

Extraction of Single and Double Differential Cross-Sections on Argon for CC1 μ 2p0 π Event Topologies in the SBND

Emilio Peláez Cisneros

July 24, 2024

Abstract

The precise measurement of cross-sections for a variety of interactions is critical to the success of upcoming flagship neutrino experiments. Of special interest are neutrino interactions that leave the nucleus in a 2-particle 2-hole state (2p2h). This note will present cross-section measurements for the production of 2p2h states on Argon. Using SBND data collected from the **period** of operation, we select events corresponding to a charged-current ν_μ interaction that left the Argon nucleus in a 2p2h state. These interactions produce a topology with one muon and two protons in the final state (CC1 μ 2p0 π). This analysis targets both single differential and double differential cross-section measurements for CC1 μ 2p0 π event topologies in a variety of kinematic variables. Comparisons are made to a set of theoretical models that explore different cross-section modeling configurations. Code for this analysis is available on [GitHub](#).

Contents

1	Introduction and motivation	2
2	Generator analysis	2
2.1	Signal definition	2
2.2	Generators	2
2.3	Variables definition	3
2.4	Pre-FSI events	16
2.5	Double differential plots	16
2.6	Pure MEC events	16
3	SBND analysis	32
3.1	Fiducial volume	32
3.2	Signal definition	32
3.3	Variable plots	33
3.4	Interaction and topology breakdown	33
3.5	Signal efficiency	33
3.6	Migration and response matrices	44
3.7	Systematics	51
3.8	Closure test	51
4	Cross-section results	56
5	Appendices	57
5.1	Cross section systematics	57
5.2	Flux systematics	286
6	References	365

1 Introduction and motivation

2 Since many current and next generation neutrino oscillation experiments will utilize dense nuclear targets,
3 such as liquid argon (LAr), it is critical to characterize the impact of nuclear effects on neutrino cross-sections.
4 One area of interest are neutrino events that eject 2 nucleons from the nucleus, leaving it with 2 holes: known
5 as 2-particle 2-hole states (2p2h). The general picture is that the neutrino has a charged-current interaction
6 with a neutron in the nucleus, producing a proton with significant momentum; this proton interacts with
7 another proton, producing the 2p2h state. While the majority of 2p2h states are caused by Meson Exchange
8 Currents (MEC) [15], some nuclear effects, such as Short-Range Nucleon-Nucleon correlations (SRC) [10],
9 can also produce these states. In an accelerator-based liquid argon time projection chamber (LArTPC)
10 experiment, such as SBND, a charged-current (CC) muon neutrino (ν_μ) interaction that results in a 2p2h
11 state would have a final state topology of 1 muon, 2 protons, and no charged or neutral pions. While
12 there are existing measurements of CC1 μ 2p0 π events on argon, the analyses were statistically limited and
13 no cross-sections were extracted [1, 19]. There was a previous report with single differential cross-section
14 measurements from the MicroBooNE detector [20], but this document presents the first double differential
15 cross-section measurements of CC1 μ 2p0 π topologies on argon, using data collected from the period of SBND
16 operations.

17 2 Generator analysis

18 2.1 Signal definition

19 We choose charged-current muon neutrino interactions that result in one muon, two protons, no charged pions
20 with $P_\pi > 70$ MeV/c, no neutral pions or heavier mesons, and any number of neutrons. These interactions
21 are denoted as CC1 μ 2p0 π . We require the momentum of the muon and protons to be in the following ranges
22 (in MeV/c):

$$100 < P_P < 1200 \quad 300 < P_\mu < 1000 \quad (1)$$

23 2.2 Generators

24 The following generators are used to create events, which are then discriminated using the signal definition
25 above: NuWro, GiBUU, NEUT, GENIE G18, GENIE AR23. Information about these generators is
26 summarized in Table 1.

Name	Generator/Configuration
G18	GENIE v3.0.6 G18_10a_02_11a
AR23	G18 with SuSAv2 MEC model
NuWro	NuWro 19.02.1
NEUT	NEUT v5.4.0
GiBUU	GiBUU 2021

Table 1: Generator and configuration data.

27 The GENIE configurations we used are:

- 28 (i) GENIE G18 [2, 3]: This modern model configuration uses the local Fermi gas (LFG) model [9],
29 the Nieves CCQE scattering prescription [23], which includes Coulomb corrections for the outgoing
30 muon [11], and random phase approximation (RPA) corrections [22]. Additionally, it uses the
31 Nieves MEC model [25], the KuzminLyubushkin-Naumov Berger-Sehgal RES [6, 28, 16], Berger-Sehgal
32 COH [7] and Bodek-Yang DIS [29] scattering models with the PYTHIA [26] hadronization part, and
33 the hA2018 FSI model [4].
- 34 (ii) GENIE AR23: Same as the G18 model configuration but using the SuSAv2 MEC model.

35 The alternative event generators are:

- 36 (i) NuWro [12]: Includes the LFG model [9], the Llewellyn Smith model for QE events [18], the Nieves
37 model for MEC events [24], the AdlerRarita-Schwinger formalism to calculate the Δ resonance explicitly [13],
38 the Berger-Sehgal (BS) COH [7] scattering model, an intranuclear cascade model for FSI [24],
39 and a coupling to PYTHIA [26] for hadronization.
- 40 (ii) NEUT [14]: Corresponds to the combination of the LFG model [8, 9], the Nieves CCQE scattering
41 prescription [23], the Nieves MEC model using a lookup table [25], the Berger Sehgal RES [6, 13, 5]
42 and BS COH [7] scattering models, FSI with medium corrections for pions [2, 3], and PYTHIA [26]
43 purposes.
- 44 (iii) GiBUU [21]: Uses similar models to GENIE, but they are implemented in a coherent way by solving
45 the Boltzmann-Uehling-Uhlenbeck transport equation [21]. The modeling includes the LFG model [9],
46 a standard CCQE expression [17], an empirical MEC model, and a dedicated spin dependent resonance
47 amplitude calculation following the MAID analysis [21]. The DIS model is from PYTHIA [26]. GiBUU's
48 FSI treatment propagates the hadrons through the residual nucleus in a nuclear potential consistent
49 with the initial state.

50 2.3 Variables definition

51 Given the momentum vectors for the leading proton \vec{p}_L , recoil proton \vec{p}_R , and muon \vec{p}_μ , we define several
52 variables. First, we define the momenta and opening angle of each variable, denoted as $|\vec{p}|$ and $\cos(\theta_{\vec{p}})$, with
53 the appropriate index for each momentum vector. These variables are plotted in Figure 1.

54 We also define variables relating the multiple momentum vectors. First, the opening angle between the
55 protons in the lab frame, given by

$$\cos(\theta_{\vec{p}_L, \vec{p}_R}) = \frac{\vec{p}_L \cdot \vec{p}_R}{|\vec{p}_L| |\vec{p}_R|}. \quad (2)$$

56 Then, the opening angle between the total proton momentum ($\vec{p}_{\text{sum}} = \vec{p}_L + \vec{p}_R$) and the muon, given by

$$\cos(\theta_{\vec{p}_\mu, \vec{p}_{\text{sum}}}) = \frac{\vec{p}_\mu \cdot \vec{p}_{\text{sum}}}{|\vec{p}_\mu| |\vec{p}_{\text{sum}}|}. \quad (3)$$

57 The momentum transverse to the direction of the neutrino beam, which we denote $\delta\vec{P}_T$ and is given by

$$\delta\vec{P}_T = \vec{p}_T^\mu + \vec{p}_T^L + \vec{p}_T^R. \quad (4)$$

58 For the transverse momentum, we will be interested in its magnitude $|\delta\vec{P}_T|$. Finally, the angular orientation
59 of the transverse momentum with respect to the transverse muon is defined as

$$\delta\alpha_T = \cos^{-1} \left(\frac{-\vec{p}_T^\mu \cdot \delta\vec{P}_T}{|\vec{p}_T^\mu| |\delta\vec{P}_T|} \right). \quad (5)$$

60 We plot the differential cross sections of these variables for the given generators in Figure 2. We can also
61 see the cross section by event type for all variables and all generators in Figures 3 to 12.

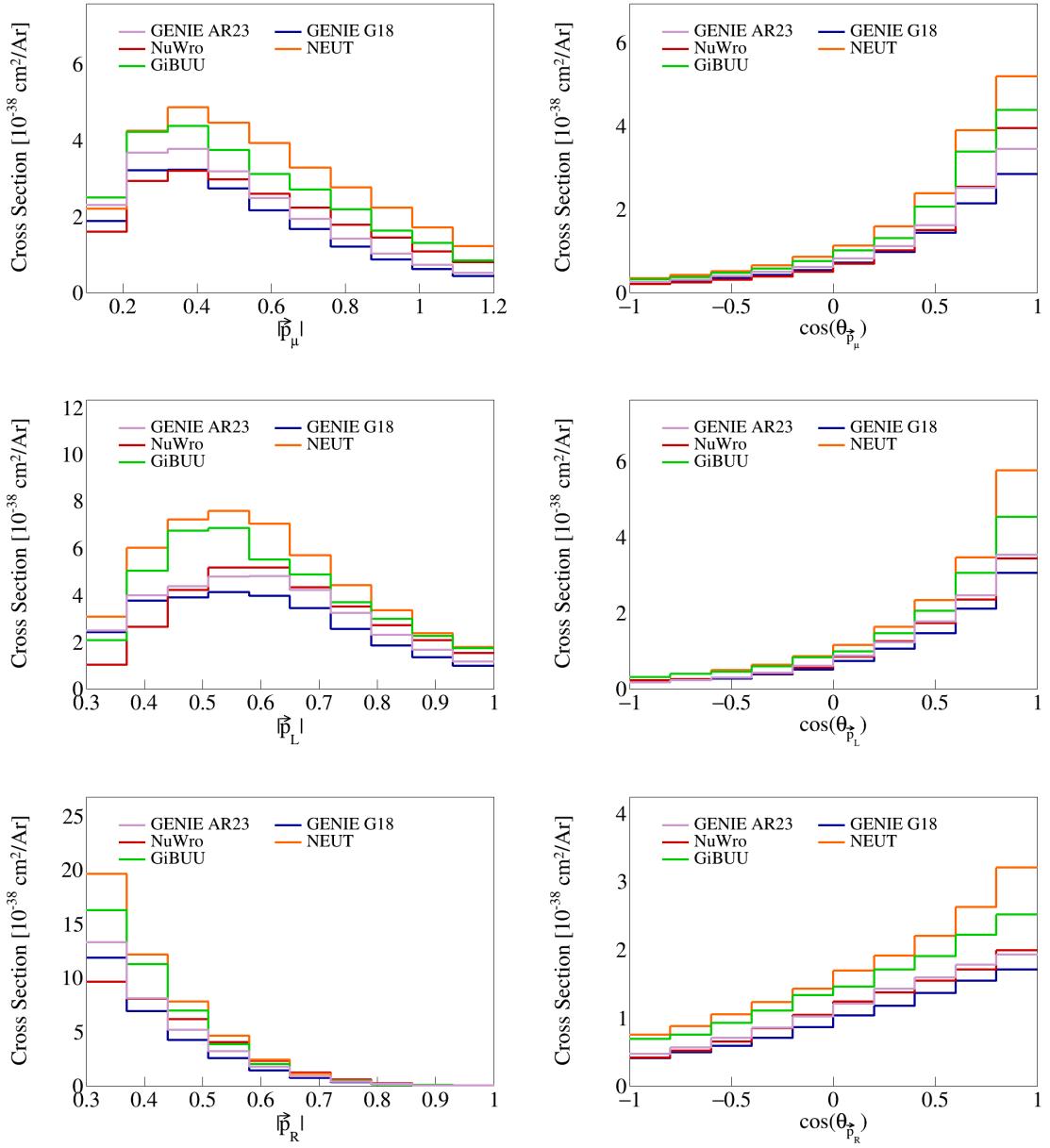


Figure 1: Cross sections for momentum and opening angles of individual particles.

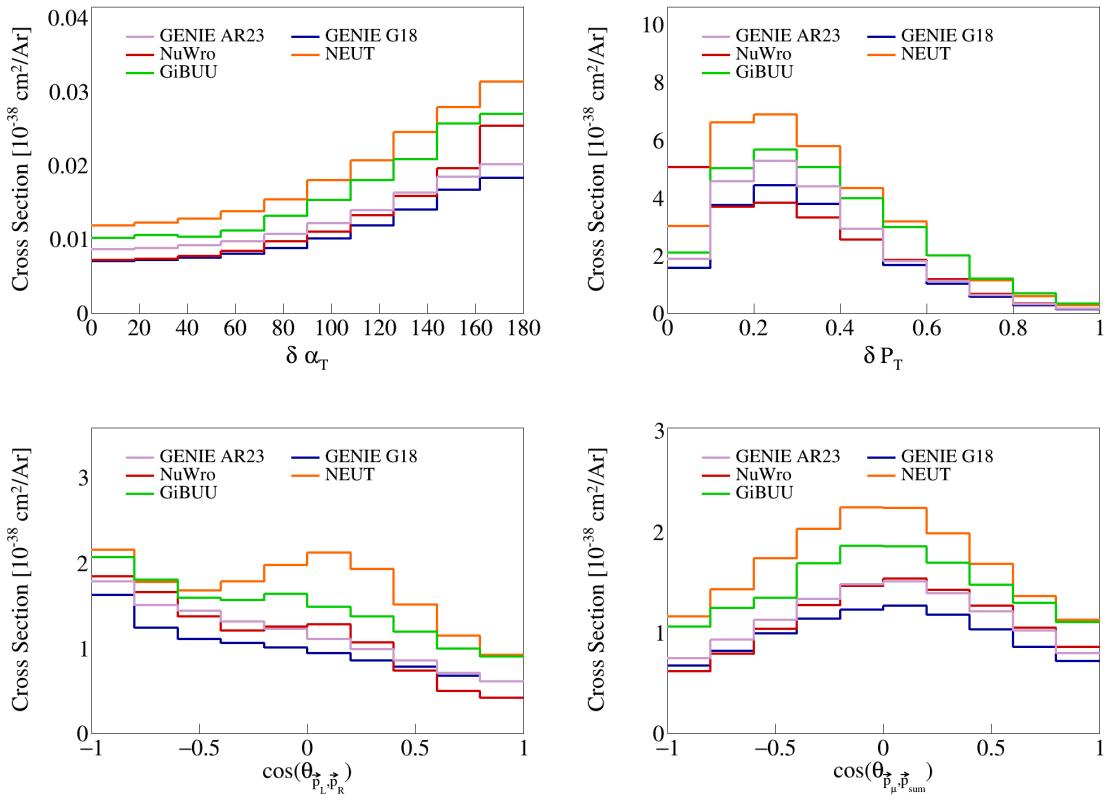


Figure 2: Cross sections for opening angles and transverse momentum.

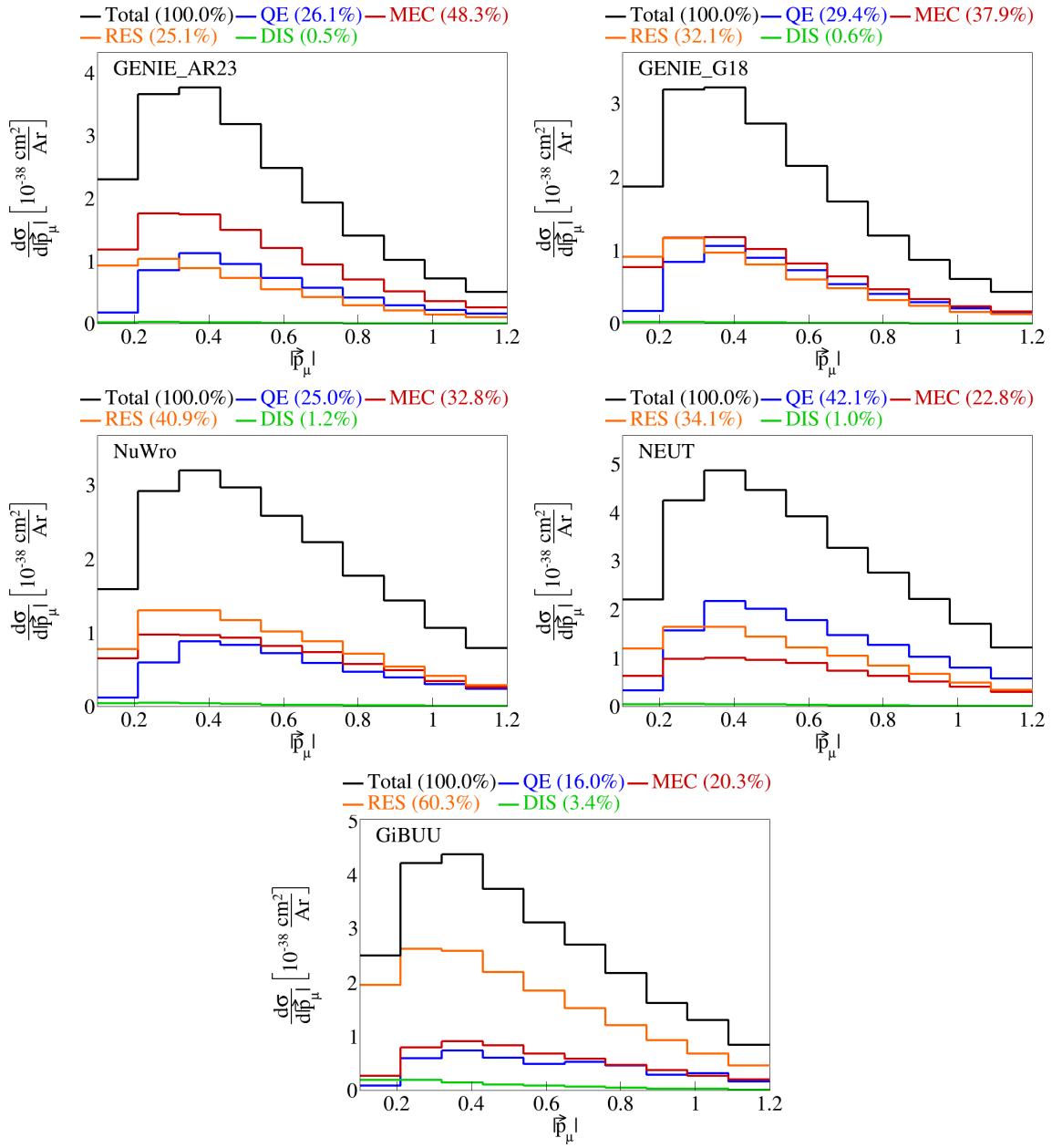


Figure 3: Event interaction breakdown for $|\vec{p}_\mu|$.

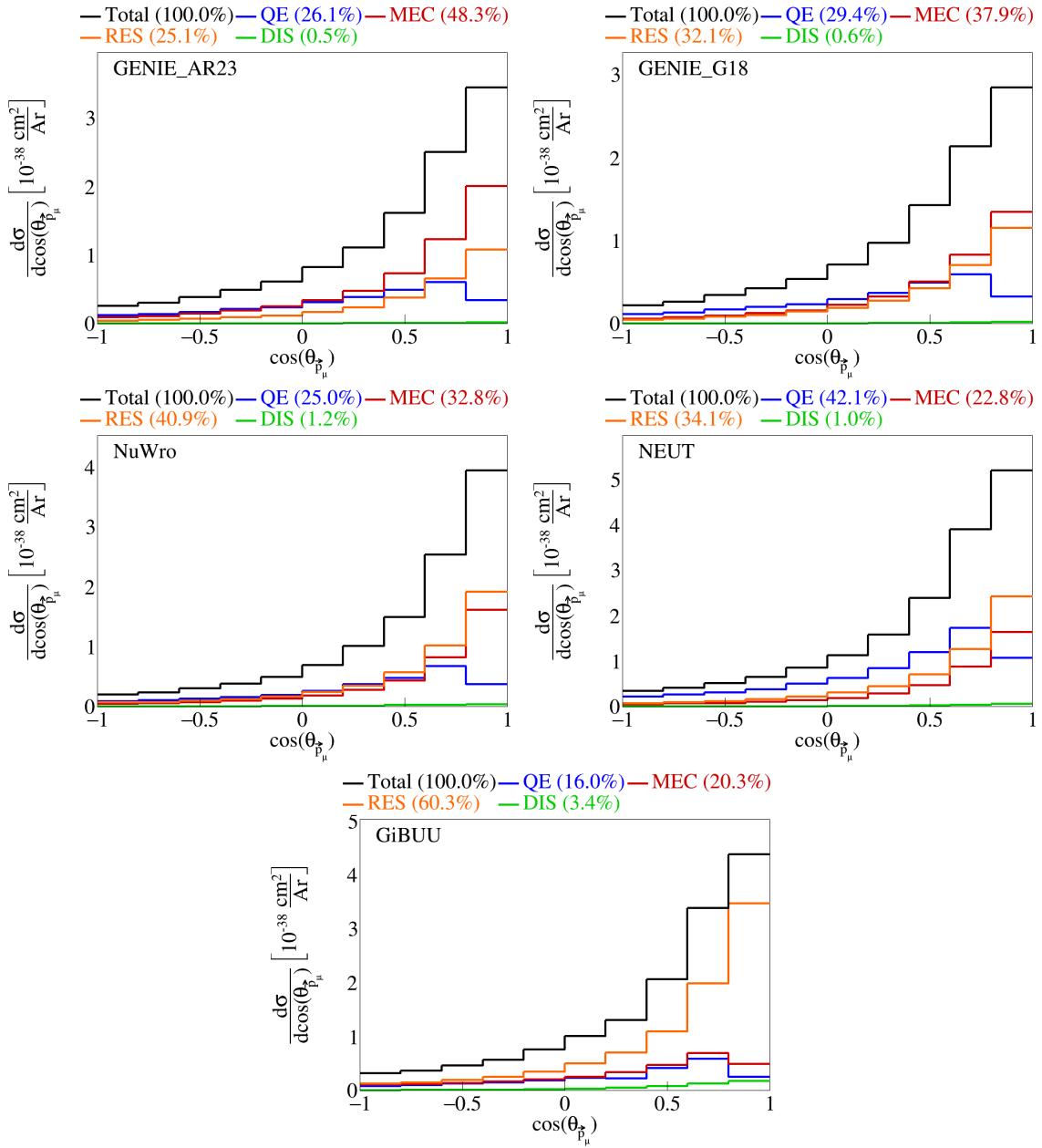


Figure 4: Event interaction breakdown for $\cos(\theta_{\vec{p}_\mu})$.

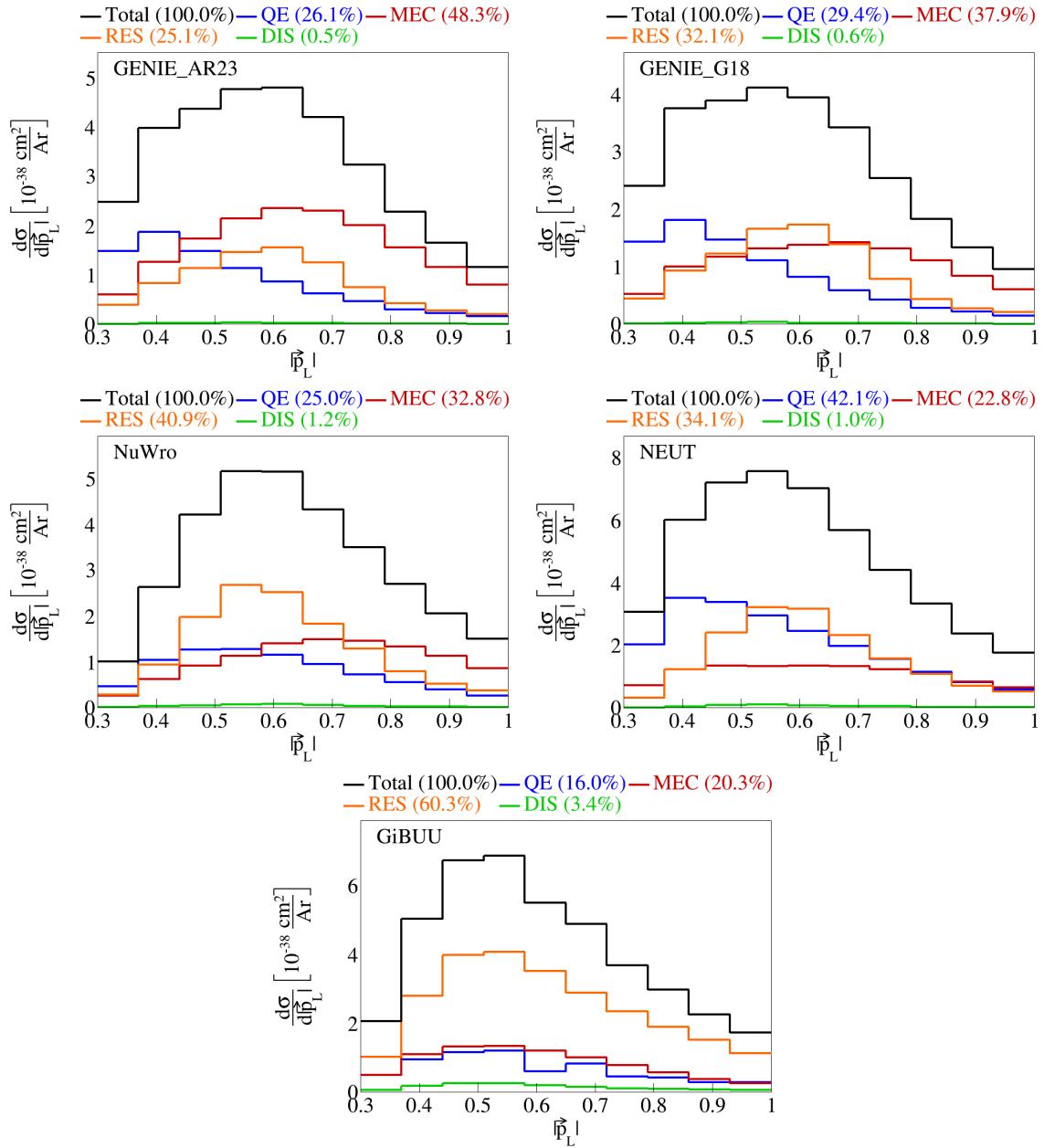


Figure 5: Event interaction breakdown for $|\vec{p}_L|$.

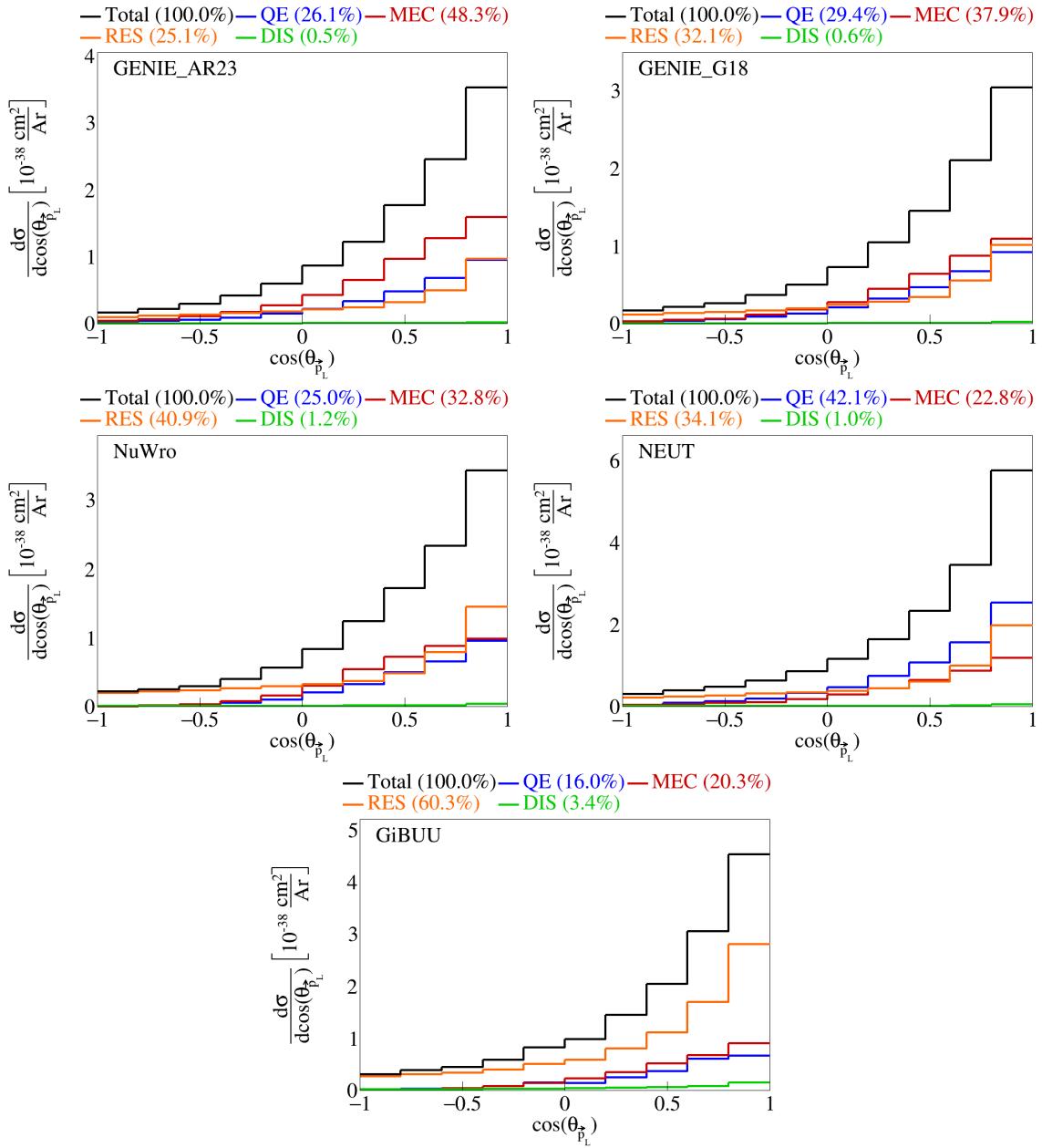


Figure 6: Event interaction breakdown for $\cos(\theta_{\vec{p}_L})$.

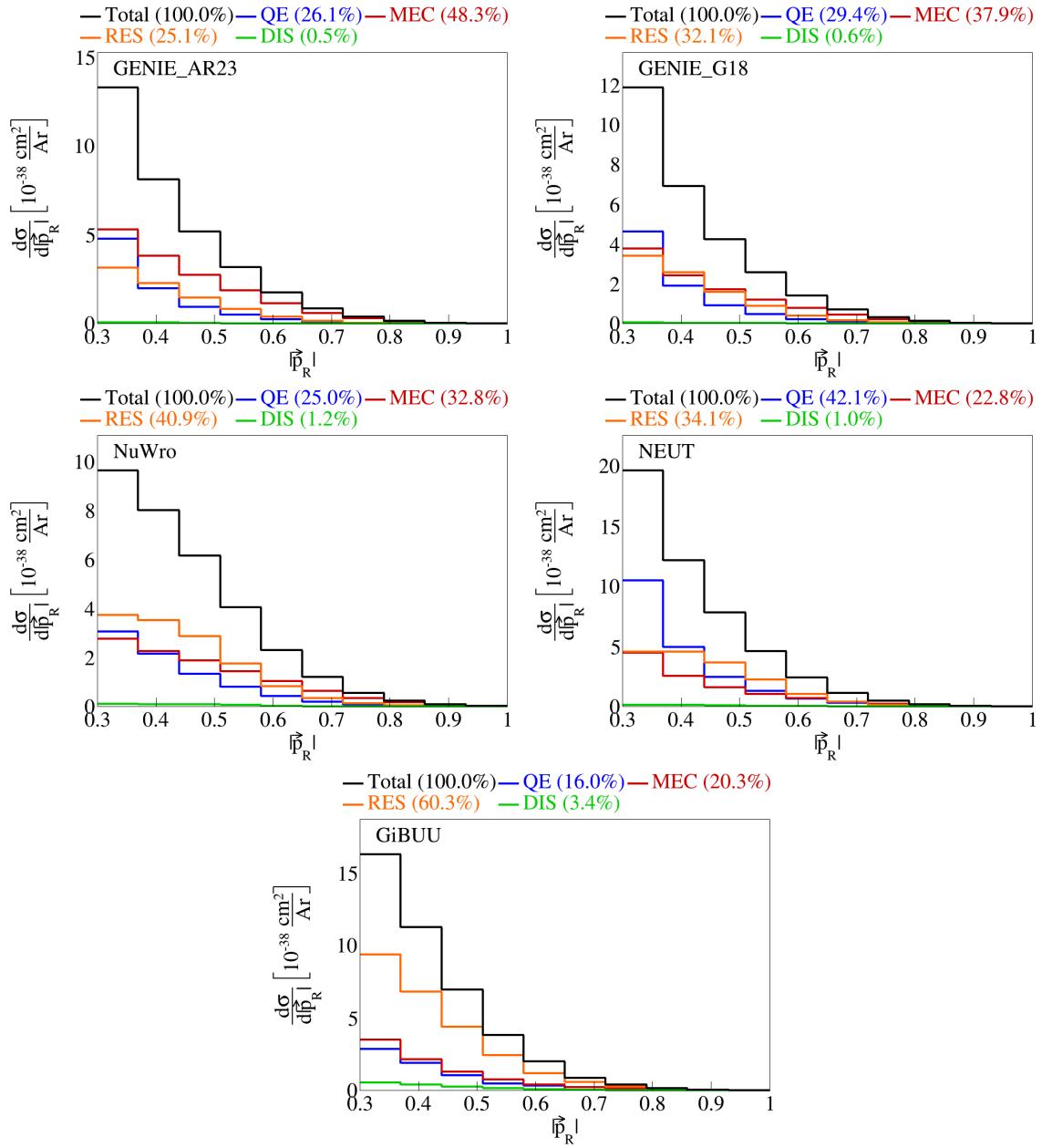


Figure 7: Event interaction breakdown for $|\vec{p}_R|$.

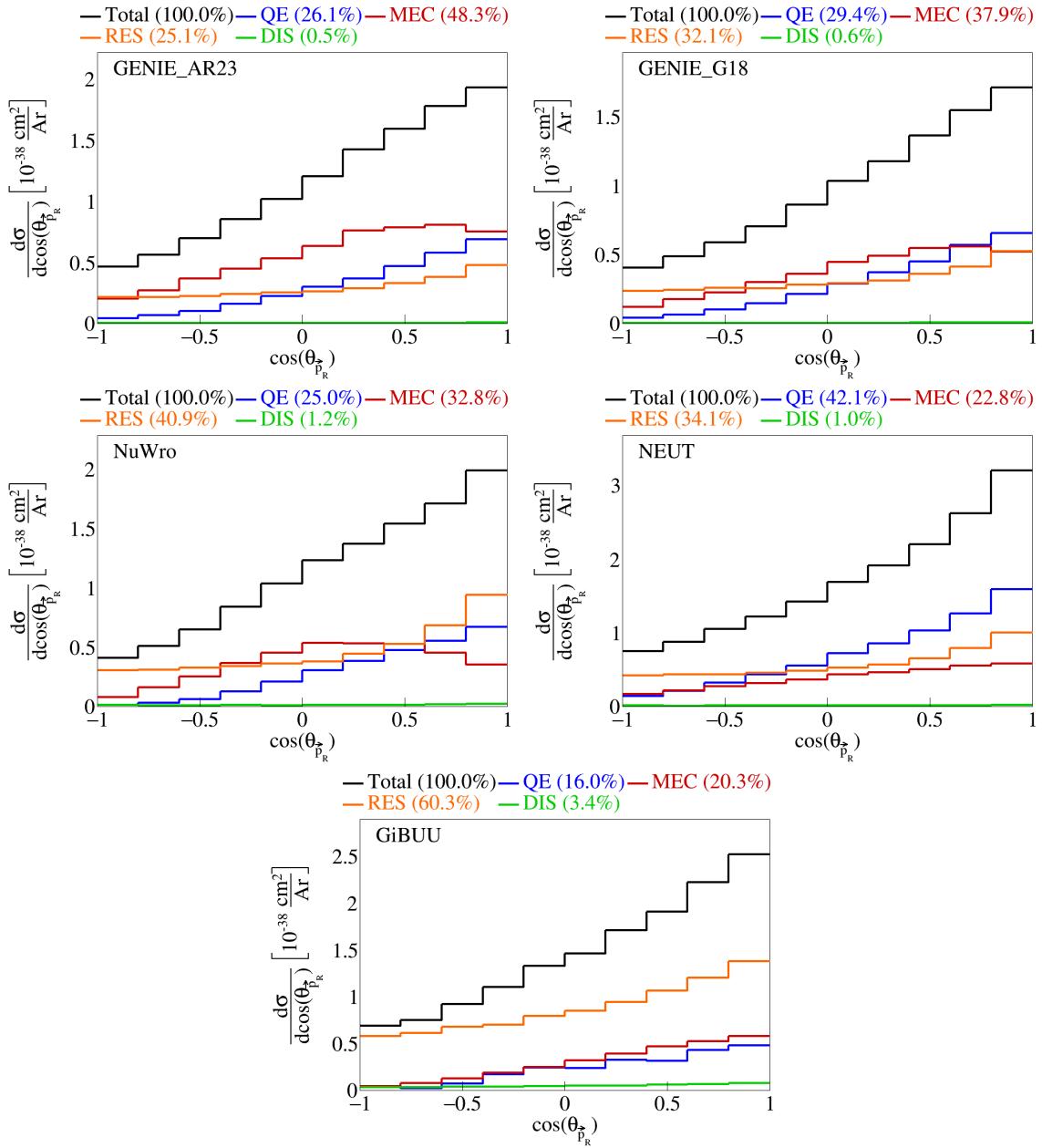


Figure 8: Event interaction breakdown for $\cos(\theta_{\vec{p}_R})$.

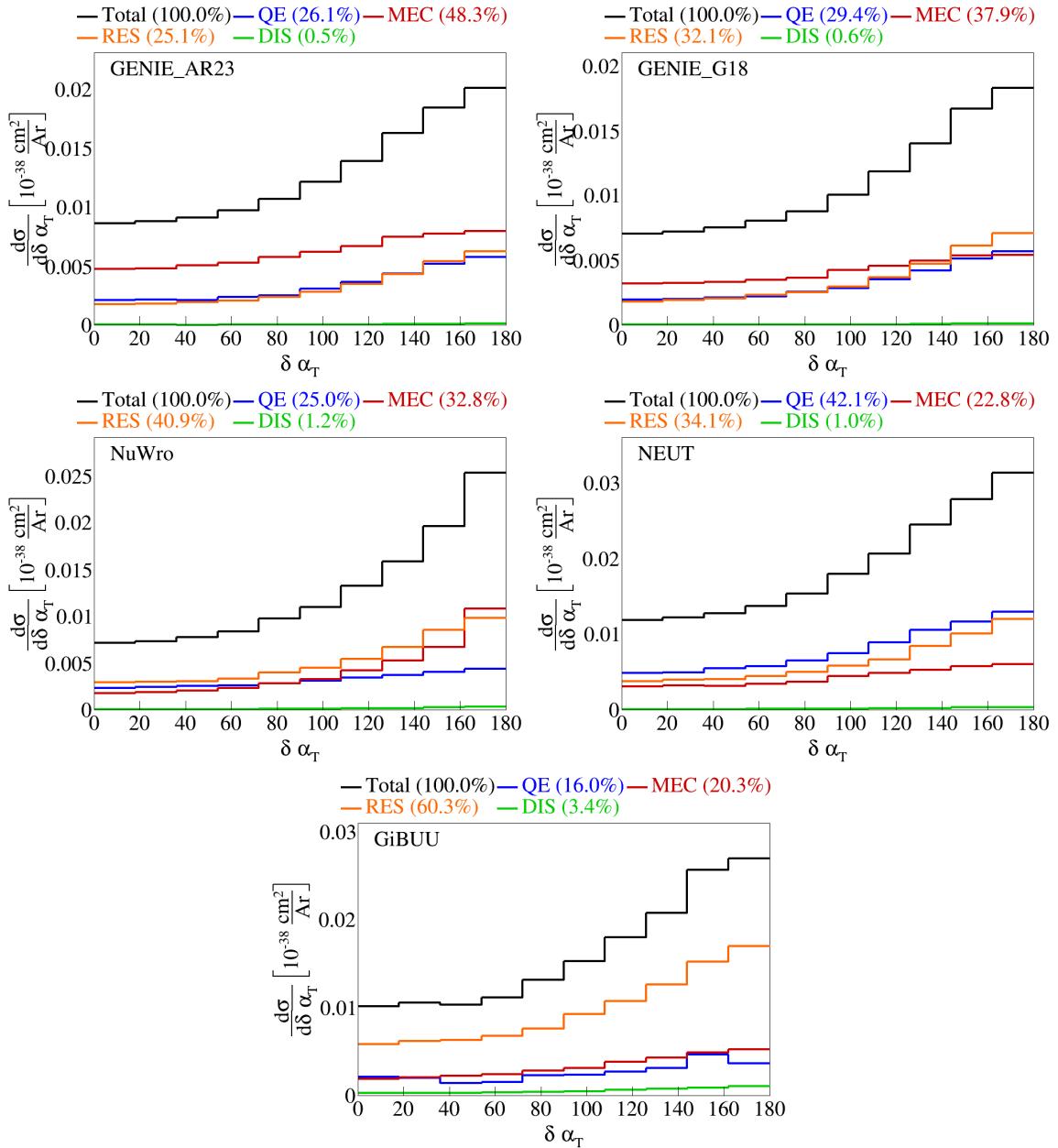


Figure 9: Event interaction breakdown for $\delta \alpha_T$.

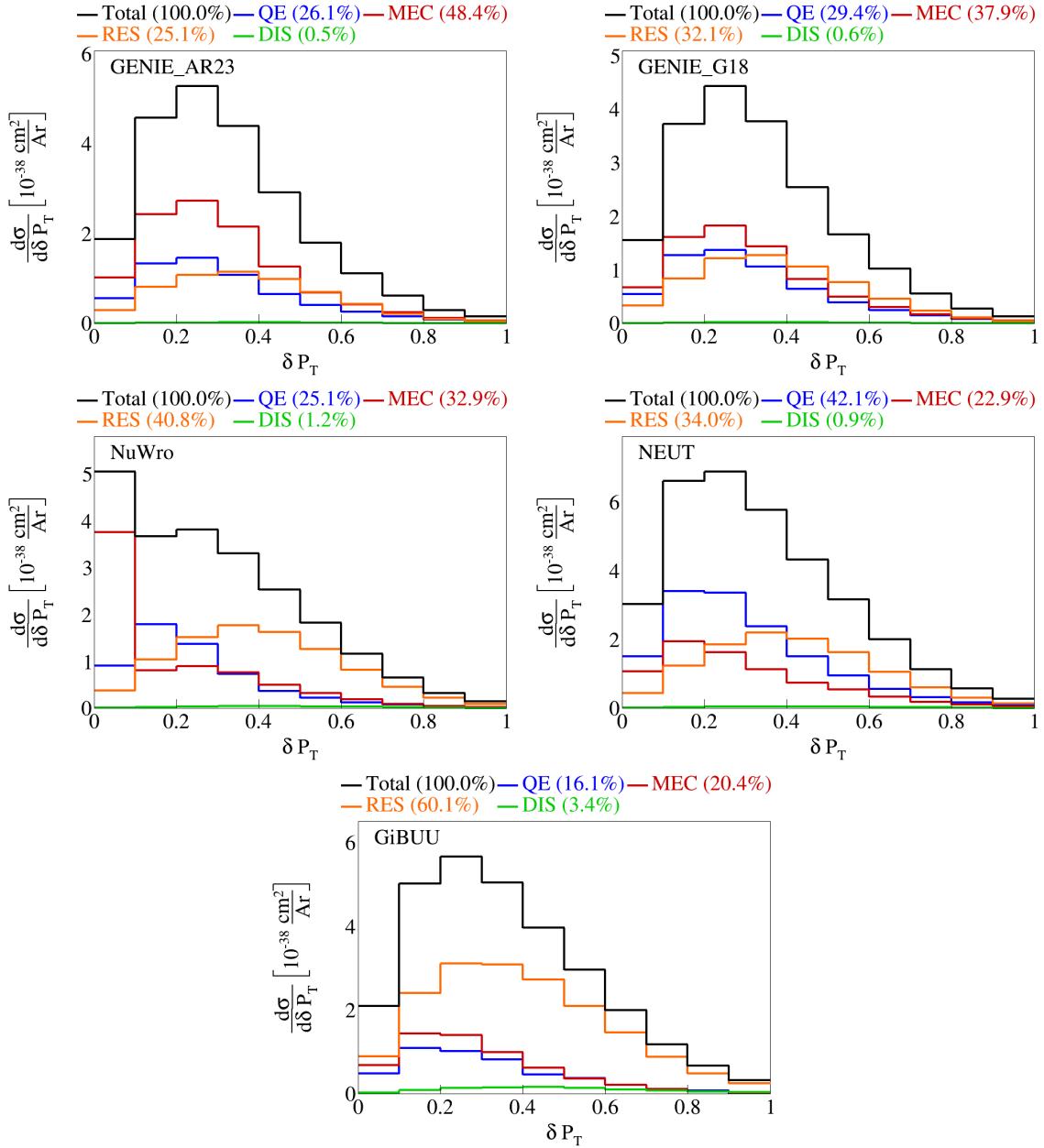


Figure 10: Event interaction breakdown for $|\delta\vec{P}_T|$.

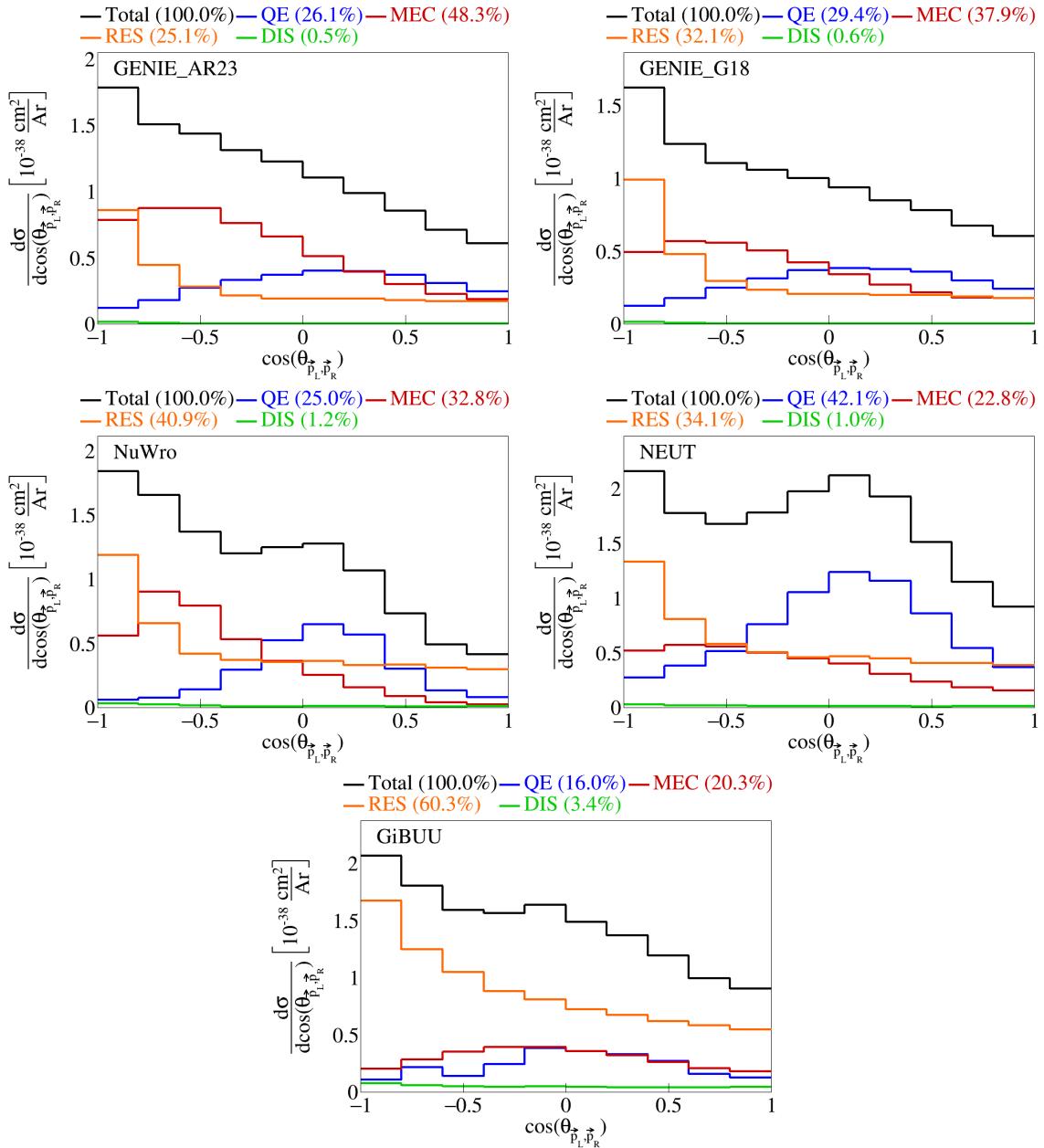


Figure 11: Event interaction breakdown for $\cos(\theta_{\vec{p}_L, \vec{p}_R})$.

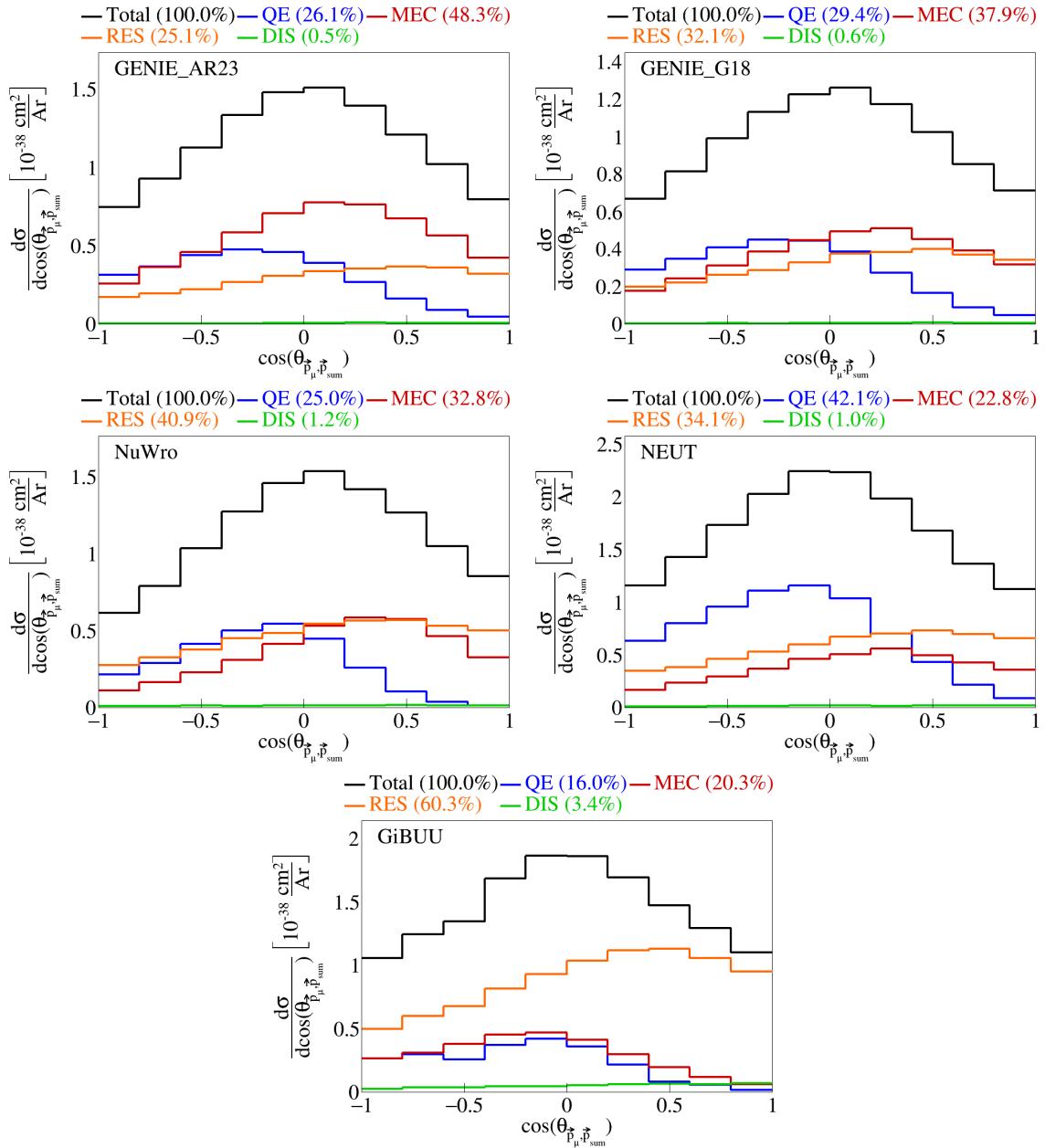


Figure 12: Event interaction breakdown for $\cos(\theta_{\vec{p}_\mu, \vec{p}_{\text{sum}}})$.

62 **2.4 Pre-FSI events**

63 To investigate why the percentage of MEC events for some generators is low, we performed event selection
64 before any final state interactions took place and plotted the interaction breakdown. For both GENIE tunes,
65 NEUT, and NuWro, we got 100% MEC events pre-FSI. For GiBUU, only 4.1% MEC versus 76.2% RES and
66 16% DIS events pre-FSI. The interaction breakdown for $|\vec{p}_\mu|$ for all the generators are shown in Figure 13.
67 Since GiBUU is the outlier, we checked the specific interaction mode for the resonance events. We got that
68 10 has 39.3%, 11 has 34.7%, 12 has 0.0136%, 13 has 26 %, and 27, 22, and 23 all have zero percent of the
69 resonance events. We also checked the event interaction breakdown for GiBUU samples generated without
70 final state interactions, in which we found that 100% of the events are MEC, shown in Figure 14.

71 Note that the difference between these two GiBUU samples is that in the former, the samples were
72 generated with final state interactions, and then we look at the state before the final state interactions
73 reportedly took place, and in the latter the event generation was done without any final state interactions.

74 **2.5 Double differential plots**

75 For our double differential variables, we look at δP_T , $\delta \alpha_T$, $\cos(\theta_{\vec{p}_L, \vec{p}_R})$, and $\cos(\theta_{\vec{p}_\mu, \vec{p}_{\text{sum}}})$ in $\cos(\theta_{\vec{p}_\mu})$. We
76 have two bins for $\cos(\theta_{\vec{p}_\mu})$, the first one going from -1 to 0.5 and the second from 0.5 to 1. Therefore, these
77 are irregular bins, with the first holding a larger range than the second. These plots are shown in Figure 15.
78 Note that, in these plots, the horizontal axis is defined by bin number of the double differential measurement,
79 not the value of the variable. This is because we are representing two variables in a single axis, but we can
80 slice the plots to get our usual horizontal axis.

81 We slice the double differential plots into two plots each, so that we have the variable of interest in the
82 horizontal axis instead of bin numbers, and each slice corresponds to one bin of $\cos(\theta_{\vec{p}_\mu})$. These plots are
83 shown in Figure 16, and the plots broke down by interaction are in Figures 17 to 20. In these plots, the
84 bins contents have been reweighted appropriately, by dividing the content of each bin by the width of the
85 bin for the variable in the axis multiplied by the width of the $\cos(\theta_{\vec{p}_\mu})$ slice. Note that the plots for the
86 $0.5 < \cos(\theta_{\vec{p}_\mu}) < 1$ slice have more events in general, although they span a smaller phase space of $\cos(\theta_{\vec{p}_\mu})$,
87 as it can be seen by the scale of the vertical axis. We performed the same double differential analysis for
88 the events before final state interactions. These are shown in Figure 21, and the corresponding interaction
89 breakdown plots are in Figures 22 to 25.

90 **2.6 Pure MEC events**

91 We also generated pure meson exchange current events using different configurations to get the MEC splines.
92 These were all generated using different tunes of GENIE: AR23, G18 with Empirical MEC model, and G18
93 with Nieves MEC model. The plots for the transverse kinematic variables are shown in Figure 26. The sliced
94 double differential plots are shown in Figure 27.

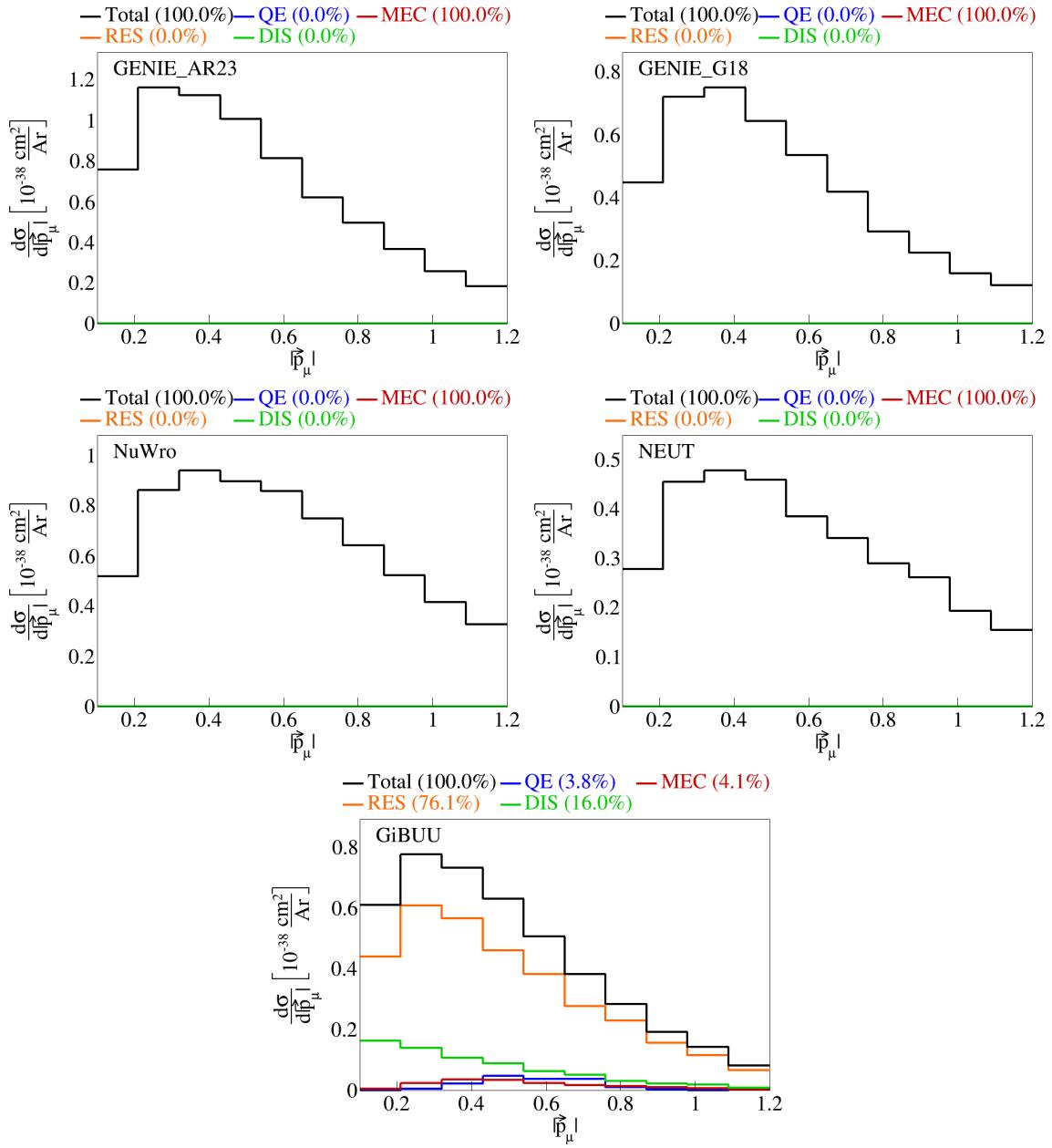


Figure 13: Event interaction breakdown of $|\vec{p}_\mu|$ before final state interactions.

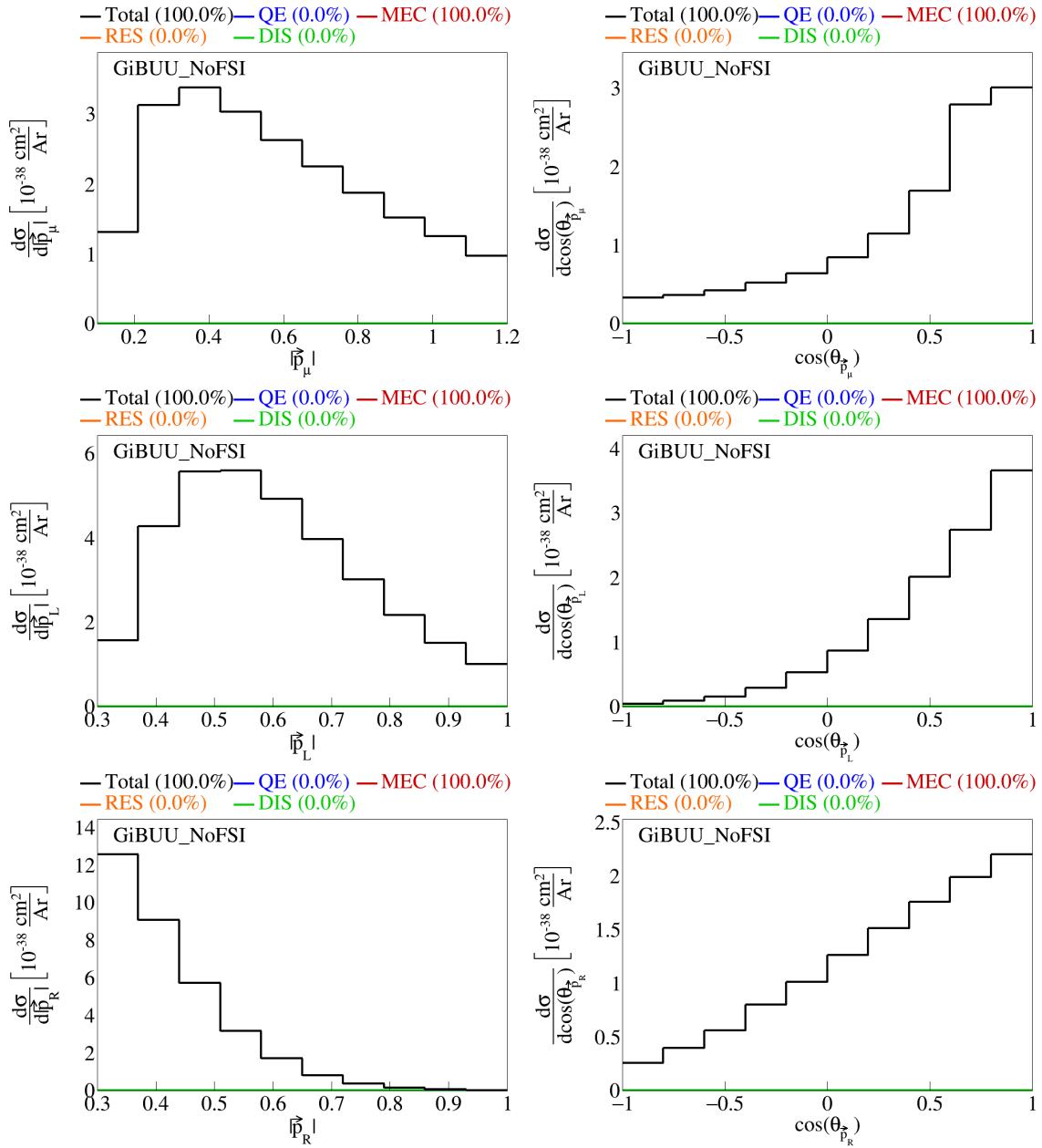


Figure 14: Event interaction breakdown for final events from GiBUU events with no FSI.

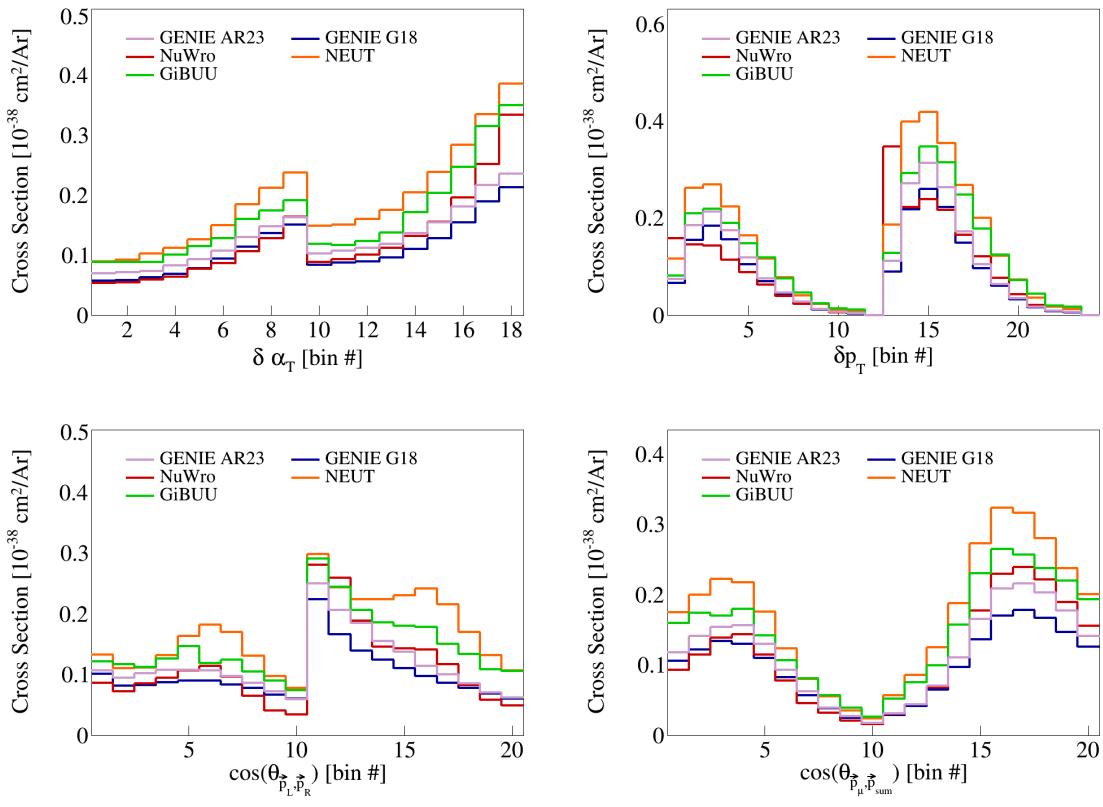


Figure 15: Double differential serial plots, all in $\cos(\theta_{\vec{p}_\mu})$.

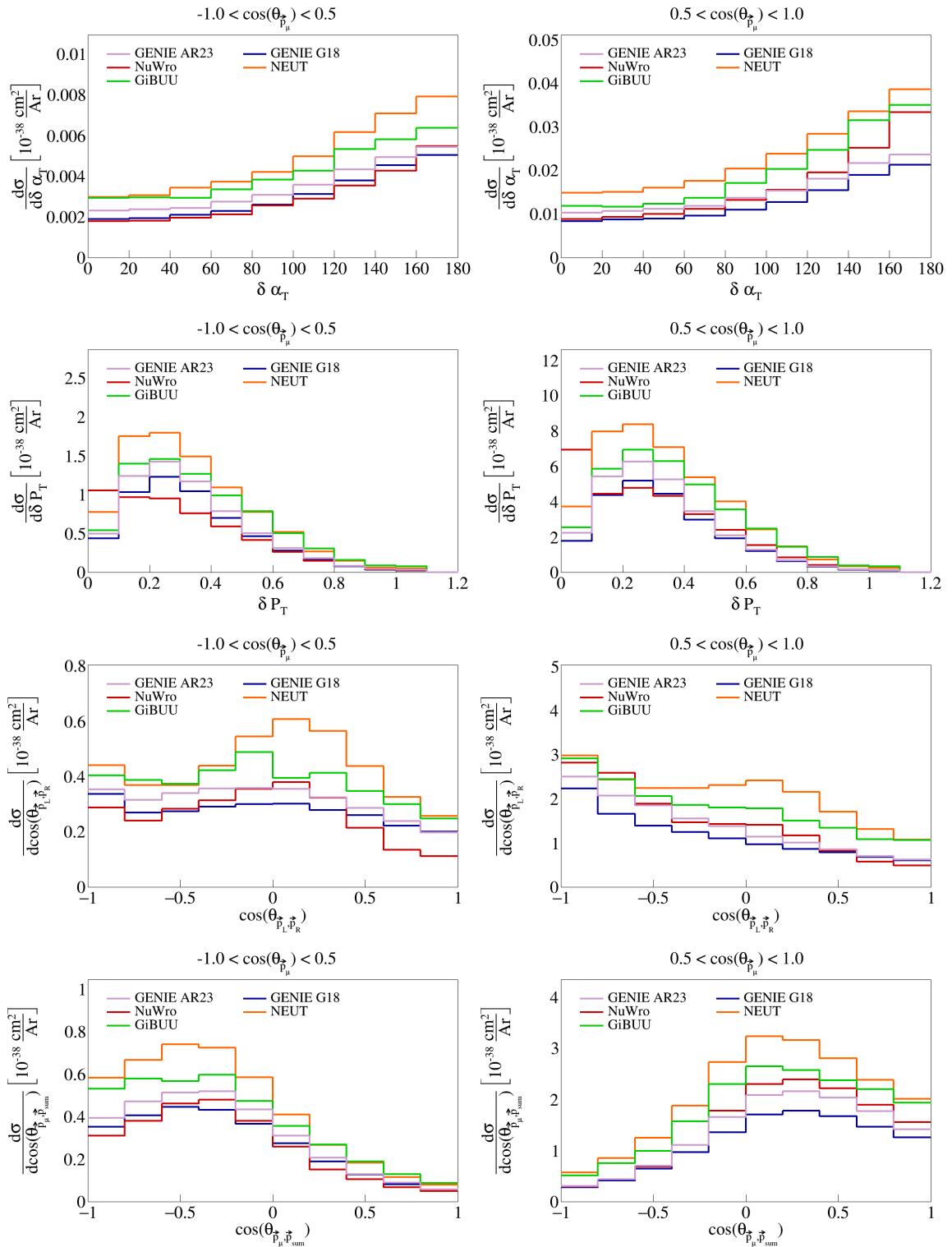


Figure 16: Sliced double differential plots.

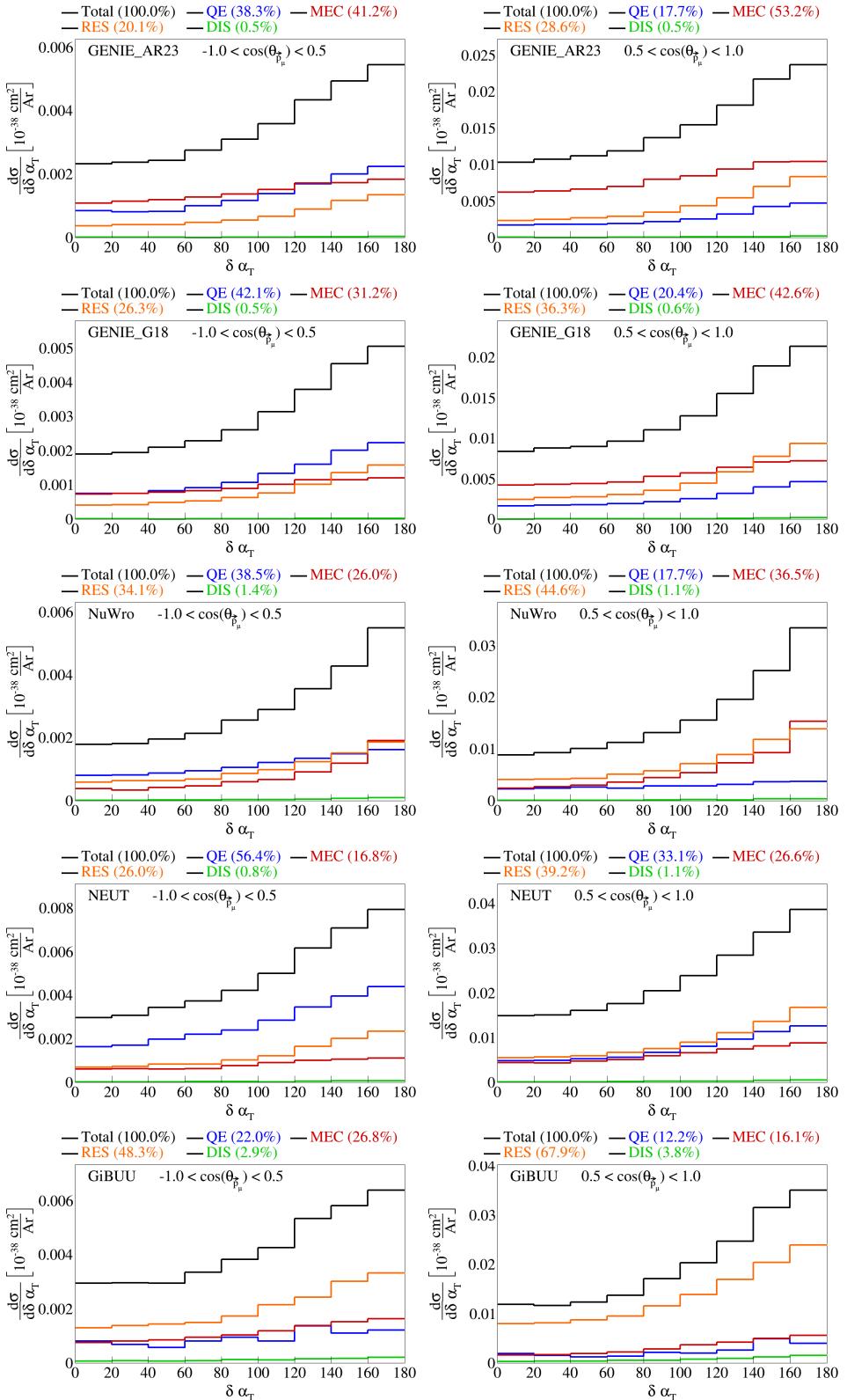


Figure 17: Interaction breakdown for sliced double differential plots for $\delta\alpha_T$ in $\cos(\theta_{\vec{p}_\mu})$.

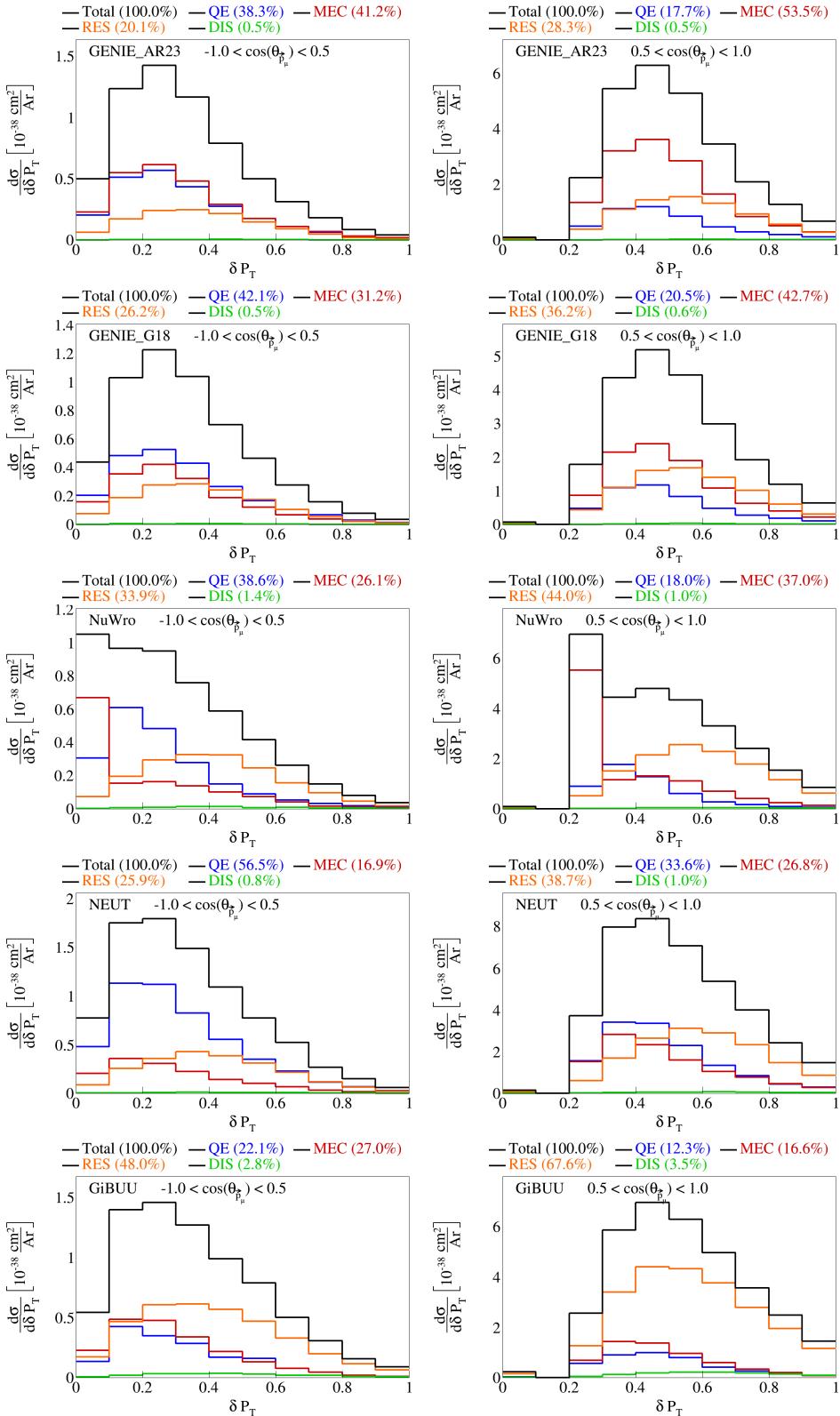


Figure 18: Interaction breakdown for sliced double differential plots for $|\delta\vec{P}_T|$ in $\cos(\theta_{\vec{p}_\mu})$.

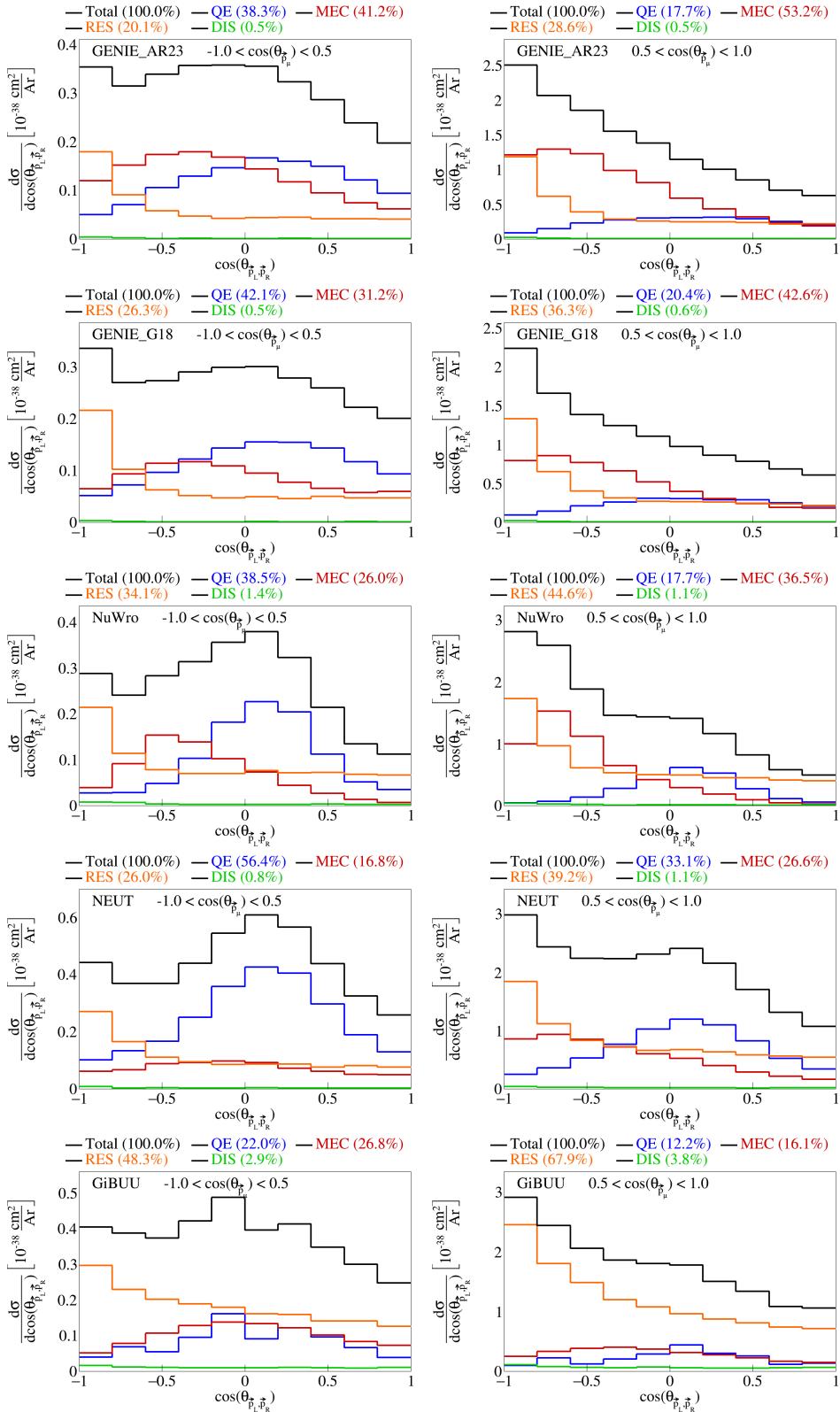


Figure 19: Interaction breakdown for sliced double differential plots for $\cos(\theta_{\vec{p}_L, \vec{p}_R})$ in $\cos(\theta_{\vec{p}_\mu})$.

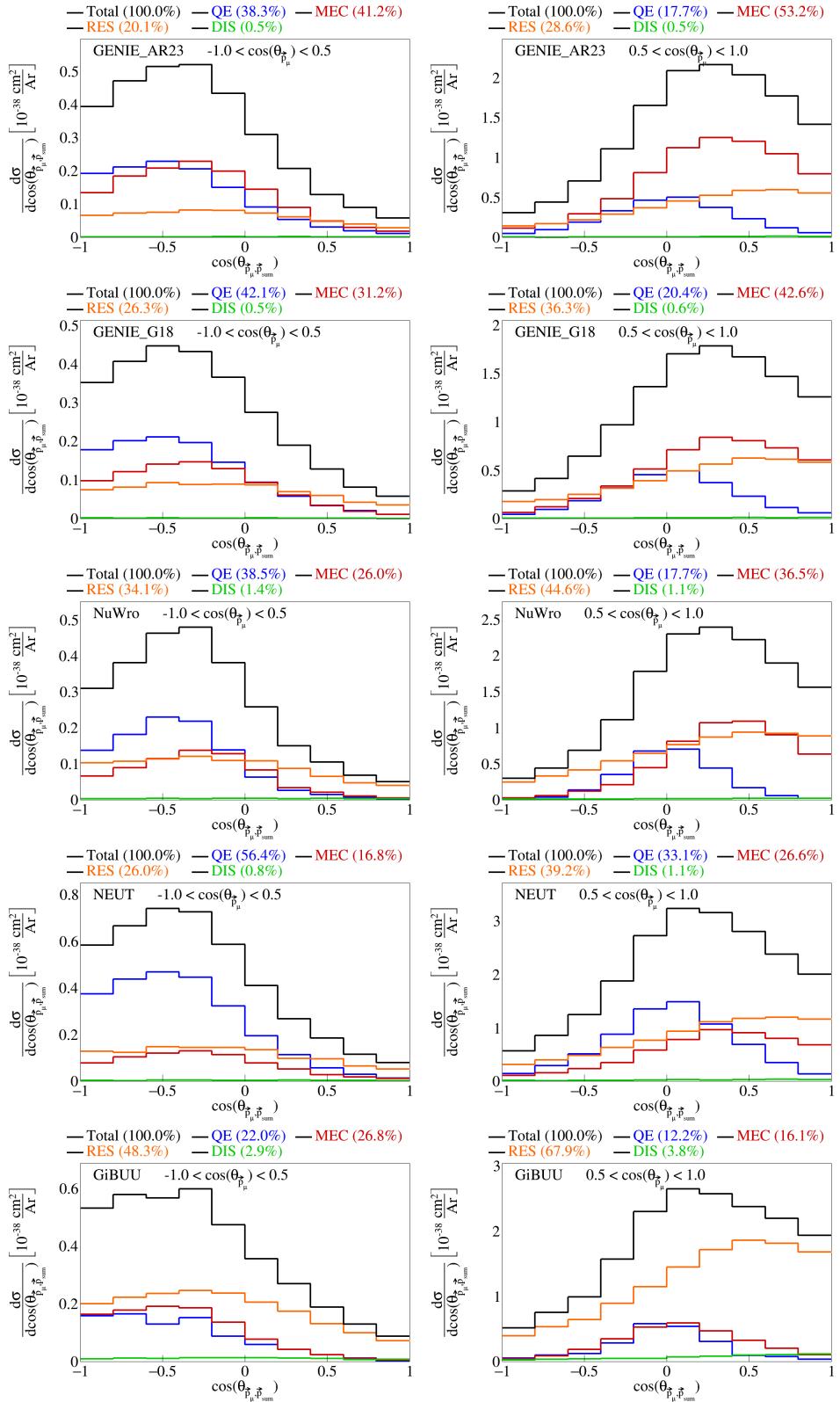


Figure 20: Interaction breakdown for sliced double differential plots for $\cos(\theta_{\vec{p}_\mu, \vec{p}_{\text{sum}}})$ in $\cos(\theta_{\vec{p}_\mu})$.

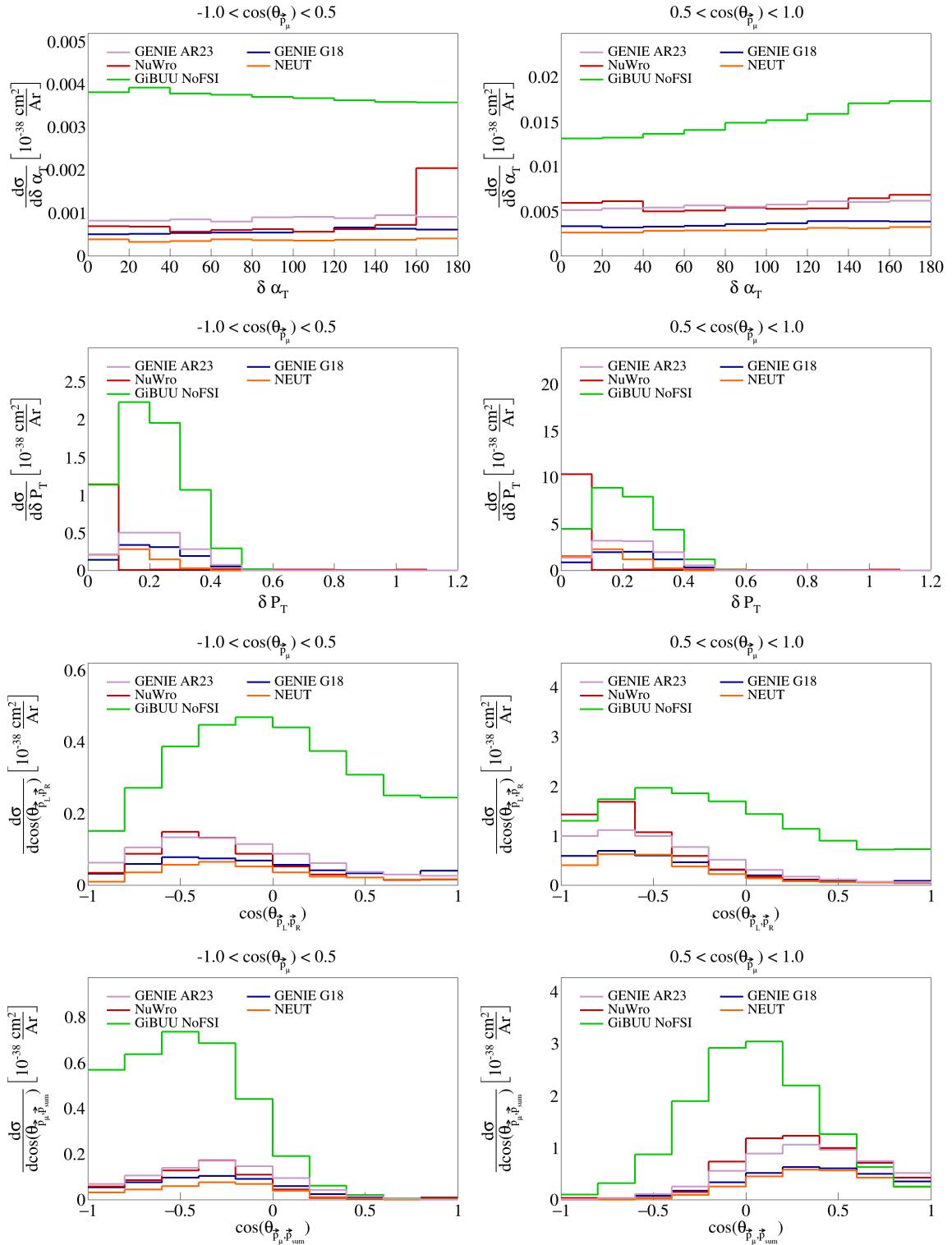


Figure 21: Sliced double differential plots for pre-FSI events.

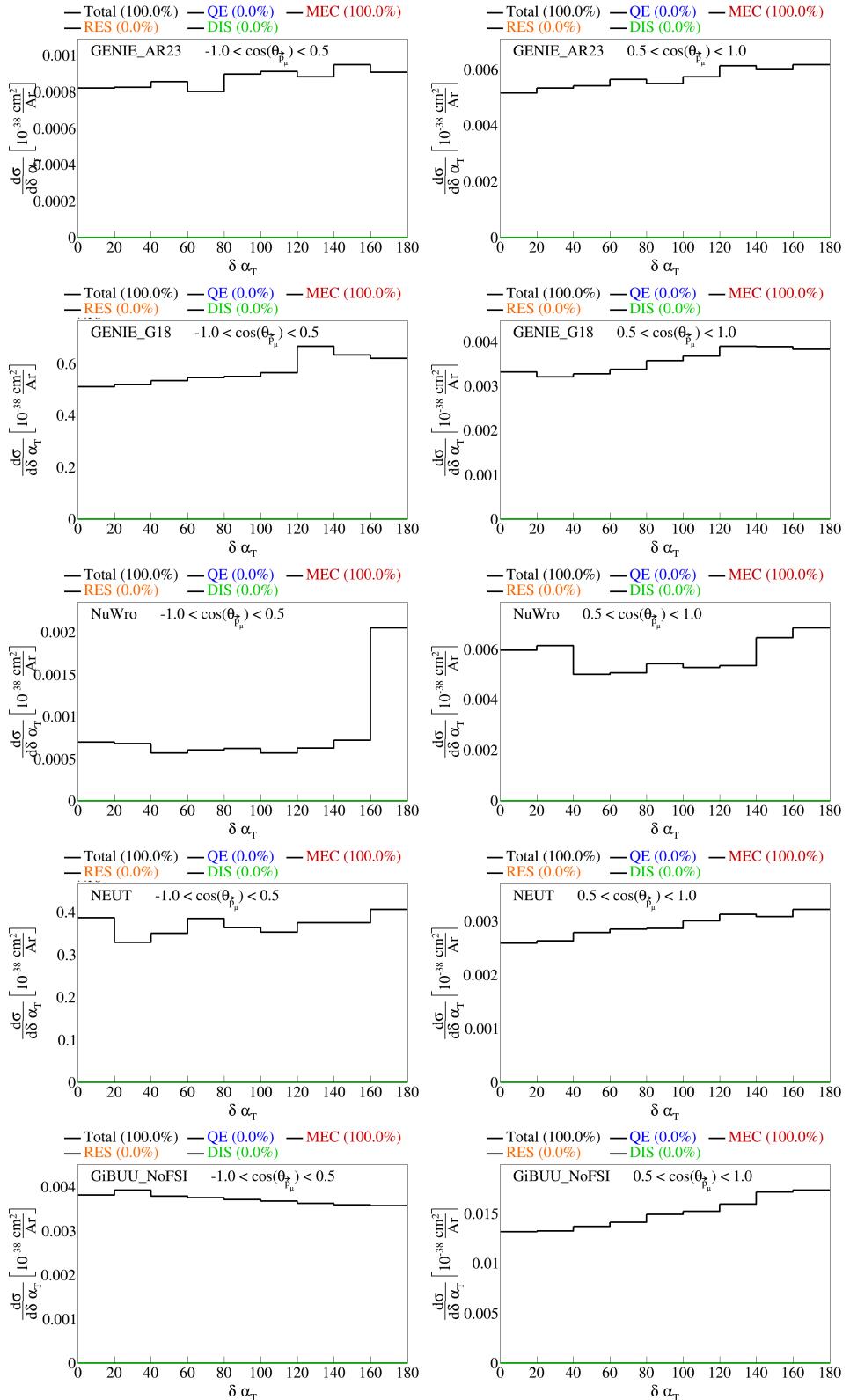


Figure 22: Interaction breakdown for sliced double differential plots for pre-FSI $\delta\alpha_T$ in $\cos(\theta_{\bar{p}_\mu})$.

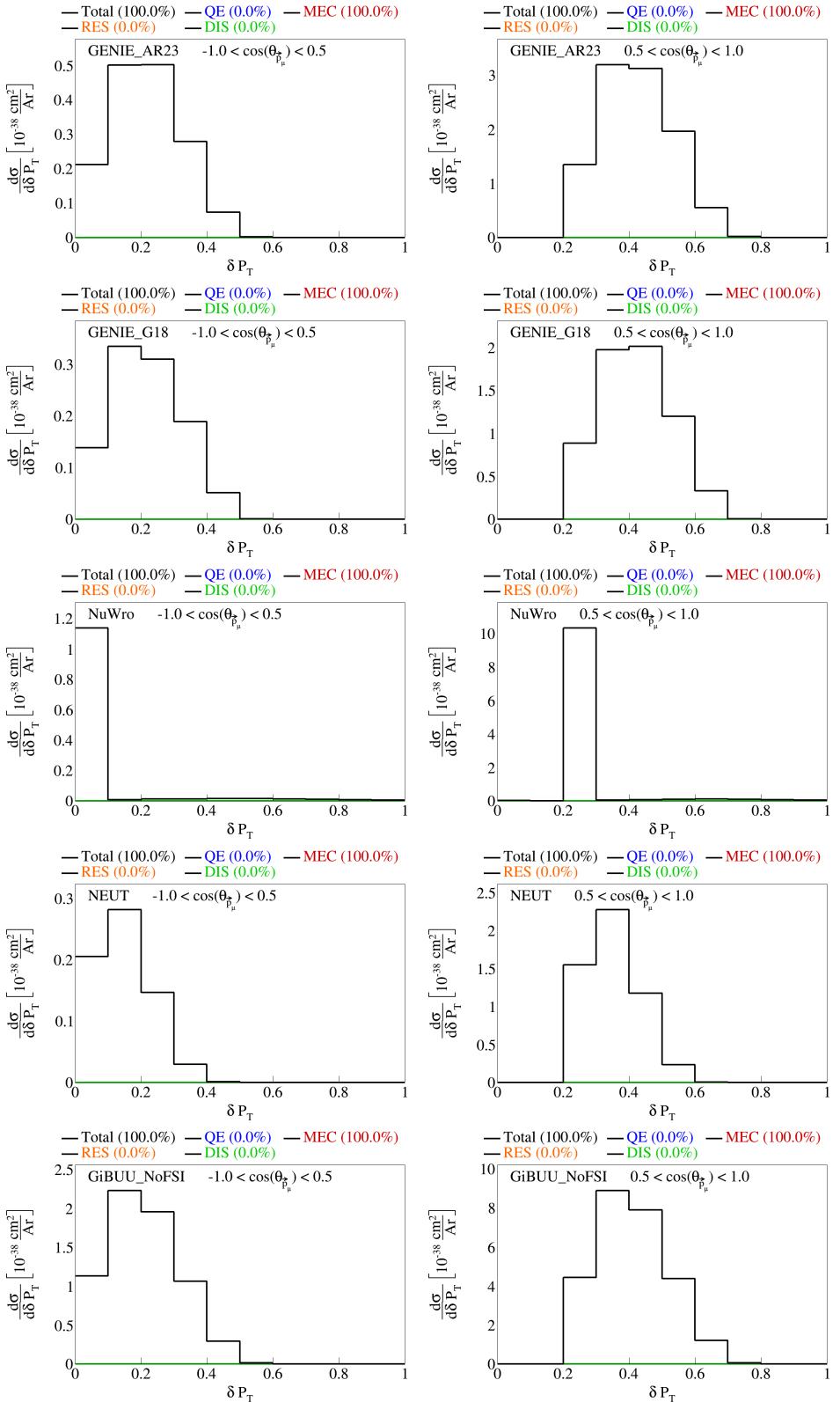


Figure 23: Interaction breakdown for sliced double differential plots for pre-FSI $|\delta \vec{P}_T|$ in $\cos(\theta_{\vec{P}_\mu})$.

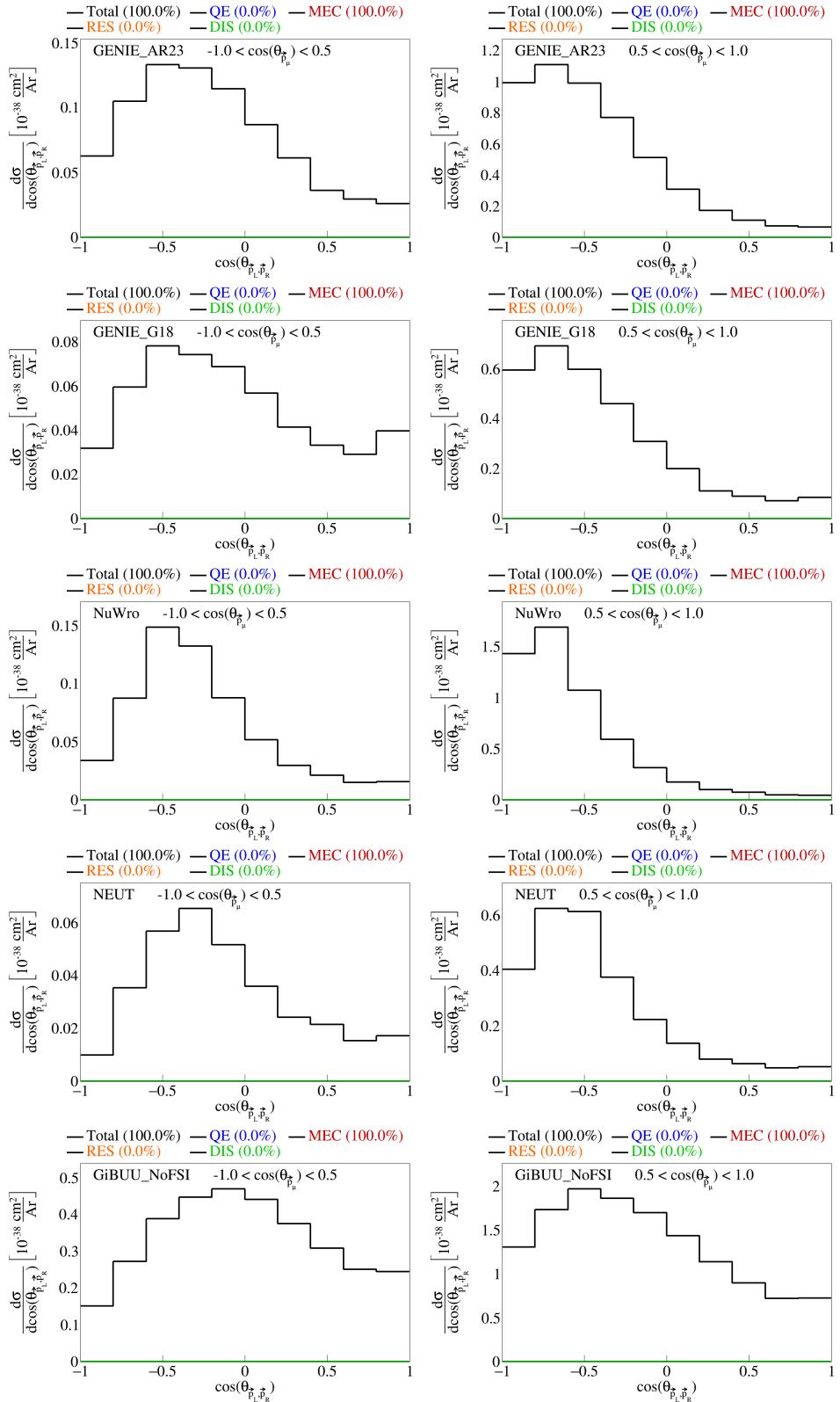


Figure 24: Interaction breakdown for sliced double differential plots for pre-FSI $\cos(\theta_{\vec{p}_L, \vec{p}_R})$ in $\cos(\theta_{\vec{p}_\mu})$.

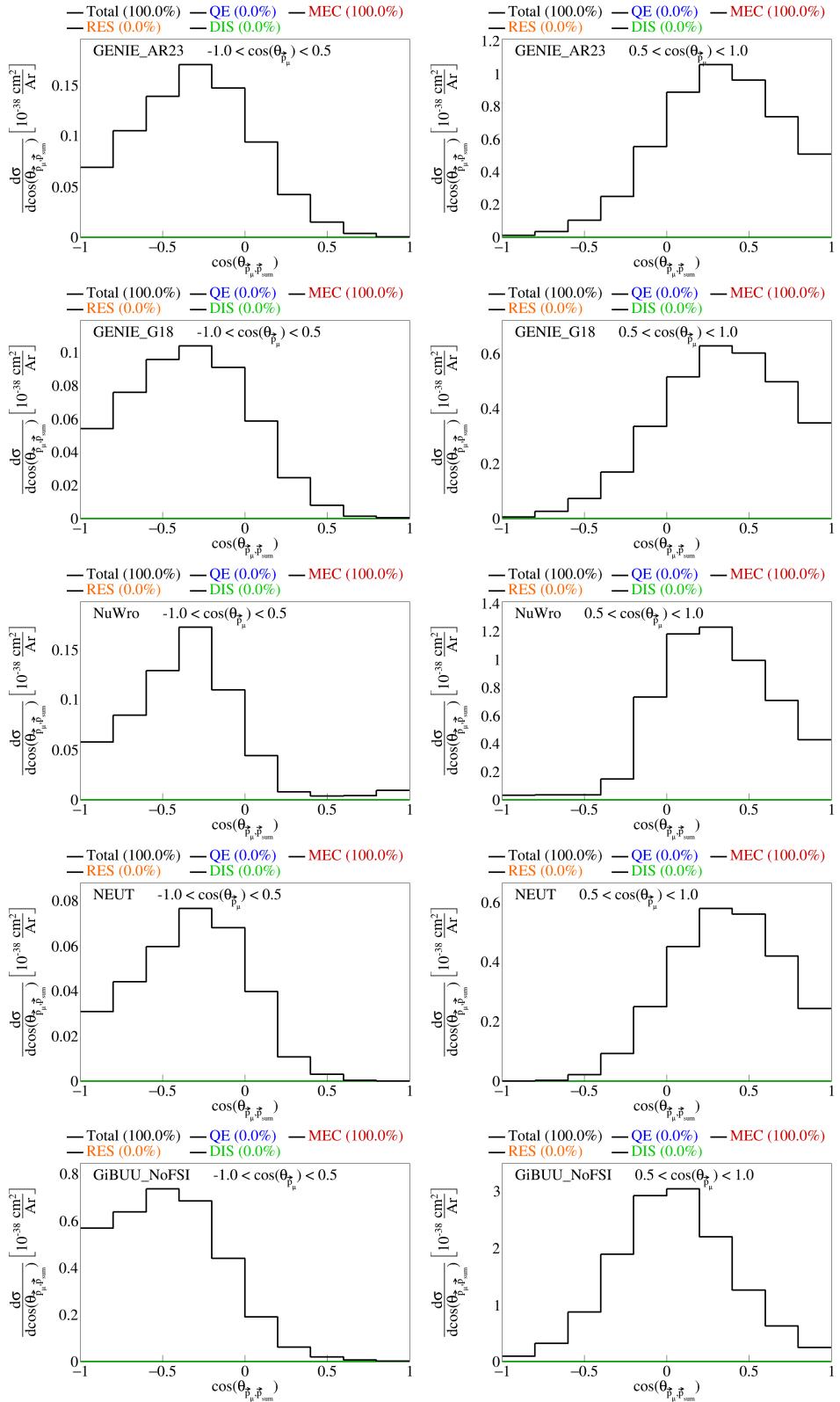


Figure 25: Interaction breakdown for sliced double differential plots for pre-FSI $\cos(\theta_{\vec{p}_\mu, \vec{p}_{\text{sum}}})$ in $\cos(\theta_{\vec{p}_\mu})$.

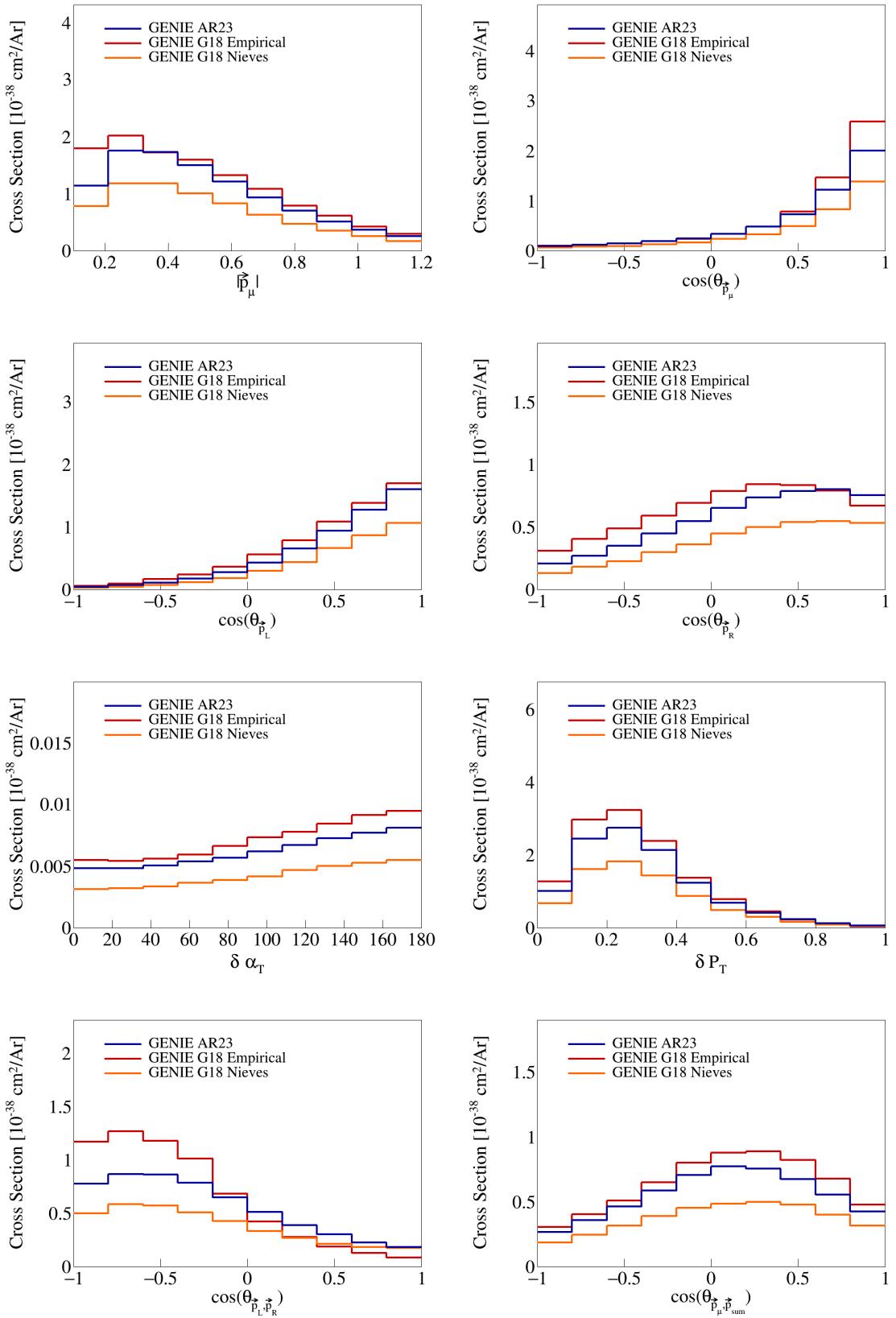


Figure 26: Variable plots for pure MEC events.

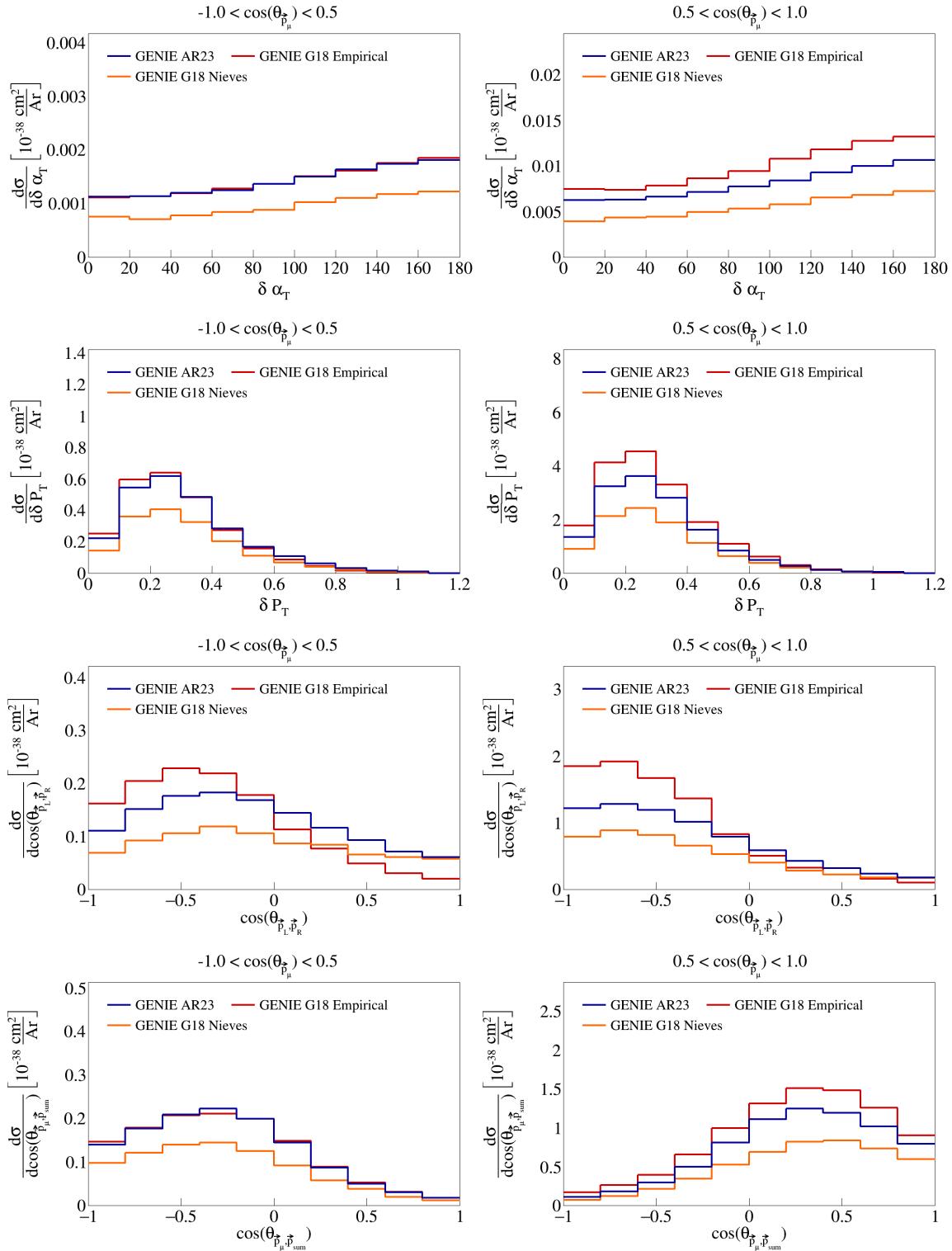


Figure 27: Sliced double differential plots for pure MEC events.

95 3 SBND analysis

96 The CAF files used for this analysis are available in the Fermilab gpvms at the path

97 `/pnfs/sbnd/persistent/users/twester/sbnd/v09_78_04/cv/*.flat.caf.root`

98 where the asterisk means that all the files in the directory with the extension `.flat.caf.root` will be used.

99 3.1 Fiducial volume

100 To perform the analysis of SBND data, we have to define the fiducial volume of the detector, which represents
101 a central part of the detector in which we will accept signals. The fiducial volume is given by the following
102 ranges:

$$5 < |x| < 180 \quad |y| < 180 \quad 10 < z < 450 \quad (6)$$

103 where x , y , and z are the coordinates in the detector frame, all in centimeters.

104 3.2 Signal definition

105 To perform analysis on experiment data, we will be using the CAFAna framework. This allows us to perform
106 cuts based on the reconstructed and Monte Carlo data (if available, i.e., only in the case of dealing with
107 simulated events), to discriminate events. To discriminate events based on their Monte Carlo data, we
108 perform a simple `TruthCut` that checks the following:

- 109 (i) That the neutrino interaction takes place in the fiducial volume.
- 110 (ii) That the neutrino is a muon neutrino.
- 111 (iii) That the interaction is a charged current interaction.
- 112 (iv) That there is only one muon in our allowed momentum range.
- 113 (v) That there are only two protons in our allowed momentum range.
- 114 (vi) That there are no charged/neutral pions in our defined momenta ranges.

115 Using the reconstructed event data, the cut we have to use is not as simple as in the Monte Carlo data
116 case. We now have to use a `Cut` that looks at different variables of the reconstructed event to determine if
117 it is a signal event. We perform the following cuts:

- 118 (i) Cosmic: that the event is not a cosmic event by Pandora's criteria, i.e., requiring `nu_score > 0.4` to
119 check how neutrino-like the event is, and `fmatch.score < 7` with $0 < fmatch.time < 1.8$ to check the
120 event comes from the beam.
- 121 (ii) Vertex in FV: that the reconstructed vertex for the neutrino interaction takes place in the fiducial
122 volume defined above.
- 123 (iii) One muon: that there is one muon track with $L_{\text{track}} > 50$ cm, starting point in the fiducial volume,
124 $\chi^2_\mu < 30$, $\chi^2_p > 60$, with momentum in our allowed range; if there are multiple candidate tracks, the
125 one with the longest track length is chosen.
- 126 (iv) Two protons: that there are two proton tracks with $\chi^2_p < 100$, full track in the fiducial volume, and
127 that these have momentum in our allowed range.
- 128 (v) No charged pions: that there are no other reconstructed tracks with momentum in the allowed range
129 for charged pions inside the fiducial volume.
- 130 (vi) No neutral pions: that there are no reconstructed particles with a positive `trackScore` less than 0.5
131 indicating a shower, so we don't allow any neutral pions.

Cut	Number of events	Global efficiency	Signal efficiency	Purity
All	1.31823e7	-	-	-
True signal events	273751	-	-	-
All reco events	6.61683e6	100%	-	-
Cosmic cut	5.46987e6	82.6659%	89.0567%	4.45703%
Vertex in FV cut	3.10952e6	46.9941%	87.5899%	7.7111%
One muon cut	2.14513e06	32.4193%	69.629%	8.88571%
Two protons cut	137309	2.07514%	16.3503%	32.5975%
No charged pions cut	65938	0.99652%	12.1369%	50.3881%
No neutral pions cut	54088.9	0.817444%	10.929%	55.313%

Table 2: Global efficiency, selection efficiency, and purity for cuts made in signal definition.

132 Using these two discriminators on simulated events, the reconstructed events that satisfy the signal definition,
 133 and distinguish between true signal events and background events.

134 We use a one-bin histogram with lower bound 0 and upper bound of 3 in the true energy variable to get
 135 total counts of generated events, true signal events, all reconstructed events, and efficiency and purity data
 136 after each of the cuts described above is applied to the reconstructed events. These results are shown in
 137 Table 2. Counts are obtained using ROOT’s command `Histo->Integral()`. Global efficiency is defined as
 138 the ratio between events that pass the cut and reconstructed events, signal efficiency as the ratio between
 139 true events that pass the cut and the all true signal events, and purity as the ratio between true signal events
 140 that pass the cut and all events that pass the cut. The numbers reported in this table are POT normalized
 141 to 6.6×10^{20} .

142 3.3 Variable plots

143 Using all the variable definitions as we did when studying the event generators, and the signal definition
 144 based on the cuts described in the previous section, we can generate plots for SBND data. The reconstructed
 145 single differential variables corresponding to vector opening angles and magnitudes are shown in Figure 28.
 146 In these figures, three lines are shown, corresponding to: all reconstructed (all the reconstructed events that
 147 pass our signal definition), signal (reconstructed events that pass signal definition and are true signal events
 148 as determined by the `TruthCut` from our previous section), and background (reconstructed events that pass
 149 signal definition but are not true signal events) events. Similarly, the variables relating multiple vectors are
 150 shown in Figure 29, and double differential sliced variables are shown in Figure 30.

151 3.4 Interaction and topology breakdown

152 We perform an interaction and topology breakdown for the SBND data. For these breakdowns, we look at
 153 the reconstructed events that pass our signal definitions cuts and see what percentage of these are generated
 154 from different interaction modes and topologies. This helps us get a better idea of what our background
 155 signal is composed of. For the interaction breakdown, we look at quasielastic (QE), MEC (meson-exchange
 156 current), RES (resonance), and DIS (deep inelastic scattering) events. For the topology breakdown, we look
 157 at the number of protons, pions, and muons in the final state. The topologies we label are CC2p0pi (our
 158 signal definition), CC1p0pi, CC($N > 2$)p0pi, CC($N \geq 0$)p1pi, and CC0p0pi. Any other topology is labeled
 159 as “Other”. These breakdowns are shown in Figures 31 to 34.

160 3.5 Signal efficiency

161 Using the truth information about reconstructed events, we can also compute signal efficiency on a bin-by-
 162 bin basis. To be precise, signal definition on a bin i is defined as the ratio between the number of events
 163 generated in bin i and reconstructed in any bin over the number of events generated in bin i . These plots
 164 are shown in Figure 35 and Figure 36 for single-differential variables and Figure 37 for double differential
 165 variables.

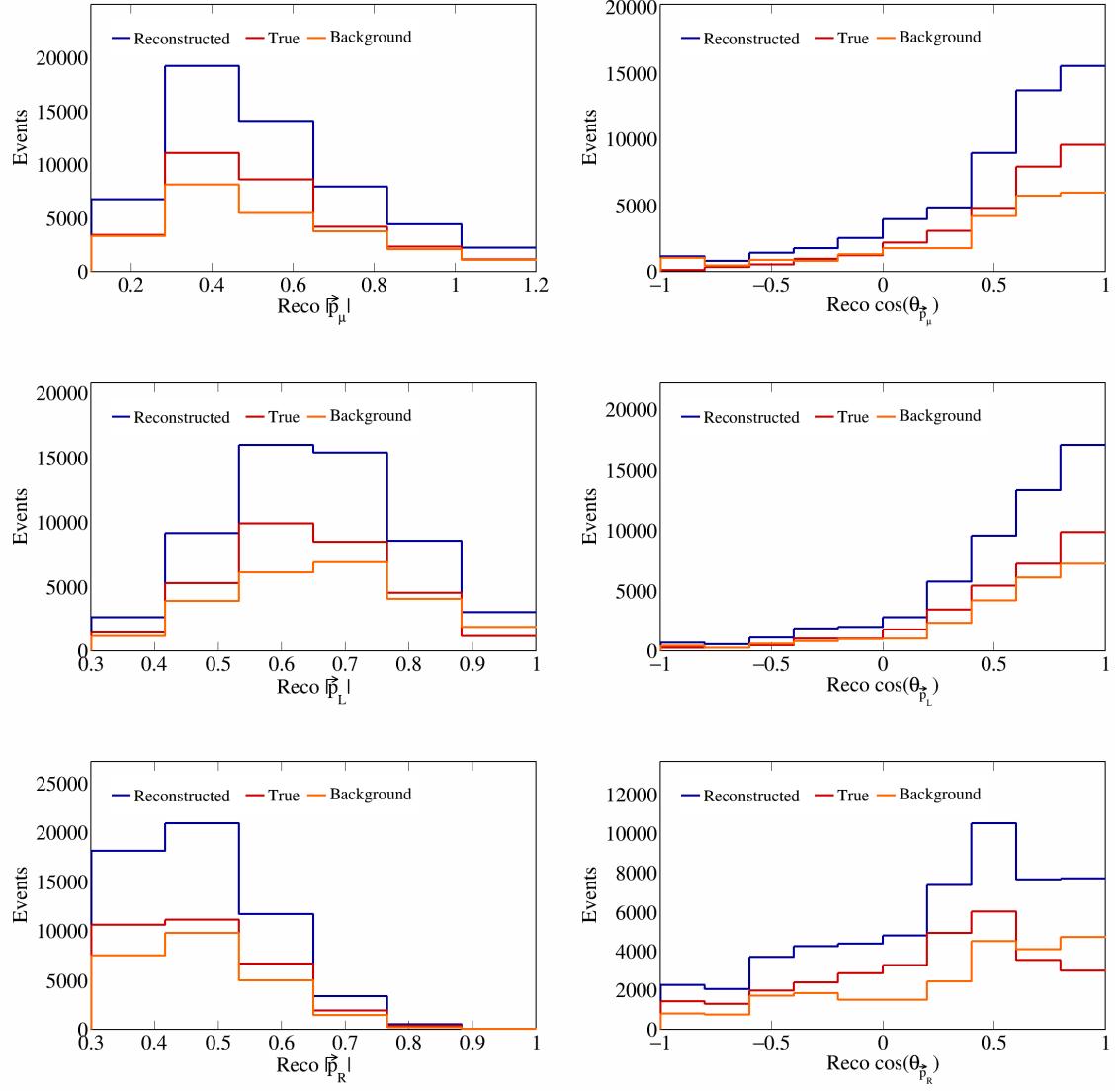


Figure 28: Vector directions and magnitudes for SBND data.

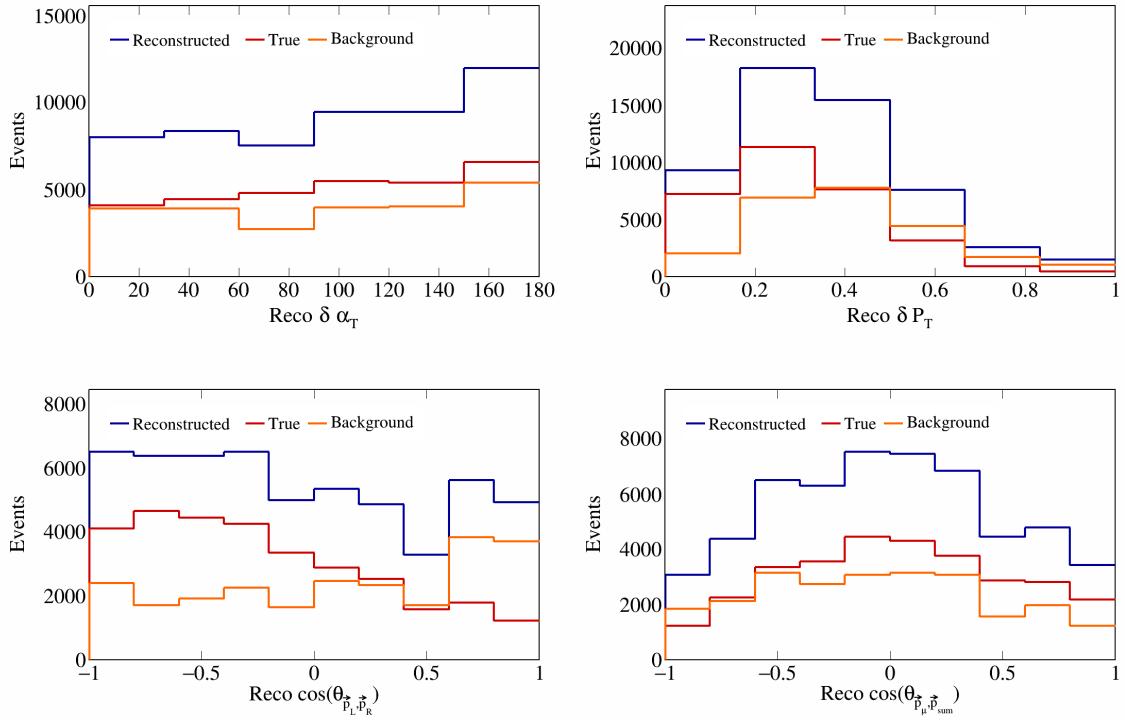


Figure 29: Vector opening angles and transverse momentum for SBND data.

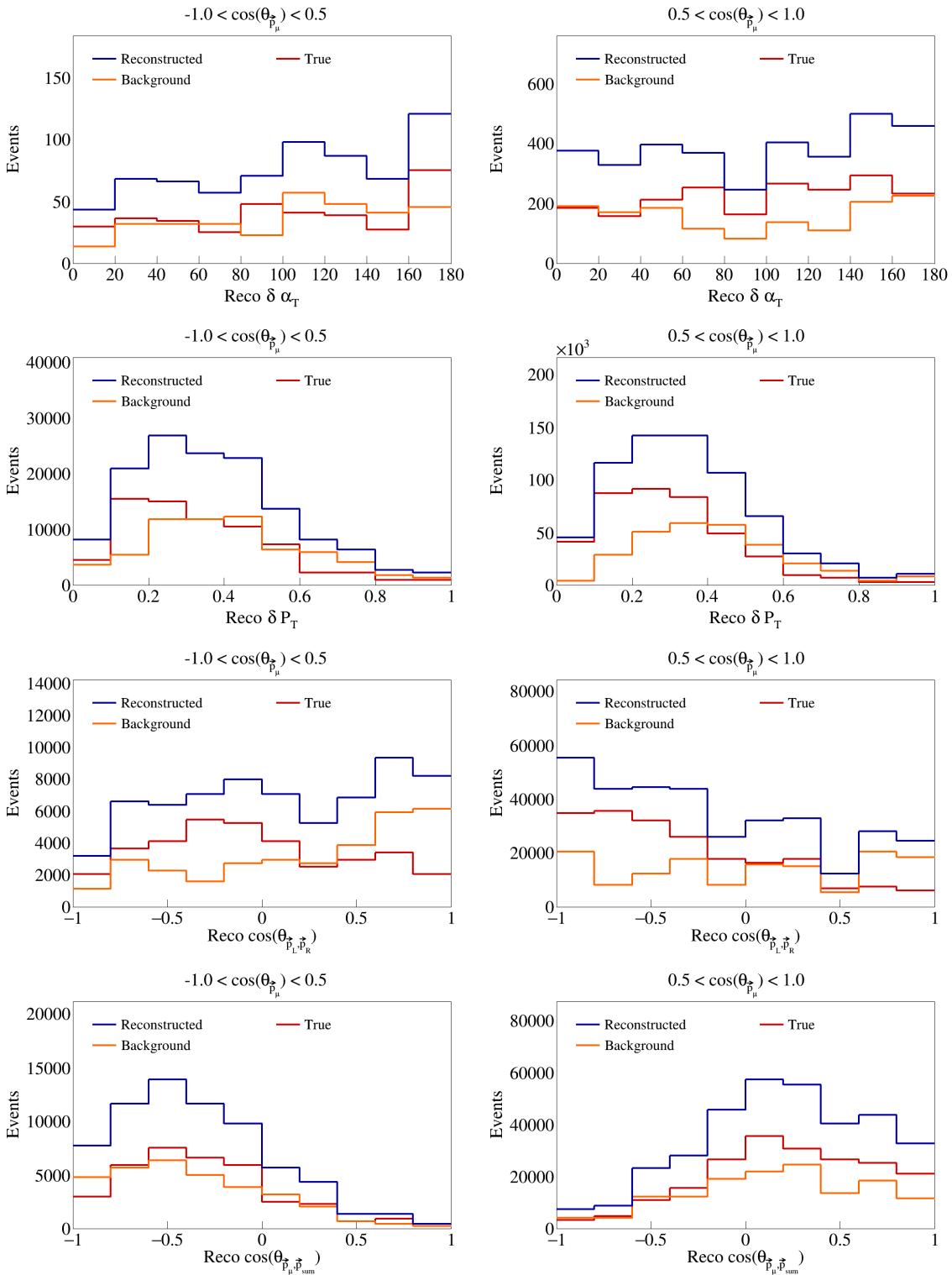


Figure 30: Sliced double differential plots for SBND events.

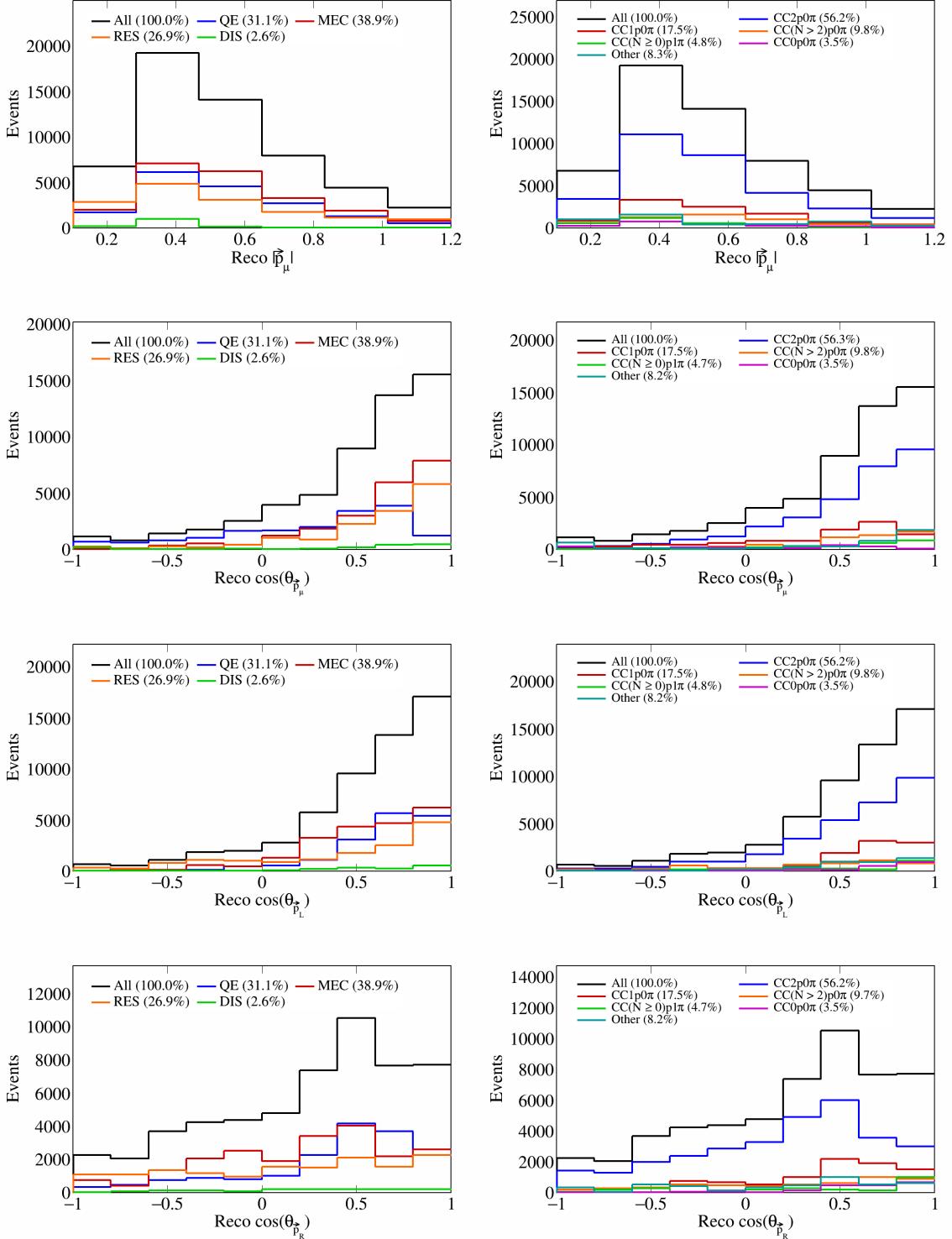


Figure 31: Interaction and topology breakdown for vector directions and magnitudes.

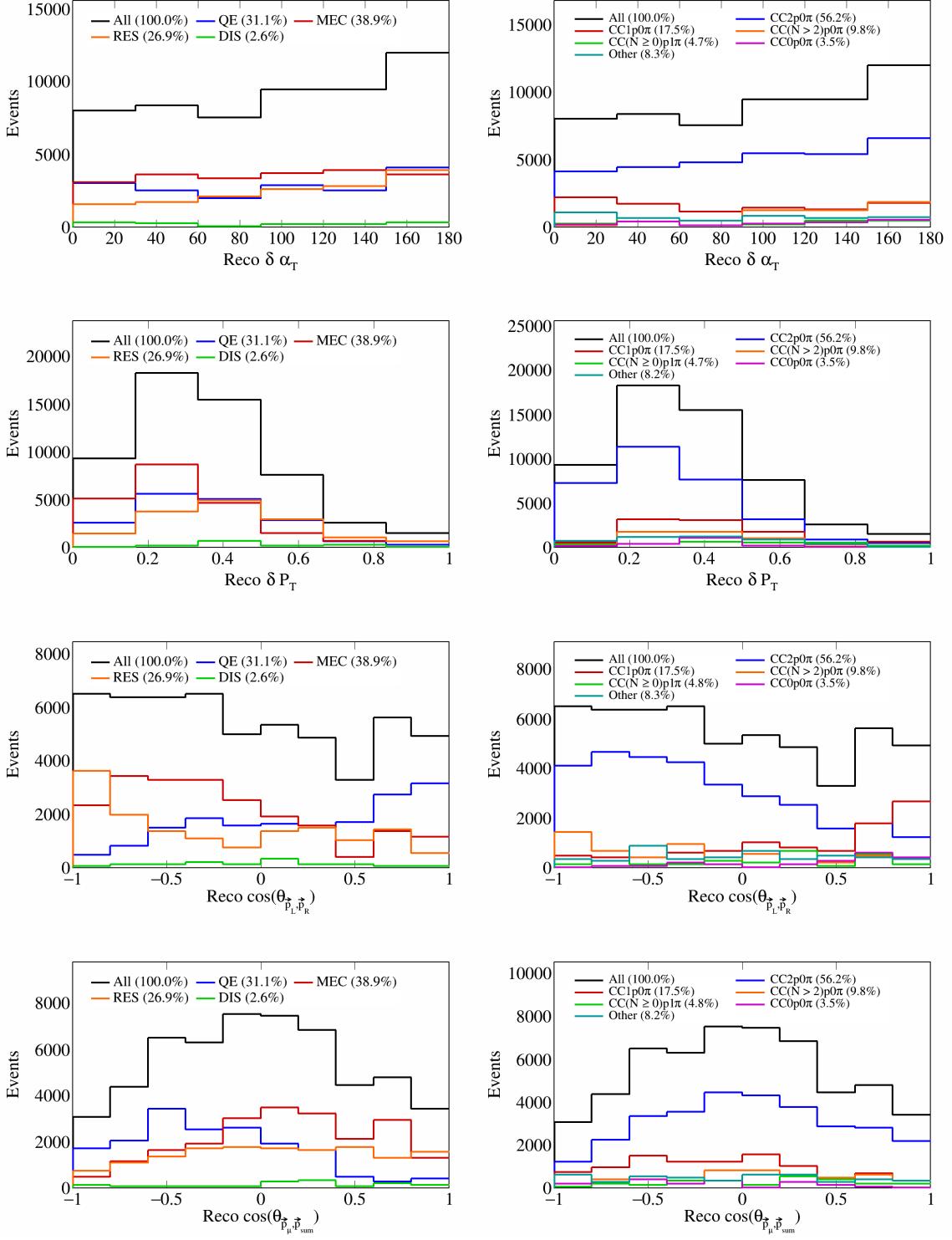


Figure 32: Interaction and topology breakdown for opening angles and transverse variables.

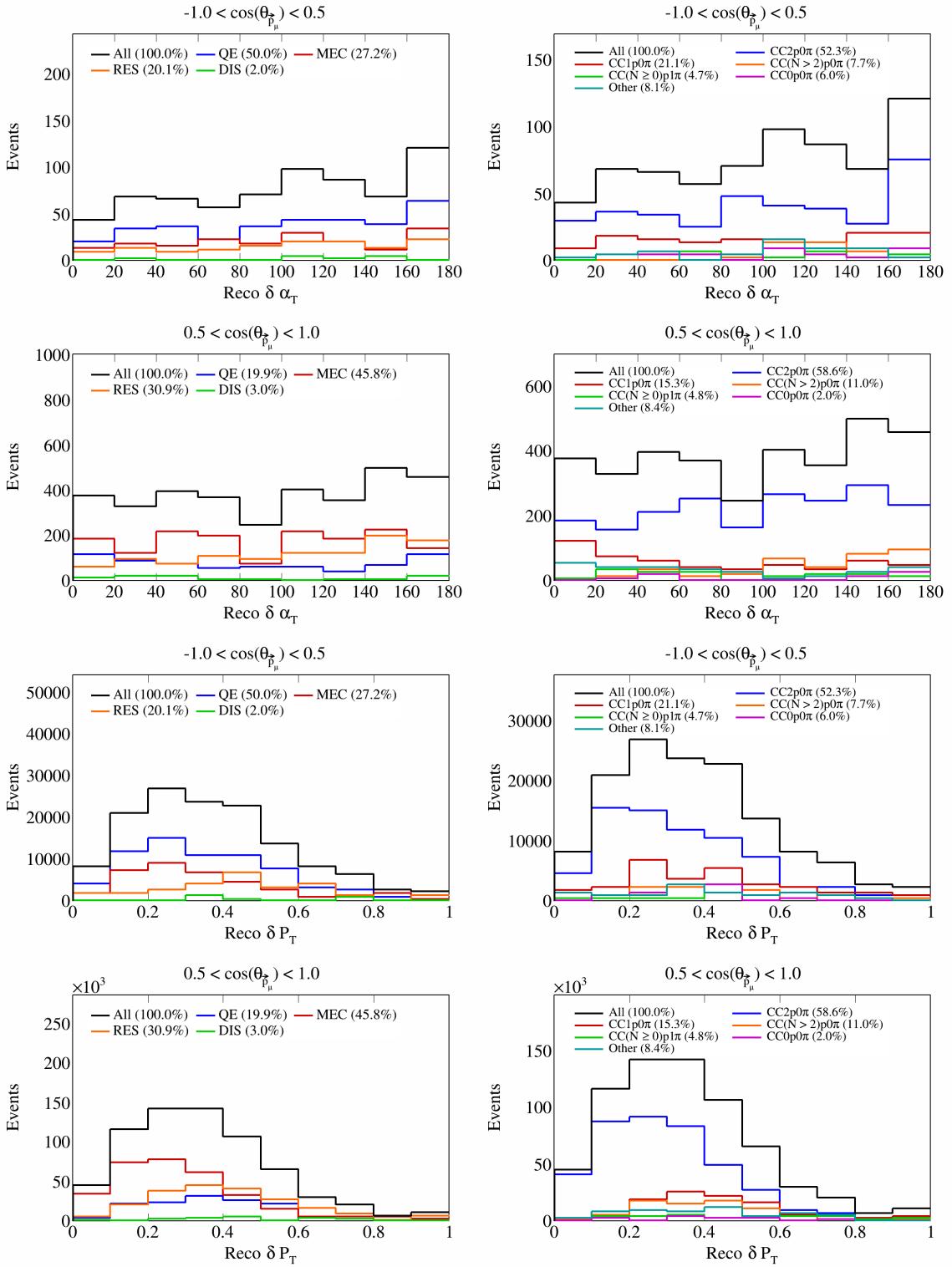


Figure 33: Interaction and topology breakdown for double differential transverse variables.

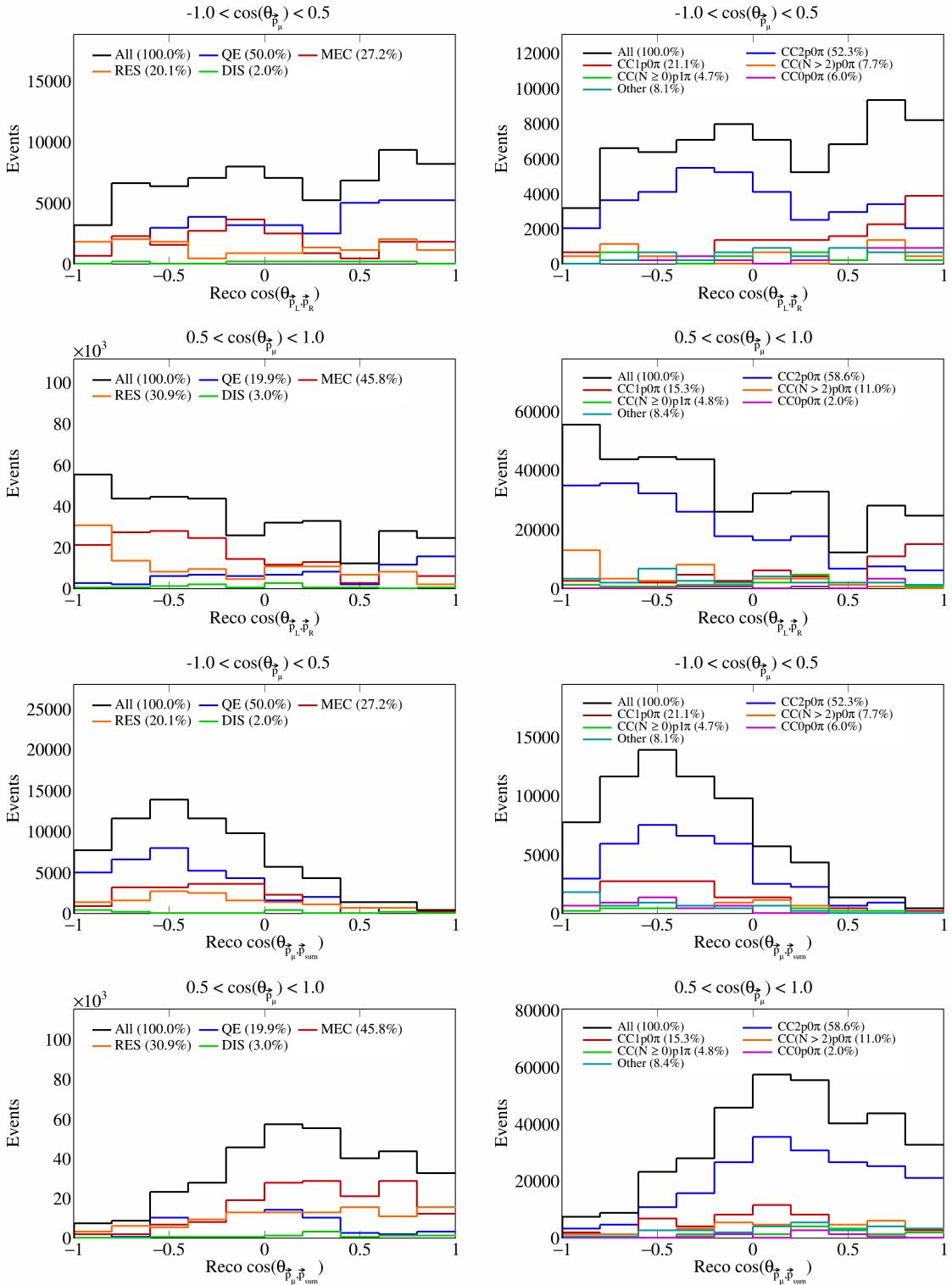


Figure 34: Interaction and topology breakdown for double differential opening angles.

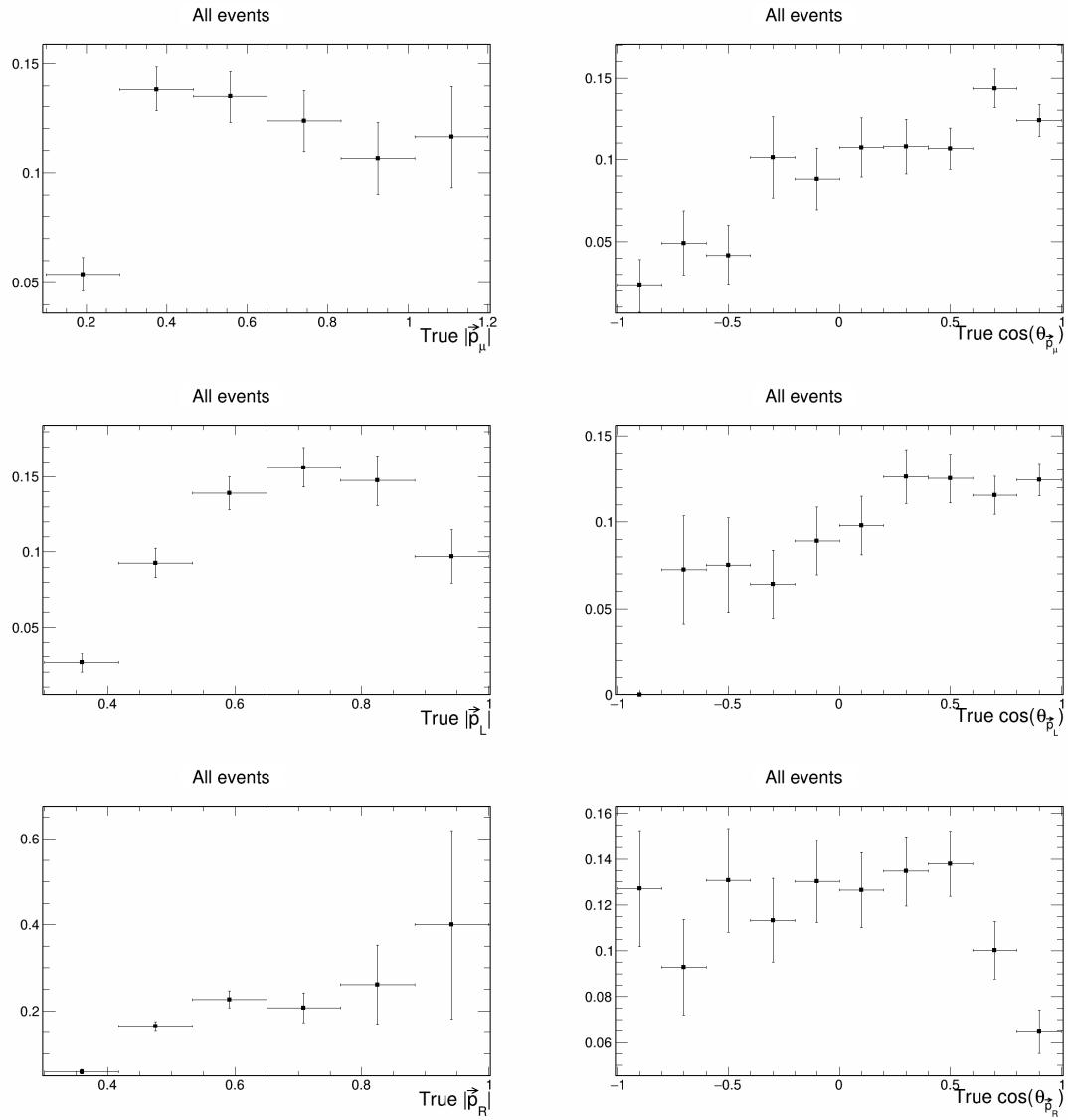


Figure 35: Signal efficiency plots for single differential vector directions and magnitudes.

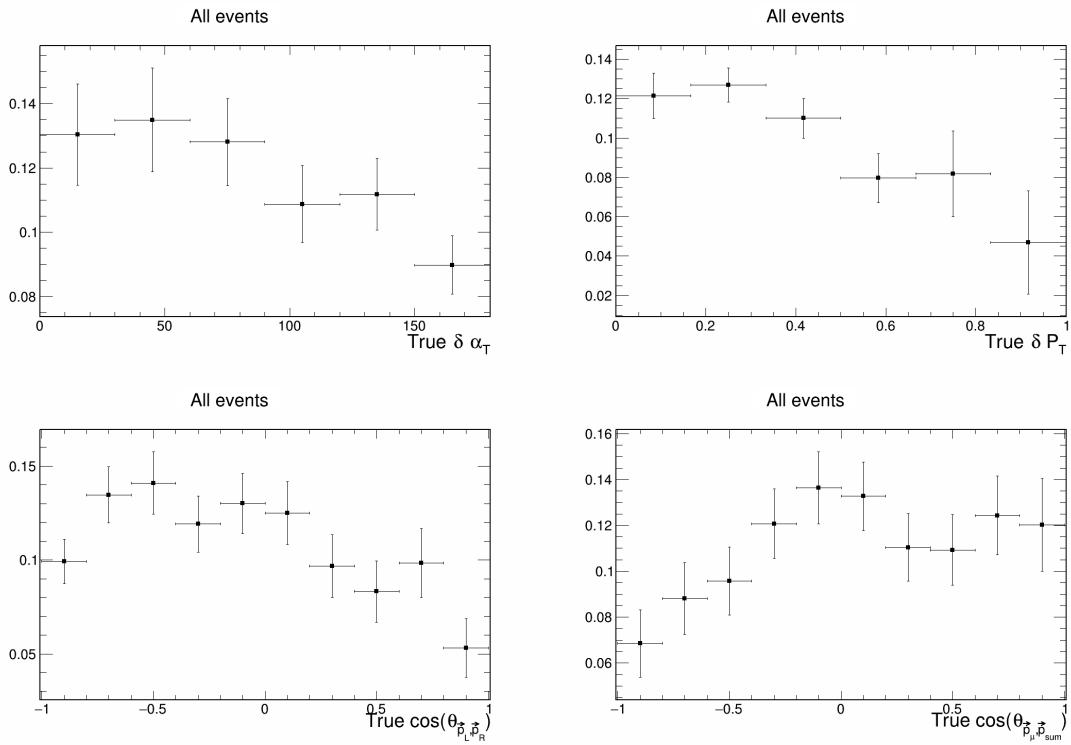


Figure 36: Signal efficiency plots for single differential vector opening angles and transverse momentum.

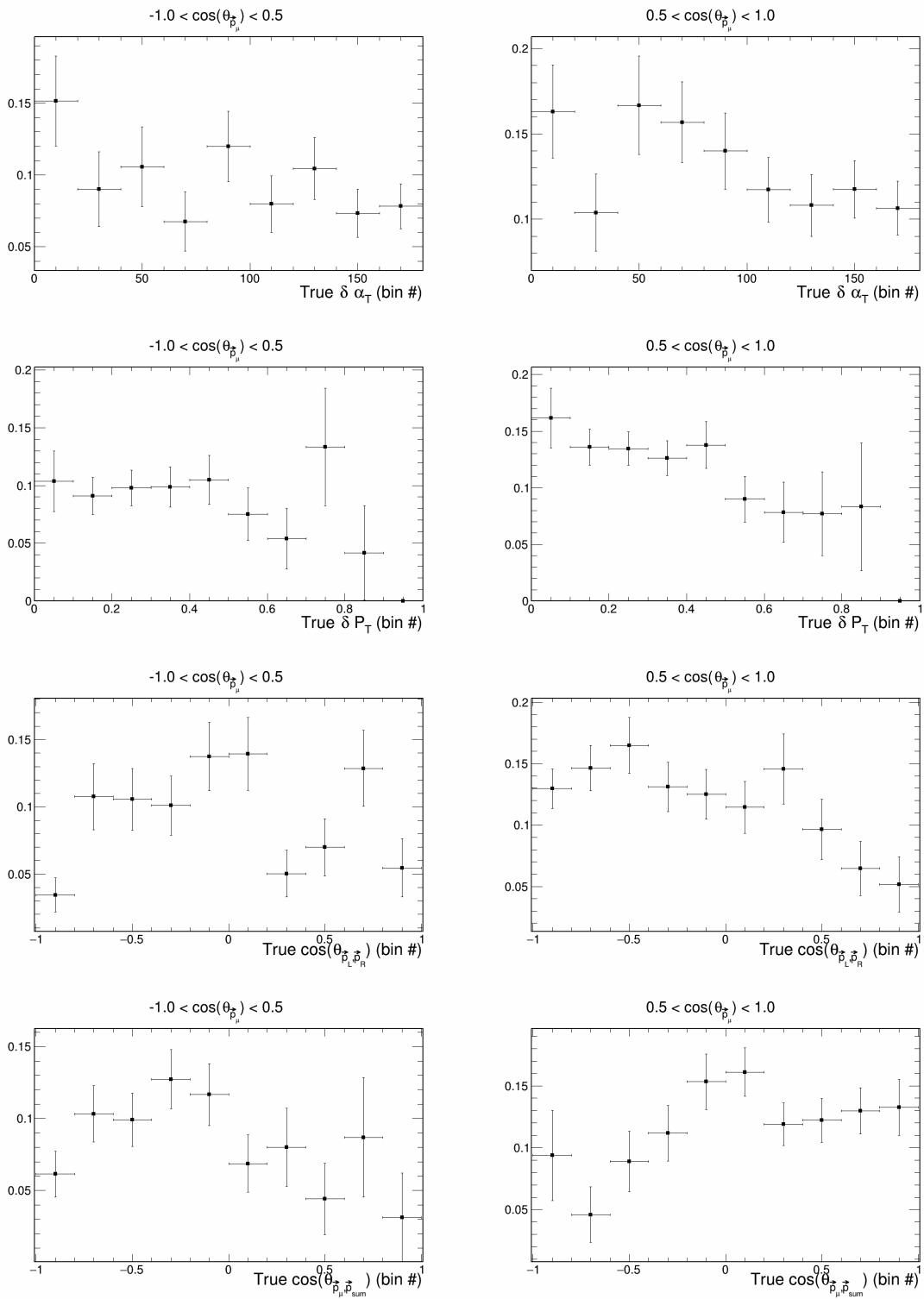


Figure 37: Signal efficiency plots for double differential variables.

166 **3.6 Migration and response matrices**

167 Further, we compute migration matrices which give us a measure of how reliable our reconstructed variables
168 are. A given column in this matrix represents a bin of the truth variable, i.e., the value with which the
169 event was generated. Then, each row corresponds to a reconstructed bin of the same variable, and each cell
170 corresponds to the probability that an event generated with the truth value corresponding to the column gets
171 reconstructed with the value corresponding to the row. For the migration matrix, we consider true signal
172 events that were reconstructed and satisfy our signal definition in the denominator. Therefore, the values in
173 each column must add up to 1. The migration matrices for the single differential variables are presented in
174 Figure 38 and Figure 39. The migration matrices for the double differential variables (given in terms of the
175 bin number) are presented in Figure 40.

176 Response matrices are computed in a similar manner, but using the total number of generated events in the
177 denominator when computing the ratios, i.e., without requiring the events to be successfully reconstructed.
178 Therefore, for these matrices, the columns of the response matrices do not have to add up to 1. The response
179 matrices for single differential variables are presented in Figure 41 and Figure 42, and the double differential
180 response matrices are given in Figure 43.

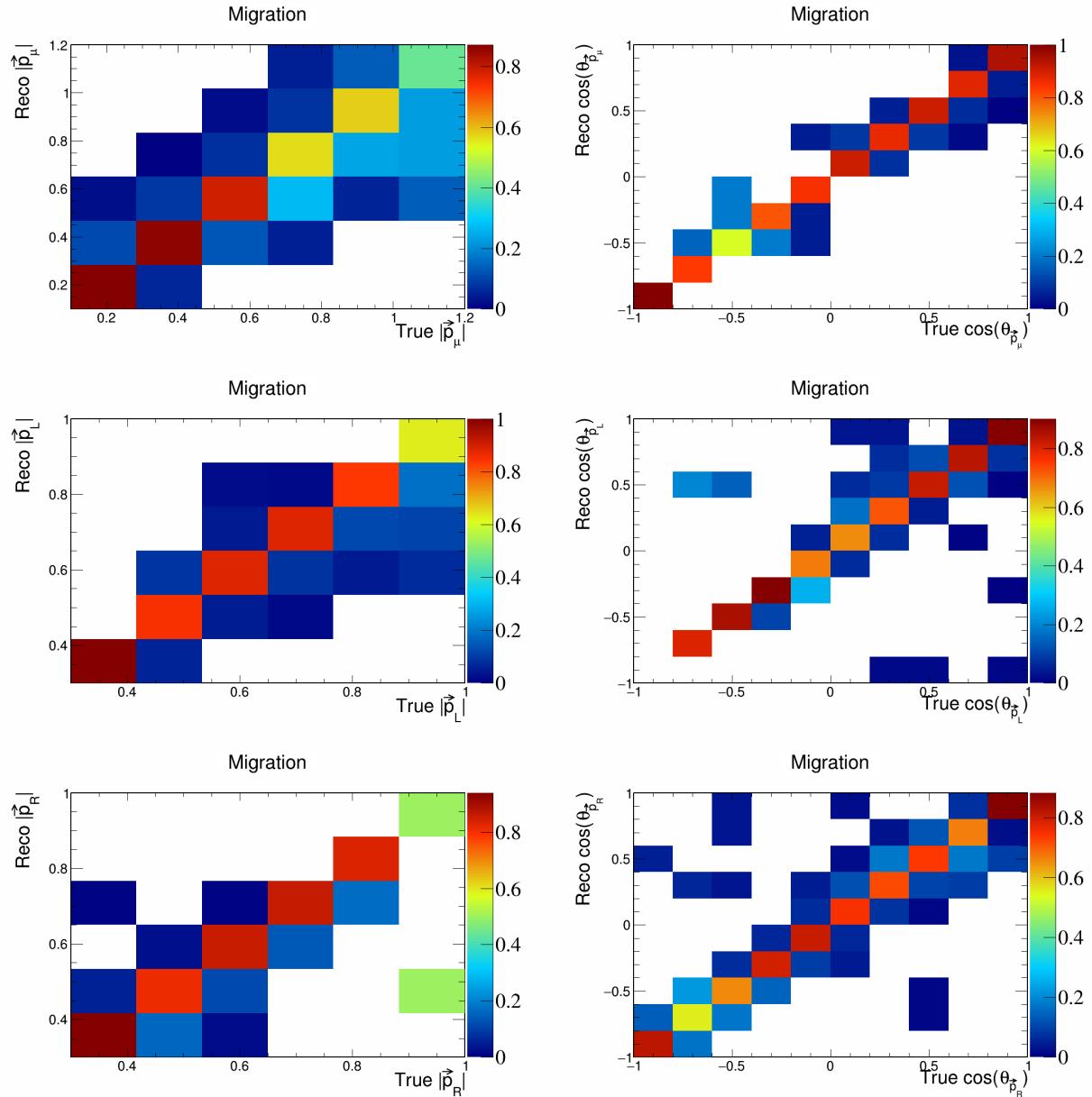


Figure 38: Migration matrices for signal differential vector directions and magnitudes.

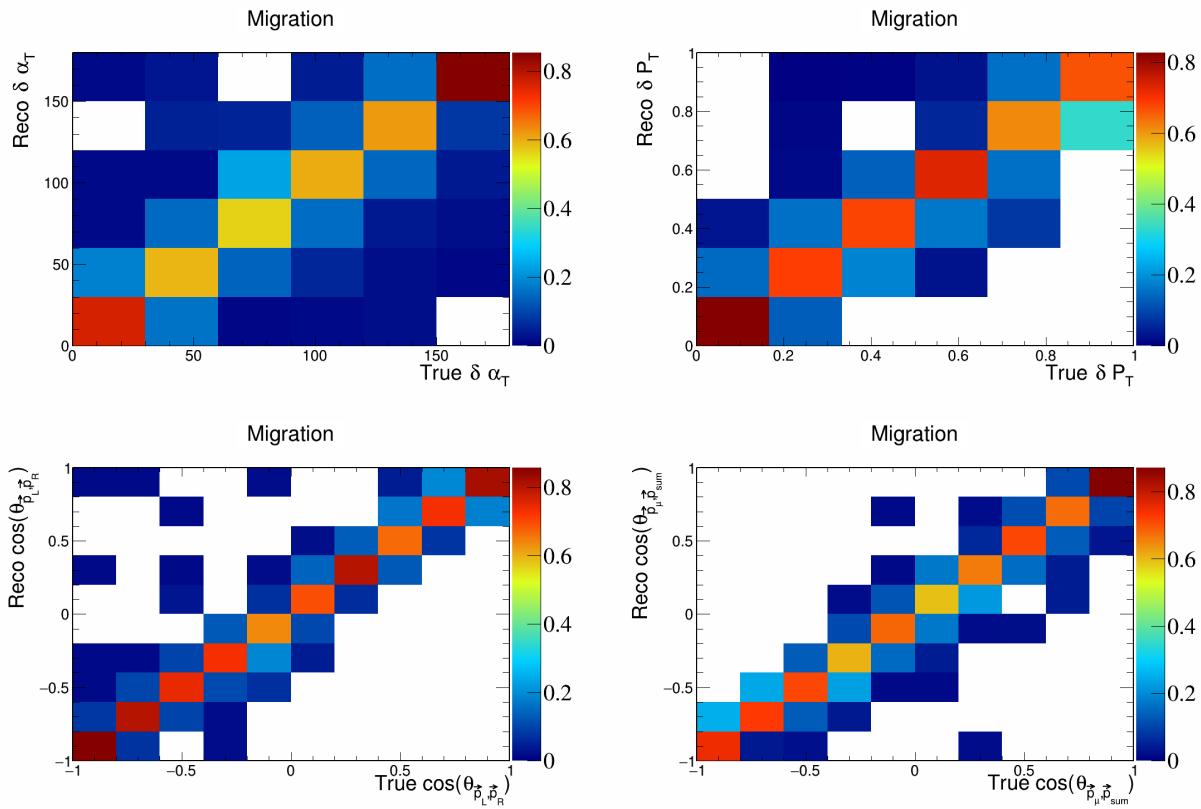


Figure 39: Migration matrices for signal differential vector opening angles and transverse momentum.

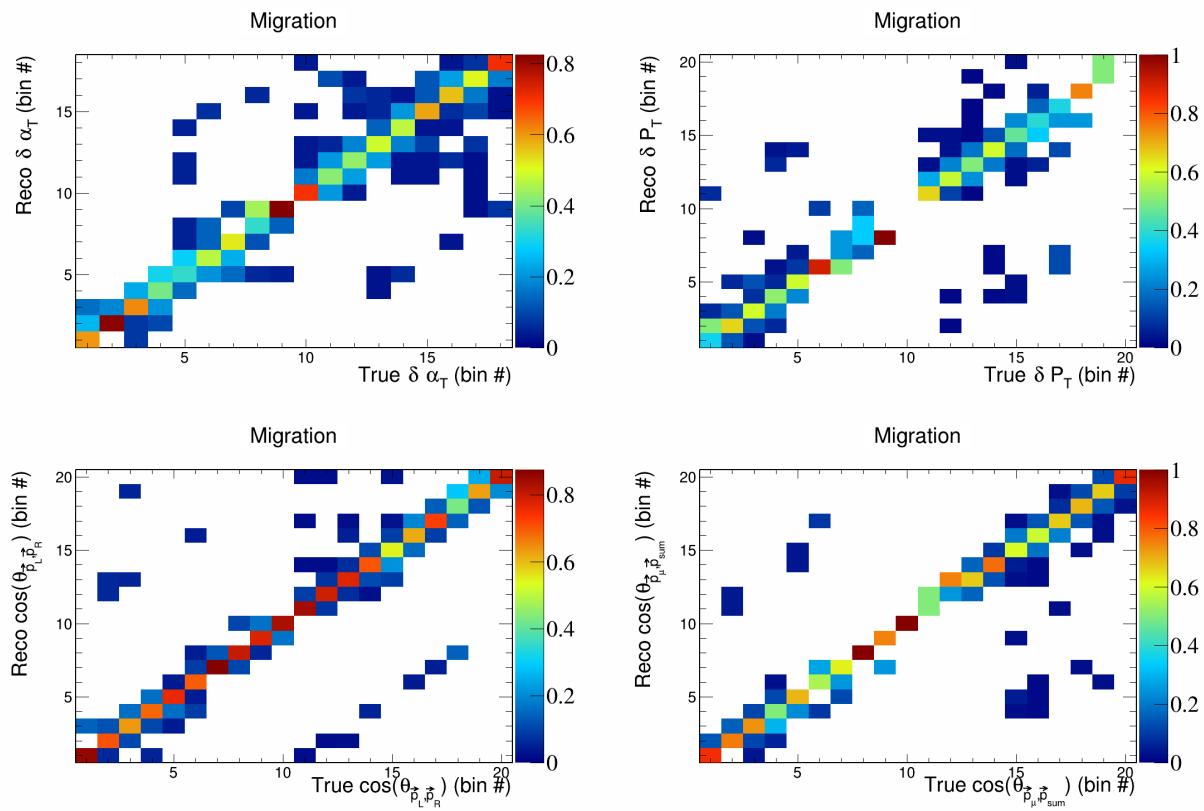


Figure 40: Migration matrices for double differential variables.

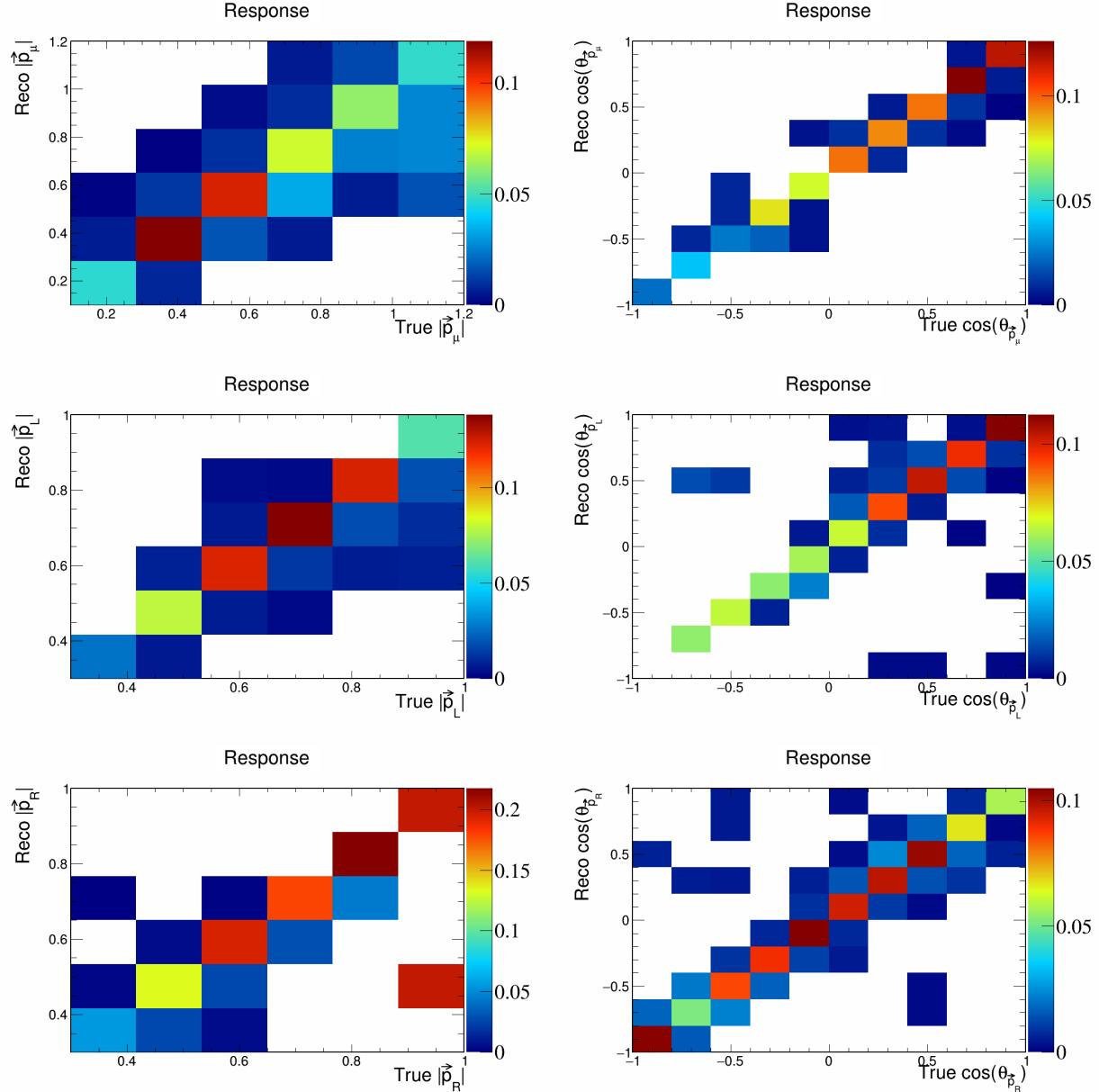


Figure 41: Response matrices for signal differential vector directions and magnitudes.

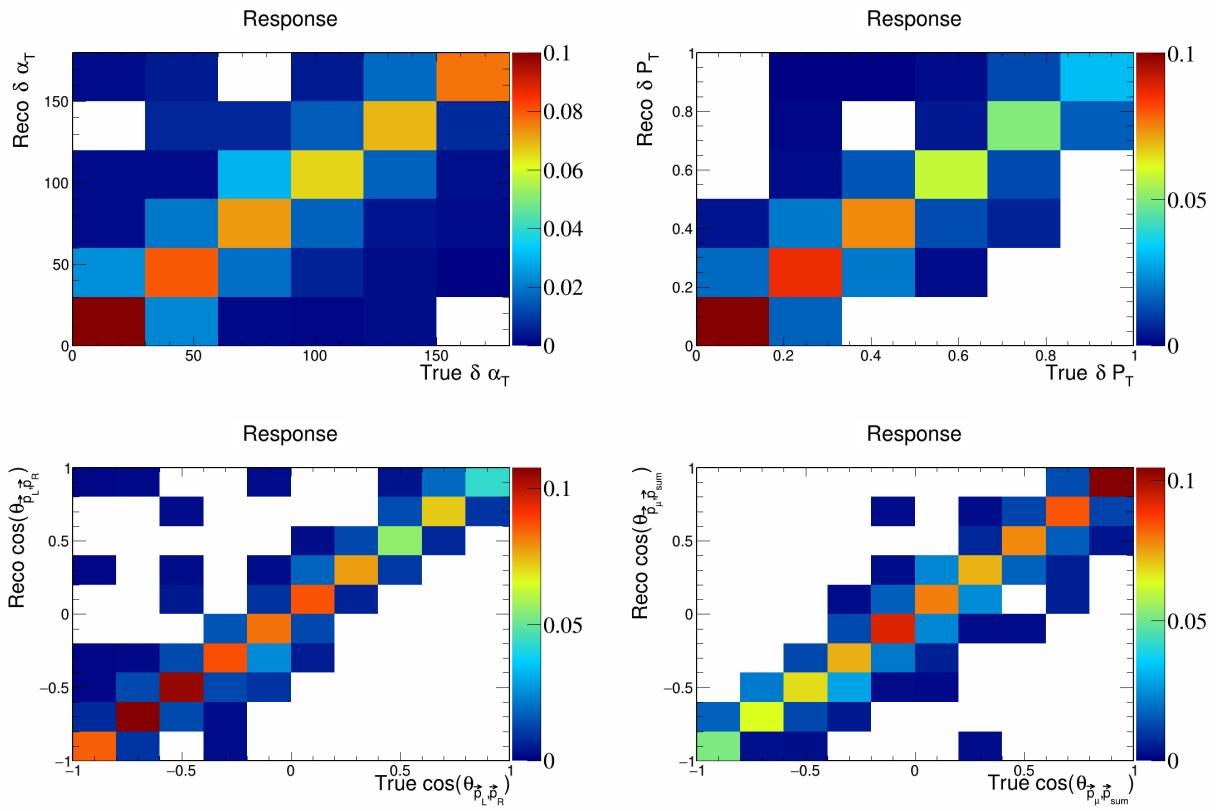


Figure 42: Response matrices for signal differential vector opening angles and transverse momentum.

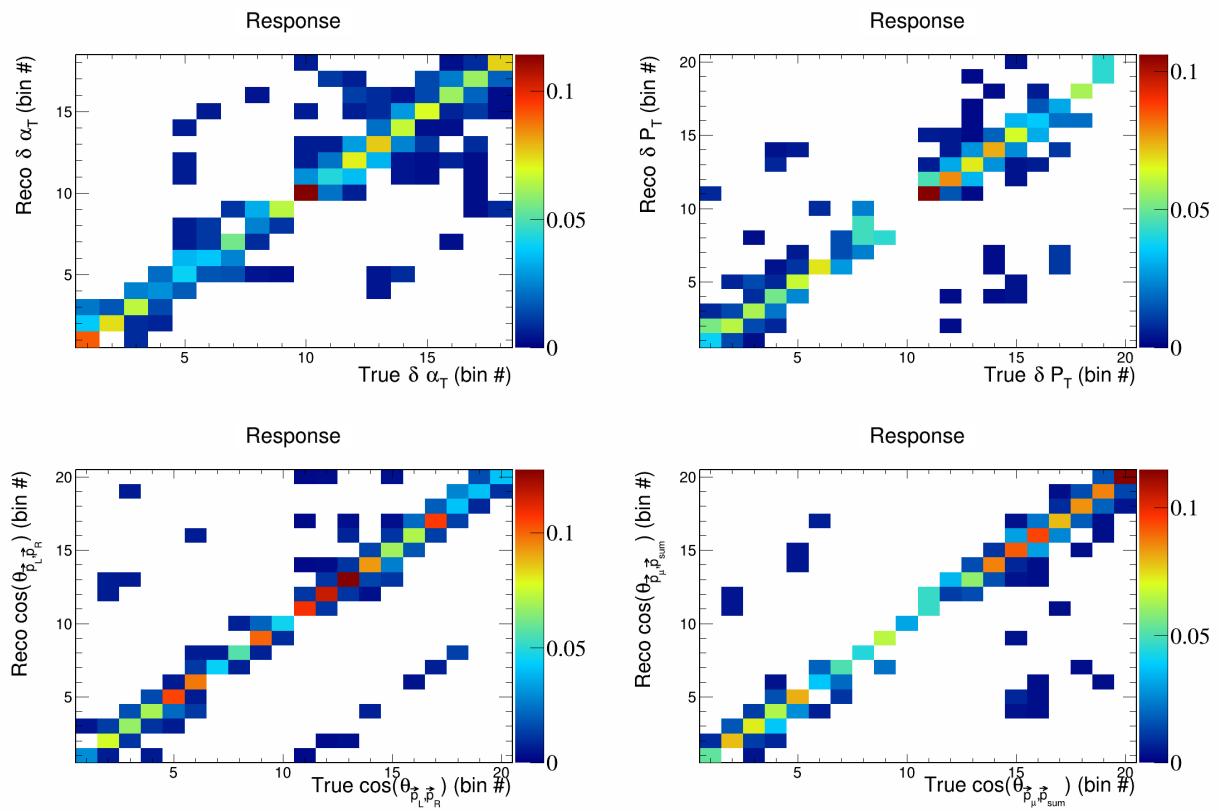


Figure 43: Response matrices for double differential variables.

181 **3.7 Systematics**

182 To include systematic uncertainties in our study, we first consider cross sectional systematics. These are
 183 variations in the cross section models used to generate the events. They can be of two types: multisigma
 184 and multisim. For the former, we consider a 1σ variation of the affected parameters, and in the latter we
 185 consider one hundred universes, each with a random variation picked from a Gaussian distribution between
 186 0σ and 1σ . From these variations, we compute the covariance matrix as

$$E_{i,j} = \frac{1}{N_{\text{Univ}}} \sum_{s=1}^{N_{\text{Univ}}} (\tilde{\sigma}_i^{\text{Var},s} - \tilde{\sigma}_i^{\text{CV}})(\tilde{\sigma}_j^{\text{Var},s} - \tilde{\sigma}_j^{\text{CV}}) \quad (7)$$

187 where $\tilde{\sigma}_i^{\text{Var},s}$ represents the variation cross section of the variable in the i -th bin in the s -th universe, and
 188 $\tilde{\sigma}_i^{\text{CV}}$ is the central value (without any variation) of the cross section in the i -th bin. Then, the fractional
 189 covariance matrix is defined as

$$F_{i,j} = \frac{E_{i,j}}{\tilde{\sigma}_i^{\text{CV}} \tilde{\sigma}_j^{\text{CV}}}. \quad (8)$$

190 And the correlation matrix is defined as

$$\rho_{i,j} = \frac{E_{i,j}}{\sqrt{E_{i,i} E_{j,j}}}. \quad (9)$$

191 In the case of a multisigma systematic, $N_{\text{Univ}} = 1$, and for a multisim systematic, $N_{\text{Univ}} = 100$. The plots
 192 for all the individual cross sectional systematics are shown in Appendix 5.1. The corresponding plots for the
 193 individual flux systematics are shown in Appendix 5.2. The total covariance matrices for each variable are
 194 shown in Figures 44 and 45.

195 **3.8 Closure test**

196 We use the total covariance matrices obtained from all the systematics and shown in the previous section
 197 to unfold our data. We perform this unfolding following the Wiener-SVD method [27], which for a given
 198 variable takes as input a response matrix, true signal histogram, a reconstructed signal histogram, and the
 199 covariance matrix. The output is the unfolded spectrum and a smearing matrix that can be used to smear
 200 true signal histograms.

201 To ensure that the unfolding techniques that we will implement work correctly, we perform a closure test,
 202 meaning that we will perform the unfolding on simulated true signal events and check that the unfolded
 203 data matches the true signal data with added smearing. We can see that the plots that perform this test
 204 in Figure 46 and Figure 47. We also note that the overall shape and magnitude of our histograms match
 205 previously reported MicroBooNE analyses.

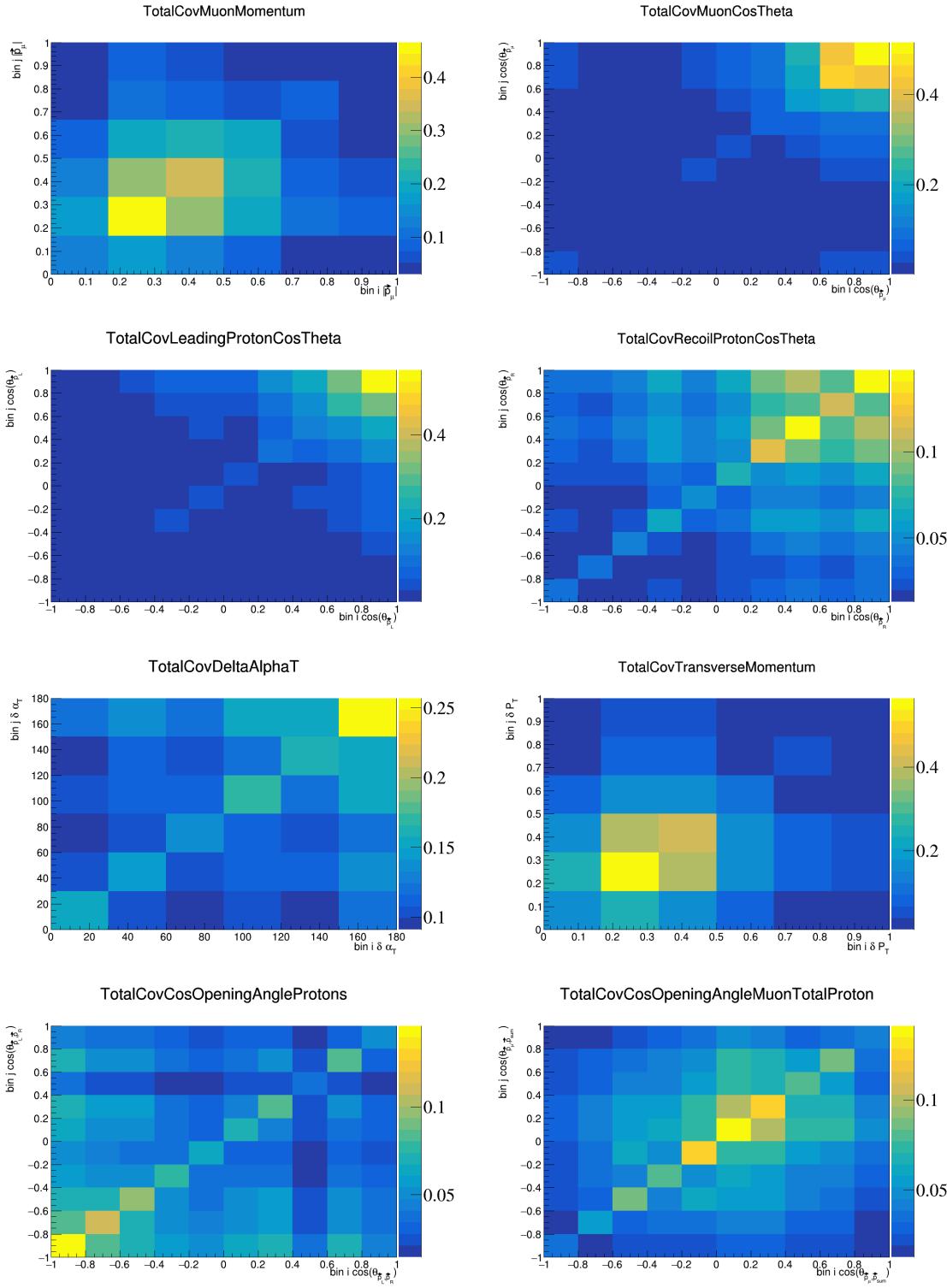


Figure 44: Total covariance matrices for single differential variables.

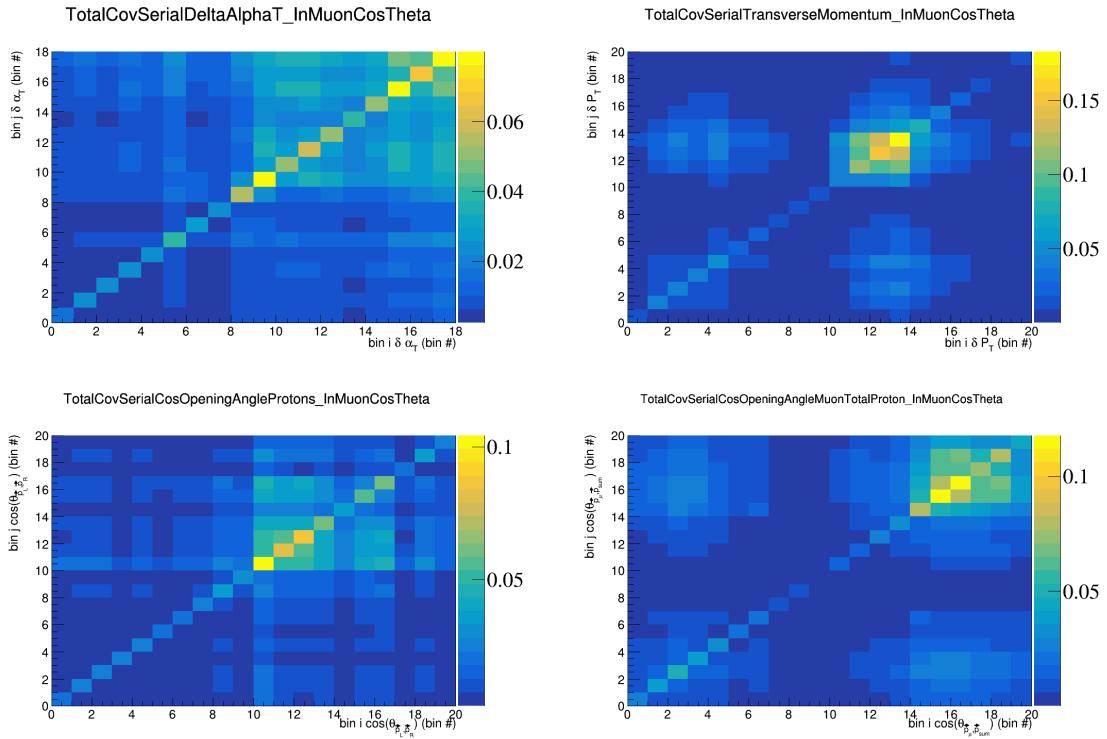


Figure 45: Total covariance matrices for double differential variables.

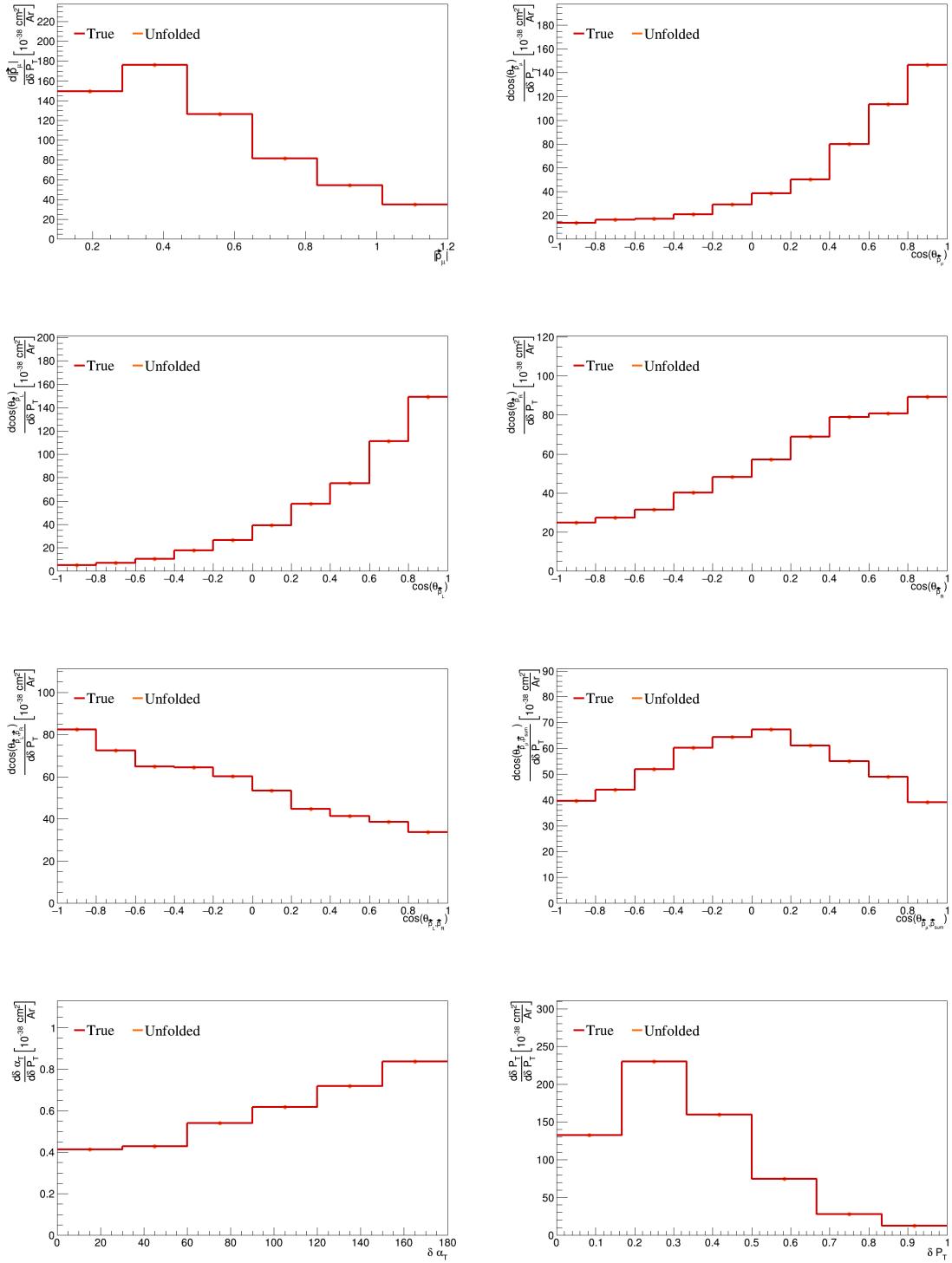


Figure 46: Closure test single differential plots.

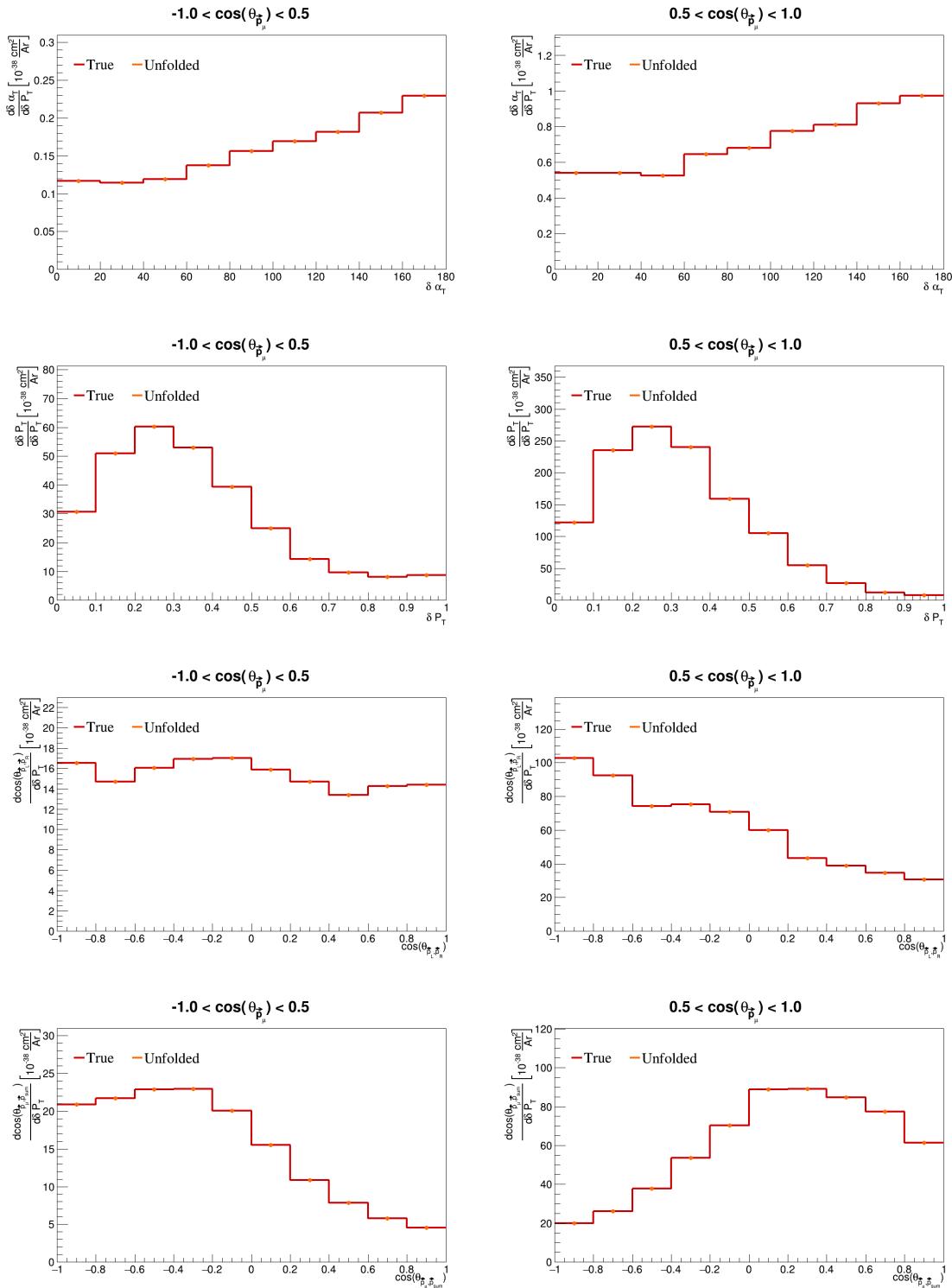


Figure 47: Closure test double differential plots.

206 **4 Cross-section results**

207 Placeholder.

208 **5 Appendices**

209 **5.1 Cross section systematics**

210 In this appendix, the variations, covariance matrices, fractional covariance matrices, and correlation matrices
 211 are plotted for all of the cross section systematics and variables.

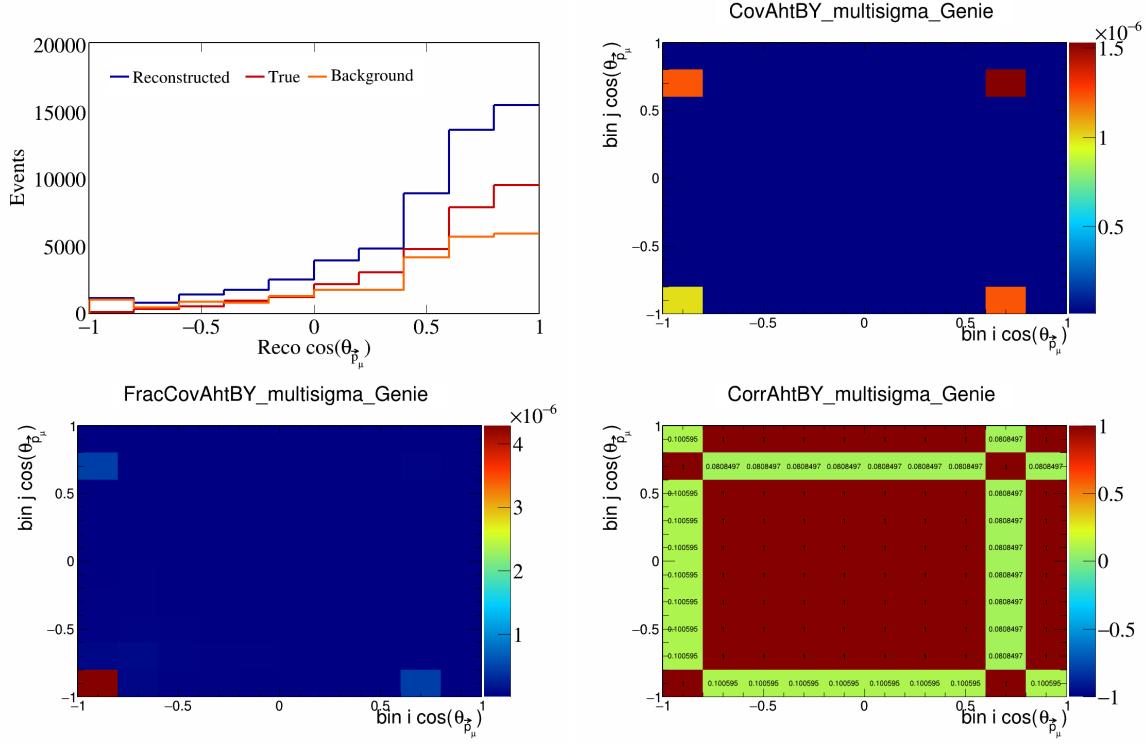


Figure 48: AhtBY variations for $\cos(\theta_{\vec{p}_\mu})$.

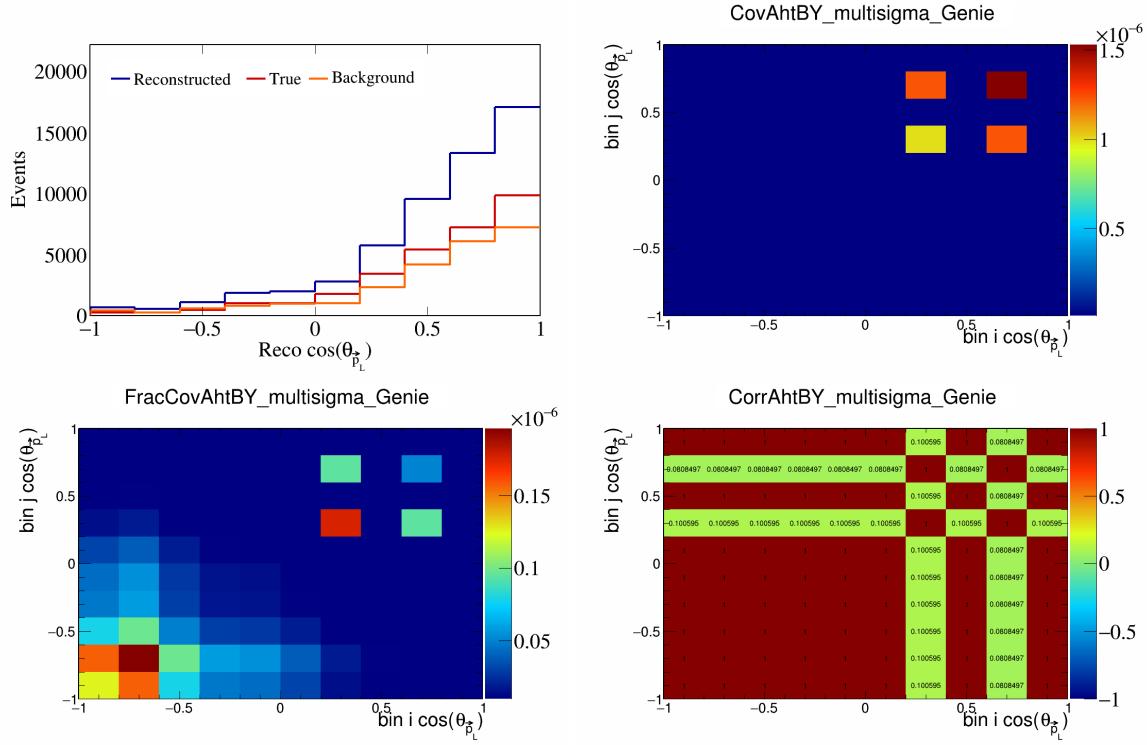


Figure 49: AhtBY variations for $\cos(\theta_{\vec{p}_L})$.

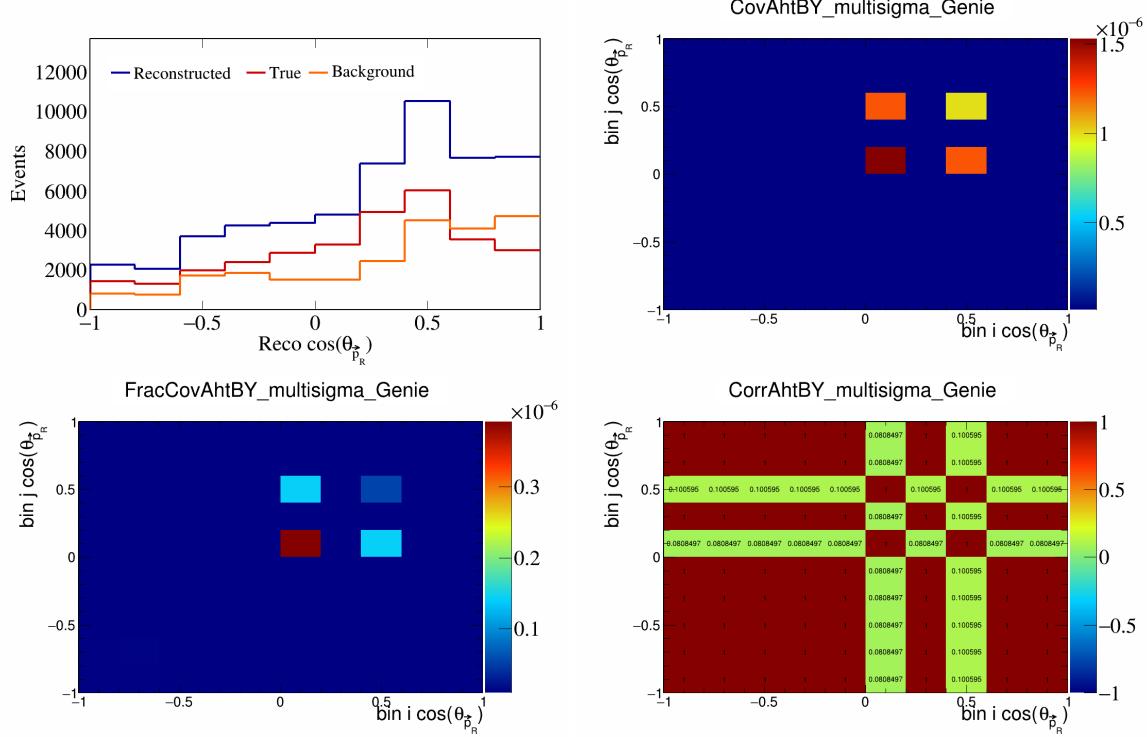


Figure 50: AhtBY variations for $\cos(\theta_{\vec{p}_R})$.

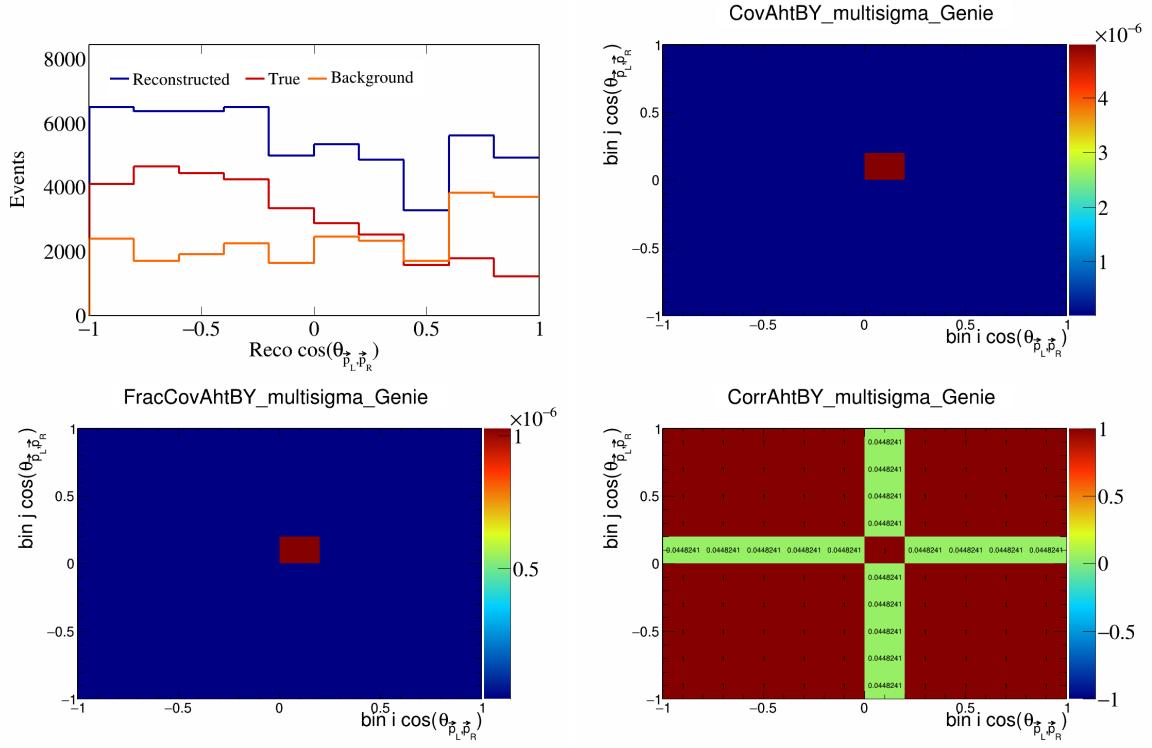


Figure 51: AhtBY variations for $\cos(\theta_{\vec{p}_L, \vec{p}_R})$.

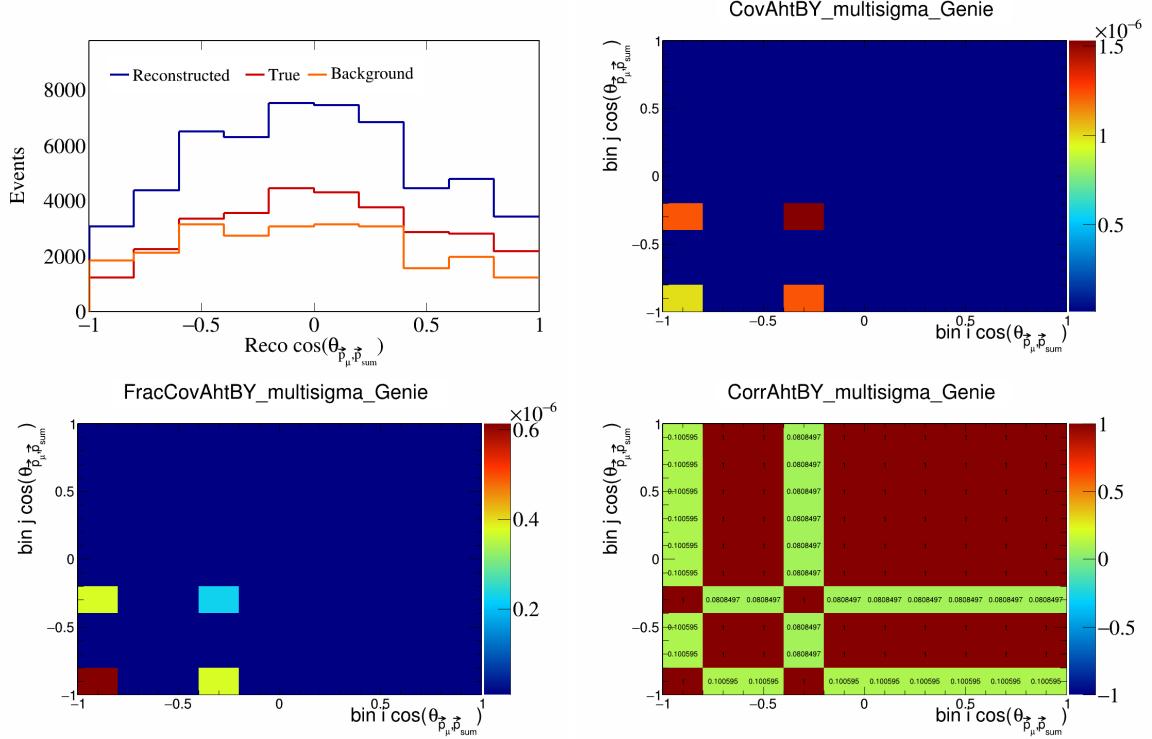


Figure 52: AhtBY variations for $\cos(\theta_{\vec{p}_\mu, \vec{p}_{\text{sum}}})$.

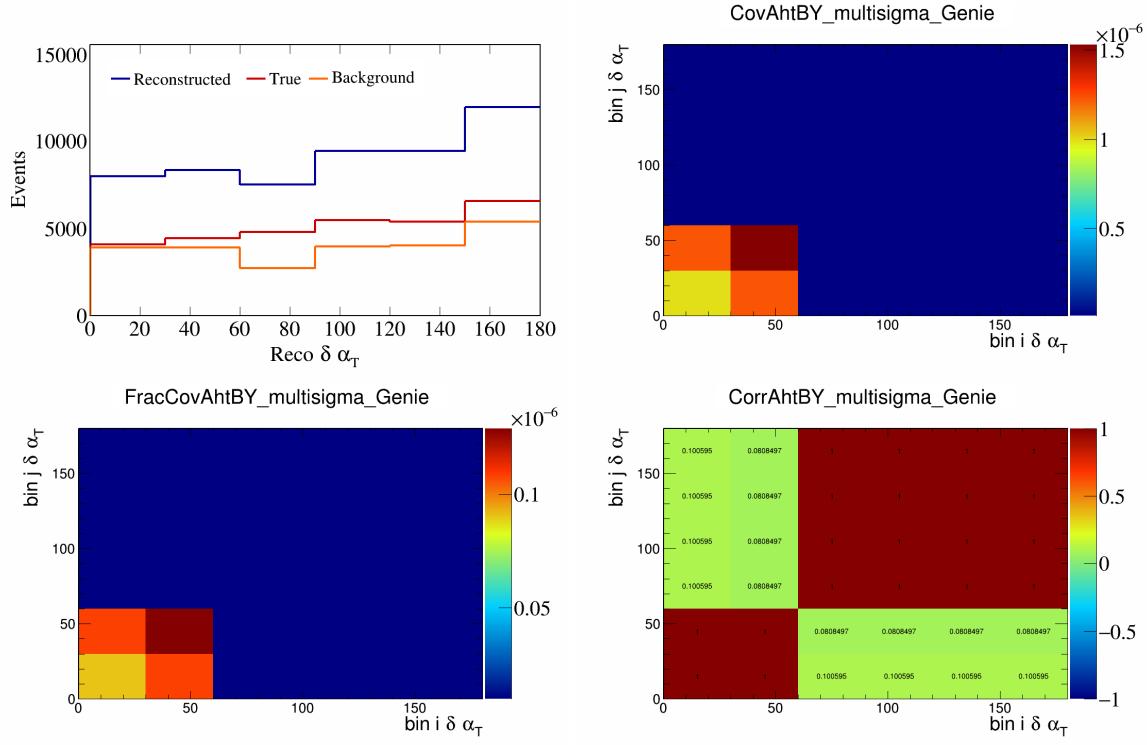


Figure 53: AhtBY variations for $\delta\alpha_T$.

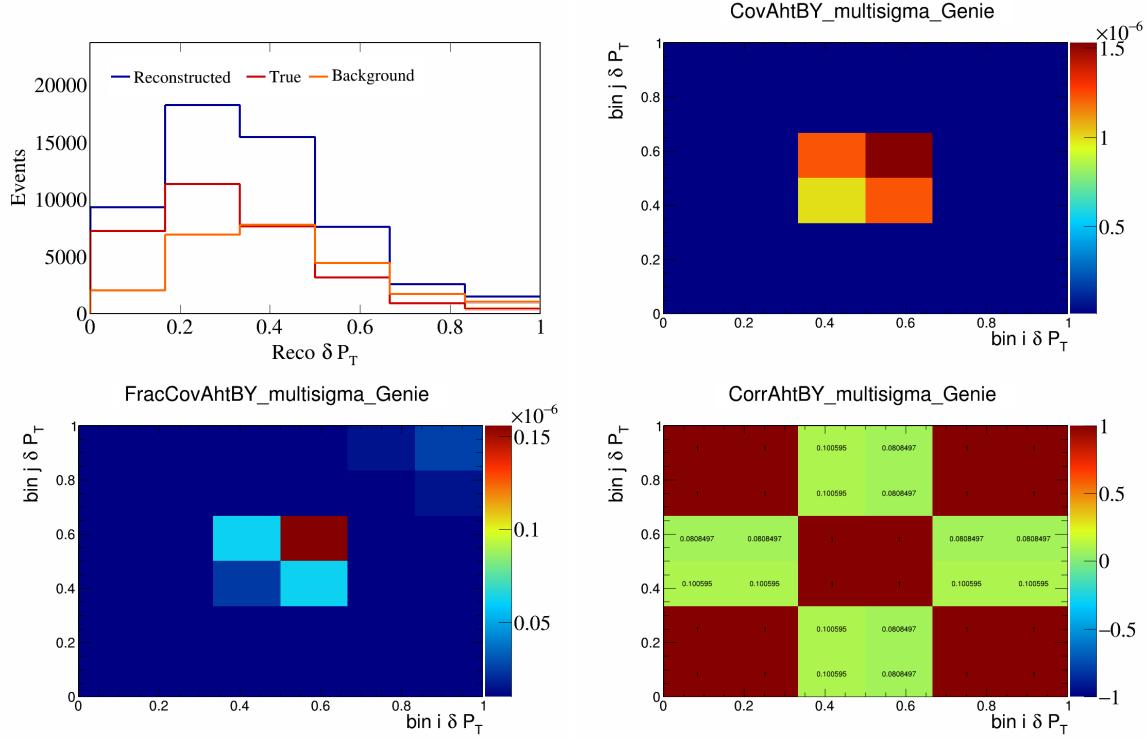


Figure 54: AhtBY variations for δP_T .

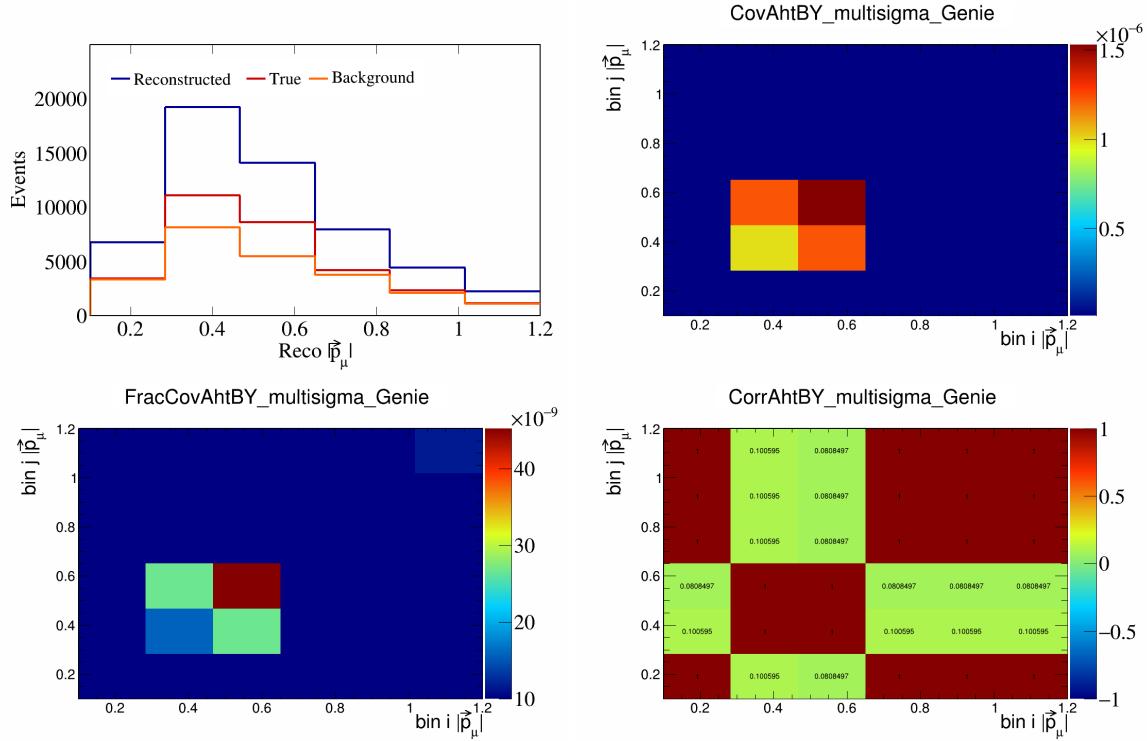


Figure 55: AhtBY variations for $|\vec{p}_\mu|$.

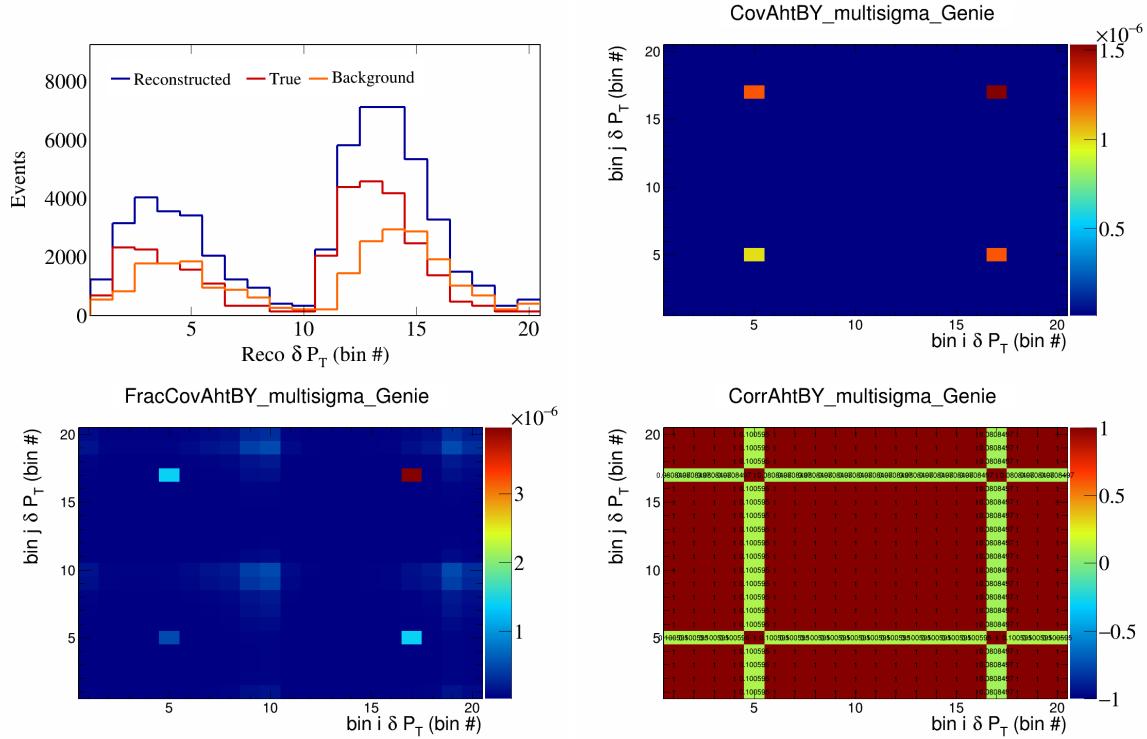


Figure 56: AhtBY variations for δP_T in $\cos(\theta_{\vec{p}_\mu})$.

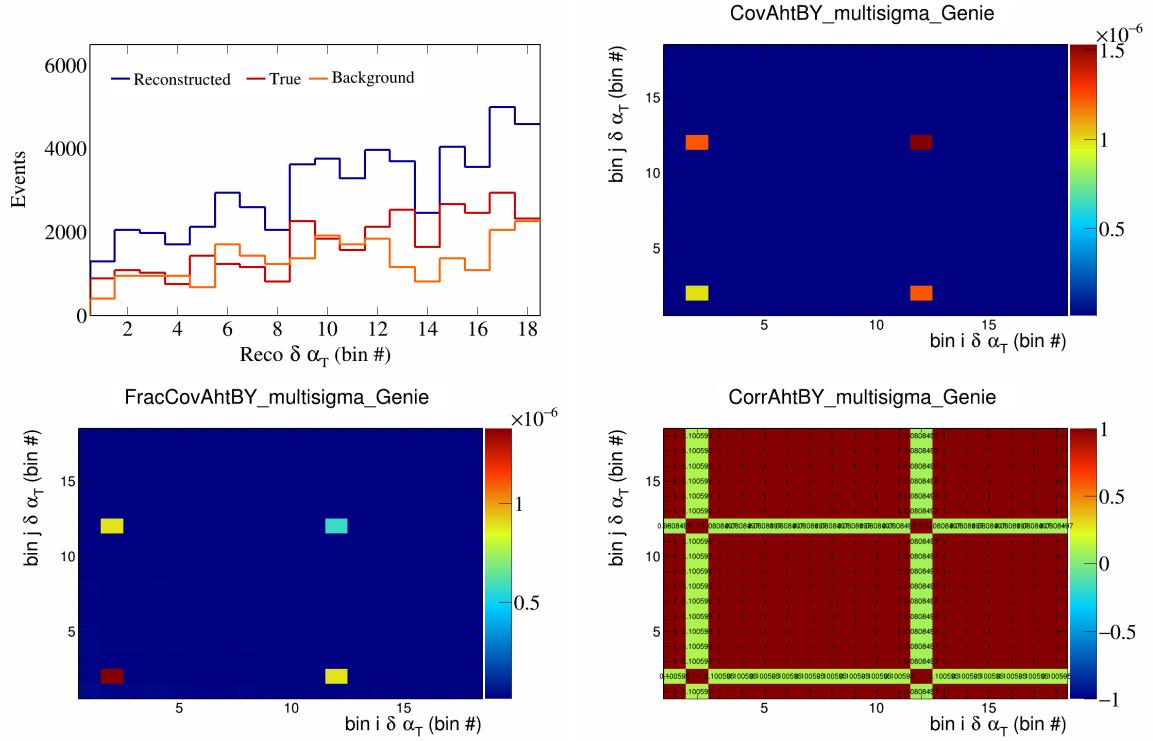


Figure 57: AhtBY variations for $\delta\alpha_T$ in $\cos(\theta_{\vec{p}_\mu})$.

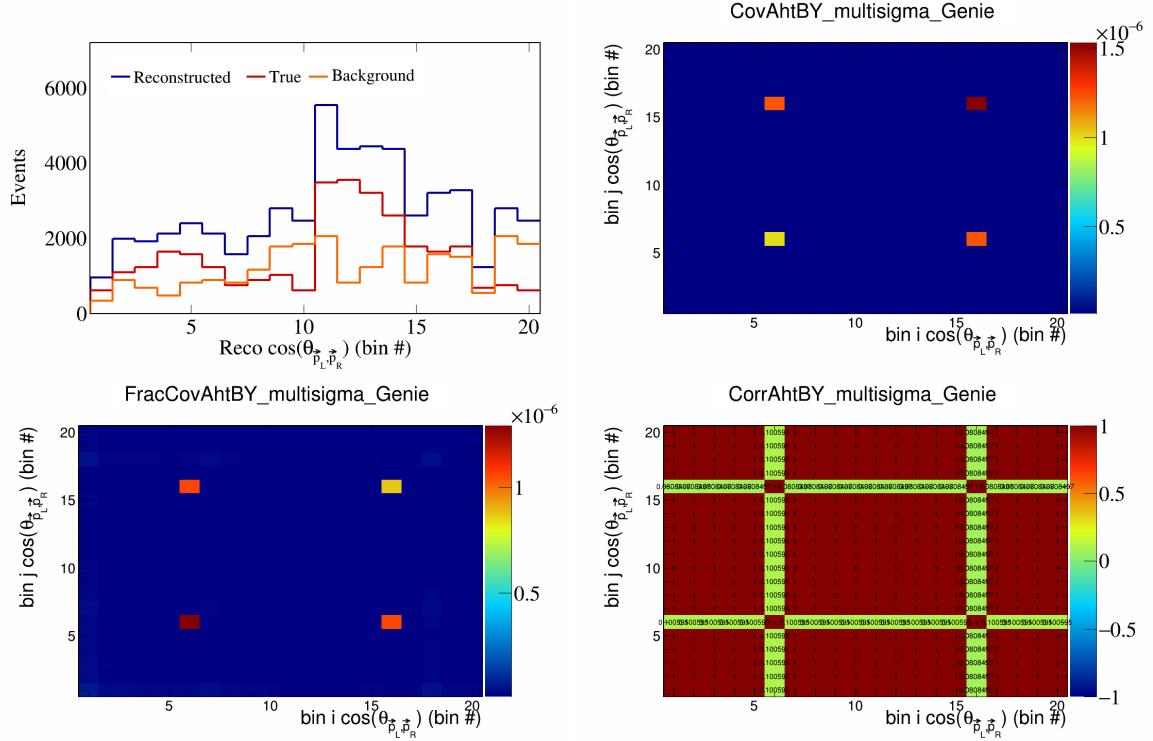


Figure 58: AhtBY variations for $\cos(\theta_{\vec{p}_L, \vec{p}_R})$ in $\cos(\theta_{\vec{p}_\mu})$.

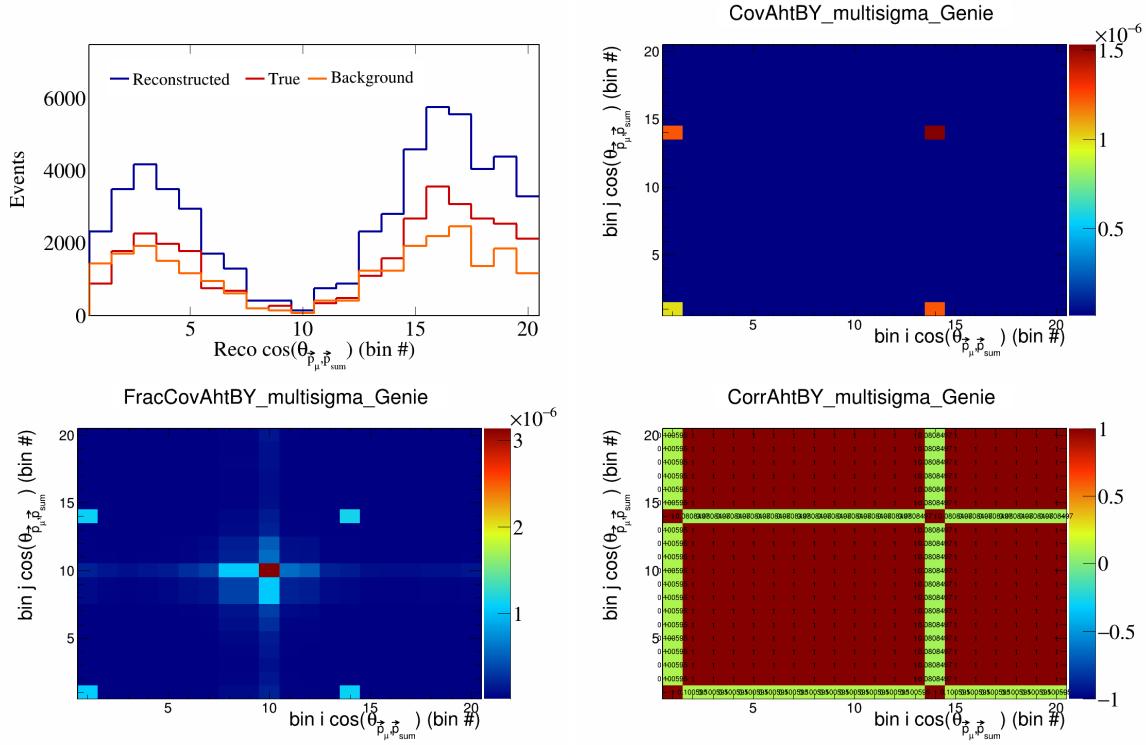


Figure 59: AhtBY variations for $\cos(\theta_{\vec{p}_\mu, \vec{p}_{\text{sum}}})$ in $\cos(\theta_{\vec{p}_\mu})$.

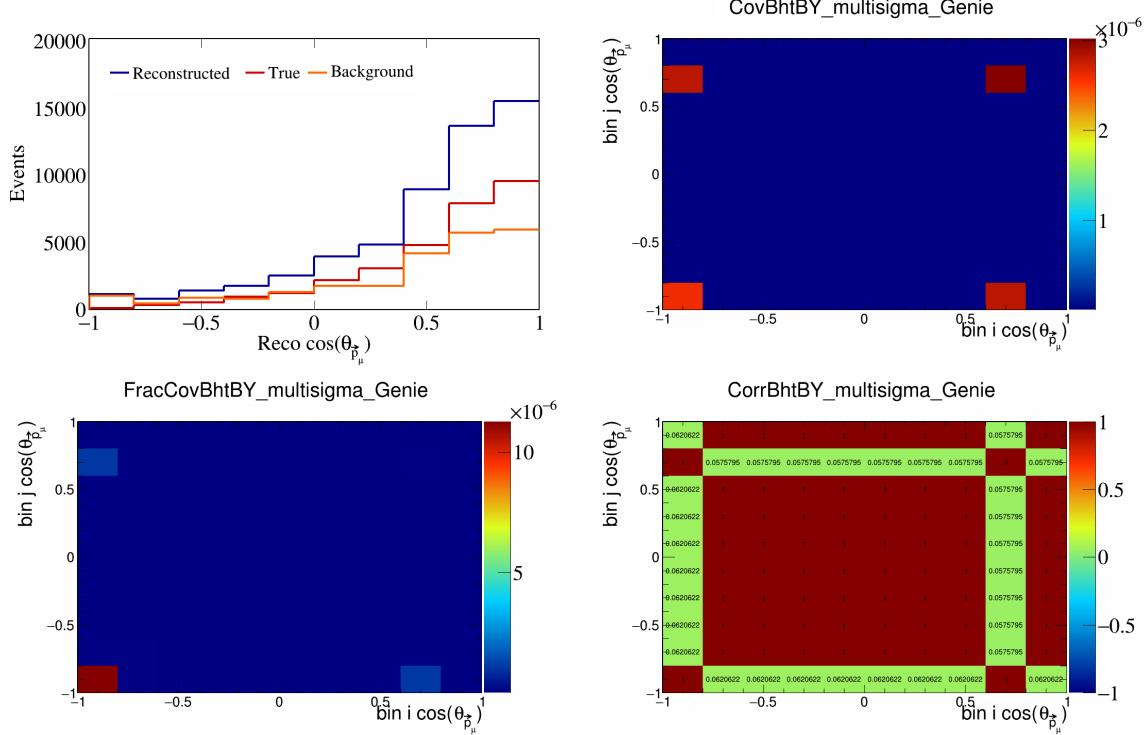


Figure 60: BhtBY variations for $\cos(\theta_{\vec{p}_\mu})$.

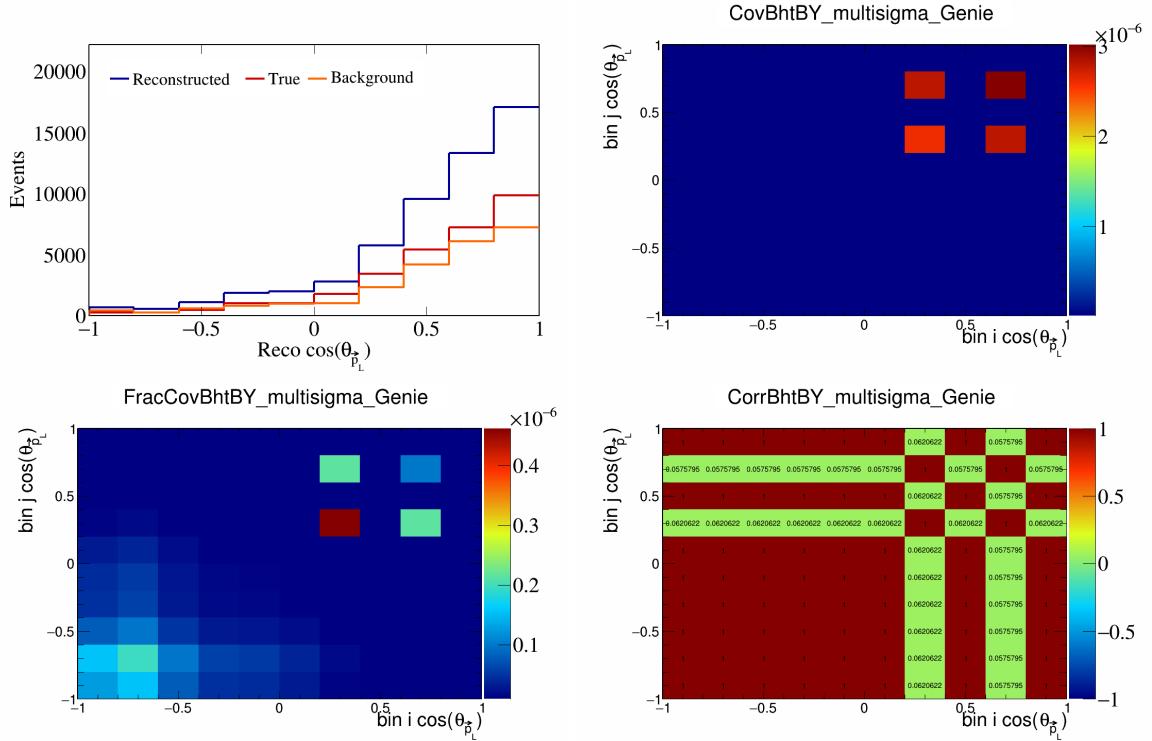


Figure 61: BhtBY variations for $\cos(\theta_{\vec{p}_L})$.

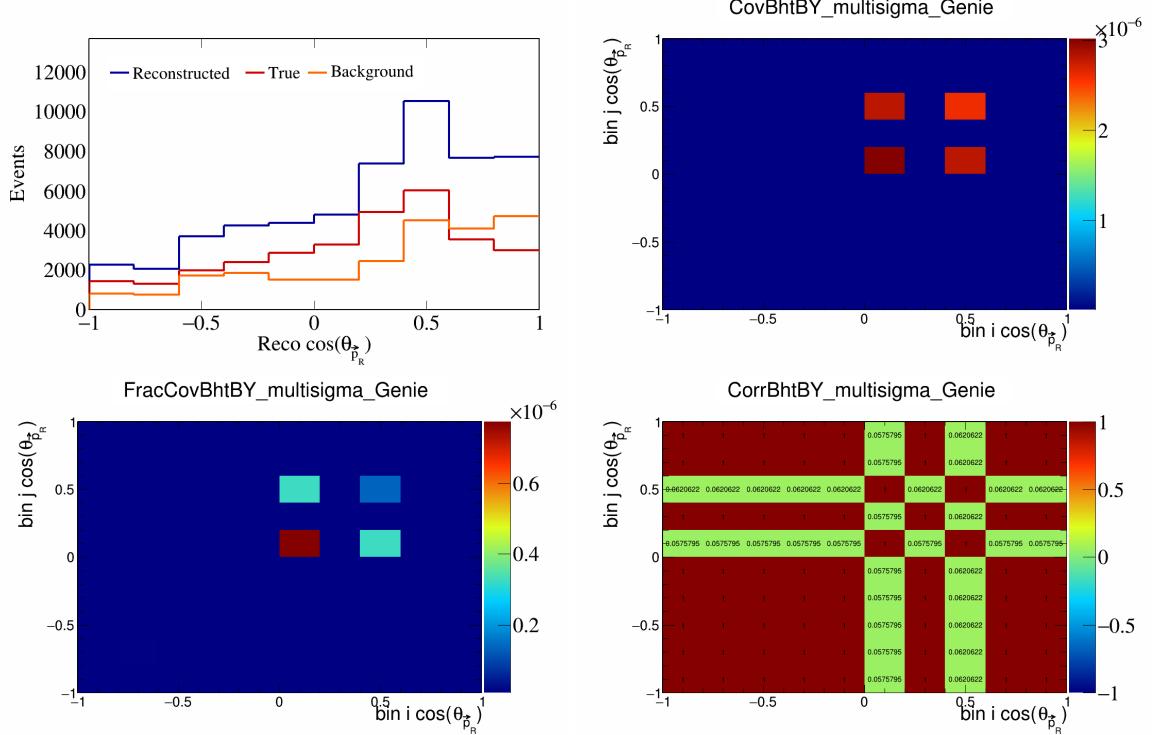


Figure 62: BhtBY variations for $\cos(\theta_{\vec{p}_R})$.

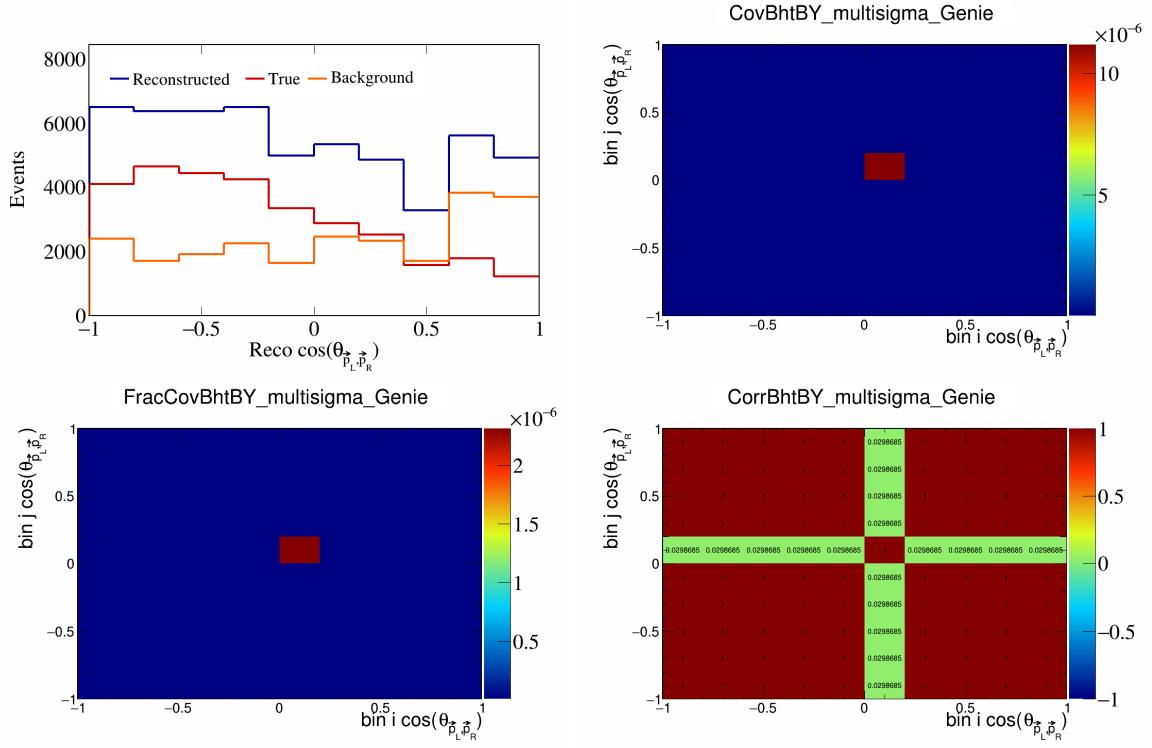


Figure 63: BhtBY variations for $\cos(\theta_{\vec{p}_L, \vec{p}_R})$.

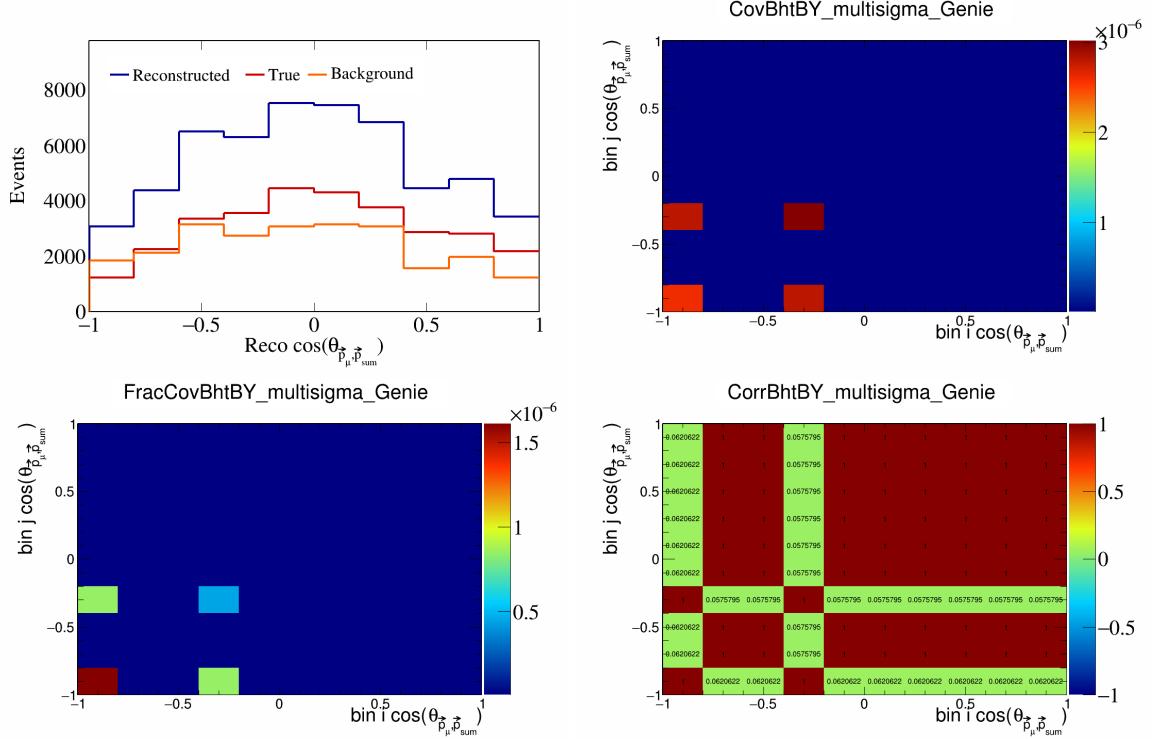


Figure 64: BhtBY variations for $\cos(\theta_{\vec{p}_\mu, \vec{p}_{\text{sum}}})$.

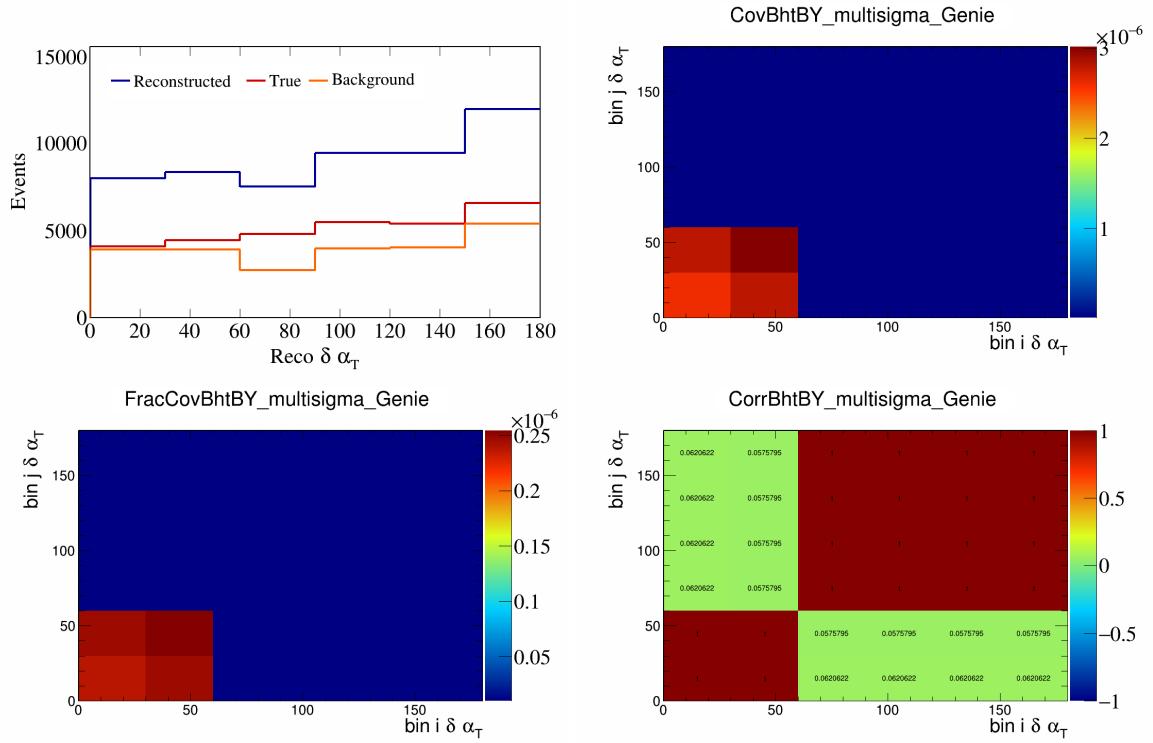


Figure 65: BhtBY variations for $\delta\alpha_T$.

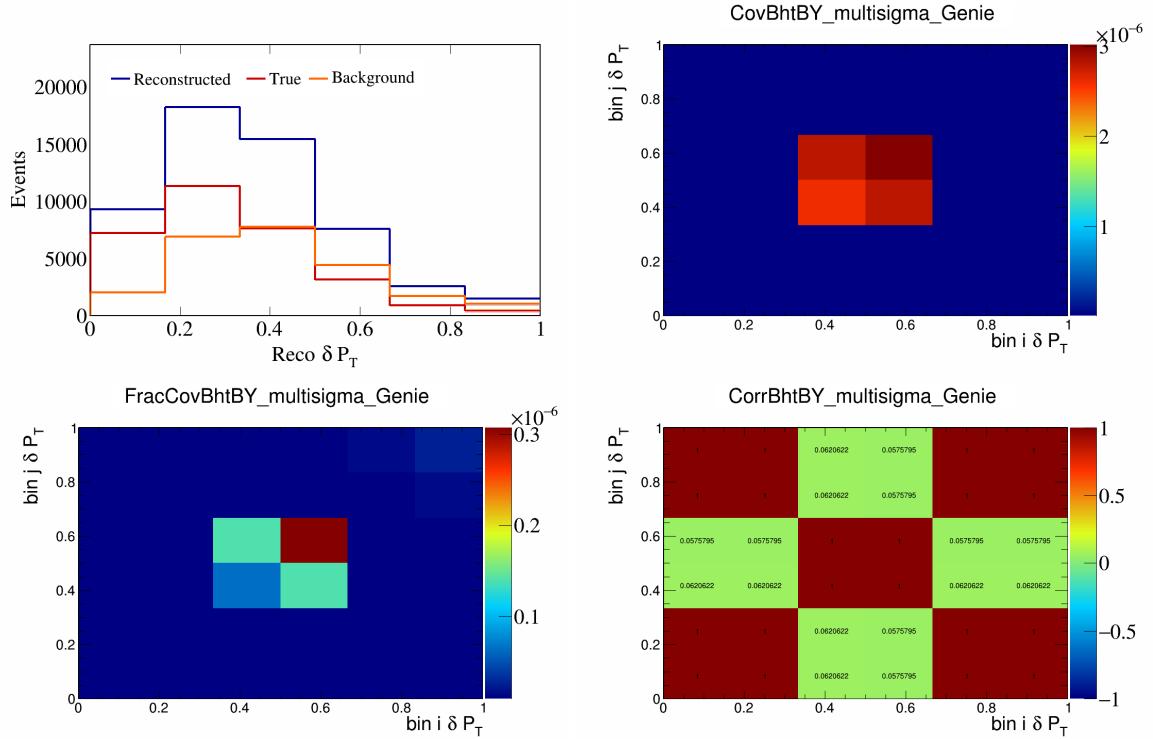


Figure 66: BhtBY variations for δP_T .

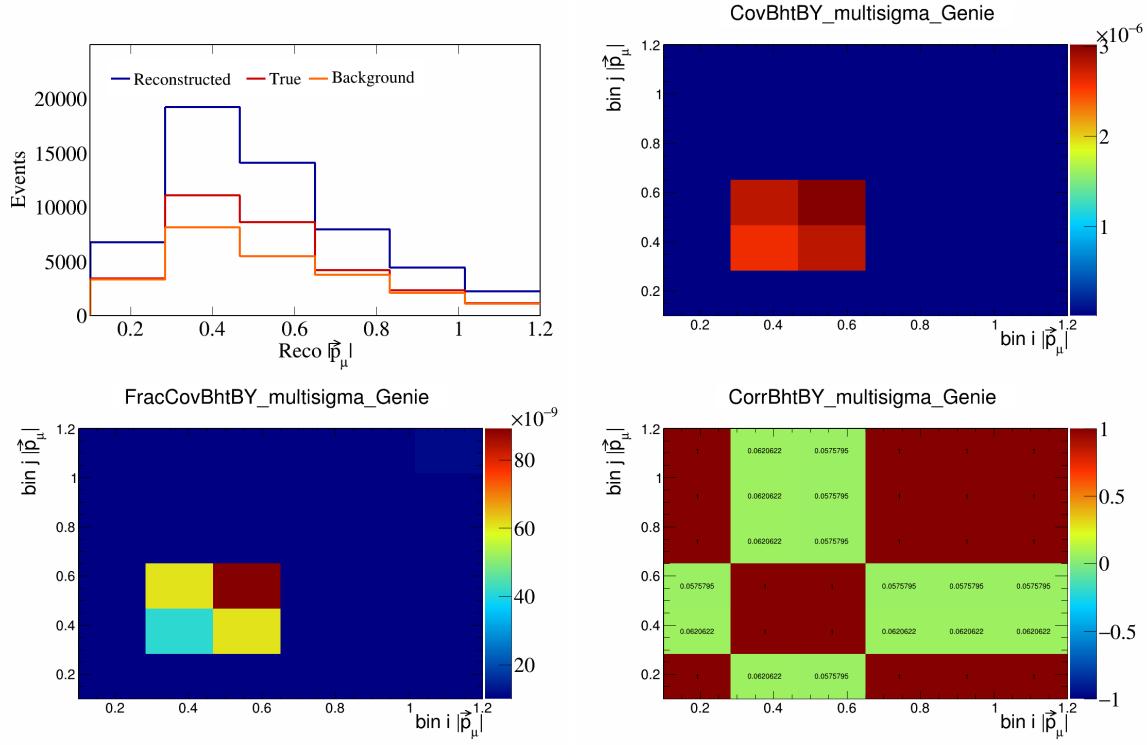


Figure 67: BhtBY variations for $|\vec{p}_\mu|$.

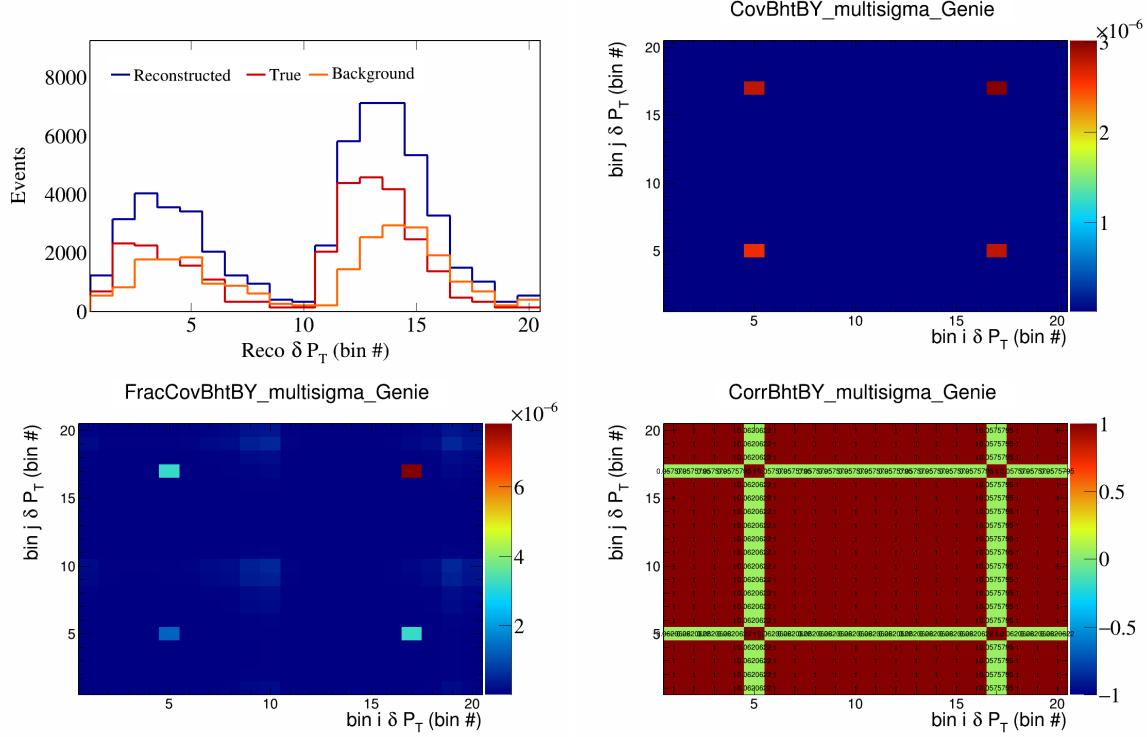


Figure 68: BhtBY variations for δP_T in $\cos(\theta_{\vec{p}_\mu})$.

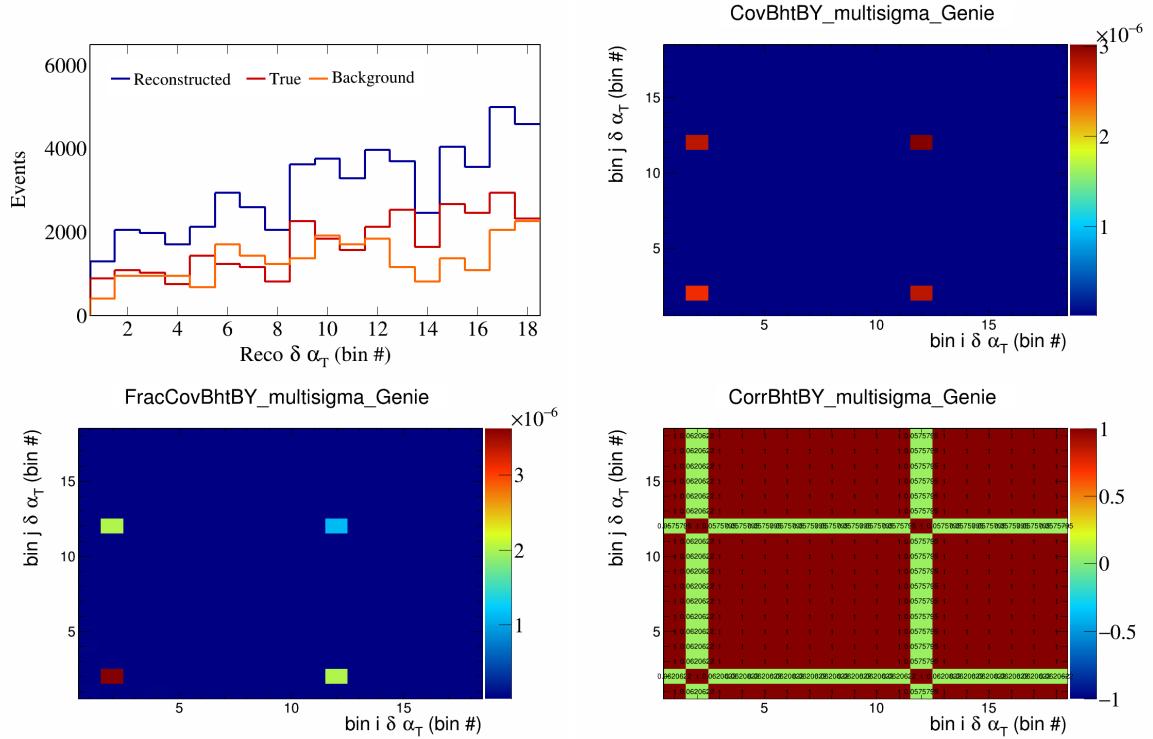


Figure 69: BhtBY variations for $\delta\alpha_T$ in $\cos(\theta_{\vec{p}_\mu})$.

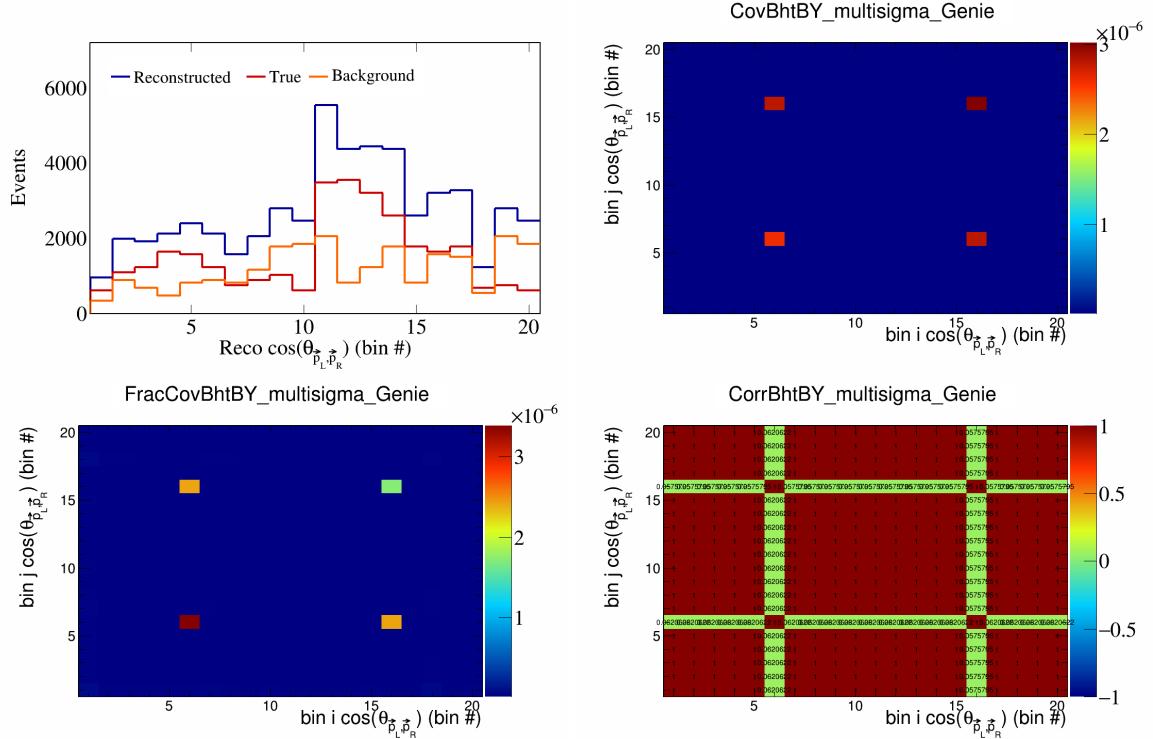


Figure 70: BhtBY variations for $\cos(\theta_{\vec{p}_L, \vec{p}_R})$ in $\cos(\theta_{\vec{p}_\mu})$.

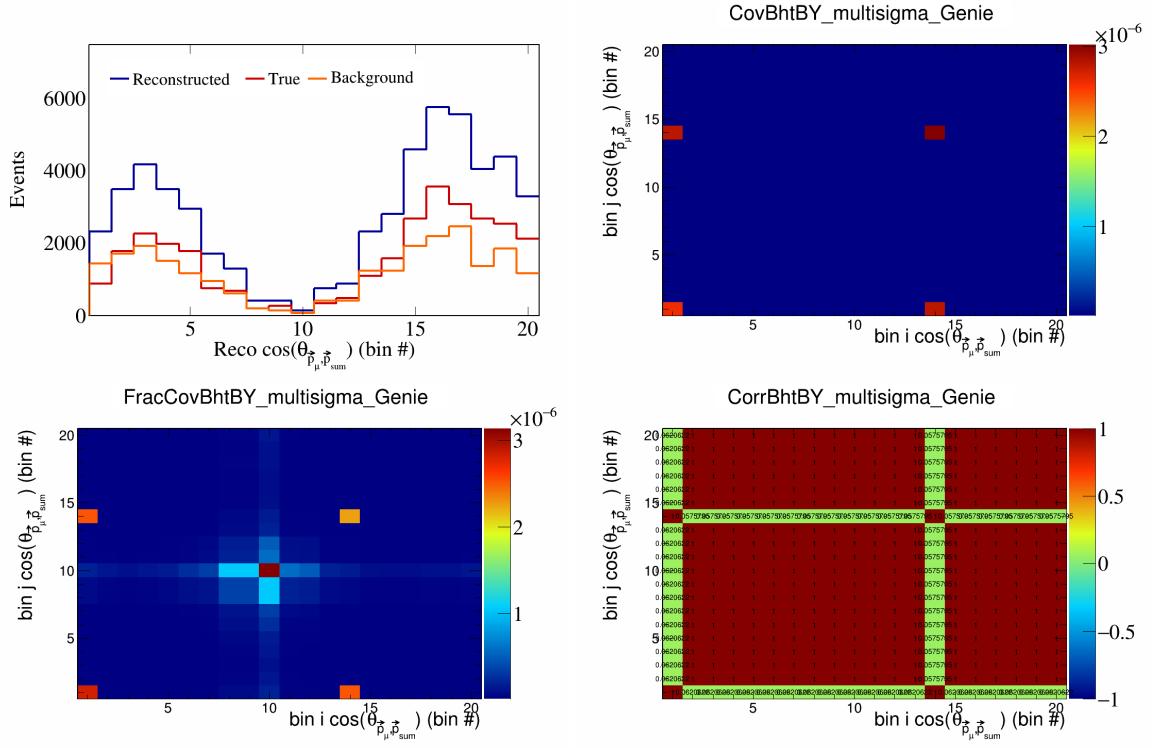


Figure 71: BhtBY variations for $\cos(\theta_{\vec{p}_\mu}^j)$ in $\cos(\theta_{\vec{p}_\mu}^i)$.

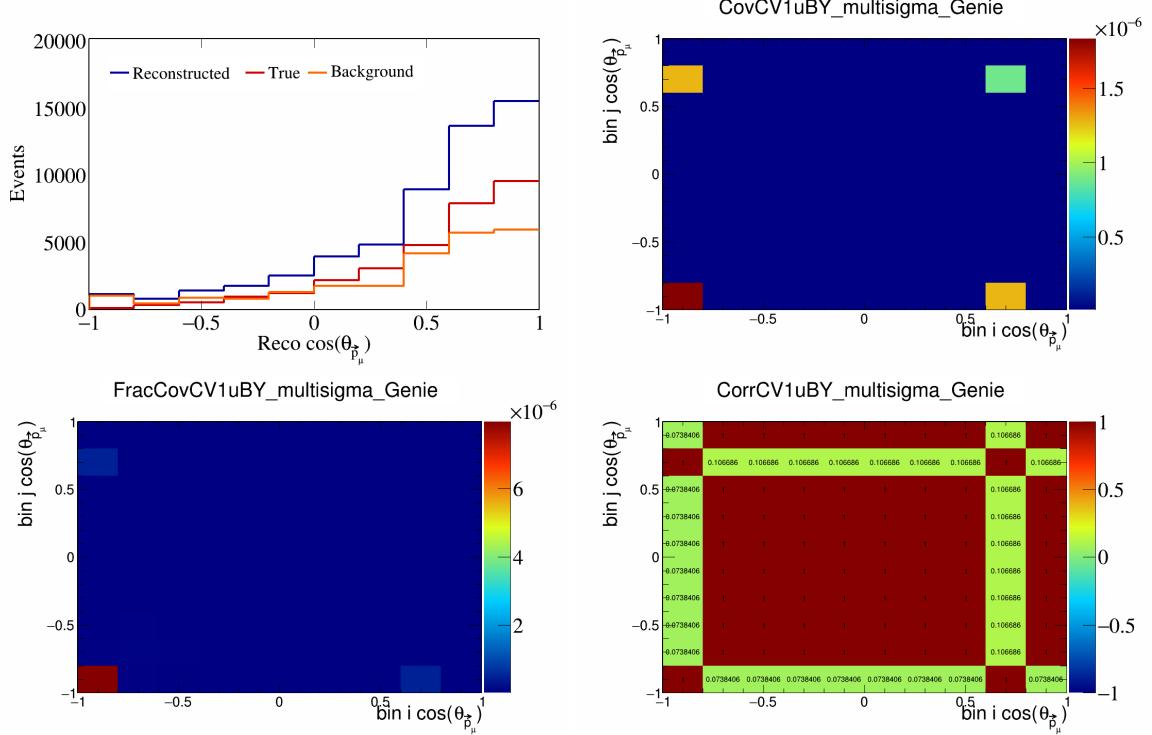


Figure 72: CV1uBY variations for $\cos(\theta_{\vec{p}_\mu}^j)$.

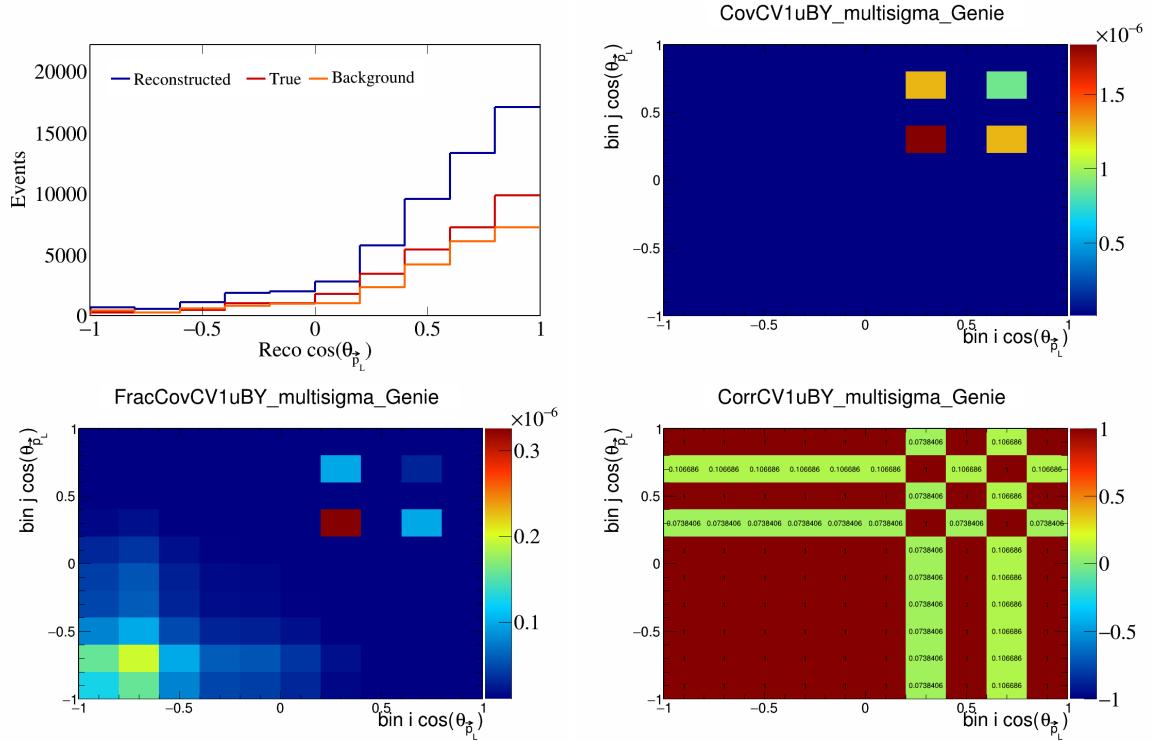


Figure 73: CV1uBY variations for $\cos(\theta_{\vec{p}_L})$.

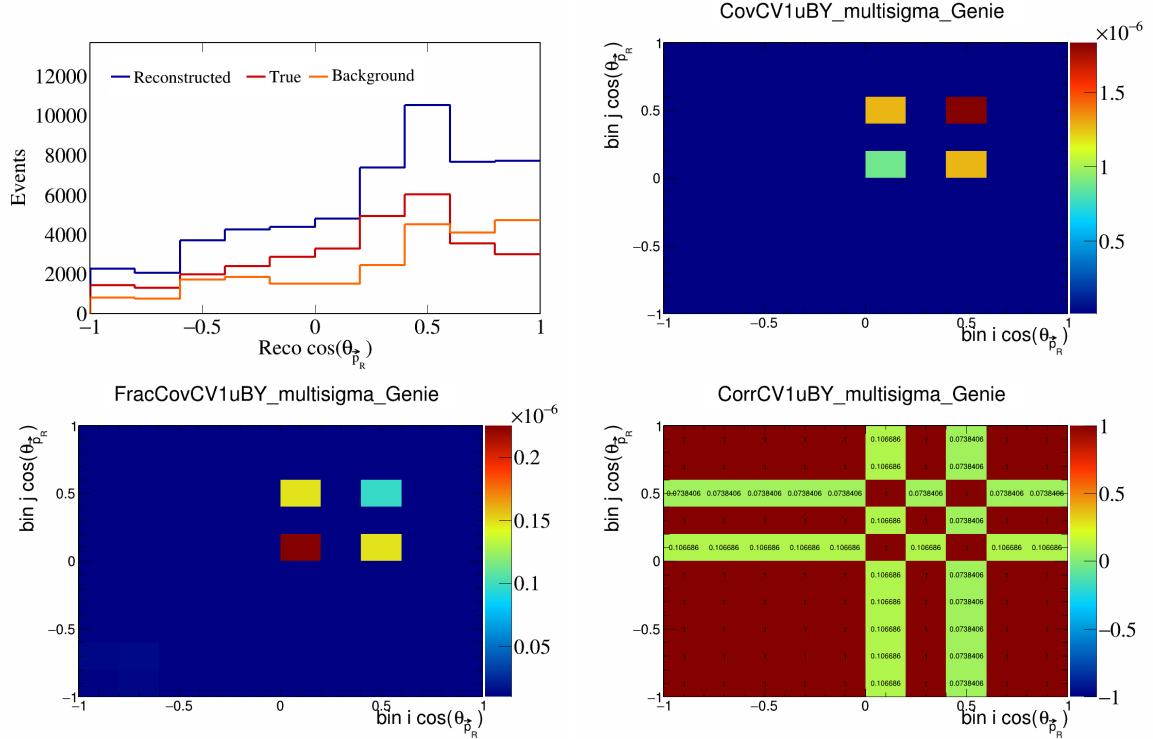


Figure 74: CV1uBY variations for $\cos(\theta_{\vec{p}_R})$.

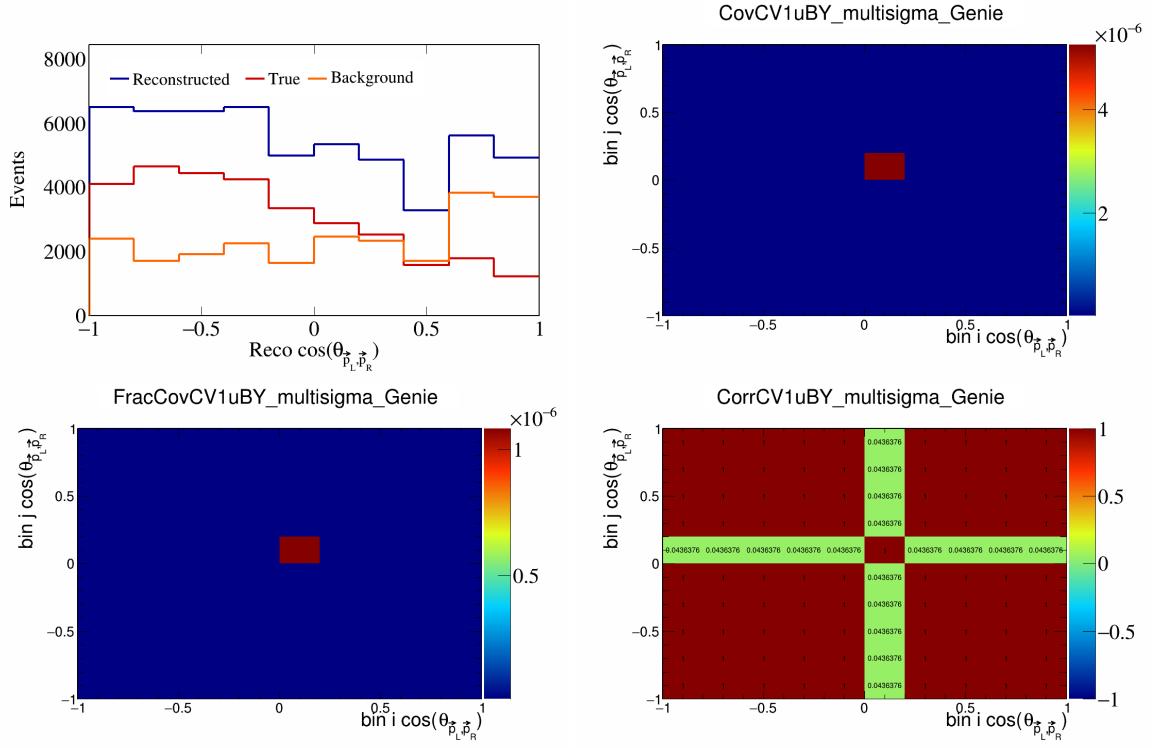


Figure 75: CV1uBY variations for $\cos(\theta_{\vec{p}_L, \vec{p}_R})$.

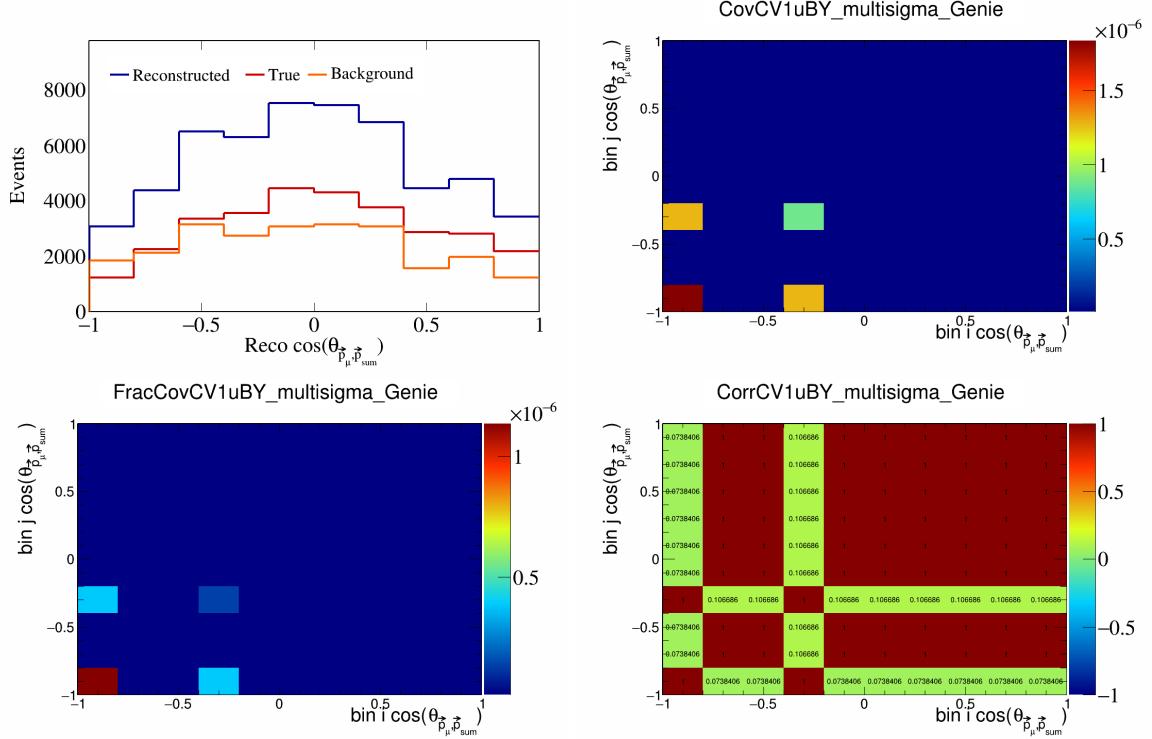


Figure 76: CV1uBY variations for $\cos(\theta_{\vec{p}_\mu, \vec{p}_{\text{sum}}})$.

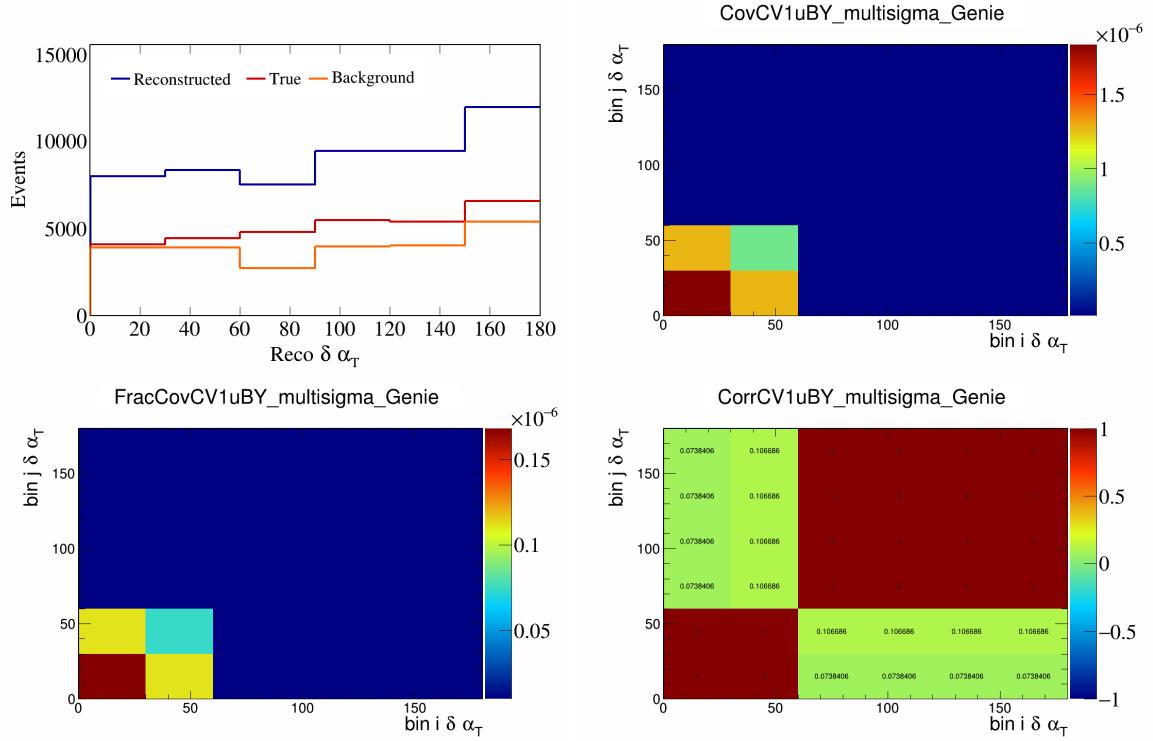


Figure 77: CV1uBY variations for $\delta\alpha_T$.

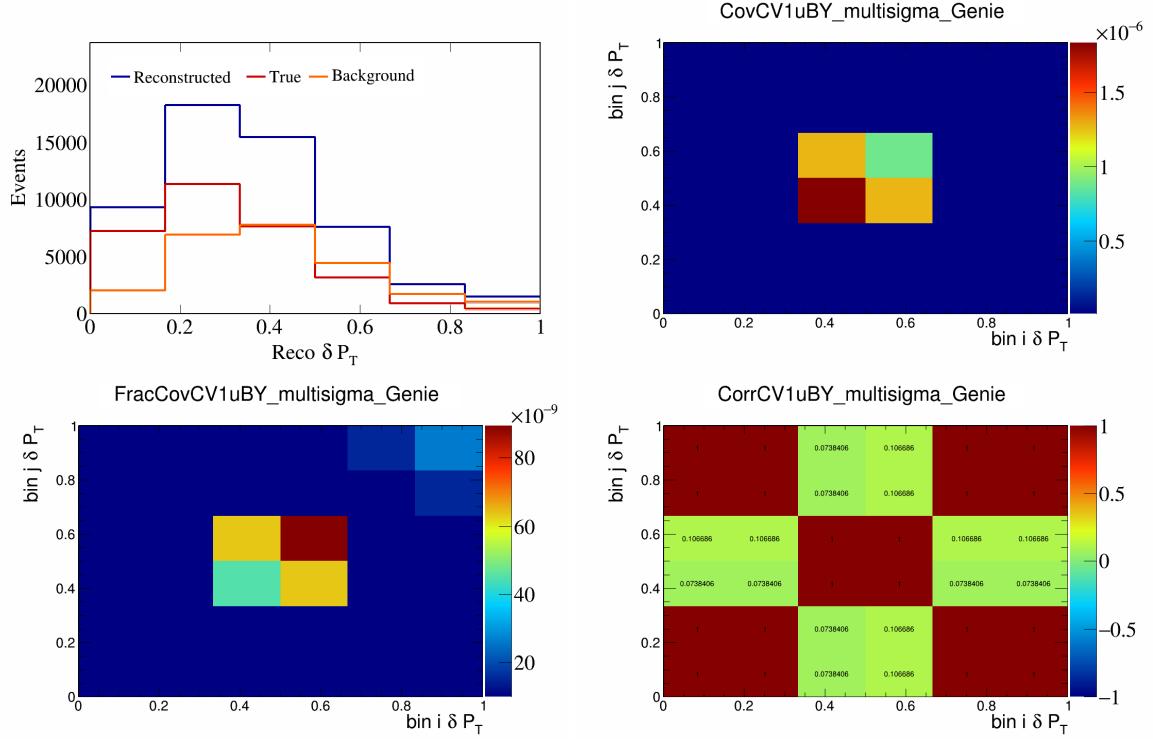


Figure 78: CV1uBY variations for δP_T .

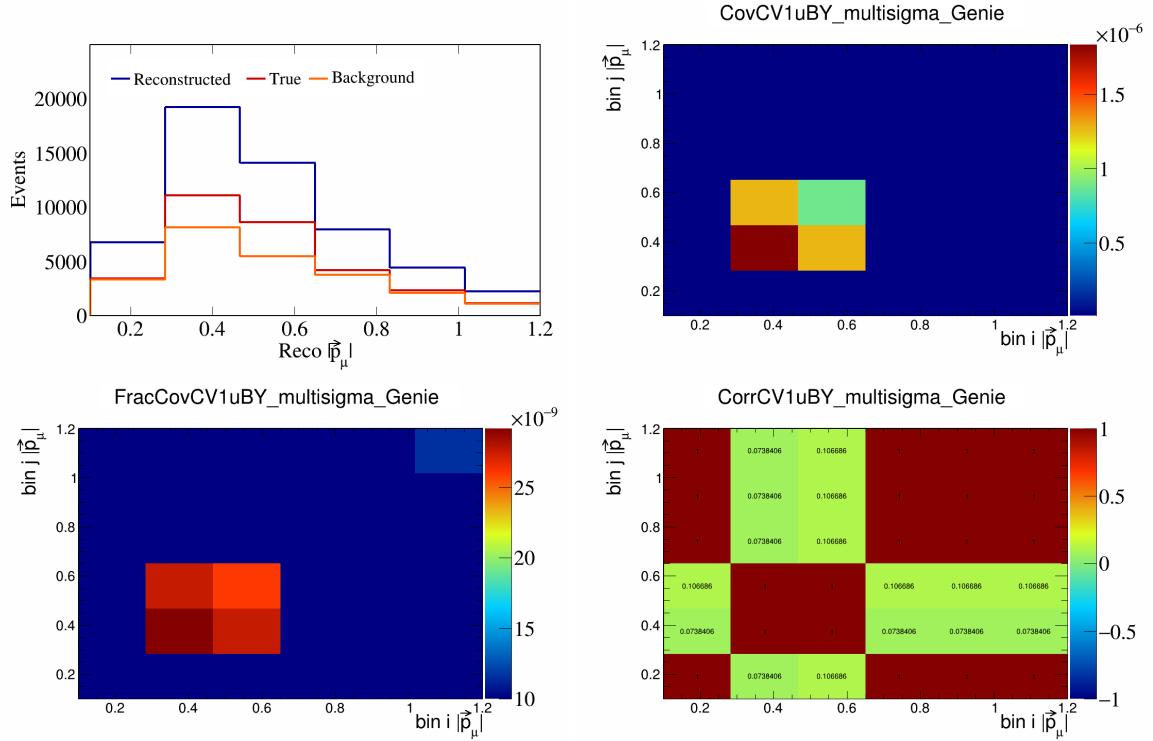


Figure 79: CV1uBY variations for $|\vec{p}_\mu|$.

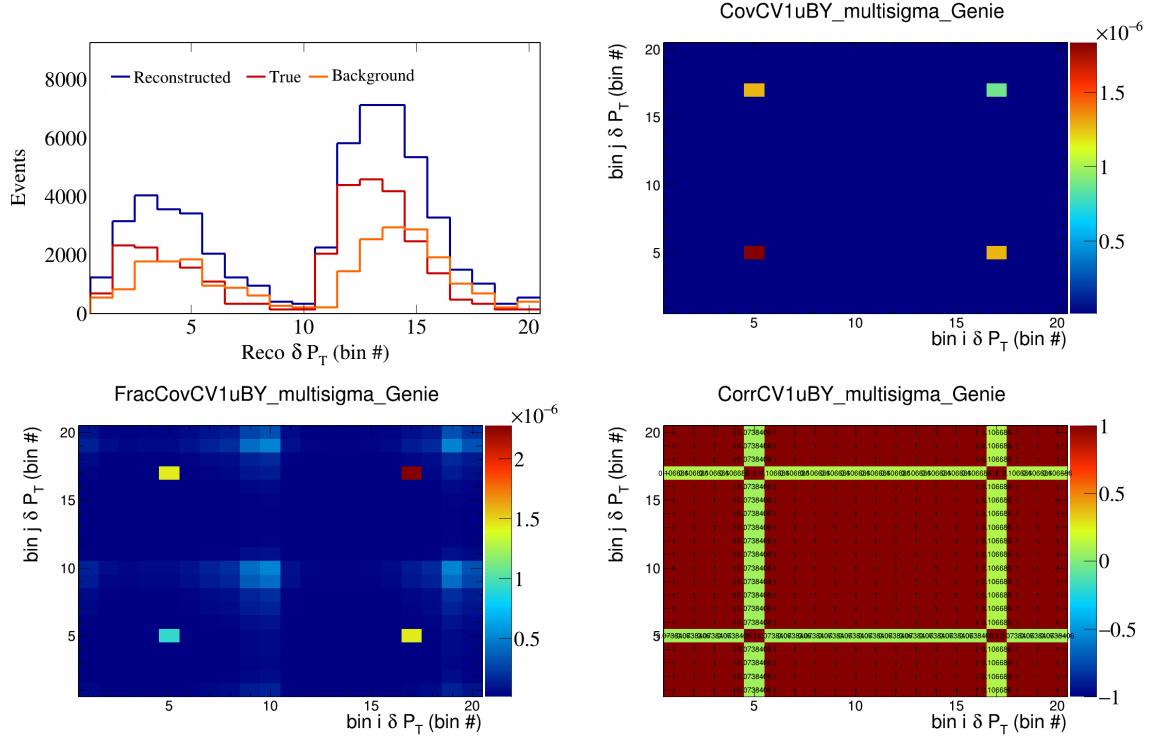


Figure 80: CV1uBY variations for δP_T in $\cos(\theta_{\vec{p}_\mu})$.

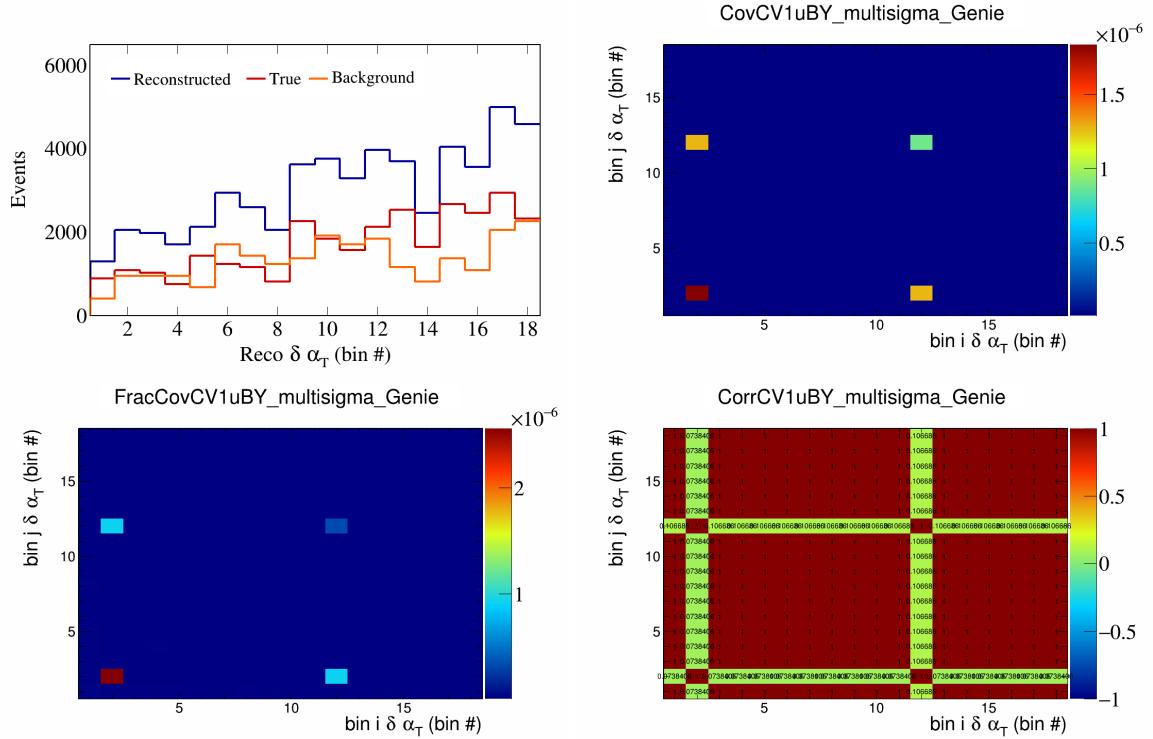


Figure 81: CV1uBY variations for $\delta\alpha_T$ in $\cos(\theta_{\vec{p}_\mu})$.

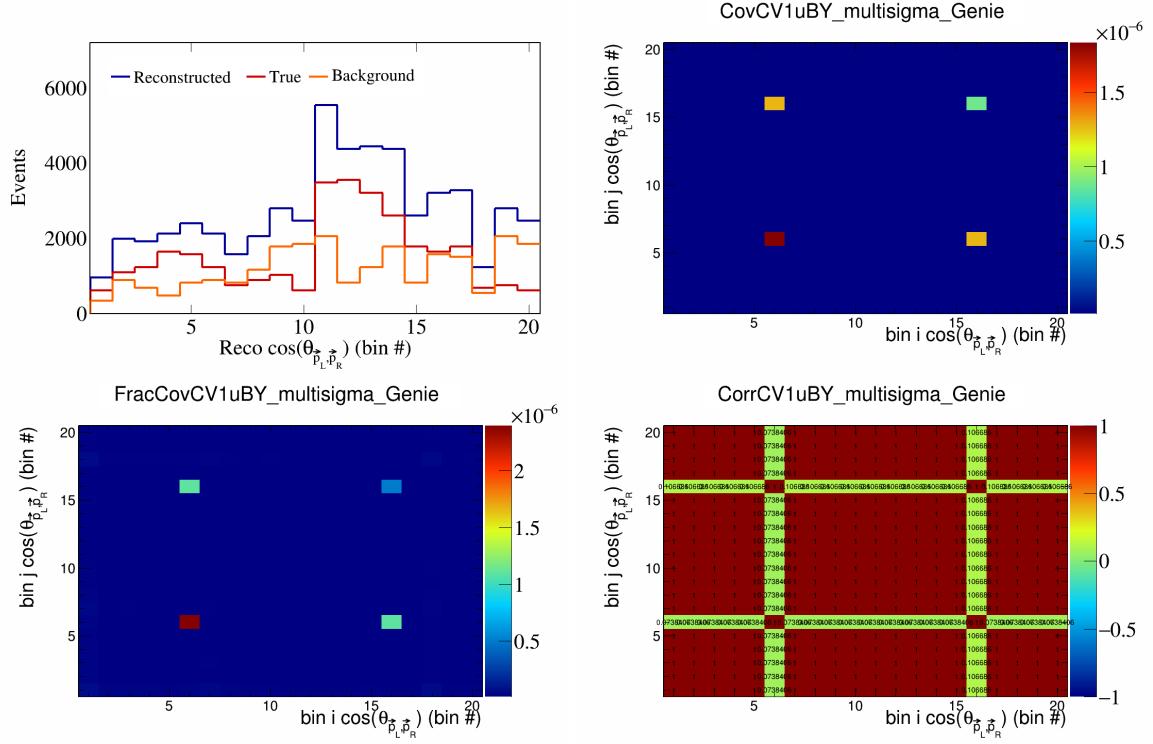


Figure 82: CV1uBY variations for $\cos(\theta_{\vec{p}_L, \vec{p}_R})$ in $\cos(\theta_{\vec{p}_\mu})$.

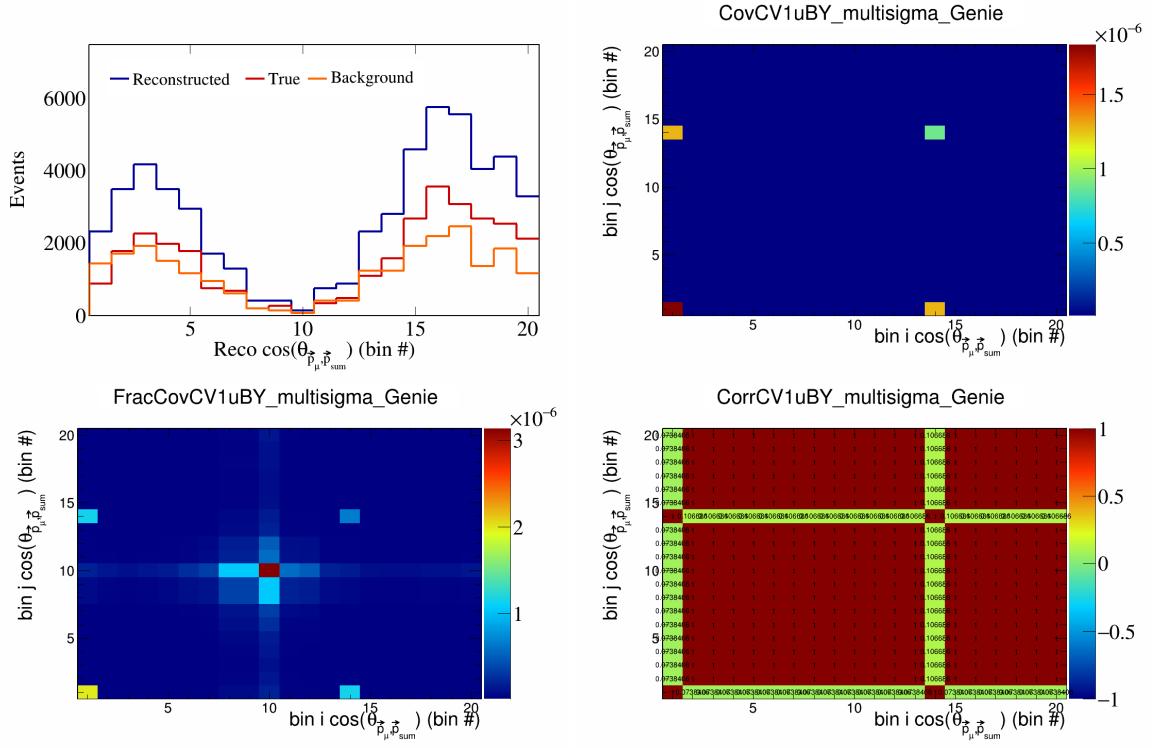


Figure 83: CV1uBY variations for $\cos(\theta_{\vec{p}_\mu, \vec{p}_{\text{sum}}})$ in $\cos(\theta_{\vec{p}_\mu})$.

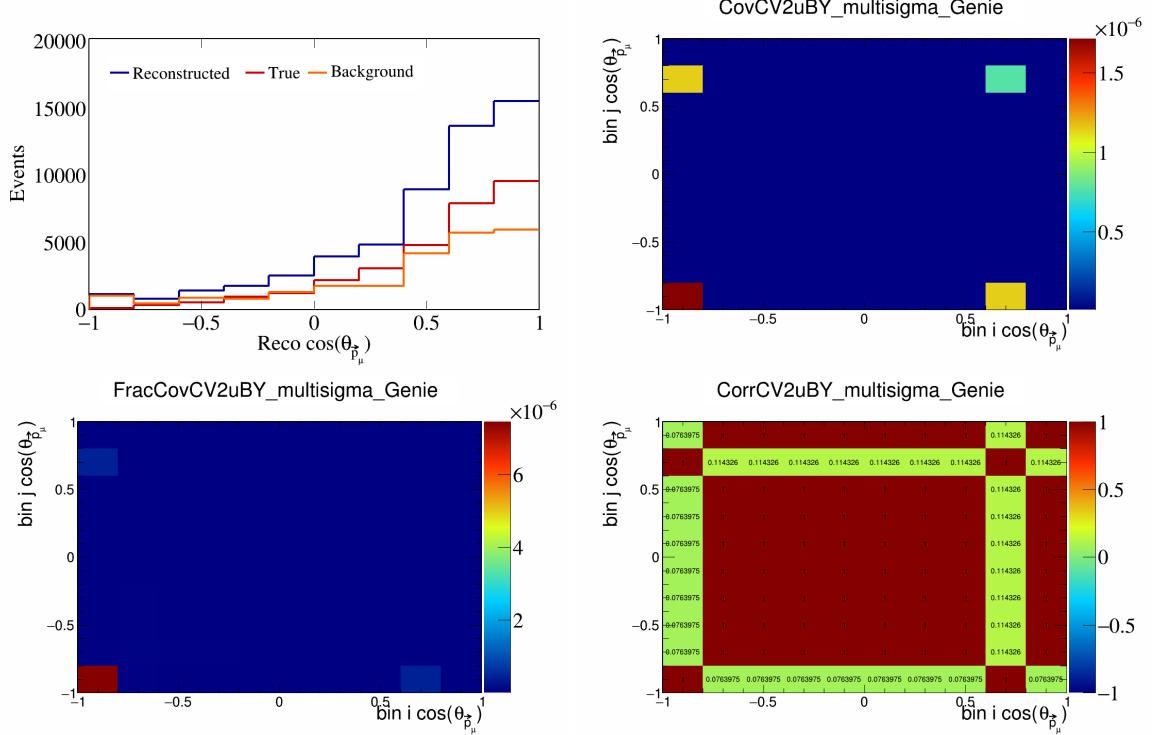


Figure 84: CV2uBY variations for $\cos(\theta_{\vec{p}_\mu})$.

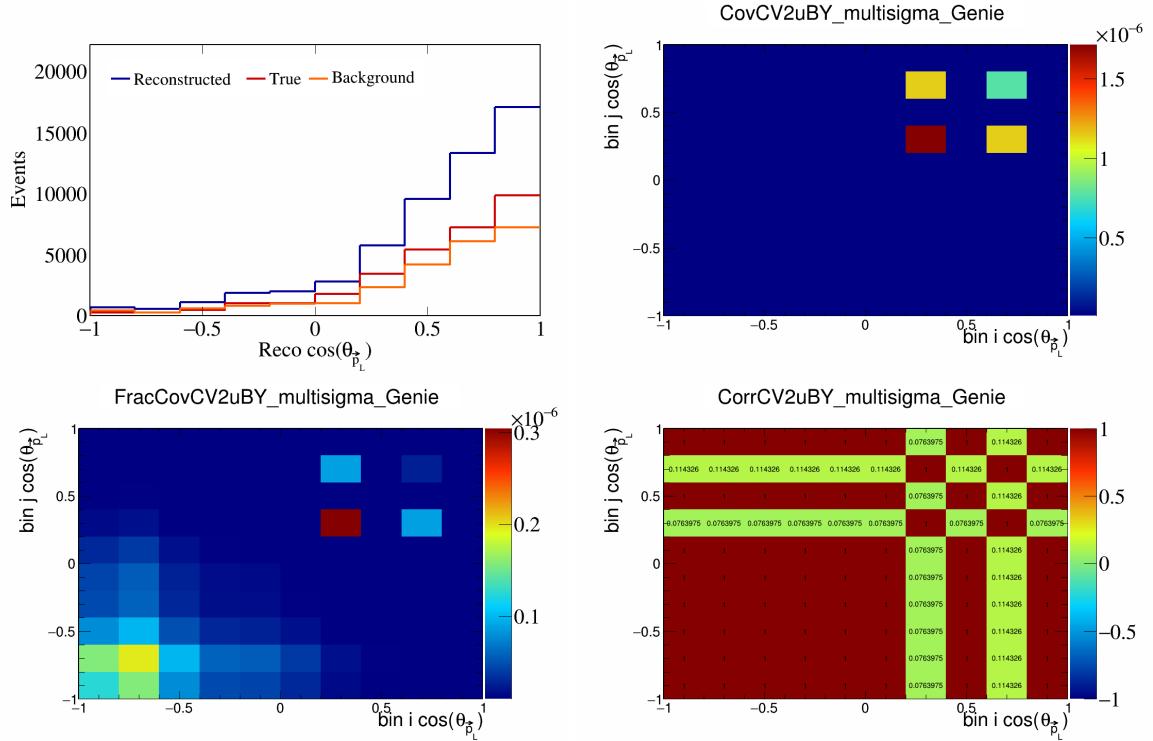


Figure 85: CV2uBY variations for $\cos(\theta_{\vec{p}_L})$.

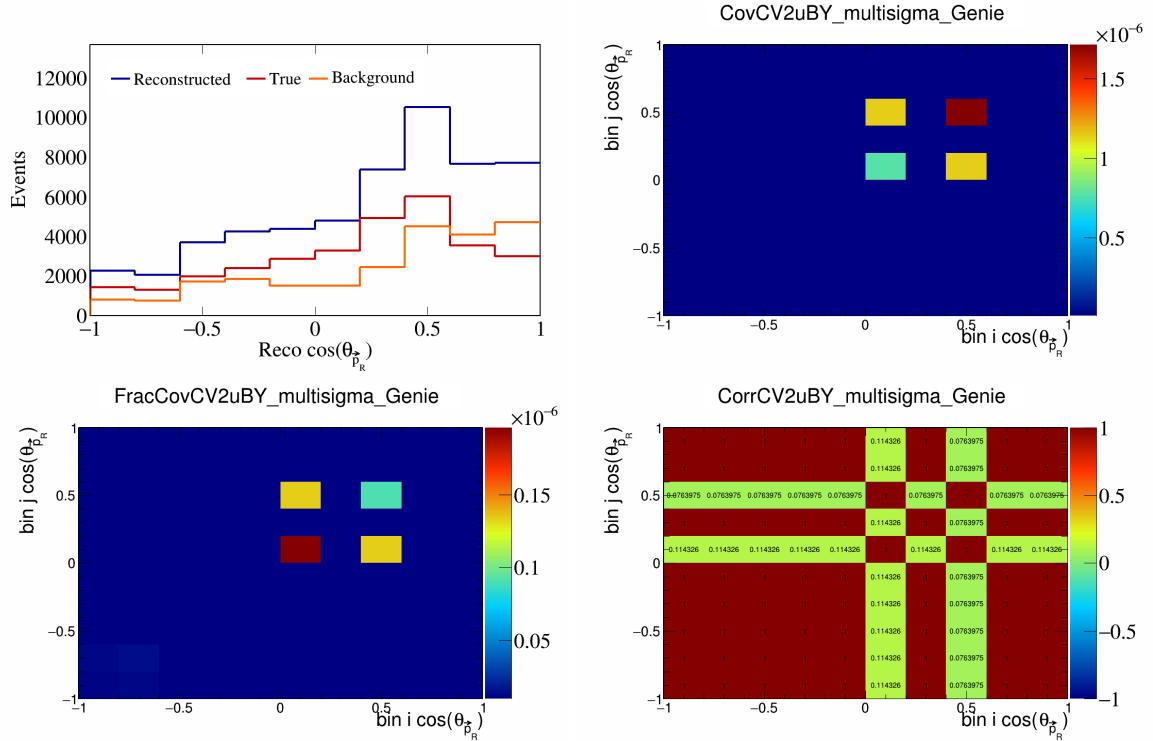


Figure 86: CV2uBY variations for $\cos(\theta_{\vec{p}_R})$.

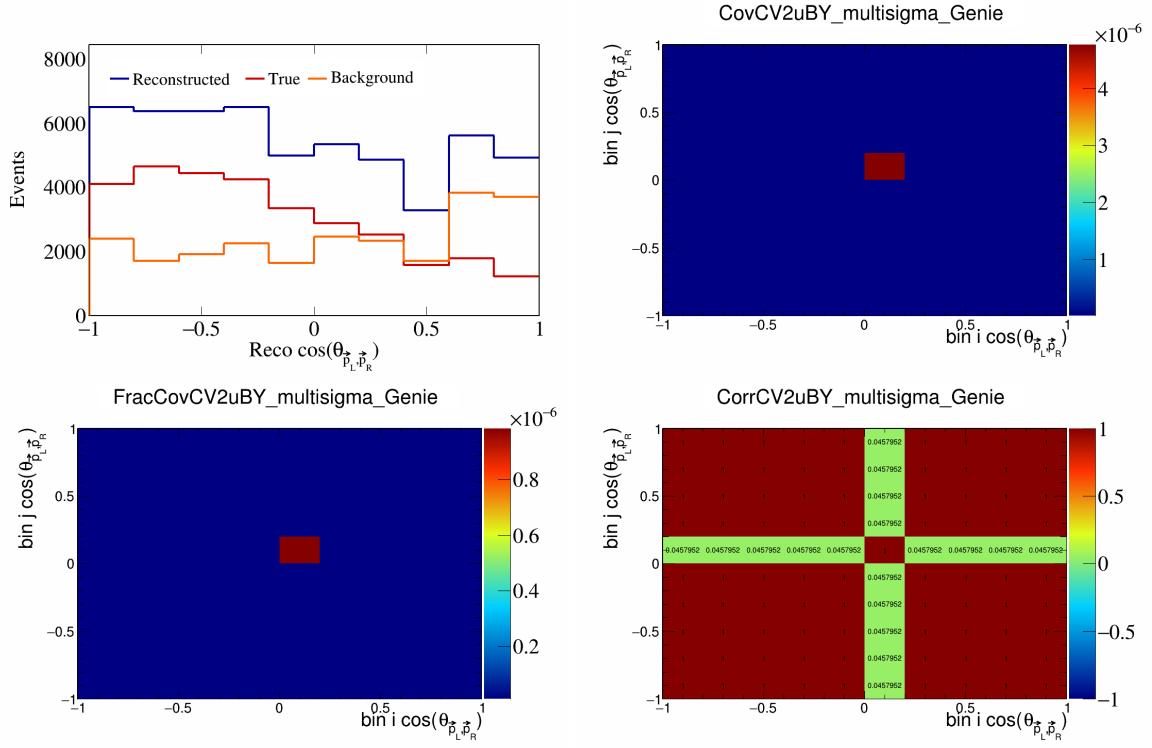


Figure 87: CV2uBY variations for $\cos(\theta_{\vec{p}_L, \vec{p}_R})$.

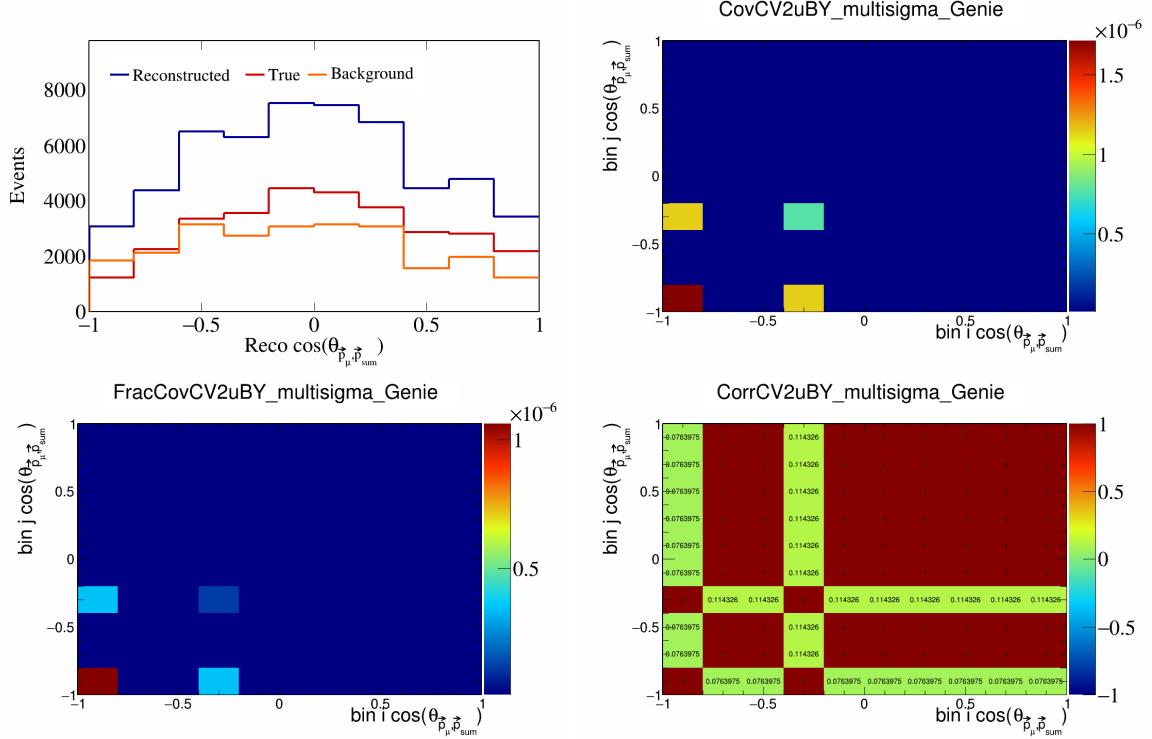


Figure 88: CV2uBY variations for $\cos(\theta_{\vec{p}_\mu, \vec{p}_{\text{sum}}})$.

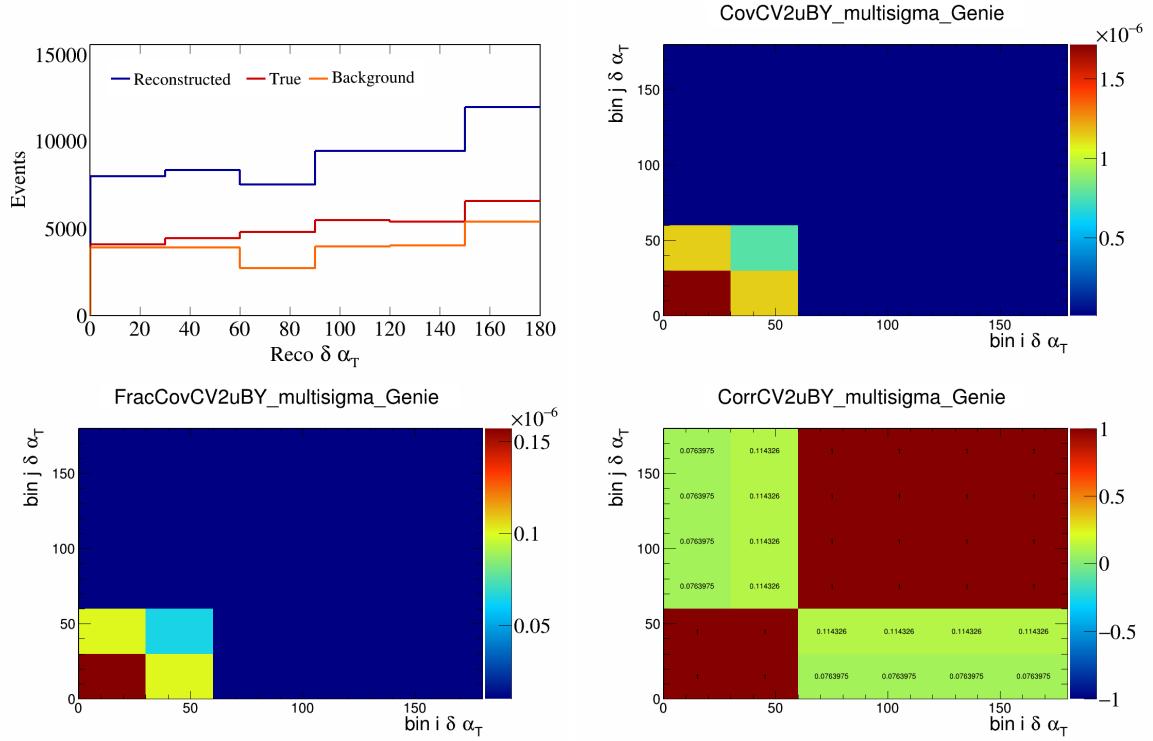


Figure 89: CV2uBY variations for $\delta\alpha_T$.

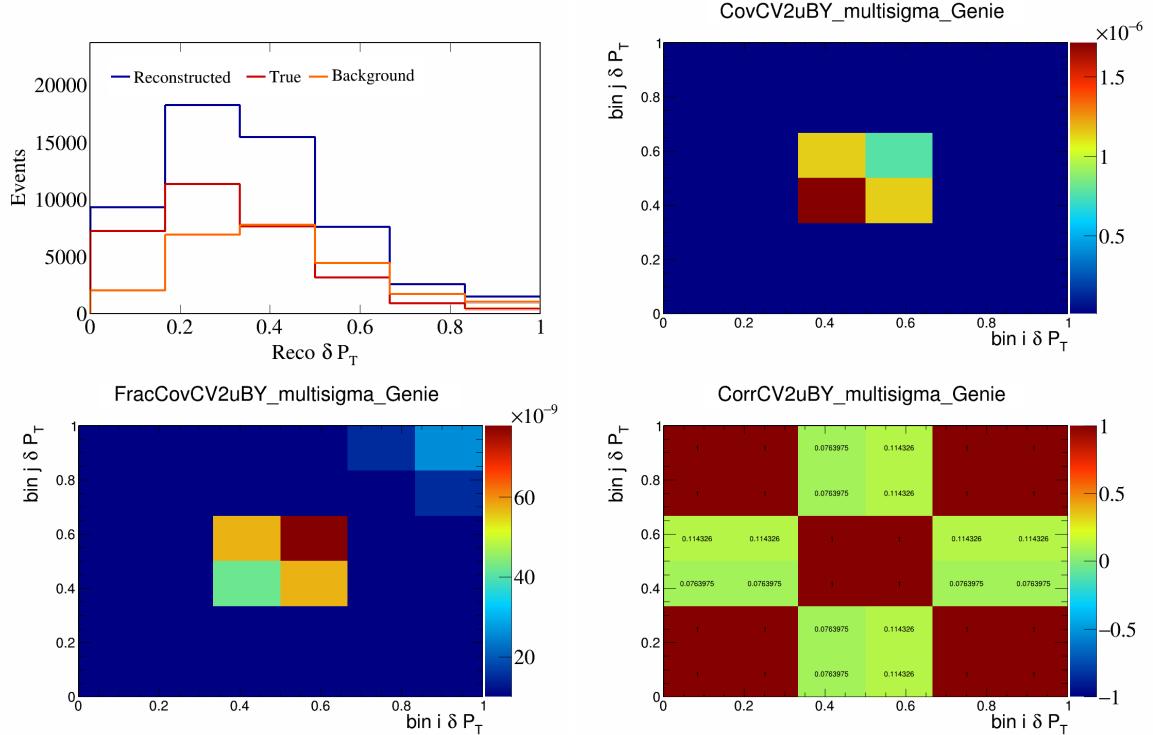


Figure 90: CV2uBY variations for δP_T .

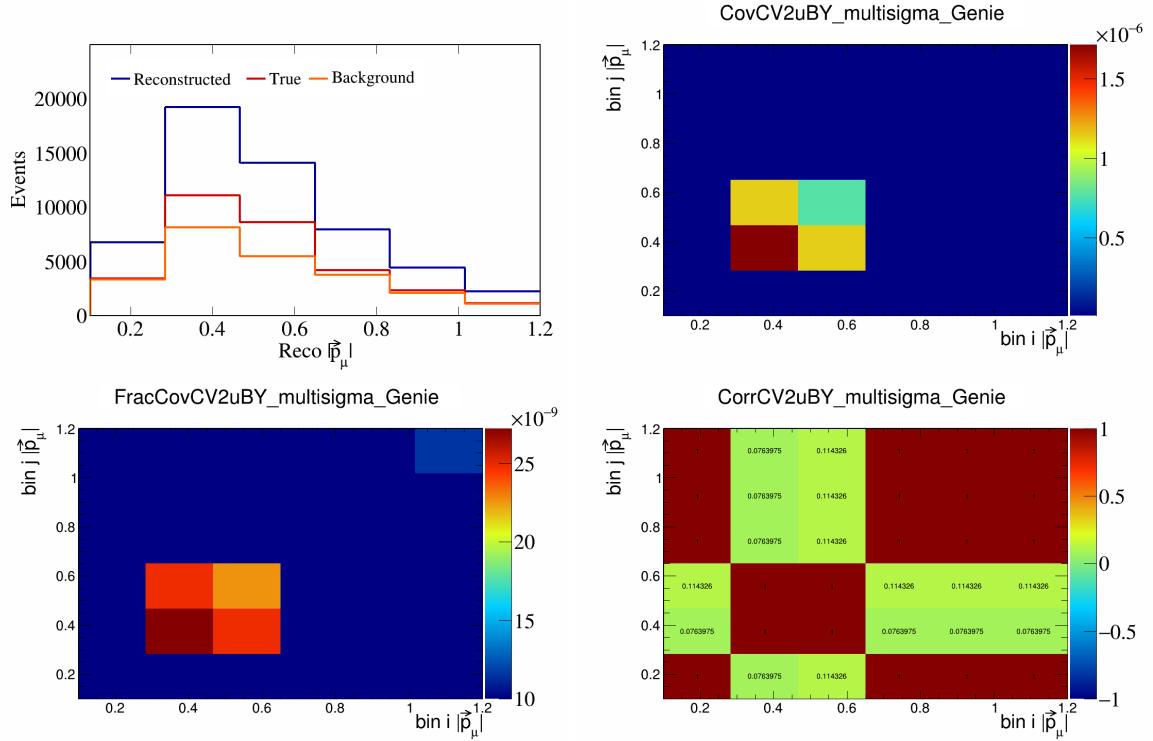


Figure 91: CV2uBY variations for $|\vec{p}_\mu|$.

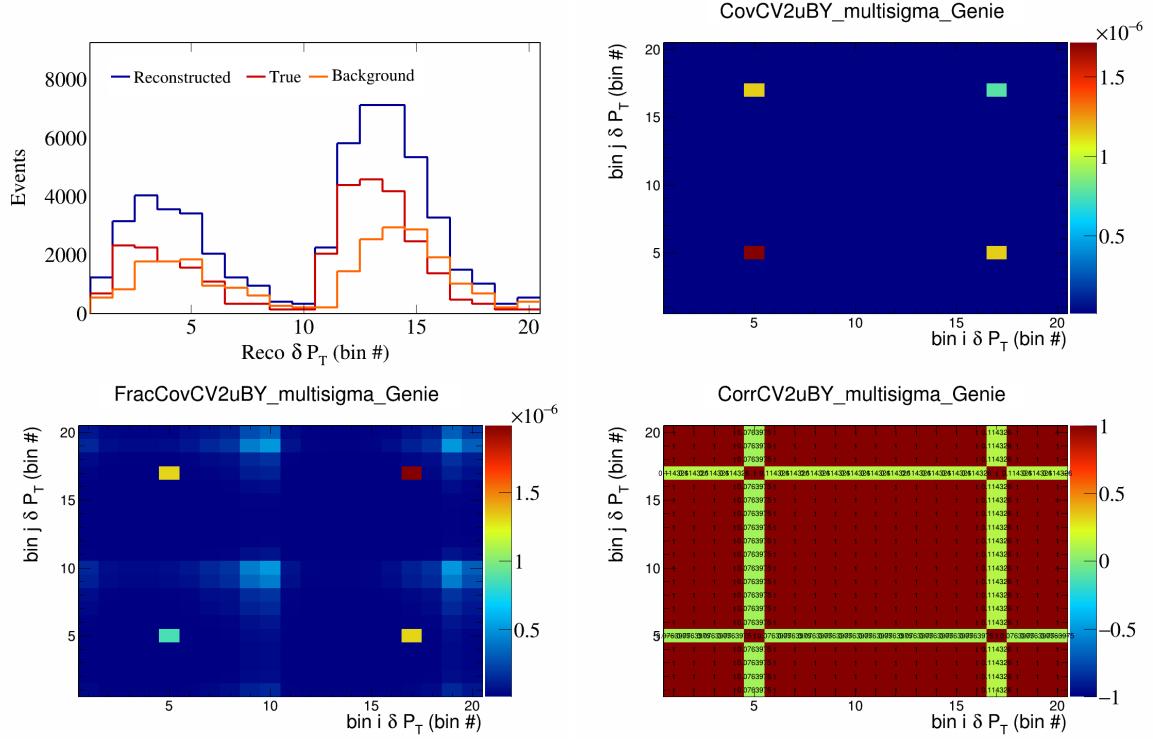


Figure 92: CV2uBY variations for δP_T in $\cos(\theta_{\vec{p}_\mu})$.

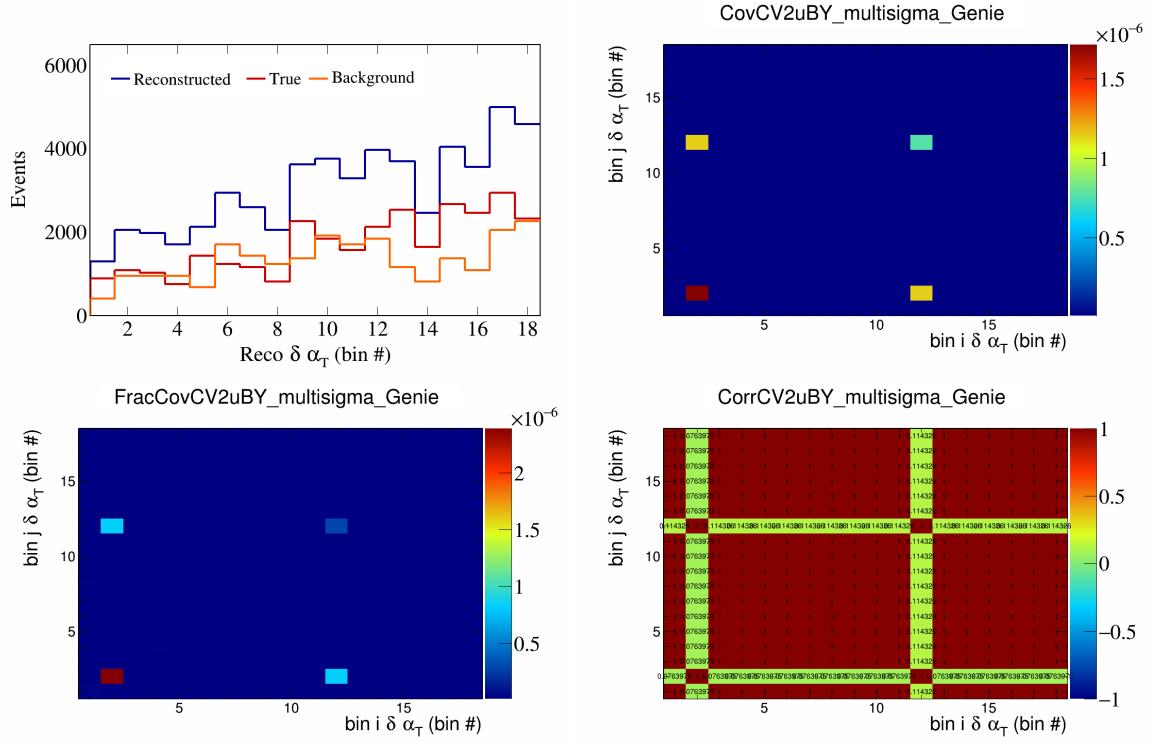


Figure 93: CV2uBY variations for $\delta\alpha_T$ in $\cos(\theta_{\vec{p}_\mu})$.

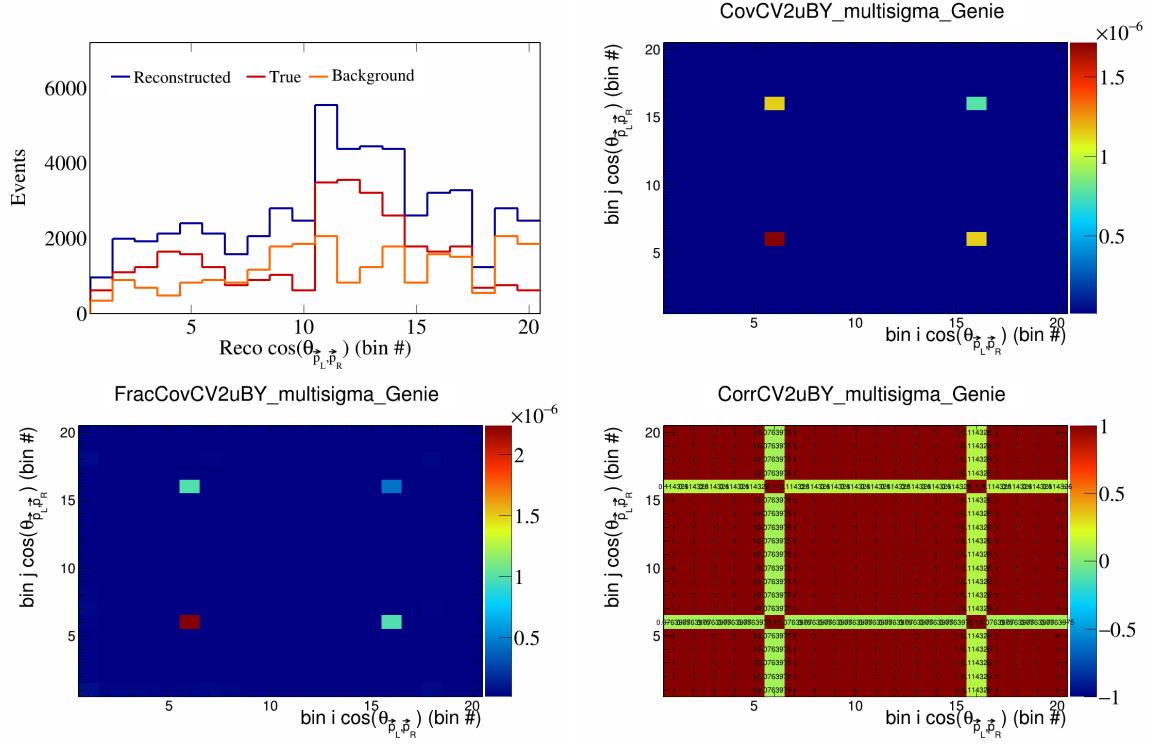


Figure 94: CV2uBY variations for $\cos(\theta_{\vec{p}_L, \vec{p}_R})$ in $\cos(\theta_{\vec{p}_\mu})$.

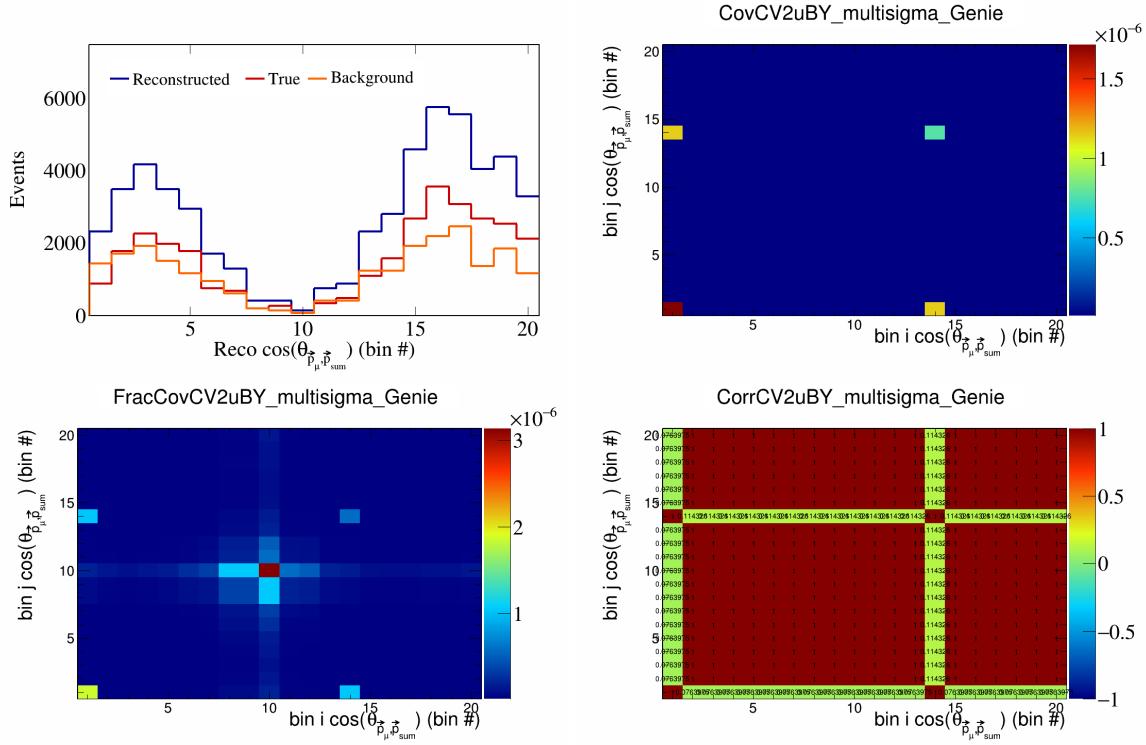


Figure 95: CV2uBY variations for $\cos(\theta_{\vec{p}_\mu}^j)$ in $\cos(\theta_{\vec{p}_\mu}^i)$.

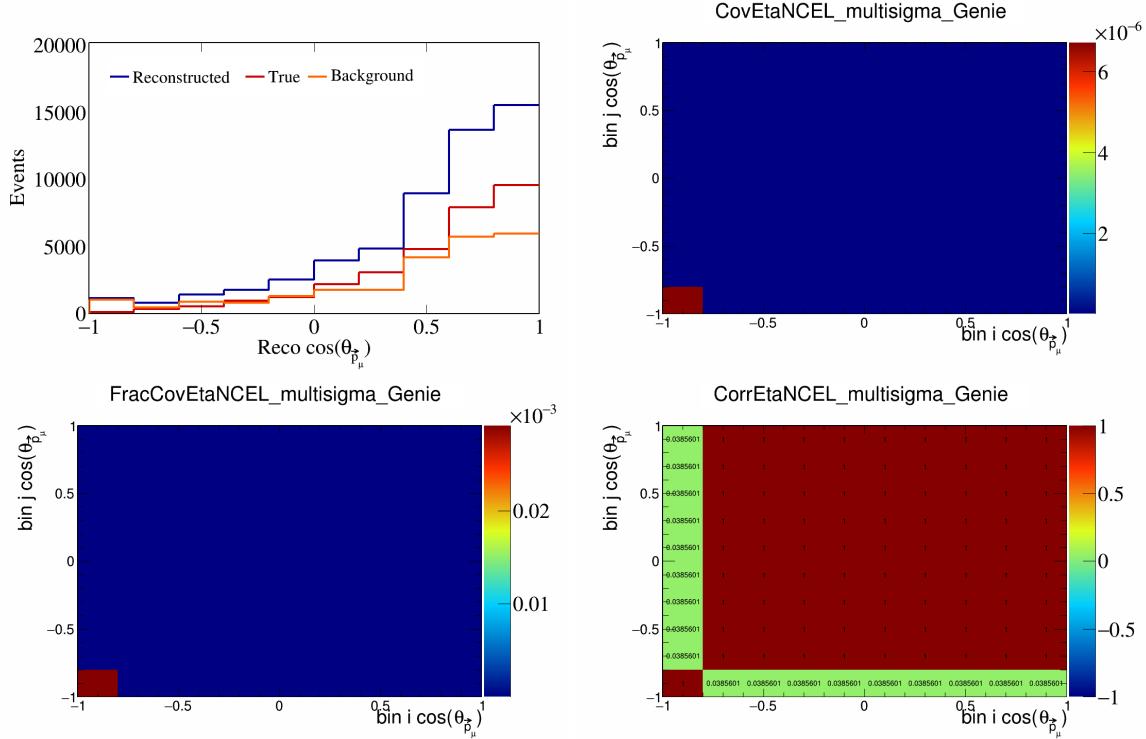


Figure 96: EtaNCEL variations for $\cos(\theta_{\vec{p}_\mu}^j)$ in $\cos(\theta_{\vec{p}_\mu}^i)$.

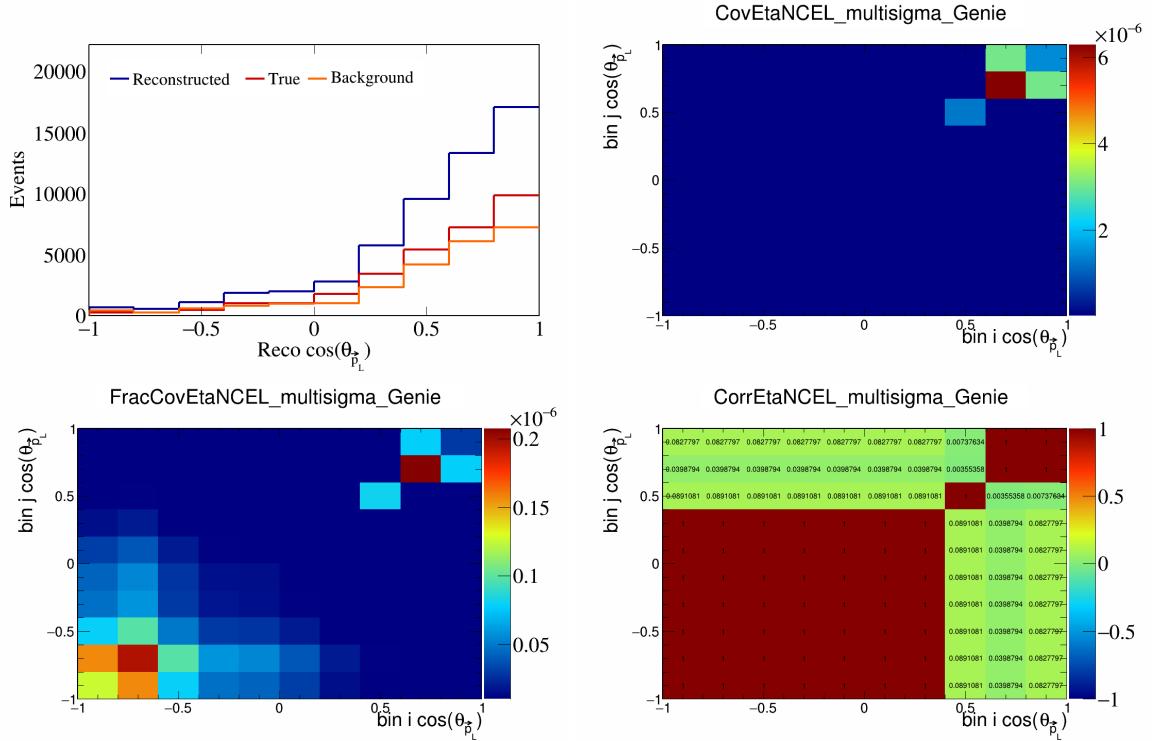


Figure 97: EtaNCEL variations for $\cos(\theta_{\vec{p}_L})$.

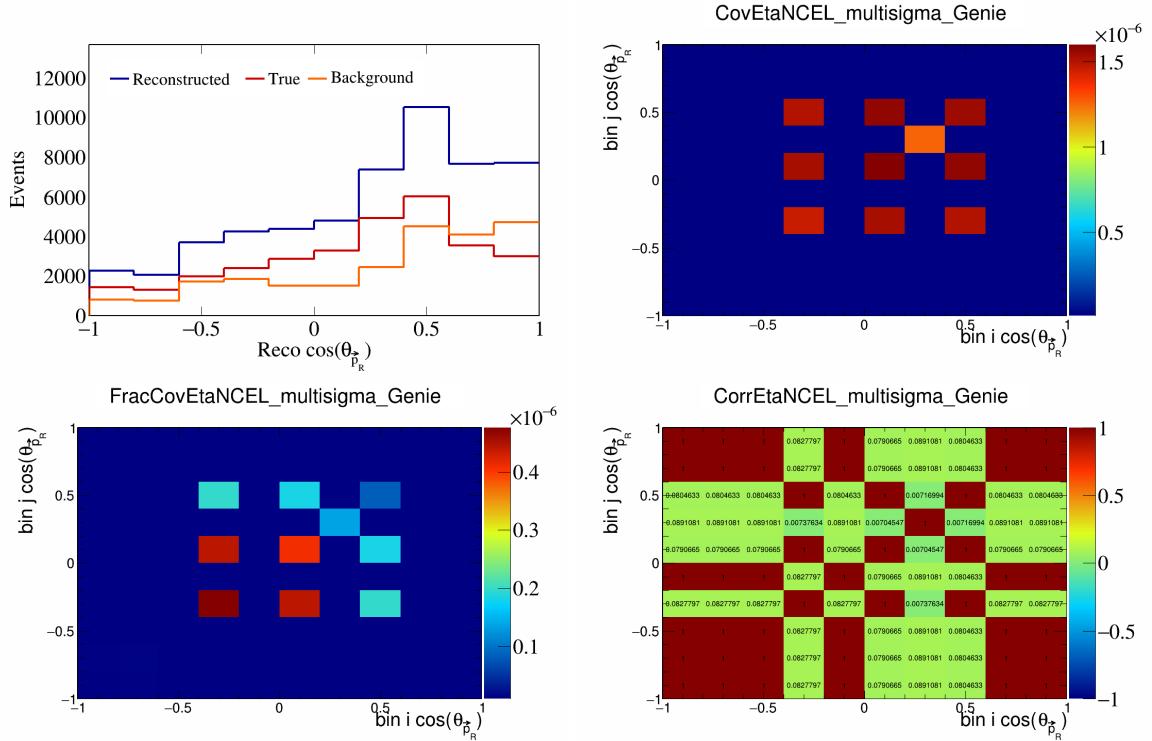


Figure 98: EtaNCEL variations for $\cos(\theta_{\vec{p}_R})$.

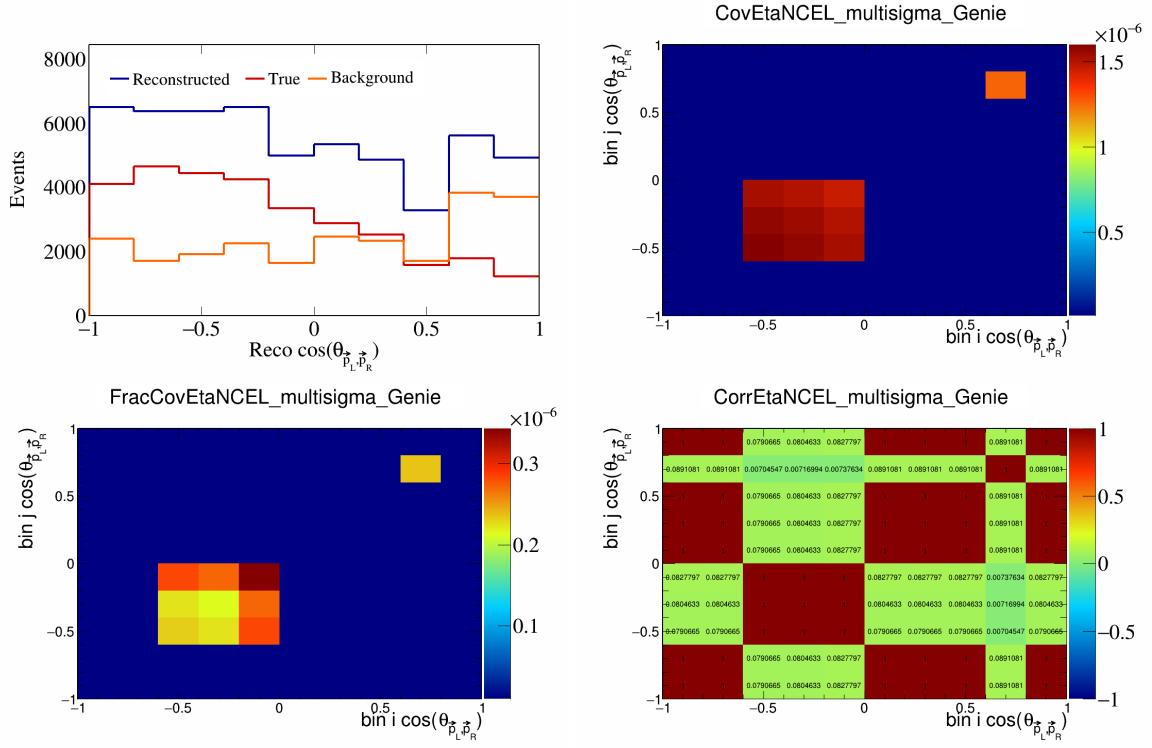


Figure 99: EtaNCEL variations for $\cos(\theta_{\vec{p}_L, \vec{p}_R})$.

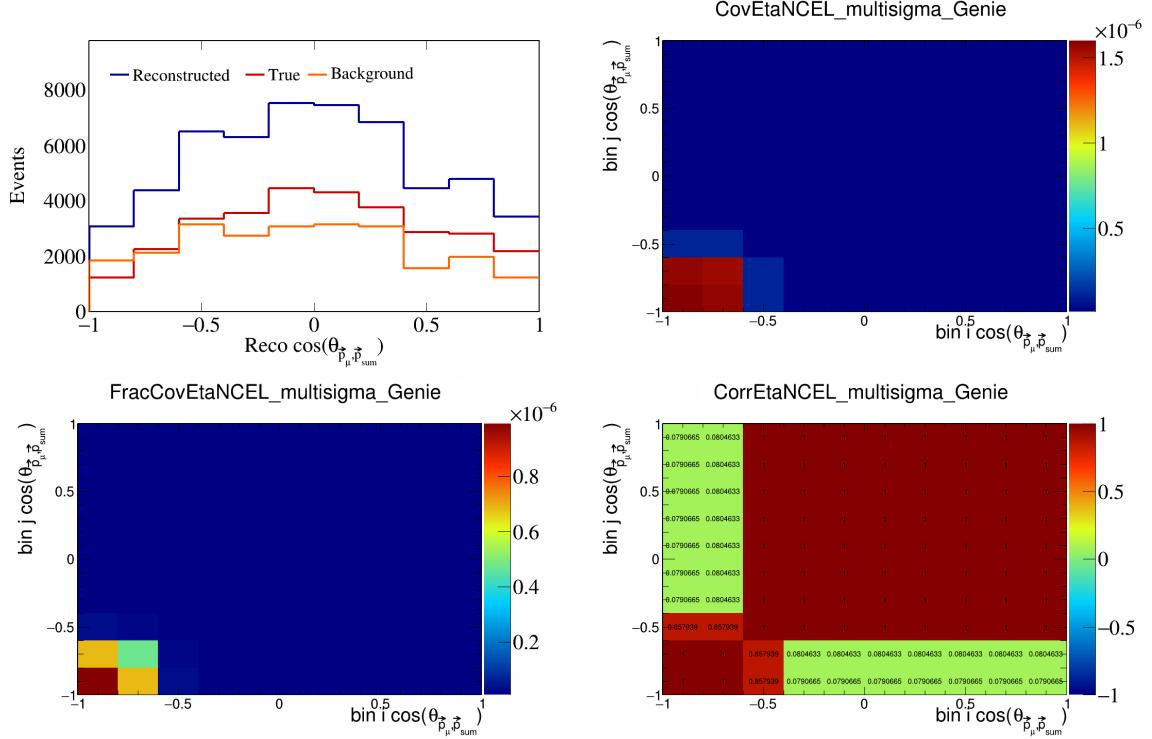


Figure 100: EtaNCEL variations for $\cos(\theta_{\vec{p}_\mu, \vec{p}_{\text{sum}}})$.

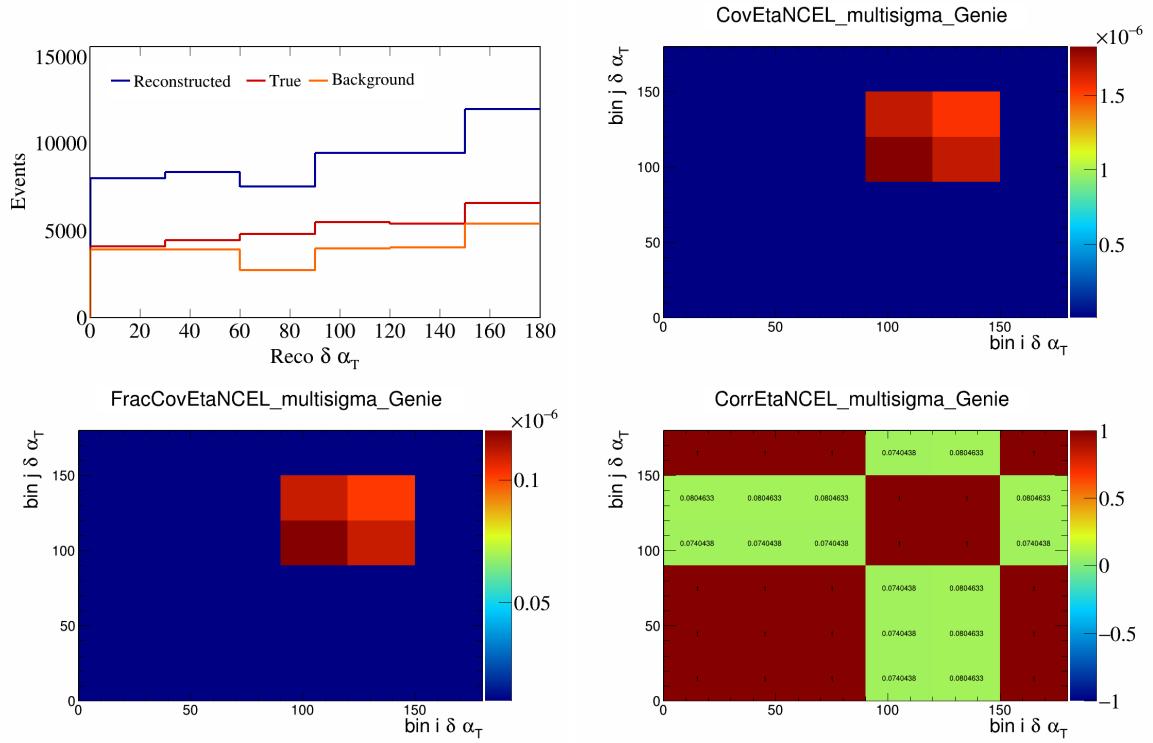


Figure 101: EtaNCEL variations for $\delta\alpha_T$.

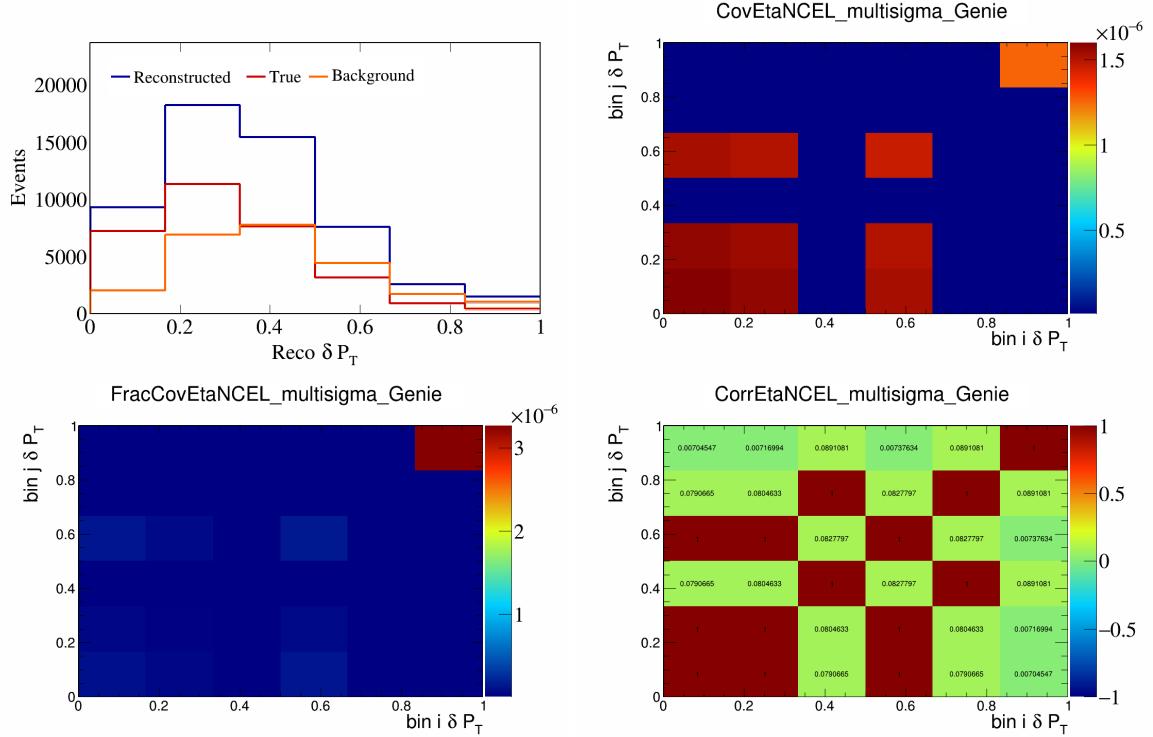


Figure 102: EtaNCEL variations for δP_T .

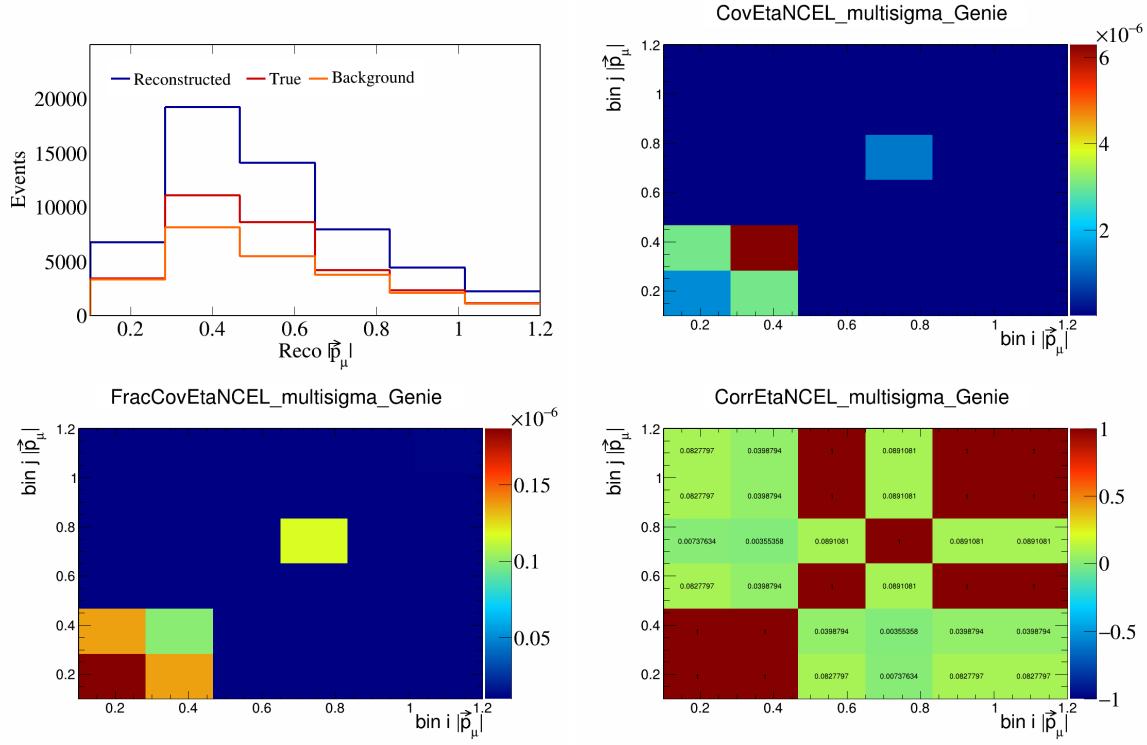


Figure 103: EtaNCEL variations for $|\vec{p}_\mu|$.

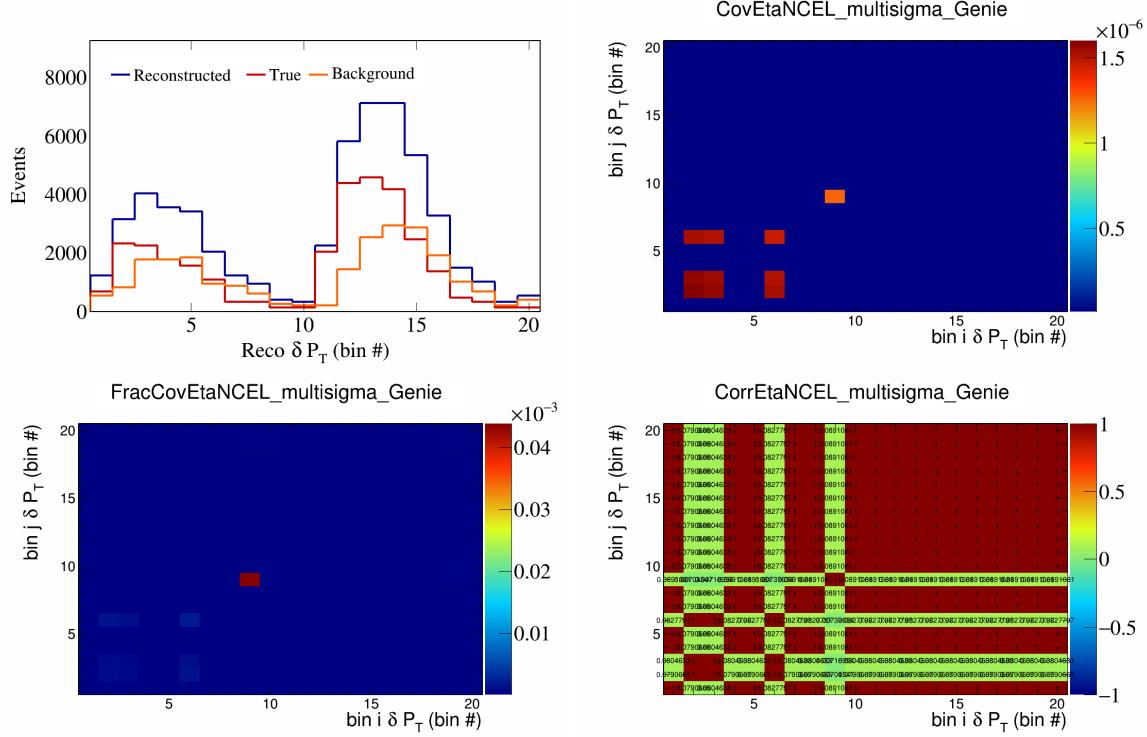


Figure 104: EtaNCEL variations for δP_T in $\cos(\theta_{\vec{p}_\mu})$.

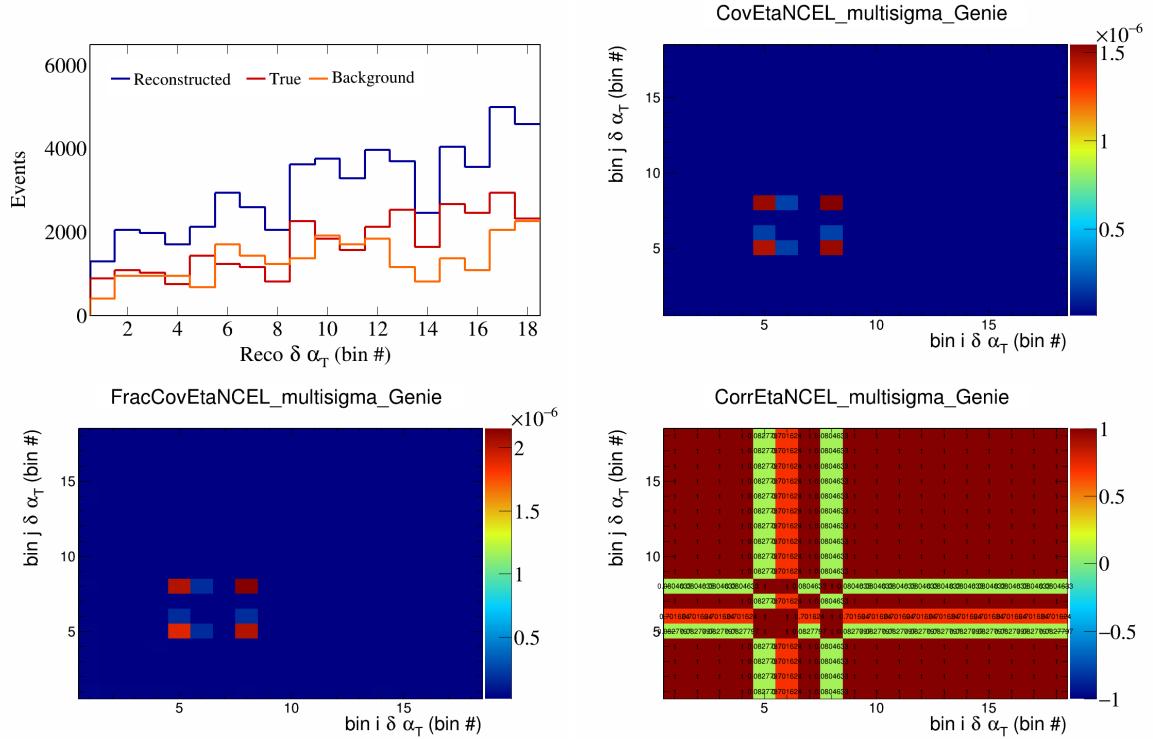


Figure 105: EtaNCEL variations for $\delta\alpha_T$ in $\cos(\theta_{\vec{p}_\mu})$.

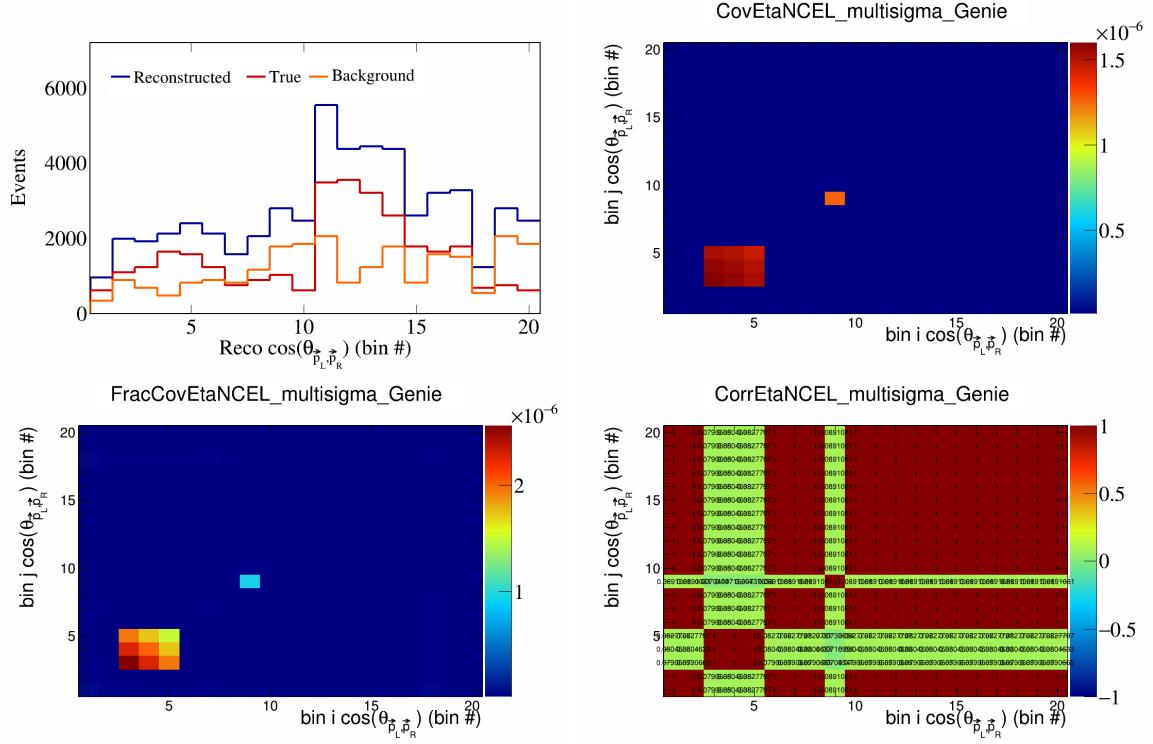


Figure 106: EtaNCEL variations for $\cos(\theta_{\vec{p}_L, \vec{p}_R})$ in $\cos(\theta_{\vec{p}_\mu})$.

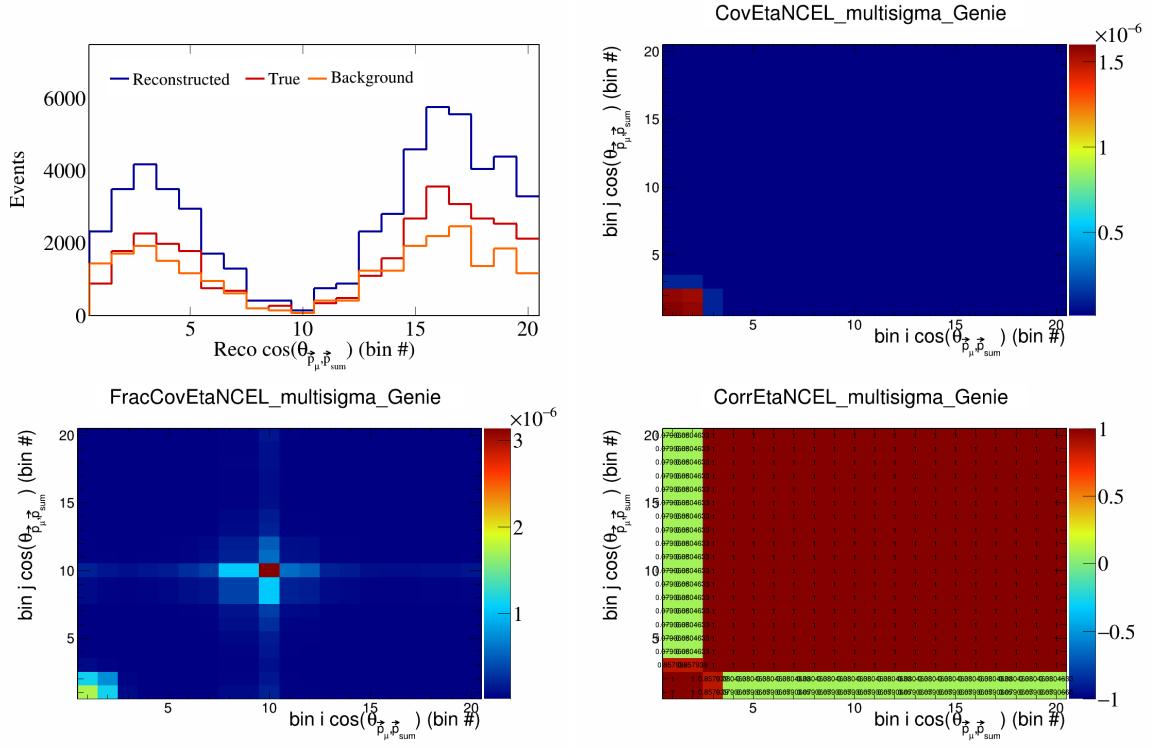


Figure 107: EtaNCEL variations for $\cos(\theta_{\vec{p}_\mu, \vec{p}_{\text{sum}}})$ in $\cos(\theta_{\vec{p}_\mu})$.

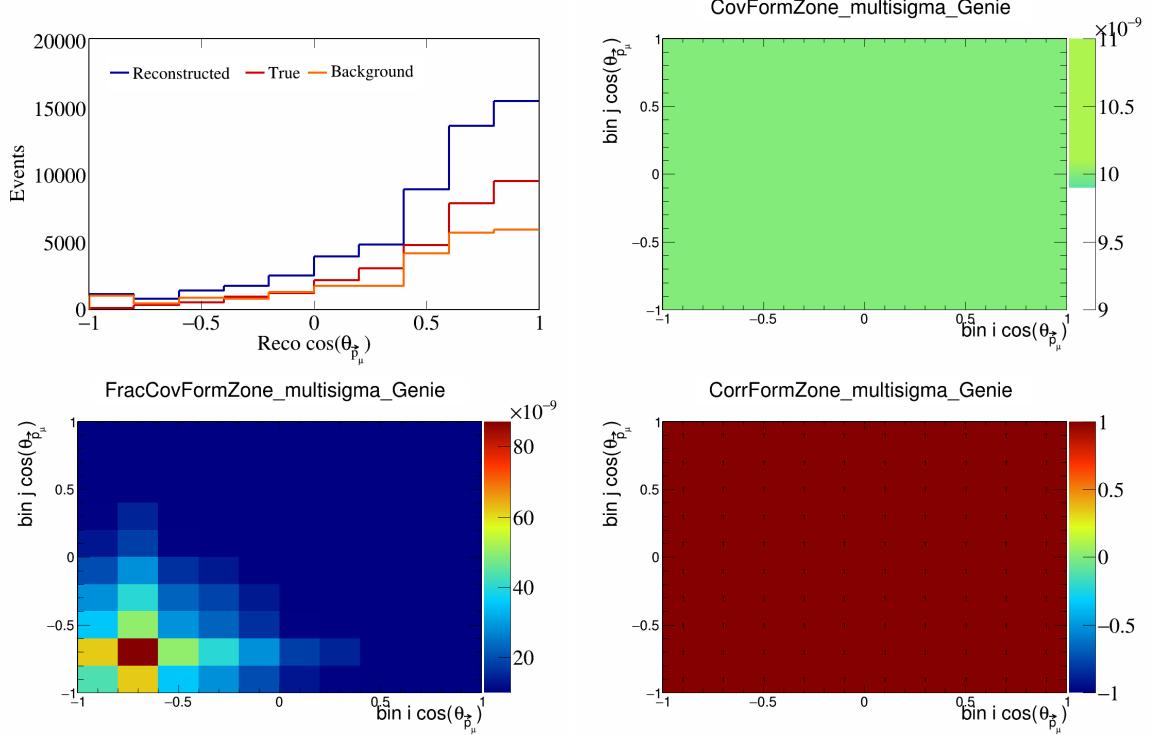


Figure 108: FormZone variations for $\cos(\theta_{\vec{p}_\mu})$.

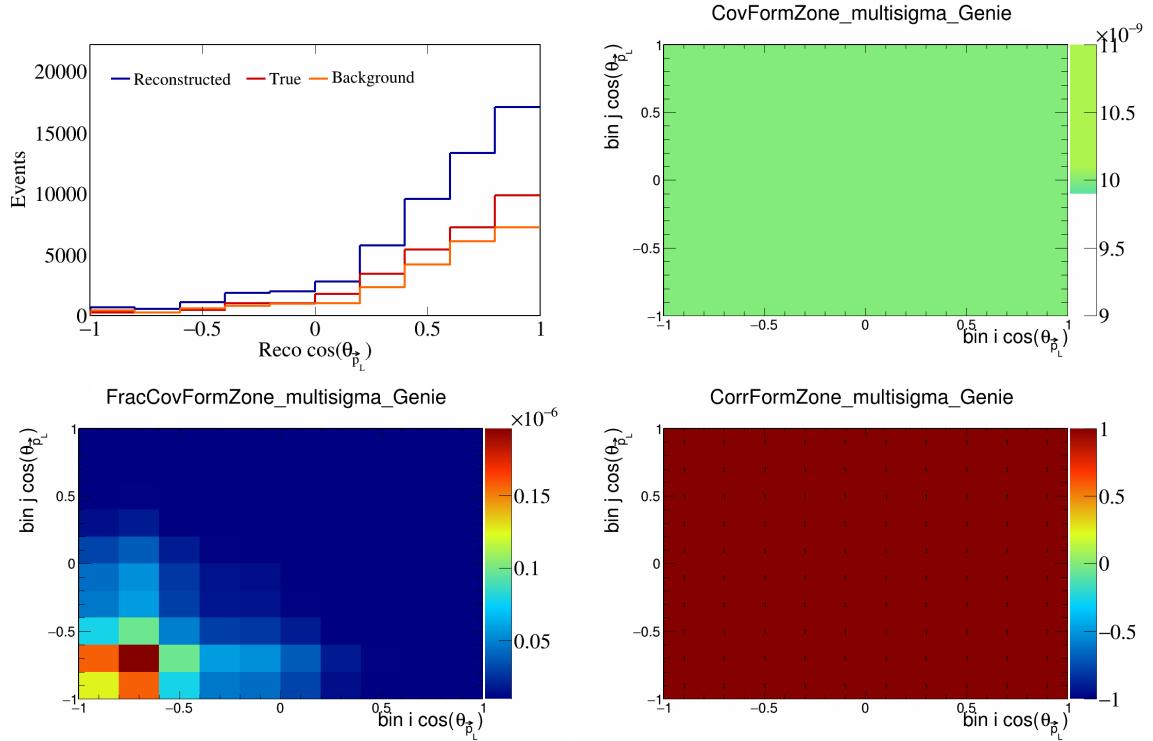


Figure 109: FormZone variations for $\cos(\theta_{\vec{p}_L})$.

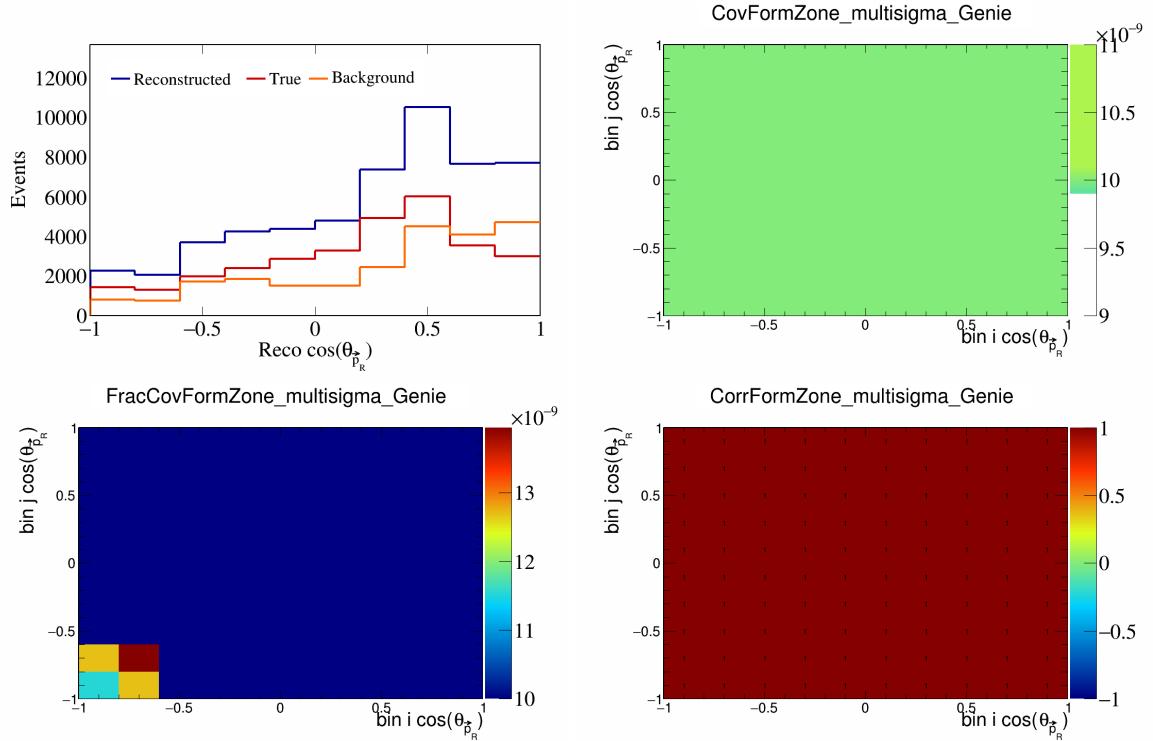


Figure 110: FormZone variations for $\cos(\theta_{\vec{p}_R})$.

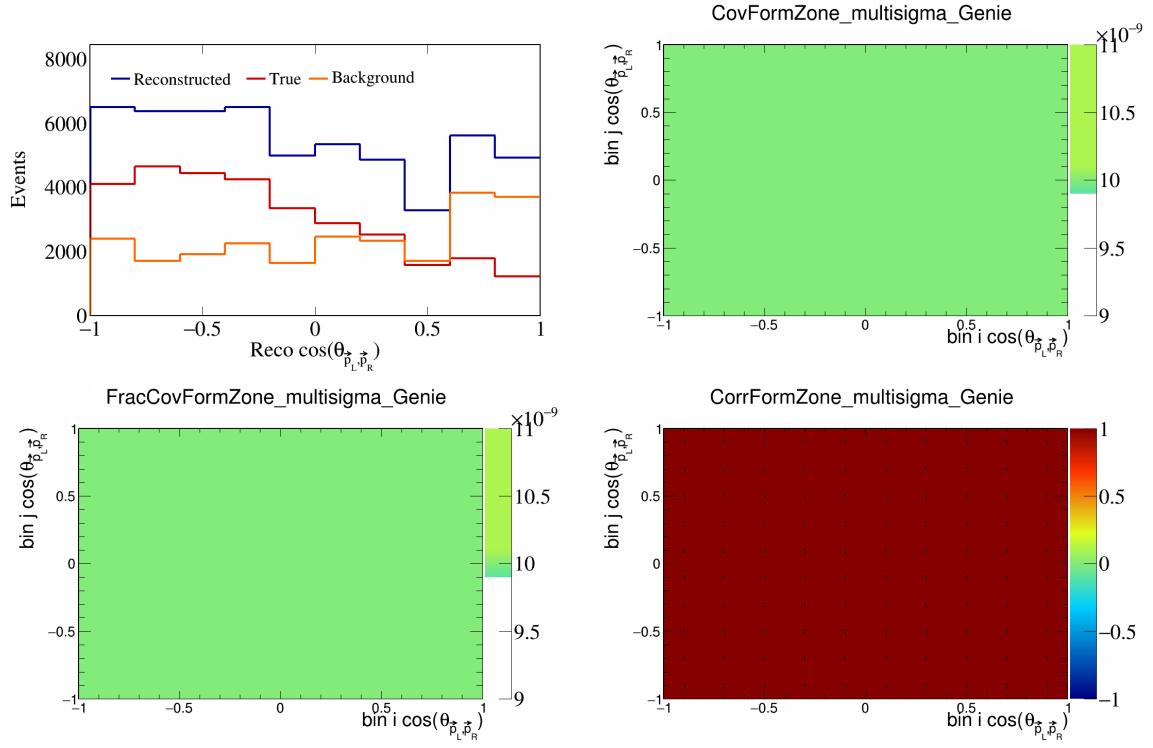


Figure 111: FormZone variations for $\cos(\theta_{\vec{p}_L, \vec{p}_R})$.

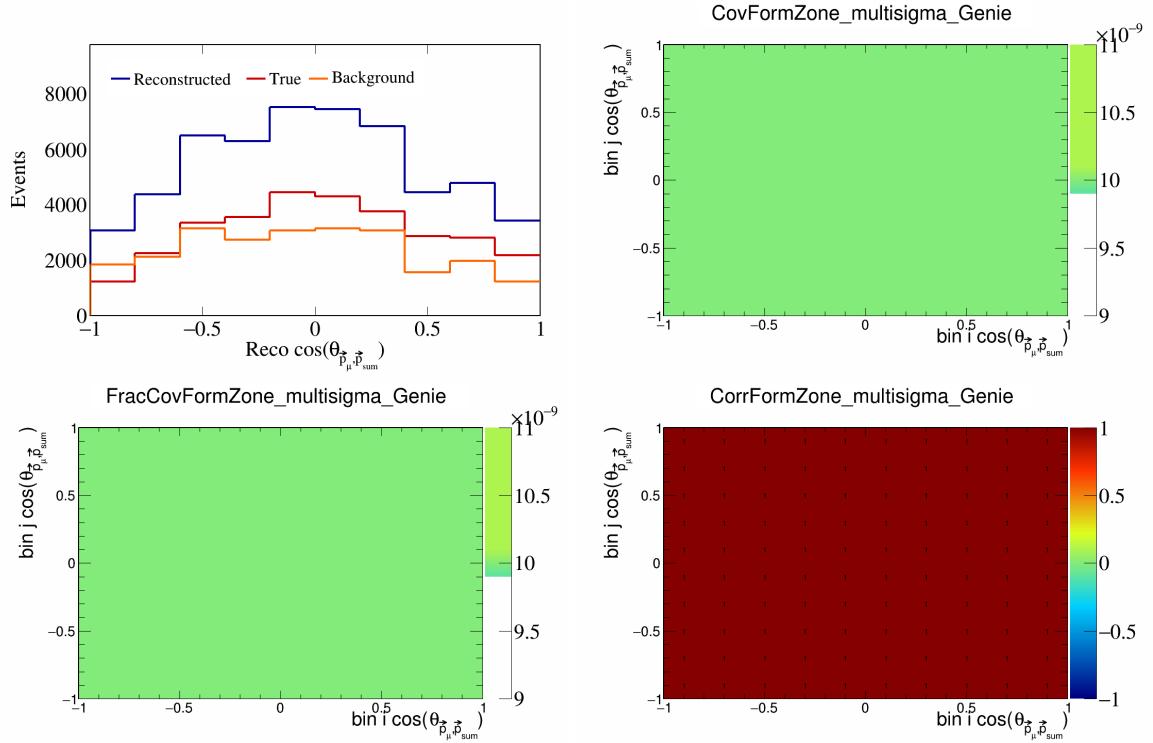


Figure 112: FormZone variations for $\cos(\theta_{\vec{p}_\mu, \vec{p}_{\text{sum}}})$.

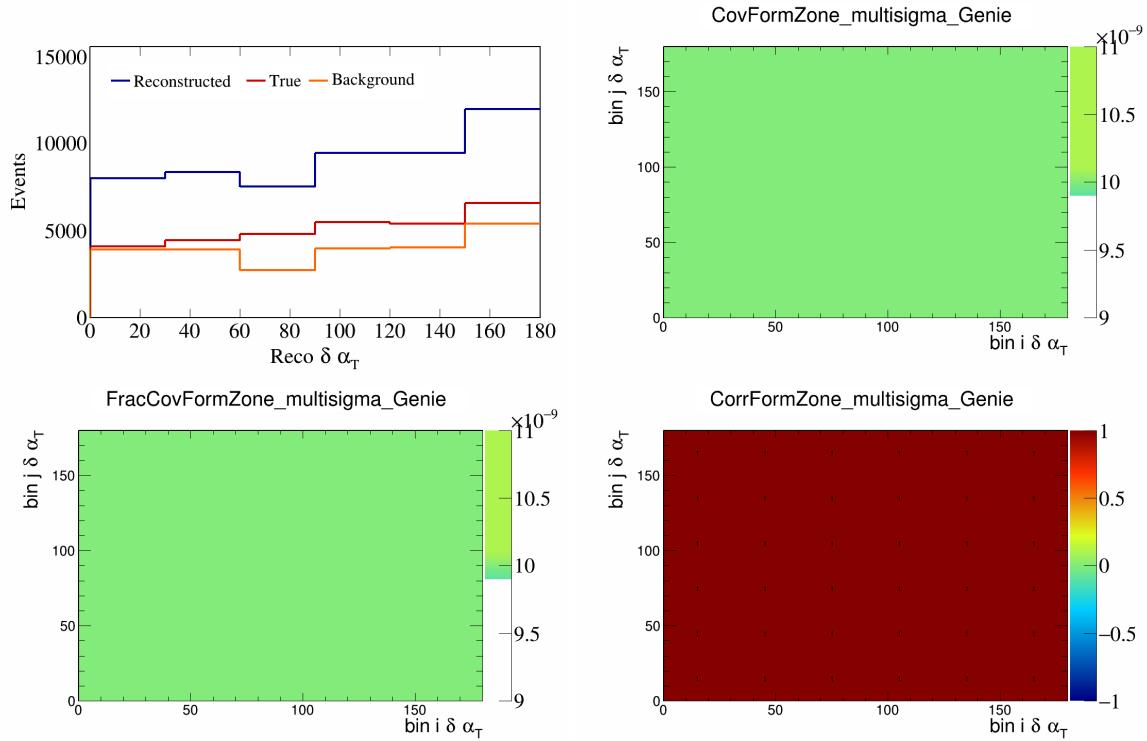


Figure 113: FormZone variations for $\delta\alpha_T$.

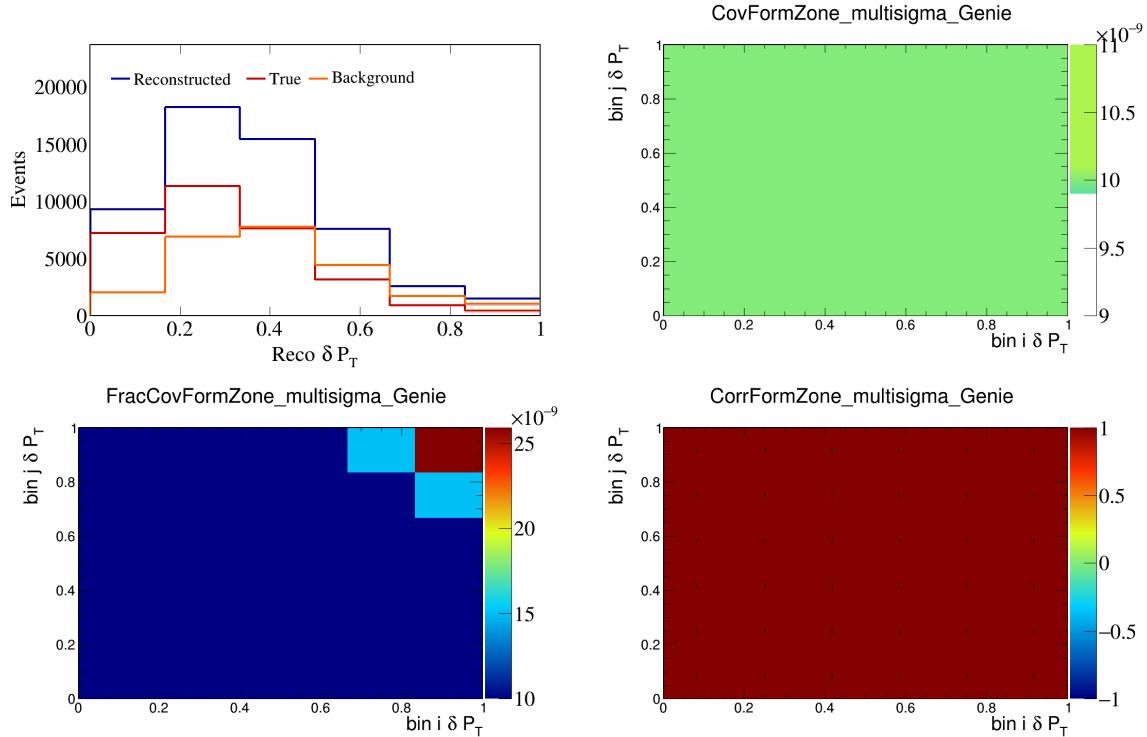


Figure 114: FormZone variations for δP_T .

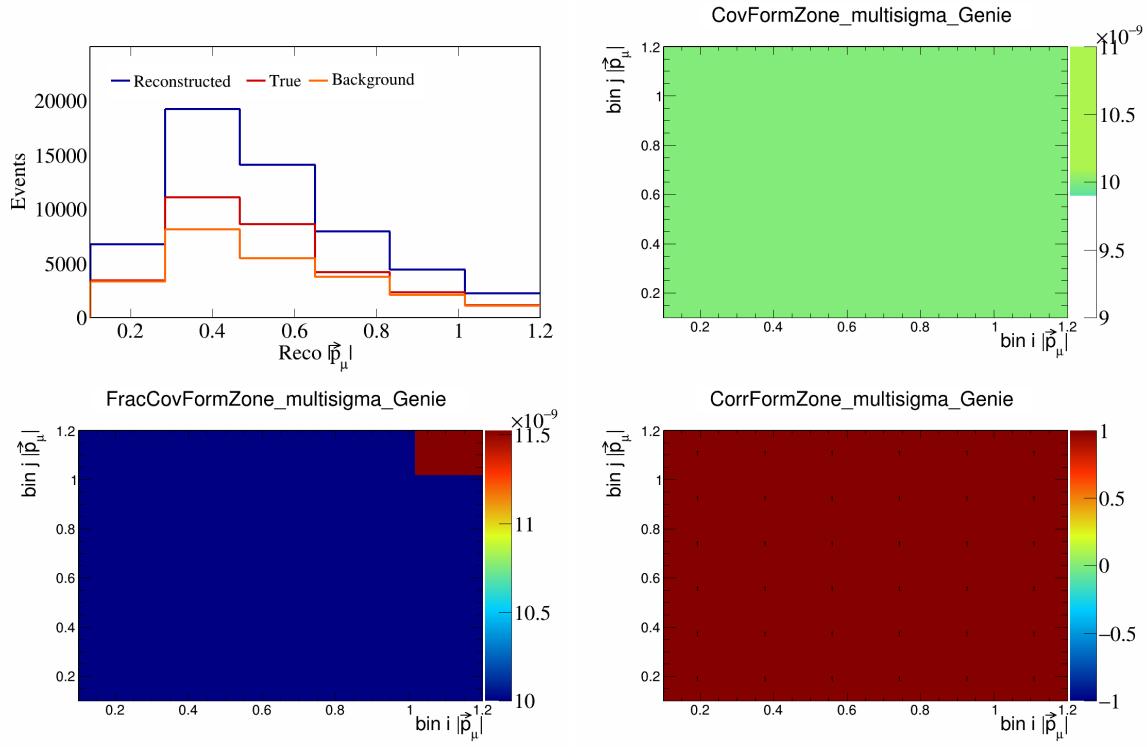


Figure 115: FormZone variations for $|\vec{p}_\mu|$.

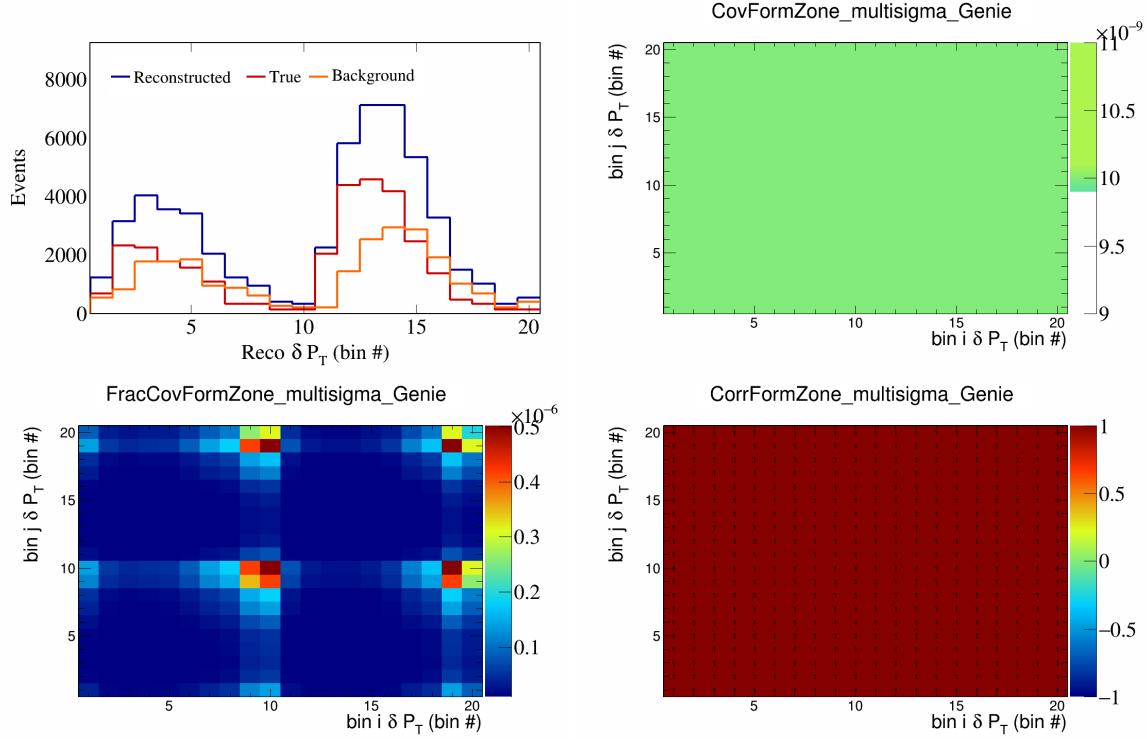


Figure 116: FormZone variations for δP_T in $\cos(\theta_{\vec{p}_\mu})$.

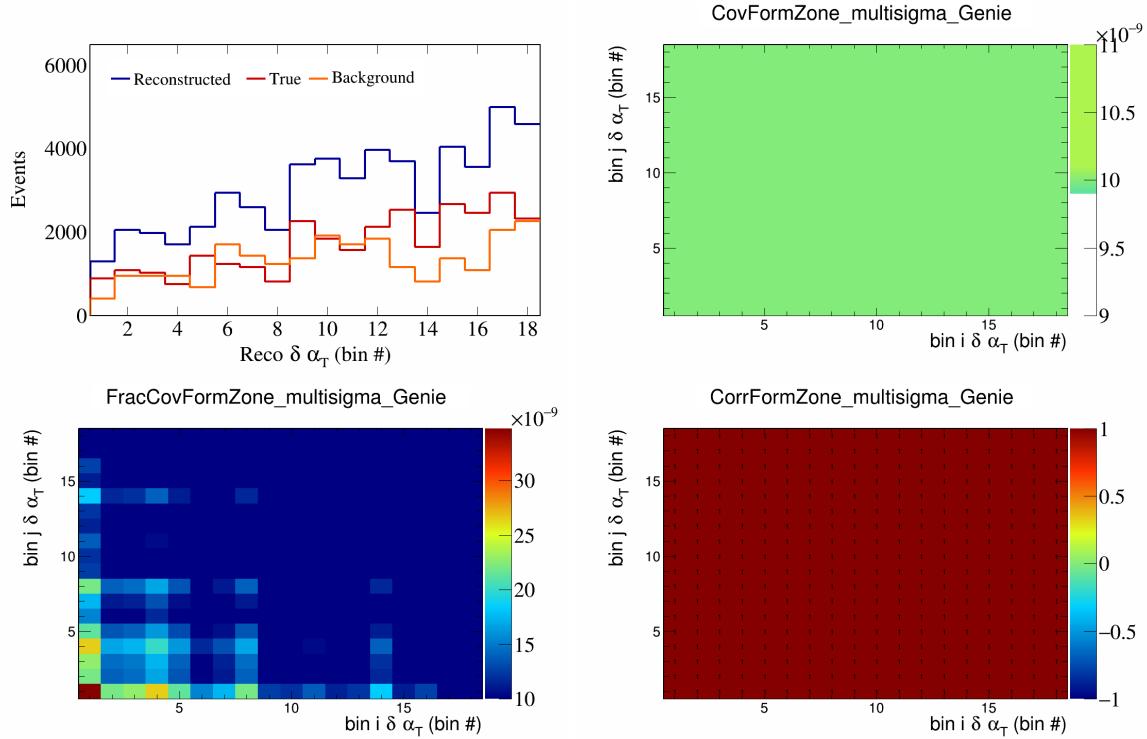


Figure 117: FormZone variations for $\delta\alpha_T$ in $\cos(\theta_{\vec{p}_\mu})$.

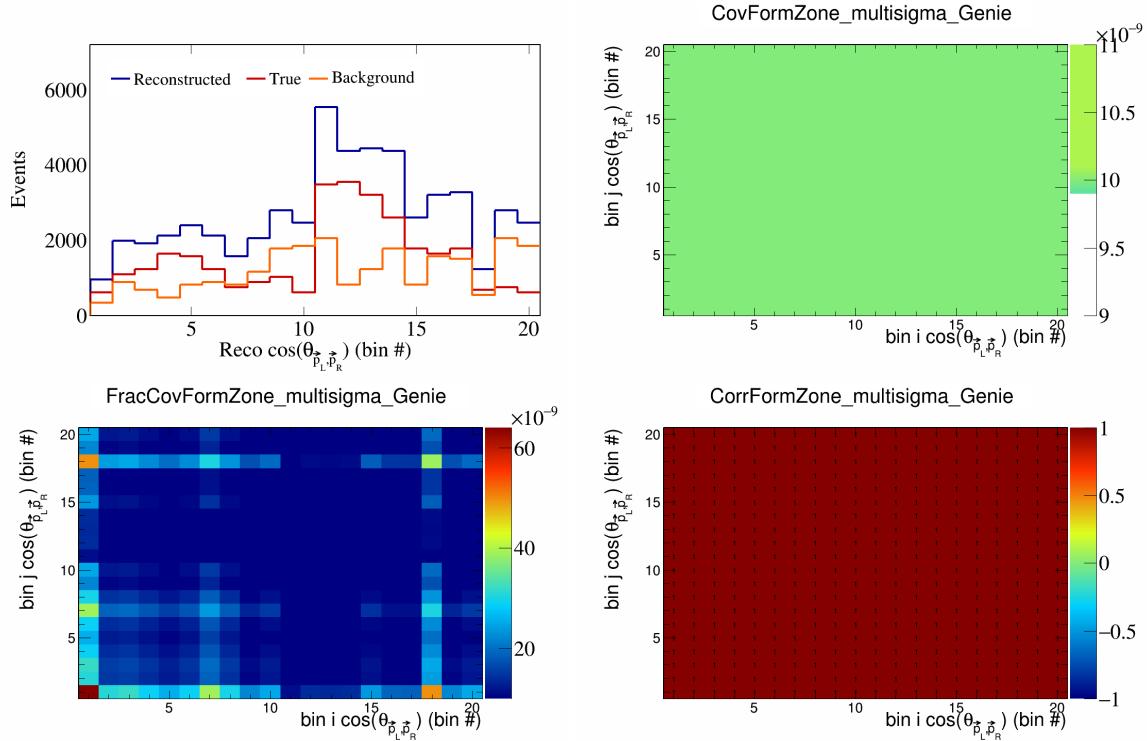


Figure 118: FormZone variations for $\cos(\theta_{\vec{p}_L, \vec{p}_R})$ in $\cos(\theta_{\vec{p}_\mu})$.

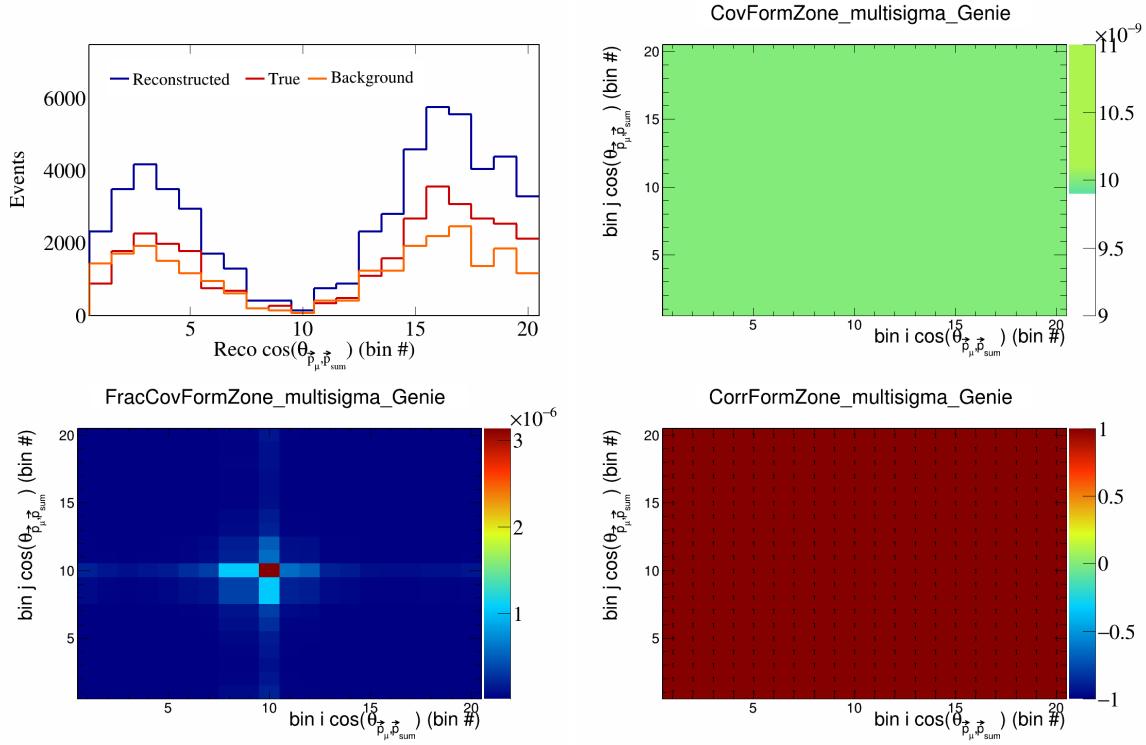


Figure 119: FormZone variations for $\cos(\theta_{\vec{p}_\mu} \cdot \vec{p}_{\text{sum}})$ in $\cos(\theta_{\vec{p}_\mu})$.

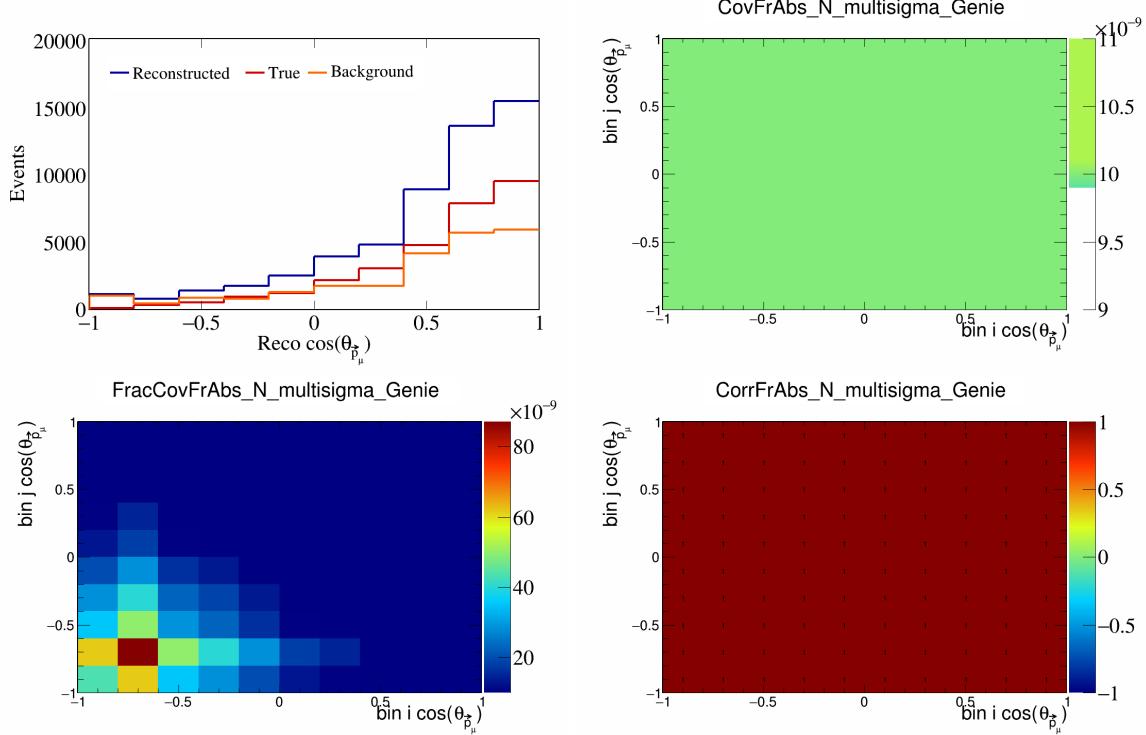


Figure 120: FrAbsN variations for $\cos(\theta_{\vec{p}_\mu})$.

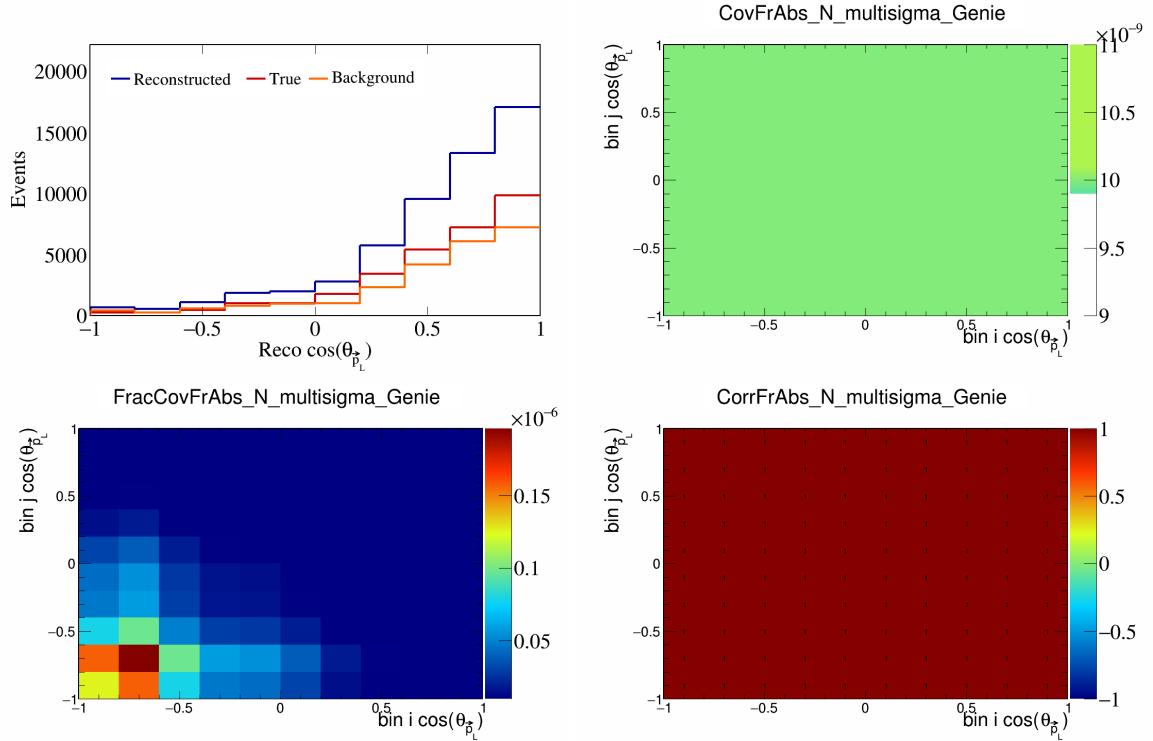


Figure 121: FrAbsN variations for $\cos(\theta_{\vec{p}_L})$.

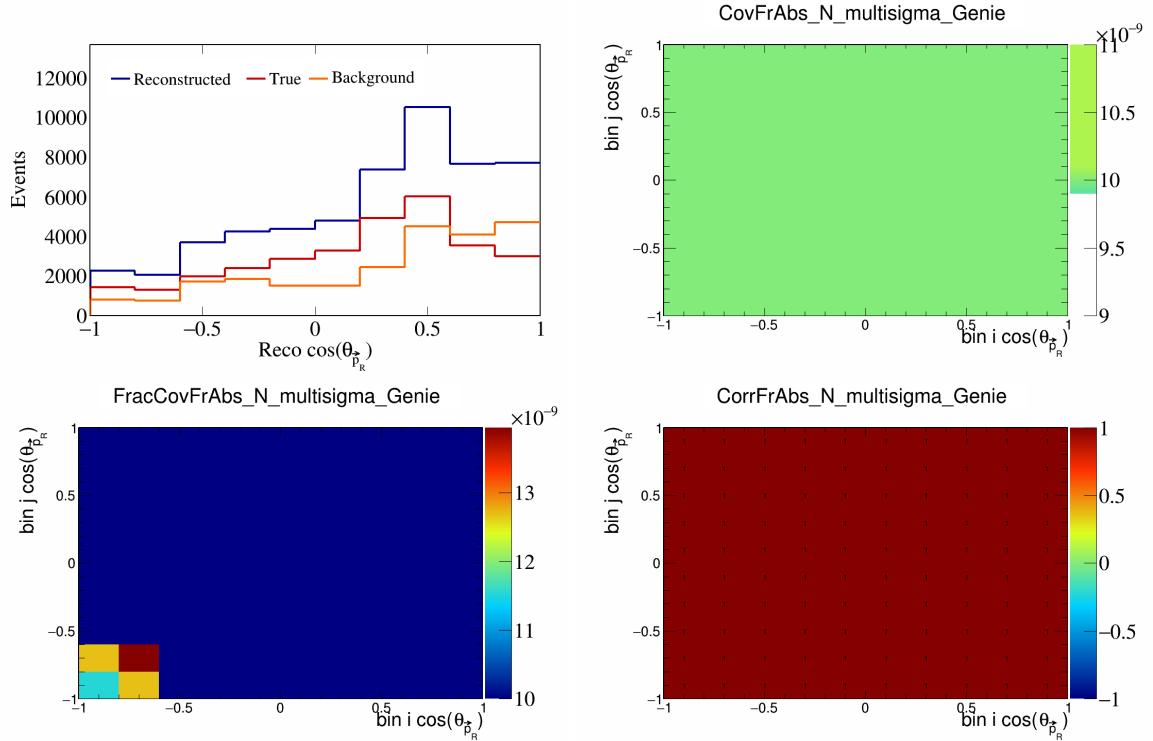


Figure 122: FrAbsN variations for $\cos(\theta_{\vec{p}_R})$.

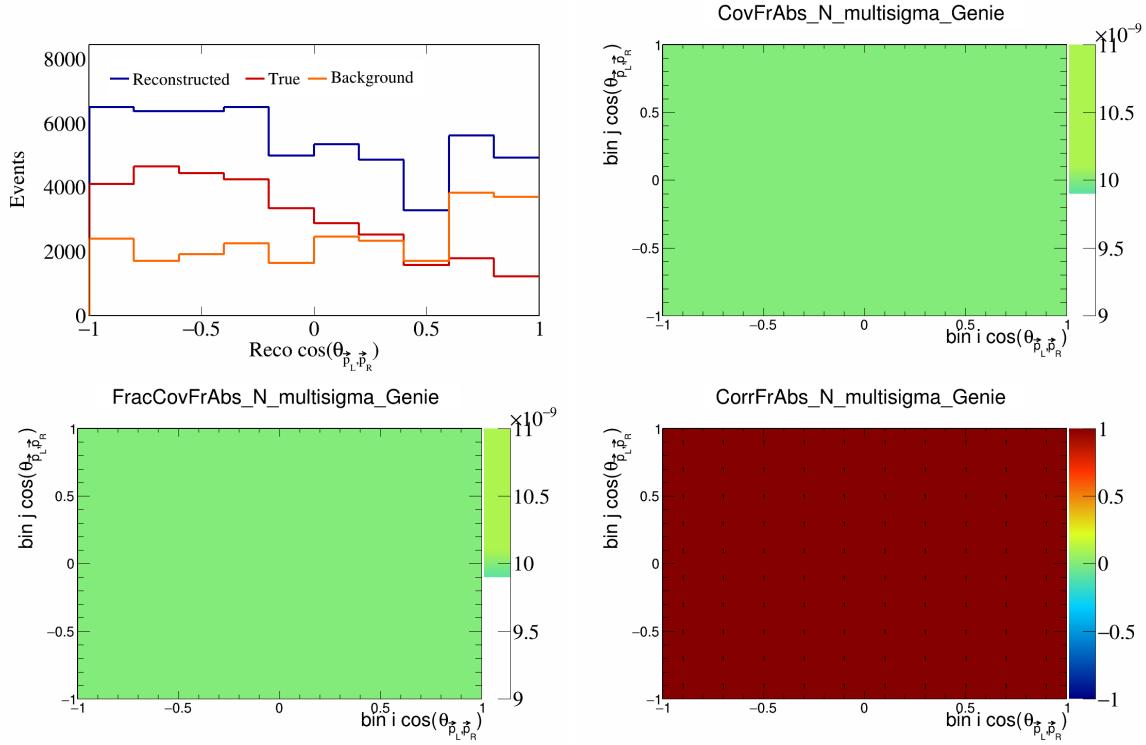


Figure 123: FrAbsN variations for $\cos(\theta_{\vec{p}_L, \vec{p}_R})$.

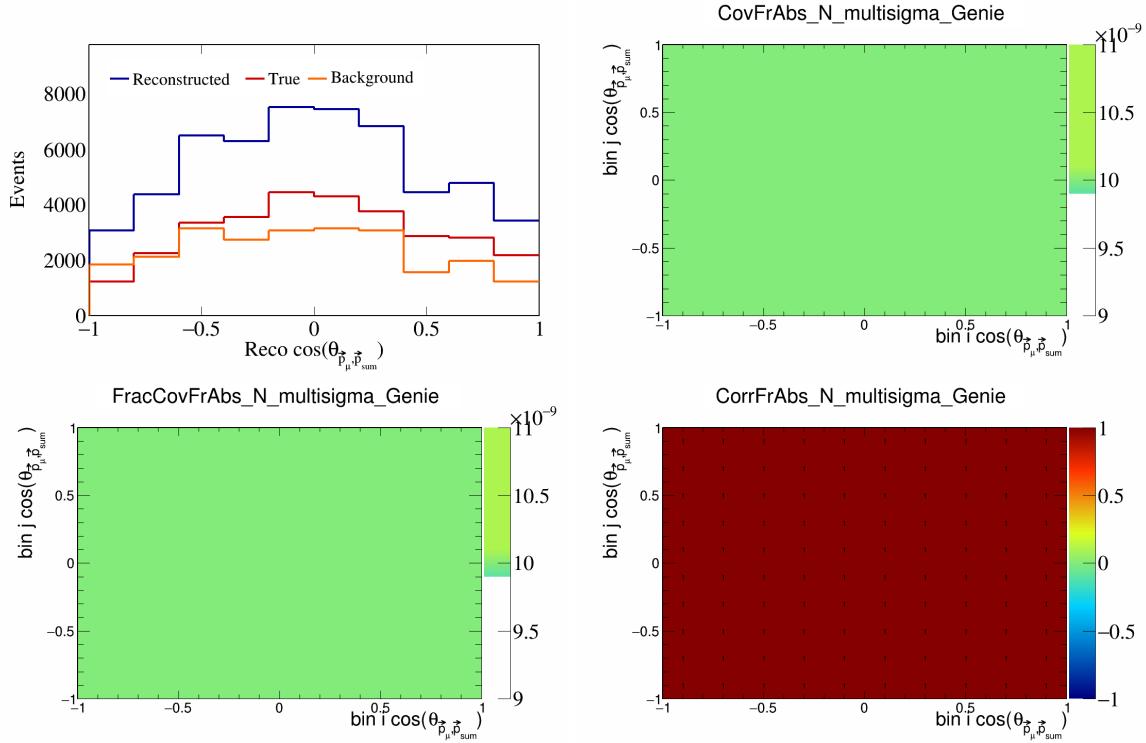


Figure 124: FrAbsN variations for $\cos(\theta_{\vec{p}_\mu, \vec{p}_{\text{sum}}})$.

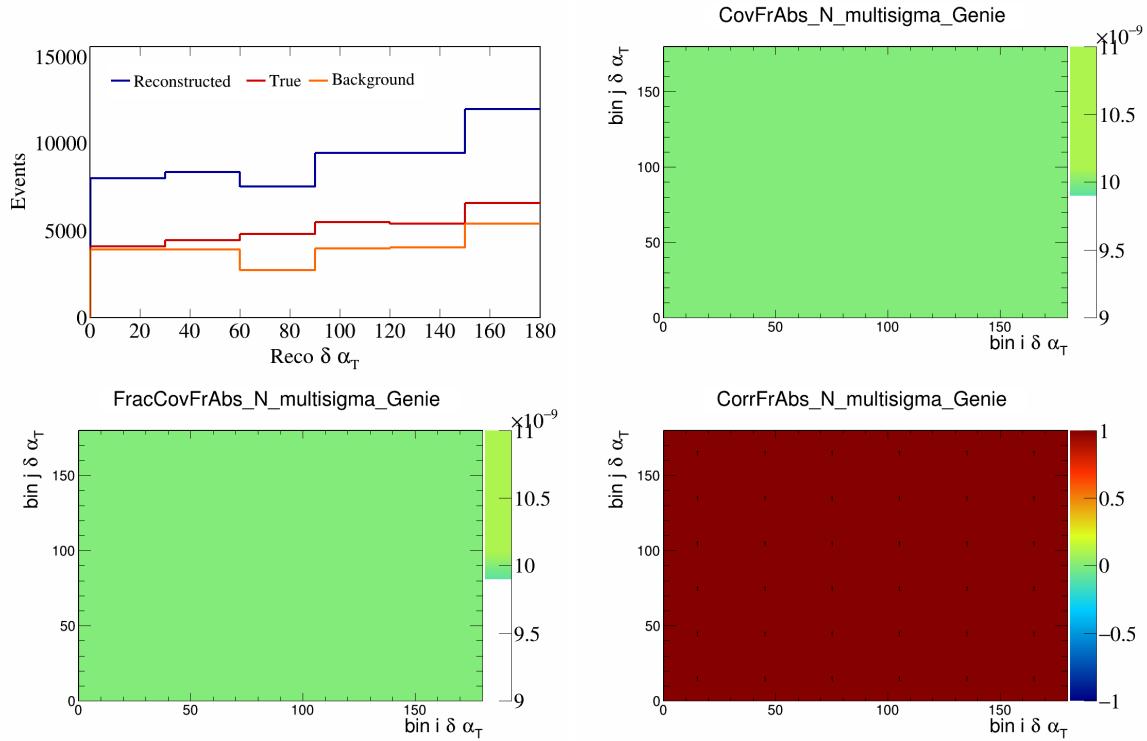


Figure 125: FrAbsN variations for $\delta\alpha_T$.

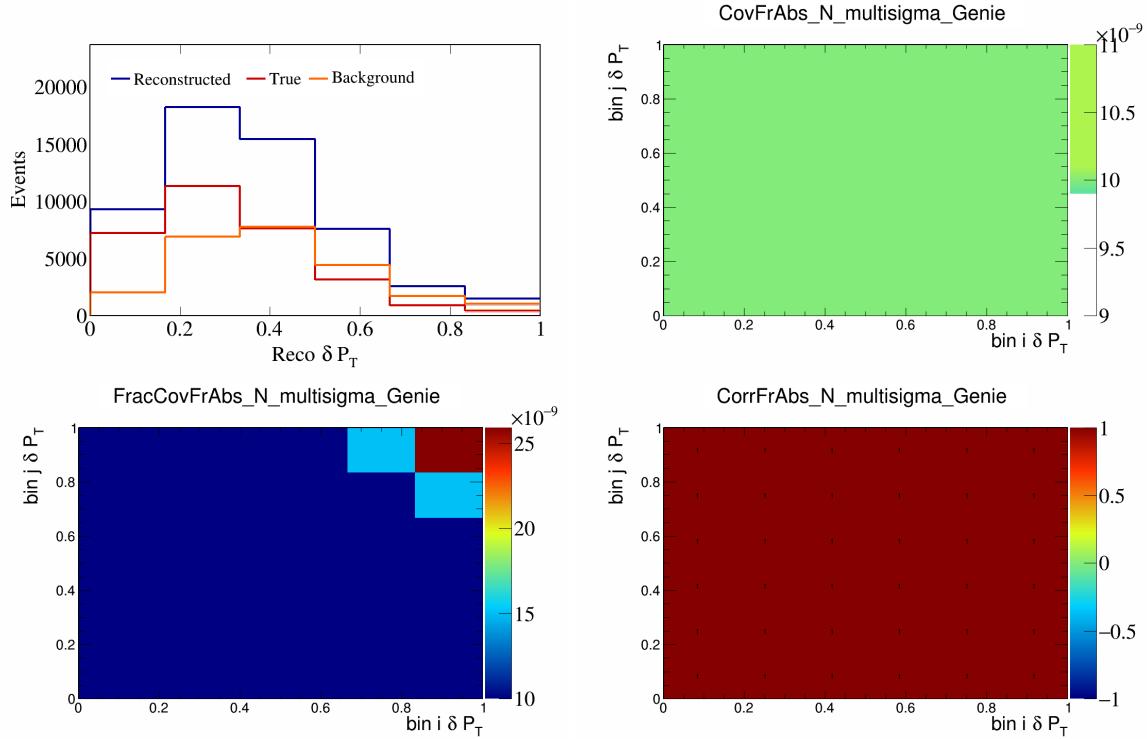


Figure 126: FrAbsN variations for δP_T .

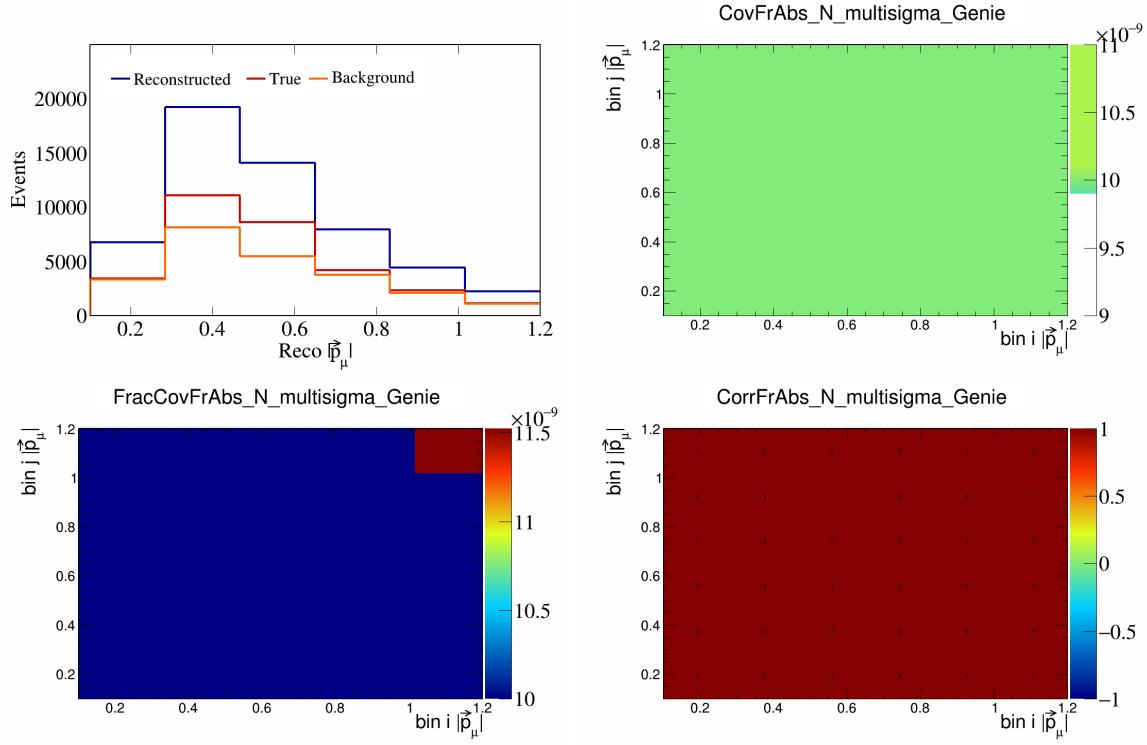


Figure 127: FrAbsN variations for $|\vec{p}_\mu|$.

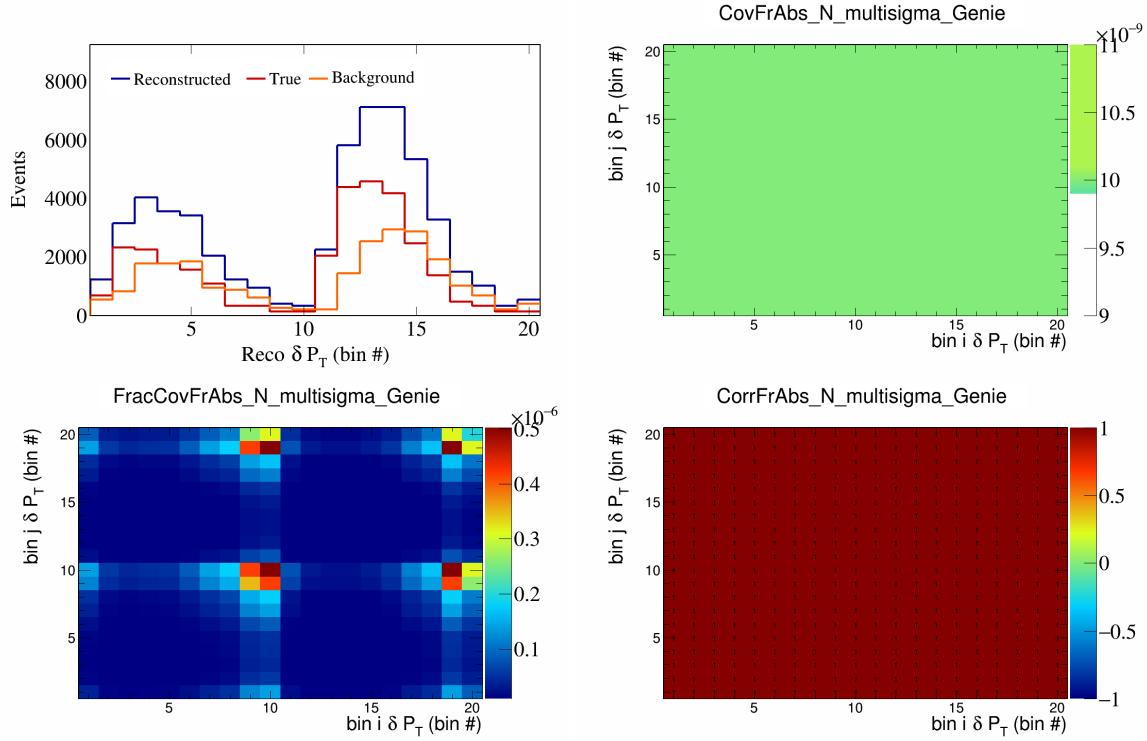


Figure 128: FrAbsN variations for δP_T in $\cos(\theta_{\vec{p}_\mu})$.

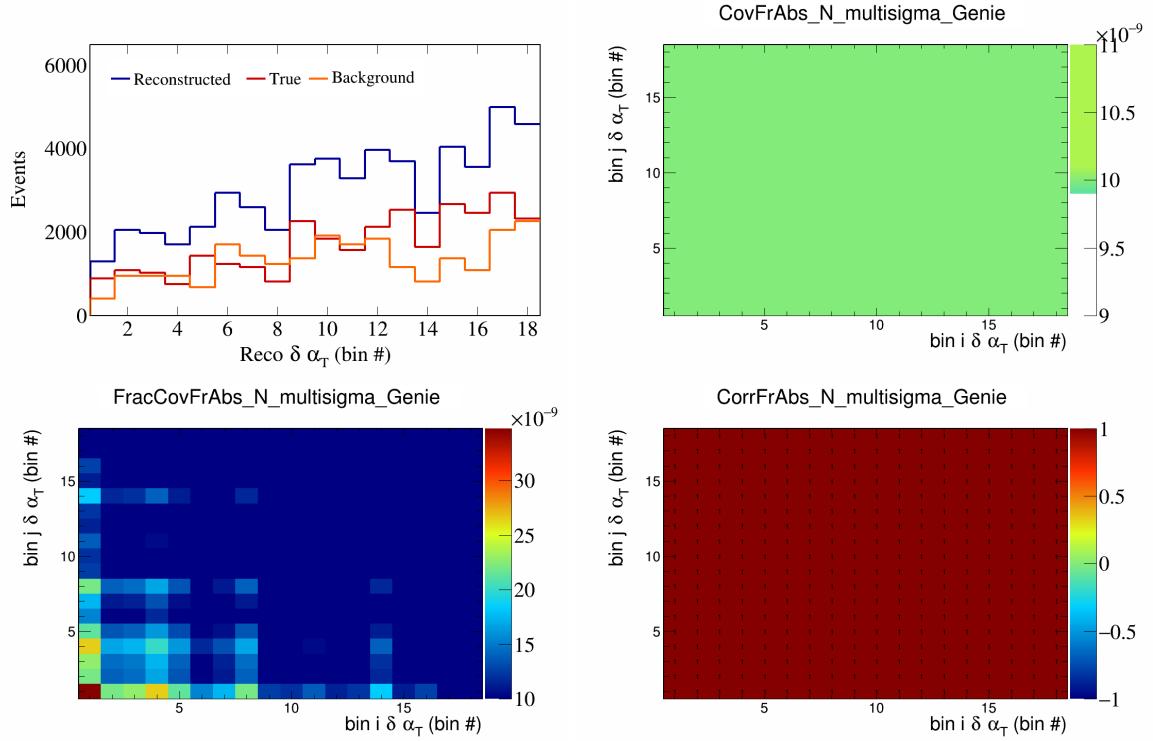


Figure 129: FrAbsN variations for $\delta\alpha_T$ in $\cos(\theta_{\vec{p}_\mu})$.

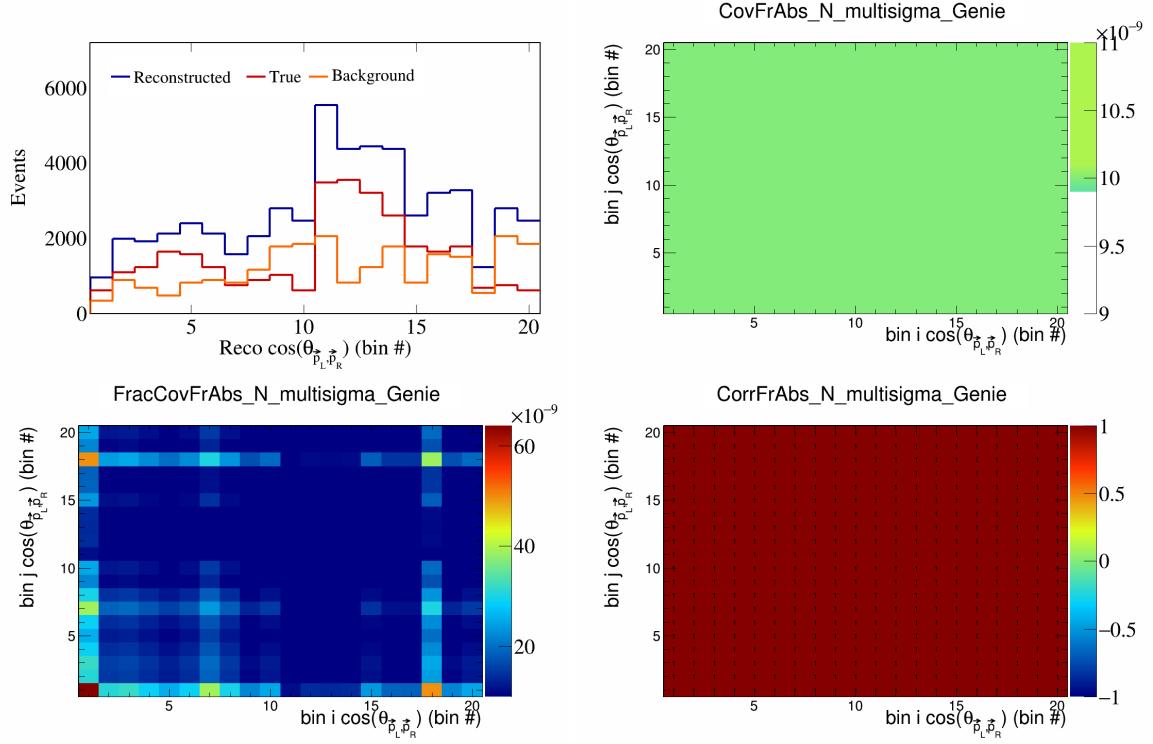


Figure 130: FrAbsN variations for $\cos(\theta_{\vec{p}_L, \vec{p}_R})$ in $\cos(\theta_{\vec{p}_\mu})$.

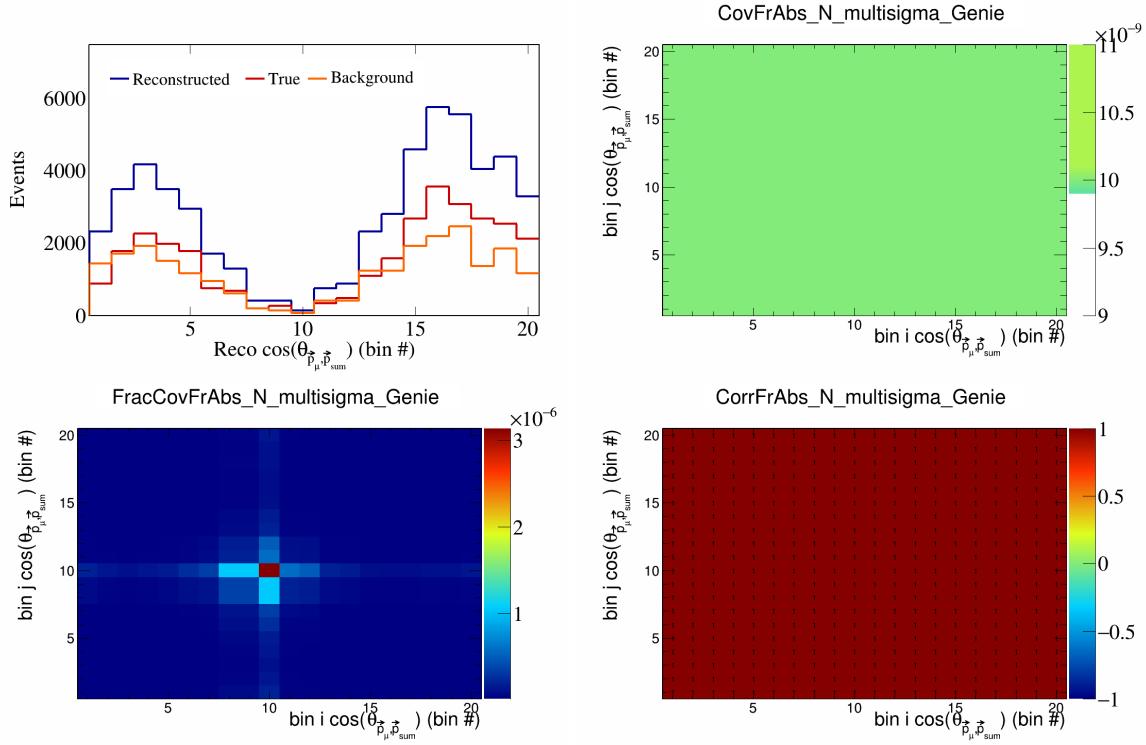


Figure 131: FrAbsN variations for $\cos(\theta_{\vec{p}_\mu})$ in $\cos(\theta_{\vec{p}_\mu})$.

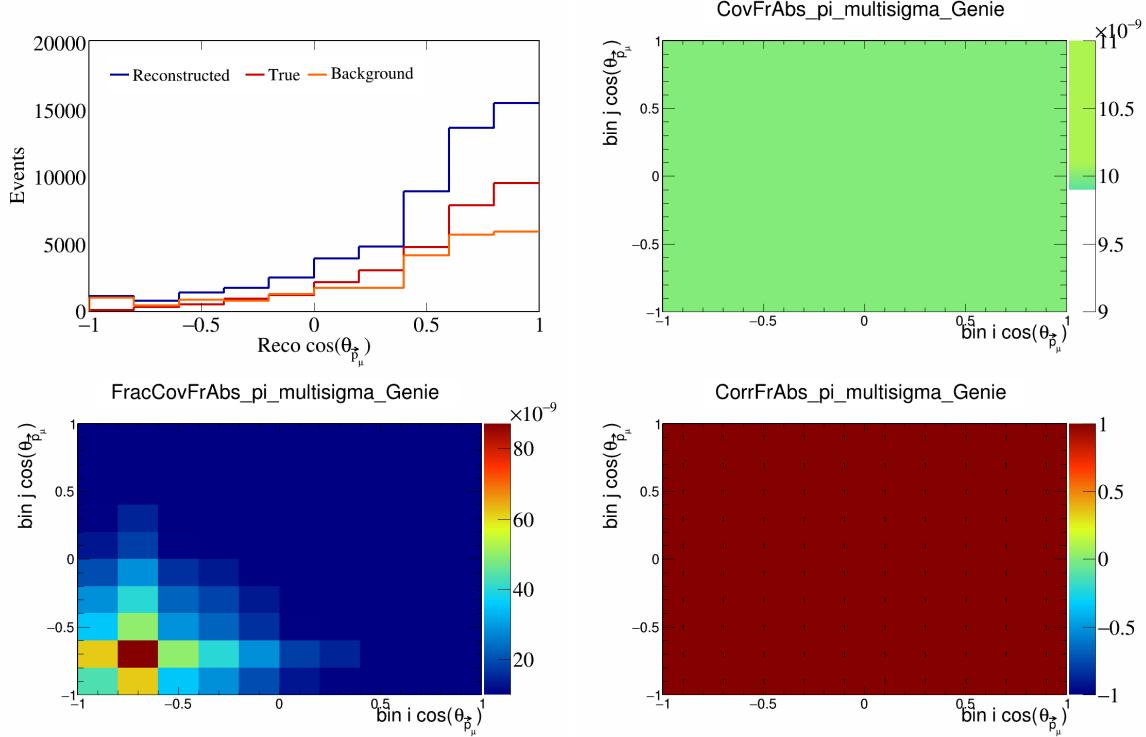


Figure 132: FrAbspi variations for $\cos(\theta_{\vec{p}_\mu})$.

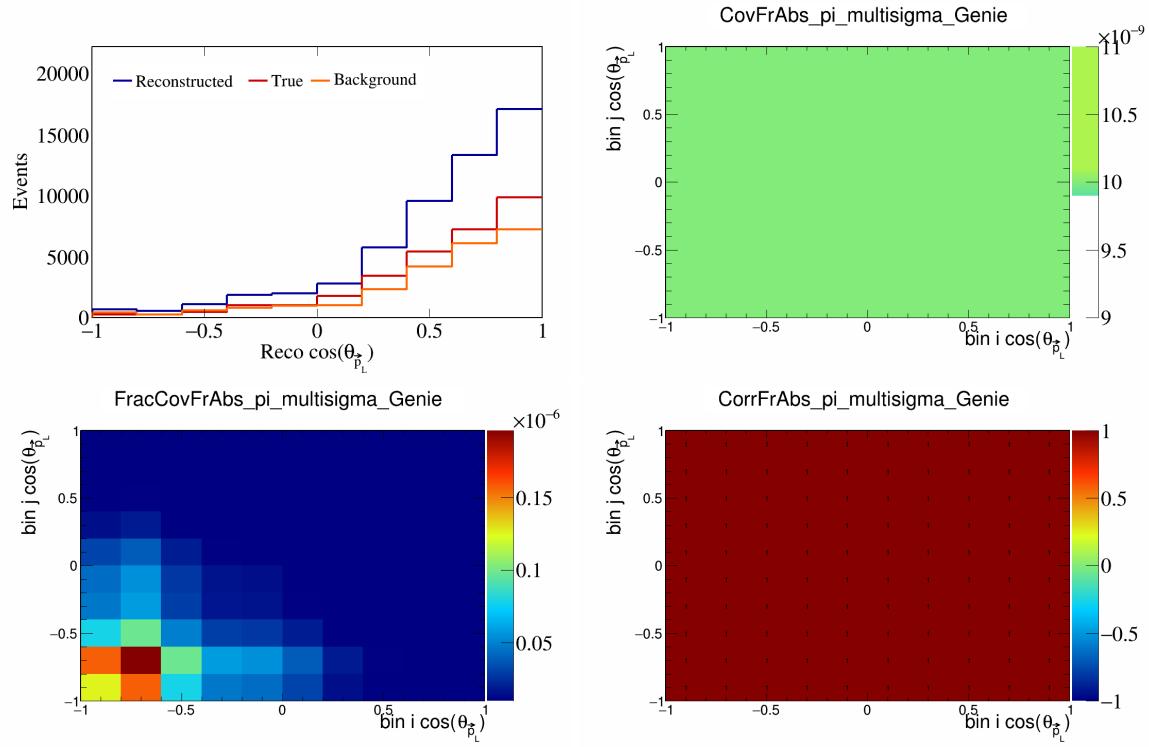


Figure 133: FrAbspi variations for $\cos(\theta_{\vec{p}_L})$.

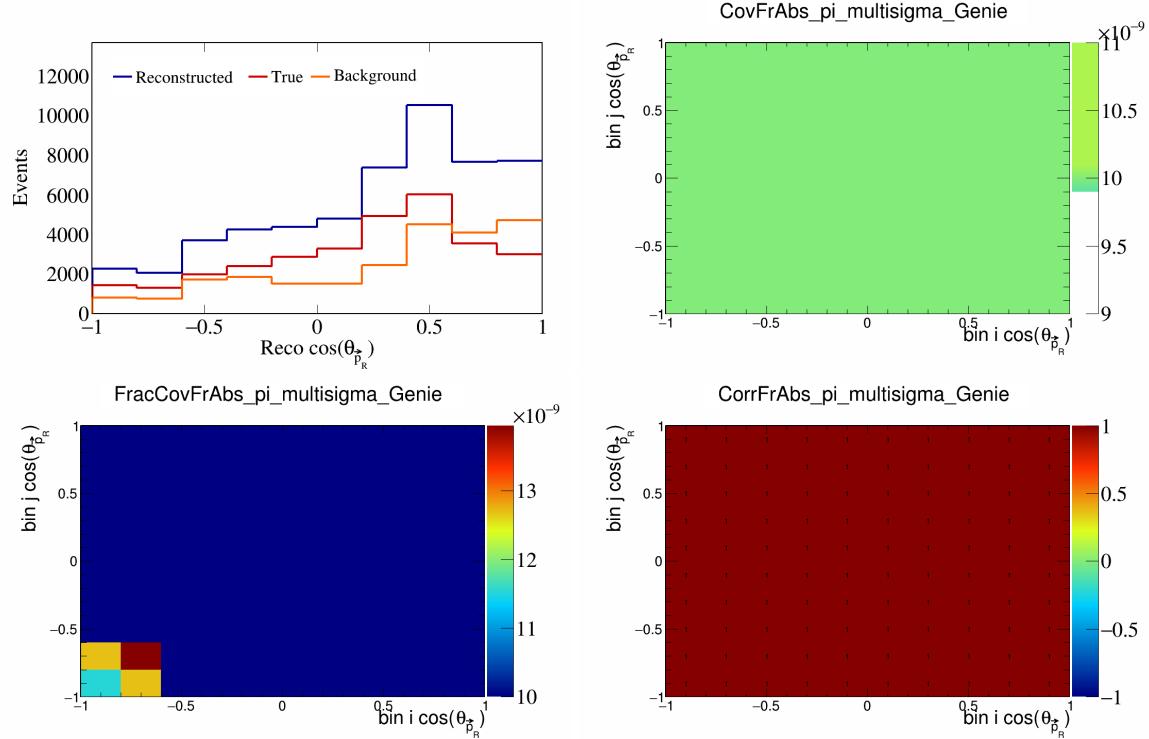


Figure 134: FrAbspi variations for $\cos(\theta_{\vec{p}_R})$.

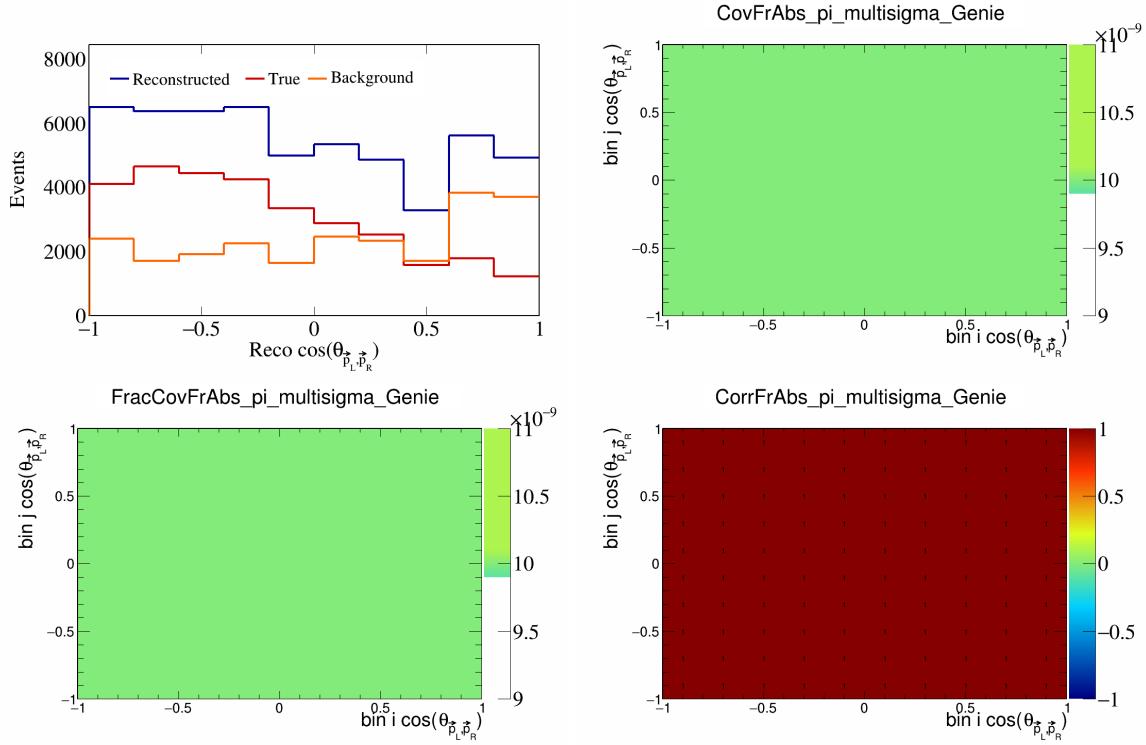


Figure 135: FrAbspi variations for $\cos(\theta_{\vec{p}_L, \vec{p}_R})$.

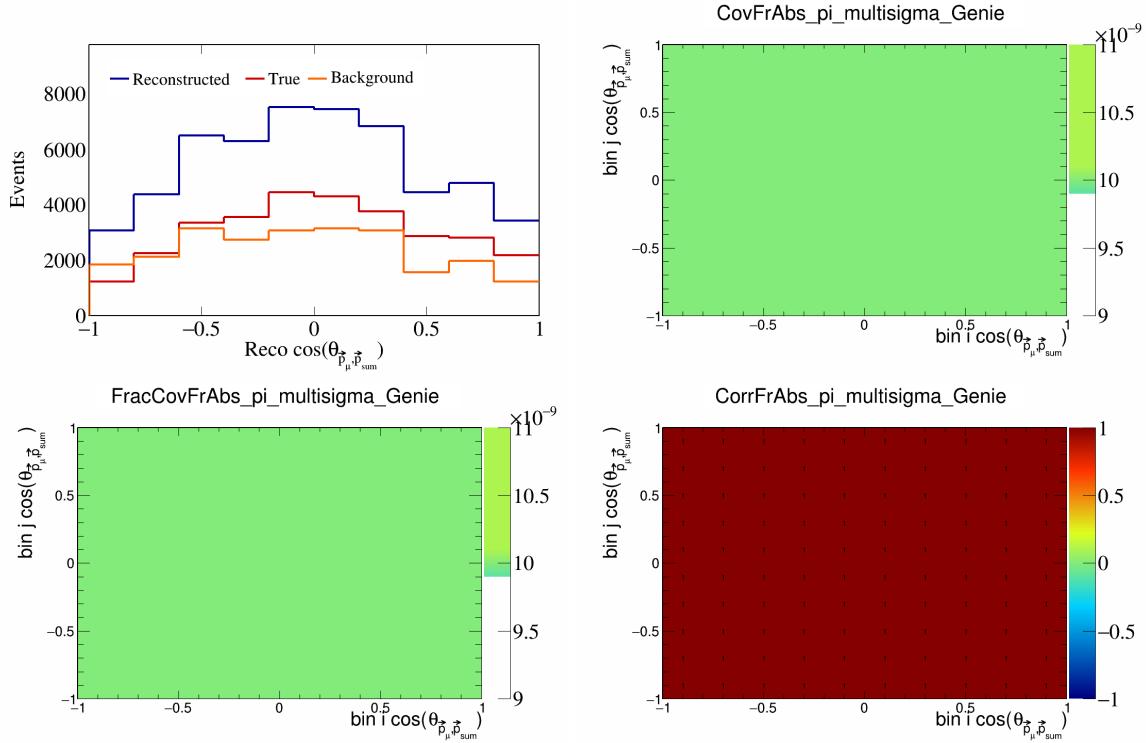


Figure 136: FrAbspi variations for $\cos(\theta_{\vec{p}_\mu, \vec{p}_{\text{sum}}})$.

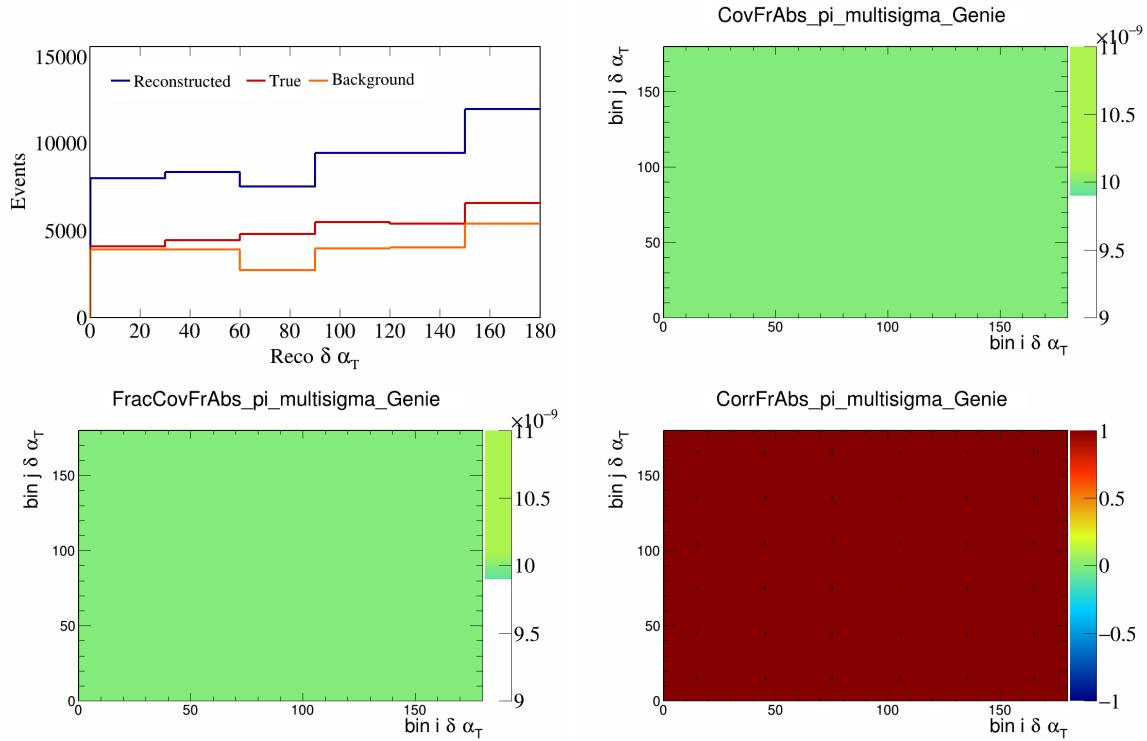


Figure 137: FrAbspi variations for $\delta \alpha_T$.

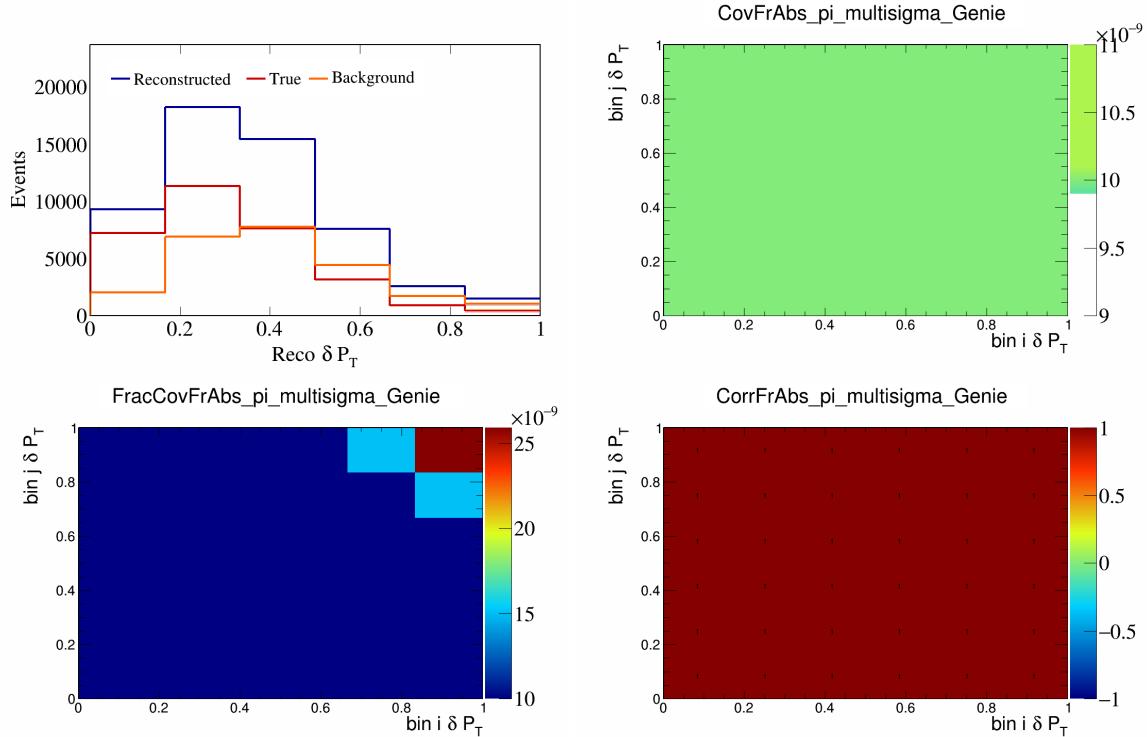


Figure 138: FrAbspi variations for δP_T .

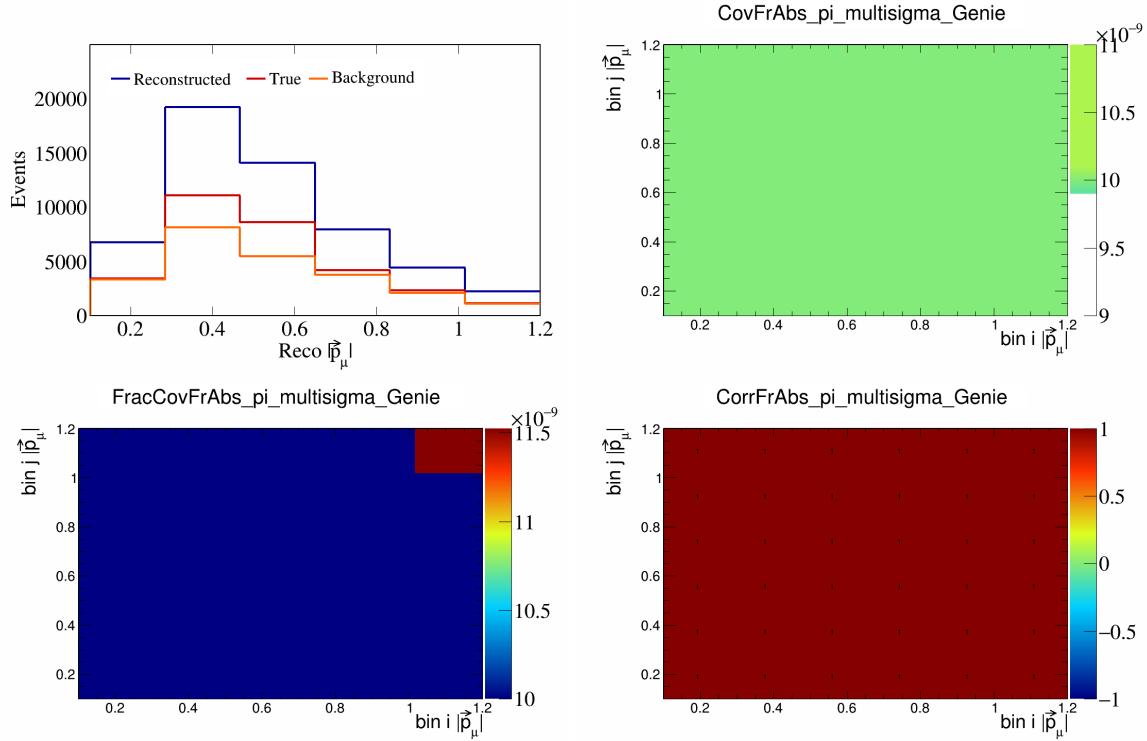


Figure 139: FrAbspi variations for $|\vec{p}_\mu|$.

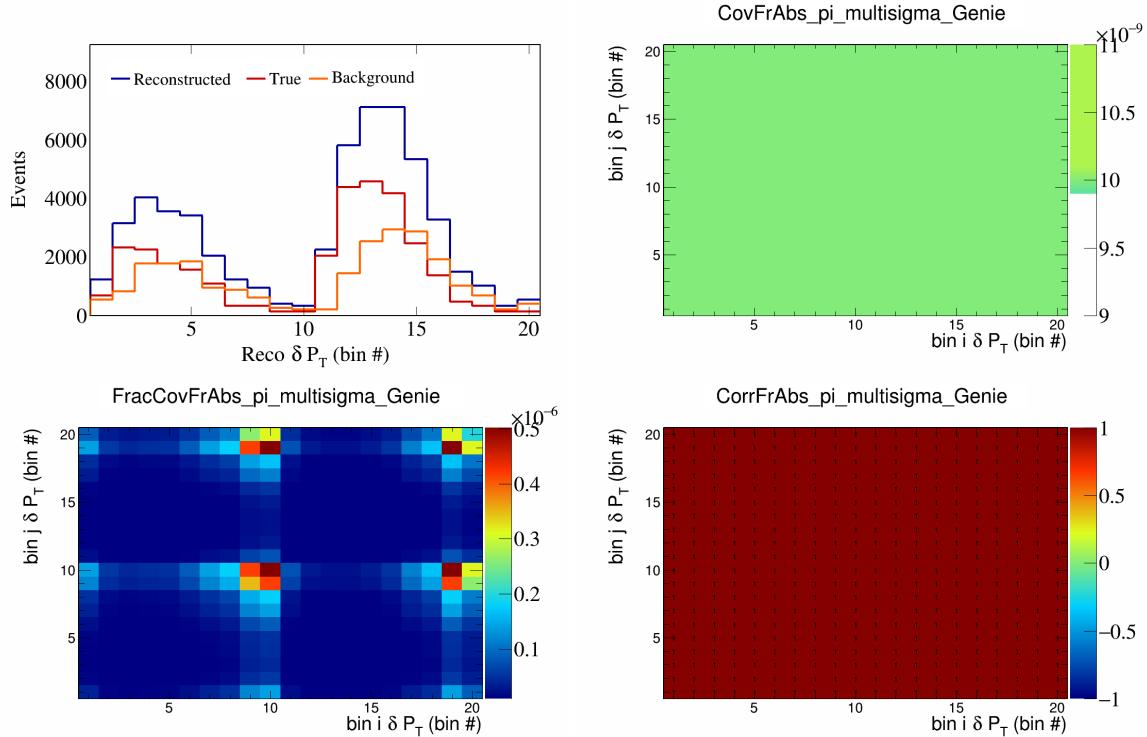


Figure 140: FrAbspi variations for δP_T in $\cos(\theta_{\vec{p}_\mu})$.

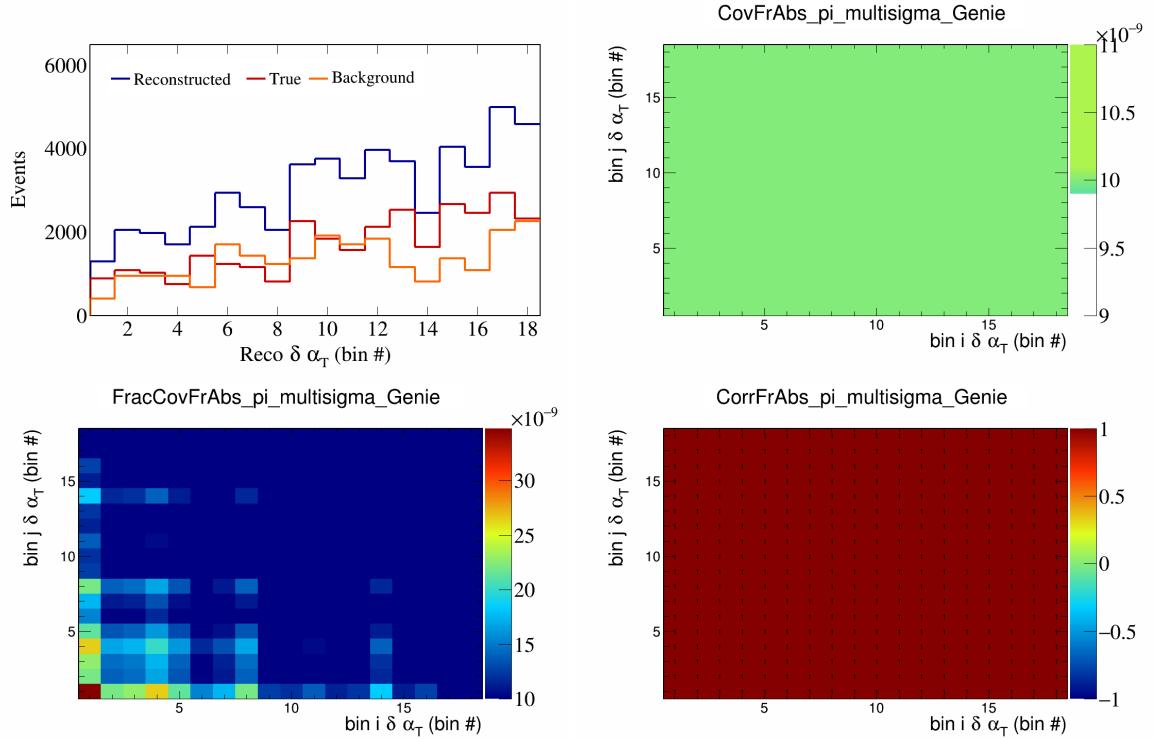


Figure 141: FrAbspi variations for $\delta\alpha_T$ in $\cos(\theta_{\vec{p}_\mu})$.

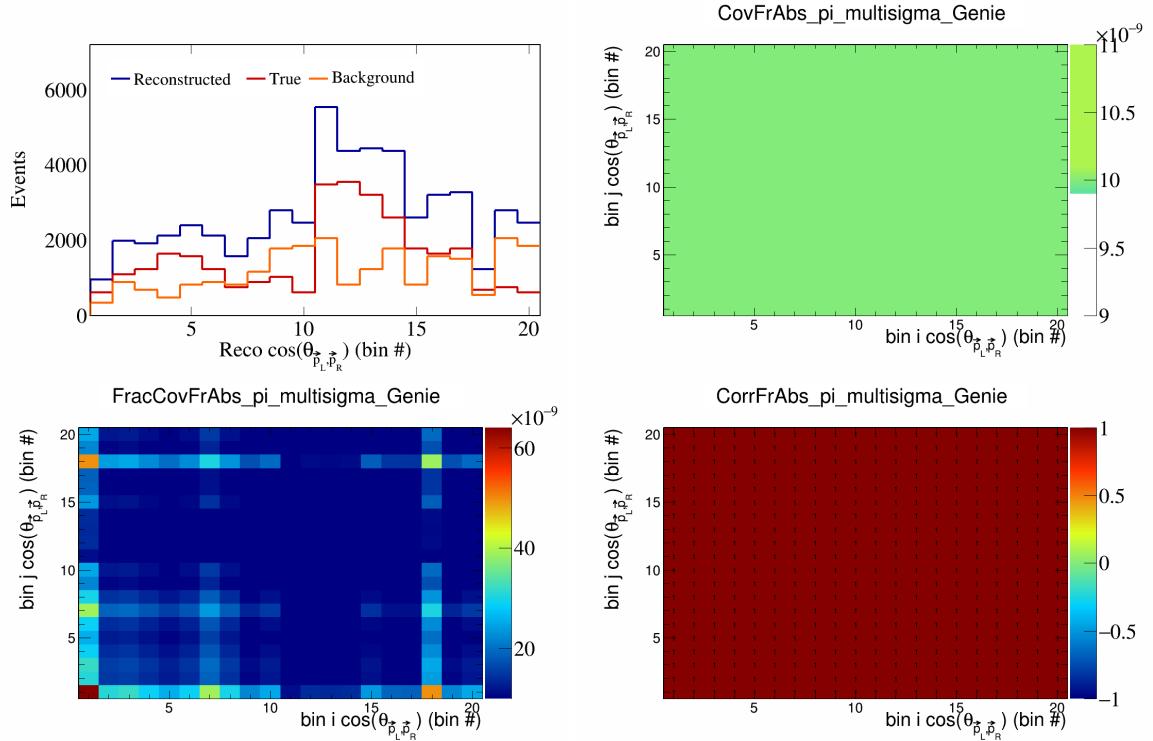


Figure 142: FrAbspi variations for $\cos(\theta_{\vec{p}_L, \vec{p}_R})$ in $\cos(\theta_{\vec{p}_\mu})$.

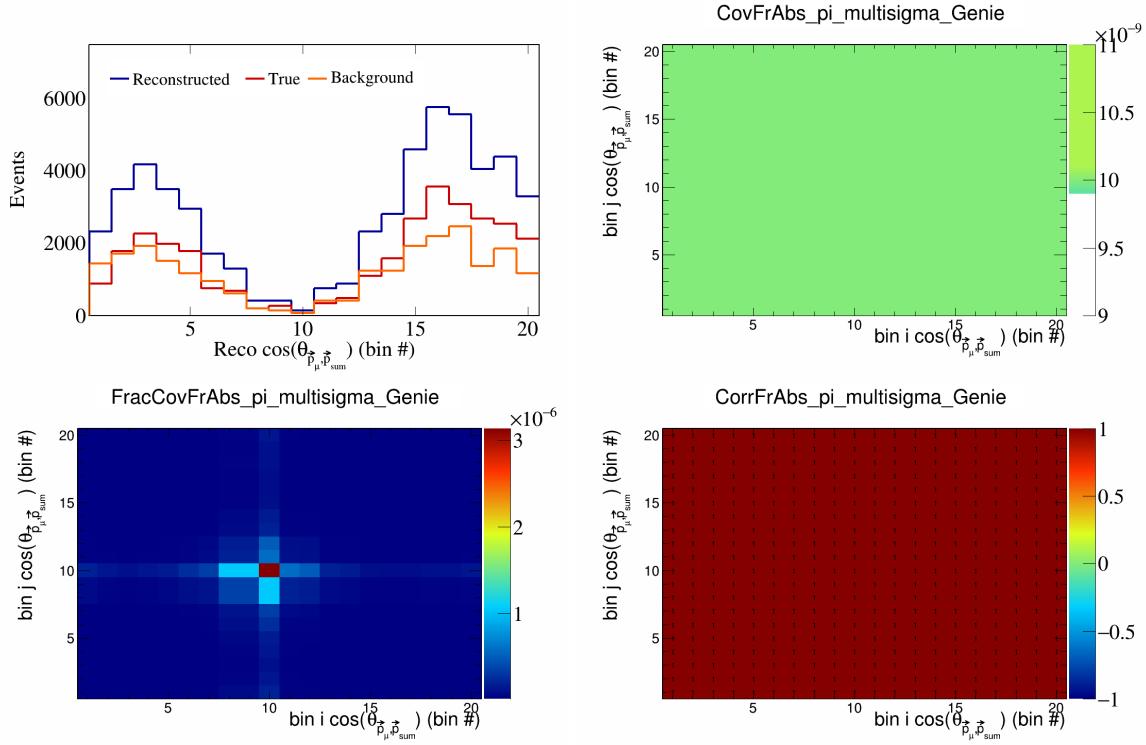


Figure 143: FrAbspi variations for $\cos(\theta_{\vec{p}_\mu})$ in $\cos(\theta_{\vec{p}_\mu})$.

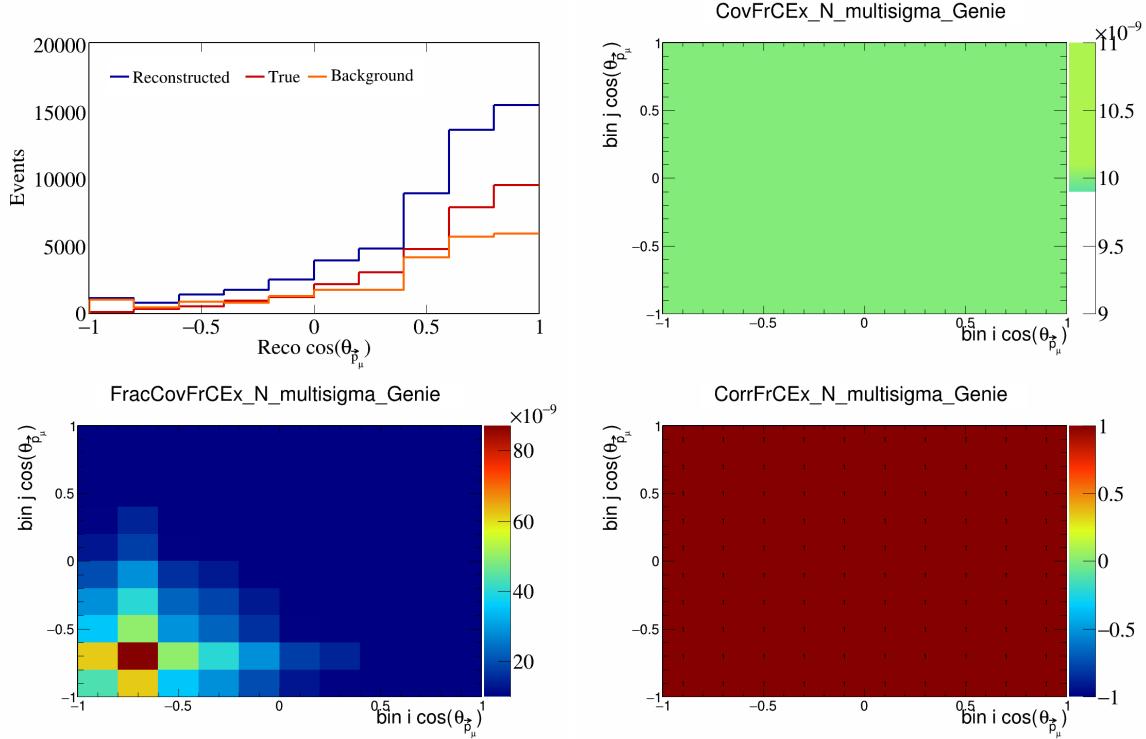


Figure 144: FrCExN variations for $\cos(\theta_{\vec{p}_\mu})$.

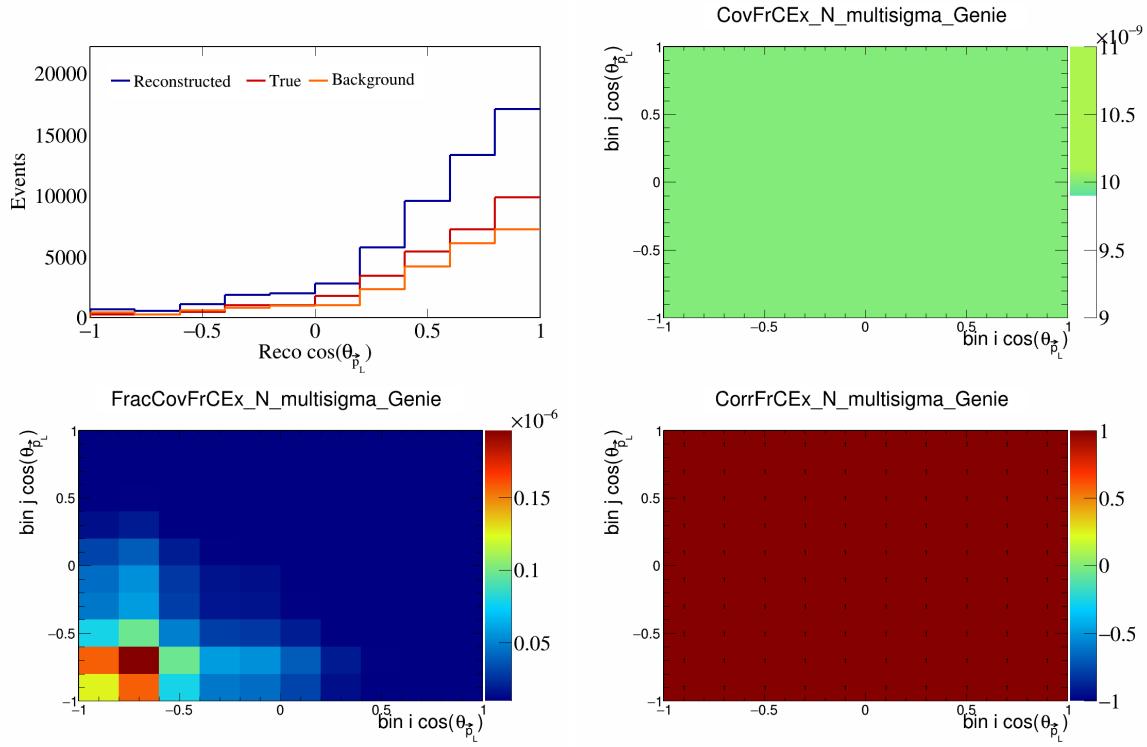


Figure 145: FrCExN variations for $\cos(\theta_{\vec{p}_L})$.

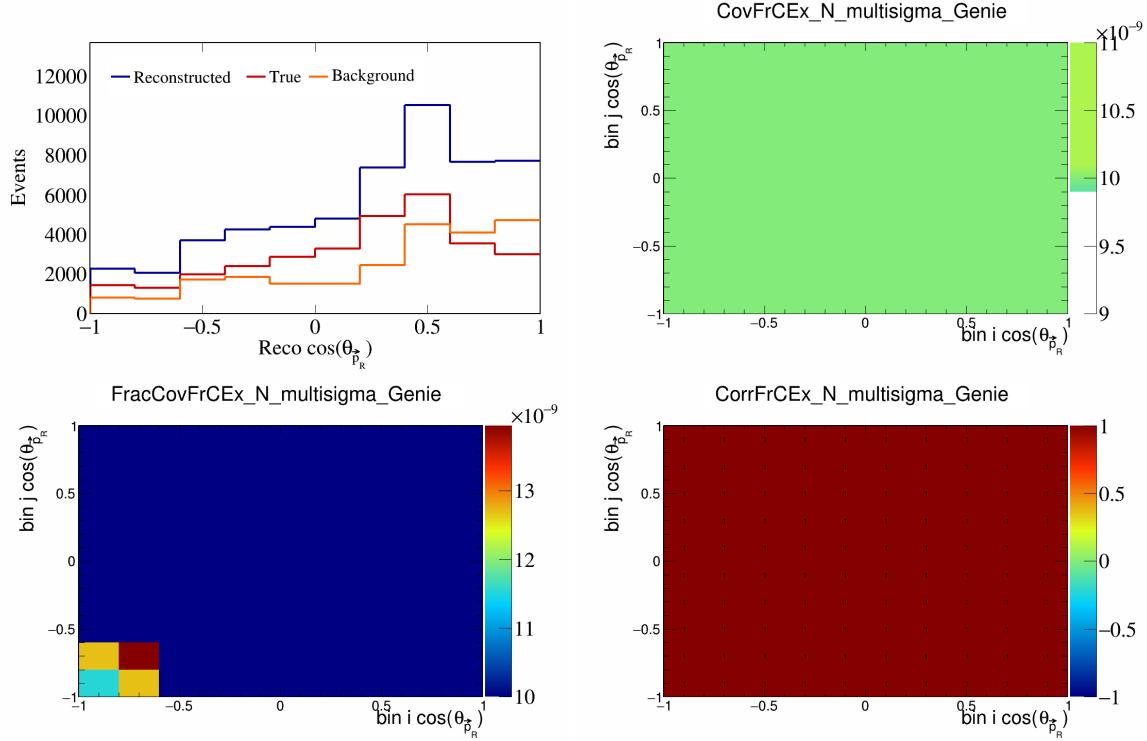


Figure 146: FrCExN variations for $\cos(\theta_{\vec{p}_R})$.

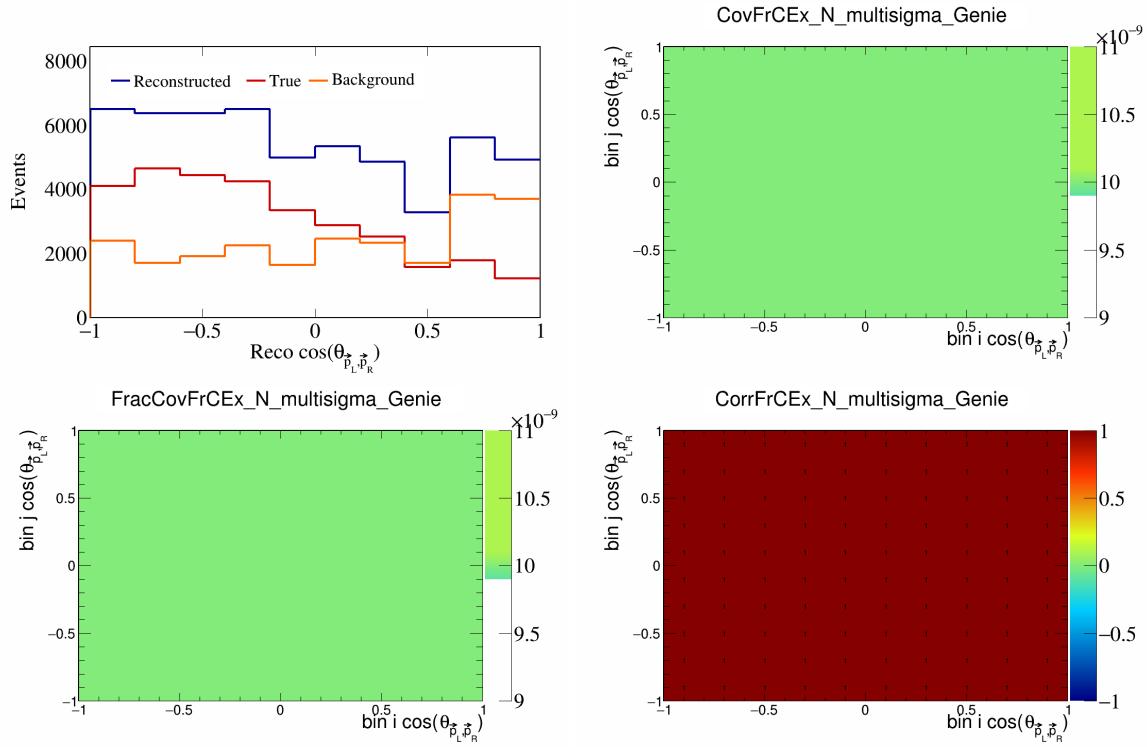


Figure 147: FrCEExN variations for $\cos(\theta_{\vec{p}_L, \vec{p}_R})$.

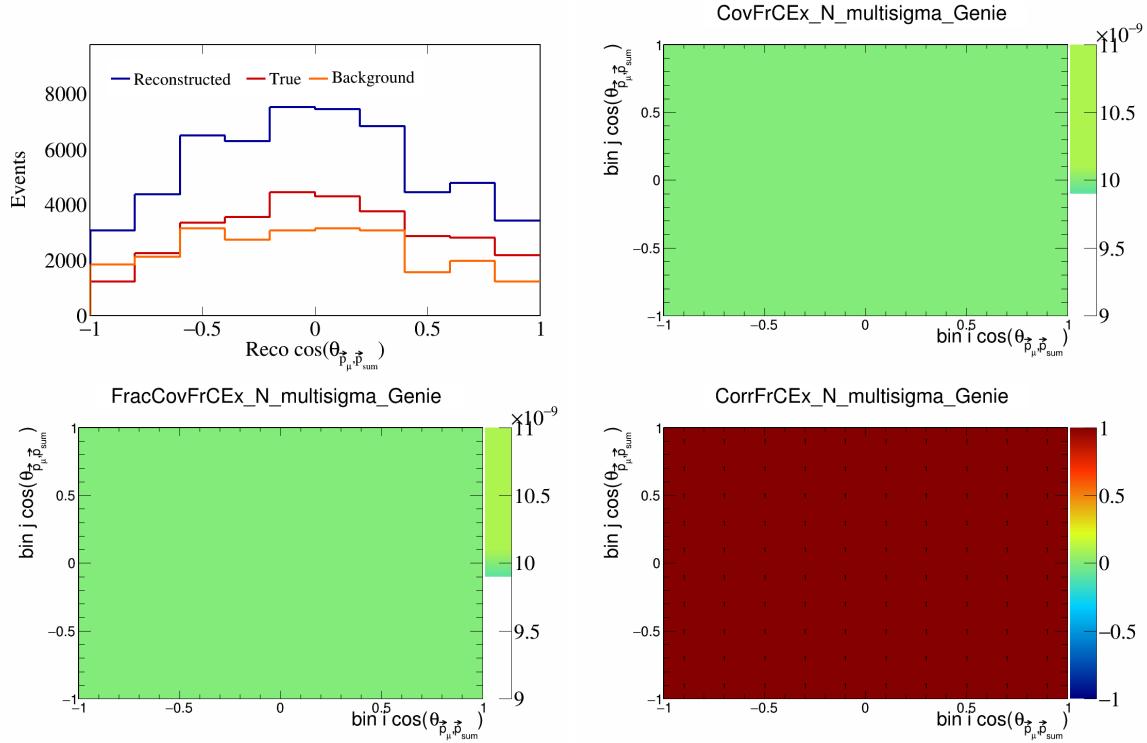


Figure 148: FrCEExN variations for $\cos(\theta_{\vec{p}_\mu, \vec{p}_{\text{sum}}})$.

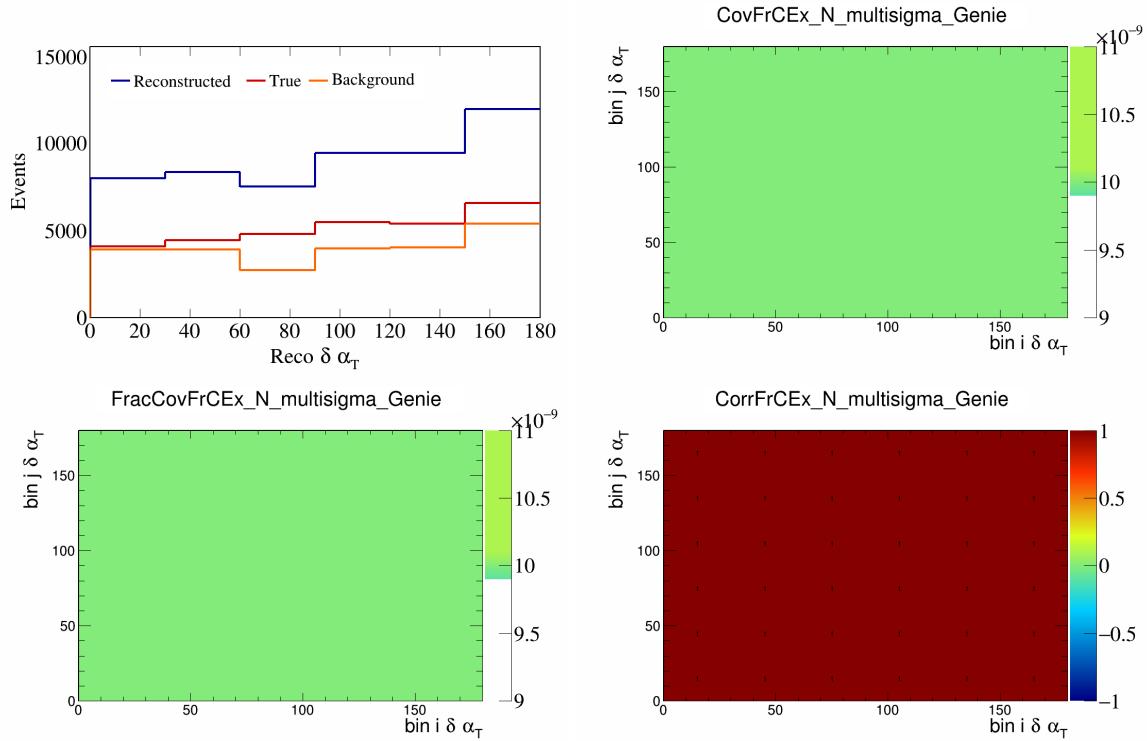


Figure 149: FrCEExN variations for $\delta\alpha_T$.

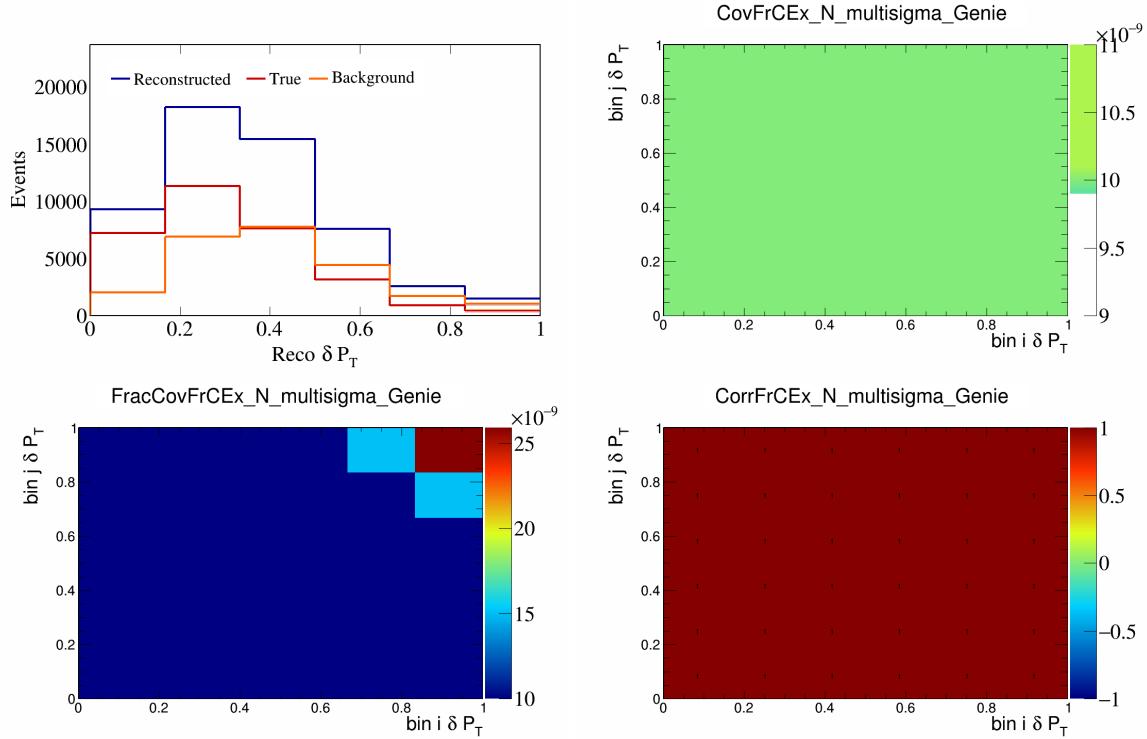


Figure 150: FrCEExN variations for δP_T .

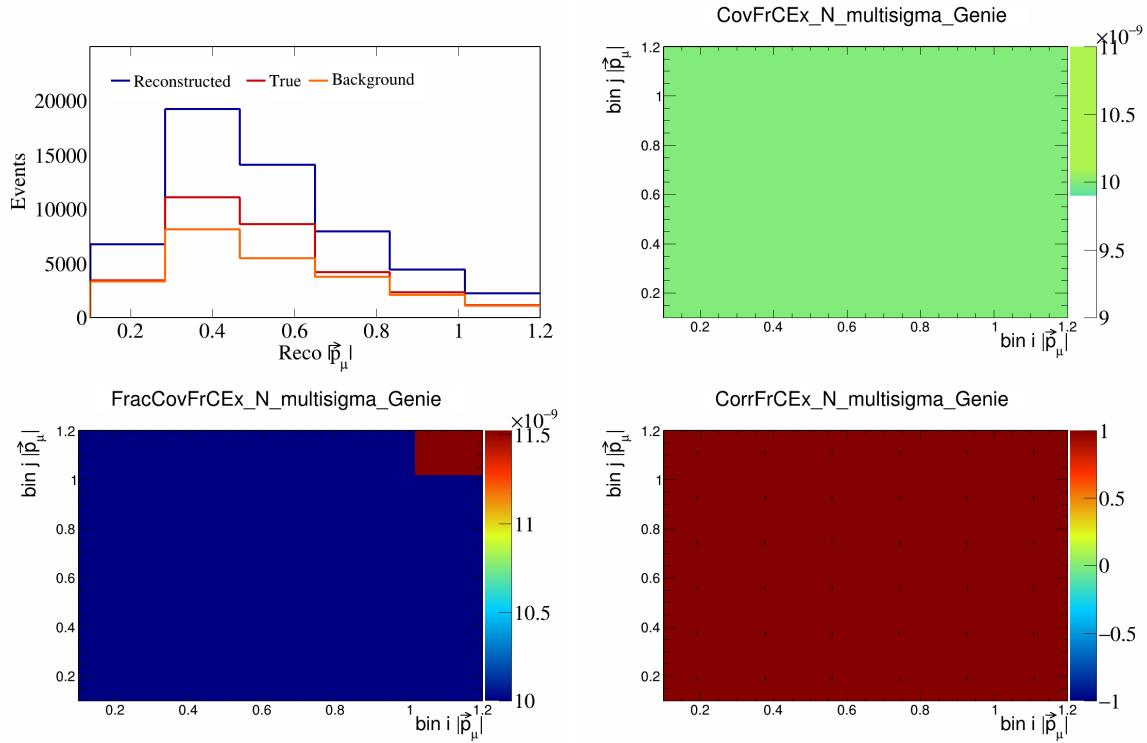


Figure 151: FrCExN variations for $|\vec{p}_\mu|$.

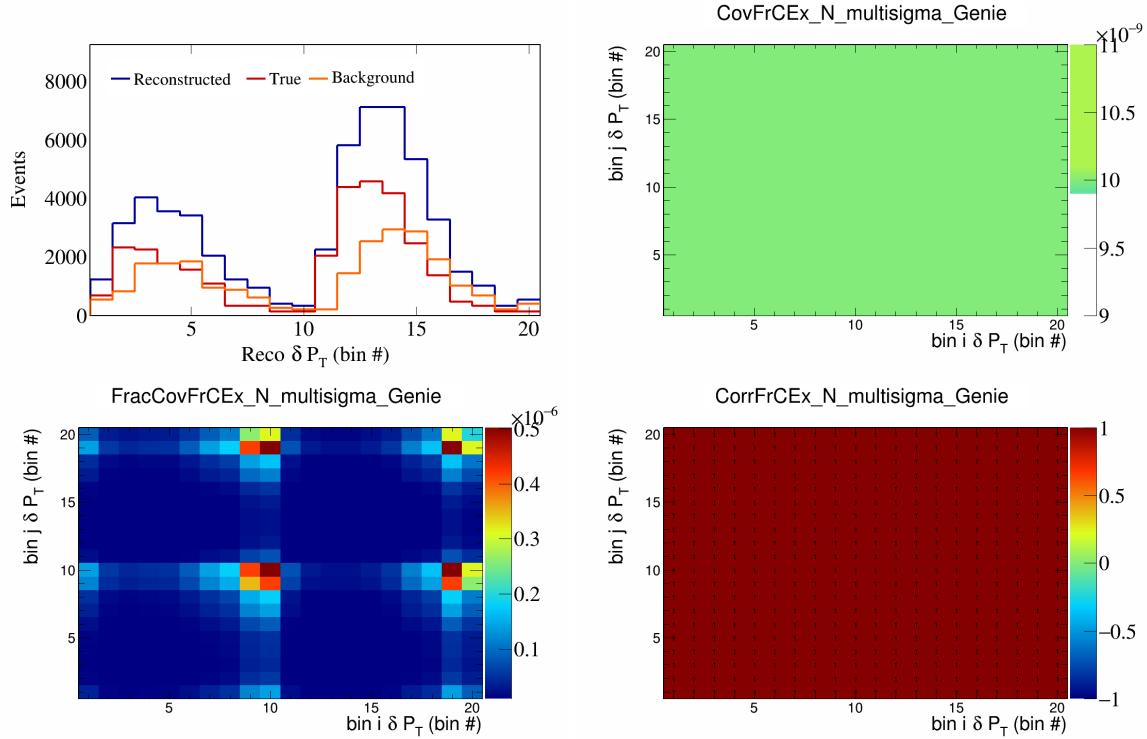


Figure 152: FrCExN variations for δP_T in $\cos(\theta_{\vec{p}_\mu})$.

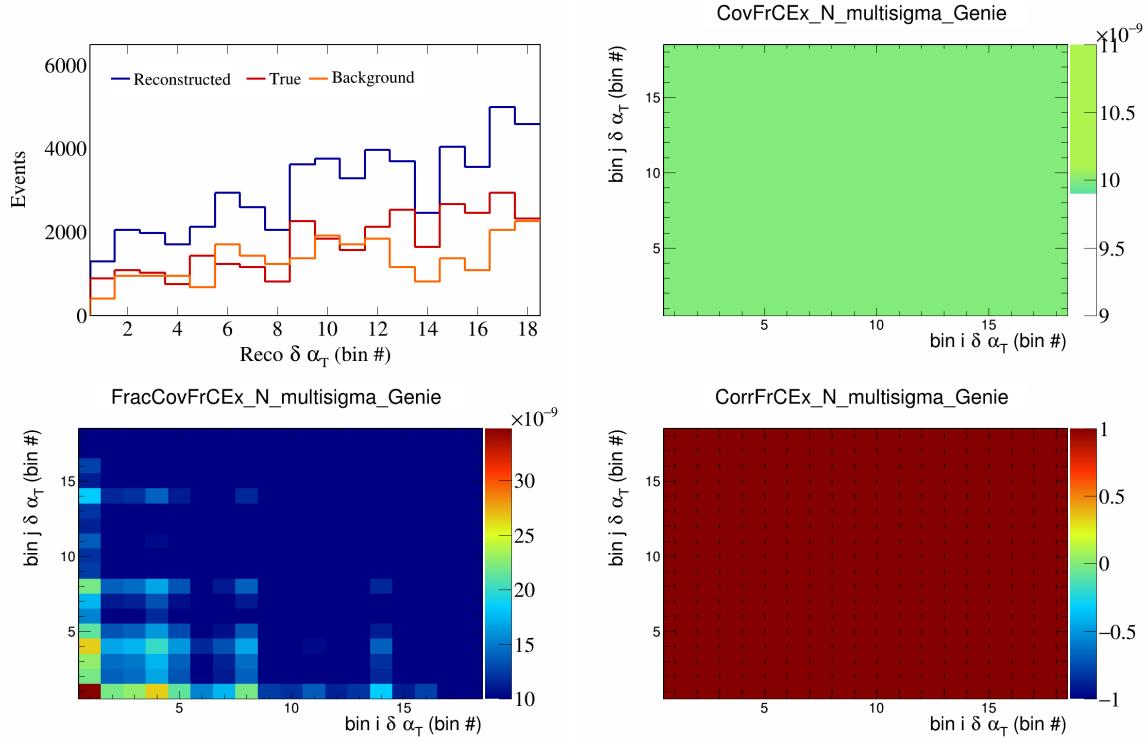


Figure 153: FrCEExN variations for $\delta \alpha_T$ in $\cos(\theta_{\vec{p}_\mu})$.

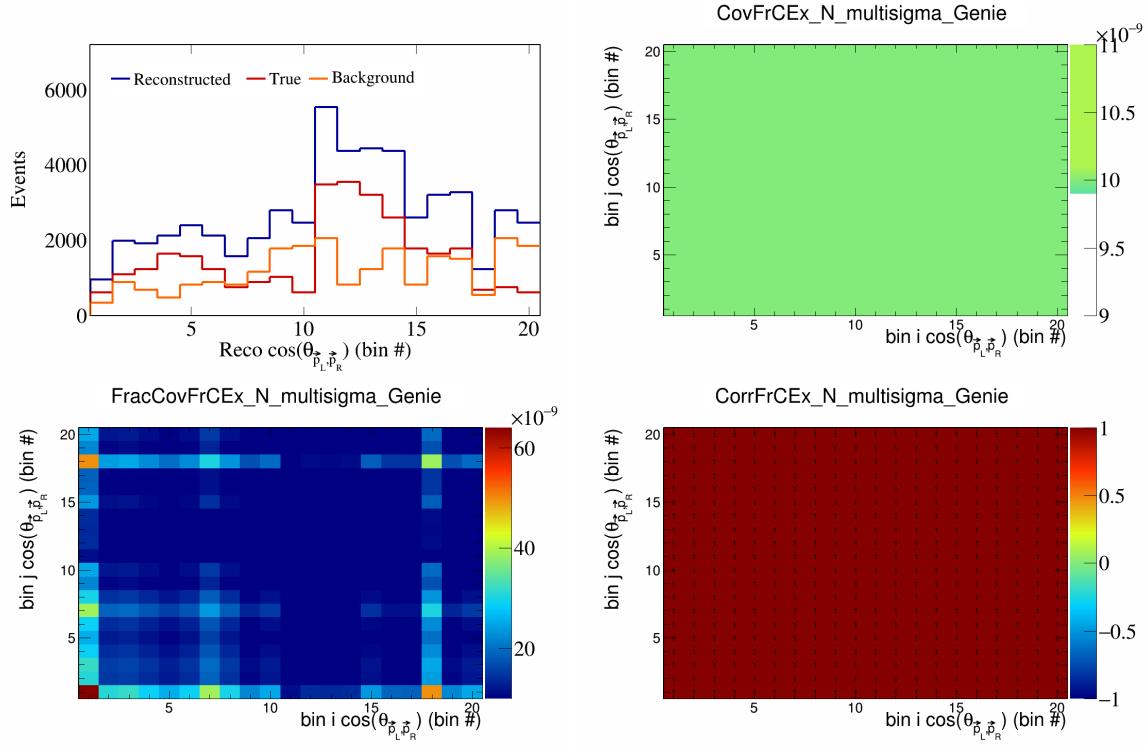


Figure 154: FrCEExN variations for $\cos(\theta_{\vec{p}_L, \vec{p}_R})$ in $\cos(\theta_{\vec{p}_\mu})$.

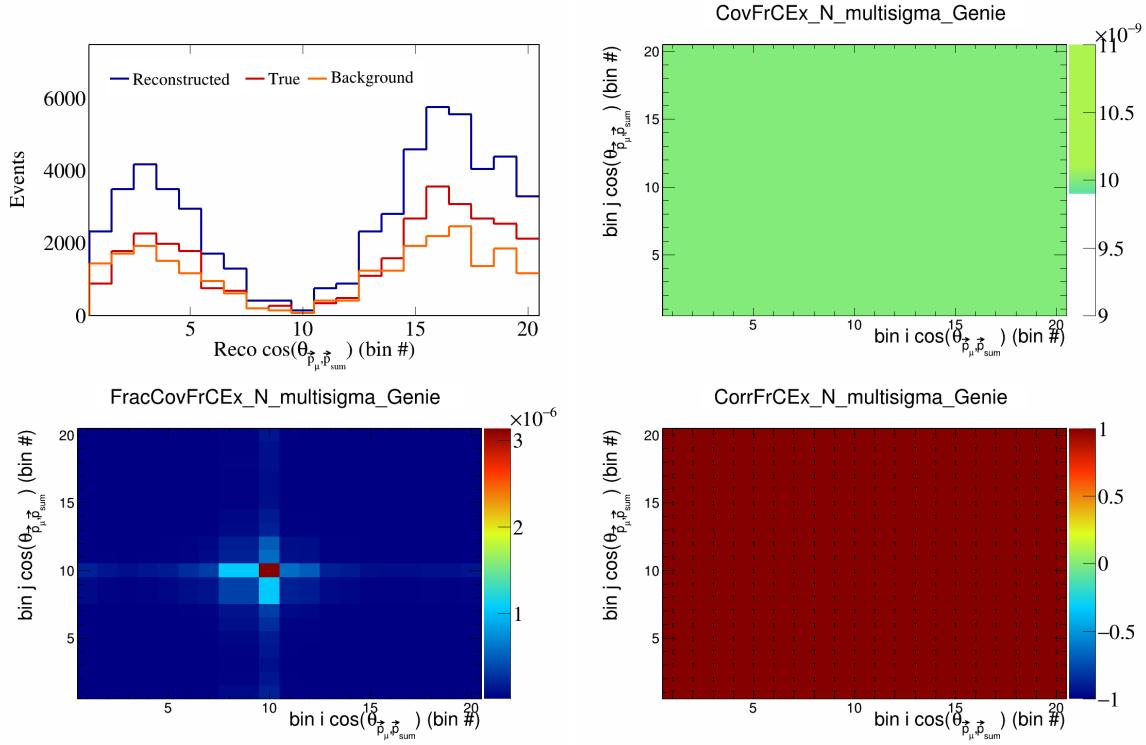


Figure 155: FrCEExN variations for $\cos(\theta_{\vec{p}_\mu, \vec{p}_{\text{sum}}})$ in $\cos(\theta_{\vec{p}_\mu})$.

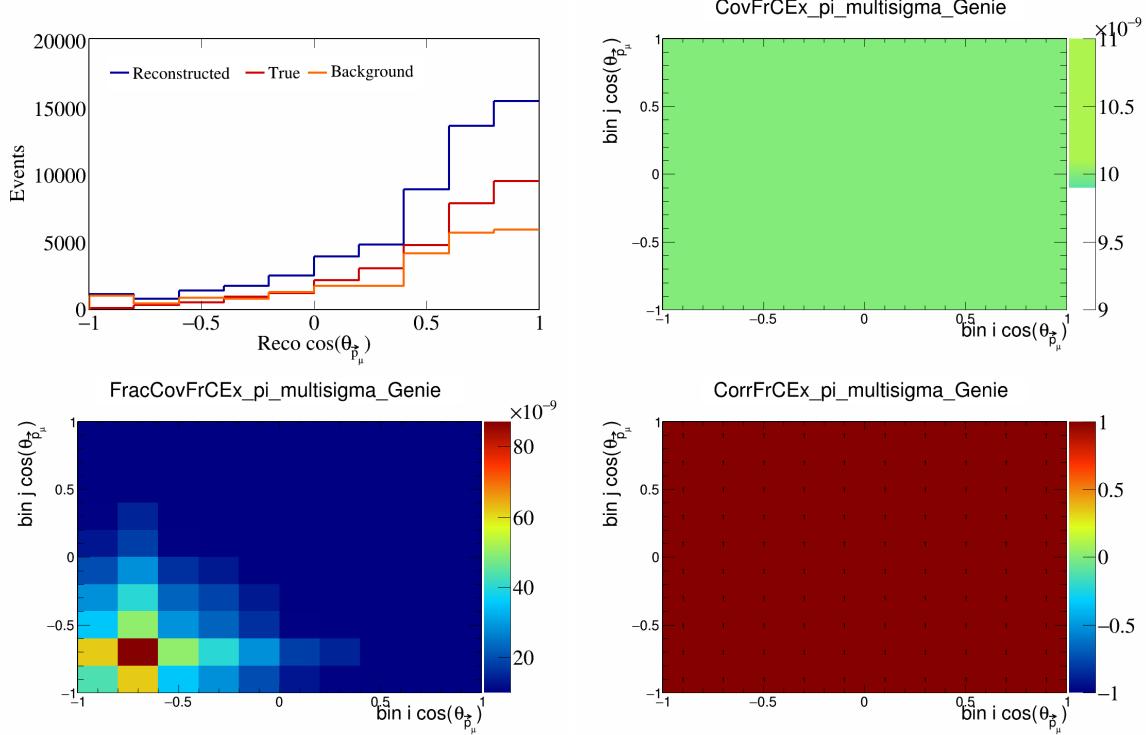


Figure 156: FrCEExpi variations for $\cos(\theta_{\vec{p}_\mu})$.

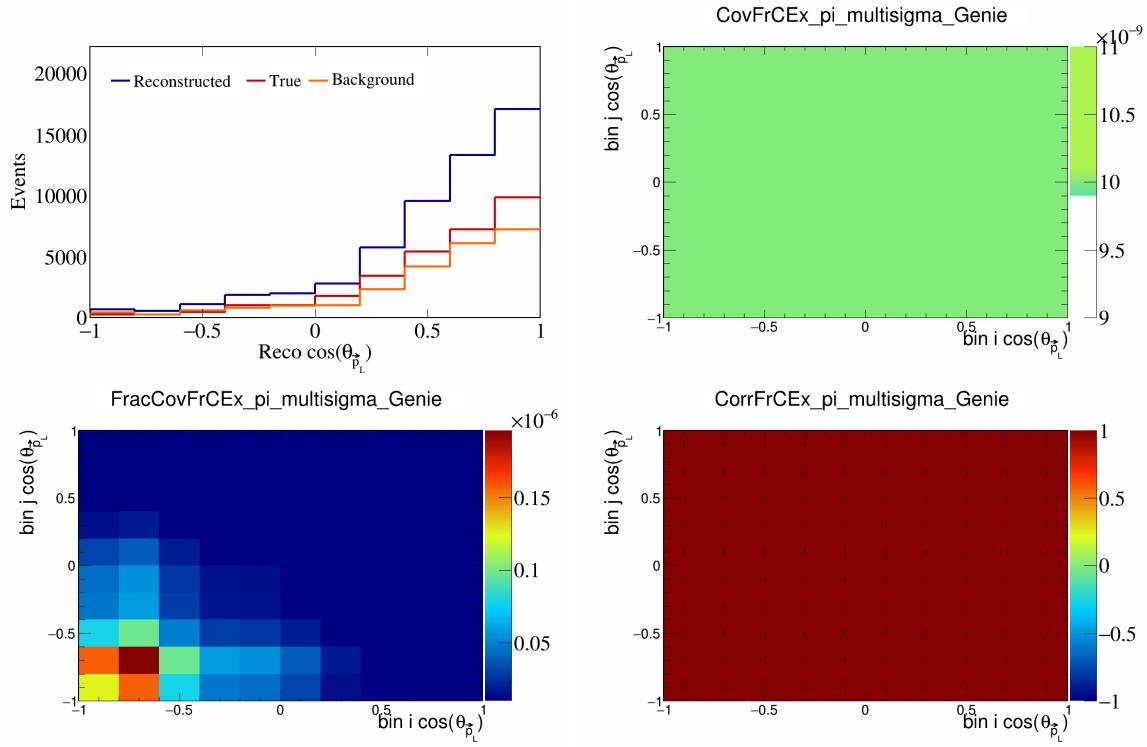


Figure 157: FrCExpi variations for $\cos(\theta_{\vec{p}_L})$.

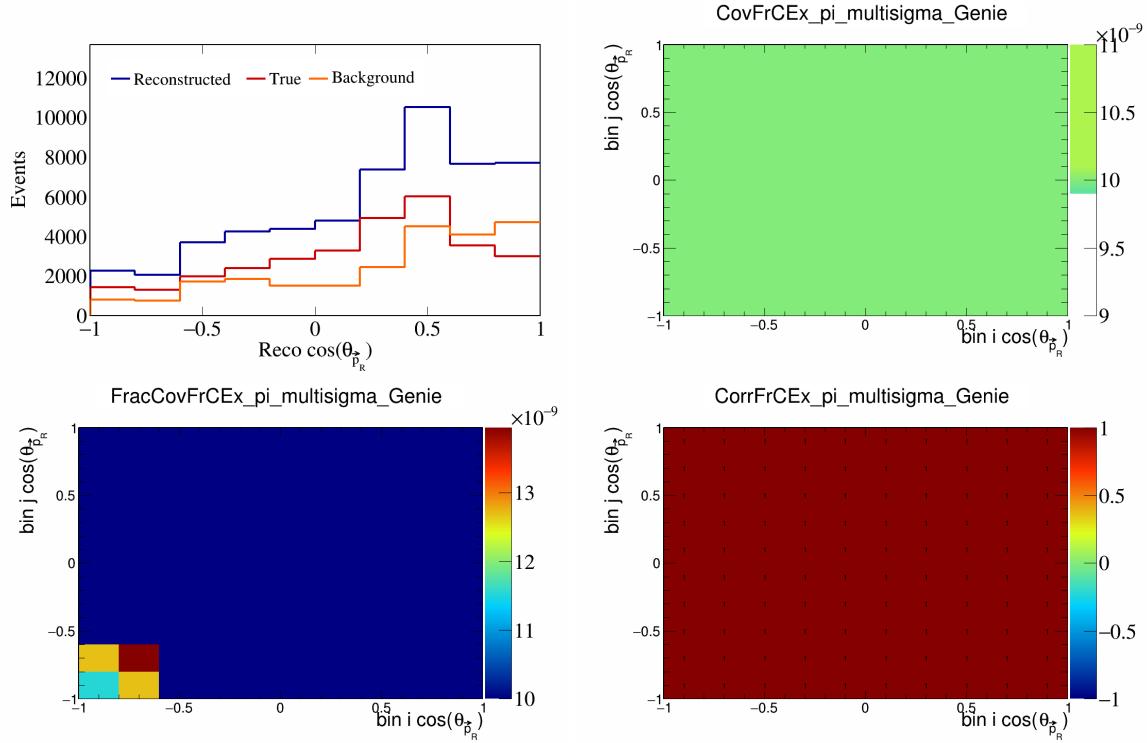


Figure 158: FrCExpi variations for $\cos(\theta_{\vec{p}_R})$.

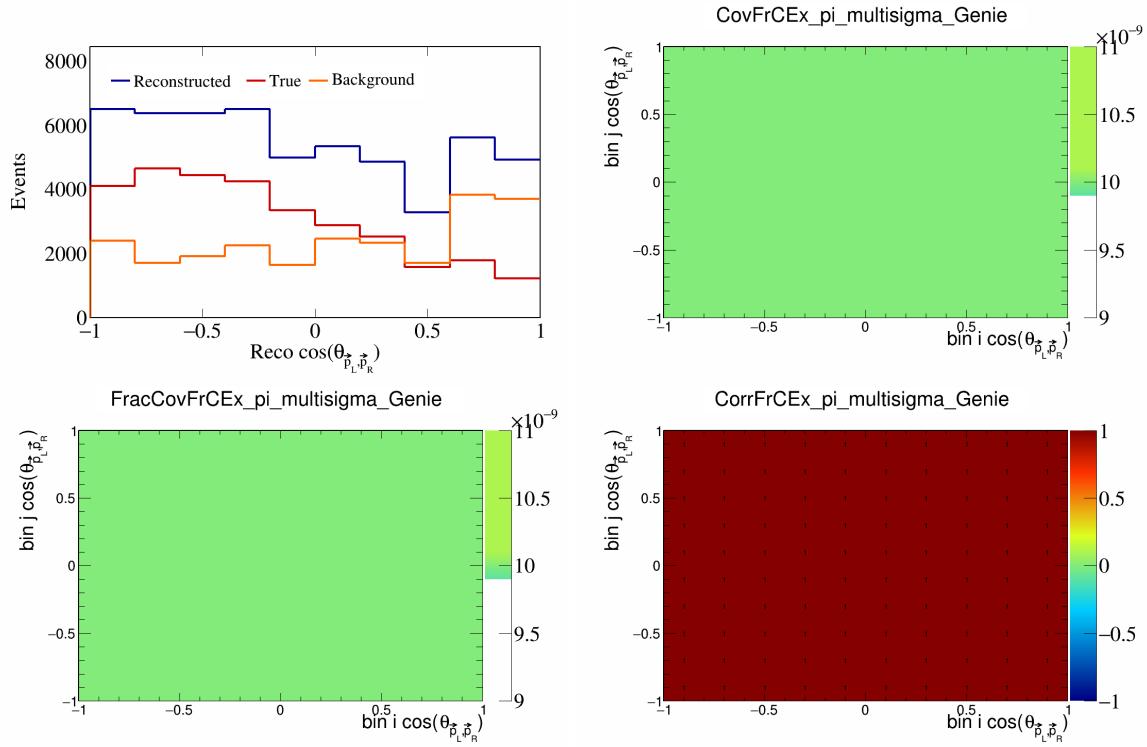


Figure 159: FrCEpi variations for $\cos(\theta_{\vec{p}_L, \vec{p}_R})$.

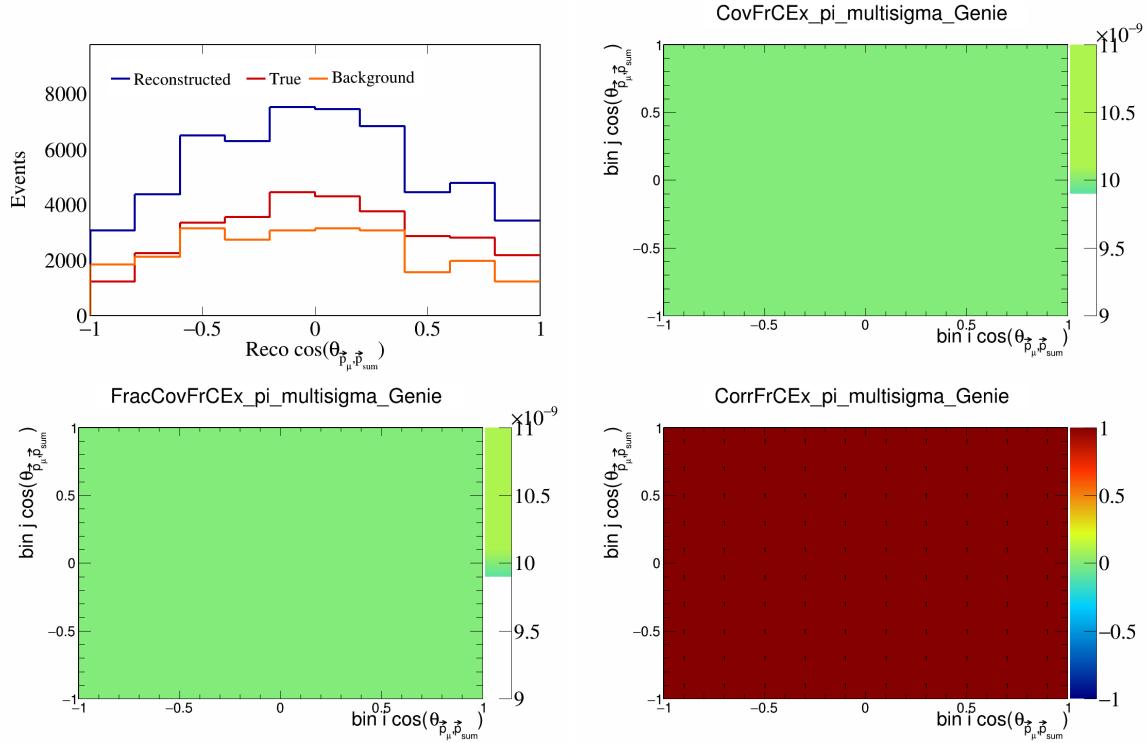


Figure 160: FrCEpi variations for $\cos(\theta_{\vec{p}_\mu, \vec{p}_{\text{sum}}})$.

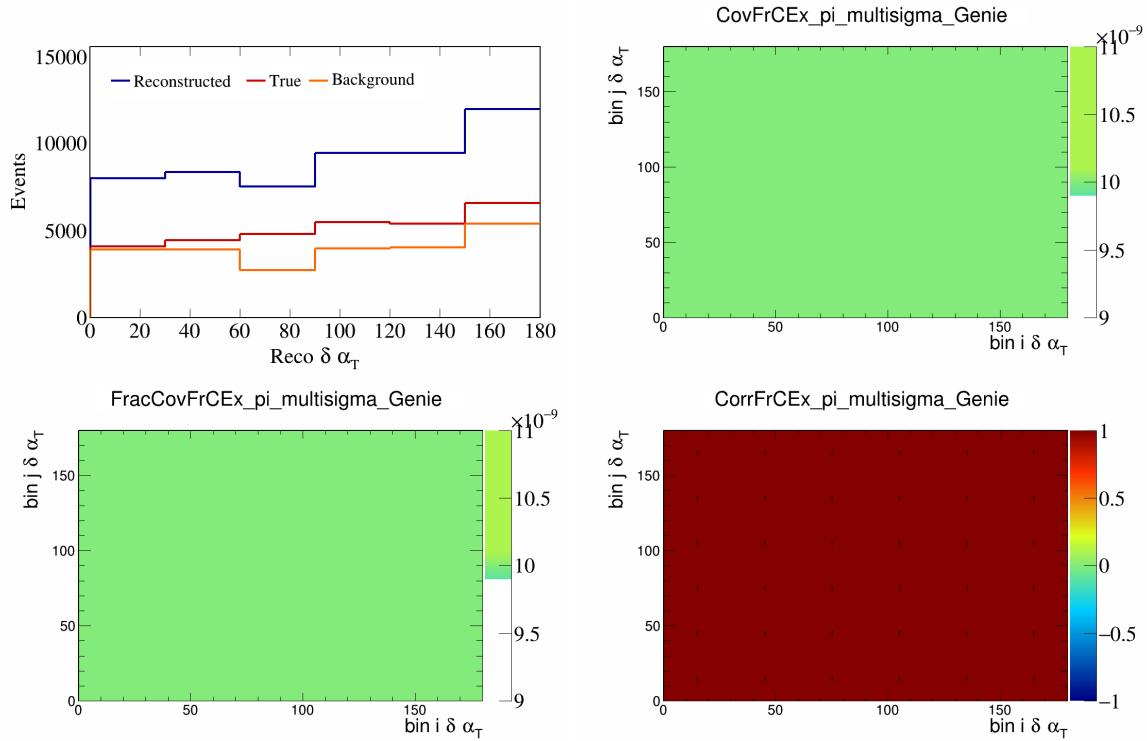


Figure 161: FrCEExpi variations for $\delta \alpha_T$.

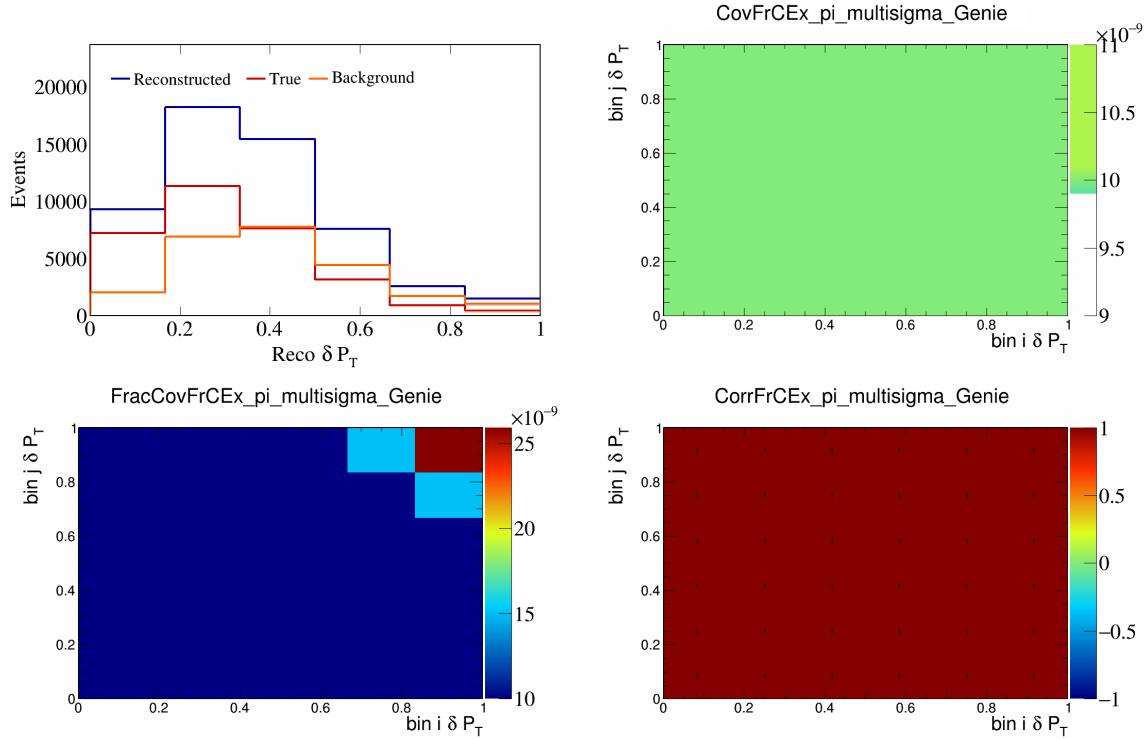


Figure 162: FrCEExpi variations for δP_T .

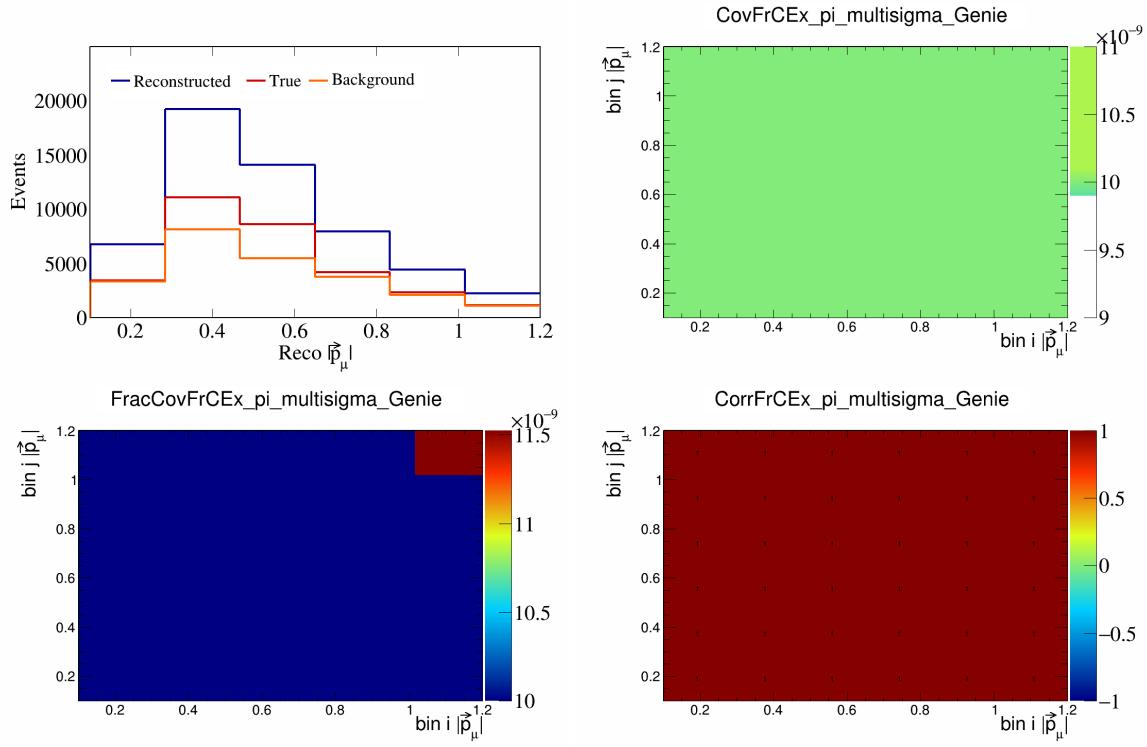


Figure 163: FrCEExpi variations for $|\vec{p}_\mu|$.

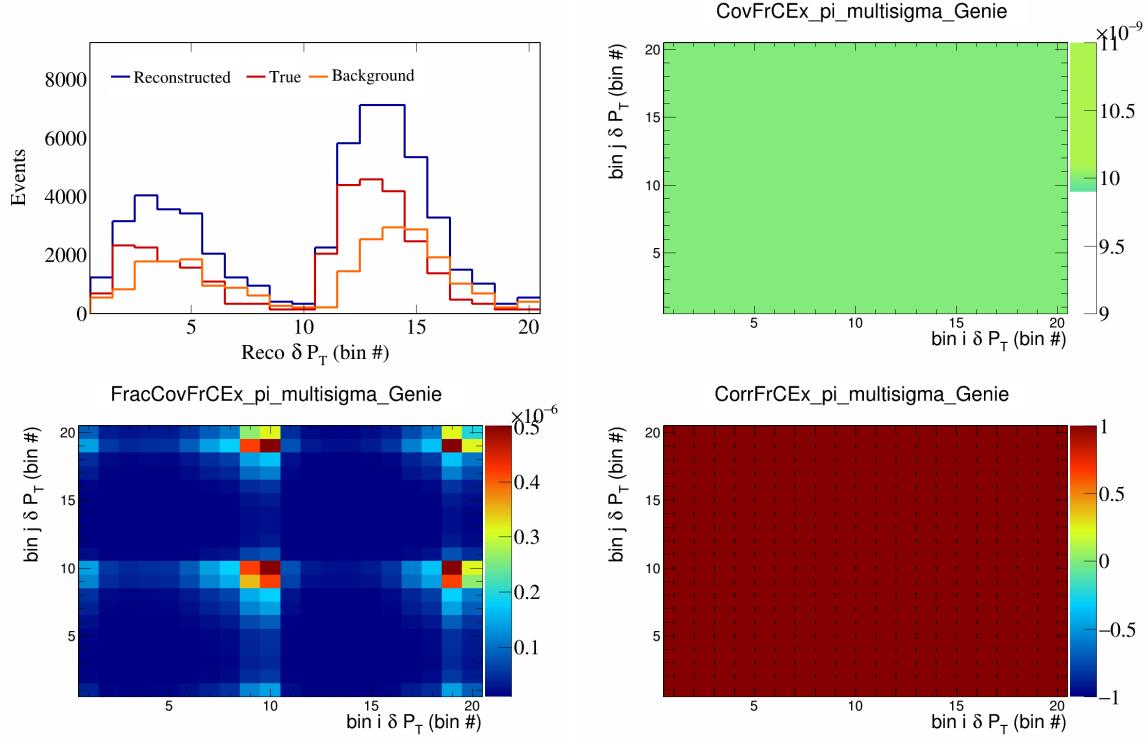


Figure 164: FrCEExpi variations for δP_T in $\cos(\theta_{\vec{p}_\mu})$.

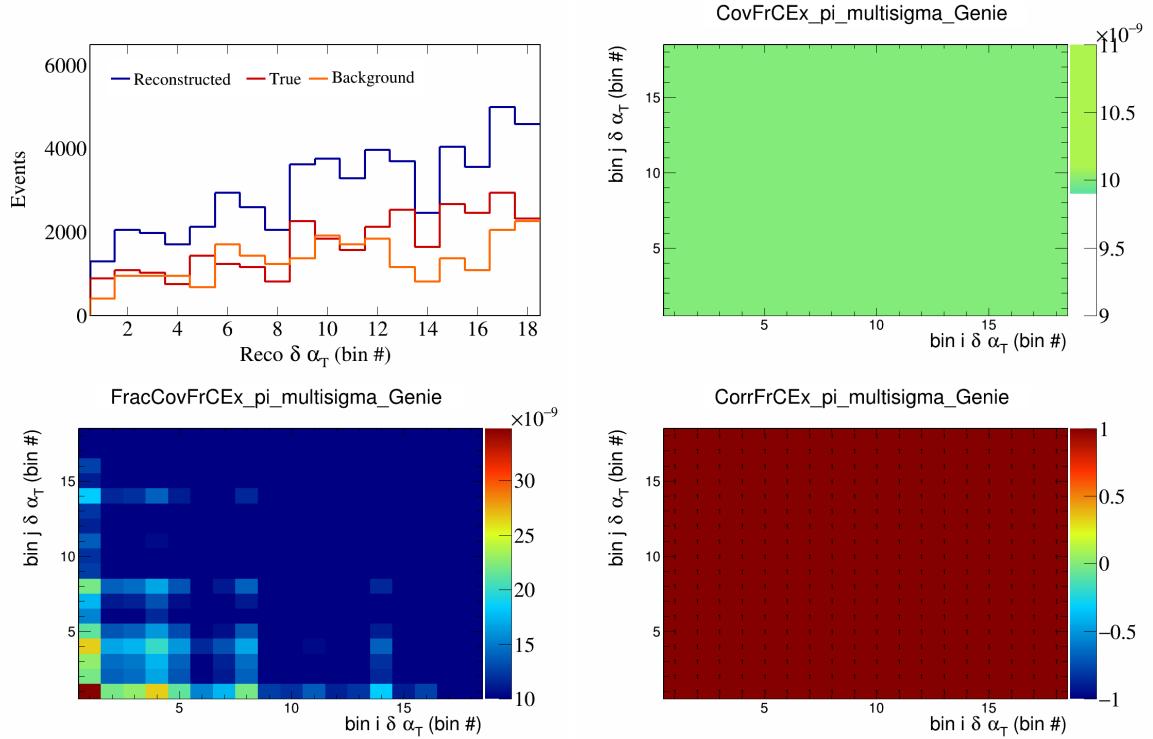


Figure 165: FrCEExpi variations for $\delta\alpha_T$ in $\cos(\theta_{\vec{p}_\mu})$.

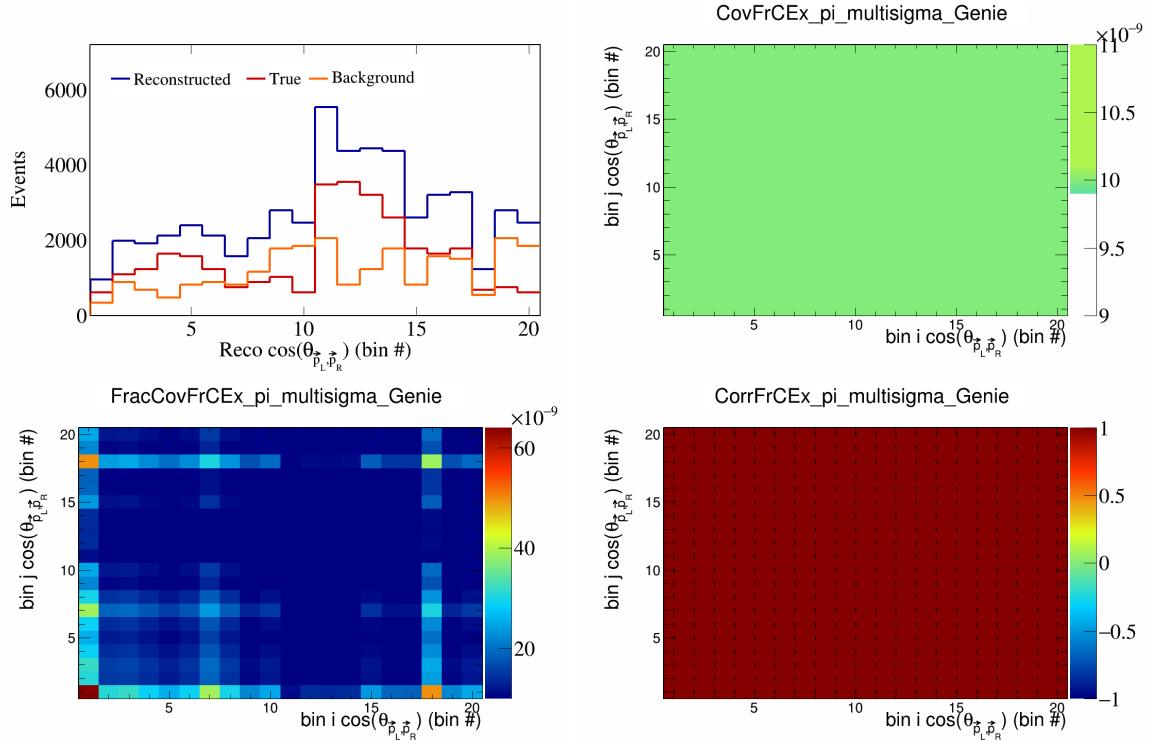


Figure 166: FrCEExpi variations for $\cos(\theta_{\vec{p}_L, \vec{p}_R})$ in $\cos(\theta_{\vec{p}_\mu})$.

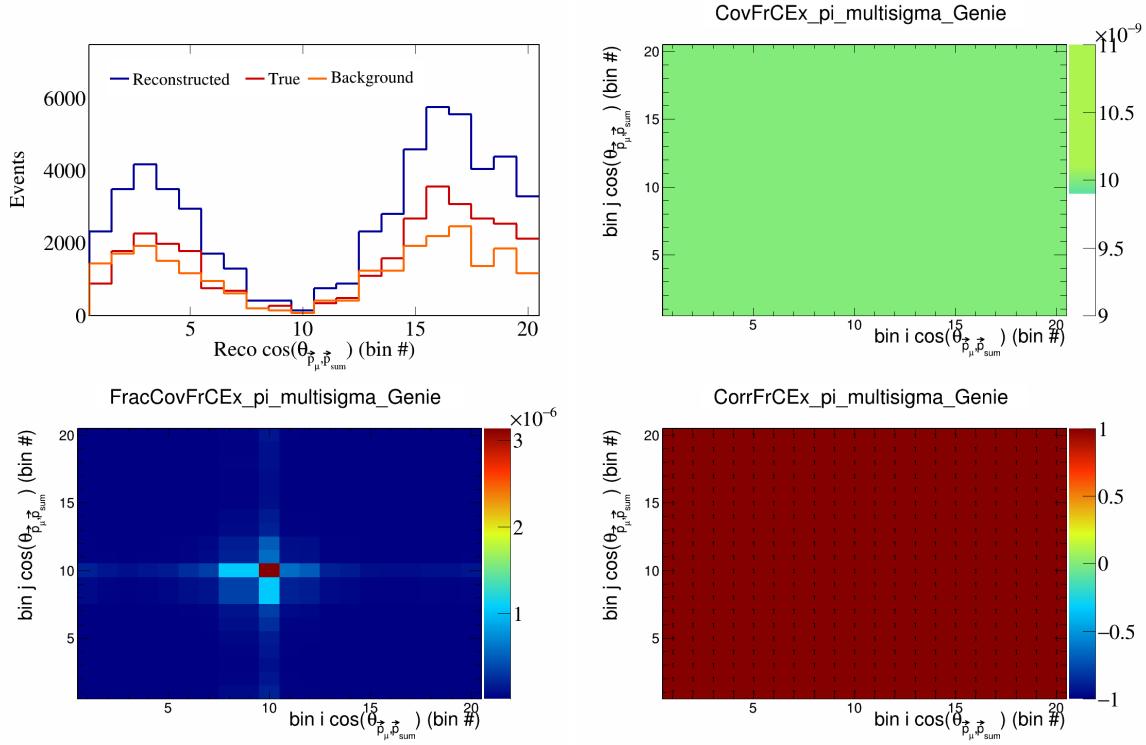


Figure 167: FrCEExpi variations for $\cos(\theta_{\vec{p}_\mu, \vec{p}_{\text{sum}}})$ in $\cos(\theta_{\vec{p}_\mu})$.

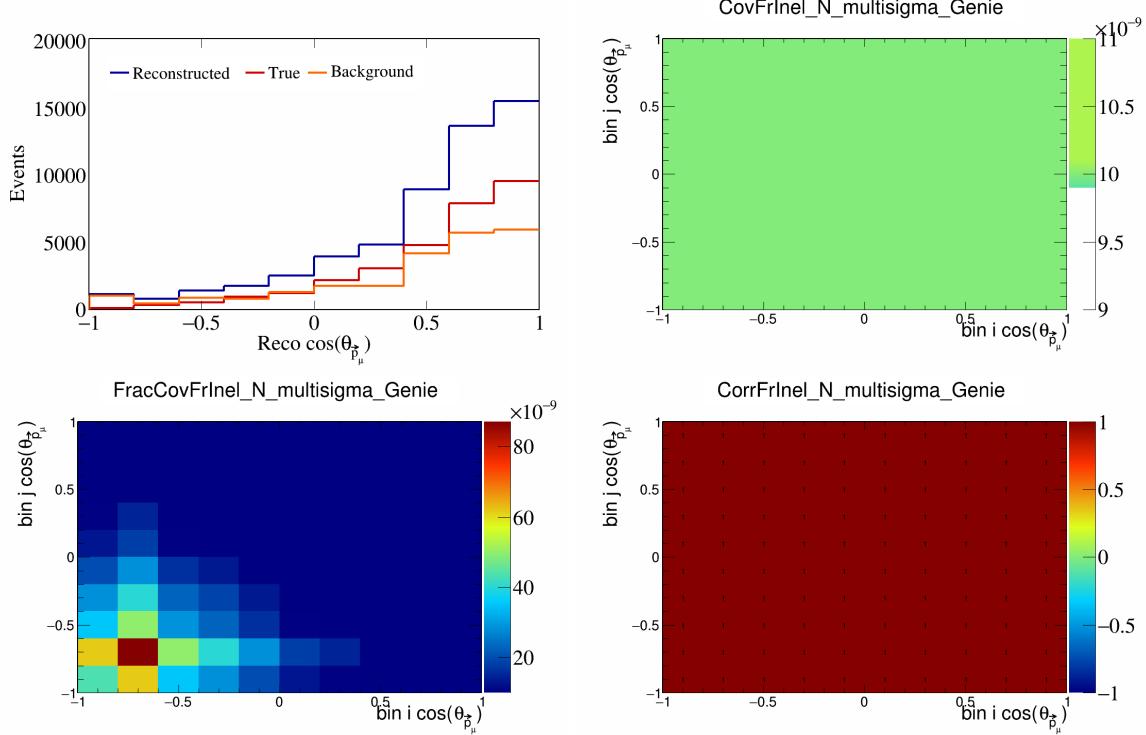


Figure 168: FrInelN variations for $\cos(\theta_{\vec{p}_\mu})$.

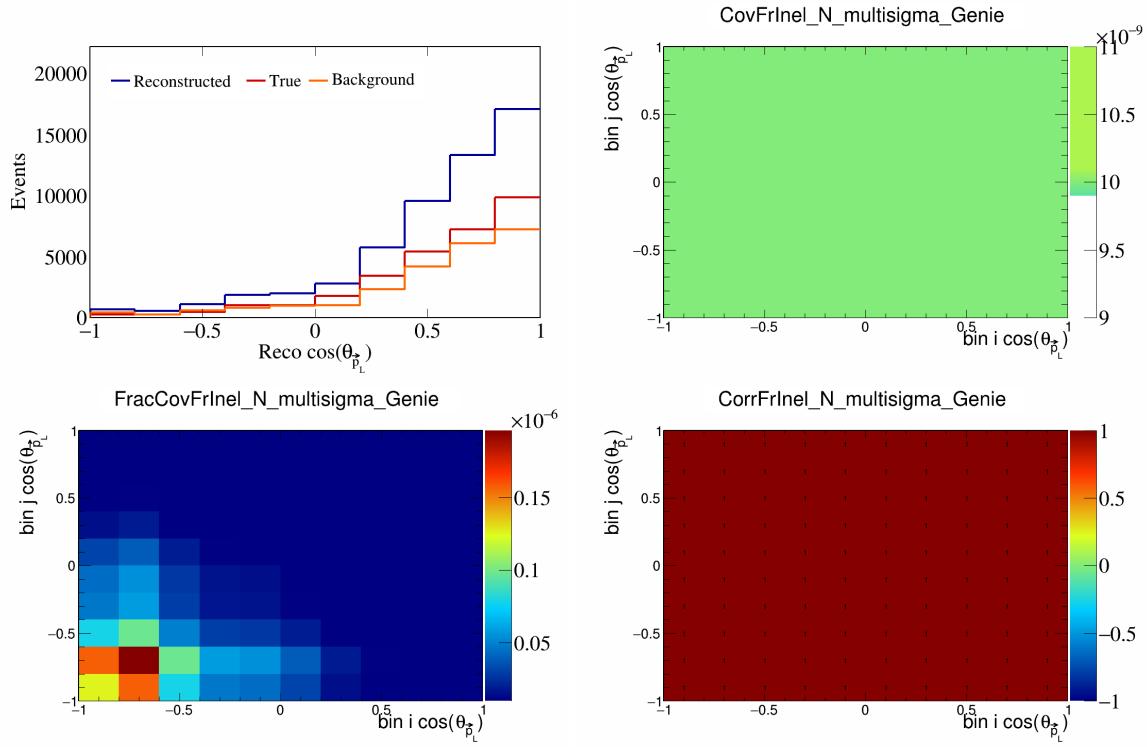


Figure 169: FrInelN variations for $\cos(\theta_{\vec{p}_L})$.

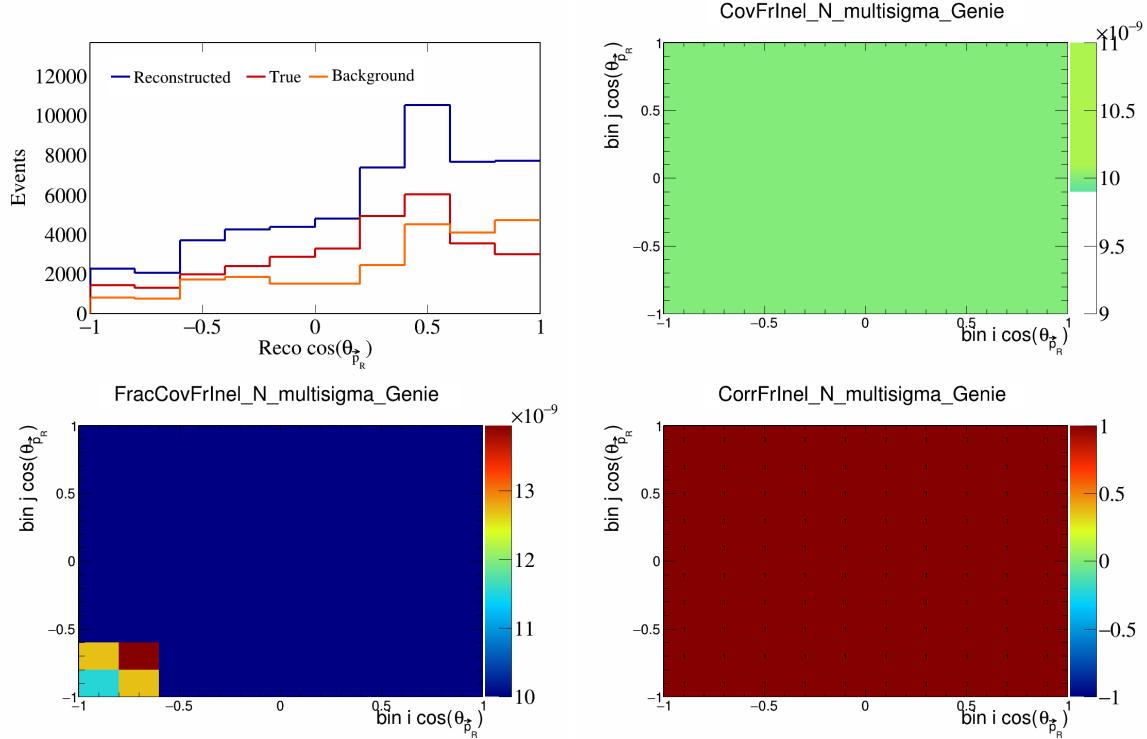


Figure 170: FrInelN variations for $\cos(\theta_{\vec{p}_R})$.

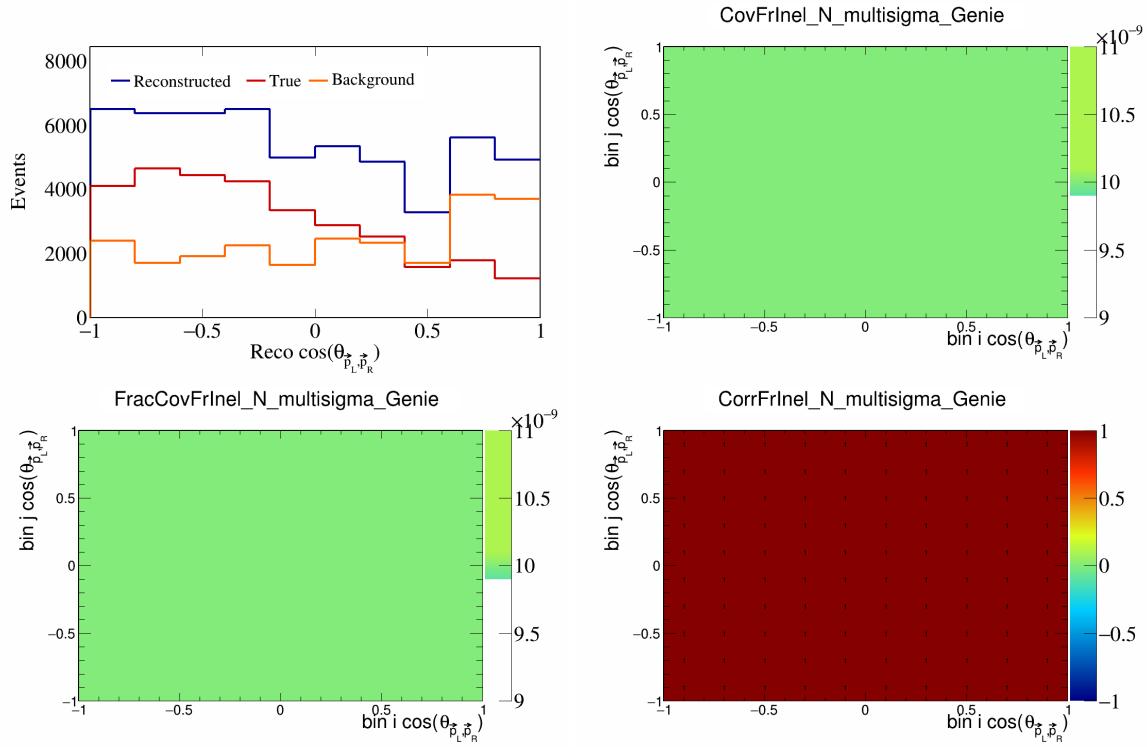


Figure 171: FrInelN variations for $\cos(\theta_{\vec{p}_L, \vec{p}_R})$.

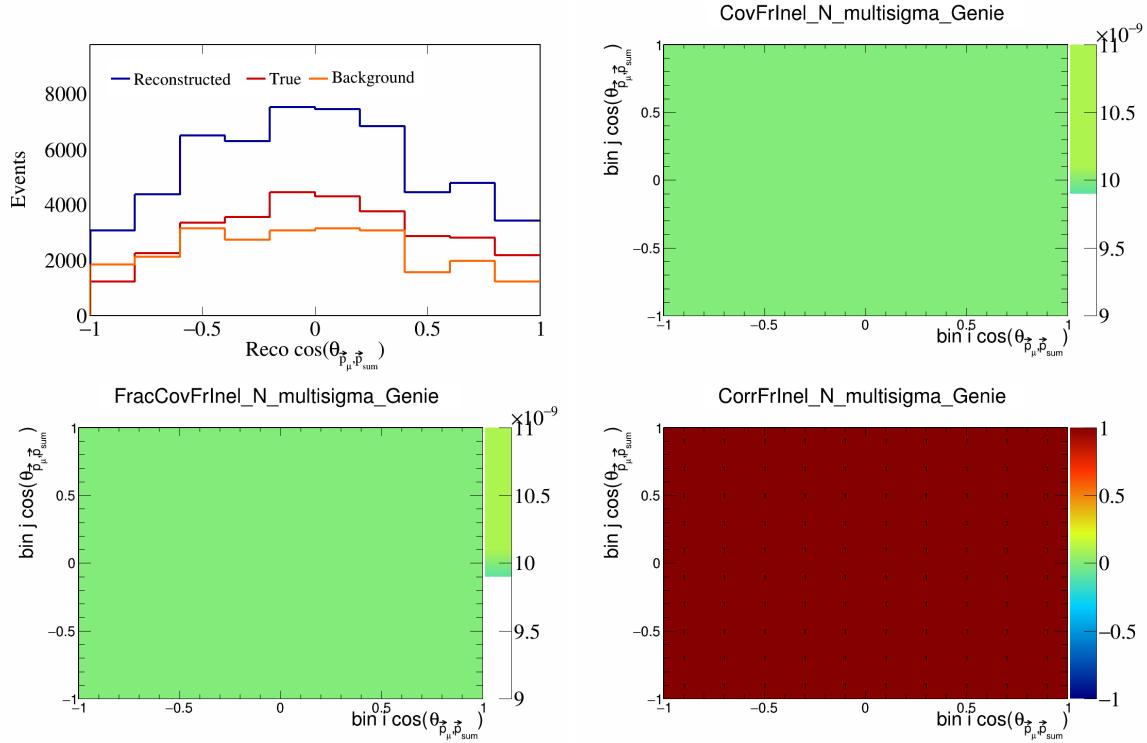


Figure 172: FrInelN variations for $\cos(\theta_{\vec{p}_\mu, \vec{p}_{\text{sum}}})$.

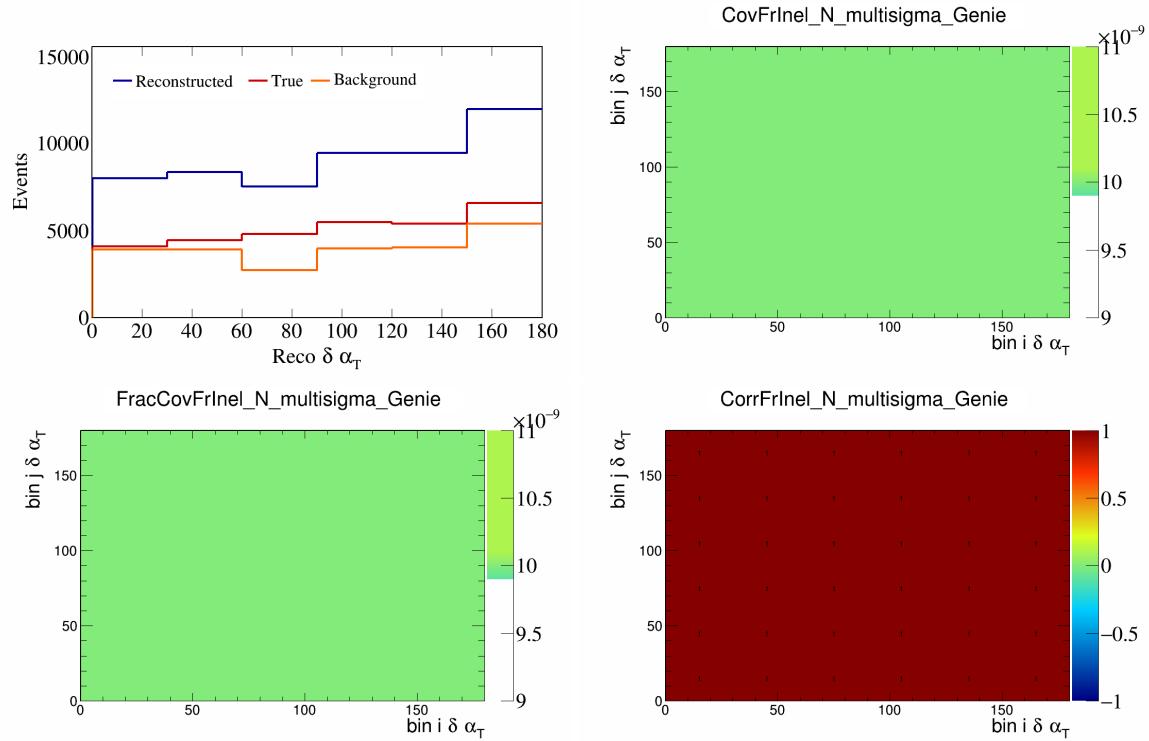


Figure 173: FrInelN variations for $\delta\alpha_T$.

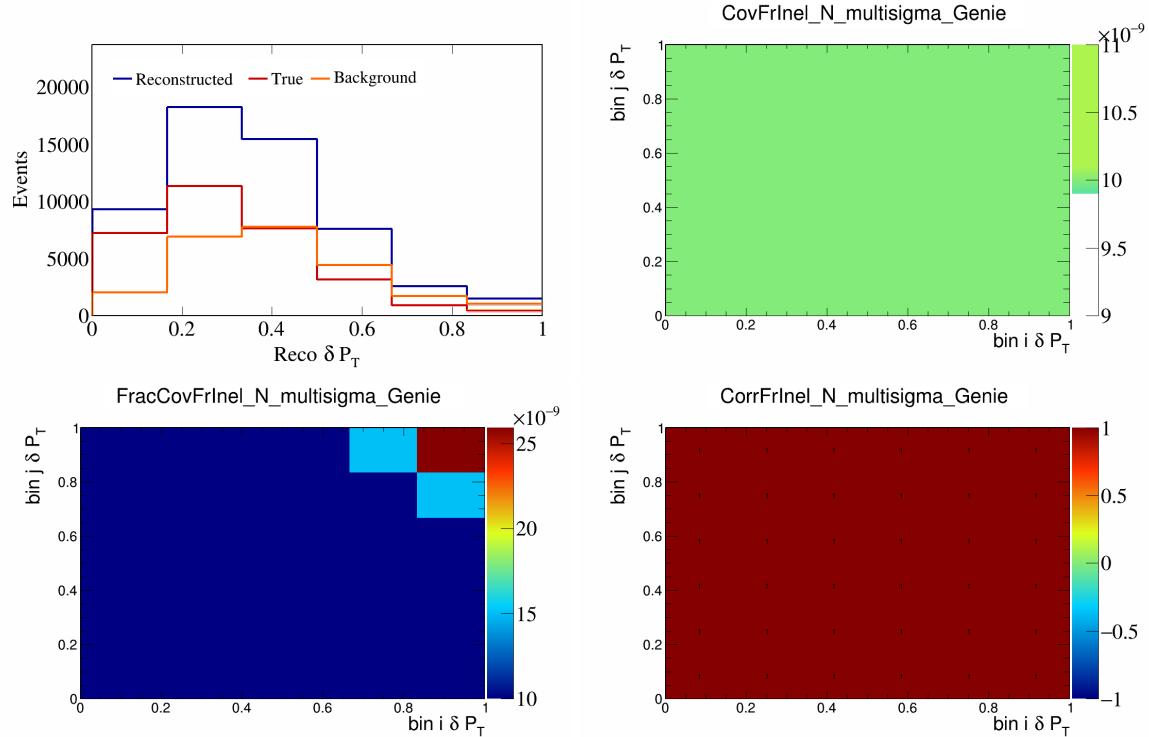


Figure 174: FrInelN variations for δP_T .

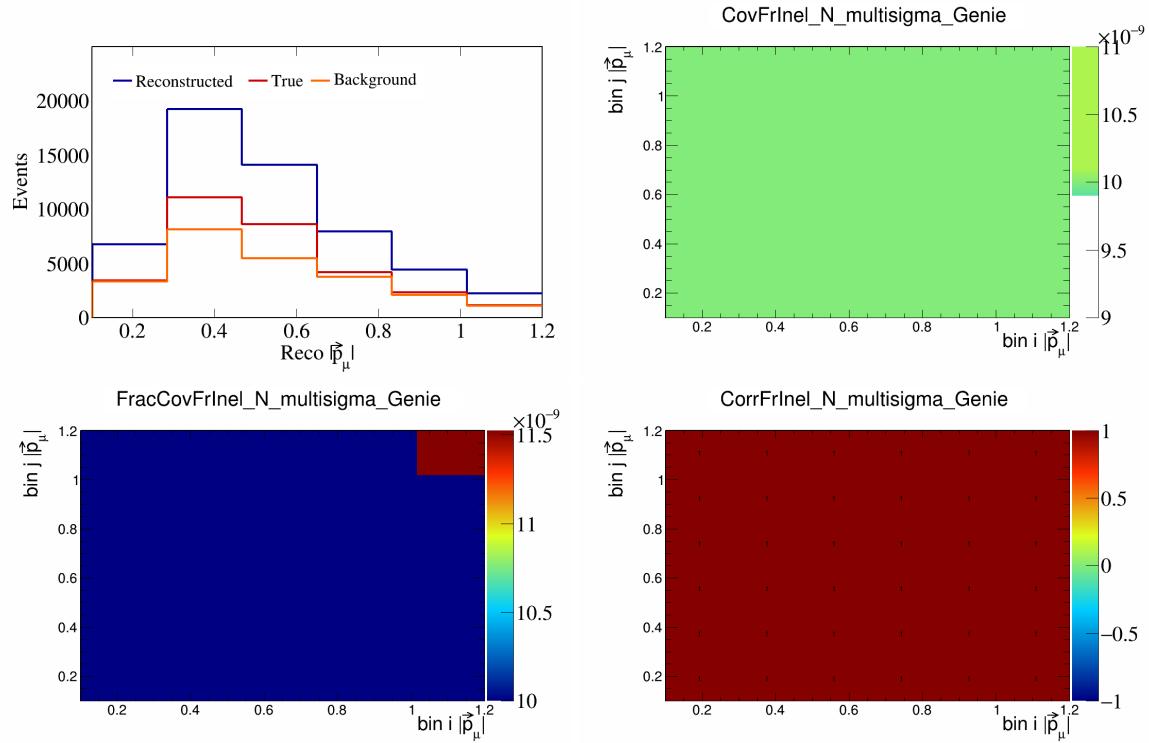


Figure 175: FrInelN variations for $|\vec{p}_\mu|$.

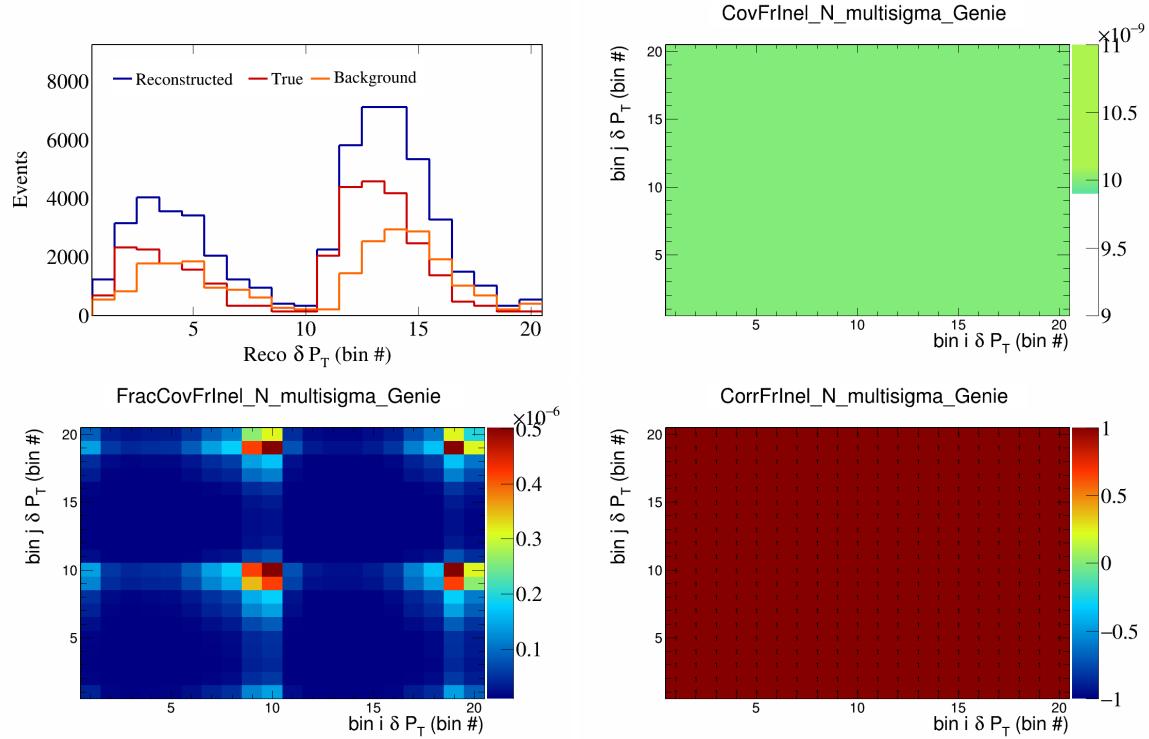


Figure 176: FrInelN variations for δP_T in $\cos(\theta_{\vec{p}_\mu})$.

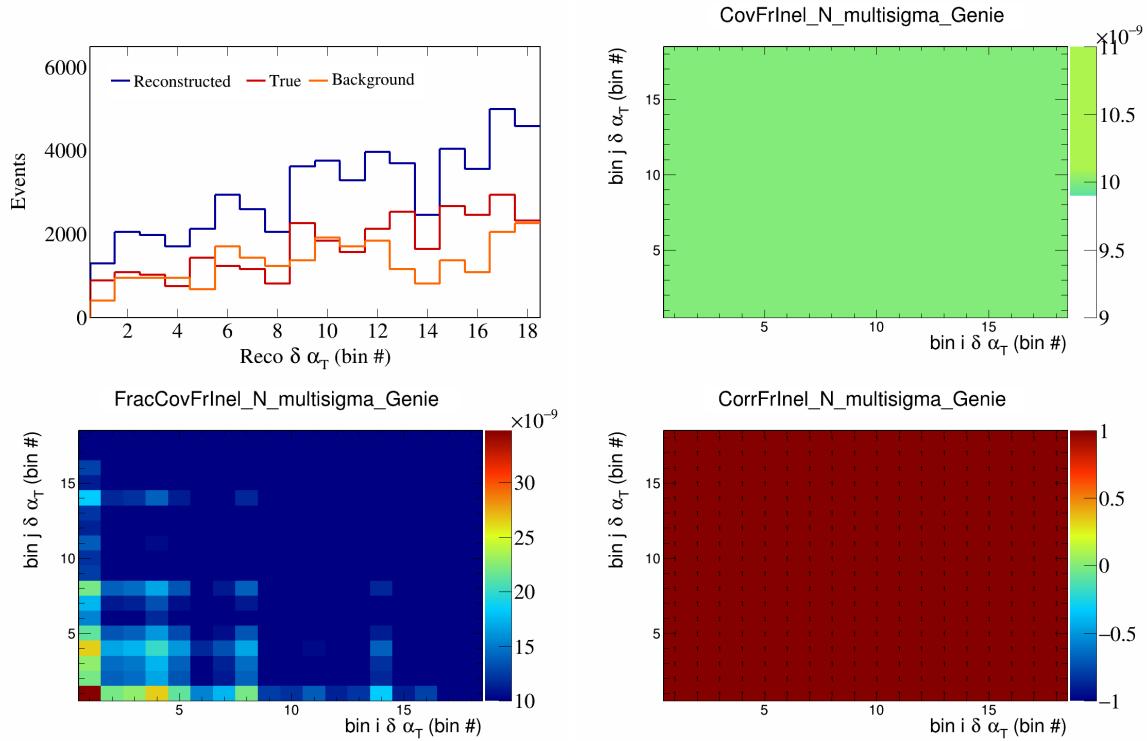


Figure 177: FrInelN variations for $\delta \alpha_T$ in $\cos(\theta_{\vec{p}_\mu})$.

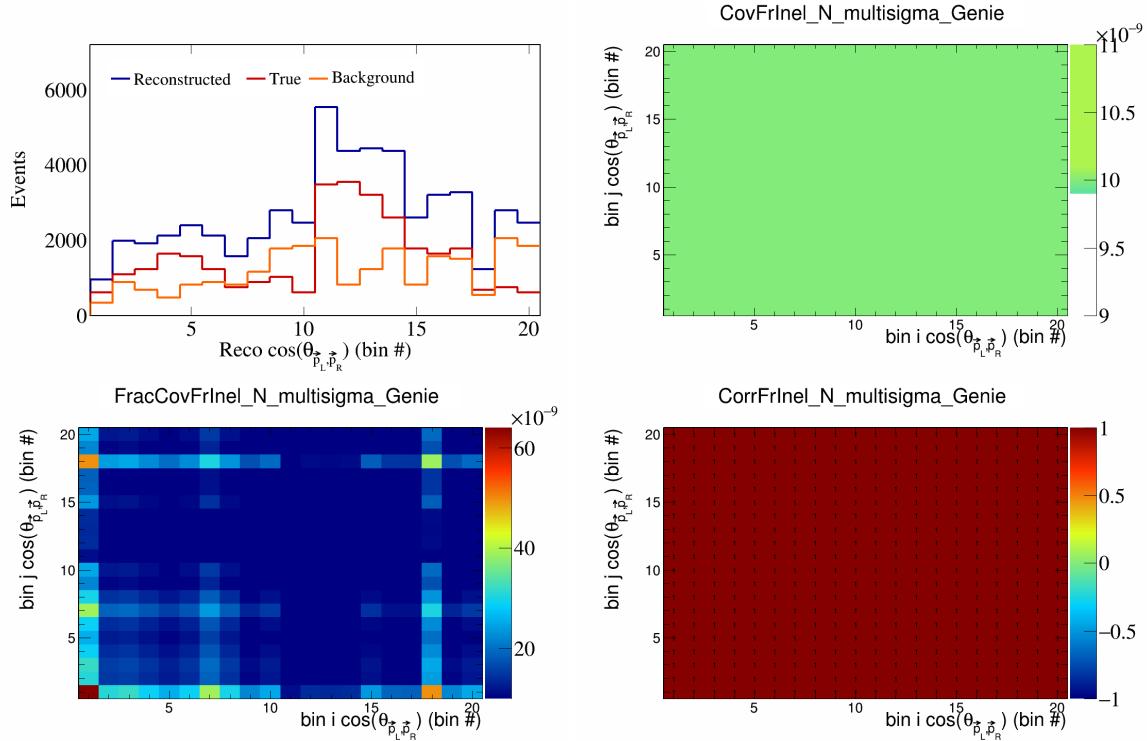


Figure 178: FrInelN variations for $\cos(\theta_{\vec{p}_L, \vec{p}_R})$ in $\cos(\theta_{\vec{p}_\mu})$.

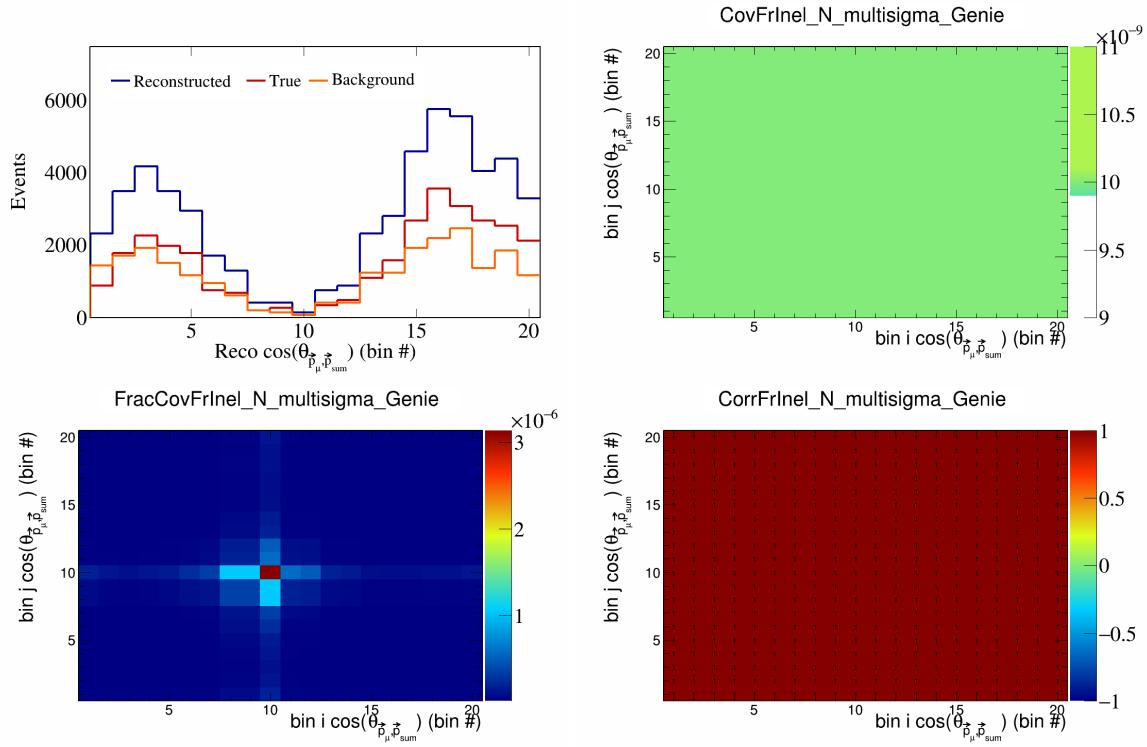


Figure 179: FrInelN variations for $\cos(\theta_{\vec{p}_\mu, \vec{p}_{\text{sum}}})$ in $\cos(\theta_{\vec{p}_\mu})$.

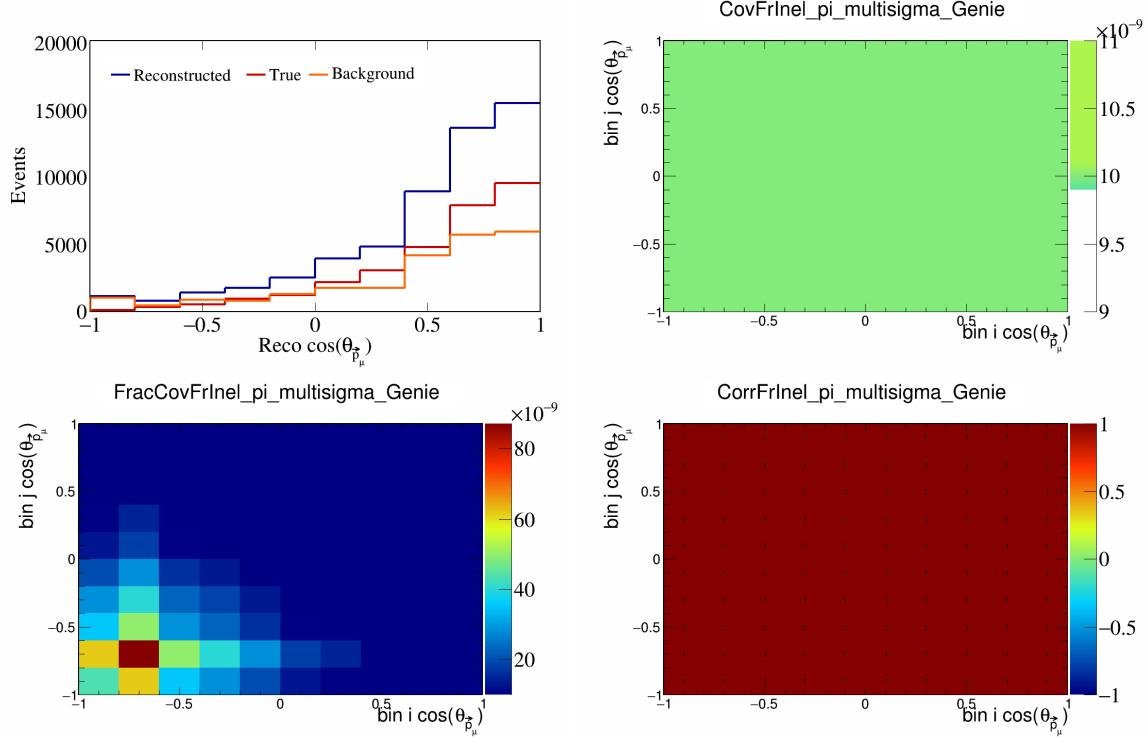


Figure 180: FrInelpi variations for $\cos(\theta_{\vec{p}_\mu})$.

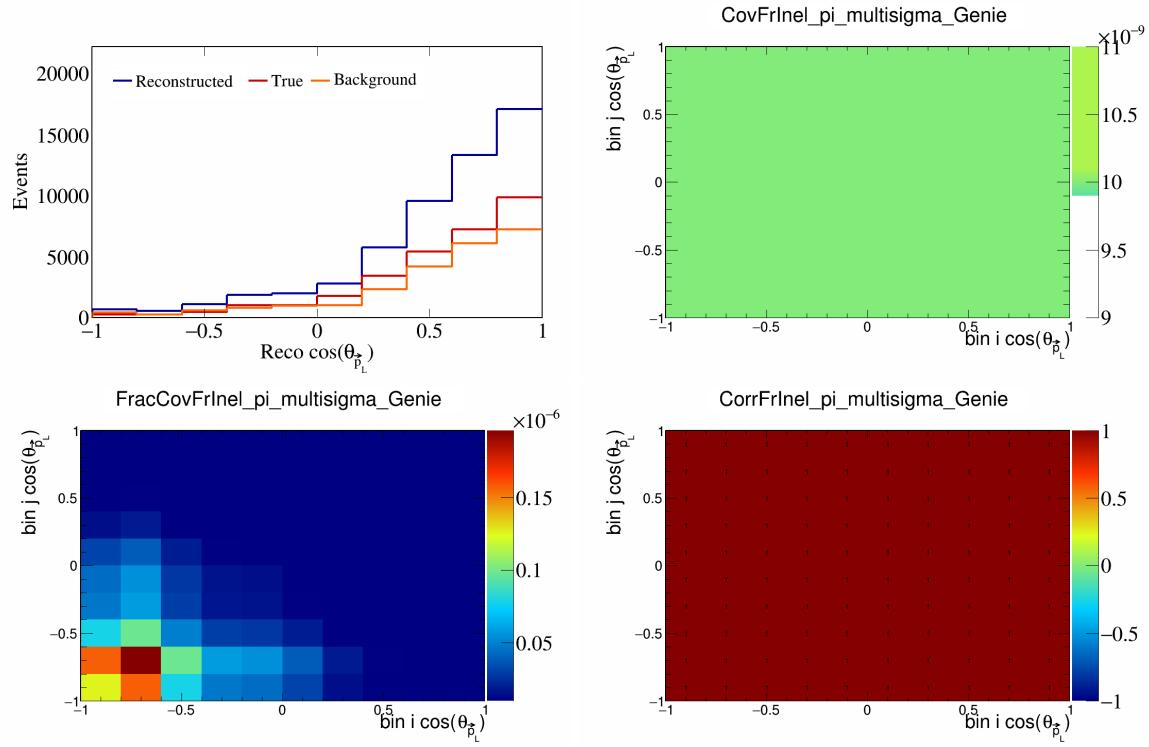


Figure 181: FrInelpi variations for $\cos(\theta_{\vec{p}_L})$.

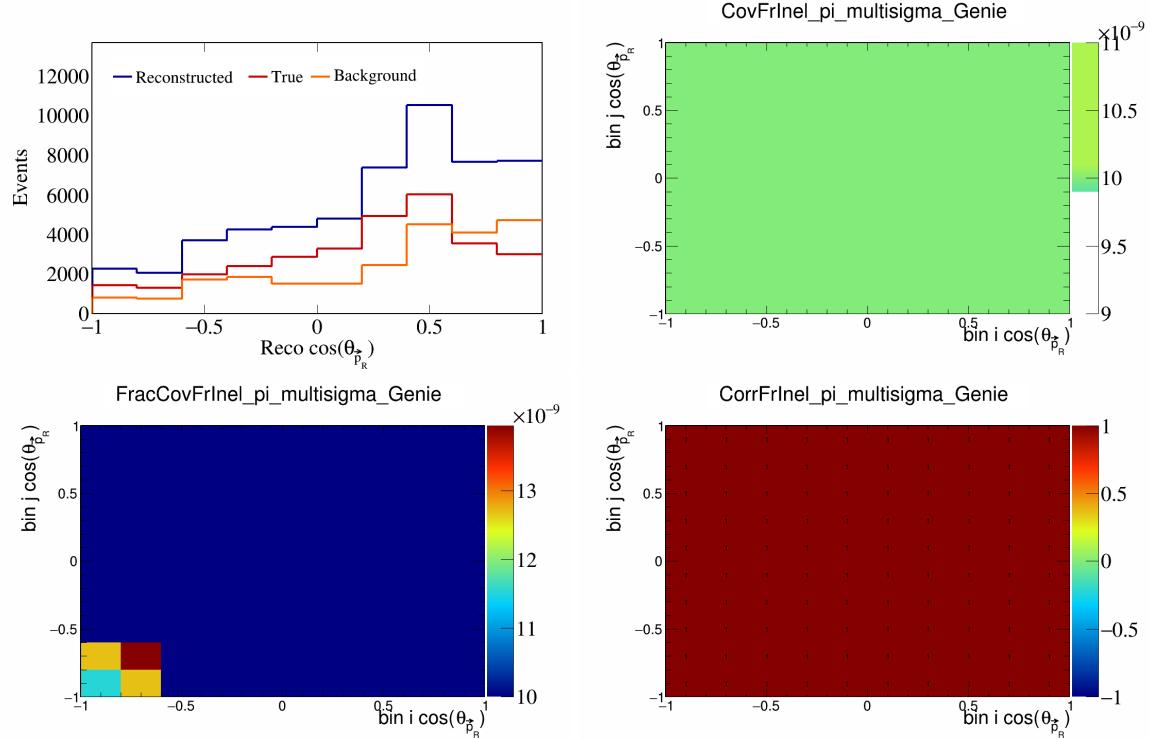


Figure 182: FrInelpi variations for $\cos(\theta_{\vec{p}_R})$.

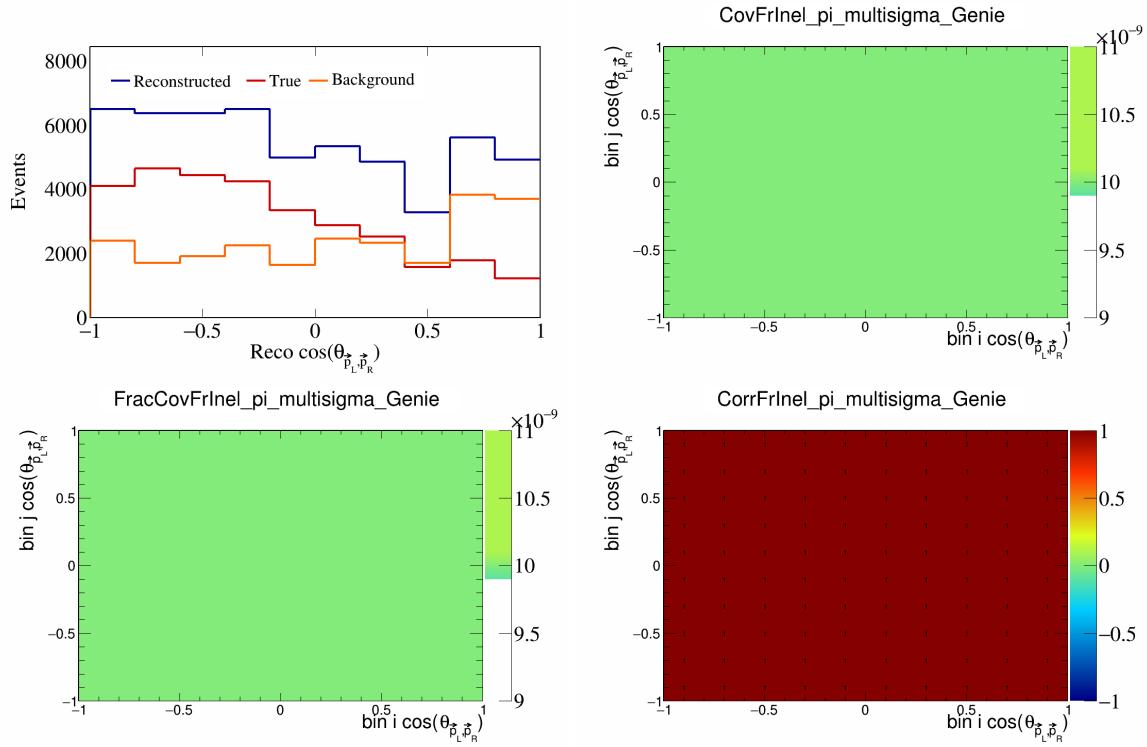


Figure 183: FrInelpi variations for $\cos(\theta_{\vec{p}_L, \vec{p}_R})$.

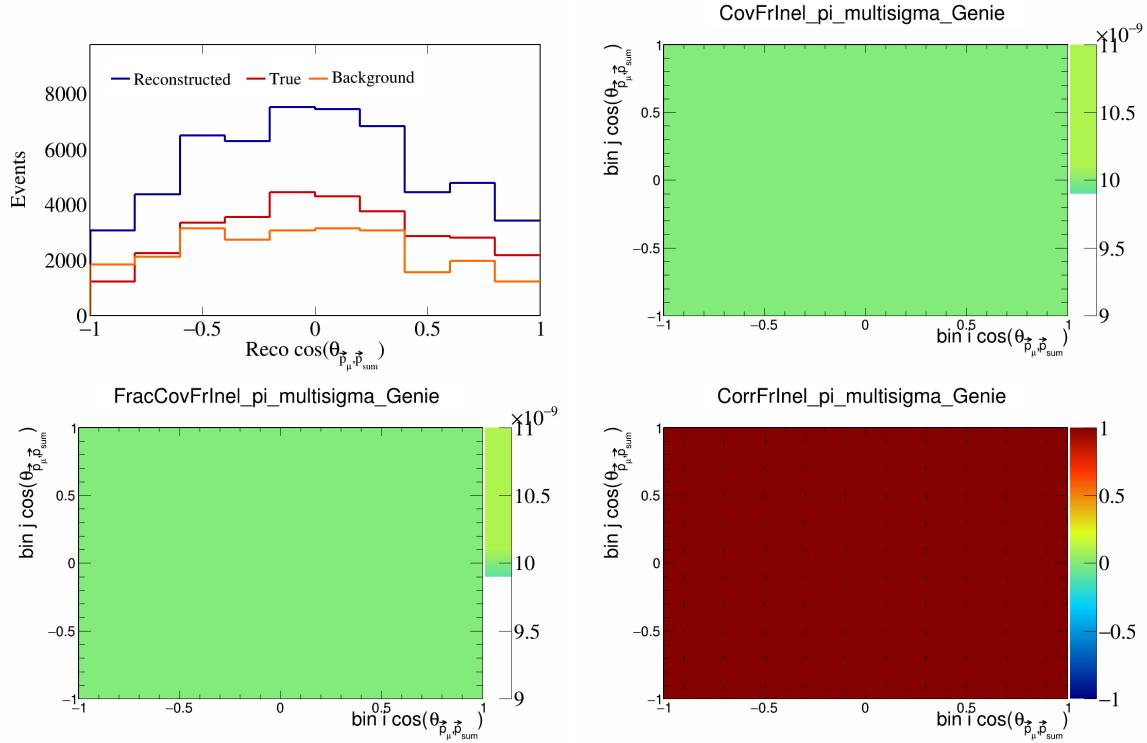


Figure 184: FrInelpi variations for $\cos(\theta_{\vec{p}_\mu, \vec{p}_{\text{sum}}})$.

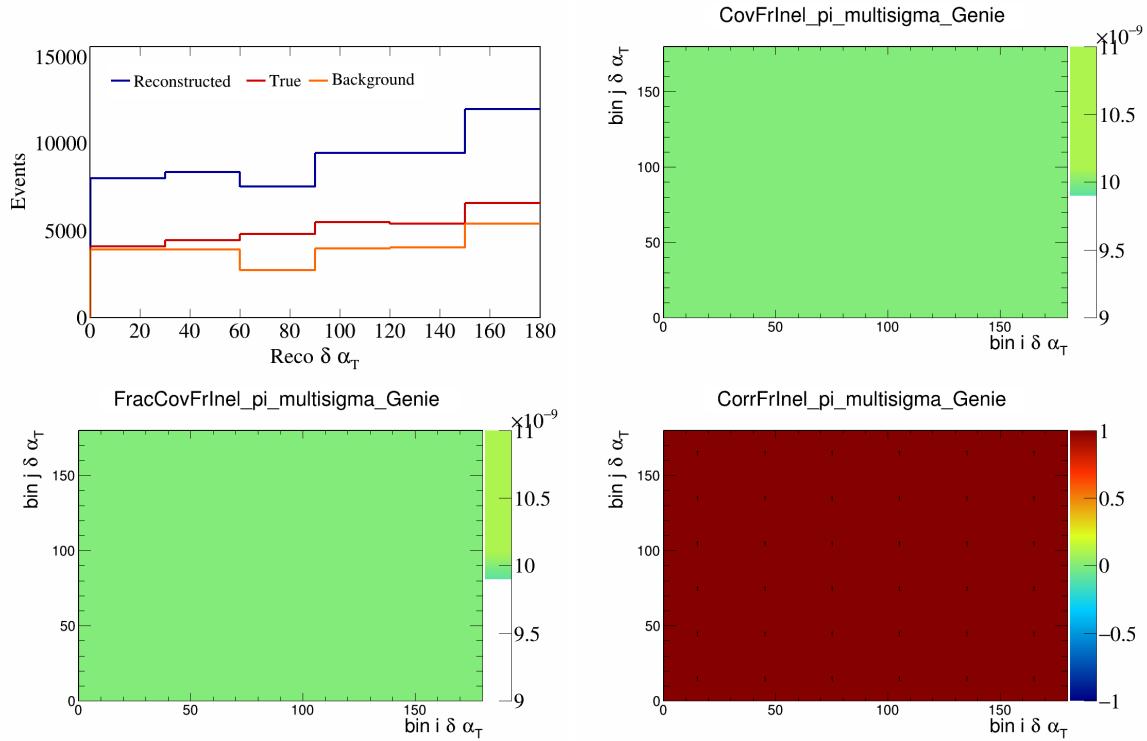


Figure 185: FrInelpi variations for $\delta\alpha_T$.

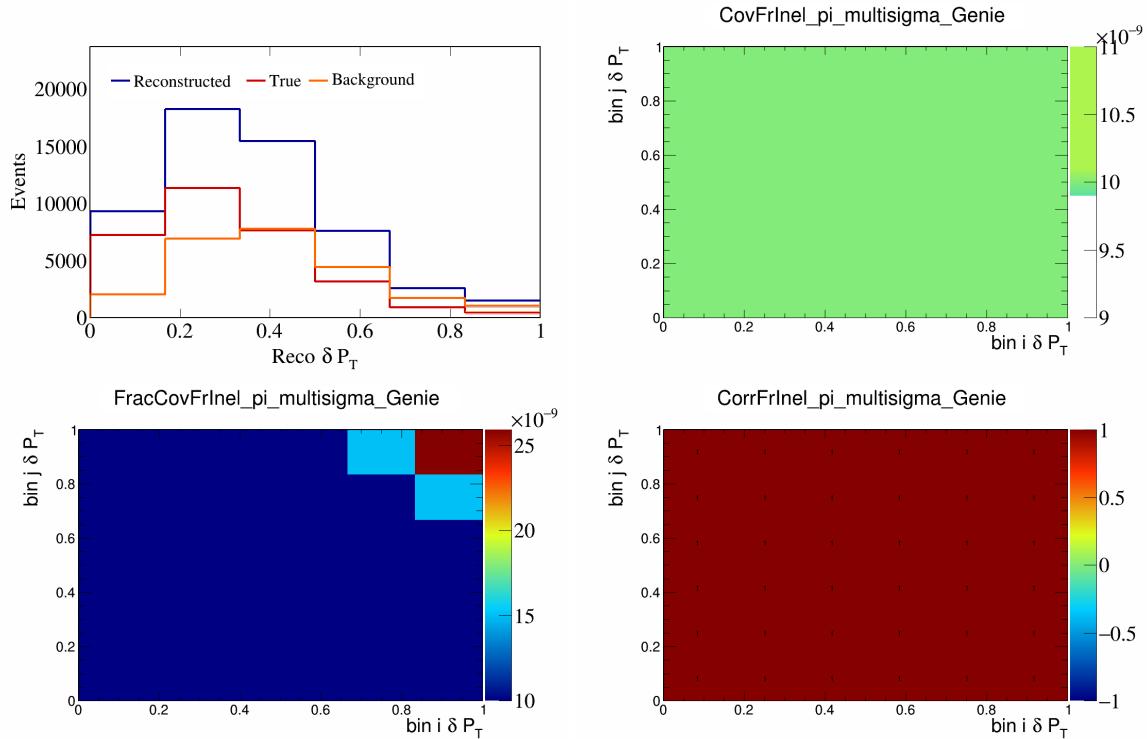


Figure 186: FrInelpi variations for δP_T .

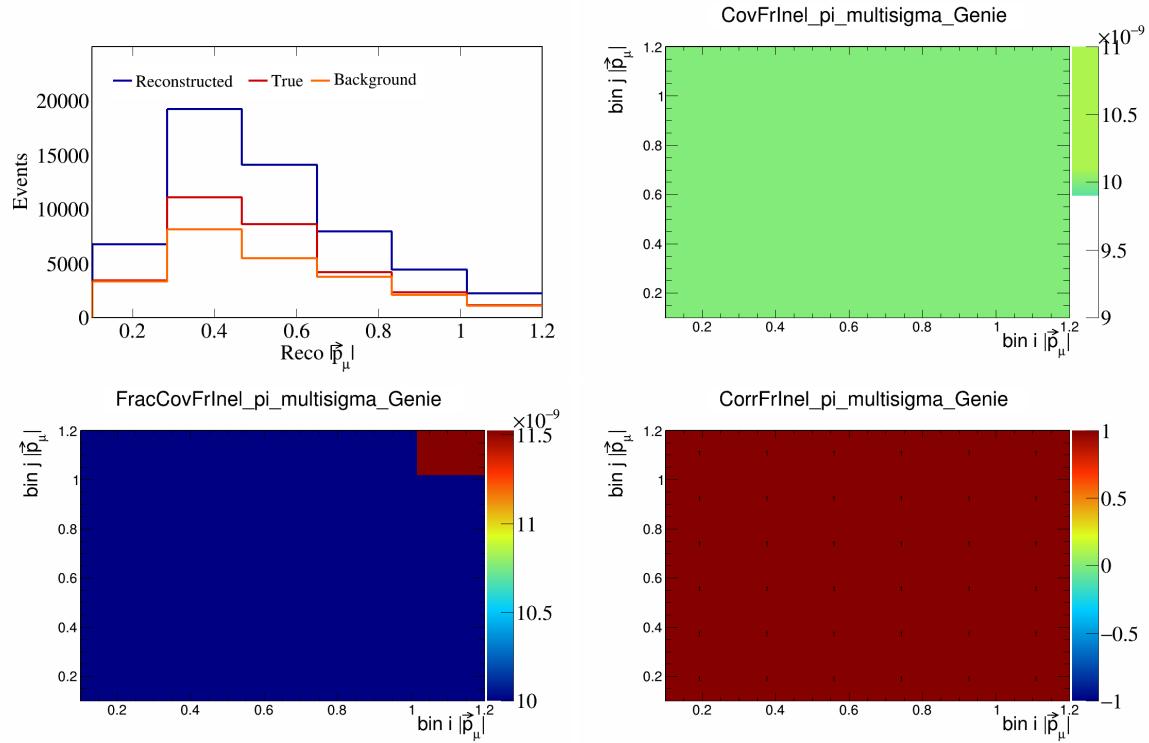


Figure 187: FrInelpi variations for $|\vec{p}_\mu|$.

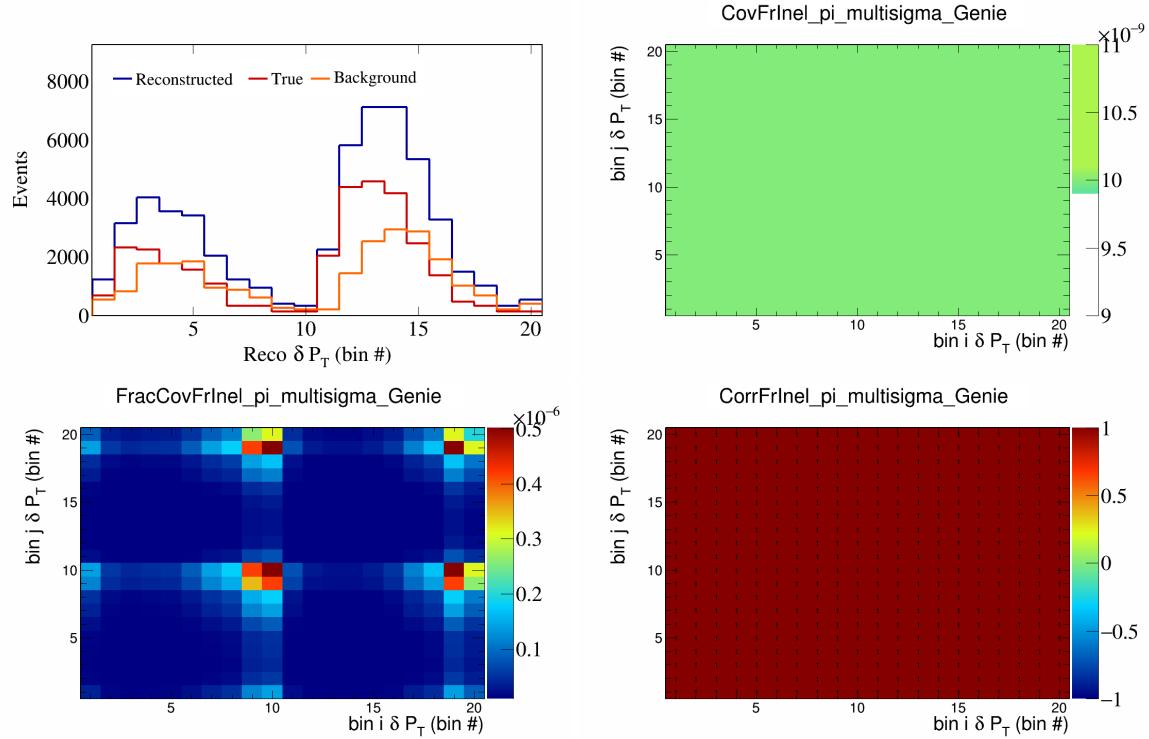


Figure 188: FrInelpi variations for δP_T in $\cos(\theta_{\vec{p}_\mu})$.

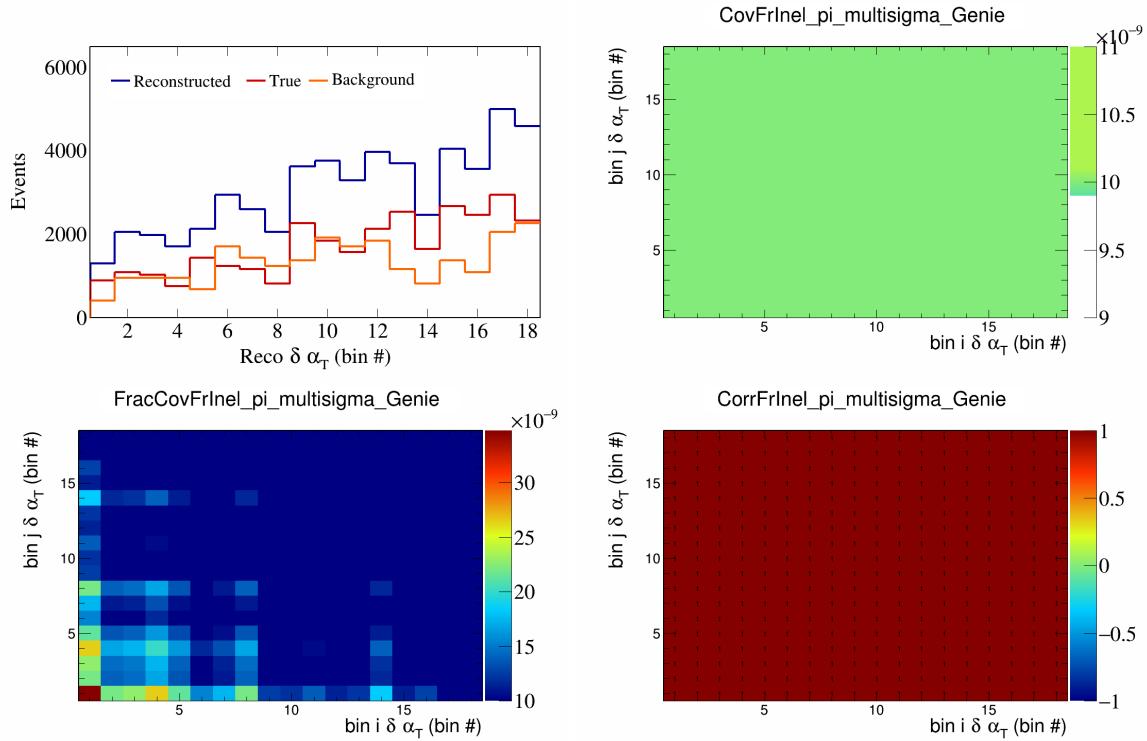


Figure 189: FrInelpi variations for $\delta\alpha_T$ in $\cos(\theta_{\vec{p}_\mu})$.

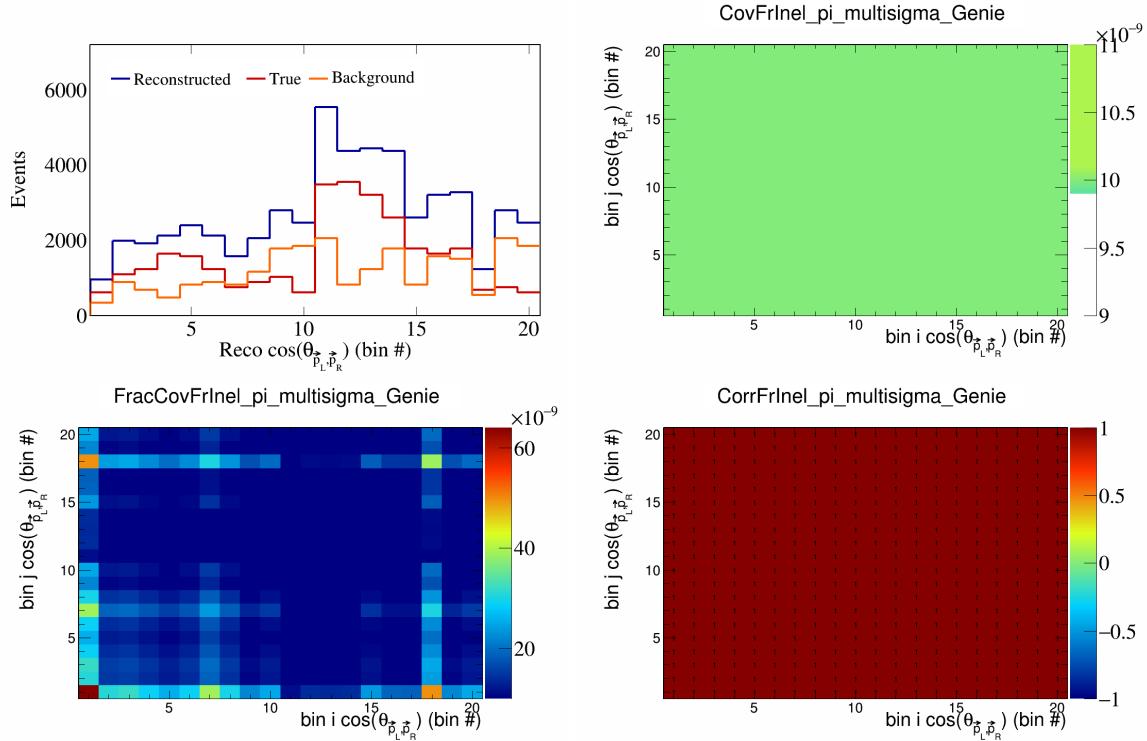


Figure 190: FrInelpi variations for $\cos(\theta_{\vec{p}_L, \vec{p}_R})$ in $\cos(\theta_{\vec{p}_\mu})$.

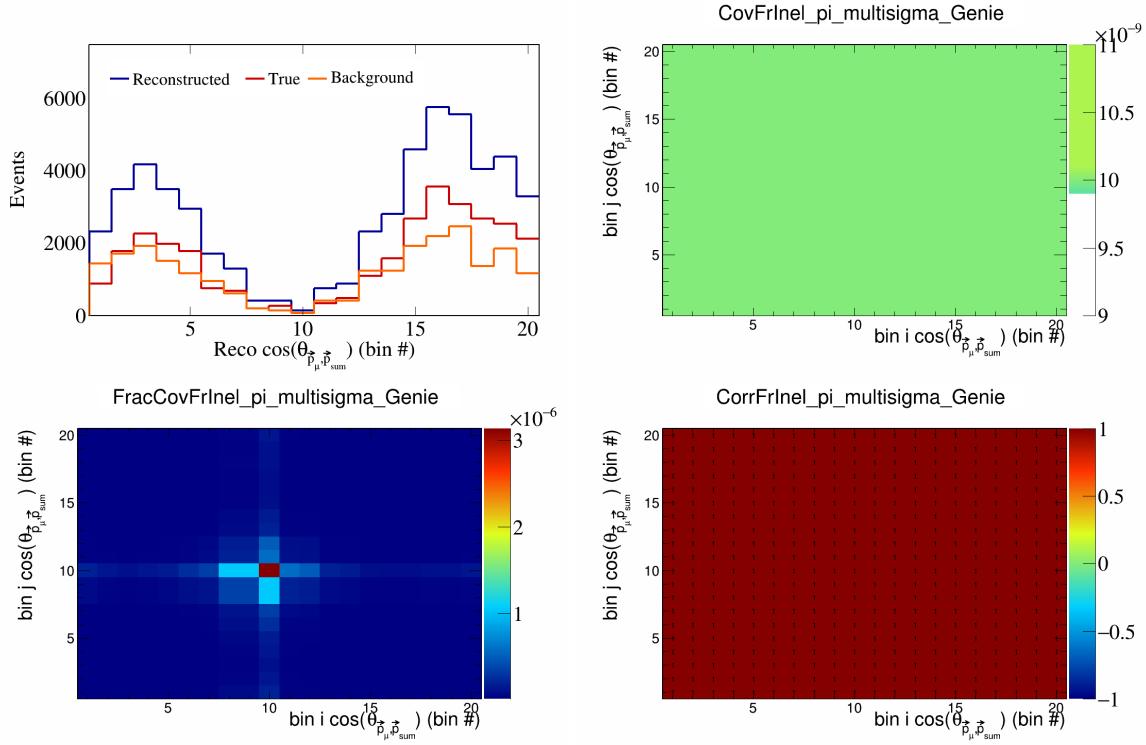


Figure 191: FrInelpi variations for $\cos(\theta_{\vec{p}_\mu, \vec{p}_{\text{sum}}})$ in $\cos(\theta_{\vec{p}_\mu})$.

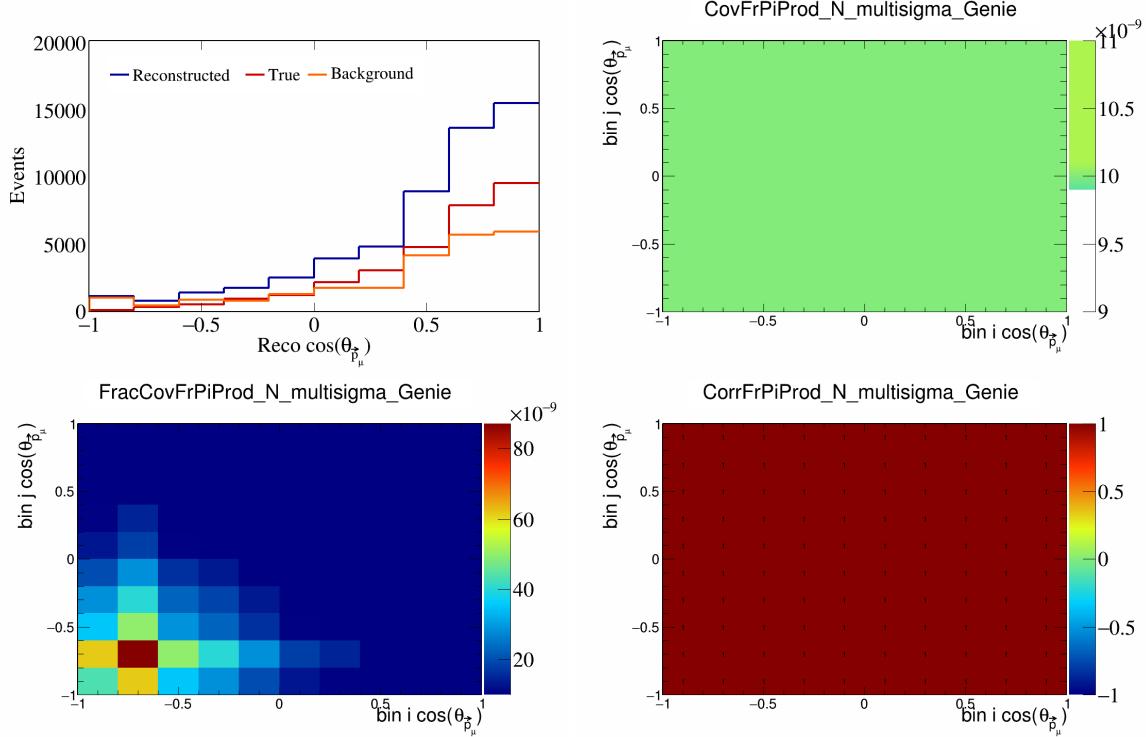


Figure 192: FrPiProdN variations for $\cos(\theta_{\vec{p}_\mu})$.

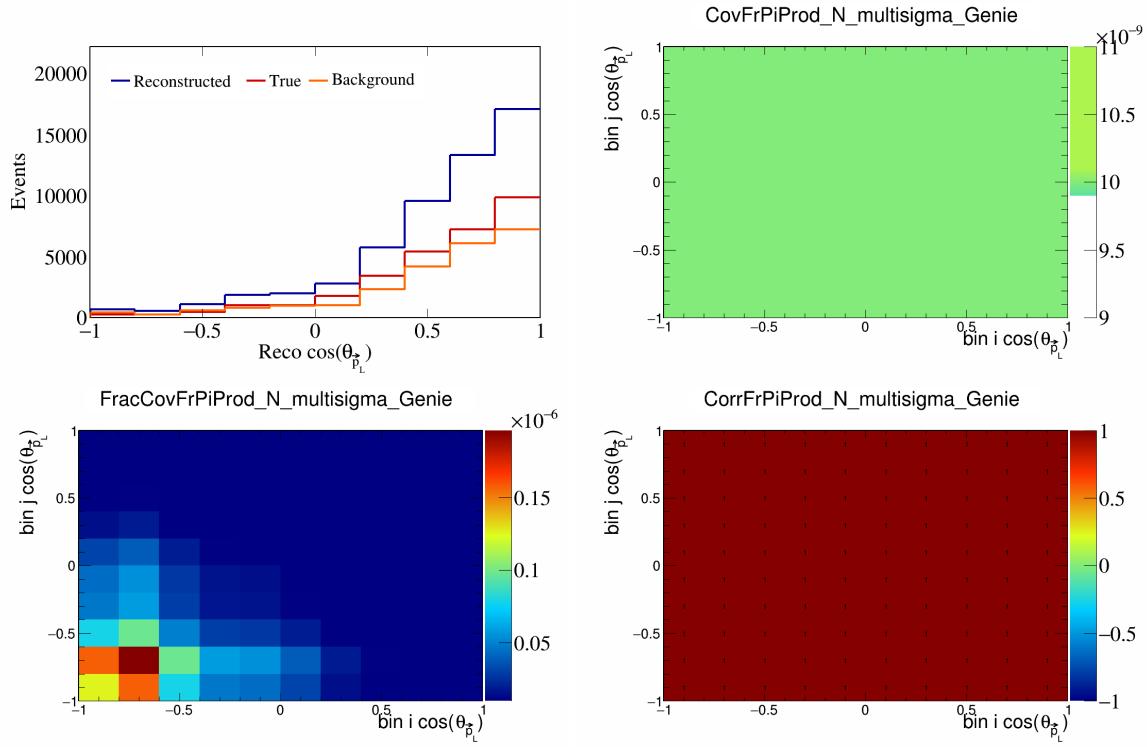


Figure 193: FrPiProdN variations for $\cos(\theta_{\vec{p}_L})$.

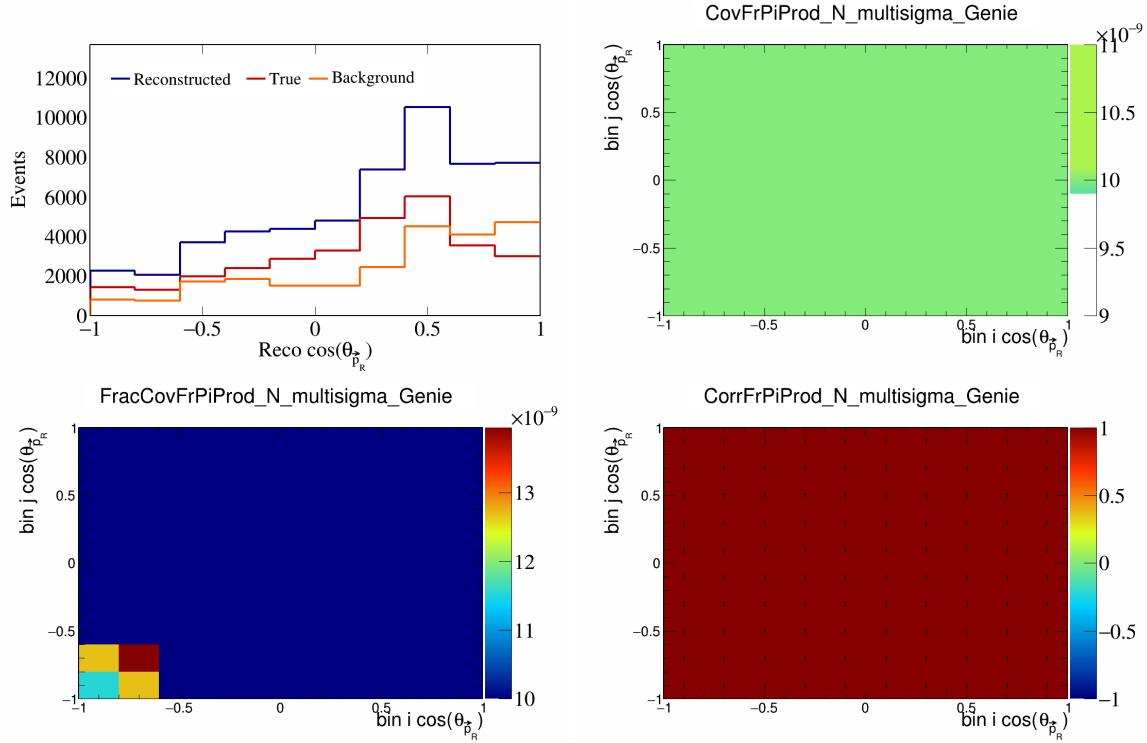


Figure 194: FrPiProdN variations for $\cos(\theta_{\vec{p}_R})$.

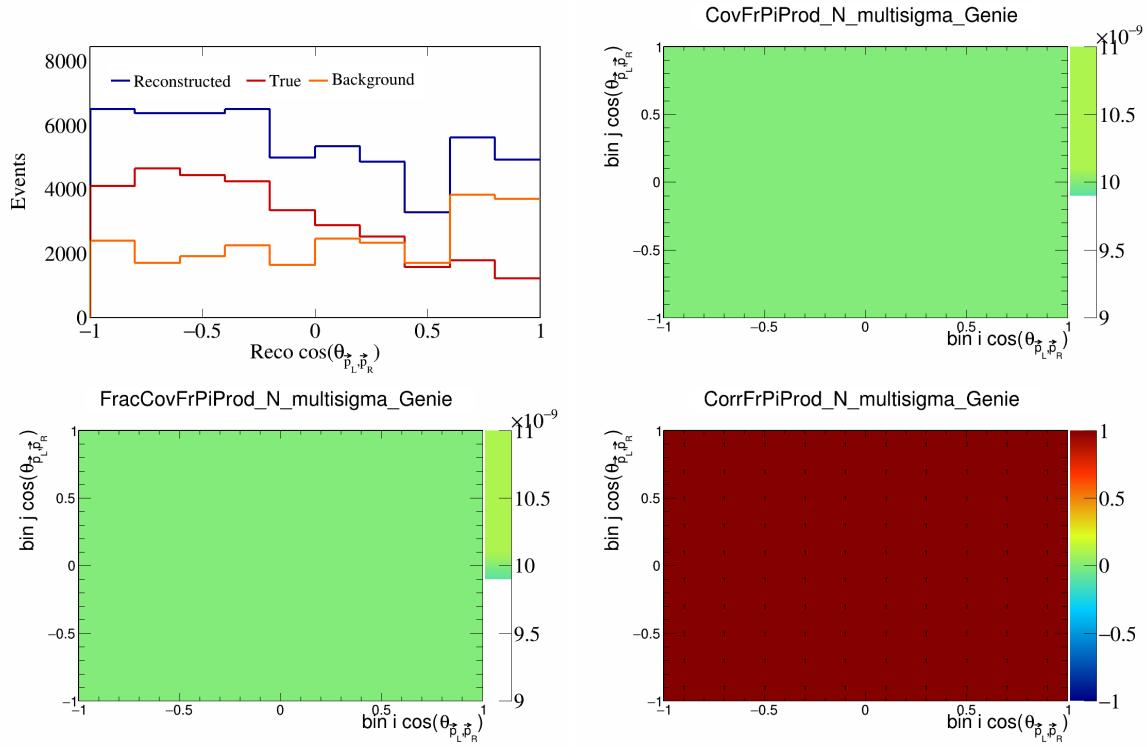


Figure 195: FrPiProdN variations for $\cos(\theta_{\vec{p}_L, \vec{p}_R})$.

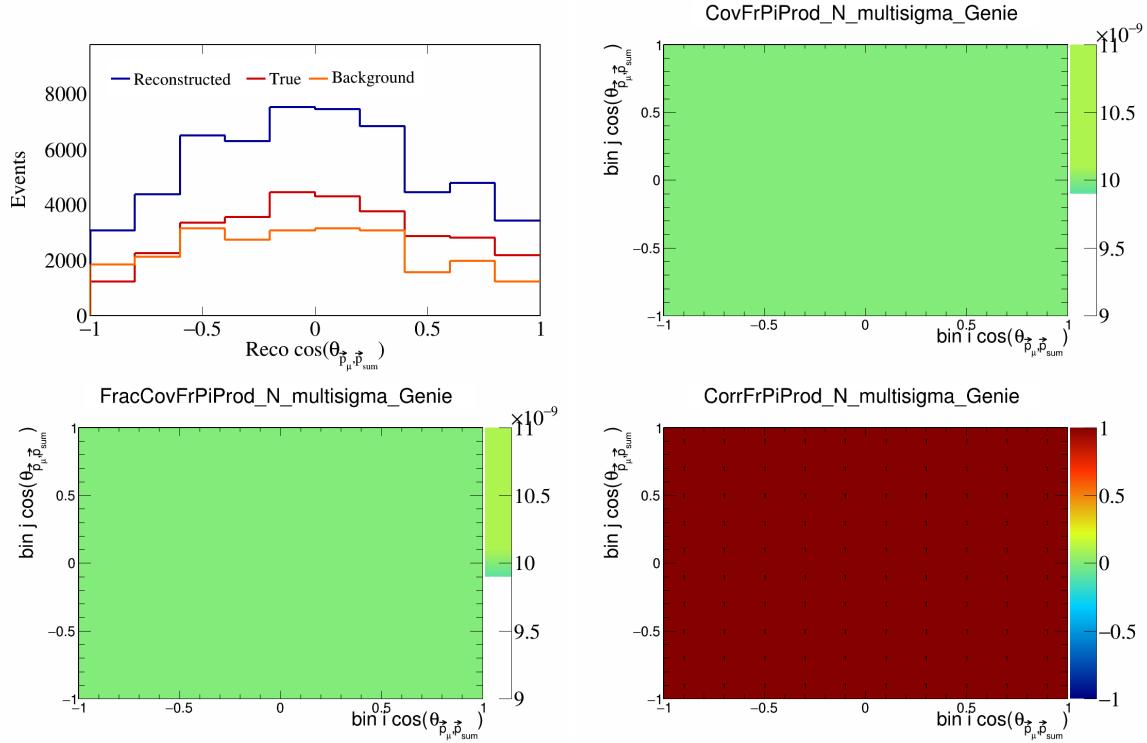


Figure 196: FrPiProdN variations for $\cos(\theta_{\vec{p}_\mu, \vec{p}_{\text{sum}}})$.

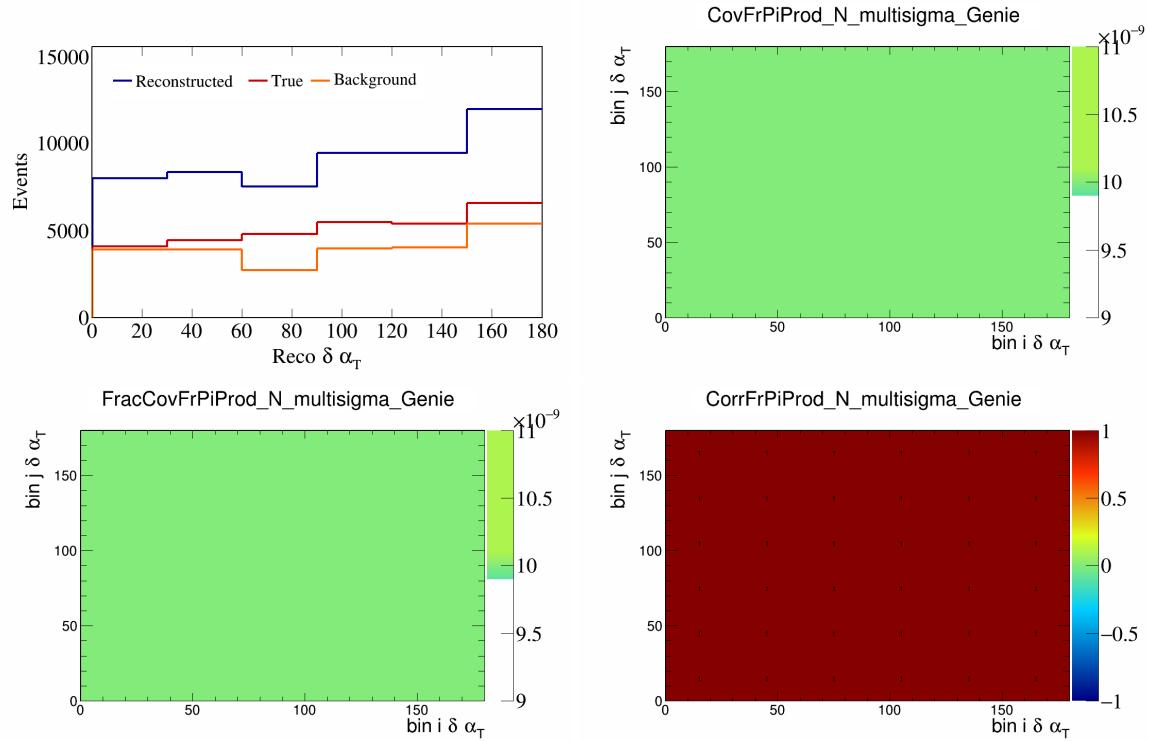


Figure 197: FrPiProdN variations for $\delta\alpha_T$.

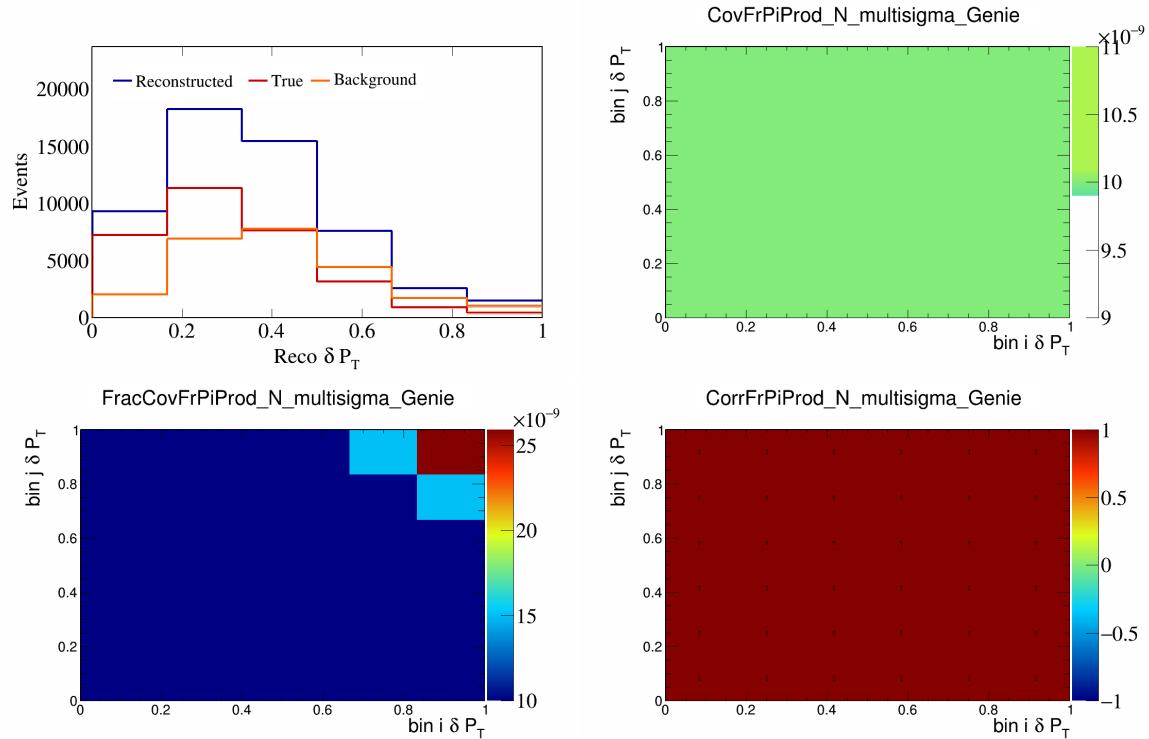


Figure 198: FrPiProdN variations for δP_T .

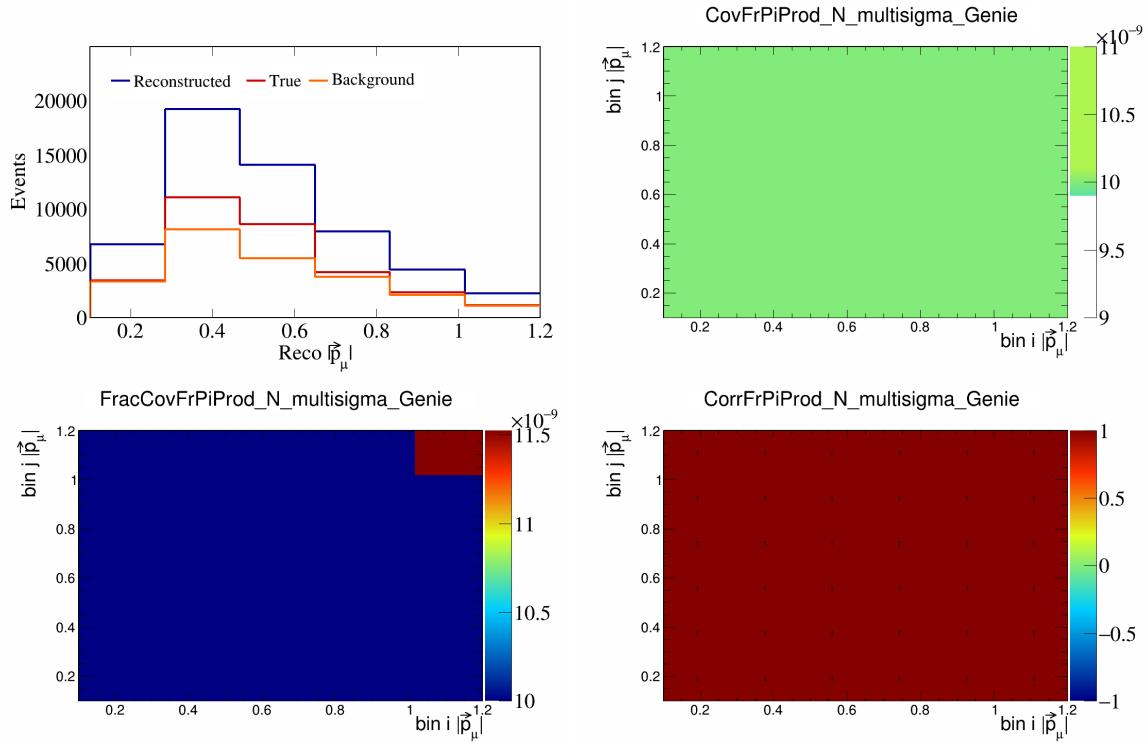


Figure 199: FrPiProdN variations for $|\vec{p}_\mu|$.

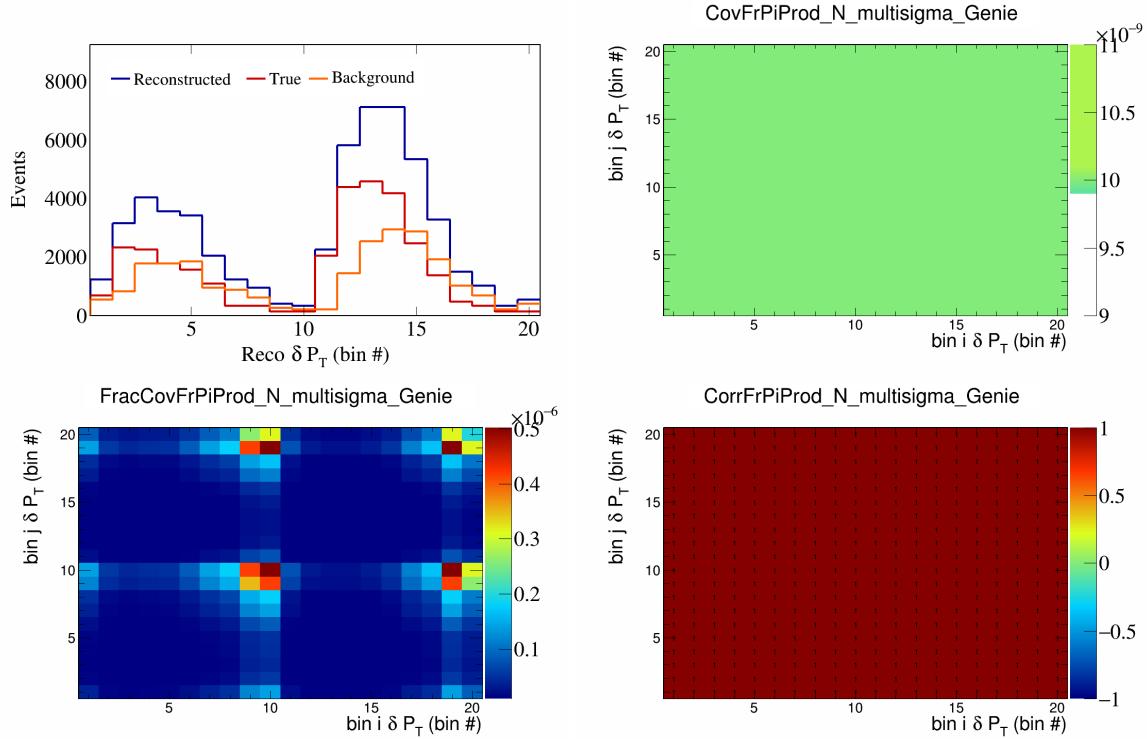


Figure 200: FrPiProdN variations for δP_T in $\cos(\theta_{\vec{p}_\mu})$.

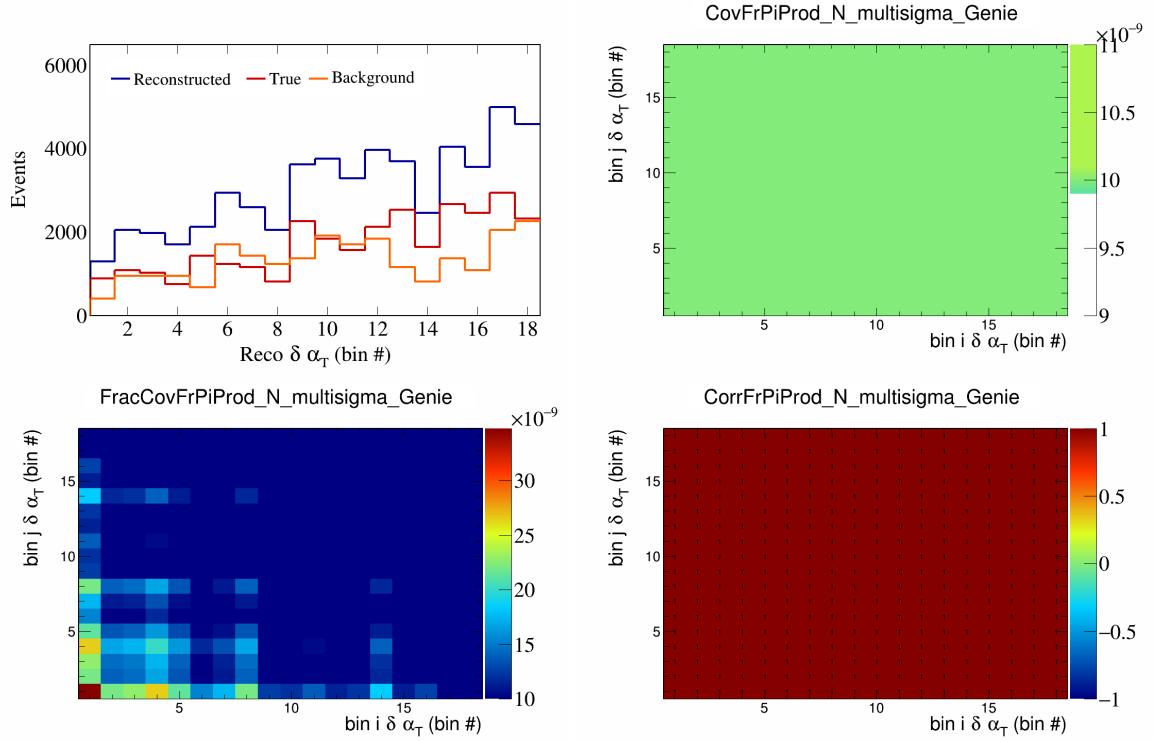


Figure 201: FrPiProdN variations for $\delta\alpha_T$ in $\cos(\theta_{\vec{p}_\mu})$.

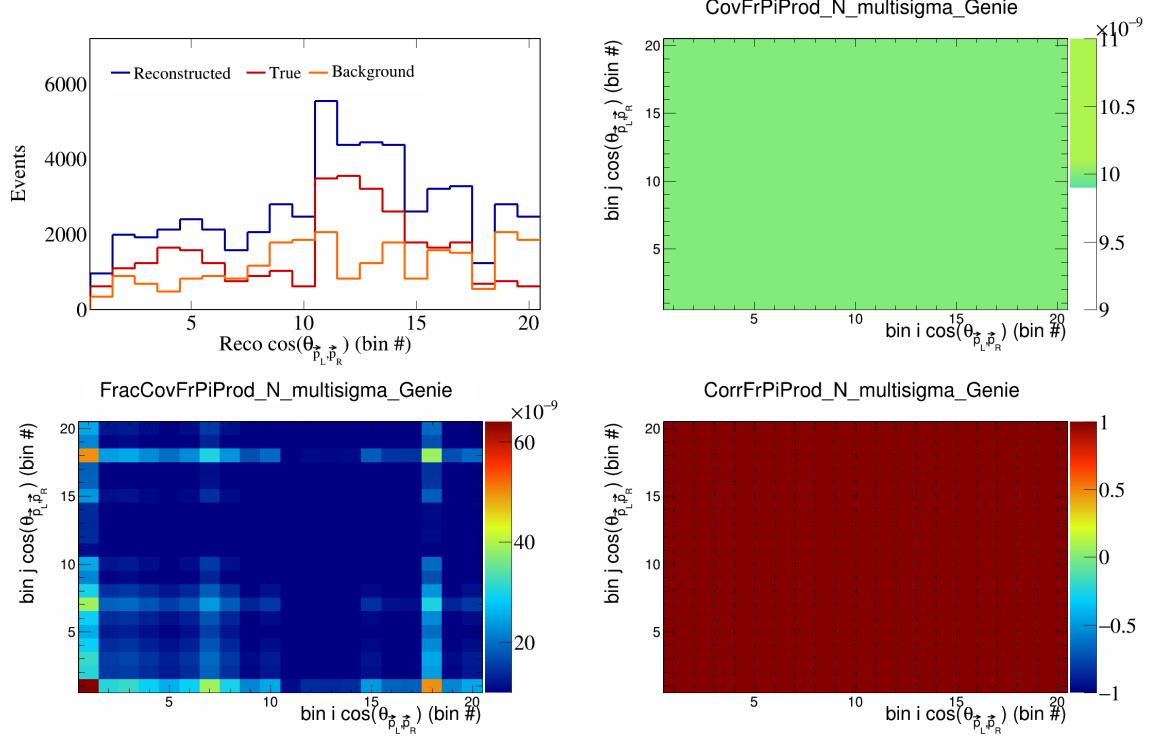


Figure 202: FrPiProdN variations for $\cos(\theta_{\vec{p}_L, \vec{p}_R})$ in $\cos(\theta_{\vec{p}_\mu})$.

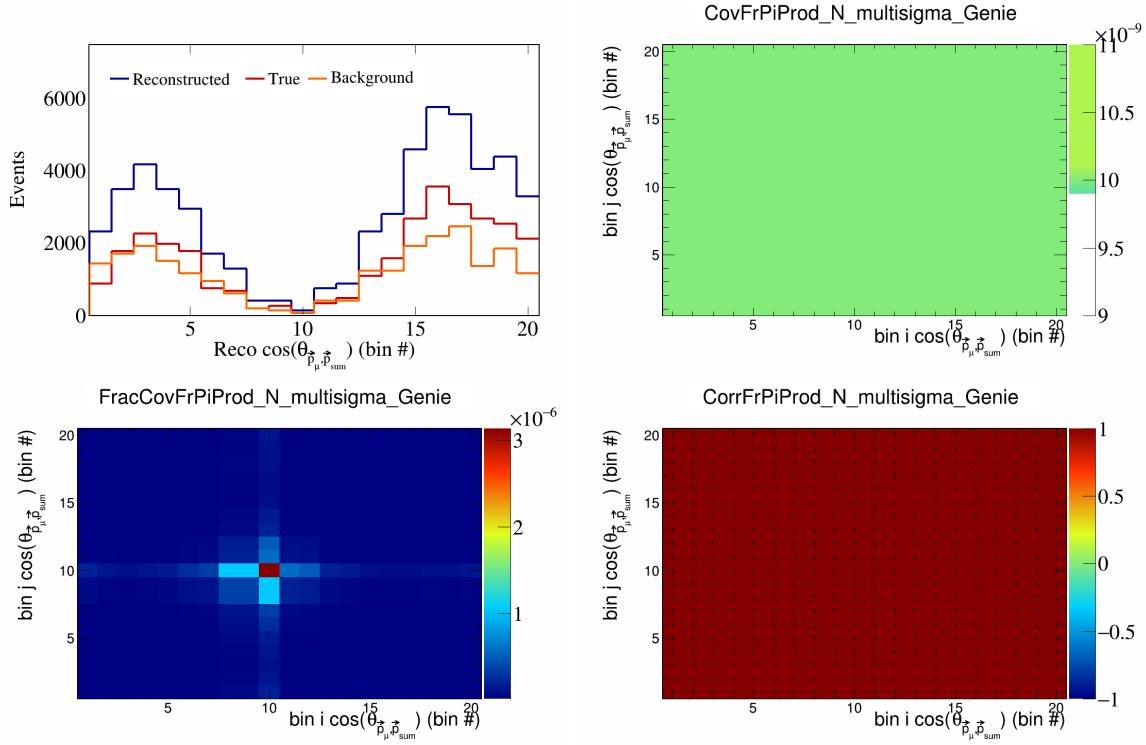


Figure 203: FrPiProdN variations for $\cos(\theta_{\vec{p}_\mu, \vec{p}_{\text{sum}}})$ in $\cos(\theta_{\vec{p}_\mu})$.

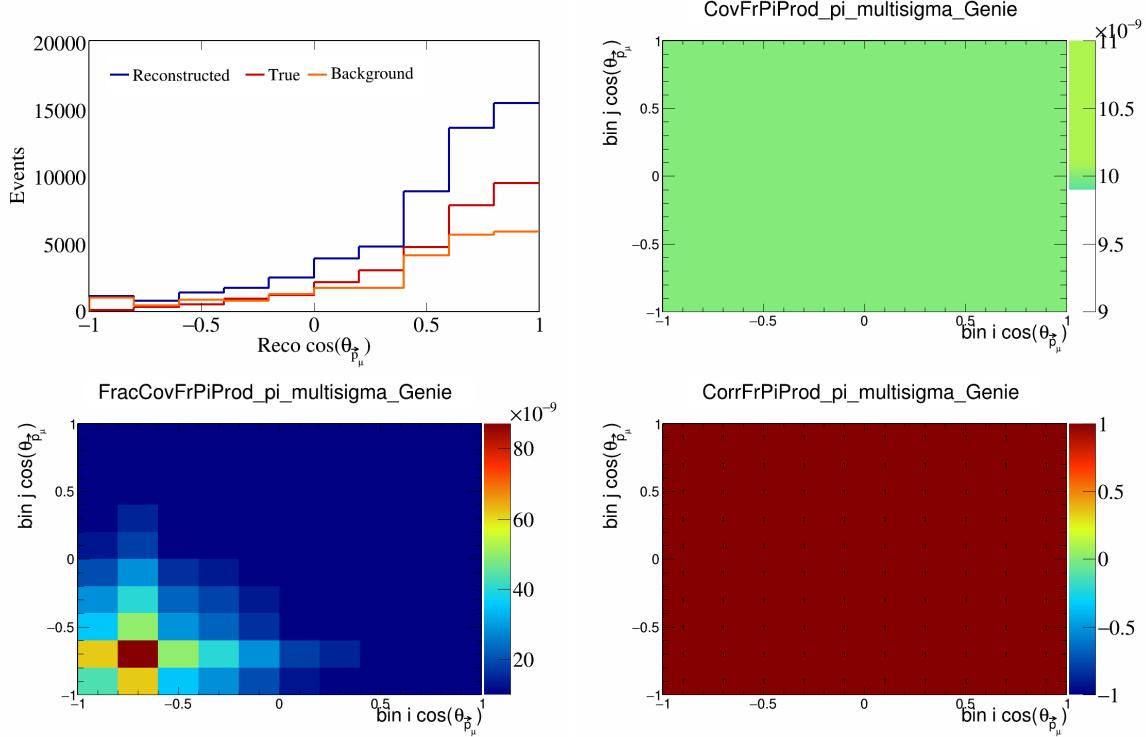


Figure 204: FrPiProdpi variations for $\cos(\theta_{\vec{p}_\mu})$.

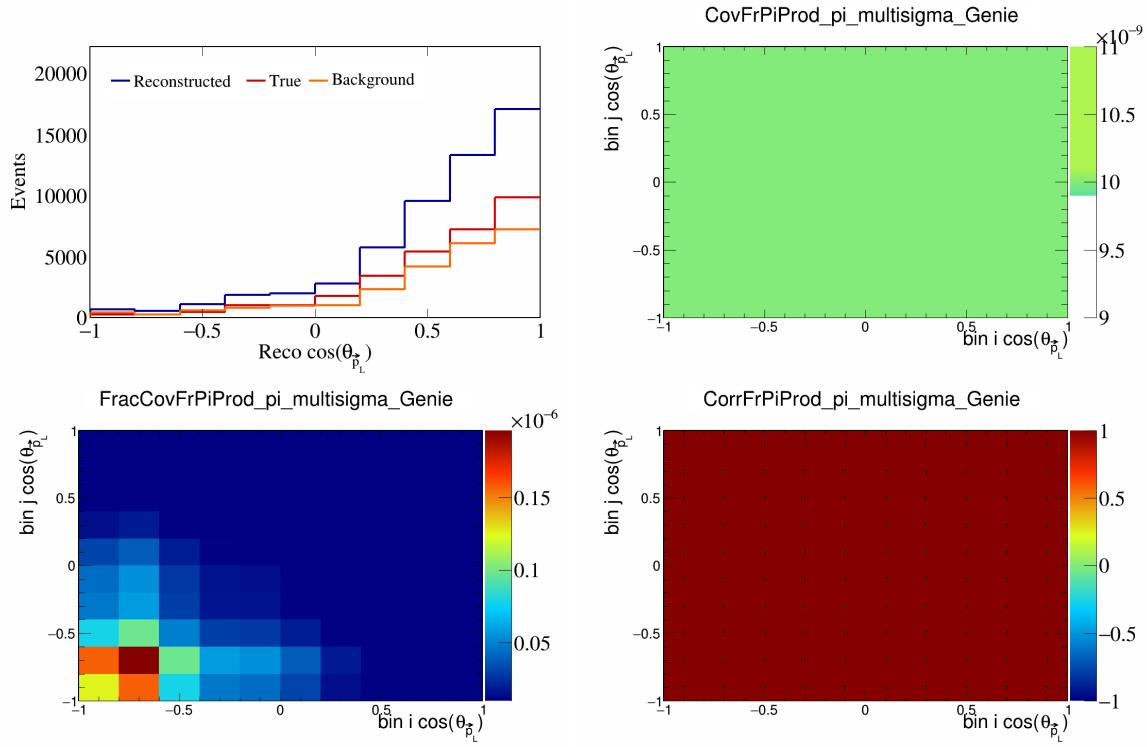


Figure 205: FrPiProdpi variations for $\cos(\theta_{\vec{p}_L})$.

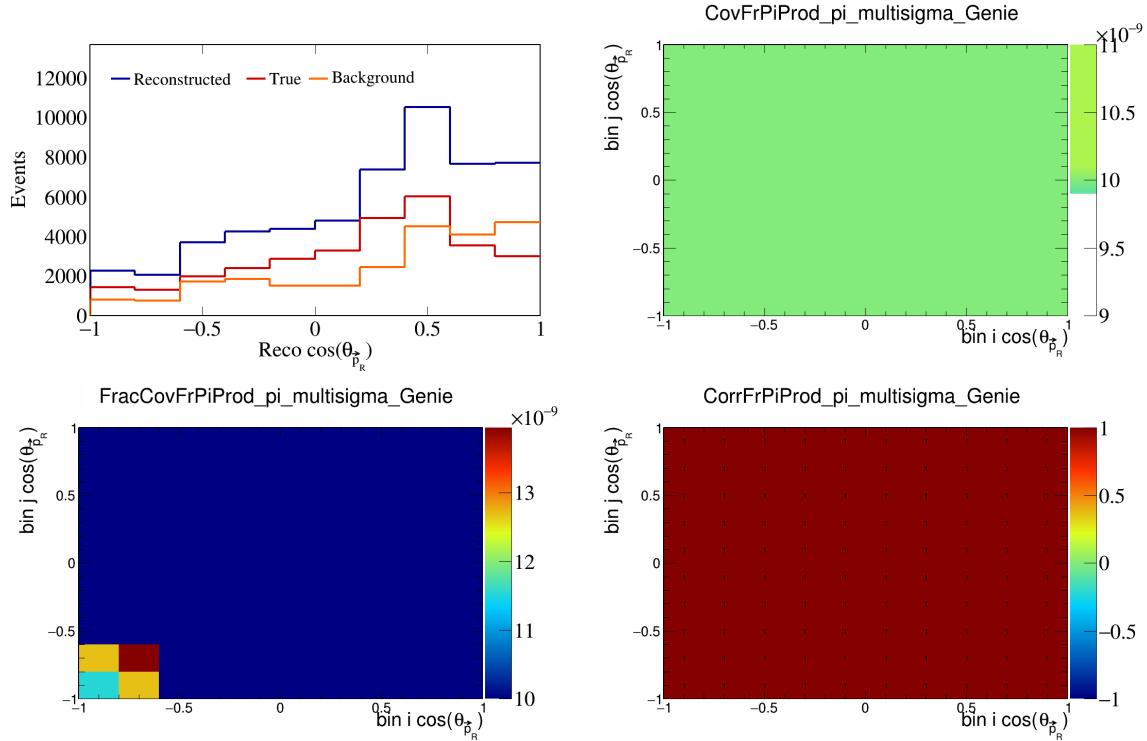


Figure 206: FrPiProdpi variations for $\cos(\theta_{\vec{p}_R})$.

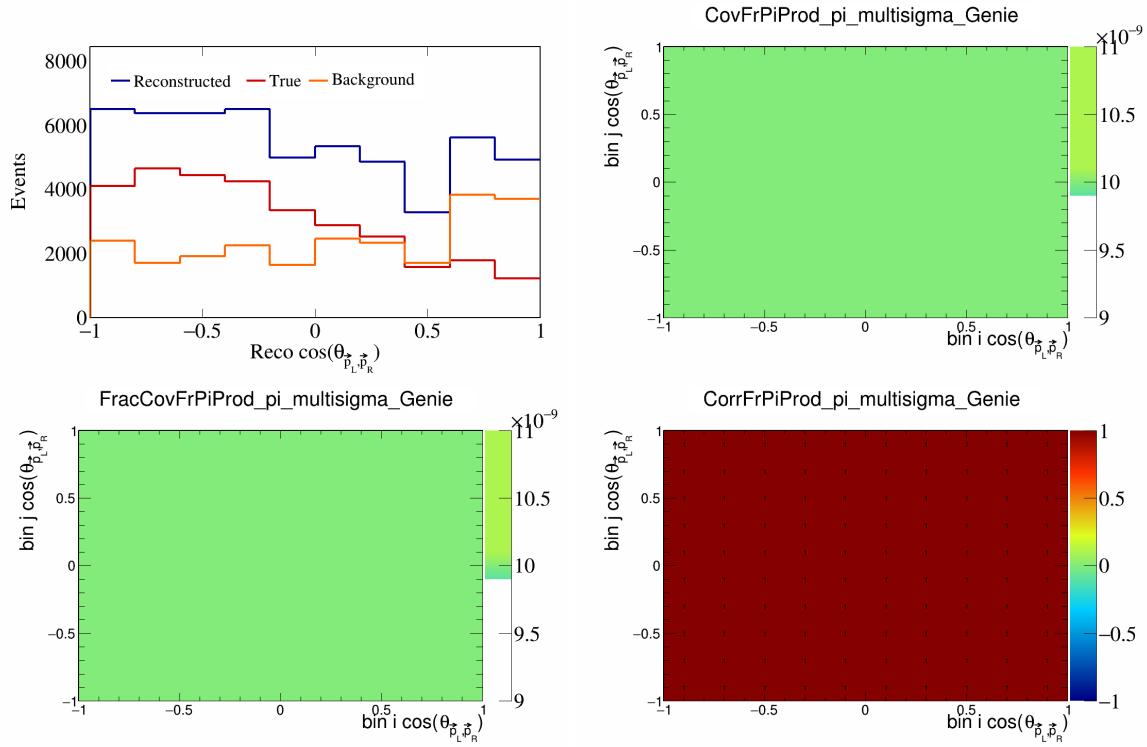


Figure 207: FrPiProdpi variations for $\cos(\theta_{\vec{p}_L, \vec{p}_R})$.

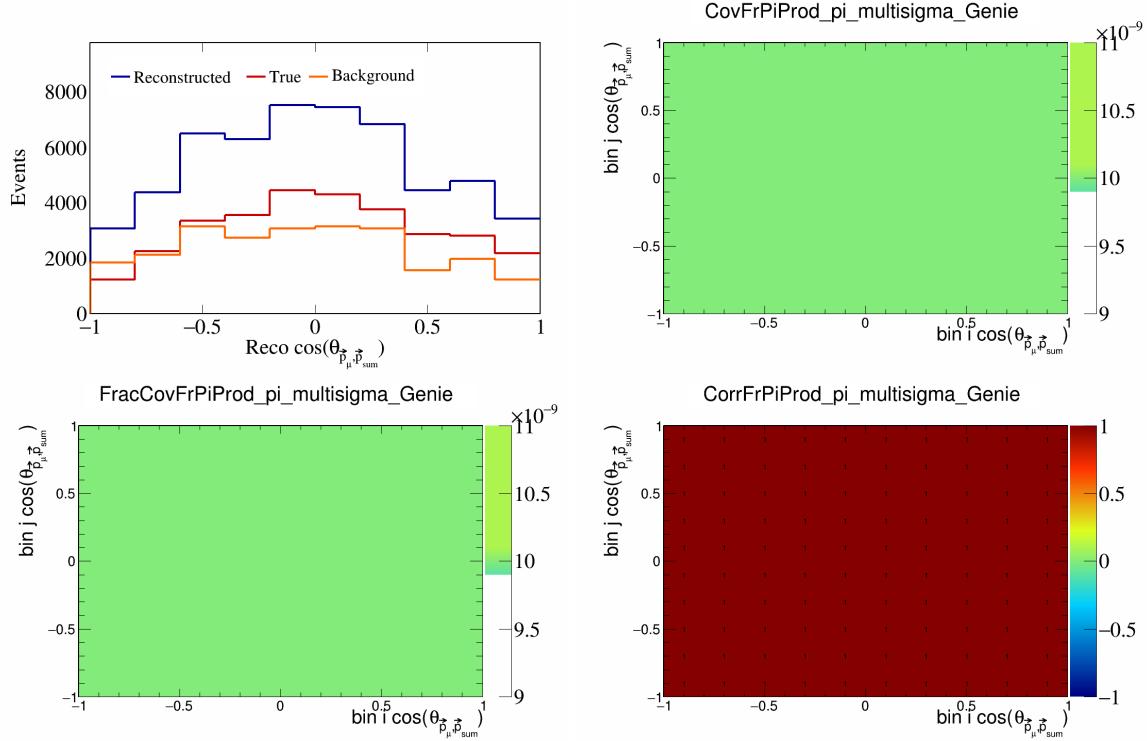


Figure 208: FrPiProdpi variations for $\cos(\theta_{\vec{p}_\mu, \vec{p}_{\text{sum}}})$.

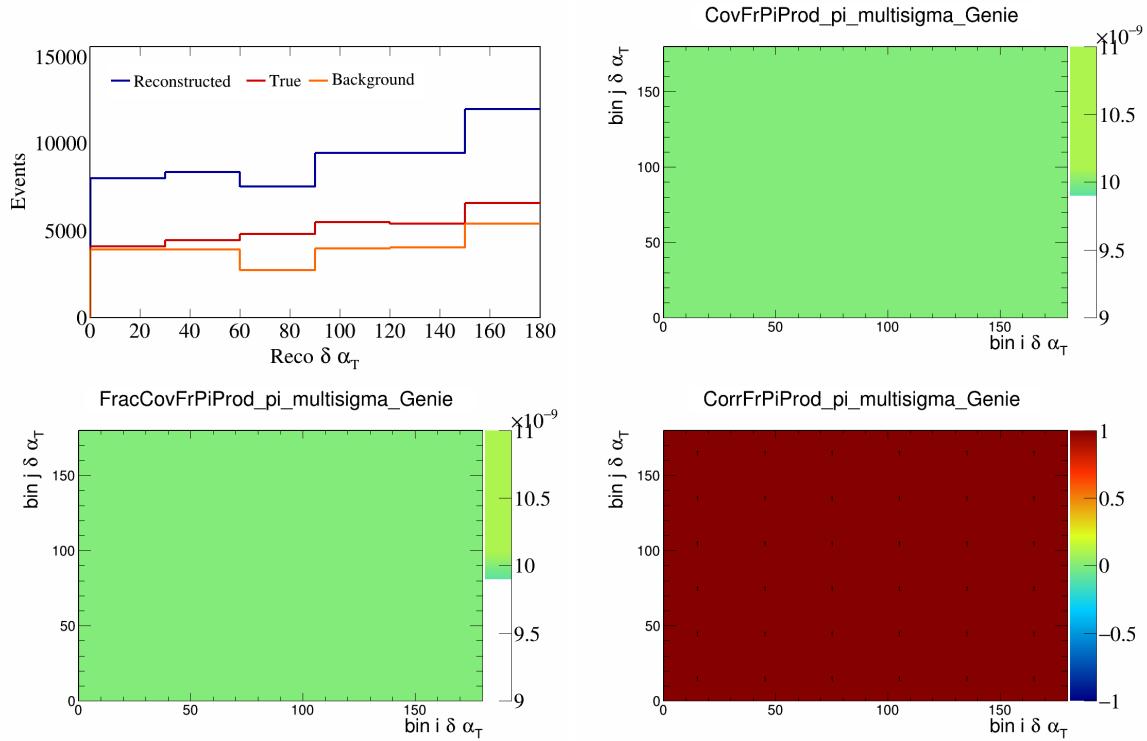


Figure 209: FrPiProdpi variations for $\delta\alpha_T$.

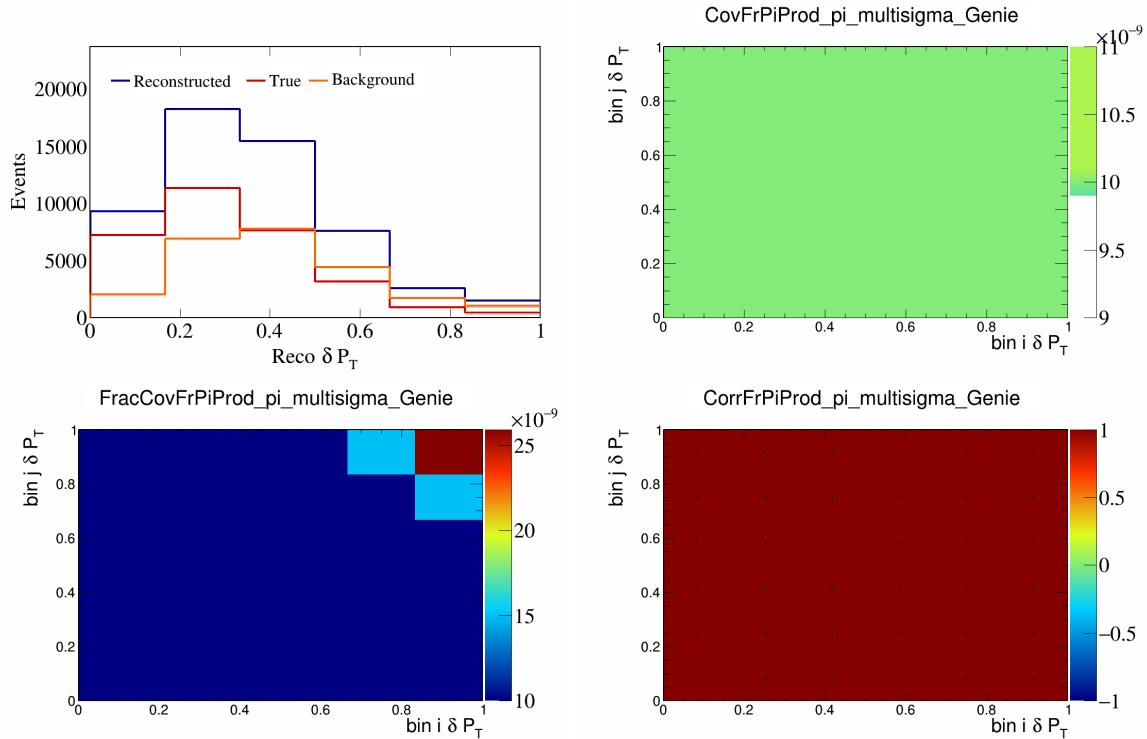


Figure 210: FrPiProdpi variations for δP_T .

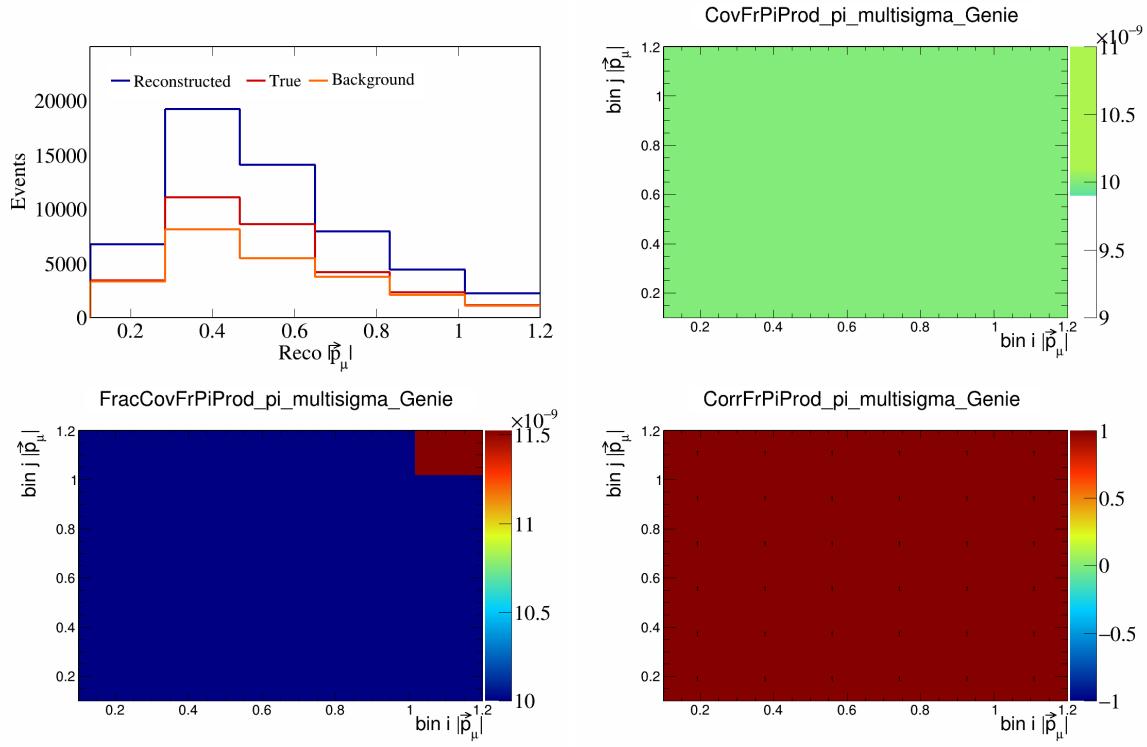


Figure 211: FrPiProdpi variations for $|\vec{p}_\mu|$.

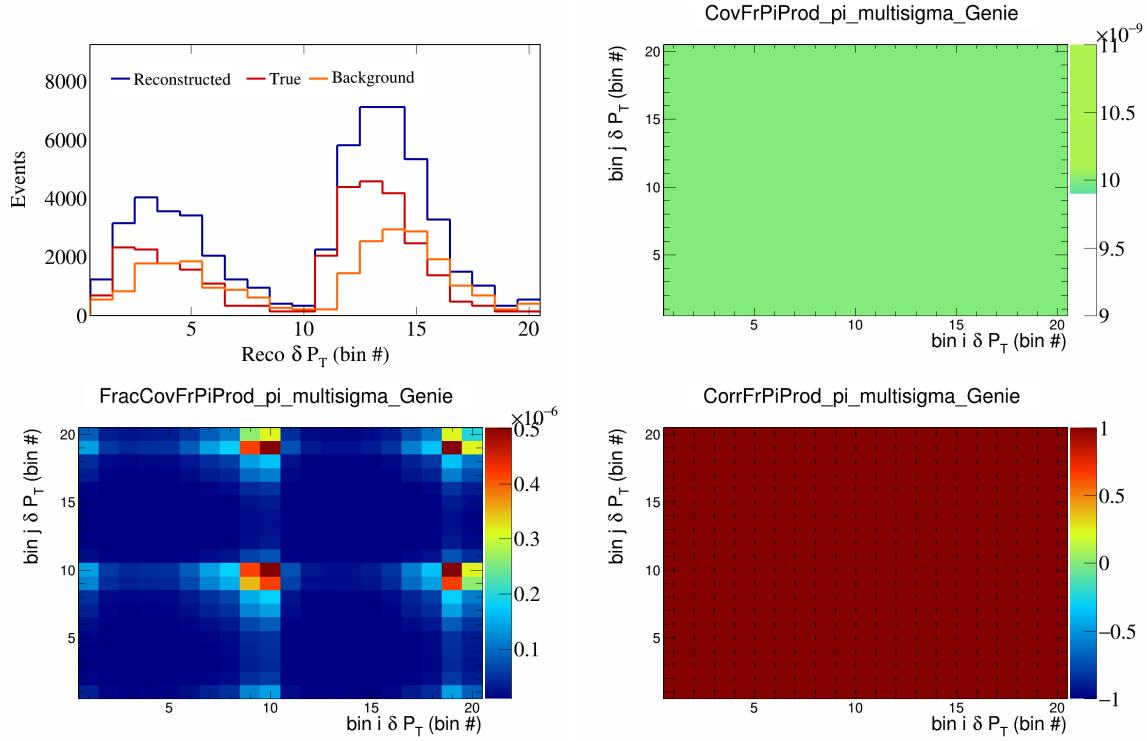


Figure 212: FrPiProdpi variations for δP_T in $\cos(\theta_{\vec{p}_\mu})$.

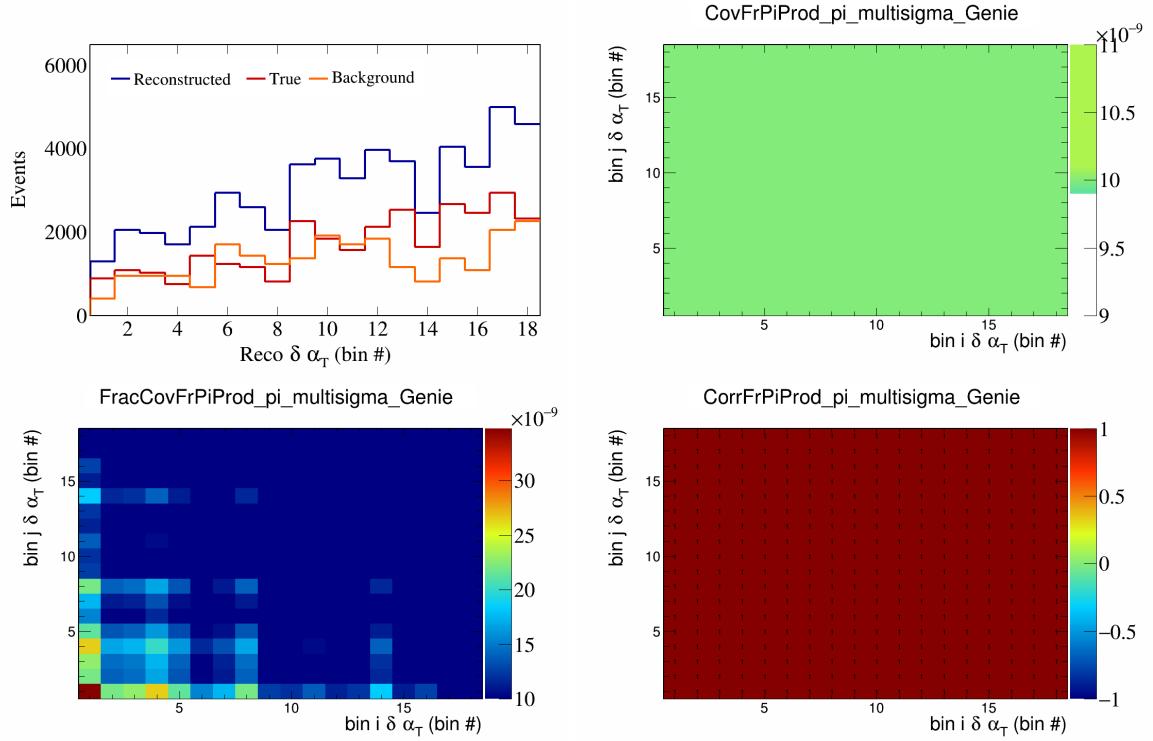


Figure 213: FrPiProdpi variations for $\delta \alpha_T$ in $\cos(\theta_{\vec{p}_\mu})$.

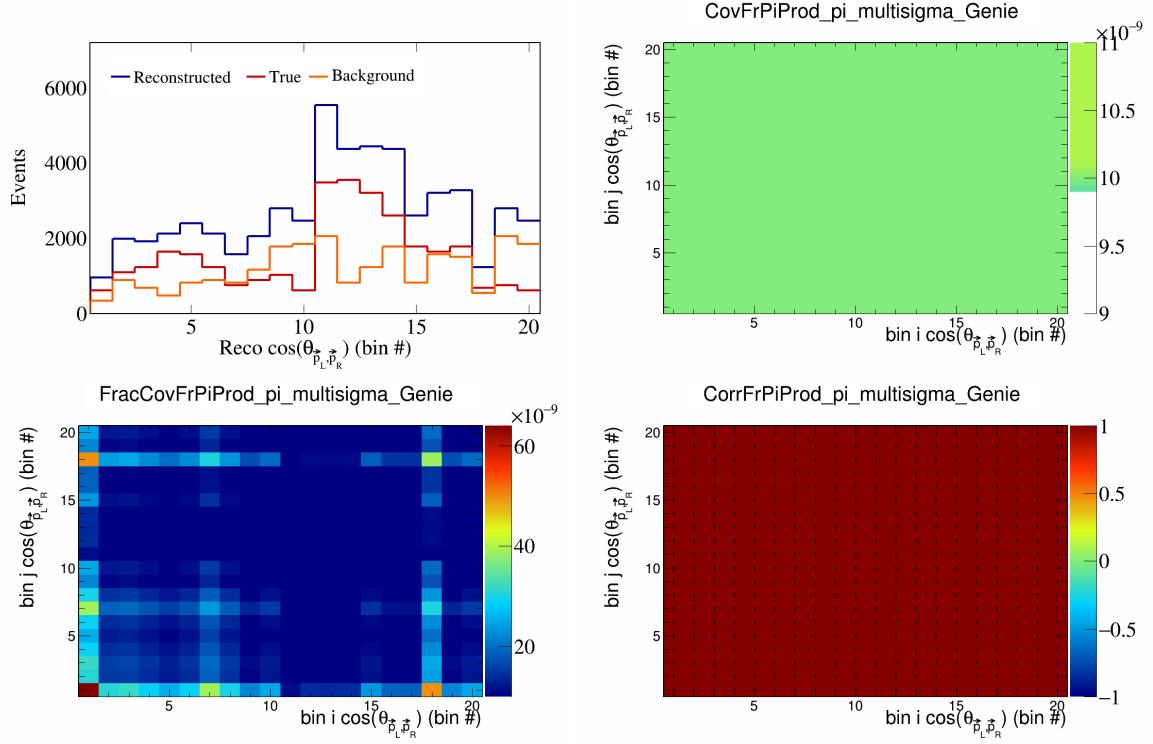


Figure 214: FrPiProdpi variations for $\cos(\theta_{\vec{p}_L, \vec{p}_R})$ in $\cos(\theta_{\vec{p}_\mu})$.

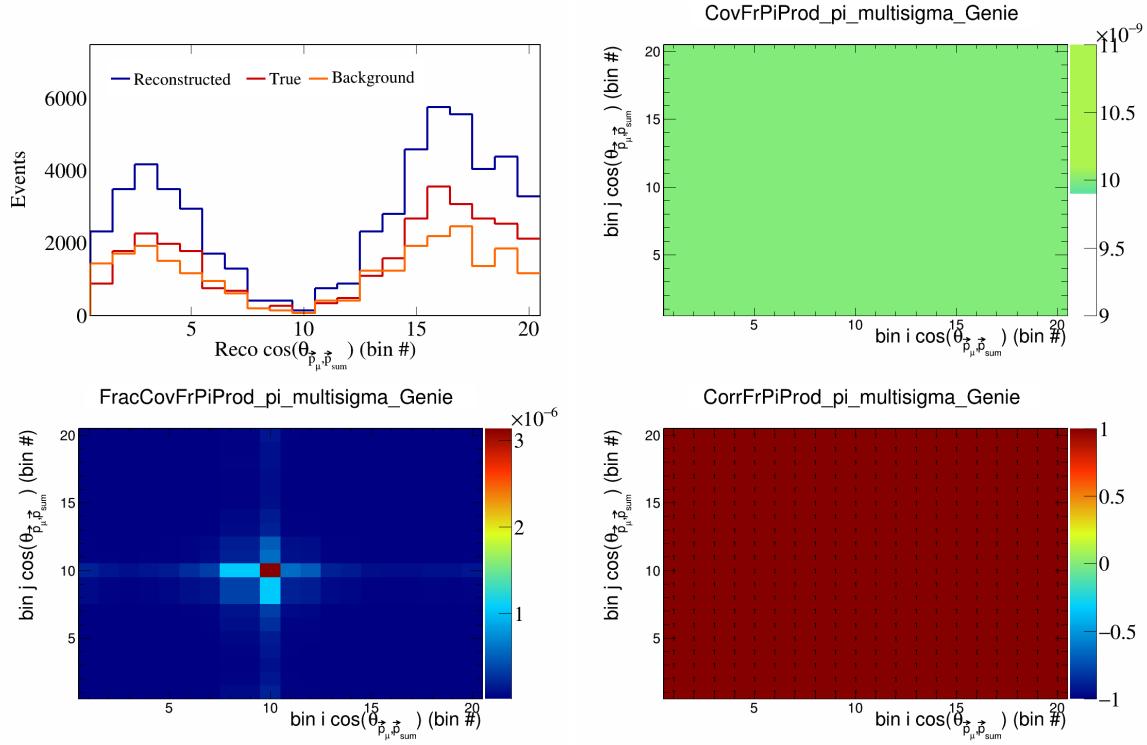


Figure 215: FrPiProdpi variations for $\cos(\theta_{\vec{p}_\mu, \vec{p}_{\text{sum}}})$ in $\cos(\theta_{\vec{p}_\mu})$.

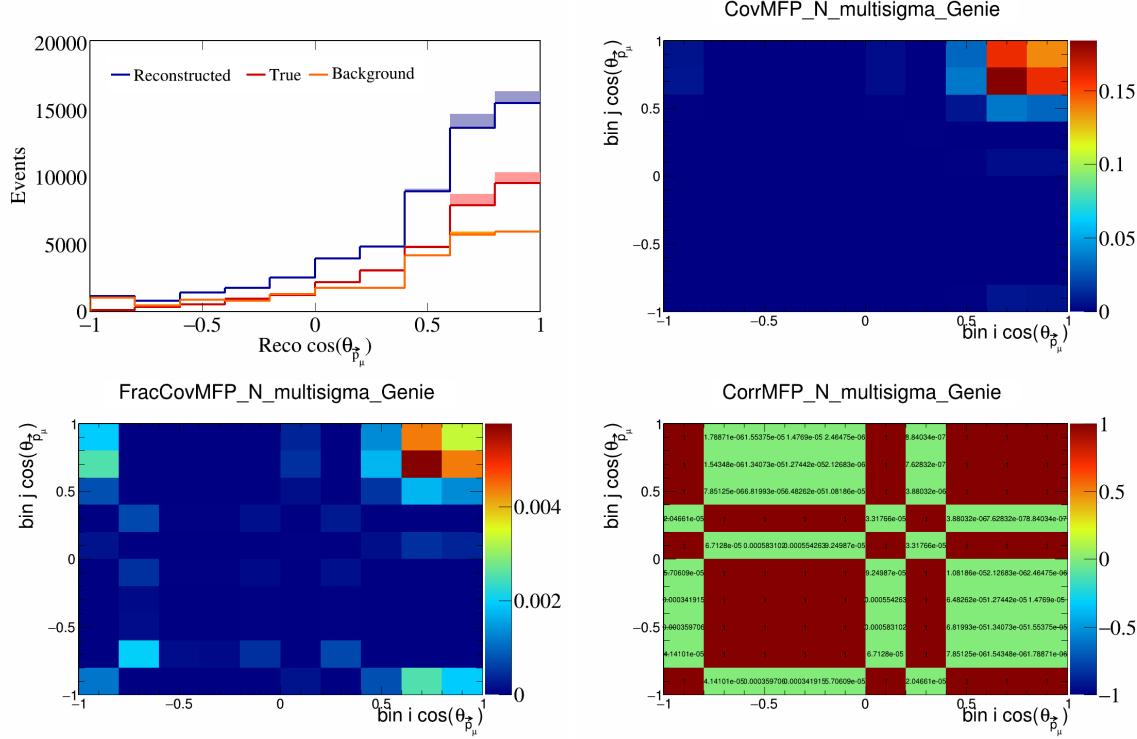


Figure 216: MFPN variations for $\cos(\theta_{\vec{p}_\mu})$.

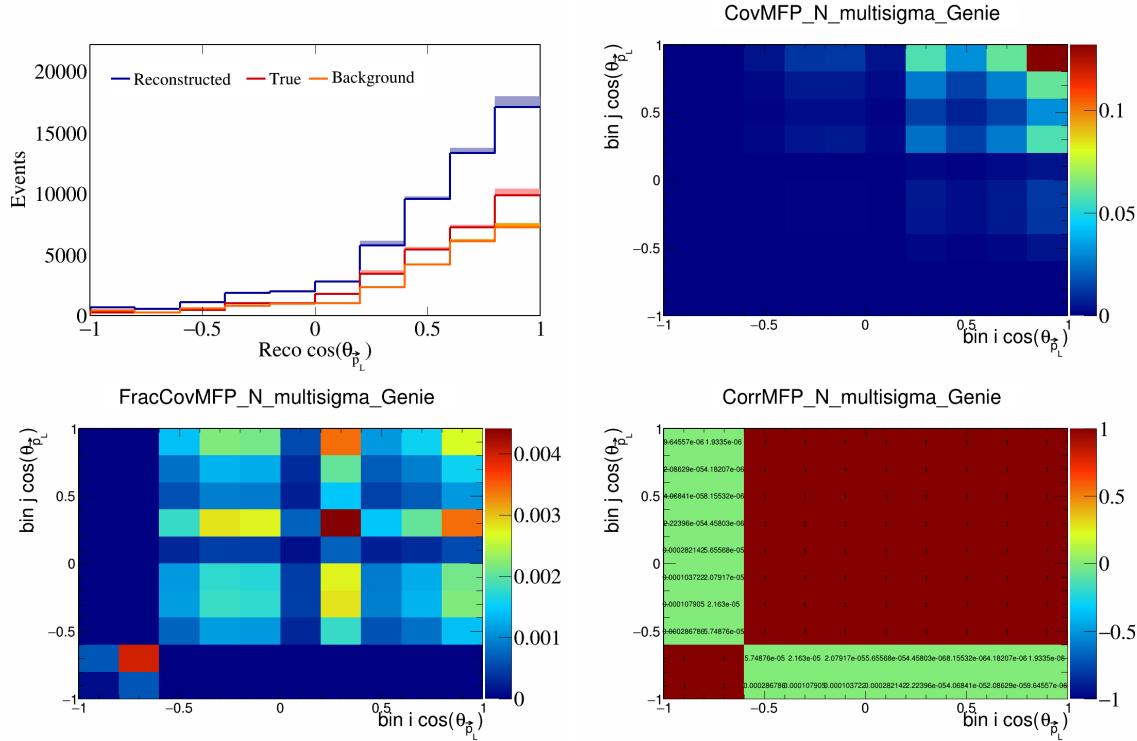


Figure 217: MFPN variations for $\cos(\theta_{\vec{p}_L})$.

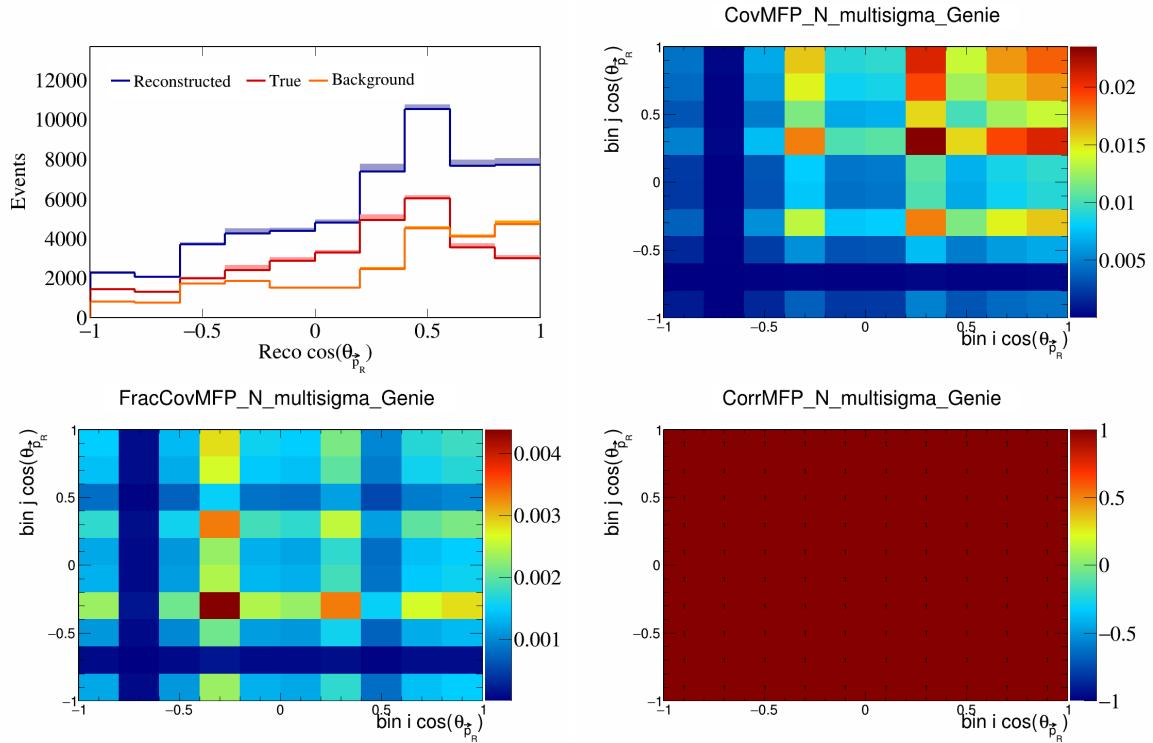


Figure 218: MFPN variations for $\cos(\theta_{\vec{p}_R})$.

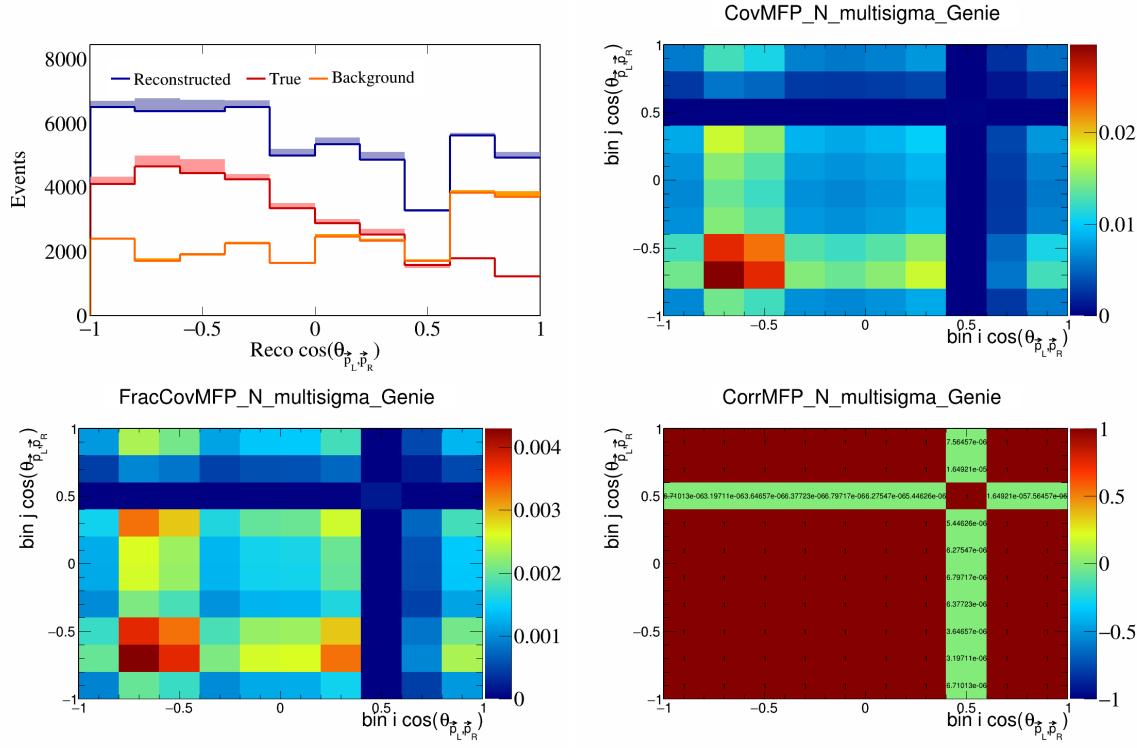


Figure 219: MFPN variations for $\cos(\theta_{\vec{p}_L, \vec{p}_R})$.

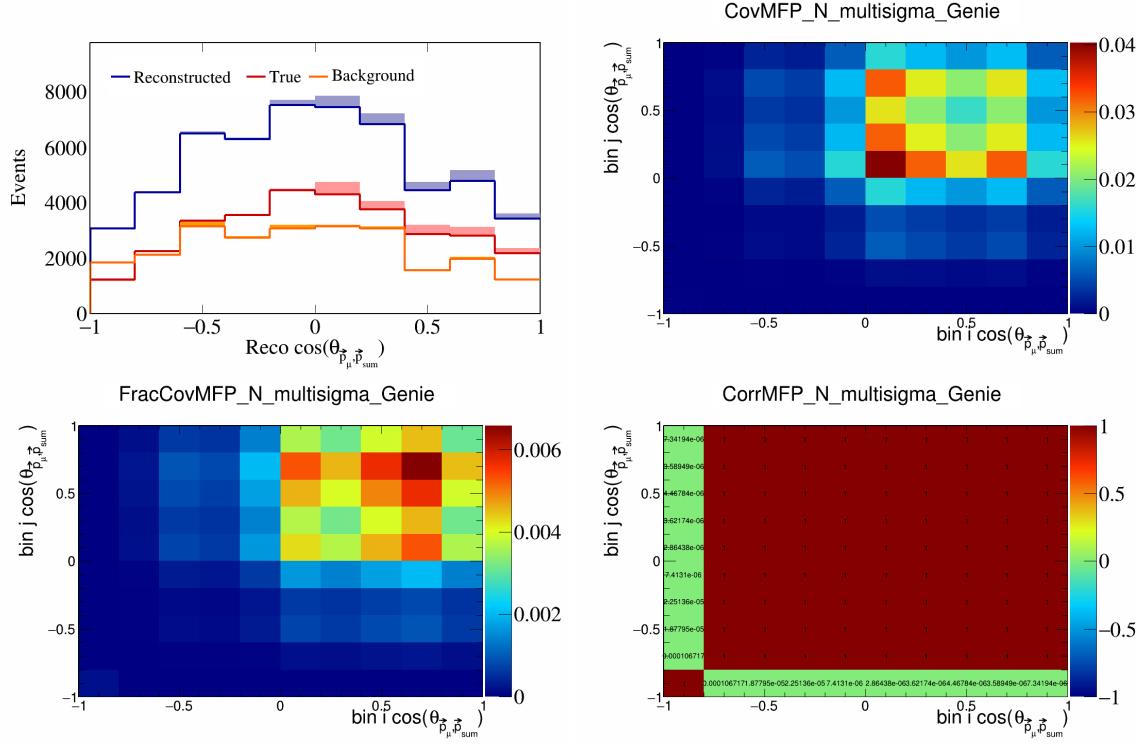


Figure 220: MFPN variations for $\cos(\theta_{\vec{p}_\mu, \vec{p}_{\text{sum}}})$.

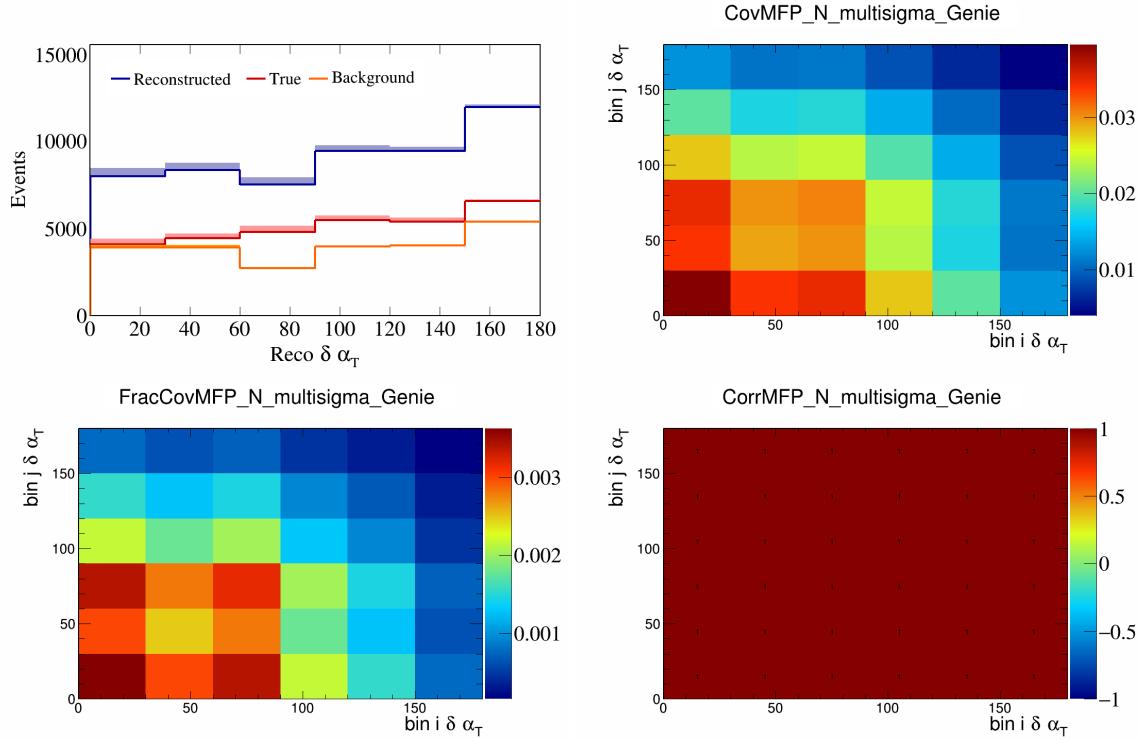


Figure 221: MFPN variations for $\delta\alpha_T$.

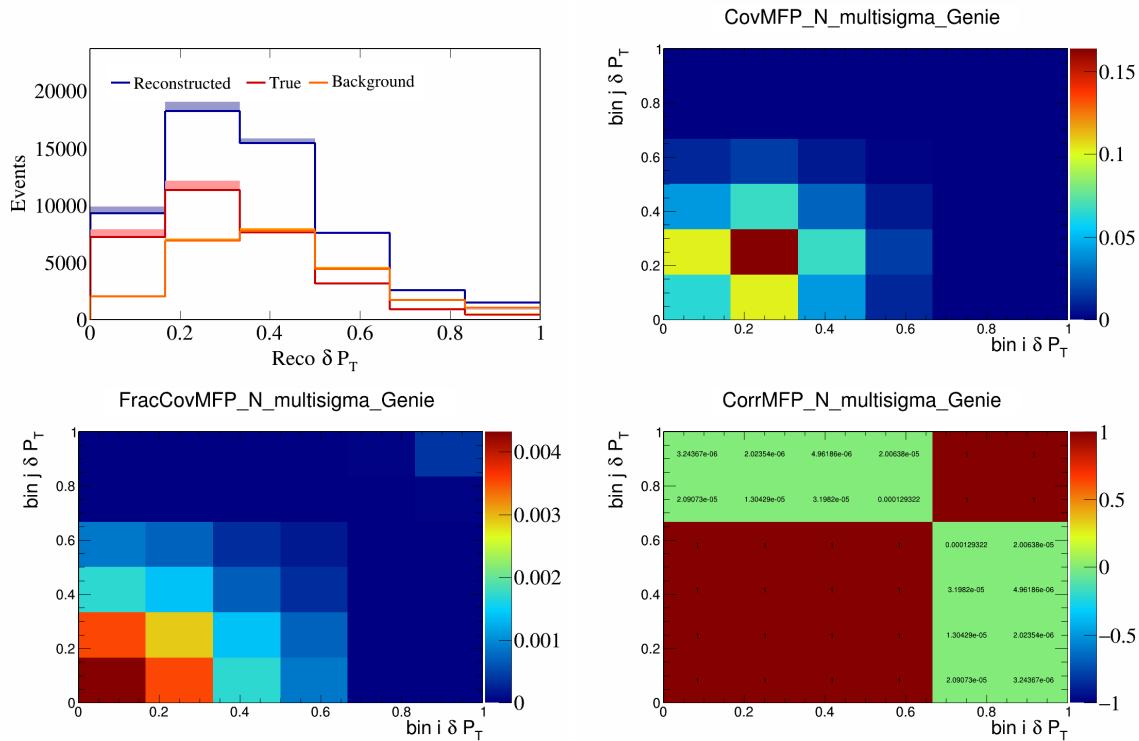


Figure 222: MFPN variations for δP_T .

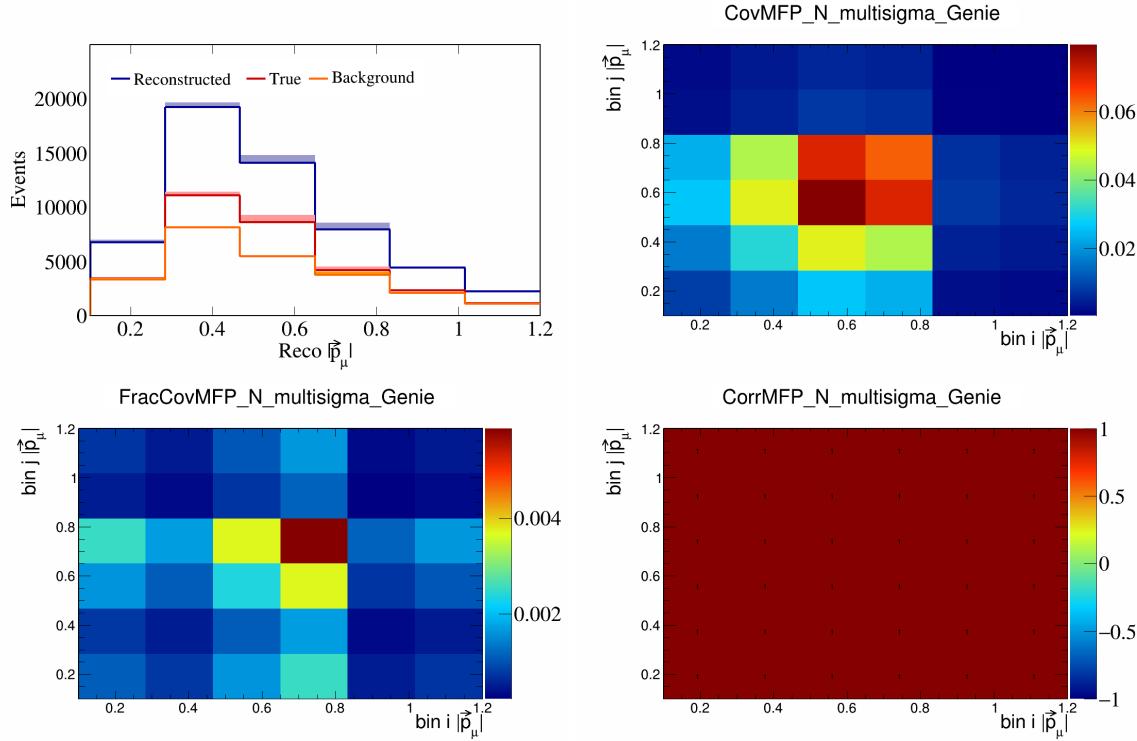


Figure 223: MFPN variations for $|\vec{p}_\mu|$.

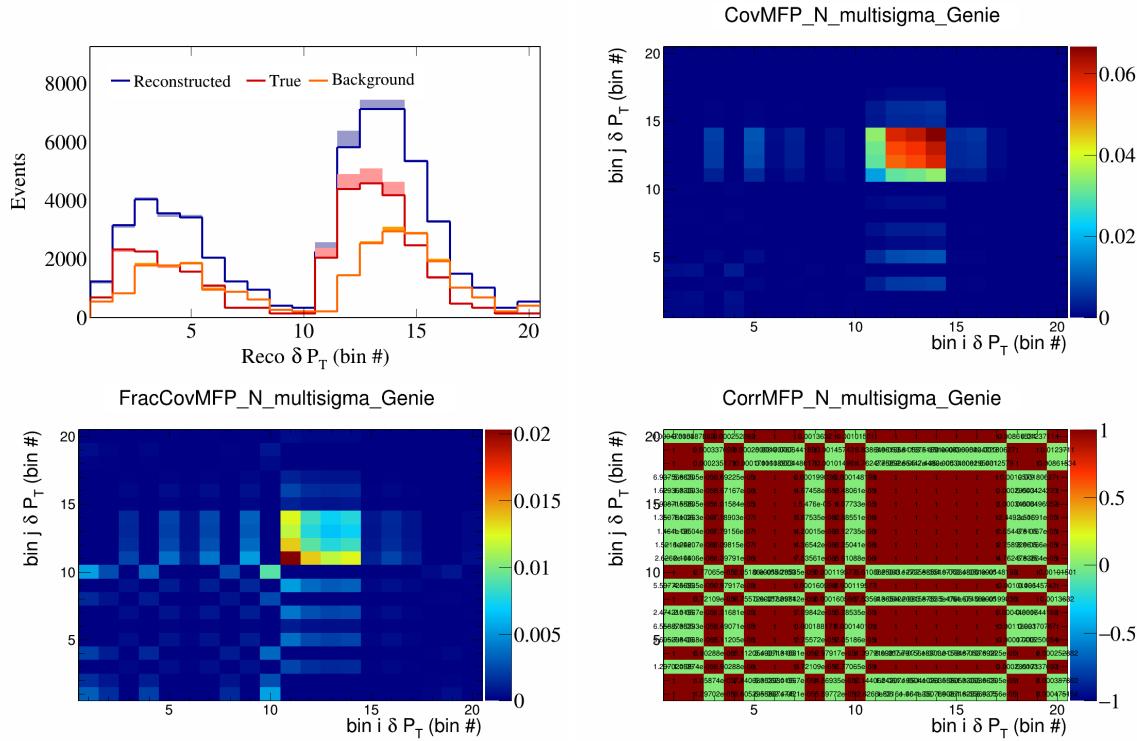


Figure 224: MFPN variations for δP_T in $\cos(\theta_{\vec{p}_\mu})$.

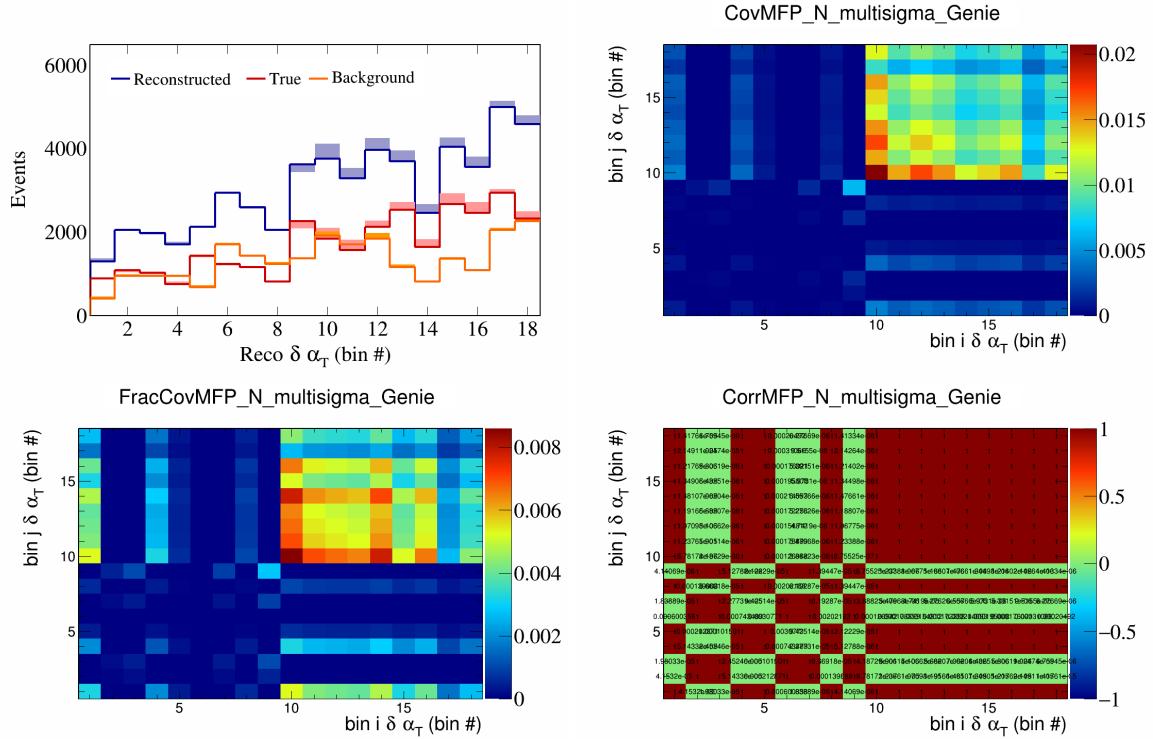


Figure 225: MFPN variations for $\delta\alpha_T$ in $\cos(\theta_{\vec{p}_\mu})$.

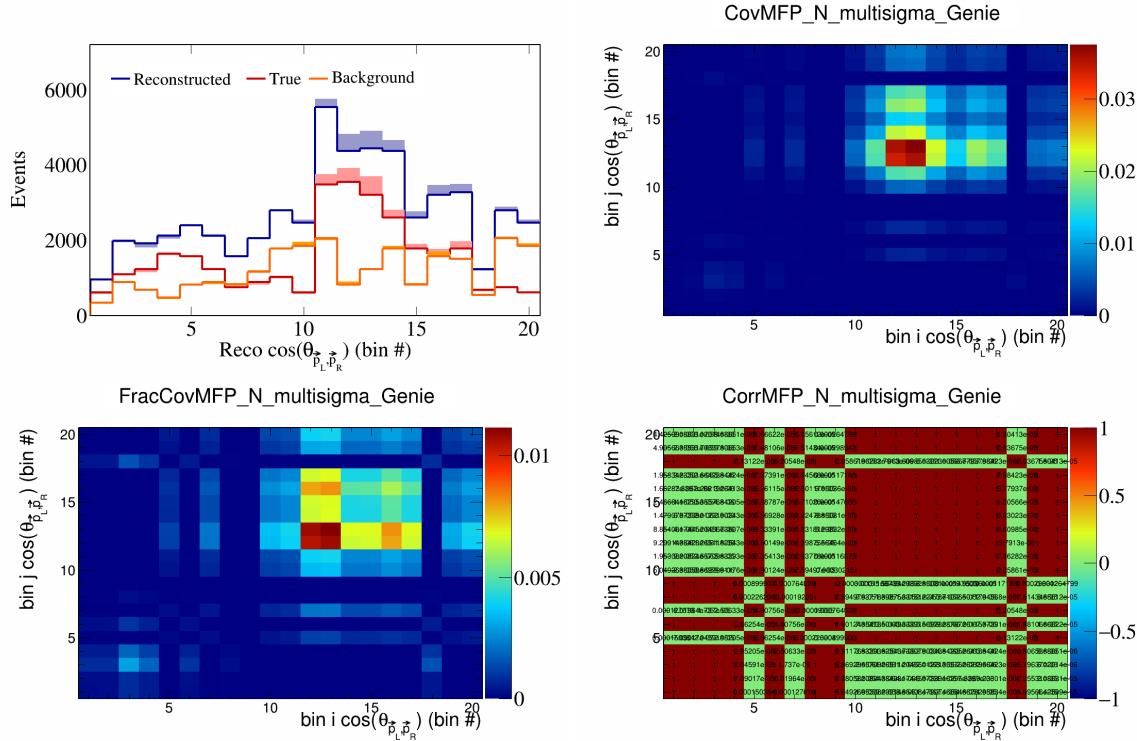


Figure 226: MFPN variations for $\cos(\theta_{\vec{p}_L, \vec{p}_R})$ in $\cos(\theta_{\vec{p}_\mu})$.

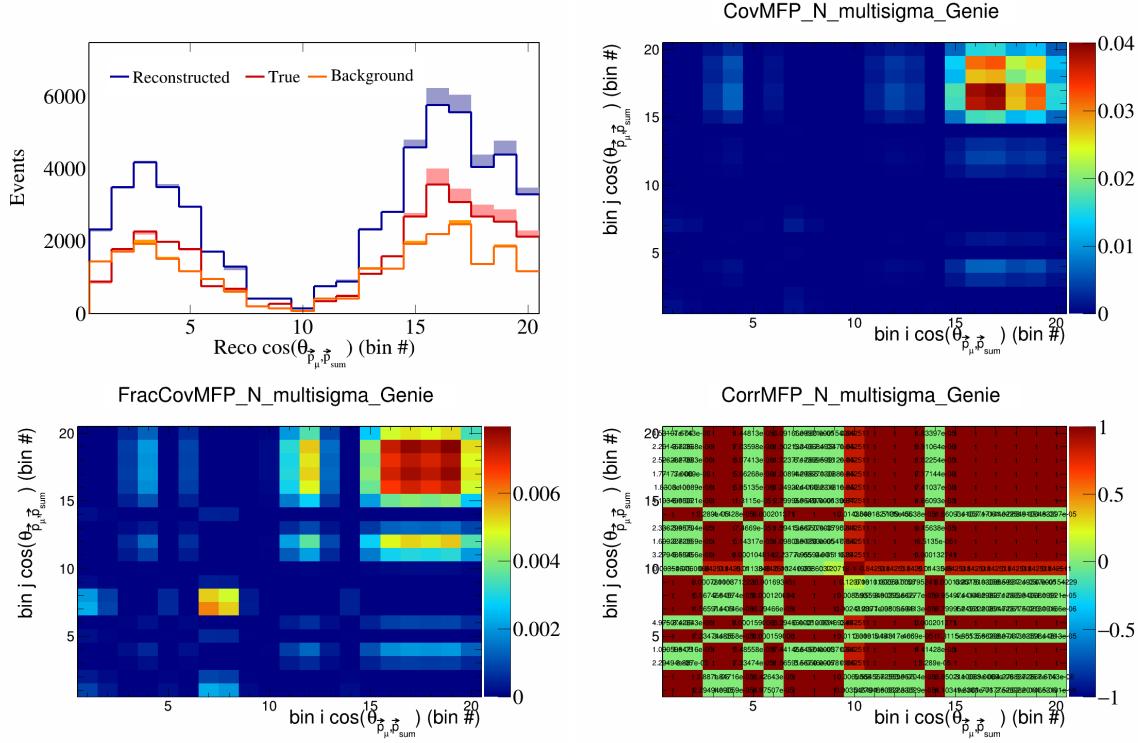


Figure 227: MFPN variations for $\cos(\theta_{\vec{p}_\mu, \vec{p}_{\text{sum}}})$ in $\cos(\theta_{\vec{p}_\mu})$.

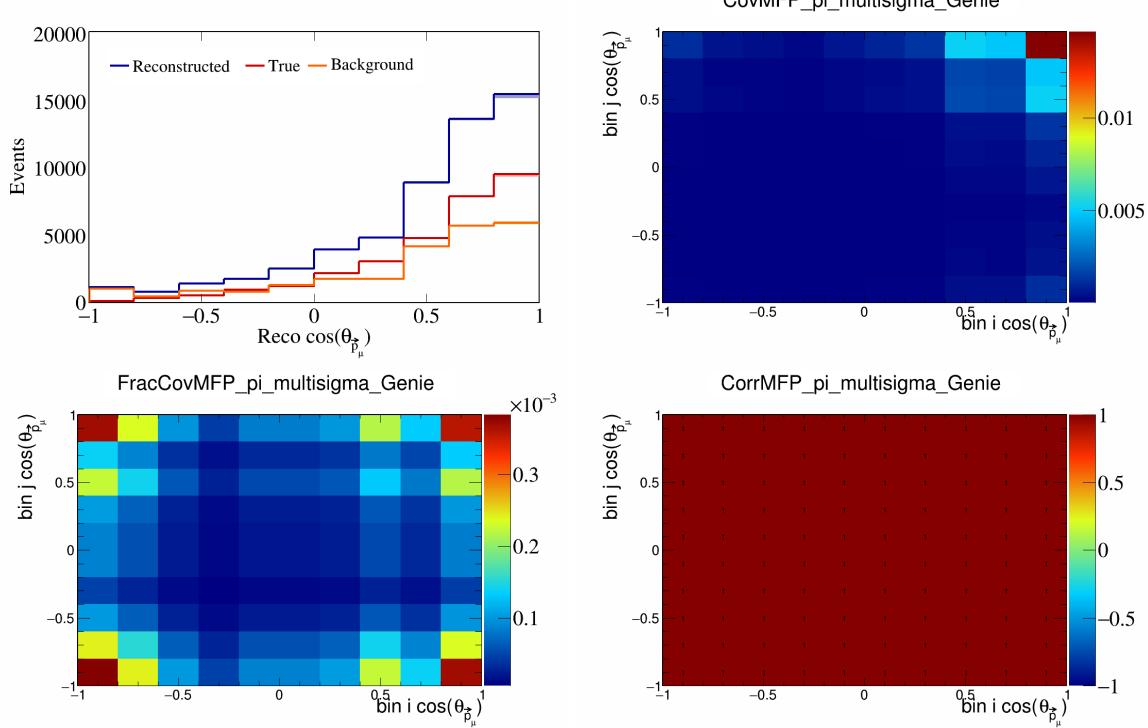


Figure 228: MFPPi variations for $\cos(\theta_{\vec{p}_\mu})$.

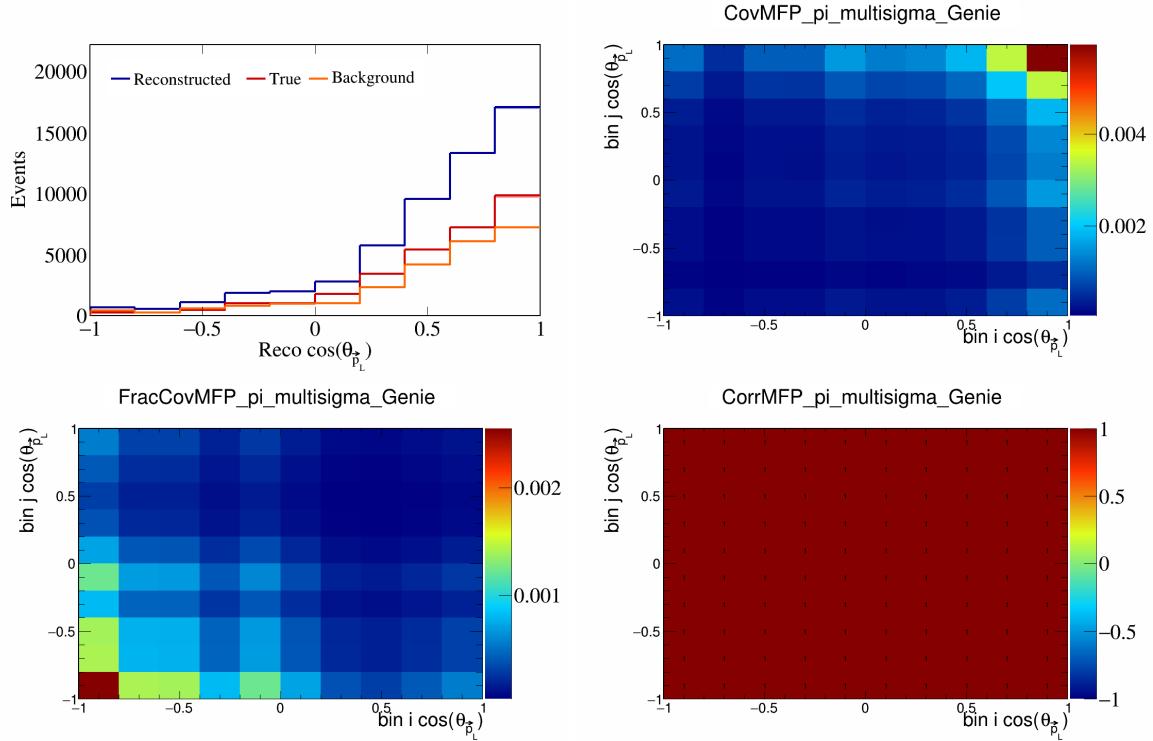


Figure 229: MFPpi variations for $\cos(\theta_{\vec{p}_L})$.

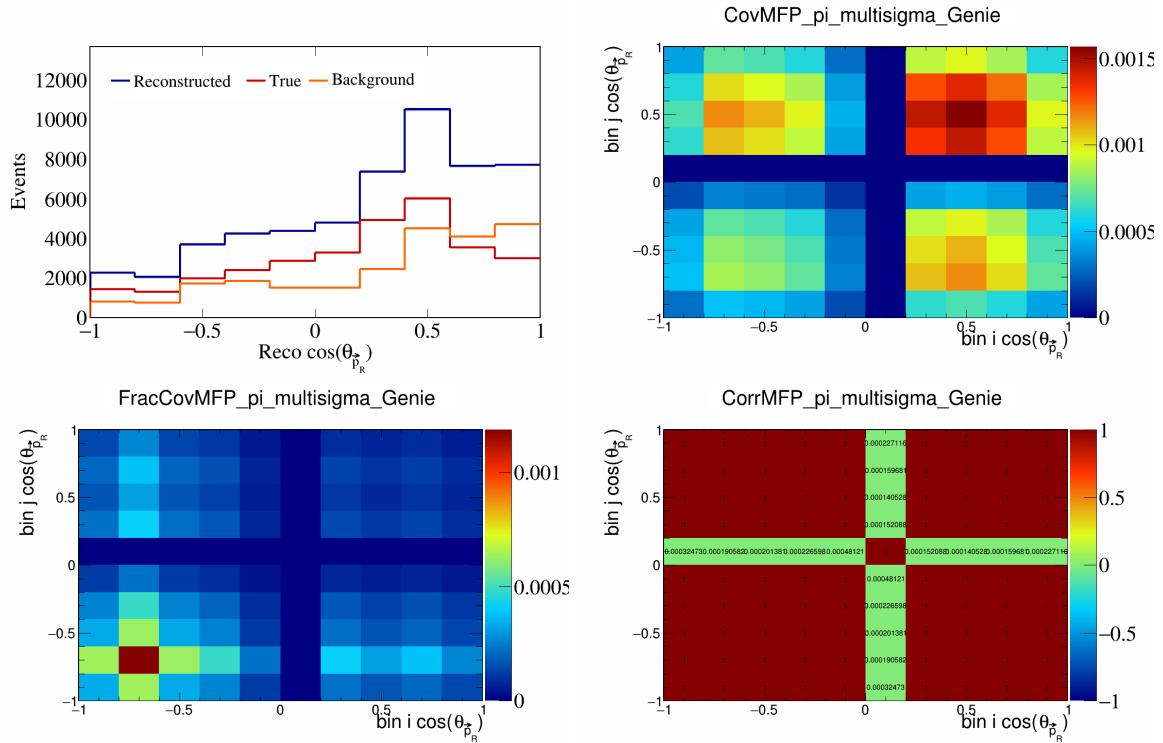


Figure 230: MFPpi variations for $\cos(\theta_{\vec{p}_R})$.

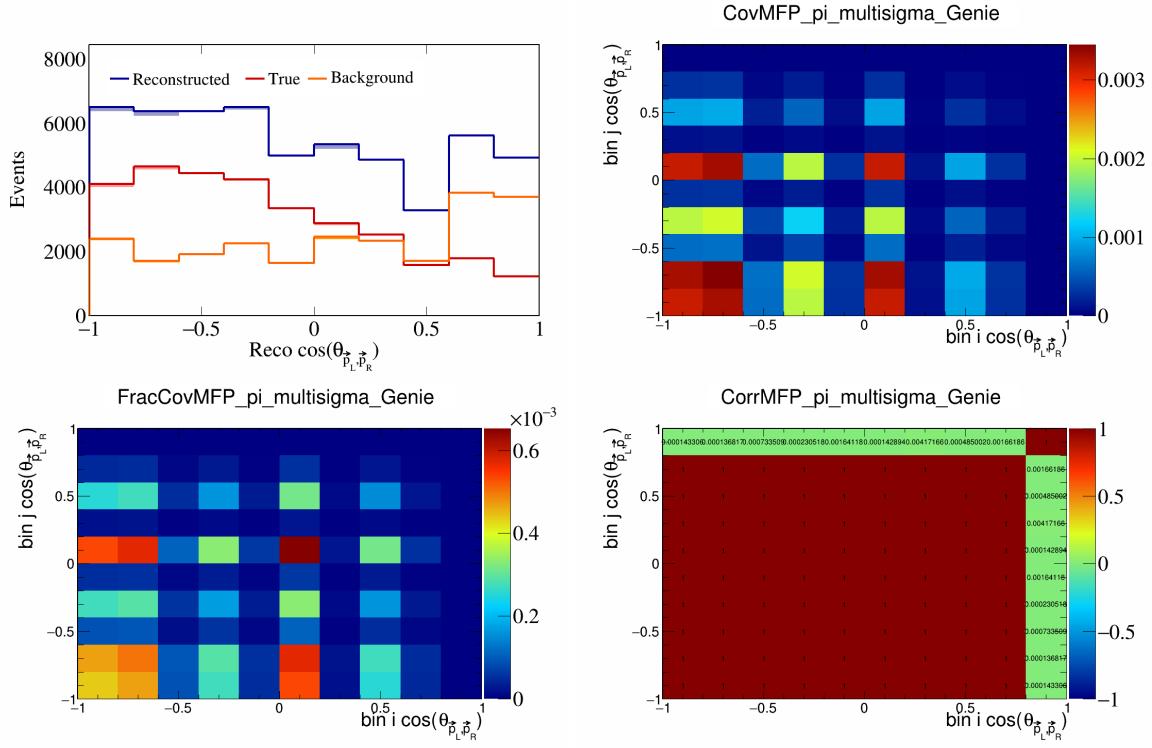


Figure 231: MFPpi variations for $\cos(\theta_{\vec{p}_L, \vec{p}_R})$.

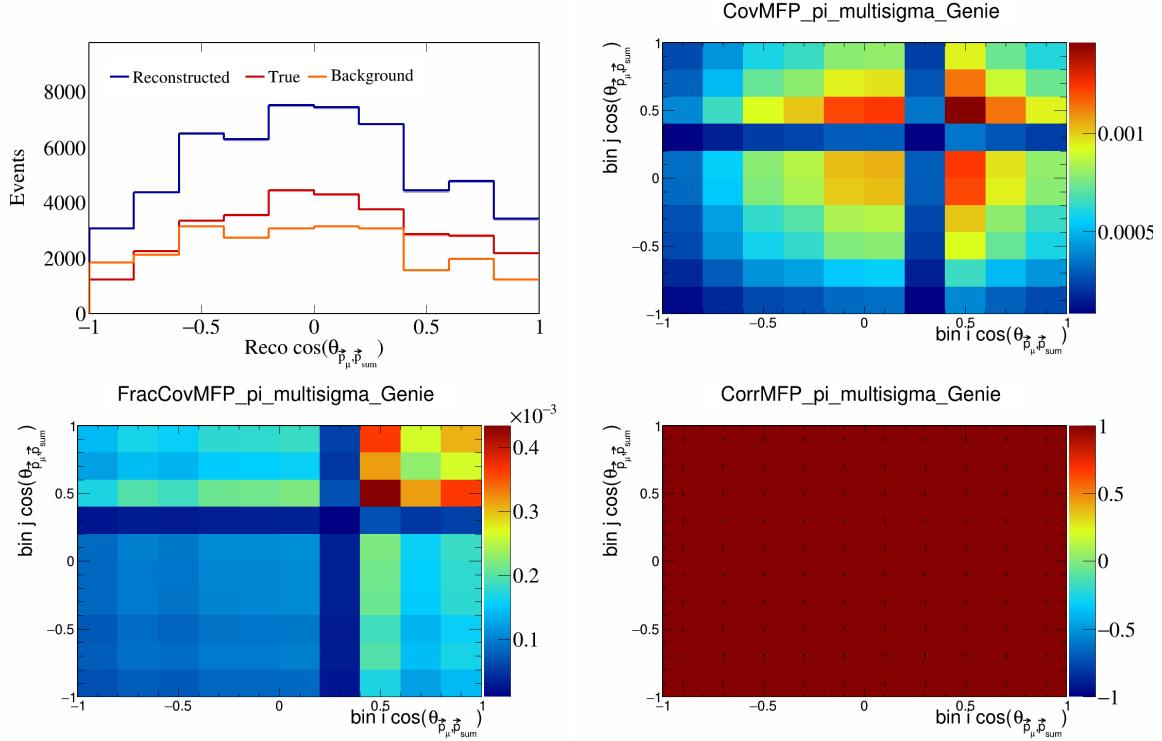


Figure 232: MFPpi variations for $\cos(\theta_{\vec{p}_\mu, \vec{p}_{\text{sum}}})$.

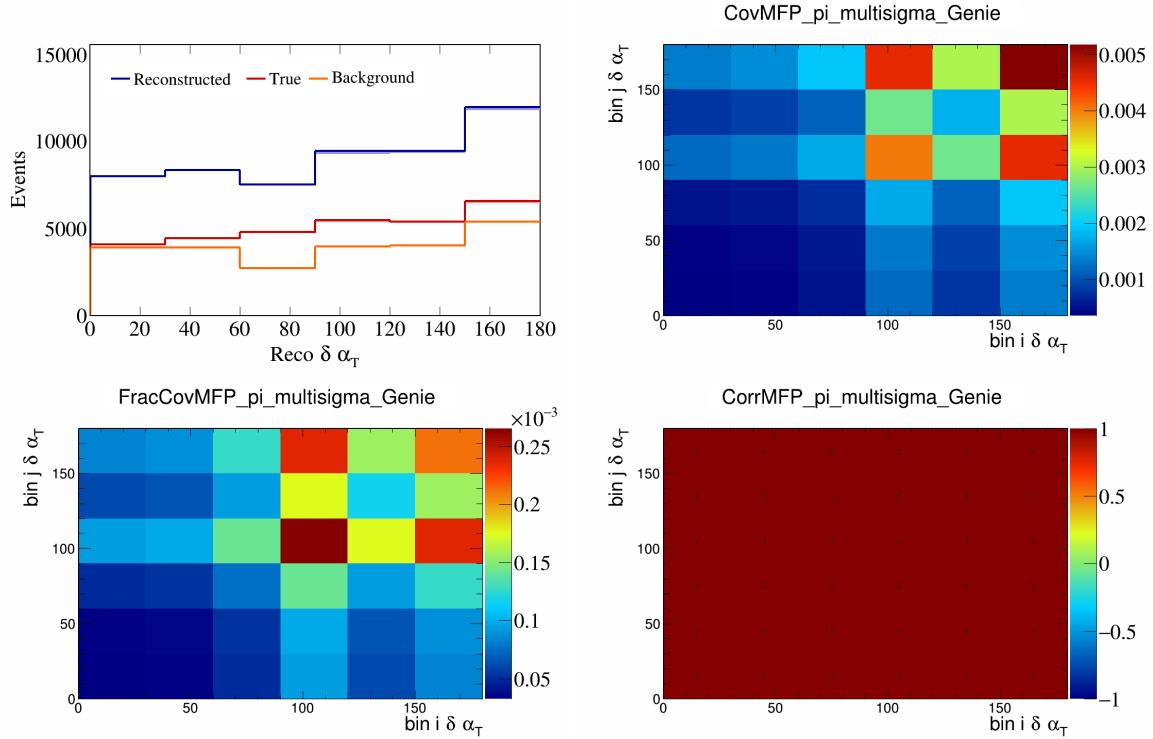


Figure 233: MFPPi variations for $\delta\alpha_T$.

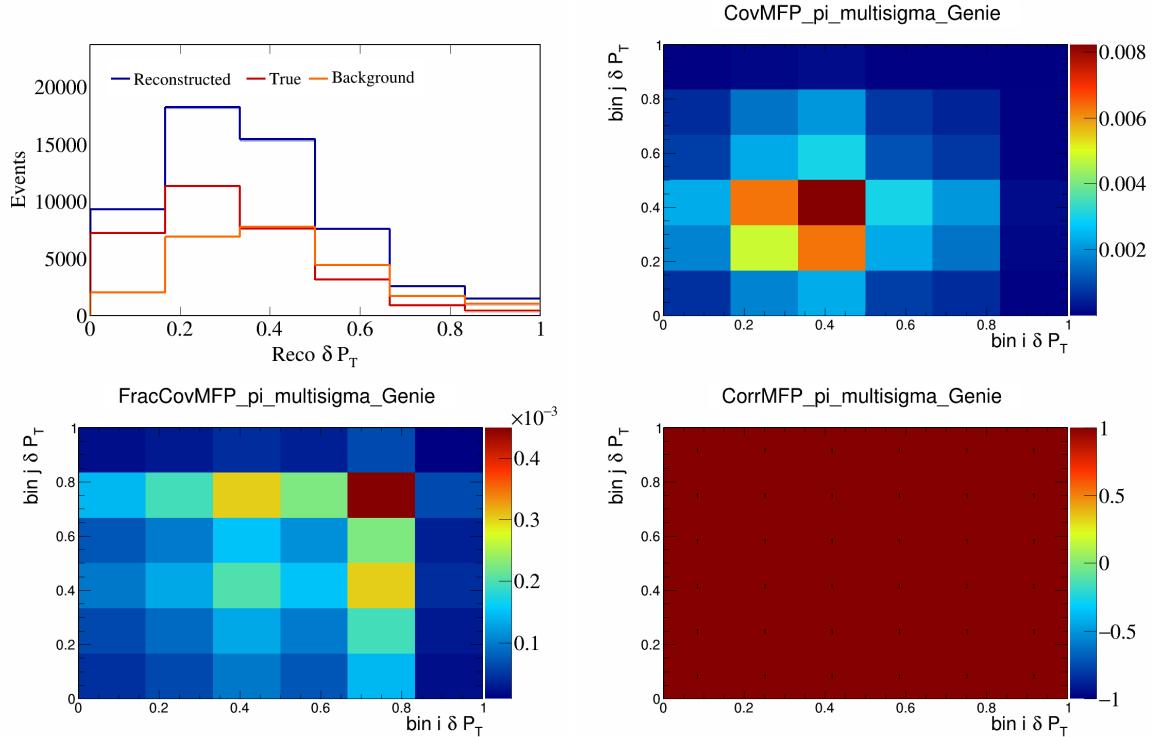


Figure 234: MFPPi variations for δP_T .

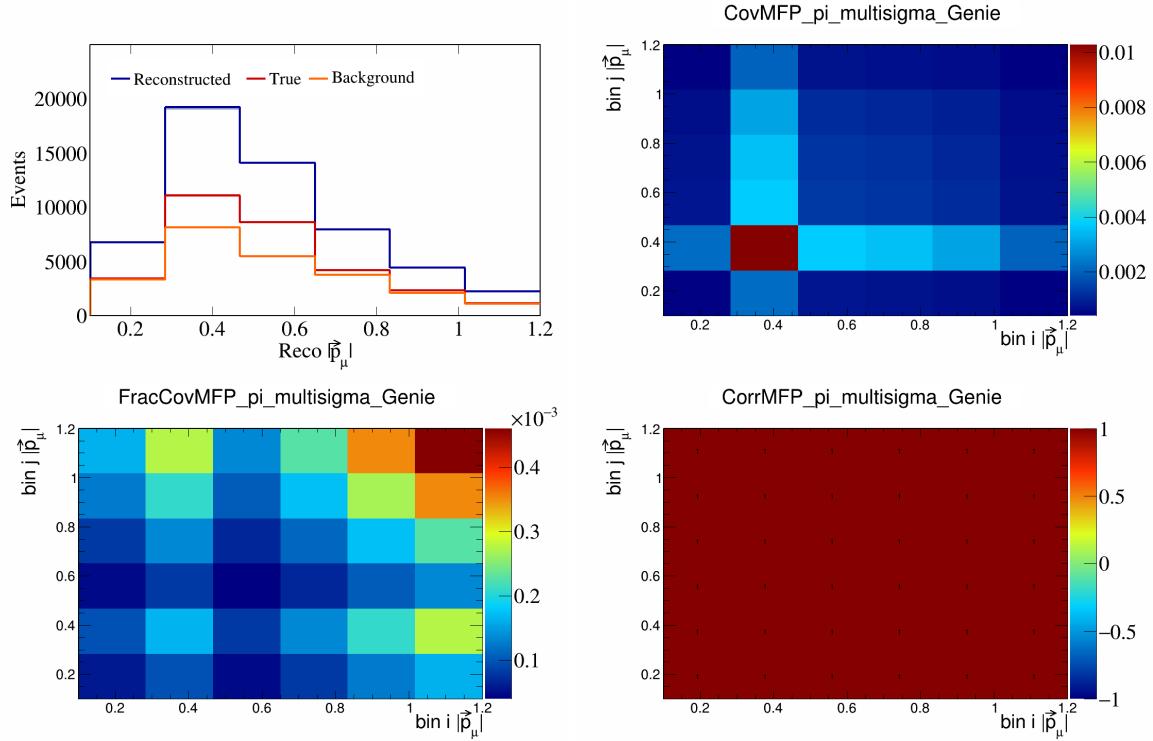


Figure 235: MFPpi variations for $|\vec{p}_\mu|$.

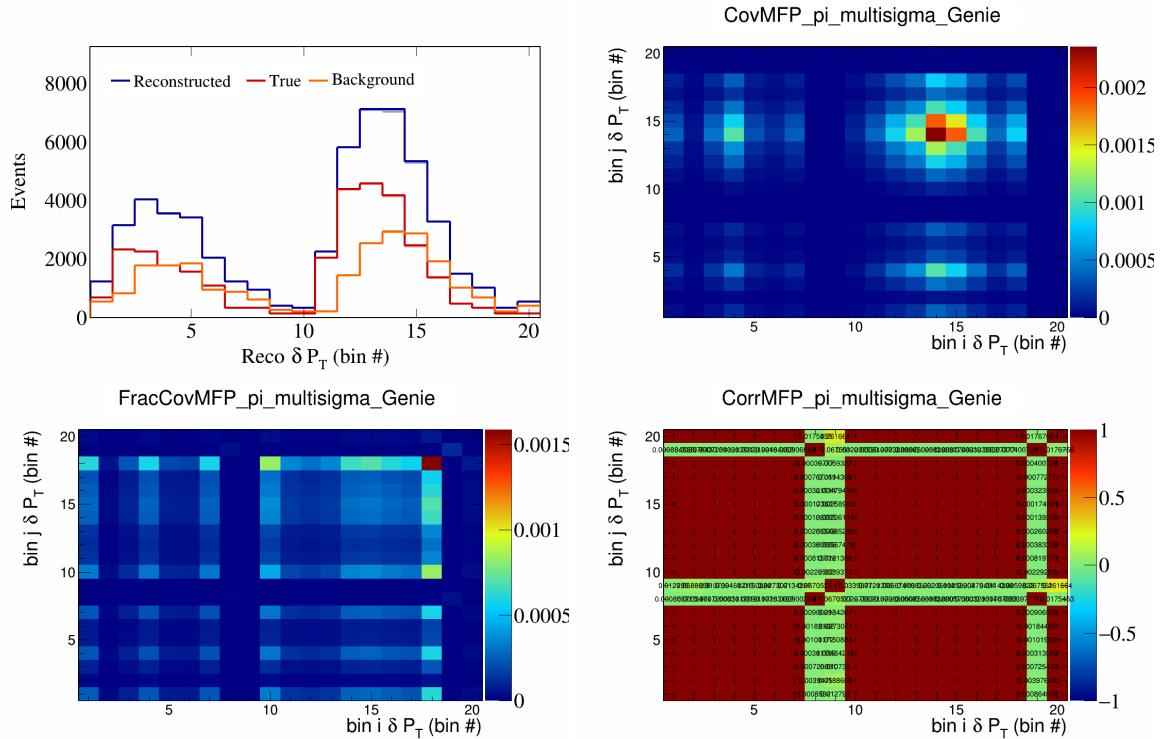


Figure 236: MFPpi variations for δP_T in $\cos(\theta_{\vec{p}_\mu})$.

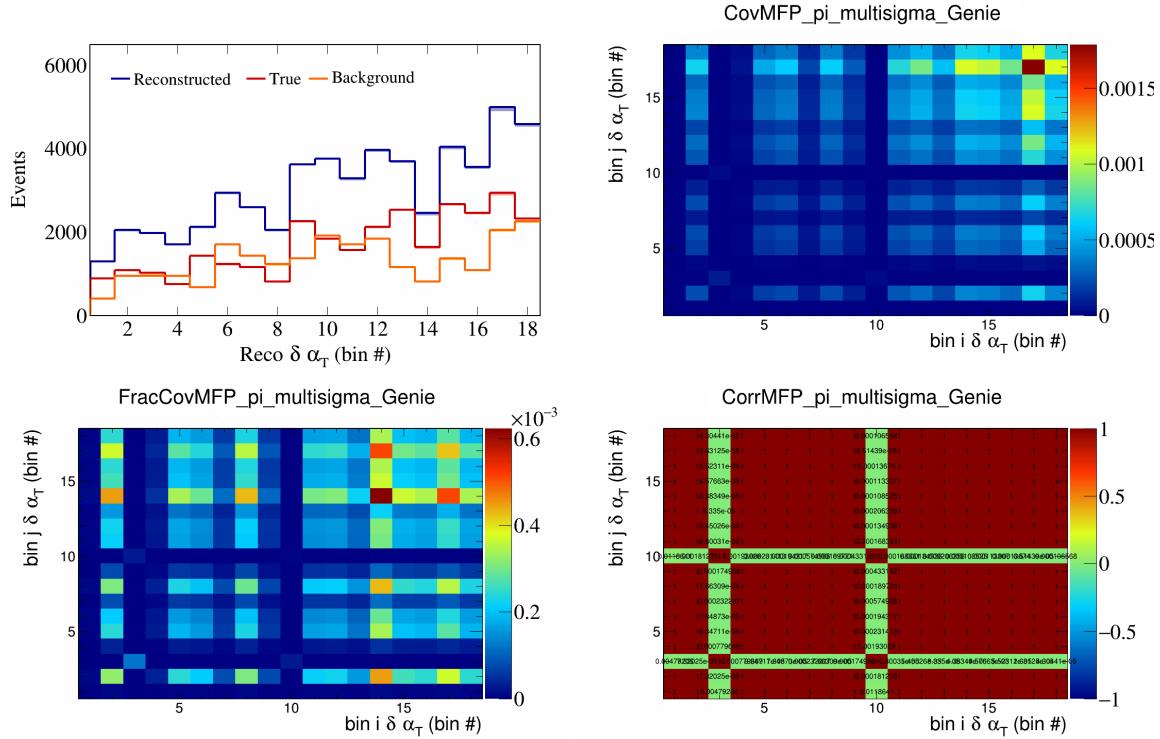


Figure 237: MFPpi variations for $\delta\alpha_T$ in $\cos(\theta_{\vec{p}_\mu})$.

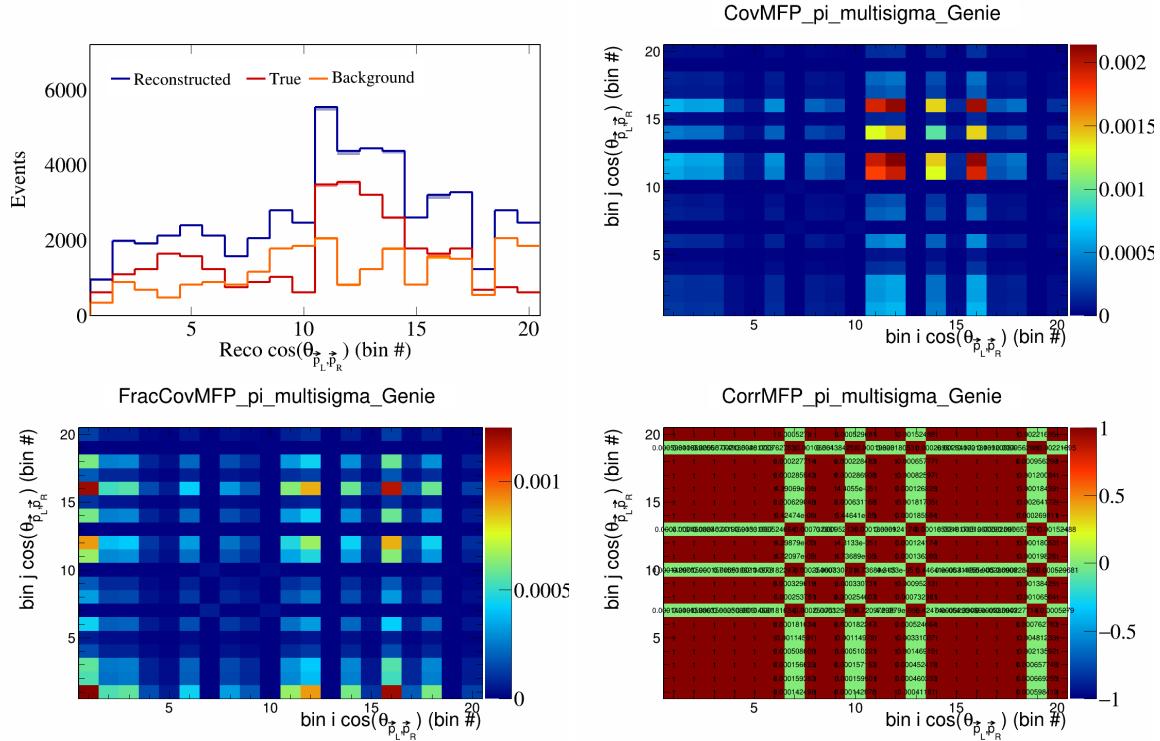


Figure 238: MFPpi variations for $\cos(\theta_{\vec{p}_L, \vec{p}_R})$ in $\cos(\theta_{\vec{p}_\mu})$.

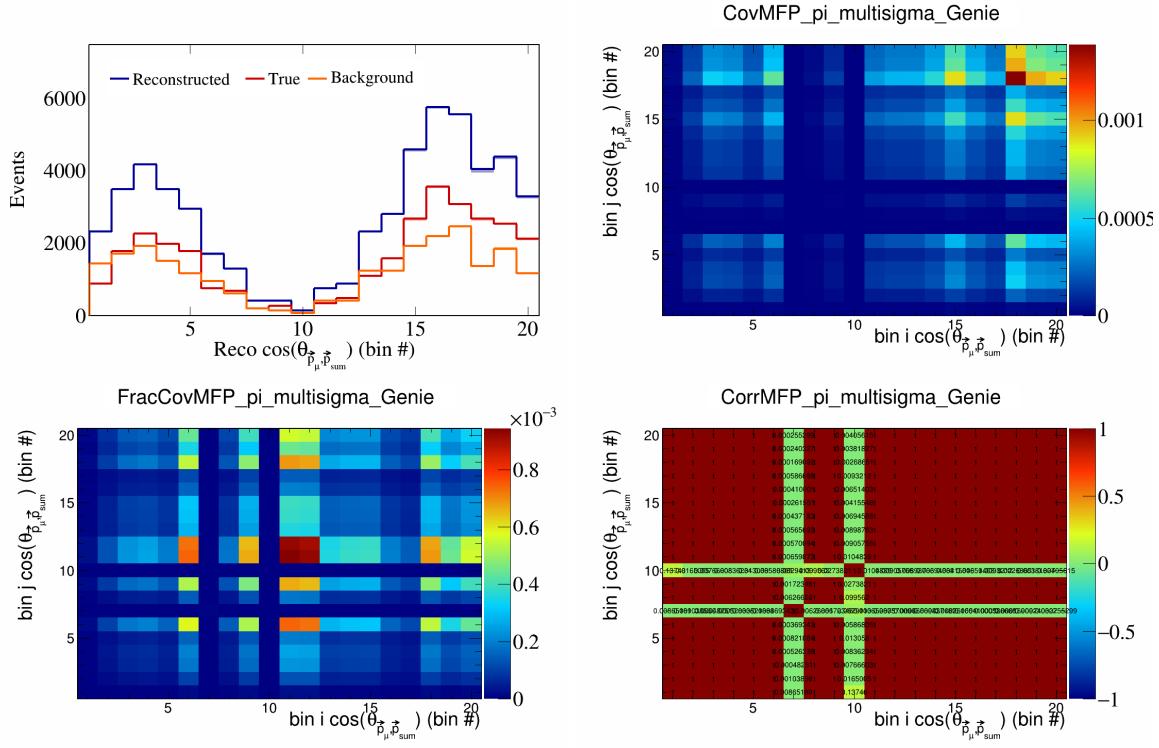


Figure 239: MFPpi variations for $\cos(\theta_{\vec{p}_\mu, \vec{p}_{\text{sum}}})$ in $\cos(\theta_{\vec{p}_\mu})$.

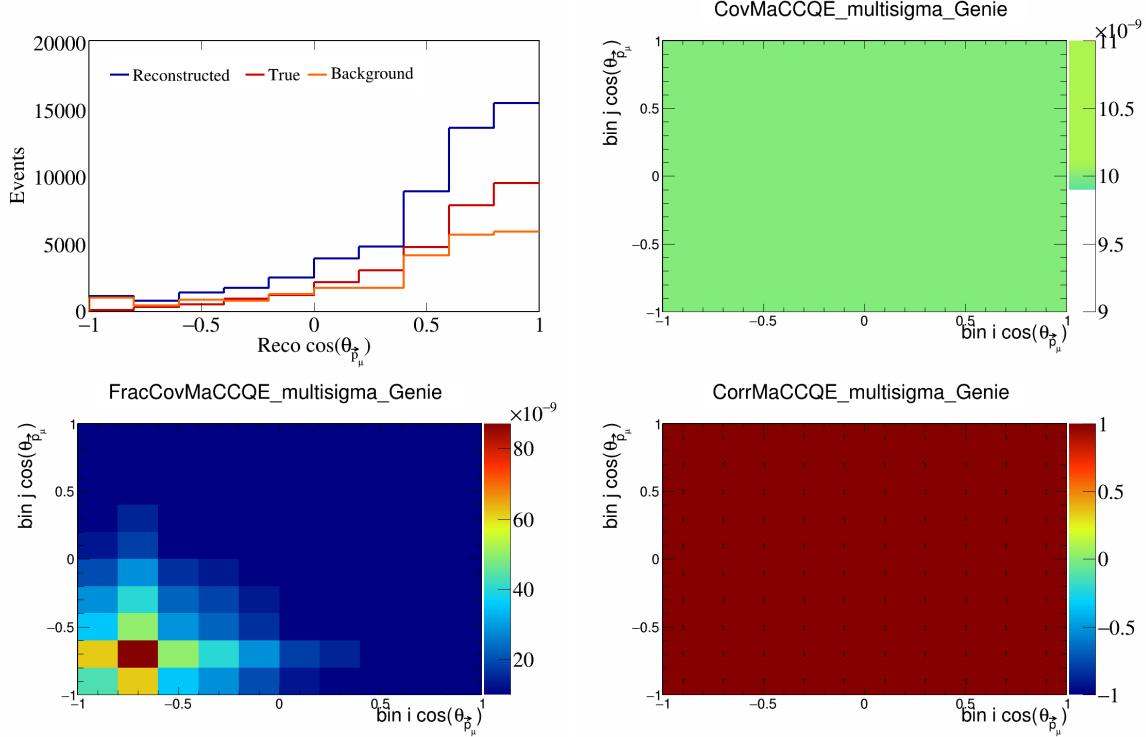


Figure 240: MaCCQE variations for $\cos(\theta_{\vec{p}_\mu})$.

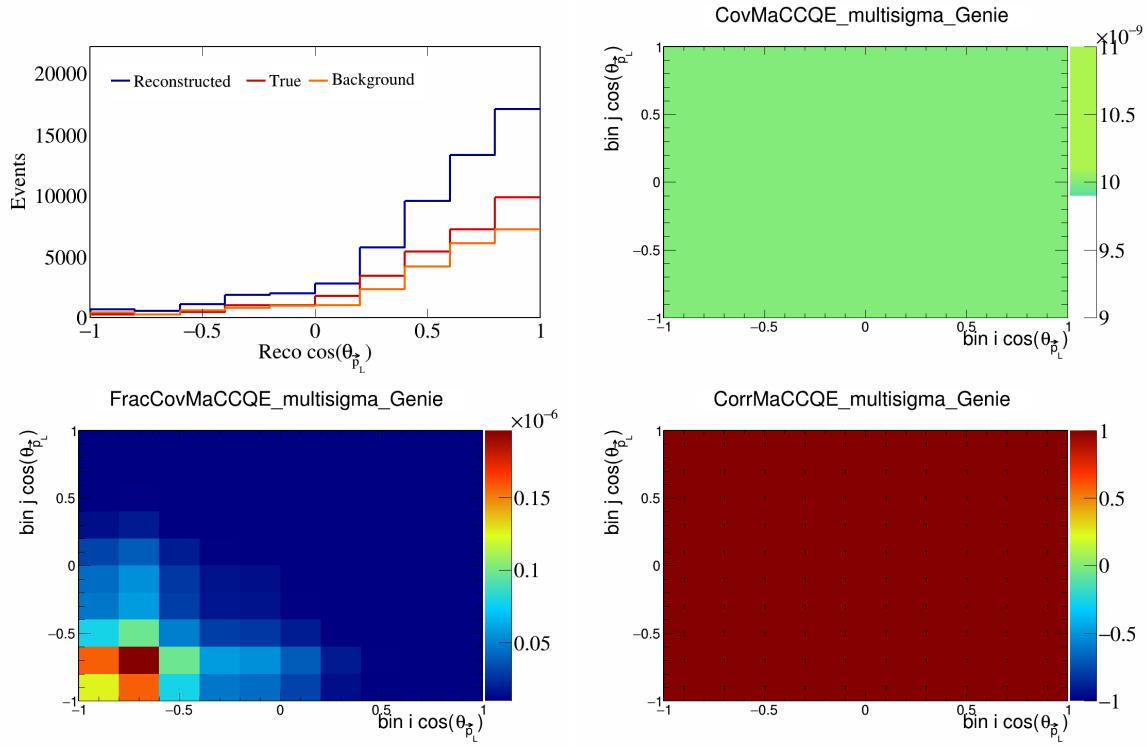


Figure 241: MaCCQE variations for $\cos(\theta_{\vec{p}_L})$.

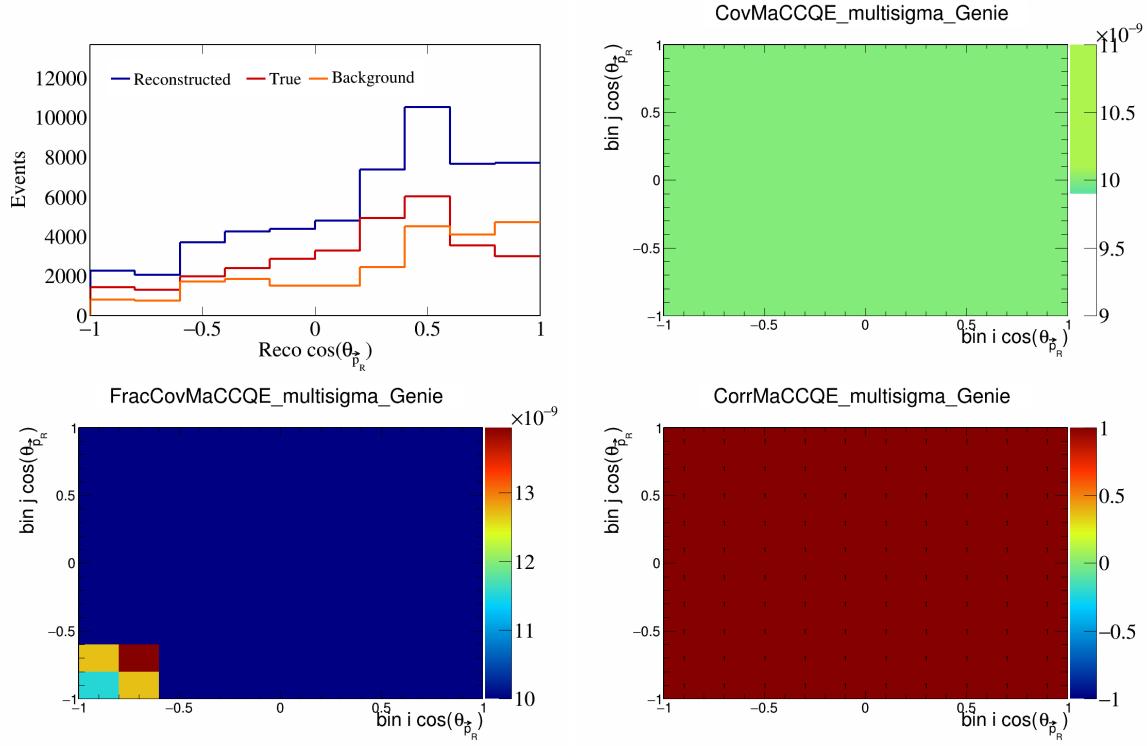


Figure 242: MaCCQE variations for $\cos(\theta_{\vec{p}_R})$.

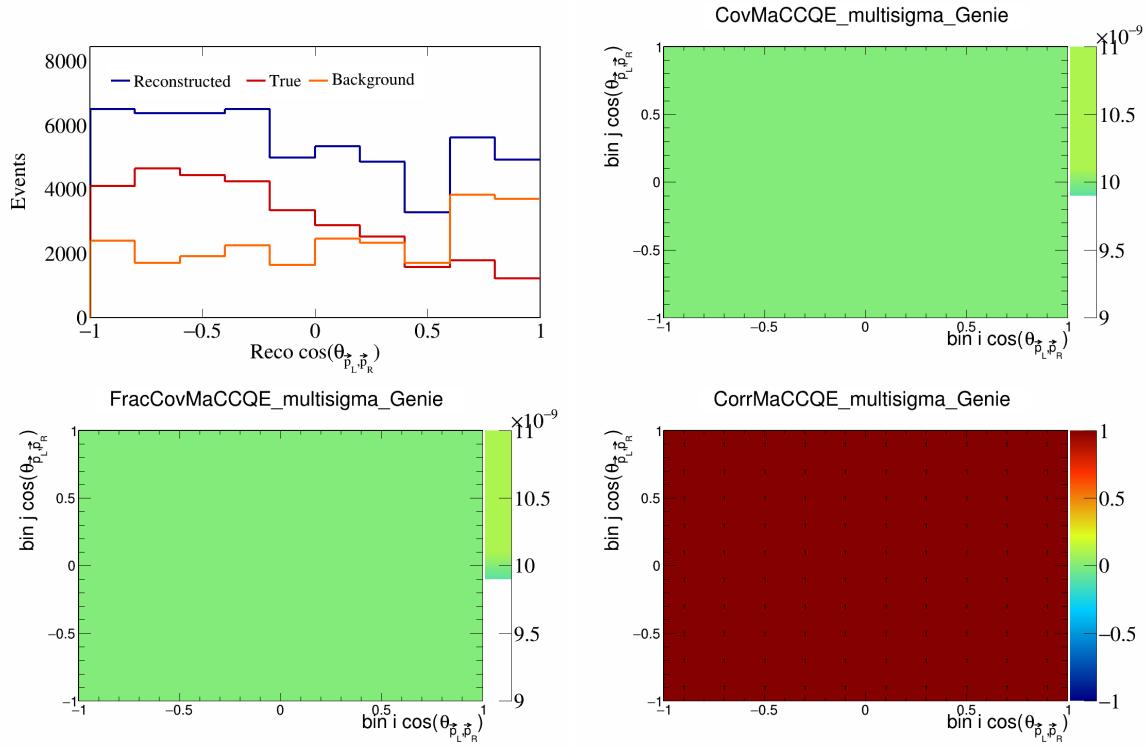


Figure 243: MaCCQE variations for $\cos(\theta_{\vec{p}_L, \vec{p}_R})$.

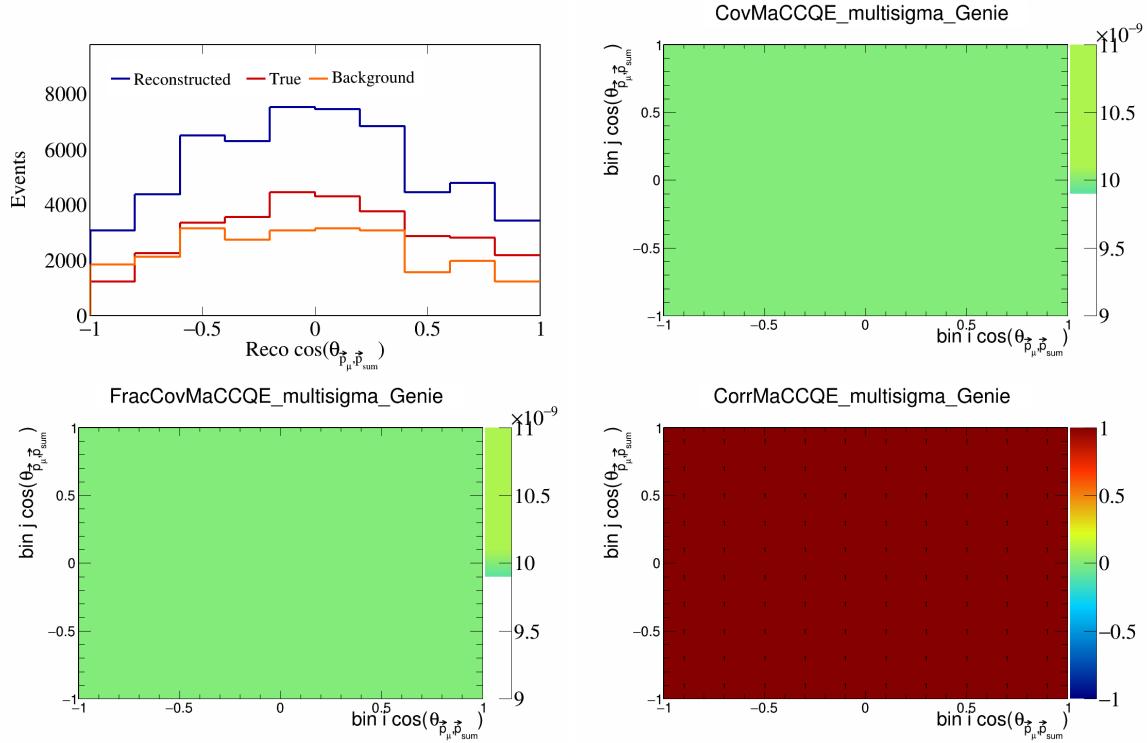


Figure 244: MaCCQE variations for $\cos(\theta_{\vec{p}_\mu, \vec{p}_{\text{sum}}})$.

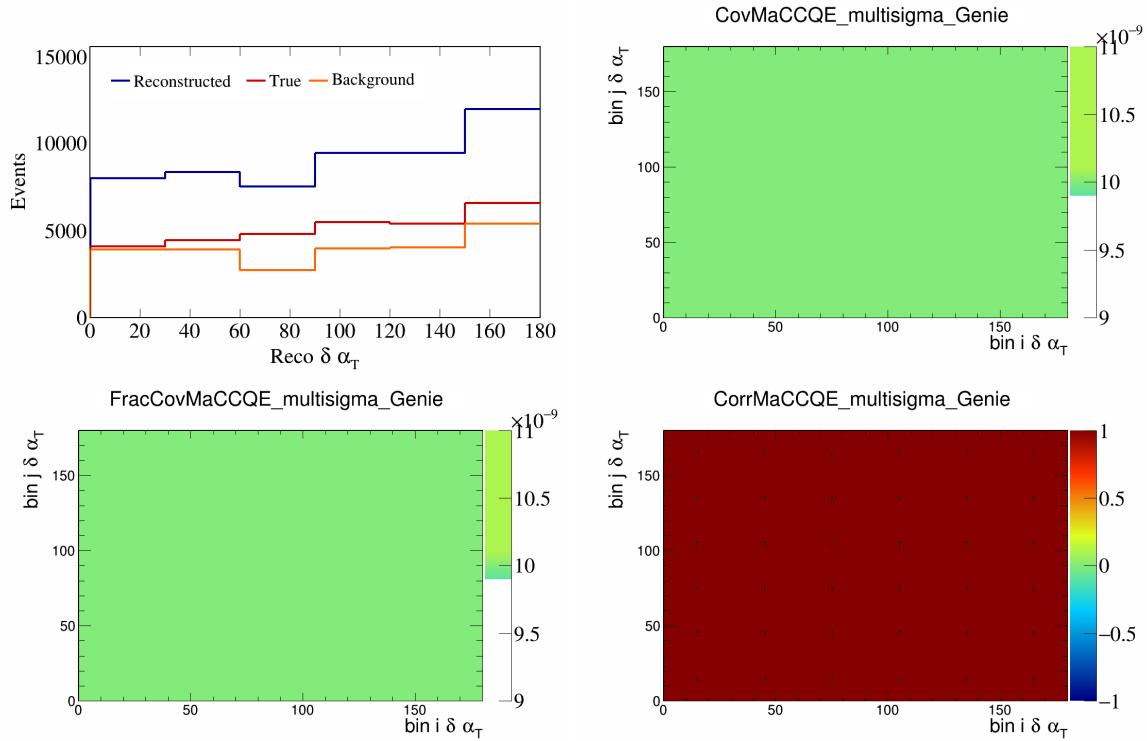


Figure 245: MaCCQE variations for $\delta\alpha_T$.

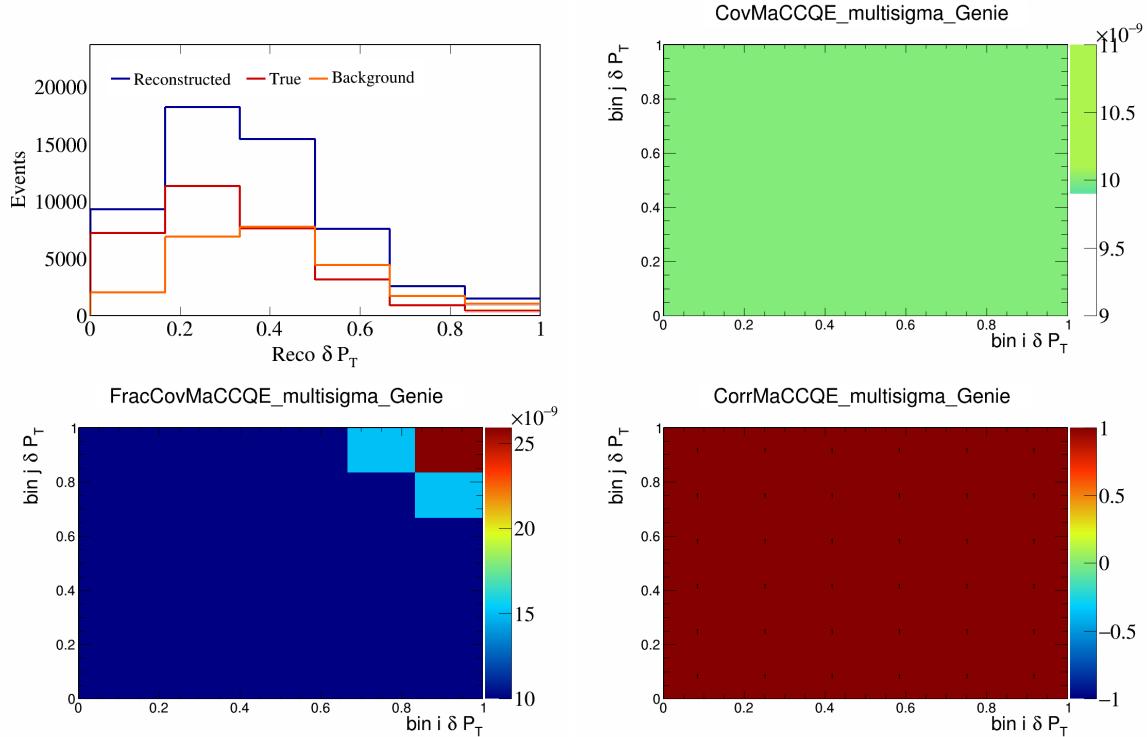


Figure 246: MaCCQE variations for δP_T .

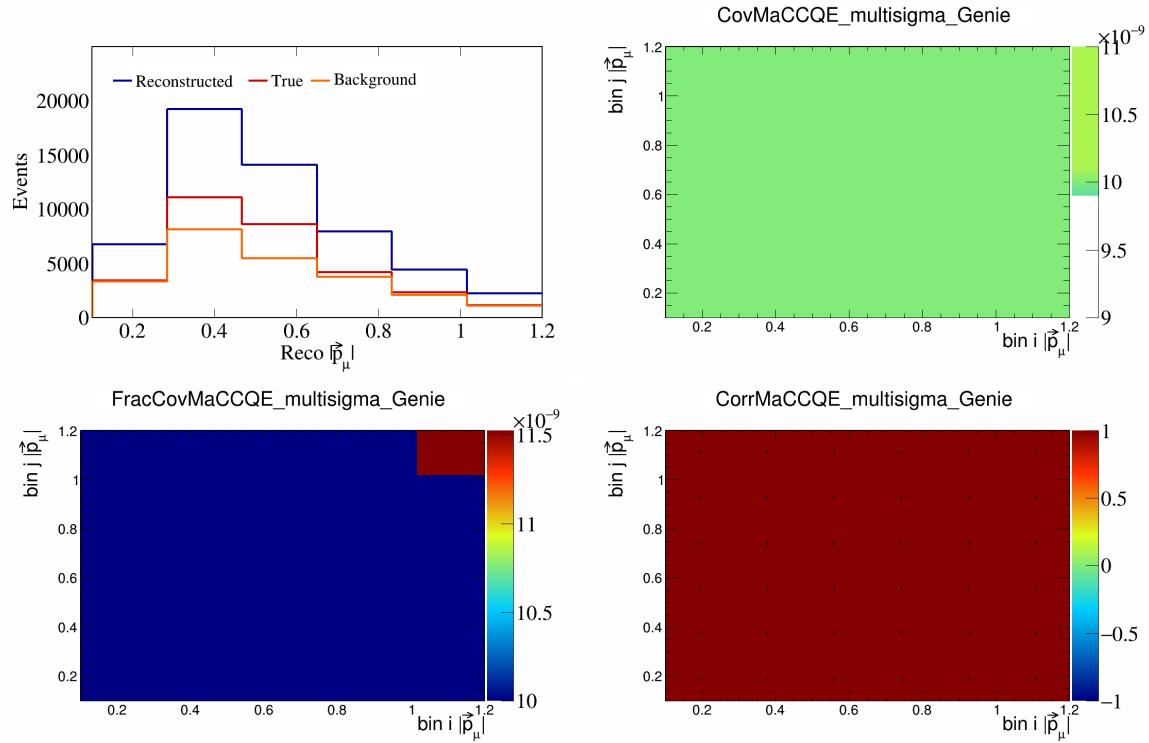


Figure 247: MaCCQE variations for $|\vec{p}_\mu|$.

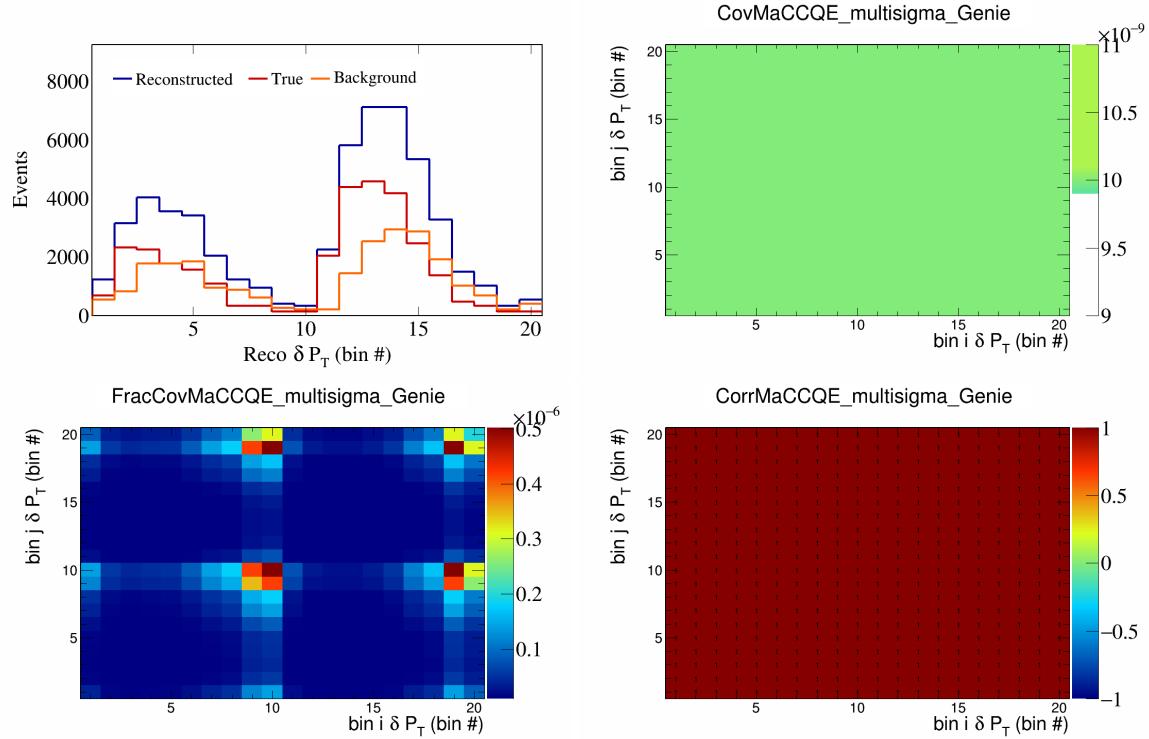


Figure 248: MaCCQE variations for δP_T in $\cos(\theta_{\vec{p}_\mu})$.

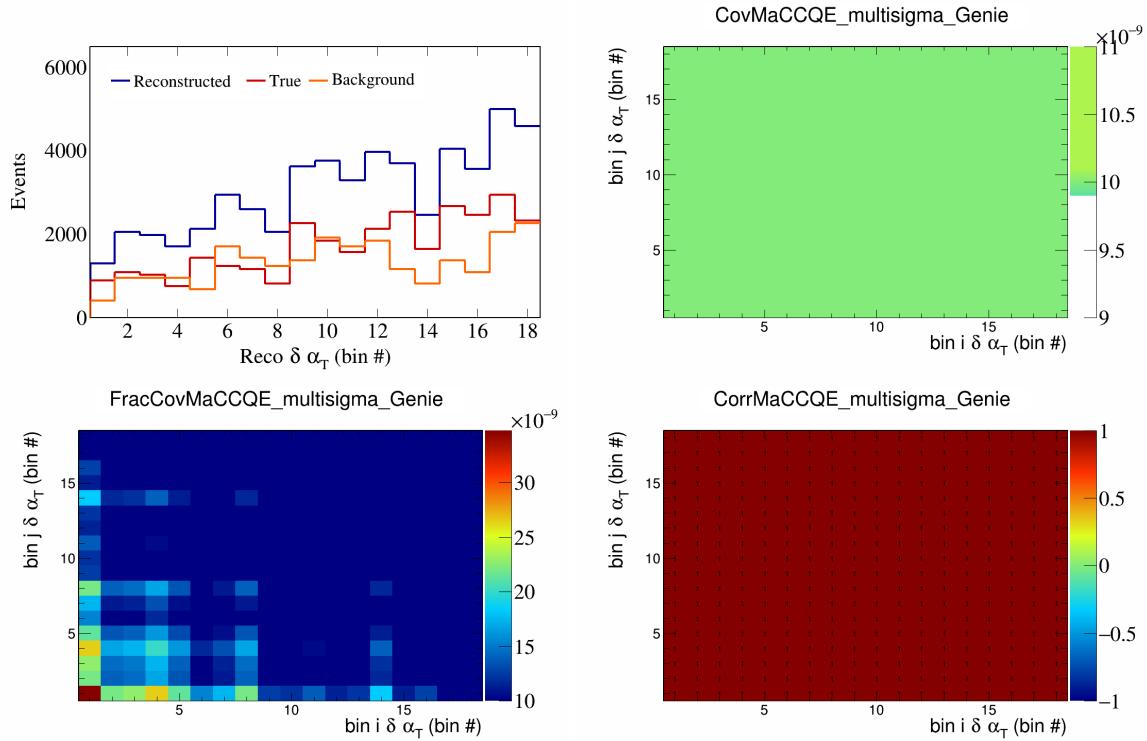


Figure 249: MaCCQE variations for $\delta\alpha_T$ in $\cos(\theta_{\vec{p}_\mu})$.

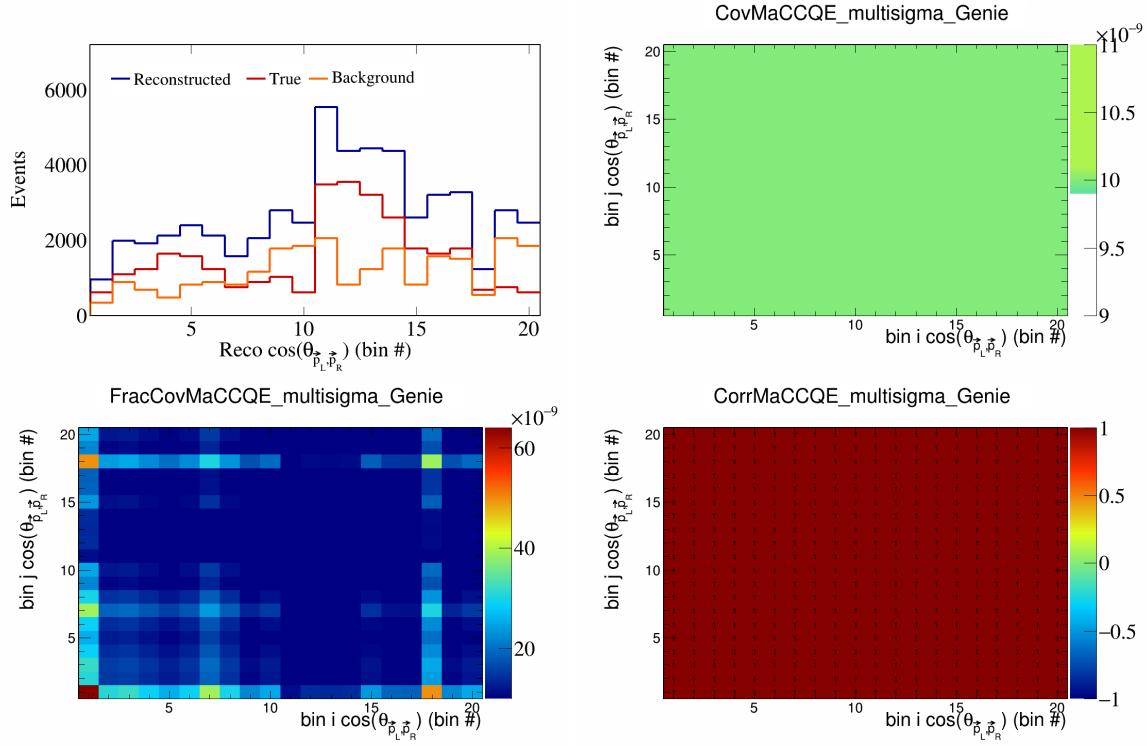


Figure 250: MaCCQE variations for $\cos(\theta_{\vec{p}_L, \vec{p}_R})$ in $\cos(\theta_{\vec{p}_\mu})$.

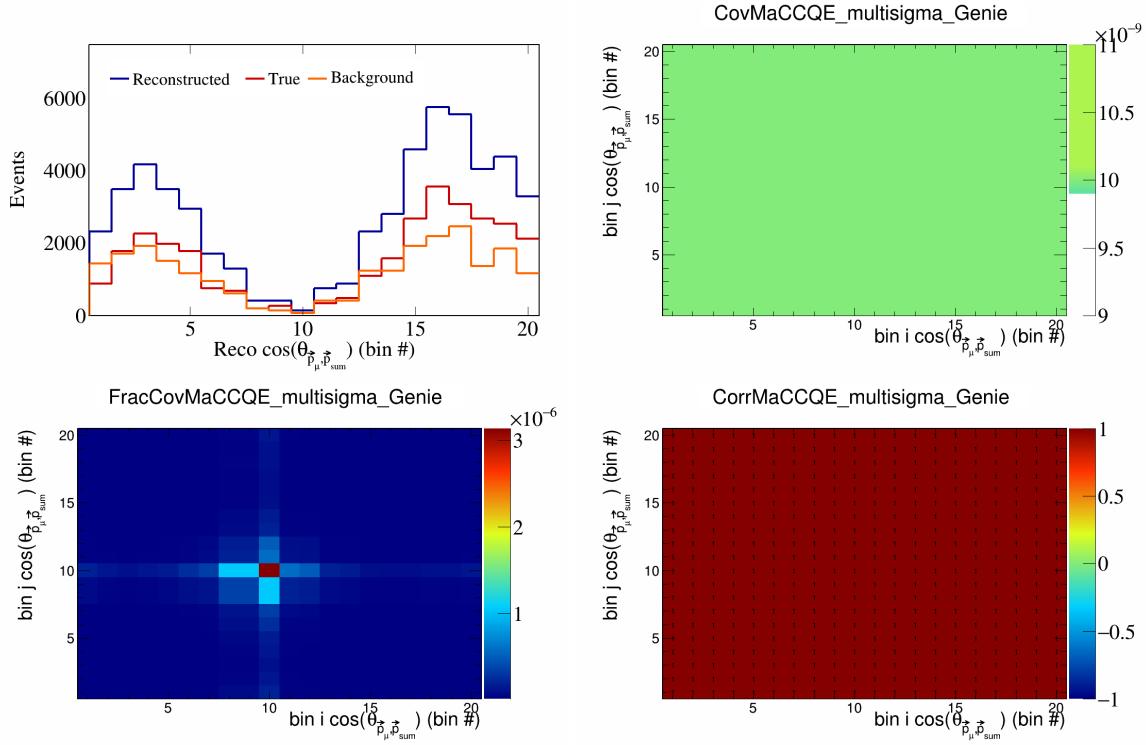


Figure 251: MaCCQE variations for $\cos(\theta_{\vec{p}_\mu, \vec{p}_{\text{sum}}})$ in $\cos(\theta_{\vec{p}_\mu})$.

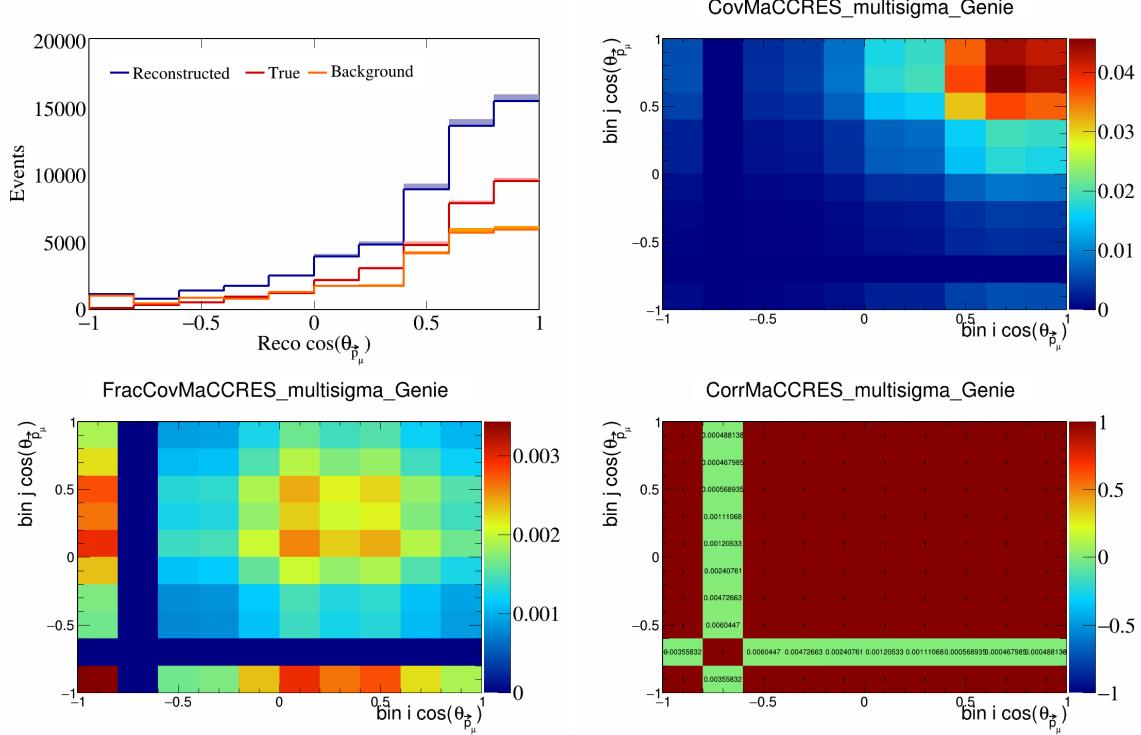


Figure 252: MaCCRES variations for $\cos(\theta_{\vec{p}_\mu, \vec{p}_{\text{sum}}})$ in $\cos(\theta_{\vec{p}_\mu})$.

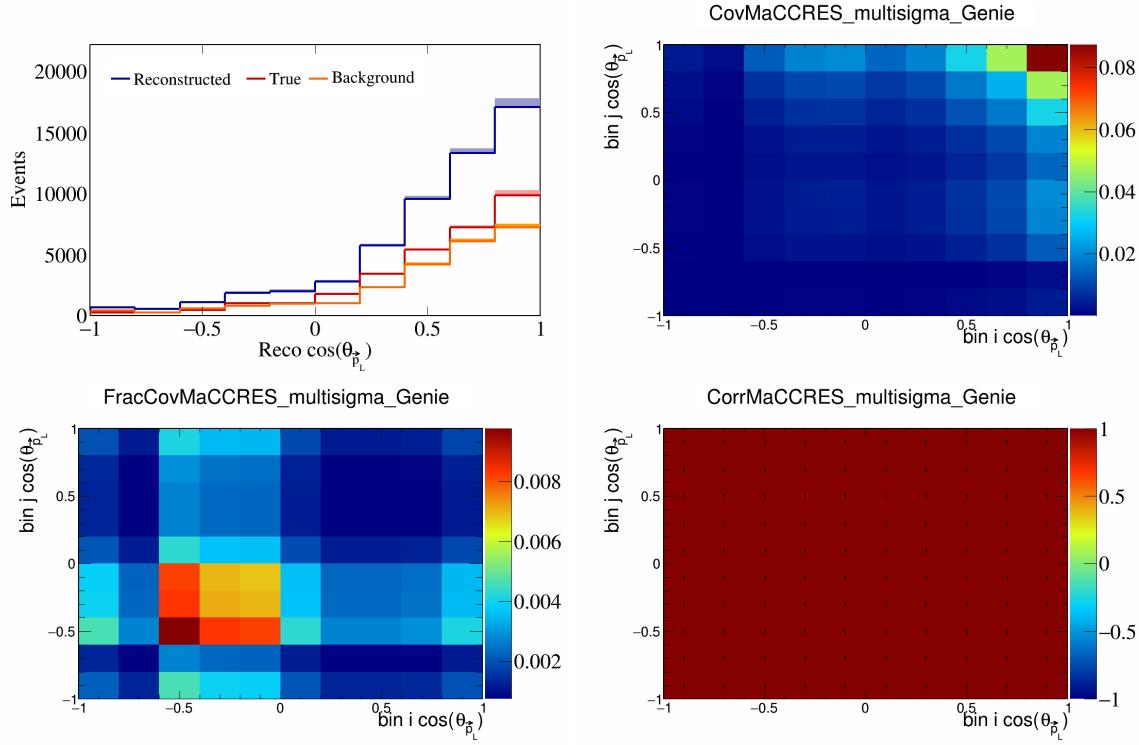


Figure 253: MaCCRES variations for $\cos(\theta_{\vec{p}_L})$.

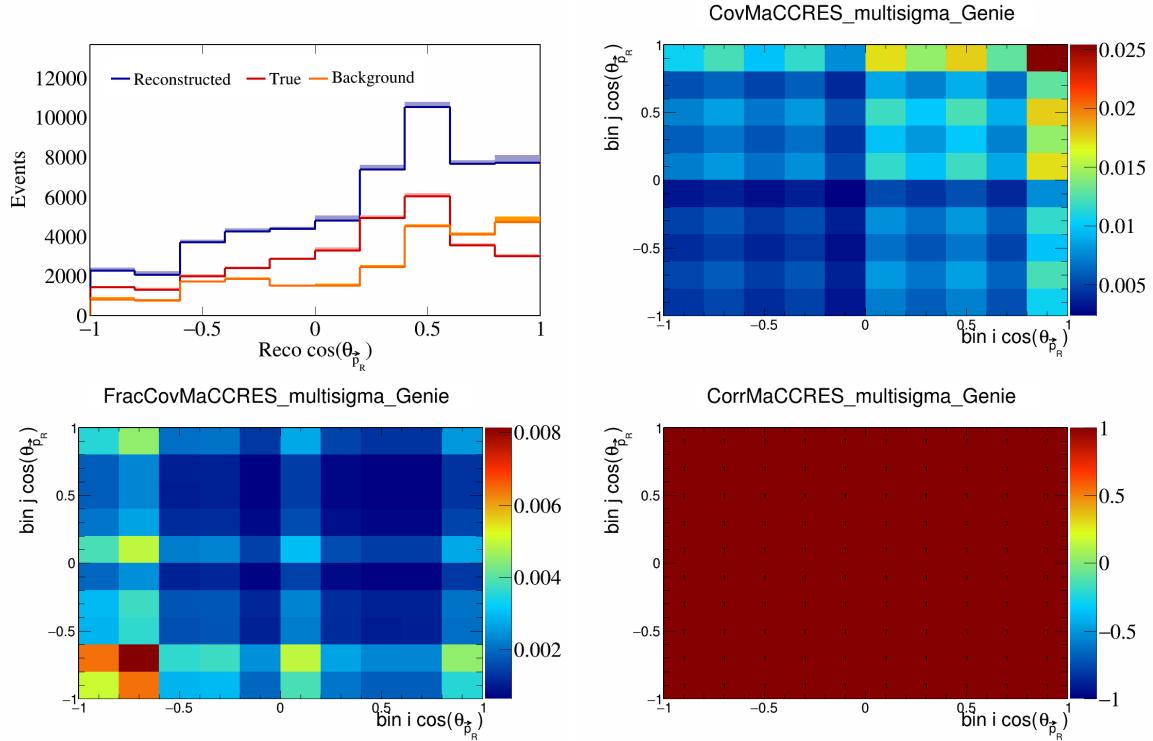


Figure 254: MaCCRES variations for $\cos(\theta_{\vec{p}_R})$.

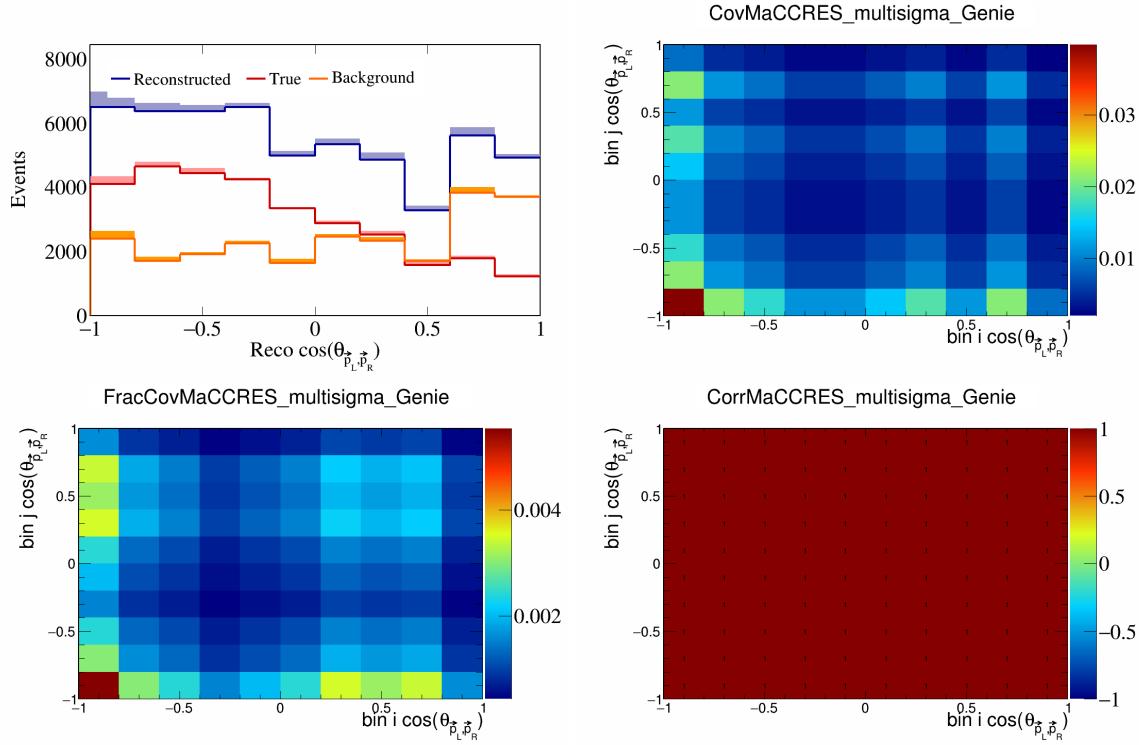


Figure 255: MaCCRES variations for $\cos(\theta_{\vec{p}_L, \vec{p}_R})$.

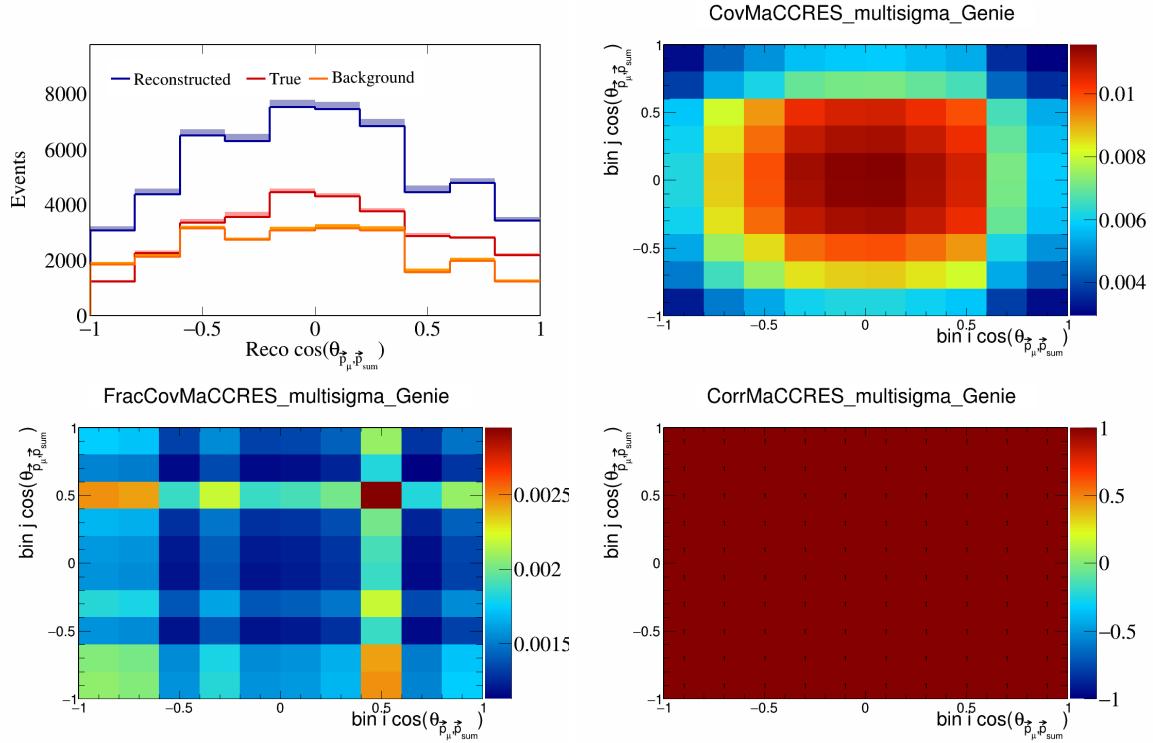


Figure 256: MaCCRES variations for $\cos(\theta_{\vec{p}_\mu, \vec{p}_{\text{sum}}})$.

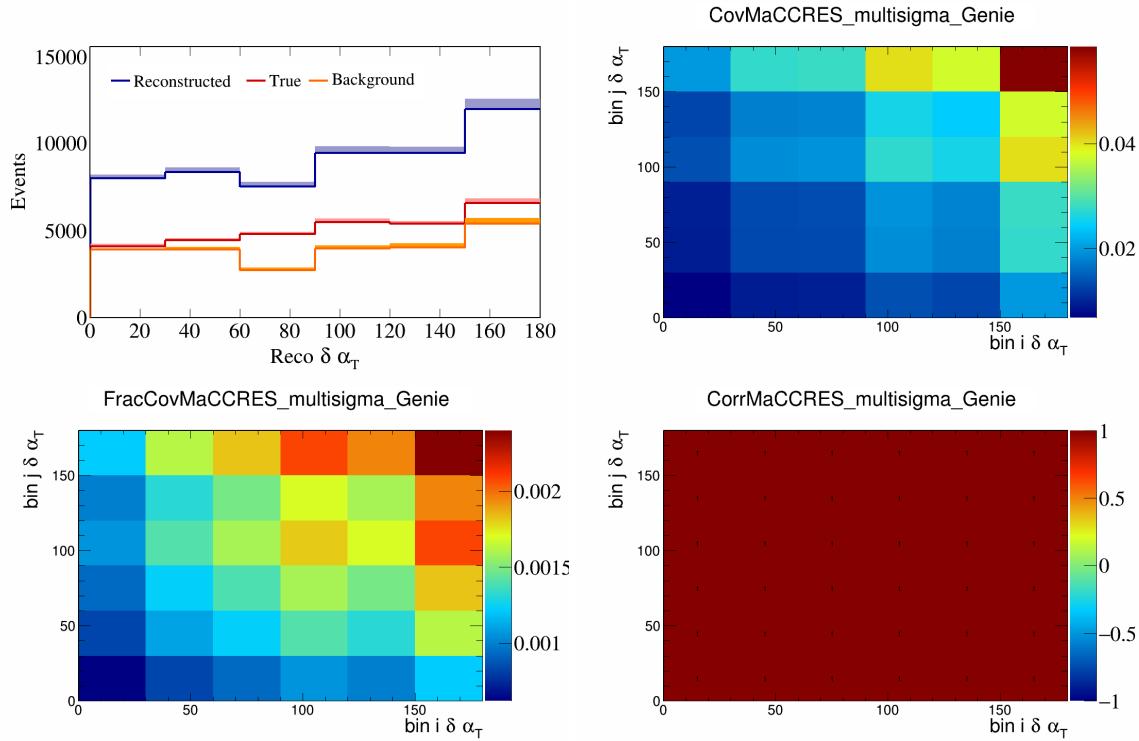


Figure 257: MaCCRES variations for $\delta\alpha_T$.

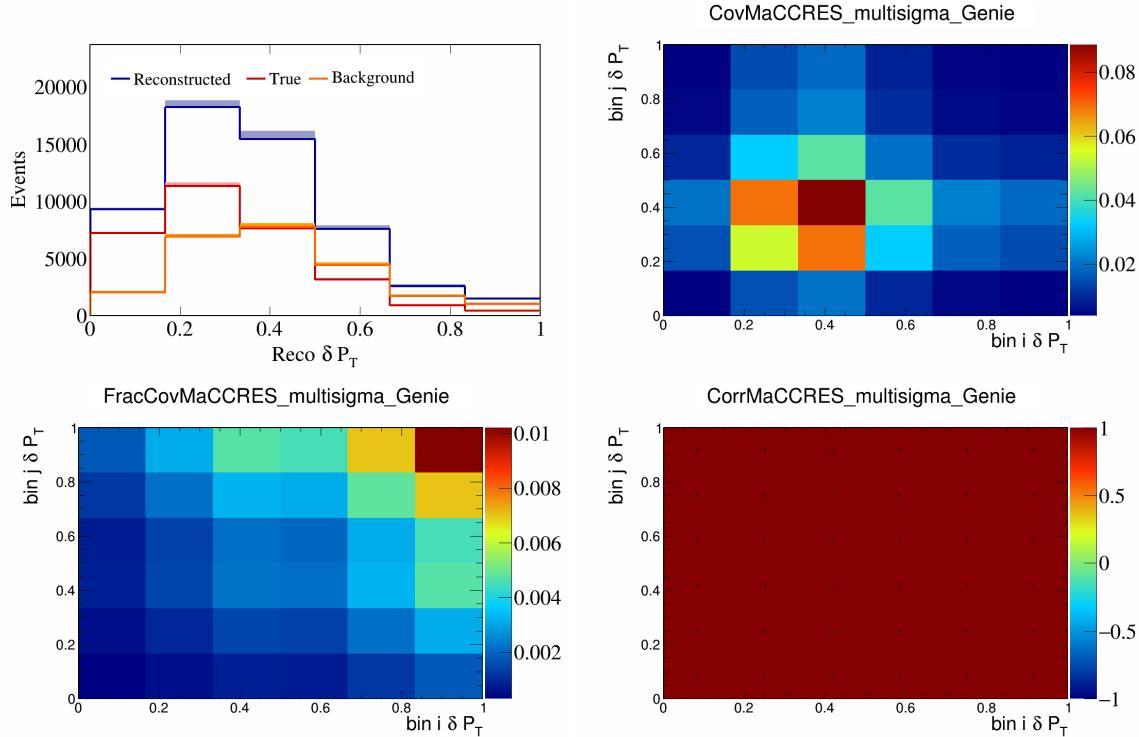


Figure 258: MaCCRES variations for δP_T .

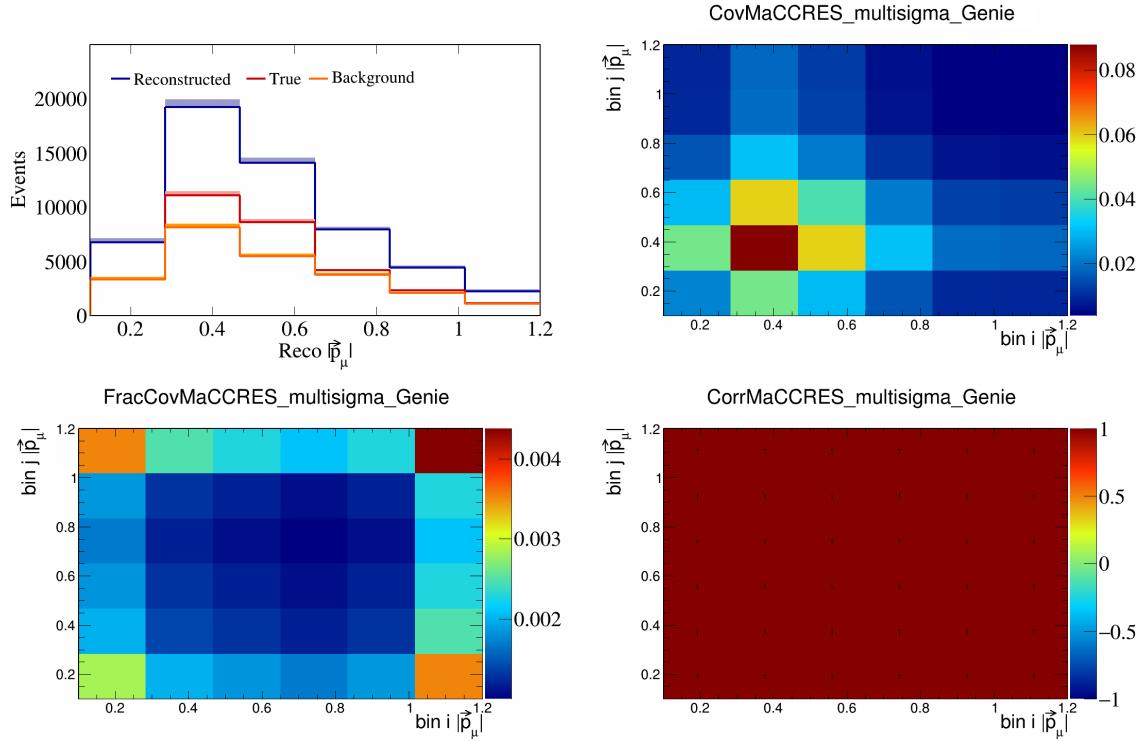


Figure 259: MaCCRES variations for $|\vec{p}_\mu|$.

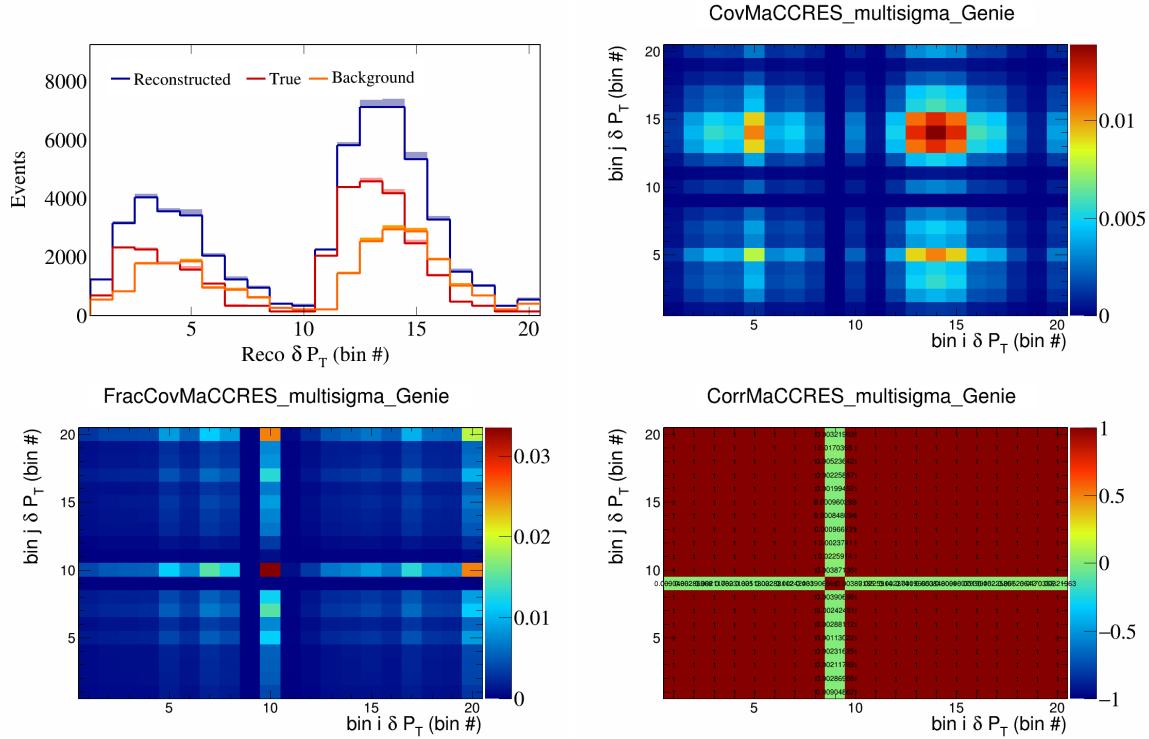


Figure 260: MaCCRES variations for δP_T in $\cos(\theta_{\vec{p}_\mu})$.

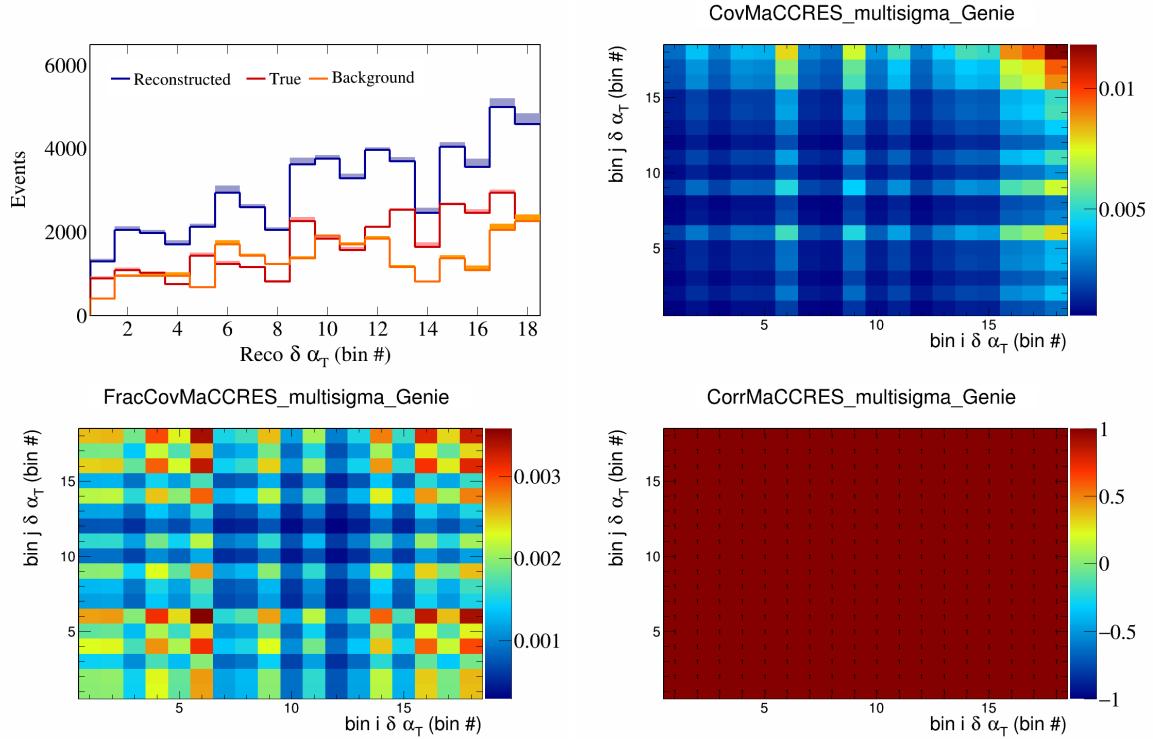


Figure 261: MaCCRES variations for $\delta \alpha_T$ in $\cos(\theta_{\vec{p}_\mu})$.

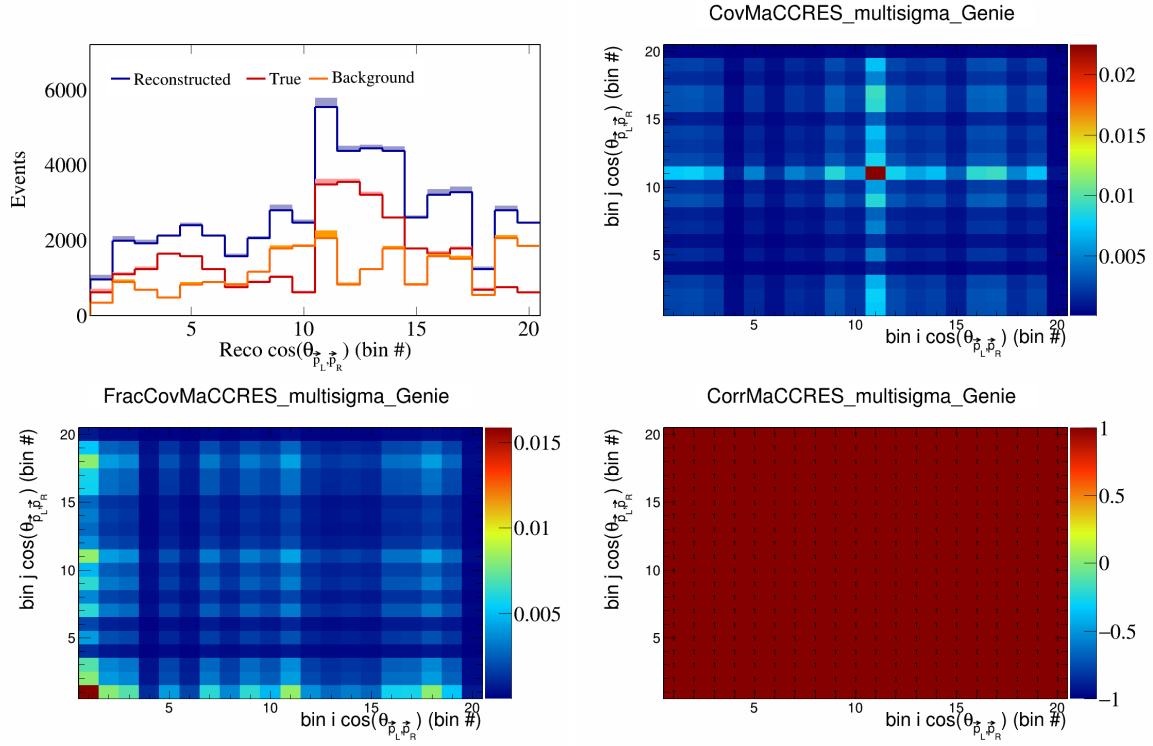


Figure 262: MaCCRES variations for $\cos(\theta_{\vec{p}_L, \vec{p}_R})$ in $\cos(\theta_{\vec{p}_\mu})$.

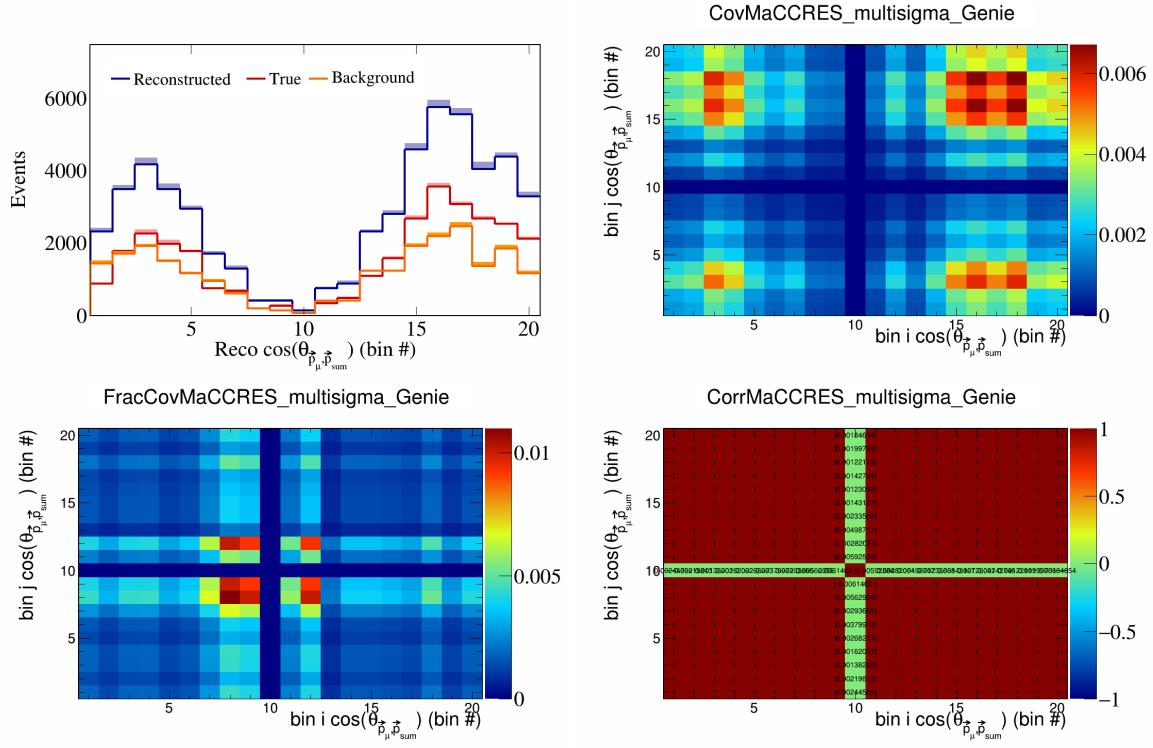


Figure 263: MaCCRES variations for $\cos(\theta_{\vec{p}_\mu, \vec{p}_{\text{sum}}})$ in $\cos(\theta_{\vec{p}_\mu})$.

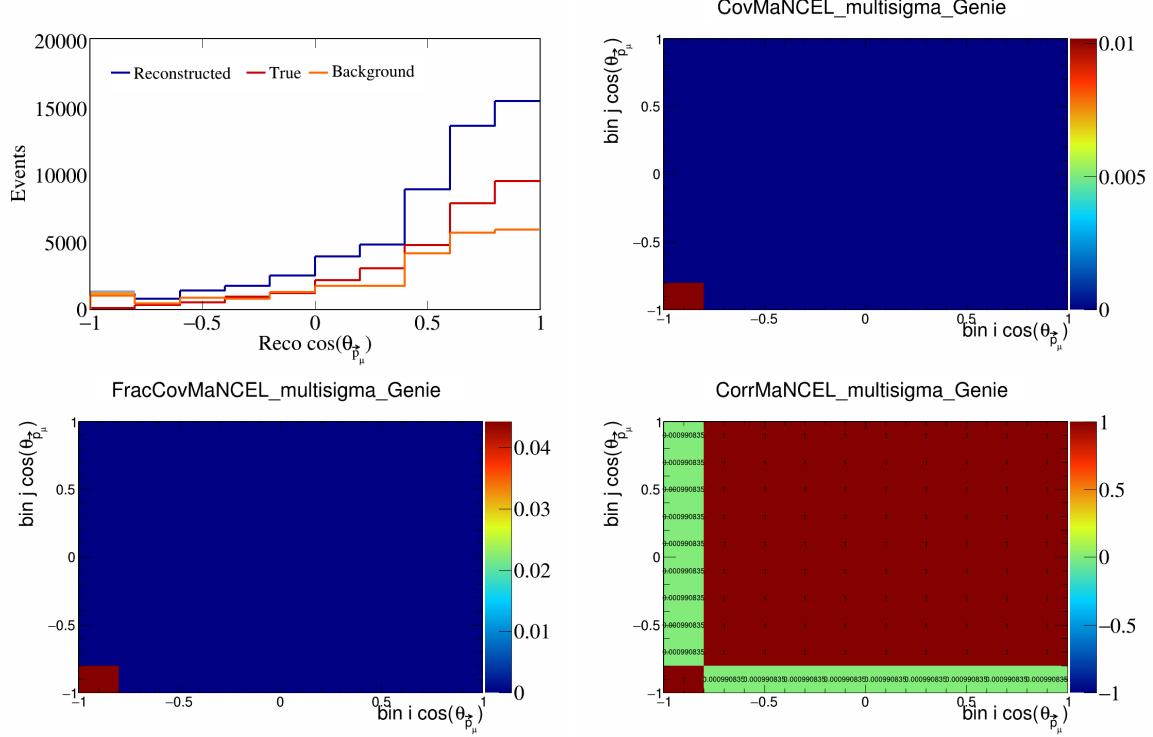


Figure 264: MaNCEL variations for $\cos(\theta_{\vec{p}_\mu})$.

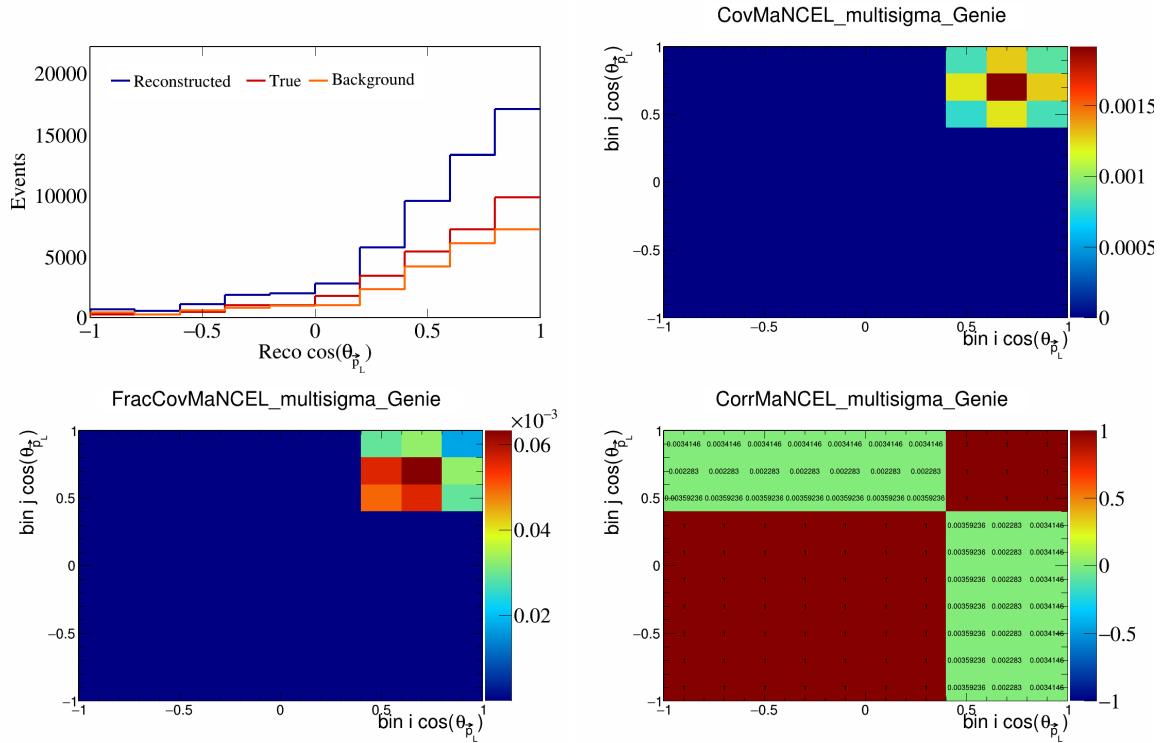


Figure 265: MaNCEL variations for $\cos(\theta_{\vec{p}_L})$.

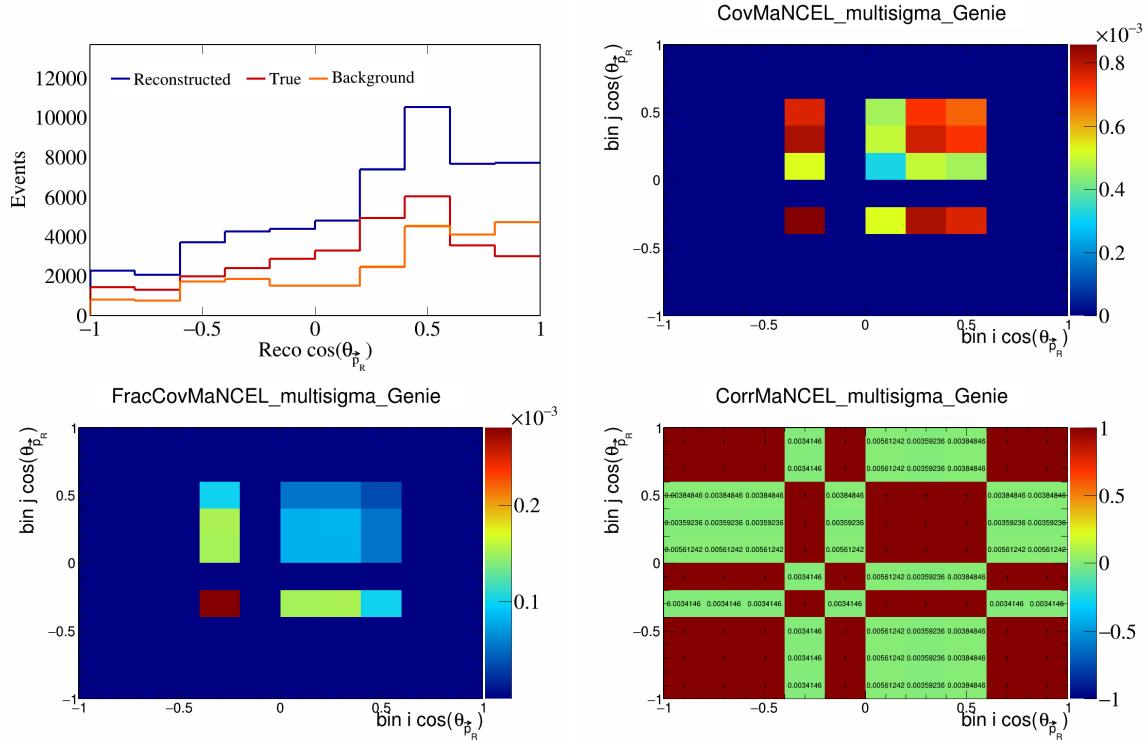


Figure 266: MaNCEL variations for $\cos(\theta_{\vec{p}_R})$.

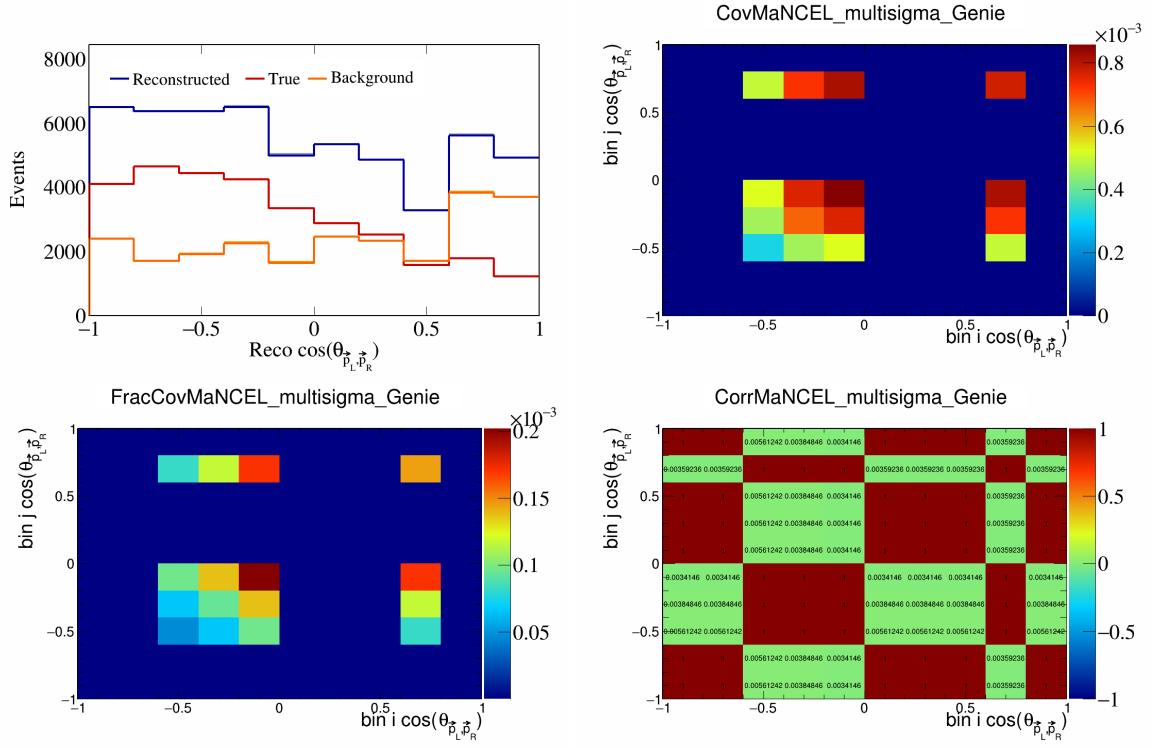


Figure 267: MaNCEL variations for $\cos(\theta_{\vec{p}_L, \vec{p}_R})$.

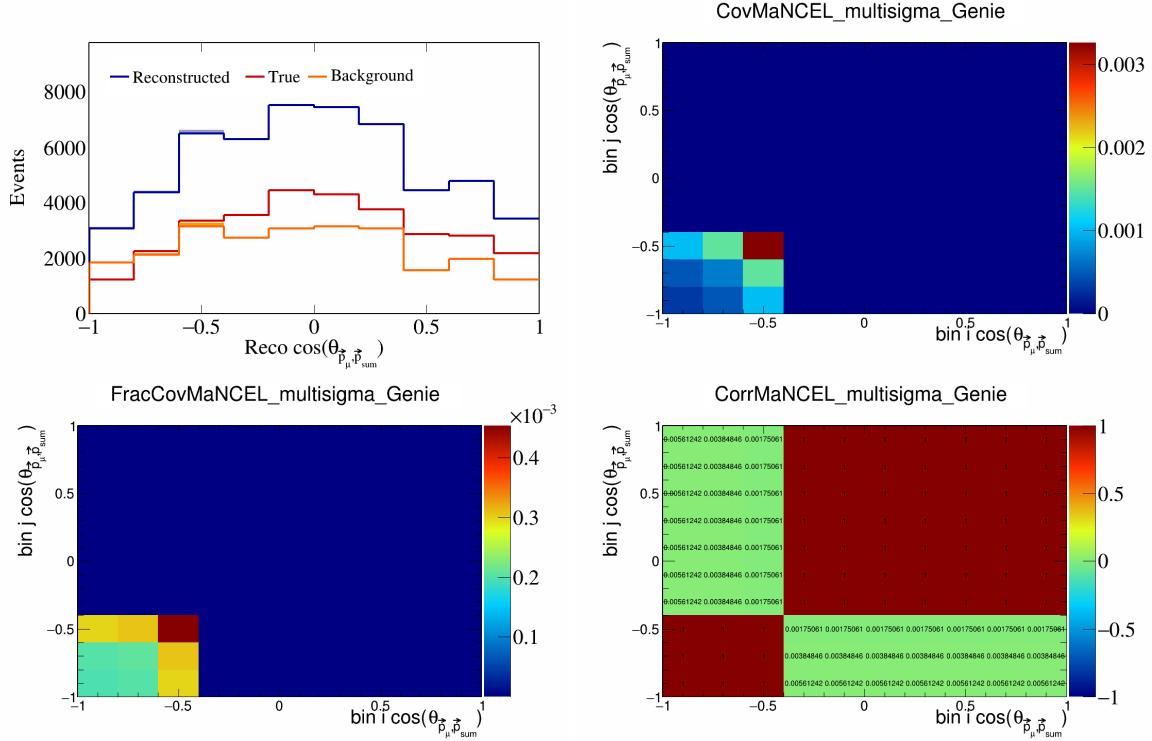


Figure 268: MaNCEL variations for $\cos(\theta_{\vec{p}_\mu, \vec{p}_{\text{sum}}})$.

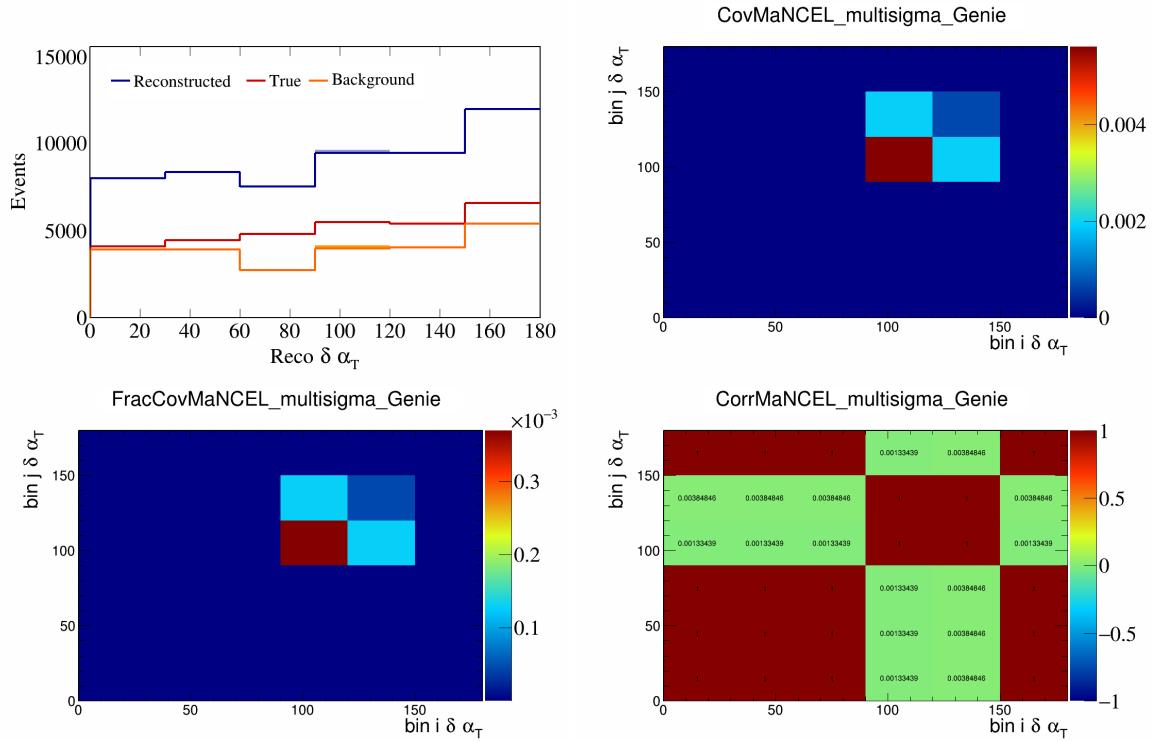


Figure 269: MaNCEL variations for $\delta\alpha_T$.

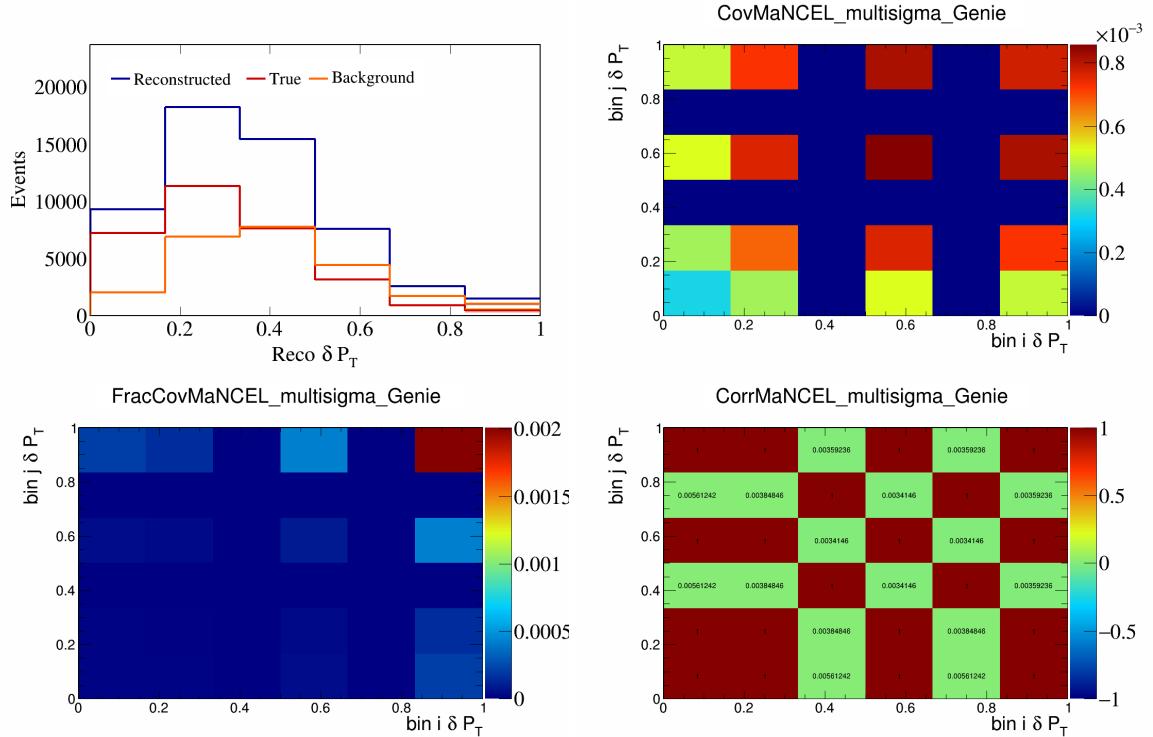


Figure 270: MaNCEL variations for δP_T .

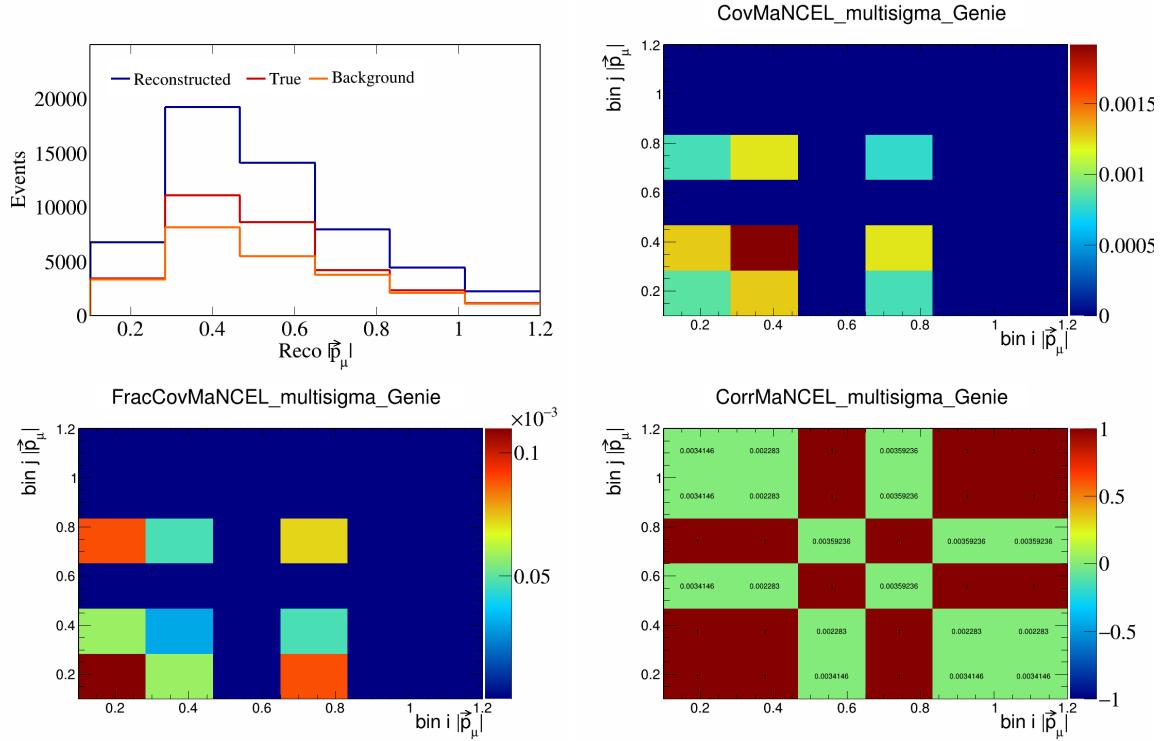


Figure 271: MaNCEL variations for $|\vec{p}_\mu|$.

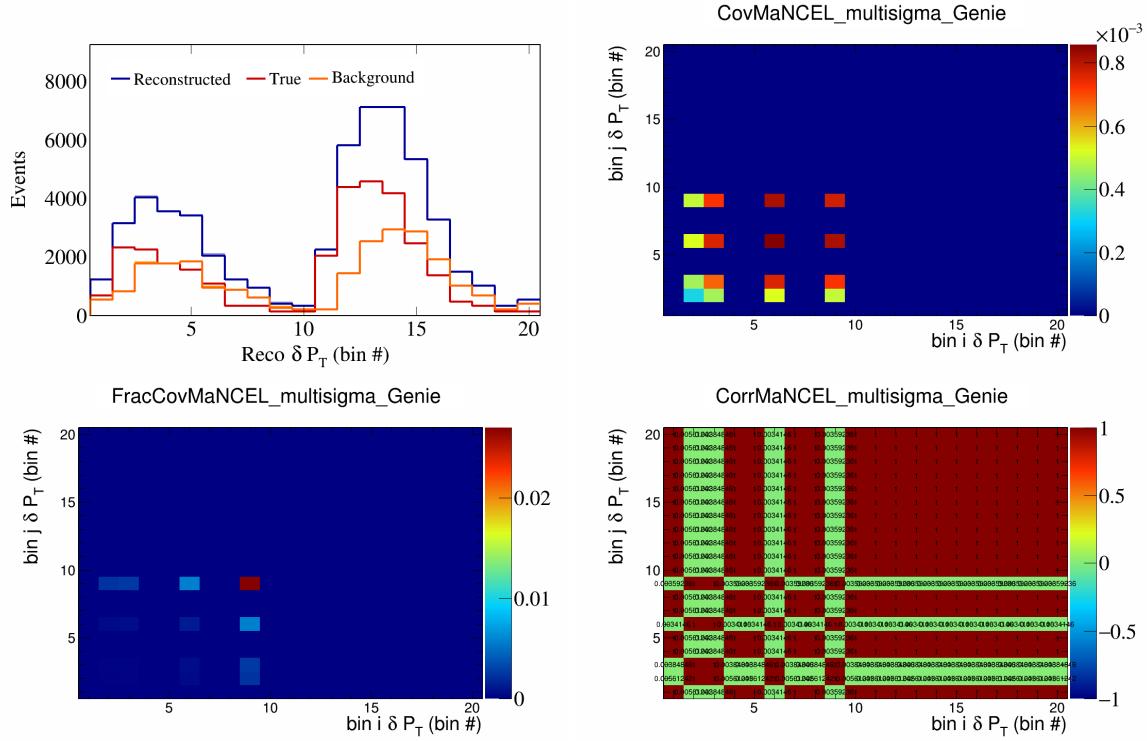


Figure 272: MaNCEL variations for δP_T in $\cos(\theta_{\vec{p}_\mu})$.

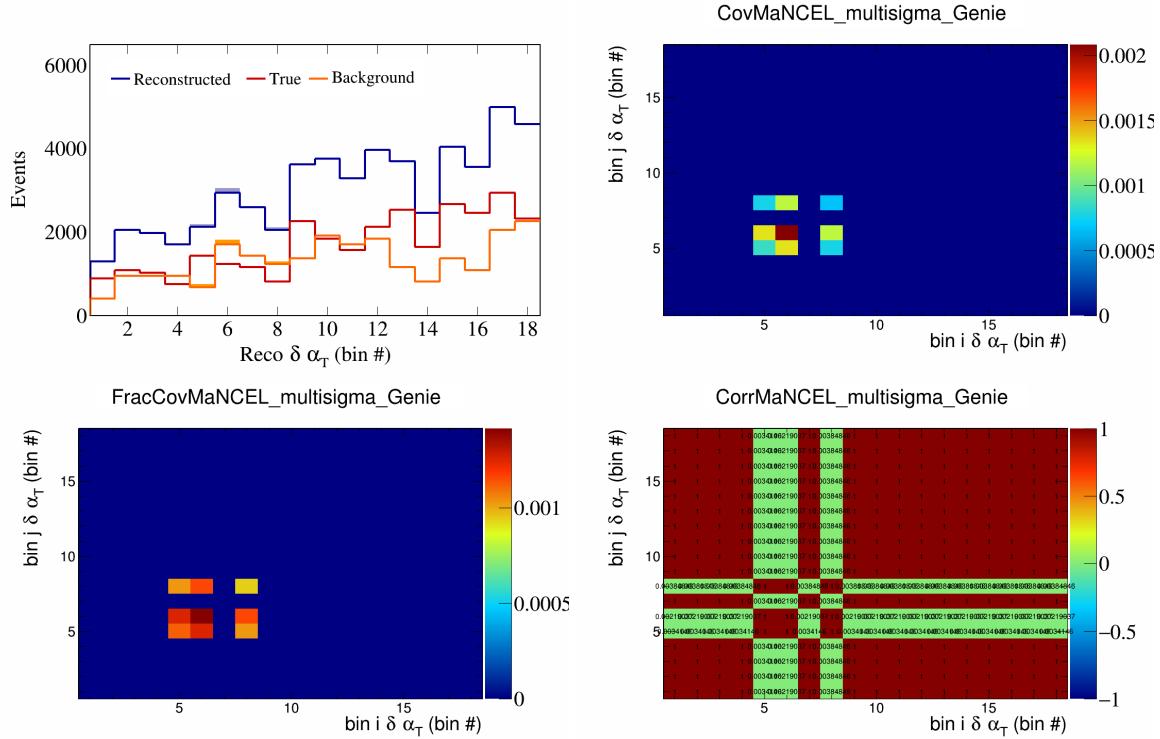


Figure 273: MaNCEL variations for $\delta \alpha_T$ in $\cos(\theta_{\vec{p}_\mu})$.

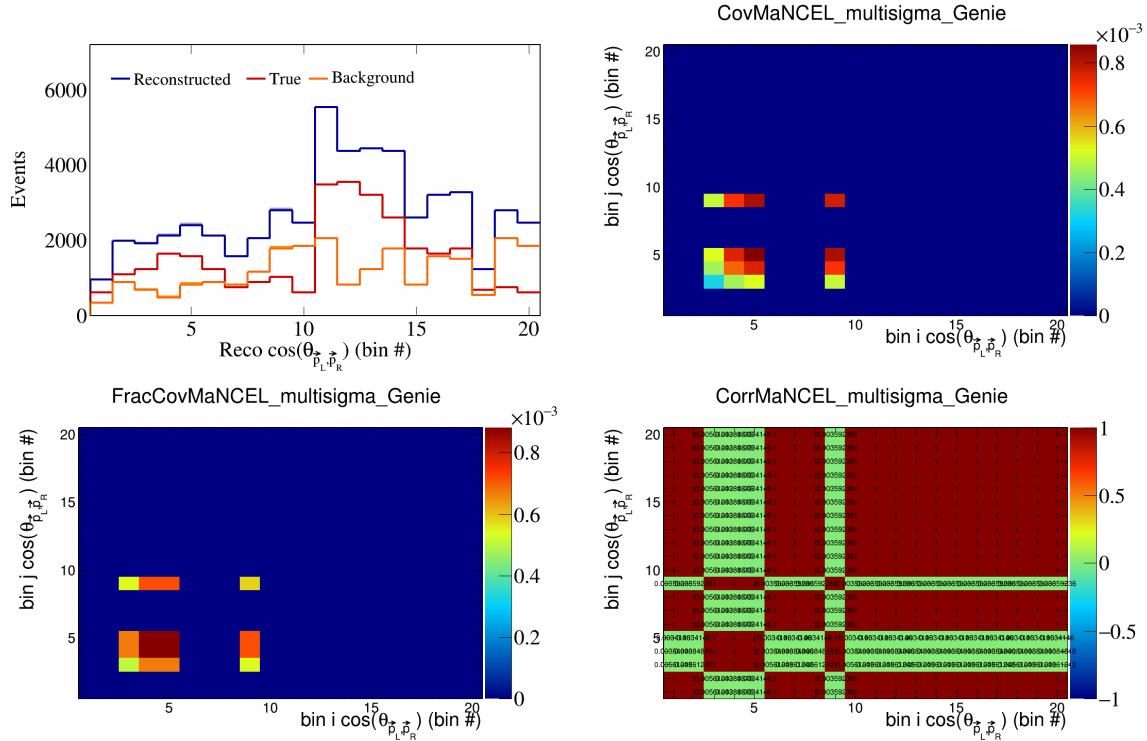


Figure 274: MaNCEL variations for $\cos(\theta_{\vec{p}_L, \vec{p}_R})$ in $\cos(\theta_{\vec{p}_\mu})$.

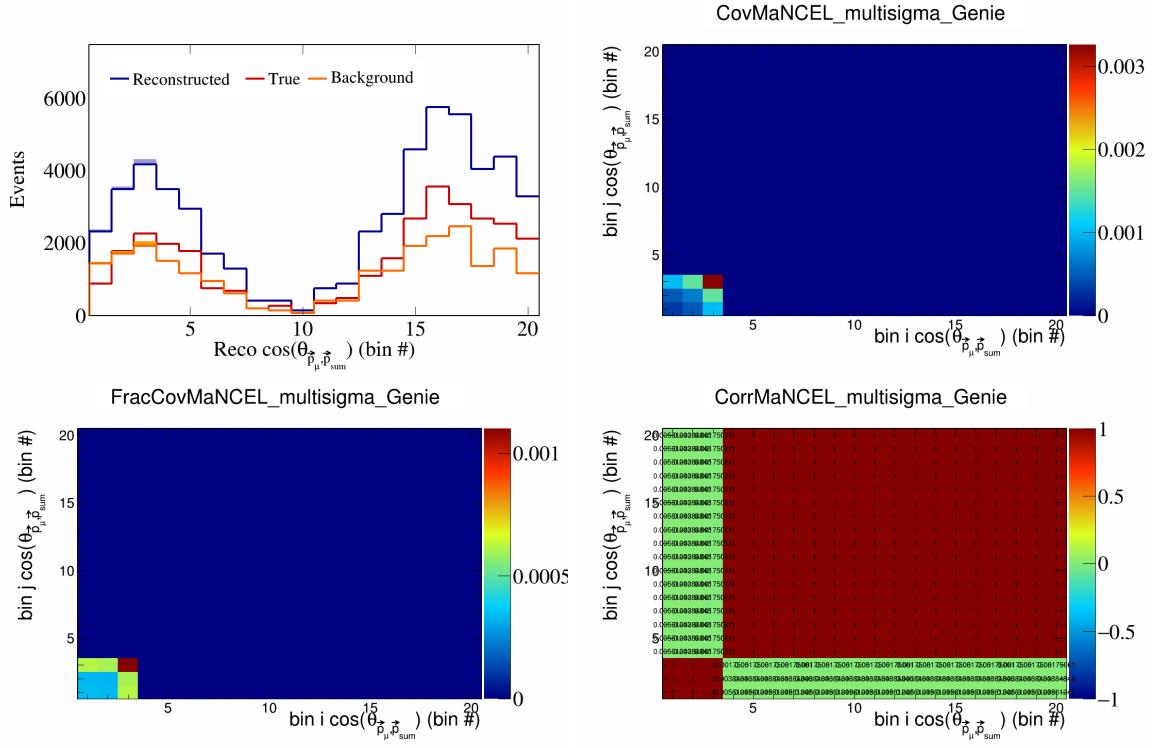


Figure 275: MaNCEL variations for $\cos(\theta_{\vec{p}_\mu, \vec{p}_{\text{sum}}})$ in $\cos(\theta_{\vec{p}_\mu})$.

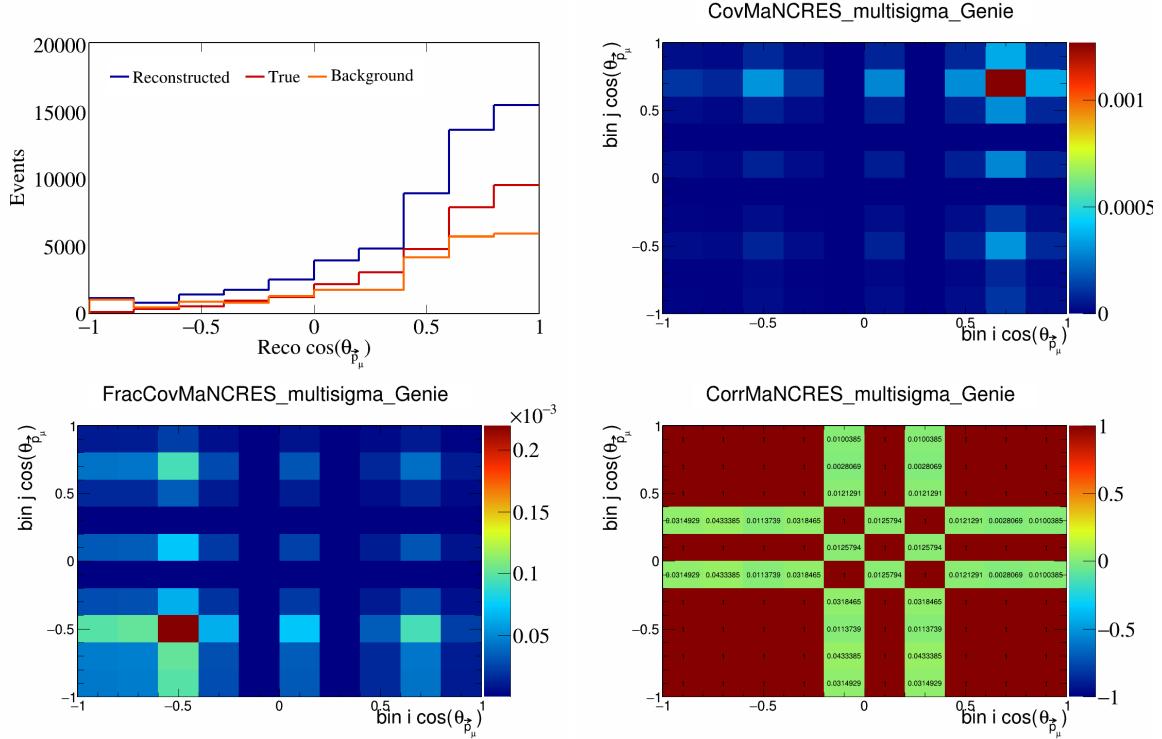


Figure 276: MaNCRES variations for $\cos(\theta_{\vec{p}_\mu})$.

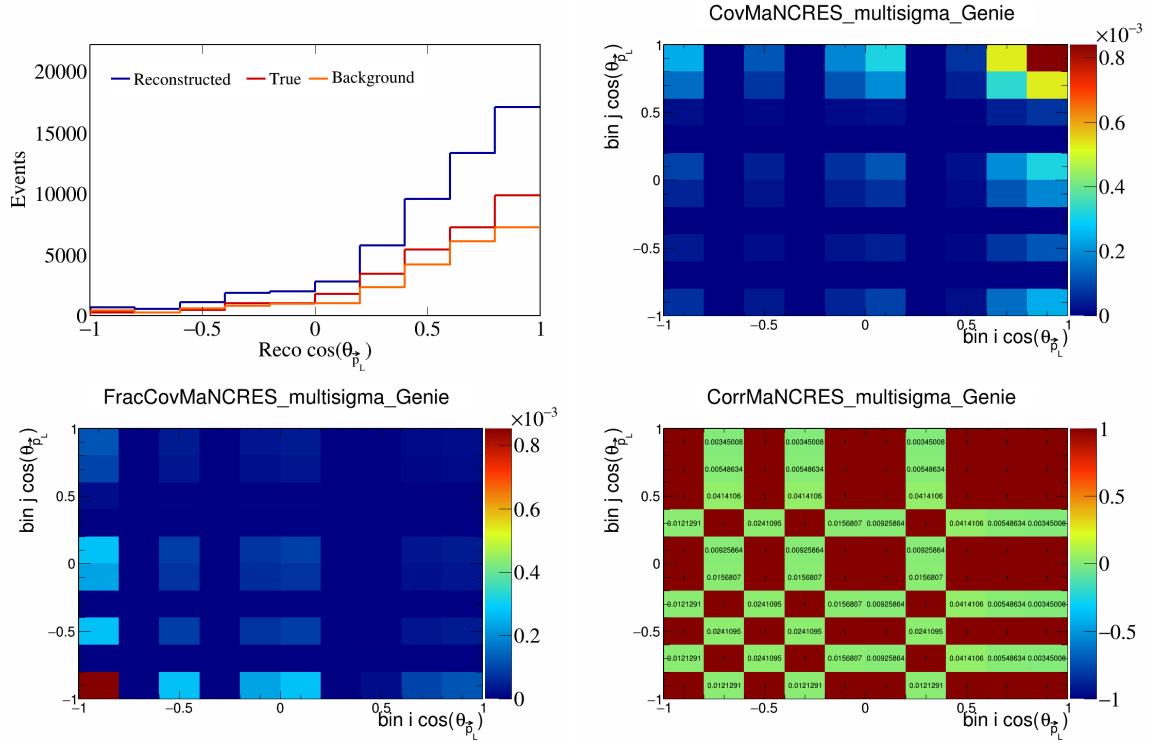


Figure 277: MaNCRES variations for $\cos(\theta_{\vec{p}_L})$.

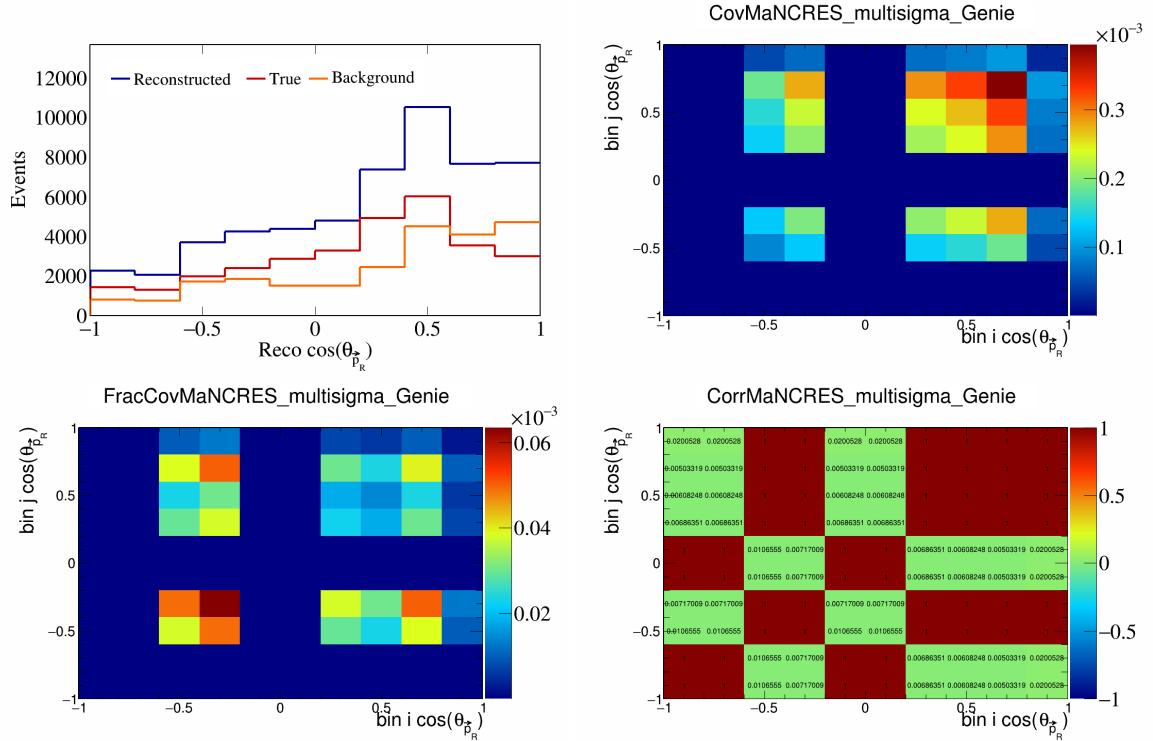


Figure 278: MaNCRES variations for $\cos(\theta_{\vec{p}_R})$.

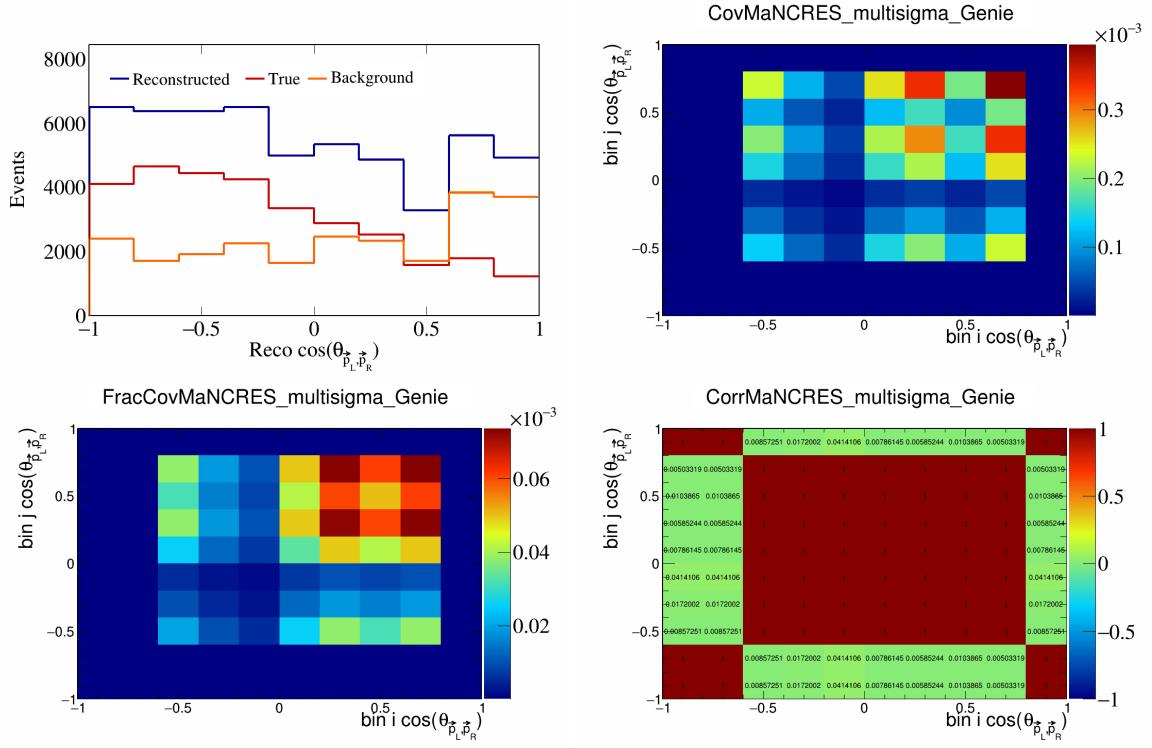


Figure 279: MaNCRES variations for $\cos(\theta_{\vec{p}_L, \vec{p}_R})$.

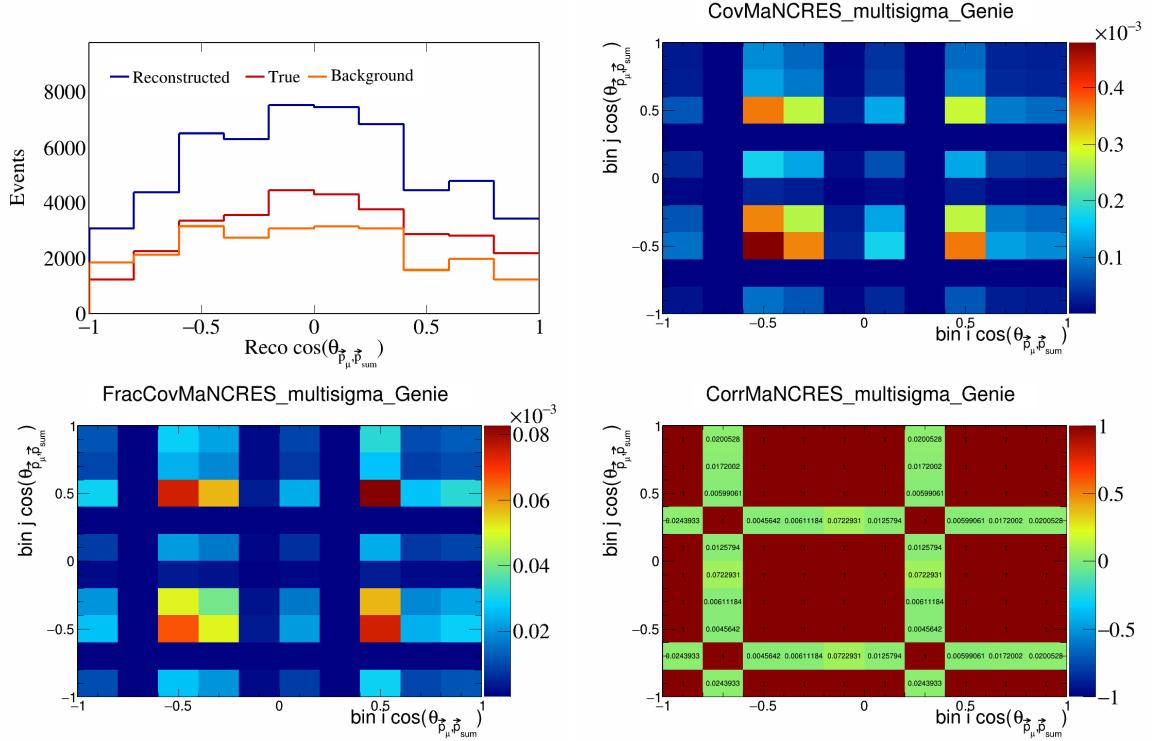


Figure 280: MaNCRES variations for $\cos(\theta_{\vec{p}_\mu, \vec{p}_{\text{sum}}})$.

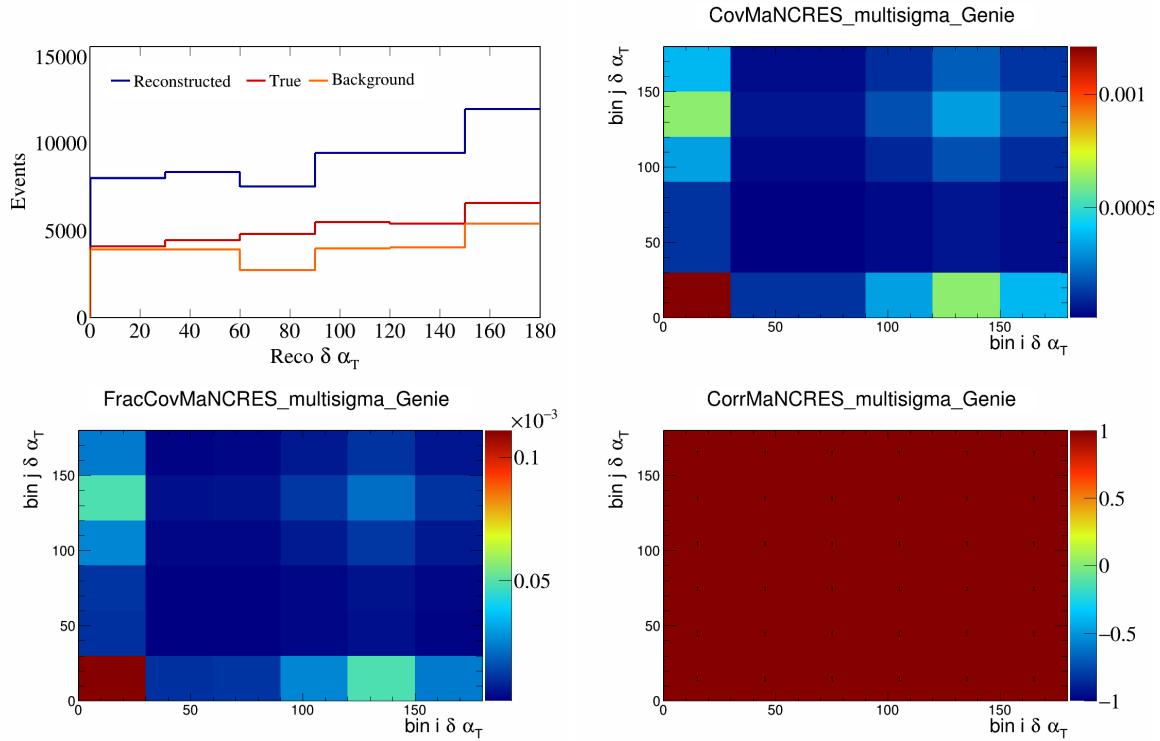


Figure 281: MaNCRES variations for $\delta\alpha_T$.

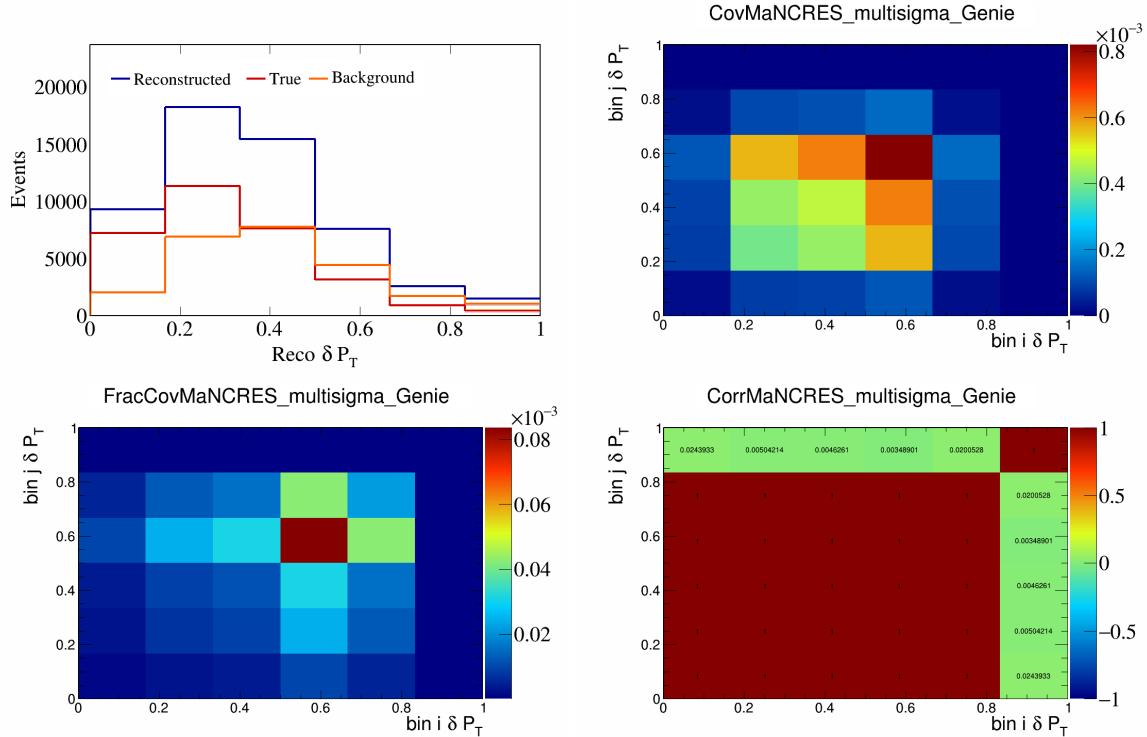


Figure 282: MaNCRES variations for δP_T .

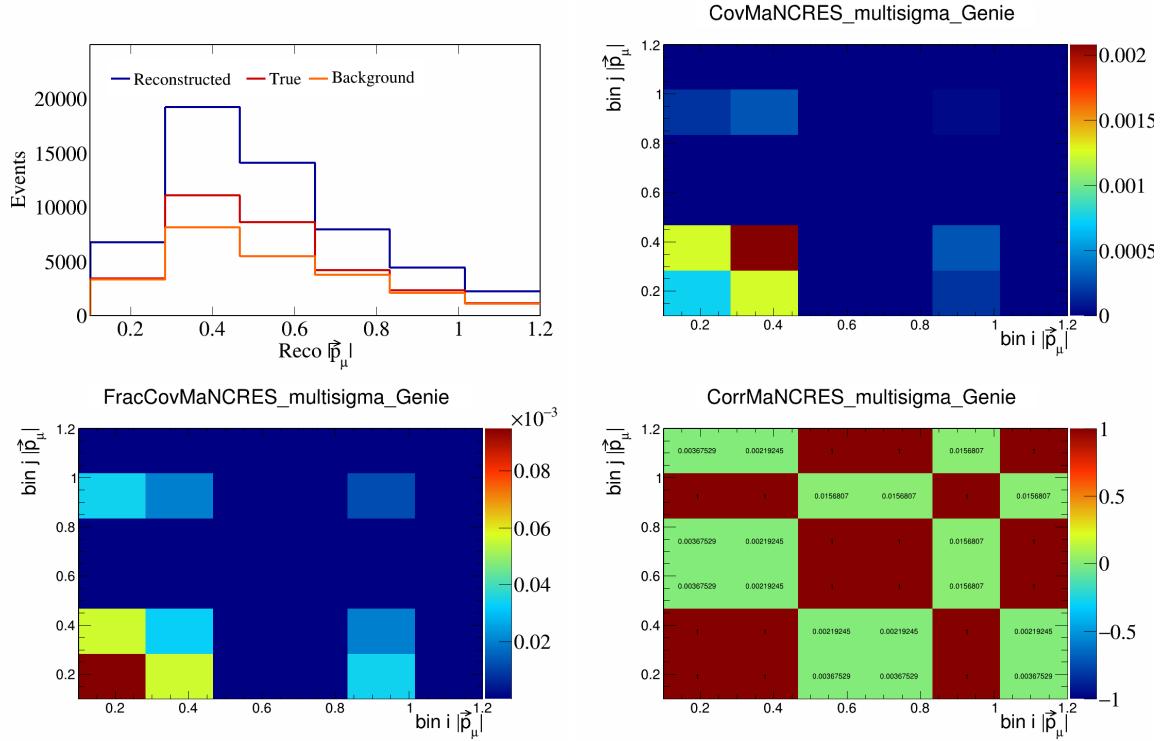


Figure 283: MaNCRES variations for $|\vec{p}_\mu|$.

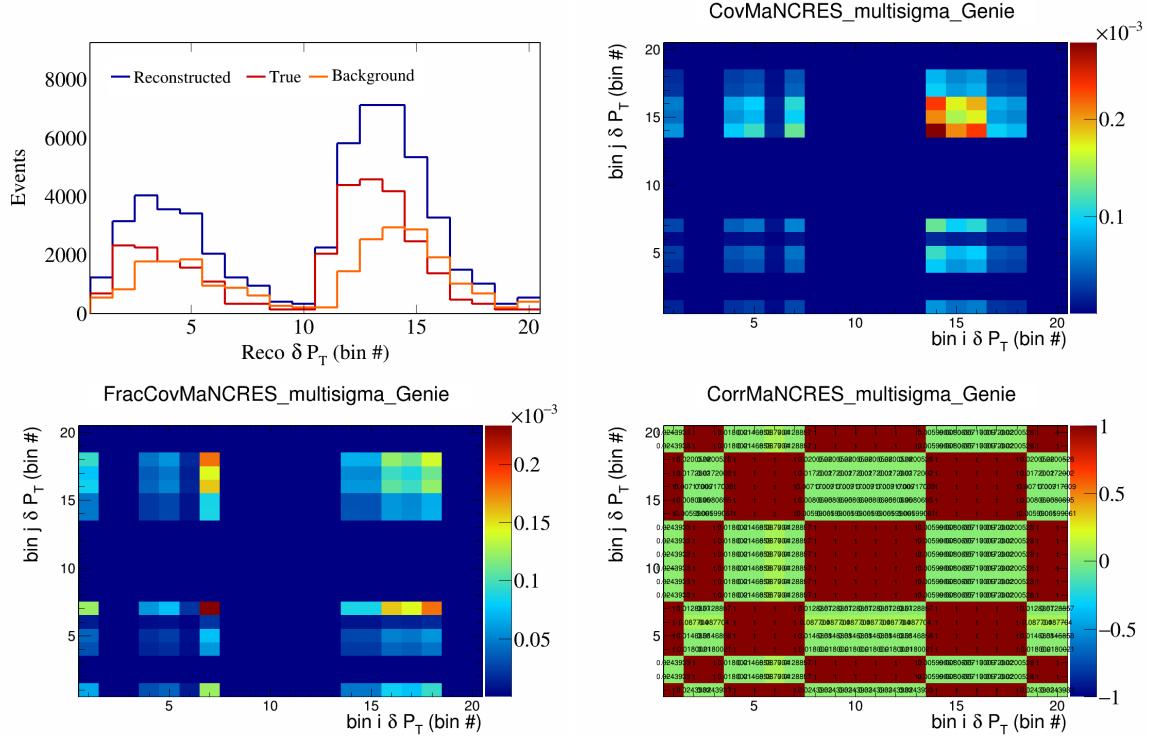


Figure 284: MaNCRES variations for δP_T in $\cos(\theta_{\vec{p}_\mu})$.

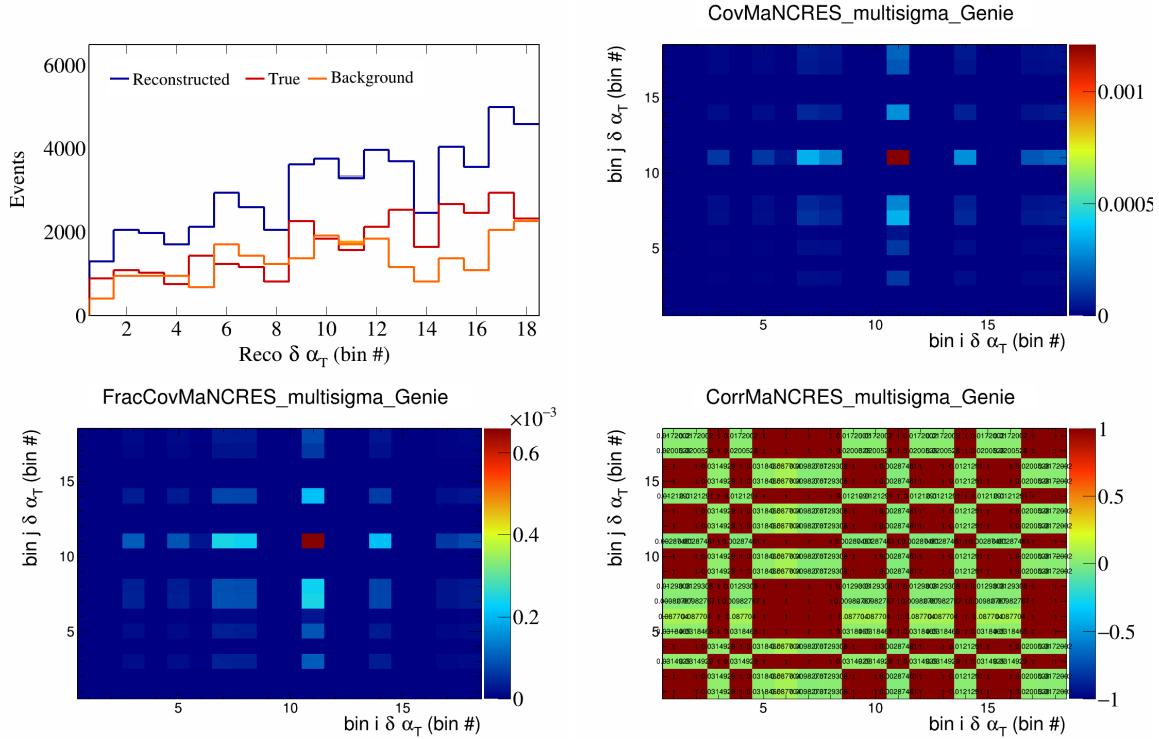


Figure 285: MaNCRES variations for $\delta\alpha_T$ in $\cos(\theta_{\vec{p}_\mu})$.

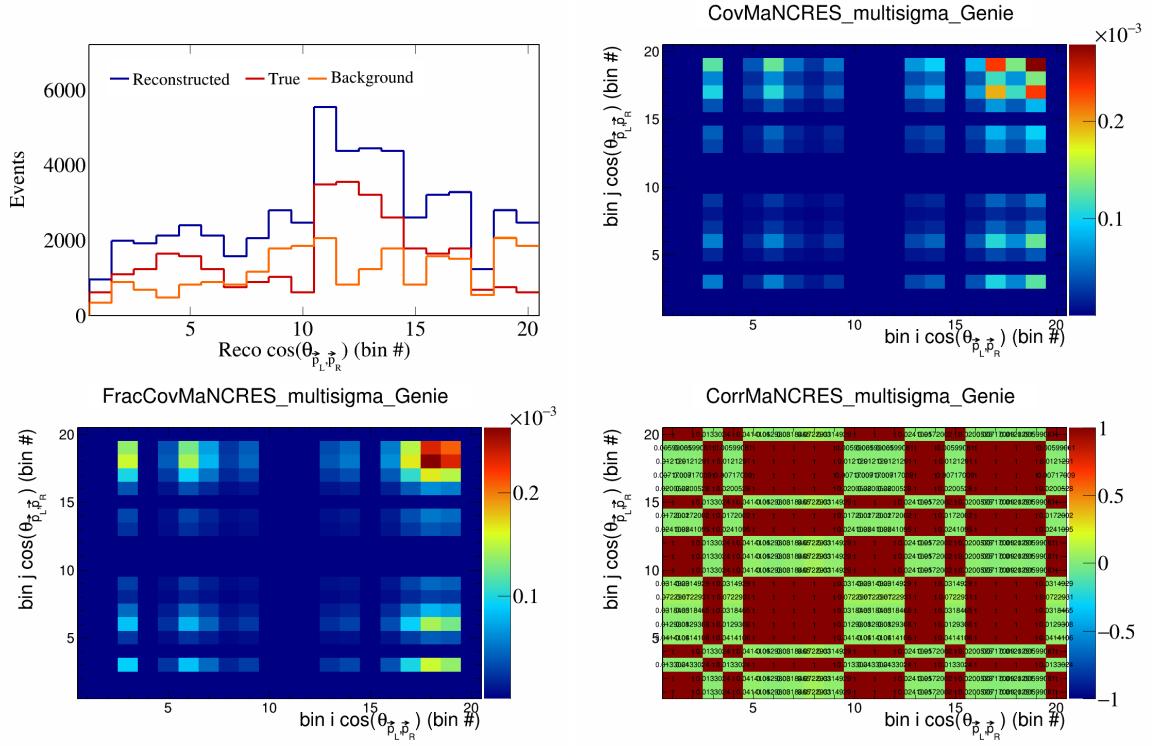


Figure 286: MaNCRES variations for $\cos(\theta_{p_L, p_R})$ in $\cos(\theta_{\vec{p}_\mu})$.

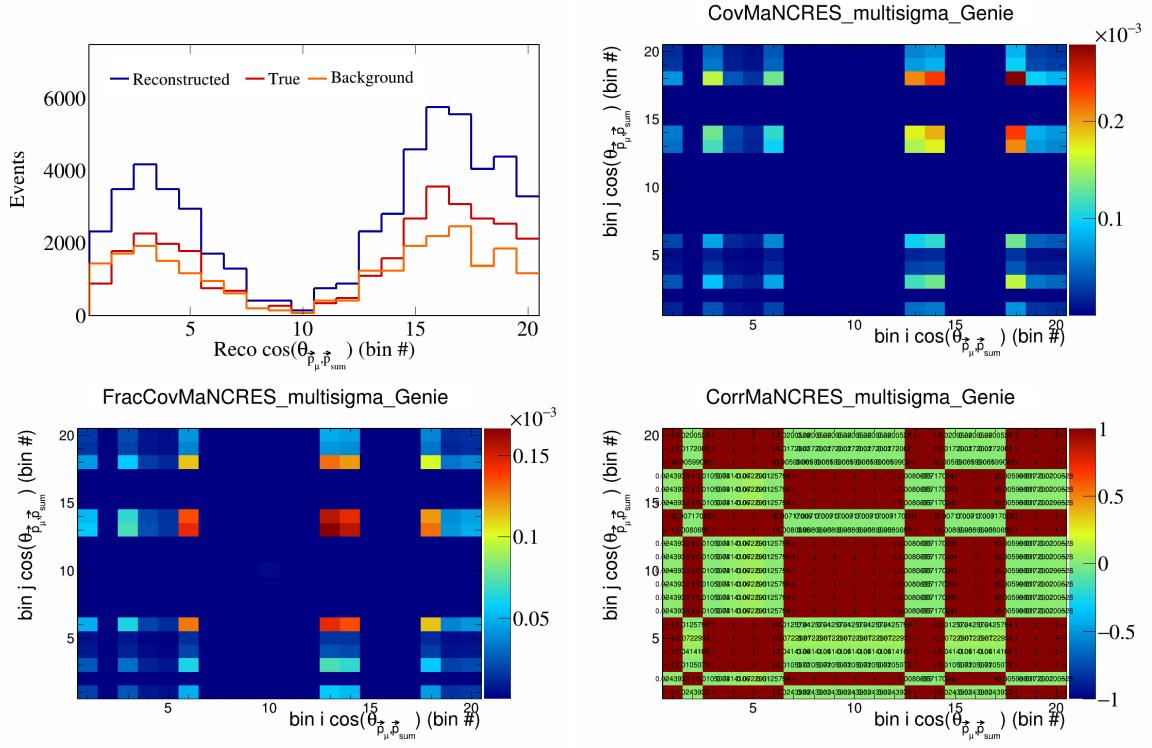


Figure 287: MaNCRES variations for $\cos(\theta_{\vec{p}_\mu, \vec{p}_{\text{sum}}})$ in $\cos(\theta_{\vec{p}_\mu})$.

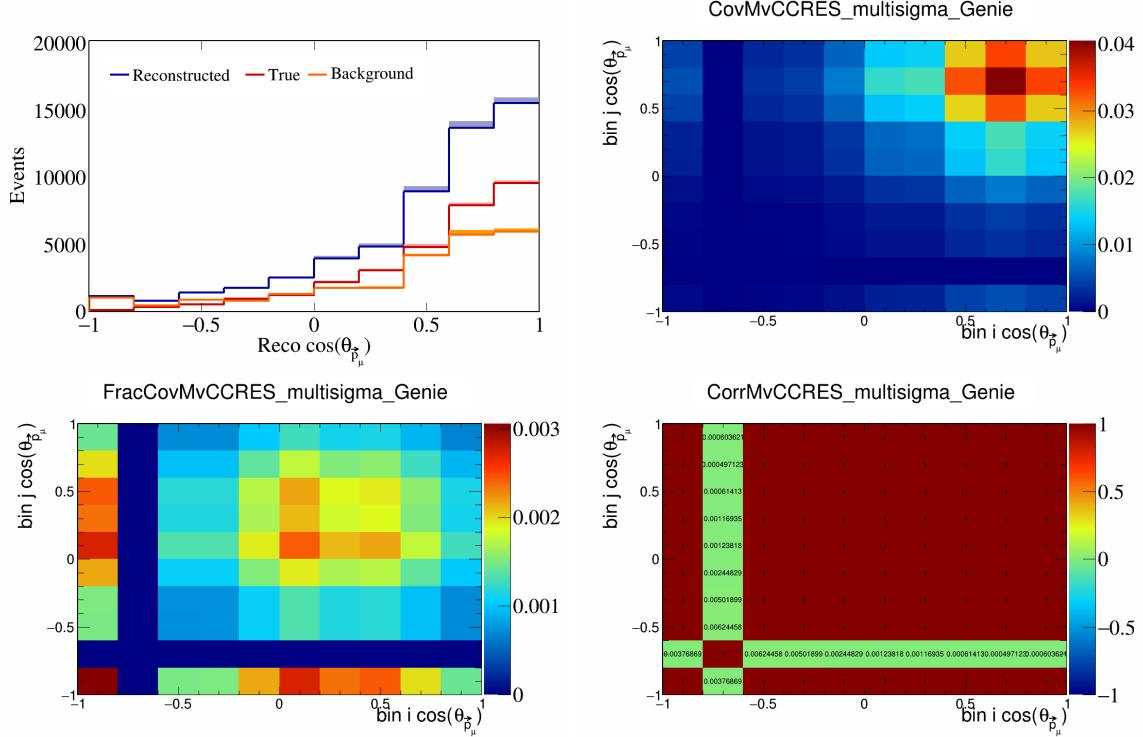


Figure 288: MvCCRES variations for $\cos(\theta_{\vec{p}_\mu})$.

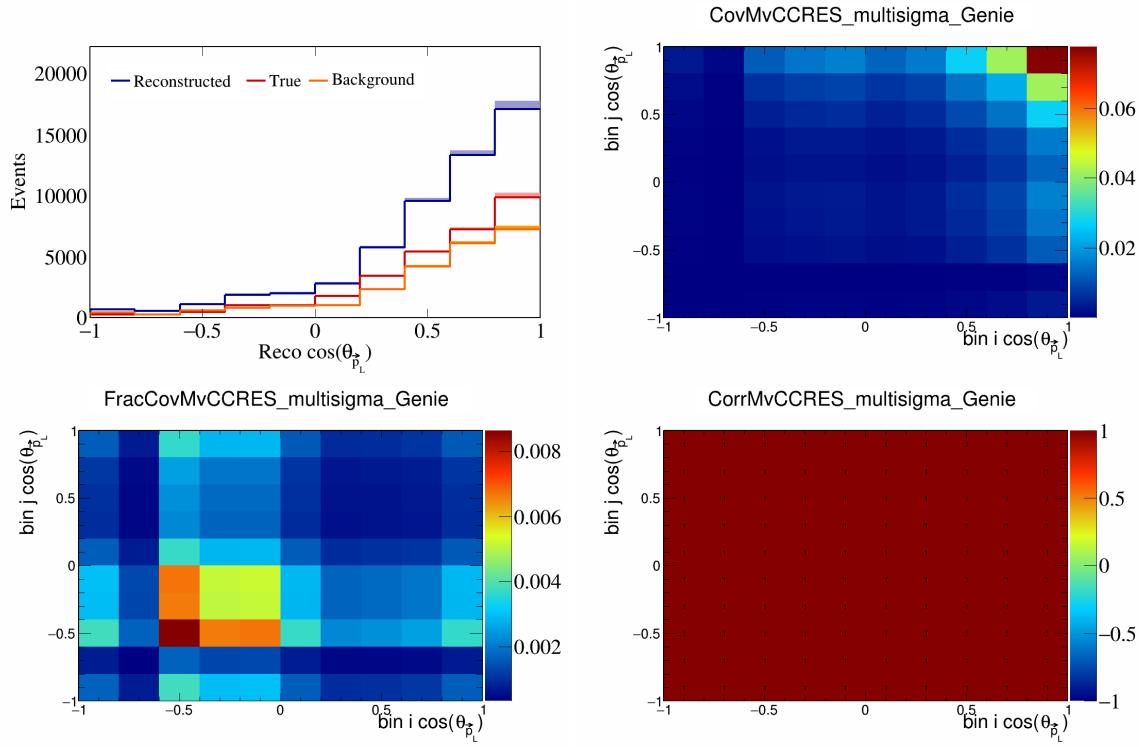


Figure 289: MvCCRES variations for $\cos(\theta_{\vec{p}_L})$.

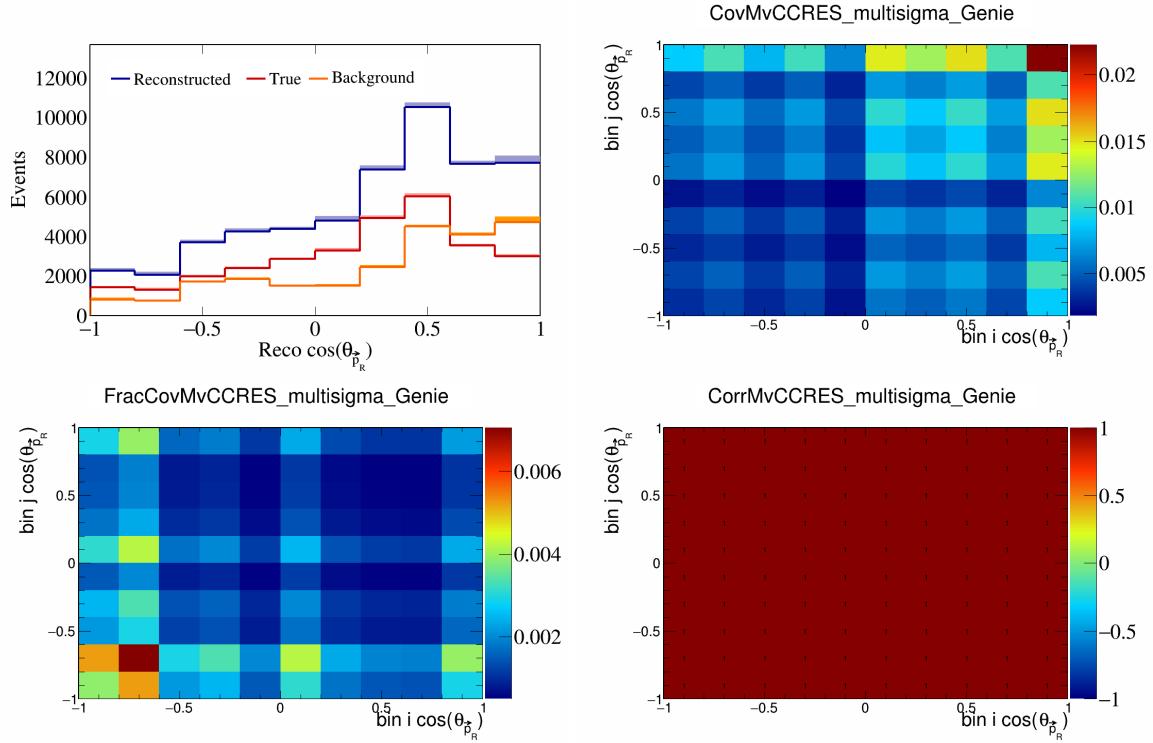


Figure 290: MvCCRES variations for $\cos(\theta_{\vec{p}_R})$.

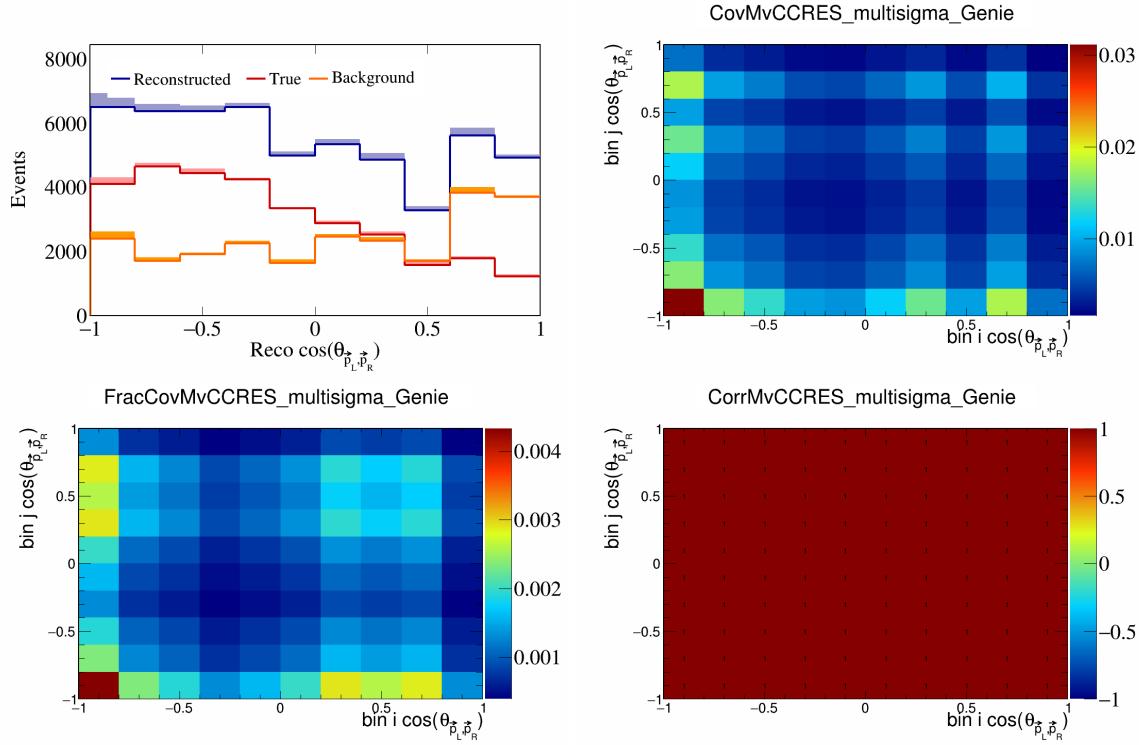


Figure 291: MvCCRES variations for $\cos(\theta_{\vec{p}_L, \vec{p}_R})$.

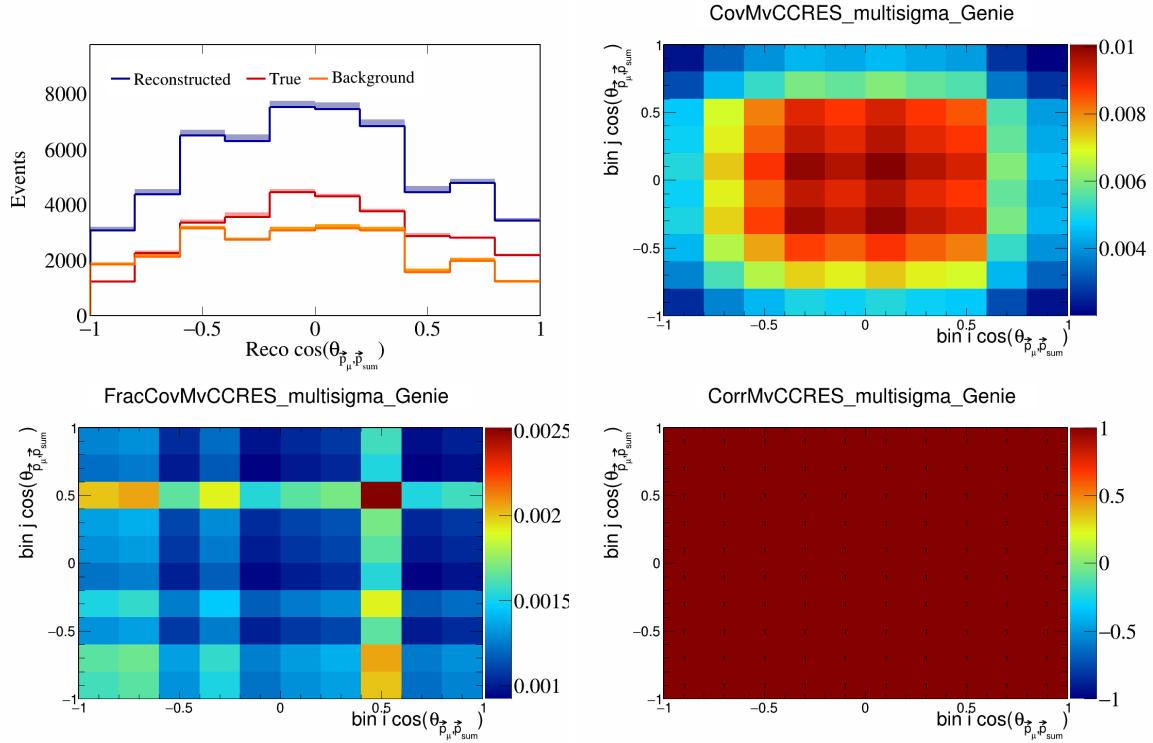


Figure 292: MvCCRES variations for $\cos(\theta_{\vec{p}_\mu, \vec{p}_{\text{sum}}})$.

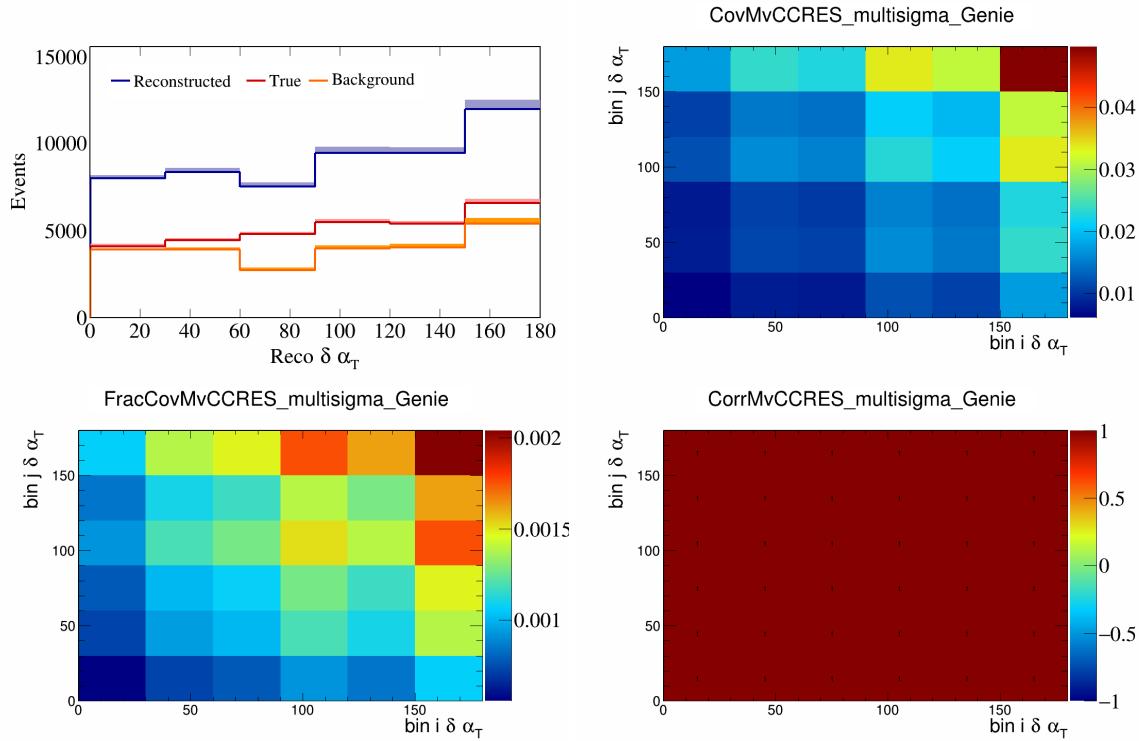


Figure 293: MvCCRES variations for $\delta\alpha_T$.

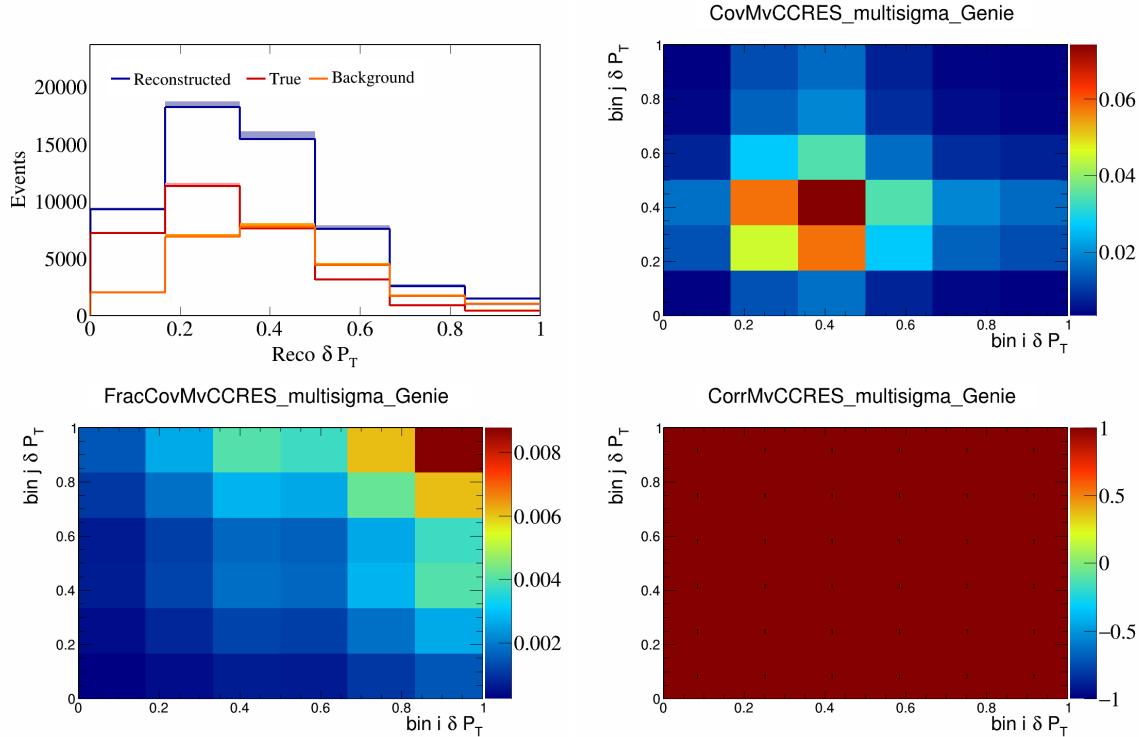


Figure 294: MvCCRES variations for δP_T .

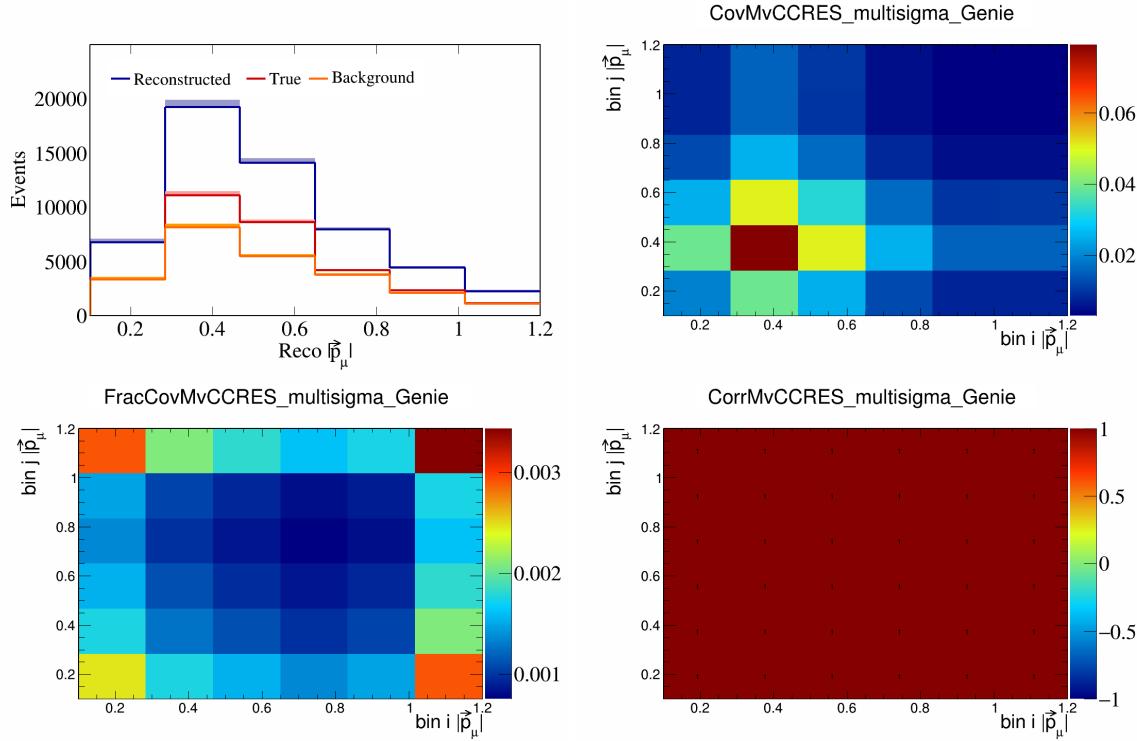


Figure 295: MvCCRES variations for $|\vec{p}_\mu|$.

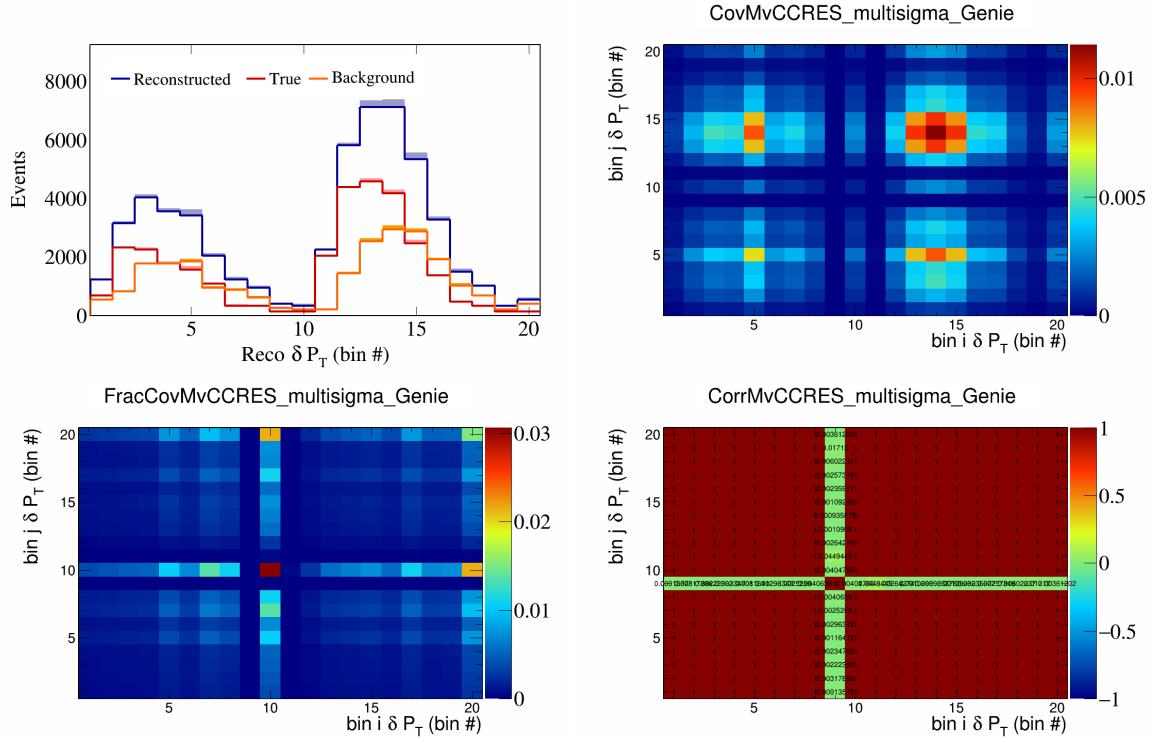


Figure 296: MvCCRES variations for δP_T in $\cos(\theta_{\vec{p}_\mu})$.

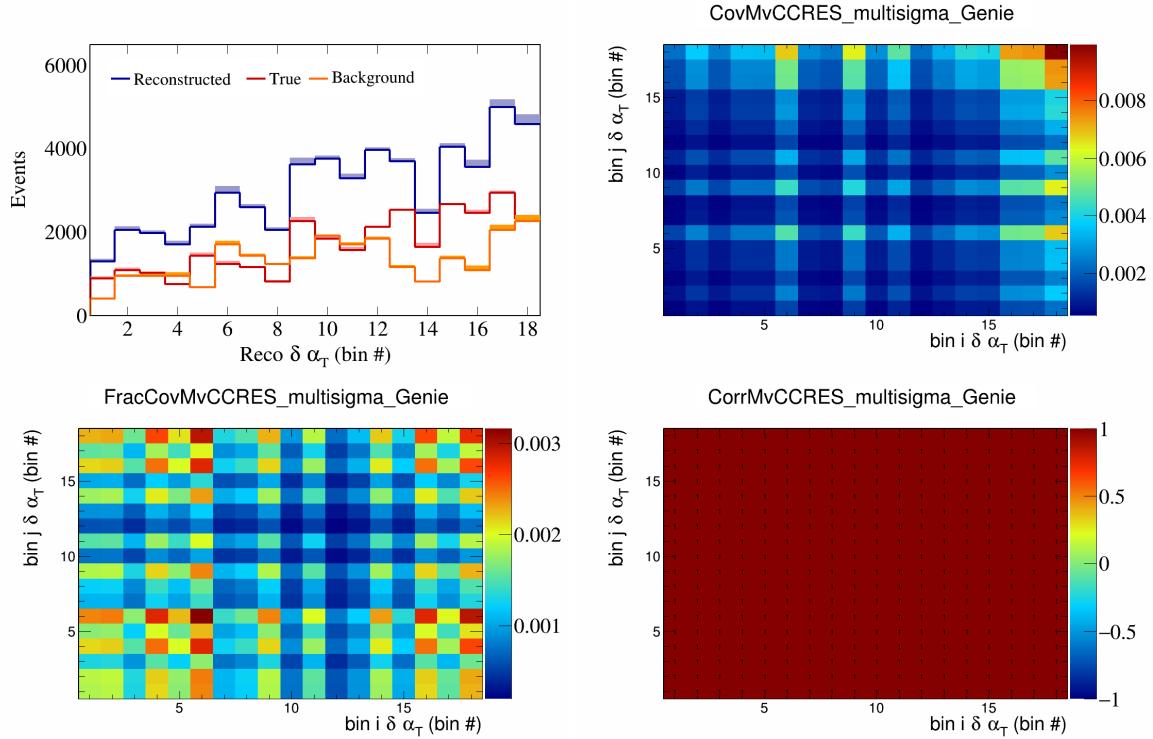


Figure 297: MvCCRES variations for $\delta\alpha_T$ in $\cos(\theta_{\vec{p}_\mu})$.

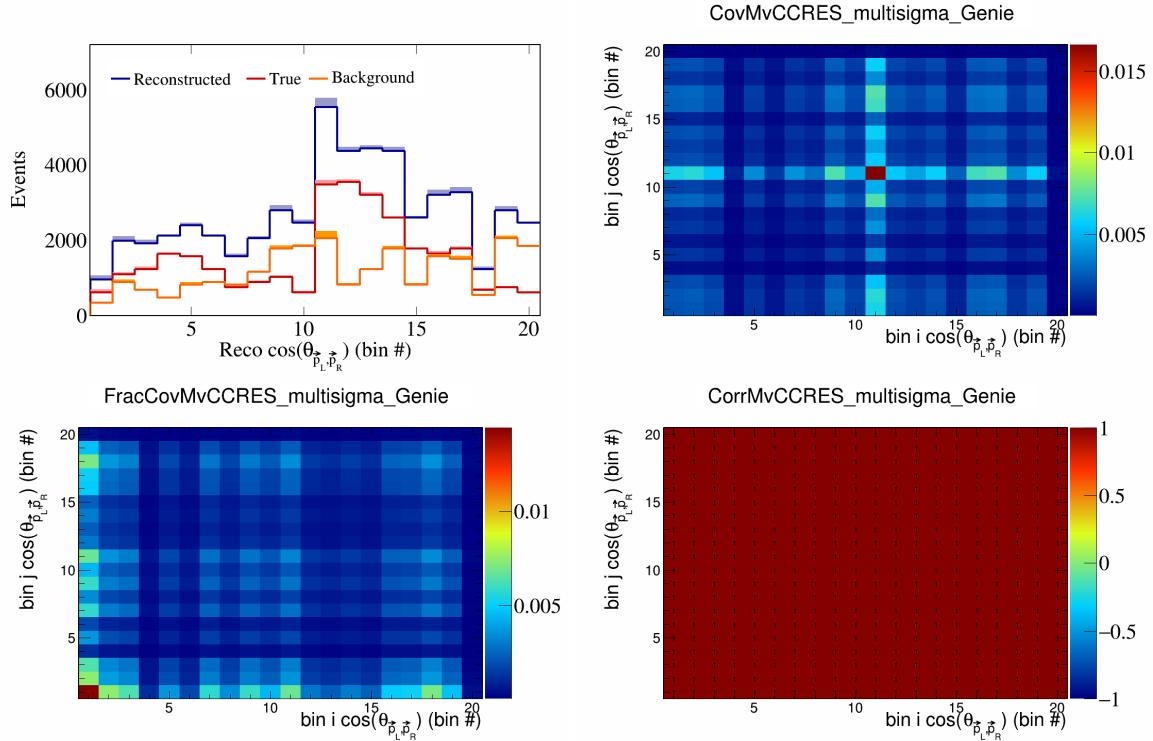


Figure 298: MvCCRES variations for $\cos(\theta_{\vec{p}_L, \vec{p}_R})$ in $\cos(\theta_{\vec{p}_\mu})$.

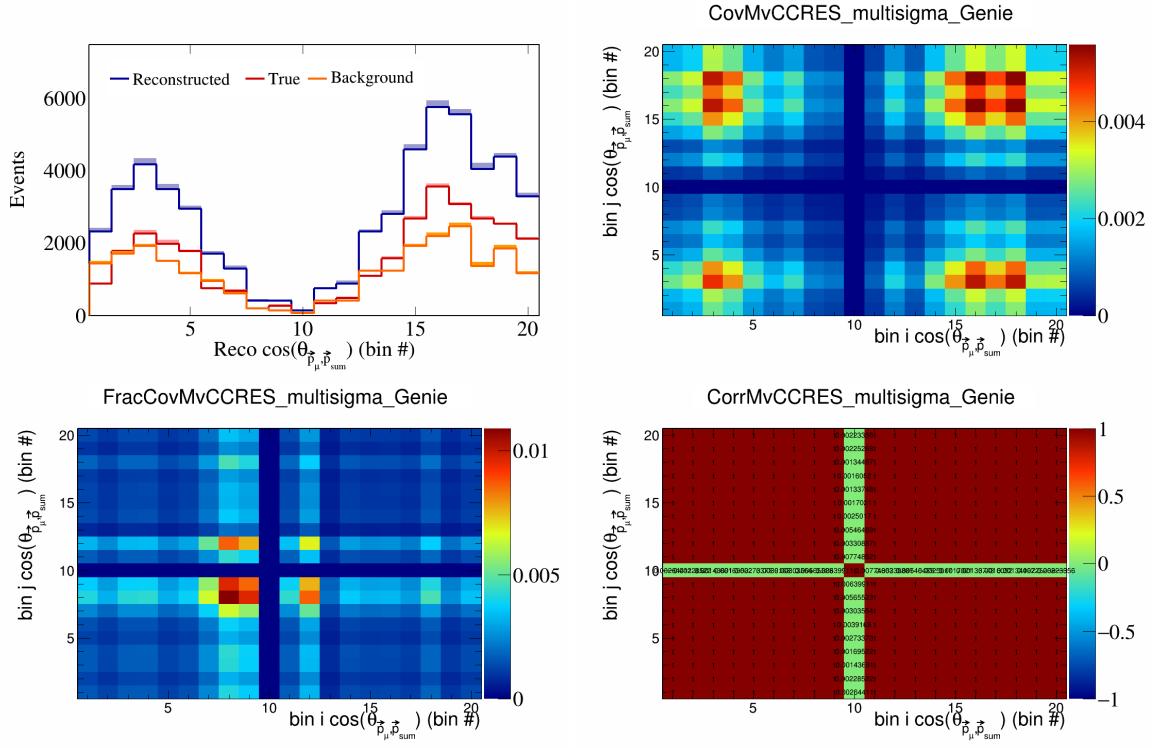


Figure 299: MvCCRES variations for $\cos(\theta_{\vec{p}_\mu, \vec{p}_{\text{sum}}})$ in $\cos(\theta_{\vec{p}_\mu})$.

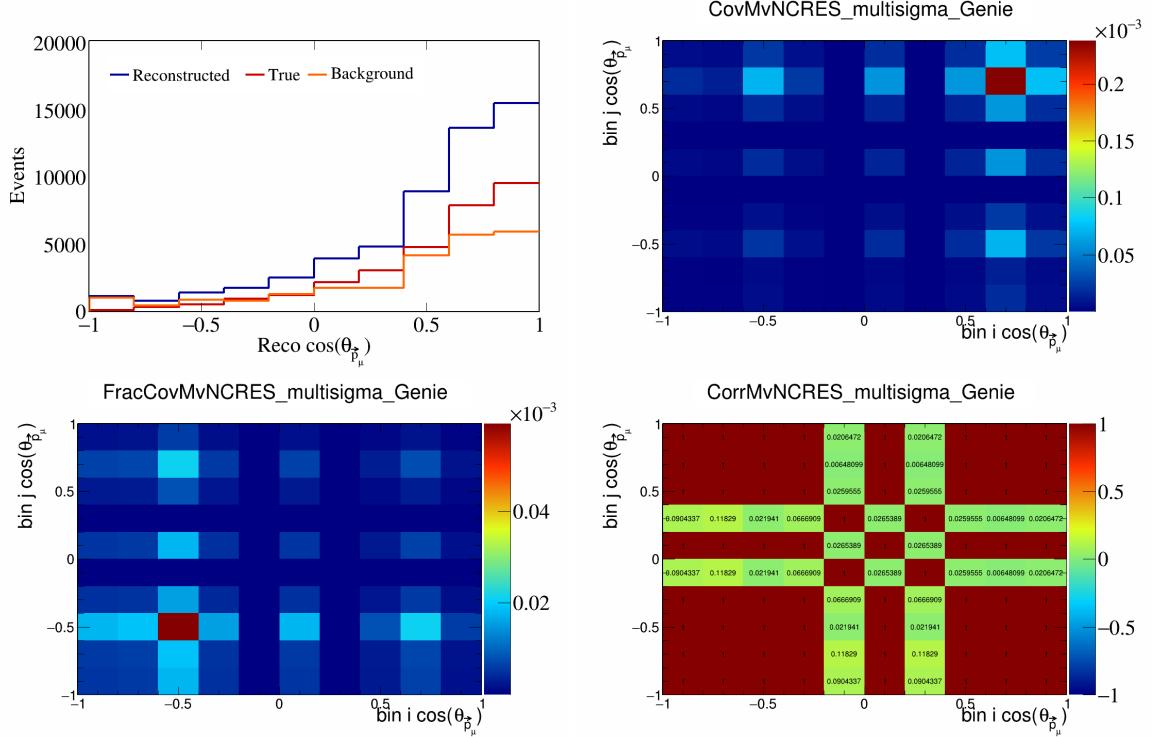


Figure 300: MvNCRES variations for $\cos(\theta_{\vec{p}_\mu})$.

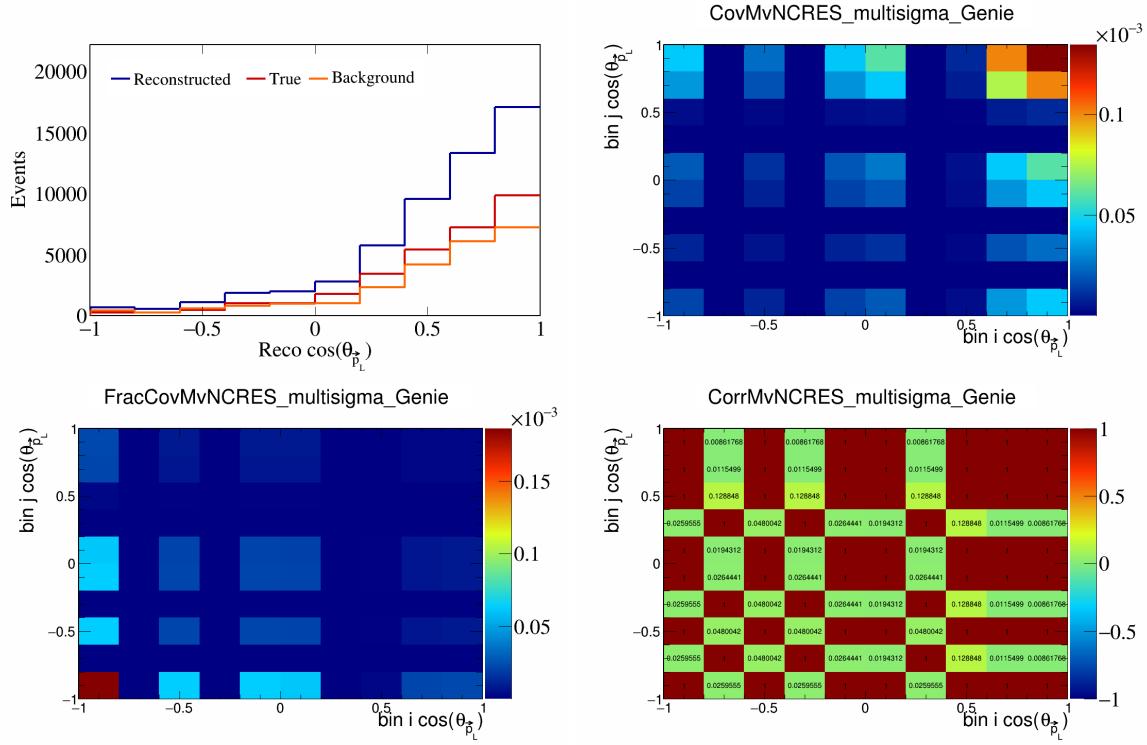


Figure 301: MvNCRES variations for $\cos(\theta_{\vec{p}_L})$.

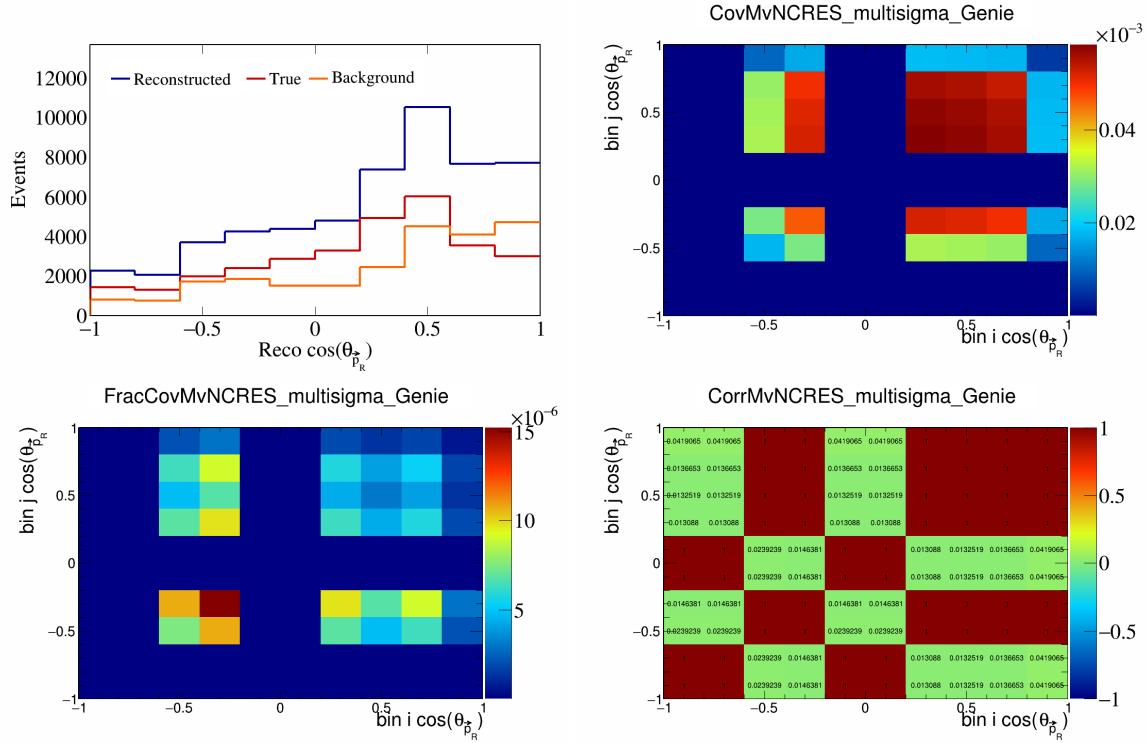


Figure 302: MvNCRES variations for $\cos(\theta_{\vec{p}_R})$.

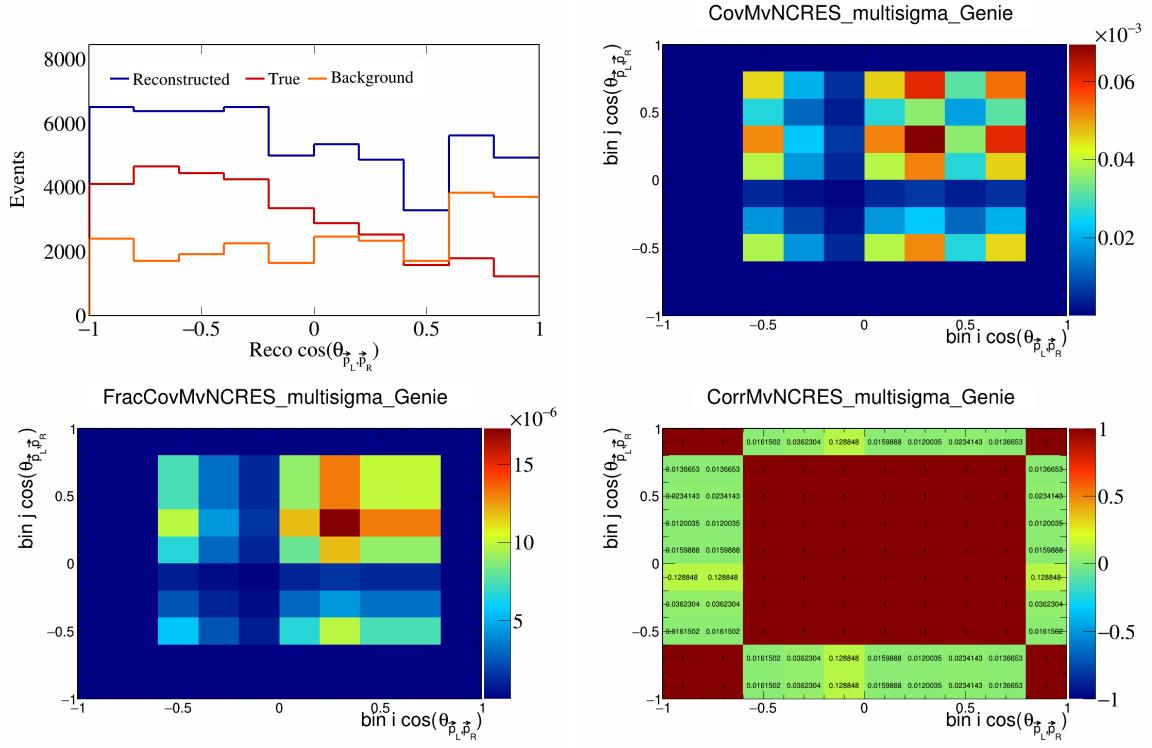


Figure 303: MvNCRES variations for $\cos(\theta_{\vec{p}_L, \vec{p}_R})$.

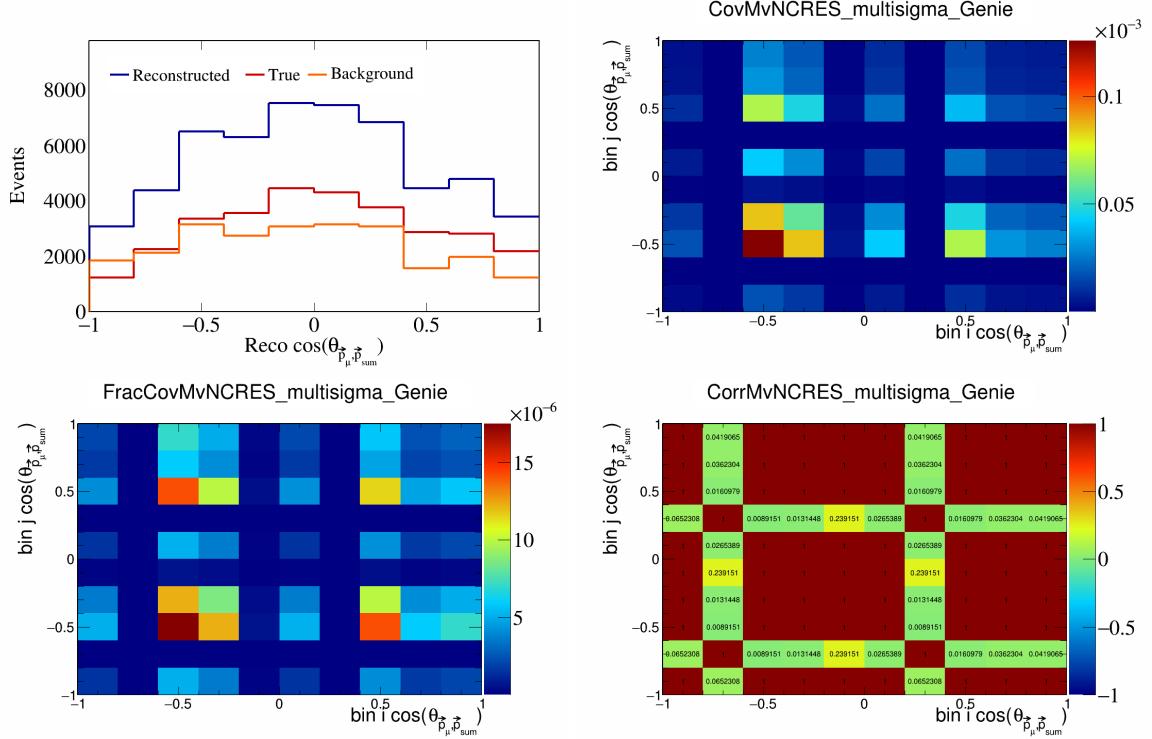


Figure 304: MvNCRES variations for $\cos(\theta_{\vec{p}_\mu, \vec{p}_{\text{sum}}})$.

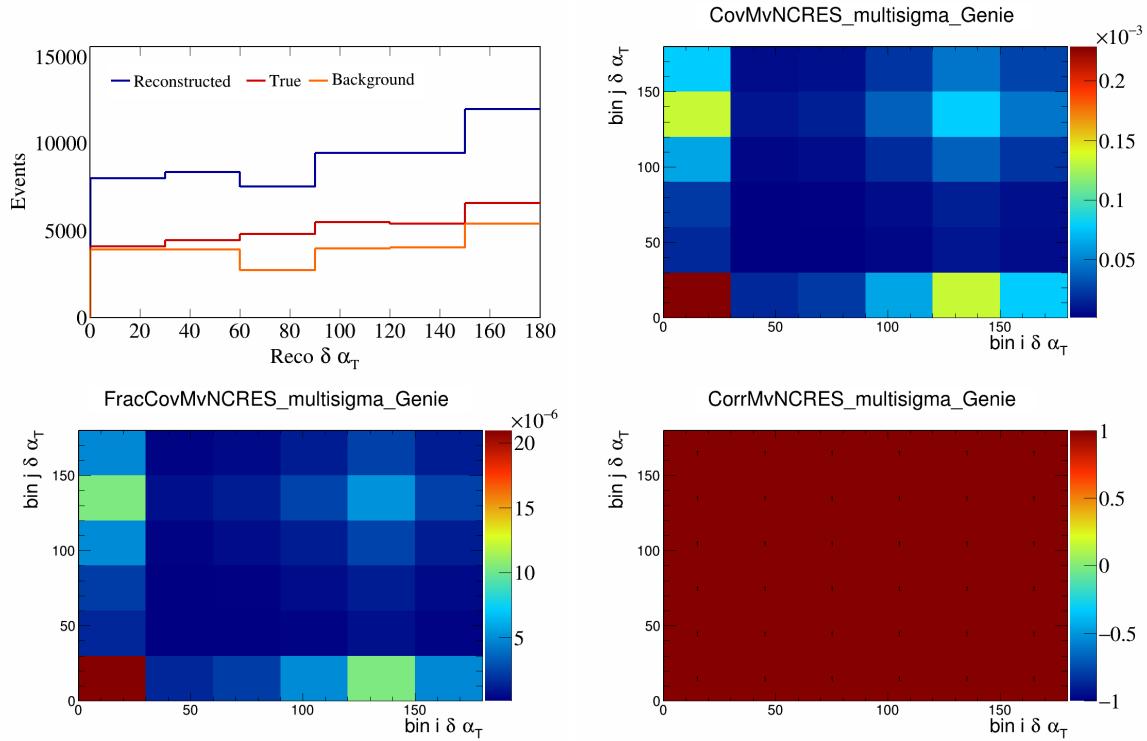


Figure 305: MvNCRES variations for $\delta\alpha_T$.

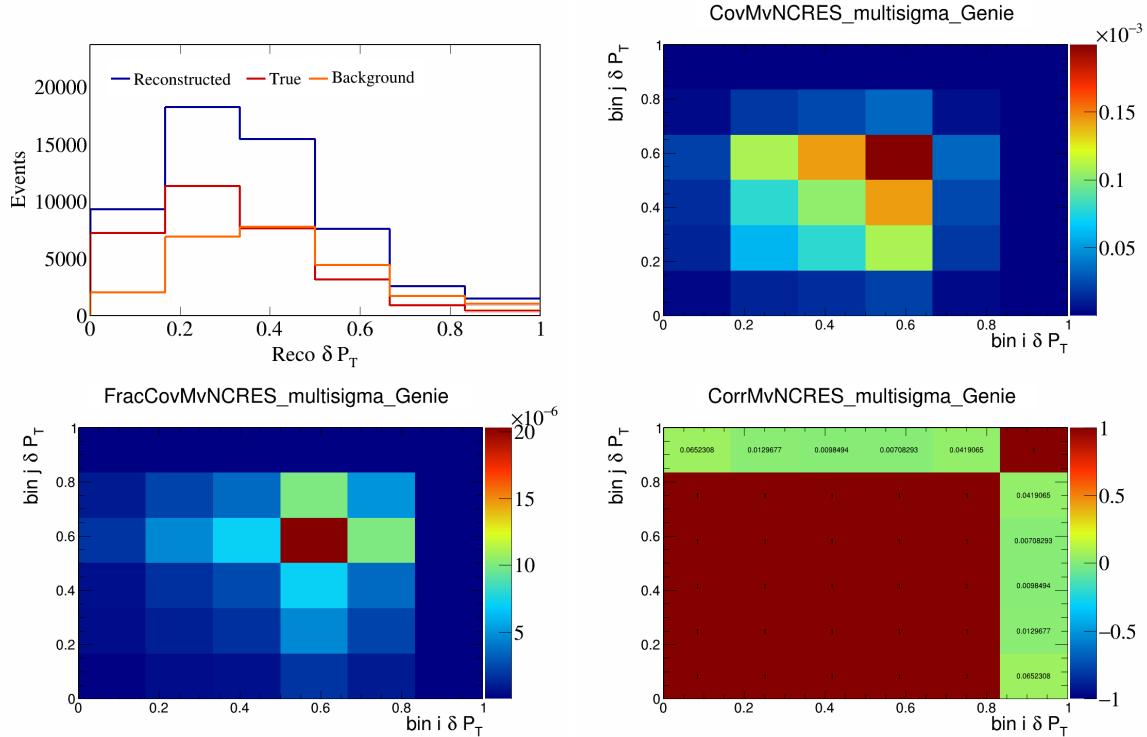


Figure 306: MvNCRES variations for δP_T .

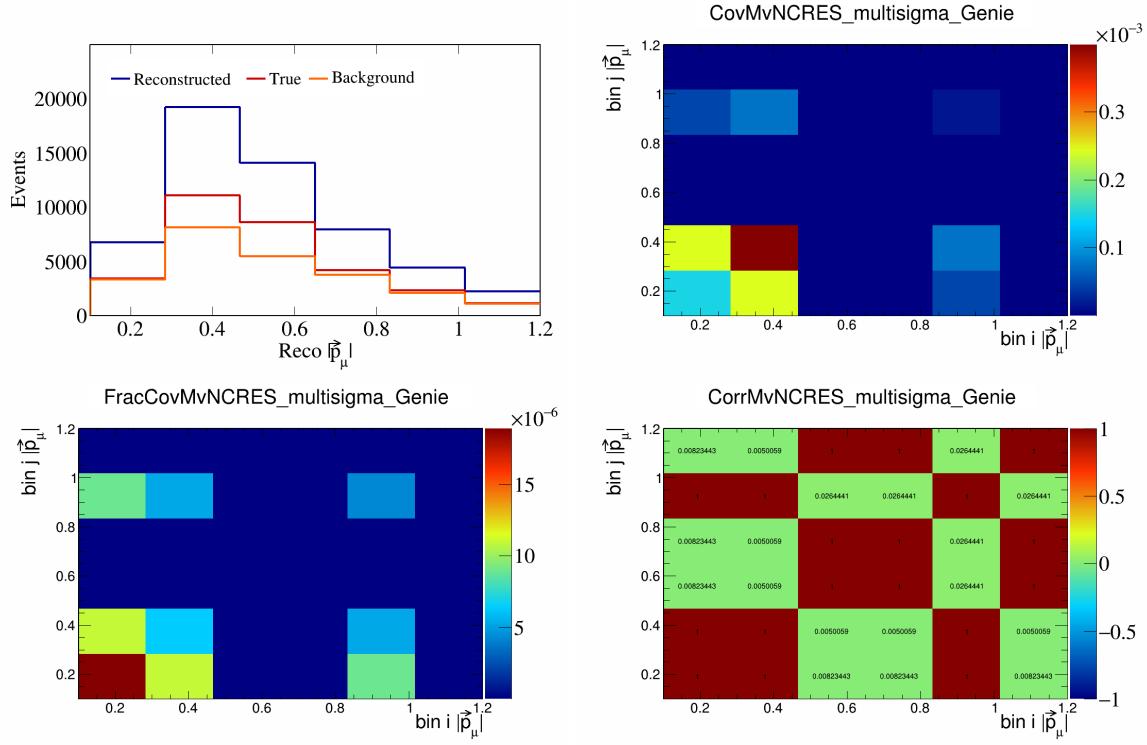


Figure 307: MvNCRES variations for $|\vec{p}_\mu|$.

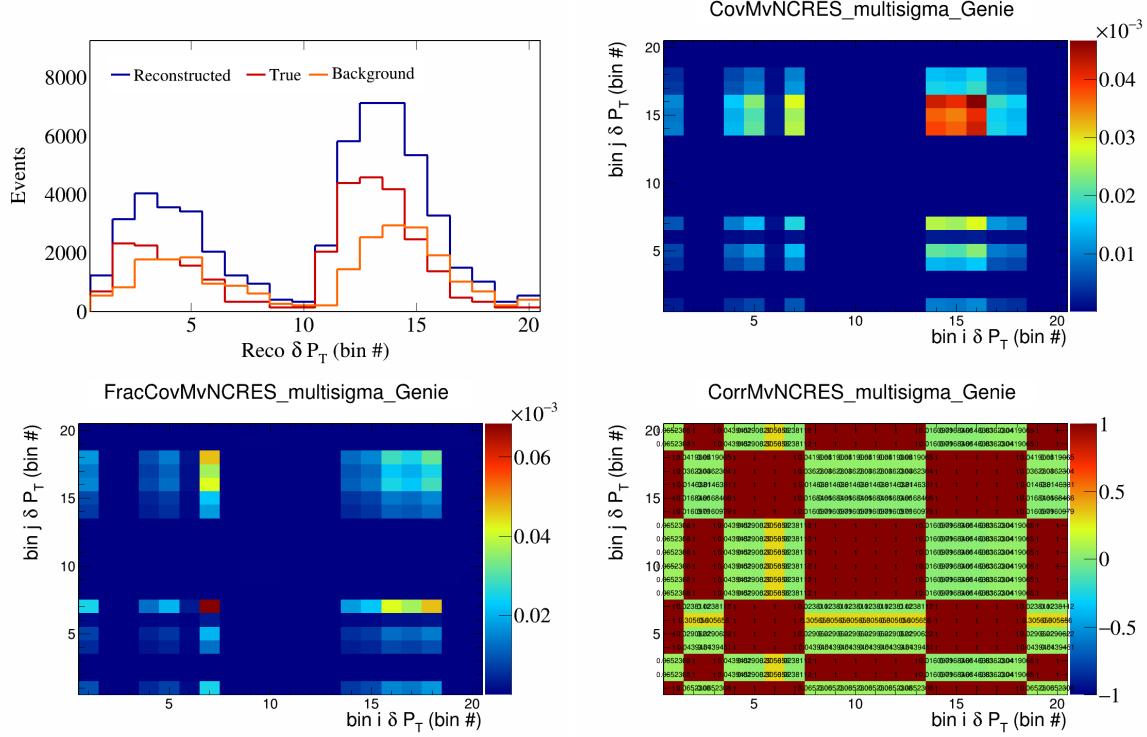


Figure 308: MvNCRES variations for δP_T in $\cos(\theta_{\vec{p}_\mu})$.

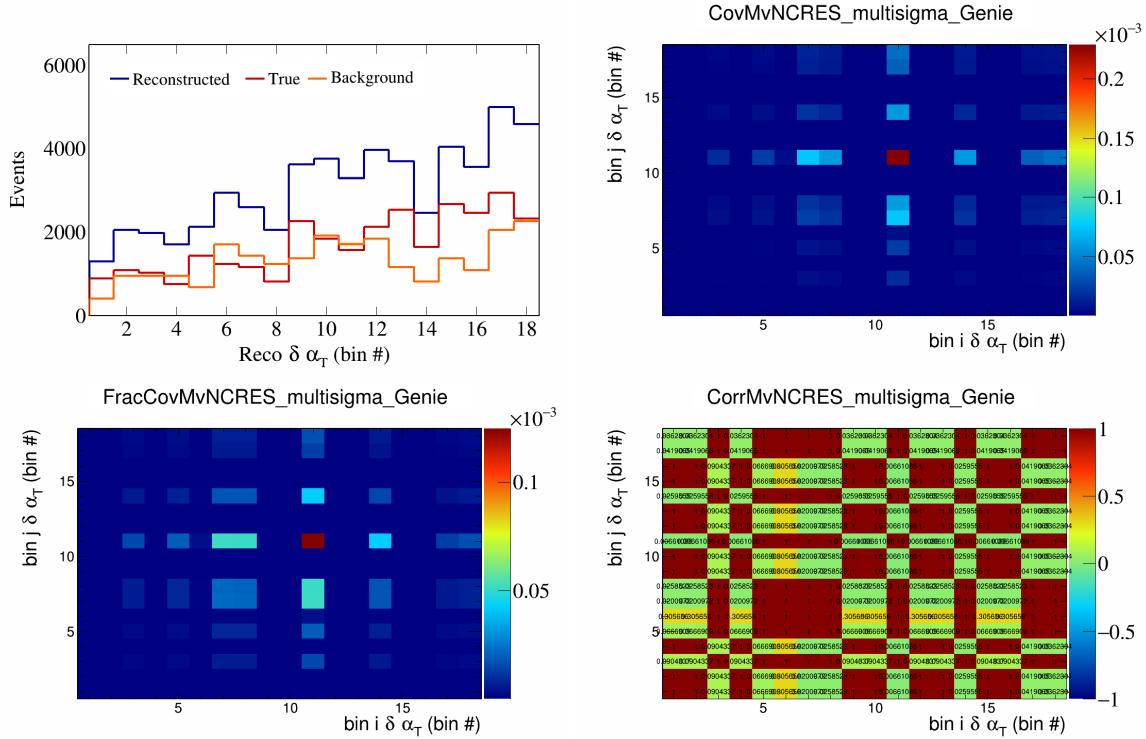


Figure 309: MvNCRES variations for $\delta \alpha_T$ in $\cos(\theta_{\vec{p}_\mu})$.

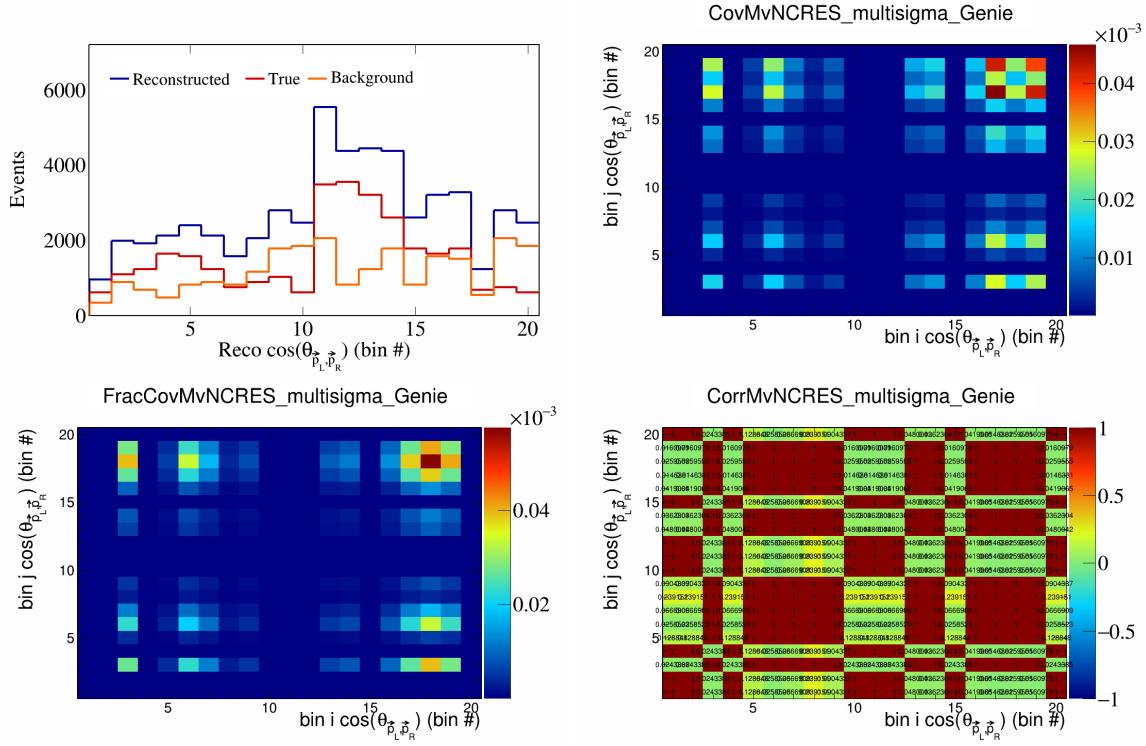


Figure 310: MvNCRES variations for $\cos(\theta_{\vec{p}_L, \vec{p}_R})$ in $\cos(\theta_{\vec{p}_\mu})$.

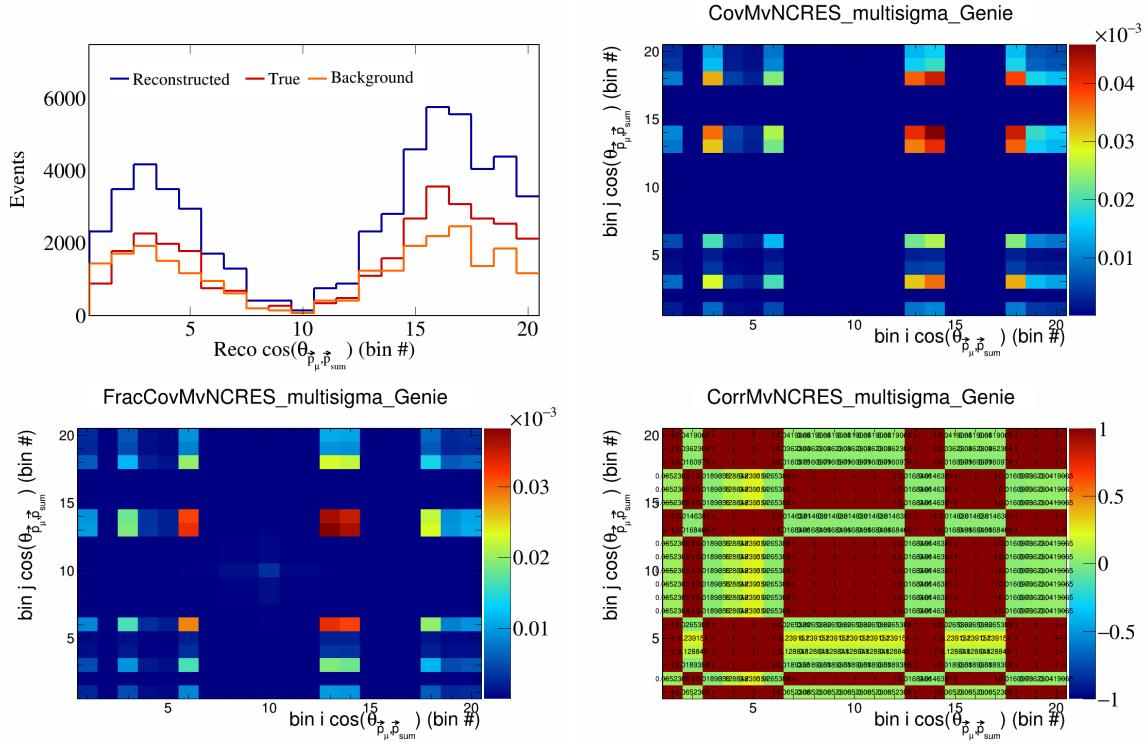


Figure 311: MyNCRES variations for $\cos(\theta_{\vec{p}_\mu, \vec{p}_{\text{sum}}})$ in $\cos(\theta_{\vec{p}_\mu})$.

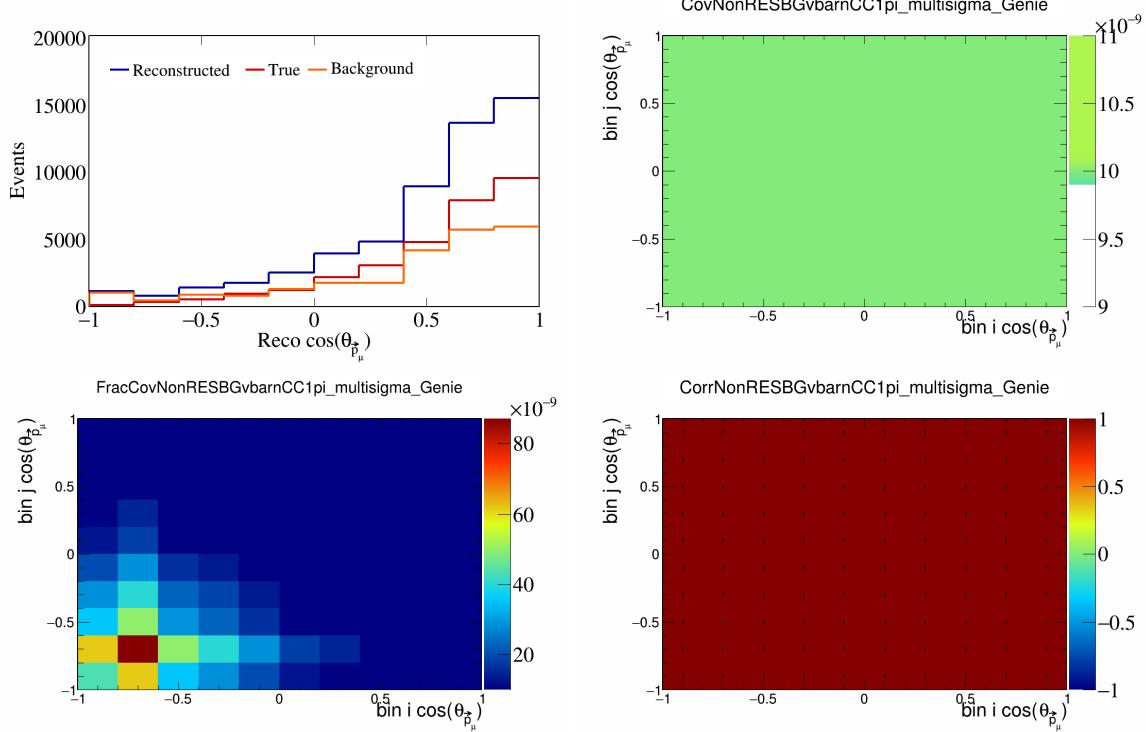


Figure 312: NonRESBGvbarCC1pi variations for $\cos(\theta_{\vec{p}_\mu})$.

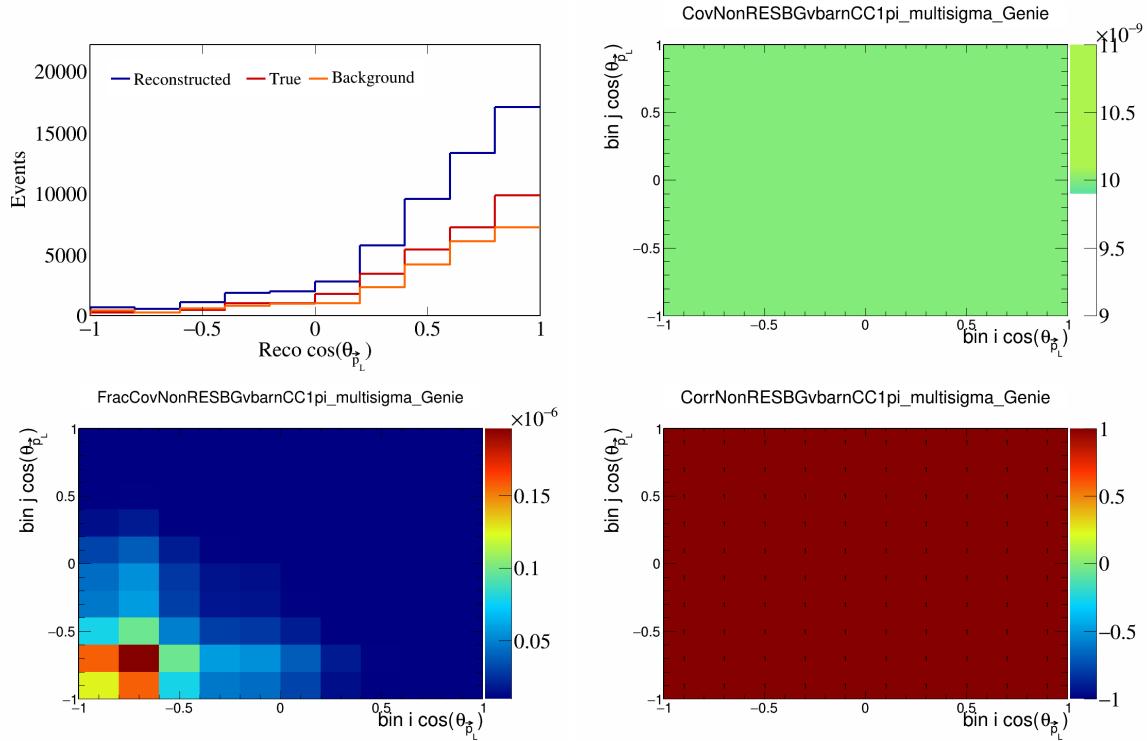


Figure 313: NonRESBGvbarCC1pi variations for $\cos(\theta_{\vec{p}_L})$.

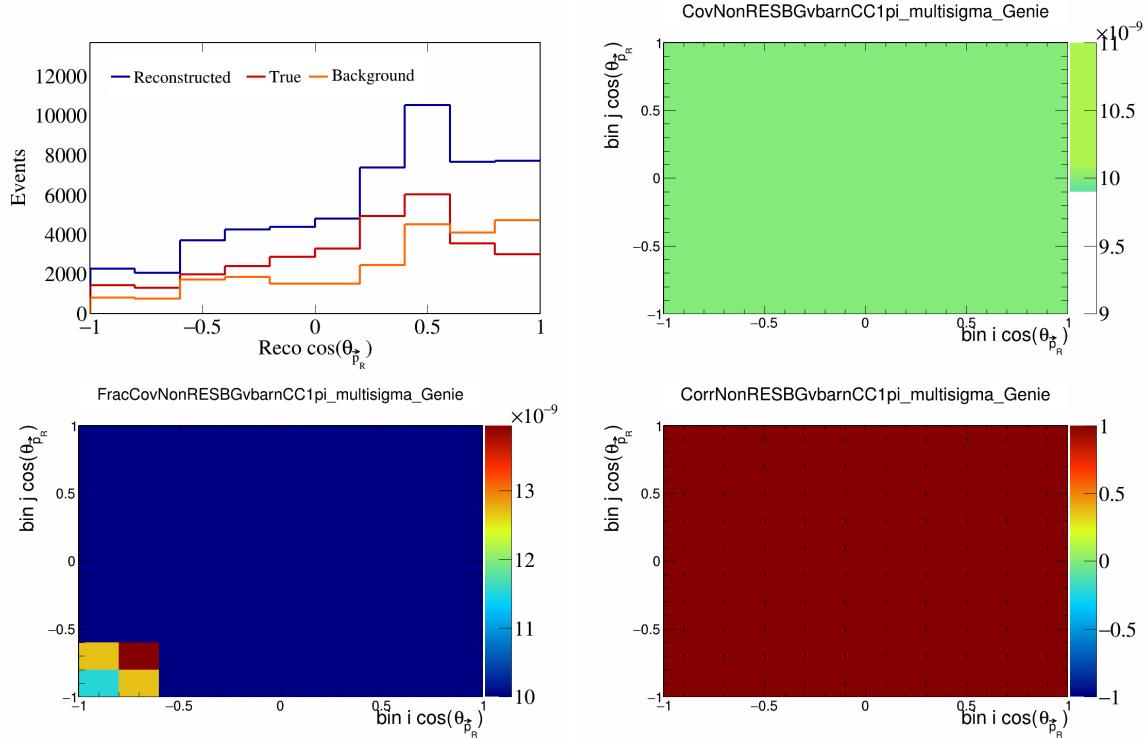


Figure 314: NonRESBGvbarCC1pi variations for $\cos(\theta_{\vec{p}_R})$.

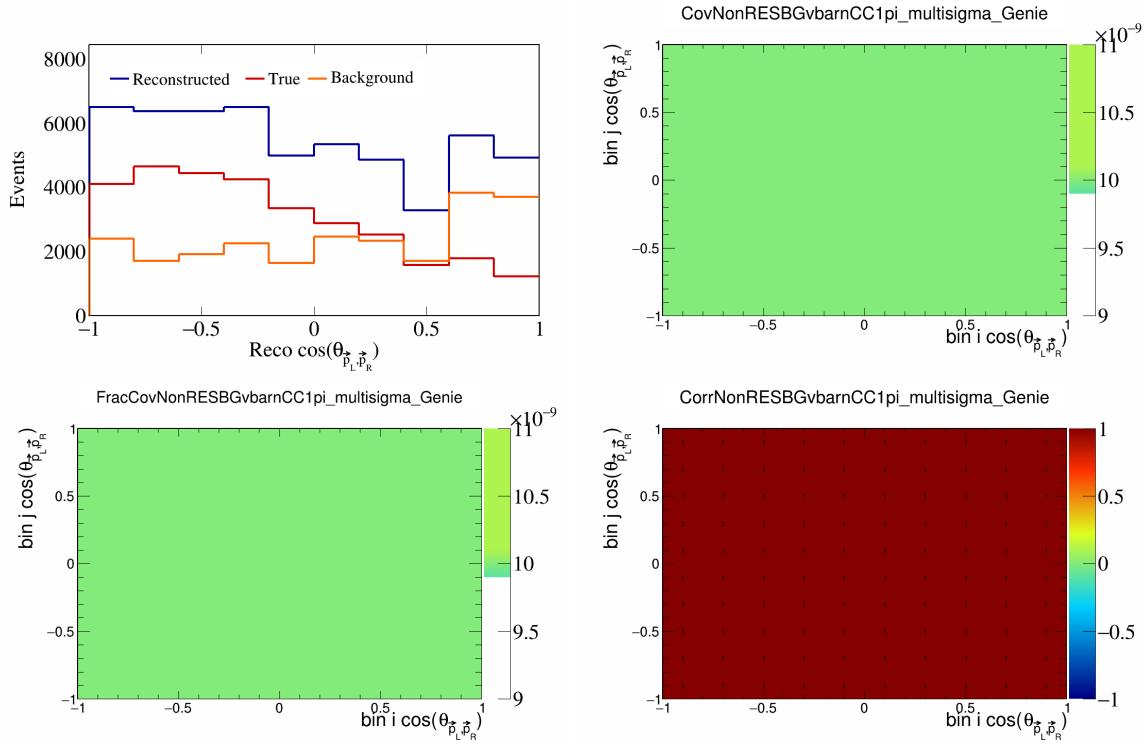


Figure 315: NonRESBGvbarCC1pi variations for $\cos(\theta_{\vec{p}_L, \vec{p}_R})$.

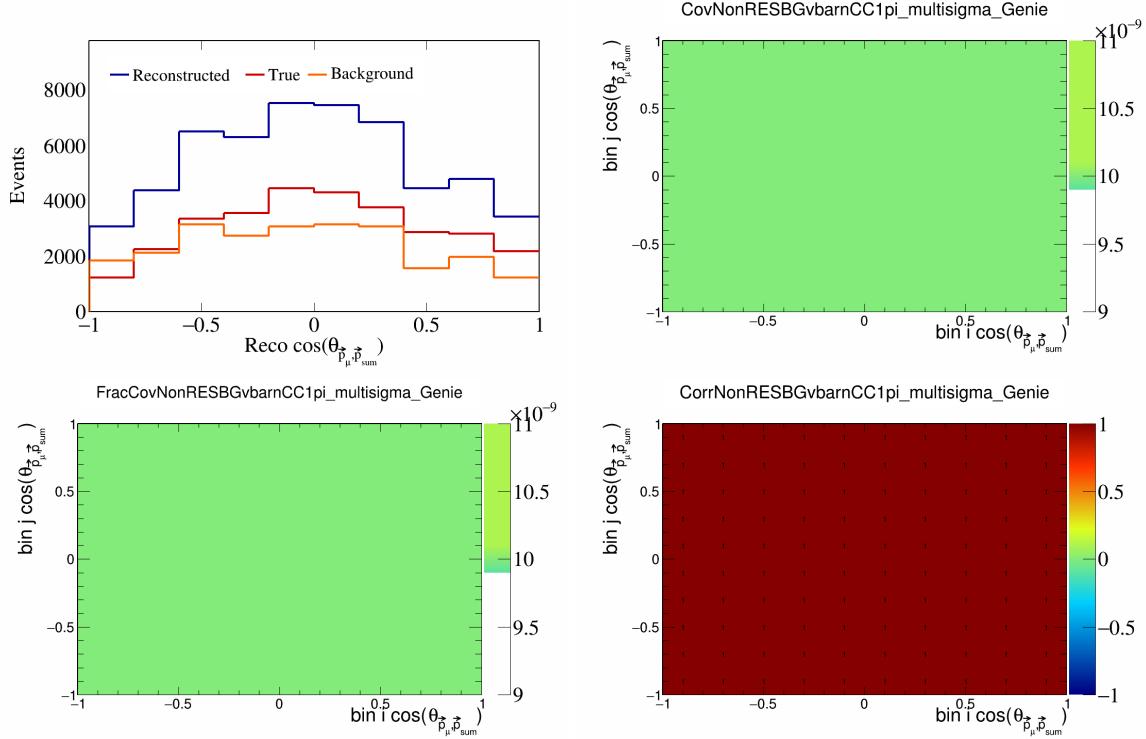


Figure 316: NonRESBGvbarCC1pi variations for $\cos(\theta_{\vec{p}_\mu, \vec{p}_{\text{sum}}})$.

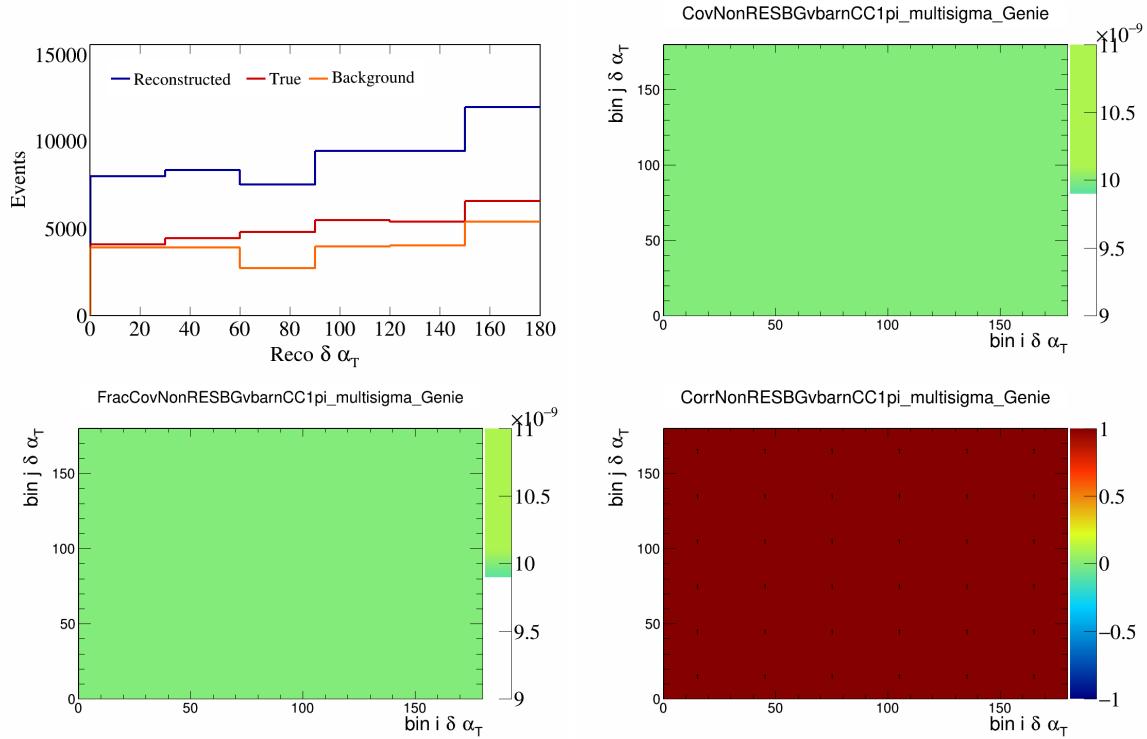


Figure 317: NonRESBGvbarCC1pi variations for $\delta\alpha_T$.

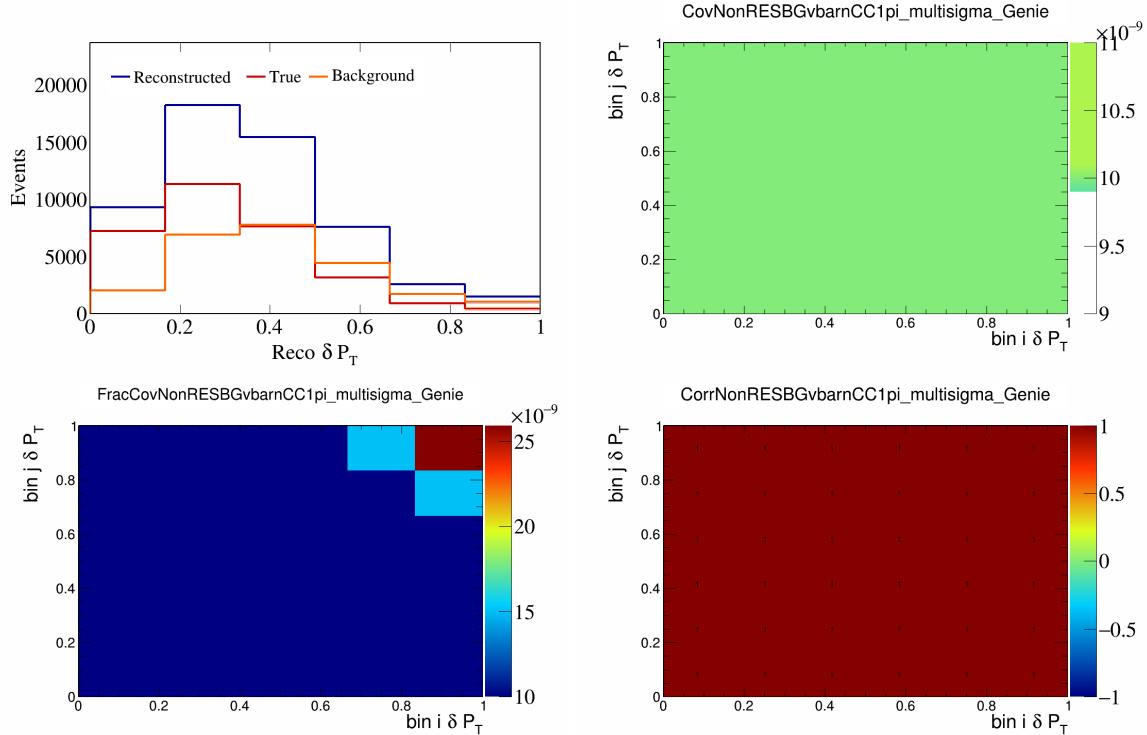


Figure 318: NonRESBGvbarCC1pi variations for δP_T .

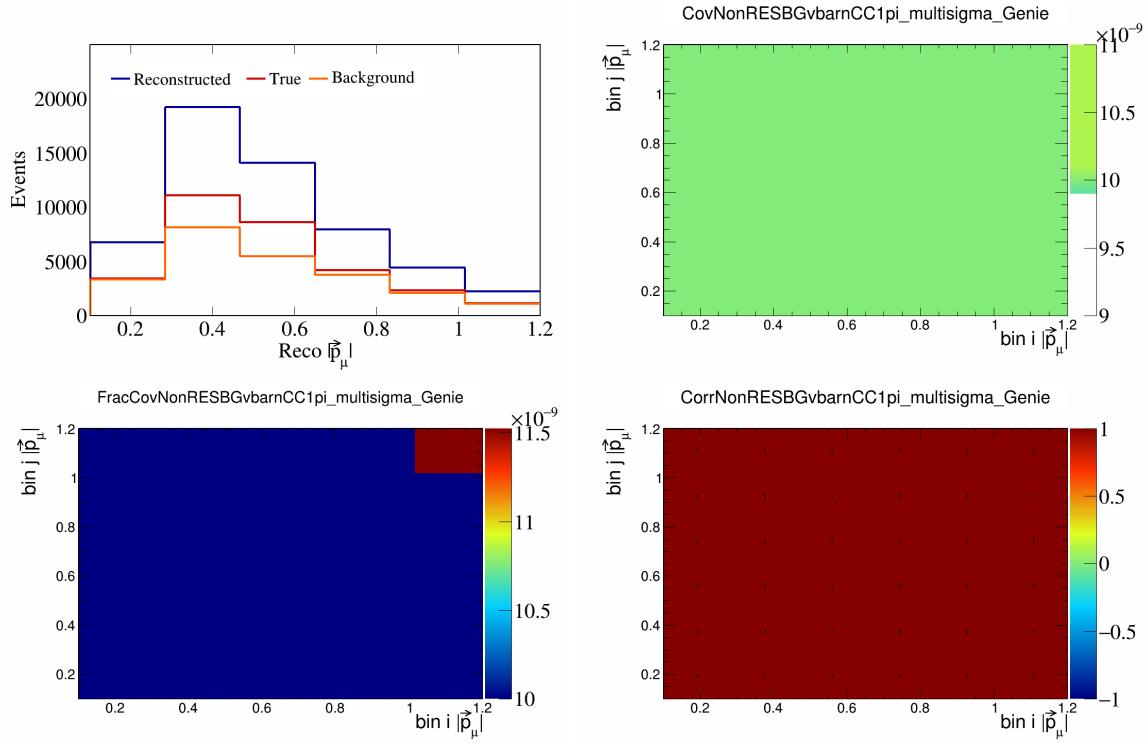


Figure 319: NonRESBGvbarCC1pi variations for $|\vec{p}_\mu|$.

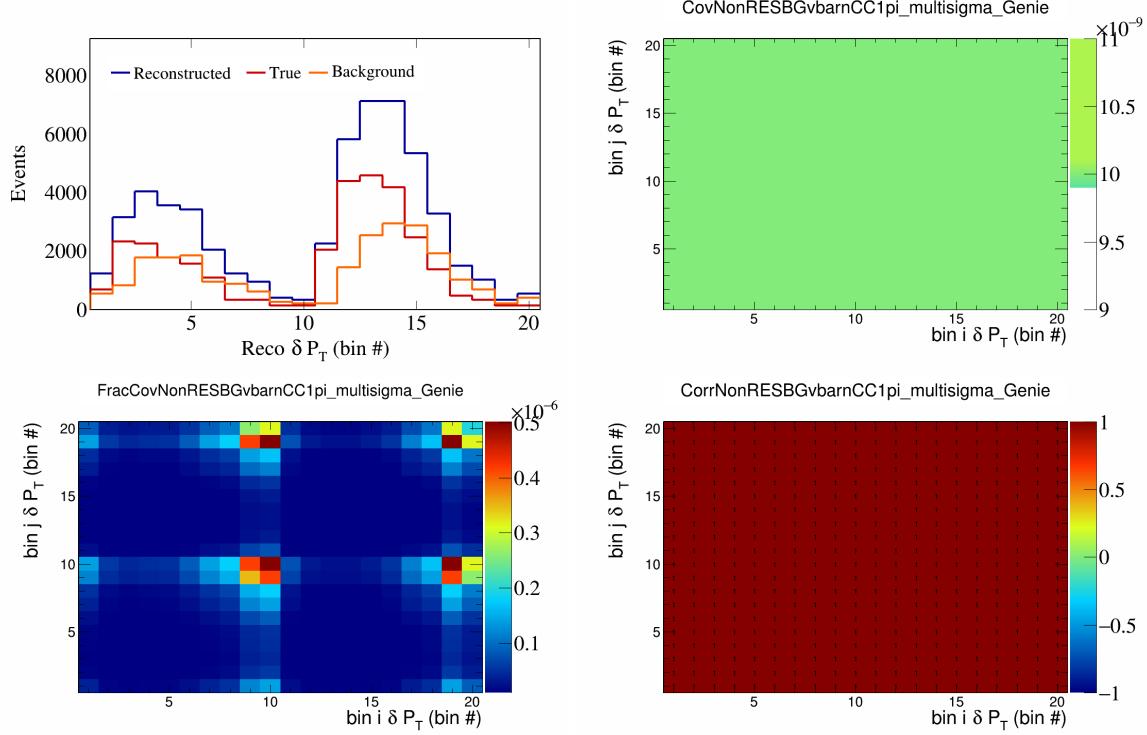


Figure 320: NonRESBGvbarCC1pi variations for δP_T in $\cos(\theta_{\vec{p}_\mu})$.

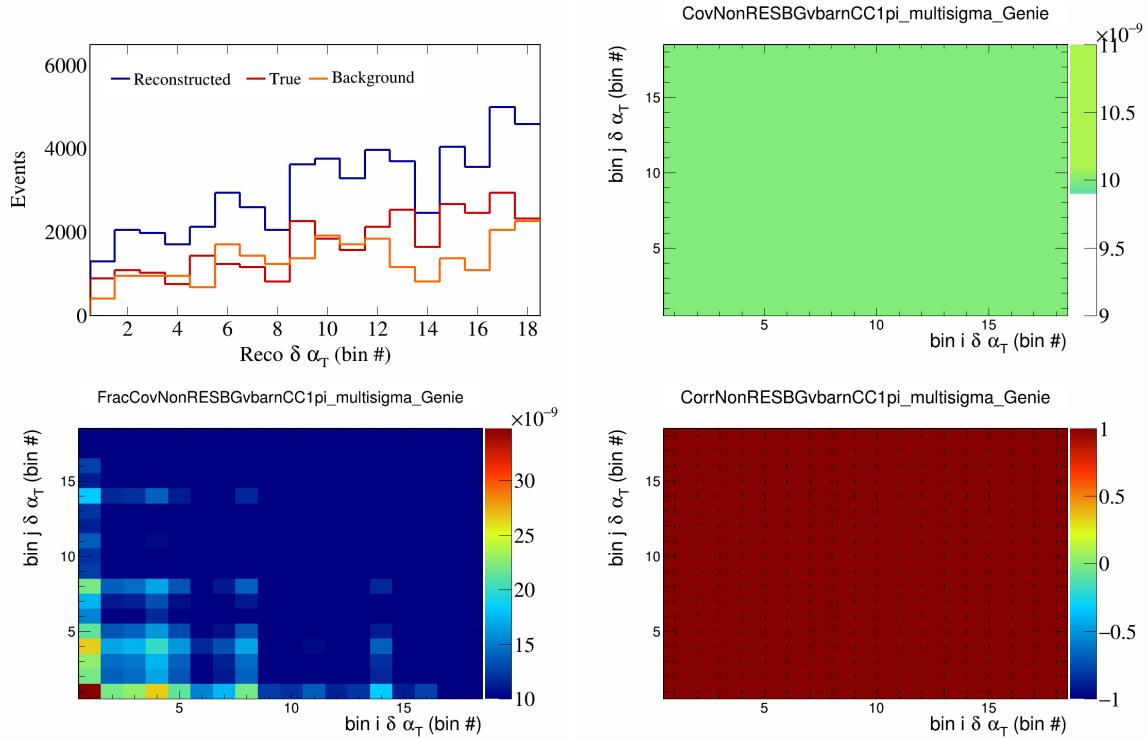


Figure 321: NonRESBGvbarCC1pi variations for $\delta\alpha_T$ in $\cos(\theta_{\vec{p}_\mu})$.

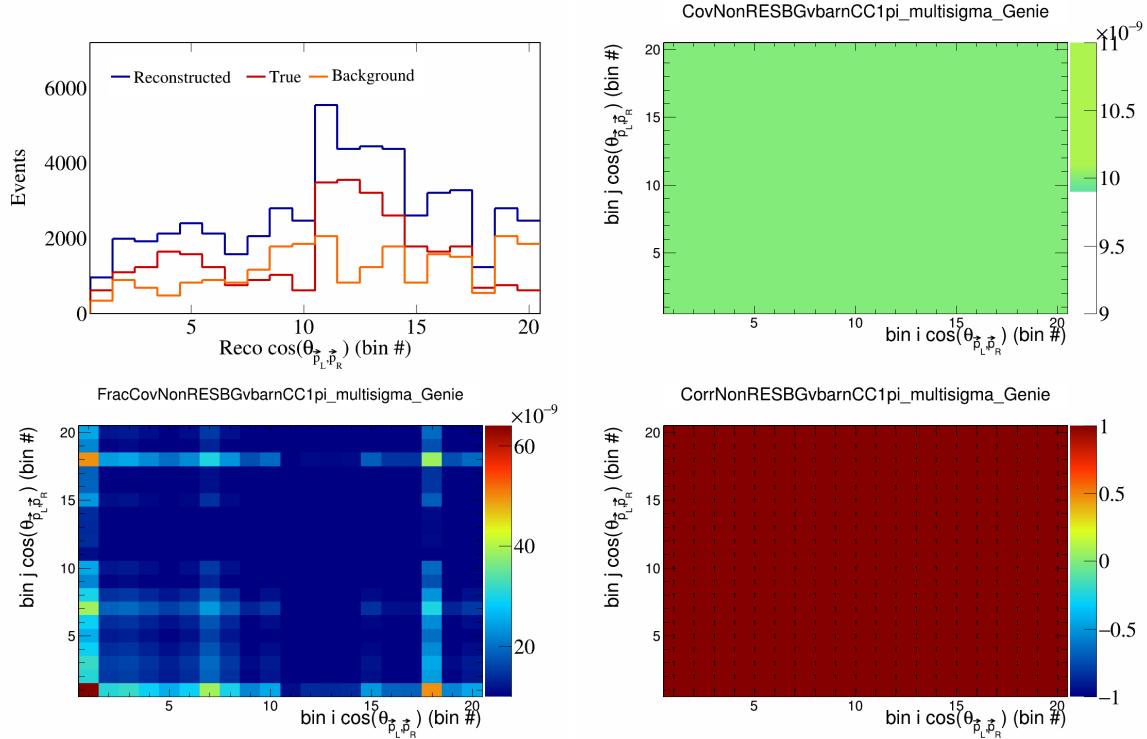


Figure 322: NonRESBGvbarCC1pi variations for $\cos(\theta_{\vec{p}_L, \vec{p}_R})$ in $\cos(\theta_{\vec{p}_\mu})$.

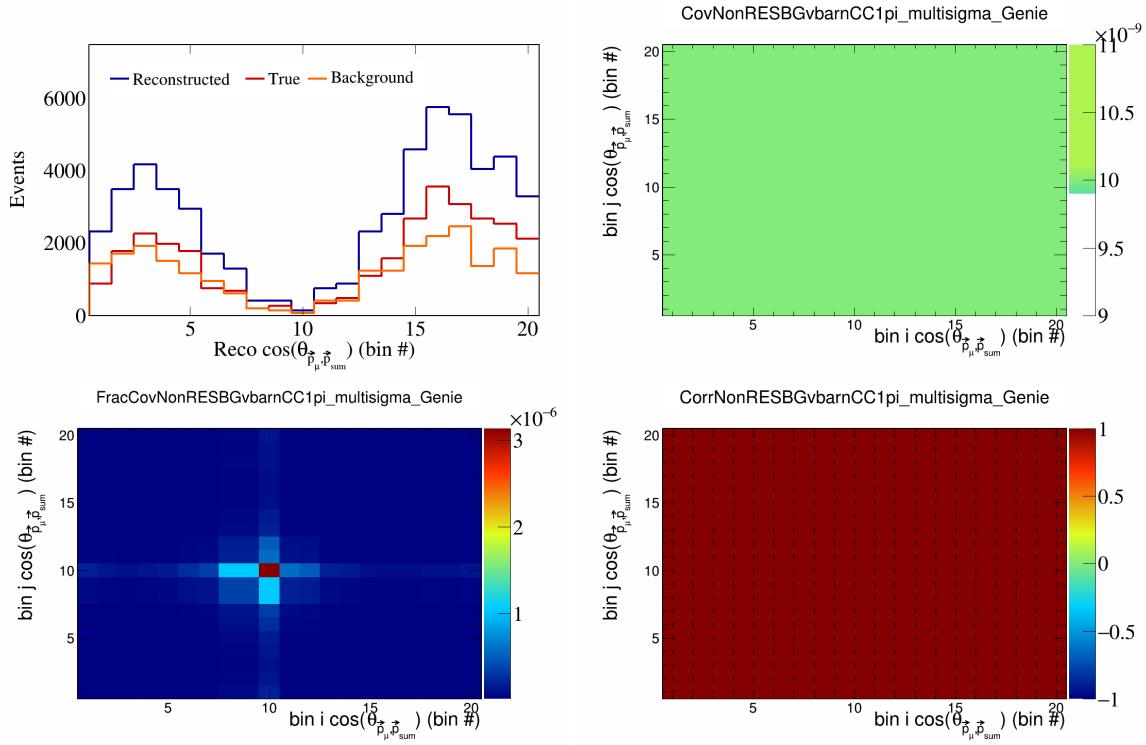


Figure 323: NonRESBGvbarCC1pi variations for $\cos(\theta_{\vec{p}_\mu, \vec{p}_{\text{sum}}})$ in $\cos(\theta_{\vec{p}_\mu})$.

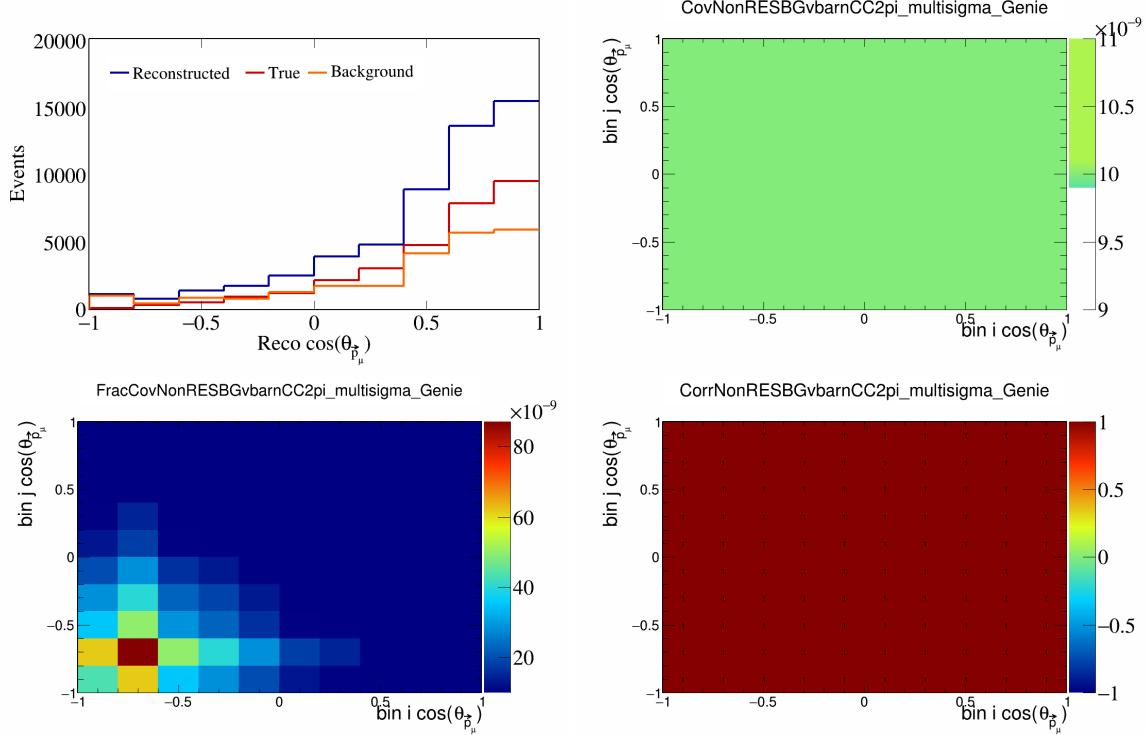


Figure 324: NonRESBGvbarCC2pi variations for $\cos(\theta_{\vec{p}_\mu})$.

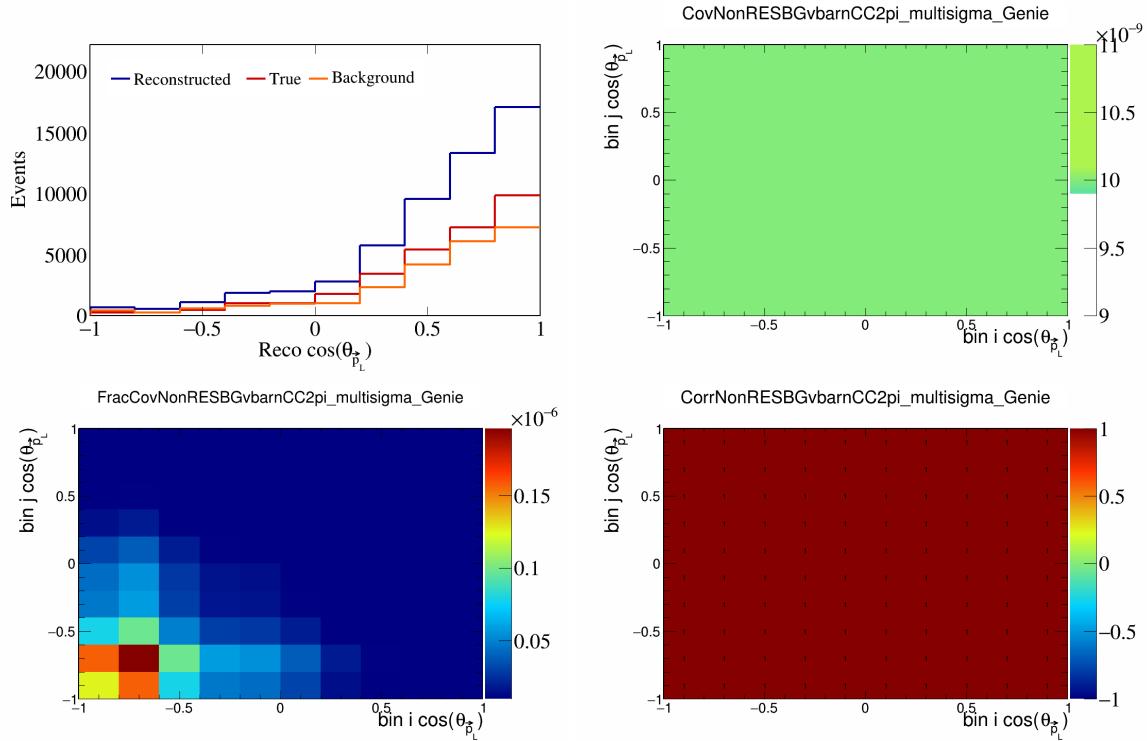


Figure 325: NonRESBGvbarCC2pi variations for $\cos(\theta_{\vec{p}_L})$.

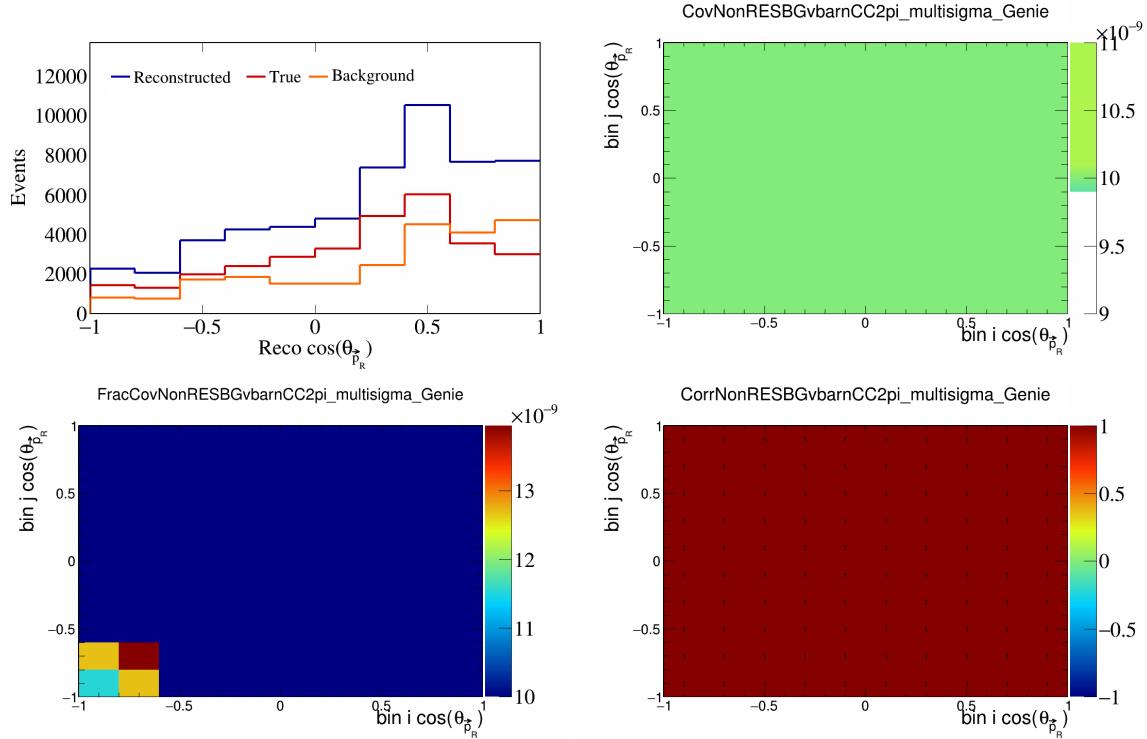


Figure 326: NonRESBGvbarCC2pi variations for $\cos(\theta_{\vec{p}_R})$.

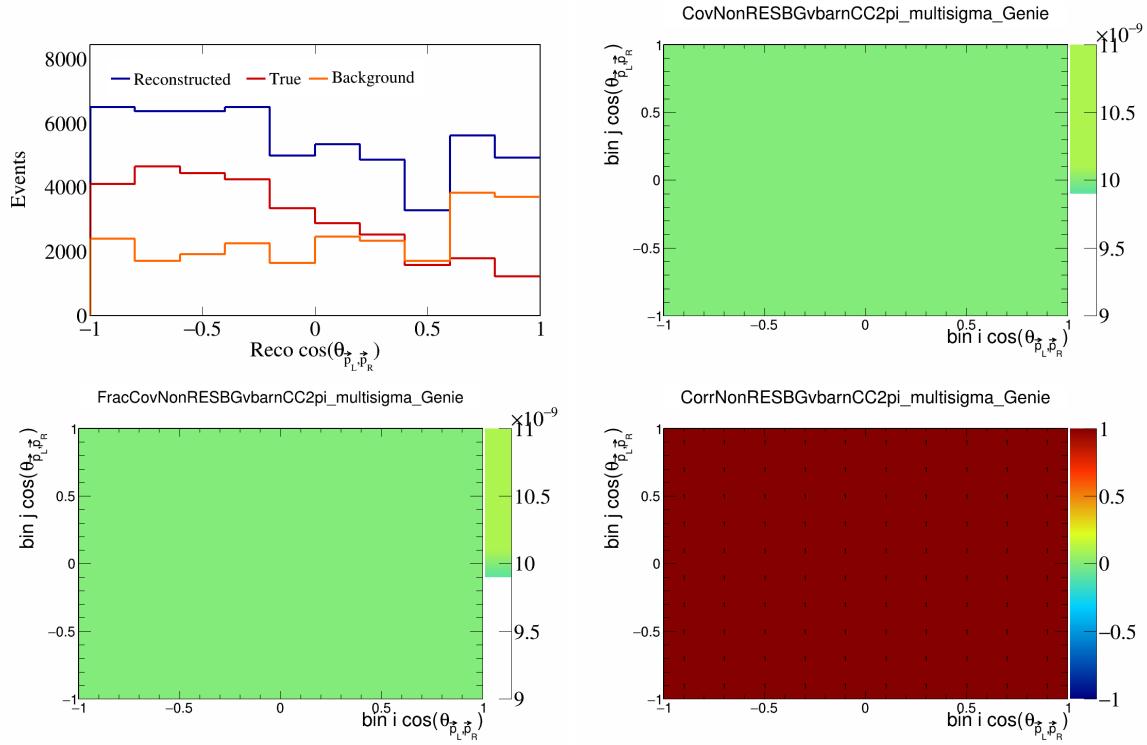


Figure 327: NonRESBGvbarCC2pi variations for $\cos(\theta_{\vec{p}_L, \vec{p}_R})$.

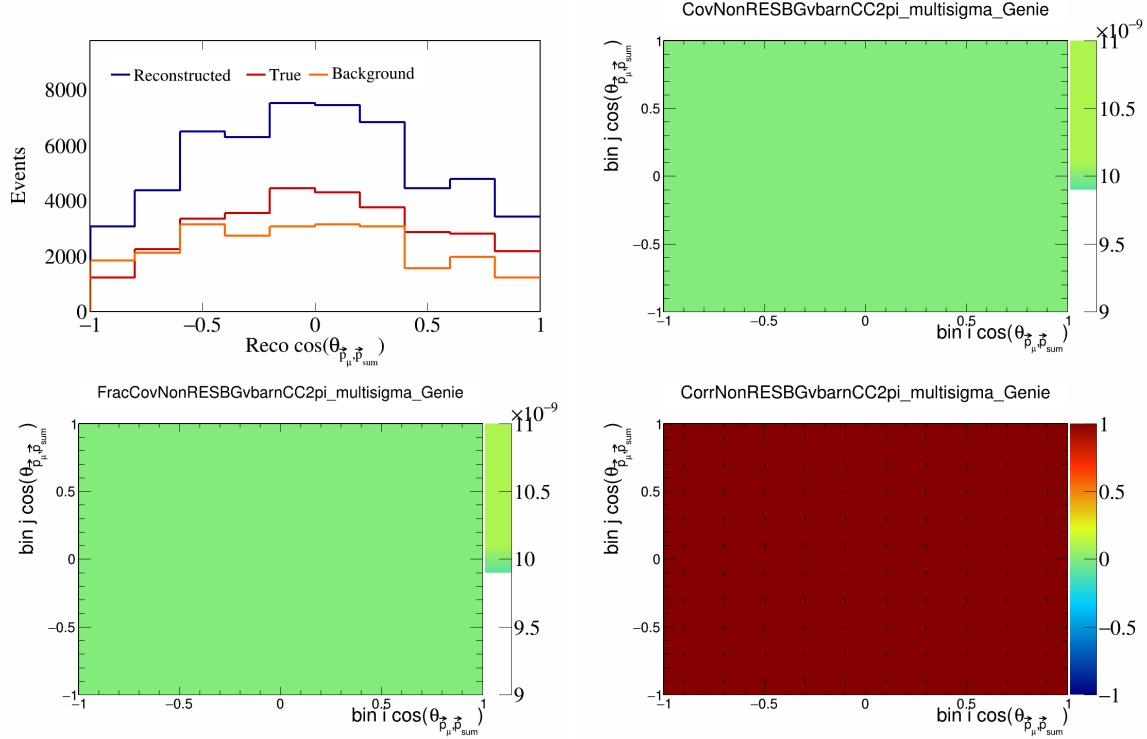


Figure 328: NonRESBGvbarCC2pi variations for $\cos(\theta_{\vec{p}_\mu, \vec{p}_{\text{sum}}})$.

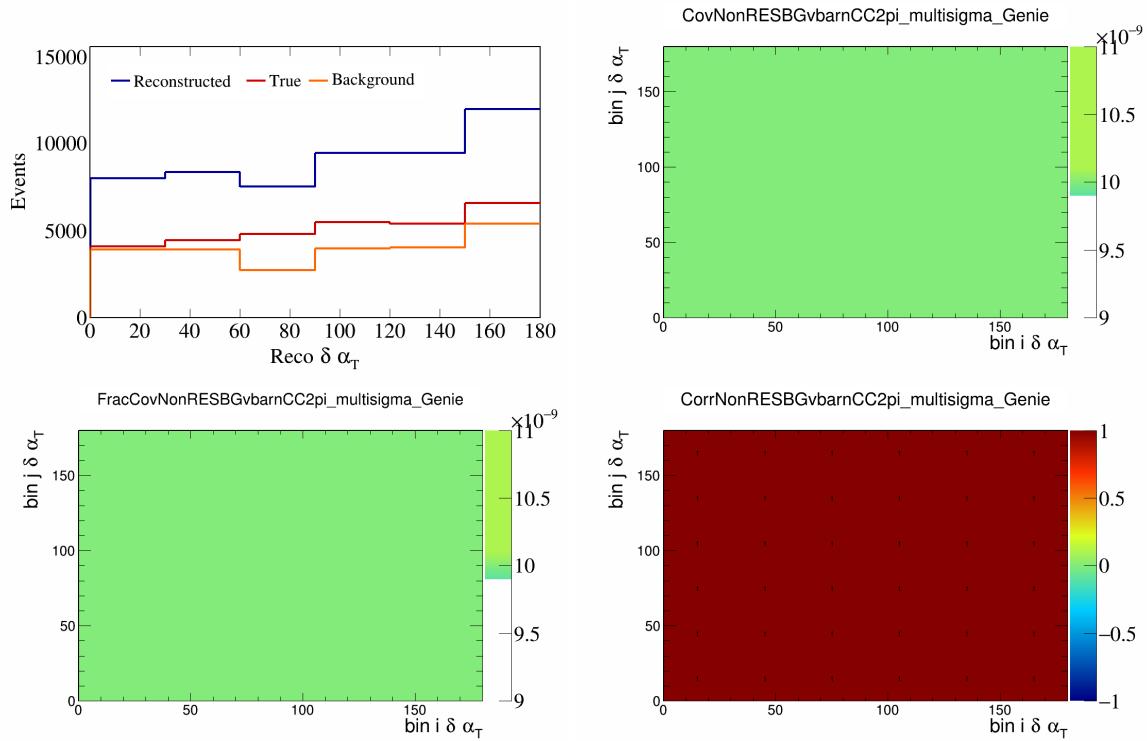


Figure 329: NonRESBGvbarCC2pi variations for $\delta\alpha_T$.

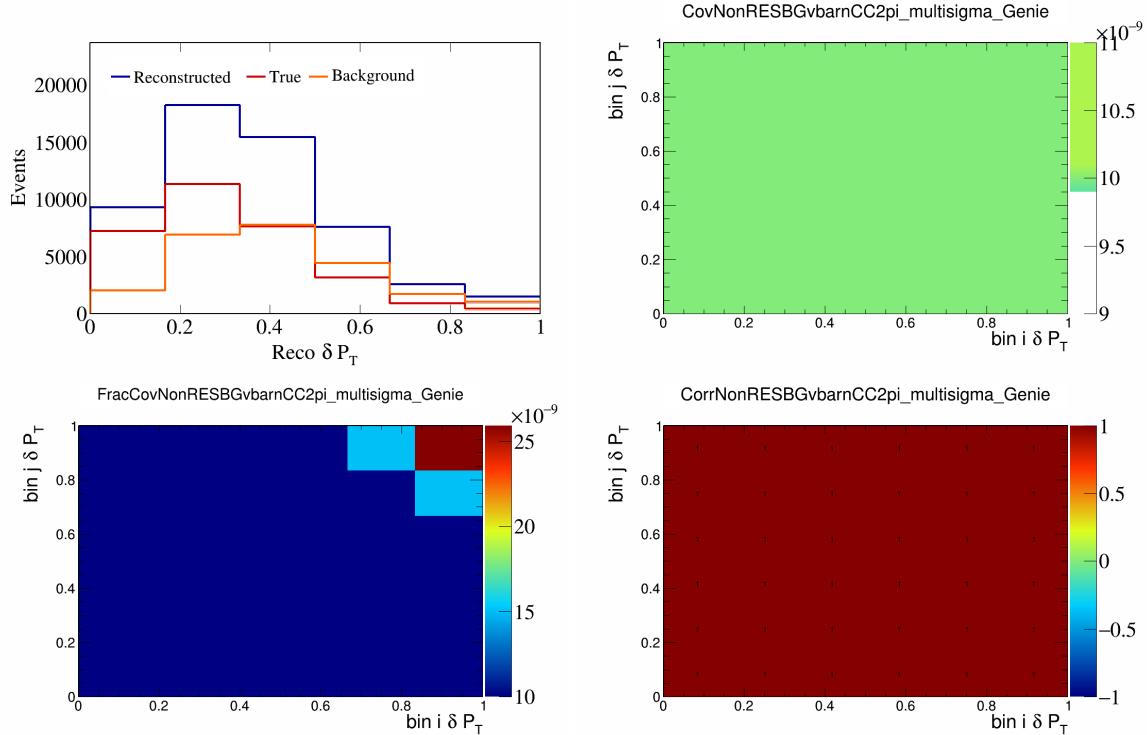


Figure 330: NonRESBGvbarCC2pi variations for δP_T .

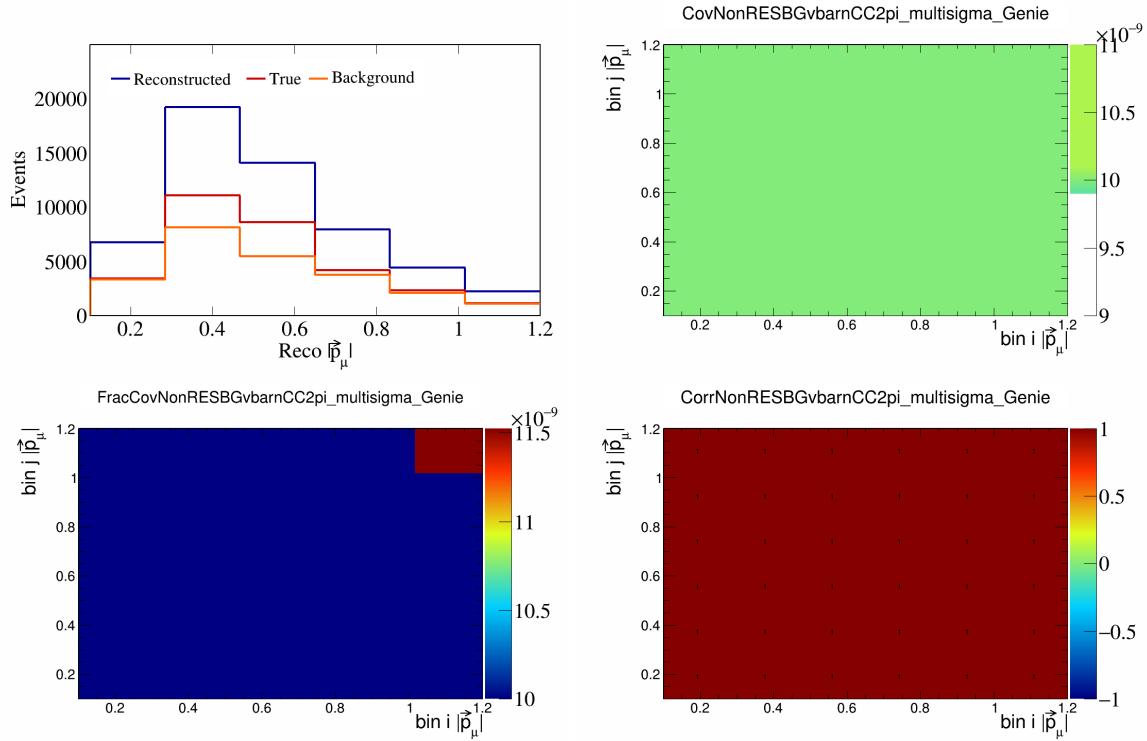


Figure 331: NonRESBGvbarCC2pi variations for $|\vec{p}_\mu|$.

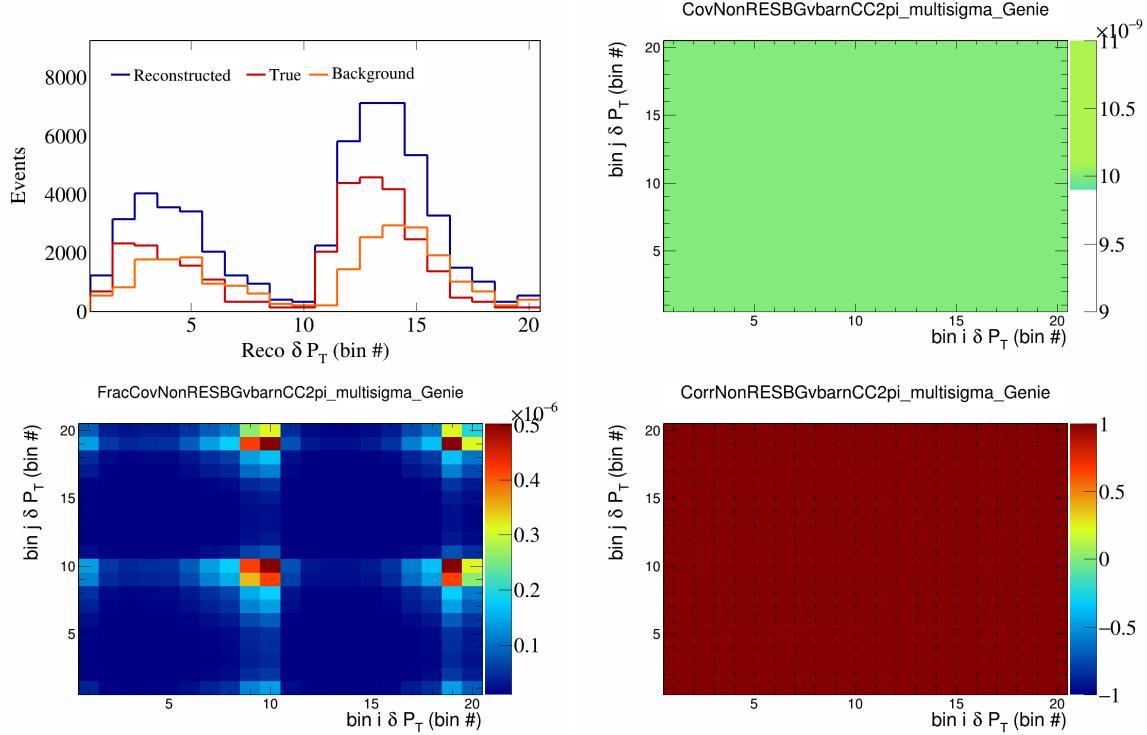


Figure 332: NonRESBGvbarCC2pi variations for δP_T in $\cos(\theta_{\vec{p}_\mu})$.

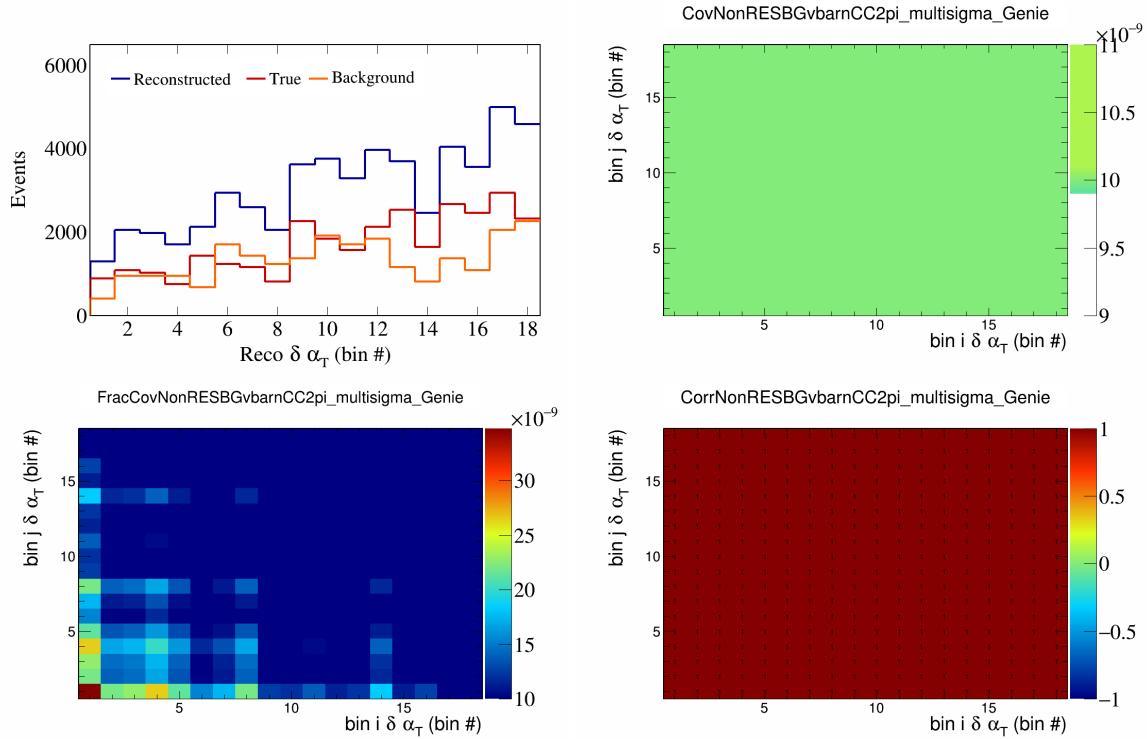


Figure 333: NonRESBGvbarCC2pi variations for $\delta\alpha_T$ in $\cos(\theta_{\vec{p}_\mu})$.

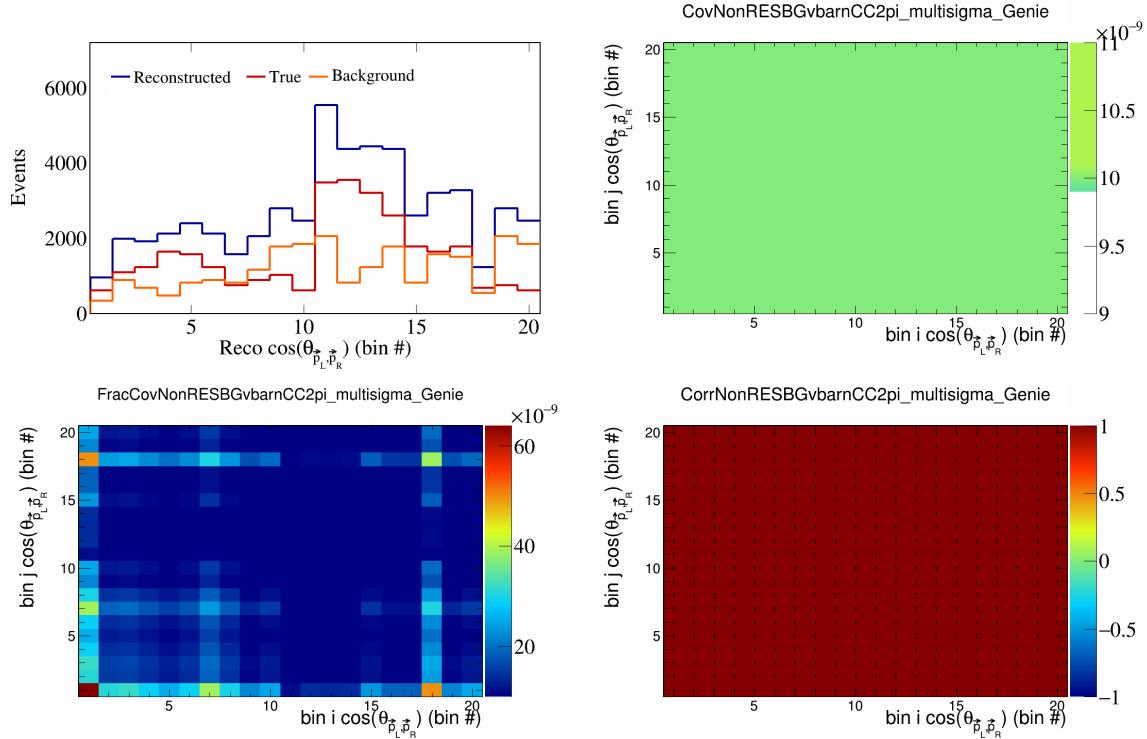


Figure 334: NonRESBGvbarCC2pi variations for $\cos(\theta_{\vec{p}_L, \vec{p}_R})$ in $\cos(\theta_{\vec{p}_\mu})$.

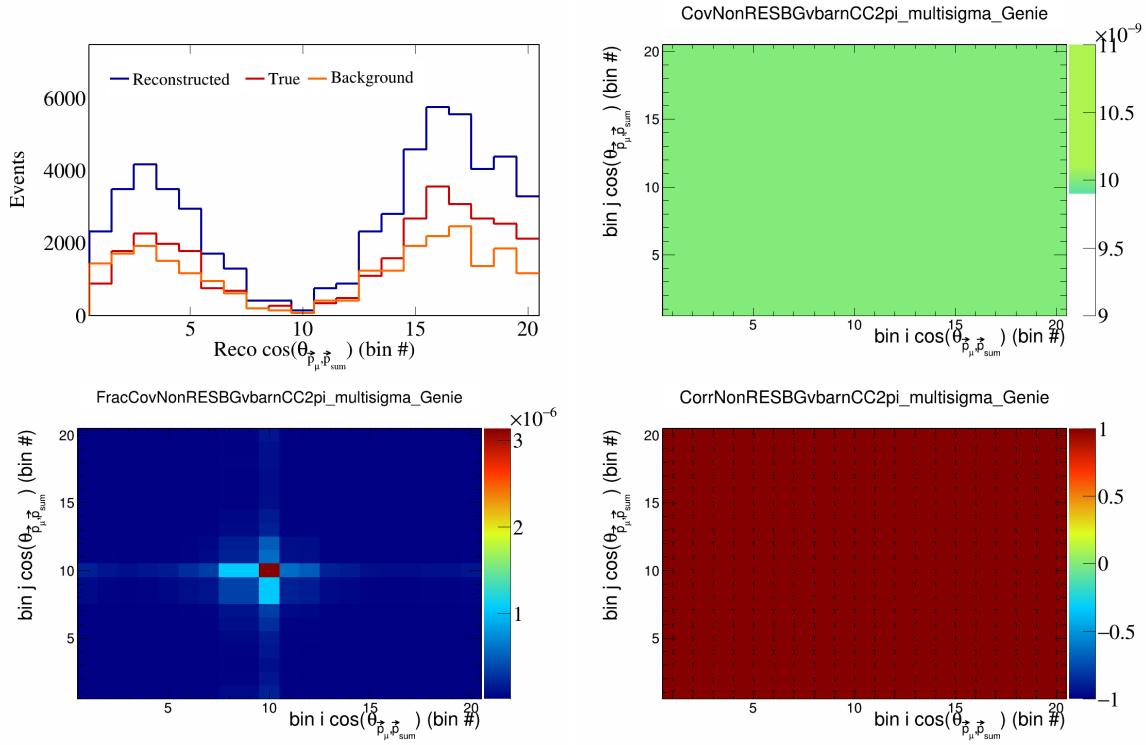


Figure 335: NonRESBGvbarCC2pi variations for $\cos(\theta_{\vec{p}_\mu})$ in $\cos(\theta_{\vec{p}_\mu})$.

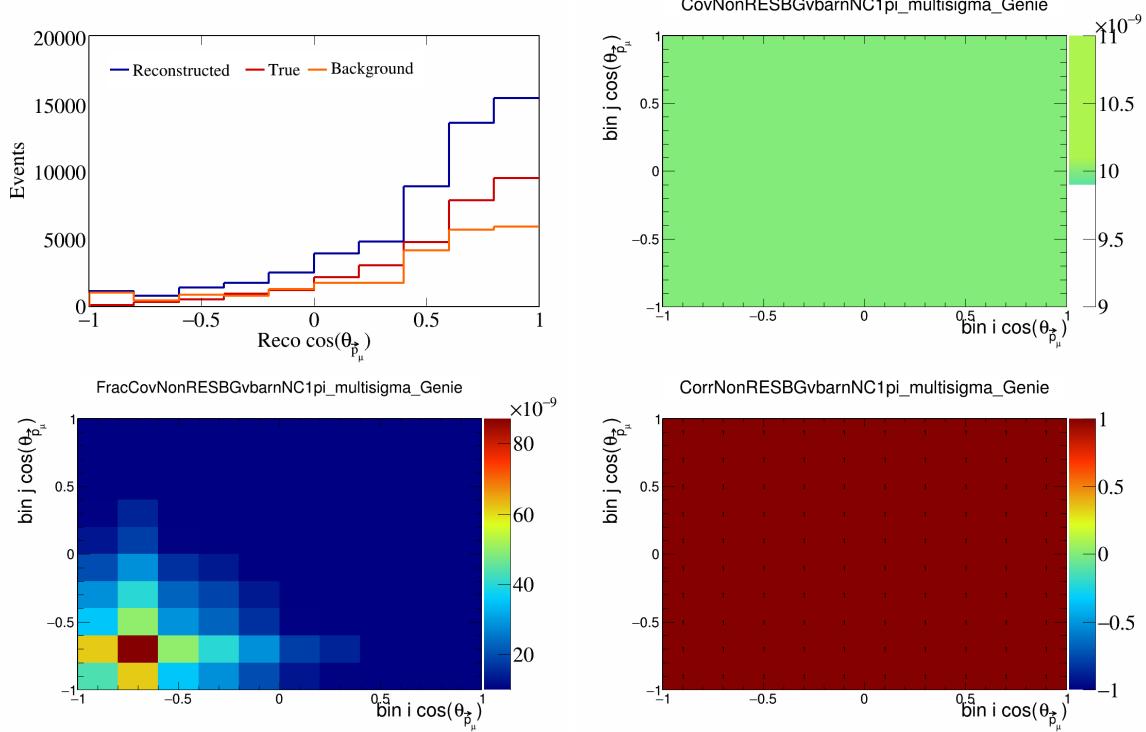


Figure 336: NonRESBGvbarNC1pi variations for $\cos(\theta_{\vec{p}_\mu})$.

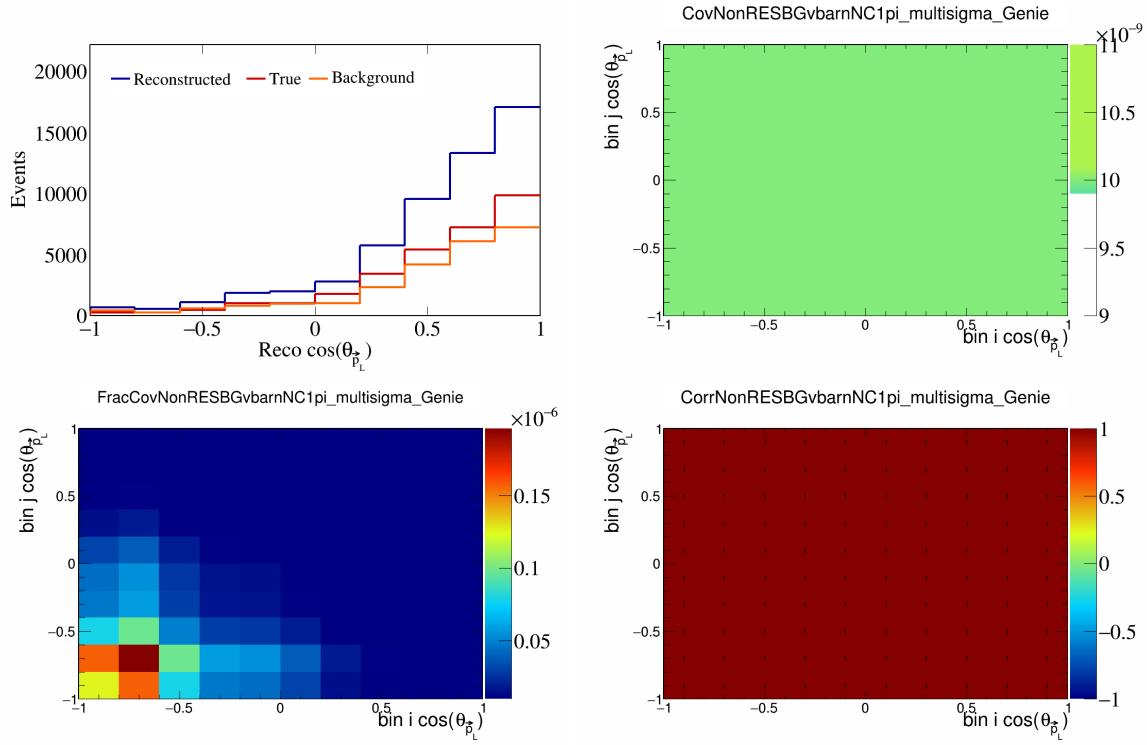


Figure 337: NonRESBGvbarNC1pi variations for $\cos(\theta_{\vec{p}_L})$.

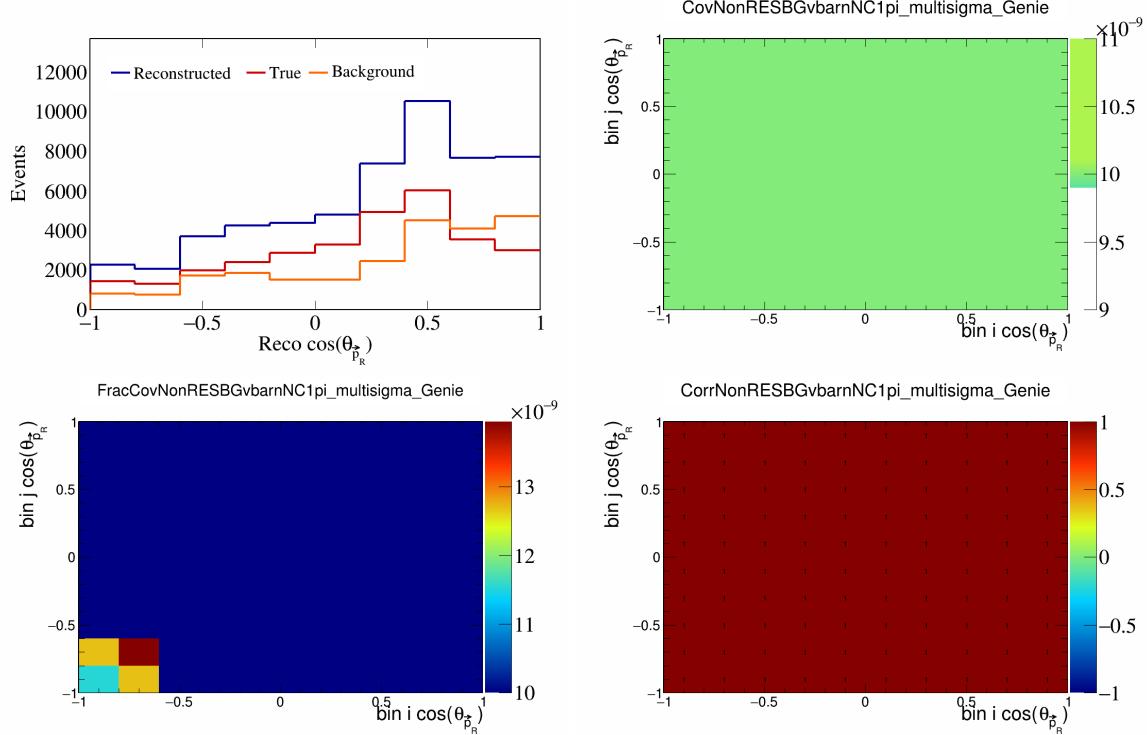


Figure 338: NonRESBGvbarNC1pi variations for $\cos(\theta_{\vec{p}_R})$.

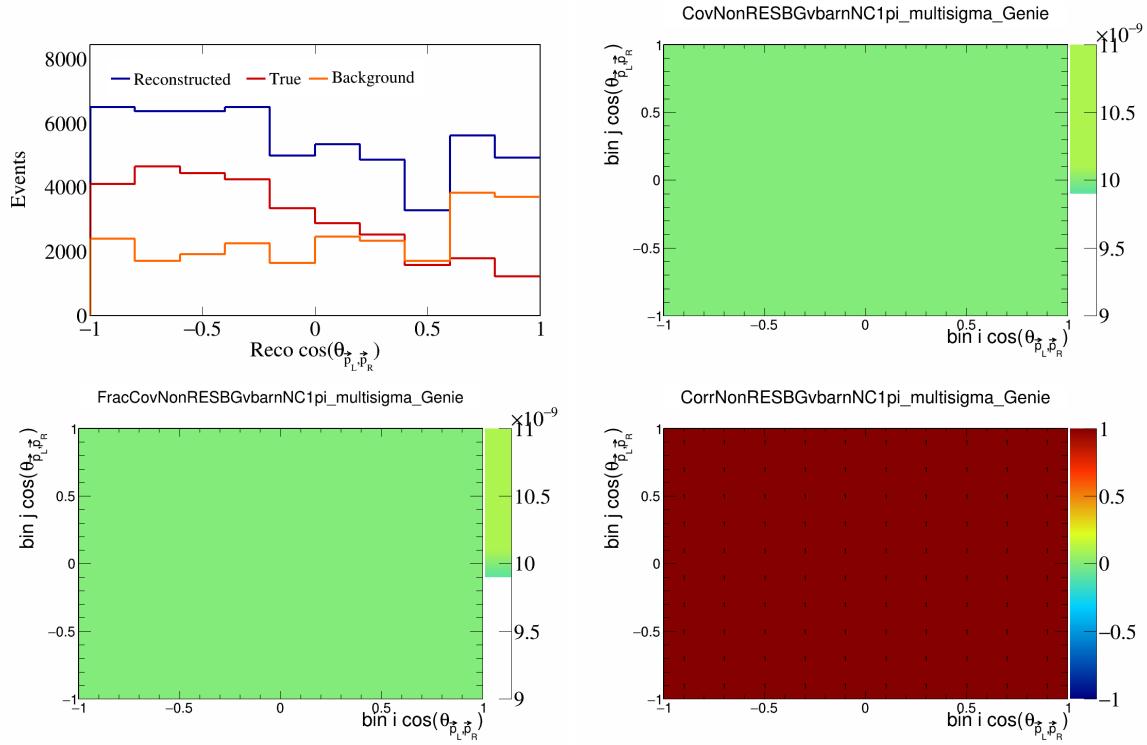


Figure 339: NonRESBGvbarNC1pi variations for $\cos(\theta_{\vec{p}_L, \vec{p}_R})$.

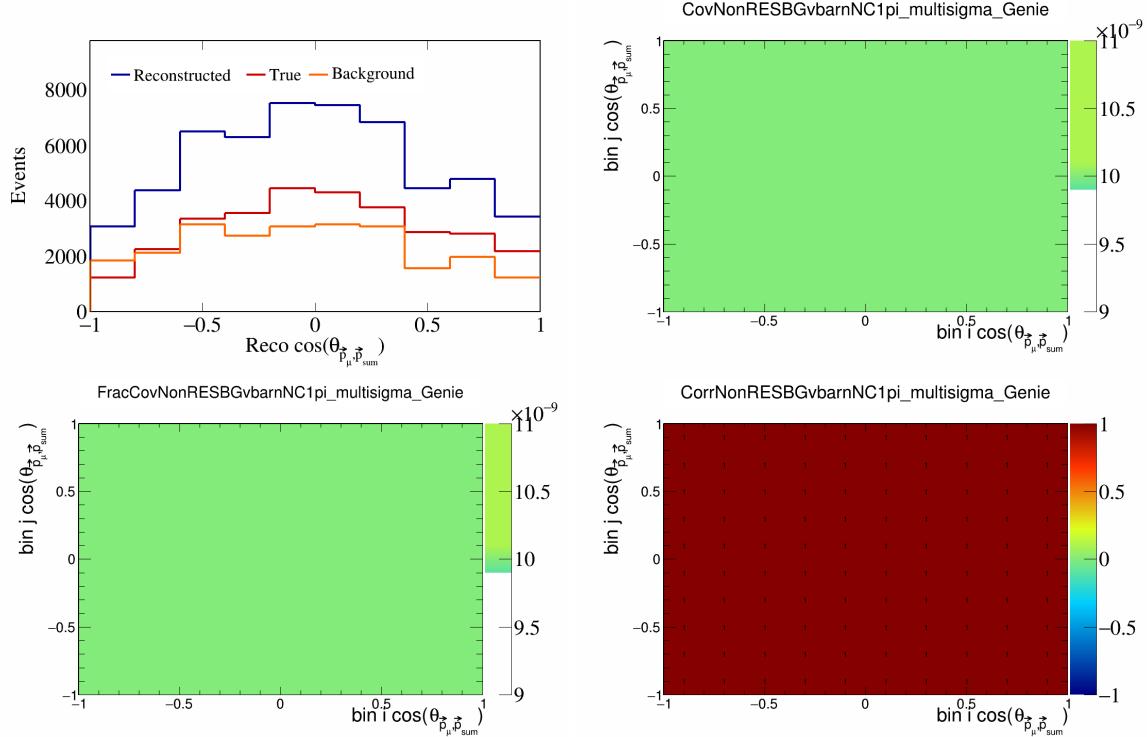


Figure 340: NonRESBGvbarNC1pi variations for $\cos(\theta_{\vec{p}_\mu, \vec{p}_{\text{sum}}})$.

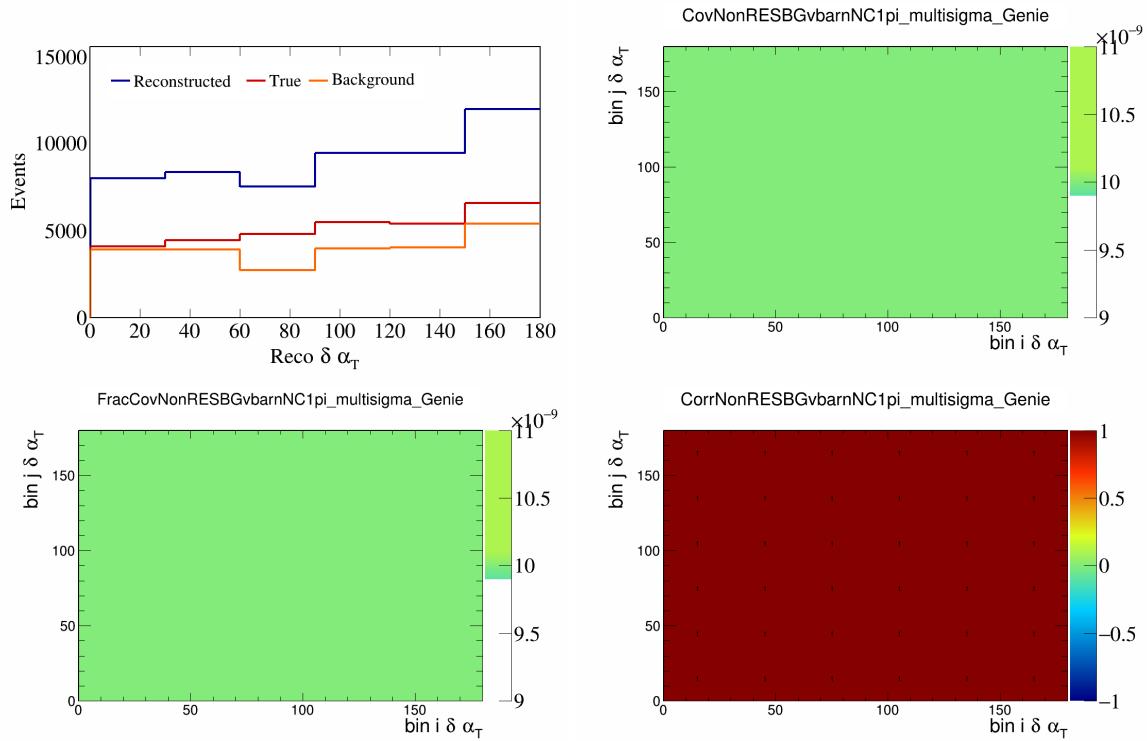


Figure 341: NonRESBGvbarNC1pi variations for $\delta\alpha_T$.

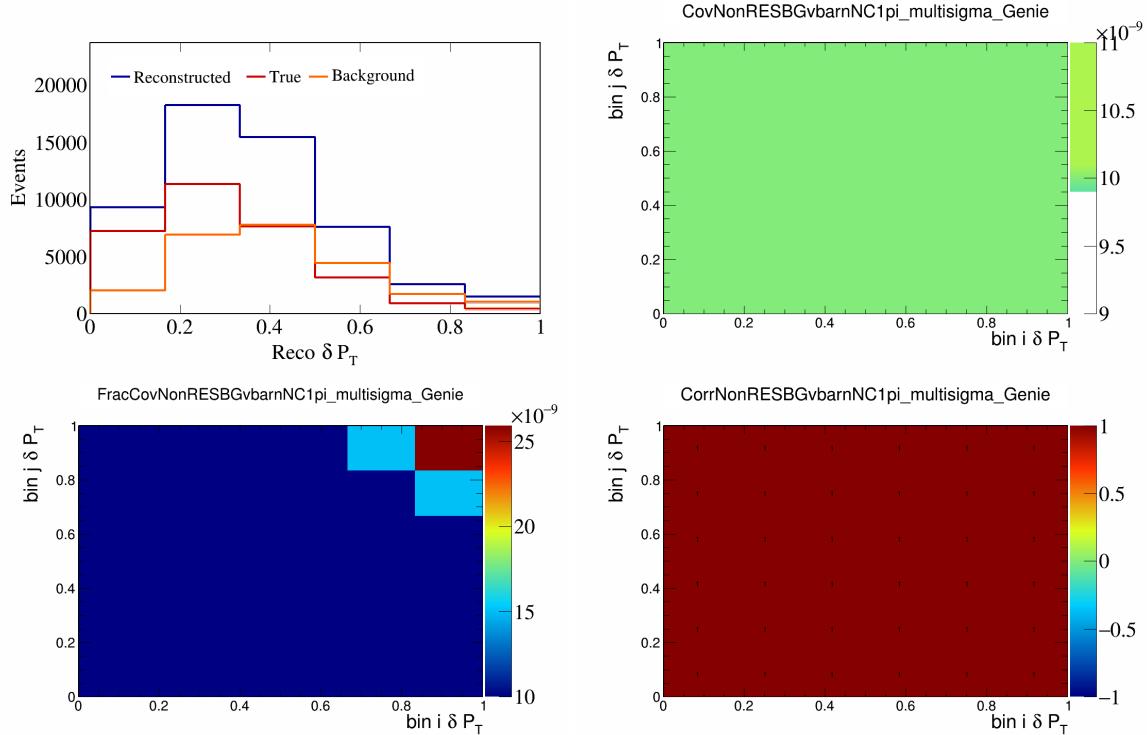


Figure 342: NonRESBGvbarNC1pi variations for δP_T .

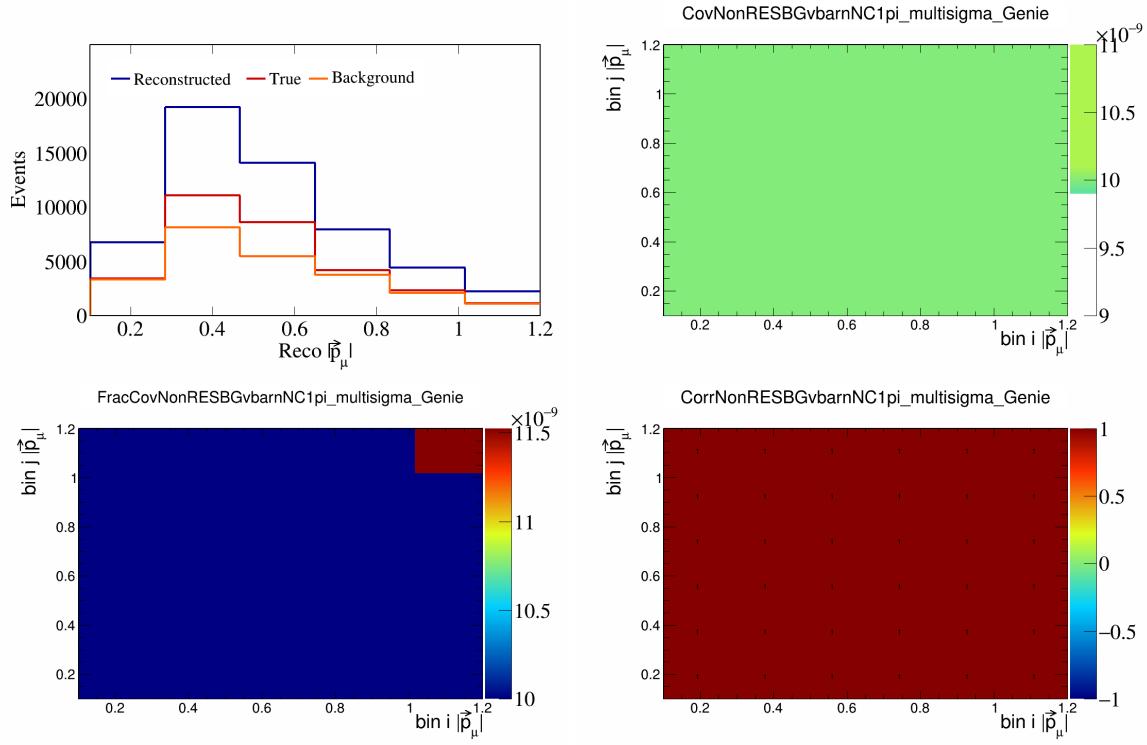


Figure 343: NonRESBGvbarNC1pi variations for $|\vec{p}_\mu|$.

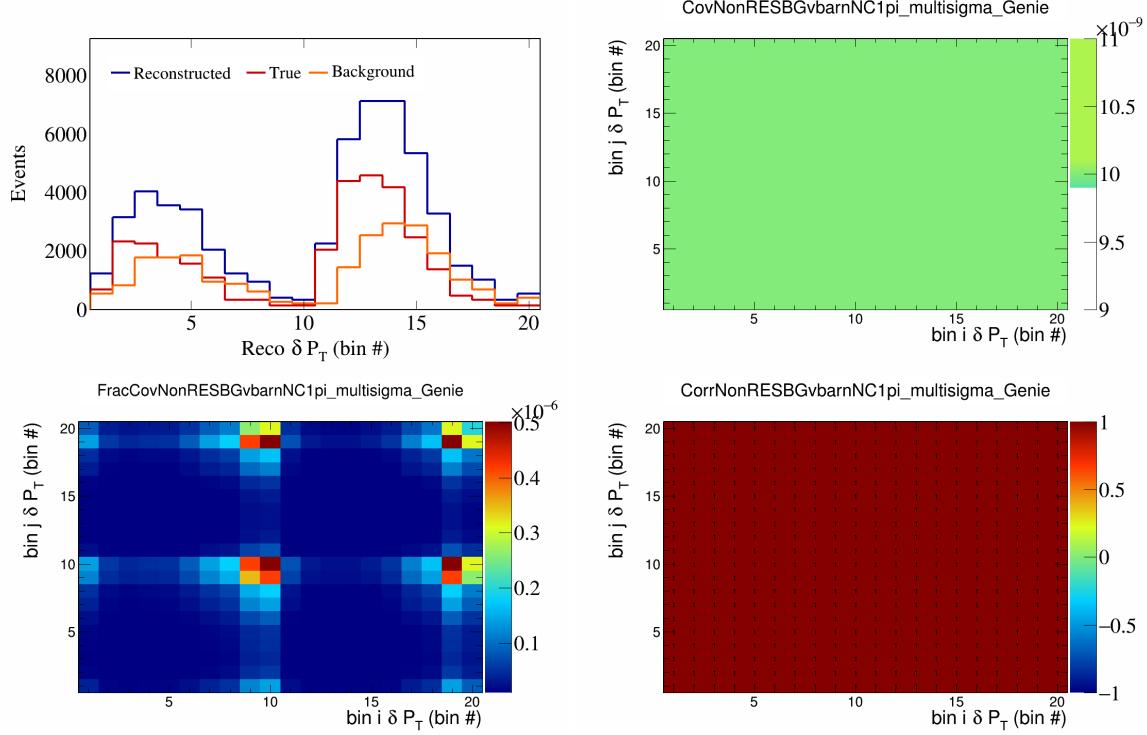


Figure 344: NonRESBGvbarNC1pi variations for δP_T in $\cos(\theta_{\vec{p}_\mu})$.

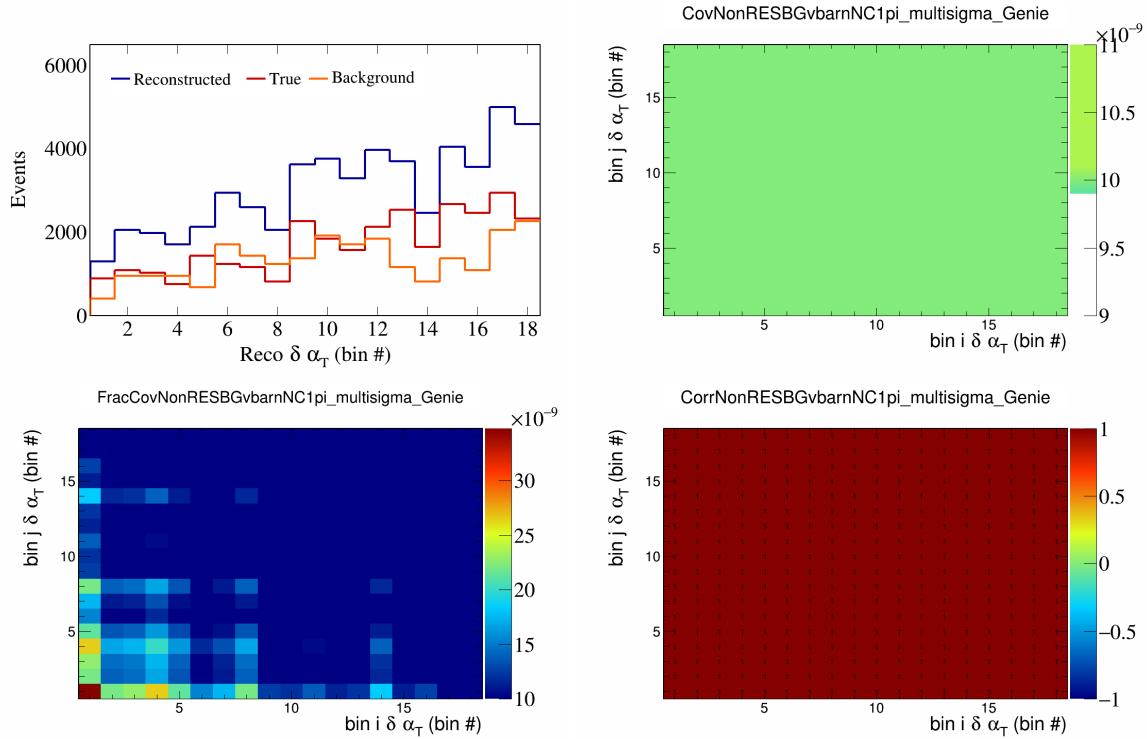


Figure 345: NonRESBGvbarNC1pi variations for $\delta\alpha_T$ in $\cos(\theta_{\vec{p}_\mu})$.

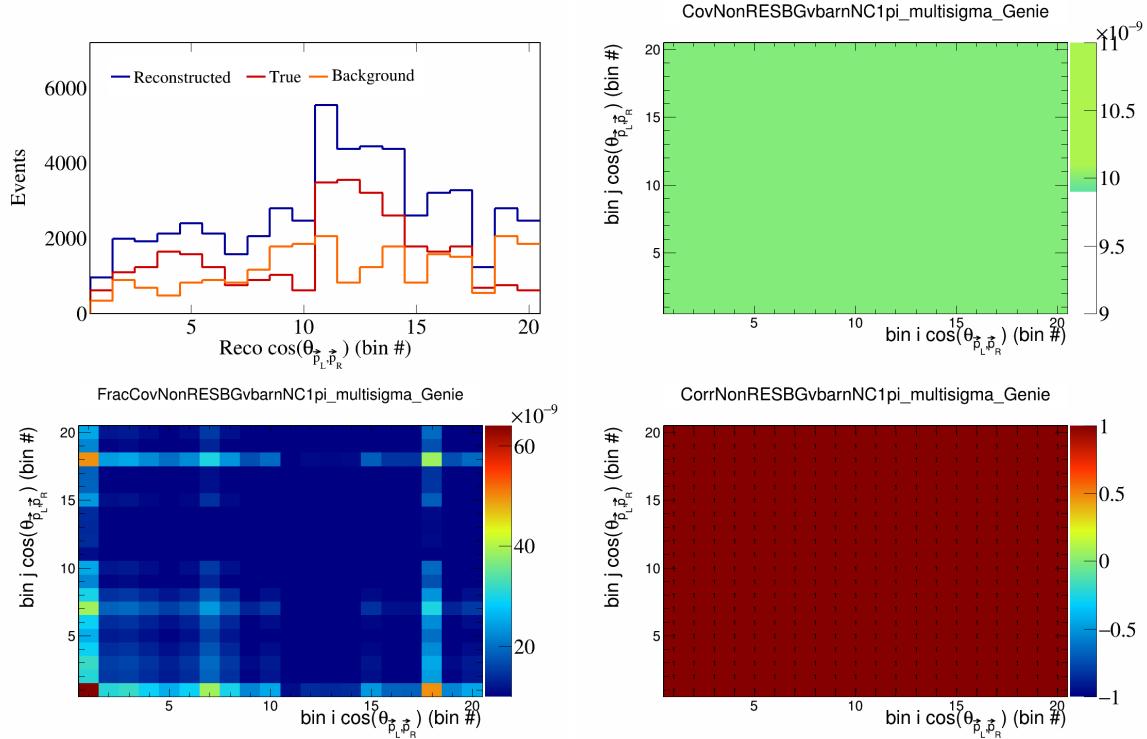


Figure 346: NonRESBGvbarNC1pi variations for $\cos(\theta_{\vec{p}_L, \vec{p}_R})$ in $\cos(\theta_{\vec{p}_\mu})$.

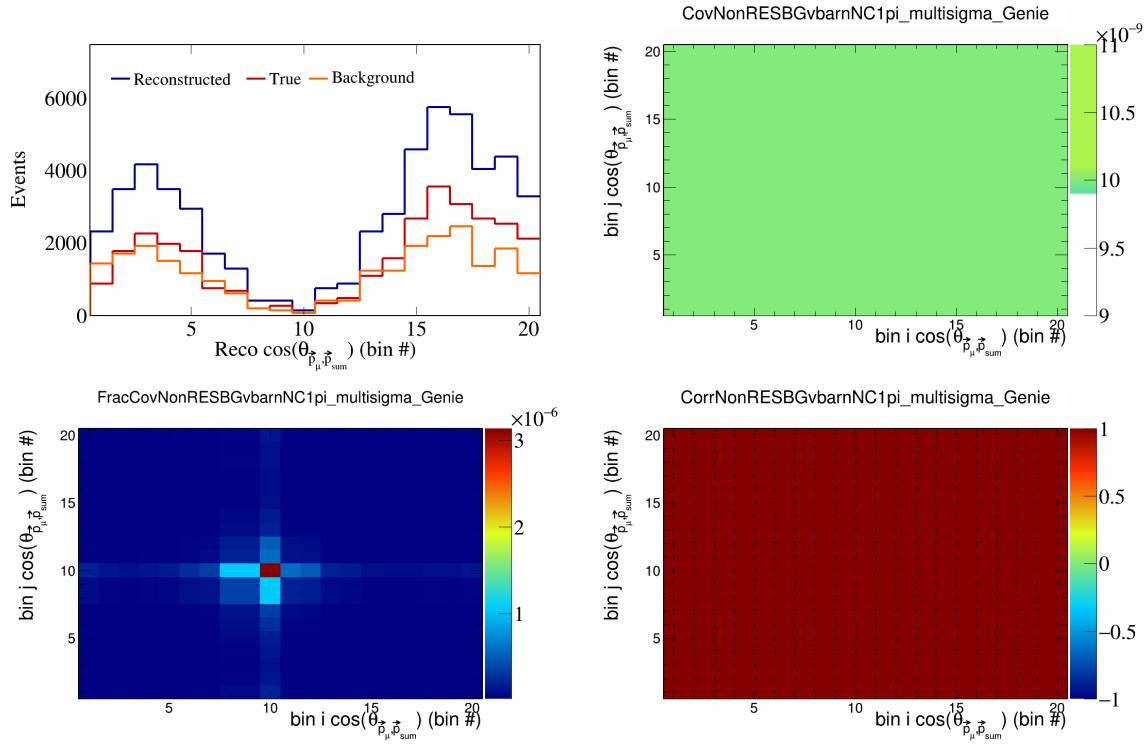


Figure 347: NonRESBGvbarNC1pi variations for $\cos(\theta_{\vec{p}_\mu, \vec{p}_{\text{sum}}})$ in $\cos(\theta_{\vec{p}_\mu})$.

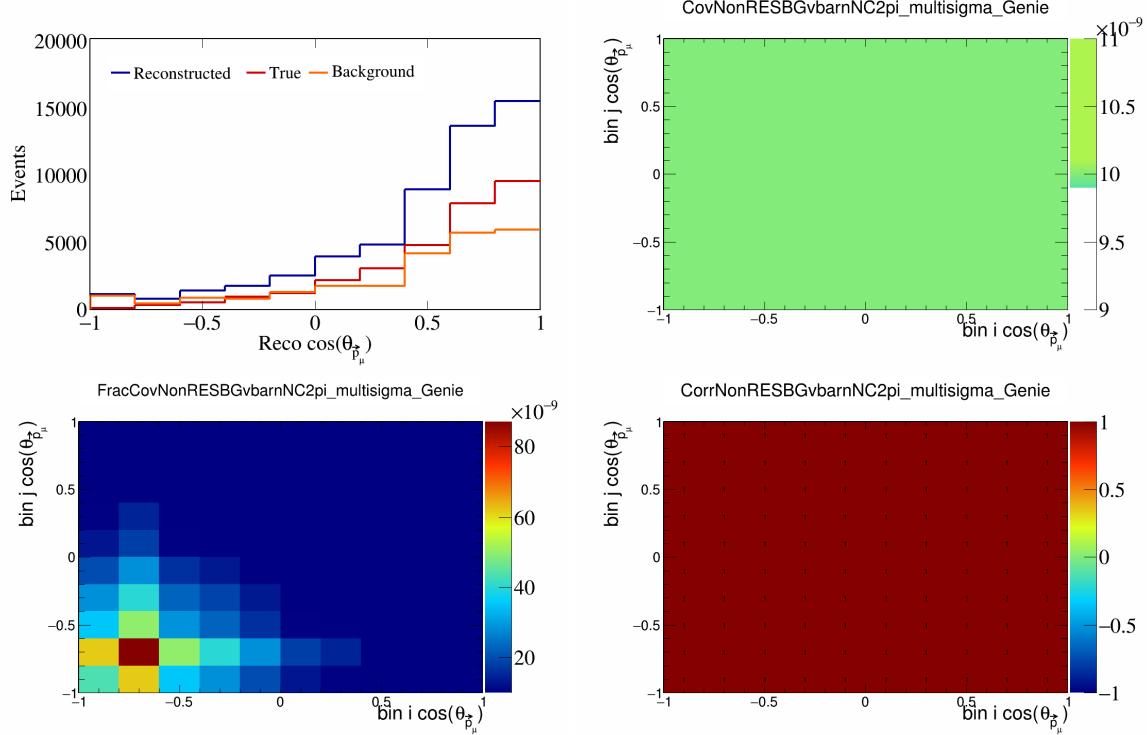


Figure 348: NonRESBGvbarNC2pi variations for $\cos(\theta_{\vec{p}_\mu})$.

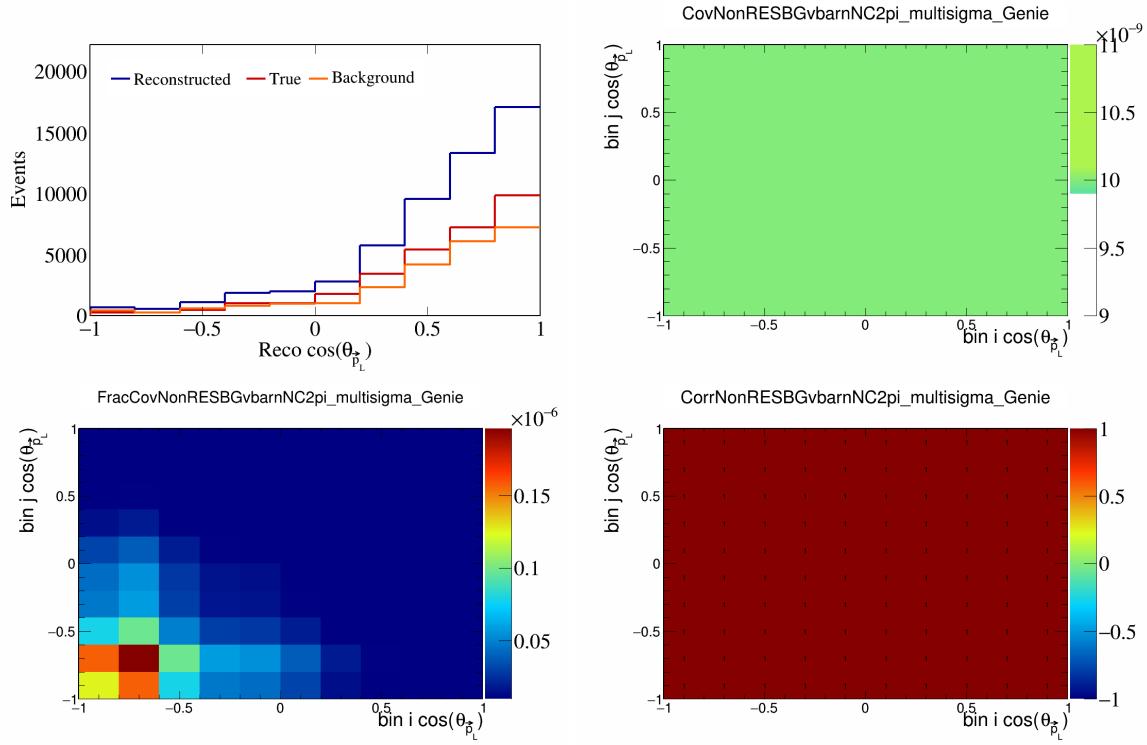


Figure 349: NonRESBGvbarNC2pi variations for $\cos(\theta_{\vec{p}_L})$.

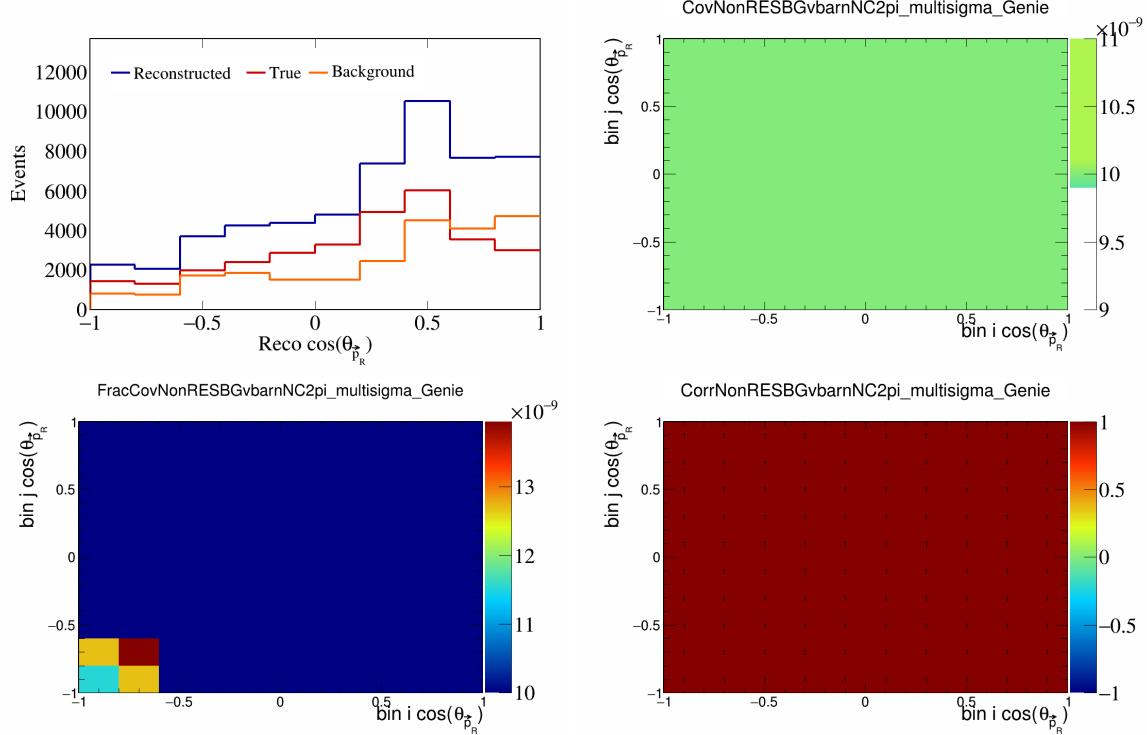


Figure 350: NonRESBGvbarNC2pi variations for $\cos(\theta_{\vec{p}_R})$.

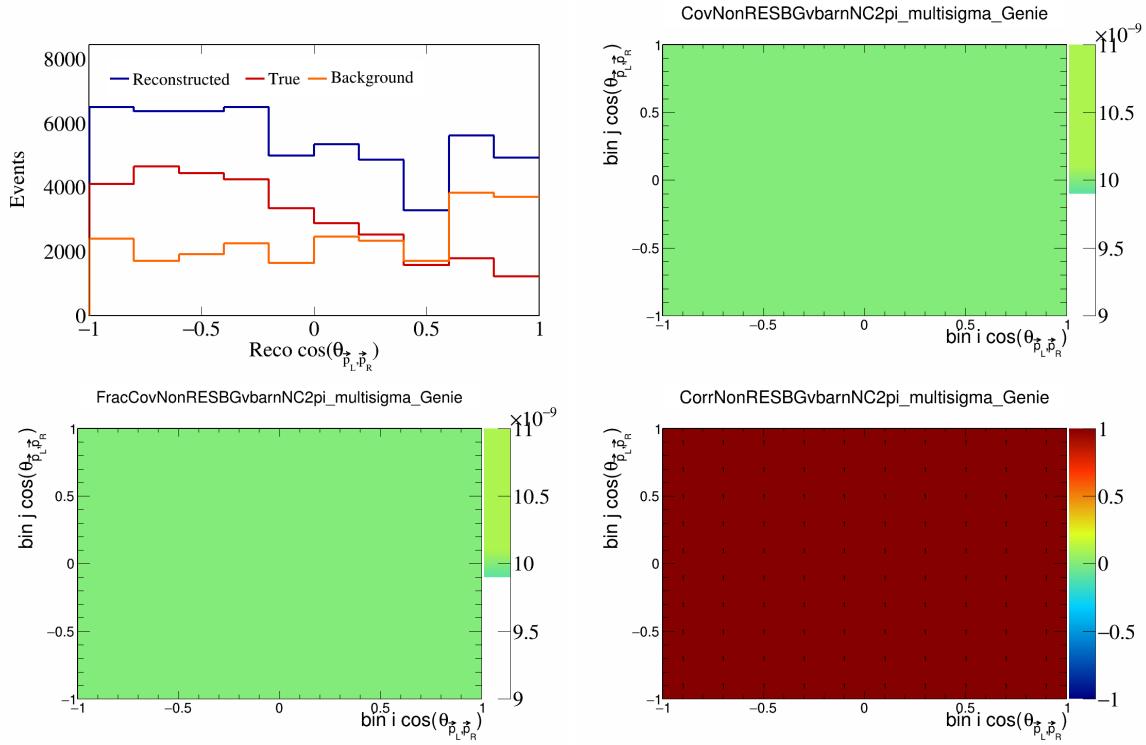


Figure 351: NonRESBGvbarNC2pi variations for $\cos(\theta_{\vec{p}_L, \vec{p}_R})$.

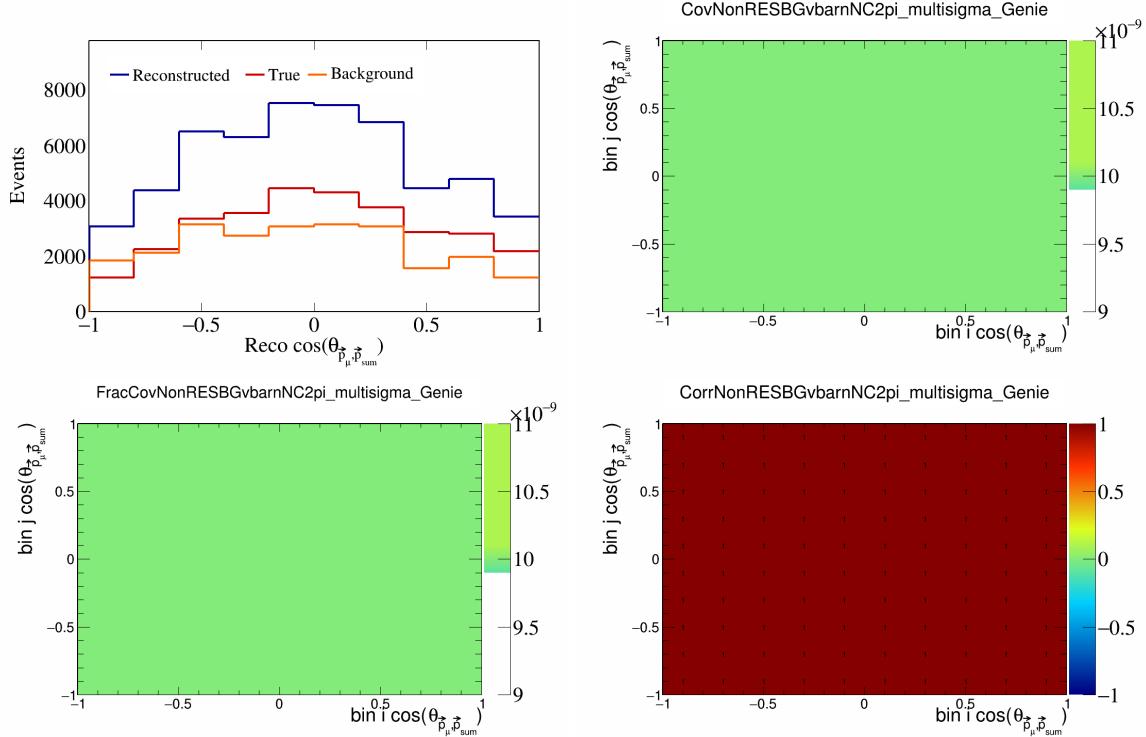


Figure 352: NonRESBGvbarNC2pi variations for $\cos(\theta_{\vec{p}_\mu, \vec{p}_{\text{sum}}})$.

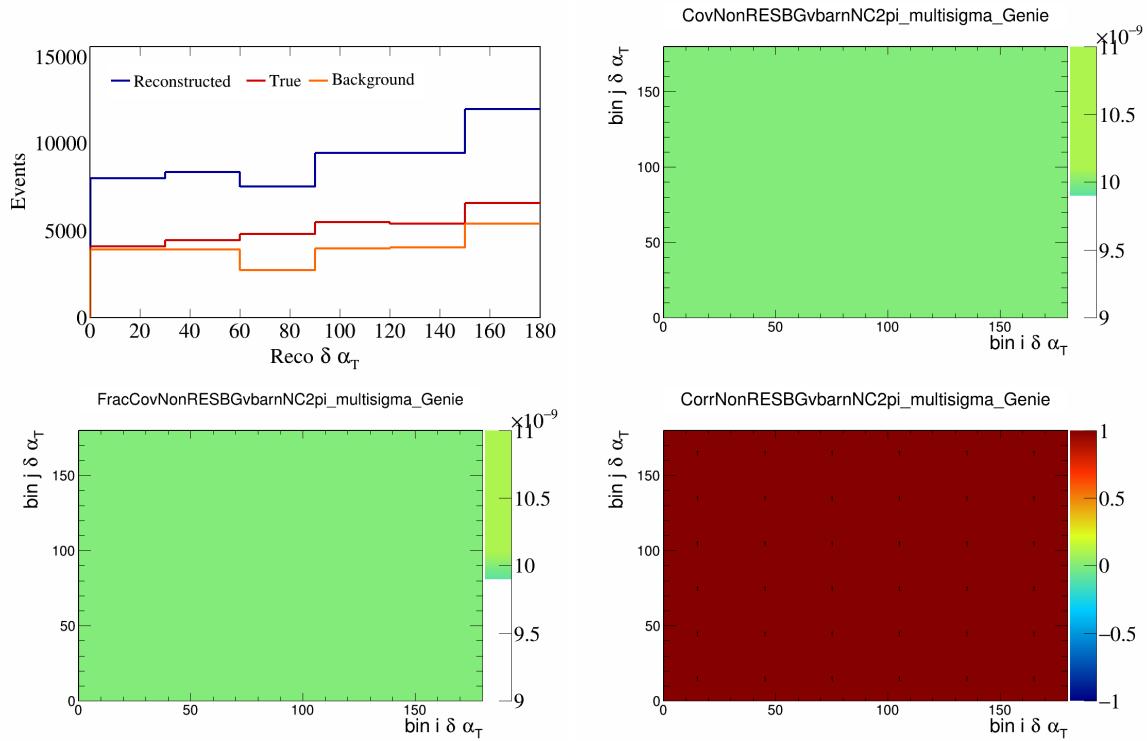


Figure 353: NonRESBGvbarNC2pi variations for $\delta\alpha_T$.

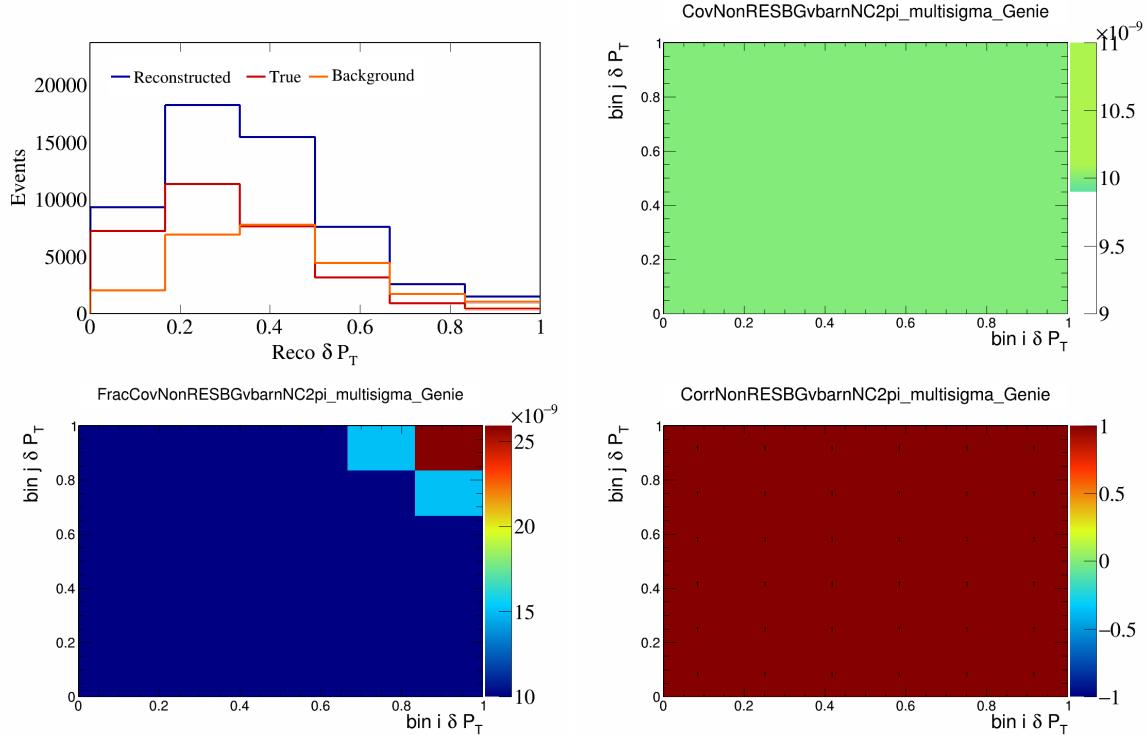


Figure 354: NonRESBGvbarNC2pi variations for δP_T .

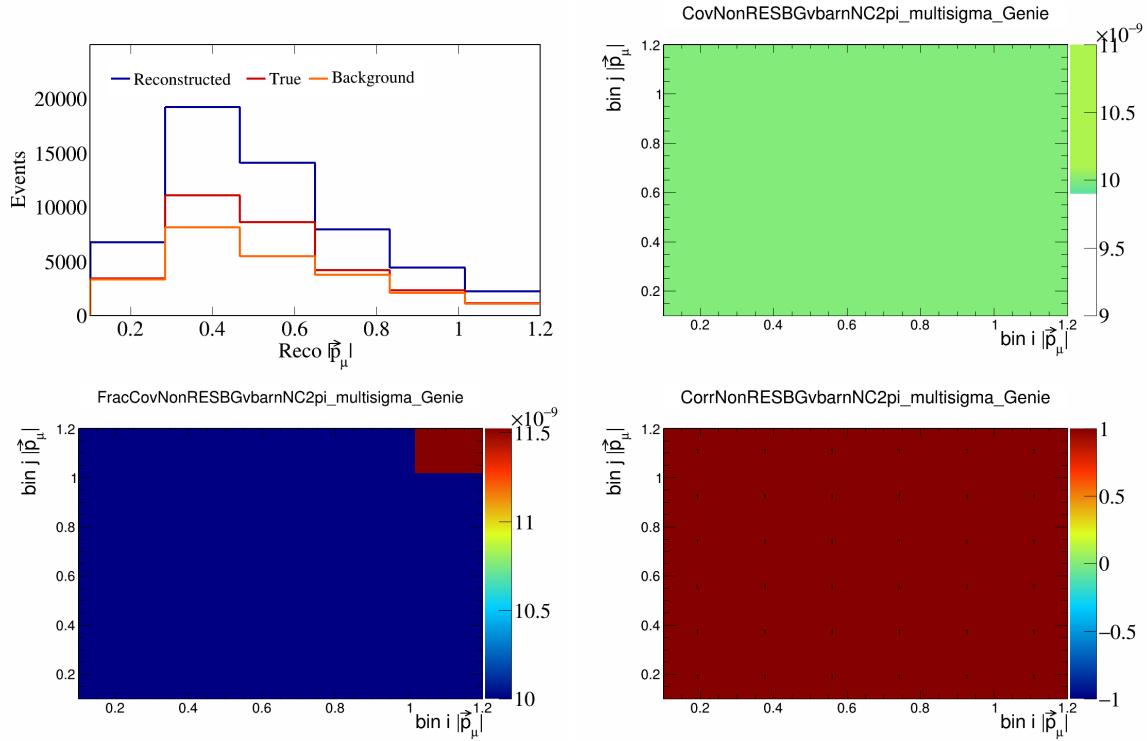


Figure 355: NonRESBGvbarNC2pi variations for $|\vec{p}_\mu|$.

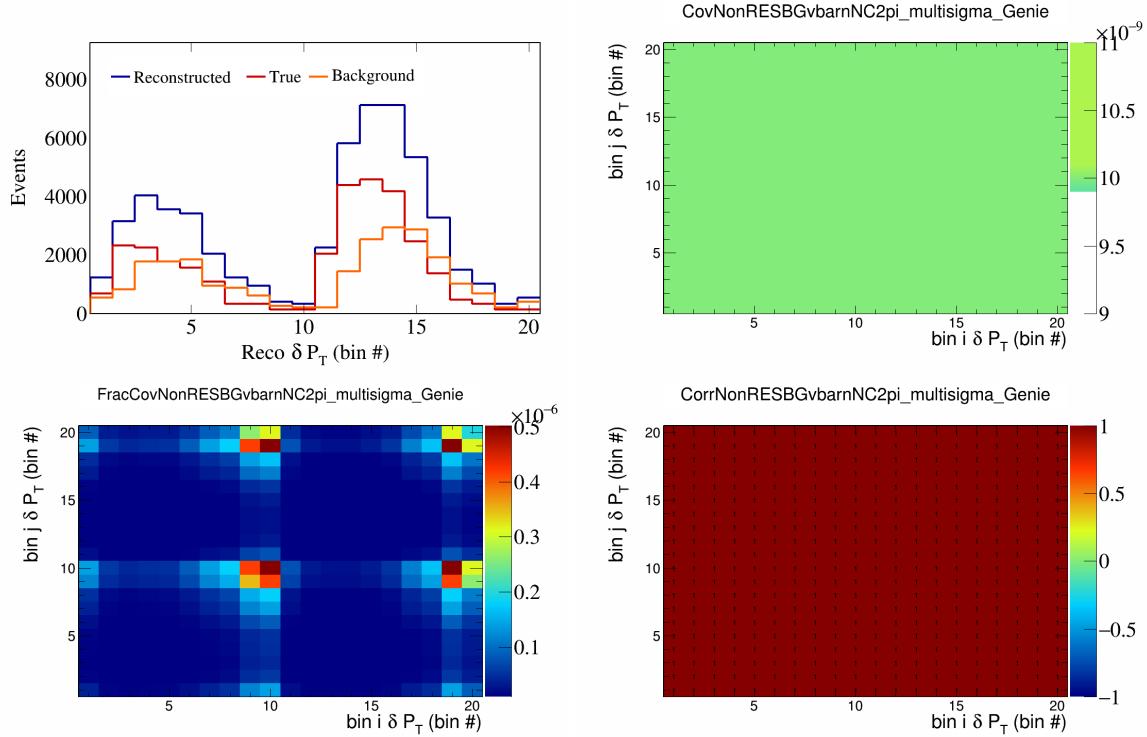


Figure 356: NonRESBGvbarNC2pi variations for δP_T in $\cos(\theta_{\vec{p}_\mu})$.

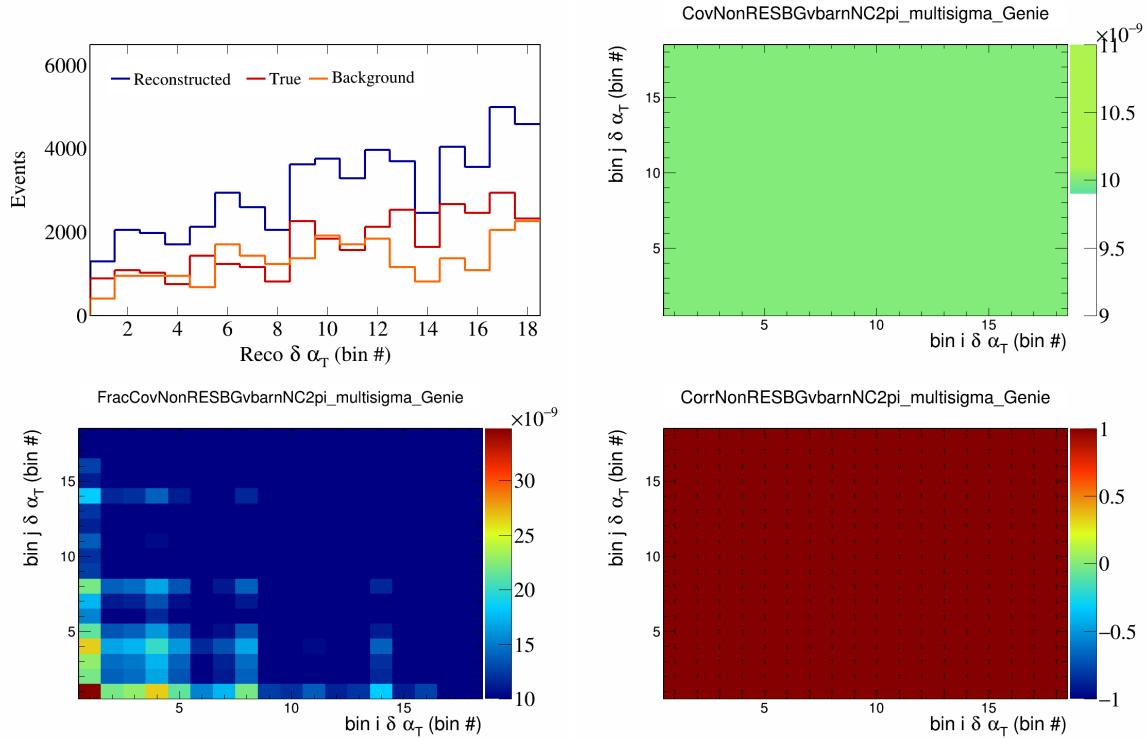


Figure 357: NonRESBGvbarNC2pi variations for $\delta\alpha_T$ in $\cos(\theta_{\vec{p}_\mu})$.

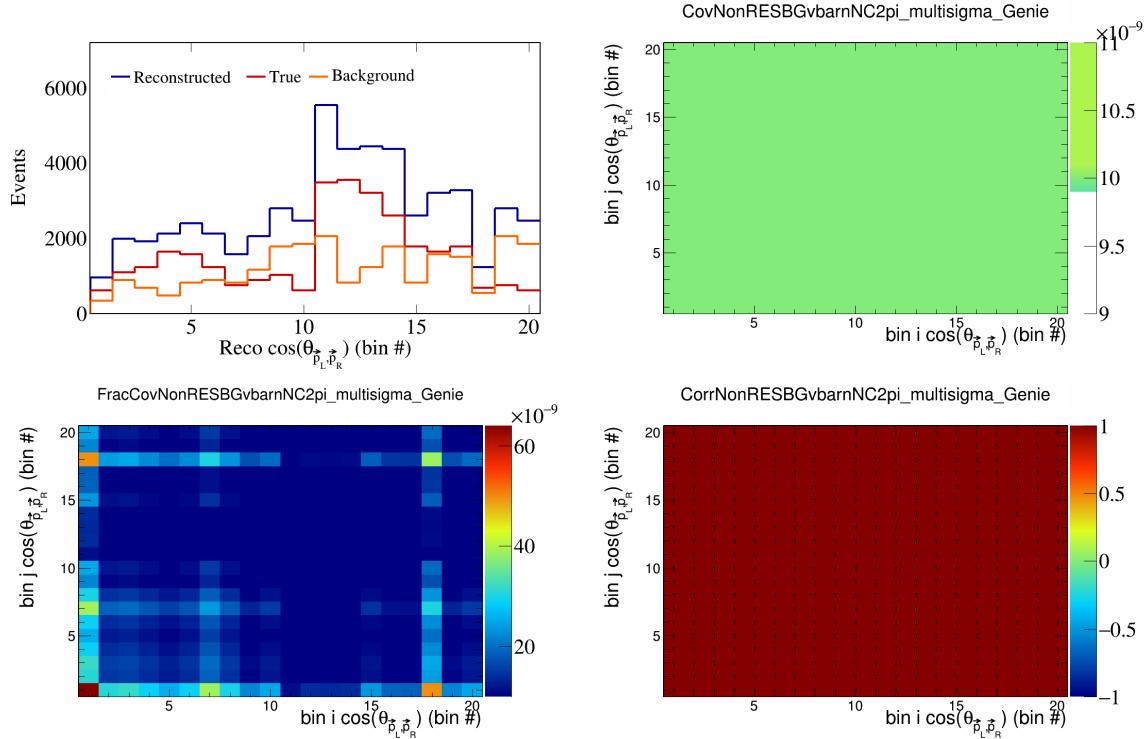


Figure 358: NonRESBGvbarNC2pi variations for $\cos(\theta_{\vec{p}_L, \vec{p}_R})$ in $\cos(\theta_{\vec{p}_\mu})$.

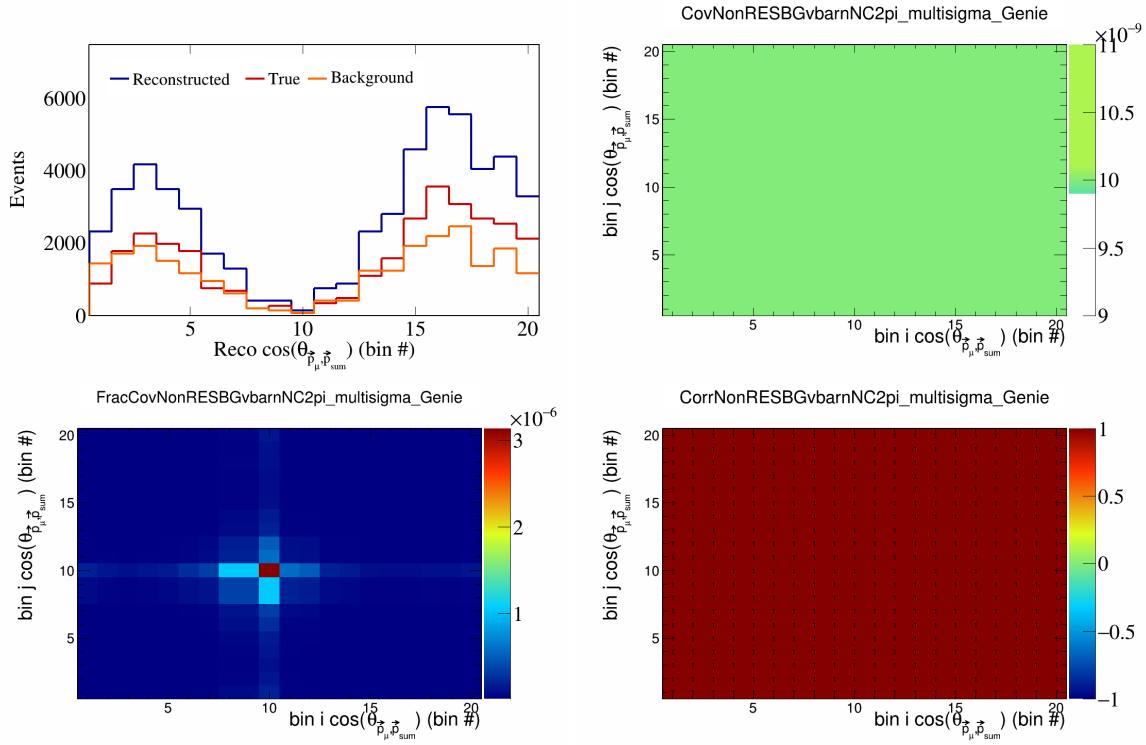


Figure 359: NonRESBGvbarNC2pi variations for $\cos(\theta_{\vec{p}_\mu, \vec{p}_{\text{sum}}})$ in $\cos(\theta_{\vec{p}_\mu})$.

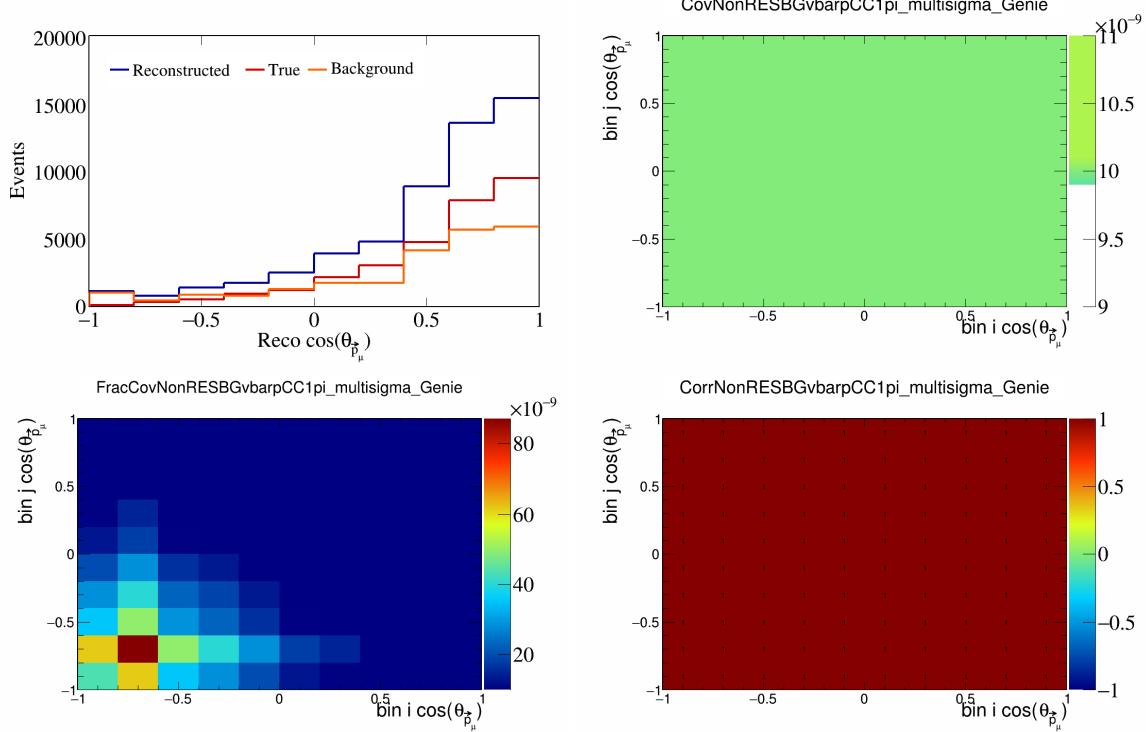


Figure 360: NonRESBGvbarCC1pi variations for $\cos(\theta_{\vec{p}_\mu})$.

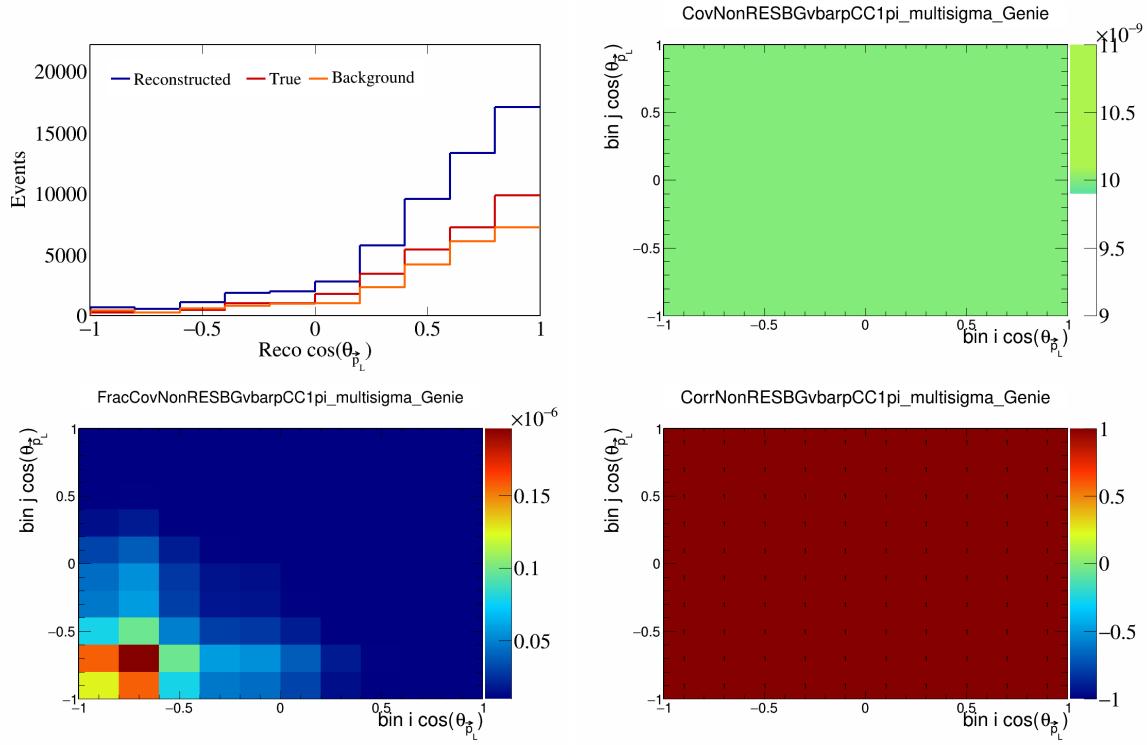


Figure 361: NonRESBGvbarpCC1pi variations for $\cos(\theta_{\vec{p}_L})$.

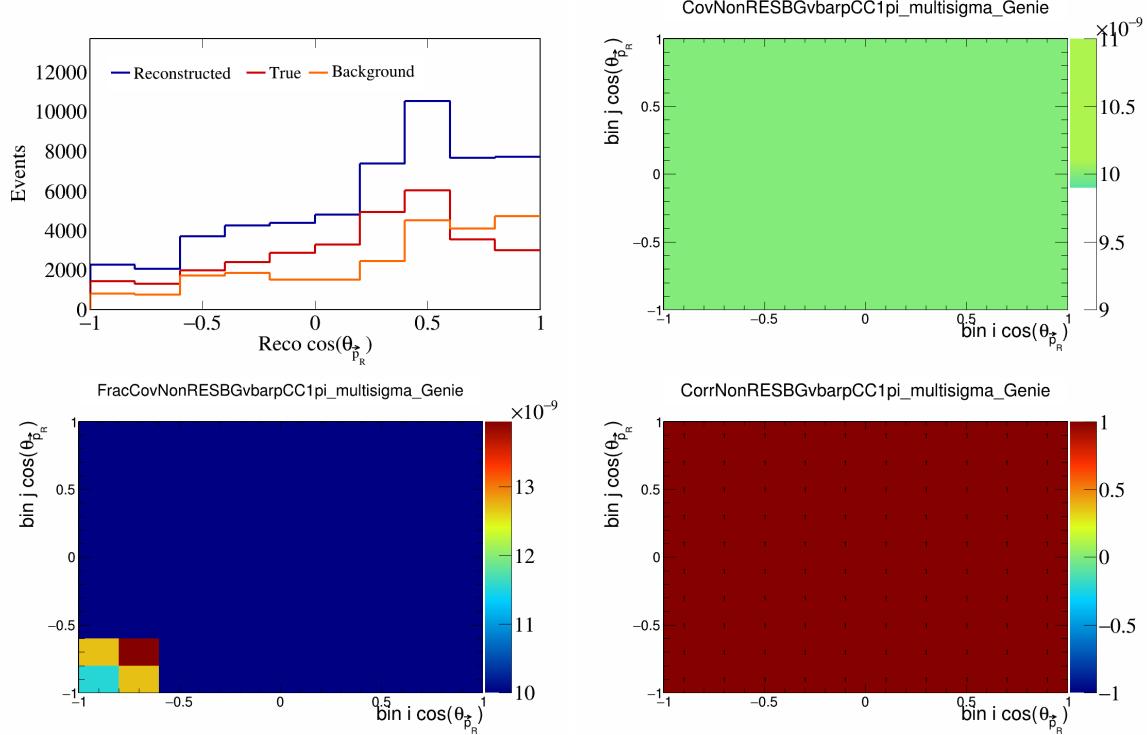


Figure 362: NonRESBGvbarpCC1pi variations for $\cos(\theta_{\vec{p}_R})$.

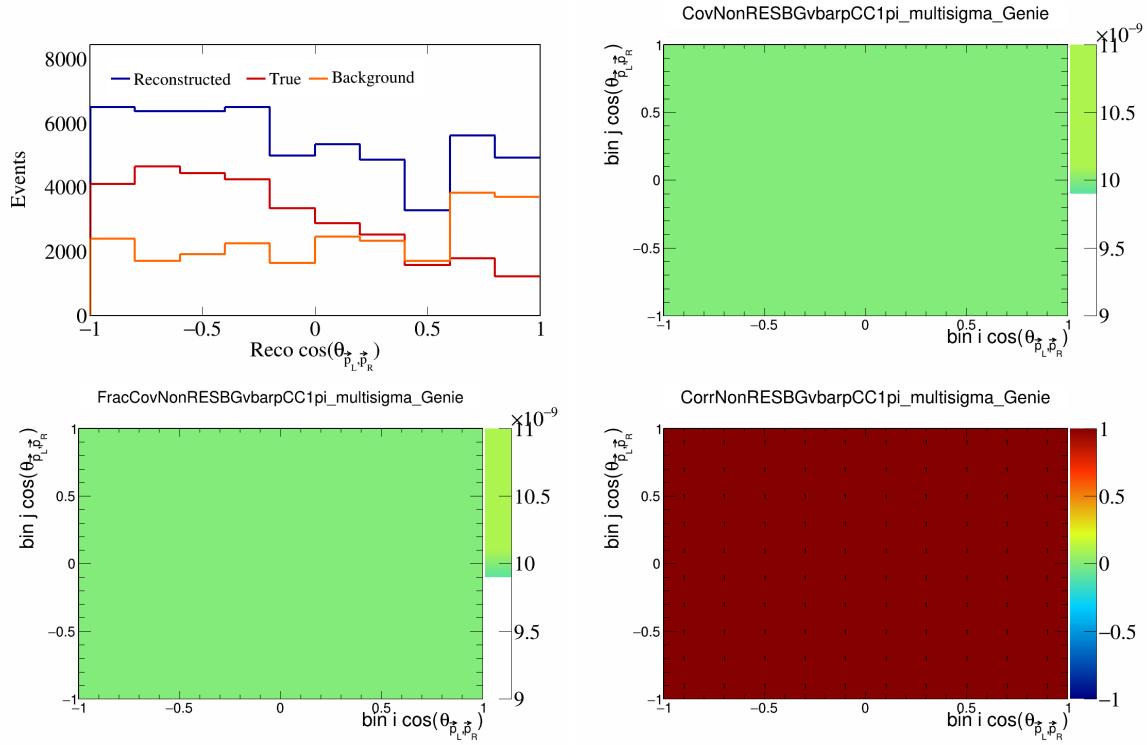


Figure 363: NonRESBGvbarpCC1pi variations for $\cos(\theta_{\vec{p}_L, \vec{p}_R})$.

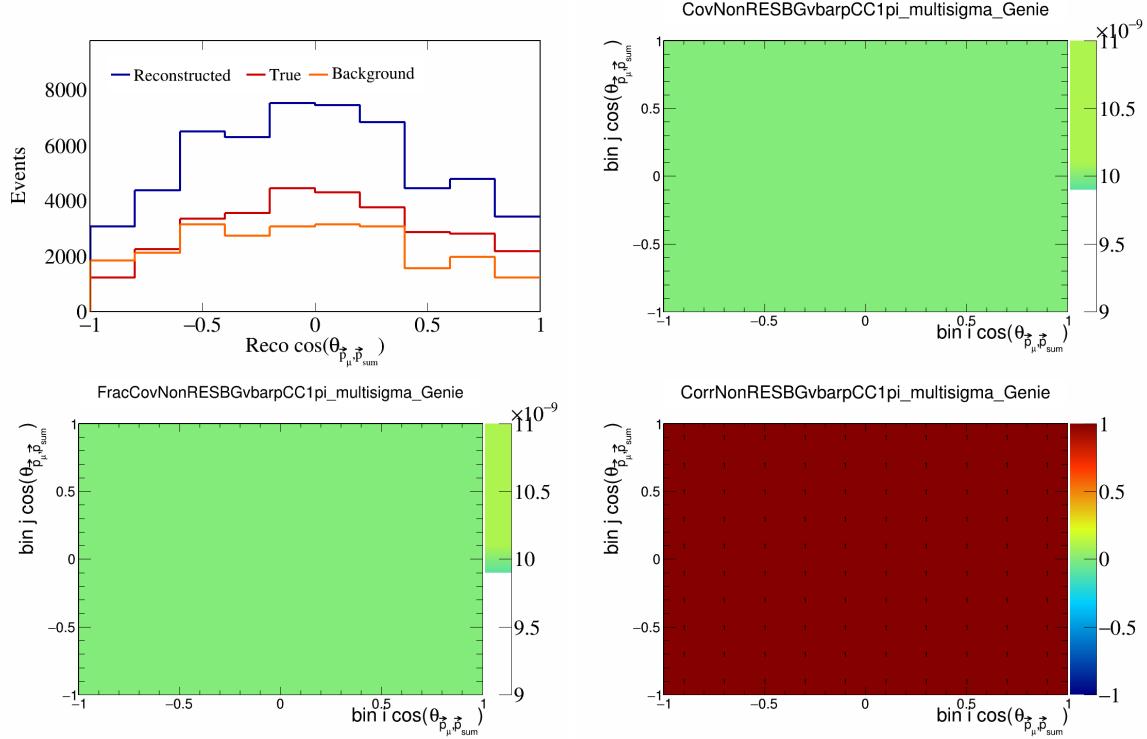


Figure 364: NonRESBGvbarpCC1pi variations for $\cos(\theta_{\vec{p}_\mu, \vec{p}_{\text{sum}}})$.

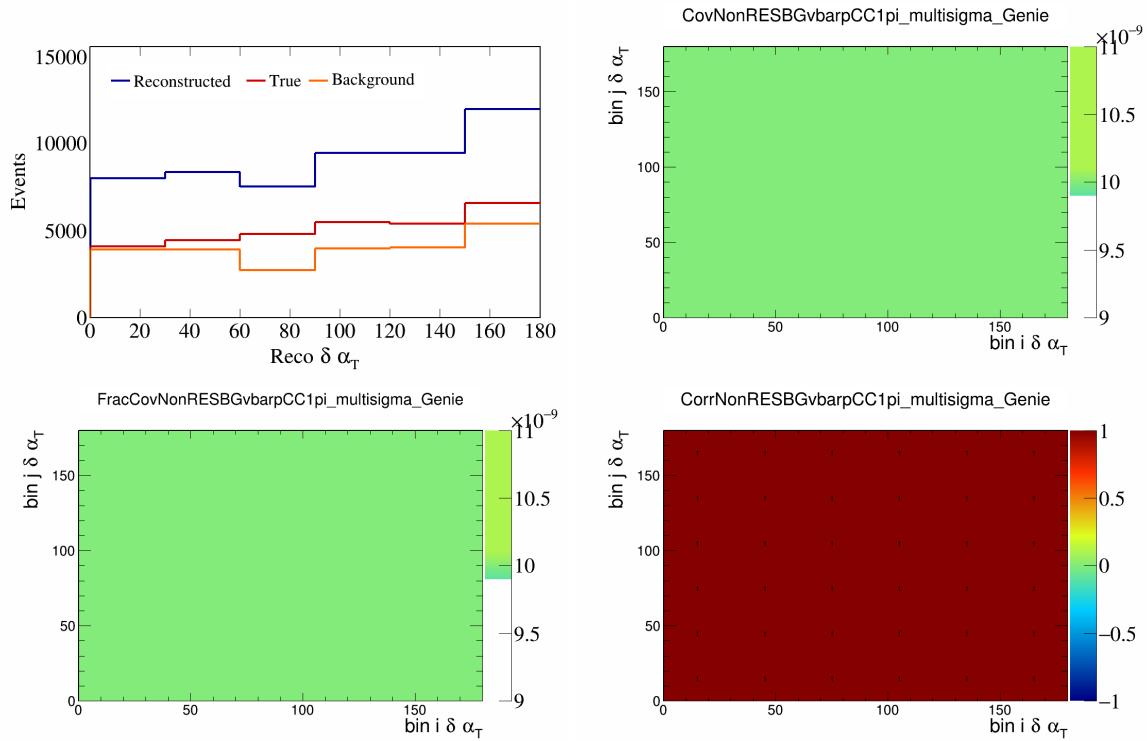


Figure 365: NonRESBGvbarpCC1pi variations for $\delta\alpha_T$.

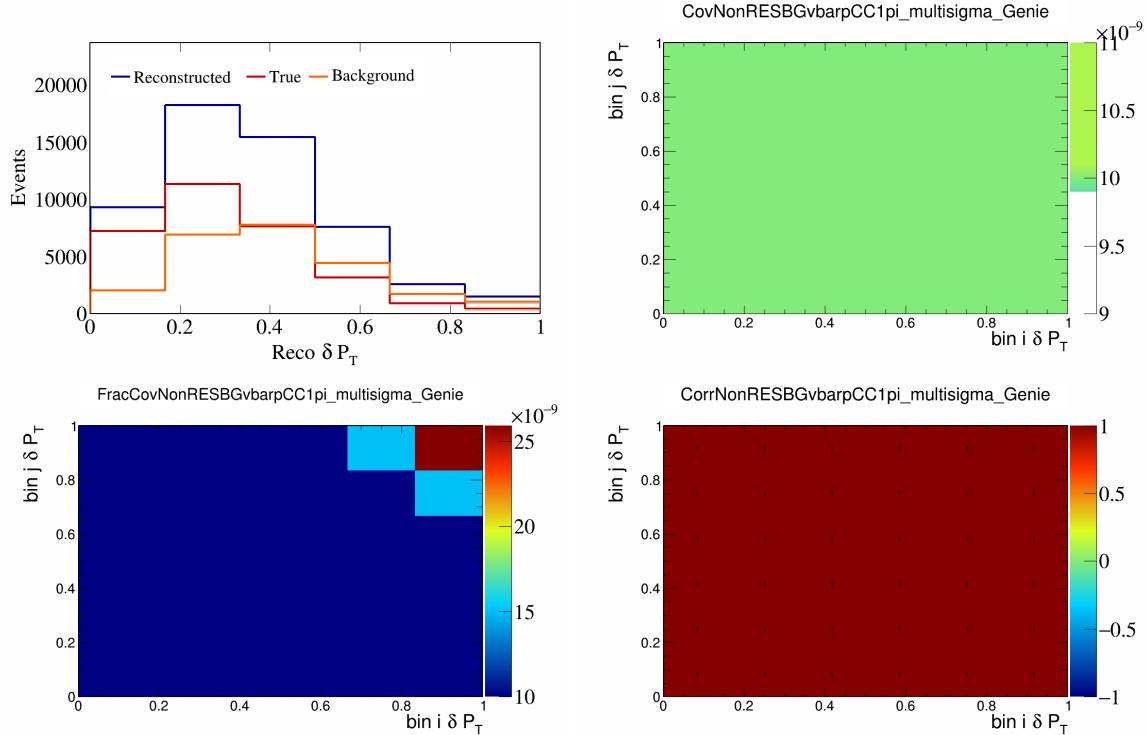


Figure 366: NonRESBGvbarpCC1pi variations for δP_T .

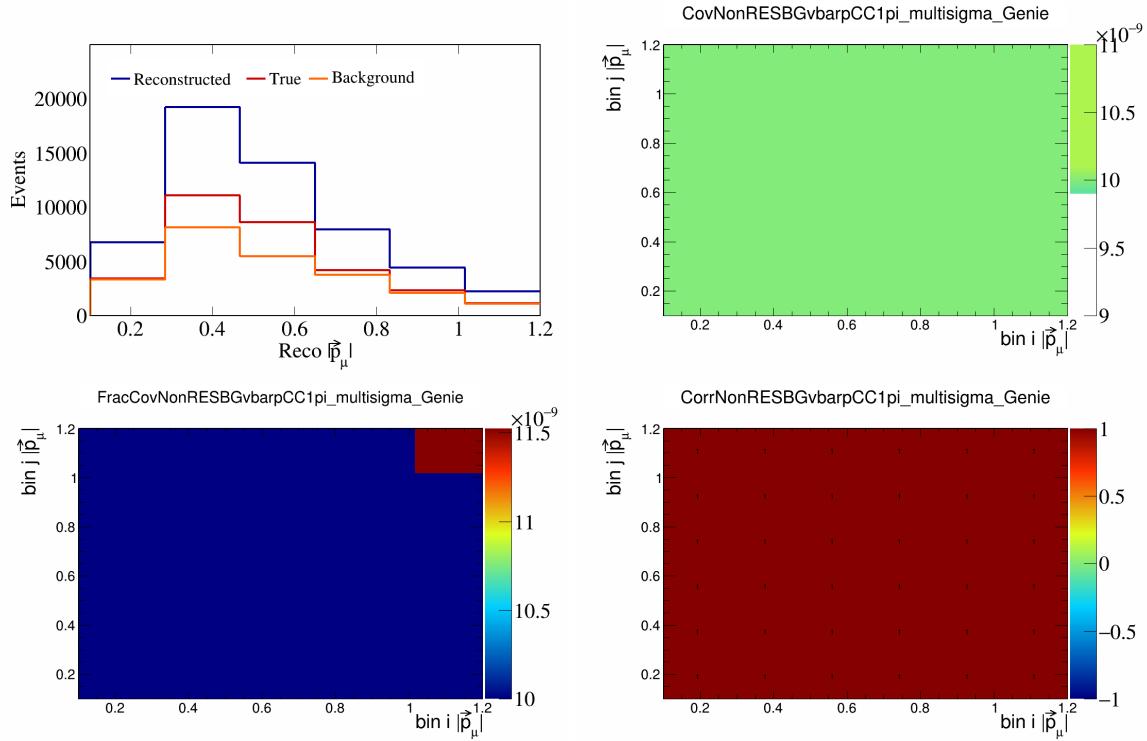


Figure 367: NonRESBGvbarpCC1pi variations for $|\vec{p}_\mu|$.

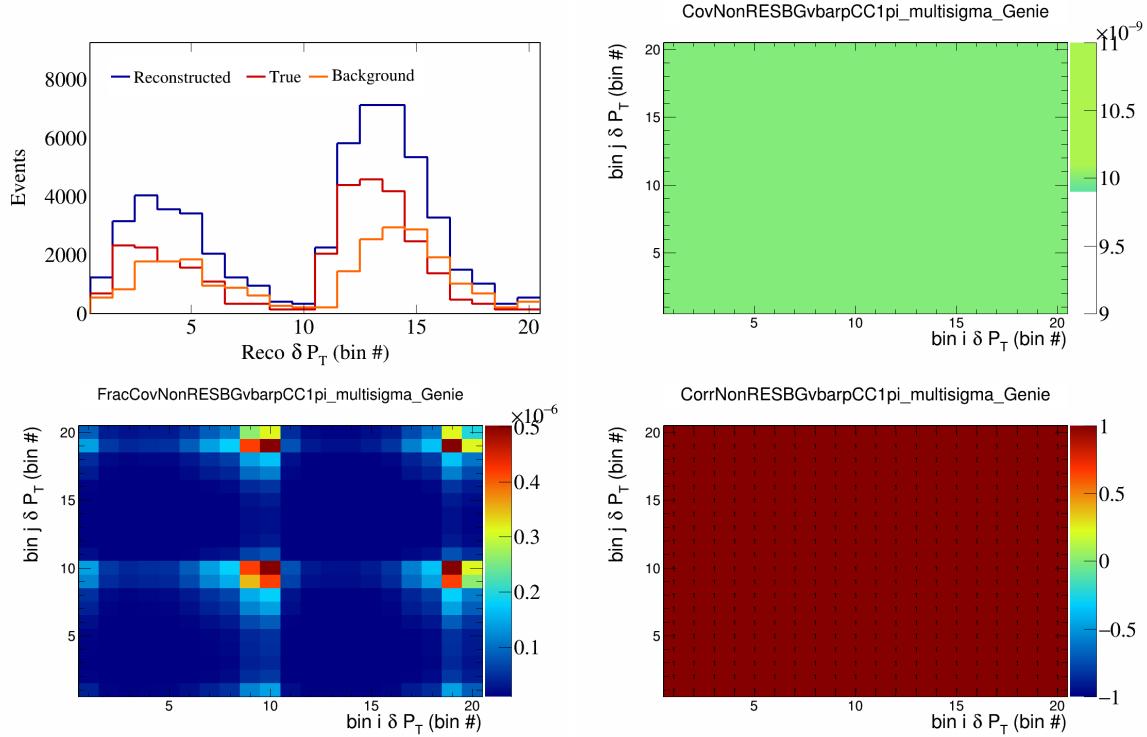


Figure 368: NonRESBGvbarpCC1pi variations for δP_T in $\cos(\theta_{\vec{p}_\mu})$.

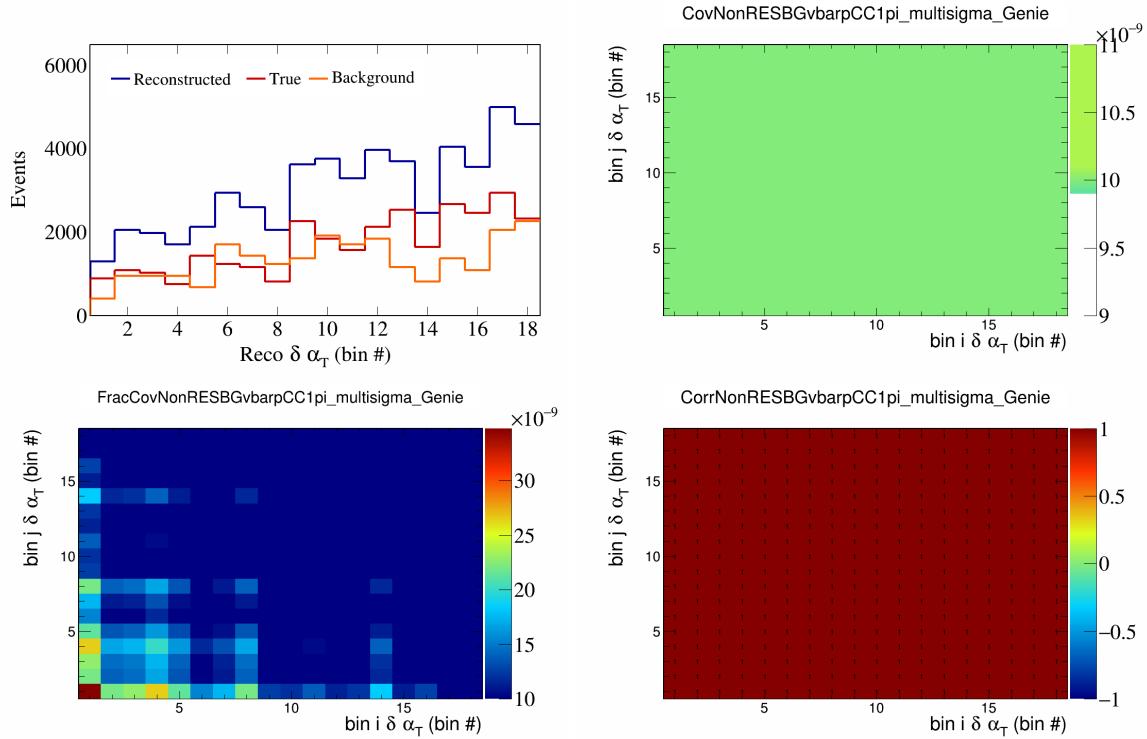


Figure 369: NonRESBGvbarpCC1pi variations for $\delta\alpha_T$ in $\cos(\theta_{\vec{p}_\mu})$.

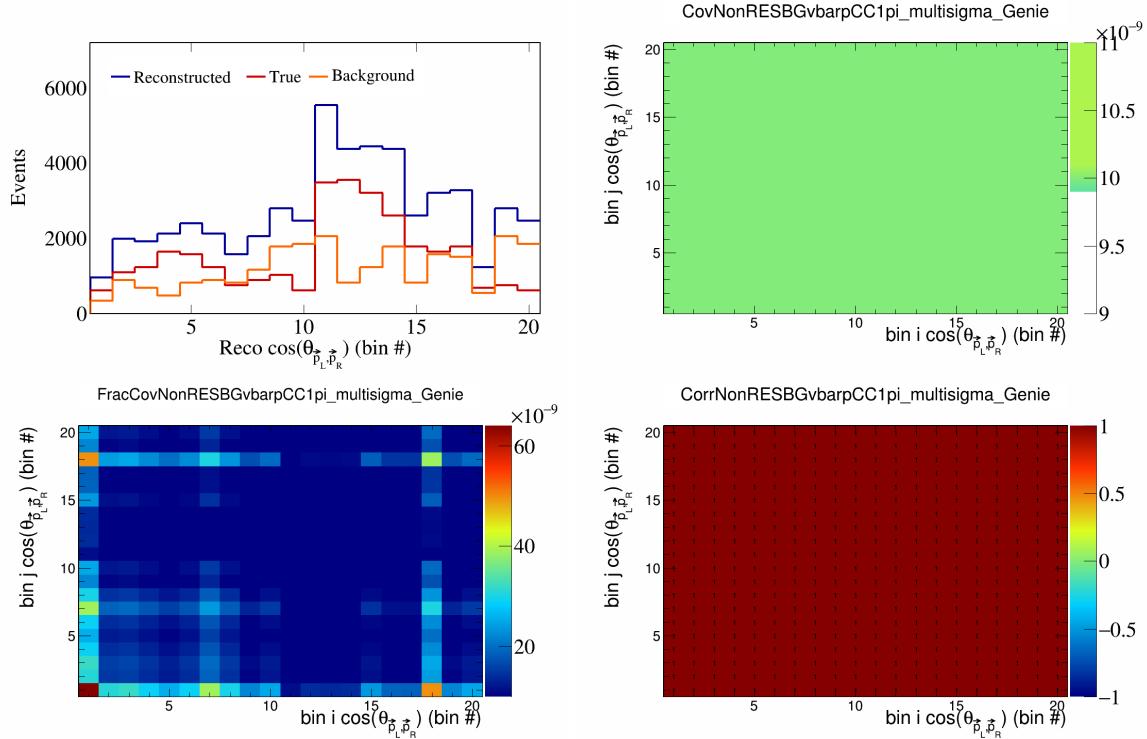


Figure 370: NonRESBGvbarpCC1pi variations for $\cos(\theta_{\vec{p}_L, \vec{p}_R})$ in $\cos(\theta_{\vec{p}_\mu})$.

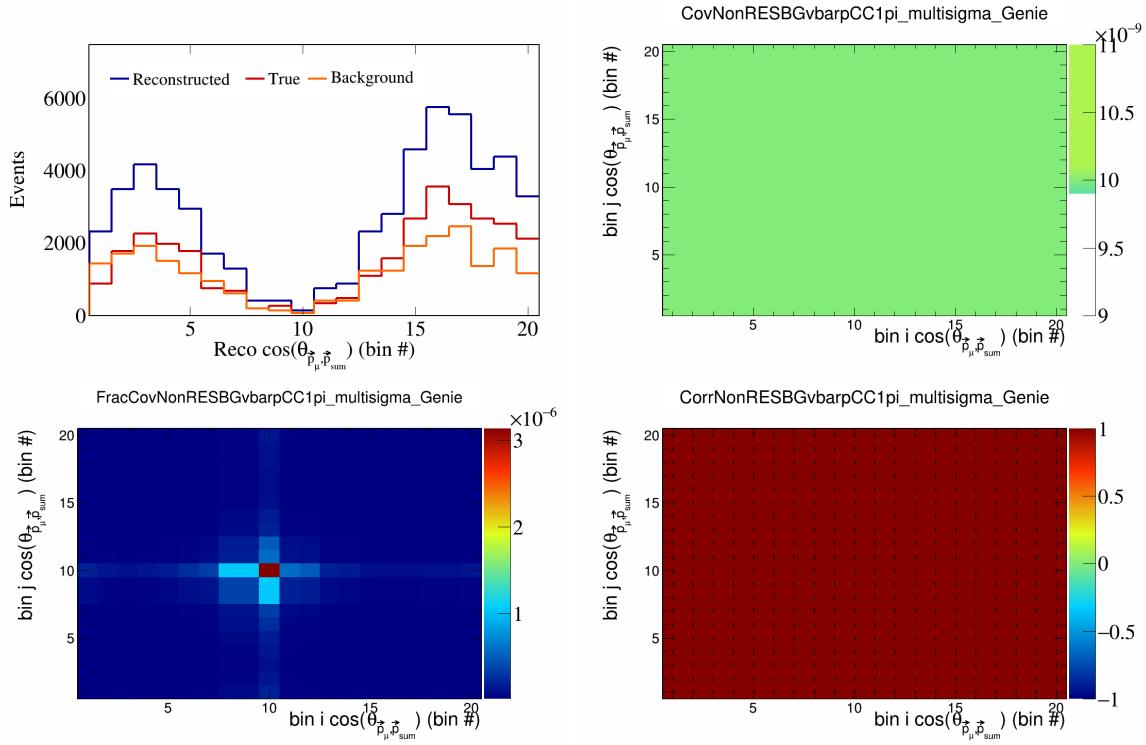


Figure 371: NonRESBGvbarpCC1pi variations for $\cos(\theta_{\vec{p}_\mu, \vec{p}_{\text{sum}}})$ in $\cos(\theta_{\vec{p}_\mu})$.

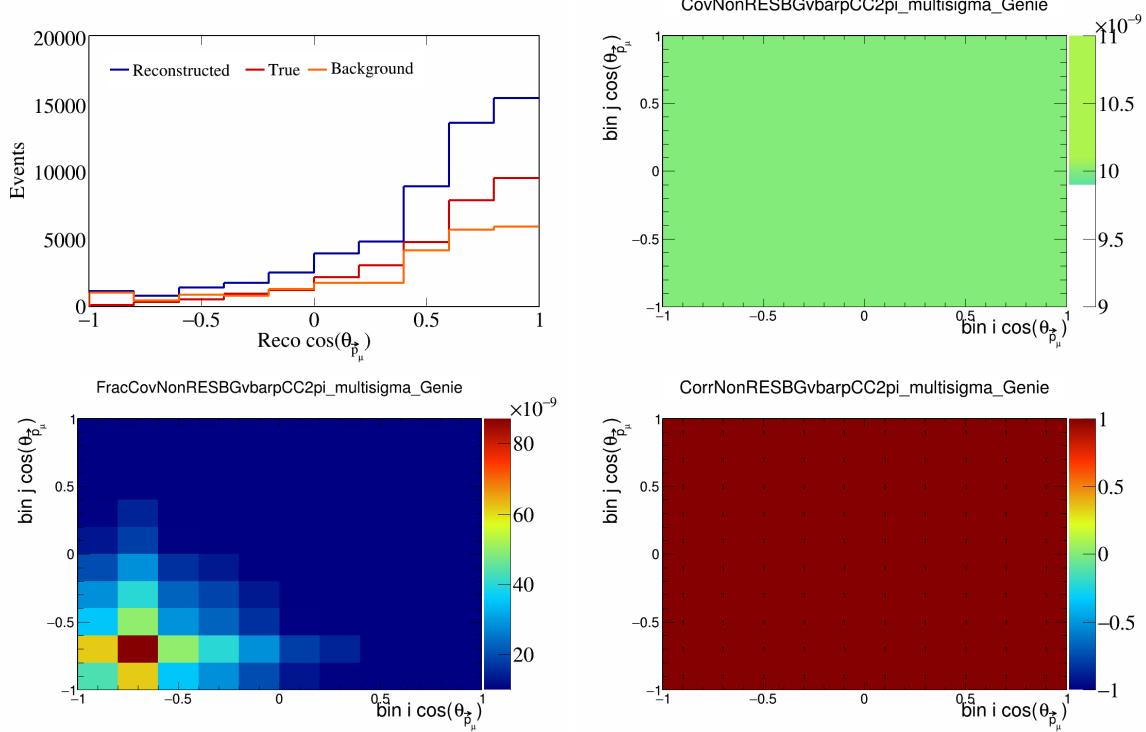


Figure 372: NonRESBGvbarpCC2pi variations for $\cos(\theta_{\vec{p}_\mu})$.

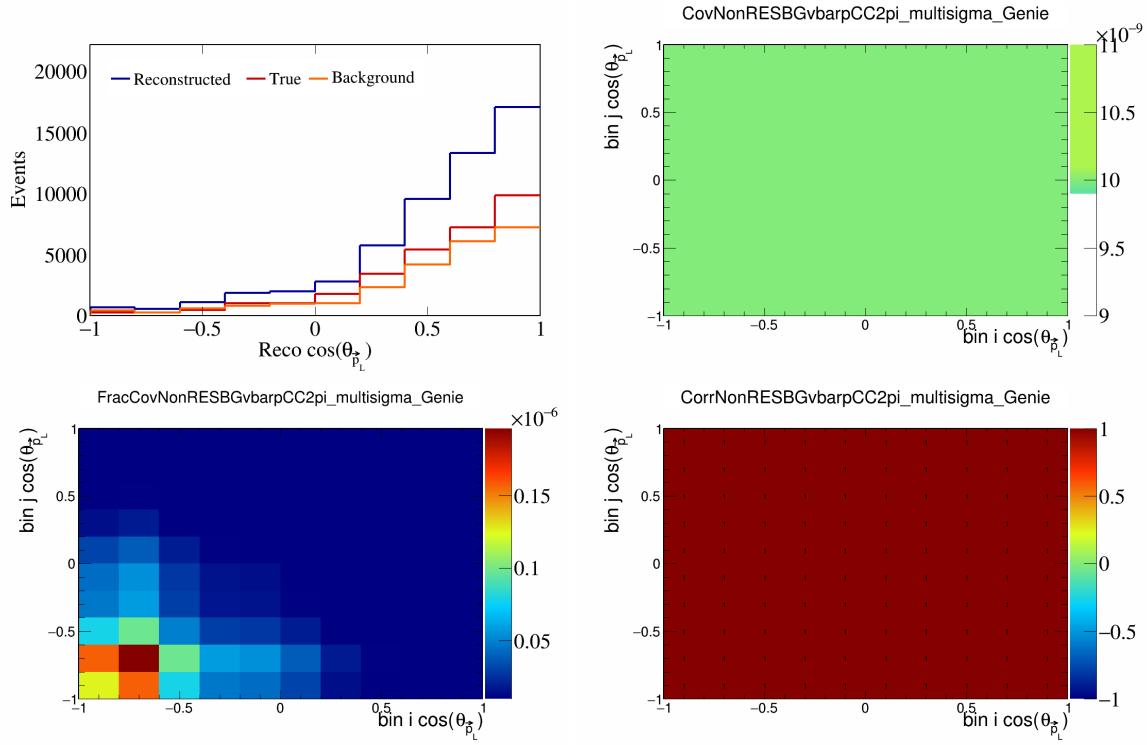


Figure 373: NonRESBGvbarpCC2pi variations for $\cos(\theta_{\vec{p}_L})$.

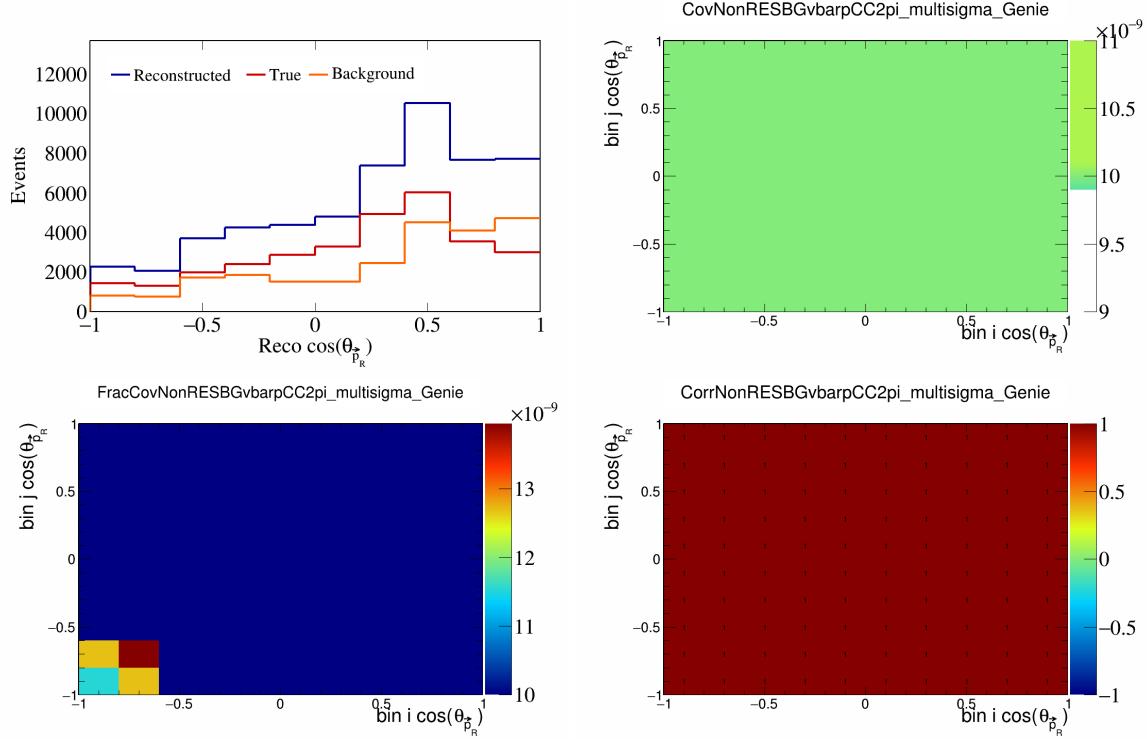


Figure 374: NonRESBGvbarpCC2pi variations for $\cos(\theta_{\vec{p}_R})$.

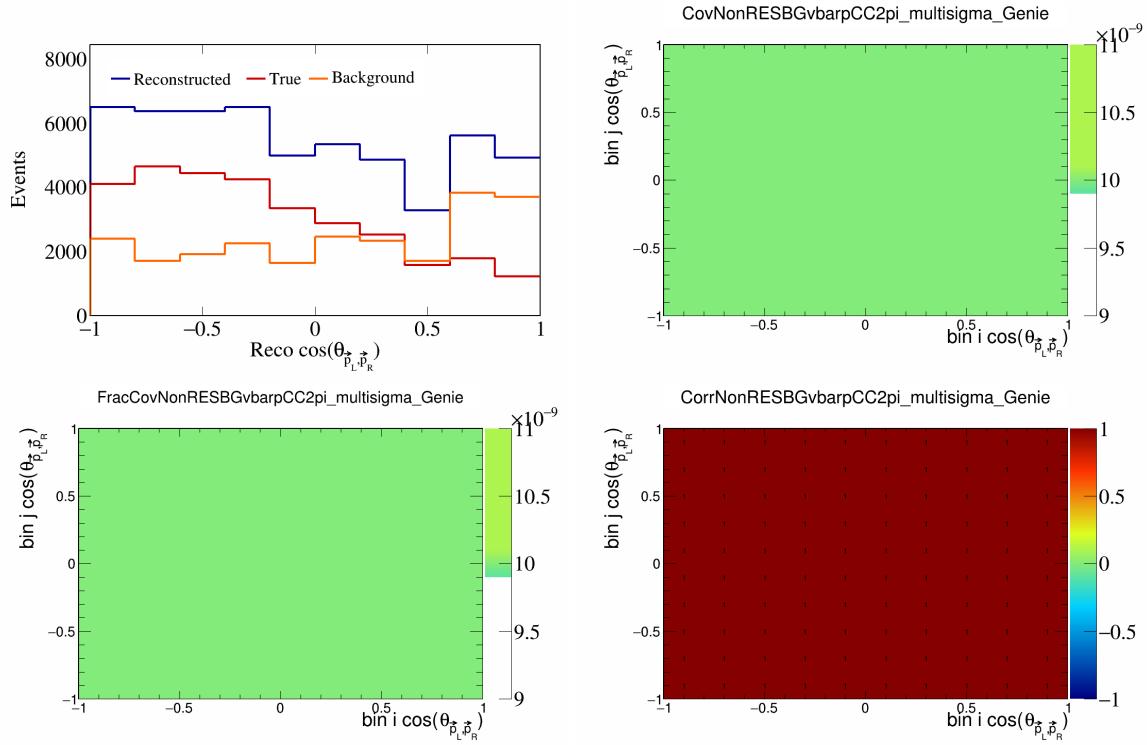


Figure 375: NonRESBGvbarpCC2pi variations for $\cos(\theta_{\vec{p}_L, \vec{p}_R})$.

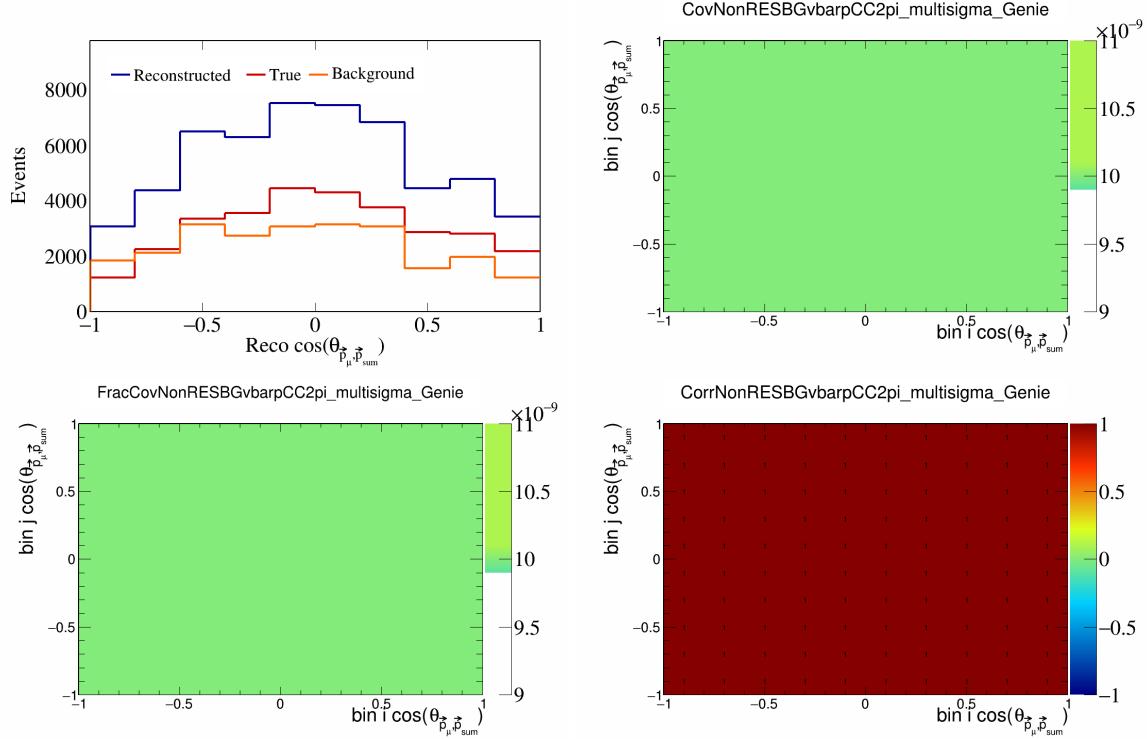


Figure 376: NonRESBGvbarpCC2pi variations for $\cos(\theta_{\vec{p}_\mu, \vec{p}_{\text{sum}}})$.

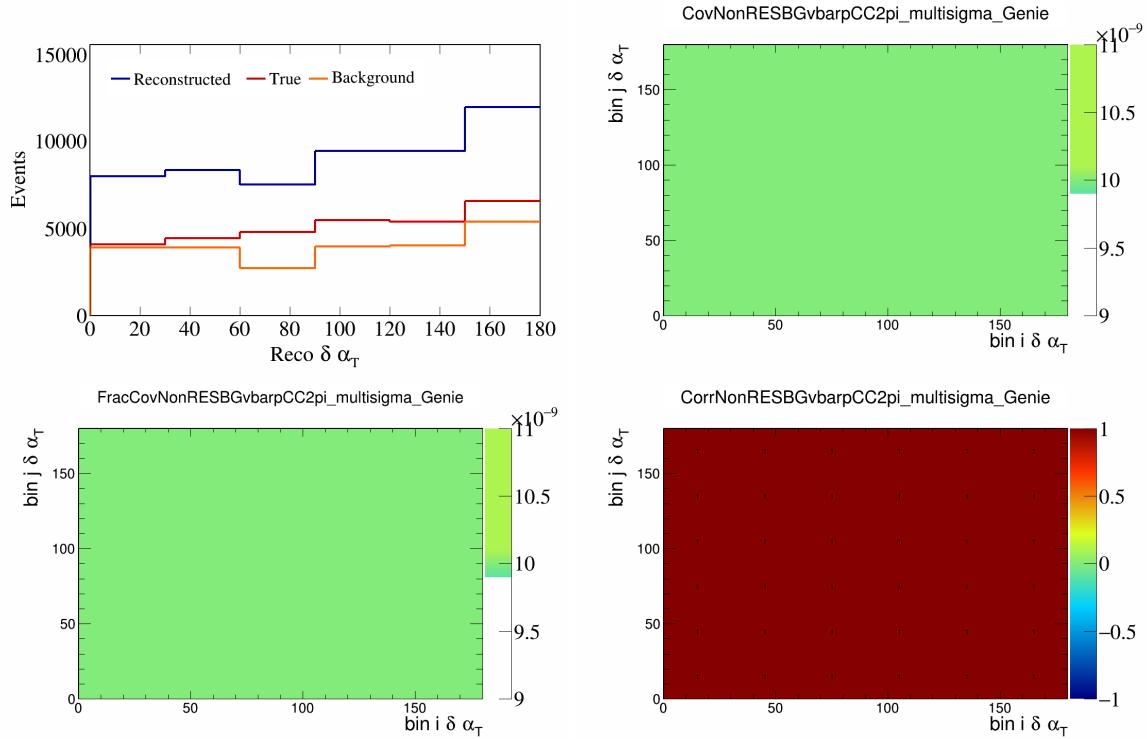


Figure 377: NonRESBGvbarpCC2pi variations for $\delta\alpha_T$.

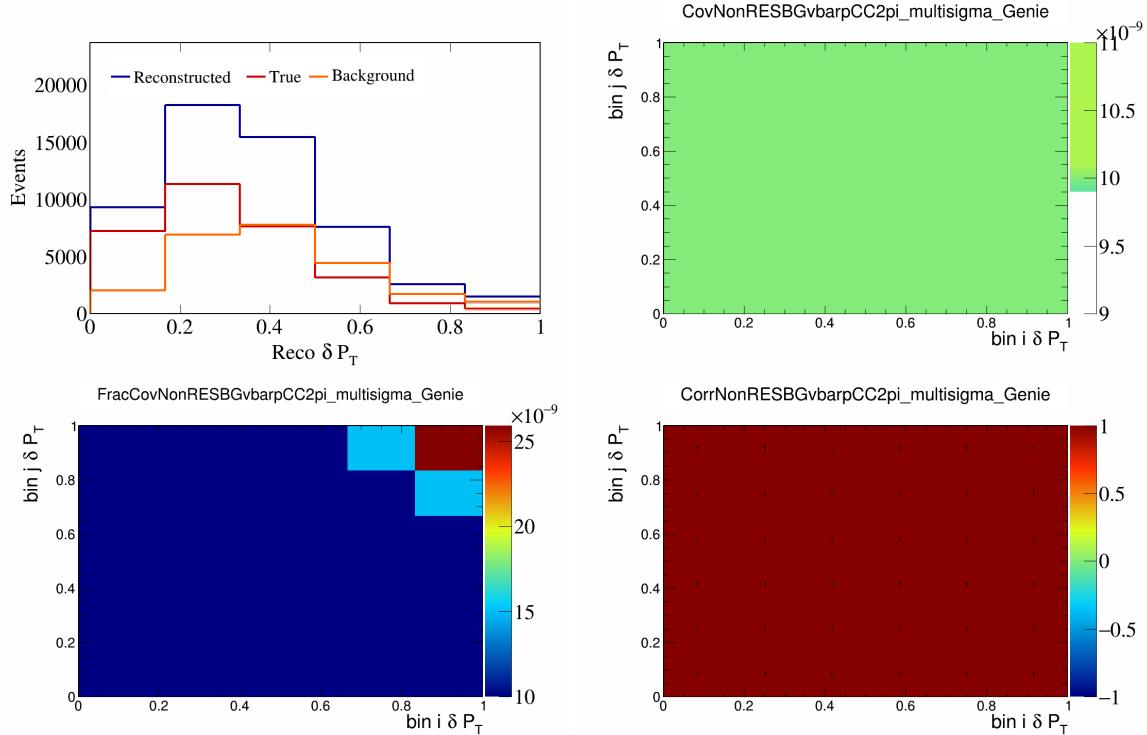


Figure 378: NonRESBGvbarpCC2pi variations for δP_T .

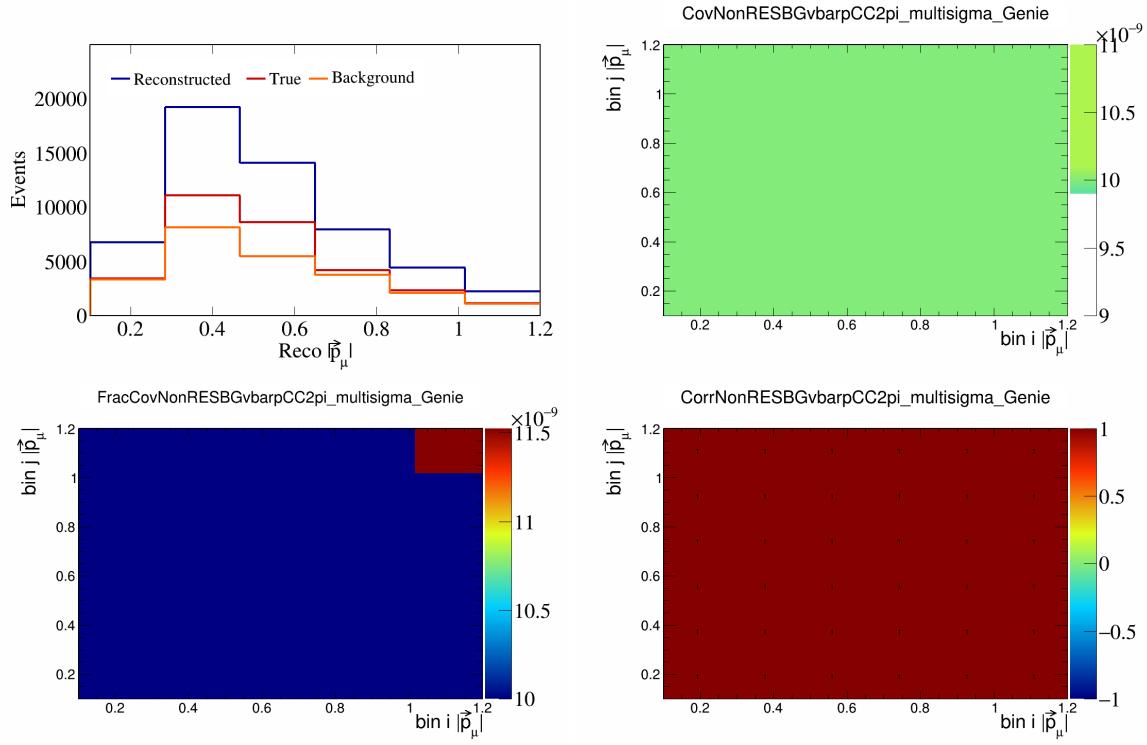


Figure 379: NonRESBGvbarpCC2pi variations for $|\vec{p}_\mu|$.

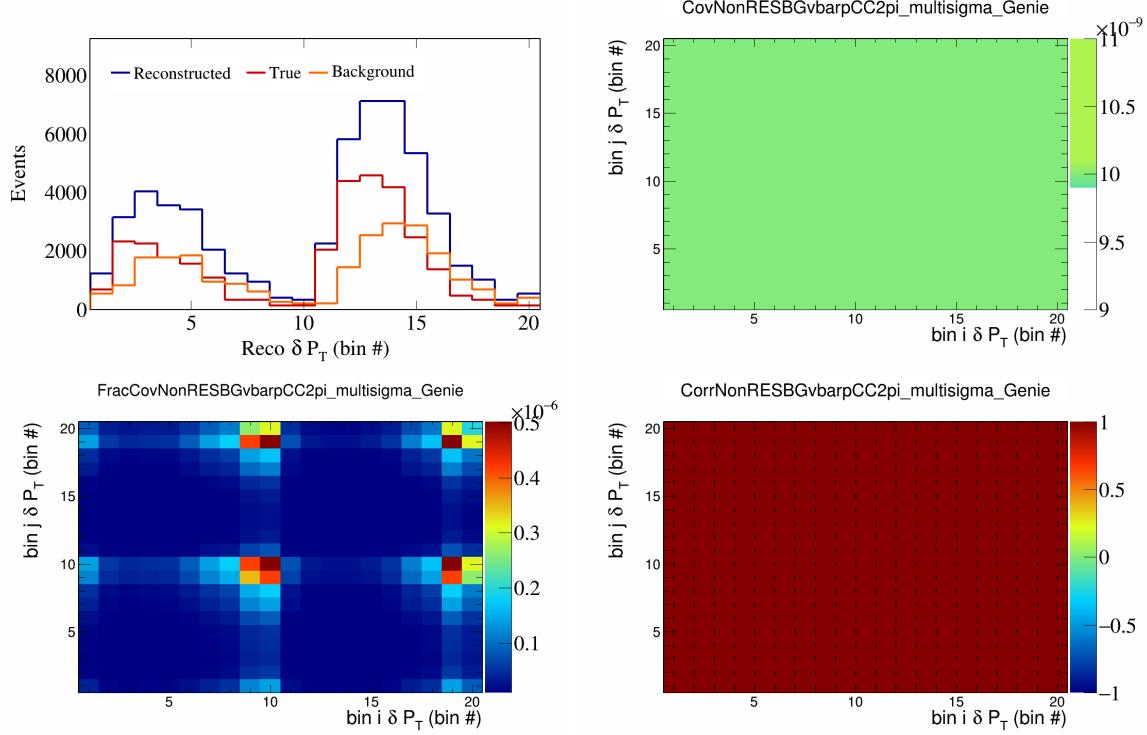


Figure 380: NonRESBGvbarpCC2pi variations for δP_T in $\cos(\theta_{\vec{p}_\mu})$.

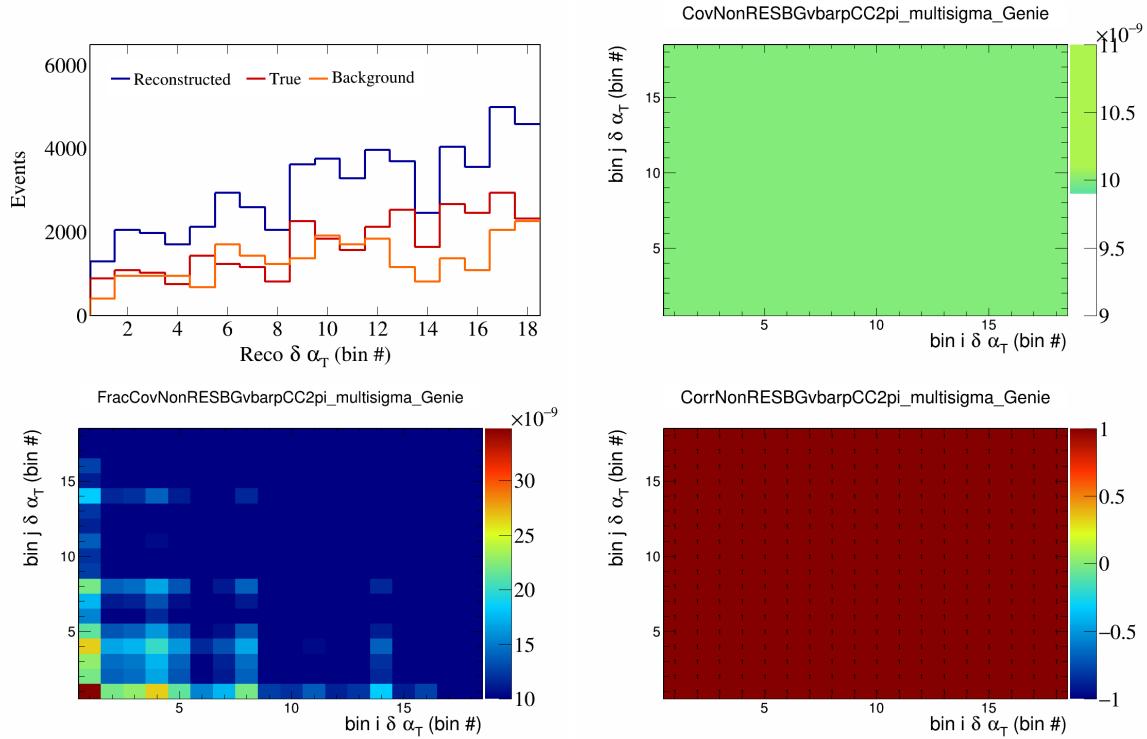


Figure 381: NonRESBGvbarpCC2pi variations for $\delta\alpha_T$ in $\cos(\theta_{\vec{p}_\mu})$.

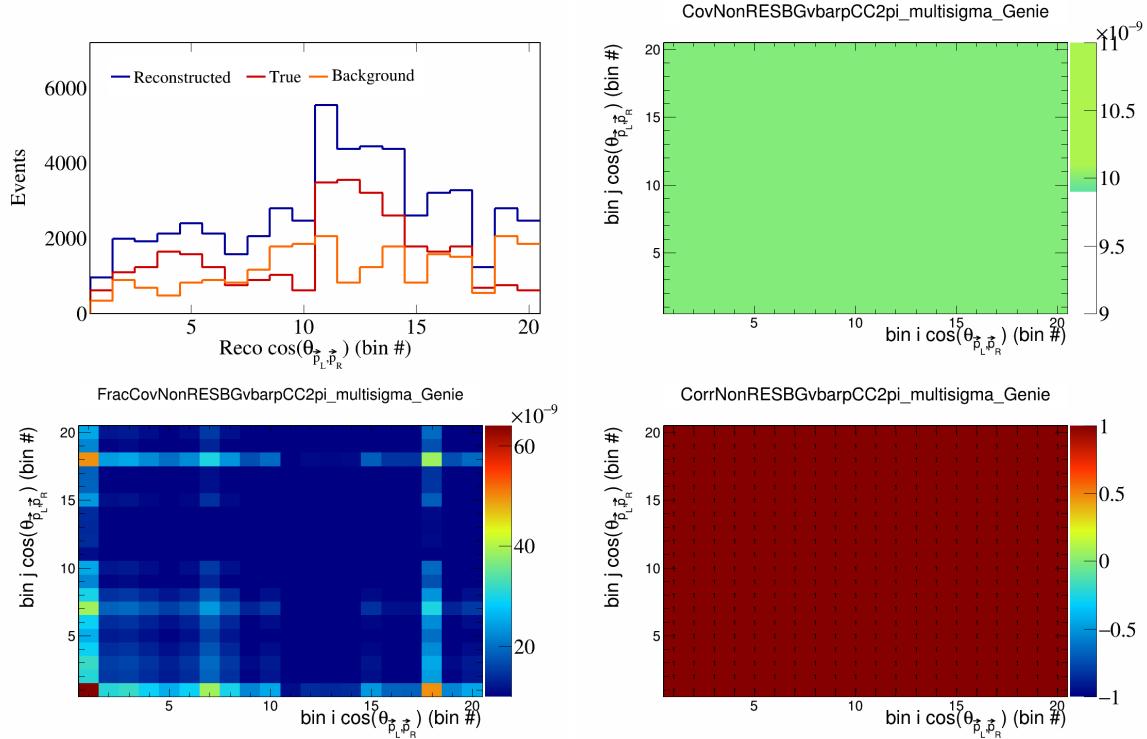


Figure 382: NonRESBGvbarpCC2pi variations for $\cos(\theta_{\vec{p}_L, \vec{p}_R})$ in $\cos(\theta_{\vec{p}_\mu})$.

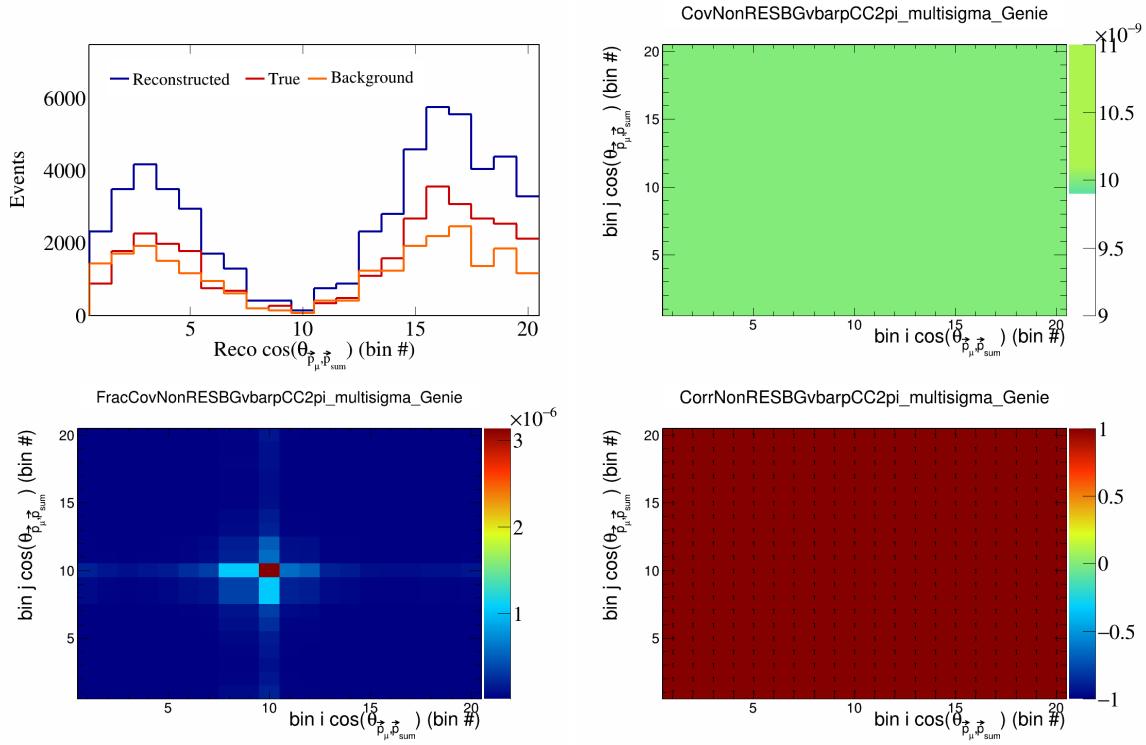


Figure 383: NonRESBGvbarpCC2pi variations for $\cos(\theta_{\vec{p}_\mu})$ in $\cos(\theta_{\vec{p}_\mu})$.

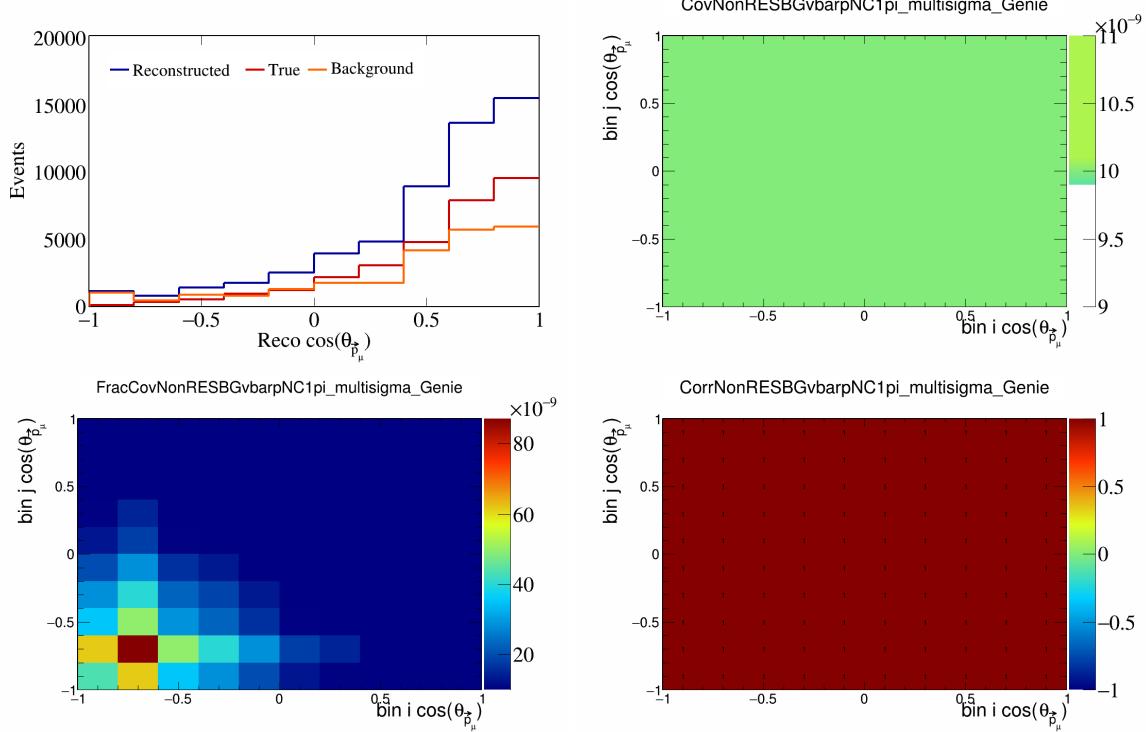


Figure 384: NonRESBGvbarpNC1pi variations for $\cos(\theta_{\vec{p}_\mu})$.

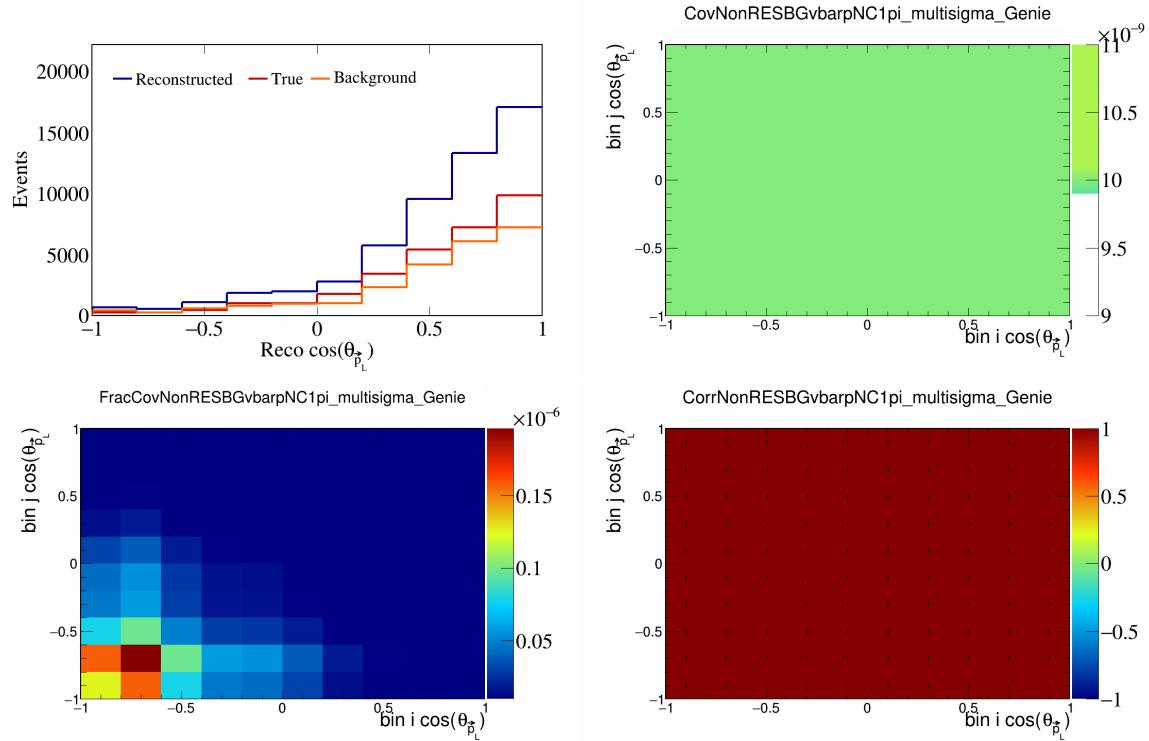


Figure 385: NonRESBGvbarpi variations for $\cos(\theta_{\vec{p}_L})$.

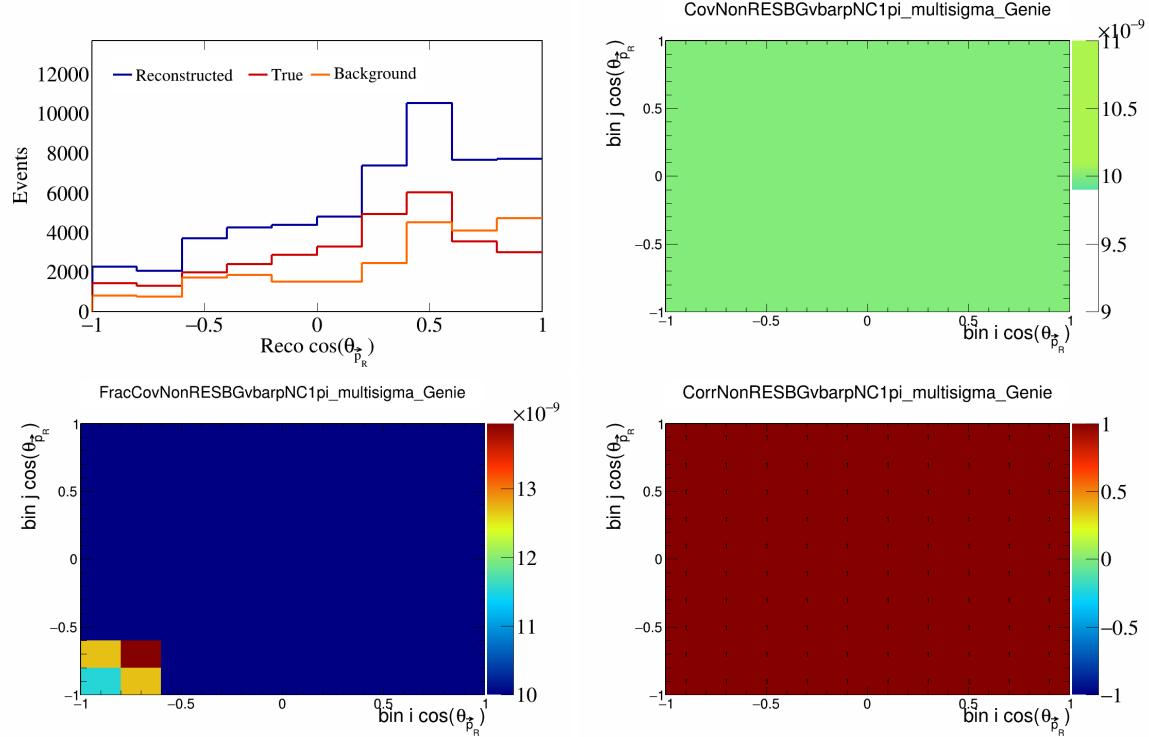


Figure 386: NonRESBGvbarpi variations for $\cos(\theta_{\vec{p}_R})$.

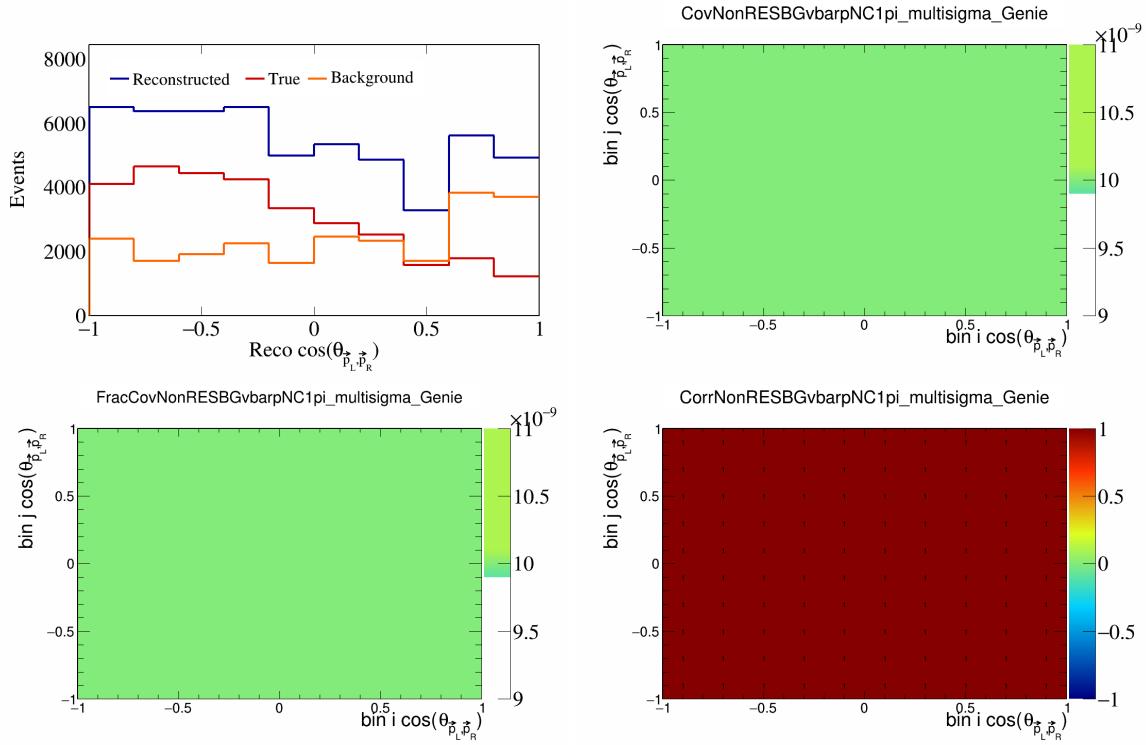


Figure 387: NonRESBGvbarpNC1pi variations for $\cos(\theta_{\vec{p}_L, \vec{p}_R})$.

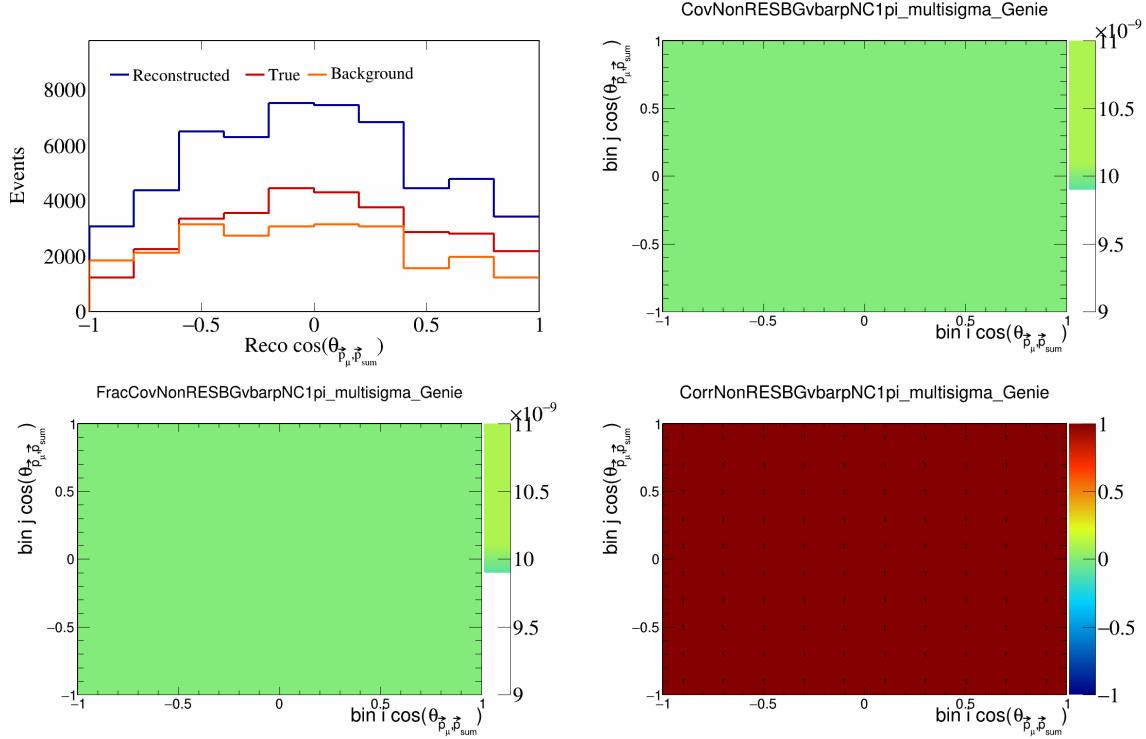


Figure 388: NonRESBGvbarpNC1pi variations for $\cos(\theta_{\vec{p}_\mu, \vec{p}_{\text{sum}}})$.

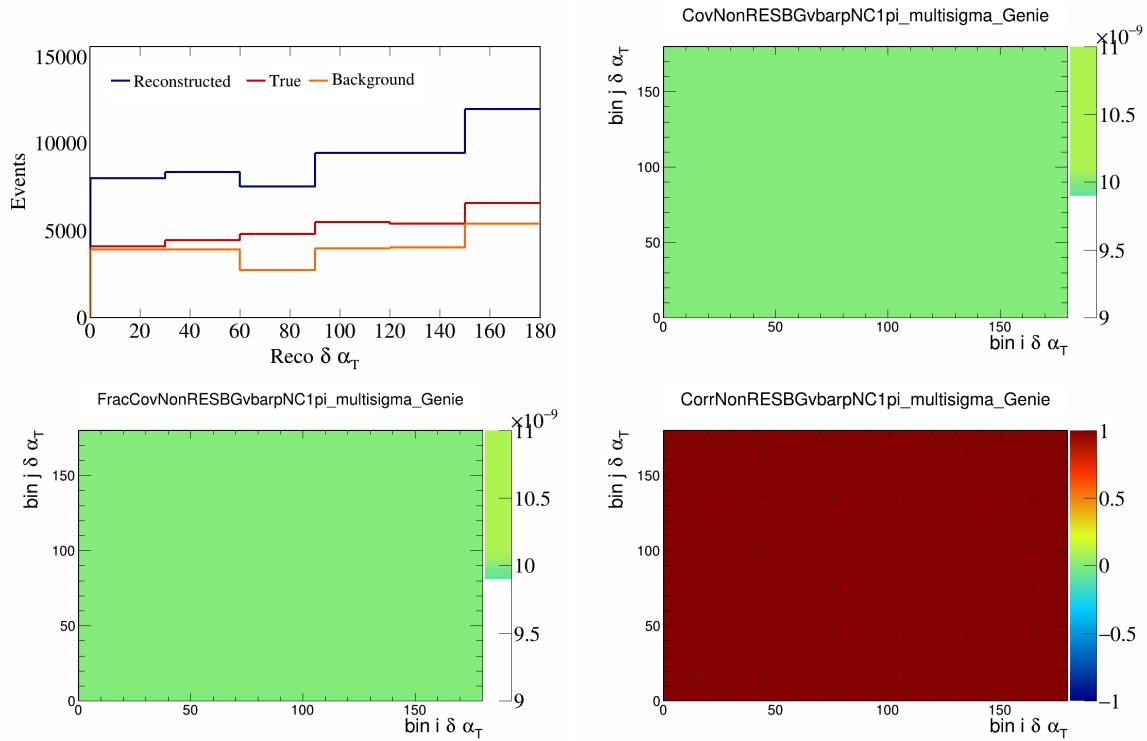


Figure 389: NonRESBGvbarpNC1pi variations for $\delta\alpha_T$.

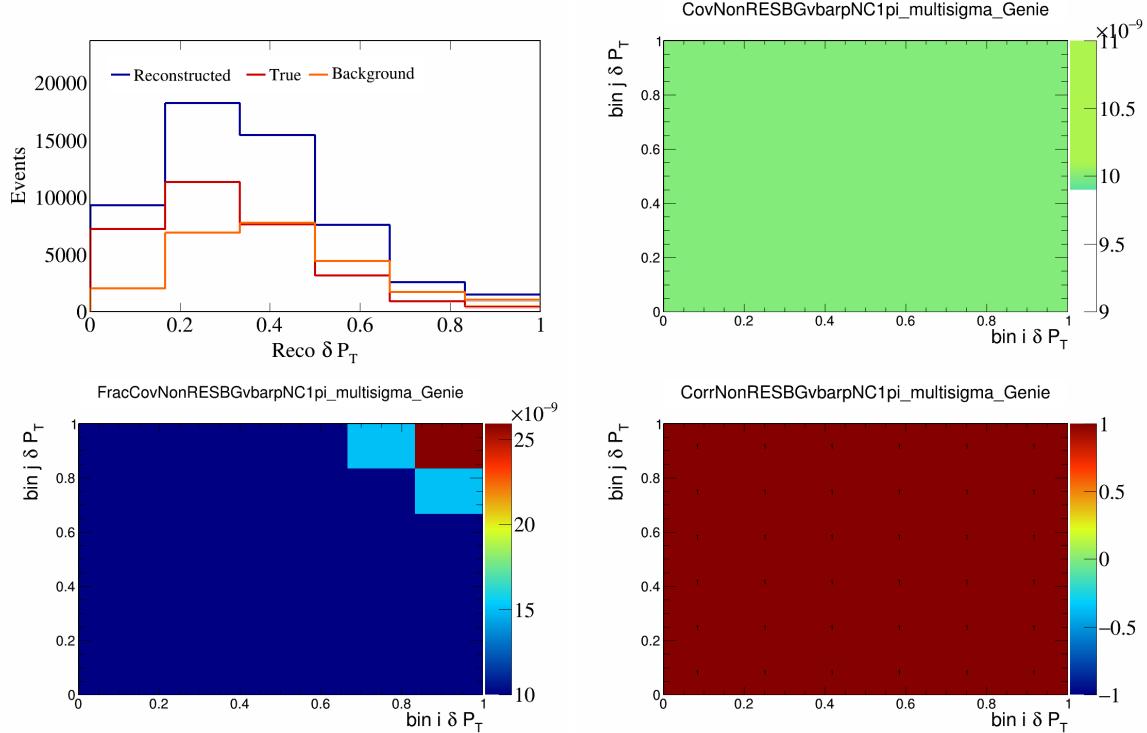


Figure 390: NonRESBGvbarpNC1pi variations for δP_T .

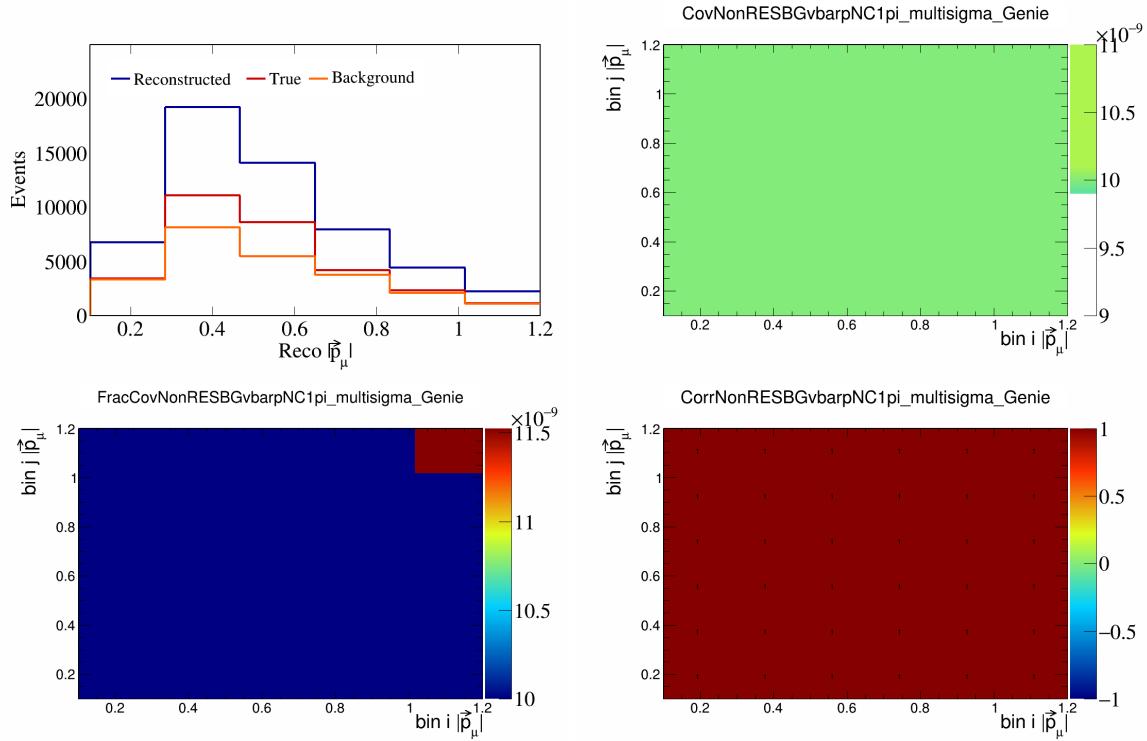


Figure 391: NonRESBGvbarpNC1pi variations for $|\vec{p}_\mu|$.

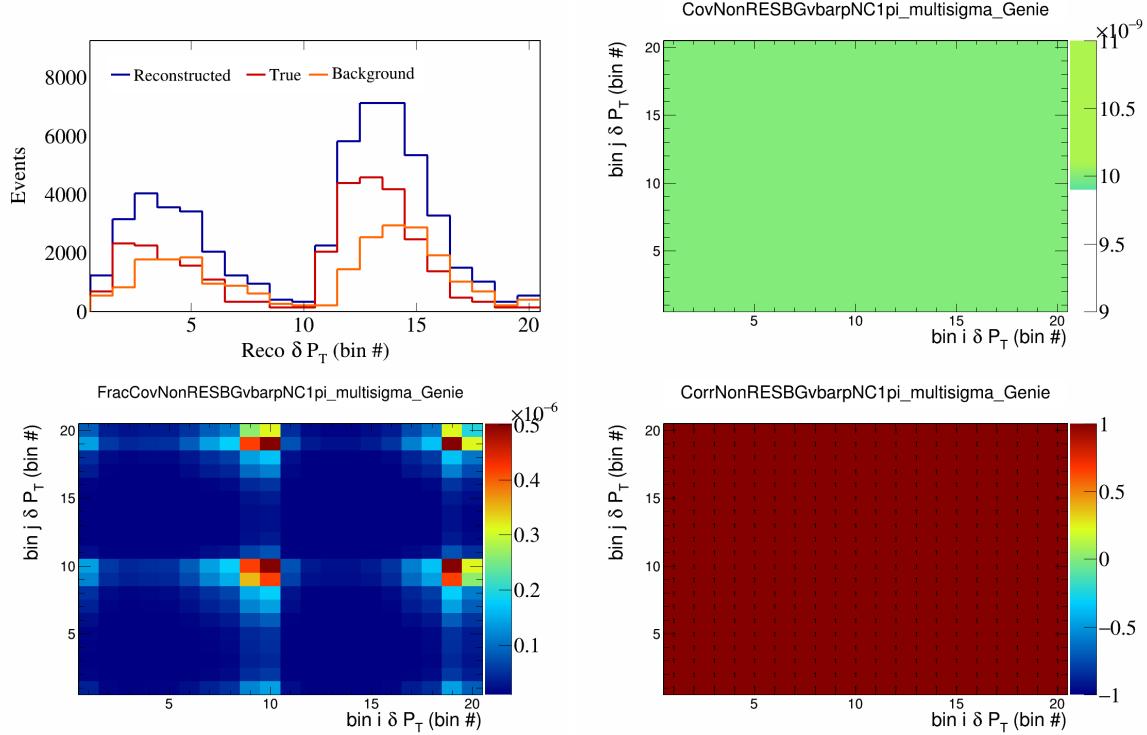


Figure 392: NonRESBGvbarpNC1pi variations for δP_T in $\cos(\theta_{\vec{p}_\mu})$.

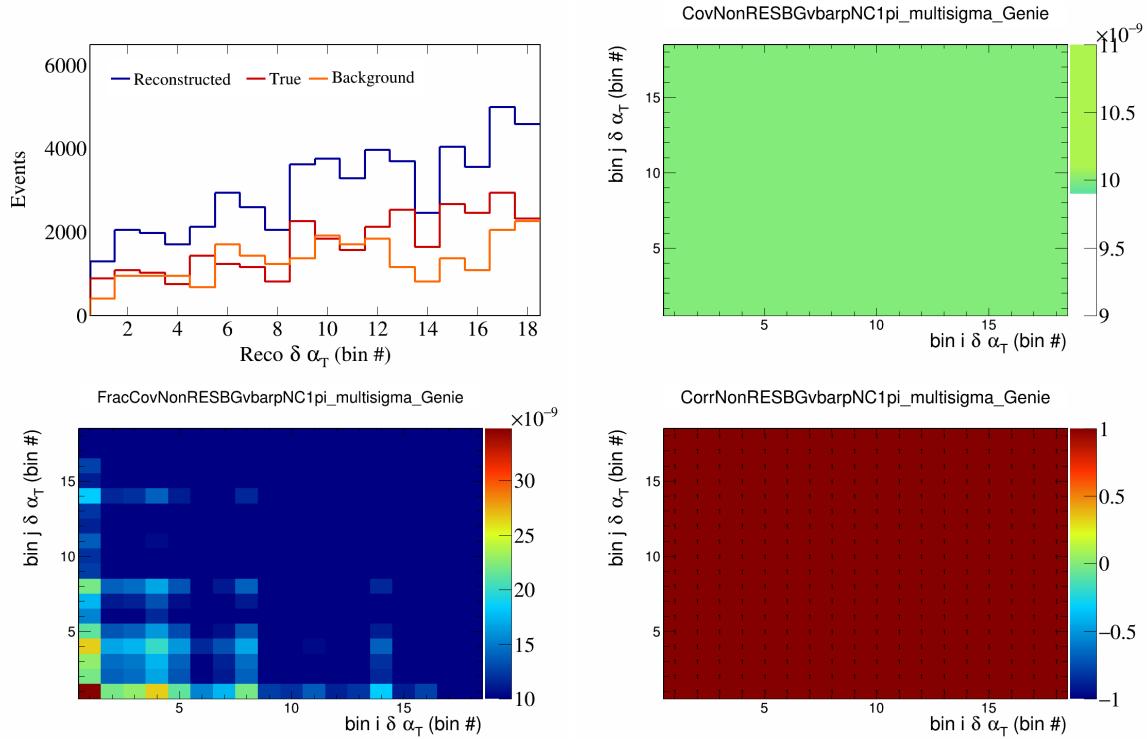


Figure 393: NonRESBGvbarpNC1pi variations for $\delta \alpha_T$ in $\cos(\theta_{\vec{p}_\mu})$.

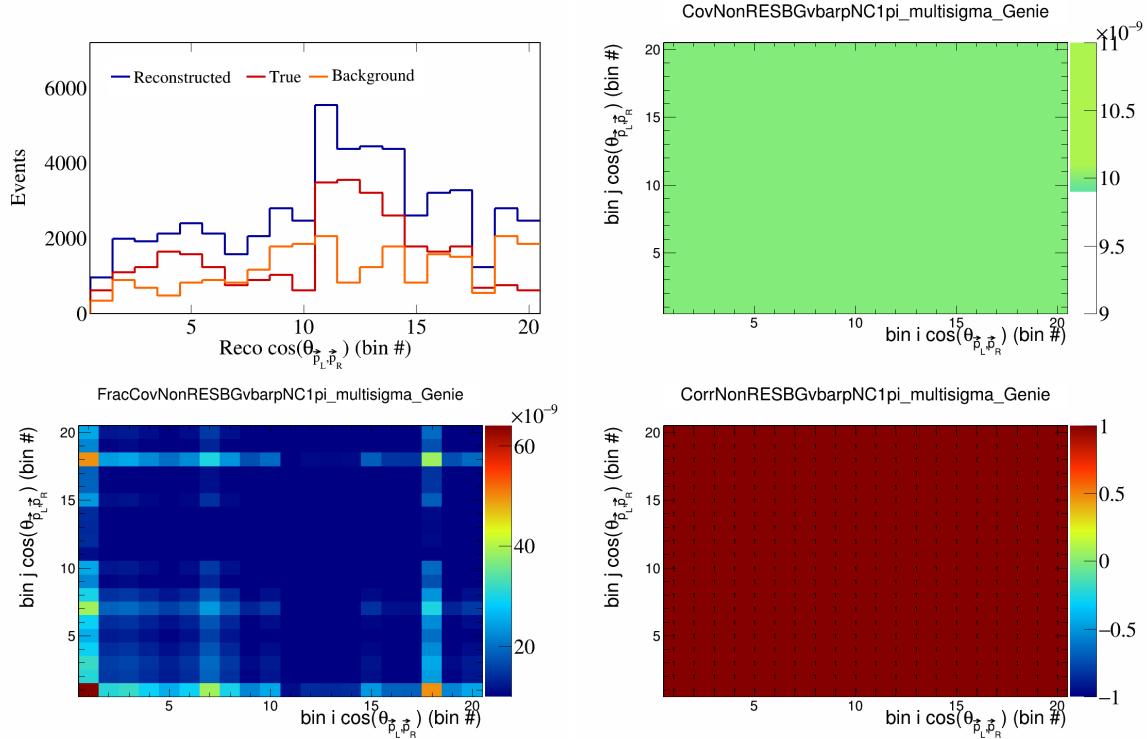


Figure 394: NonRESBGvbarpNC1pi variations for $\cos(\theta_{\vec{p}_L, \vec{p}_R})$ in $\cos(\theta_{\vec{p}_\mu})$.

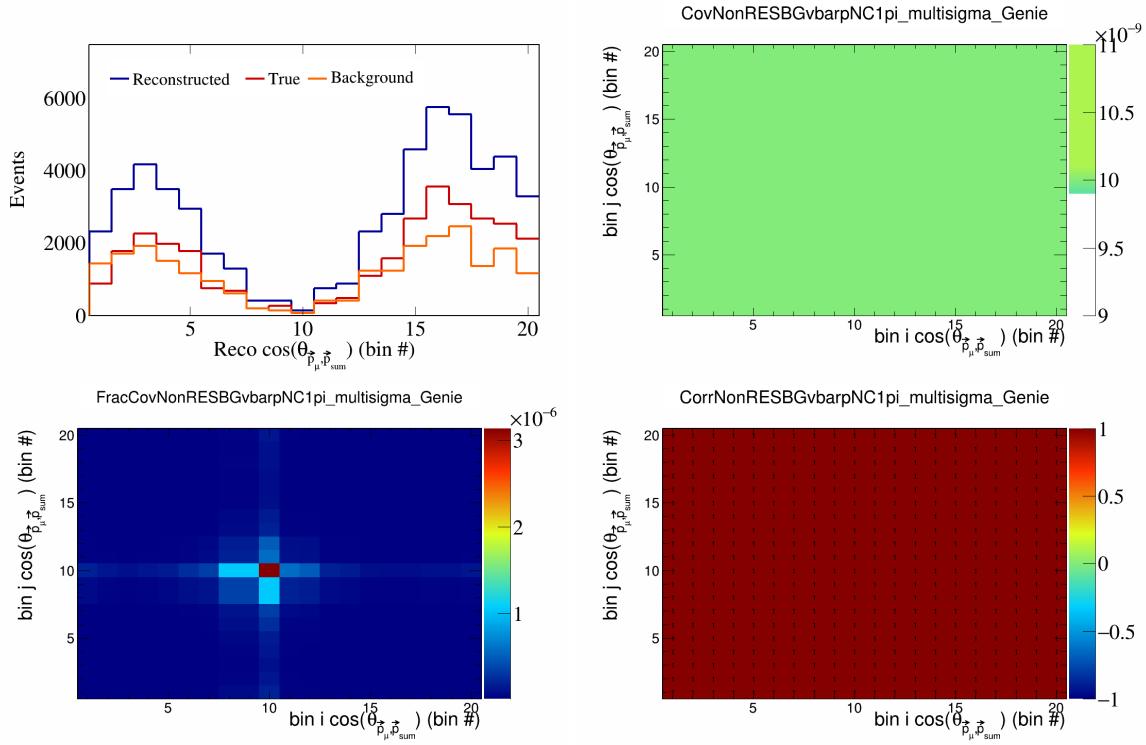


Figure 395: NonRESBGvbarpNC1pi variations for $\cos(\theta_{\vec{p}_\mu})$ in $\cos(\theta_{\vec{p}_\mu})$.

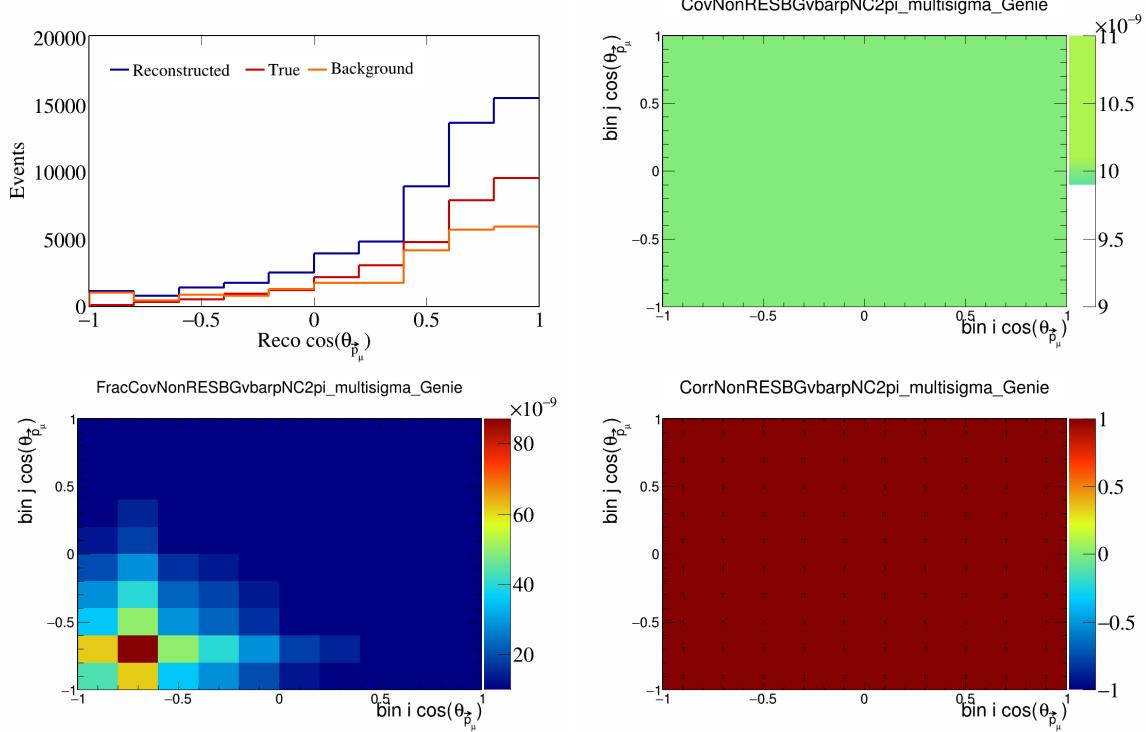


Figure 396: NonRESBGvbarpNC2pi variations for $\cos(\theta_{\vec{p}_\mu})$.

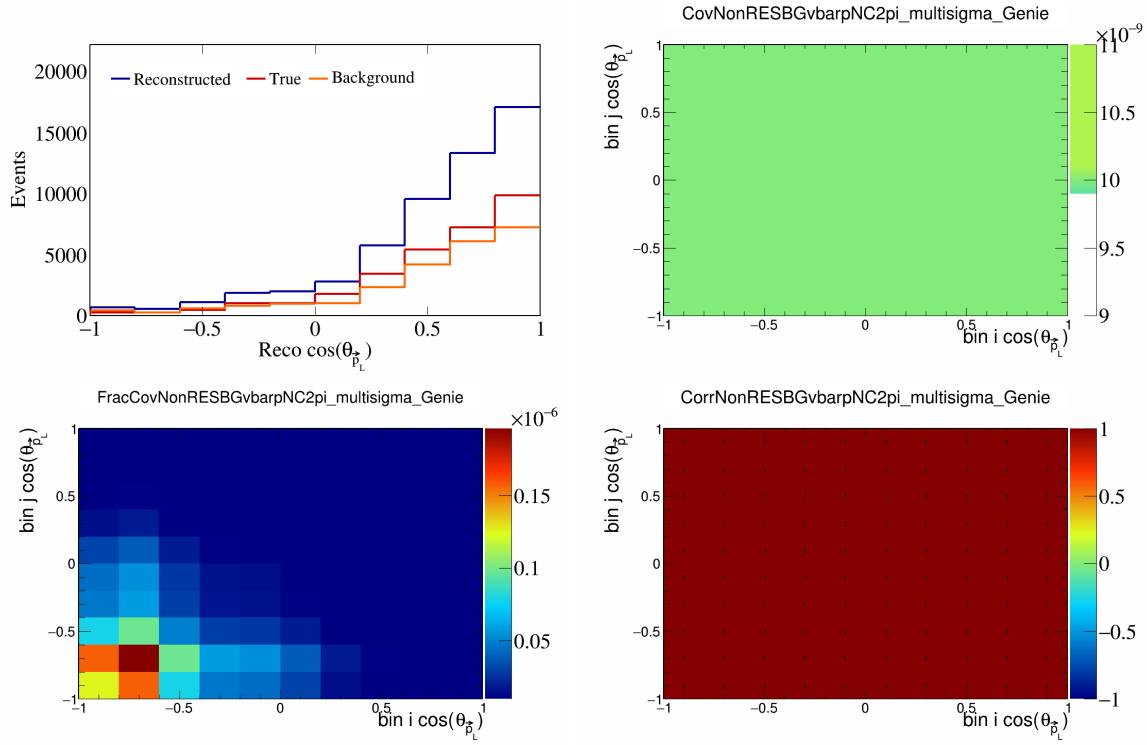


Figure 397: NonRESBGvbarpNC2pi variations for $\cos(\theta_{\vec{p}_L})$.

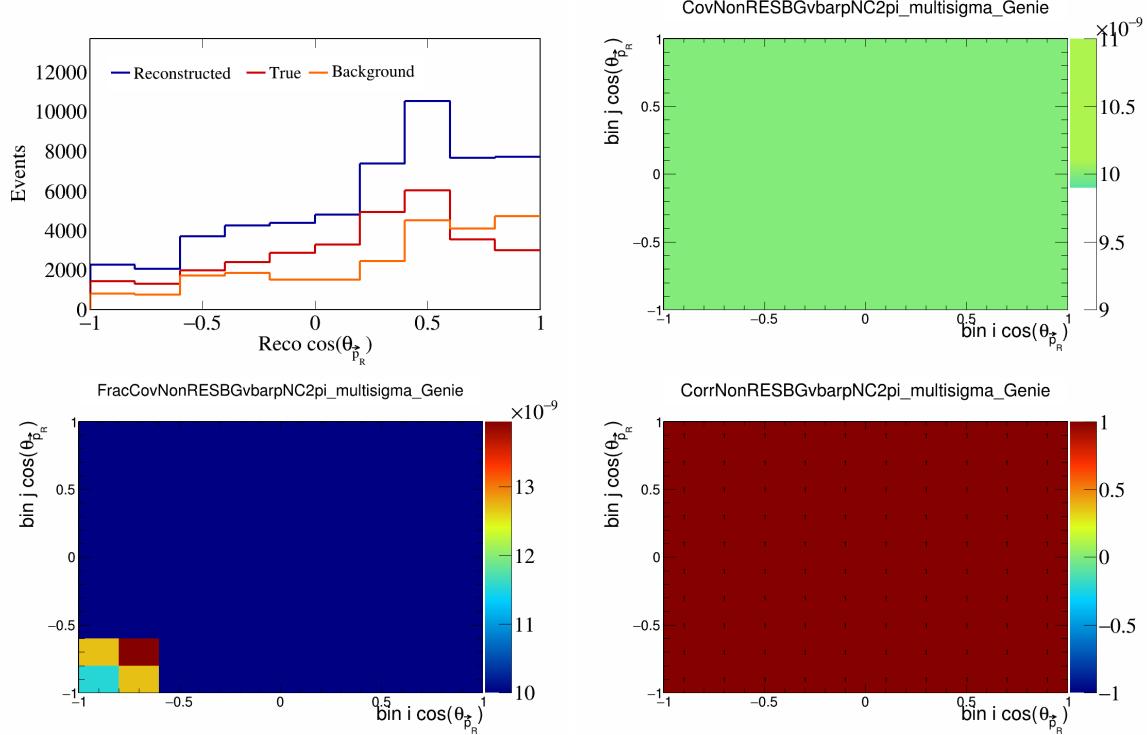


Figure 398: NonRESBGvbarpNC2pi variations for $\cos(\theta_{\vec{p}_R})$.

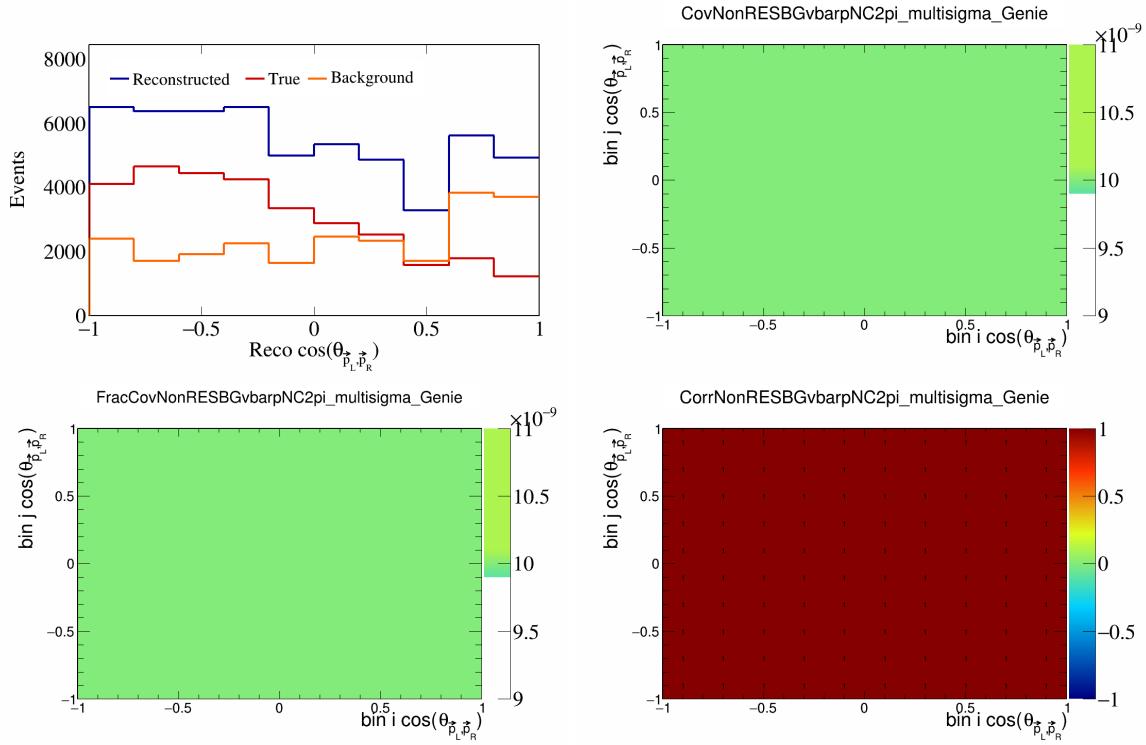


Figure 399: NonRESBGvbarpNC2pi variations for $\cos(\theta_{\vec{p}_L, \vec{p}_R})$.

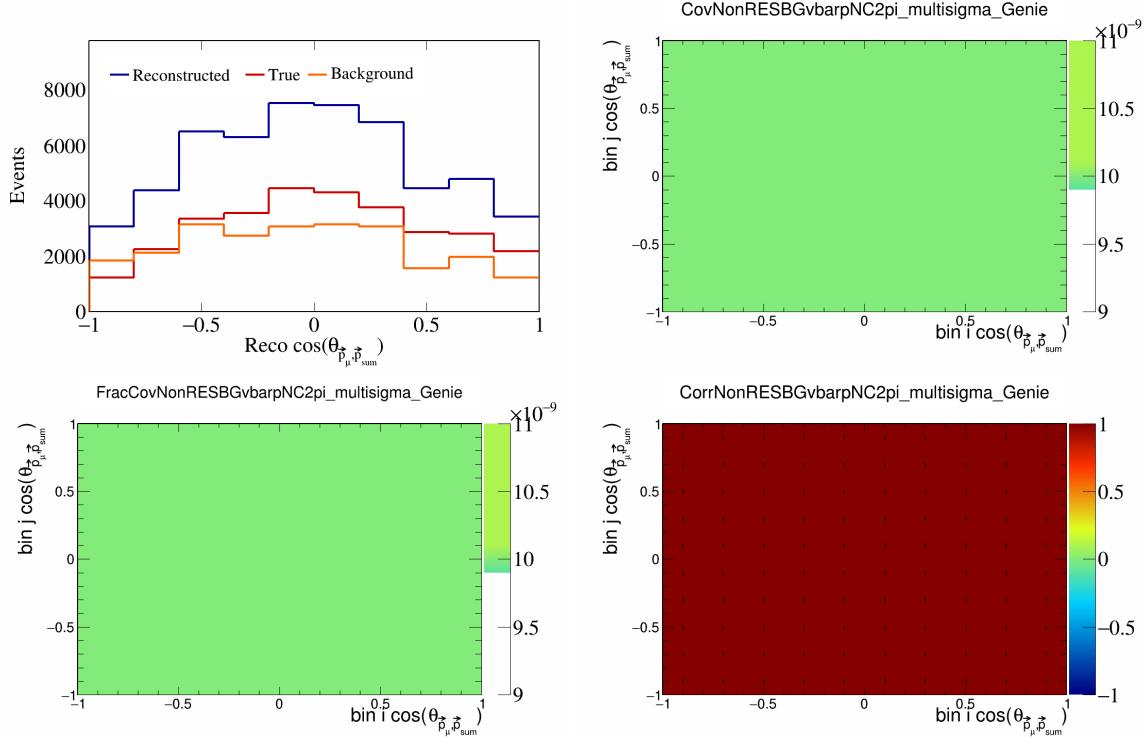


Figure 400: NonRESBGvbarpNC2pi variations for $\cos(\theta_{\vec{p}_\mu, \vec{p}_{\text{sum}}})$.

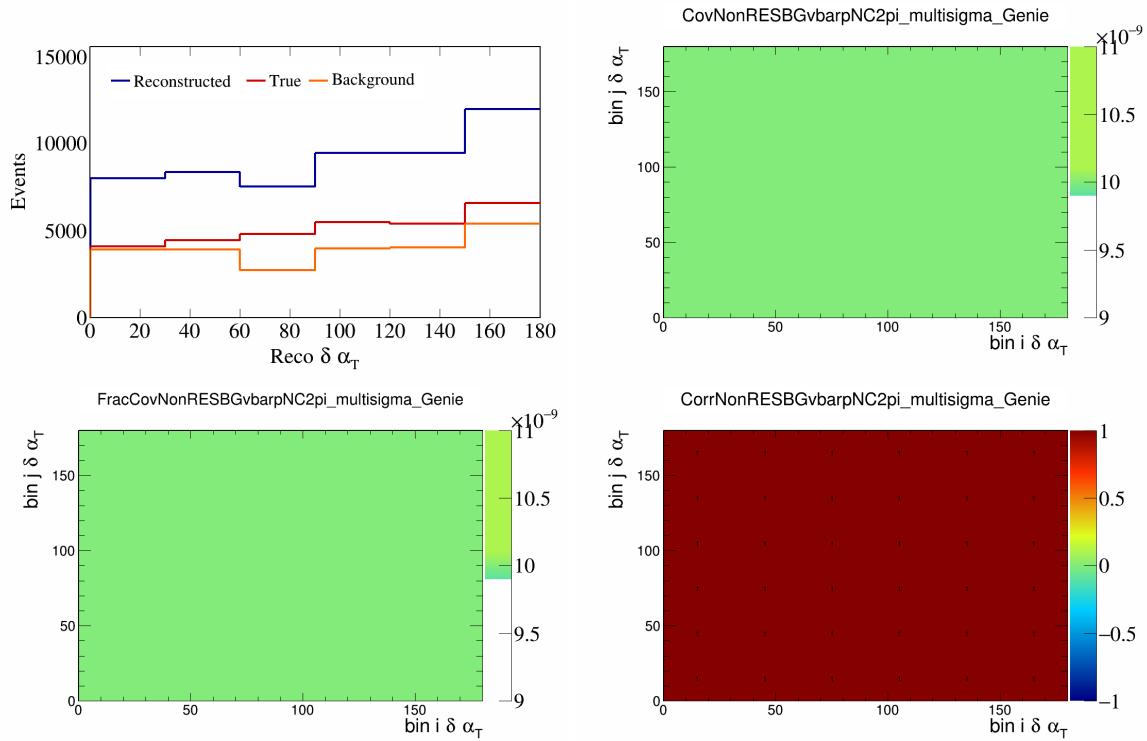


Figure 401: NonRESBGvbarpNC2pi variations for $\delta\alpha_T$.

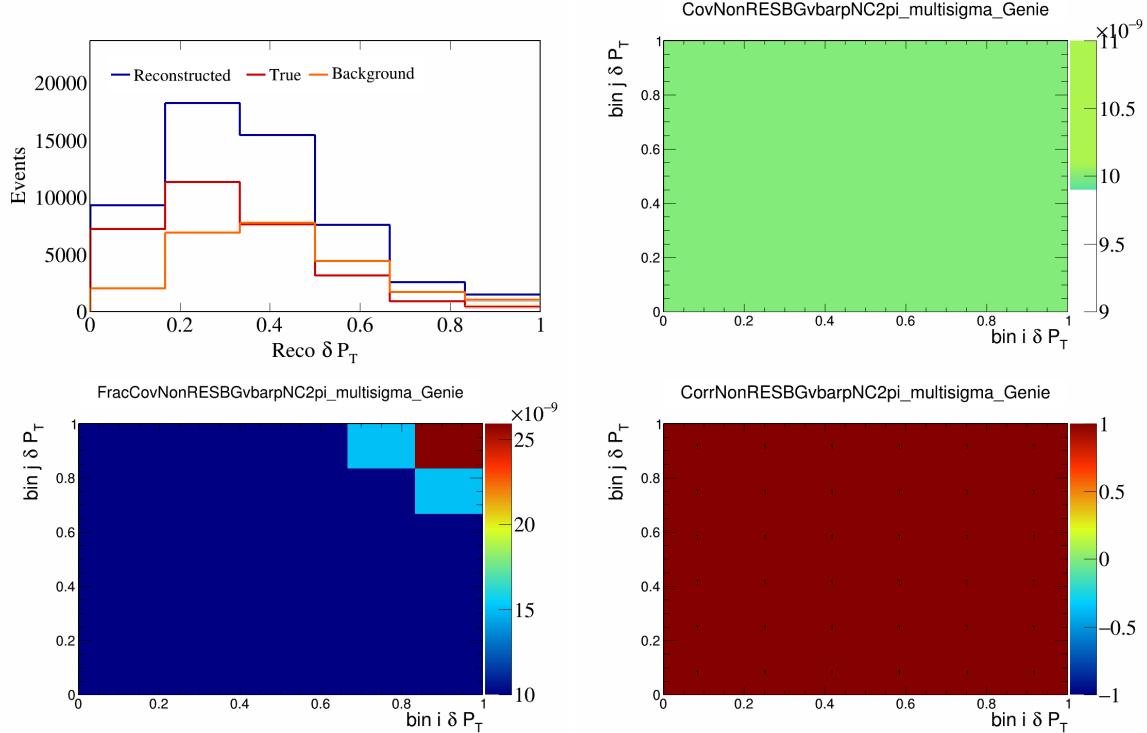


Figure 402: NonRESBGvbarpNC2pi variations for δP_T .

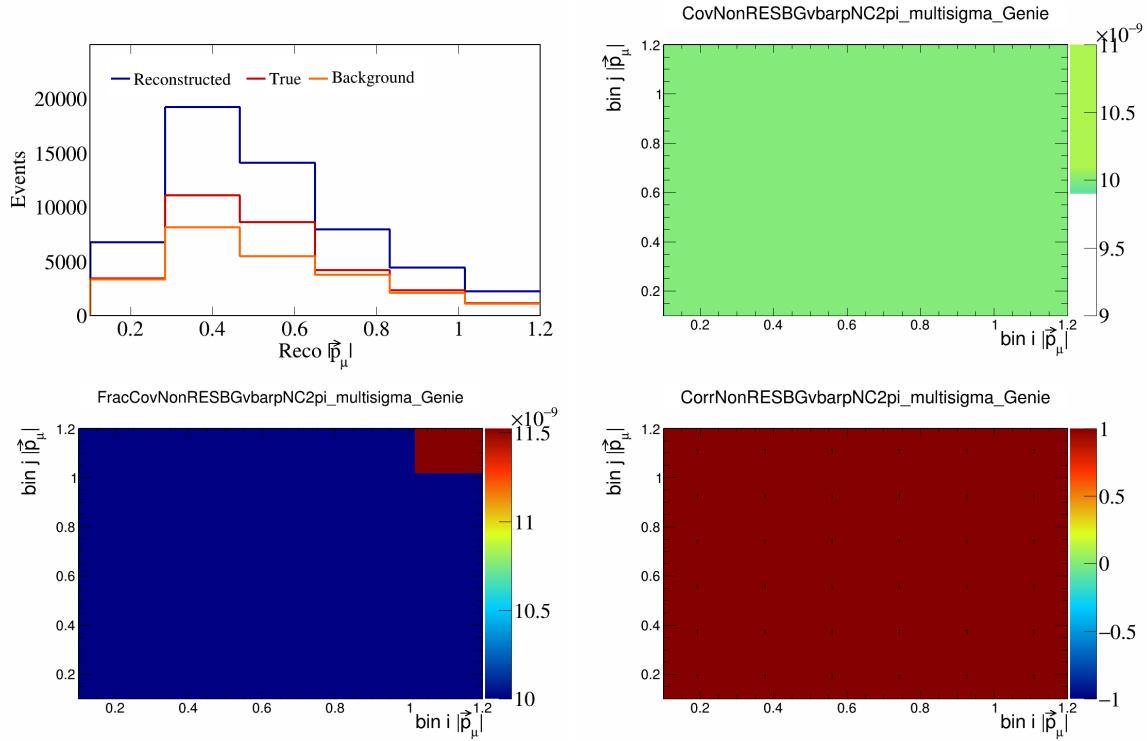


Figure 403: NonRESBGvbarpNC2pi variations for $|\vec{p}_\mu|$.

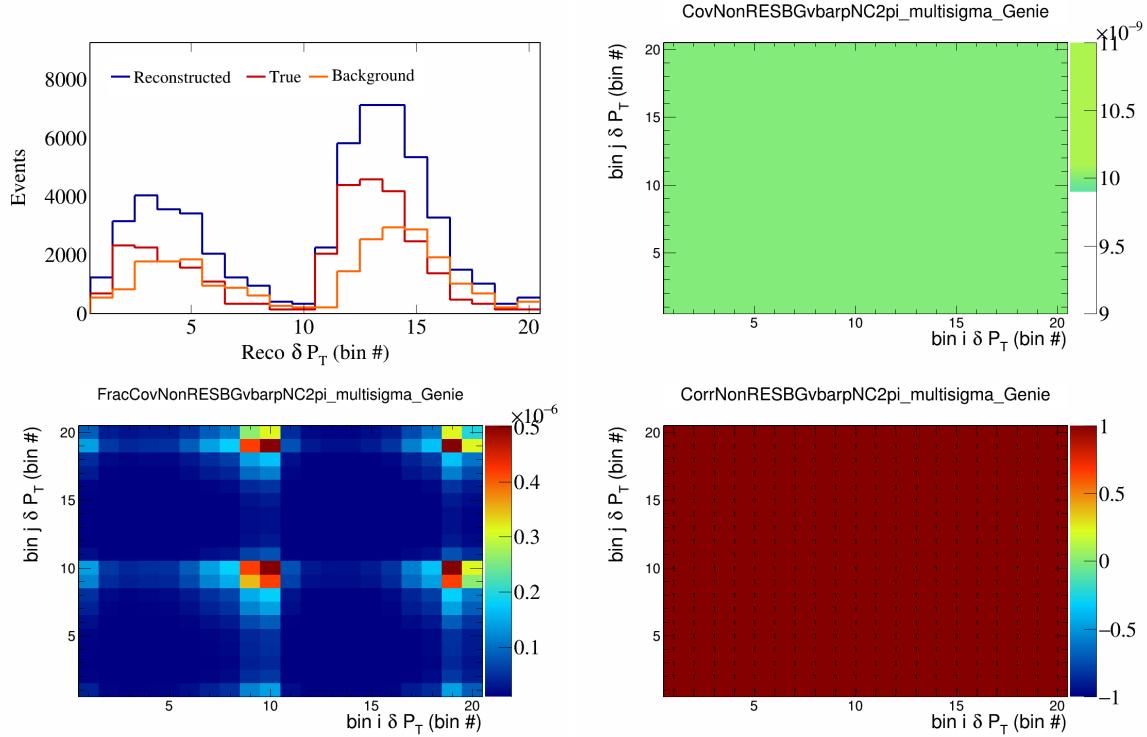


Figure 404: NonRESBGvbarpNC2pi variations for δP_T in $\cos(\theta_{\vec{p}_\mu})$.

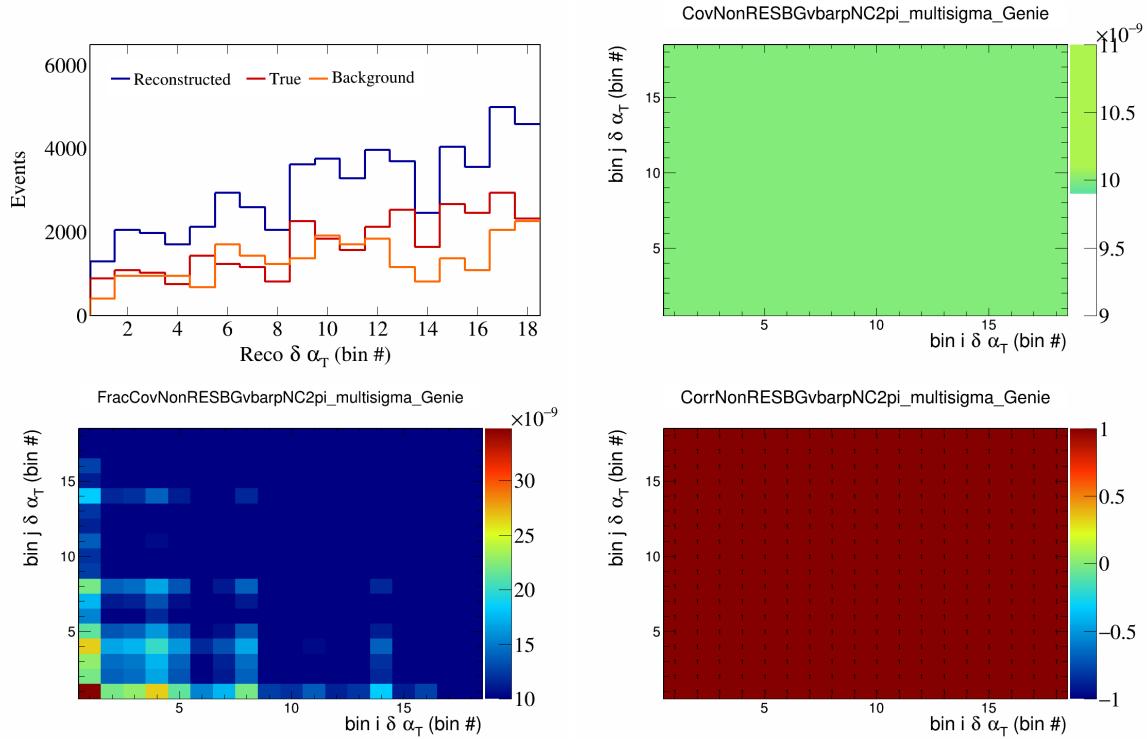


Figure 405: NonRESBGvbarpNC2pi variations for $\delta\alpha_T$ in $\cos(\theta_{\vec{p}_\mu})$.

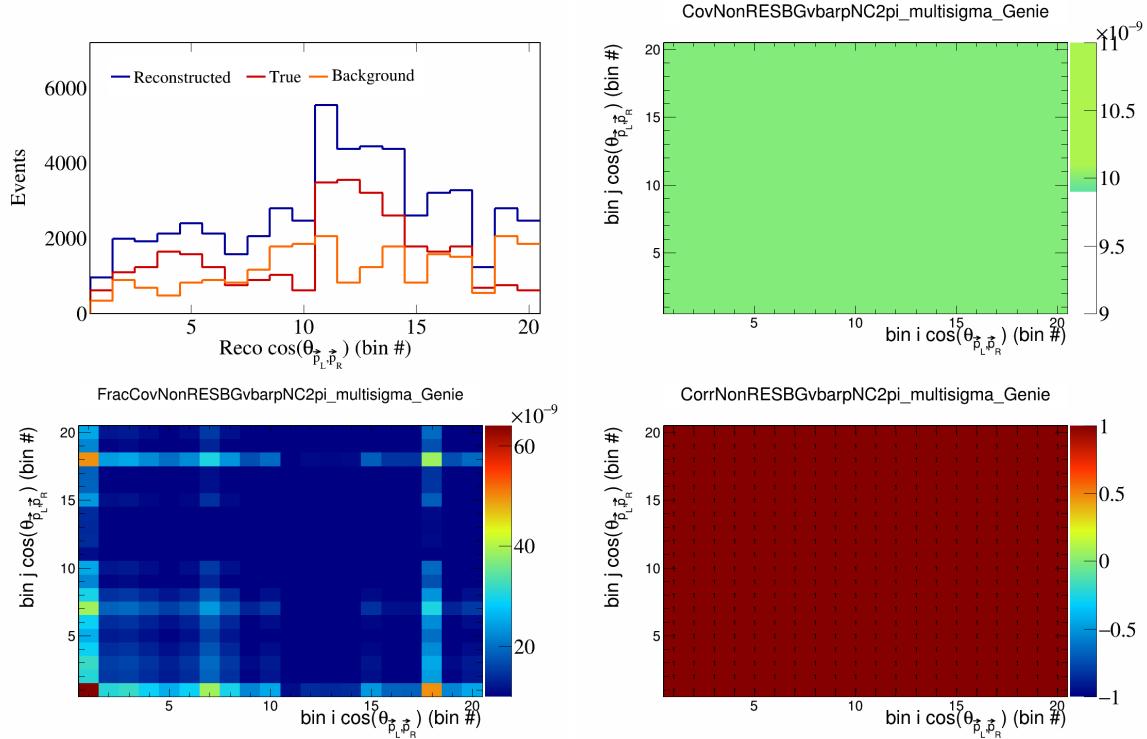


Figure 406: NonRESBGvbarpNC2pi variations for $\cos(\theta_{\vec{p}_L, \vec{p}_R})$ in $\cos(\theta_{\vec{p}_\mu})$.

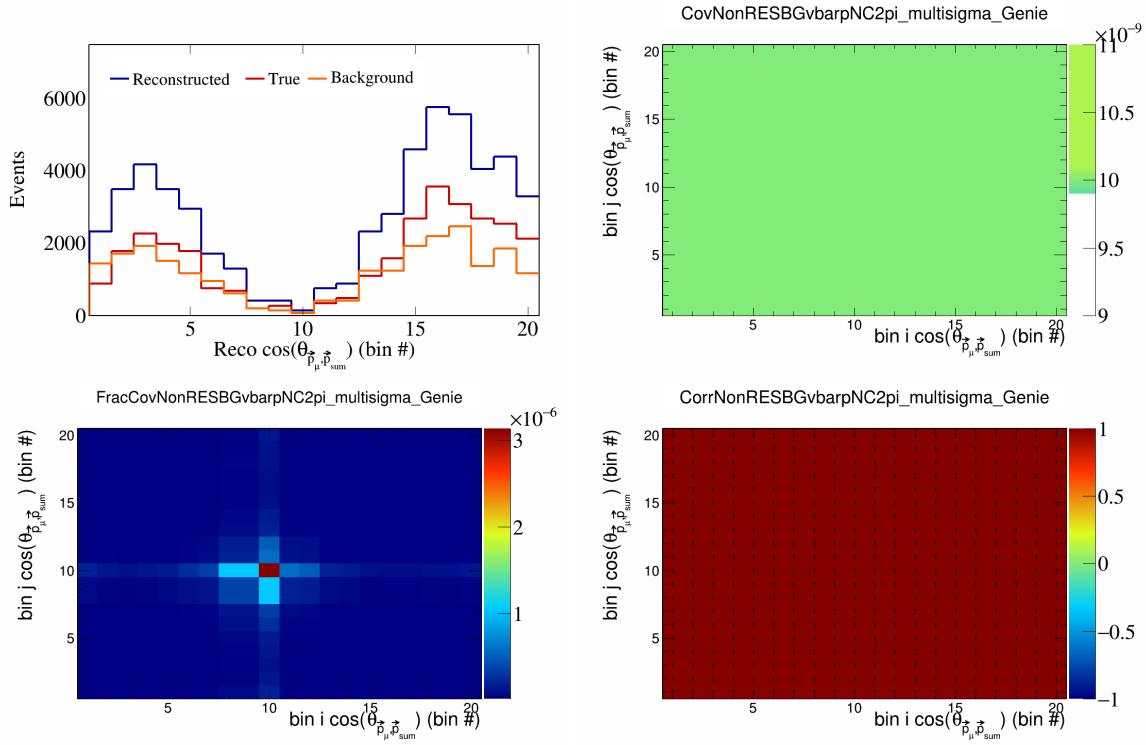


Figure 407: NonRESBGvbarpNC2pi variations for $\cos(\theta_{\vec{p}_\mu} \cdot \vec{p}_{\text{sum}})$ in $\cos(\theta_{\vec{p}_\mu})$.

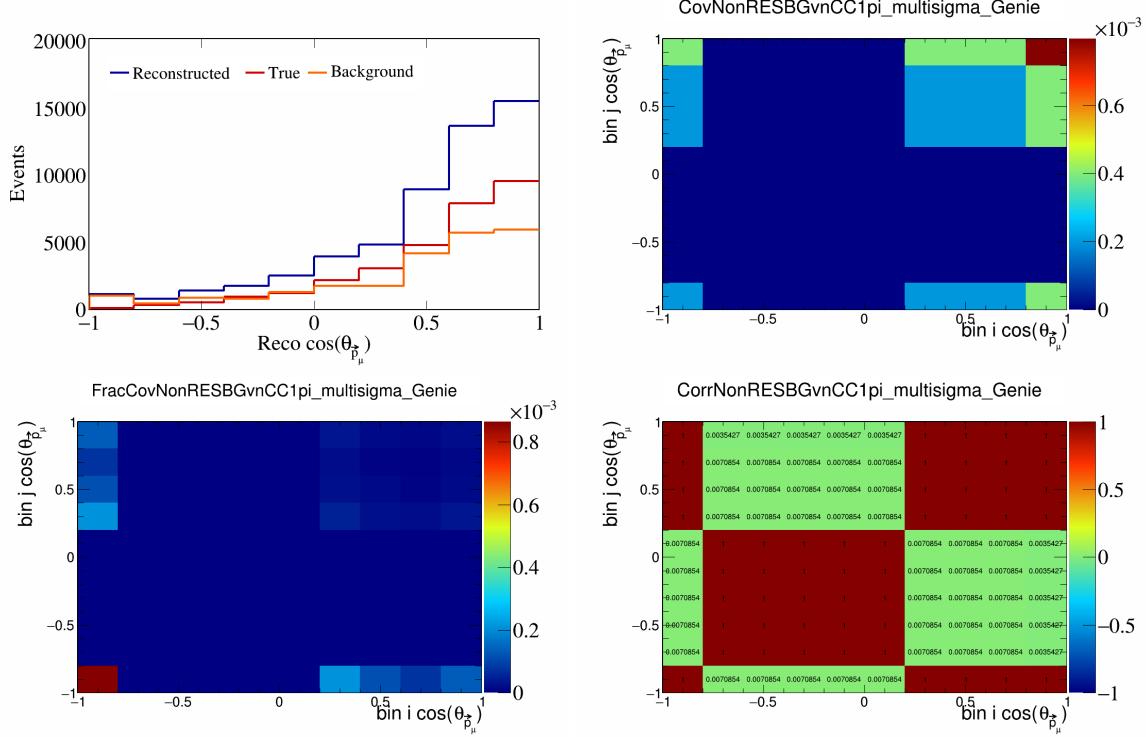


Figure 408: NonRESBGvnCC1pi variations for $\cos(\theta_{\vec{p}_\mu})$.

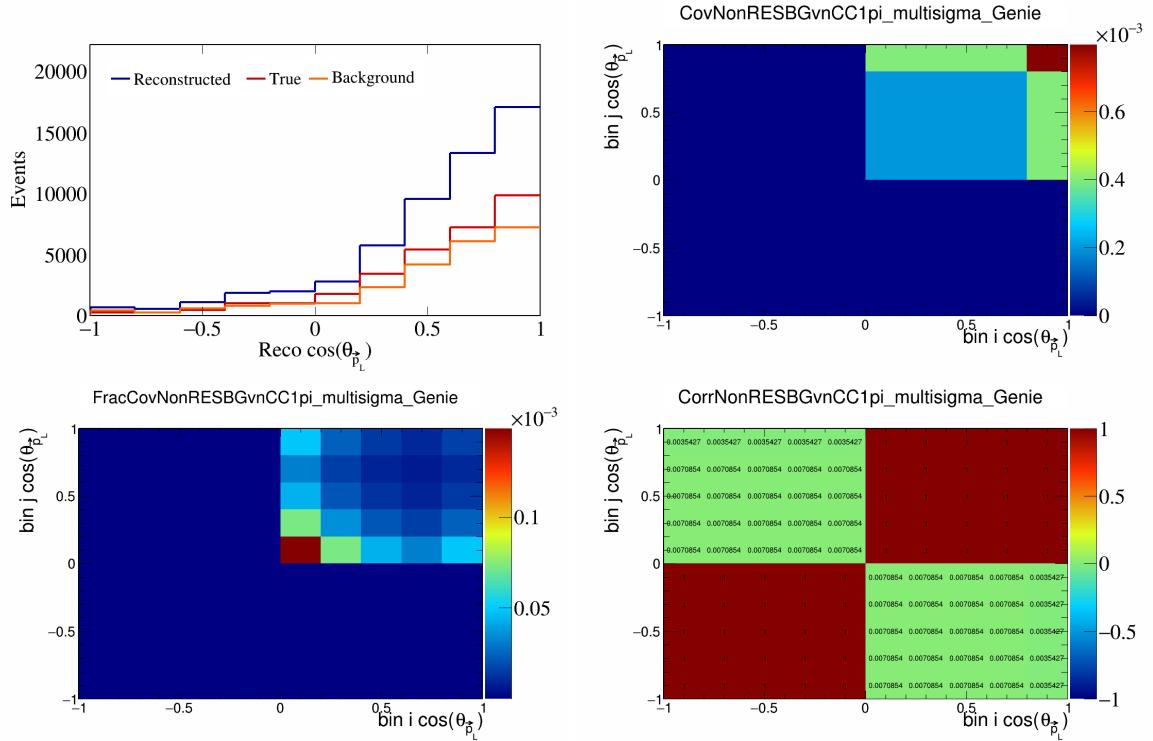


Figure 409: NonRESBGvnCC1pi variations for $\cos(\theta_{\vec{p}_L})$.

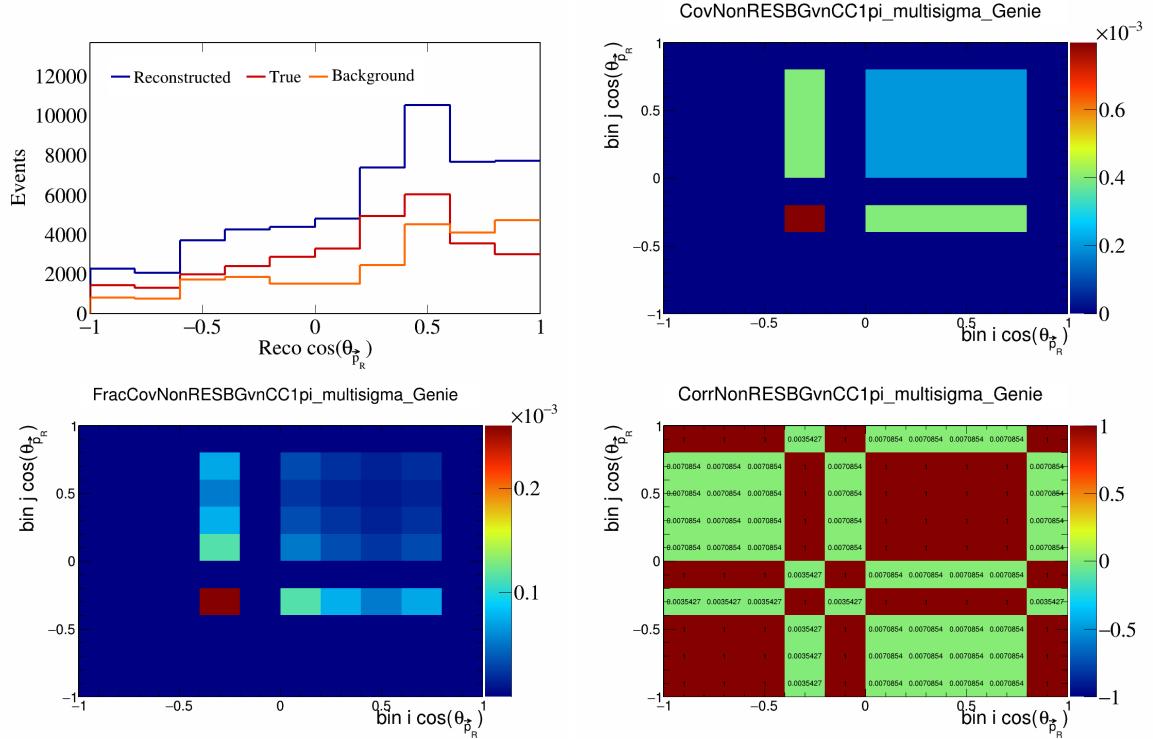


Figure 410: NonRESBGvnCC1pi variations for $\cos(\theta_{\vec{p}_R})$.

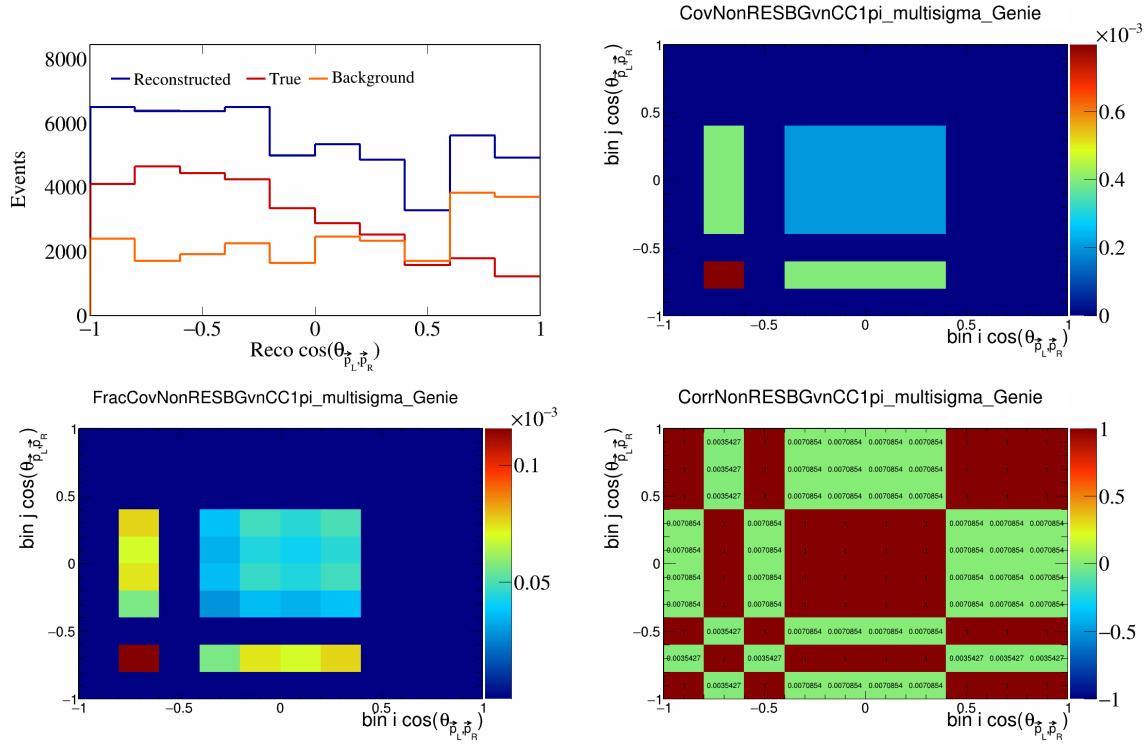


Figure 411: NonRESBGvnCC1pi variations for $\cos(\theta_{\vec{p}_L, \vec{p}_R})$.

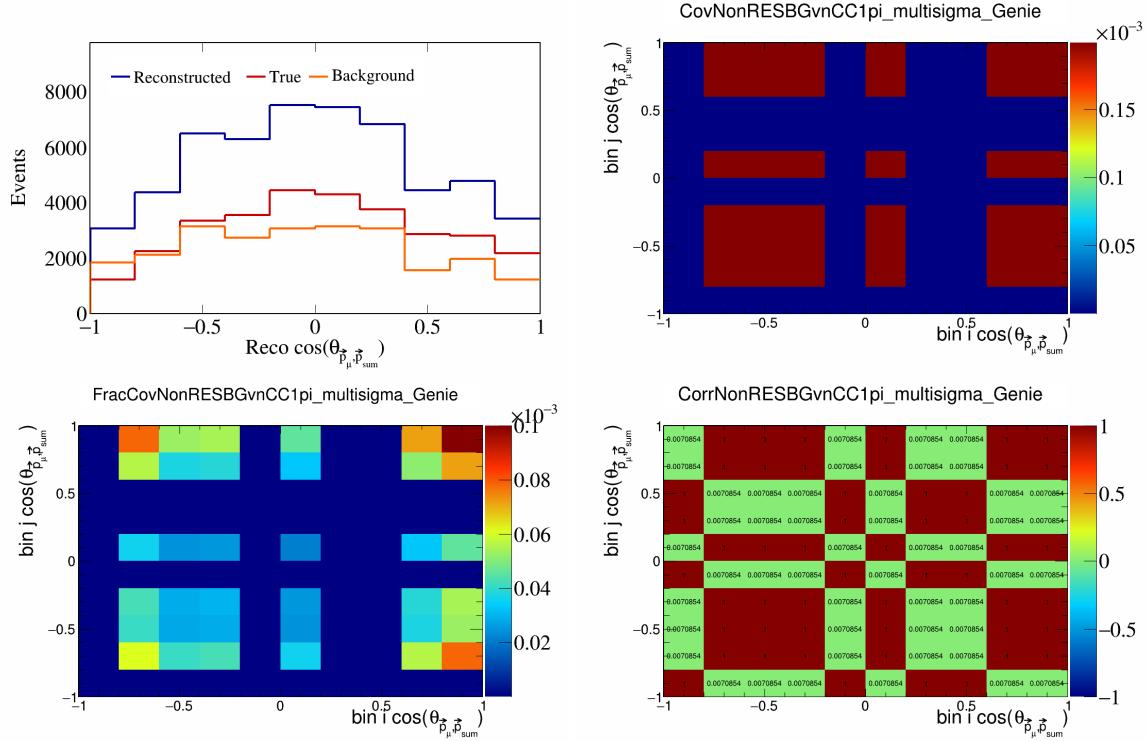


Figure 412: NonRESBGvnCC1pi variations for $\cos(\theta_{\vec{p}_\mu, \vec{p}_{\text{sum}}})$.

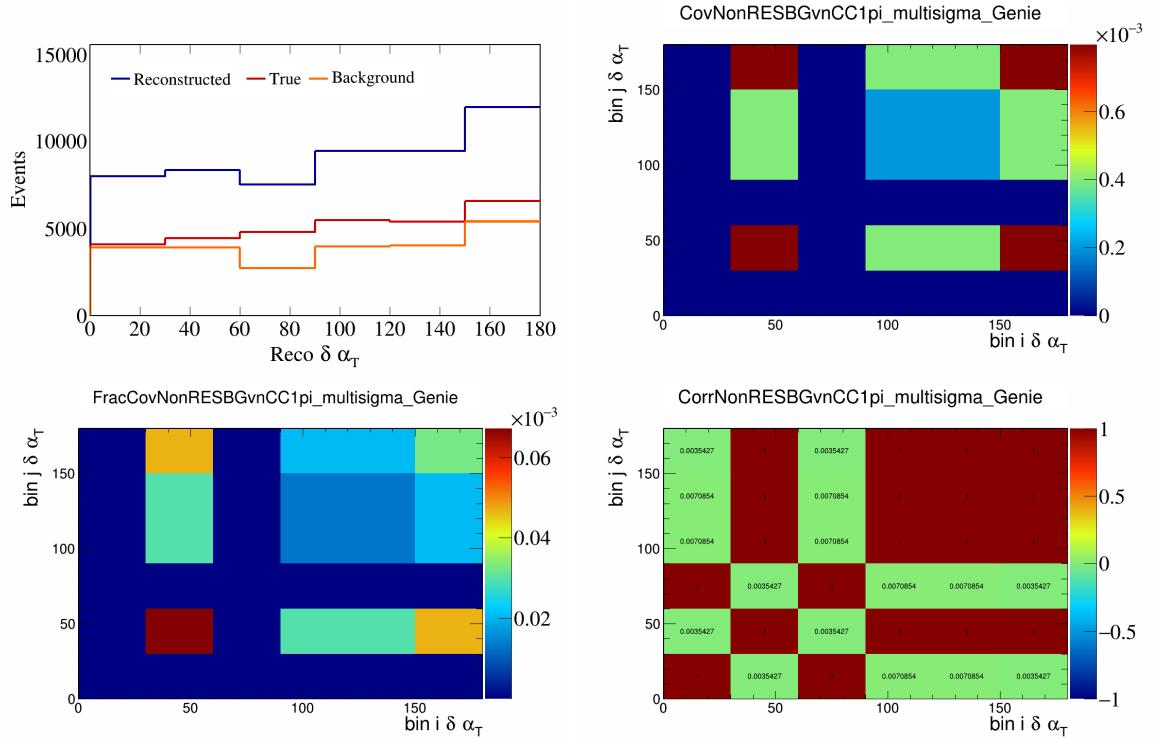


Figure 413: NonRESBGvnCC1pi variations for $\delta\alpha_T$.

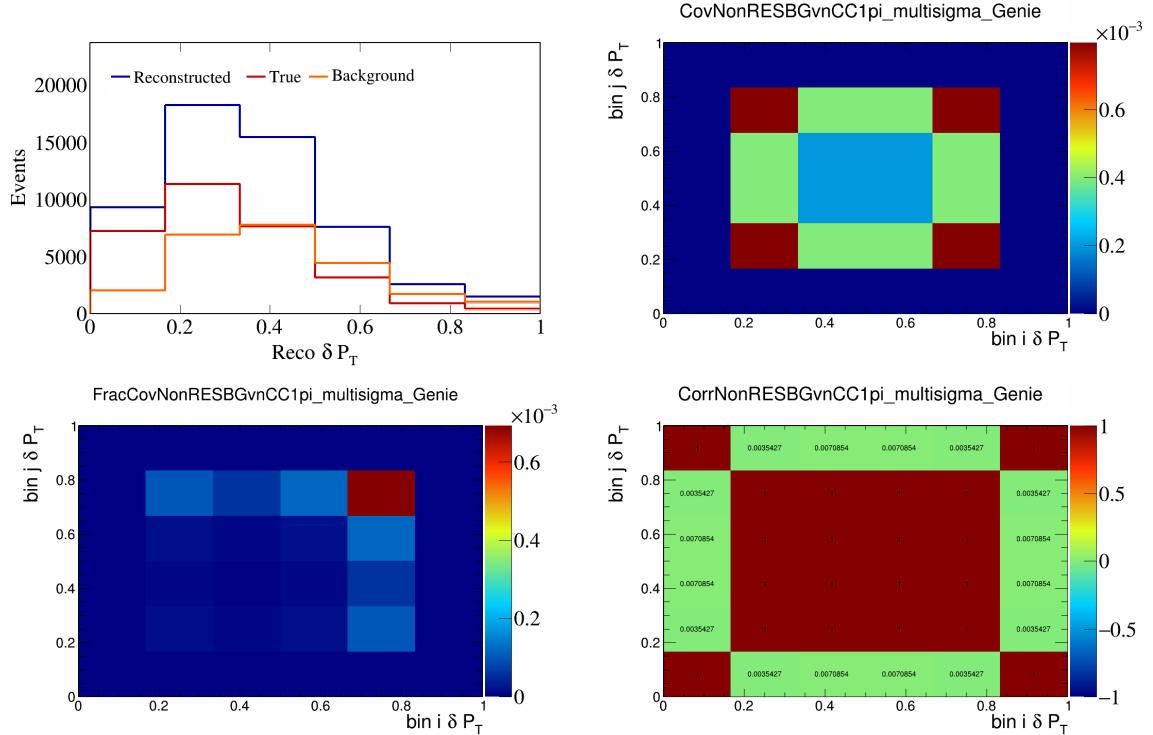


Figure 414: NonRESBGvnCC1pi variations for δP_T .

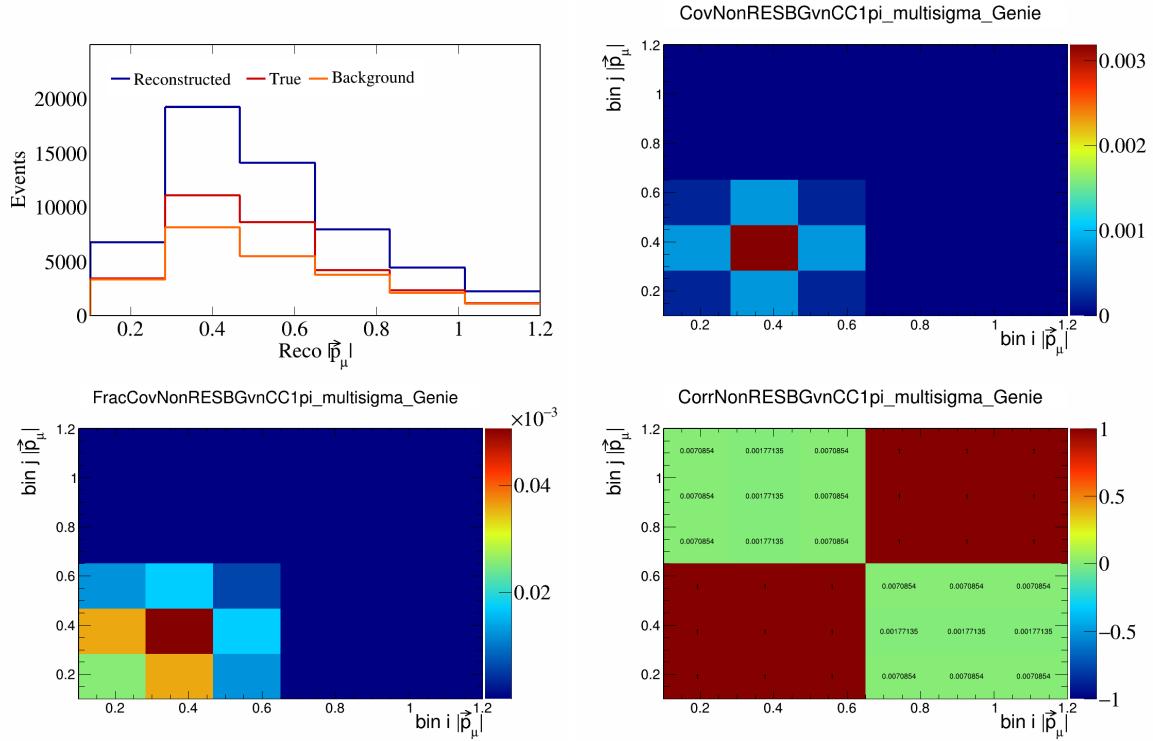


Figure 415: NonRESBGvnCC1pi variations for $|\vec{p}_\mu|$.

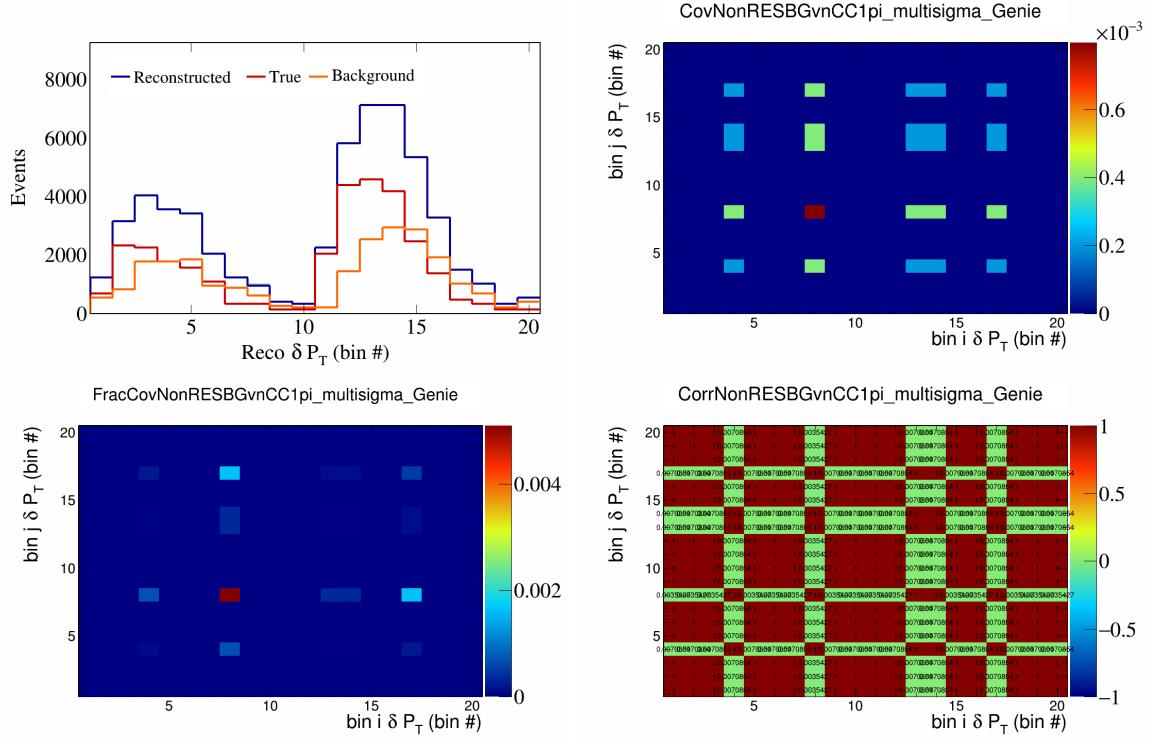


Figure 416: NonRESBGvnCC1pi variations for δP_T in $\cos(\theta_{\vec{p}_\mu})$.

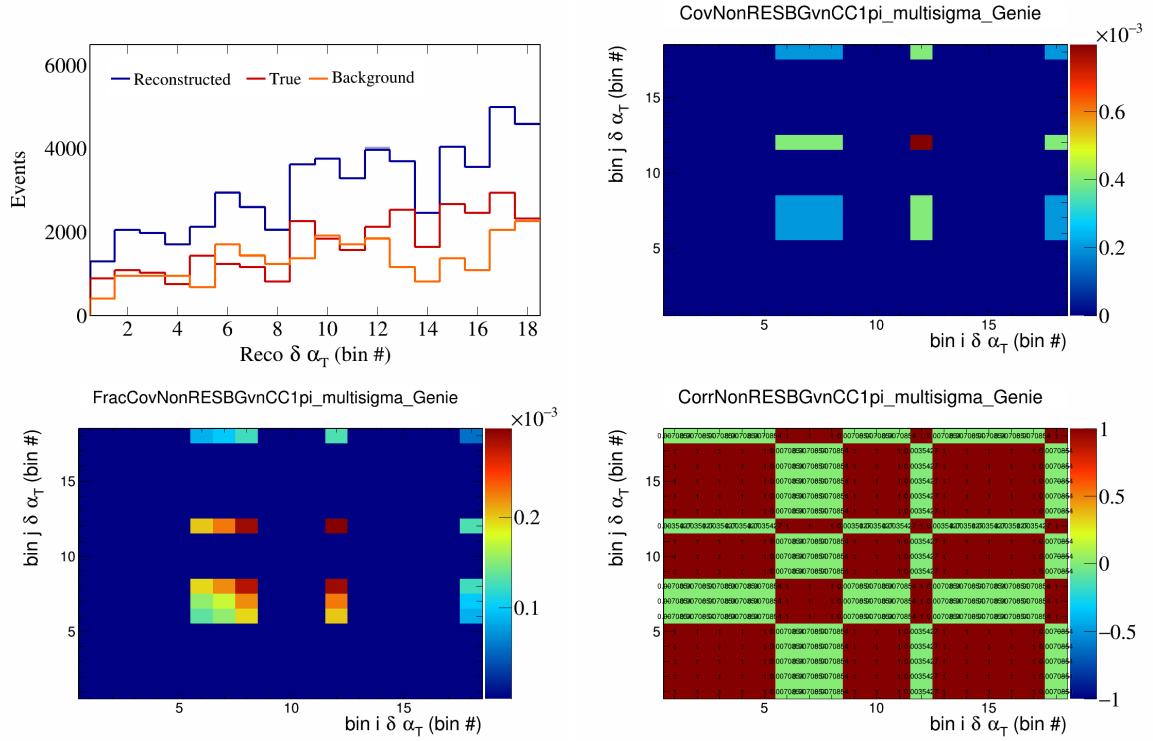


Figure 417: NonRESBGvnCC1pi variations for $\delta\alpha_T$ in $\cos(\theta_{\vec{p}_\mu})$.

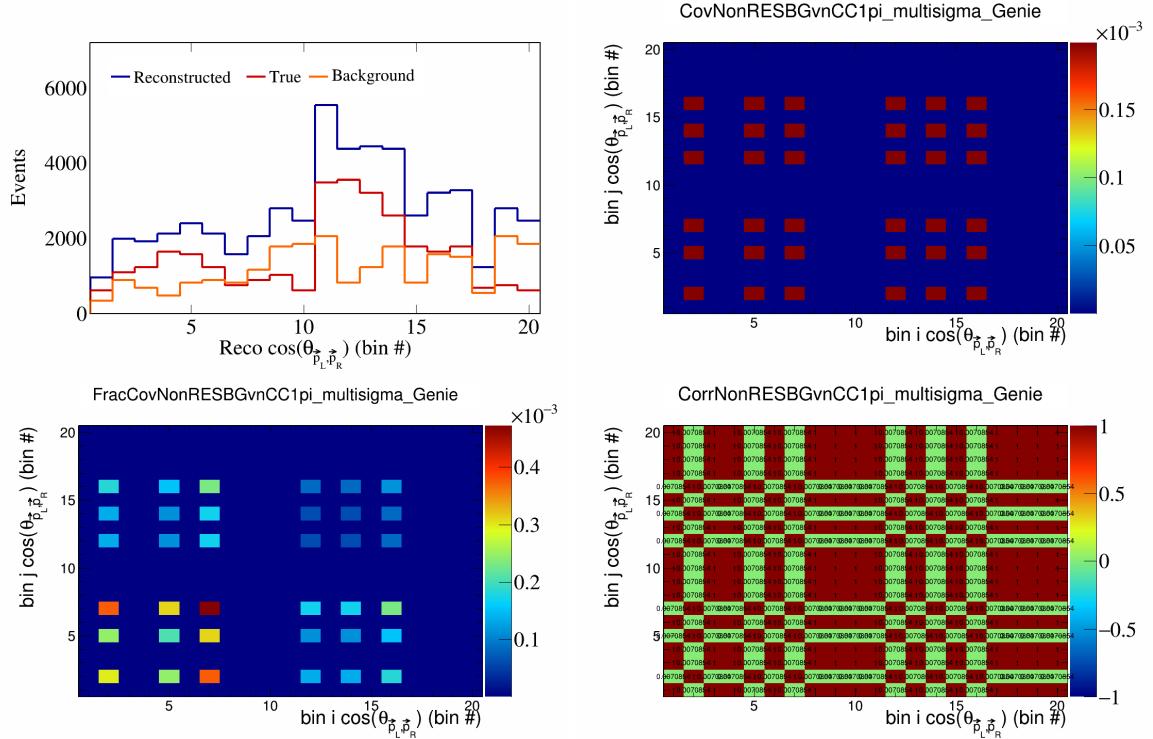


Figure 418: NonRESBGvnCC1pi variations for $\cos(\theta_{\vec{p}_L, \vec{p}_R})$ in $\cos(\theta_{\vec{p}_\mu})$.

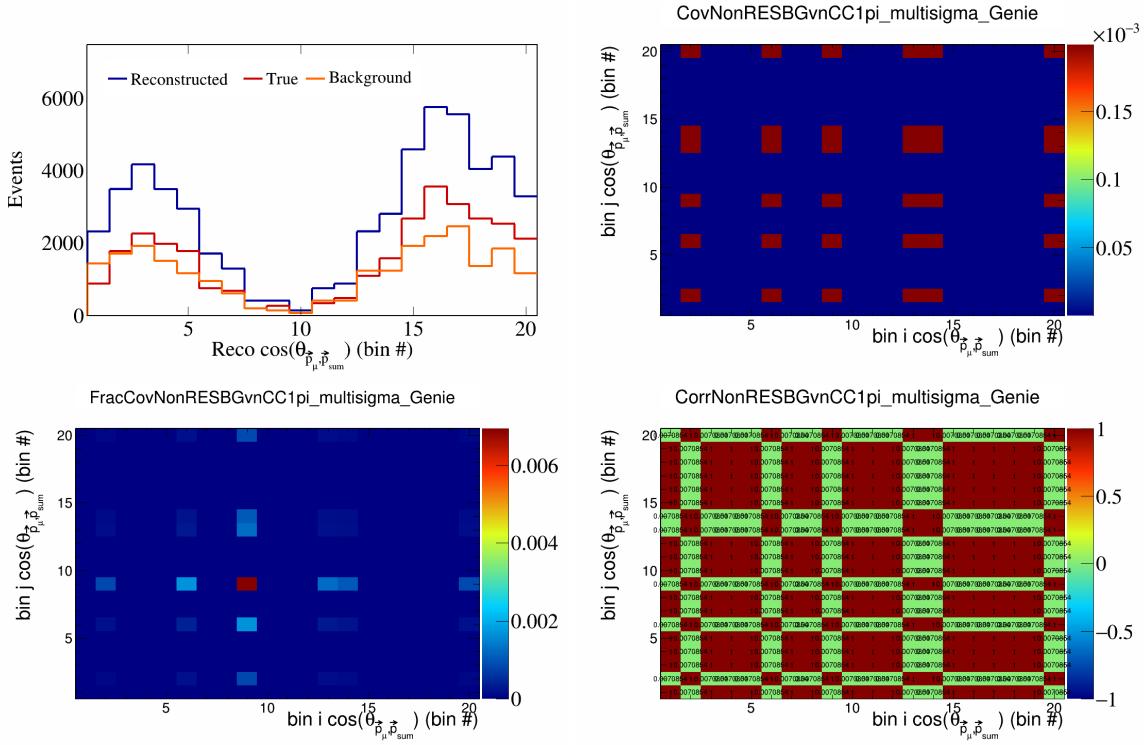


Figure 419: NonRESBGvnCC1pi variations for $\cos(\theta_{\vec{p}_\mu, \vec{p}_{\text{sum}}})$ in $\cos(\theta_{\vec{p}_\mu})$.

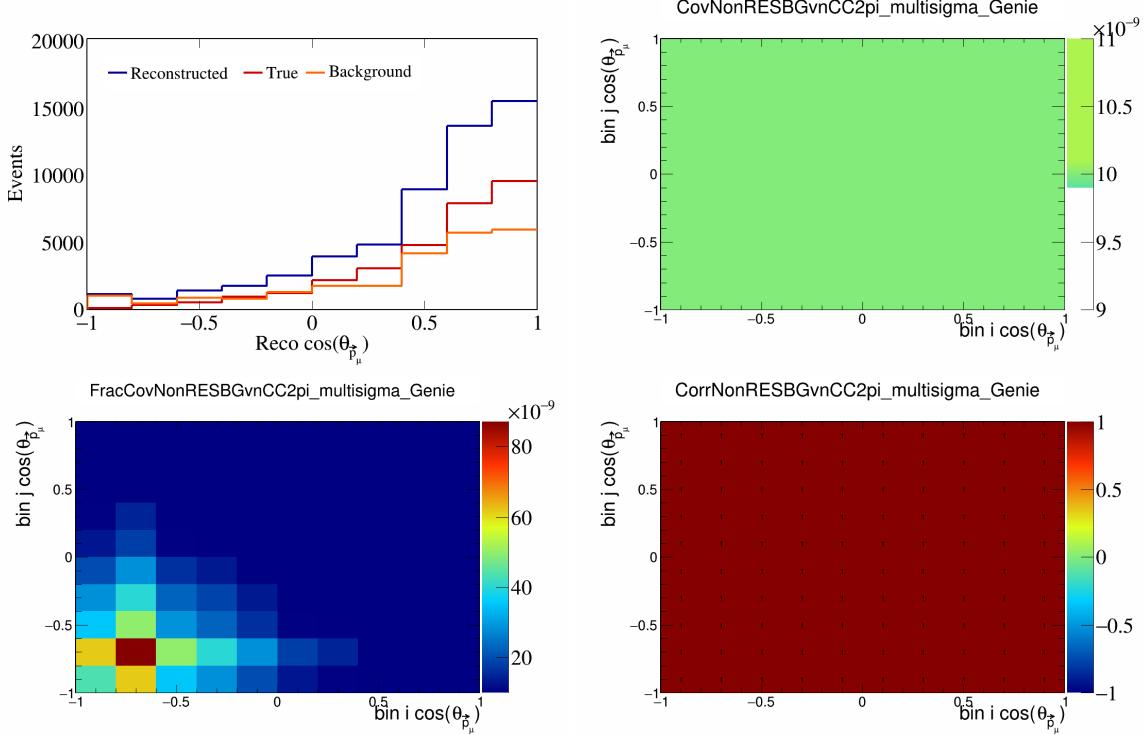


Figure 420: NonRESBGvnCC2pi variations for $\cos(\theta_{\vec{p}_\mu})$.

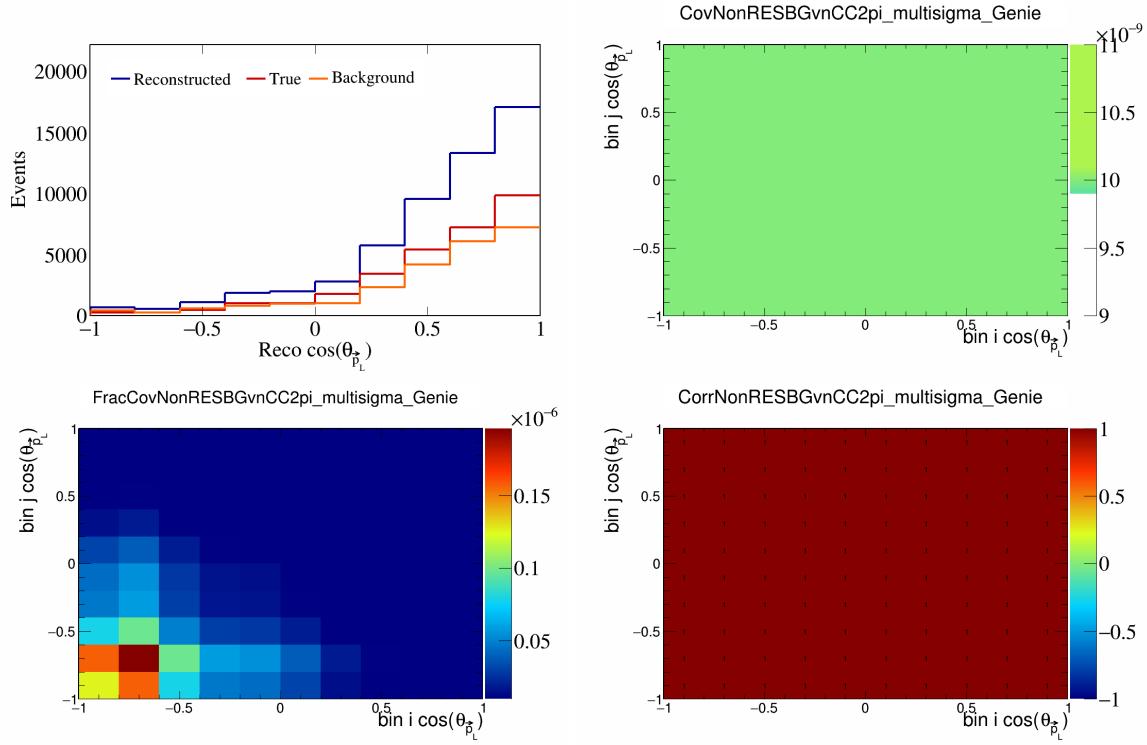


Figure 421: NonRESBGvnCC2pi variations for $\cos(\theta_{\vec{p}_L})$.

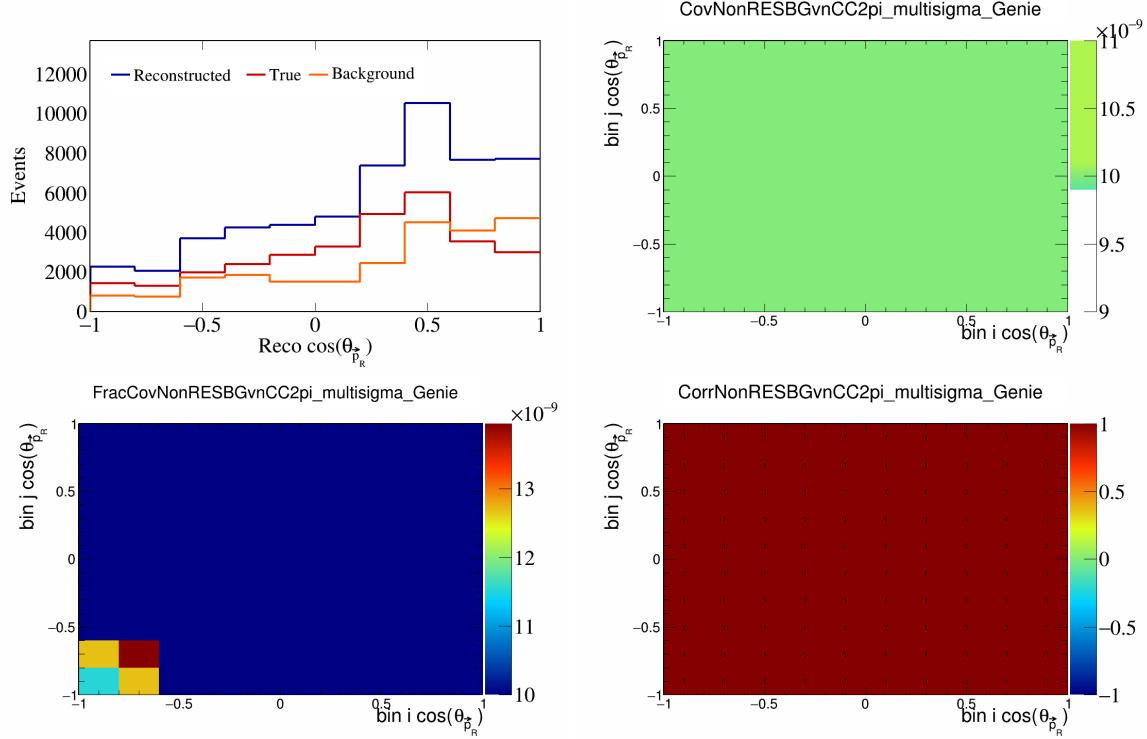


Figure 422: NonRESBGvnCC2pi variations for $\cos(\theta_{\vec{p}_R})$.

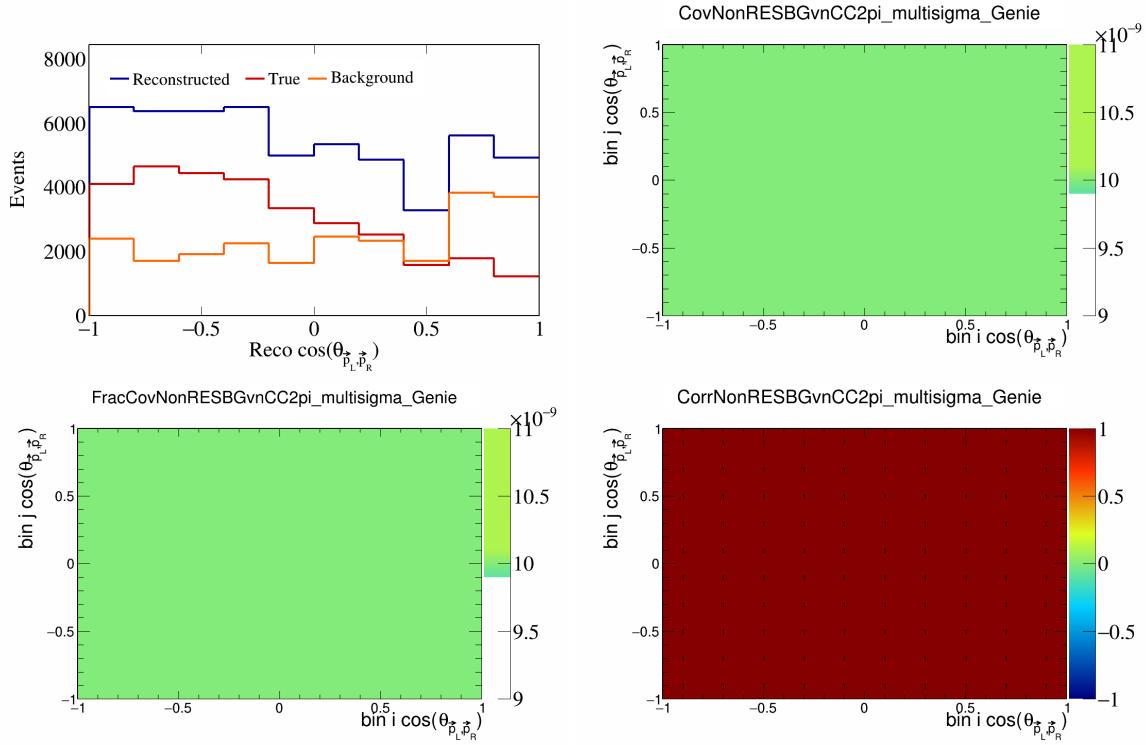


Figure 423: NonRESBGvnCC2pi variations for $\cos(\theta_{\vec{p}_L, \vec{p}_R})$.

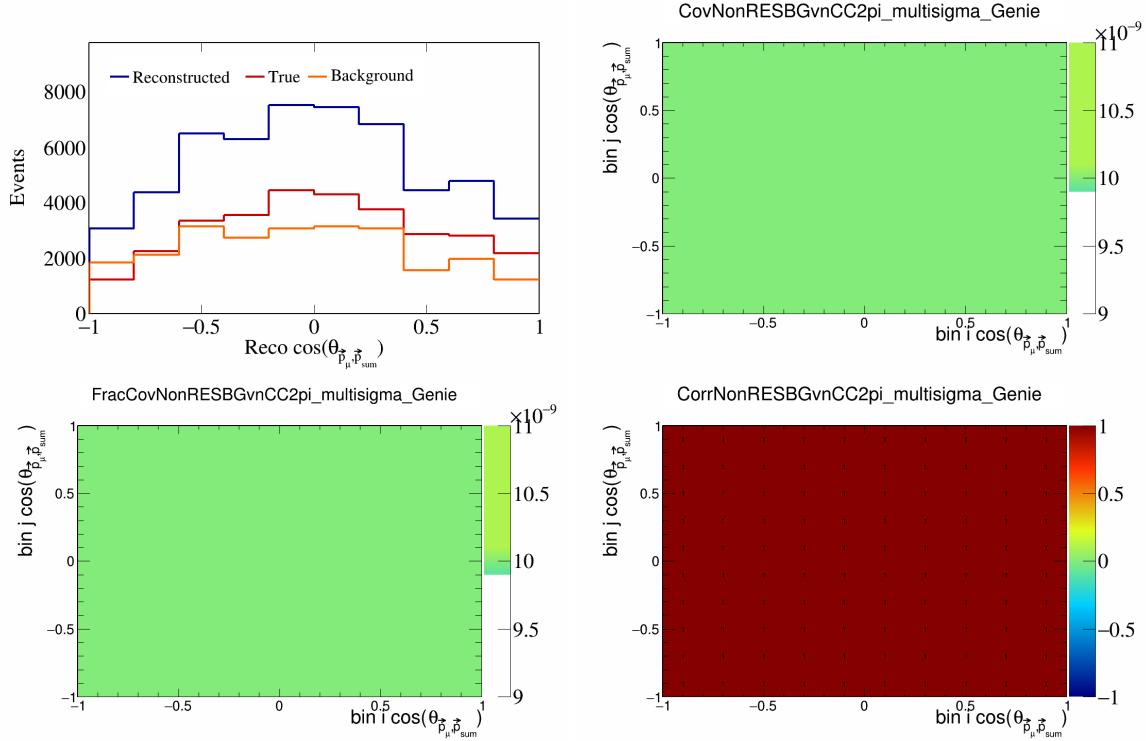


Figure 424: NonRESBGvnCC2pi variations for $\cos(\theta_{\vec{p}_\mu, \vec{p}_{\text{sum}}})$.

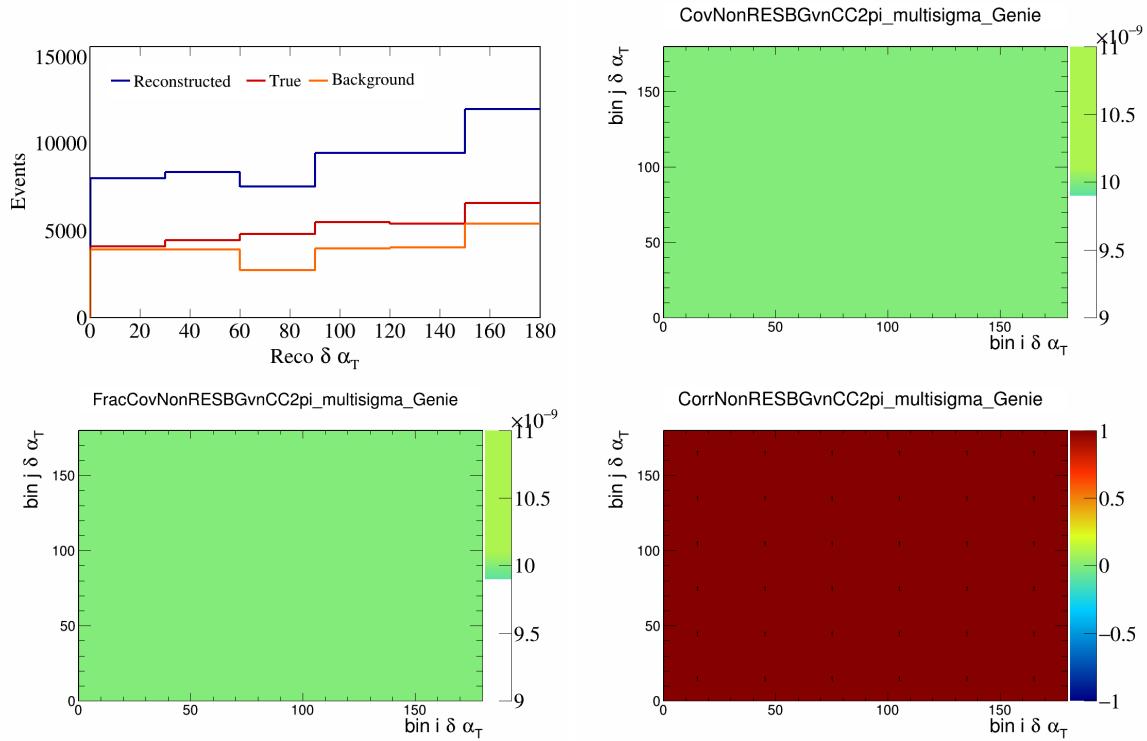


Figure 425: NonRESBGvnCC2pi variations for $\delta\alpha_T$.

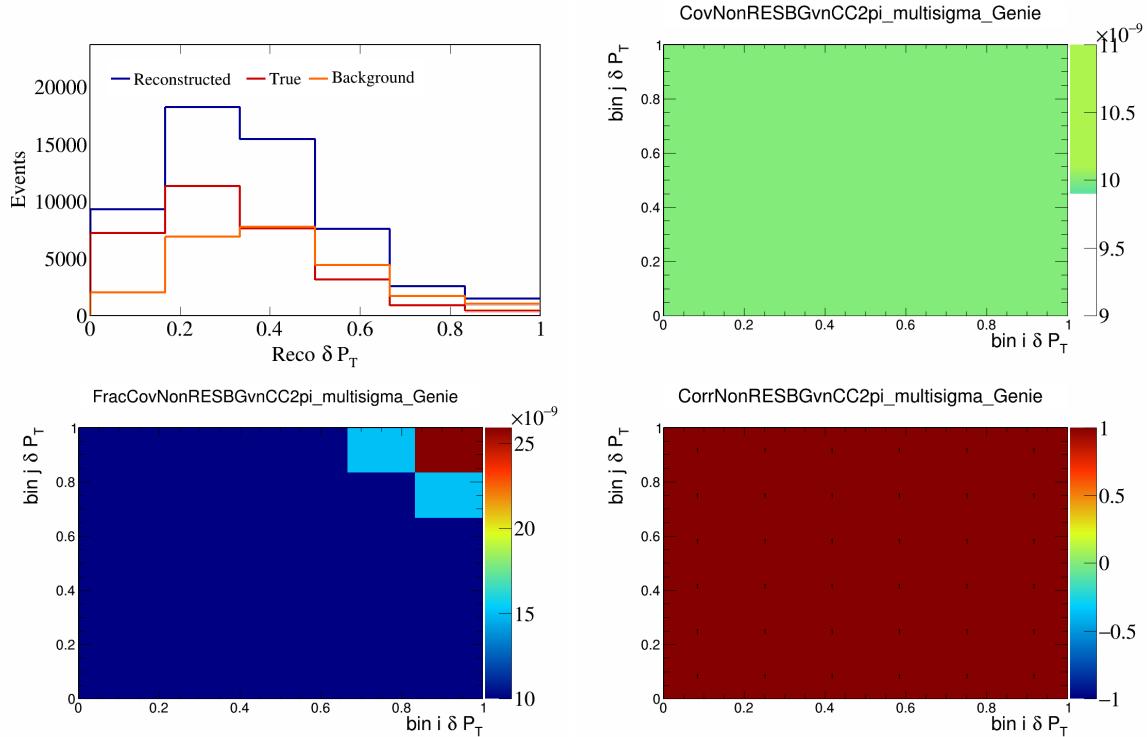


Figure 426: NonRESBGvnCC2pi variations for δP_T .

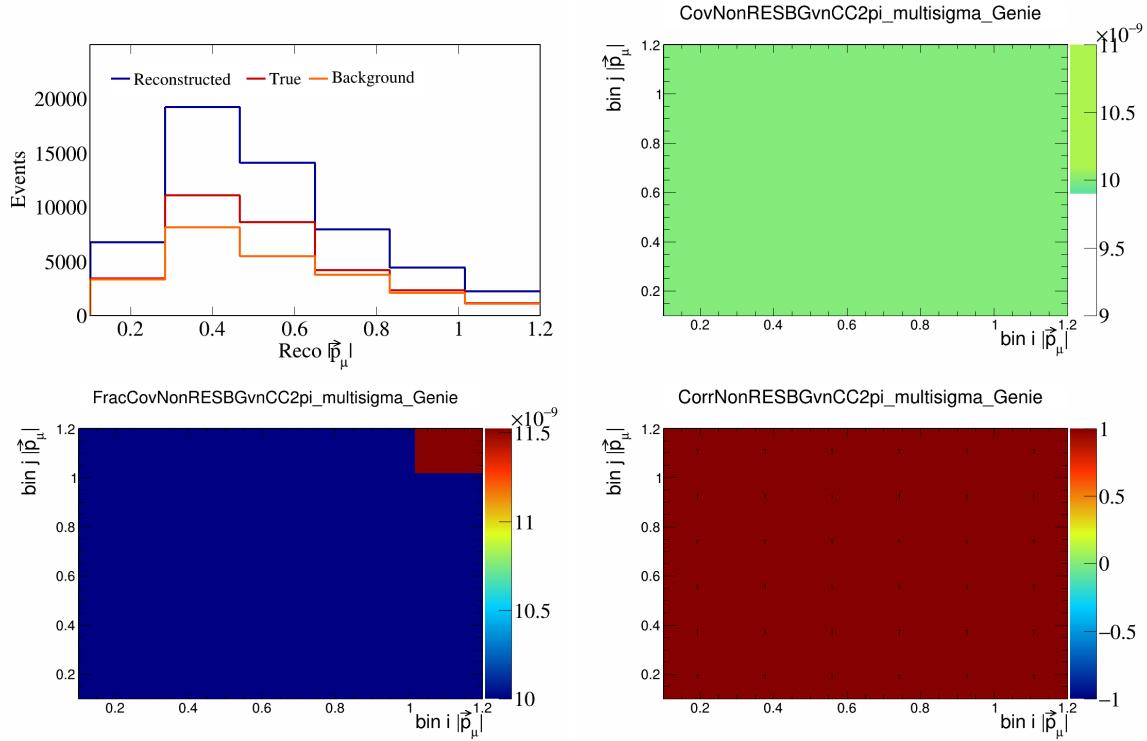


Figure 427: NonRESBGvnCC2pi variations for $|\vec{p}_\mu|$.

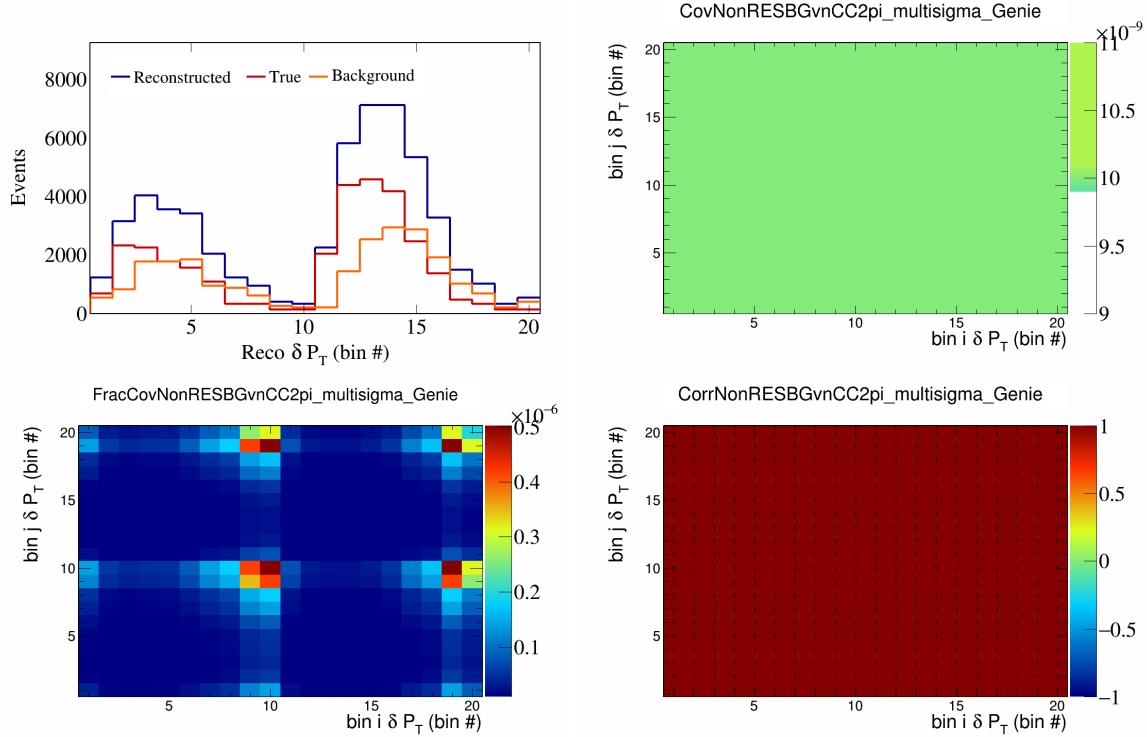


Figure 428: NonRESBGvnCC2pi variations for δP_T in $\cos(\theta_{\vec{p}_\mu})$.

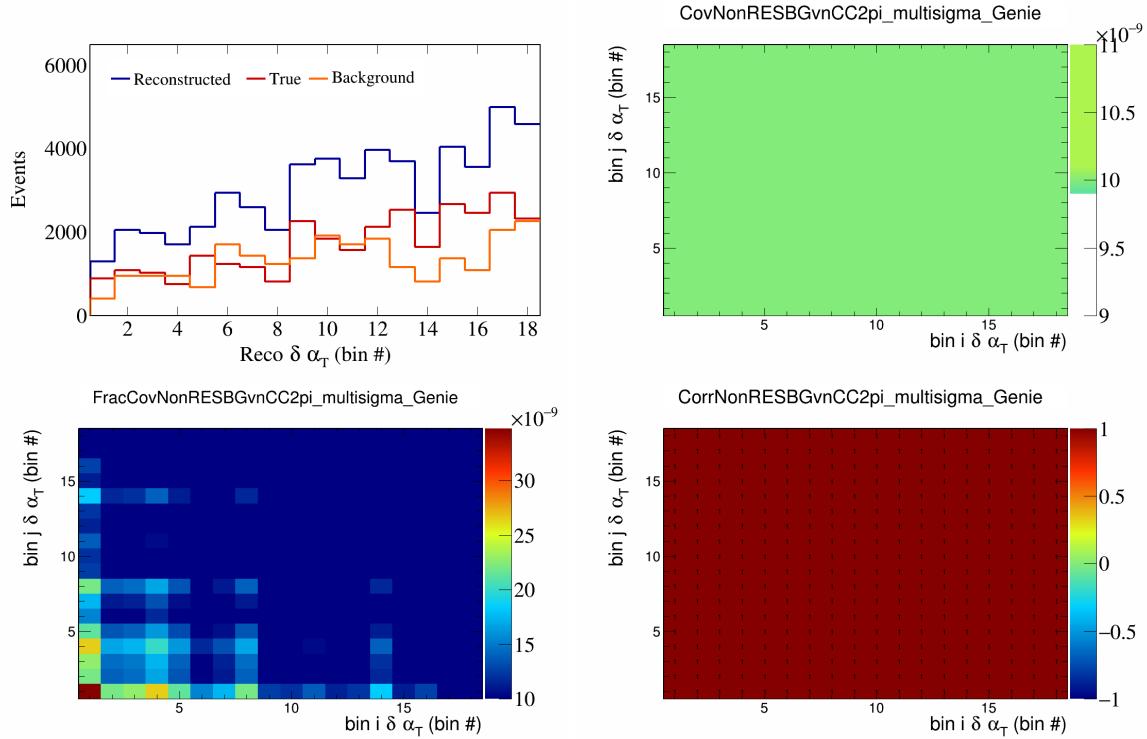


Figure 429: NonRESBGvnCC2pi variations for $\delta\alpha_T$ in $\cos(\theta_{\vec{p}_\mu})$.

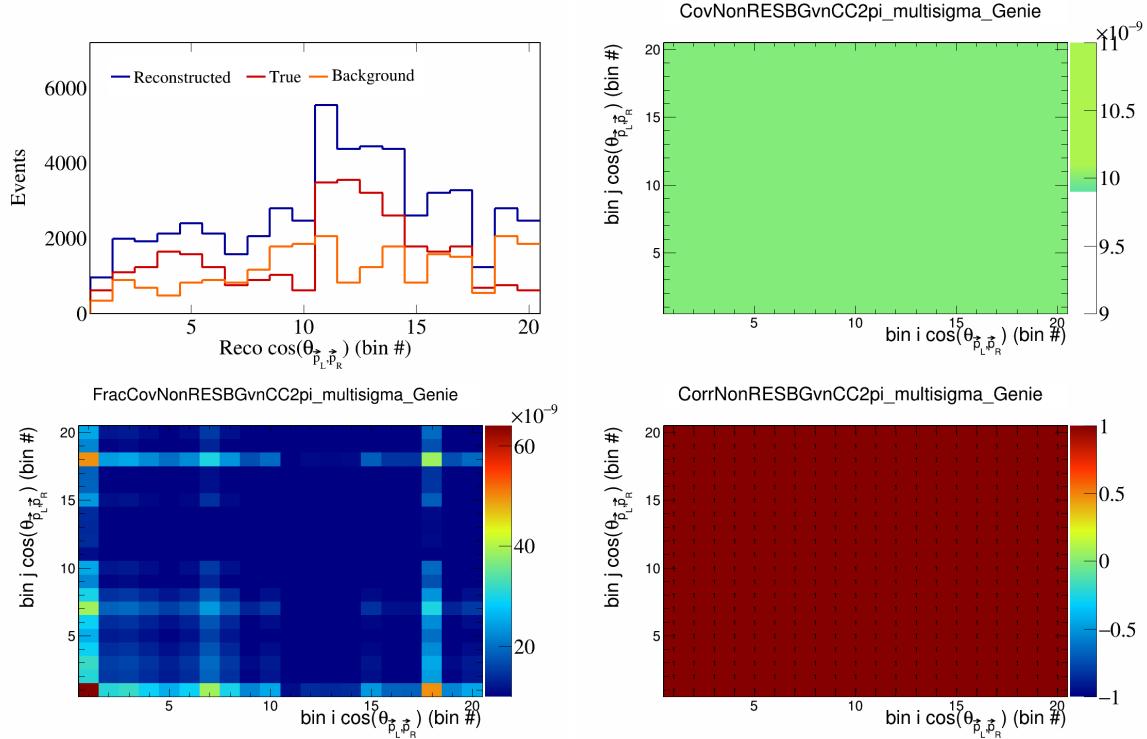


Figure 430: NonRESBGvnCC2pi variations for $\cos(\theta_{\vec{p}_L, \vec{p}_R})$ in $\cos(\theta_{\vec{p}_\mu})$.

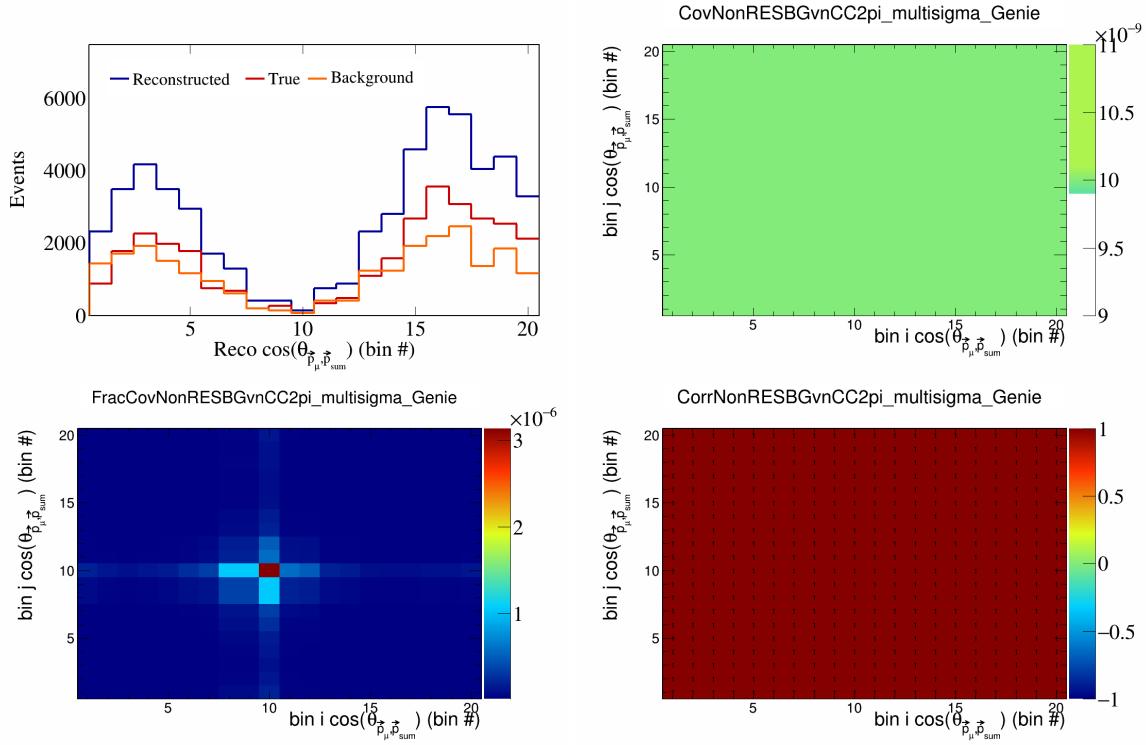


Figure 431: NonRESBGvnCC2pi variations for $\cos(\theta_{\vec{p}_\mu, \vec{p}_{\text{sum}}})$ in $\cos(\theta_{\vec{p}_\mu})$.

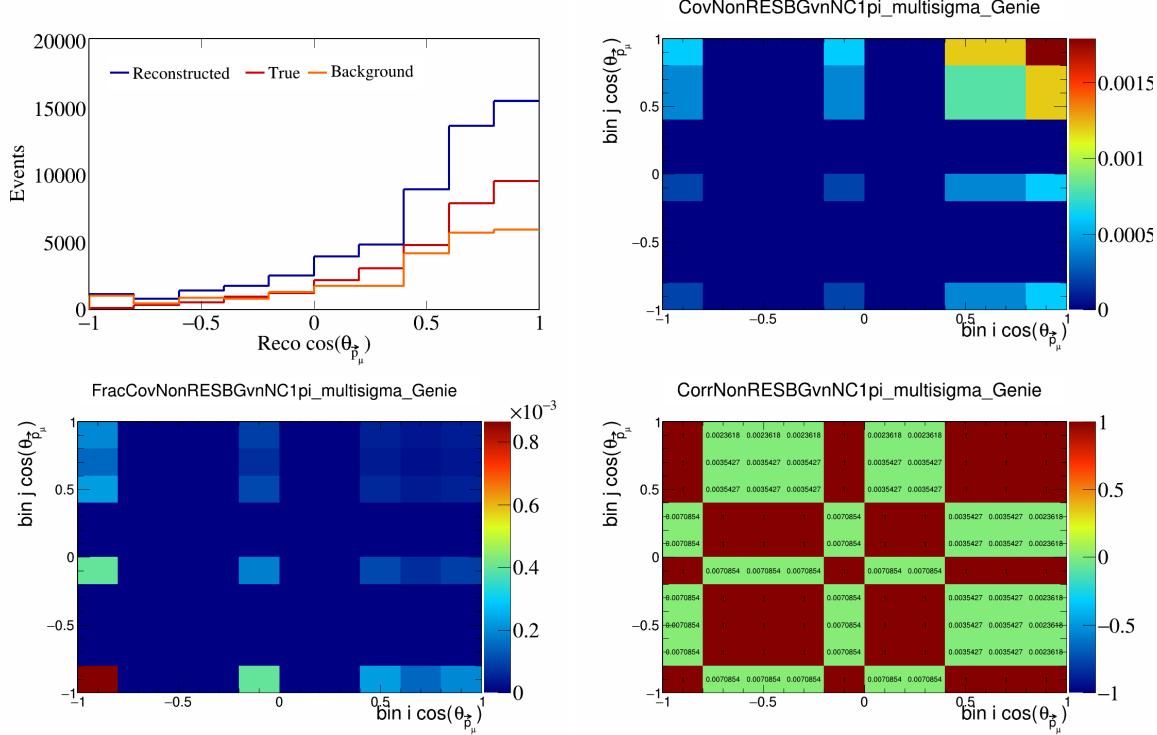


Figure 432: NonRESBGvnNC1pi variations for $\cos(\theta_{\vec{p}_\mu})$.

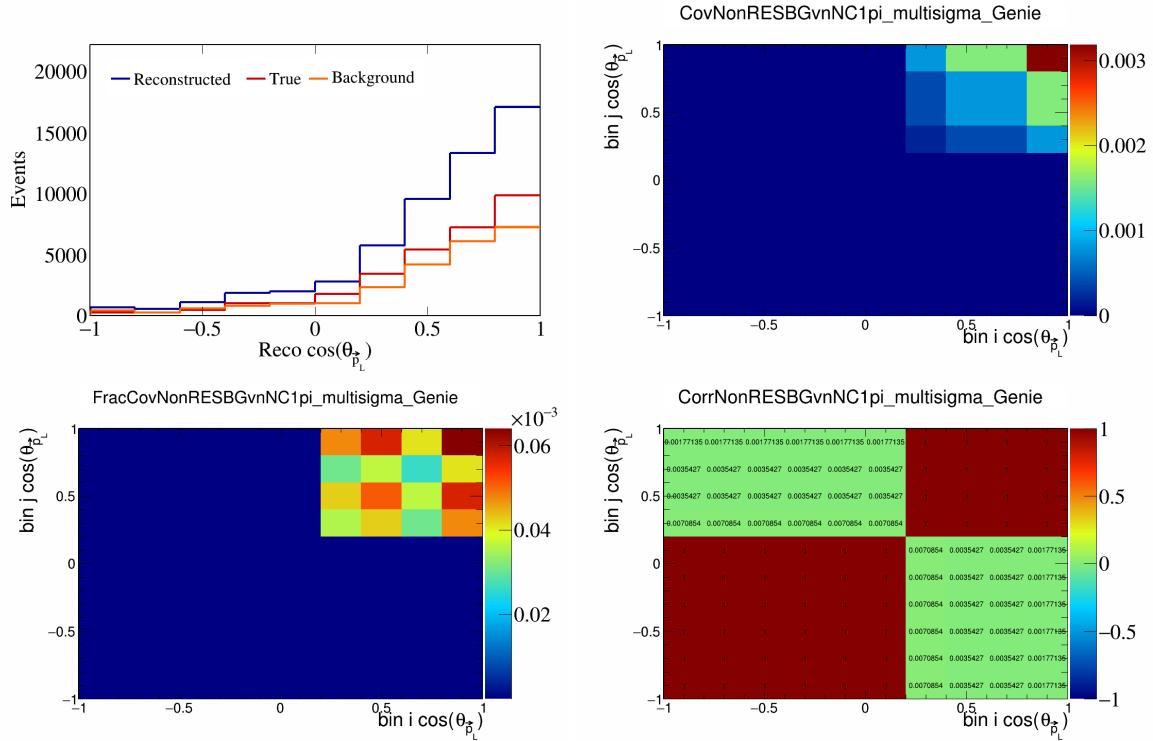


Figure 433: NonRESBGvnNC1pi variations for $\cos(\theta_{\vec{p}_L})$.

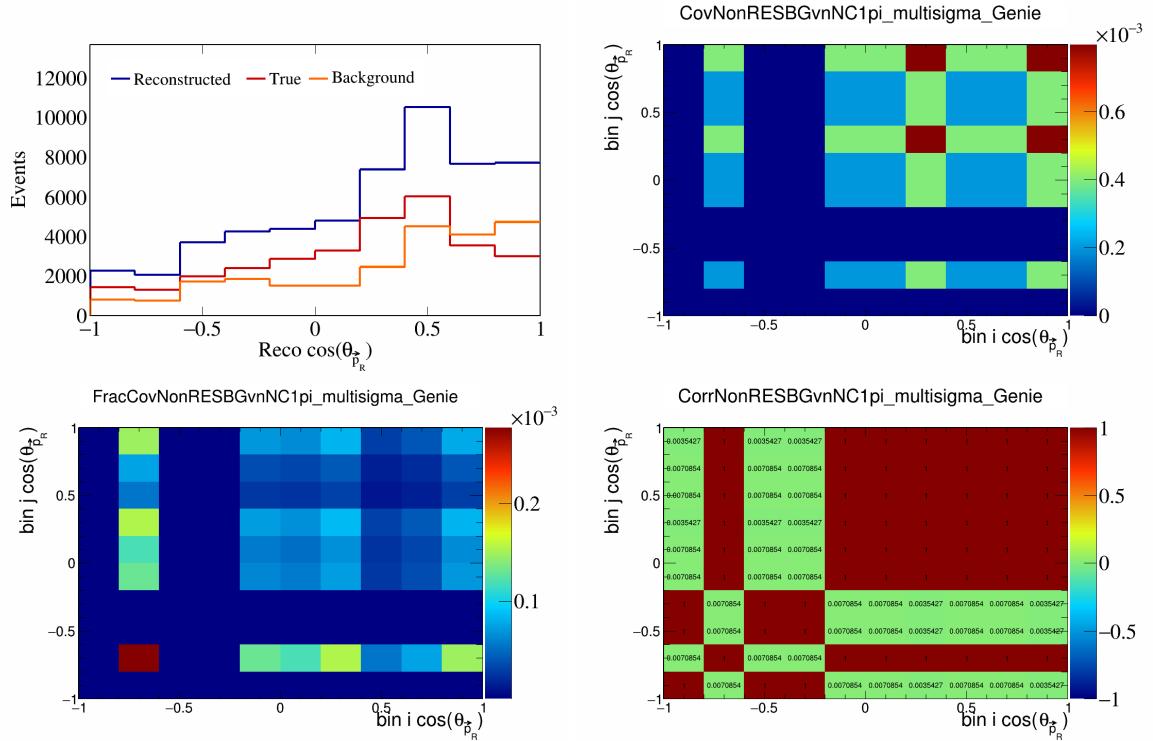


Figure 434: NonRESBGvnNC1pi variations for $\cos(\theta_{\vec{p}_R})$.

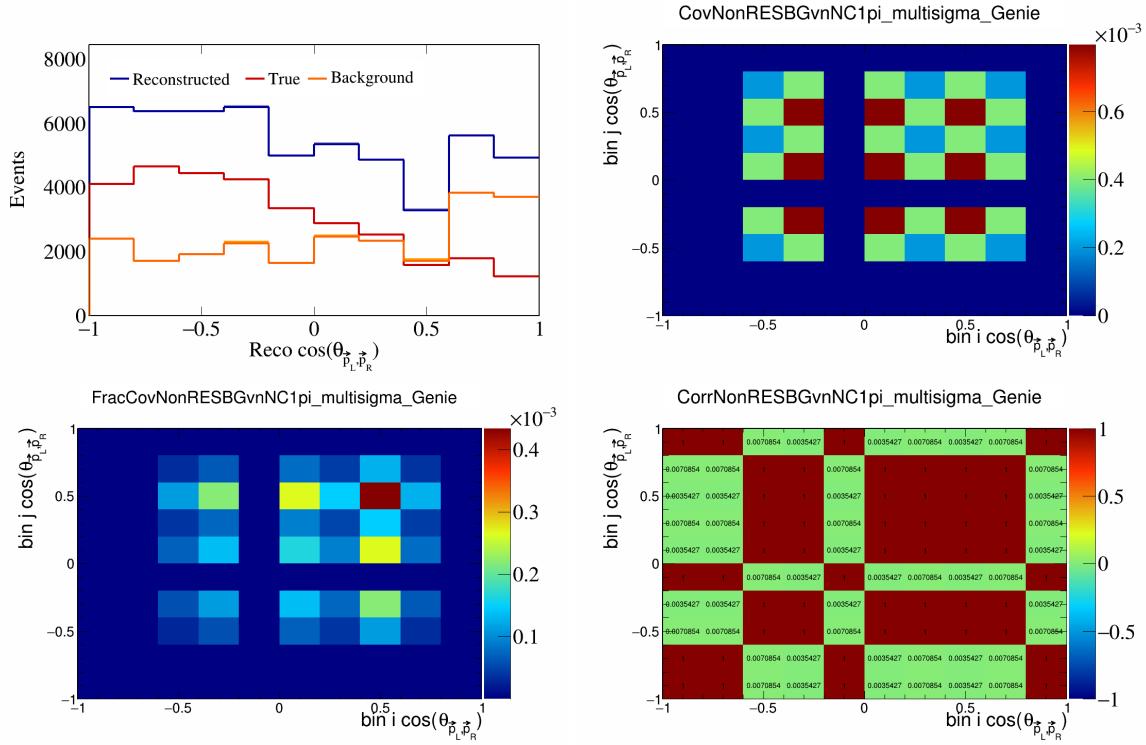


Figure 435: NonRESBGvnNC1pi variations for $\cos(\theta_{\vec{p}_L, \vec{p}_R})$.

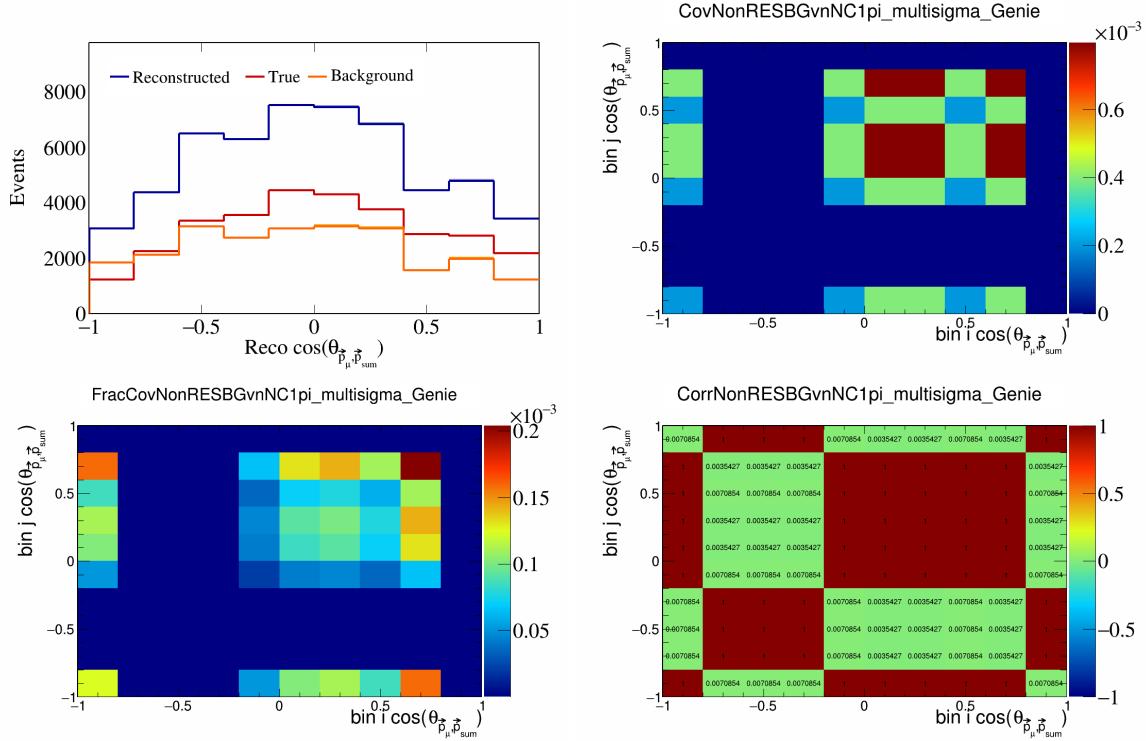


Figure 436: NonRESBGvnNC1pi variations for $\cos(\theta_{\vec{p}_\mu, \vec{p}_{\text{sum}}})$.

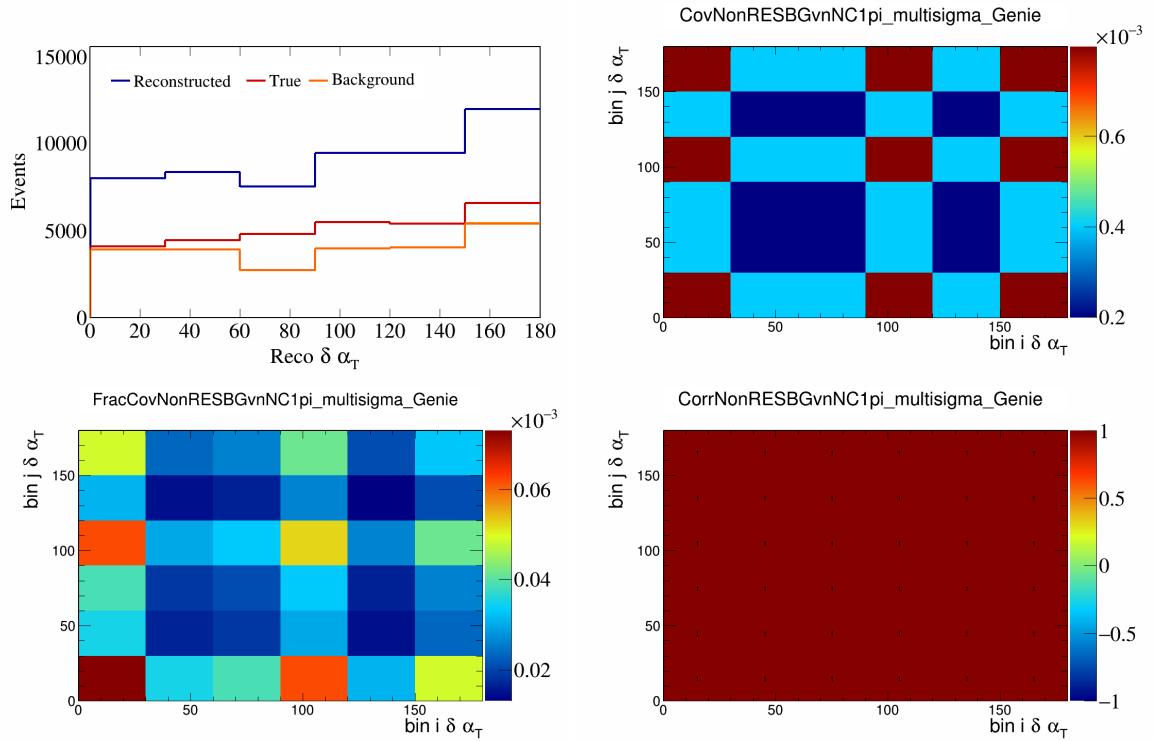


Figure 437: NonRESBGvnNC1pi variations for $\delta\alpha_T$.

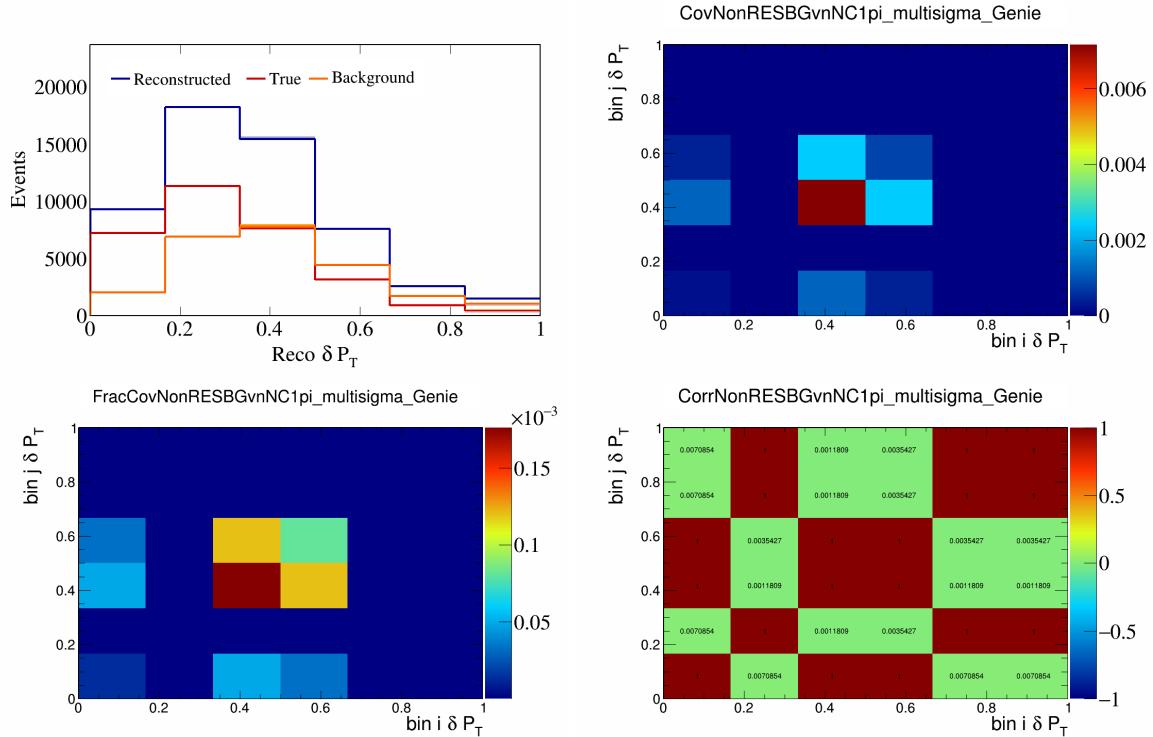


Figure 438: NonRESBGvnNC1pi variations for δP_T .

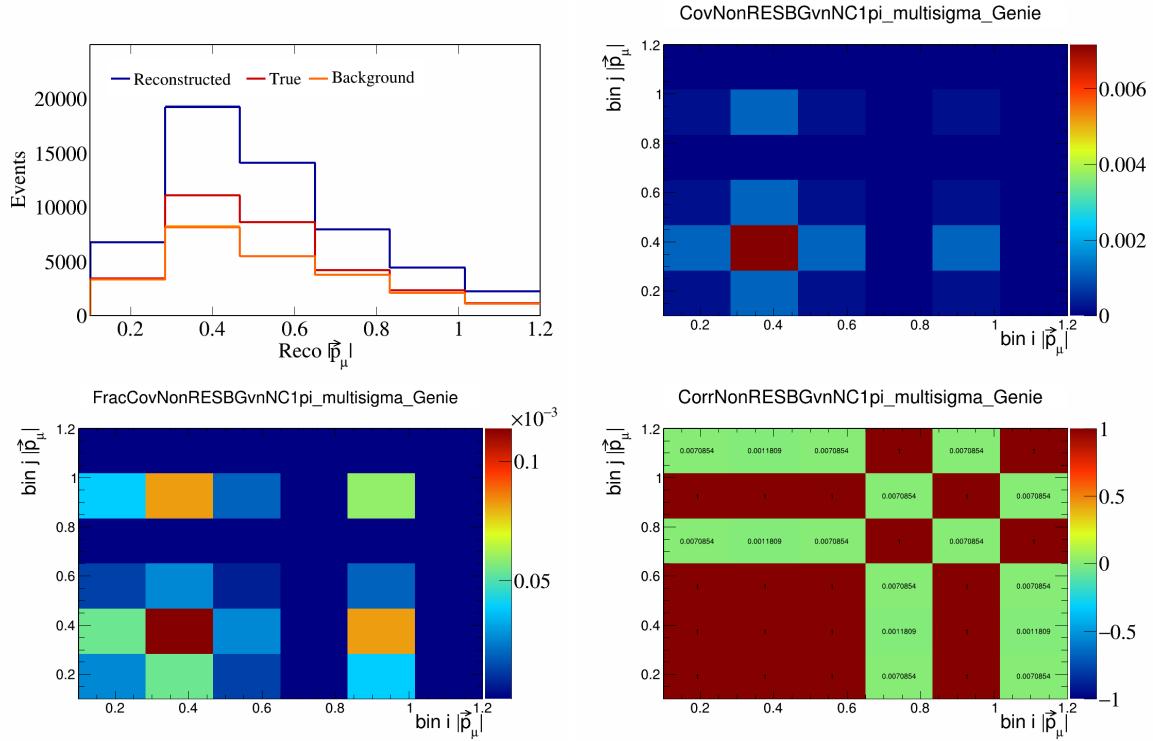


Figure 439: NonRESBGvnNC1pi variations for $|\vec{p}_\mu|$.

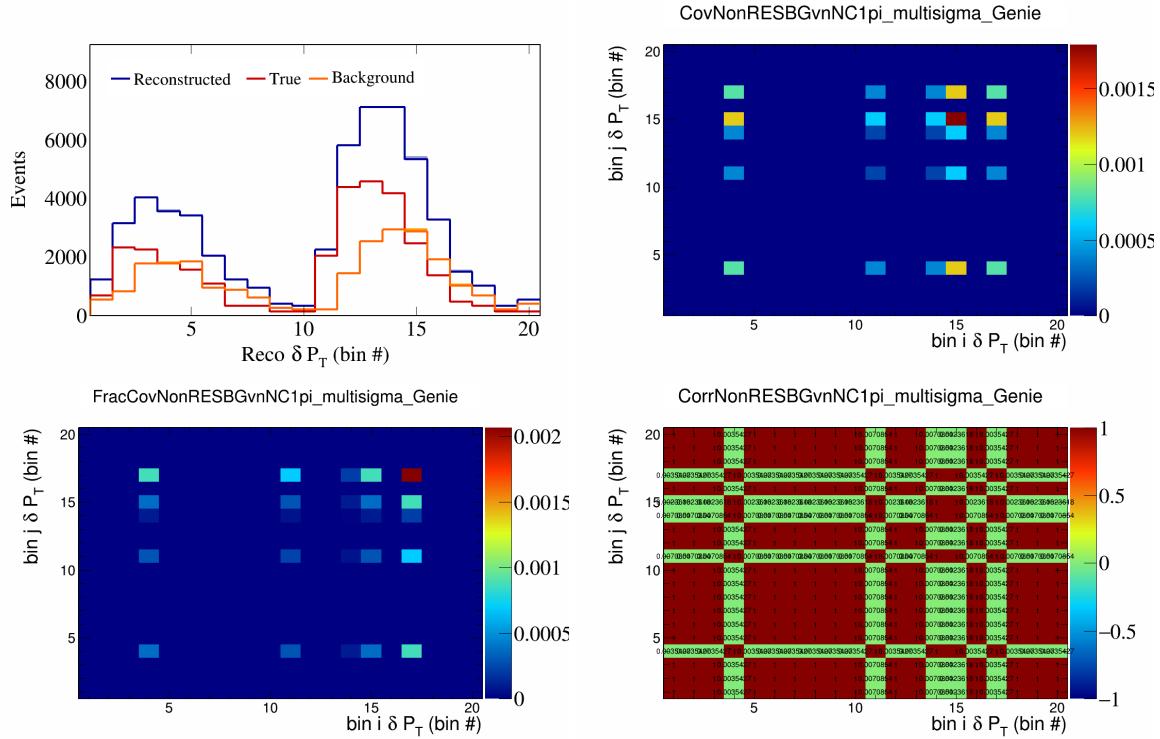


Figure 440: NonRESBGvnNC1pi variations for δP_T in $\cos(\theta_{\vec{p}_\mu})$.

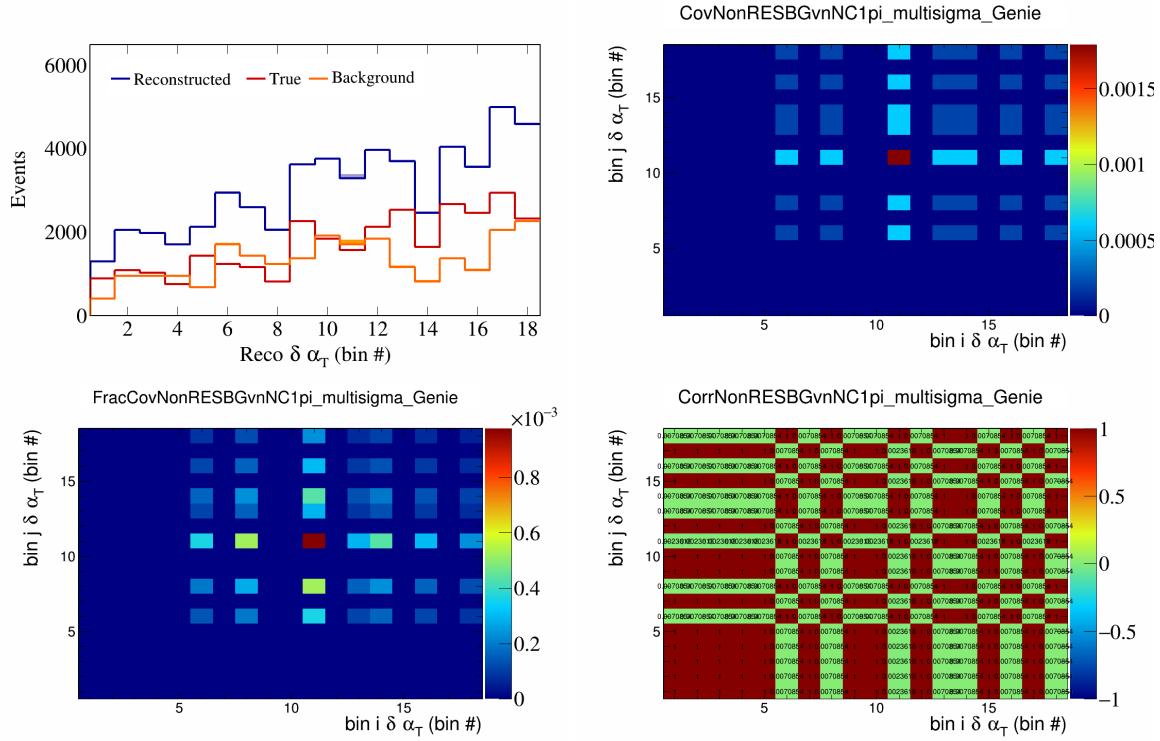


Figure 441: NonRESBGvnNC1pi variations for $\delta\alpha_T$ in $\cos(\theta_{\vec{p}_\mu})$.

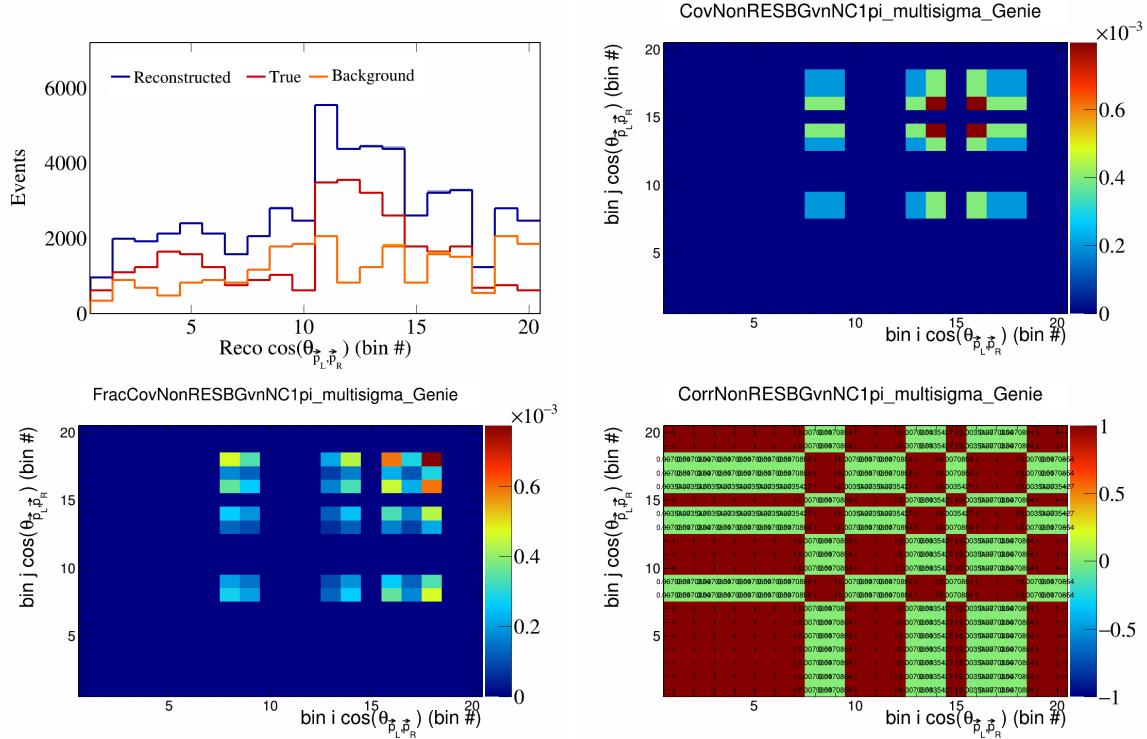


Figure 442: NonRESBGvnNC1pi variations for $\cos(\theta_{\vec{p}_L, \vec{p}_R})$ in $\cos(\theta_{\vec{p}_\mu})$.

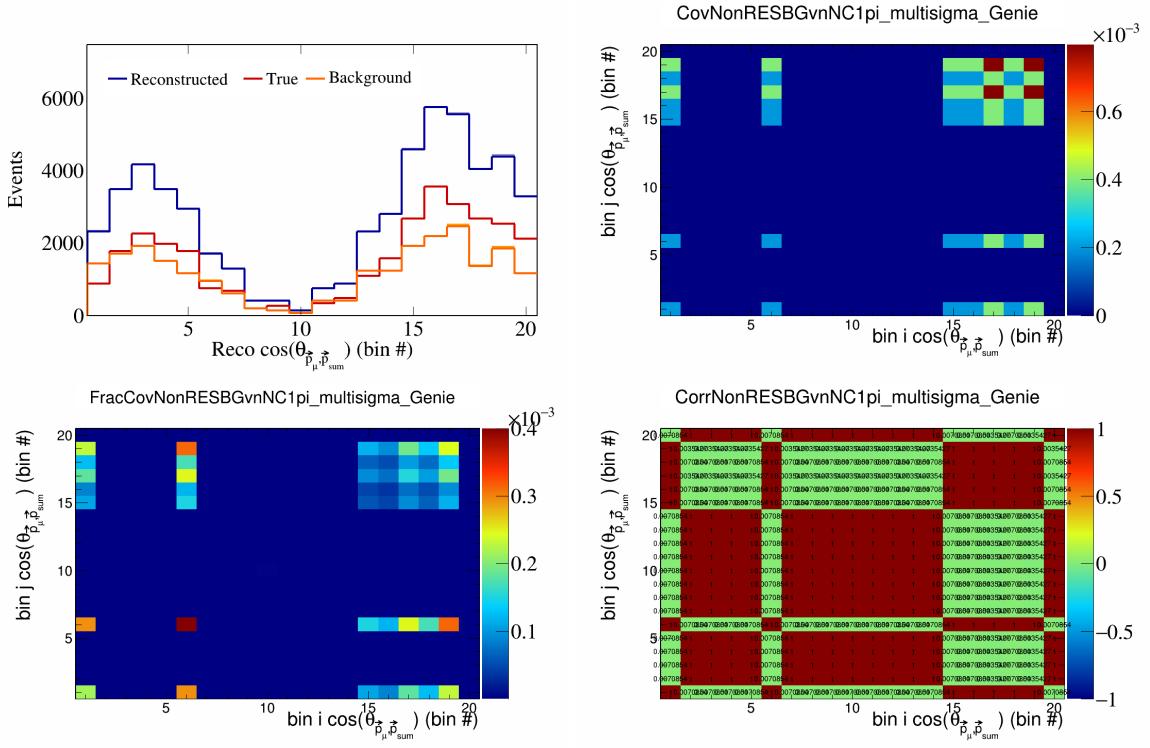


Figure 443: NonRESBGvnNC1pi variations for $\cos(\theta_{\vec{p}_\mu, \vec{p}_{\text{sum}}})$ in $\cos(\theta_{\vec{p}_\mu})$.

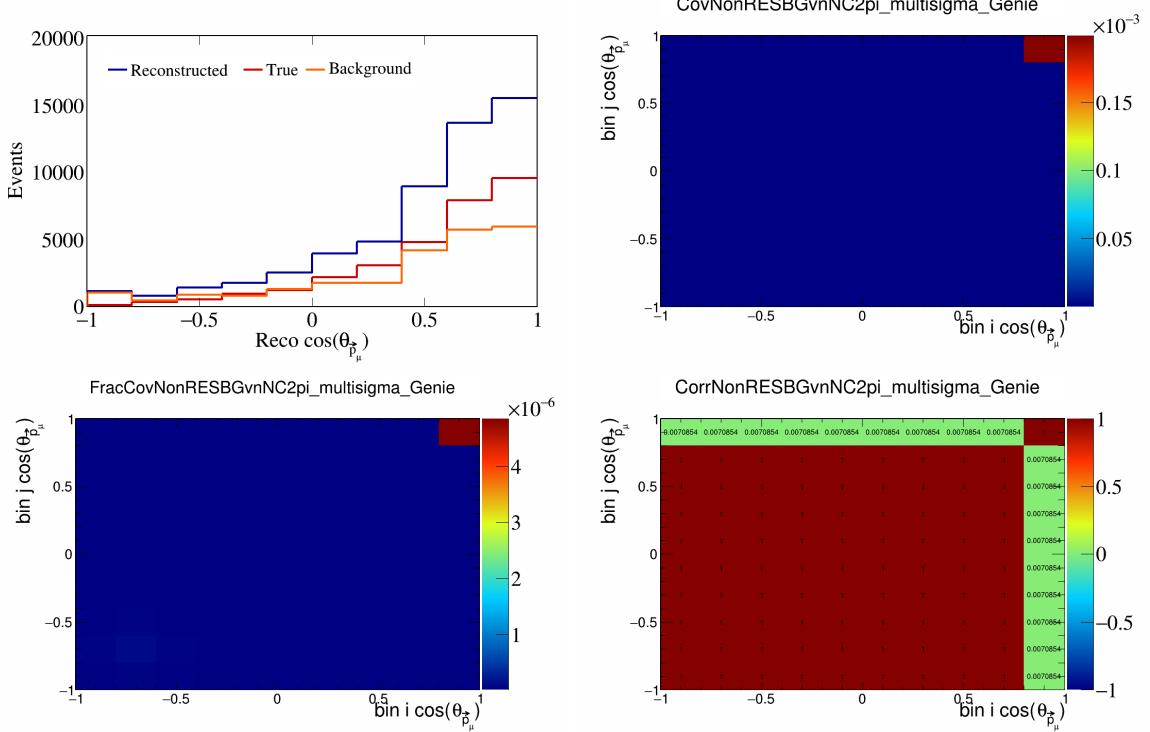


Figure 444: NonRESBGvnNC2pi variations for $\cos(\theta_{\vec{p}_\mu})$.

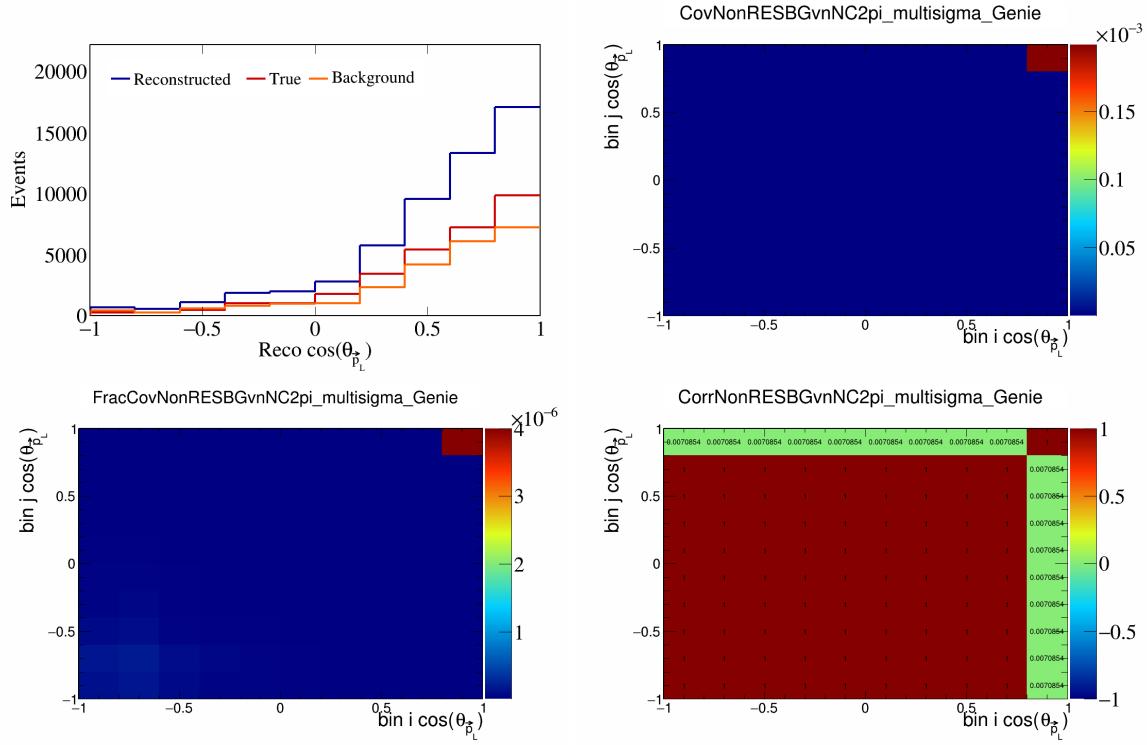


Figure 445: NonRESBGvnNC2pi variations for $\cos(\theta_{\vec{p}_L})$.

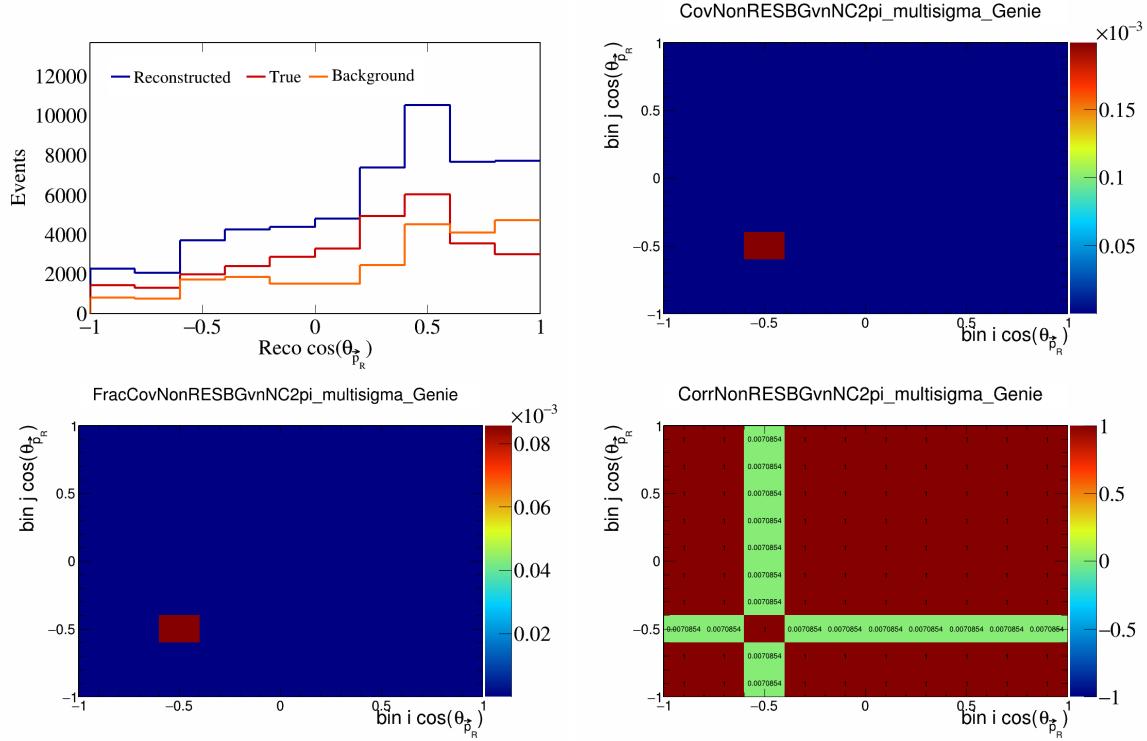


Figure 446: NonRESBGvnNC2pi variations for $\cos(\theta_{\vec{p}_R})$.

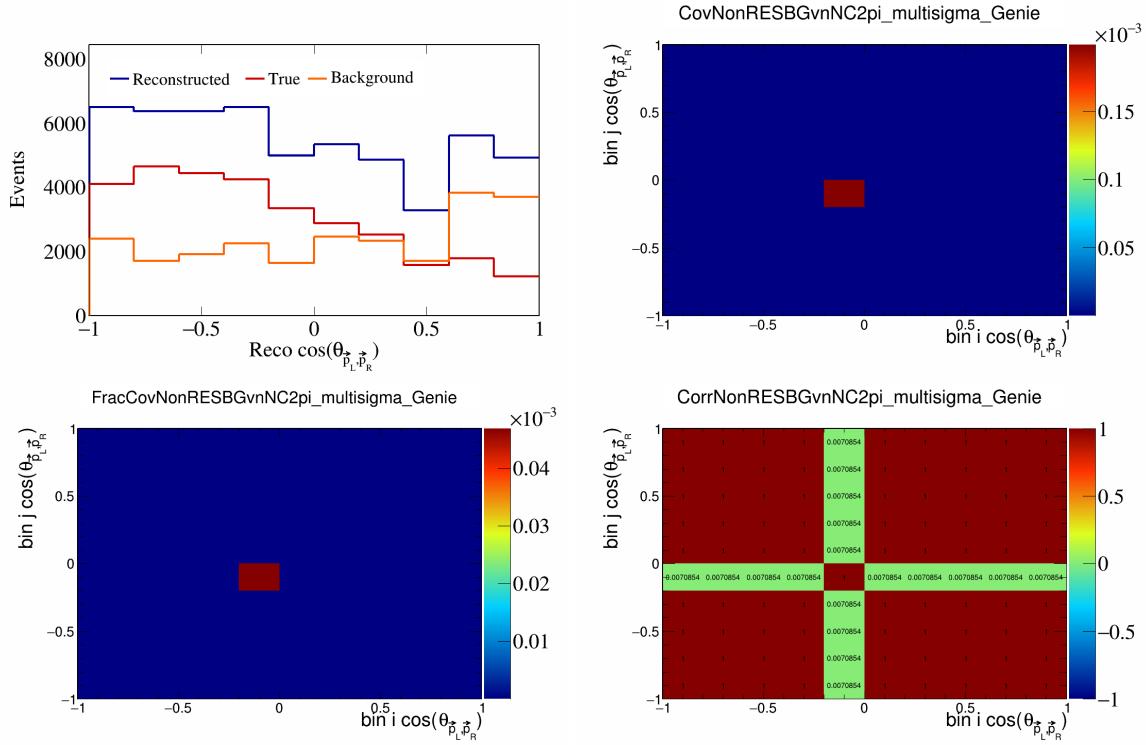


Figure 447: NonRESBGvnNC2pi variations for $\cos(\theta_{\vec{p}_L, \vec{p}_R})$.

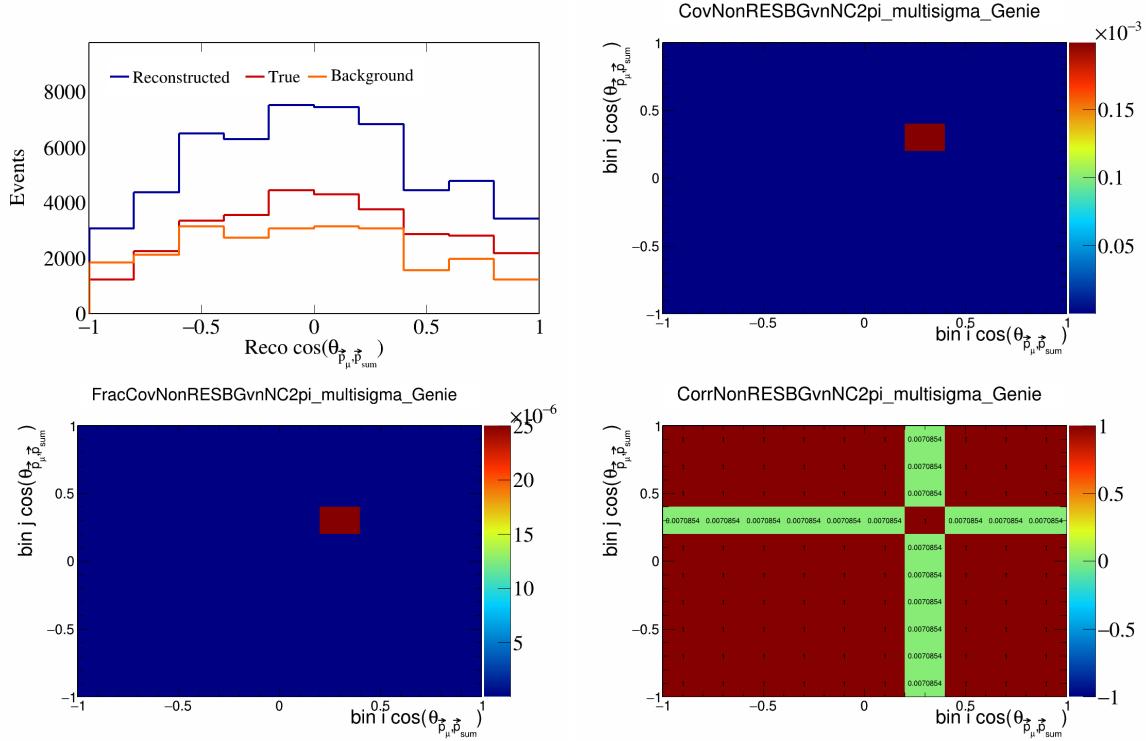


Figure 448: NonRESBGvnNC2pi variations for $\cos(\theta_{\vec{p}_\mu, \vec{p}_{\text{sum}}})$.

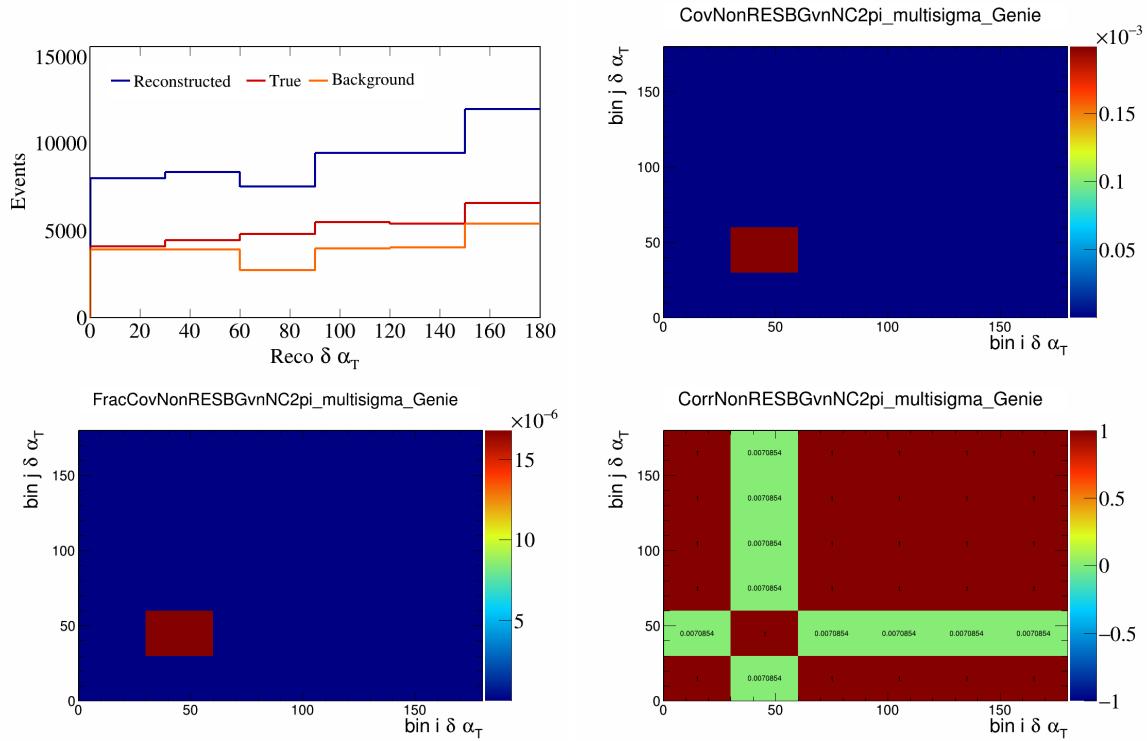


Figure 449: NonRESBGvnNC2pi variations for $\delta \alpha_T$.

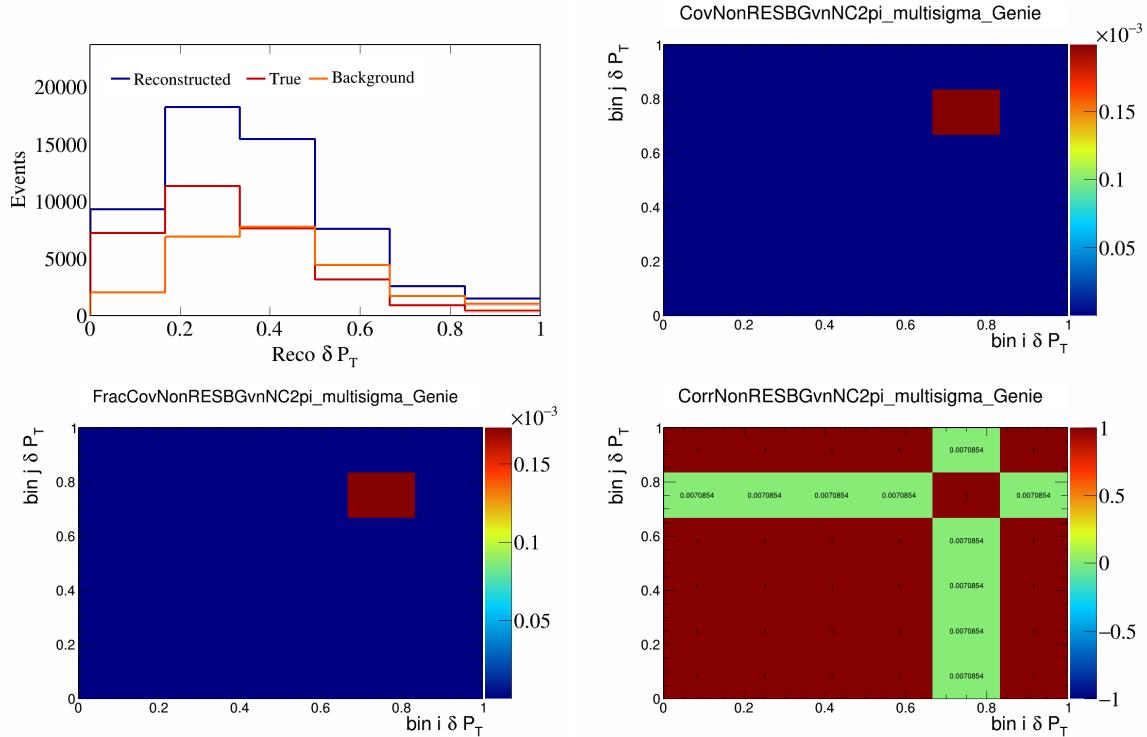


Figure 450: NonRESBGvnNC2pi variations for δP_T .

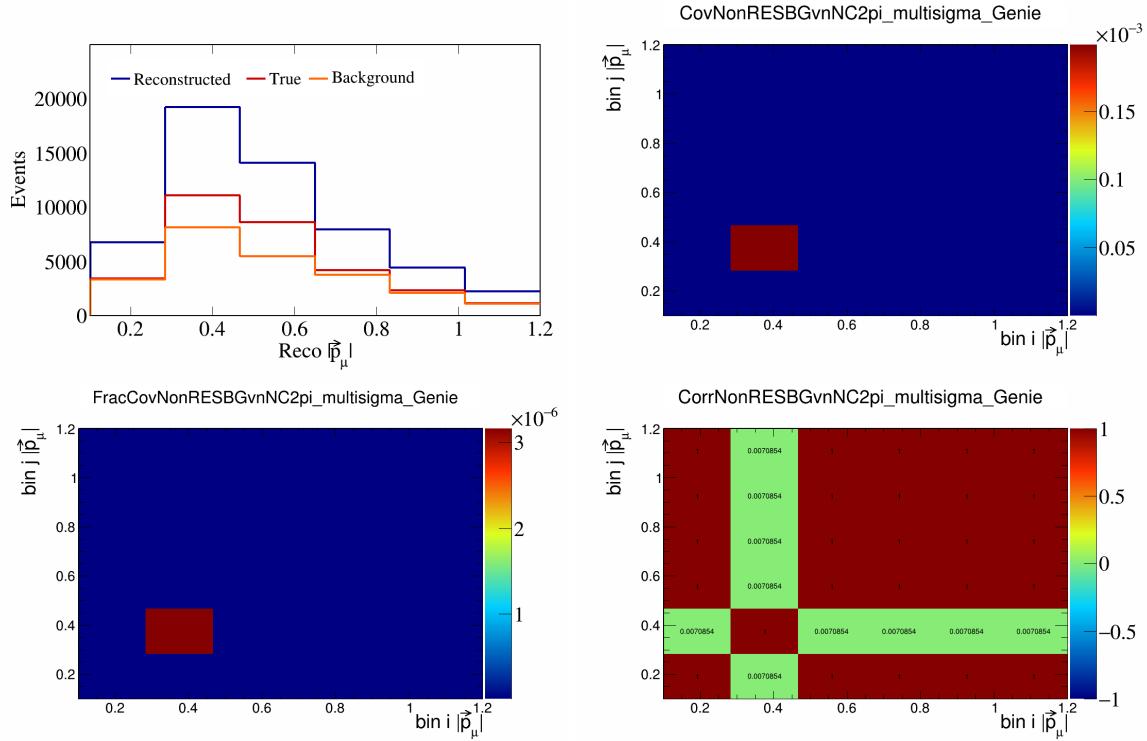


Figure 451: NonRESBGvnNC2pi variations for $|\vec{p}_\mu|$.

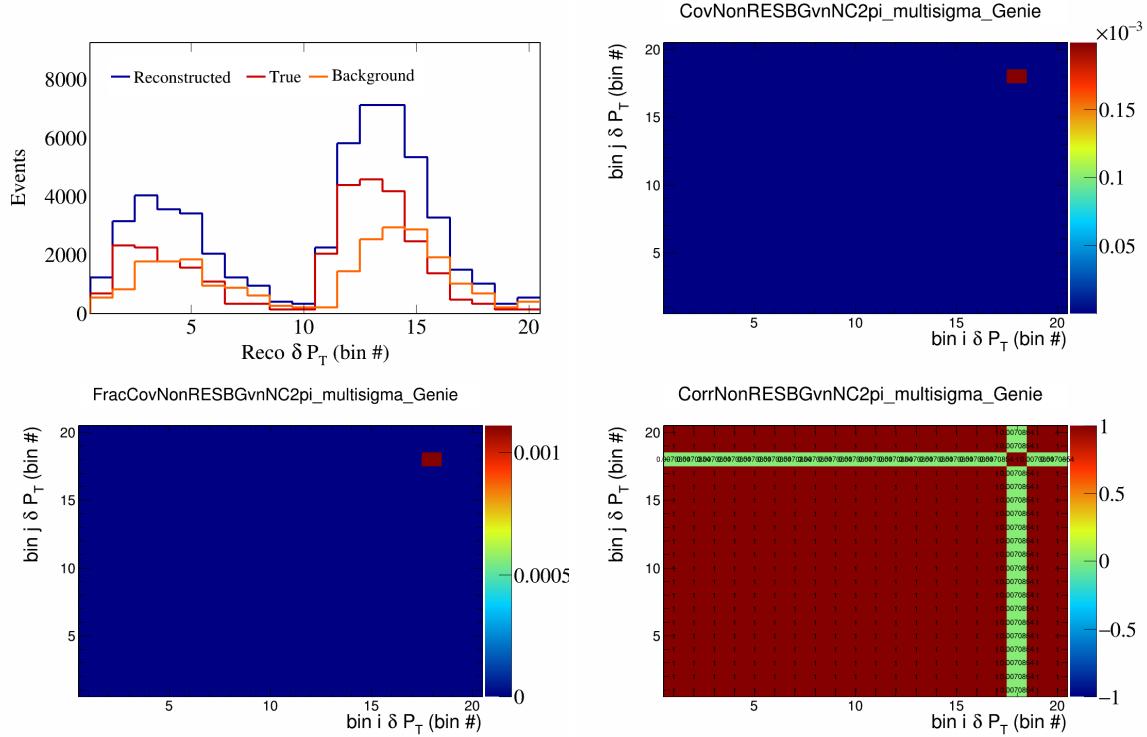


Figure 452: NonRESBGvnNC2pi variations for δP_T in $\cos(\theta_{\vec{p}_\mu})$.

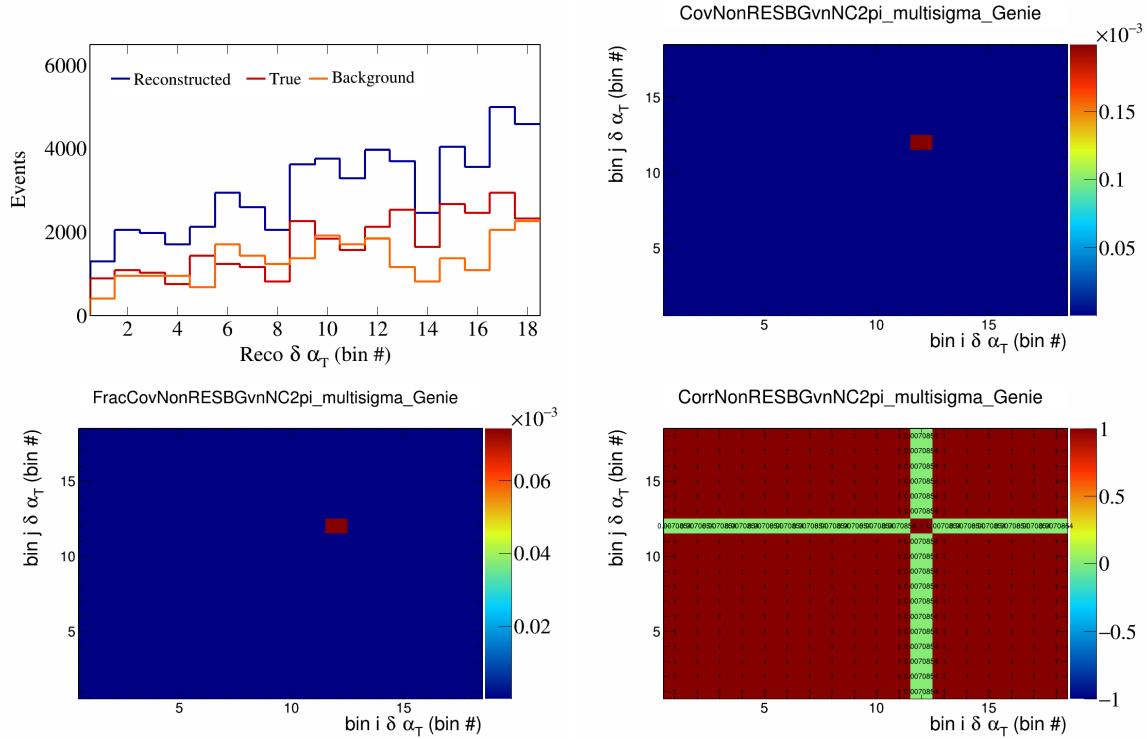


Figure 453: NonRESBGvnNC2pi variations for $\delta \alpha_T$ in $\cos(\theta_{\vec{p}_\mu})$.

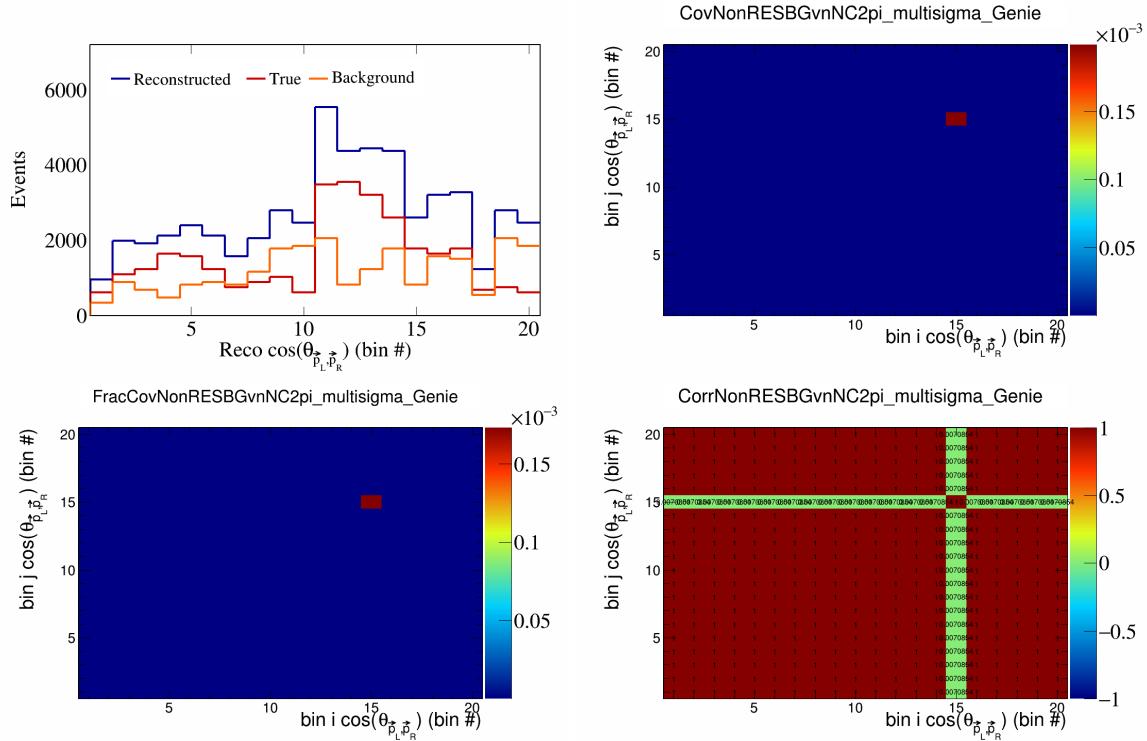


Figure 454: NonRESBGvnNC2pi variations for $\cos(\theta_{\vec{p}_L, \vec{p}_R})$ in $\cos(\theta_{\vec{p}_\mu})$.

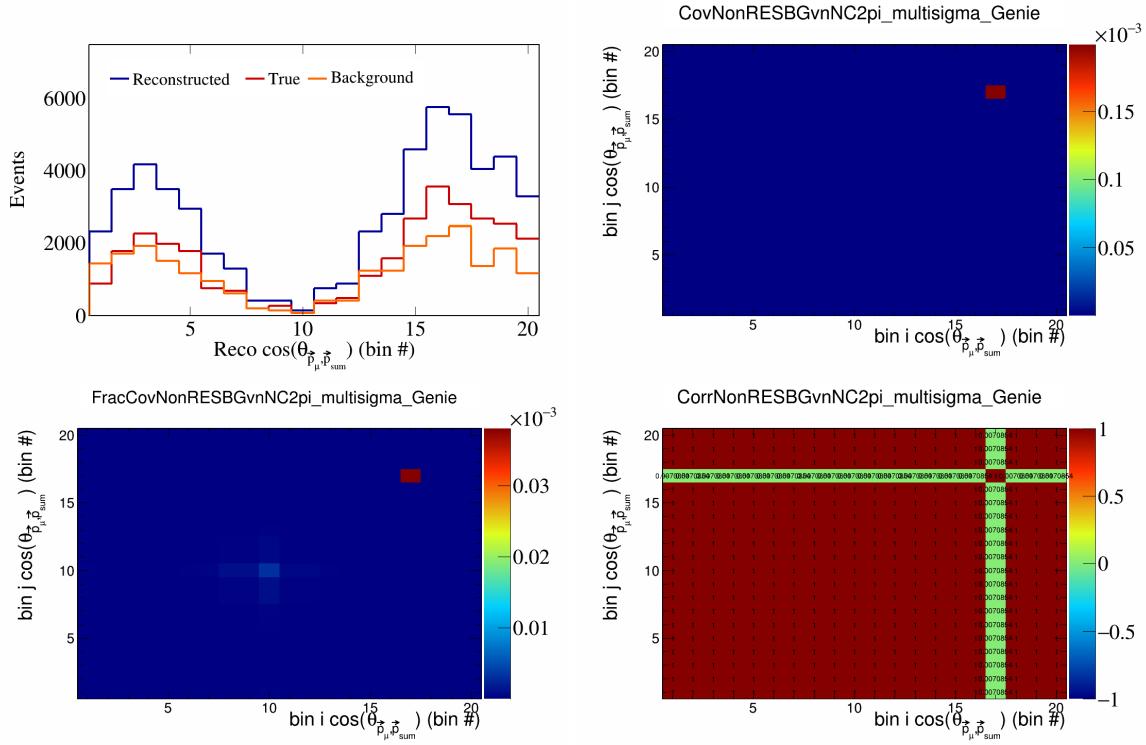


Figure 455: NonRESBGvnNC2pi variations for $\cos(\theta_{\vec{p}_\mu, \vec{p}_{\text{sum}}})$ in $\cos(\theta_{\vec{p}_\mu})$.

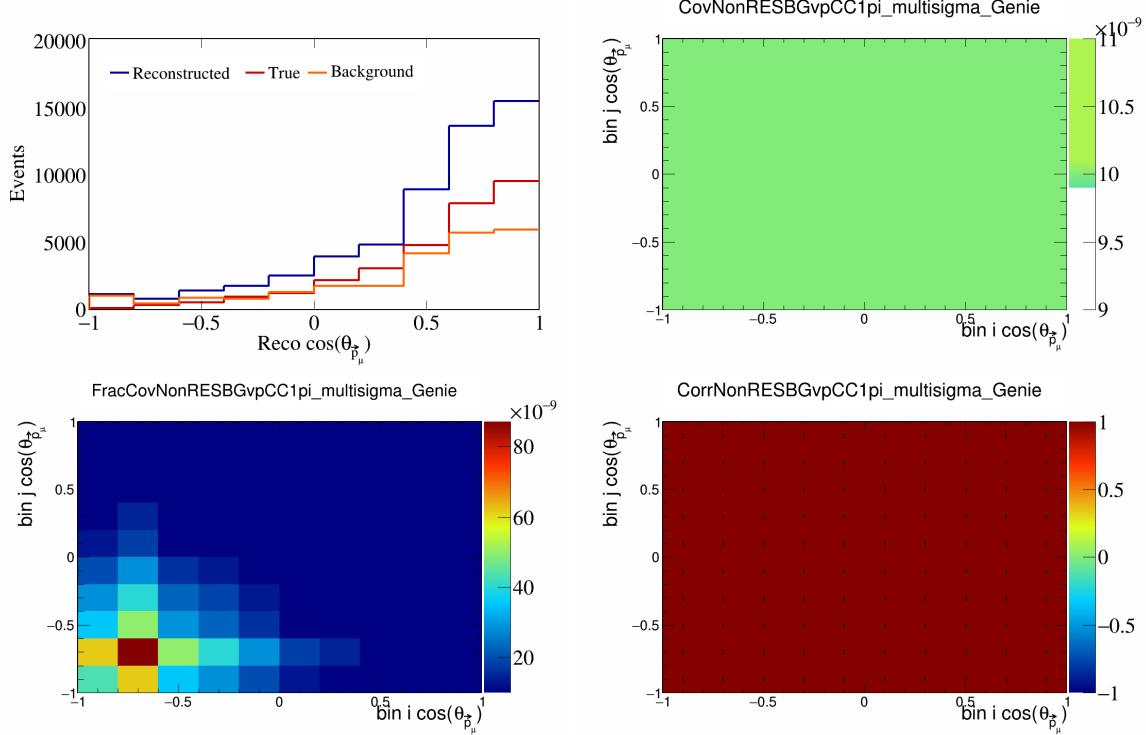


Figure 456: NonRESBGvpCC1pi variations for $\cos(\theta_{\vec{p}_\mu})$.

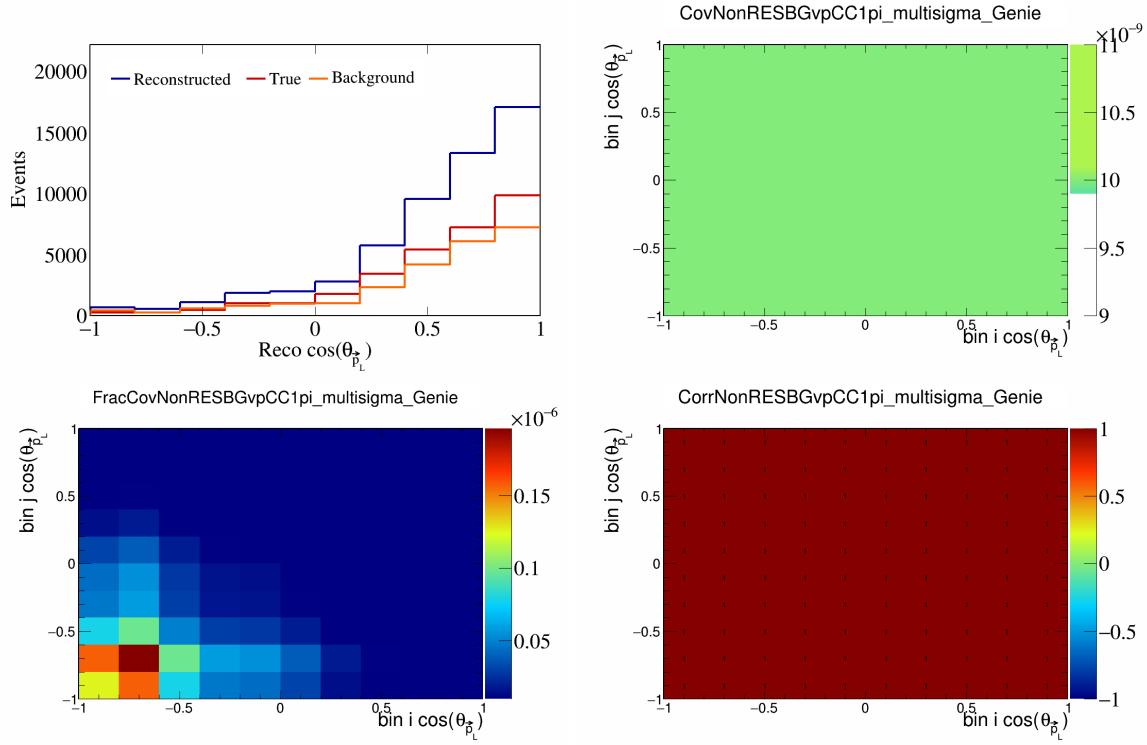


Figure 457: NonRESBGvpCC1pi variations for $\cos(\theta_{\vec{p}_L})$.

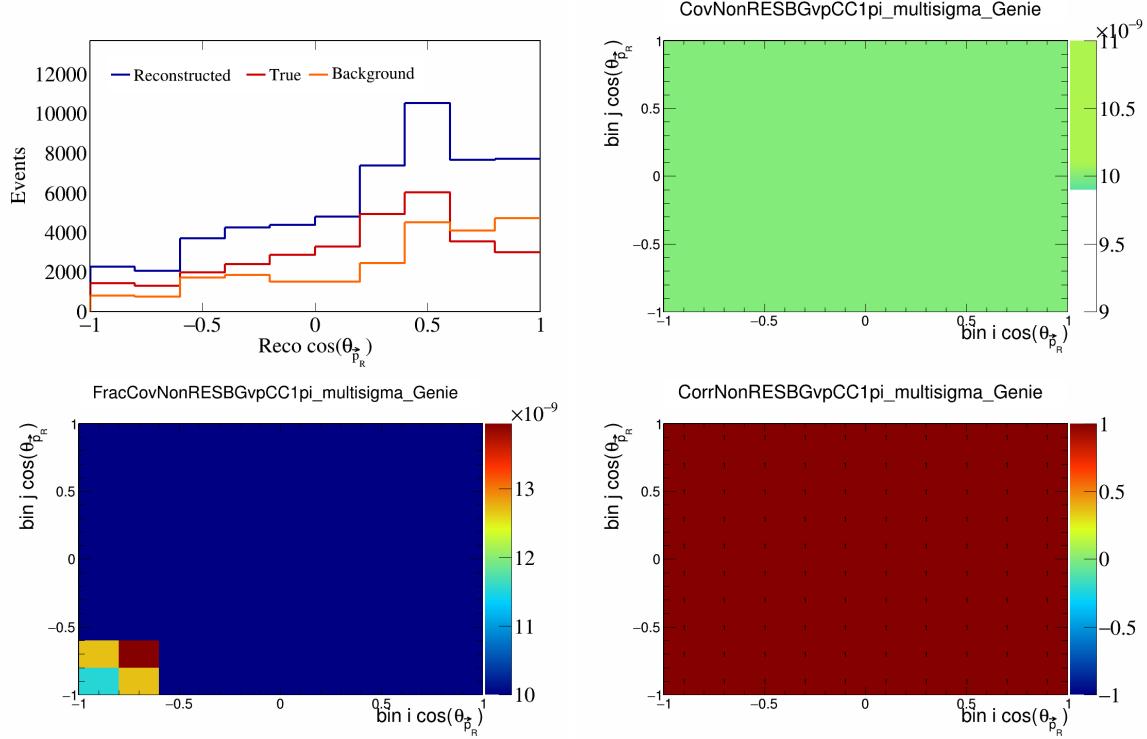


Figure 458: NonRESBGvpCC1pi variations for $\cos(\theta_{\vec{p}_R})$.

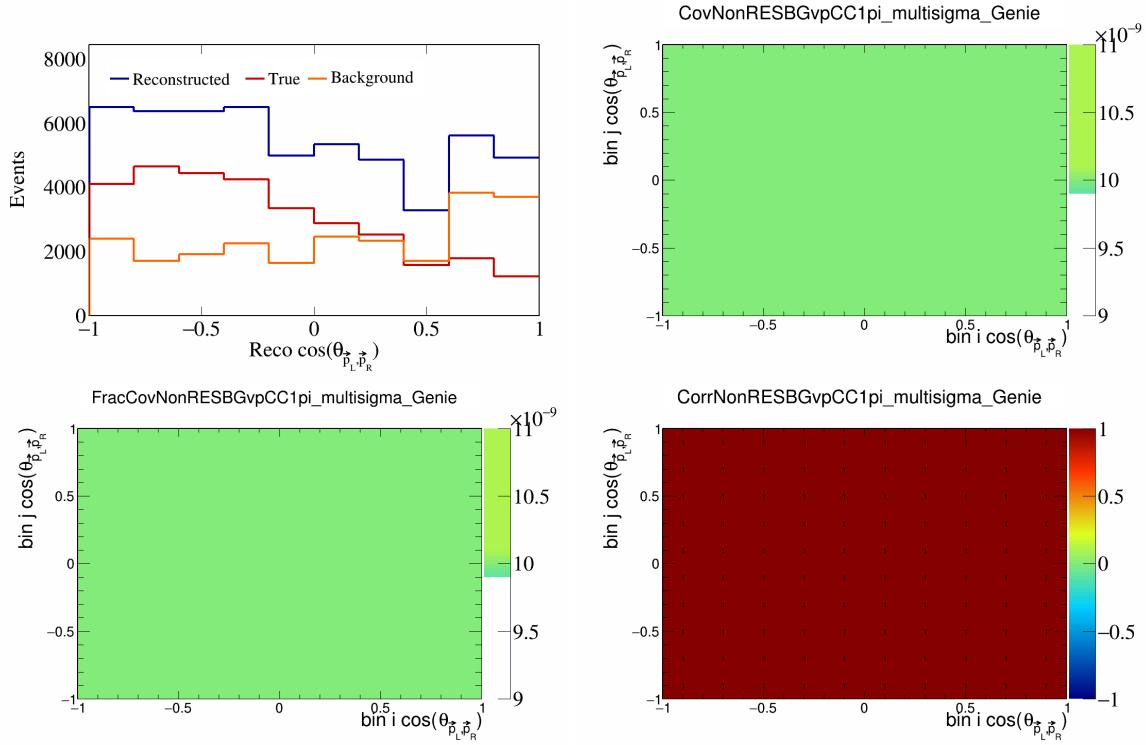


Figure 459: NonRESBGvpCC1pi variations for $\cos(\theta_{\vec{p}_L, \vec{p}_R})$.

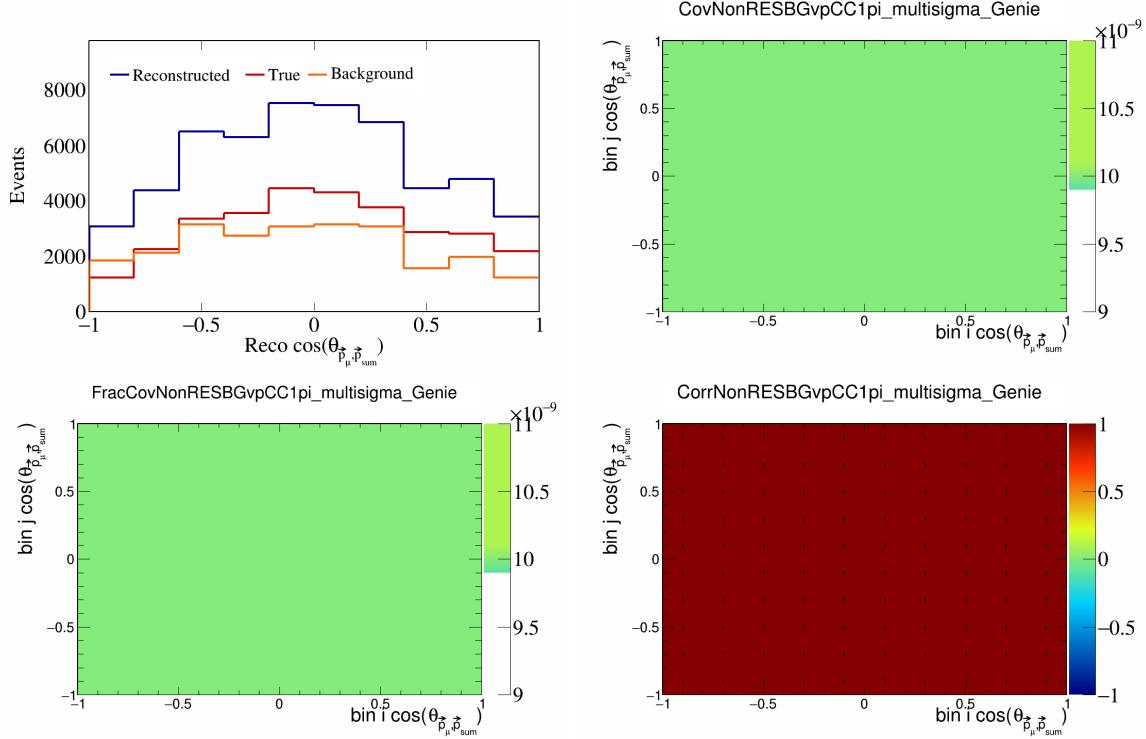


Figure 460: NonRESBGvpCC1pi variations for $\cos(\theta_{\vec{p}_\mu, \vec{p}_{\text{sum}}})$.

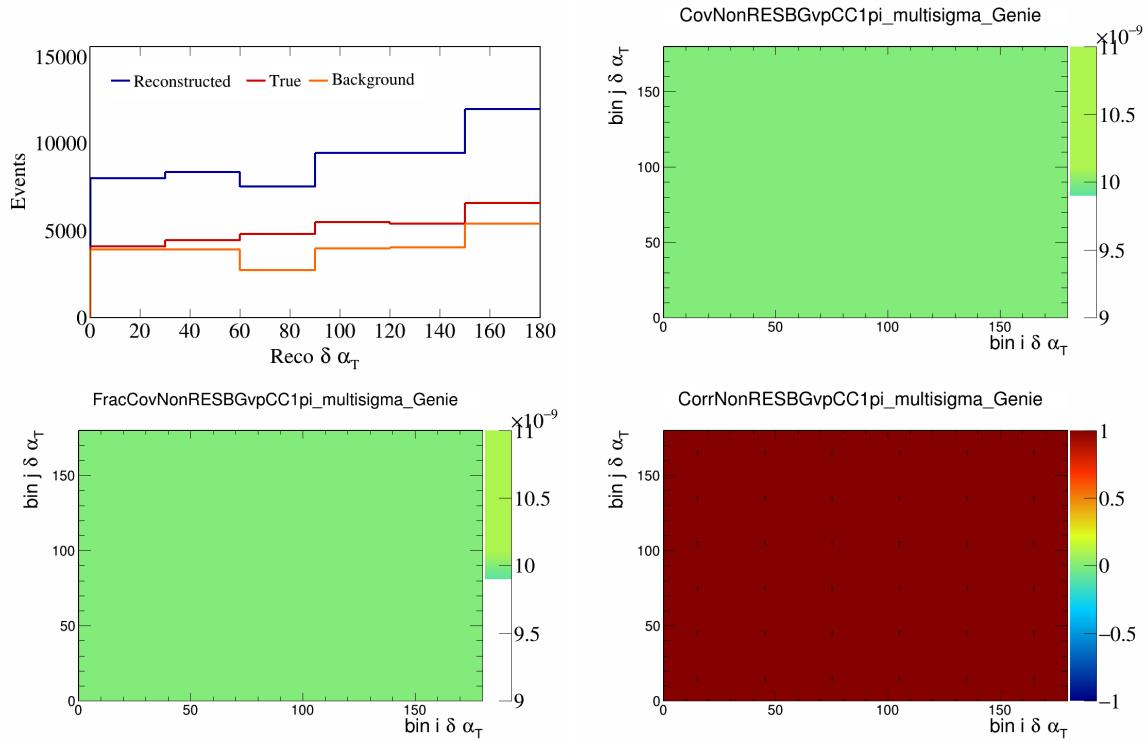


Figure 461: NonRESBGvpCC1pi variations for $\delta\alpha_T$.

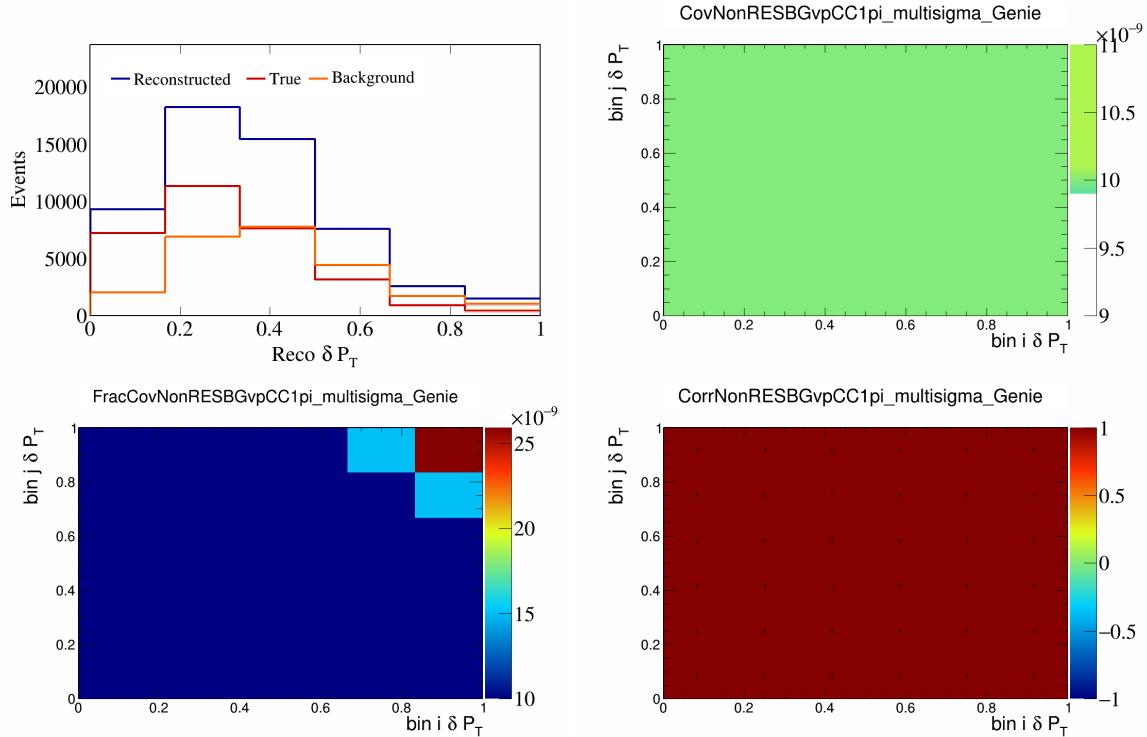


Figure 462: NonRESBGvpCC1pi variations for δP_T .

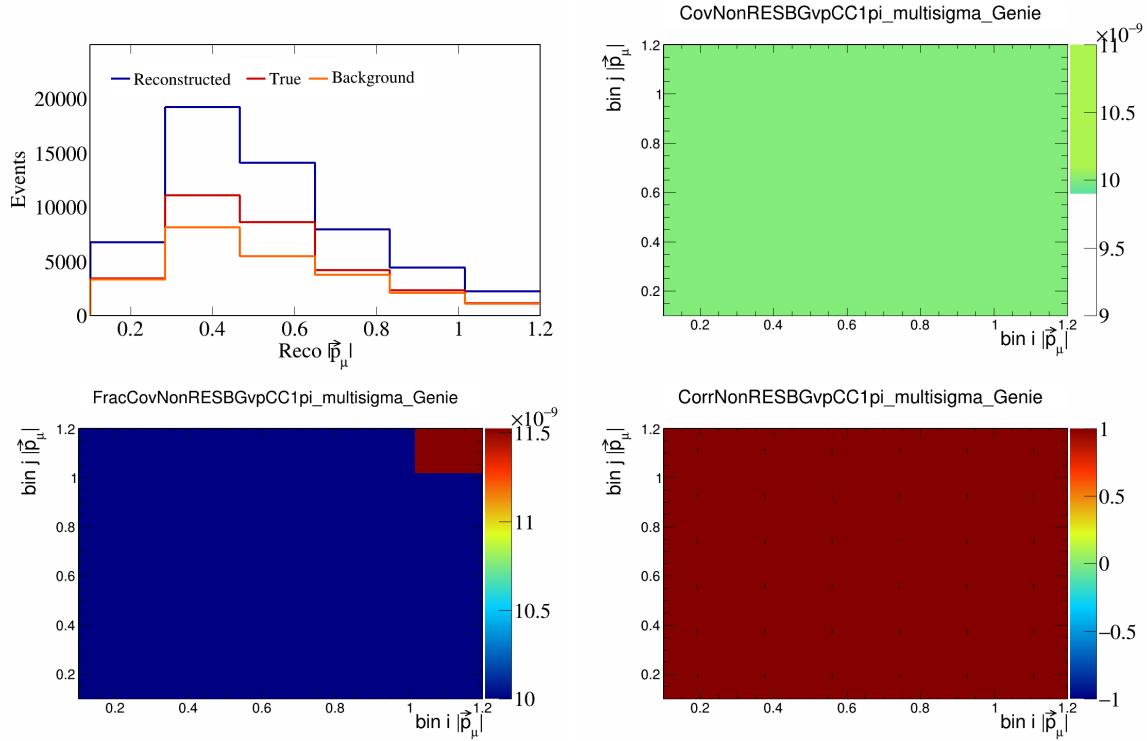


Figure 463: NonRESBGvpCC1pi variations for $|\vec{p}_\mu|$.

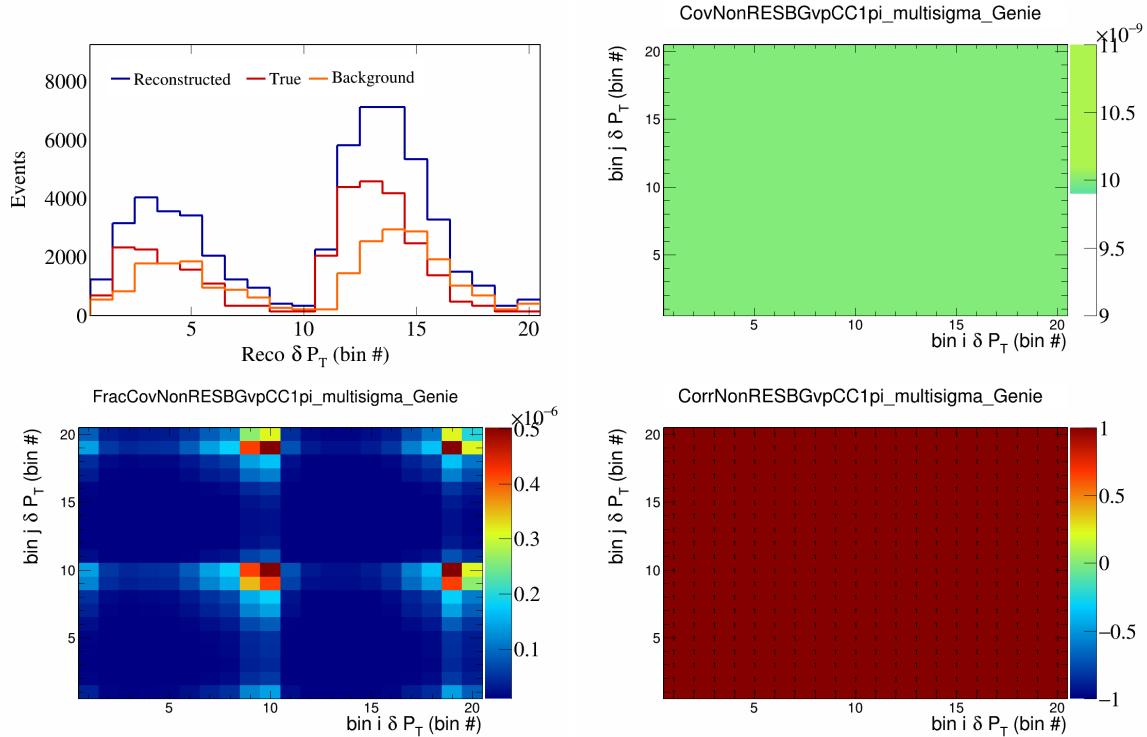


Figure 464: NonRESBGvpCC1pi variations for δP_T in $\cos(\theta_{\vec{p}_\mu})$.

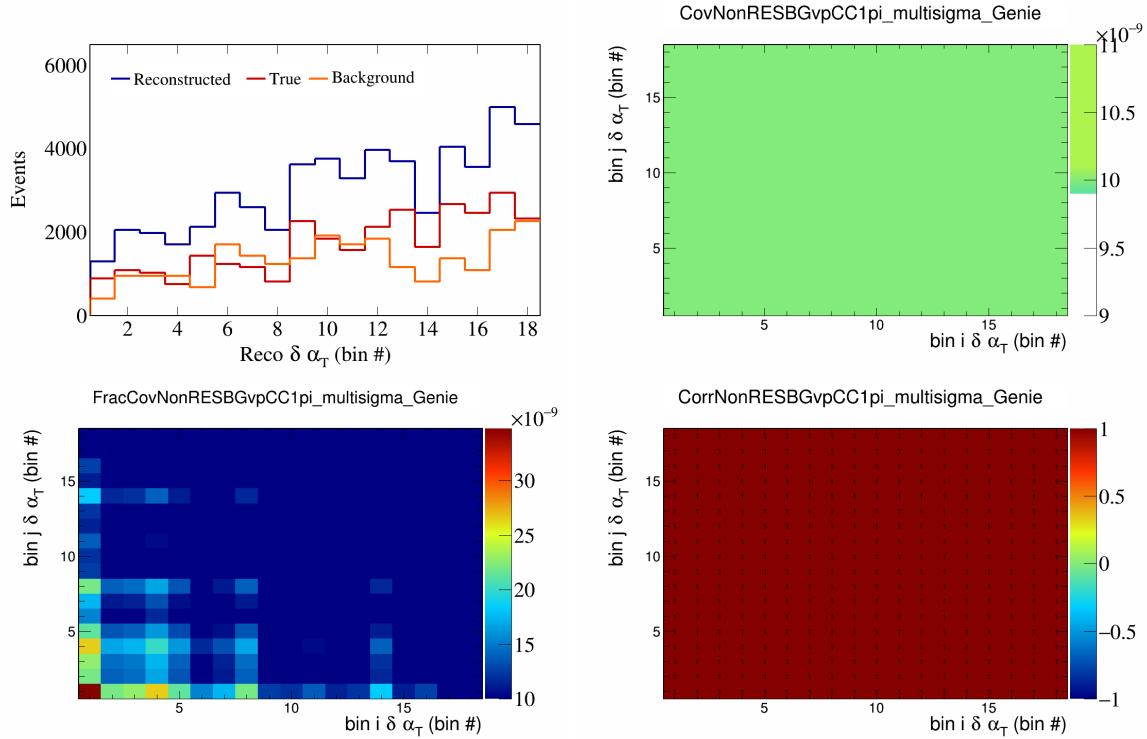


Figure 465: NonRESBGvpCC1pi variations for $\delta\alpha_T$ in $\cos(\theta_{\vec{p}_\mu})$.

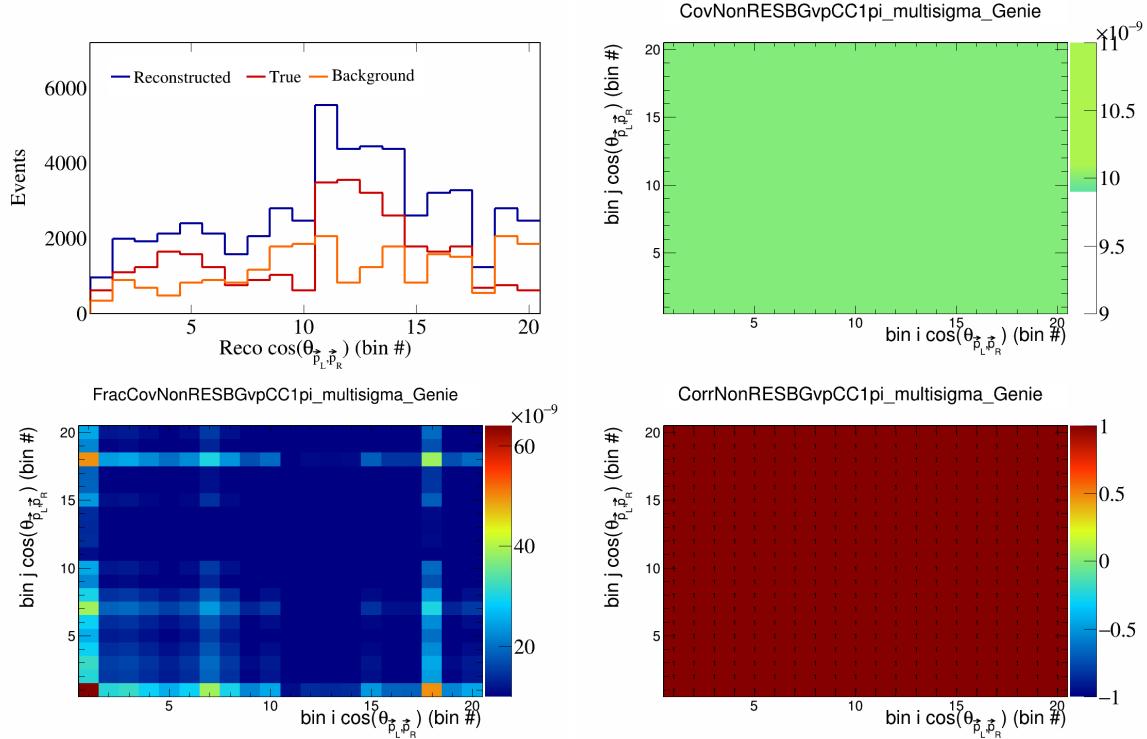


Figure 466: NonRESBGvpCC1pi variations for $\cos(\theta_{\vec{p}_L, \vec{p}_R})$ in $\cos(\theta_{\vec{p}_\mu})$.

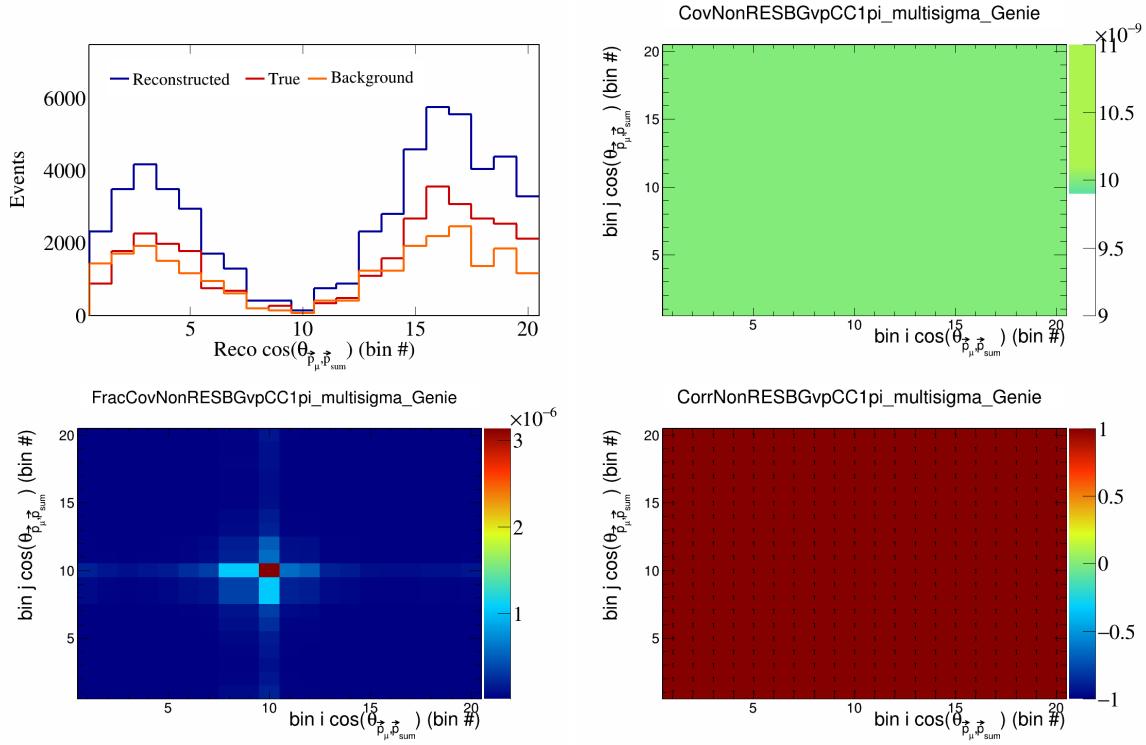


Figure 467: NonRESBGvpCC1pi variations for $\cos(\theta_{\vec{p}_\mu, \vec{p}_{\text{sum}}})$ in $\cos(\theta_{\vec{p}_\mu})$.

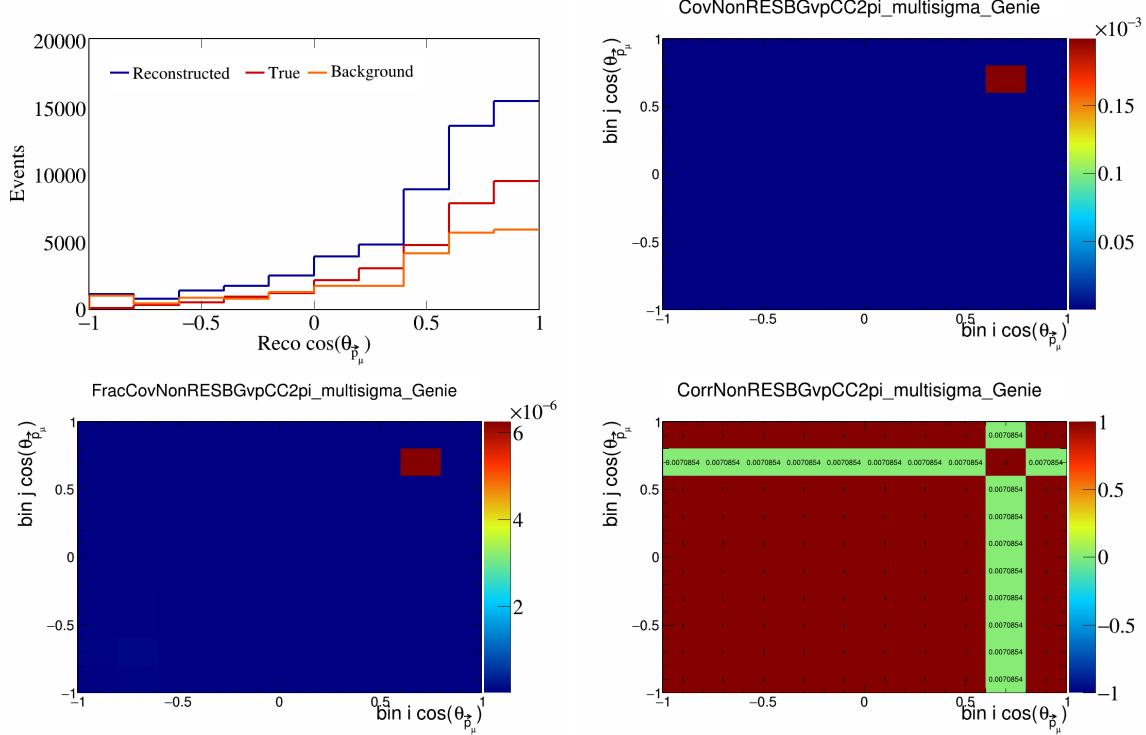


Figure 468: NonRESBGvpCC2pi variations for $\cos(\theta_{\vec{p}_\mu})$.

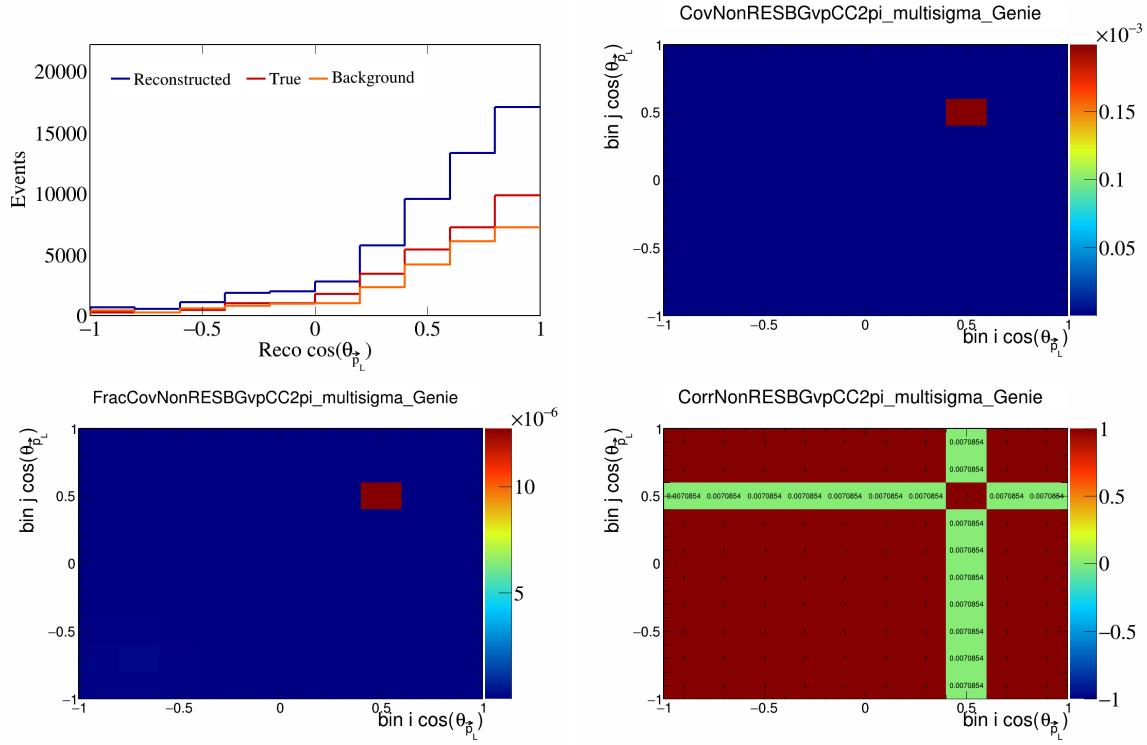


Figure 469: NonRESBGvpCC2pi variations for $\cos(\theta_{\vec{p}_L})$.

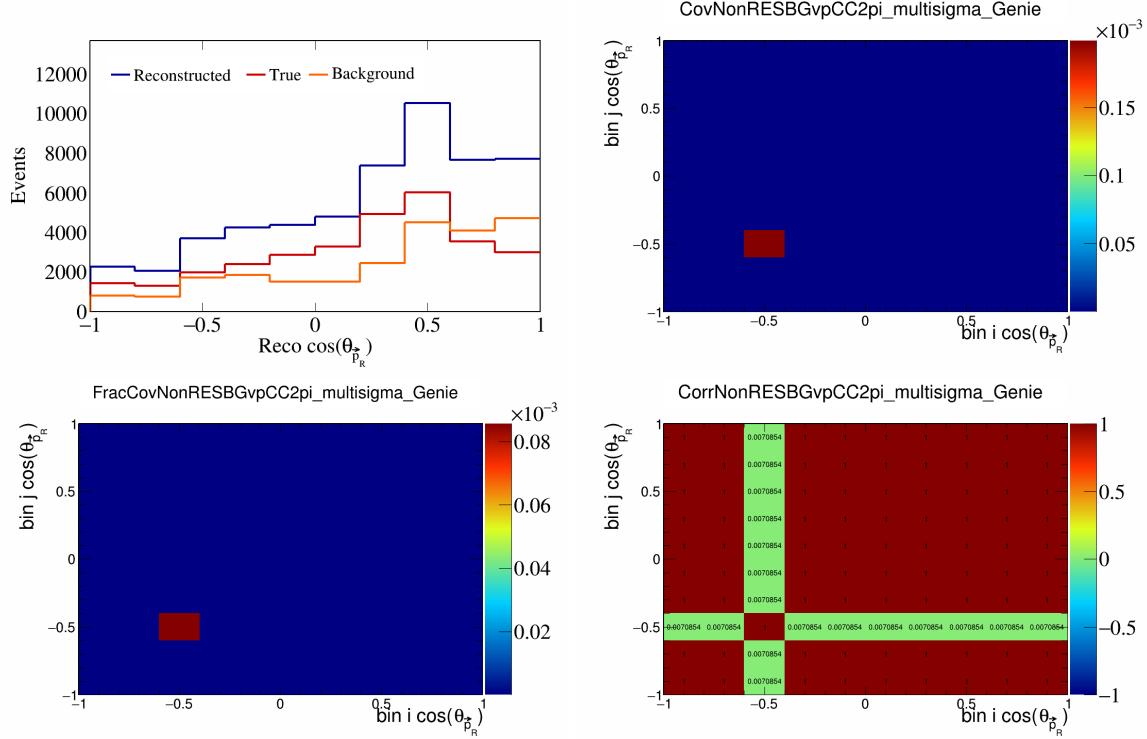


Figure 470: NonRESBGvpCC2pi variations for $\cos(\theta_{\vec{p}_R})$.

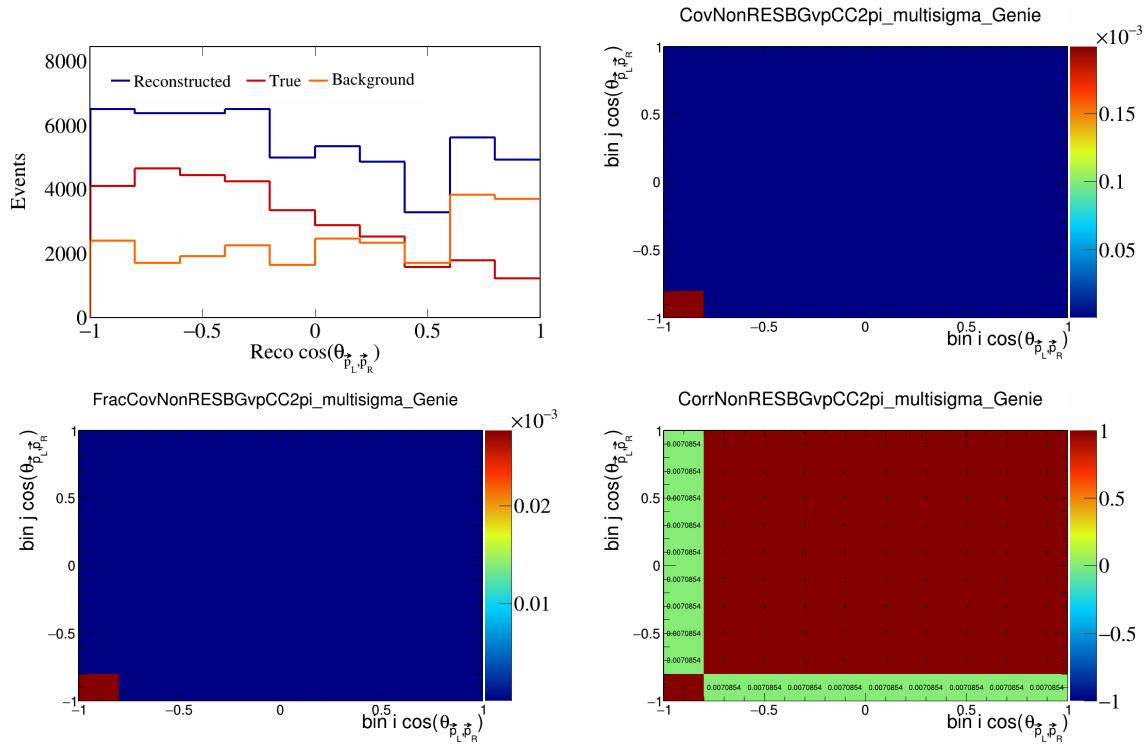


Figure 471: NonRESBGvpCC2pi variations for $\cos(\theta_{\vec{p}_L, \vec{p}_R})$.

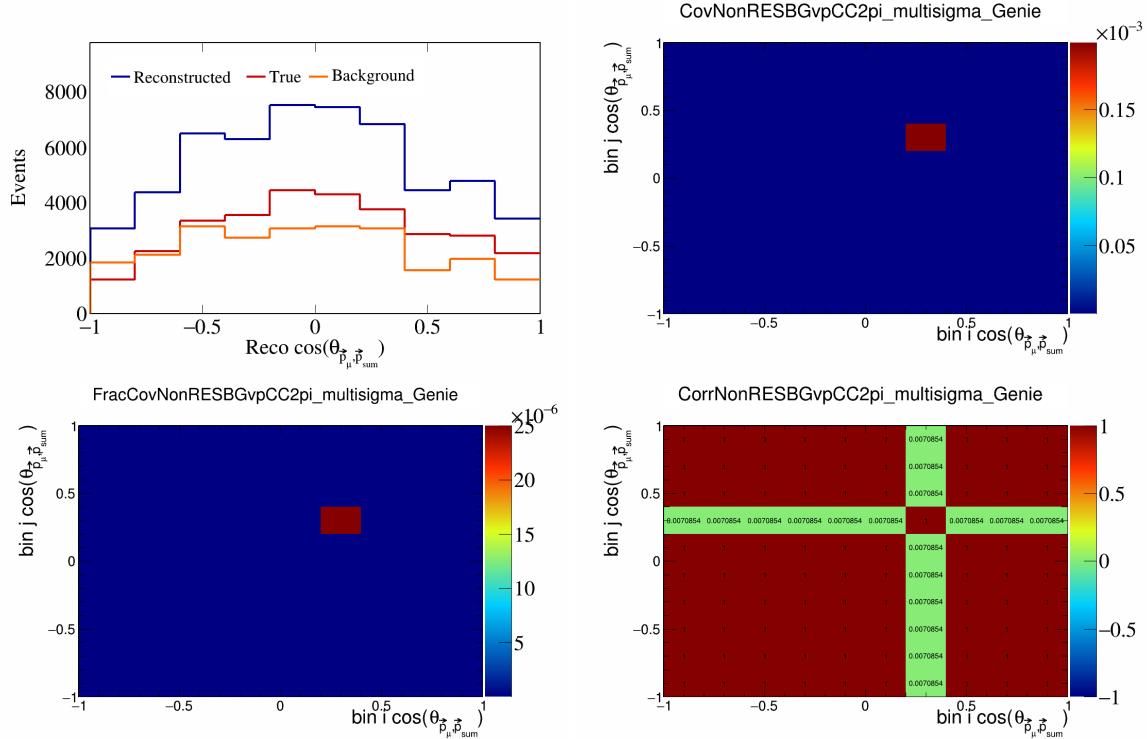


Figure 472: NonRESBGvpCC2pi variations for $\cos(\theta_{\vec{p}_\mu, \vec{p}_{\text{sum}}})$.

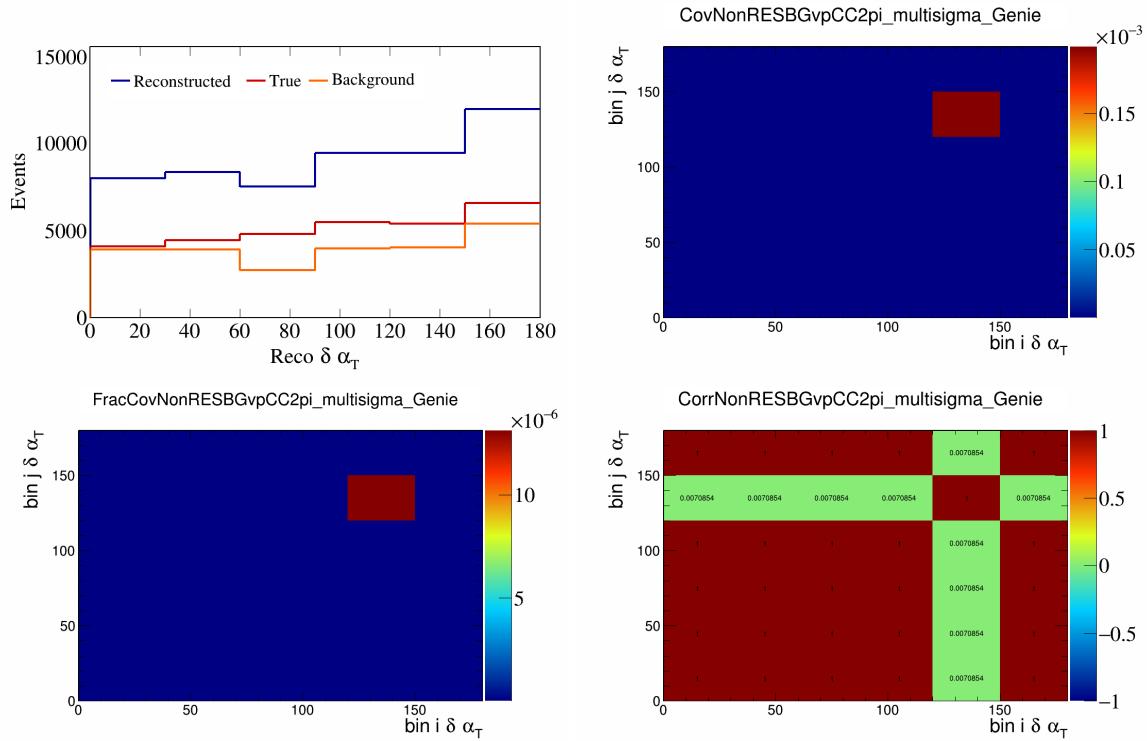


Figure 473: NonRESBGvpCC2pi variations for $\delta\alpha_T$.

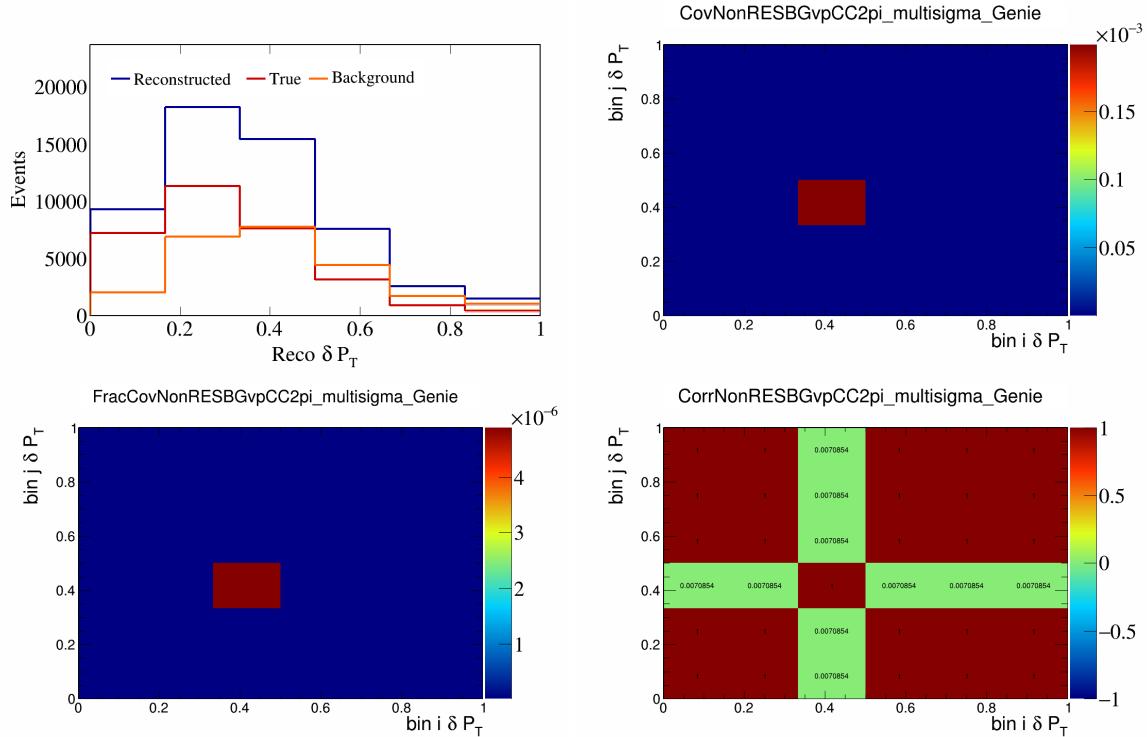


Figure 474: NonRESBGvpCC2pi variations for δP_T .

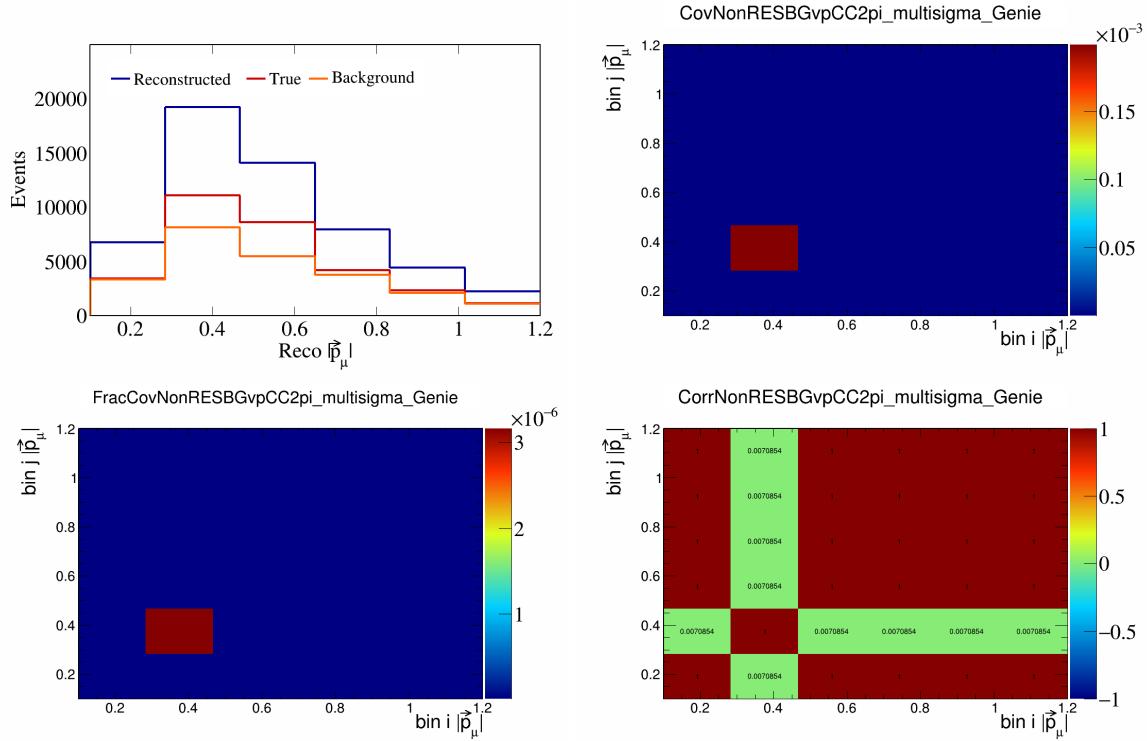


Figure 475: NonRESBGvpCC2pi variations for $|\vec{p}_\mu|$.

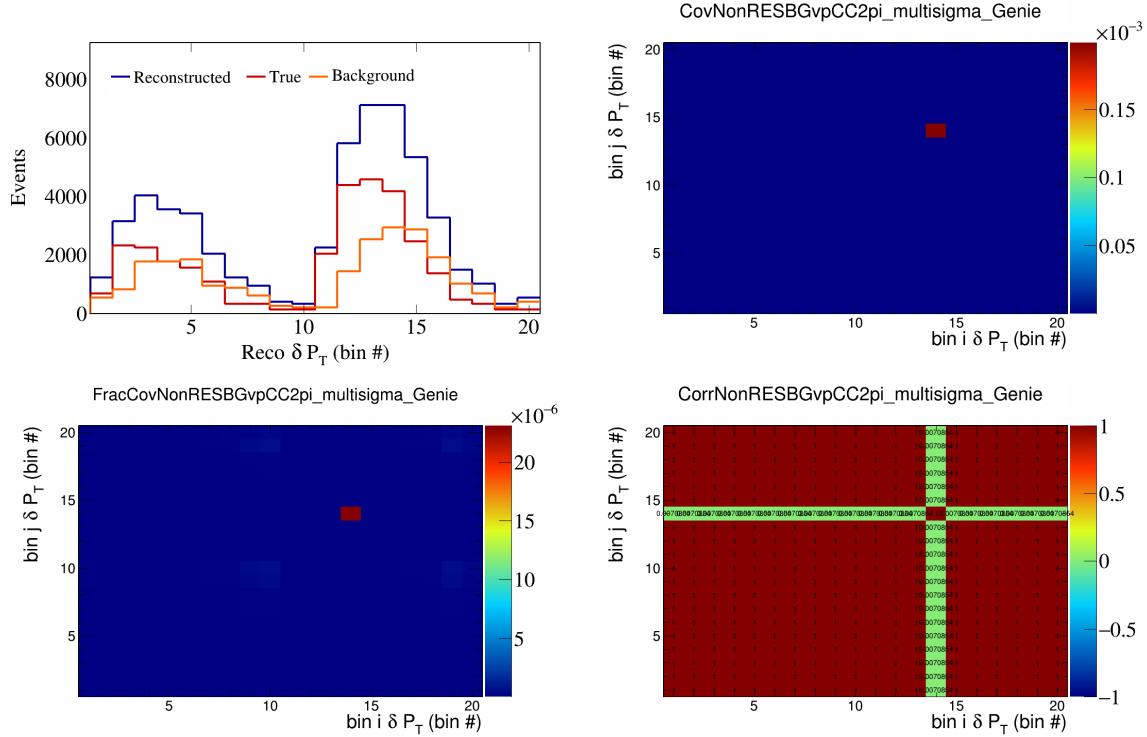


Figure 476: NonRESBGvpCC2pi variations for δP_T in $\cos(\theta_{\vec{p}_\mu})$.

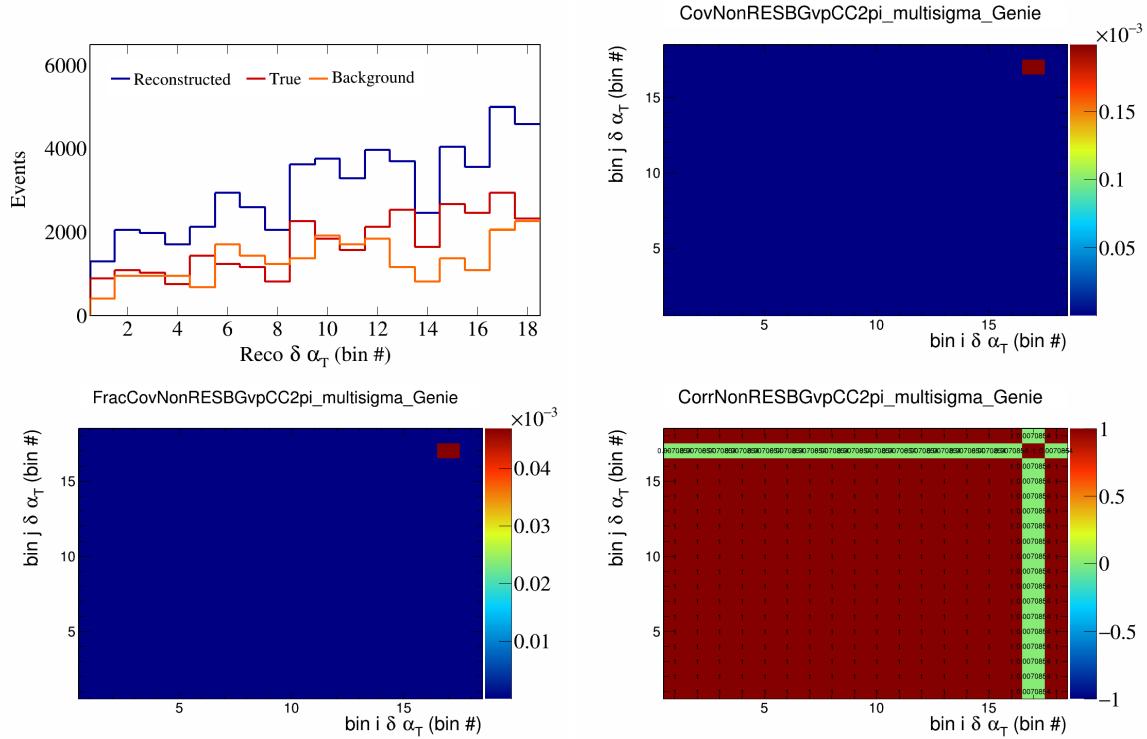


Figure 477: NonRESBGvpCC2pi variations for $\delta\alpha_T$ in $\cos(\theta_{\vec{p}_\mu})$.

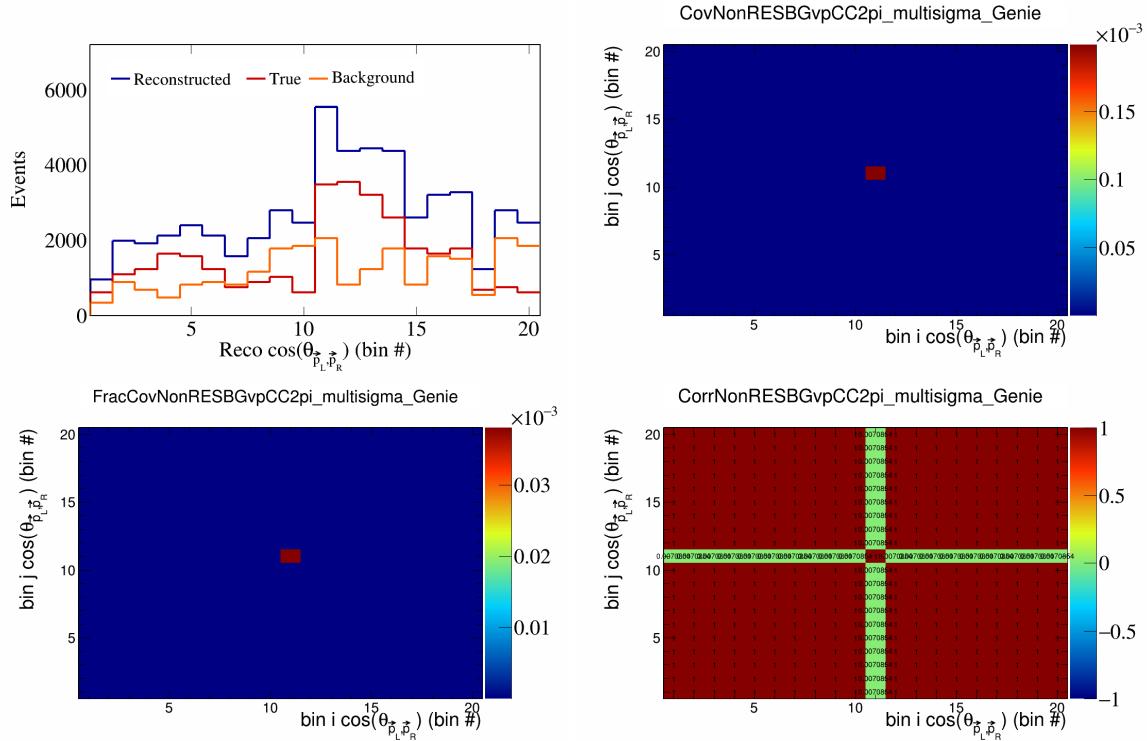


Figure 478: NonRESBGvpCC2pi variations for $\cos(\theta_{\vec{p}_L, \vec{p}_R})$ in $\cos(\theta_{\vec{p}_\mu})$.

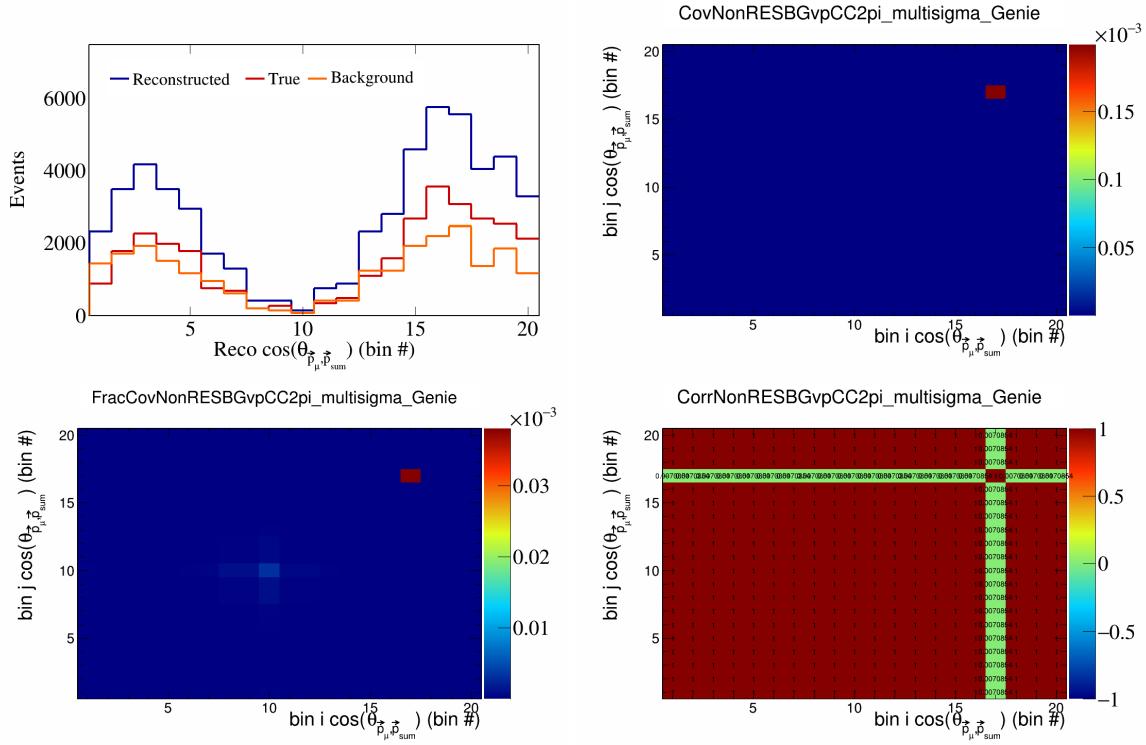


Figure 479: NonRESBGvpCC2pi variations for $\cos(\theta_{\vec{p}_\mu, \vec{p}_{\text{sum}}})$ in $\cos(\theta_{\vec{p}_\mu})$.

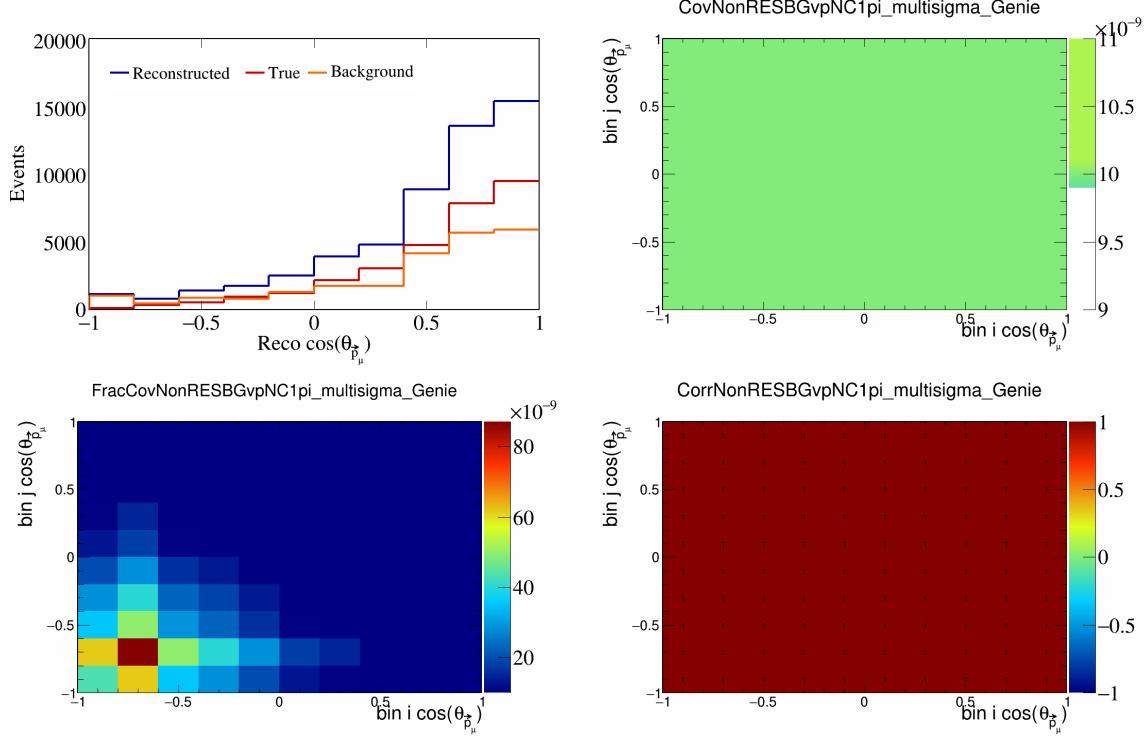


Figure 480: NonRESBGvpNC1pi variations for $\cos(\theta_{\vec{p}_\mu})$.

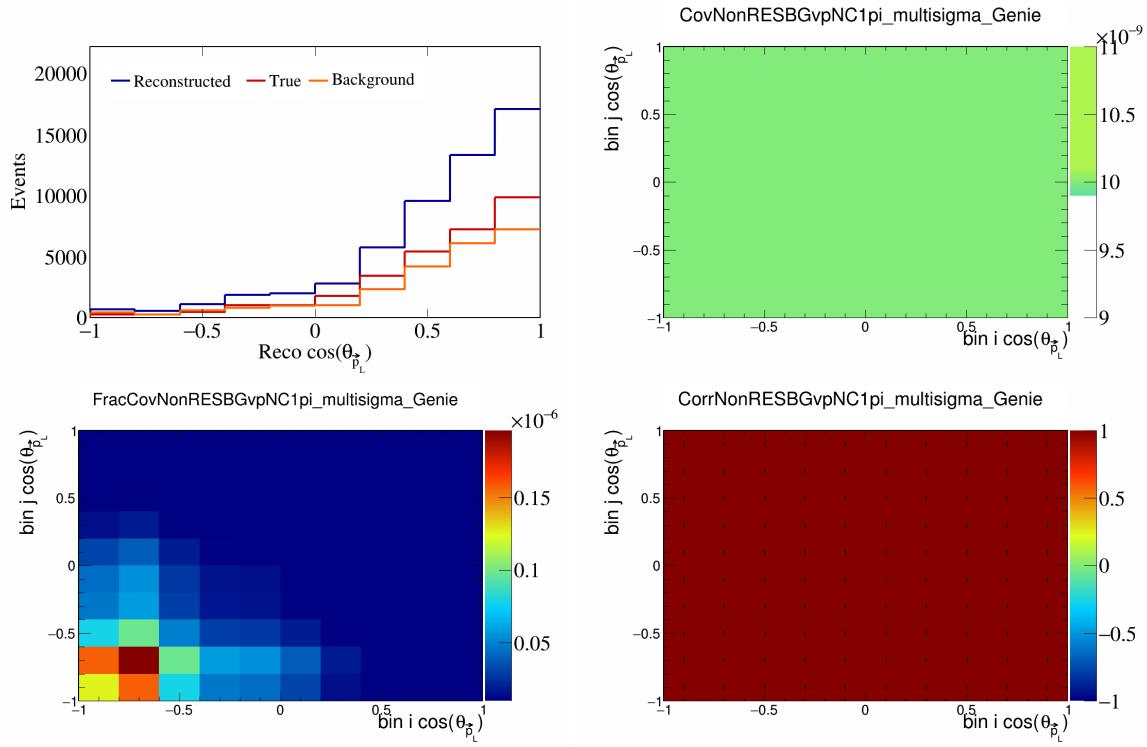


Figure 481: NonRESBGvpNC1pi variations for $\cos(\theta_{\vec{p}_L})$.

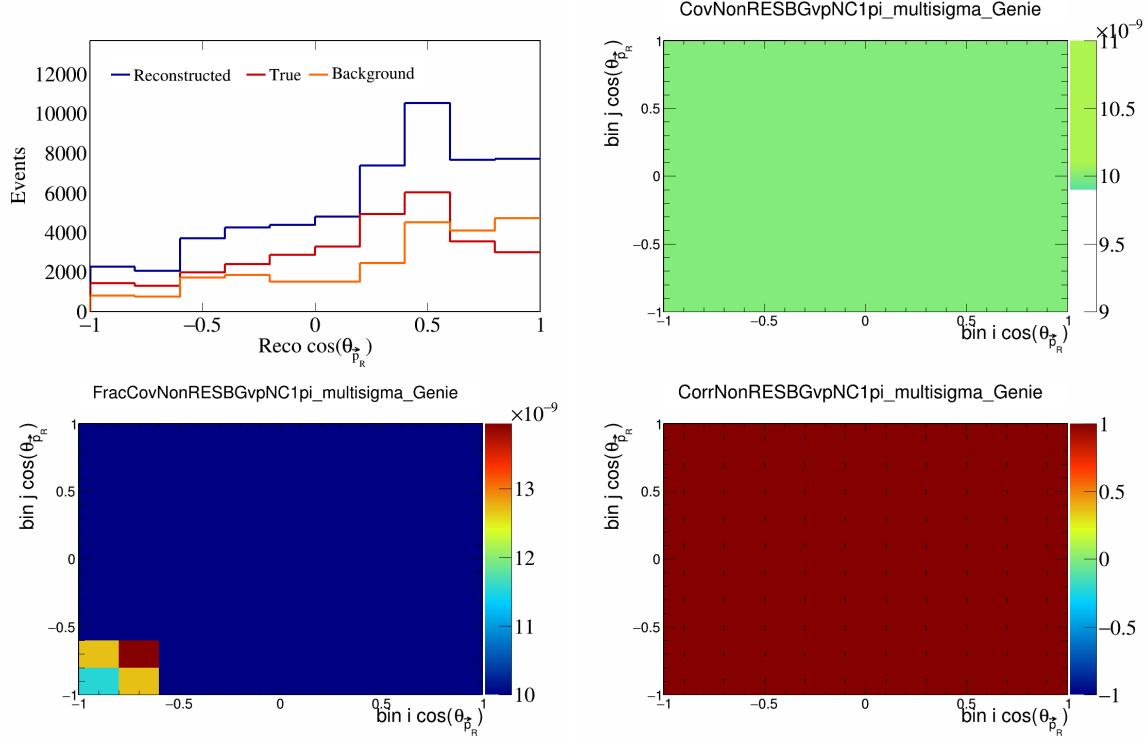


Figure 482: NonRESBGvpNC1pi variations for $\cos(\theta_{\vec{p}_R})$.

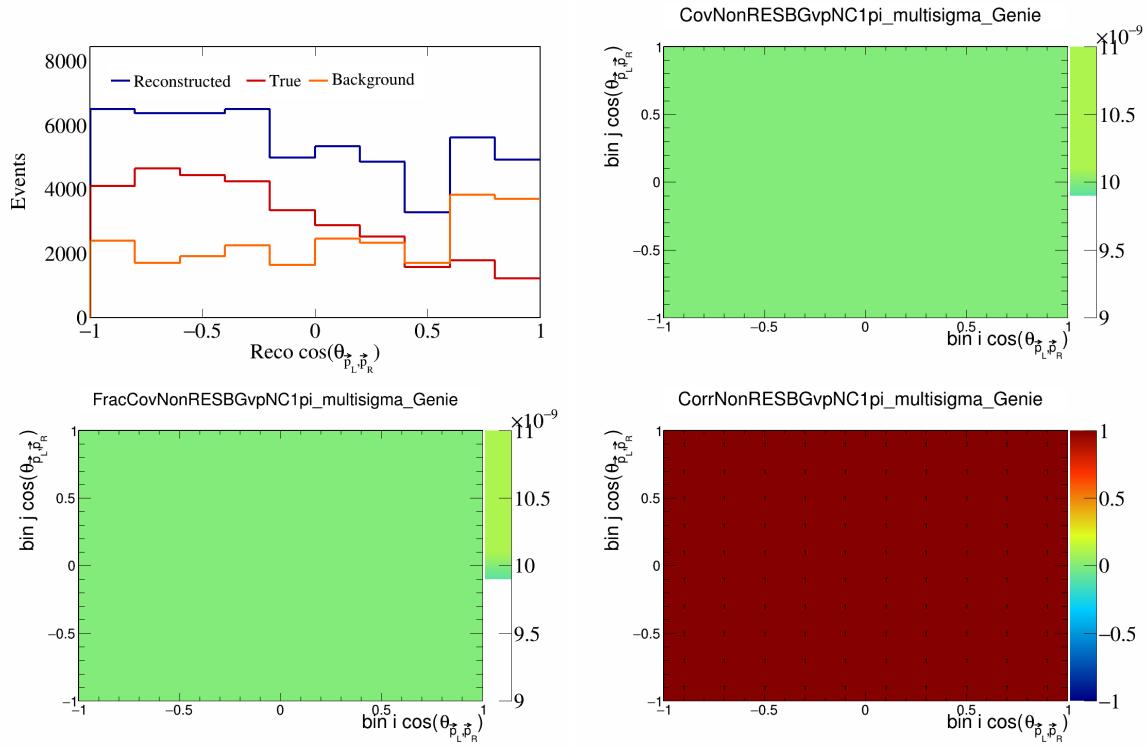


Figure 483: NonRESBGvpNC1pi variations for $\cos(\theta_{\vec{p}_L, \vec{p}_R})$.

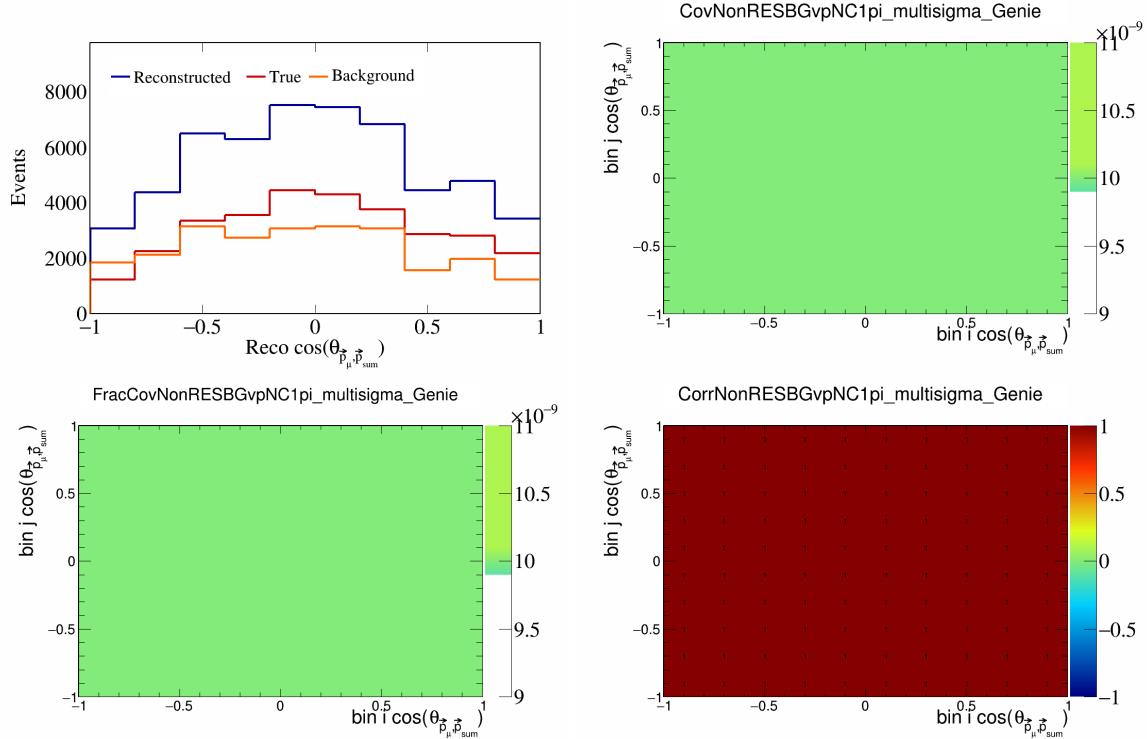


Figure 484: NonRESBGvpNC1pi variations for $\cos(\theta_{\vec{p}_\mu, \vec{p}_{\text{sum}}})$.

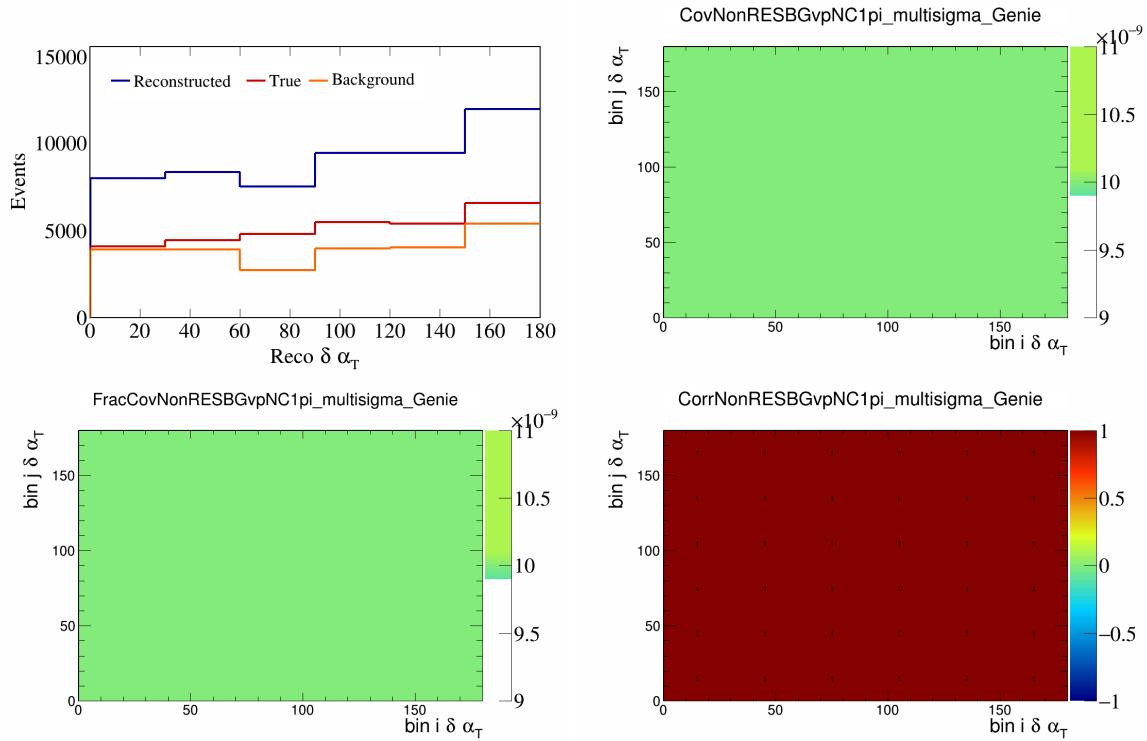


Figure 485: NonRESBGvpNC1pi variations for $\delta\alpha_T$.

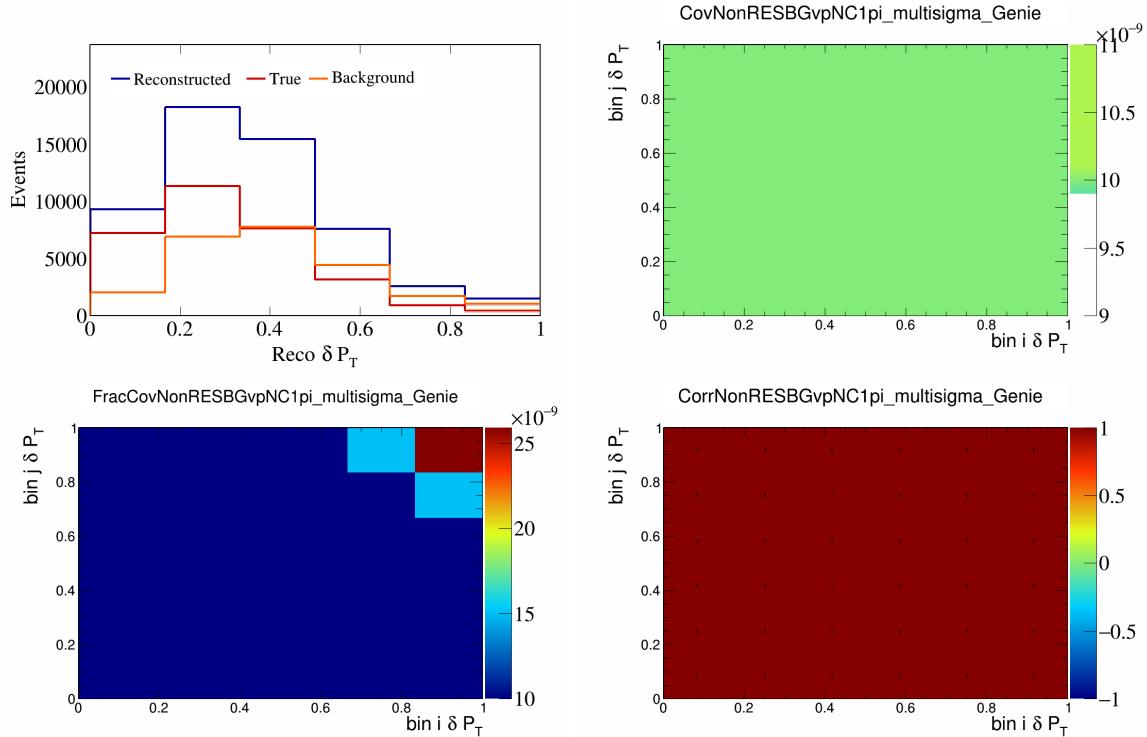


Figure 486: NonRESBGvpNC1pi variations for δP_T .

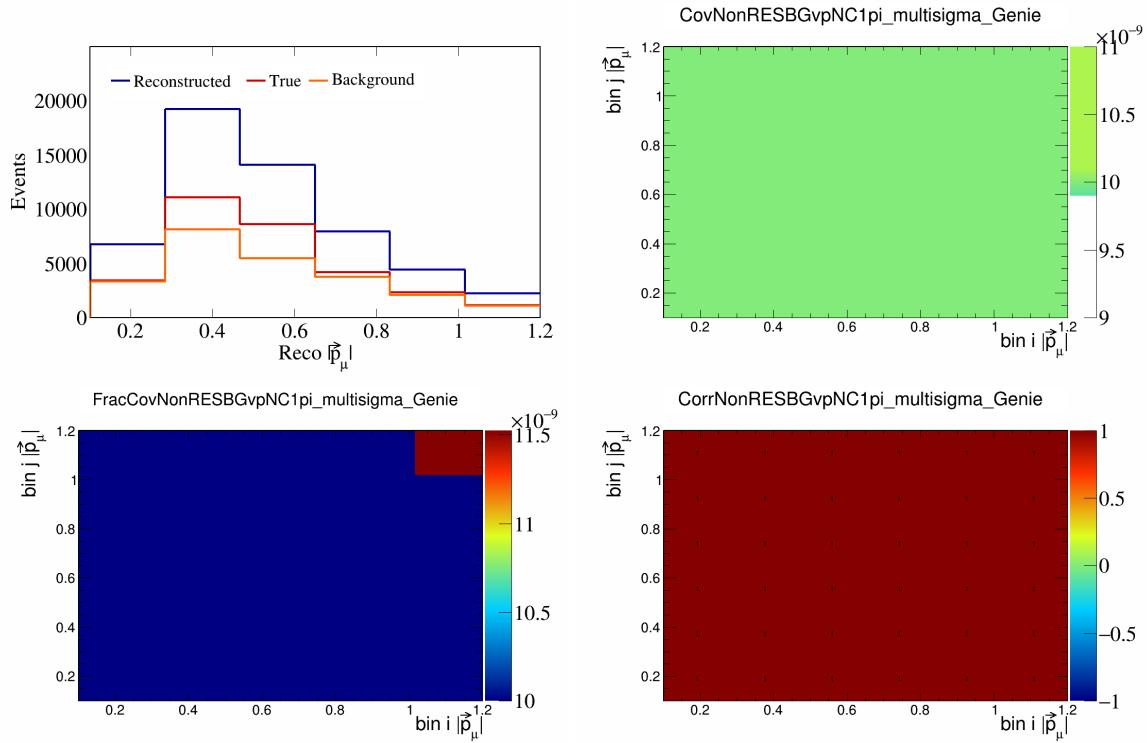


Figure 487: NonRESBGvpNC1pi variations for $|\vec{p}_\mu|$.

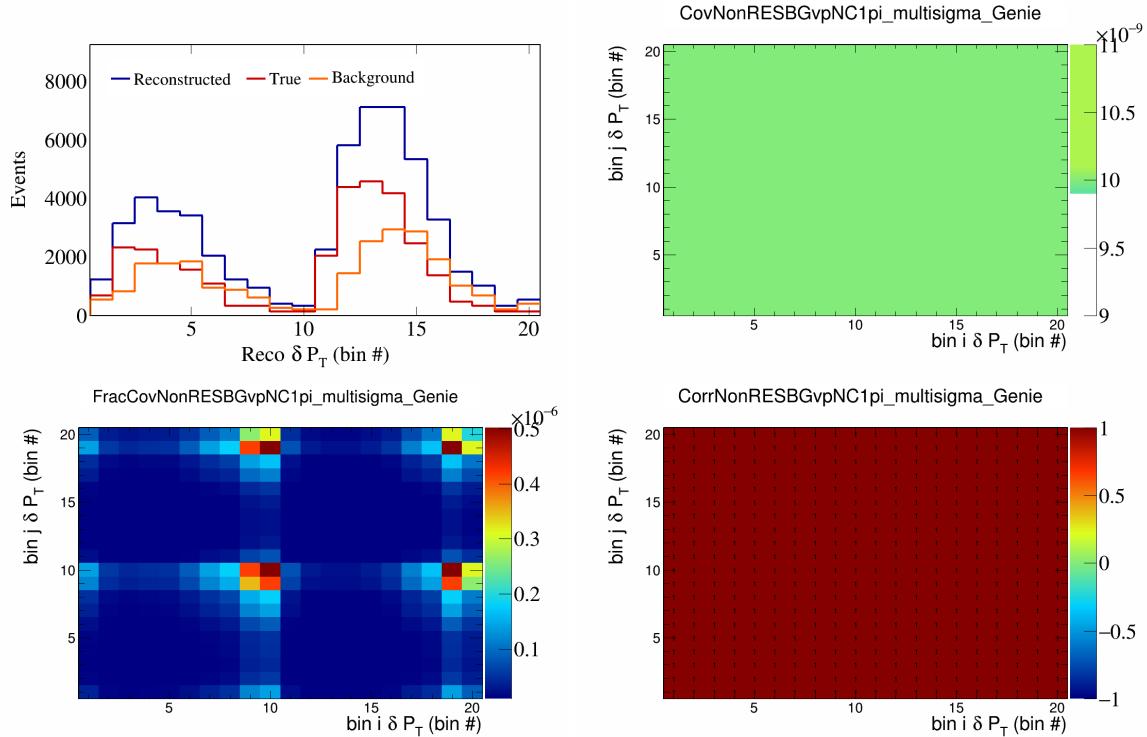


Figure 488: NonRESBGvpNC1pi variations for δP_T in $\cos(\theta_{\vec{p}_\mu})$.

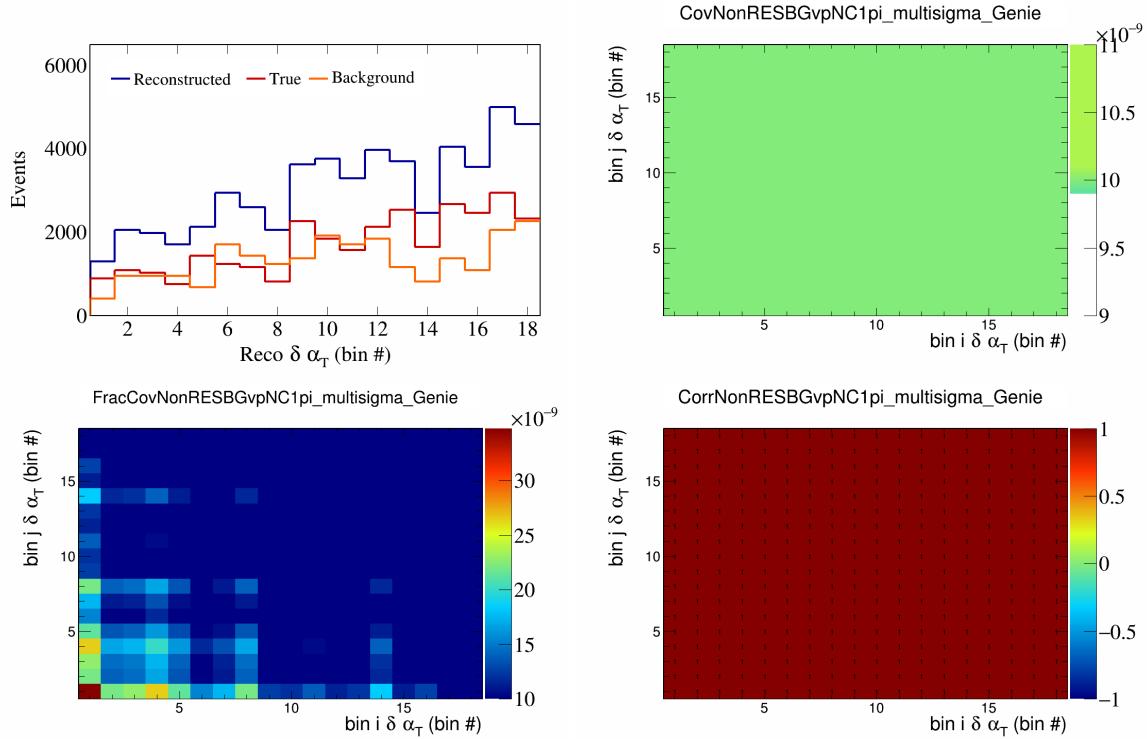


Figure 489: NonRESBGvpNC1pi variations for $\delta\alpha_T$ in $\cos(\theta_{\vec{p}_\mu})$.

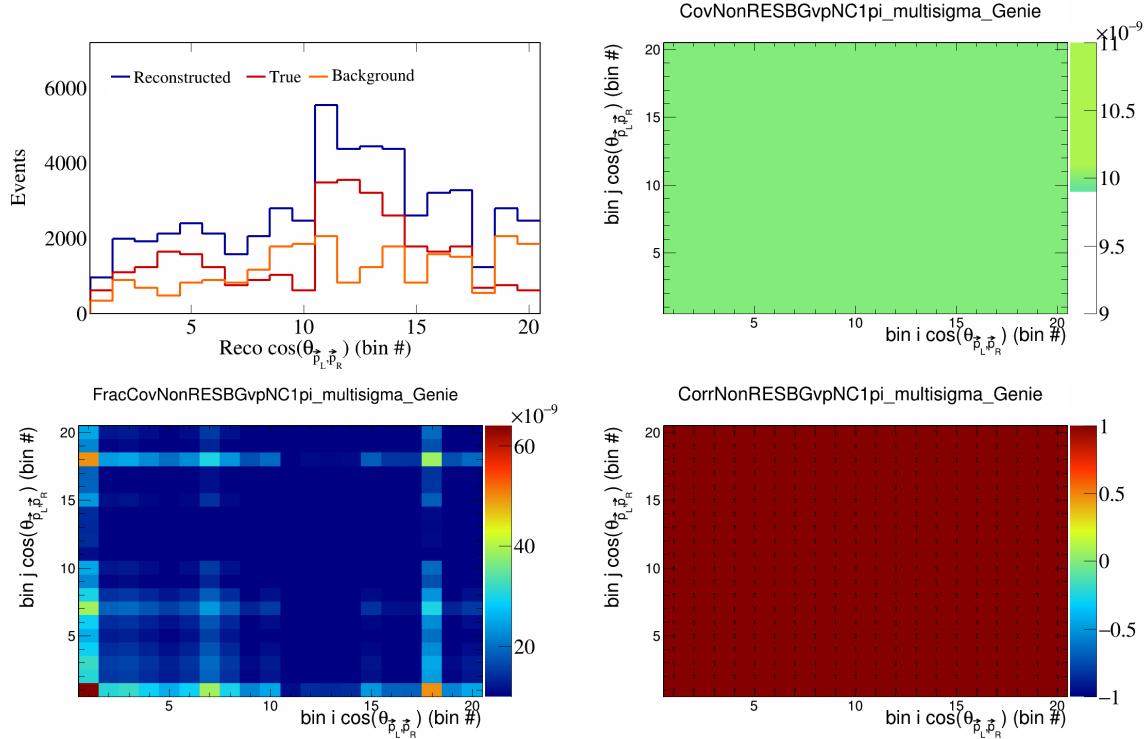


Figure 490: NonRESBGvpNC1pi variations for $\cos(\theta_{\vec{p}_L, \vec{p}_R})$ in $\cos(\theta_{\vec{p}_\mu})$.

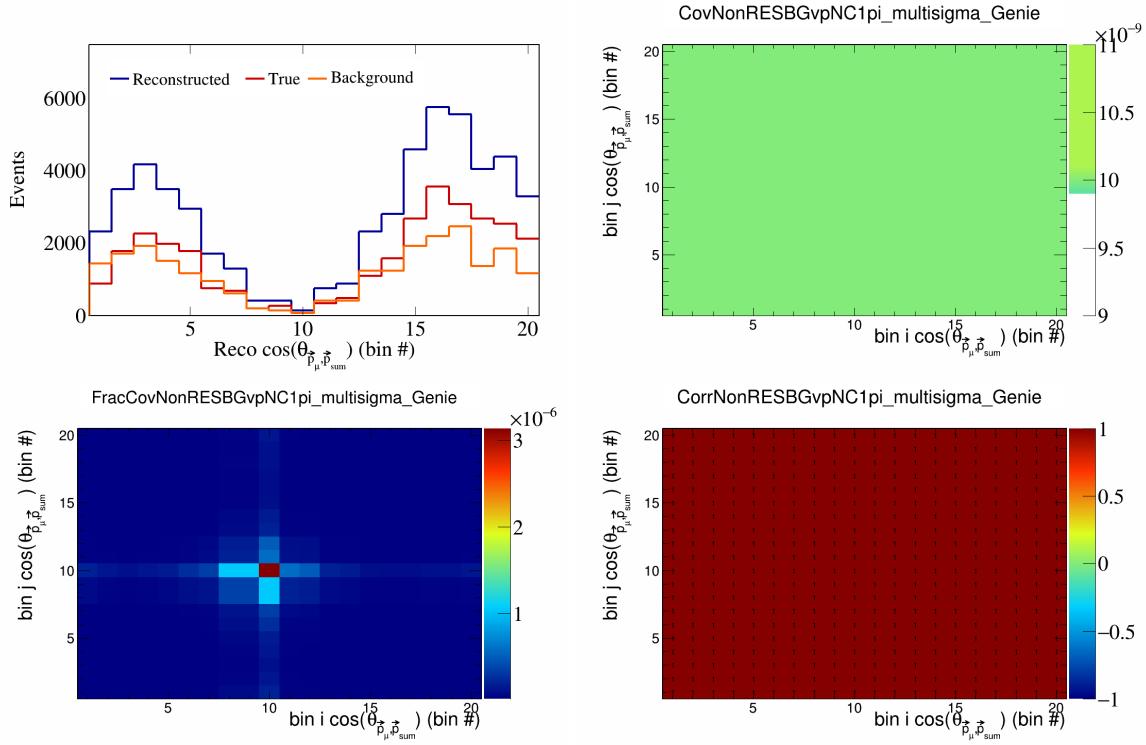


Figure 491: NonRESBGvpNC1pi variations for $\cos(\theta_{\vec{p}_\mu, \vec{p}_{\text{sum}}})$ in $\cos(\theta_{\vec{p}_\mu})$.

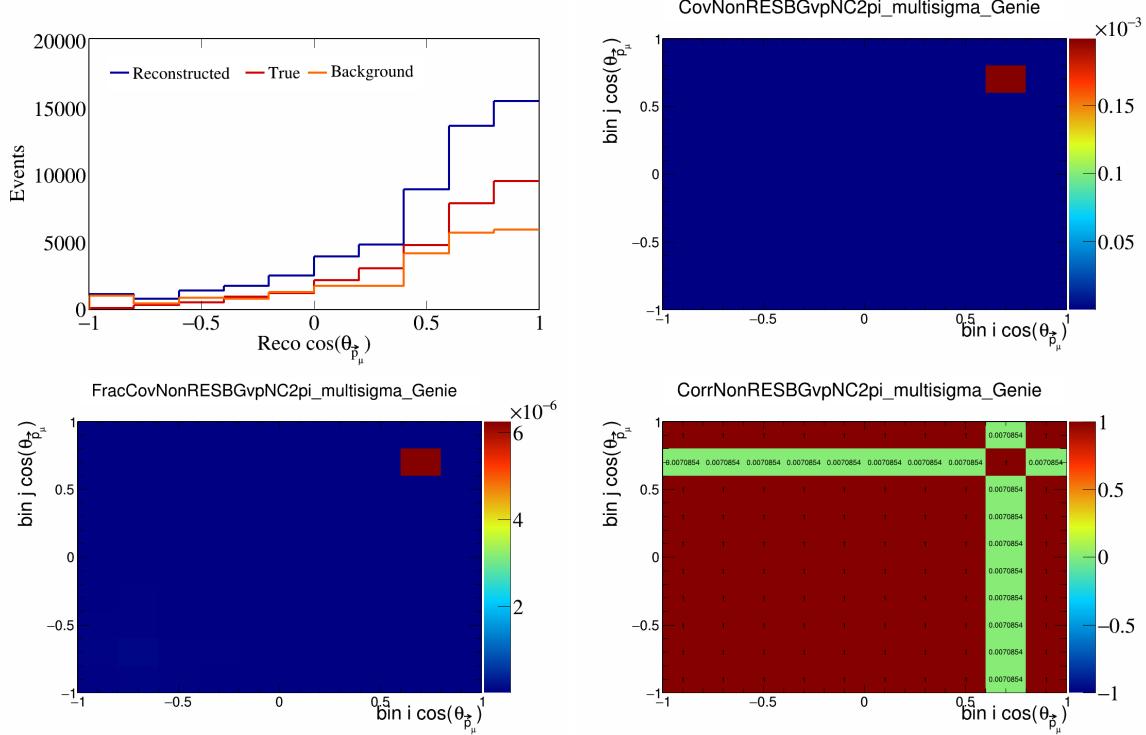


Figure 492: NonRESBGvpNC2pi variations for $\cos(\theta_{\vec{p}_\mu})$.

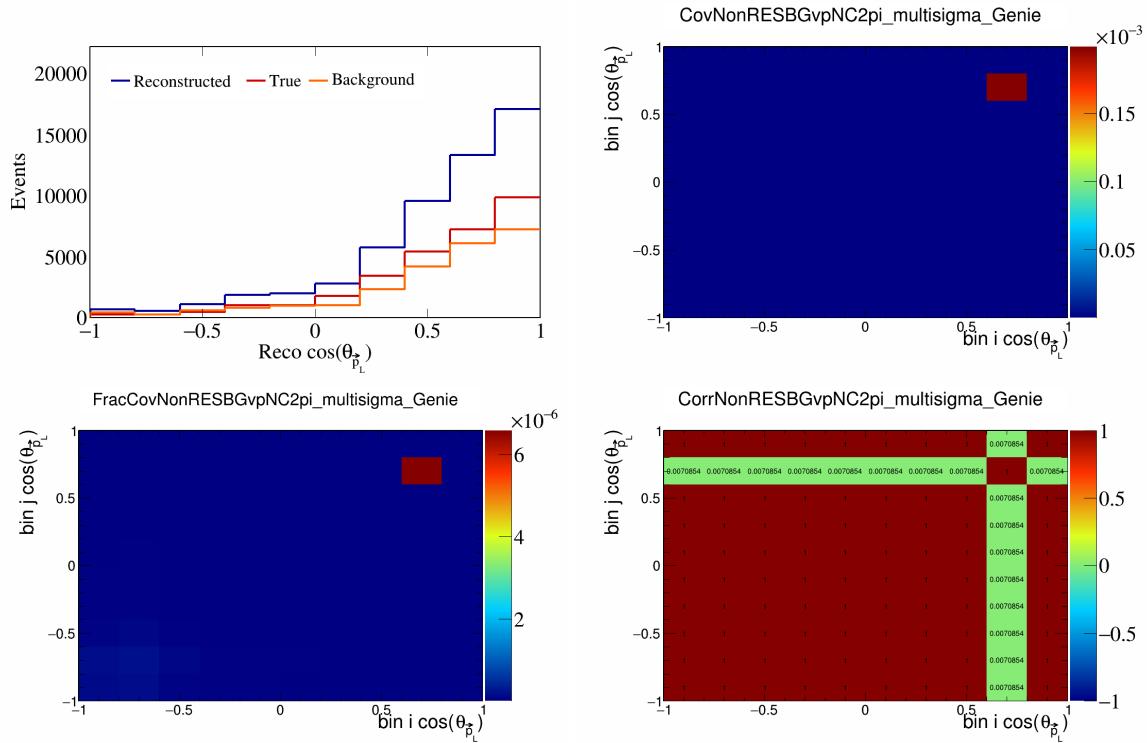


Figure 493: NonRESBGvpNC2pi variations for $\cos(\theta_{\vec{p}_L})$.

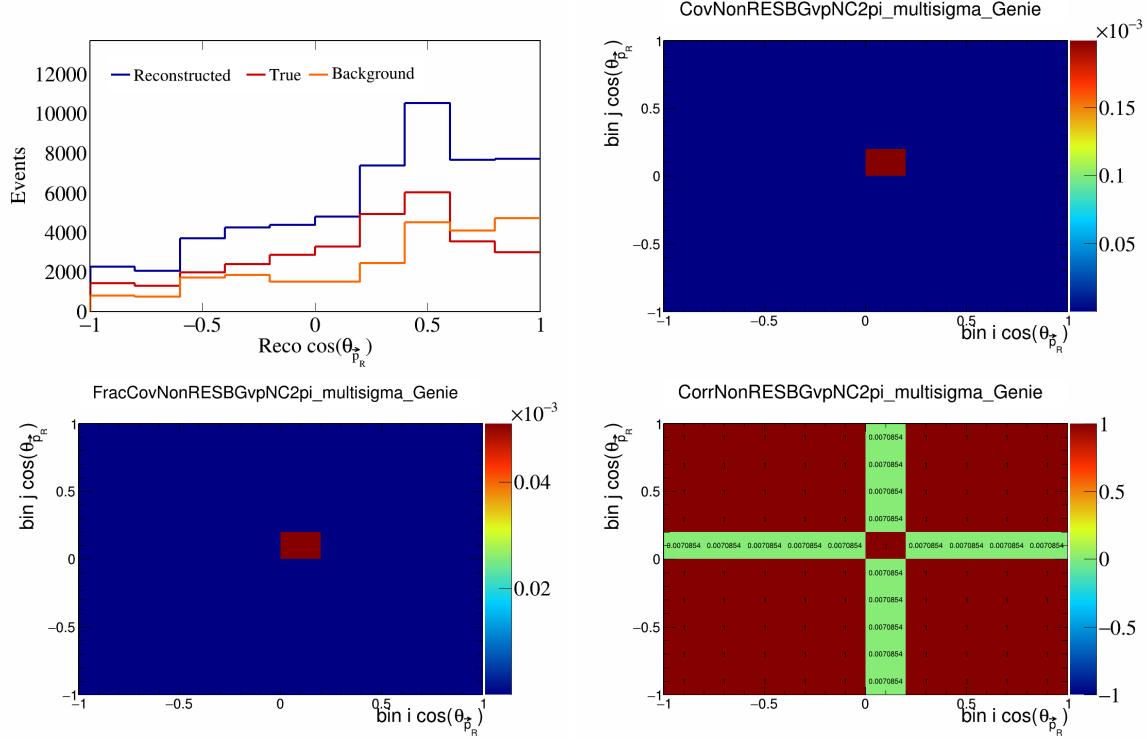


Figure 494: NonRESBGvpNC2pi variations for $\cos(\theta_{\vec{p}_R})$.

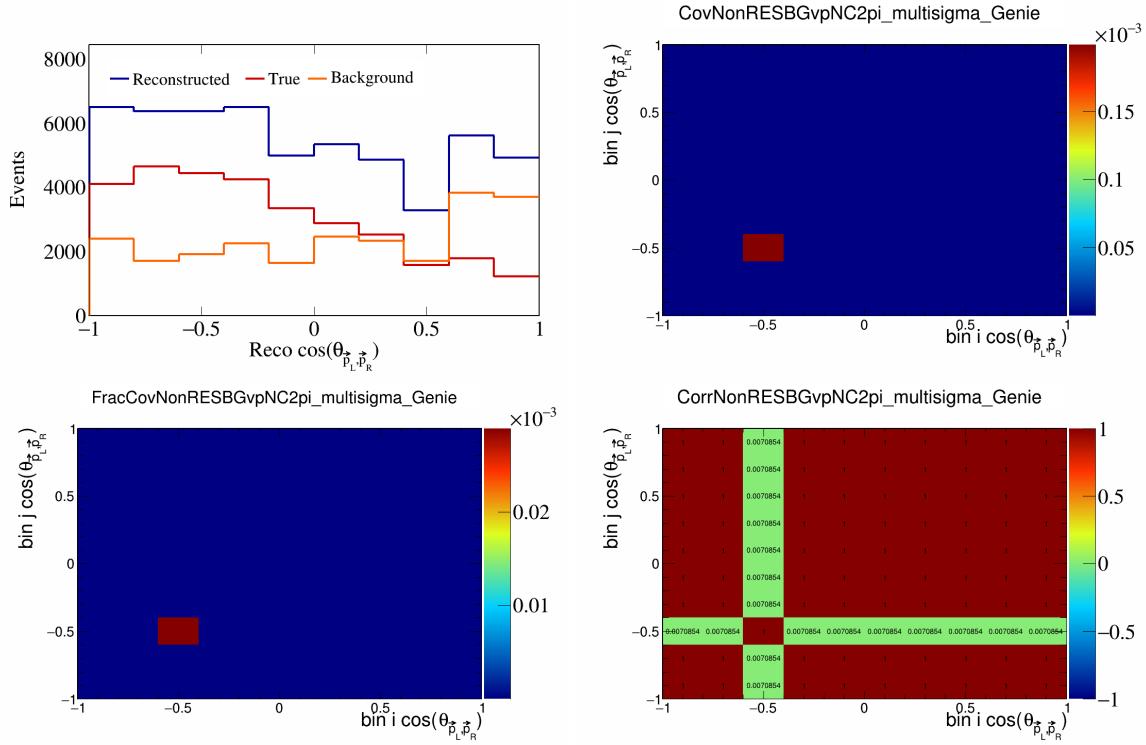


Figure 495: NonRESBGvpNC2pi variations for $\cos(\theta_{\vec{p}_L, \vec{p}_R})$.

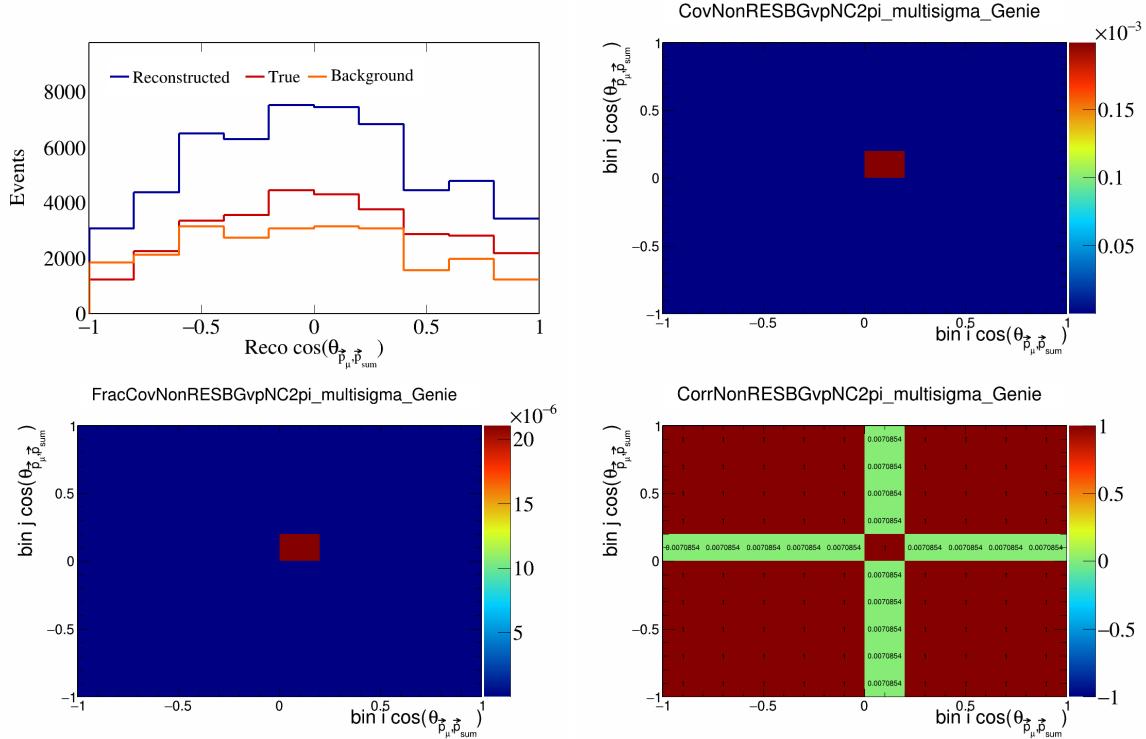


Figure 496: NonRESBGvpNC2pi variations for $\cos(\theta_{\vec{p}_\mu, \vec{p}_{\text{sum}}})$.

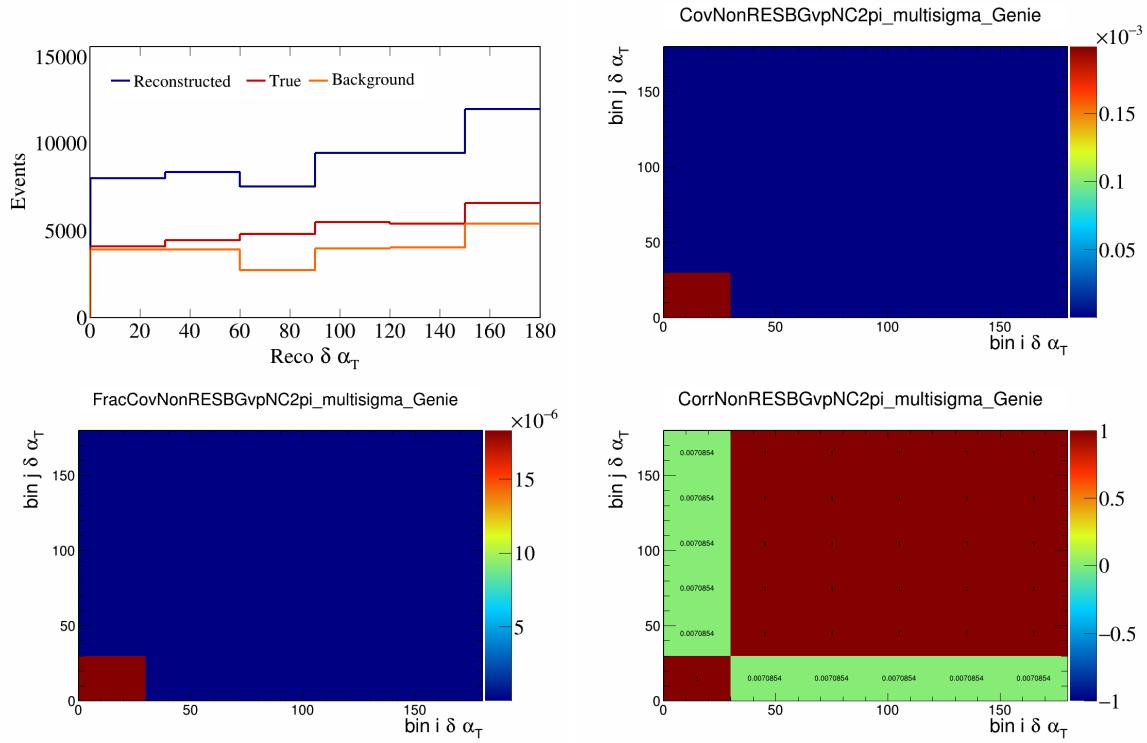


Figure 497: NonRESBGvpNC2pi variations for $\delta \alpha_T$.

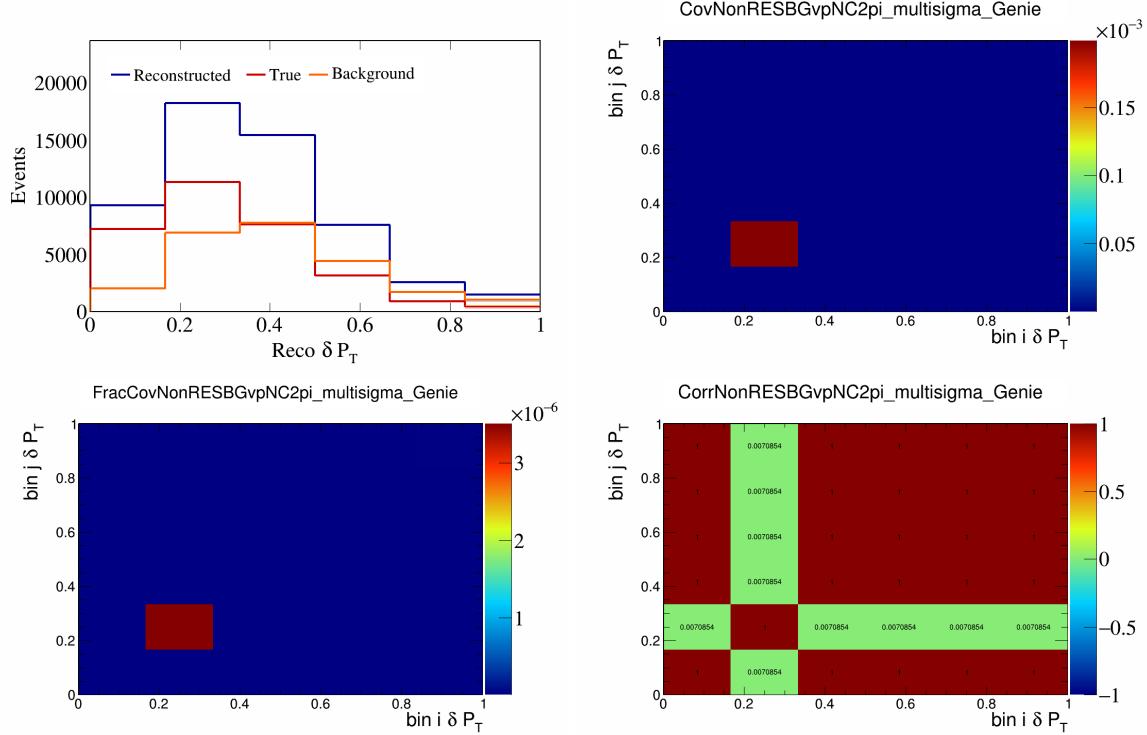


Figure 498: NonRESBGvpNC2pi variations for δP_T .

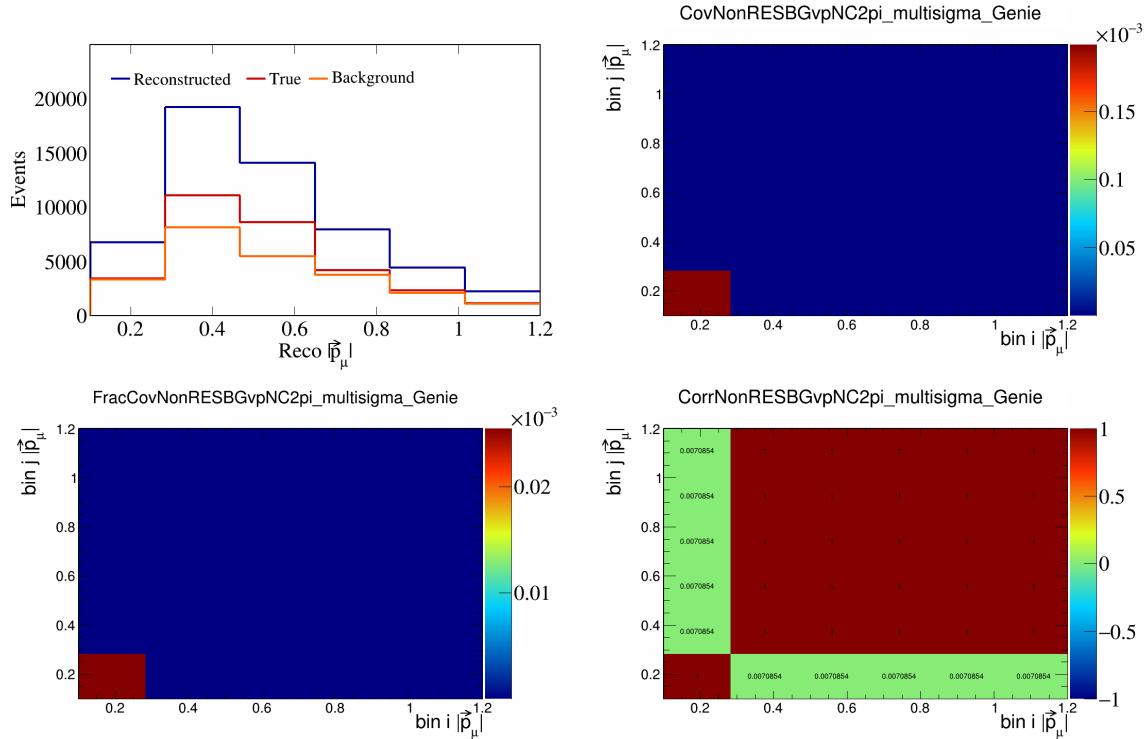


Figure 499: NonRESBGvpNC2pi variations for $|\vec{p}_\mu|$.

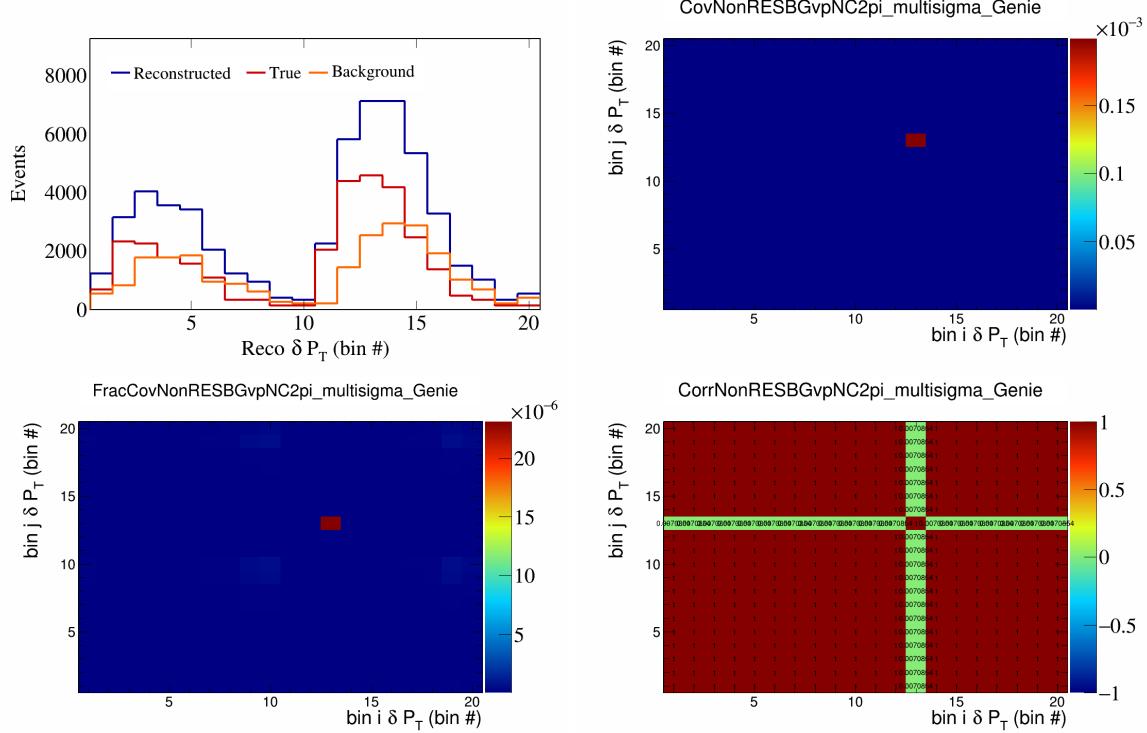


Figure 500: NonRESBGvpNC2pi variations for δP_T in $\cos(\theta_{\vec{p}_\mu})$.

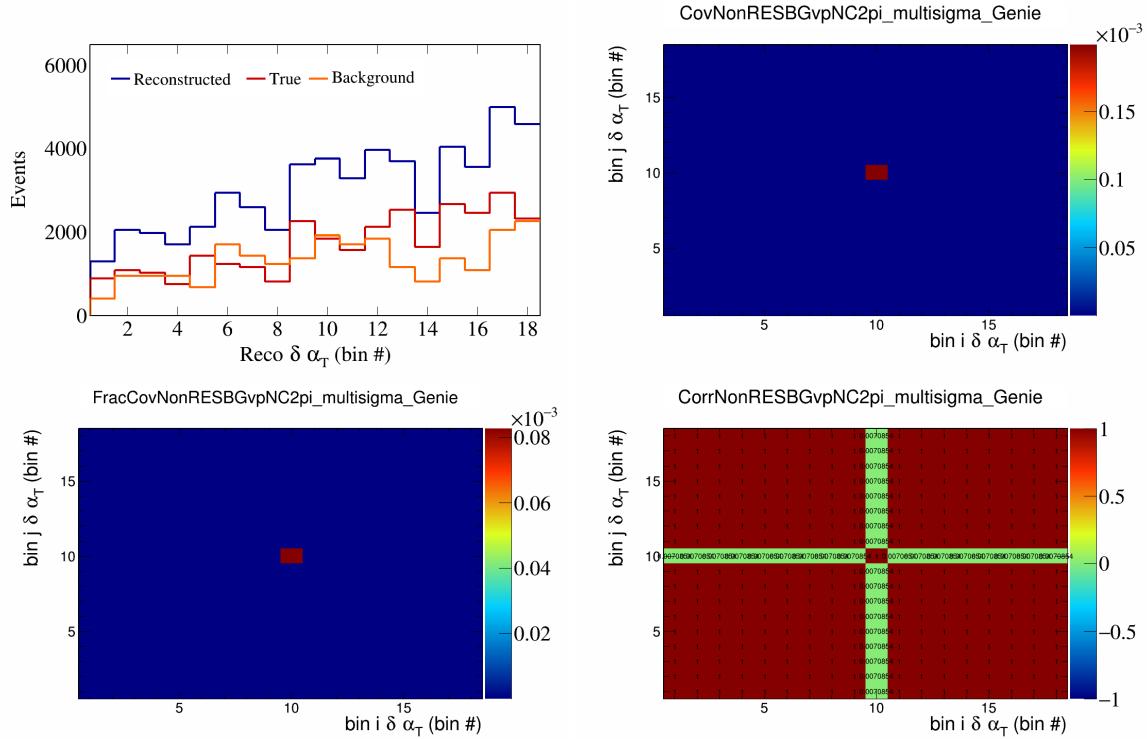


Figure 501: NonRESBGvpNC2pi variations for $\delta\alpha_T$ in $\cos(\theta_{\vec{p}_\mu})$.

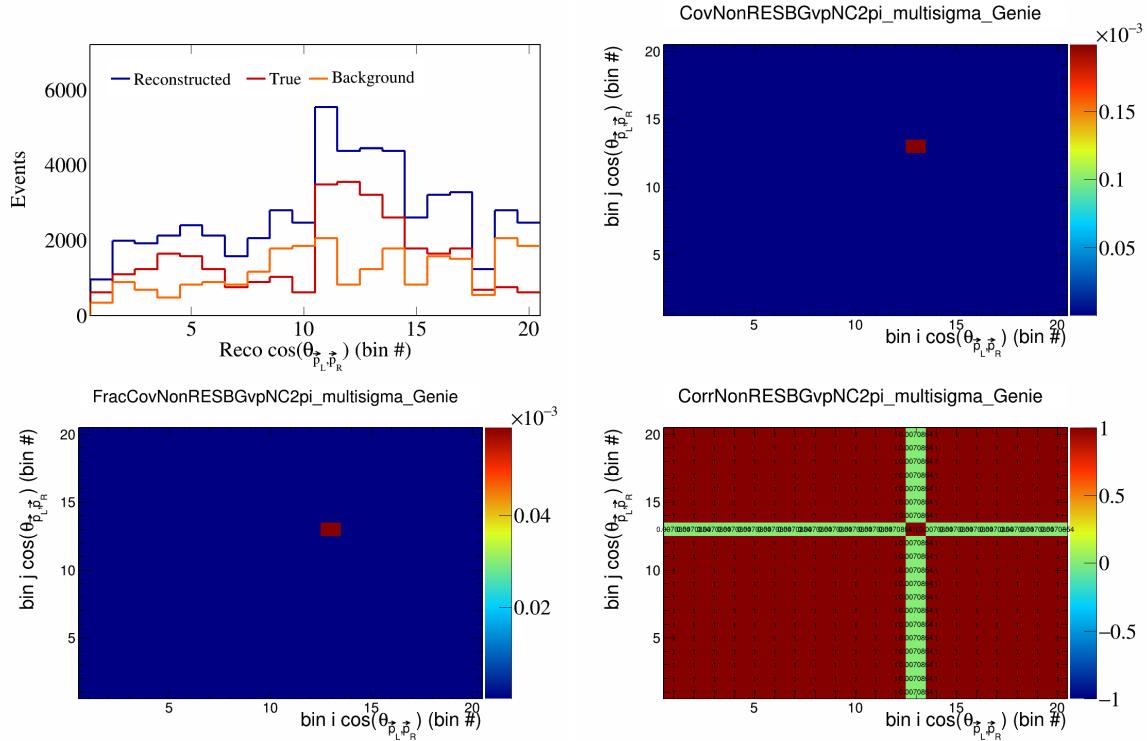


Figure 502: NonRESBGvpNC2pi variations for $\cos(\theta_{\vec{p}_L, \vec{p}_R})$ in $\cos(\theta_{\vec{p}_\mu})$.

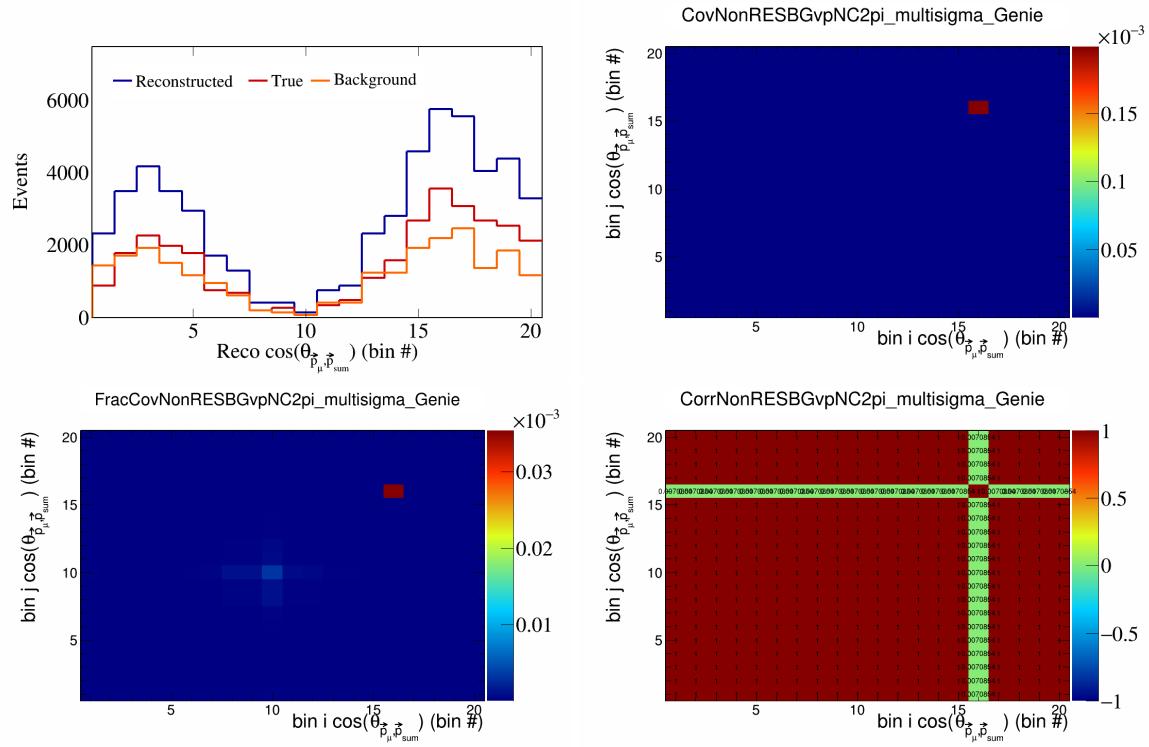


Figure 503: NonRESBGvpNC2pi variations for $\cos(\theta_{\vec{p}_\mu, \vec{p}_{\text{sum}}})$ in $\cos(\theta_{\vec{p}_\mu})$.

5.2 Flux systematics

In this appendix, the variations, covariance matrices, fractional covariance matrices, and correlation matrices are plotted for all of the flux systematics and variables.

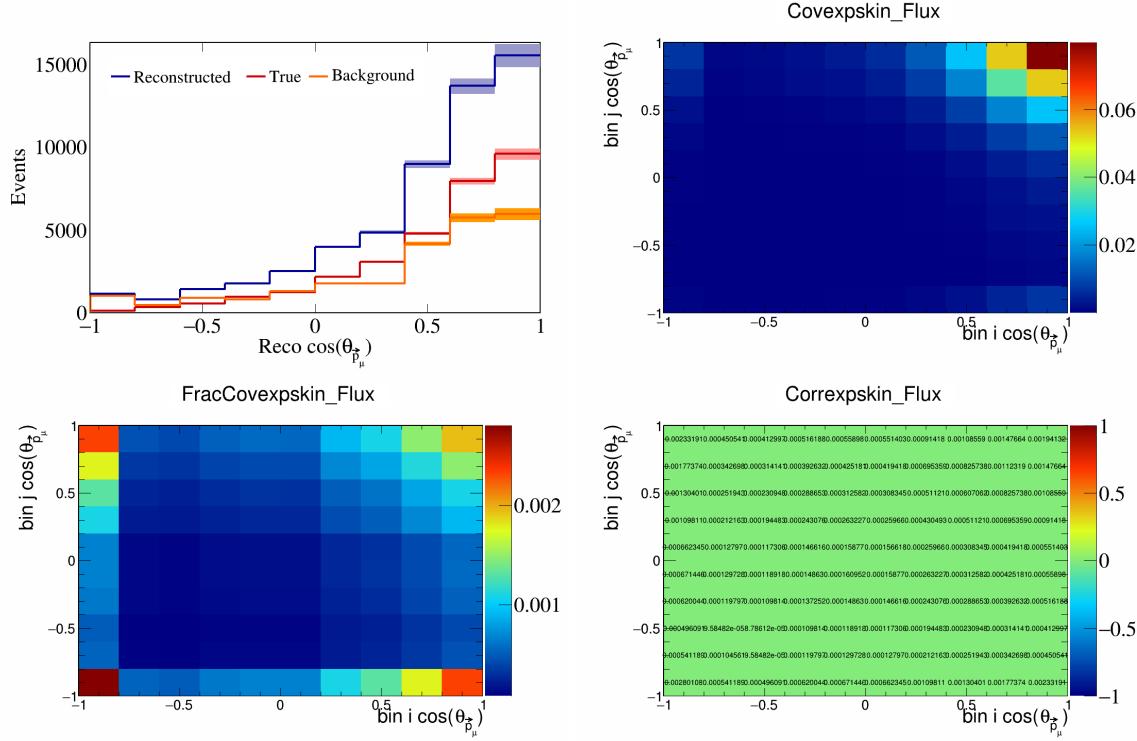


Figure 504: Epskin variations for $\cos(\theta_{\vec{p}_\mu})$.

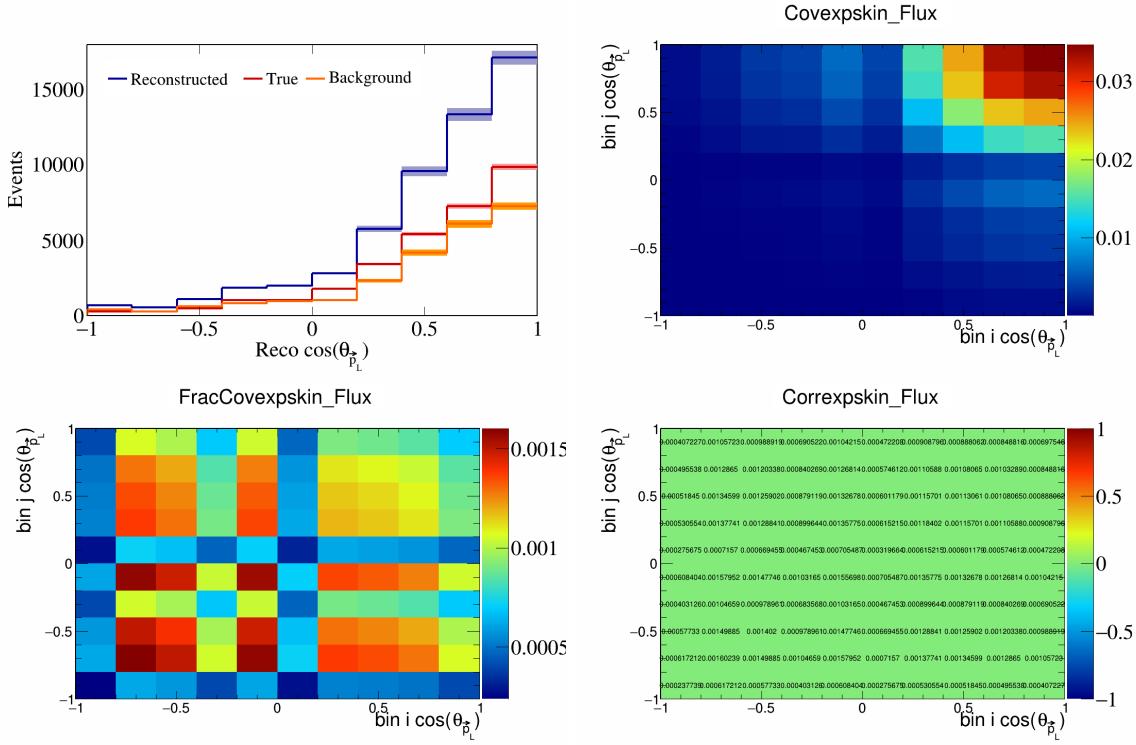


Figure 505: Expskin variations for $\cos(\theta_{\vec{p}_L})$.

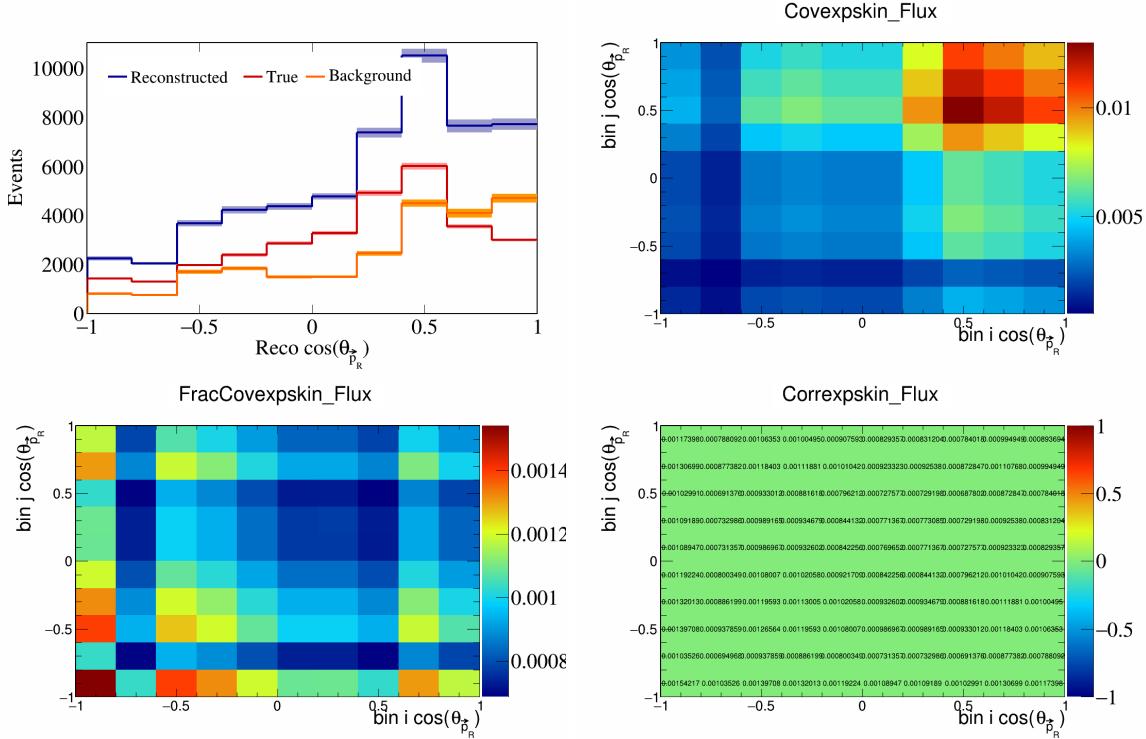


Figure 506: Expskin variations for $\cos(\theta_{\vec{p}_R})$.

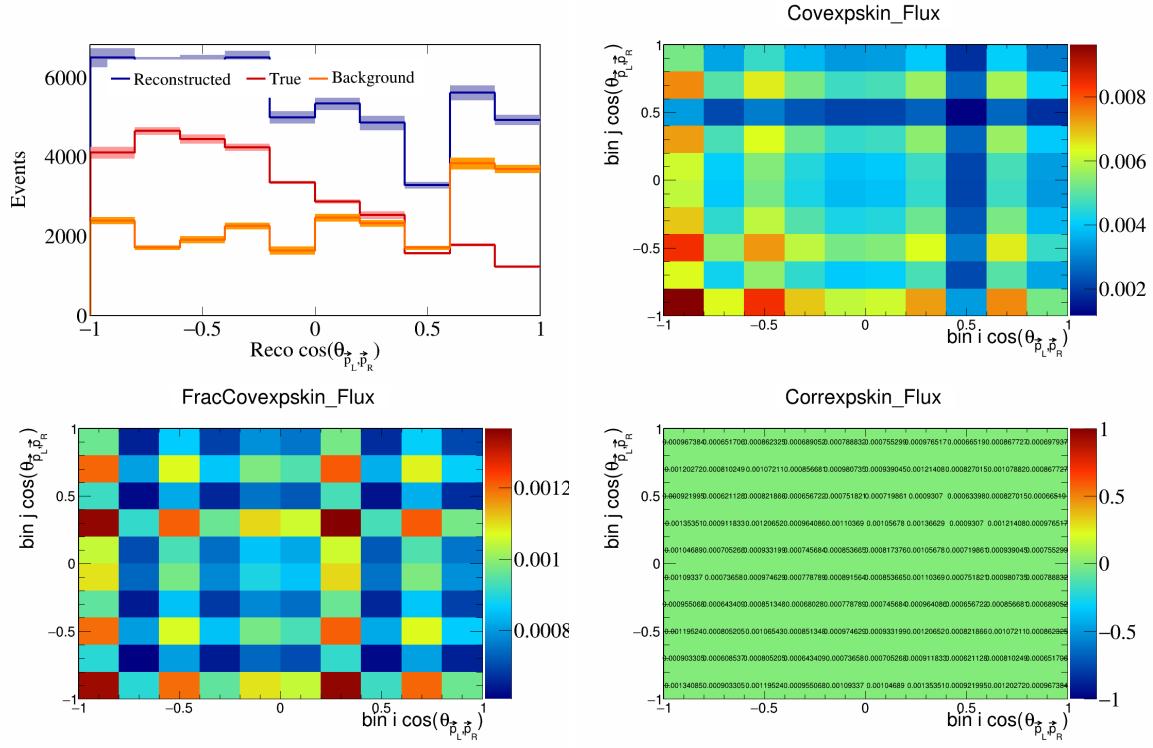


Figure 507: ExpSkin variations for $\cos(\theta_{\vec{p}_L, \vec{p}_R})$.

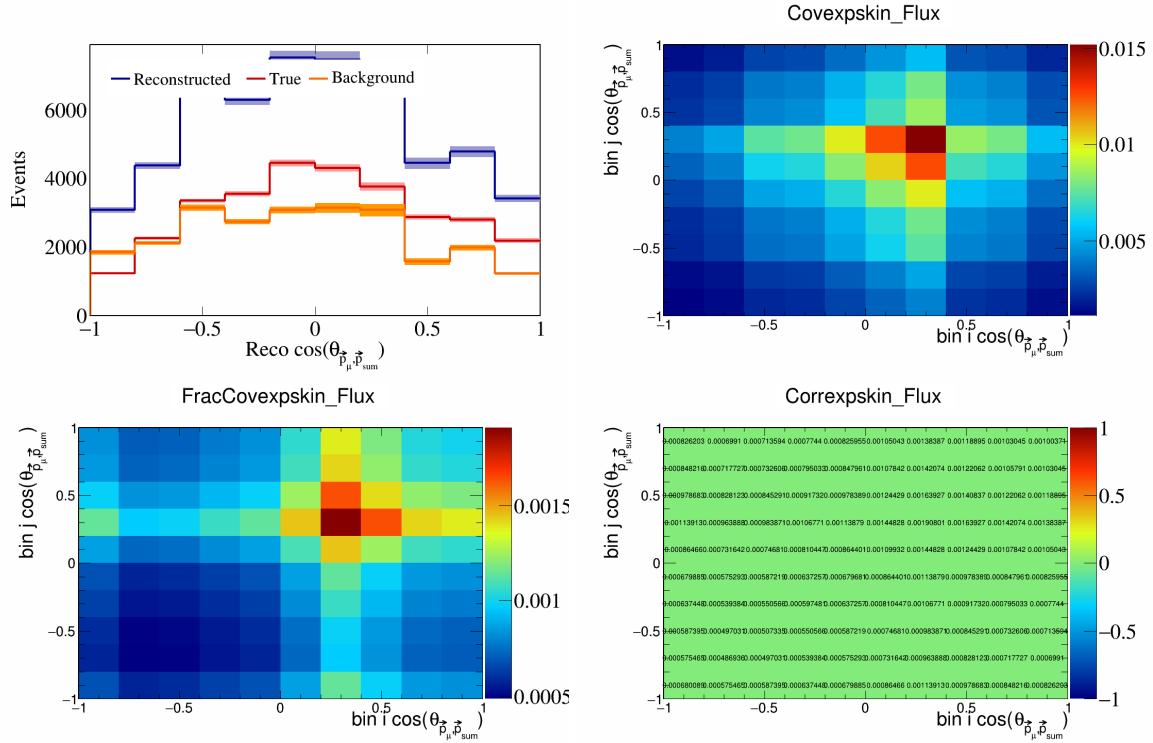


Figure 508: ExpSkin variations for $\cos(\theta_{\vec{p}_\mu, \vec{p}_{\text{sum}}})$.

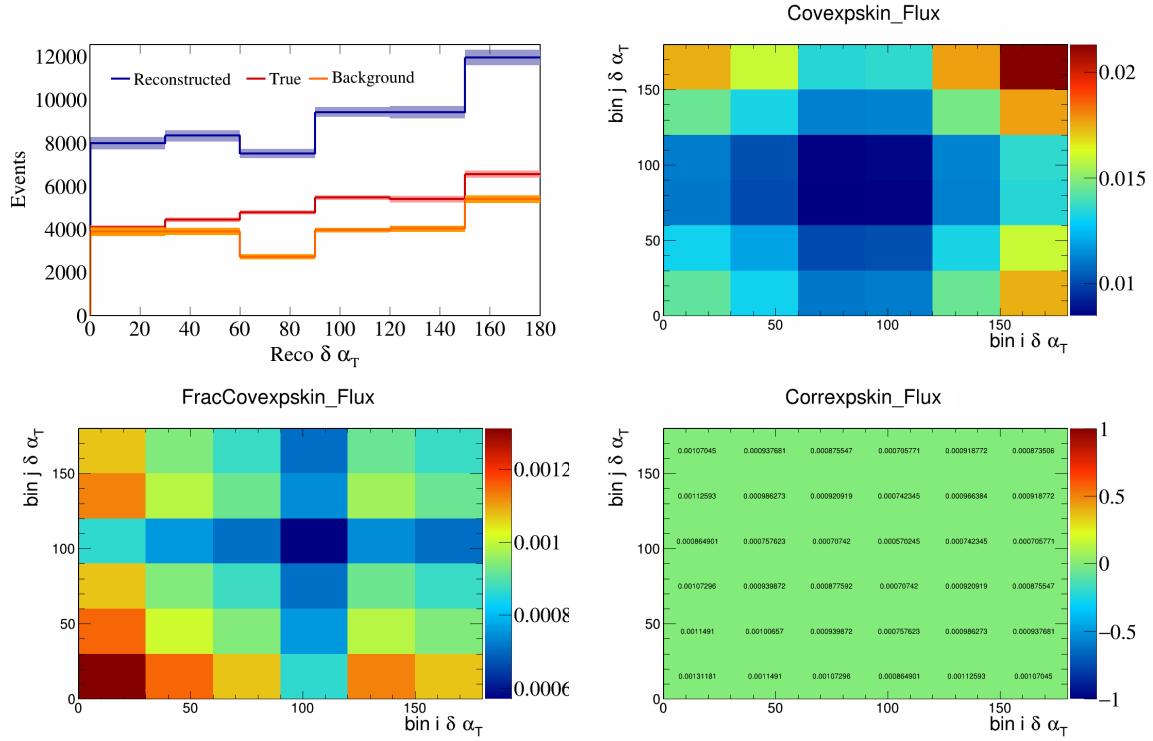


Figure 509: Expskin variations for $\delta \alpha_T$.

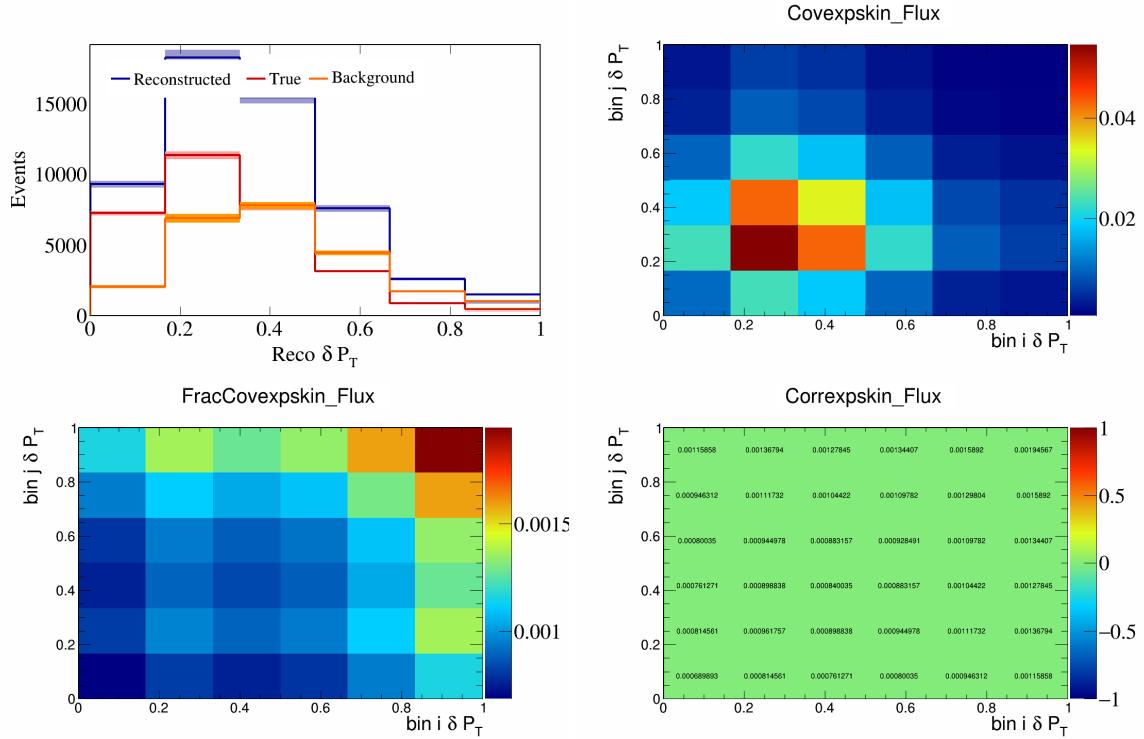


Figure 510: Expskin variations for δP_T .

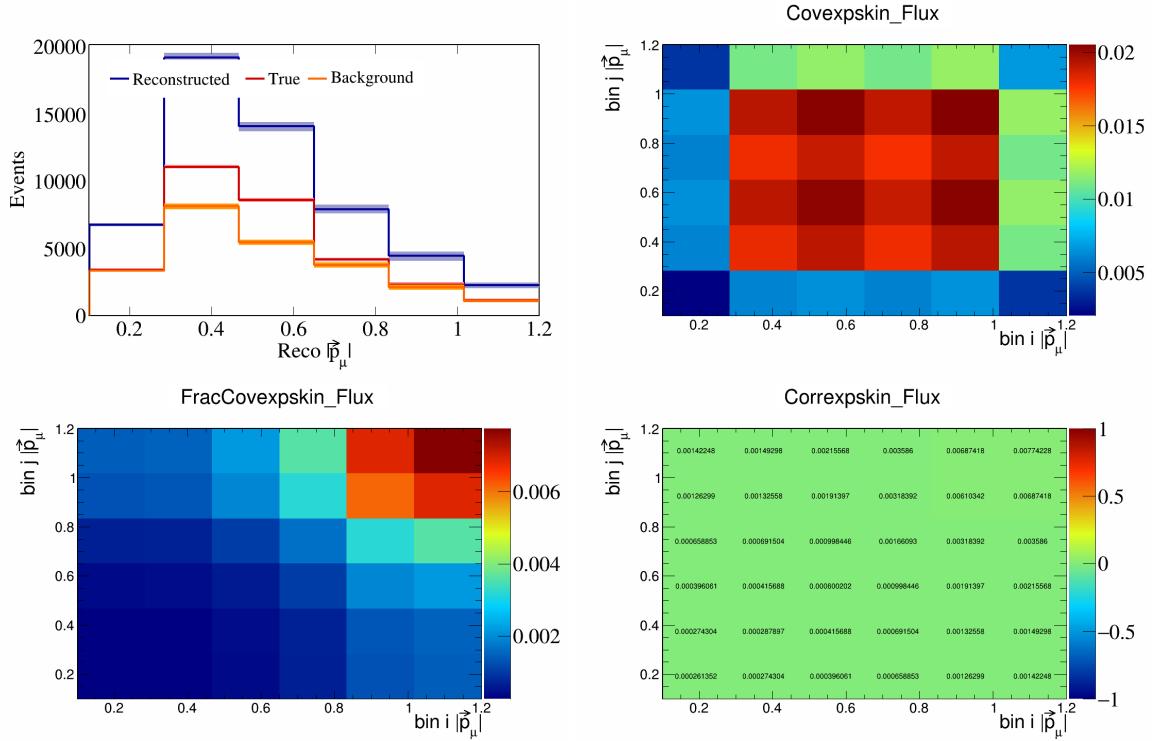


Figure 511: Expskin variations for $|\vec{p}_\mu|$.

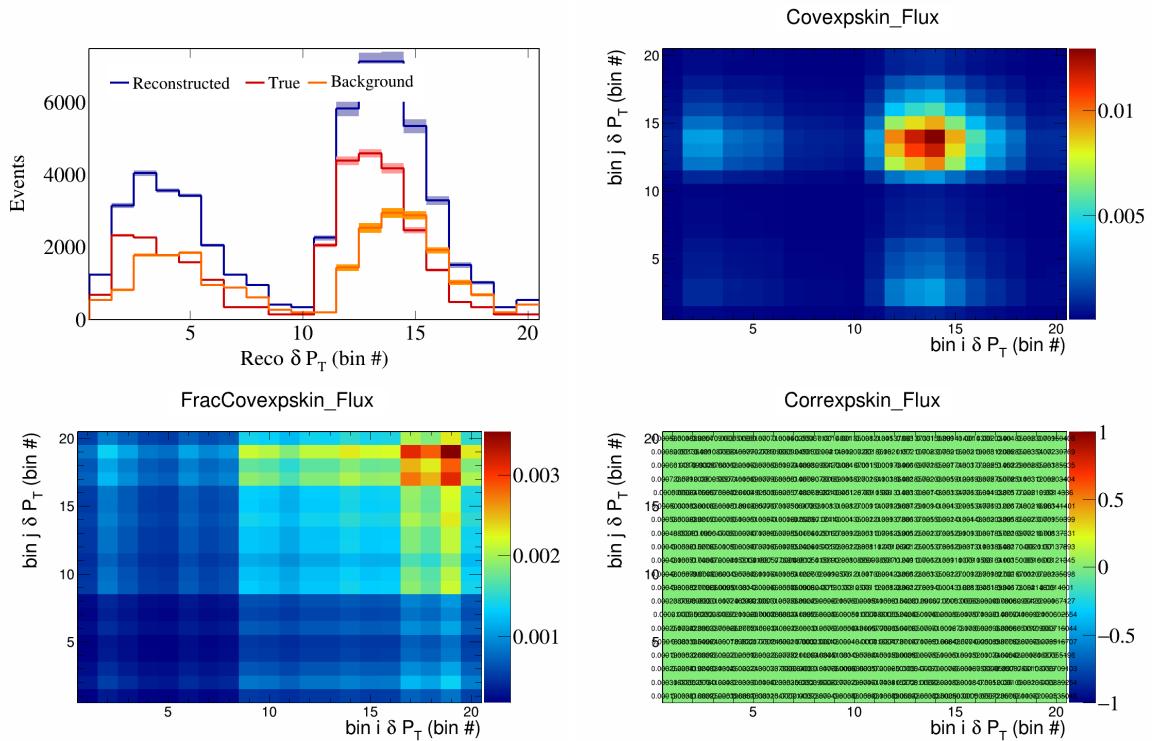


Figure 512: Expskin variations for δP_T in $\cos(\theta_{\vec{p}_\mu})$.

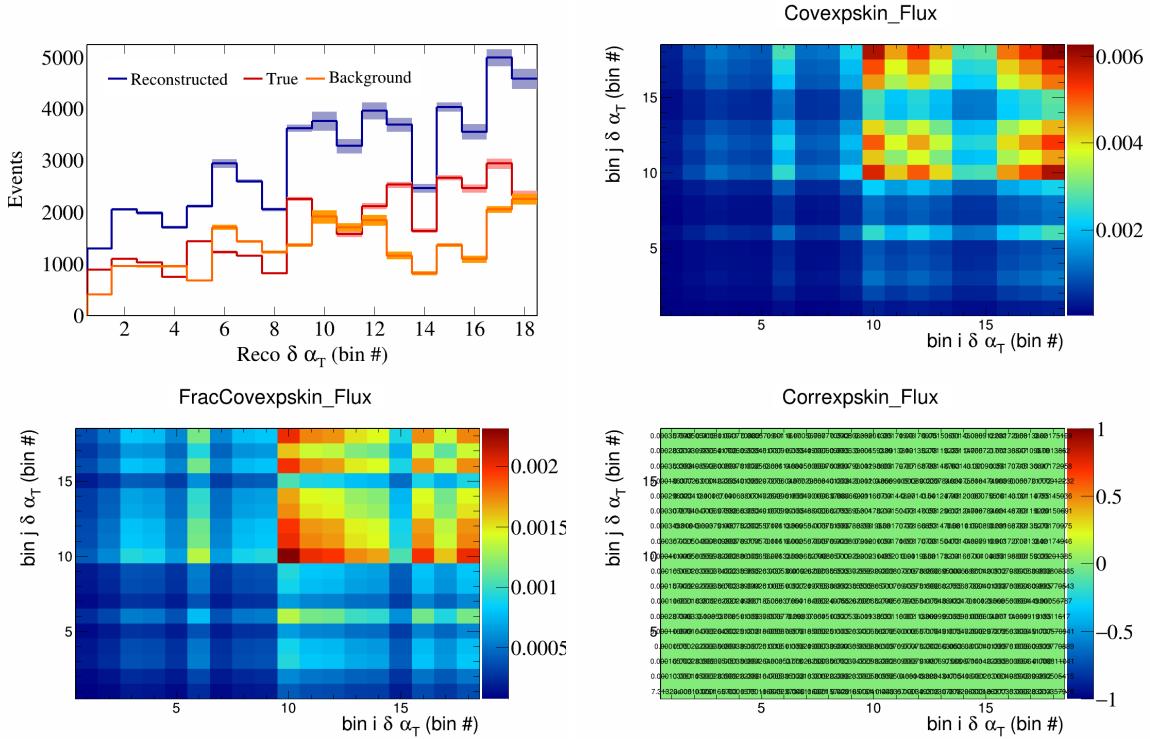


Figure 513: Expskin variations for $\delta \alpha_T$ in $\cos(\theta_{\vec{p}_\mu})$.

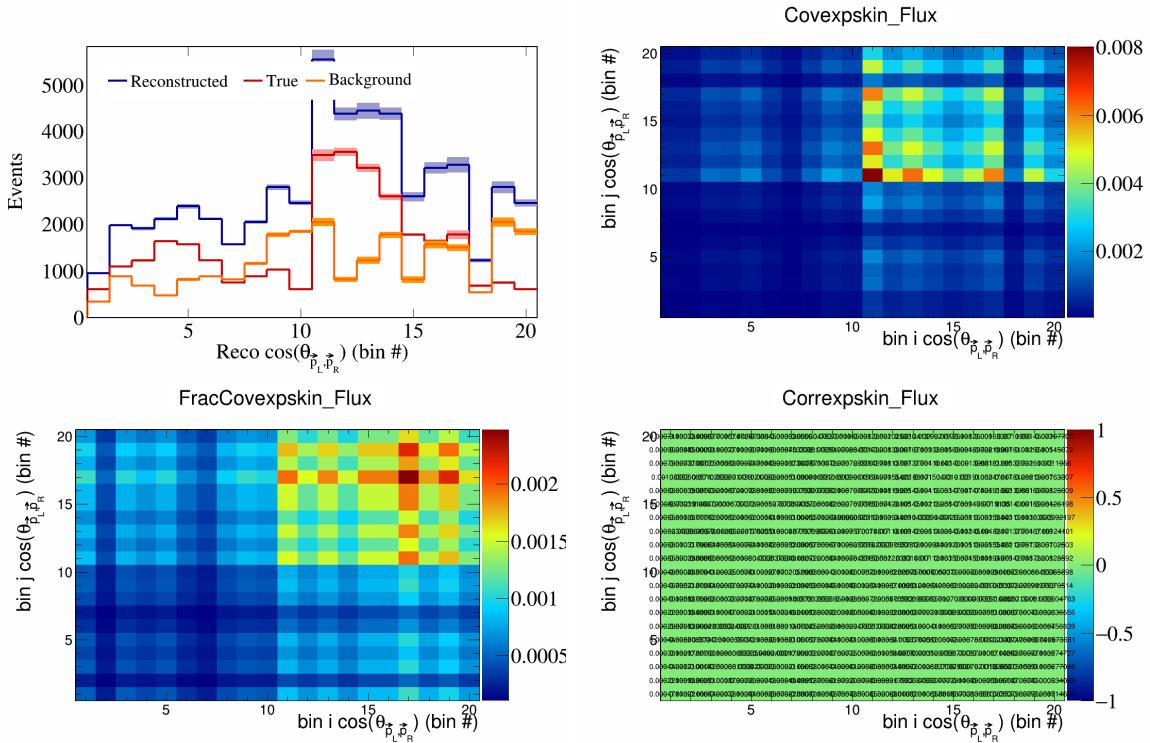


Figure 514: Expskin variations for $\cos(\theta_{\vec{p}_L, \vec{p}_R})$ in $\cos(\theta_{\vec{p}_\mu})$.

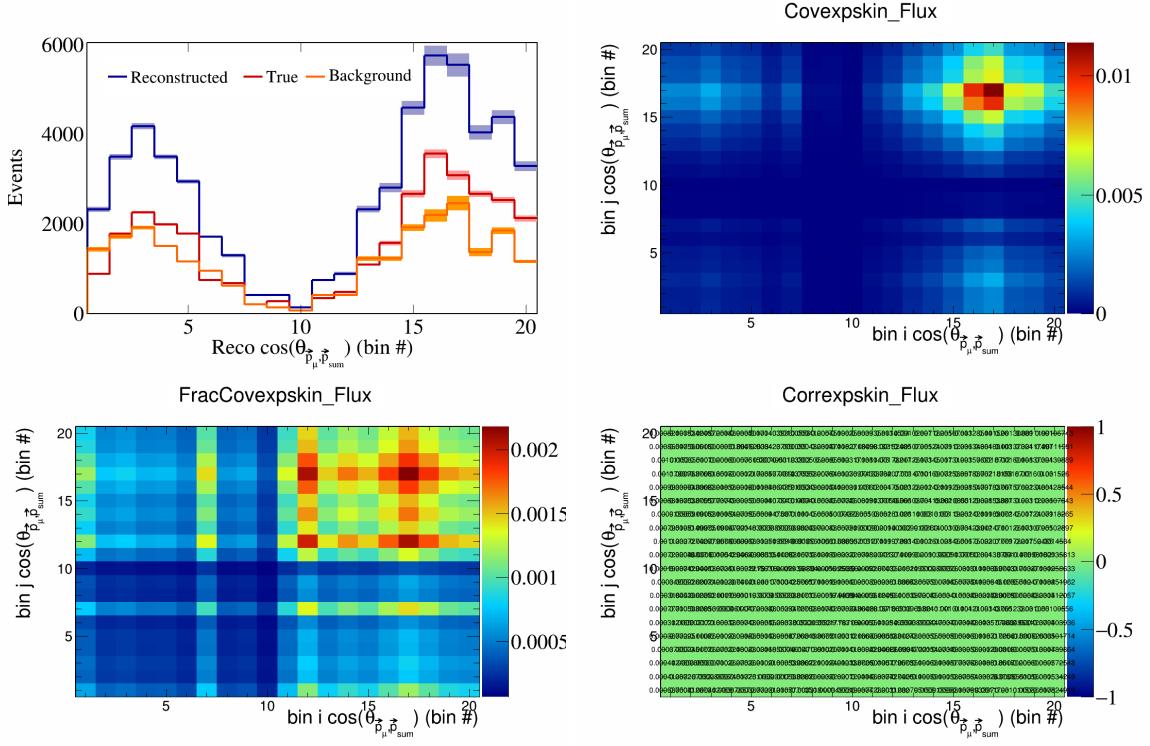


Figure 515: Expskin variations for $\cos(\theta_{\vec{p}_\mu})$ in $\cos(\theta_{\vec{p}_\mu})$.

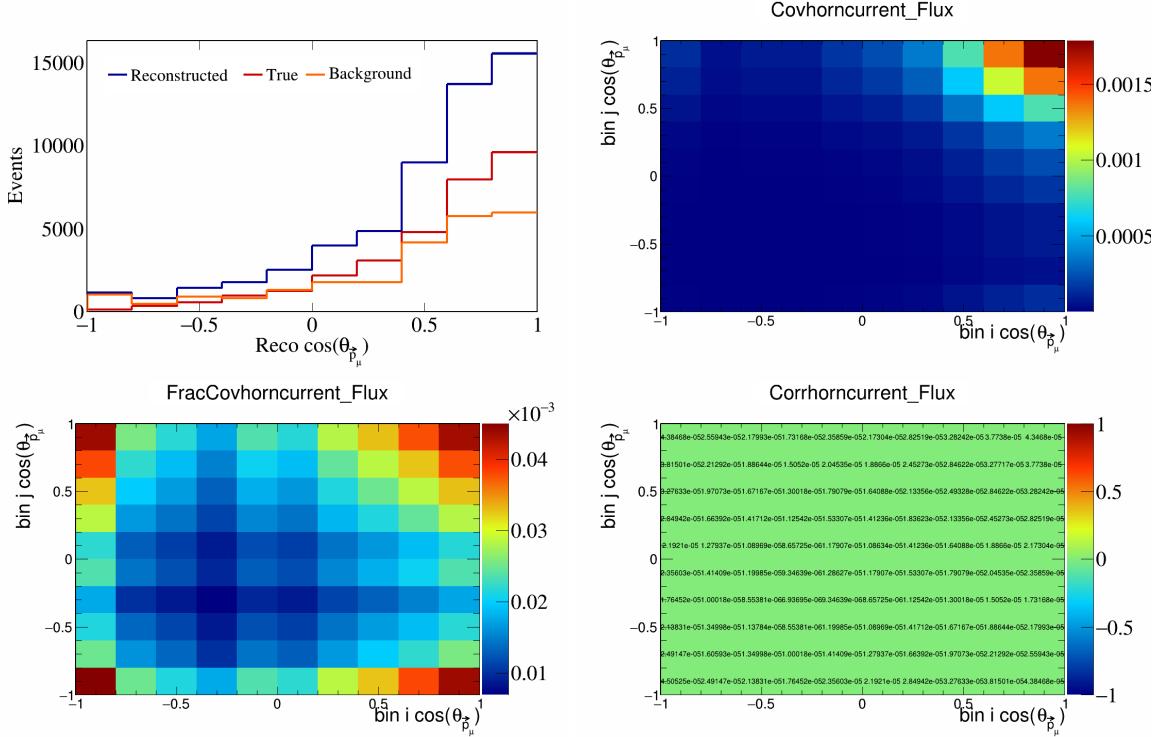


Figure 516: HornCurrent variations for $\cos(\theta_{\vec{p}_\mu})$.

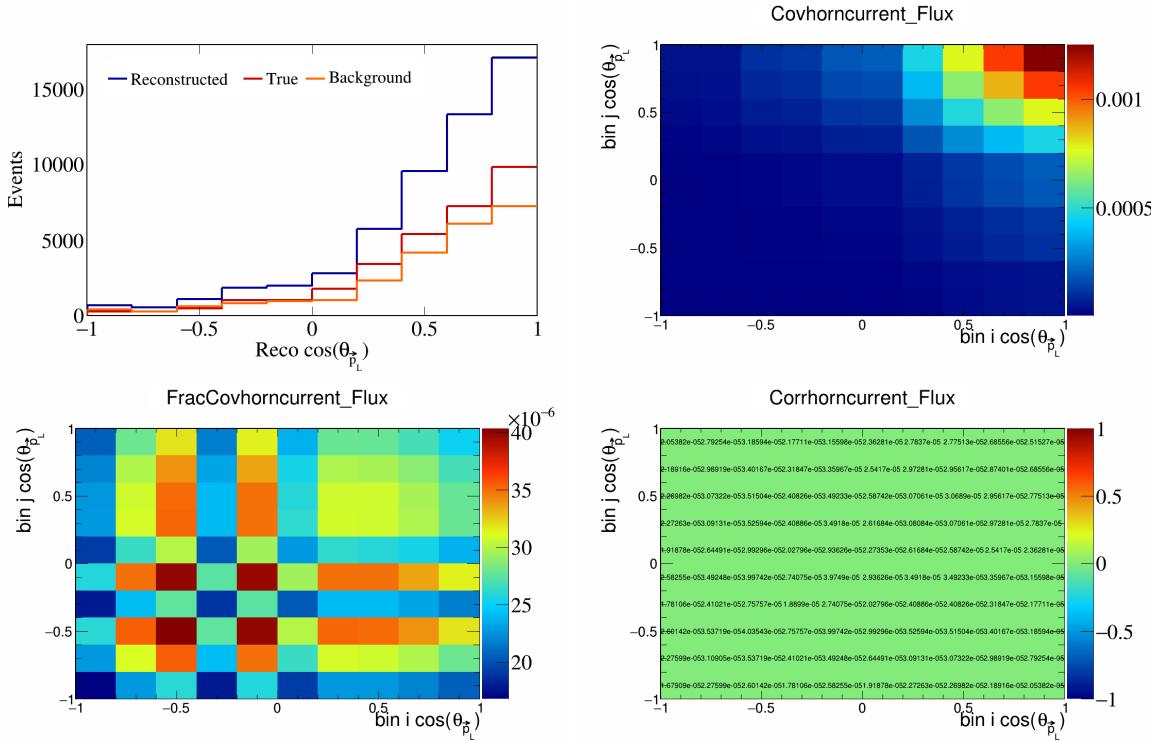


Figure 517: HornCurrent variations for $\cos(\theta_{\vec{p}_L})$.

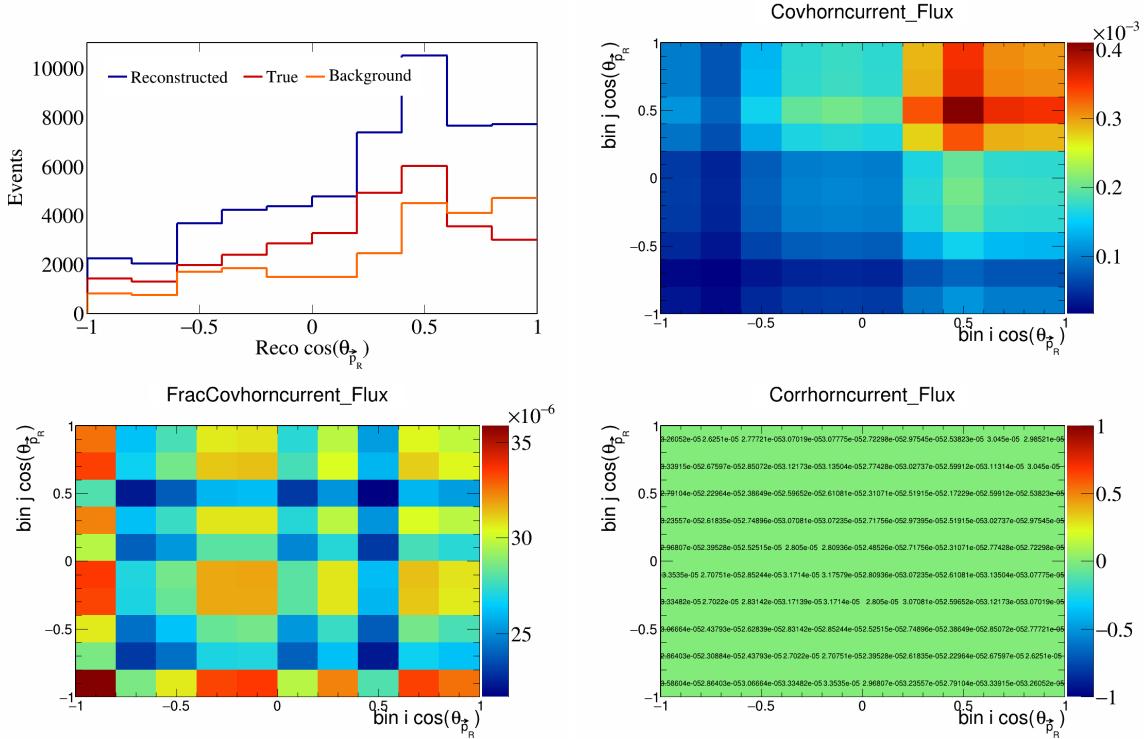


Figure 518: HornCurrent variations for $\cos(\theta_{\vec{p}_R})$.

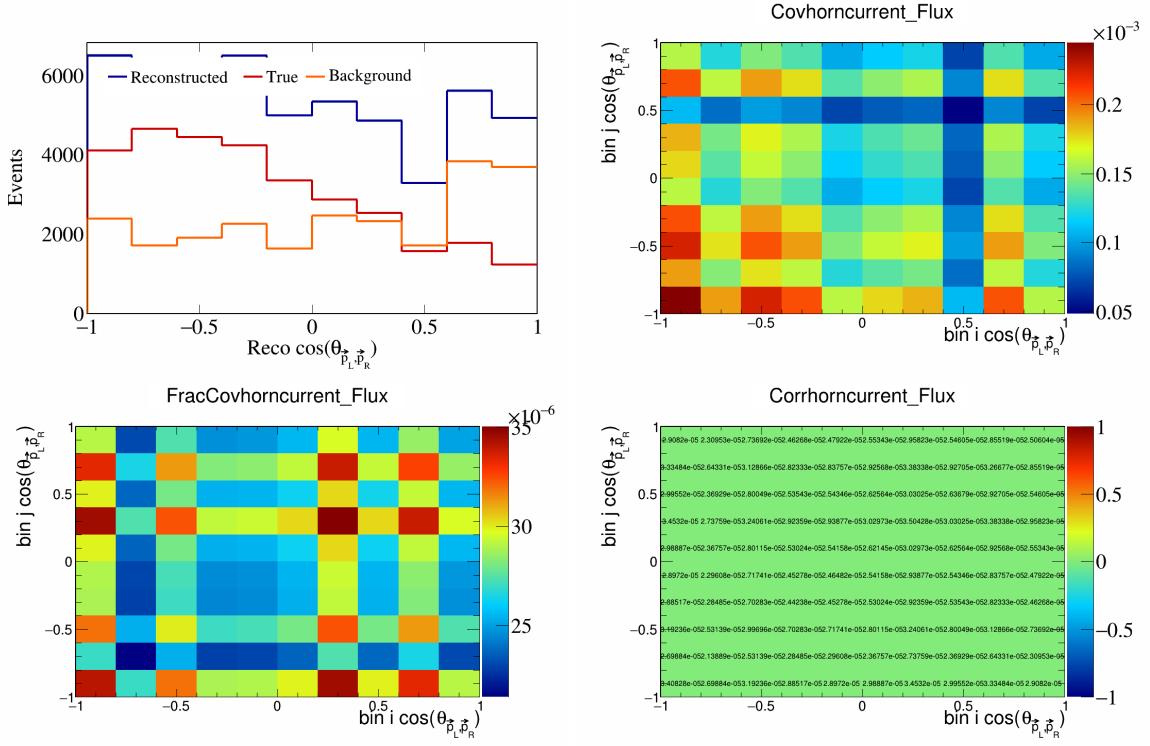


Figure 519: HornCurrent variations for $\cos(\theta_{\vec{p}_L, \vec{p}_R})$.

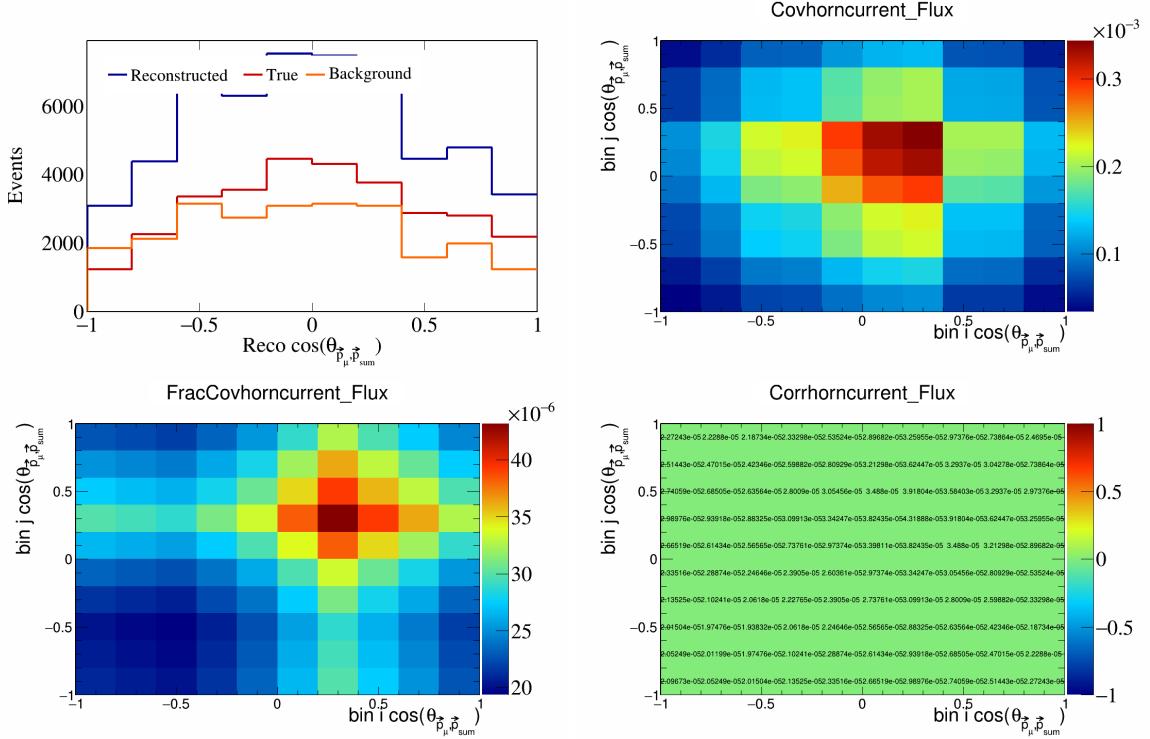


Figure 520: HornCurrent variations for $\cos(\theta_{\vec{p}_\mu, \vec{p}_{\text{sum}}})$.

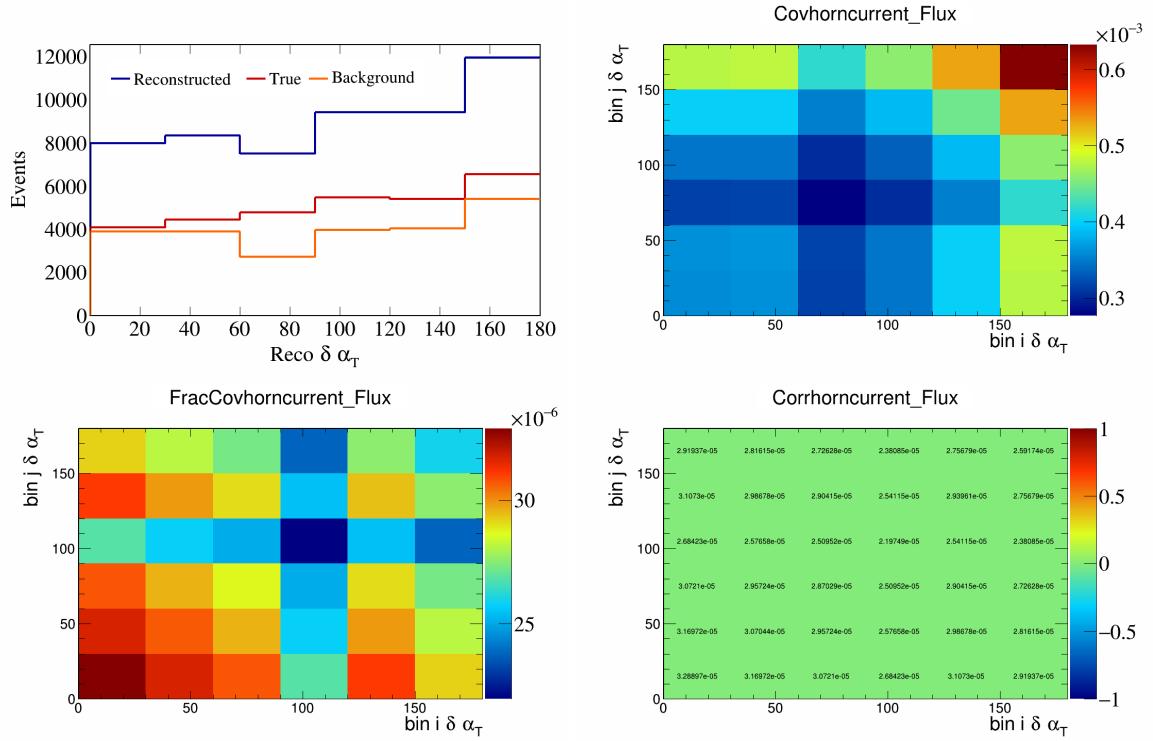


Figure 521: HornCurrent variations for $\delta\alpha_T$.

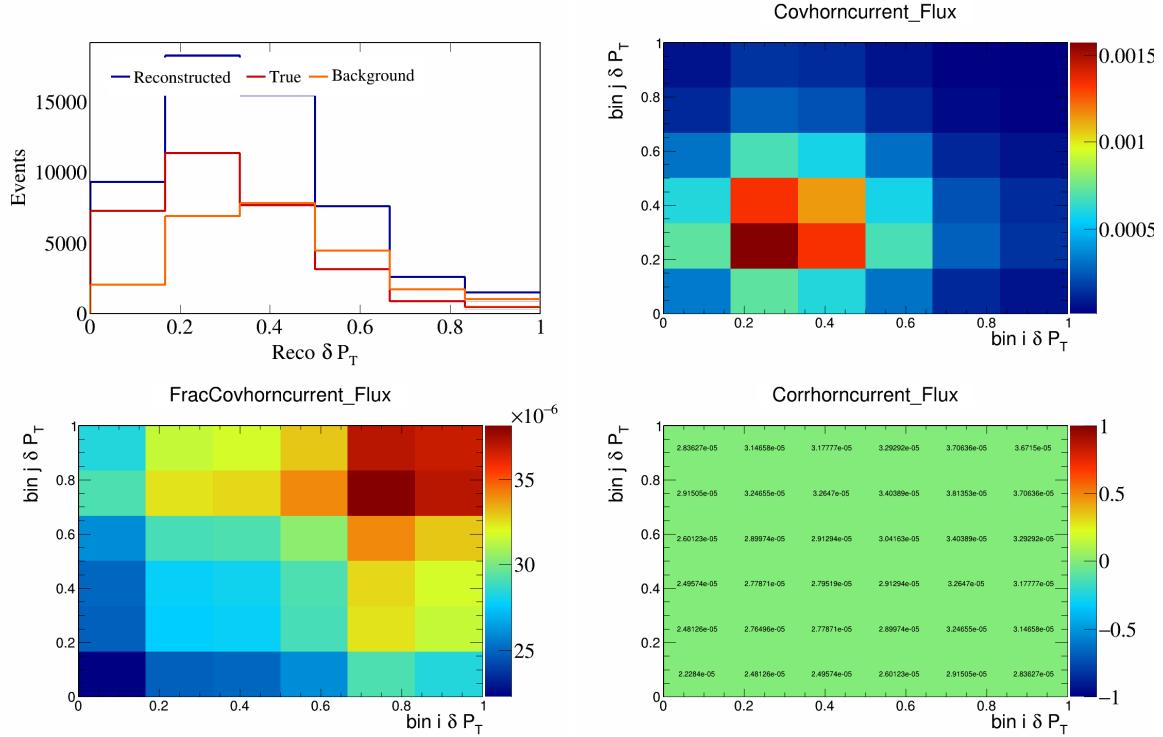


Figure 522: HornCurrent variations for δP_T .

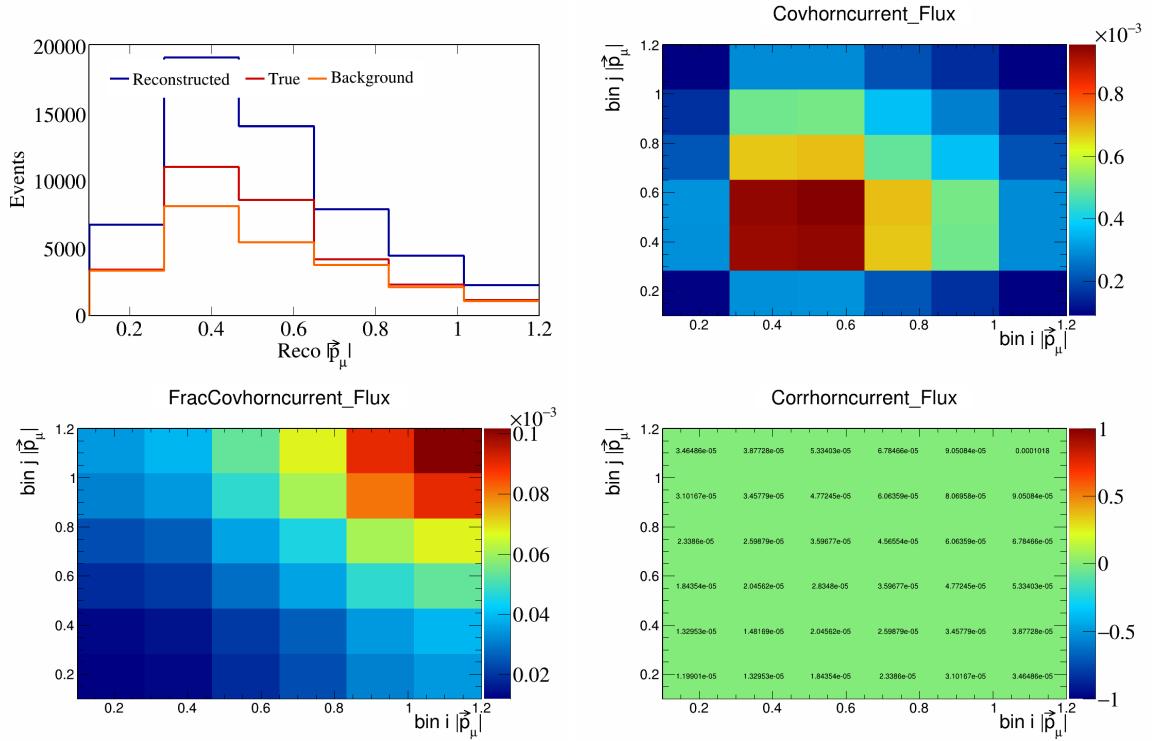


Figure 523: HornCurrent variations for $|\vec{p}_\mu|$.

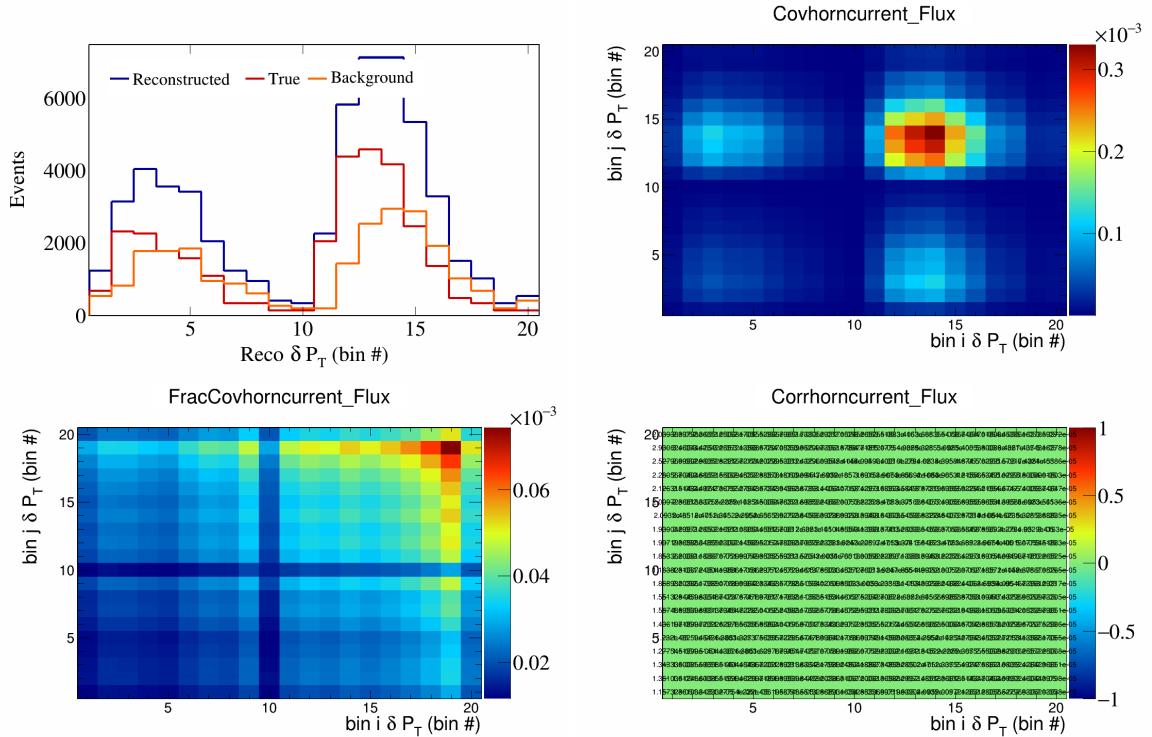


Figure 524: HornCurrent variations for δP_T in $\cos(\theta_{\vec{p}_\mu})$.

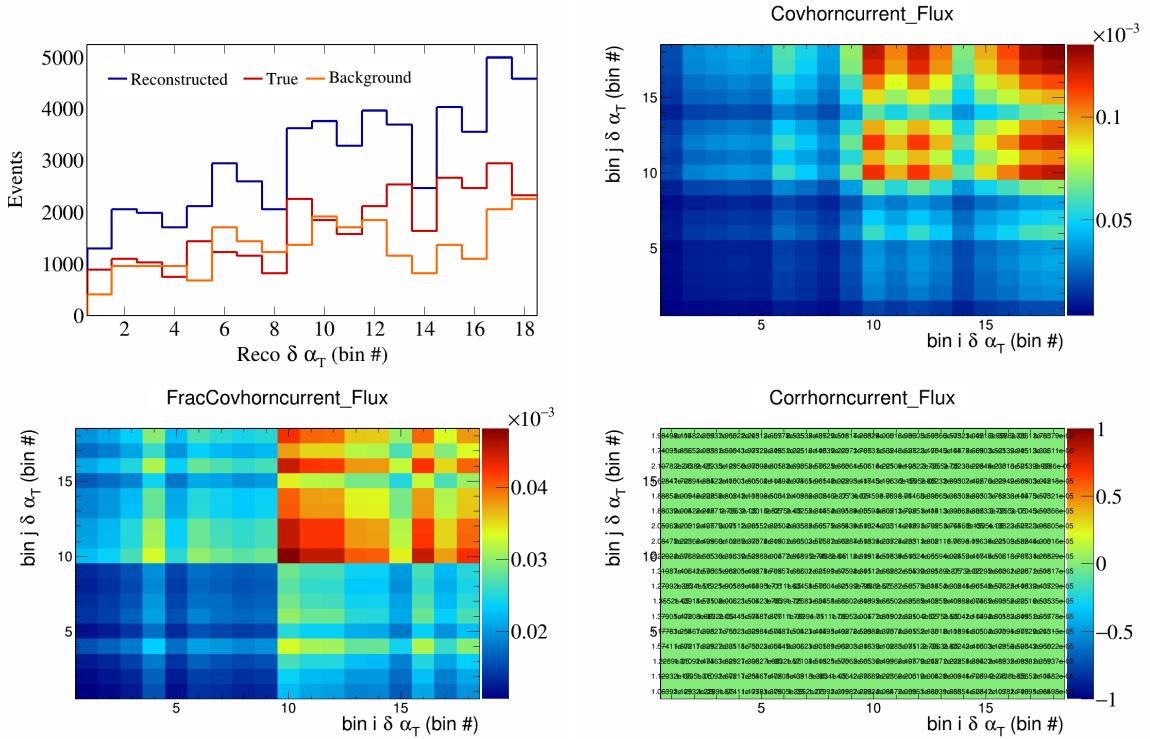


Figure 525: HornCurrent variations for $\delta\alpha_T$ in $\cos(\theta_{\vec{p}_\mu})$.

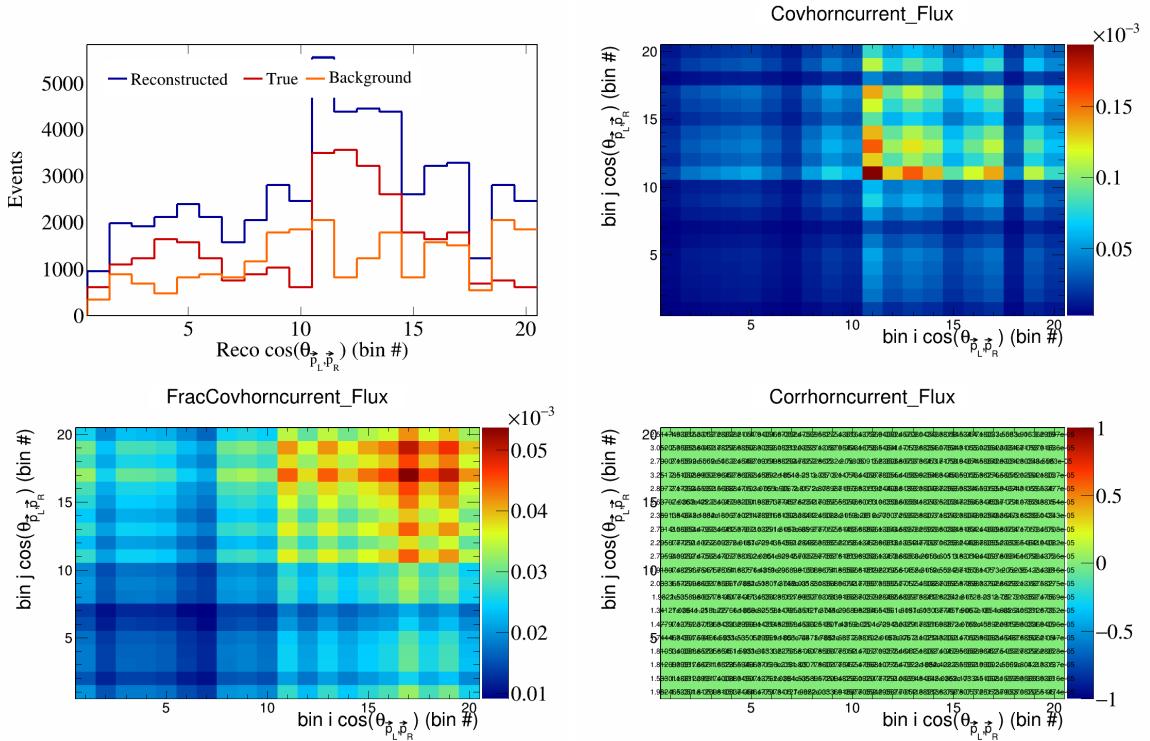


Figure 526: HornCurrent variations for $\cos(\theta_{\vec{p}_L, \vec{p}_R})$ in $\cos(\theta_{\vec{p}_\mu})$.

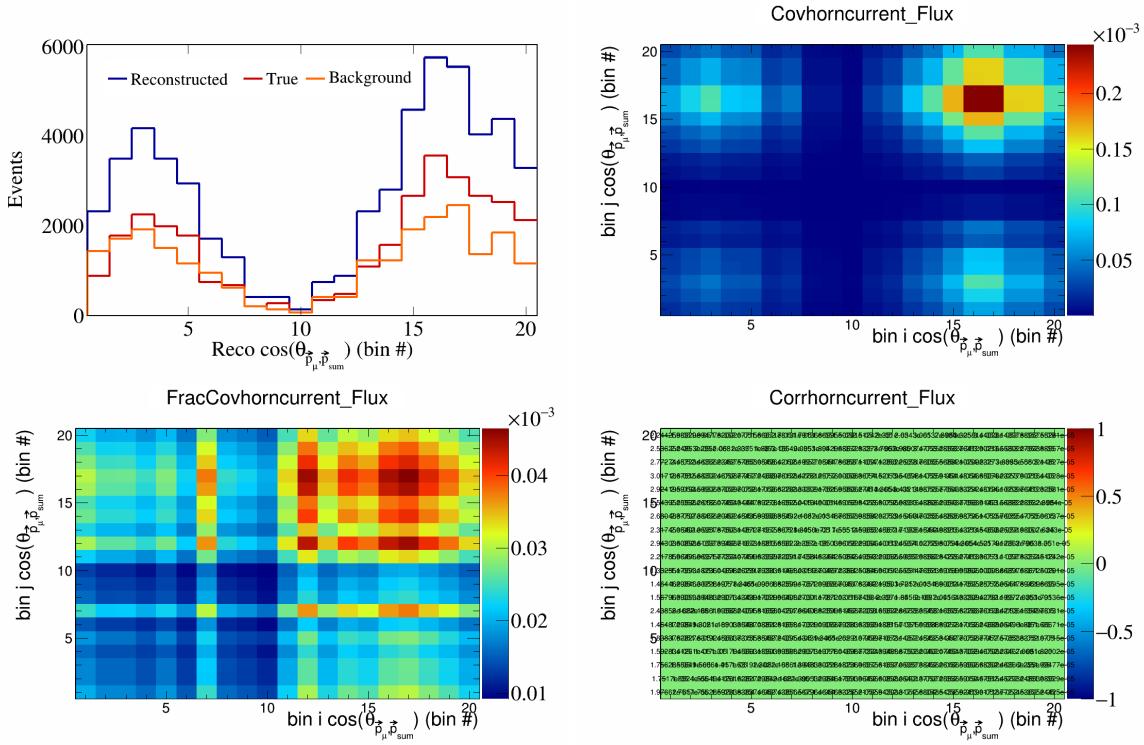


Figure 527: HornCurrent variations for $\cos(\theta_{\vec{p}_\mu \vec{p}_{\text{sum}}})$ in $\cos(\theta_{\vec{p}_\mu})$.

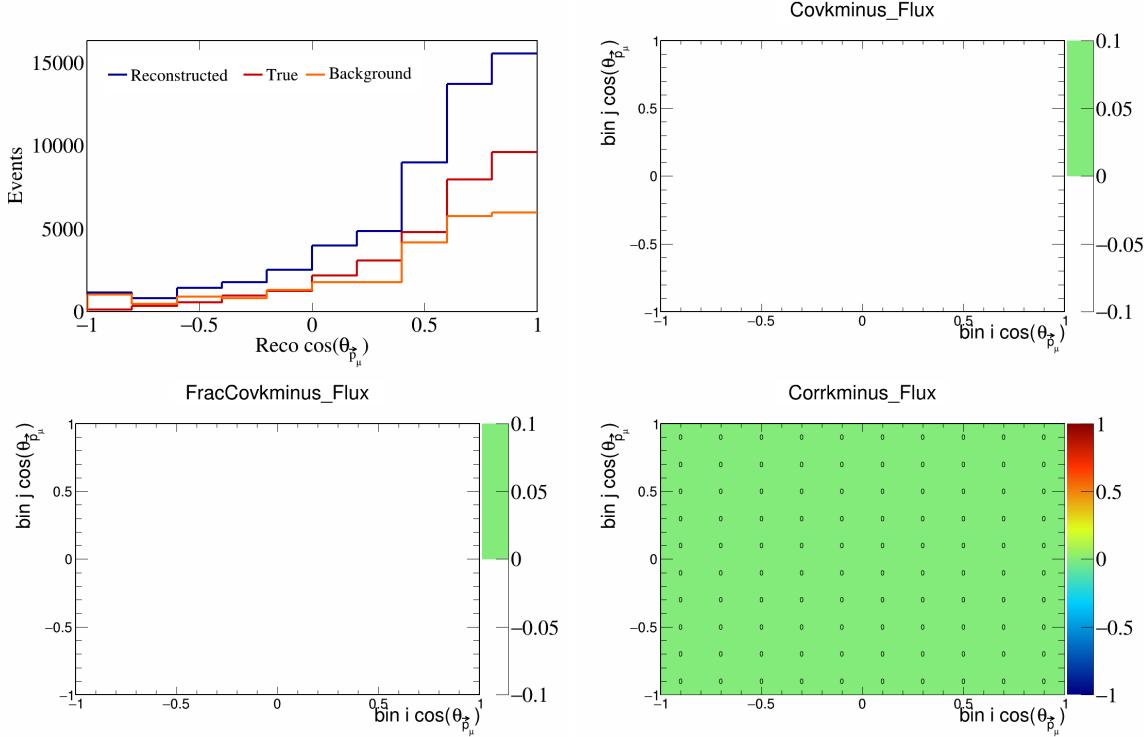


Figure 528: KMinus variations for $\cos(\theta_{\vec{p}_\mu})$.

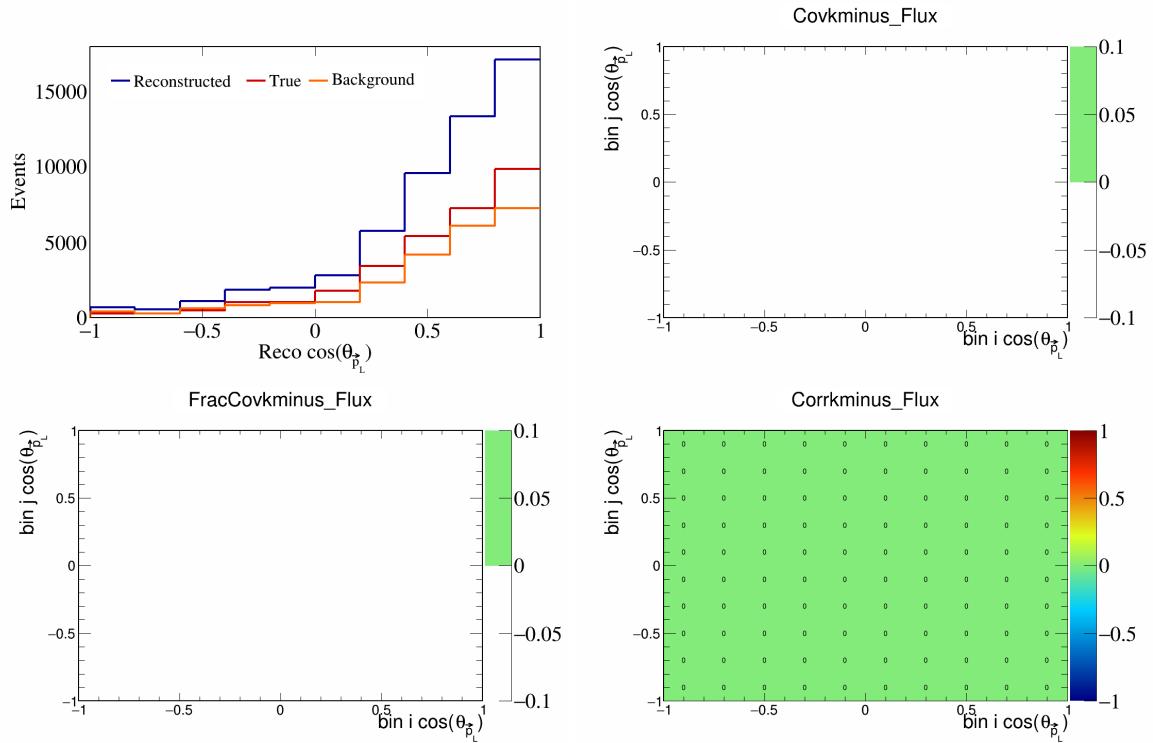


Figure 529: KMinus variations for $\cos(\theta_{\vec{p}_L})$.

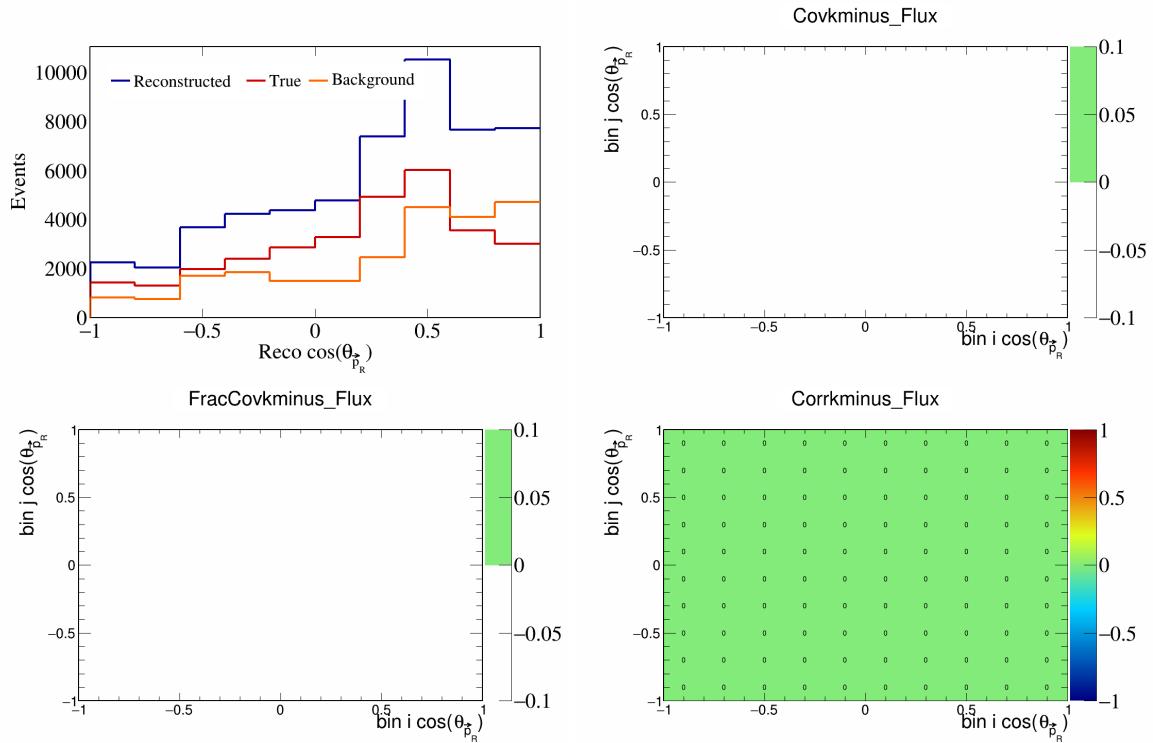


Figure 530: KMinus variations for $\cos(\theta_{\vec{p}_R})$.

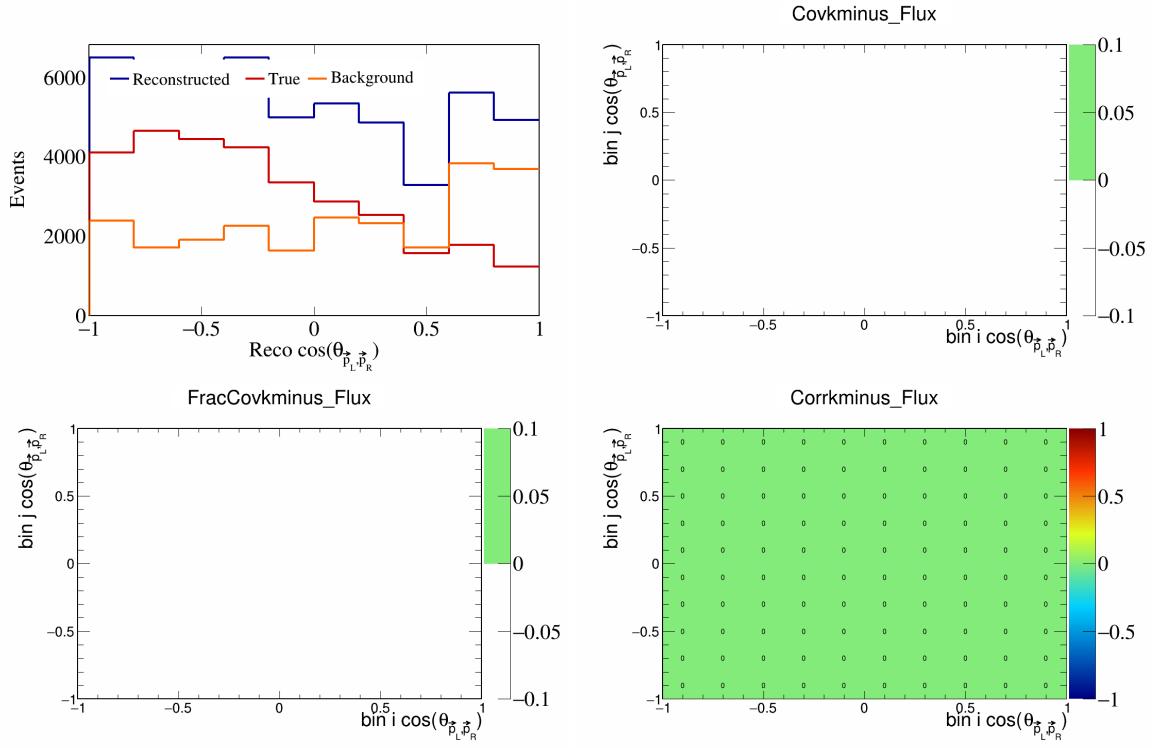


Figure 531: KMinus variations for $\cos(\theta_{\vec{p}_L, \vec{p}_R})$.

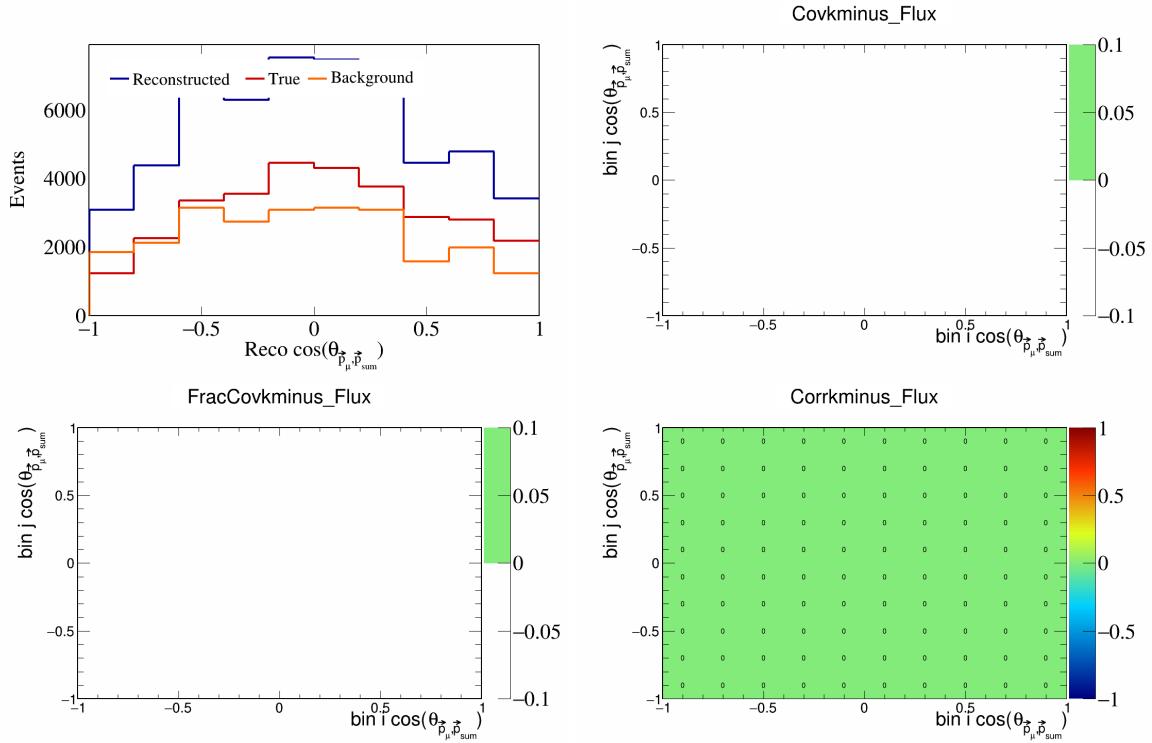


Figure 532: KMinus variations for $\cos(\theta_{\vec{p}_\mu, \vec{p}_{\text{sum}}})$.

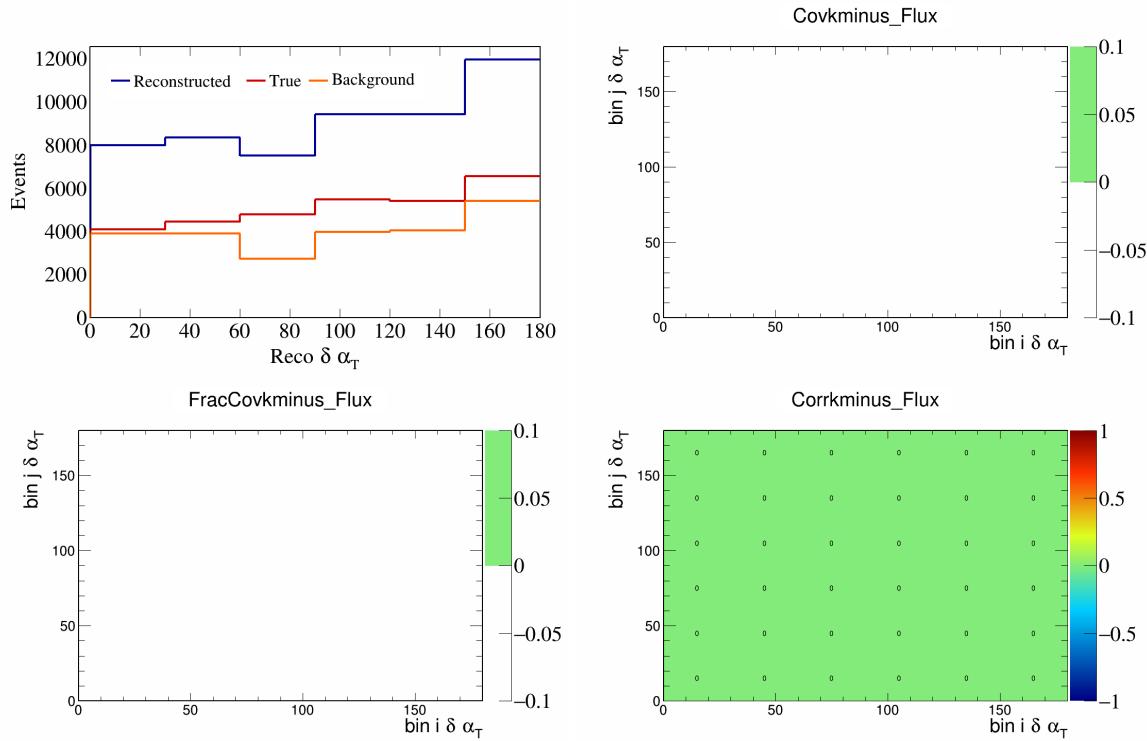


Figure 533: KMinus variations for $\delta\alpha_T$.

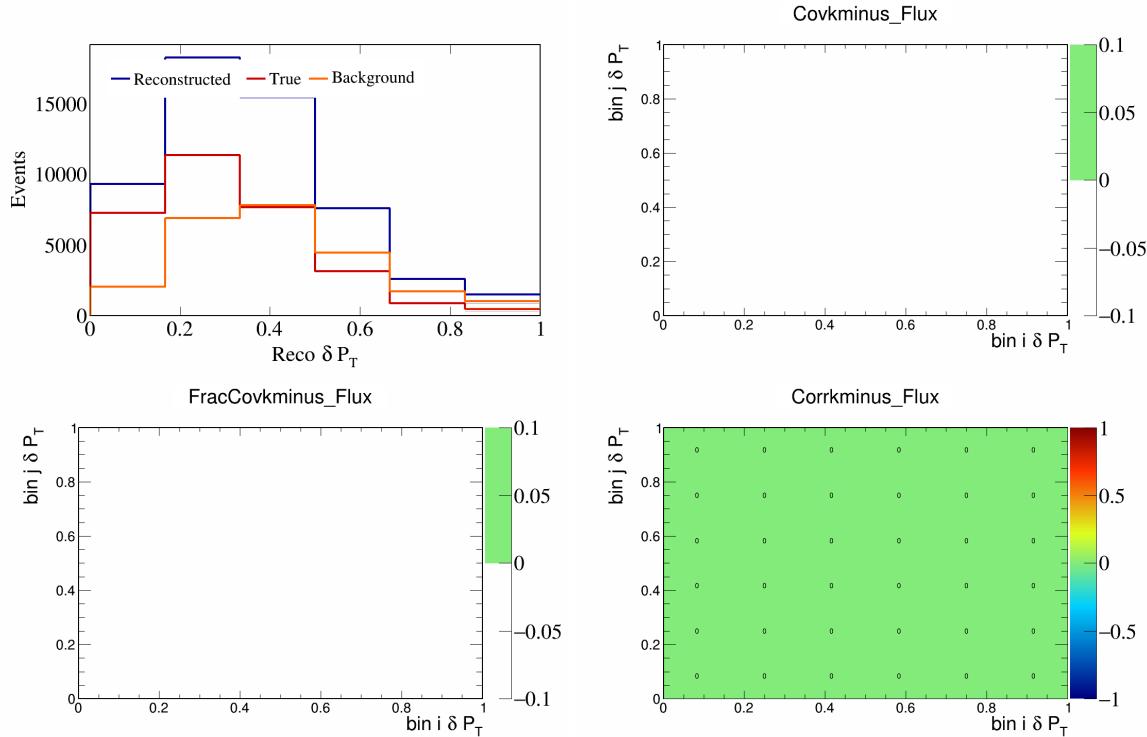


Figure 534: KMinus variations for δP_T .

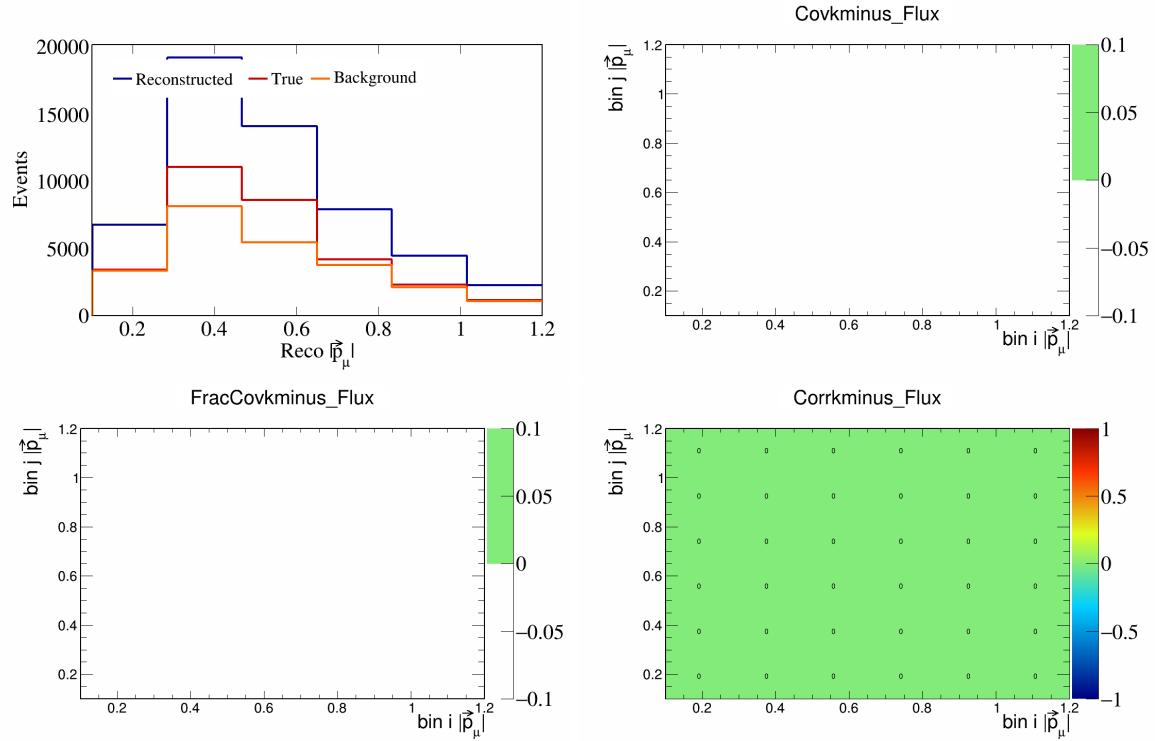


Figure 535: KMinus variations for $|\vec{p}_\mu|$.

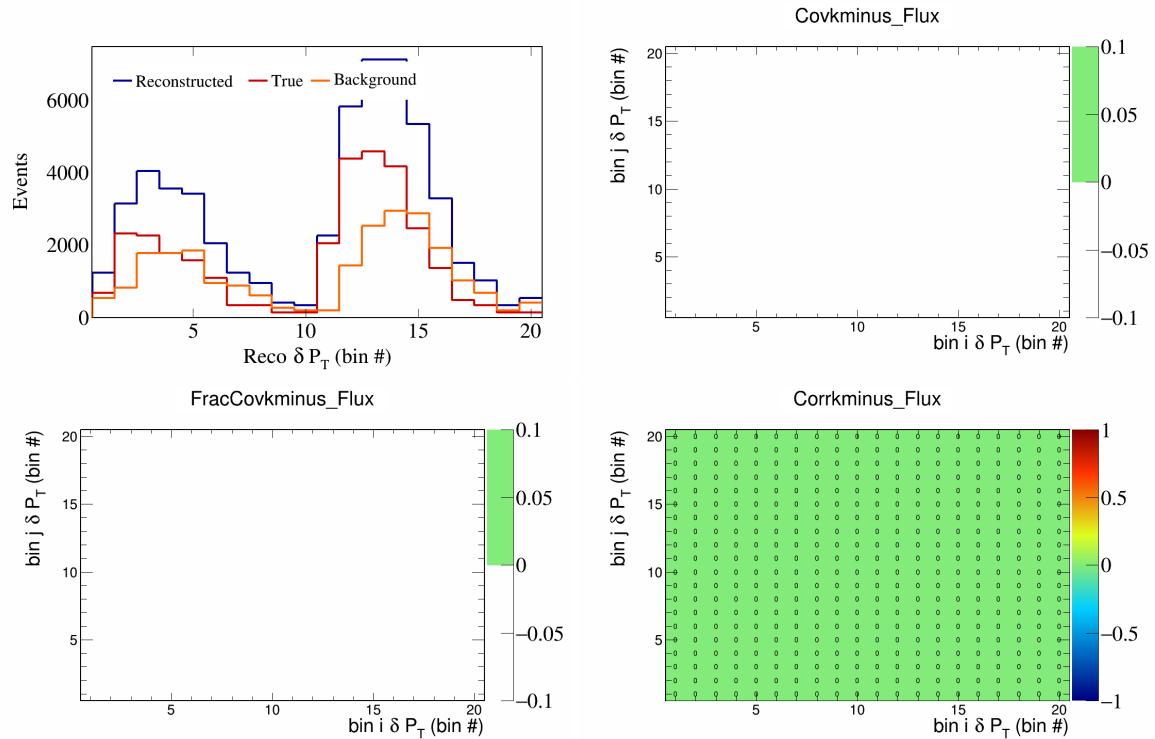


Figure 536: KMinus variations for δP_T in $\cos(\theta_{\vec{p}_\mu})$.

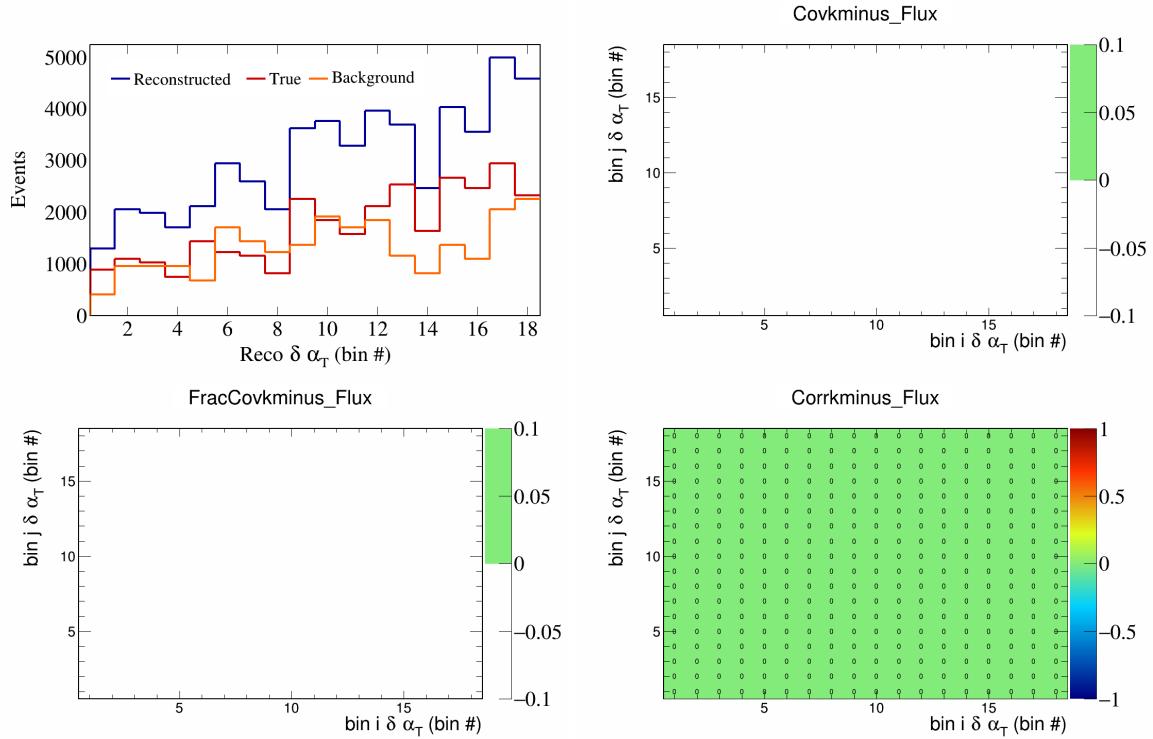


Figure 537: KMinus variations for $\delta\alpha_T$ in $\cos(\theta_{\vec{p}_\mu})$.

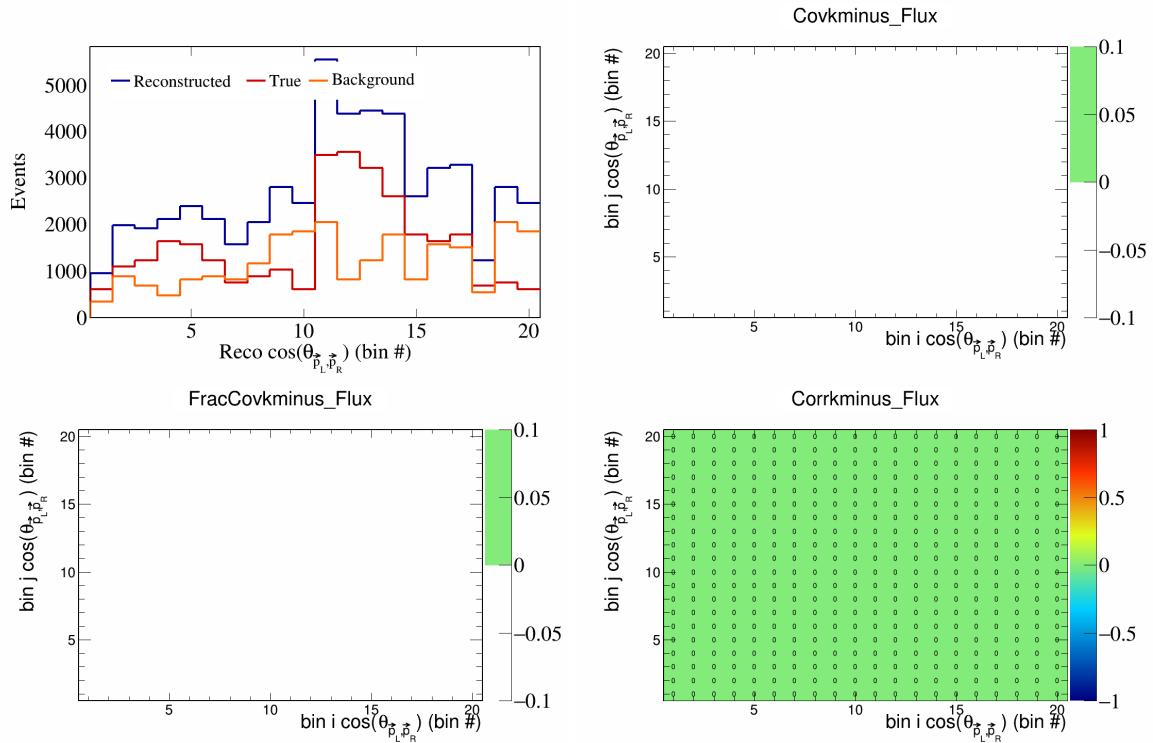


Figure 538: KMinus variations for $\cos(\theta_{\vec{p}_L, \vec{p}_R})$ in $\cos(\theta_{\vec{p}_\mu})$.

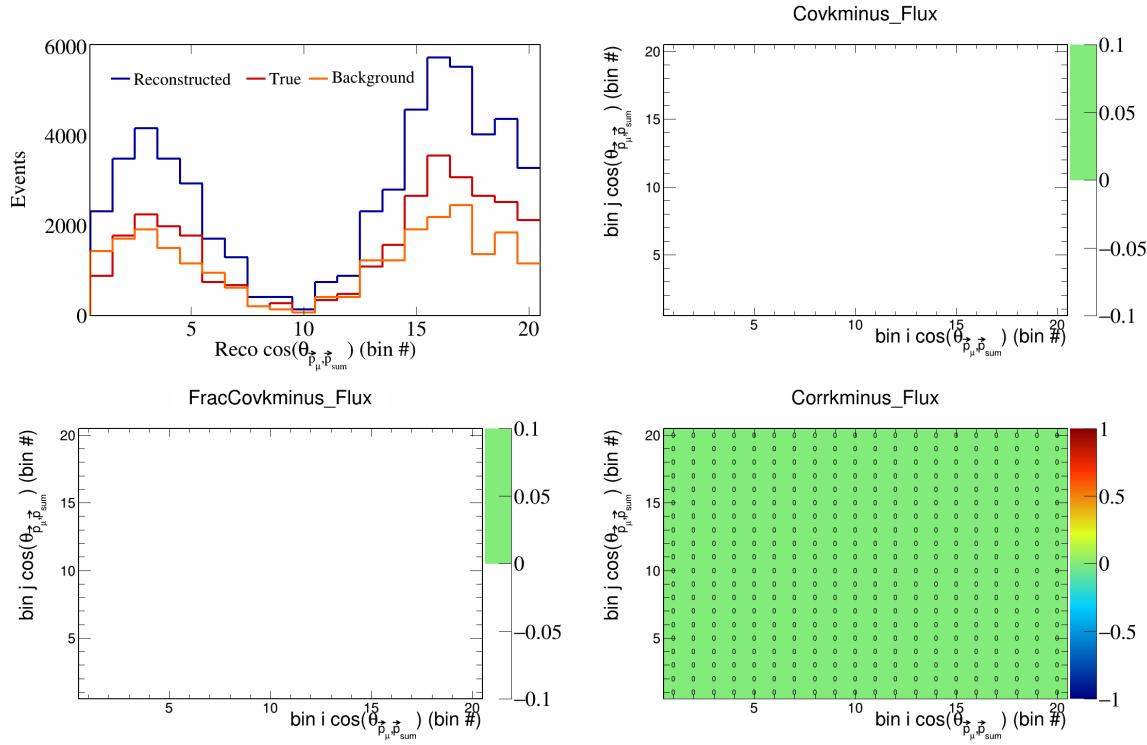


Figure 539: KMinus variations for $\cos(\theta_{\vec{p}_\mu} \vec{p}_{\text{sum}})$ in $\cos(\theta_{\vec{p}_\mu})$.

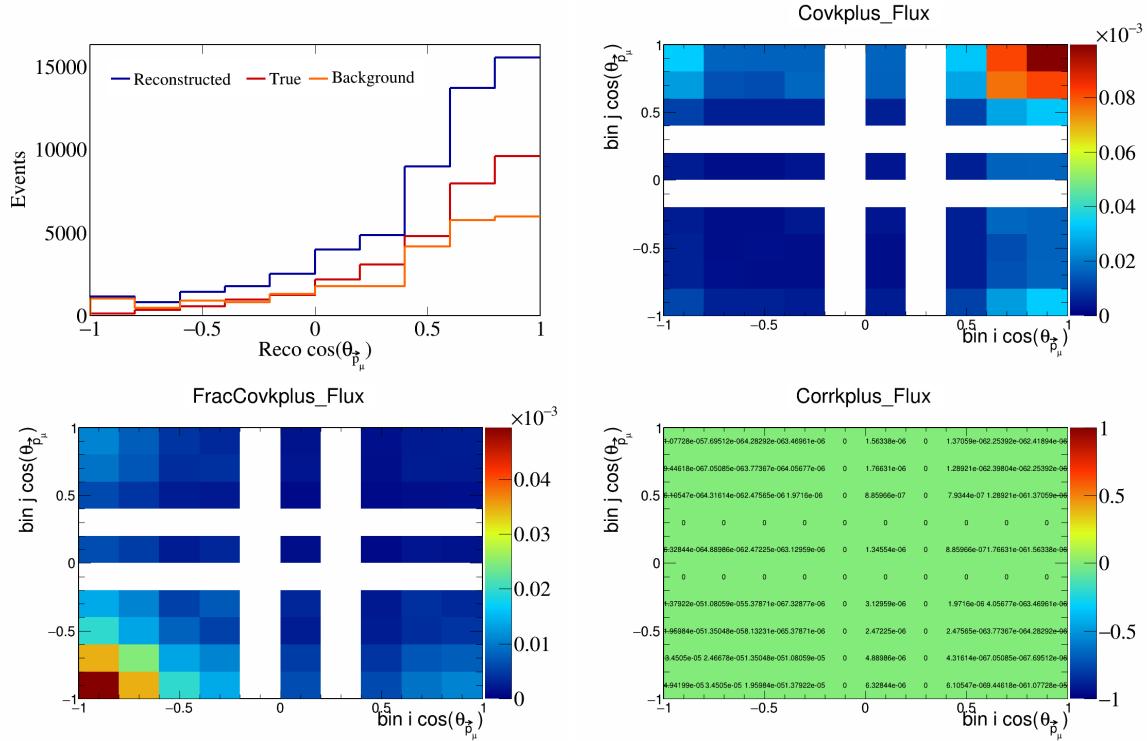


Figure 540: KPlus variations for $\cos(\theta_{\vec{p}_\mu} \vec{p}_{\text{sum}})$.

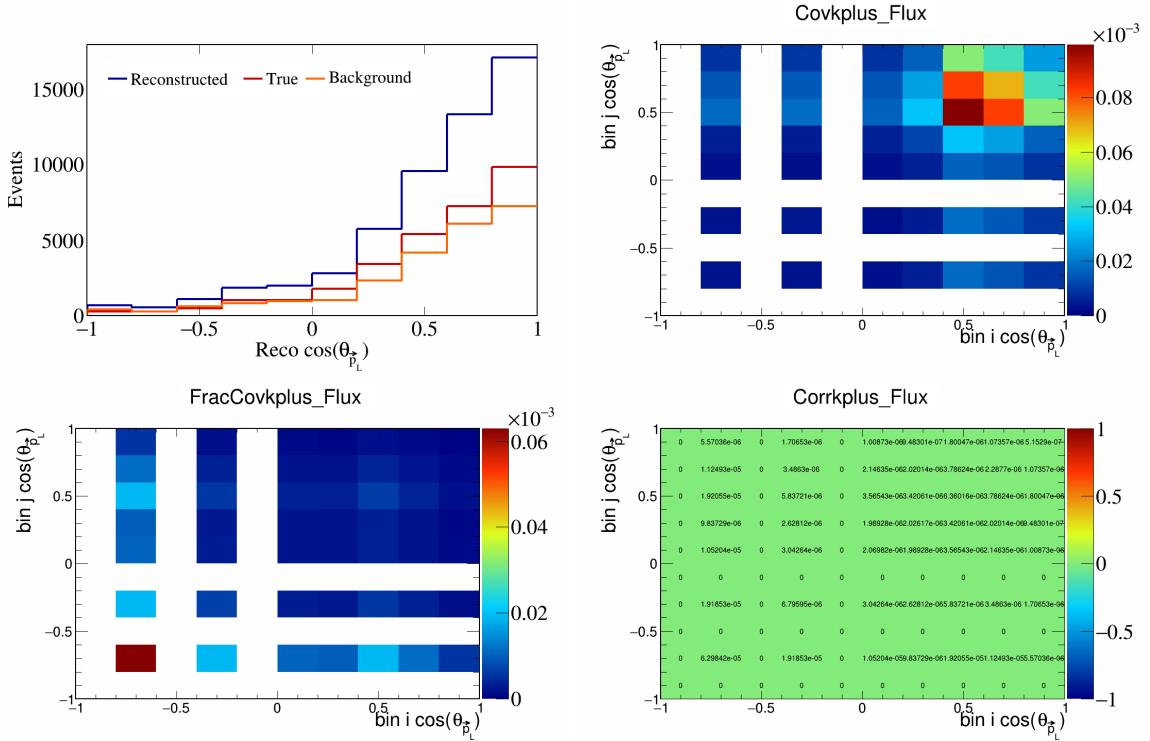


Figure 541: KPlus variations for $\cos(\theta_{\vec{p}_L})$.

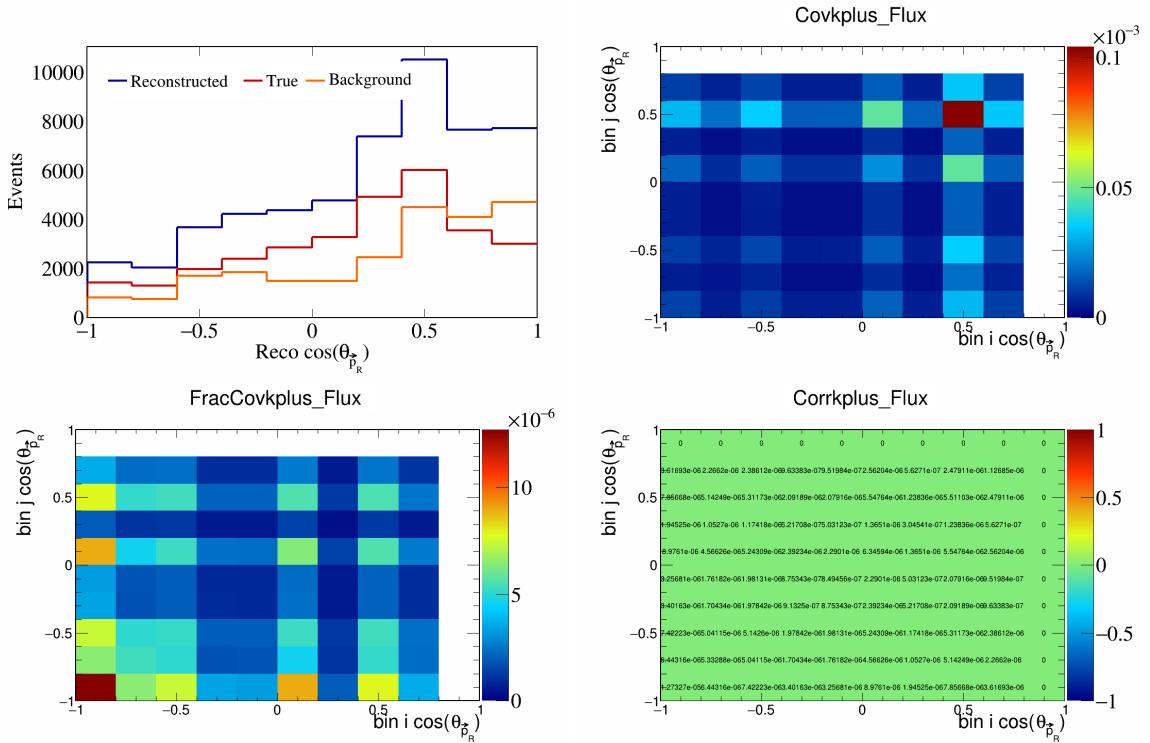


Figure 542: KPlus variations for $\cos(\theta_{\vec{p}_R})$.

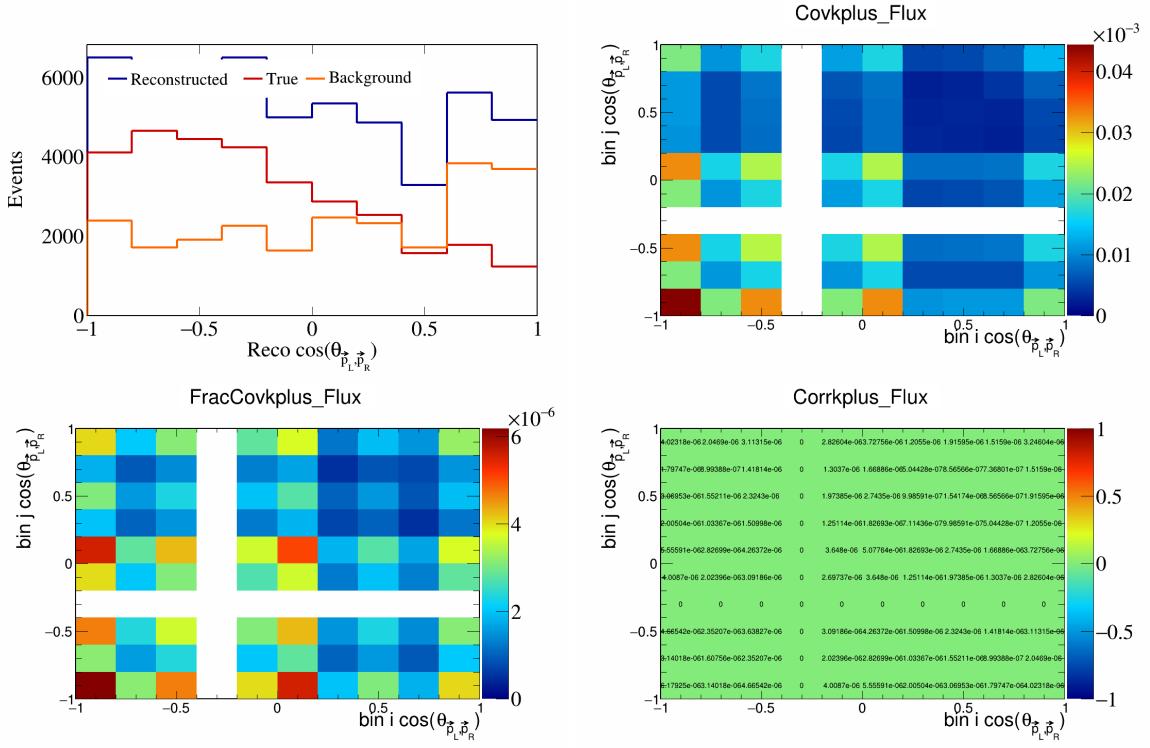


Figure 543: KPlus variations for $\cos(\theta_{\vec{p}_L, \vec{p}_R})$.

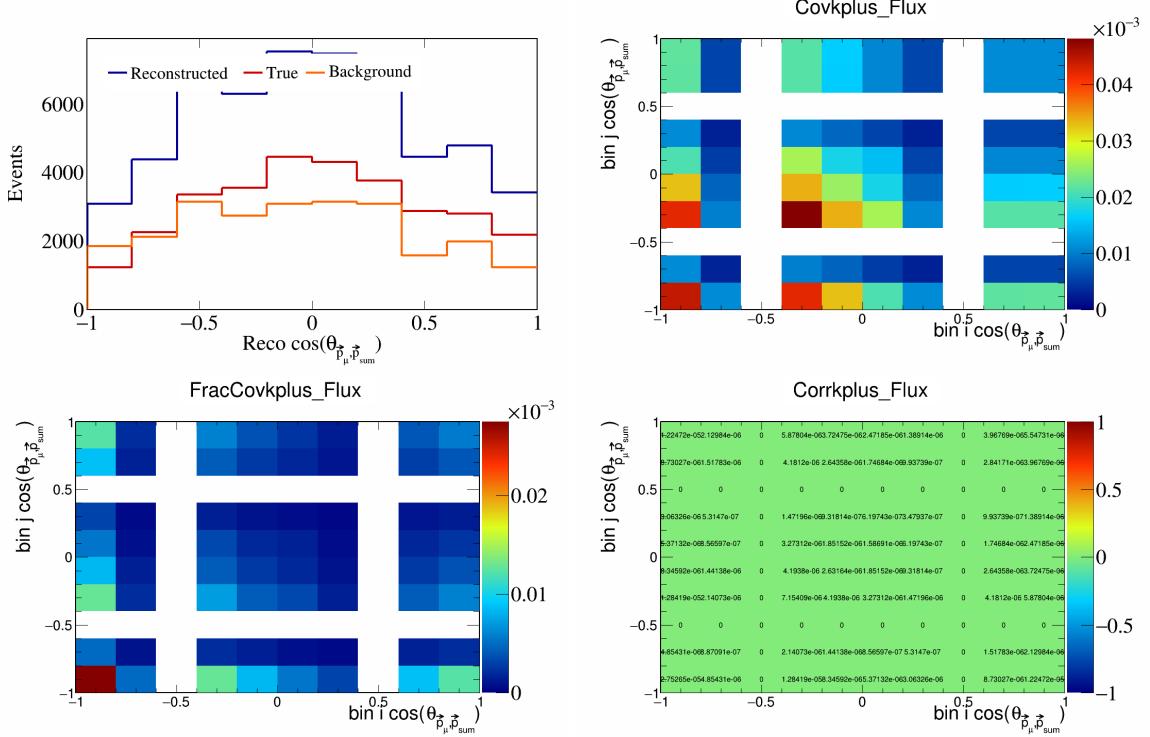


Figure 544: KPlus variations for $\cos(\theta_{\vec{p}_\mu, \vec{p}_{\text{sum}}})$.

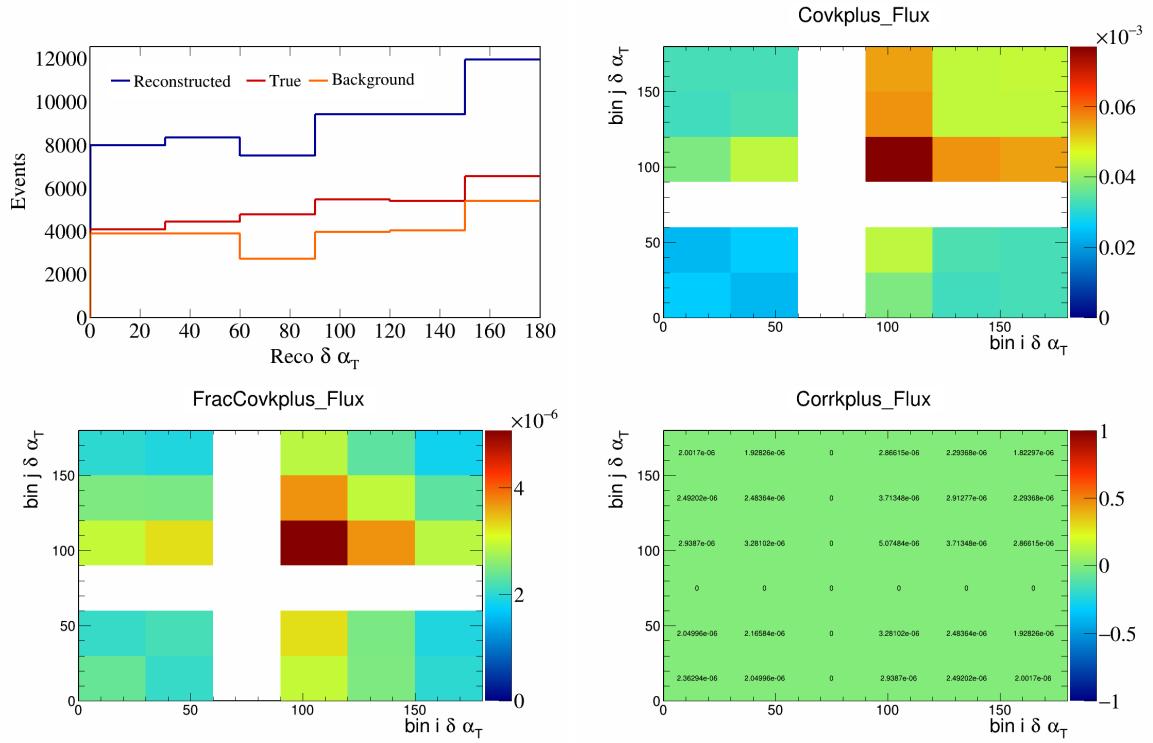


Figure 545: KPlus variations for $\delta\alpha_T$.

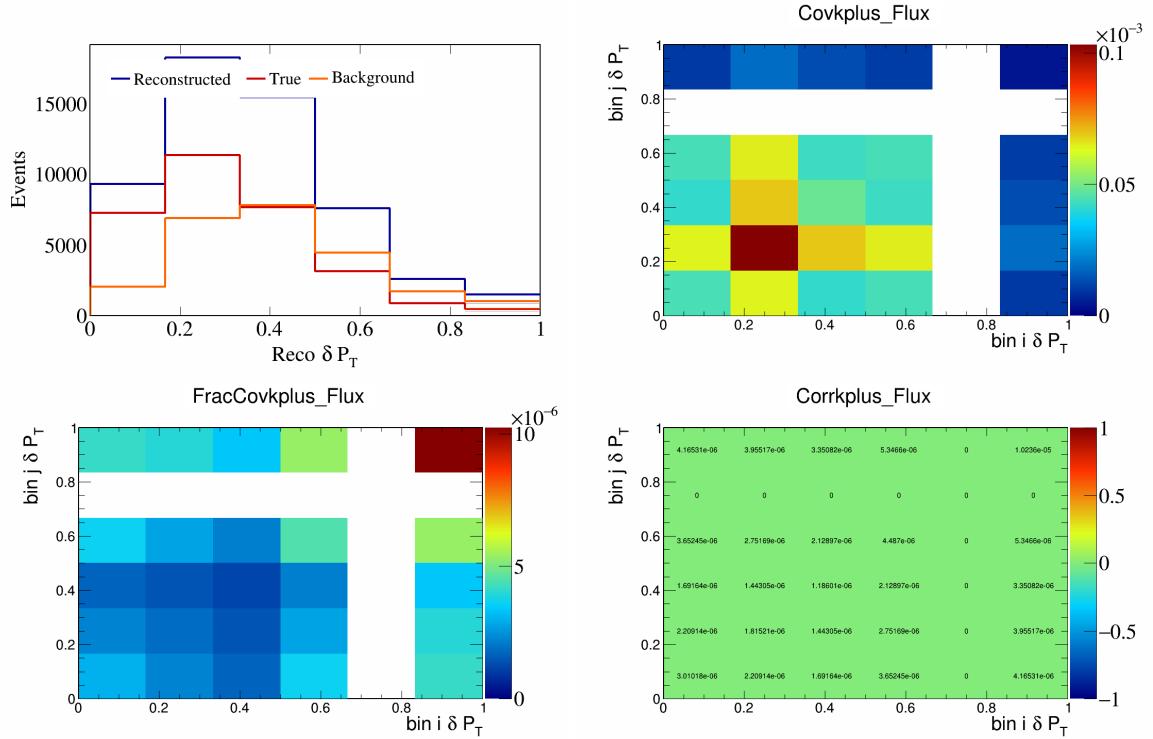


Figure 546: KPlus variations for δP_T .

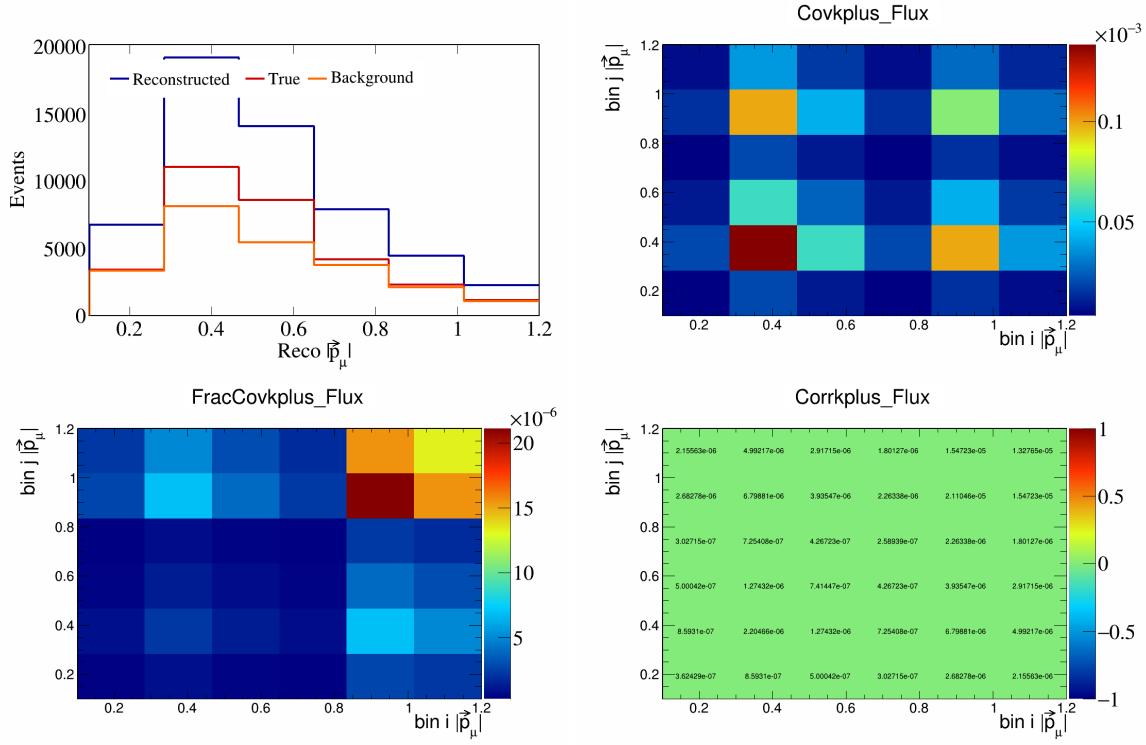


Figure 547: KPlus variations for $|\vec{p}_\mu|$.

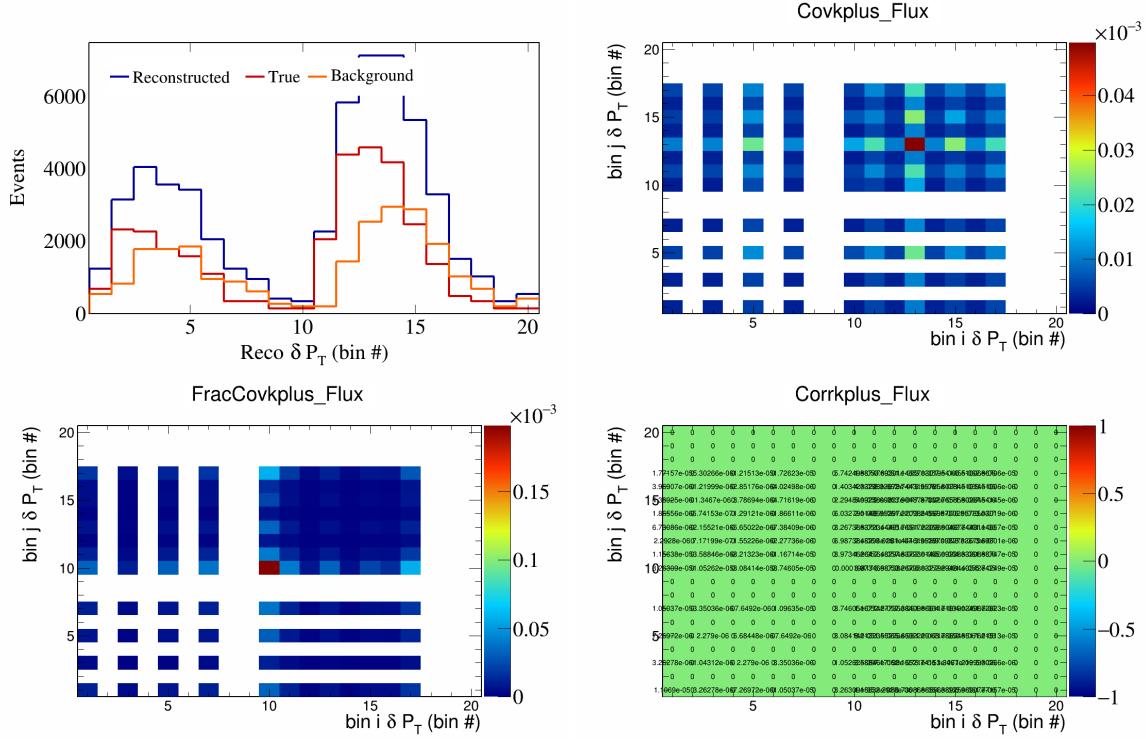


Figure 548: KPlus variations for δP_T in $\cos(\theta_{\vec{p}_\mu})$.

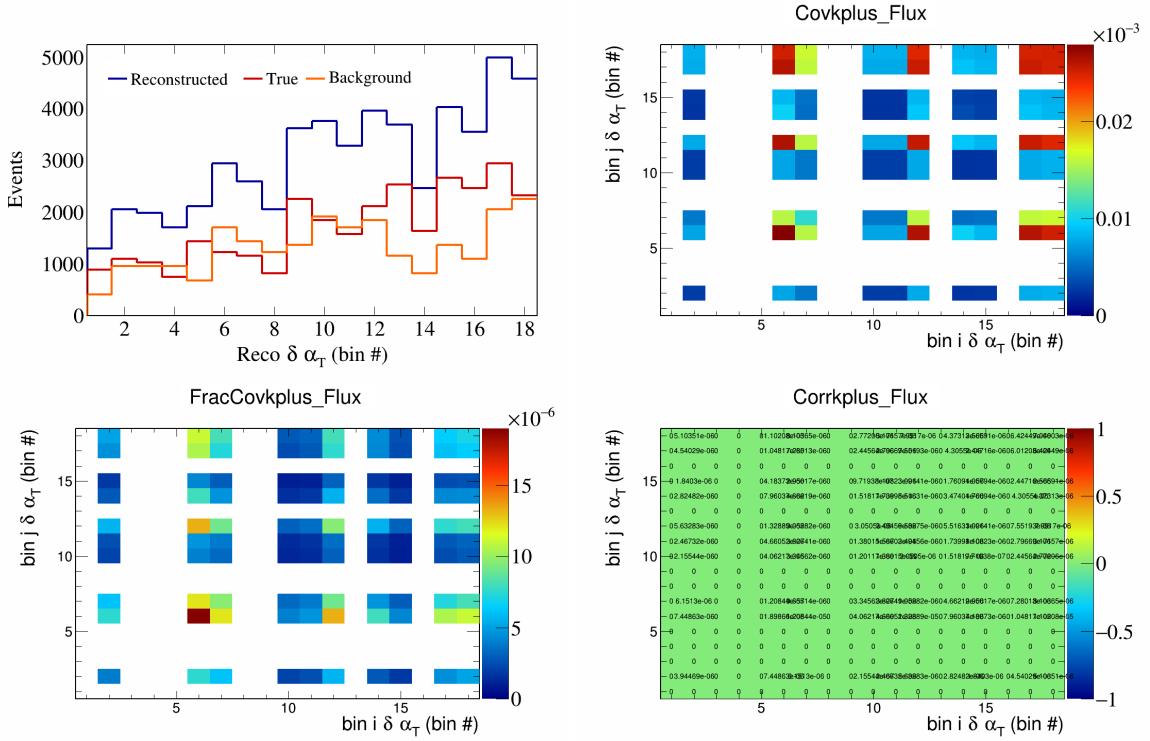


Figure 549: KPlus variations for $\delta\alpha_T$ in $\cos(\theta_{\vec{p}_\mu})$.

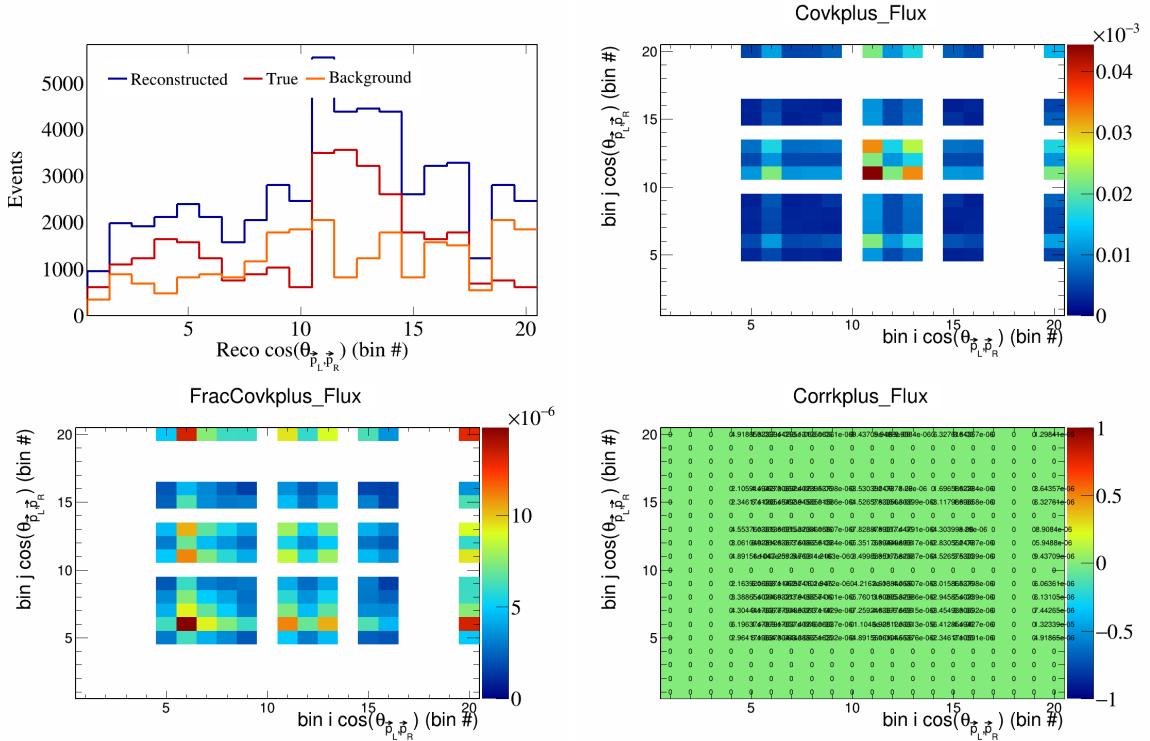


Figure 550: KPlus variations for $\cos(\theta_{p_L, p_R})$ in $\cos(\theta_{\vec{p}_\mu})$.

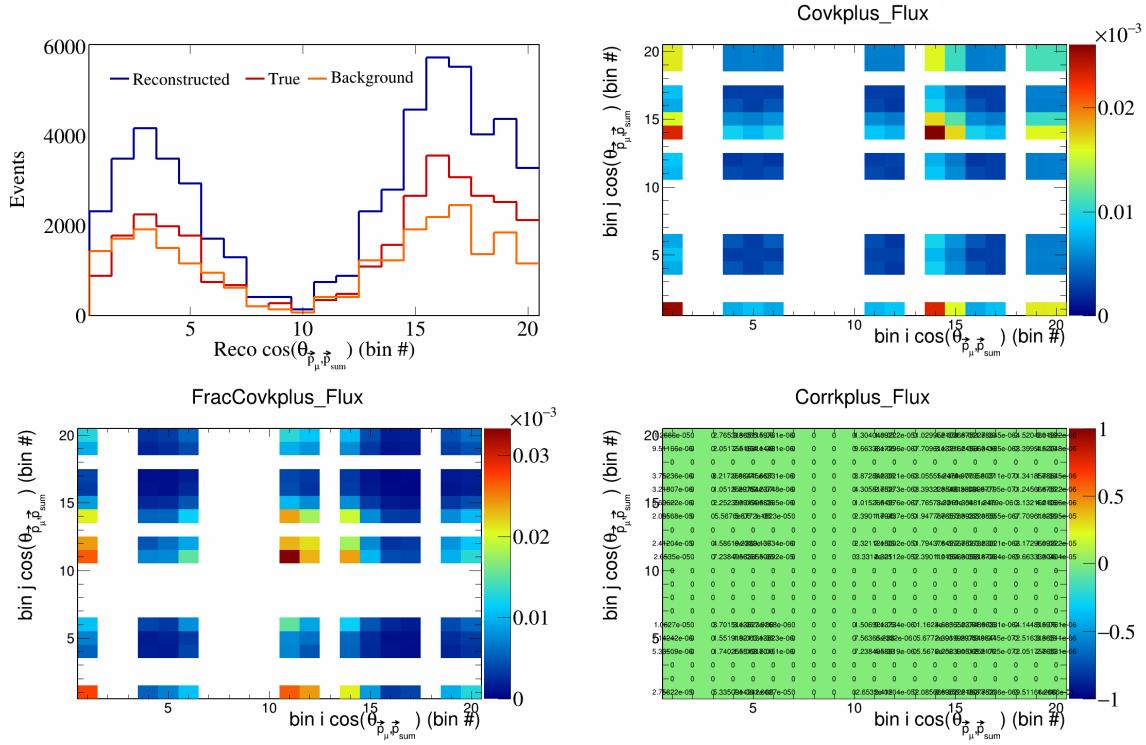


Figure 551: KPlus variations for $\cos(\theta_{\vec{p}_\mu} \vec{p}_{\text{sum}})$ in $\cos(\theta_{\vec{p}_\mu})$.

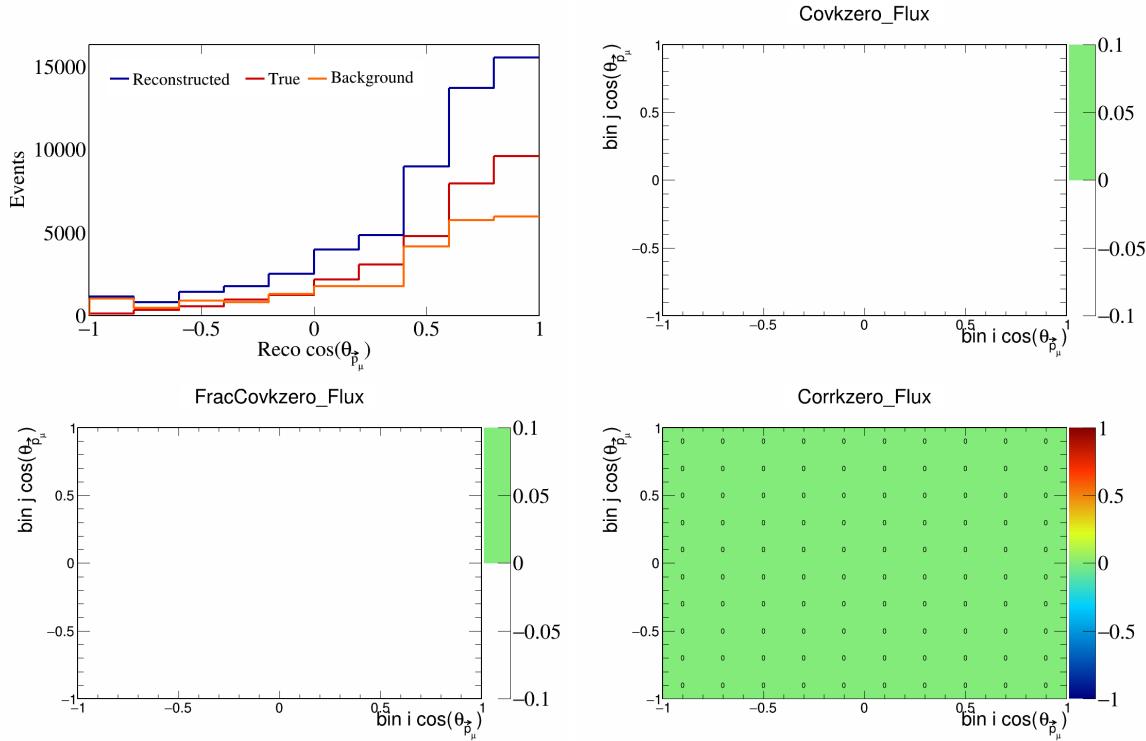


Figure 552: KZero variations for $\cos(\theta_{\vec{p}_\mu} \vec{p}_{\text{sum}})$ in $\cos(\theta_{\vec{p}_\mu})$.

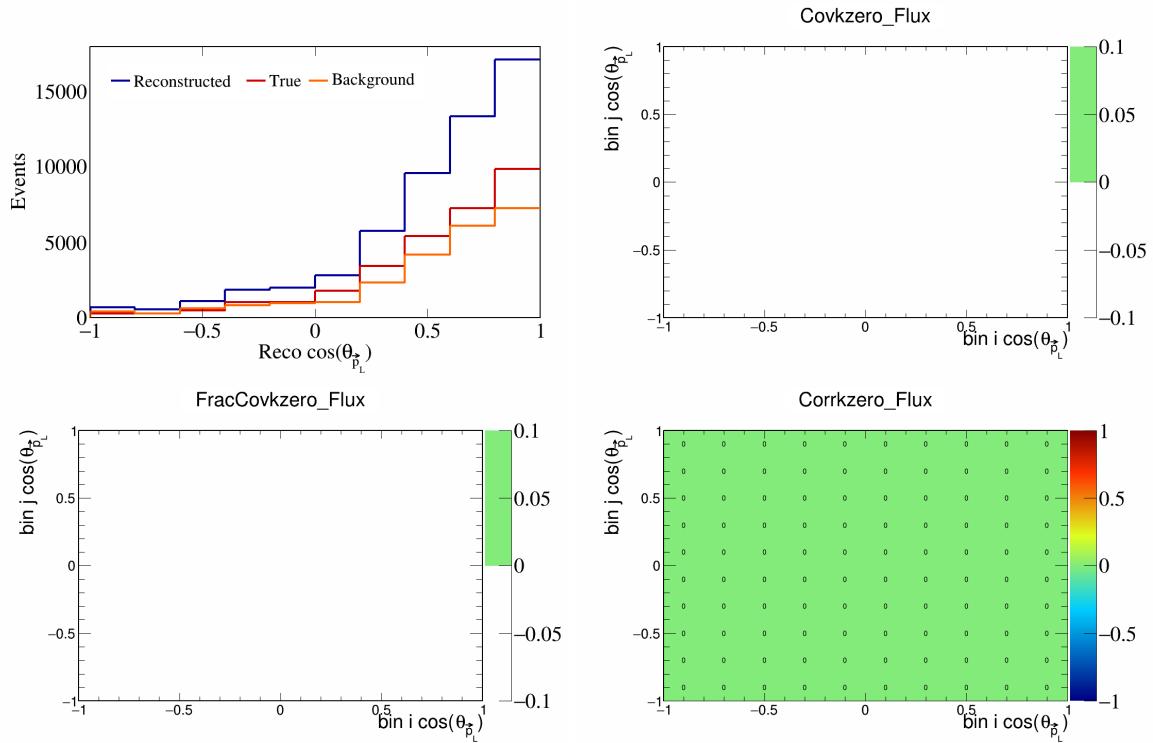


Figure 553: KZero variations for $\cos(\theta_{\vec{p}_L})$.

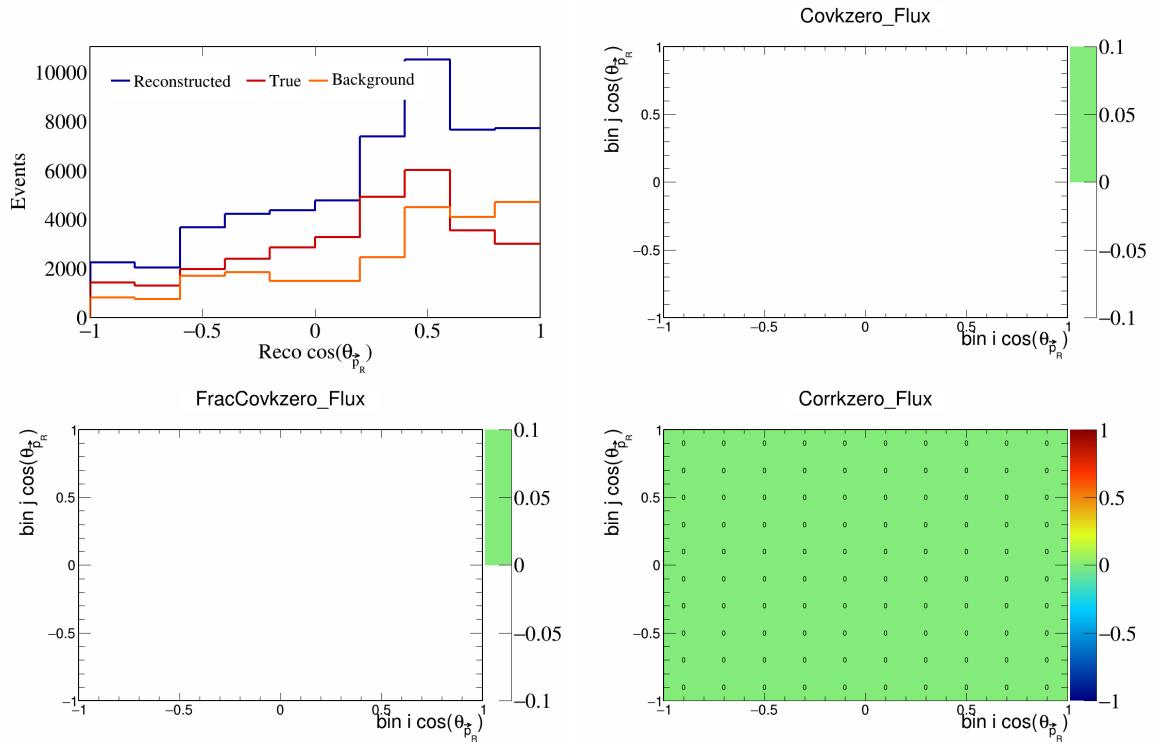


Figure 554: KZero variations for $\cos(\theta_{\vec{p}_R})$.

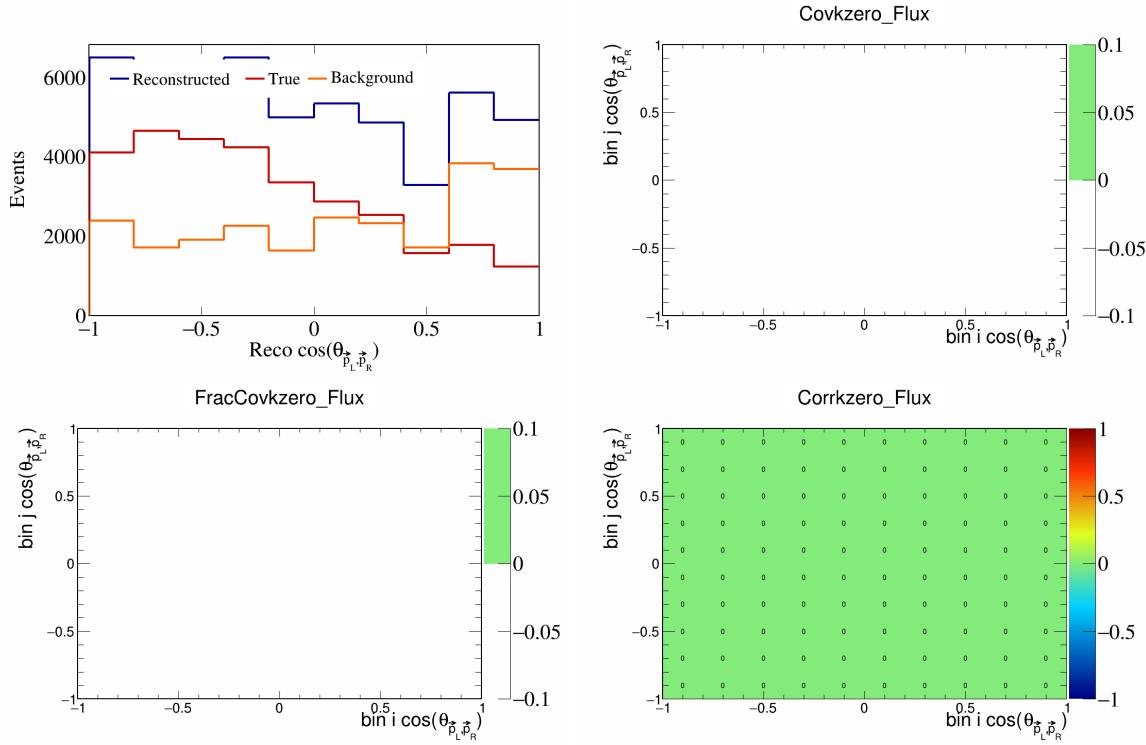


Figure 555: KZero variations for $\cos(\theta_{\vec{p}_L, \vec{p}_R})$.

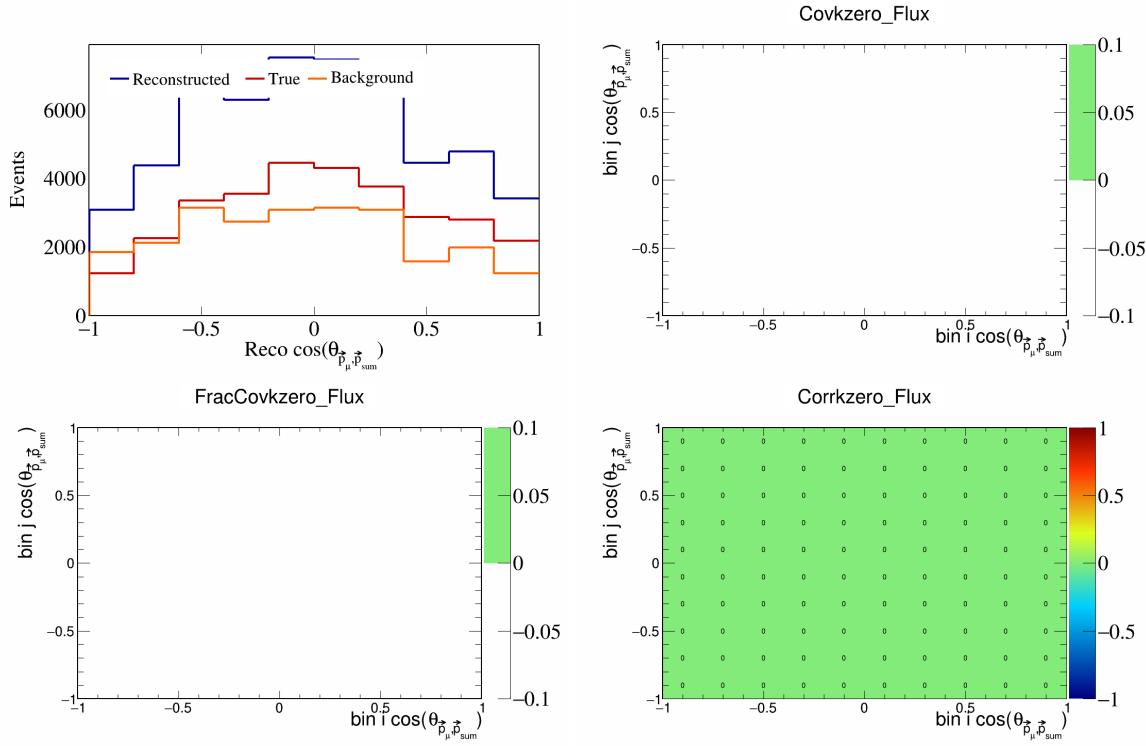


Figure 556: KZero variations for $\cos(\theta_{\vec{p}_\mu, \vec{p}_{\text{sum}}})$.

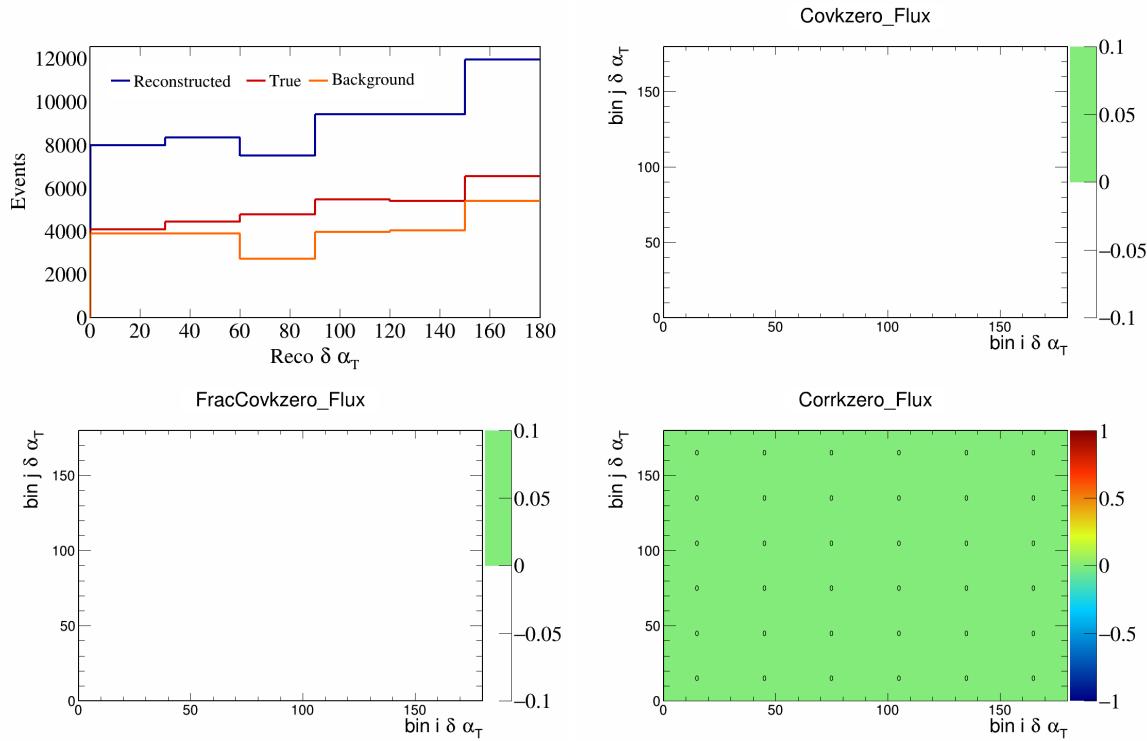


Figure 557: KZero variations for $\delta\alpha_T$.

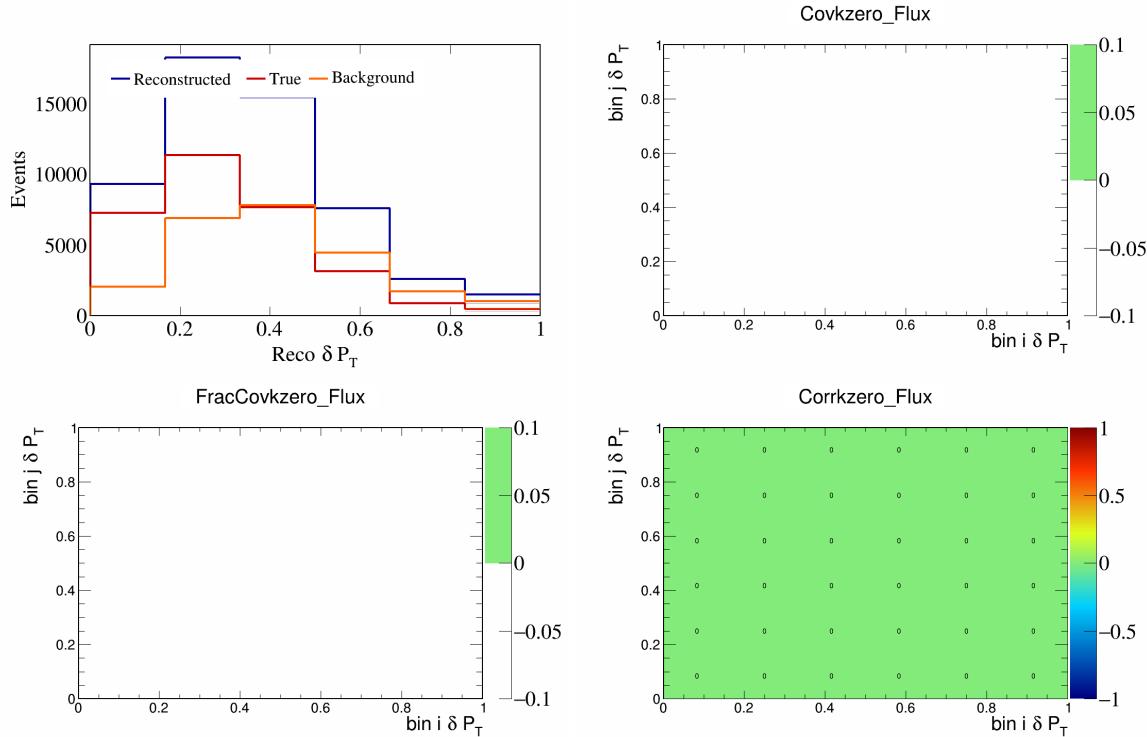


Figure 558: KZero variations for δP_T .

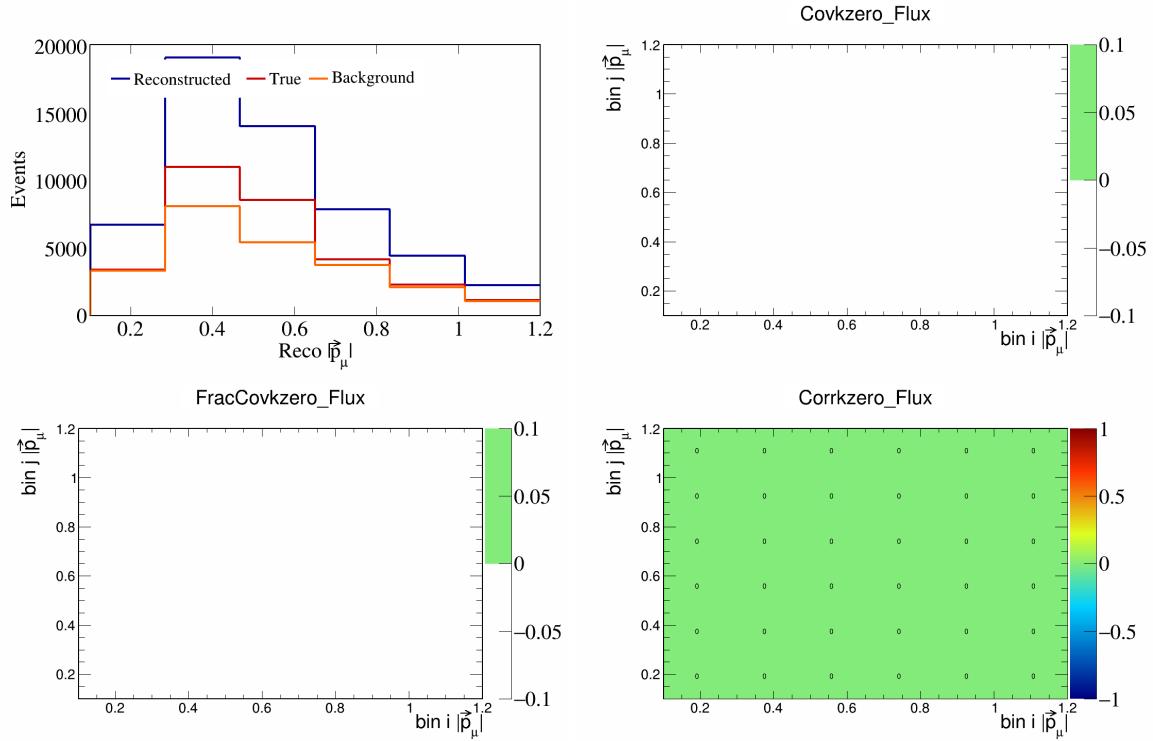


Figure 559: KZero variations for $|\vec{p}_\mu|$.

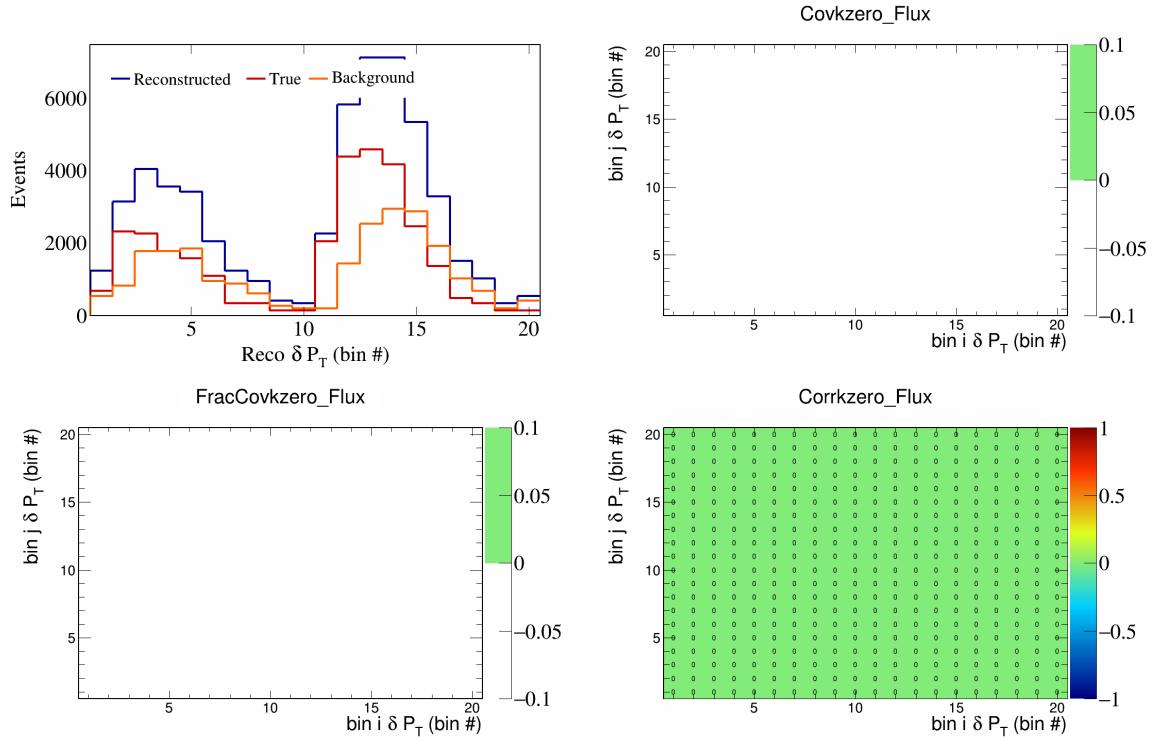


Figure 560: KZero variations for δP_T in $\cos(\theta_{\vec{p}_\mu})$.

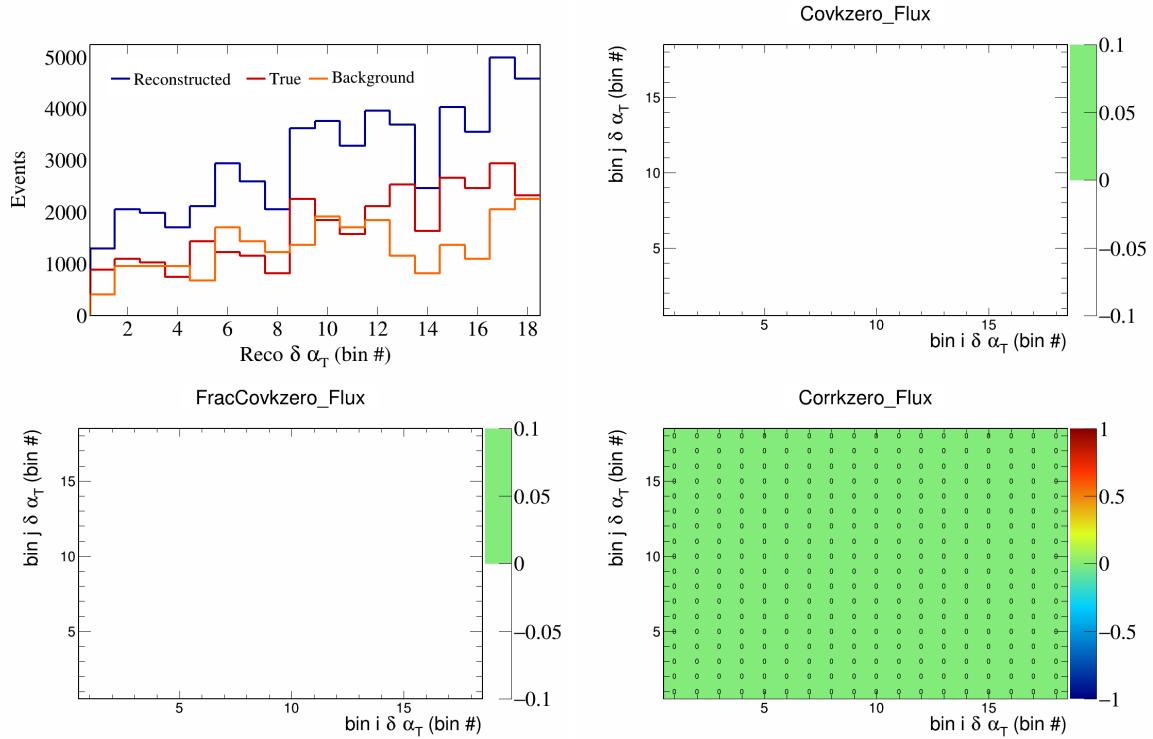


Figure 561: KZero variations for $\delta\alpha_T$ in $\cos(\theta_{\vec{p}_\mu})$.

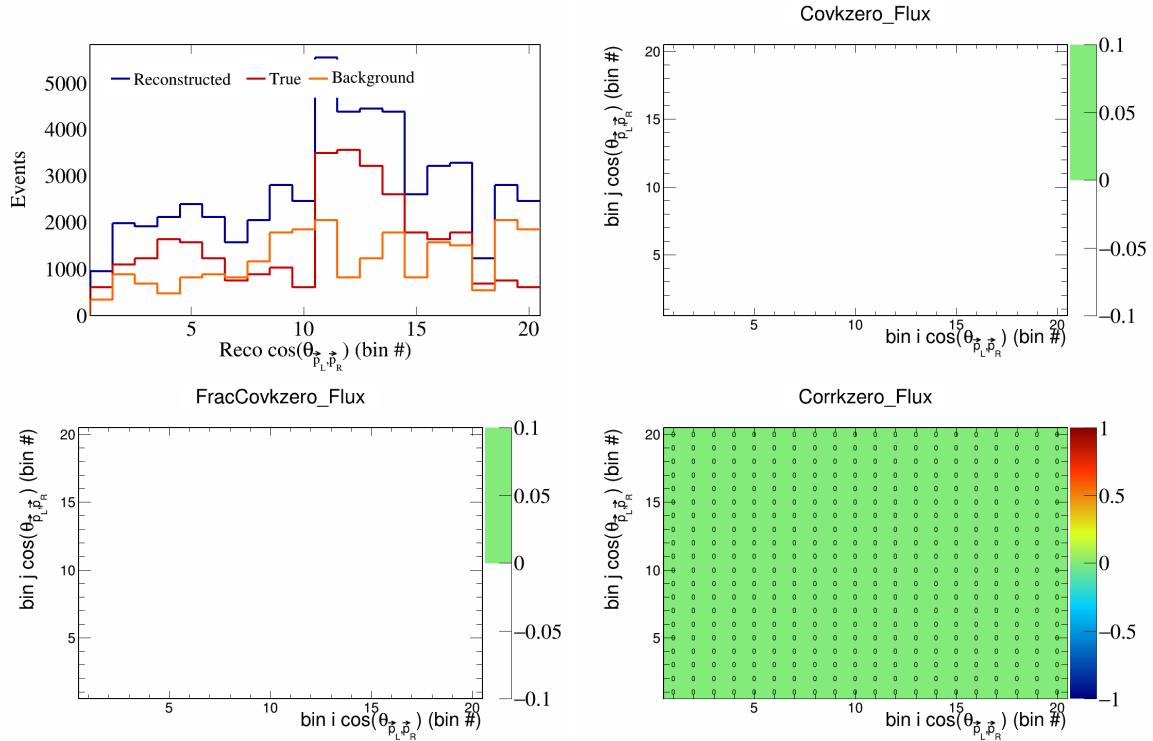


Figure 562: KZero variations for $\cos(\theta_{\vec{p}_L, \vec{p}_R})$ in $\cos(\theta_{\vec{p}_\mu})$.

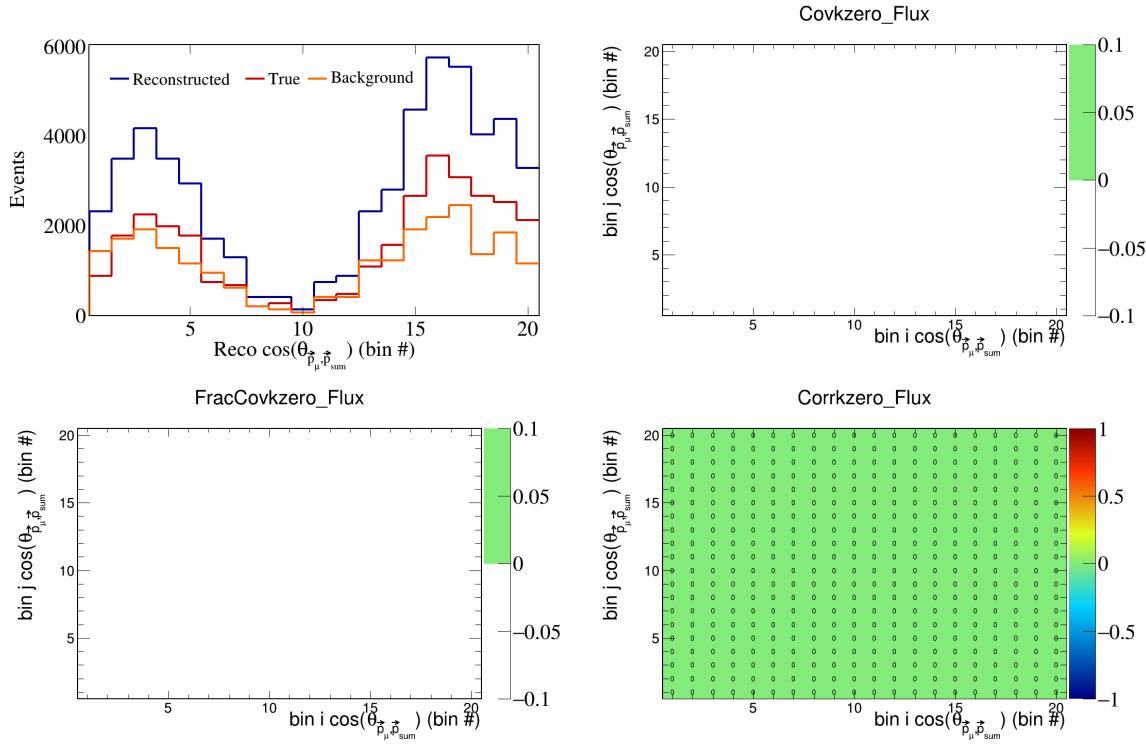


Figure 563: KZero variations for $\cos(\theta_{\vec{p}_\mu} \vec{p}_{\text{sum}})$ in $\cos(\theta_{\vec{p}_\mu})$.

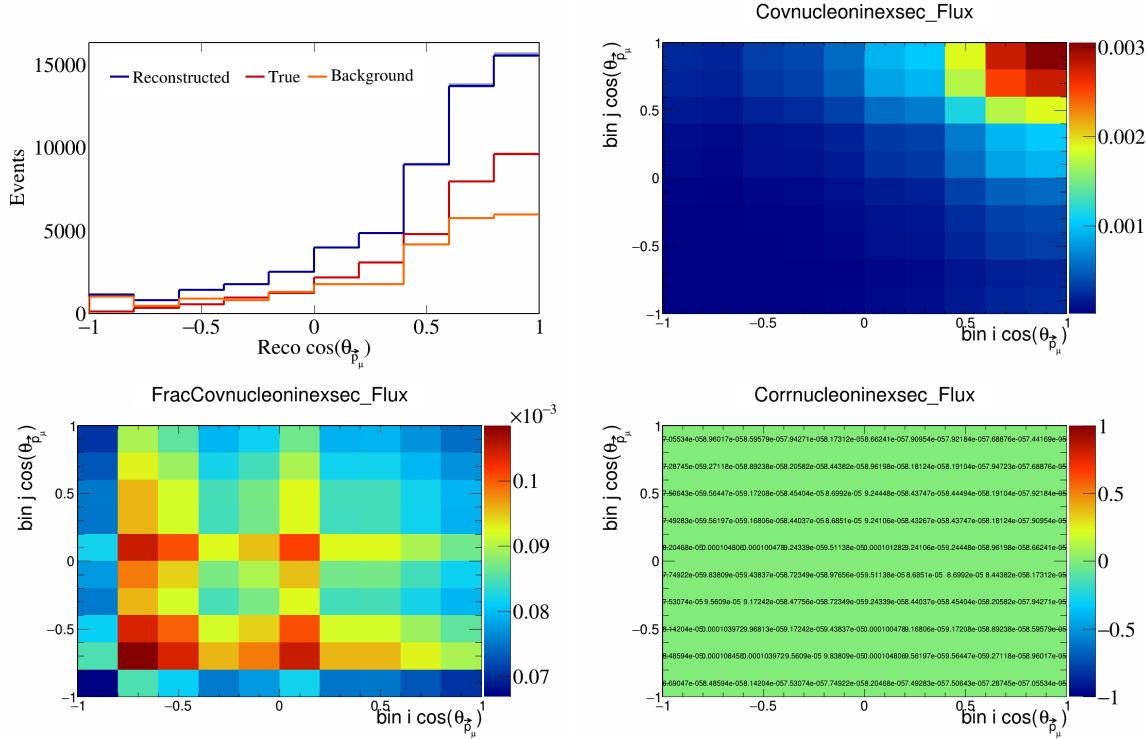


Figure 564: NucleonIneXSec variations for $\cos(\theta_{\vec{p}_\mu})$.

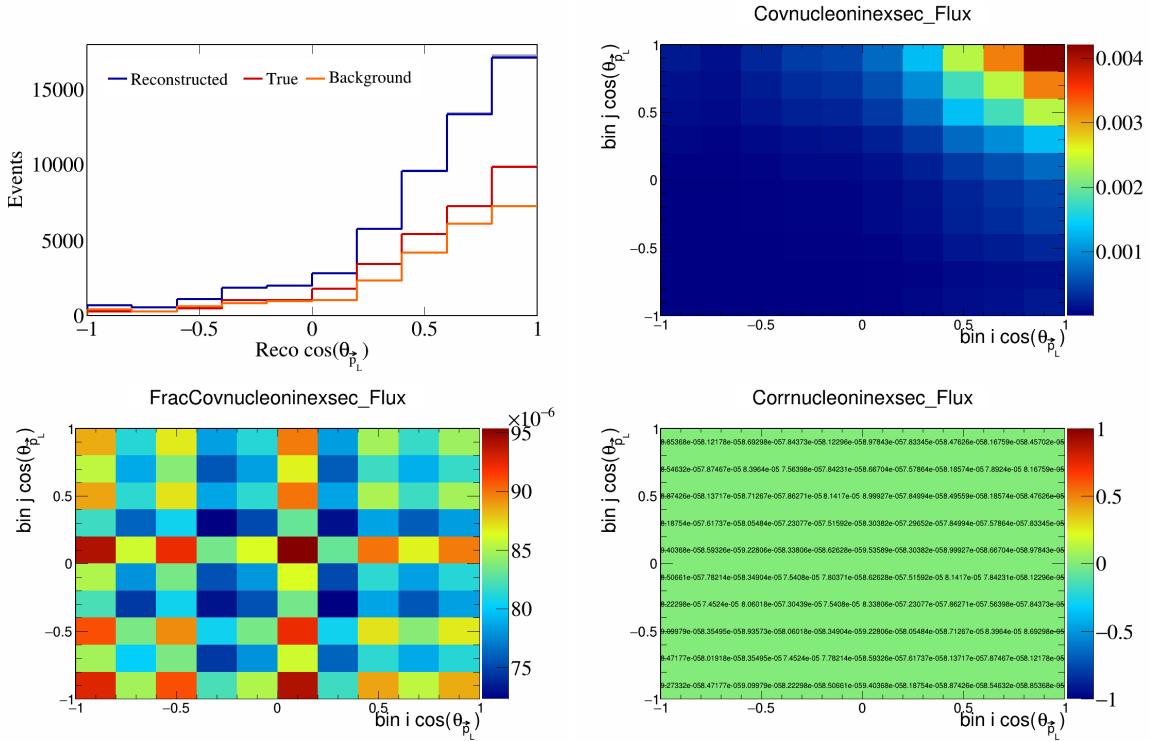


Figure 565: NucleonIneXSec variations for $\cos(\theta_{\vec{p}_L})$.

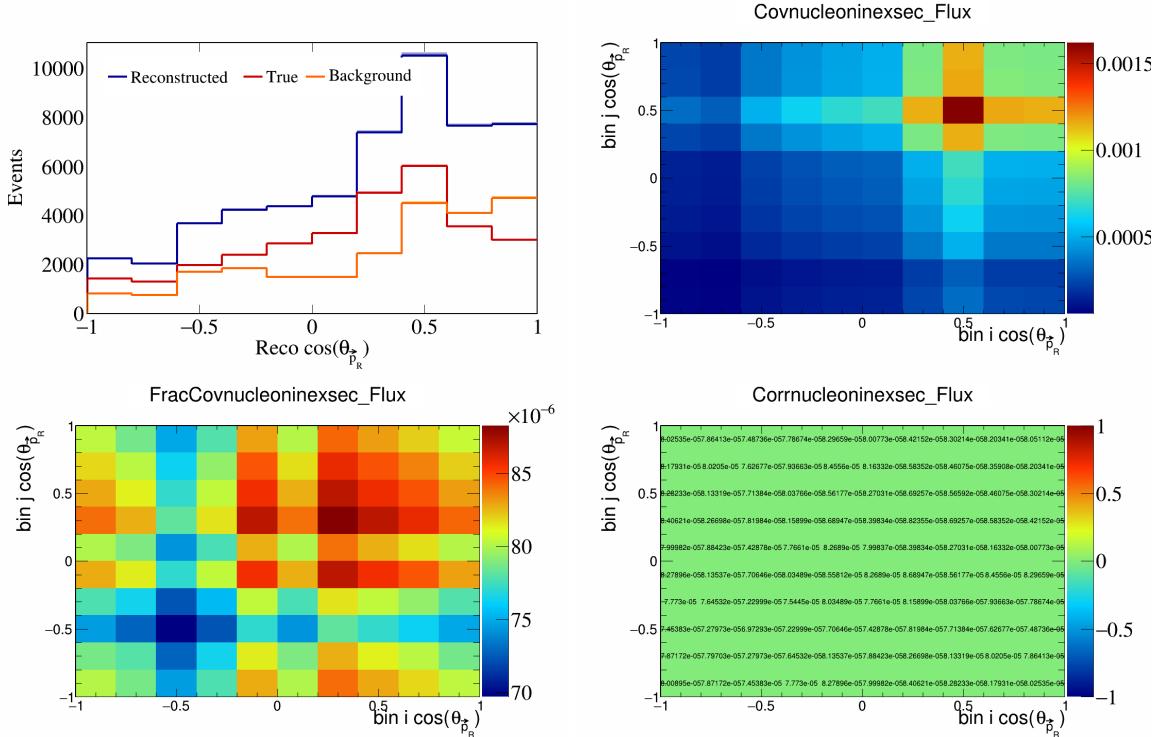


Figure 566: NucleonIneXSec variations for $\cos(\theta_{\vec{p}_R})$.

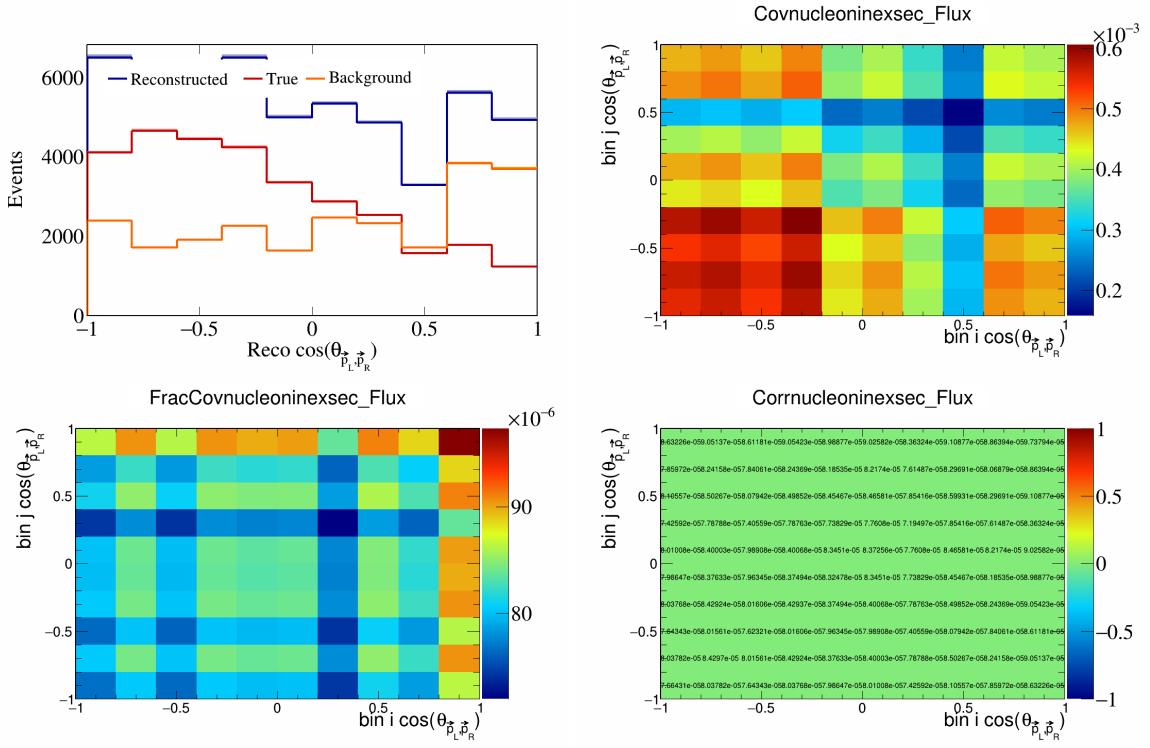


Figure 567: NucleonIneXSec variations for $\cos(\theta_{\vec{p}_L, \vec{p}_R})$.

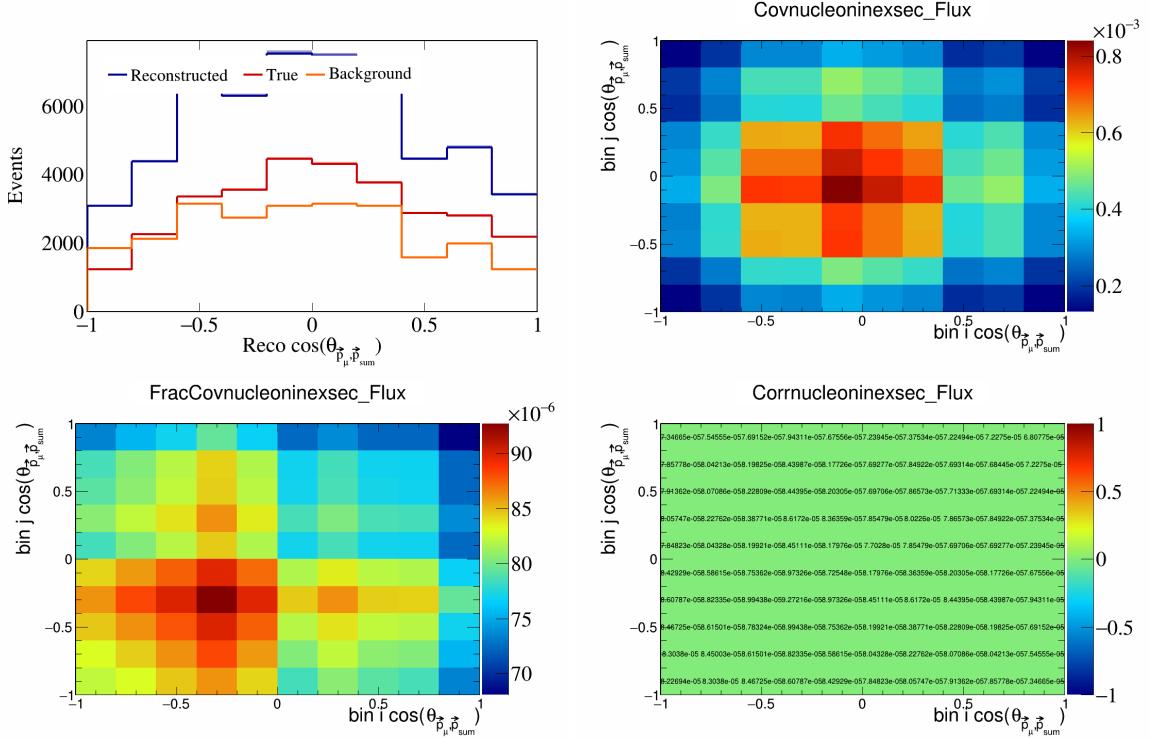


Figure 568: NucleonIneXSec variations for $\cos(\theta_{\vec{p}_\mu, \vec{p}_{\text{sum}}})$.

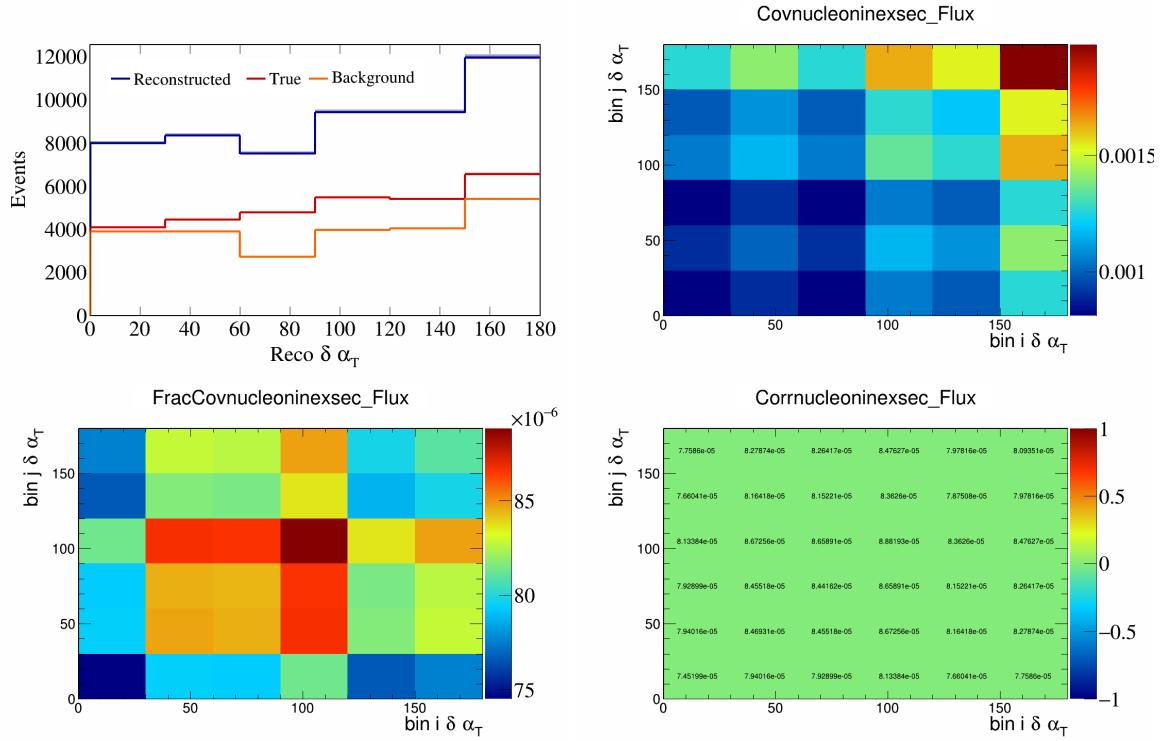


Figure 569: NucleonIneXSec variations for $\delta \alpha_T$.

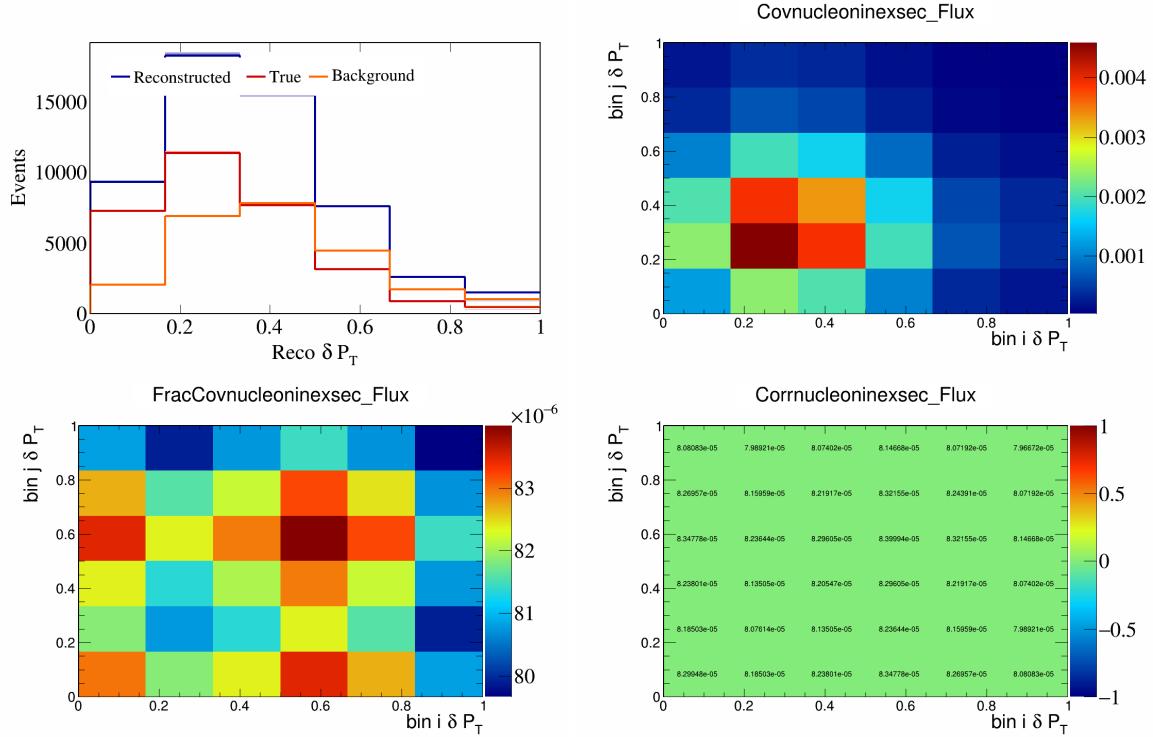


Figure 570: NucleonIneXSec variations for δP_T .

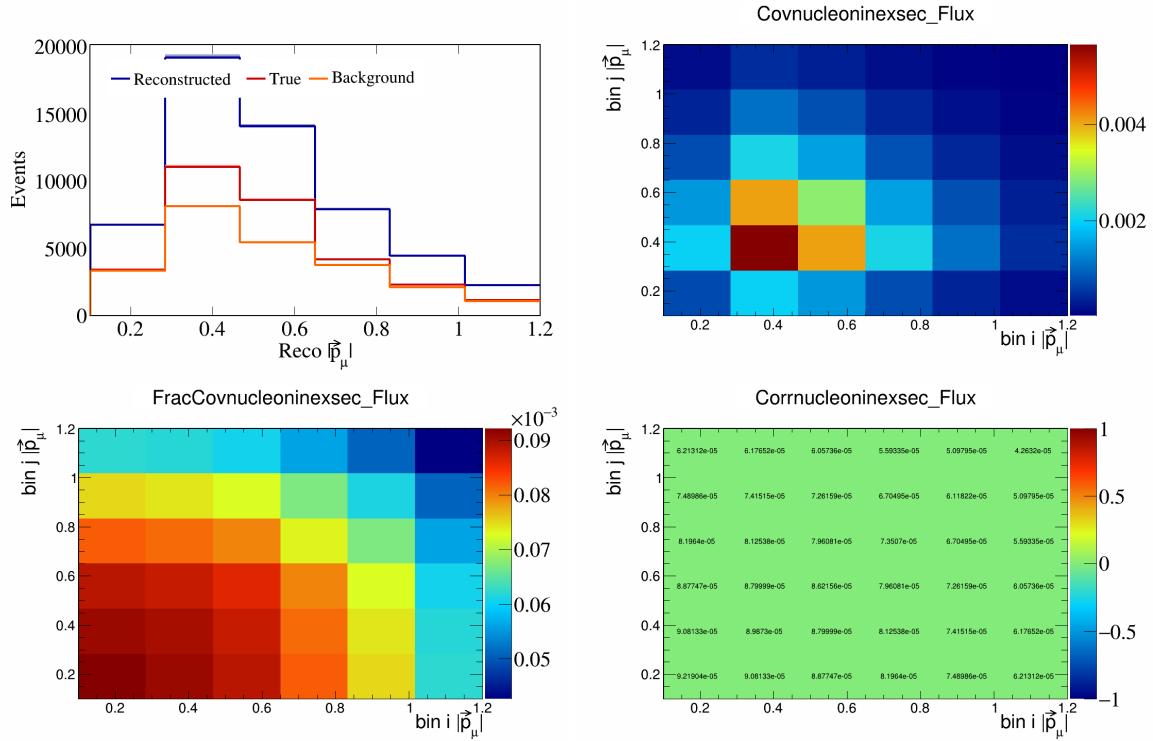


Figure 571: NucleonIneXSec variations for $|\vec{p}_\mu|$.

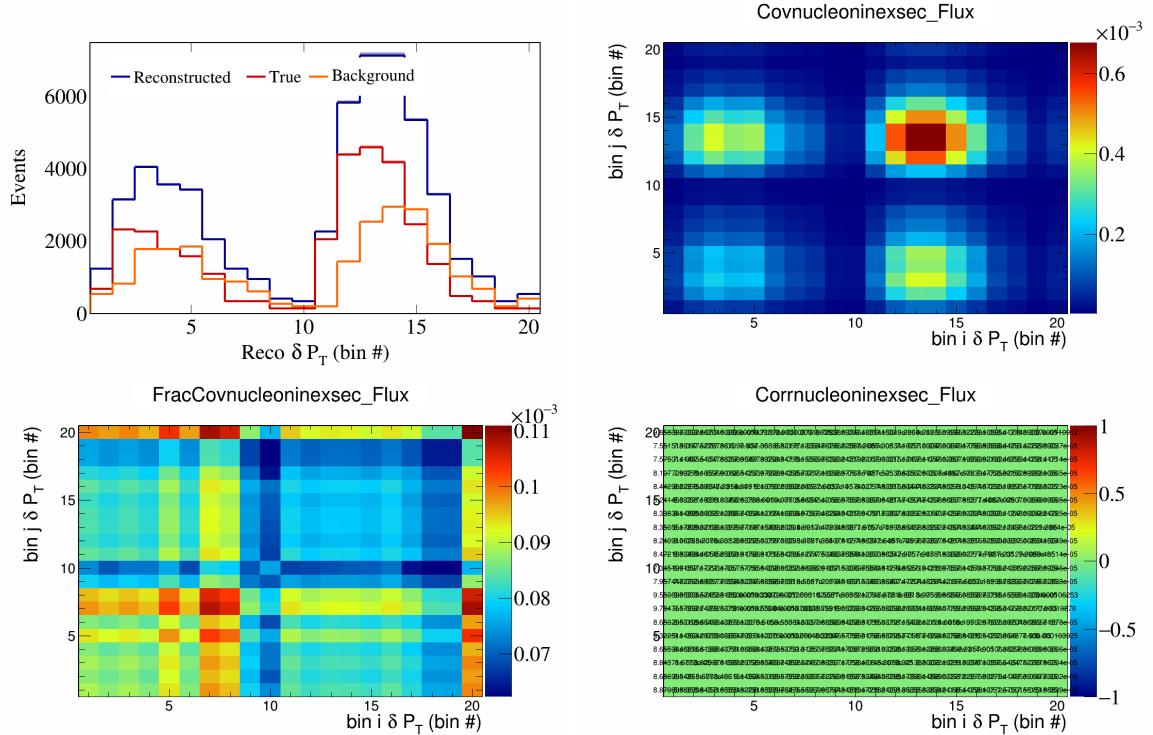


Figure 572: NucleonIneXSec variations for δP_T in $\cos(\theta_{\vec{F}})$.

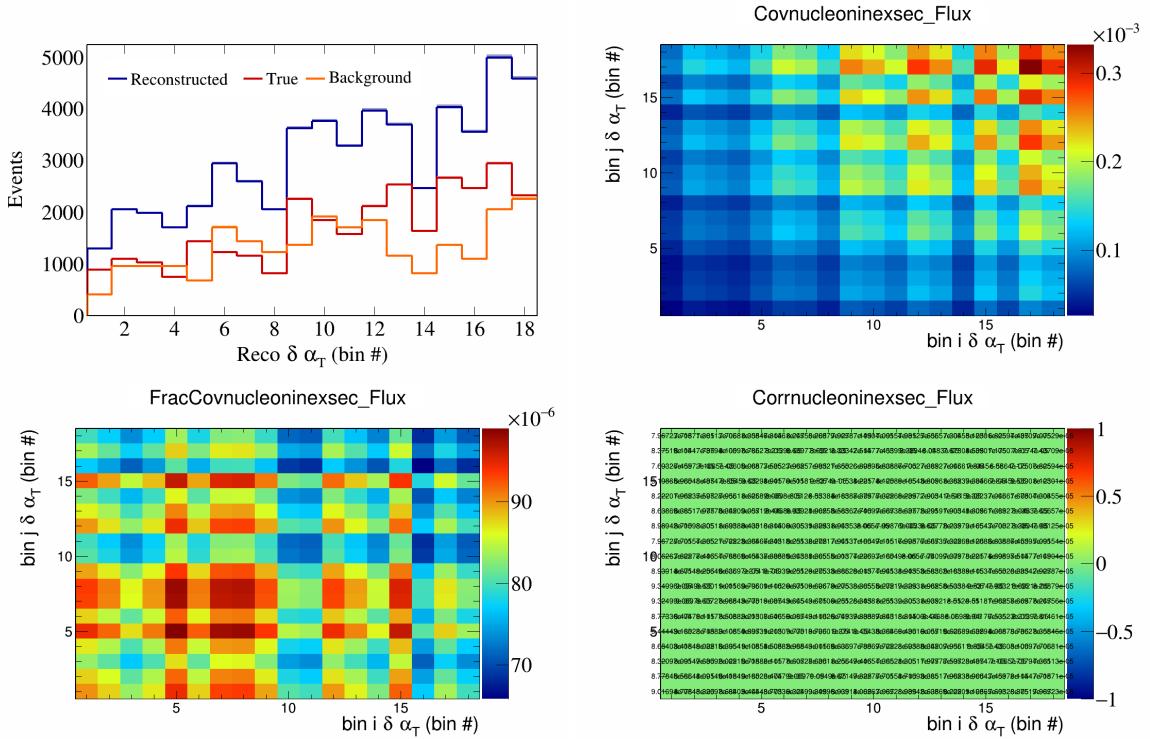


Figure 573: NucleonIneXSec variations for $\delta\alpha_T$ in $\cos(\theta_{\vec{p}_\mu})$.

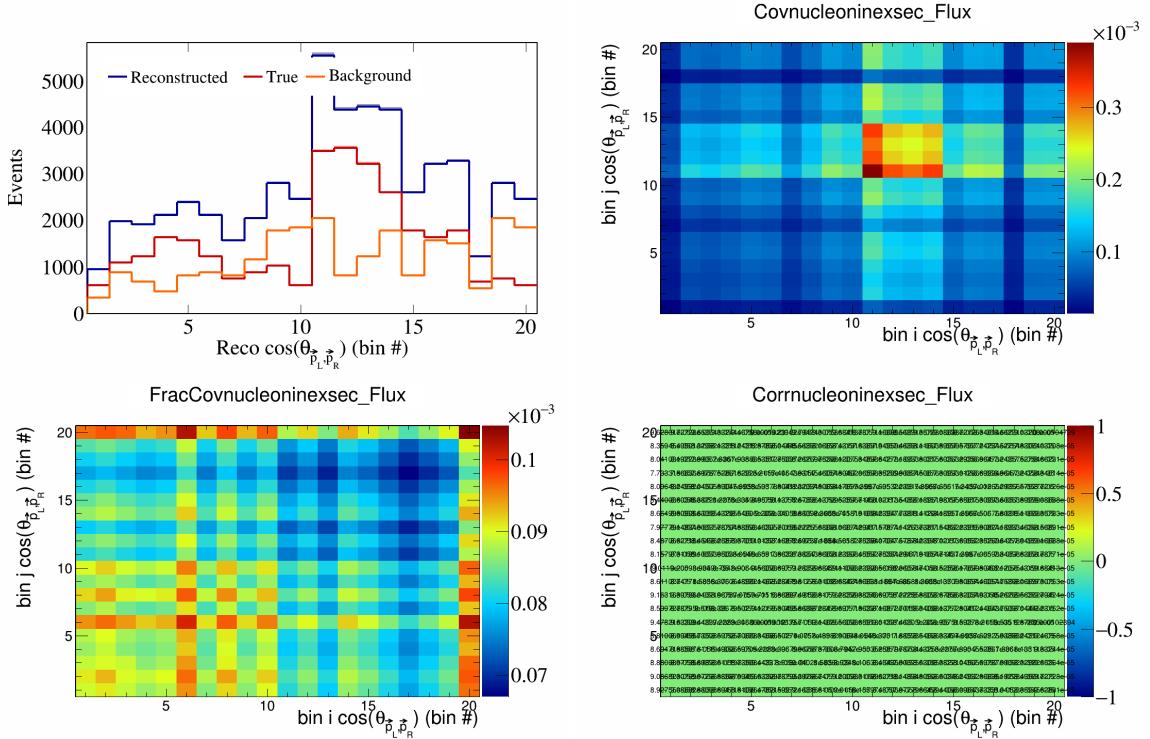


Figure 574: NucleonIneXSec variations for $\cos(\theta_{\vec{p}_L, \vec{p}_R})$ in $\cos(\theta_{\vec{p}_\mu})$.

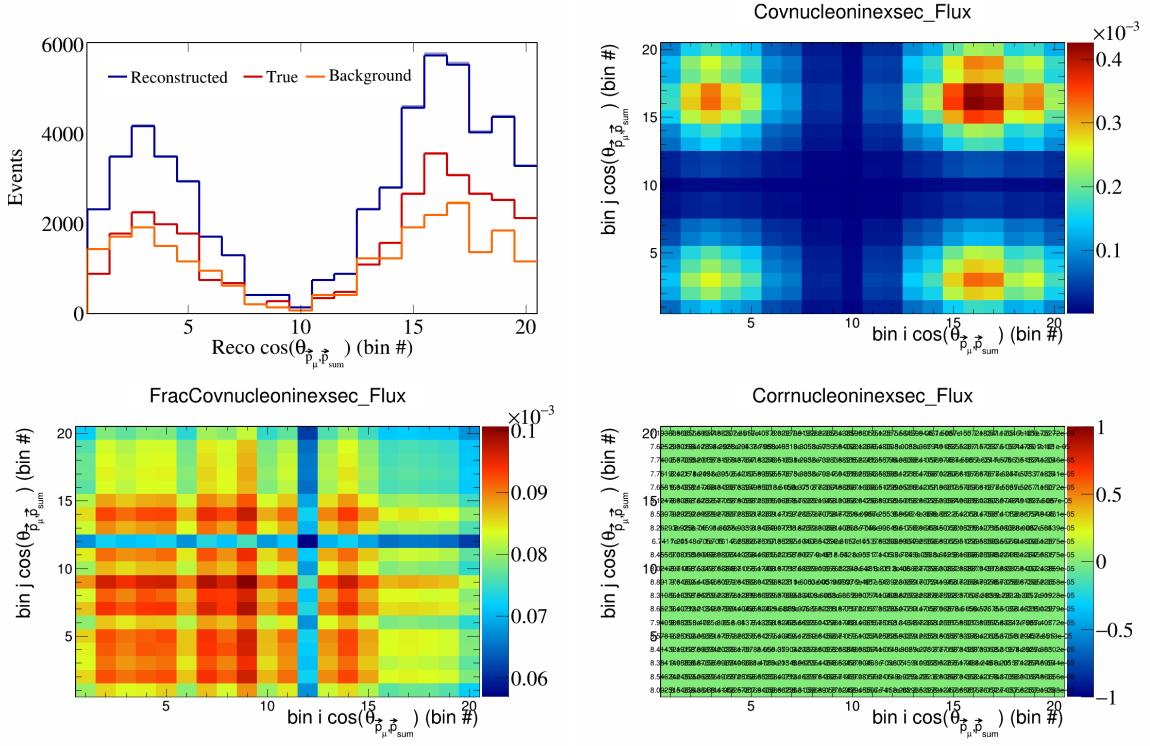


Figure 575: NucleonIneXSec variations for $\cos(\theta_{\vec{p}_\mu})$ in $\cos(\theta_{\vec{p}_\mu})$.

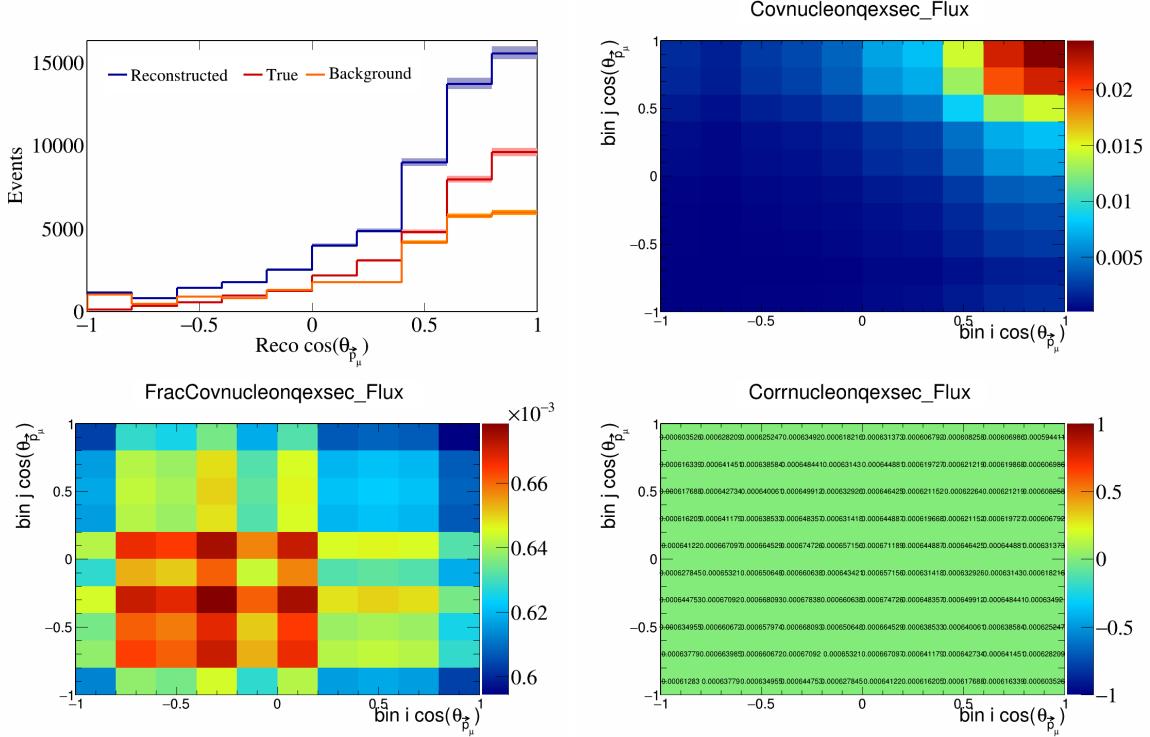


Figure 576: NucleonQeXSec variations for $\cos(\theta_{\vec{p}_\mu})$.

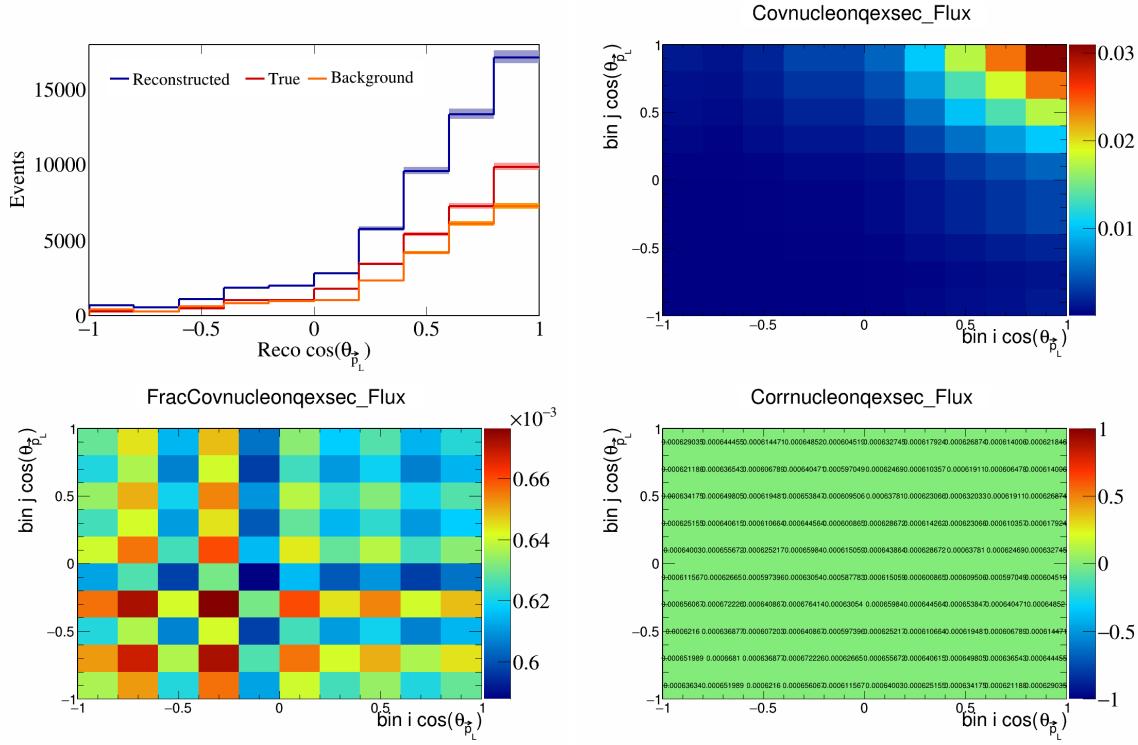


Figure 577: NucleonQeXSec variations for $\cos(\theta_{\vec{p}_L})$.

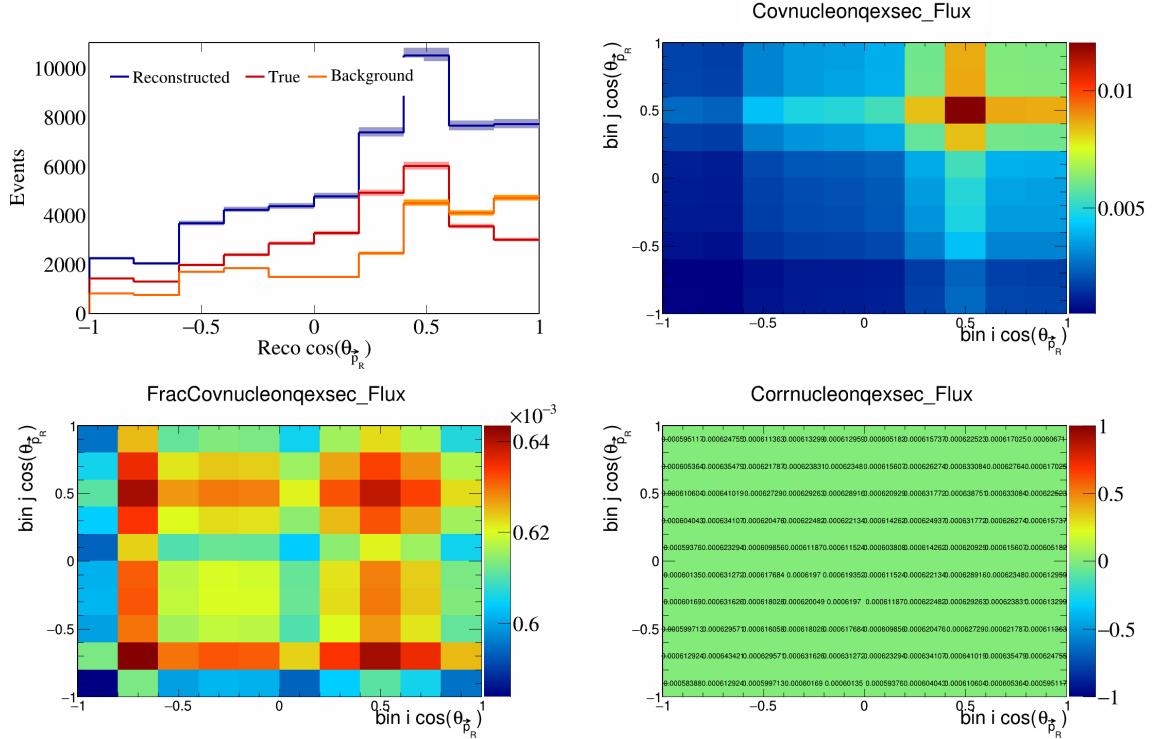


Figure 578: NucleonQeXSec variations for $\cos(\theta_{\vec{p}_R})$.

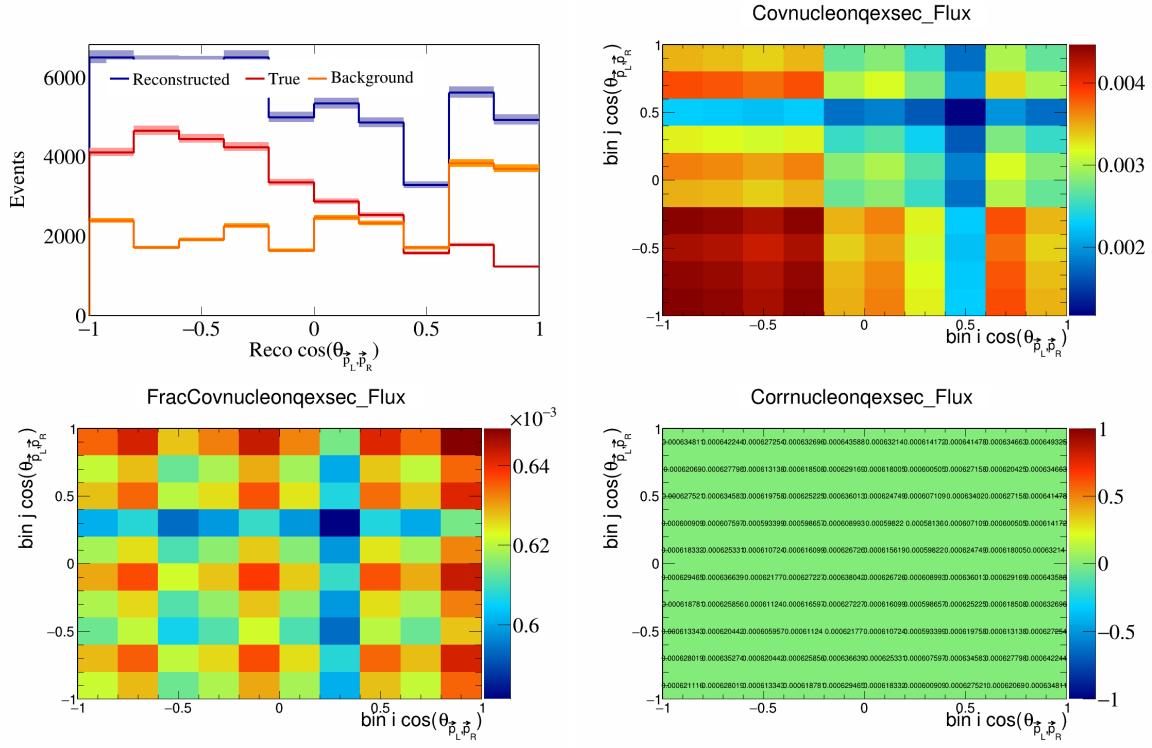


Figure 579: NucleonQeXSec variations for $\cos(\theta_{\vec{p}_L, \vec{p}_R})$.

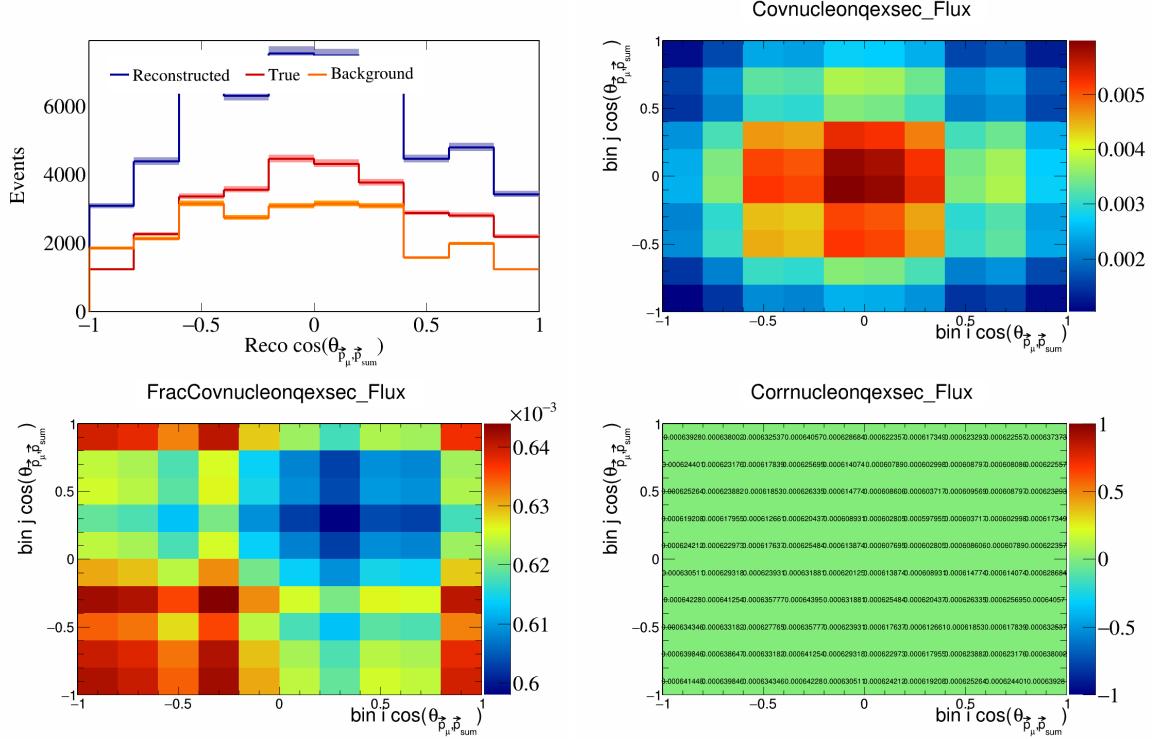


Figure 580: NucleonQeXSec variations for $\cos(\theta_{\vec{p}_\mu, \vec{p}_{\text{sum}}})$.

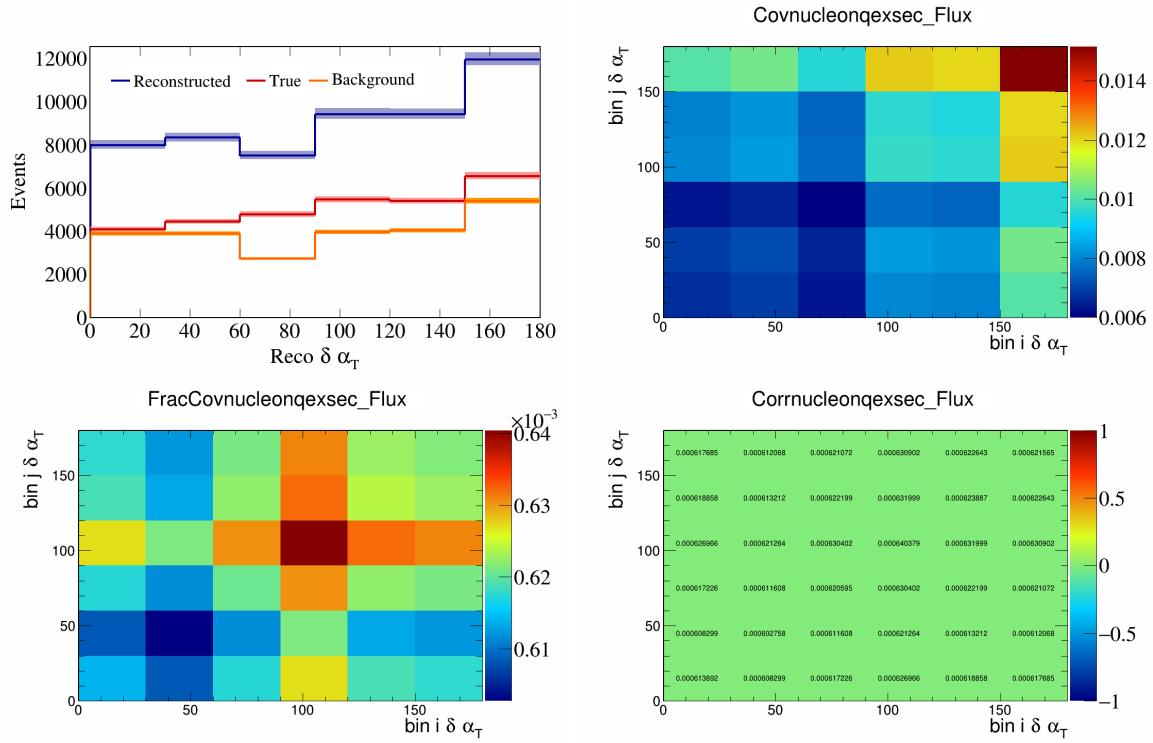


Figure 581: NucleonQeXSec variations for $\delta\alpha_T$.

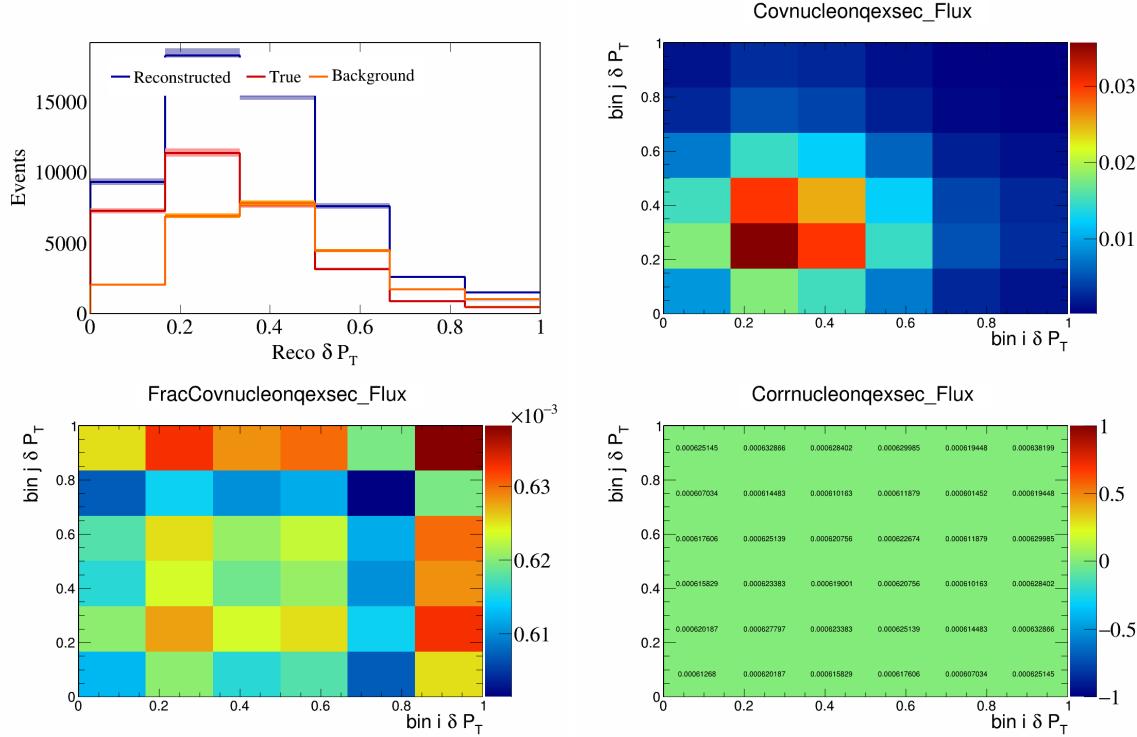


Figure 582: NucleonQeXSec variations for δP_T .

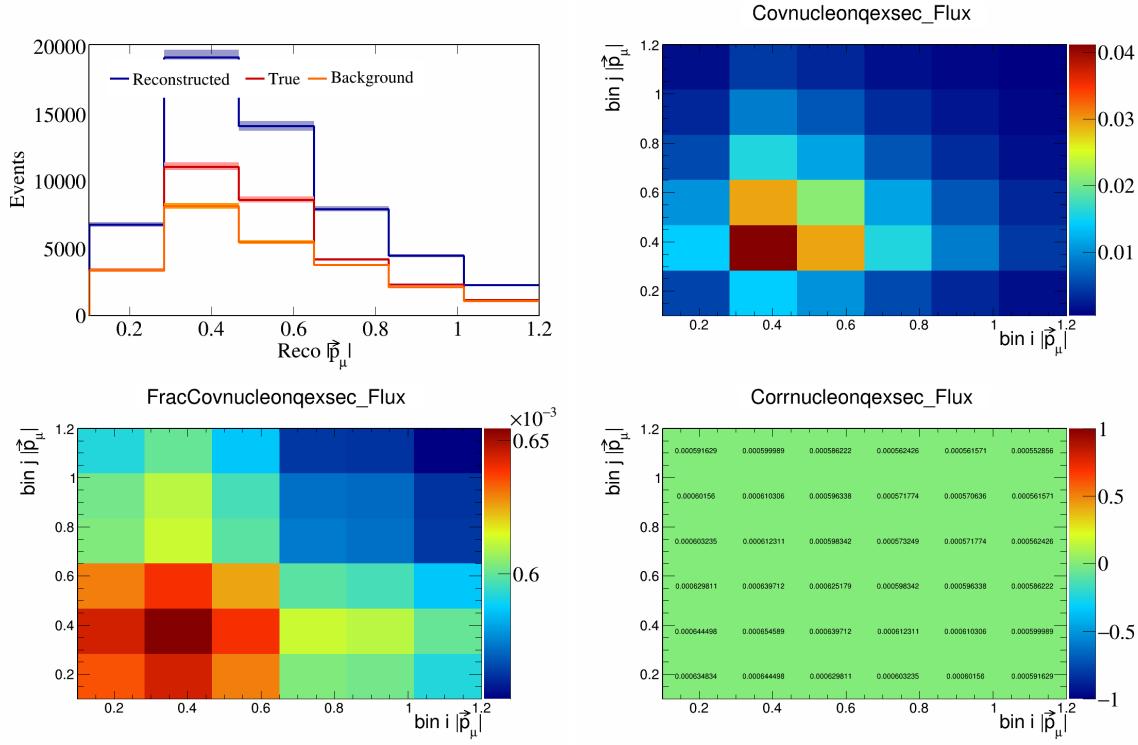


Figure 583: NucleonQeXSec variations for $|\vec{p}_\mu|$.

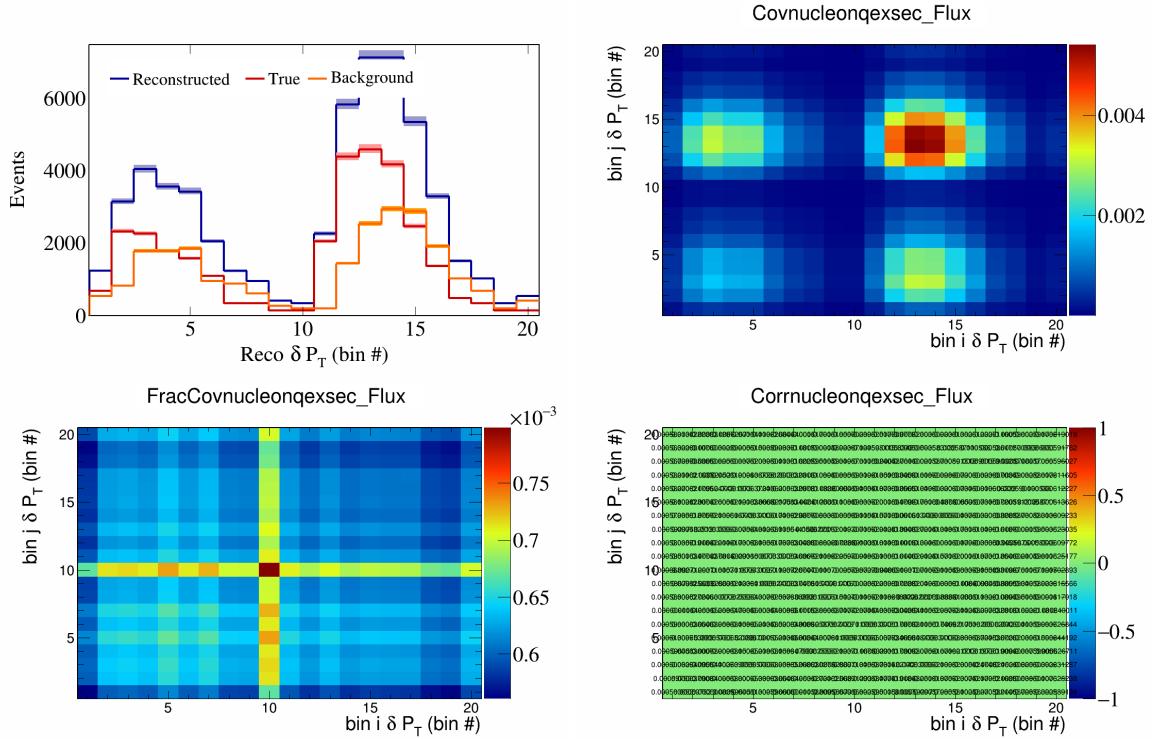


Figure 584: NucleonQeXSec variations for δP_T in $\cos(\theta_{\vec{p}_\mu})$.

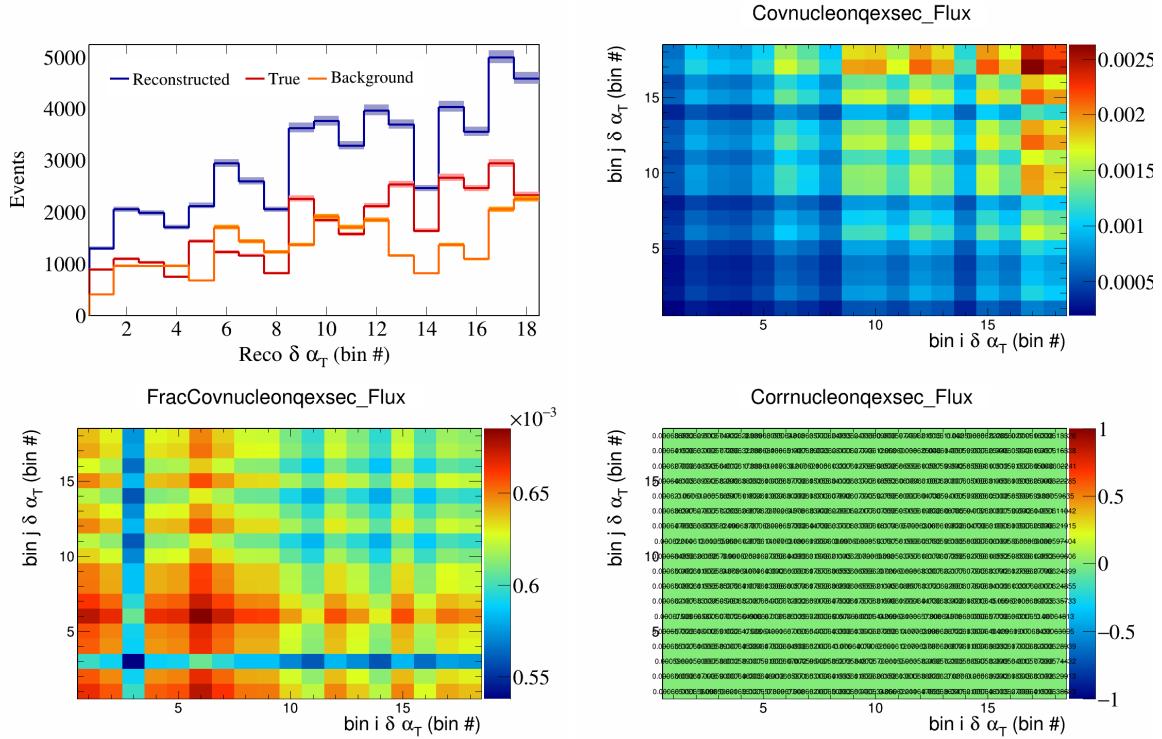


Figure 585: NucleonQeXSec variations for $\delta\alpha_T$ in $\cos(\theta_{\vec{p}_\mu})$.

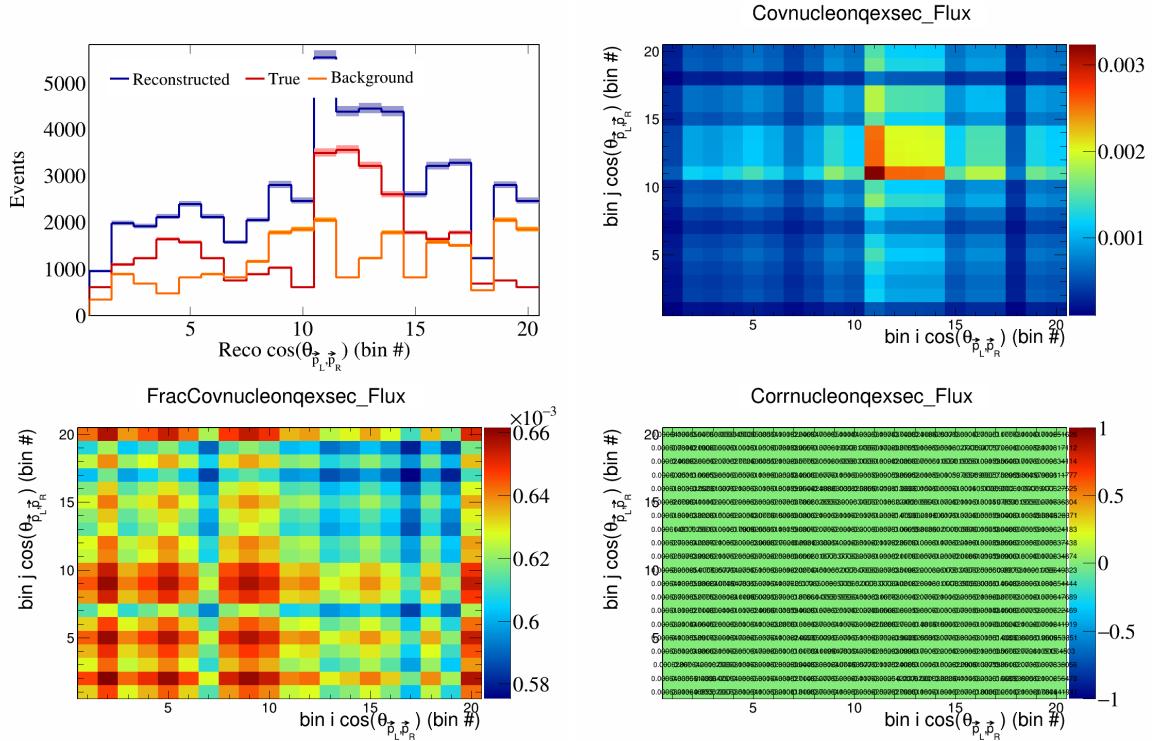


Figure 586: NucleonQeXSec variations for $\cos(\theta_{p_L, p_R})$ in $\cos(\theta_{\vec{p}_\mu})$.

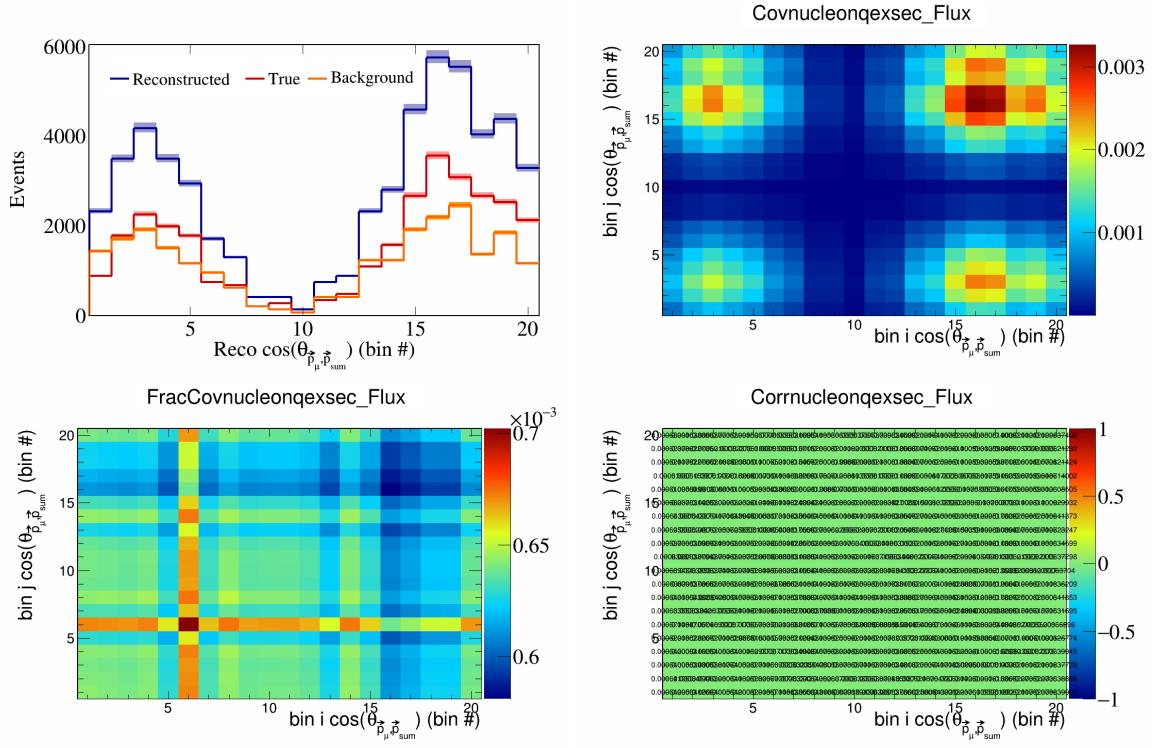


Figure 587: NucleonQeXSec variations for $\cos(\theta_{\vec{p}_\mu} \cdot \vec{p}_{\text{sum}})$ in $\cos(\theta_{\vec{p}_\mu})$.

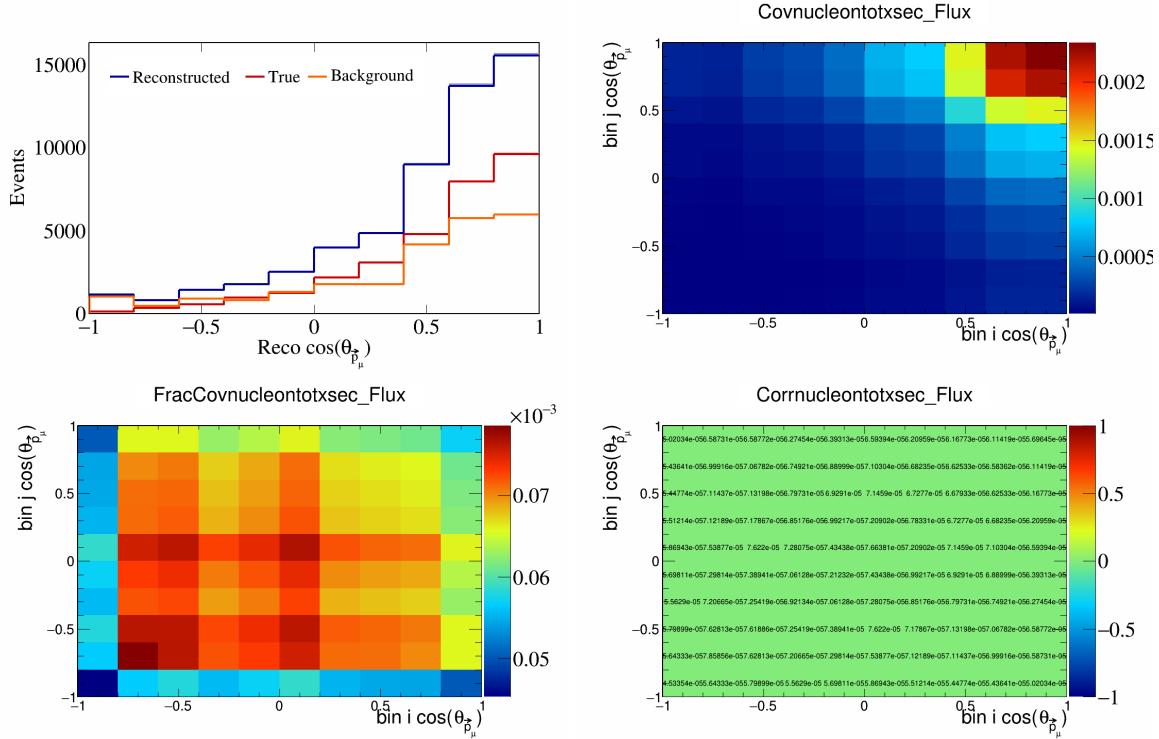


Figure 588: NucleonTotXSec variations for $\cos(\theta_{\vec{p}_\mu})$.

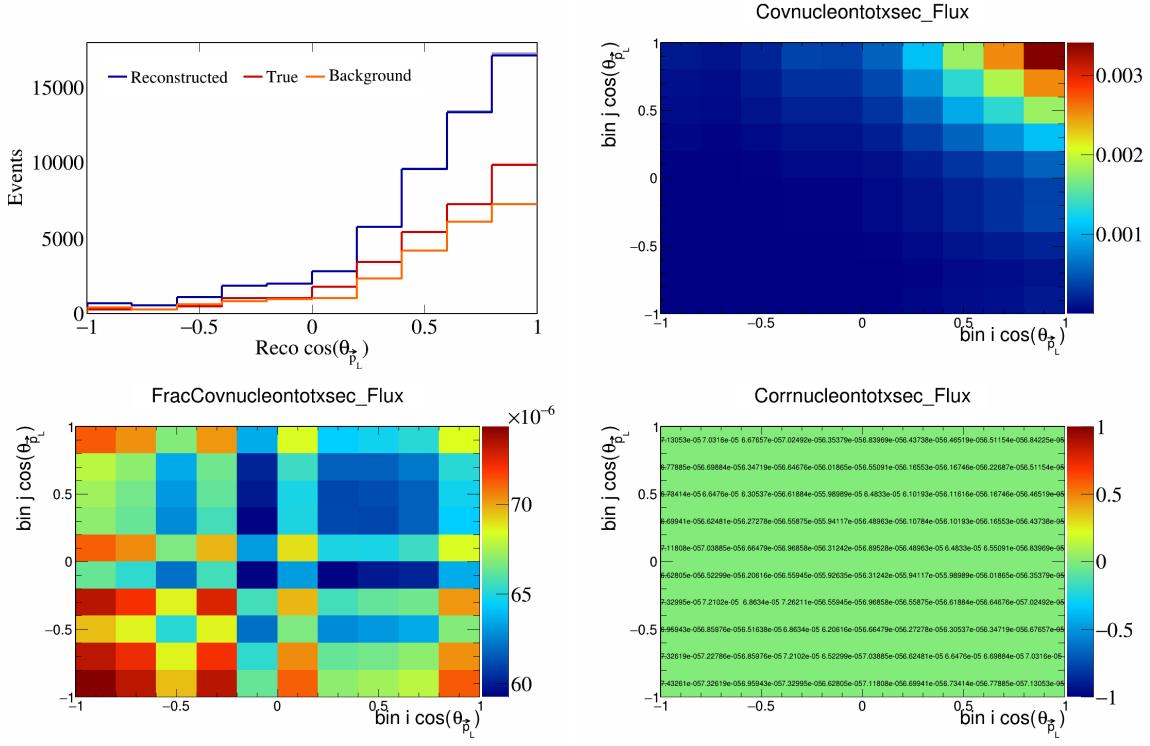


Figure 589: NucleonTotXSec variations for $\cos(\theta_{\vec{p}_L})$.

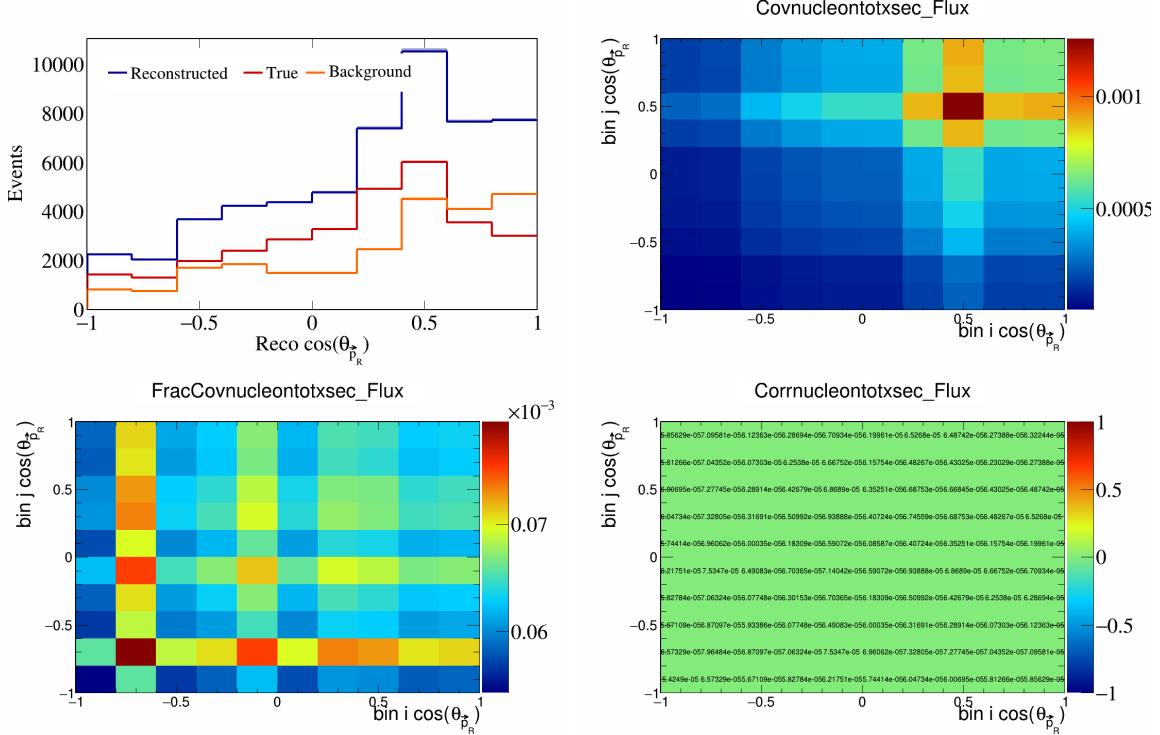


Figure 590: NucleonTotXSec variations for $\cos(\theta_{\vec{p}_R})$.

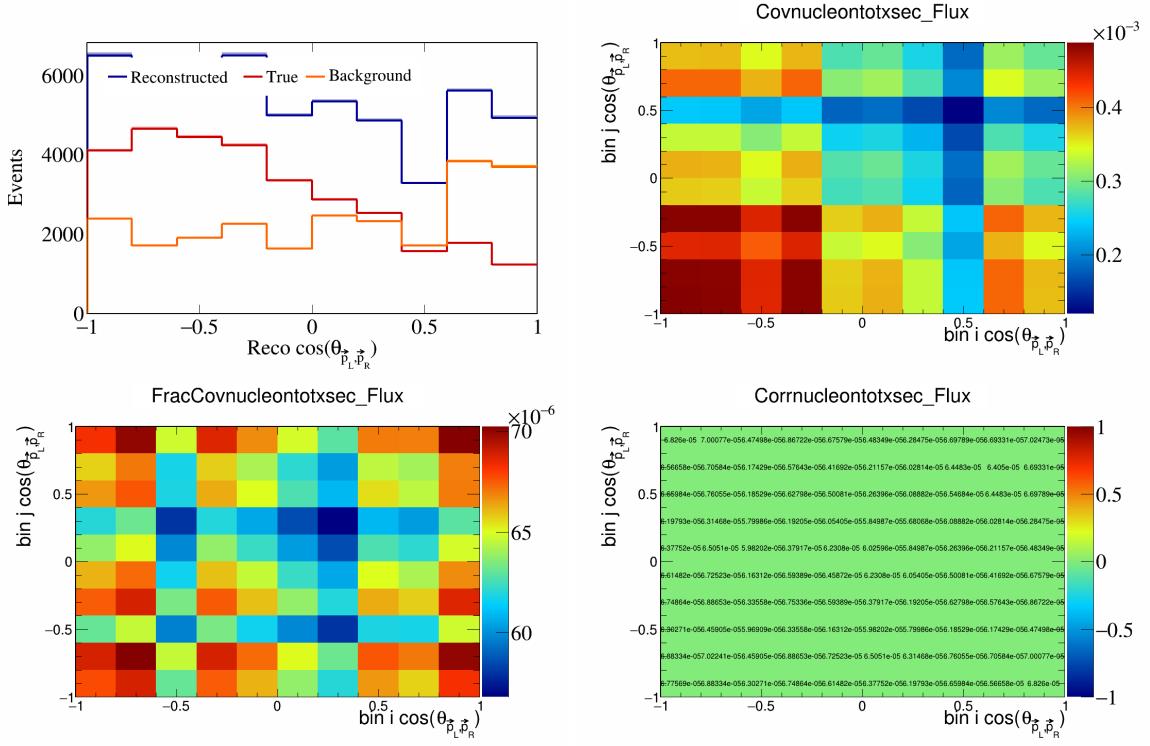


Figure 591: NucleonTotXSec variations for $\cos(\theta_{\vec{p}_L, \vec{p}_R})$.

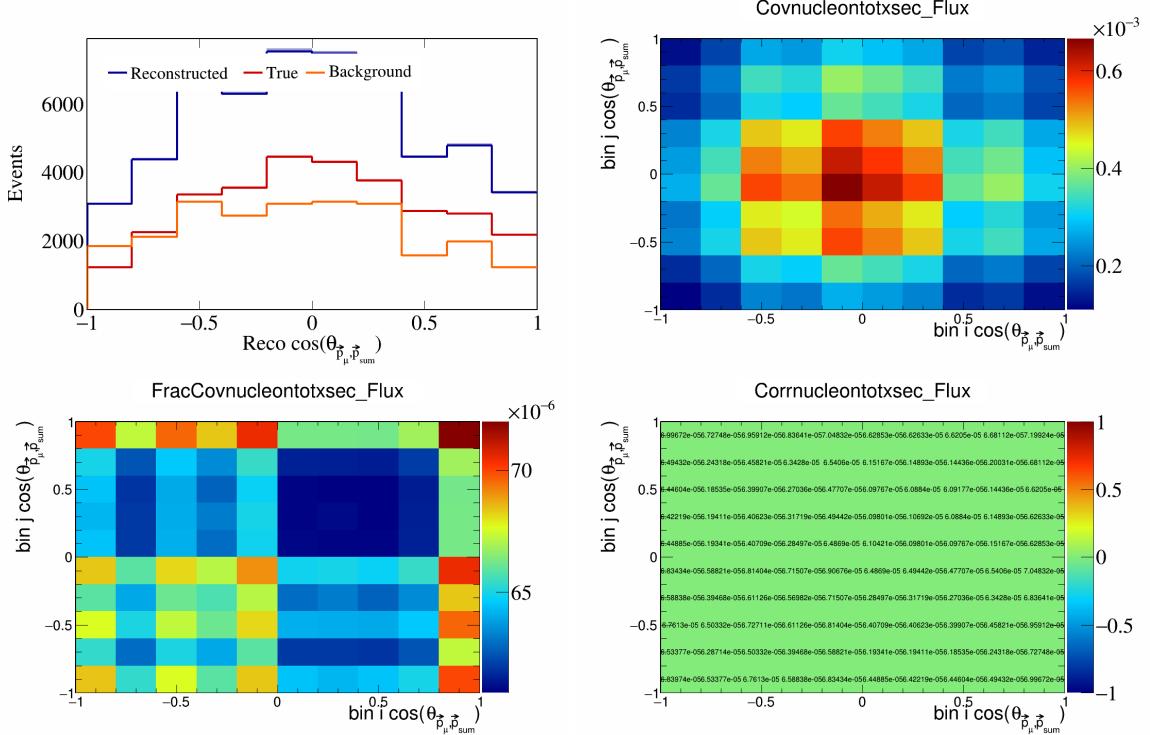


Figure 592: NucleonTotXSec variations for $\cos(\theta_{\vec{p}_\mu, \vec{p}_{\text{sum}}})$.

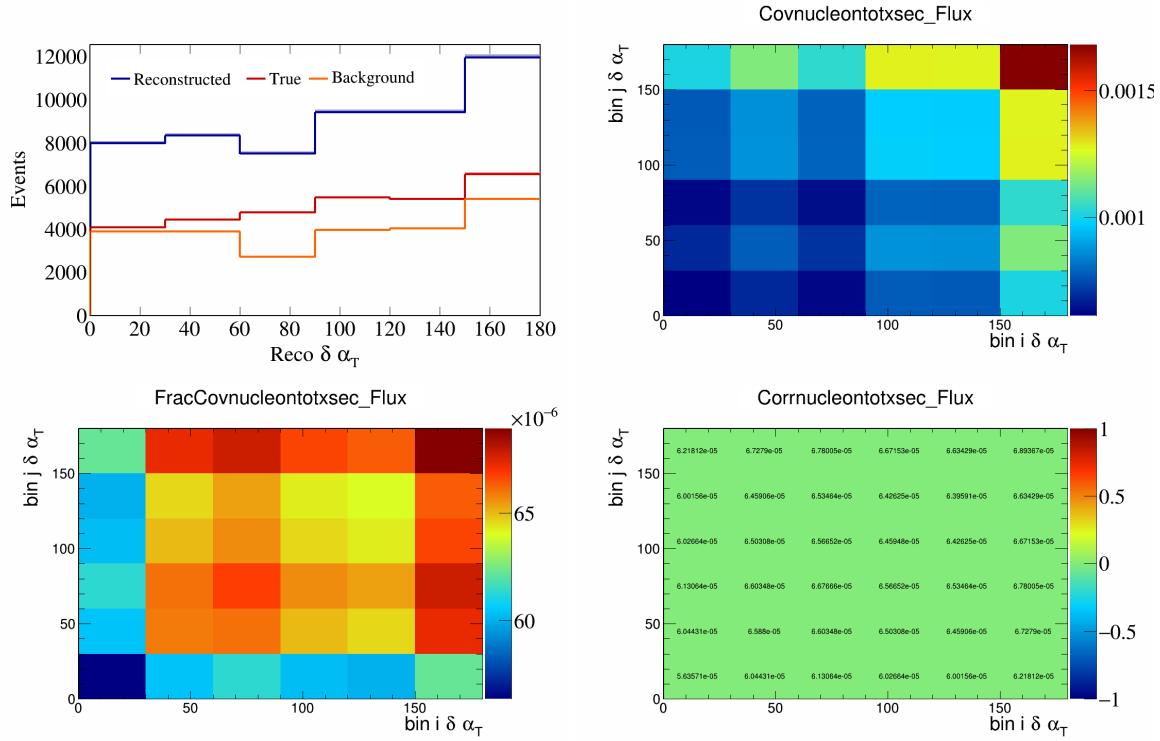


Figure 593: NucleonTotXSec variations for $\delta \alpha_T$.

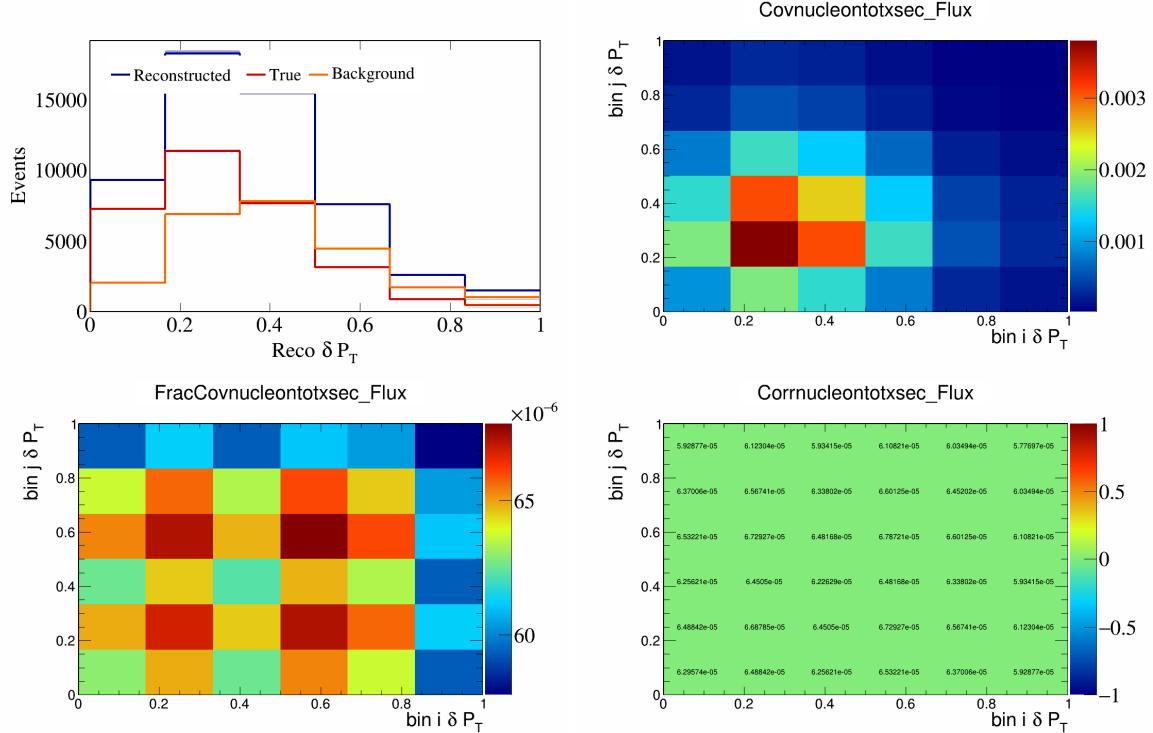


Figure 594: NucleonTotXSec variations for δP_T .

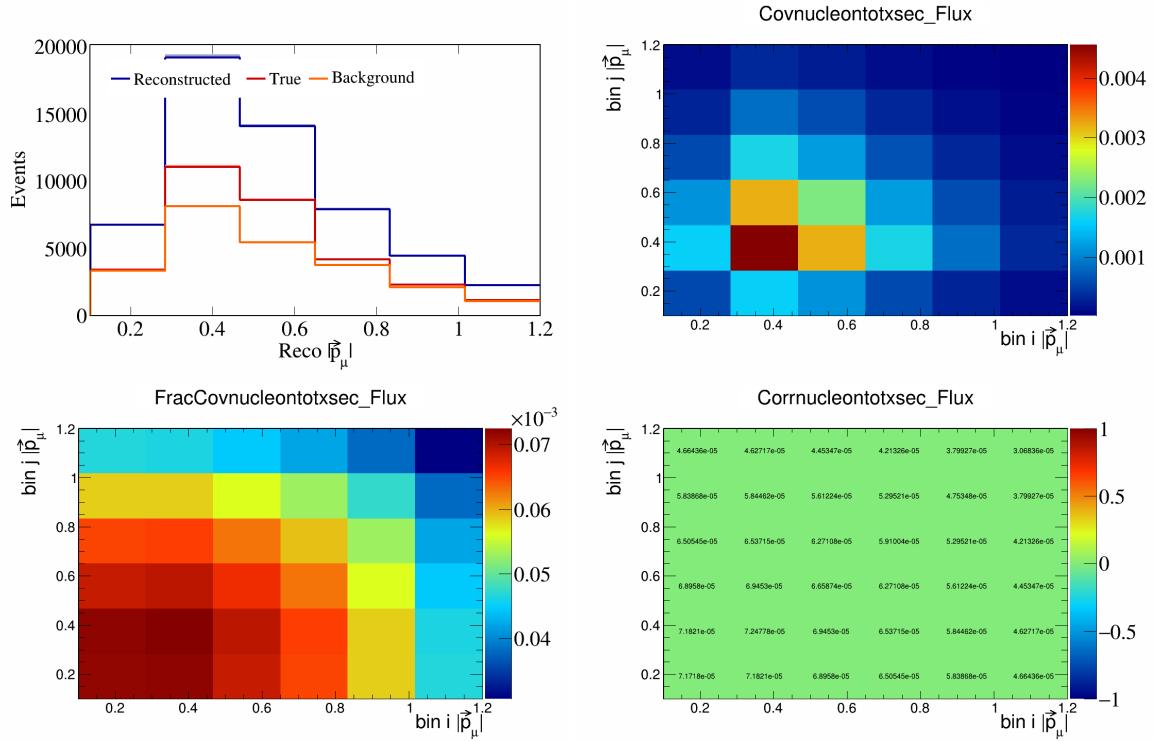


Figure 595: NucleonTotXSec variations for $|\vec{p}_\mu|$.

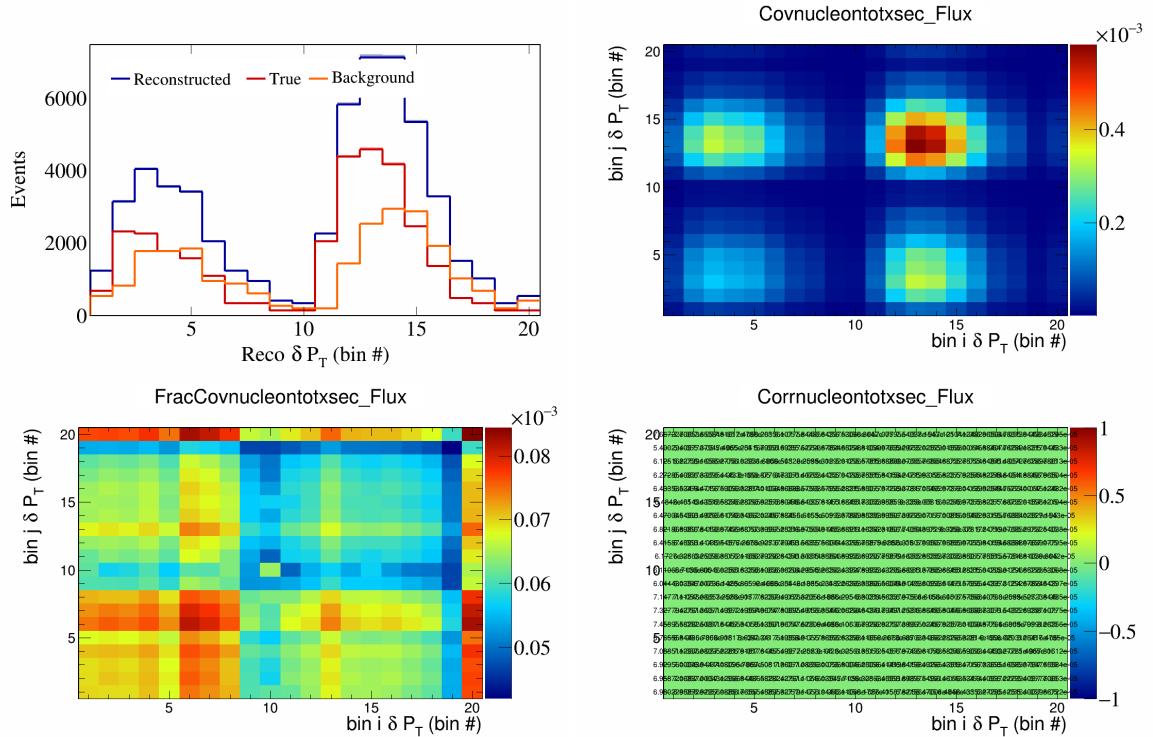


Figure 596: NucleonTotXSec variations for δP_T in $\cos(\theta_{F_\mu})$.

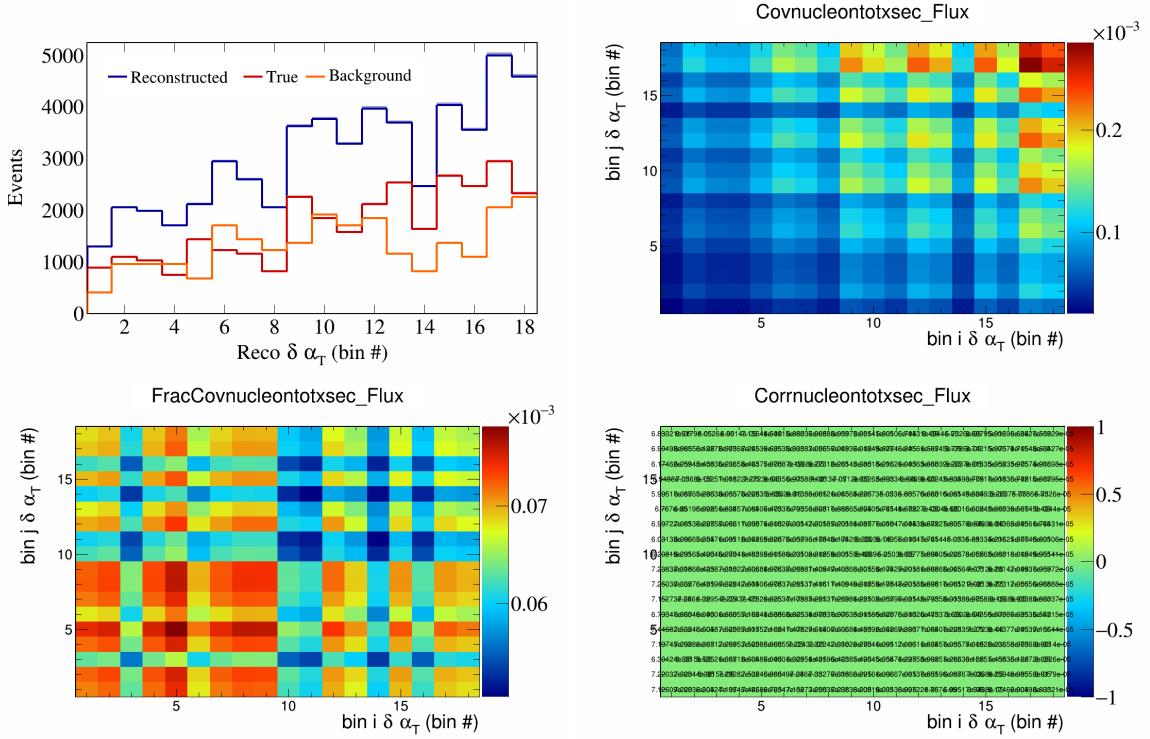


Figure 597: NucleonTotXSec variations for $\delta\alpha_T$ in $\cos(\theta_{\vec{p}_\mu})$.

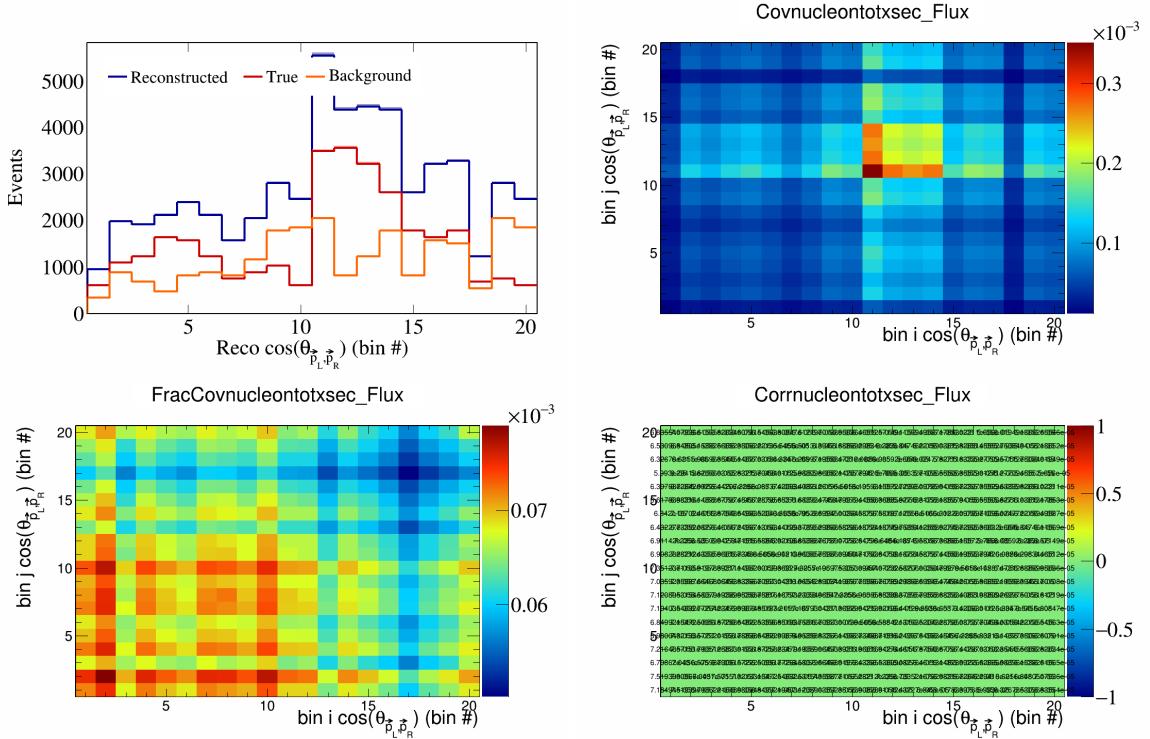


Figure 598: NucleonTotXSec variations for $\cos(\theta_{\vec{p}_L, \vec{p}_R})$ in $\cos(\theta_{\vec{p}_\mu})$.

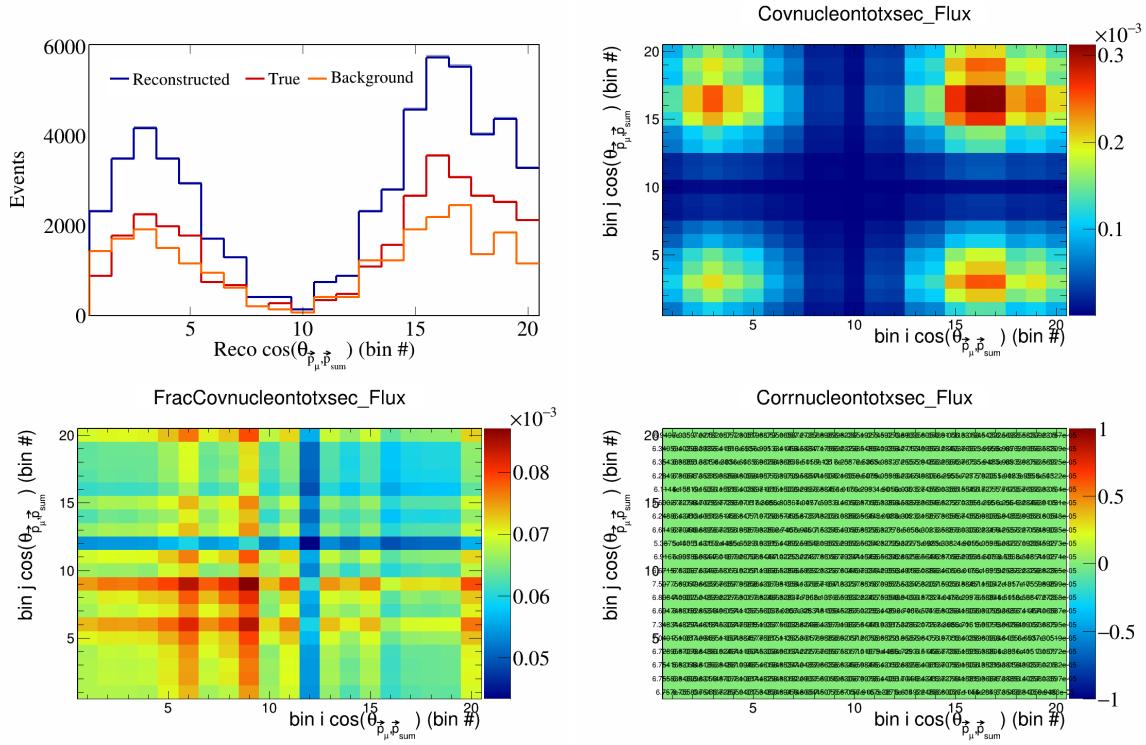


Figure 599: NucleonTotXSec variations for $\cos(\theta_{\vec{p}_\mu, \vec{p}_{\text{sum}}})$ in $\cos(\theta_{\vec{p}_\mu})$.

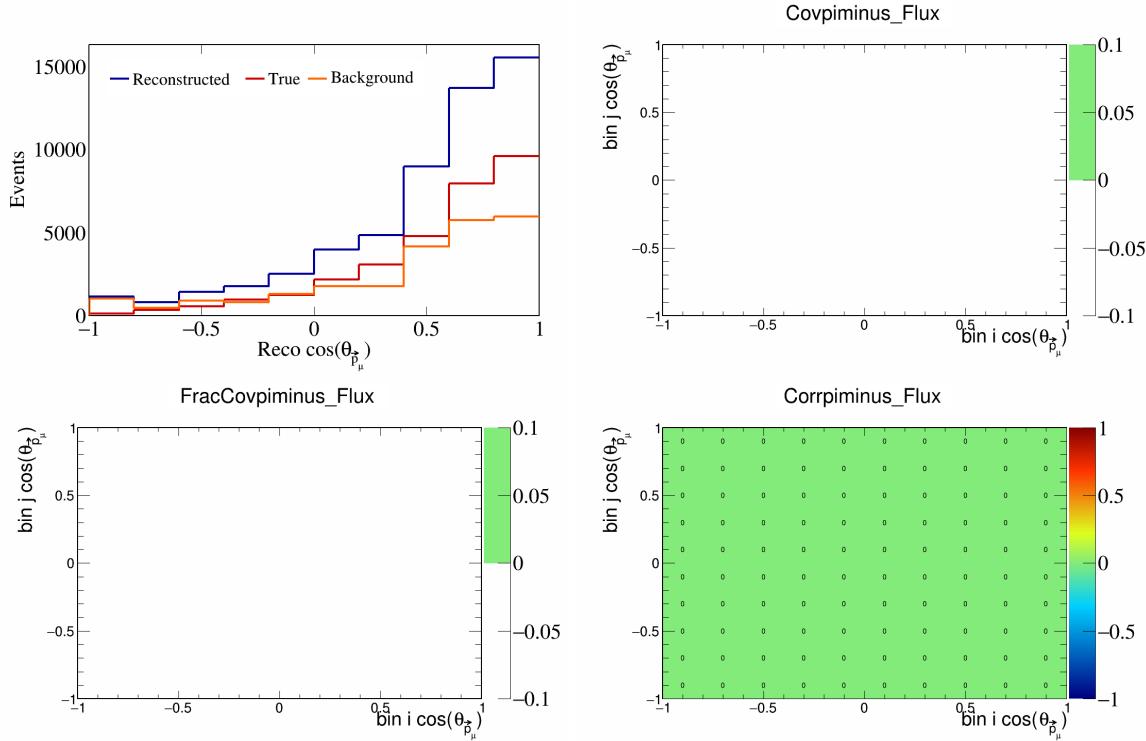


Figure 600: PiMinus variations for $\cos(\theta_{\vec{p}_\mu})$.

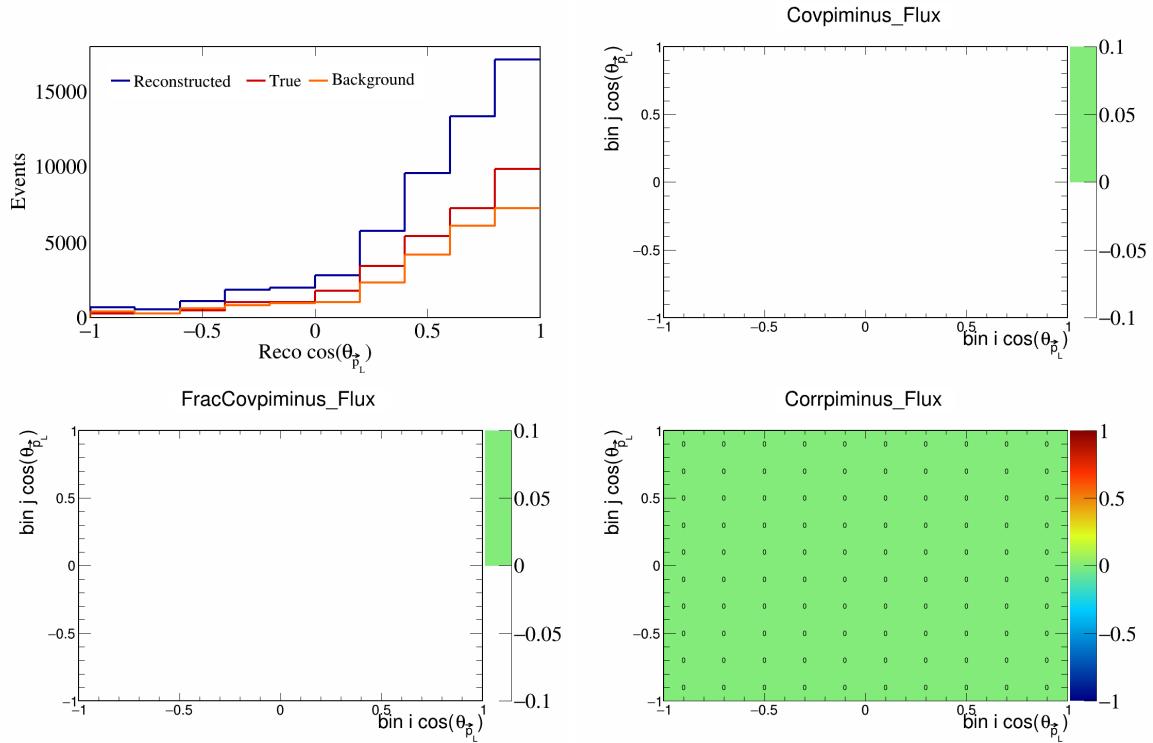


Figure 601: PiMinus variations for $\cos(\theta_{\vec{p}_L})$.

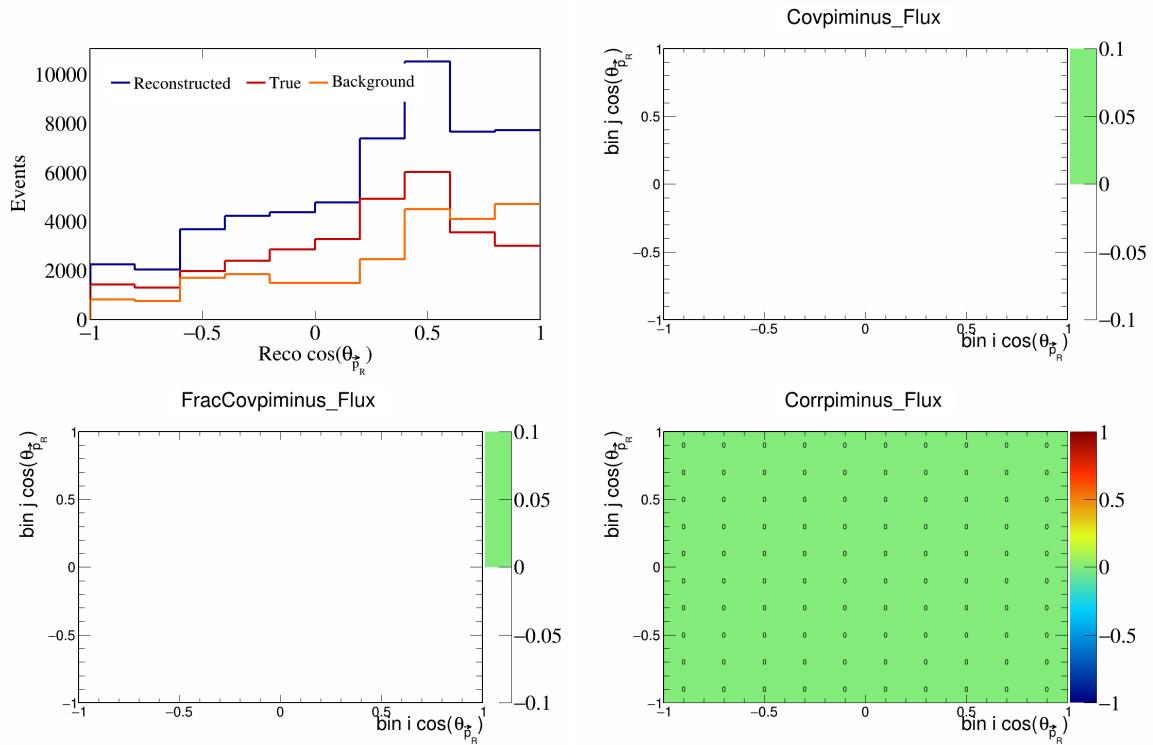


Figure 602: PiMinus variations for $\cos(\theta_{\vec{p}_R})$.

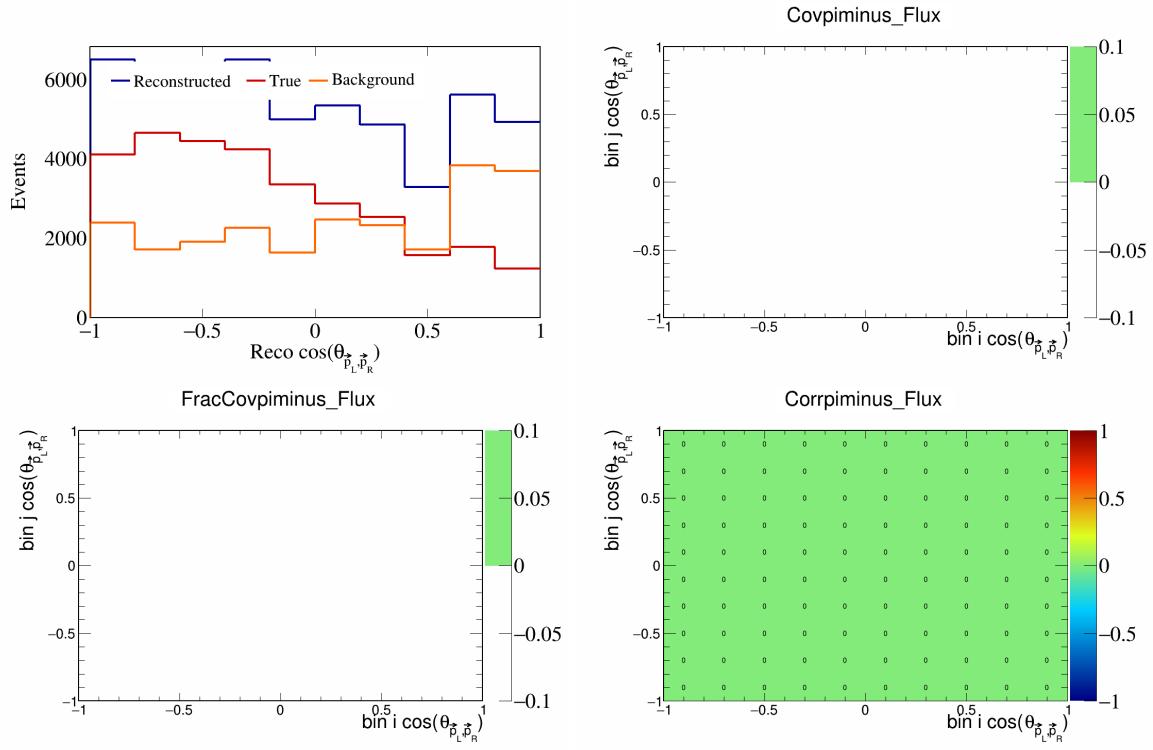


Figure 603: PiMinus variations for $\cos(\theta_{\vec{p}_L, \vec{p}_R})$.

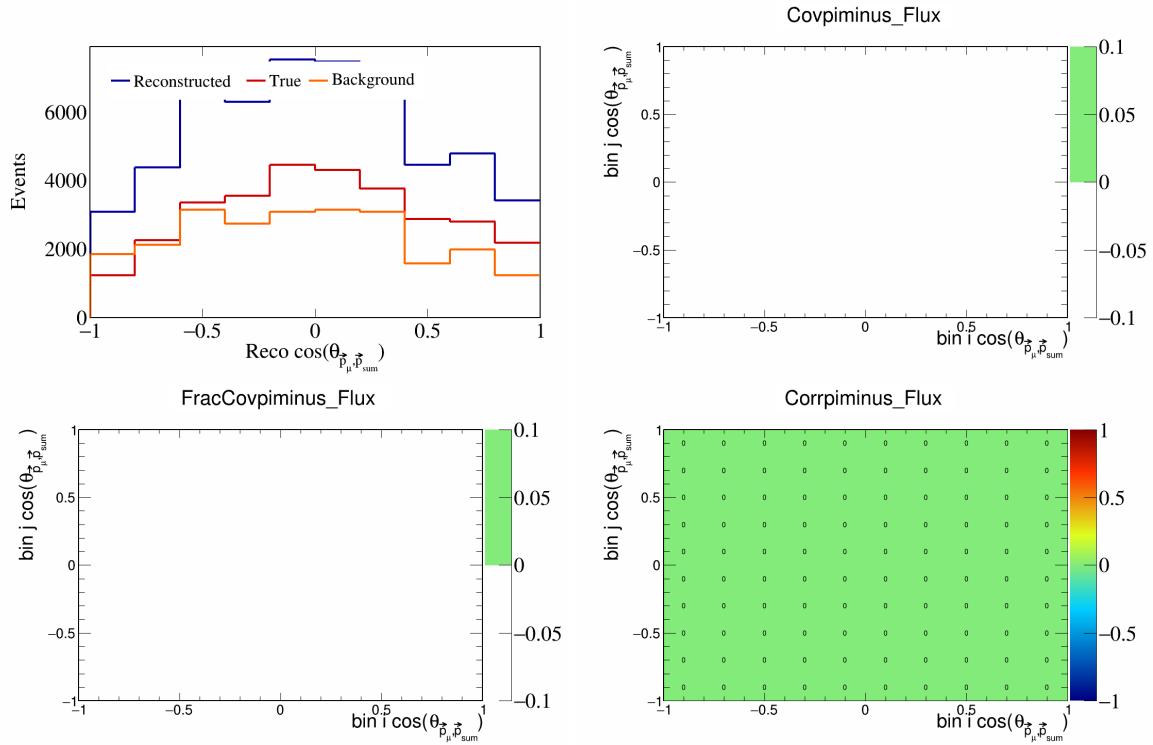


Figure 604: PiMinus variations for $\cos(\theta_{\vec{p}_\mu, \vec{p}_{\text{sum}}})$.

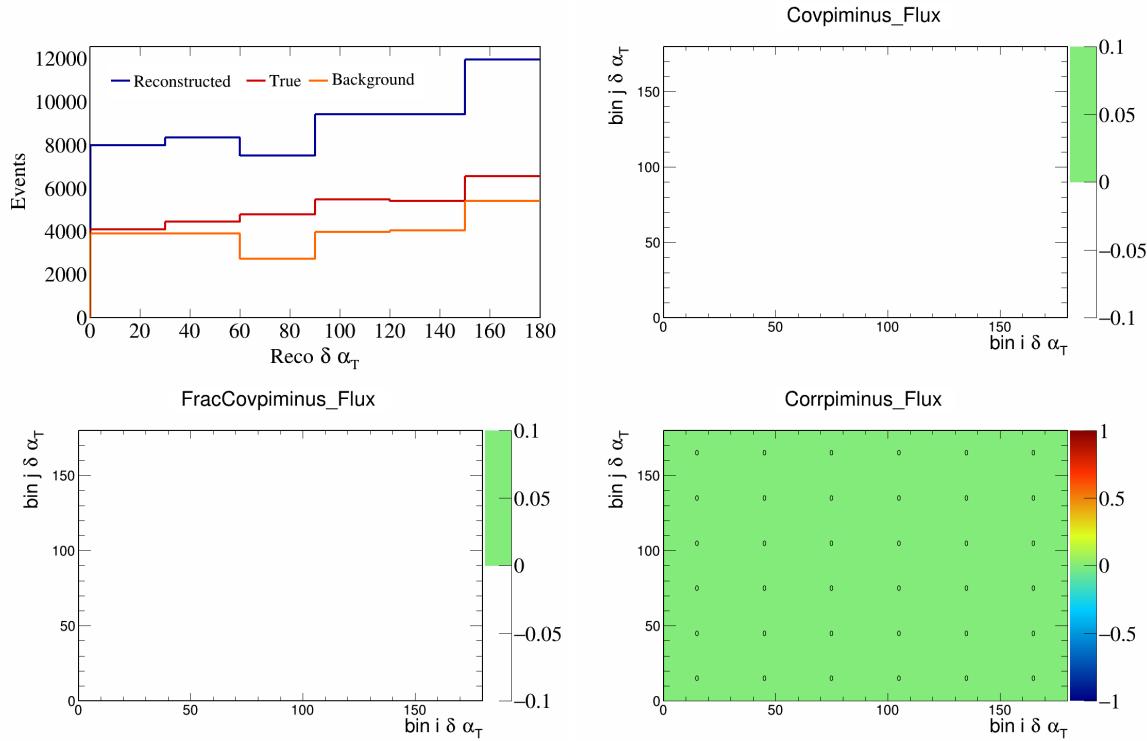


Figure 605: PiMinus variations for $\delta \alpha_T$.

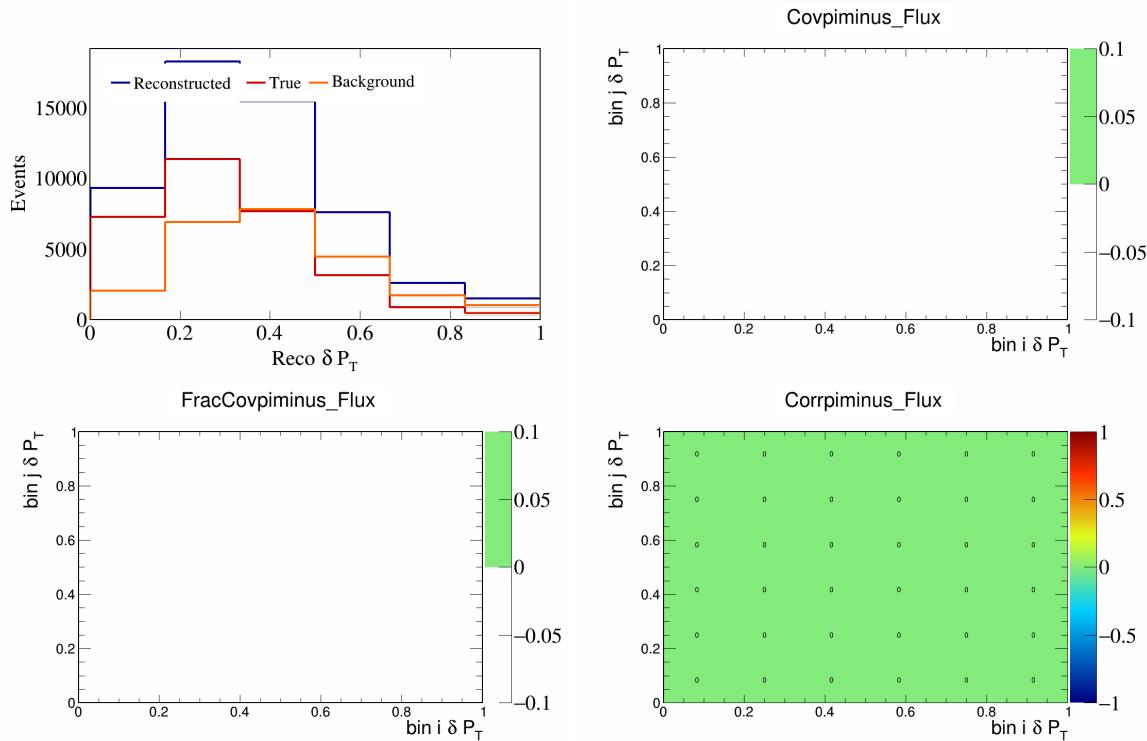


Figure 606: PiMinus variations for δP_T .

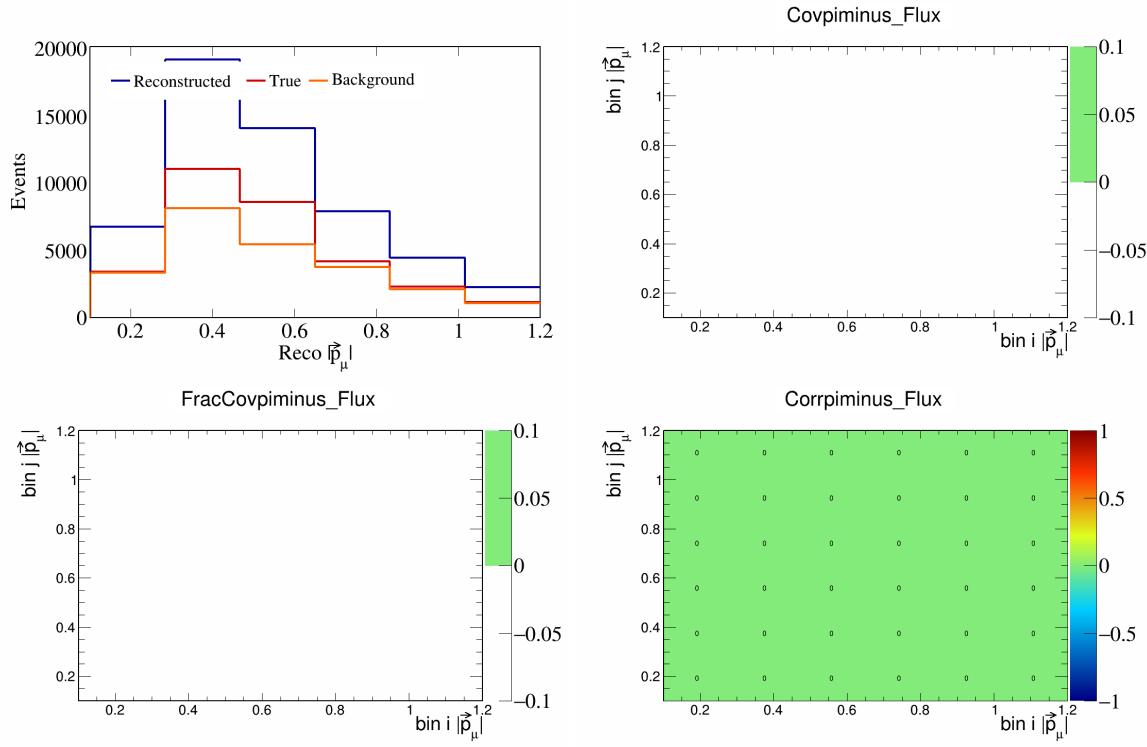


Figure 607: PiMinus variations for $|\vec{p}_\mu|$.

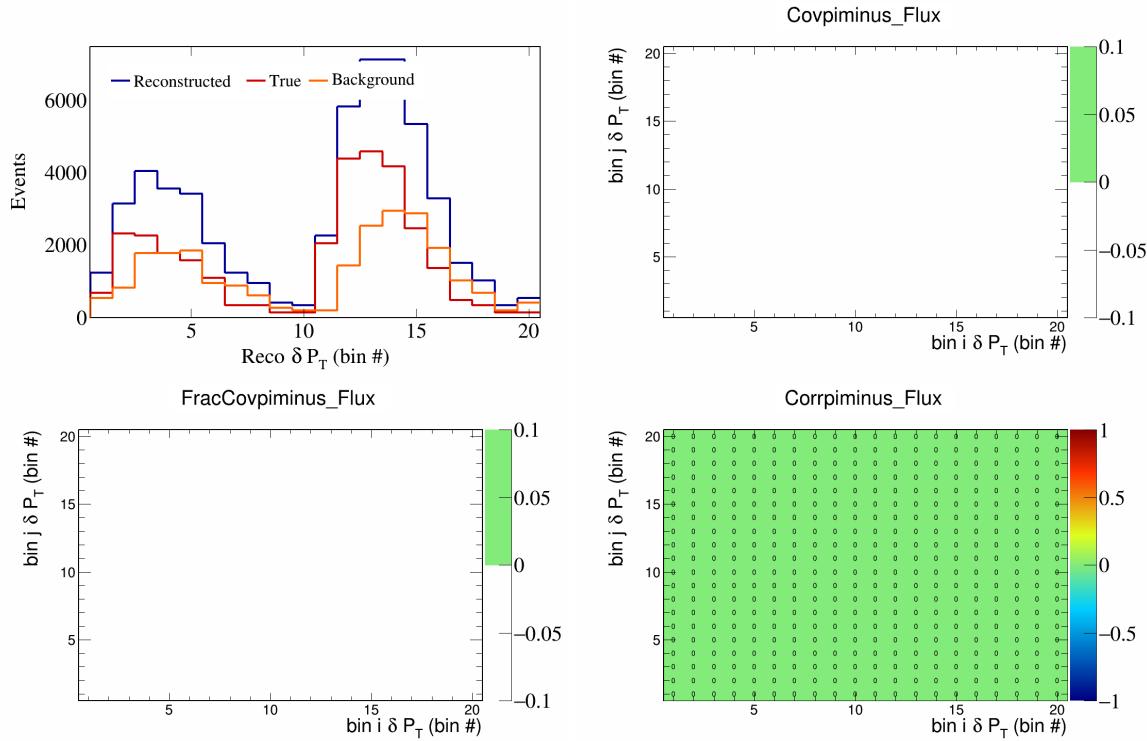


Figure 608: PiMinus variations for δP_T in $\cos(\theta_{\vec{p}_\mu})$.

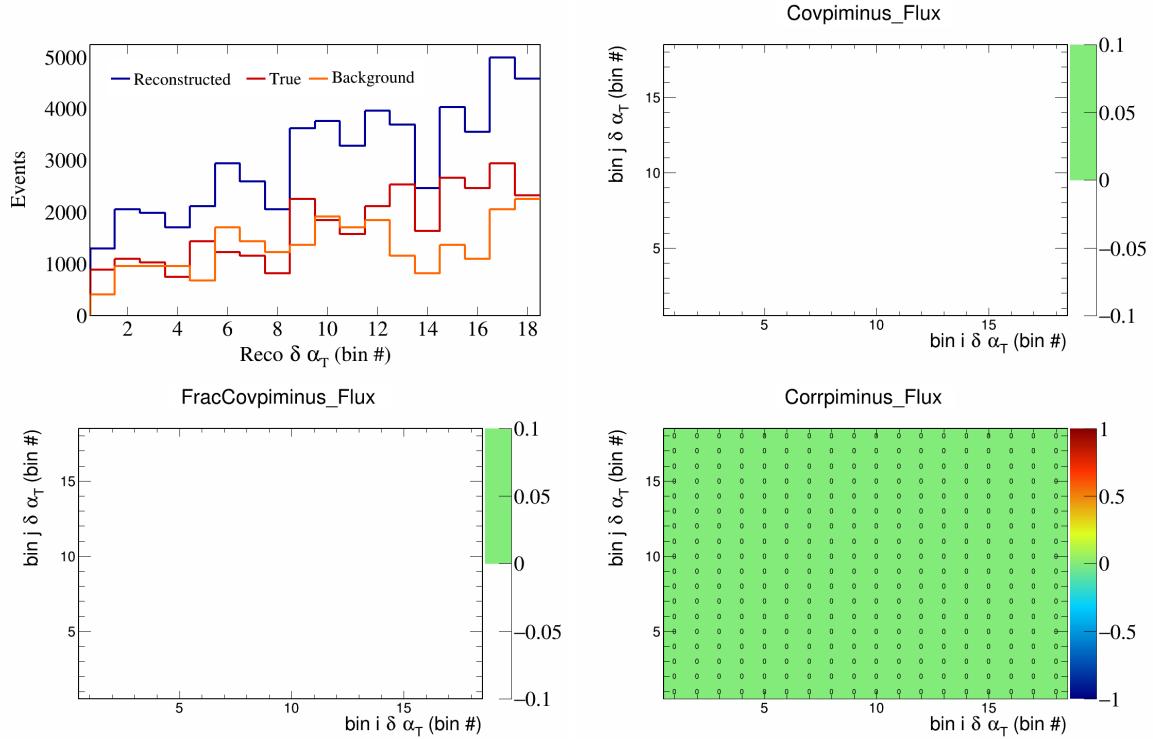


Figure 609: PiMinus variations for $\delta\alpha_T$ in $\cos(\theta_{\vec{p}_\mu})$.

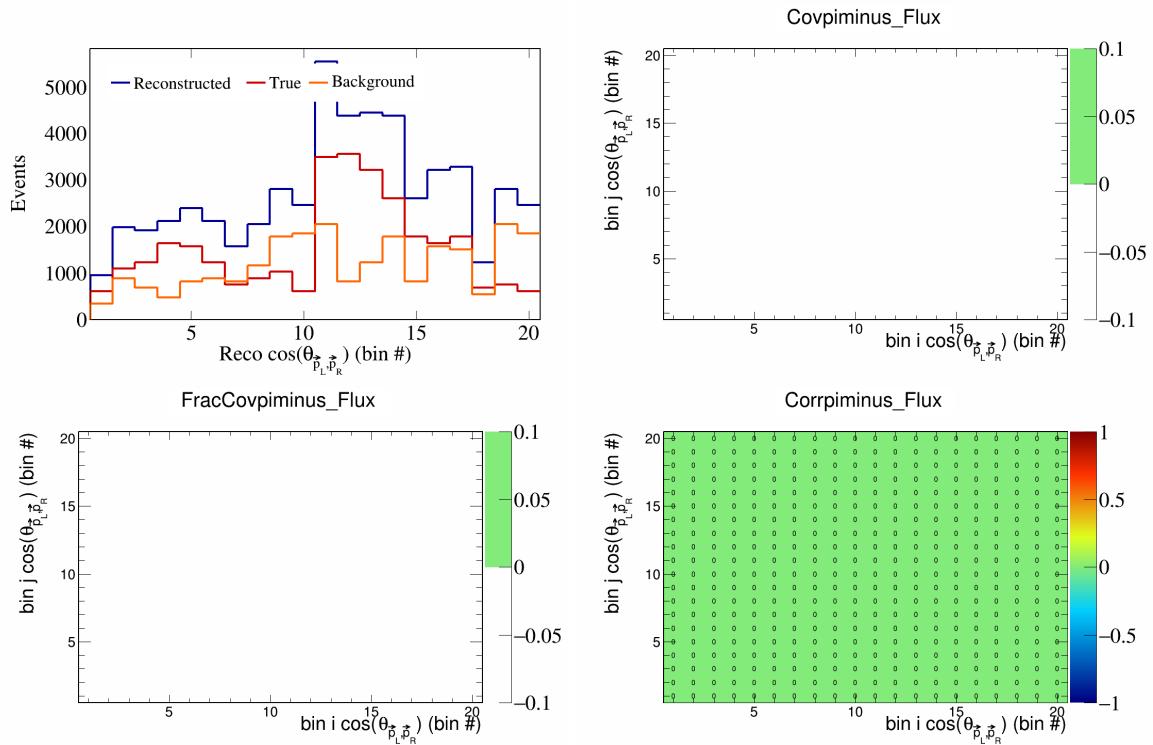


Figure 610: PiMinus variations for $\cos(\theta_{p_L, \vec{p}_R})$ in $\cos(\theta_{\vec{p}_\mu})$.

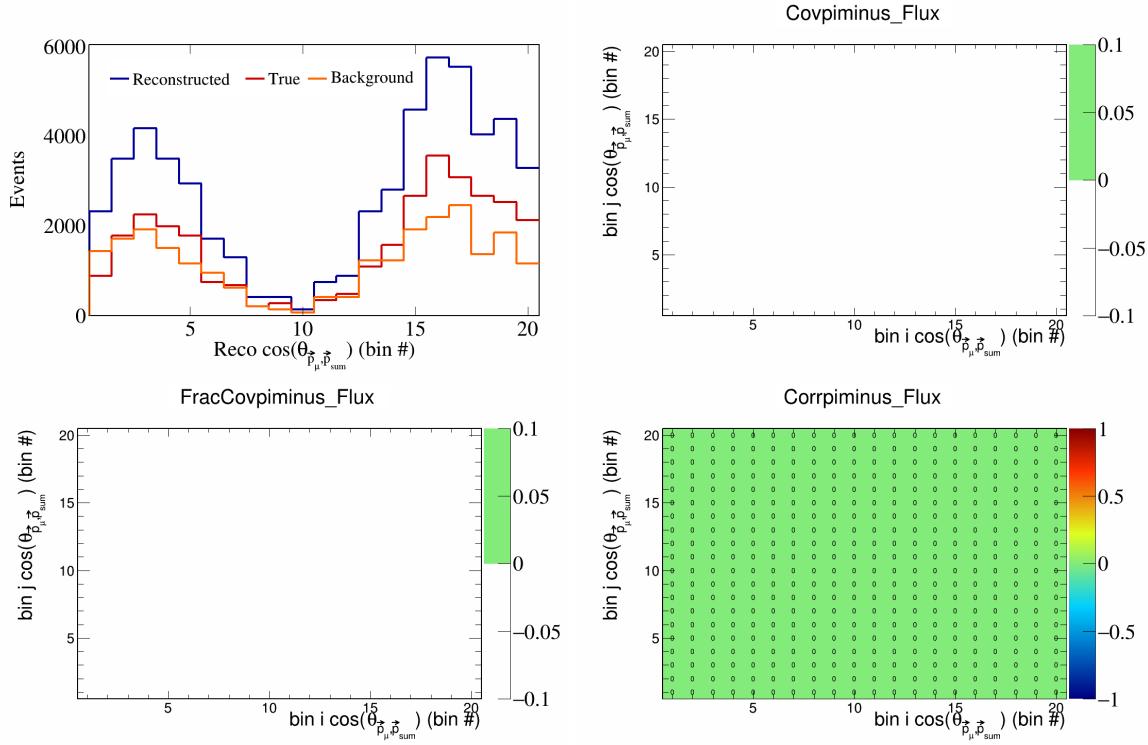


Figure 611: PiMinus variations for $\cos(\theta_{\vec{p}_\mu} \vec{p}_{\text{sum}})$ in $\cos(\theta_{\vec{p}_\mu})$.

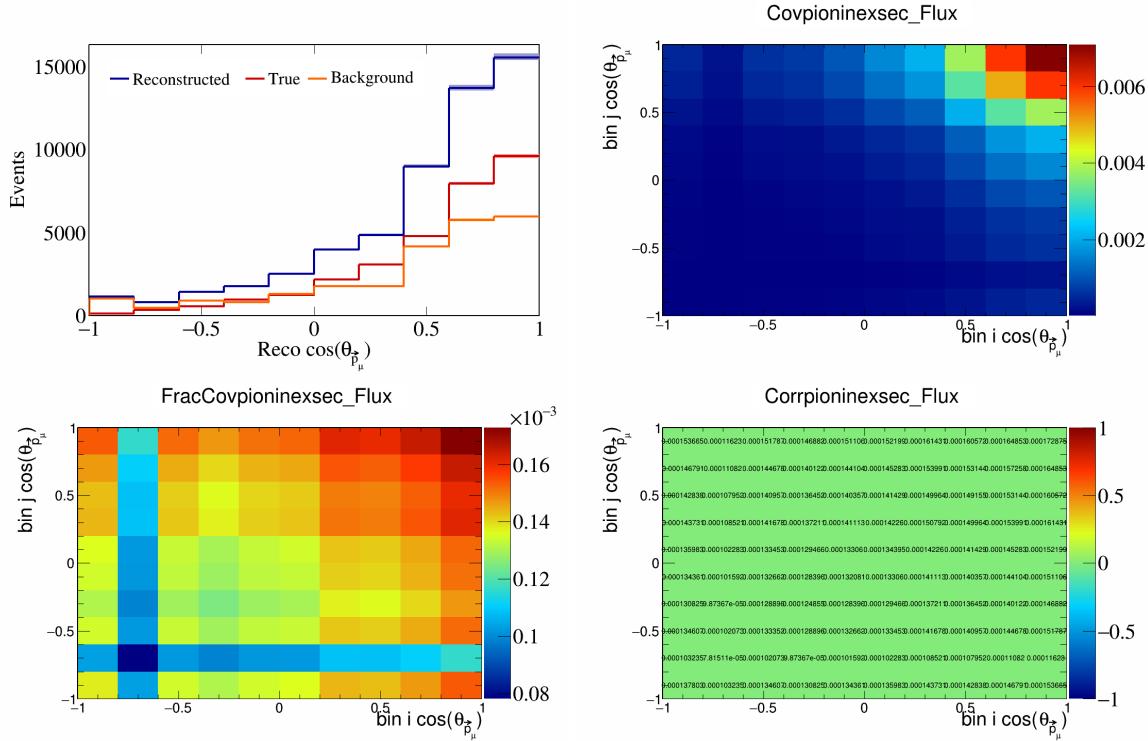


Figure 612: PionIneXSec variations for $\cos(\theta_{\vec{p}_\mu})$.

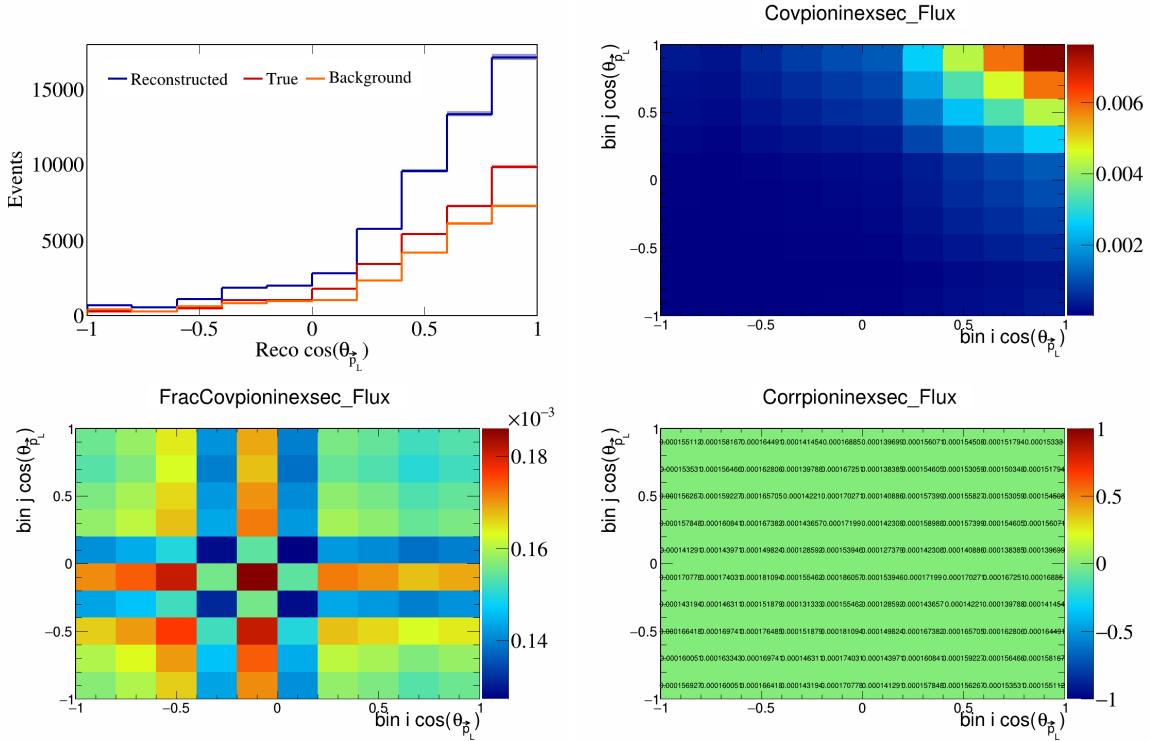


Figure 613: PionIneXSec variations for $\cos(\theta_{\vec{p}_L})$.

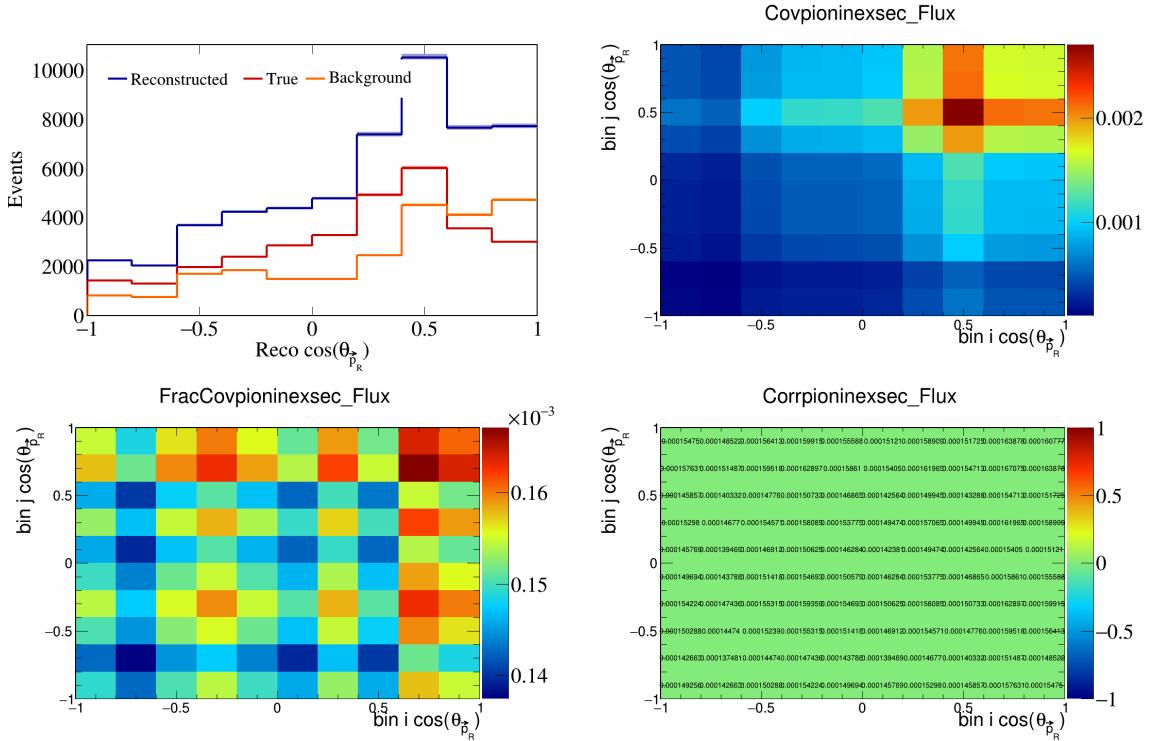


Figure 614: PionIneXSec variations for $\cos(\theta_{\vec{p}_R})$.

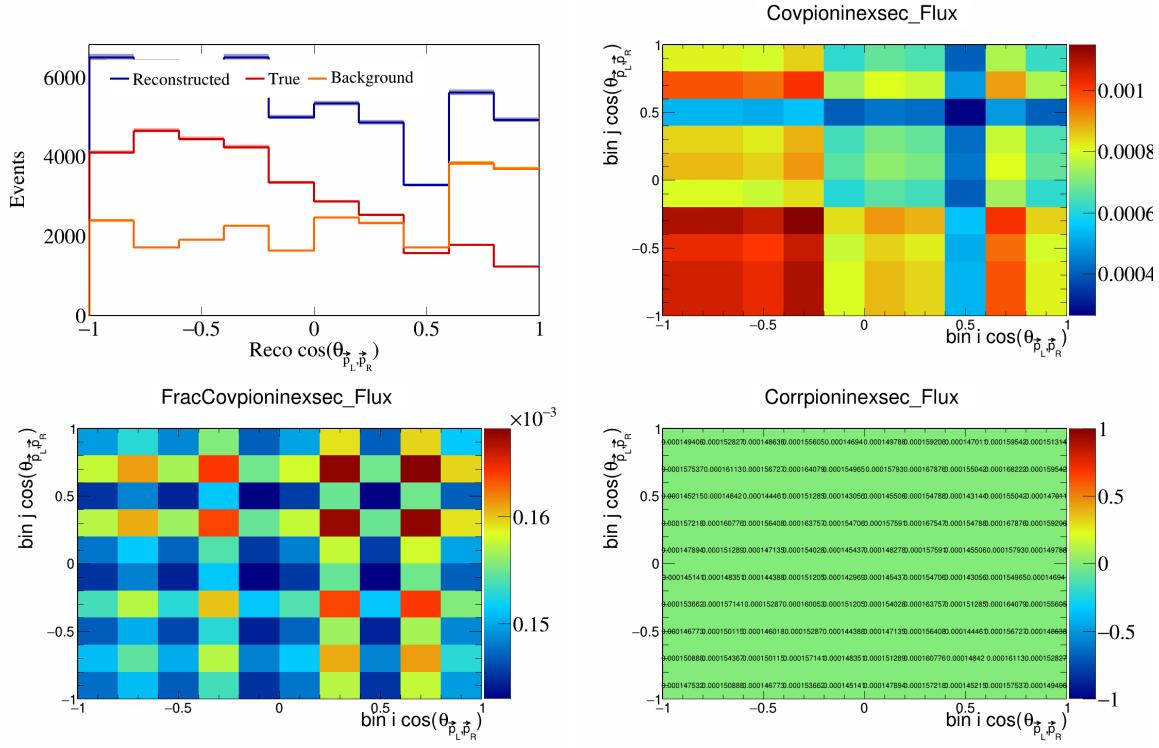


Figure 615: PionIneXSec variations for $\cos(\theta_{\vec{p}_L, \vec{p}_R})$.

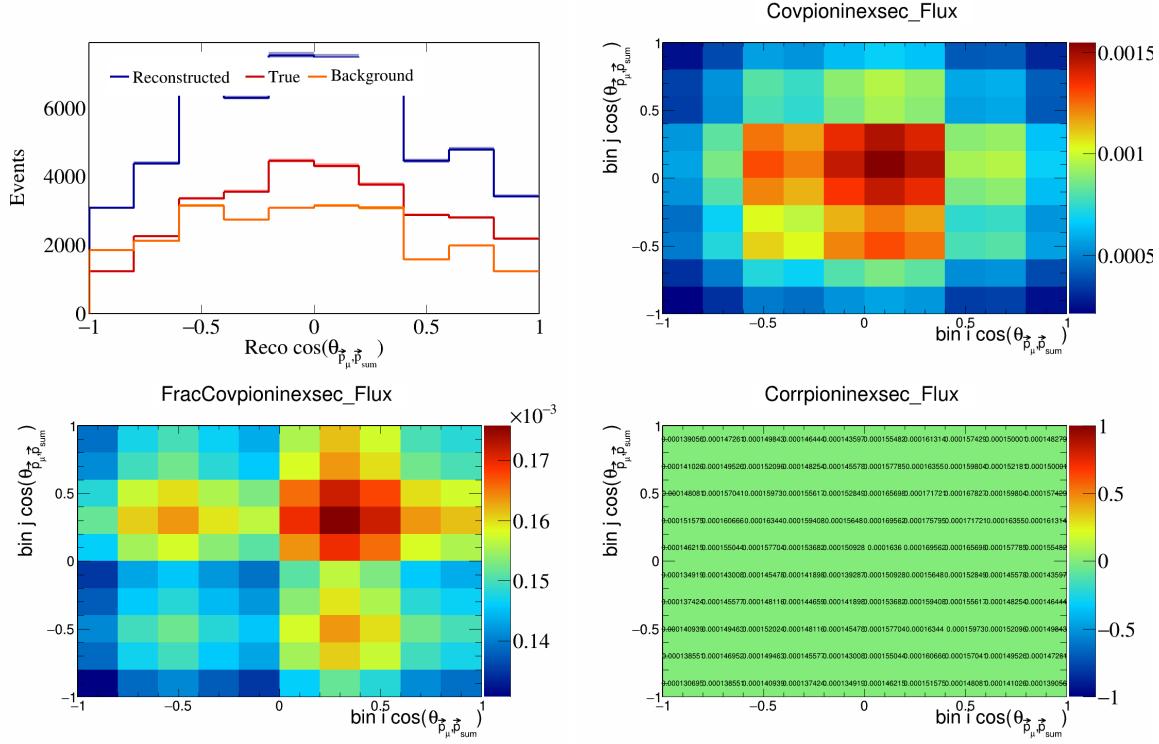


Figure 616: PionIneXSec variations for $\cos(\theta_{\vec{p}_\mu, \vec{p}_{\text{sum}}})$.

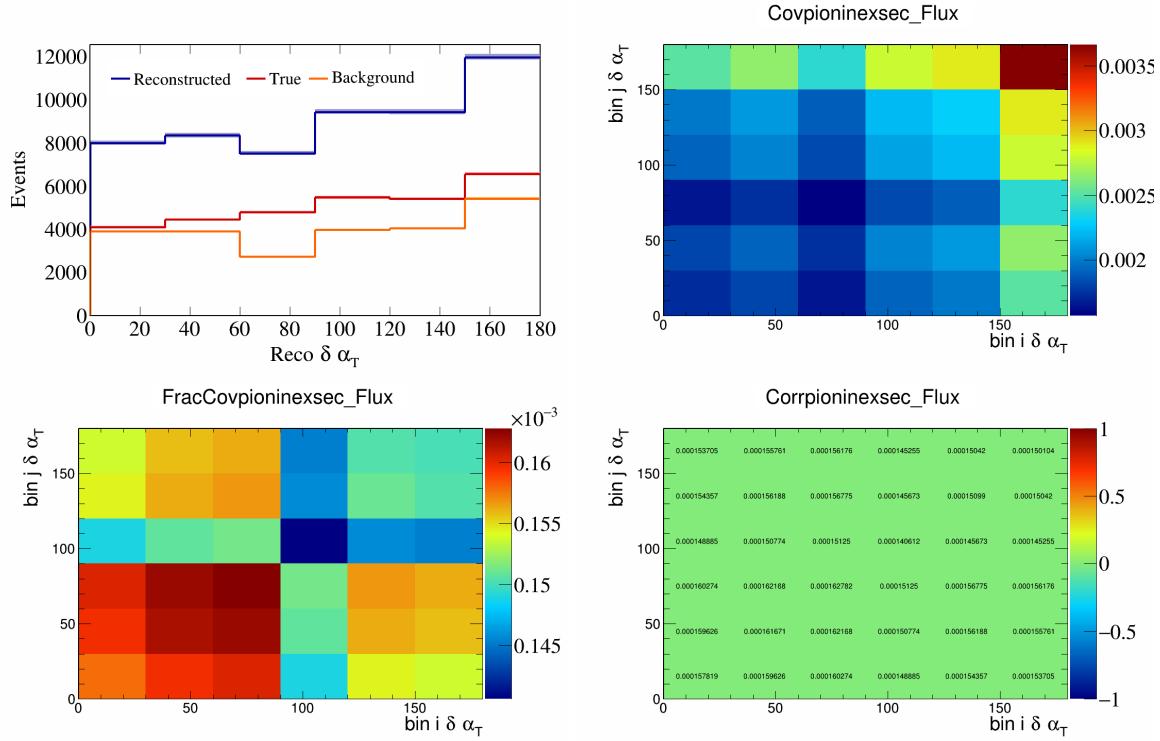


Figure 617: PionIneXSec variations for $\delta\alpha_T$.

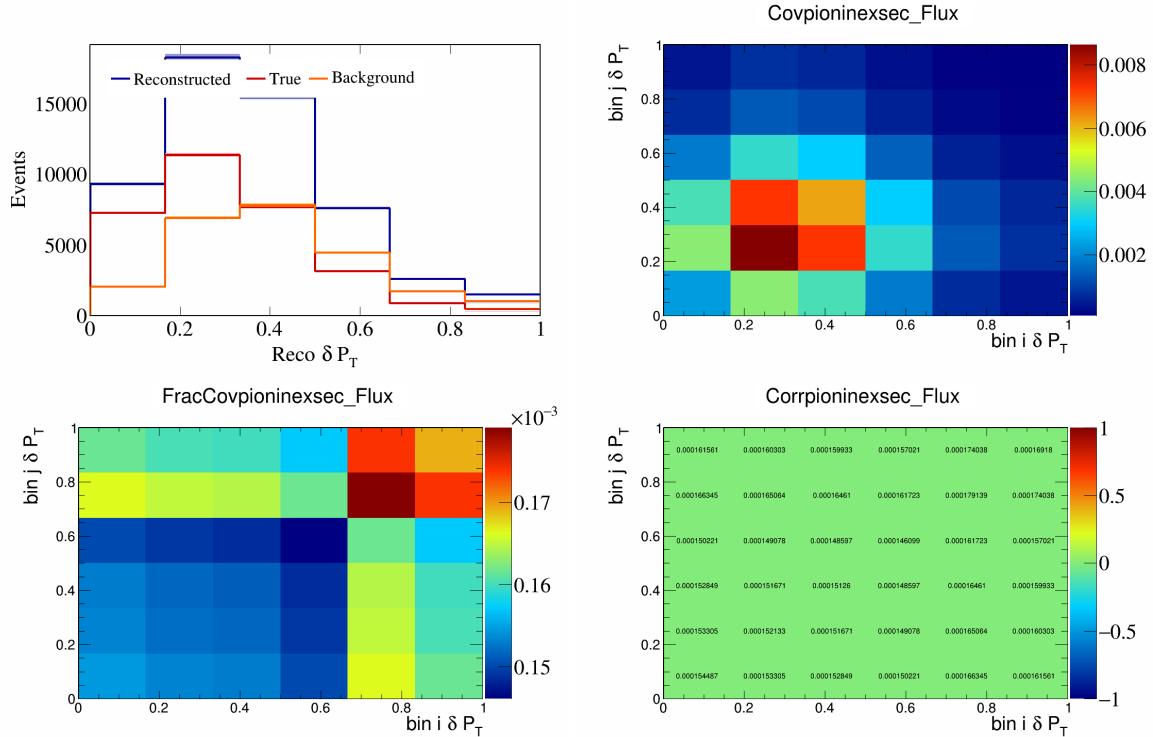


Figure 618: PionIneXSec variations for δP_T .

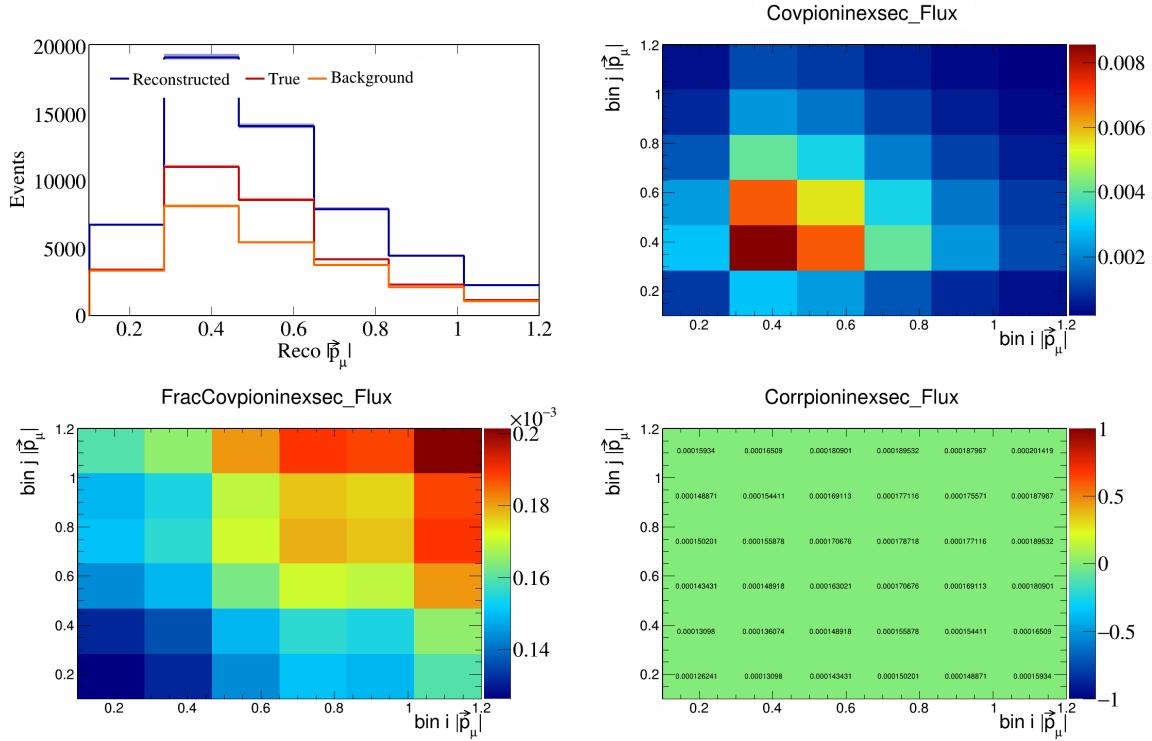


Figure 619: PionIneXSec variations for $|\vec{p}_\mu|$.

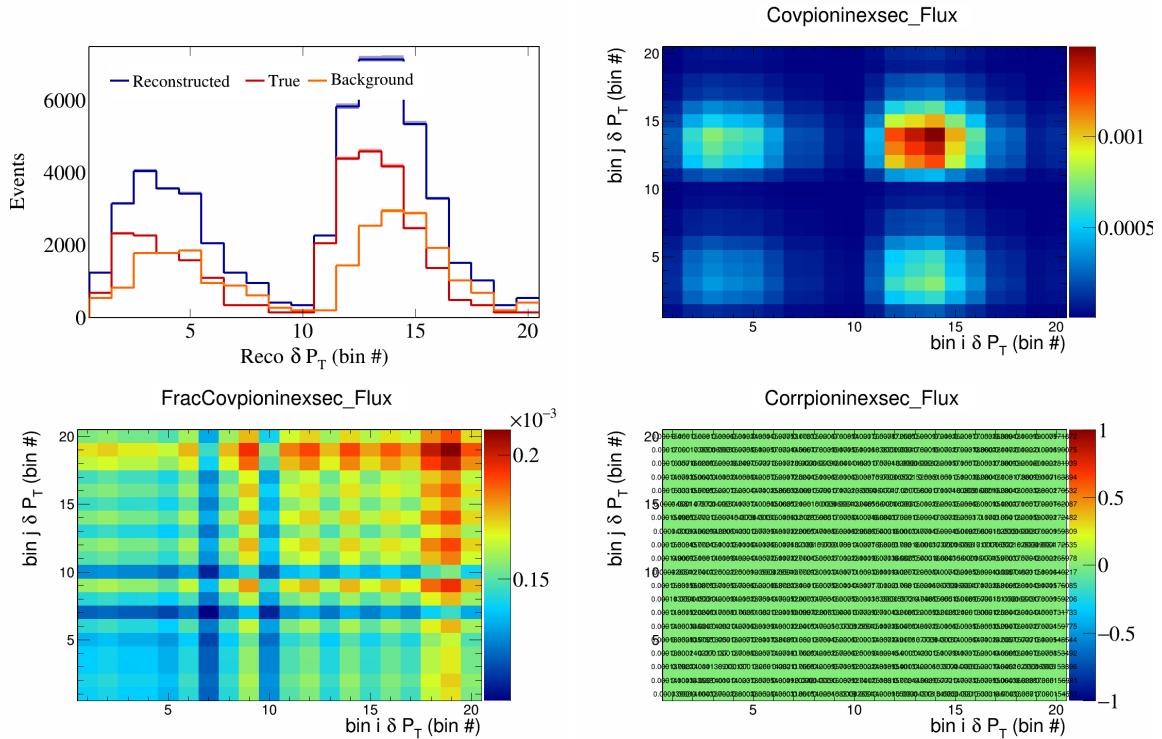


Figure 620: PionIneXSec variations for δP_T in $\cos(\theta_{\vec{p}_\mu})$.

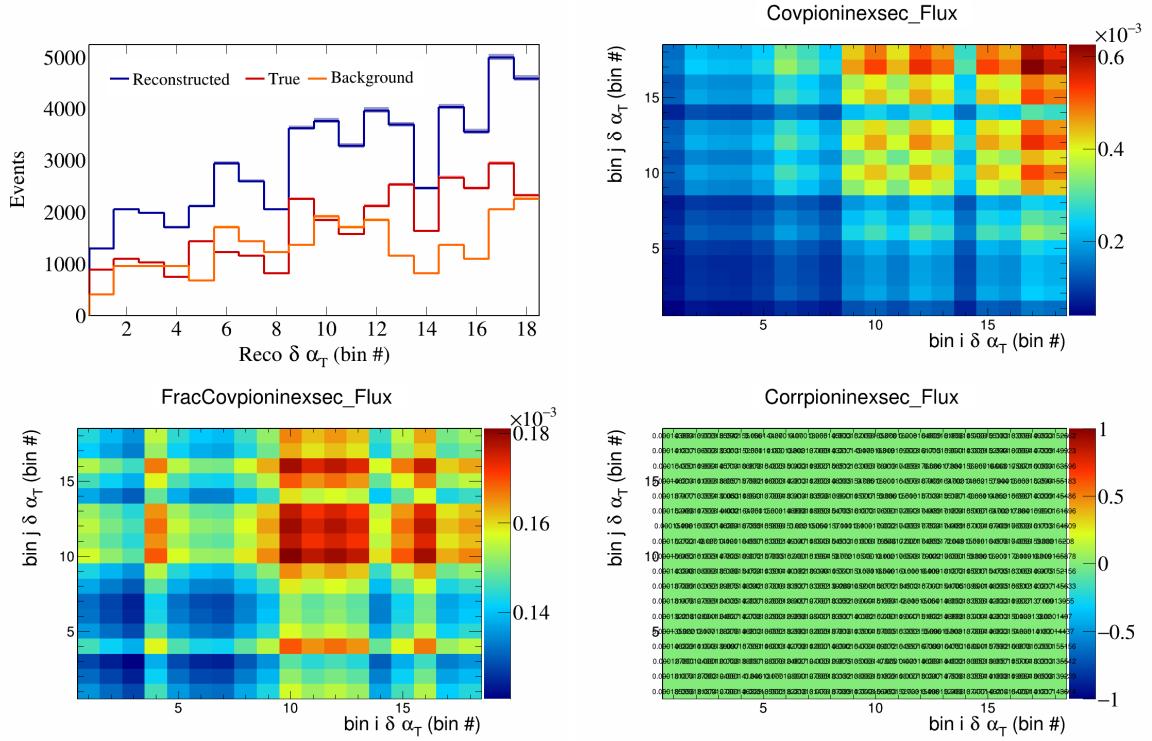


Figure 621: PionIneXSec variations for $\delta\alpha_T$ in $\cos(\theta_{\vec{p}_\mu})$.

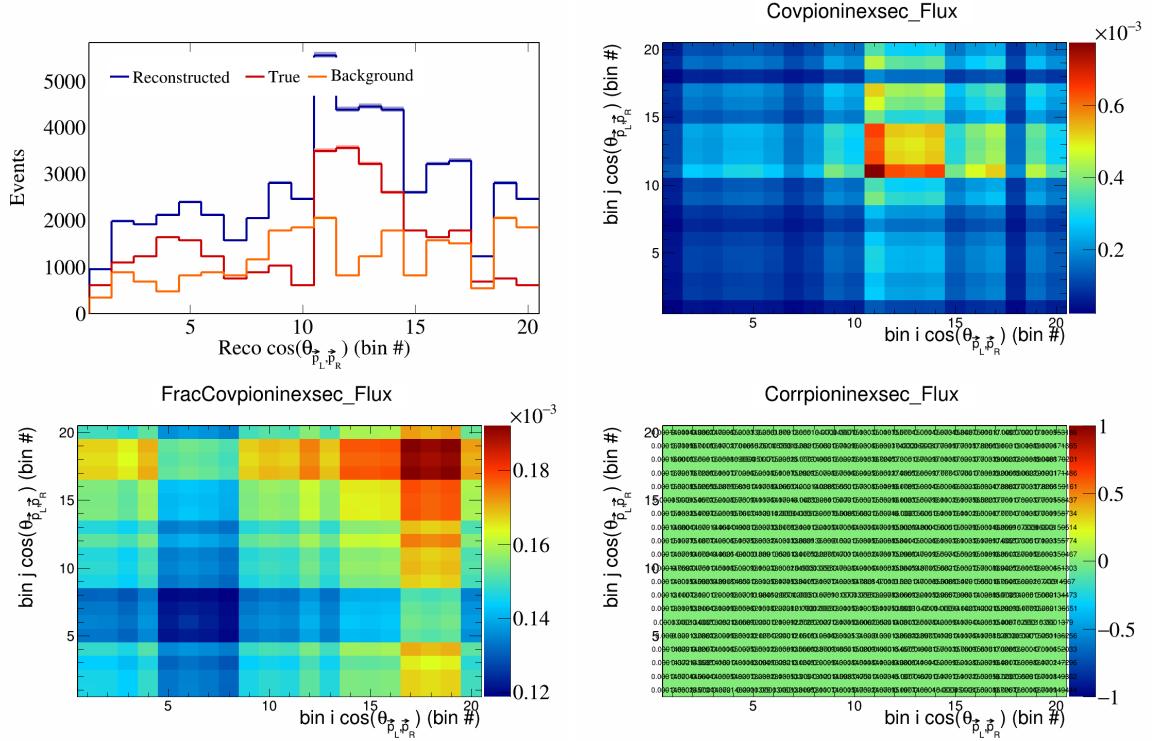


Figure 622: PionIneXSec variations for $\cos(\theta_{\vec{p}_L, \vec{p}_R})$ in $\cos(\theta_{\vec{p}_\mu})$.

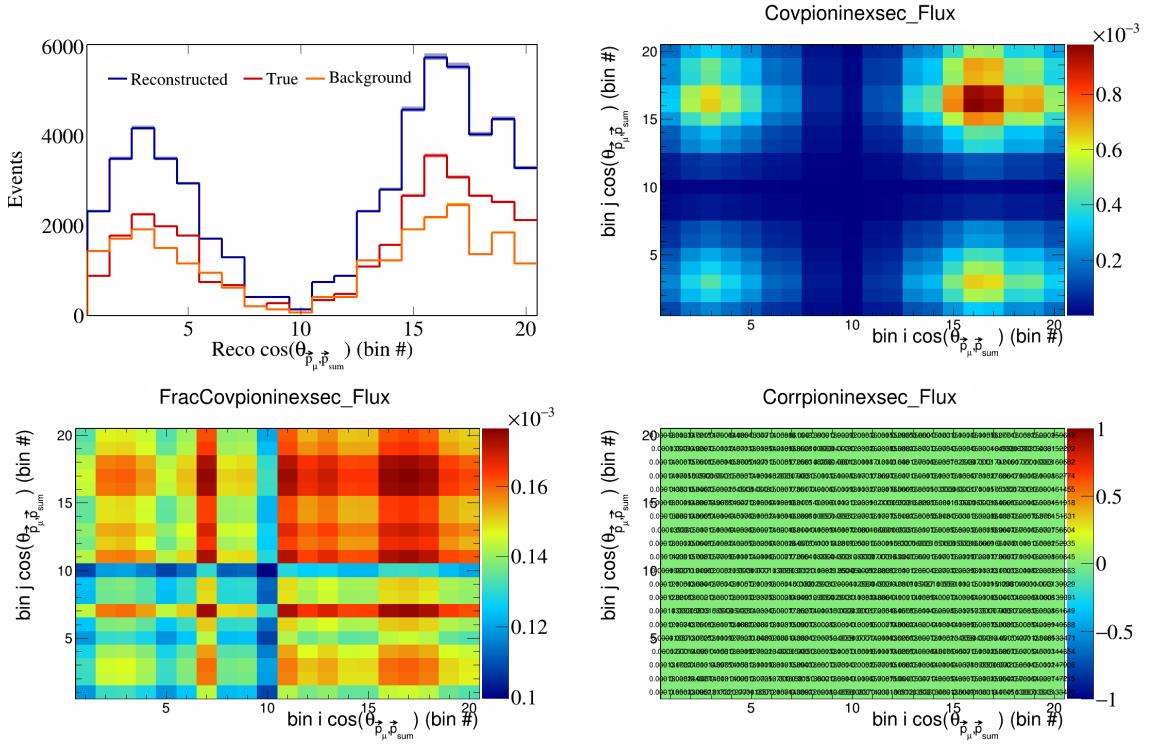


Figure 623: PionIneXSec variations for $\cos(\theta_{\vec{p}_\mu, \vec{p}_{\text{sum}}})$ in $\cos(\theta_{\vec{p}_\mu})$.

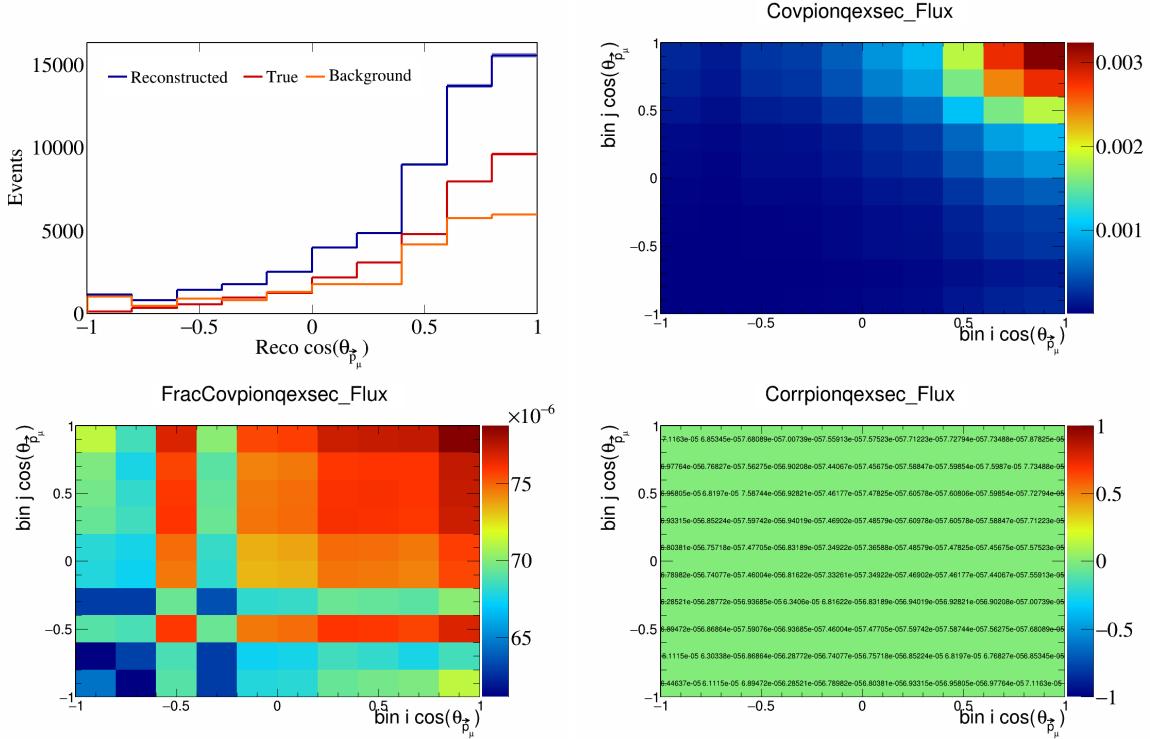


Figure 624: PionQeXSec variations for $\cos(\theta_{\vec{p}_\mu})$.

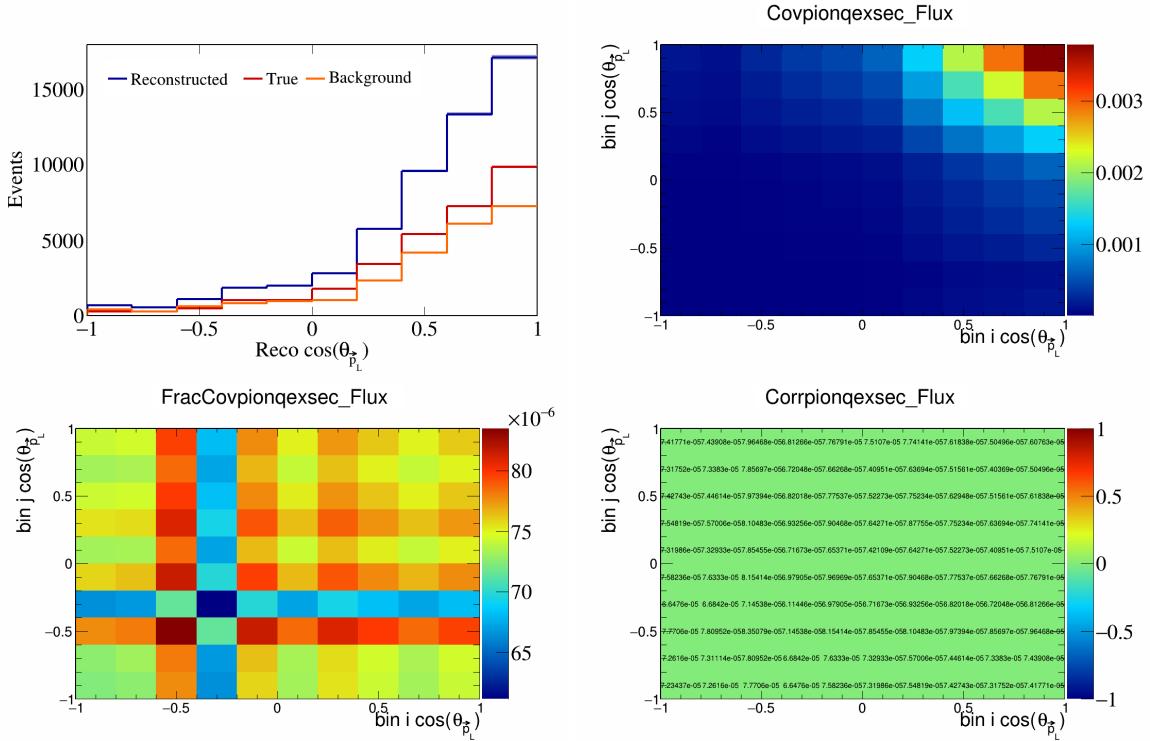


Figure 625: PionQeXSec variations for $\cos(\theta_{\vec{p}_L})$.

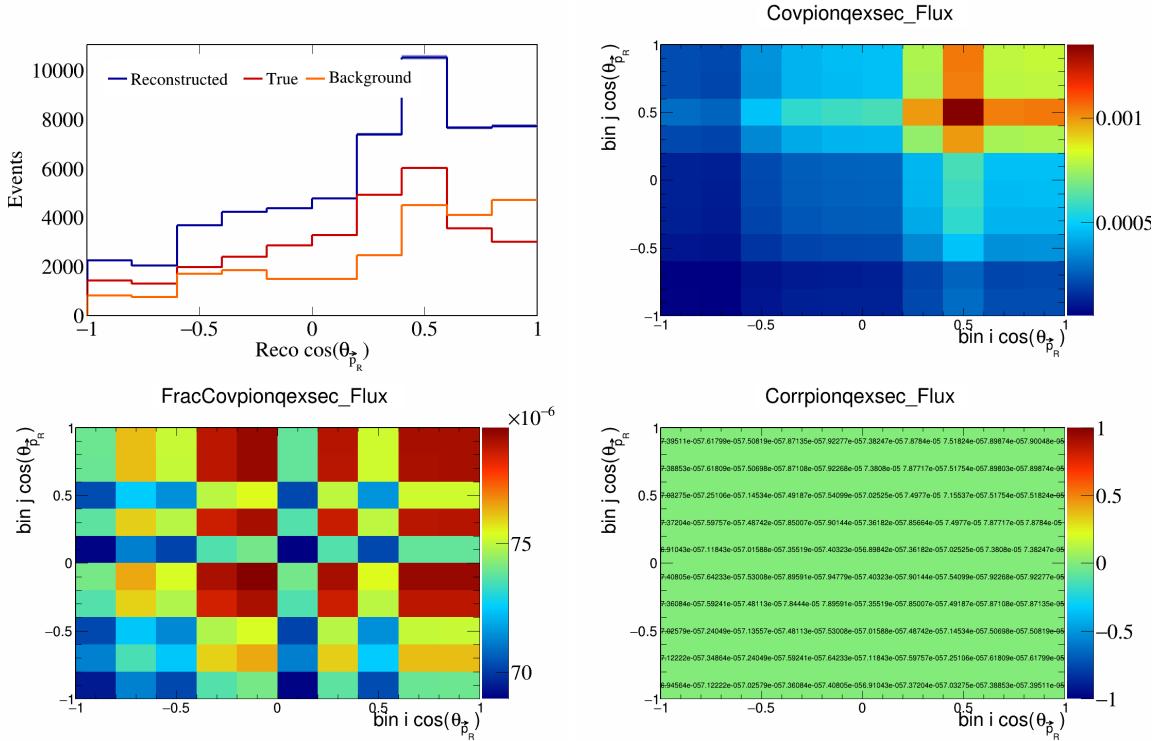


Figure 626: PionQeXSec variations for $\cos(\theta_{\vec{p}_R})$.

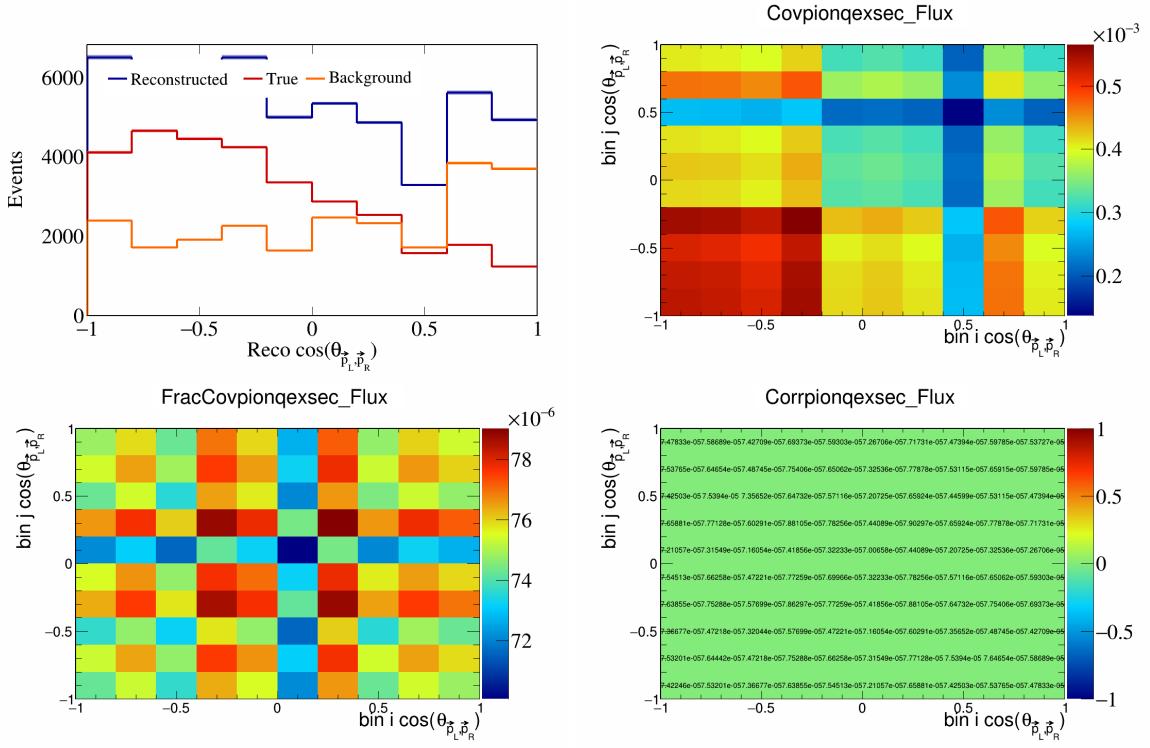


Figure 627: PionQeXSec variations for $\cos(\theta_{\vec{p}_L, \vec{p}_R})$.

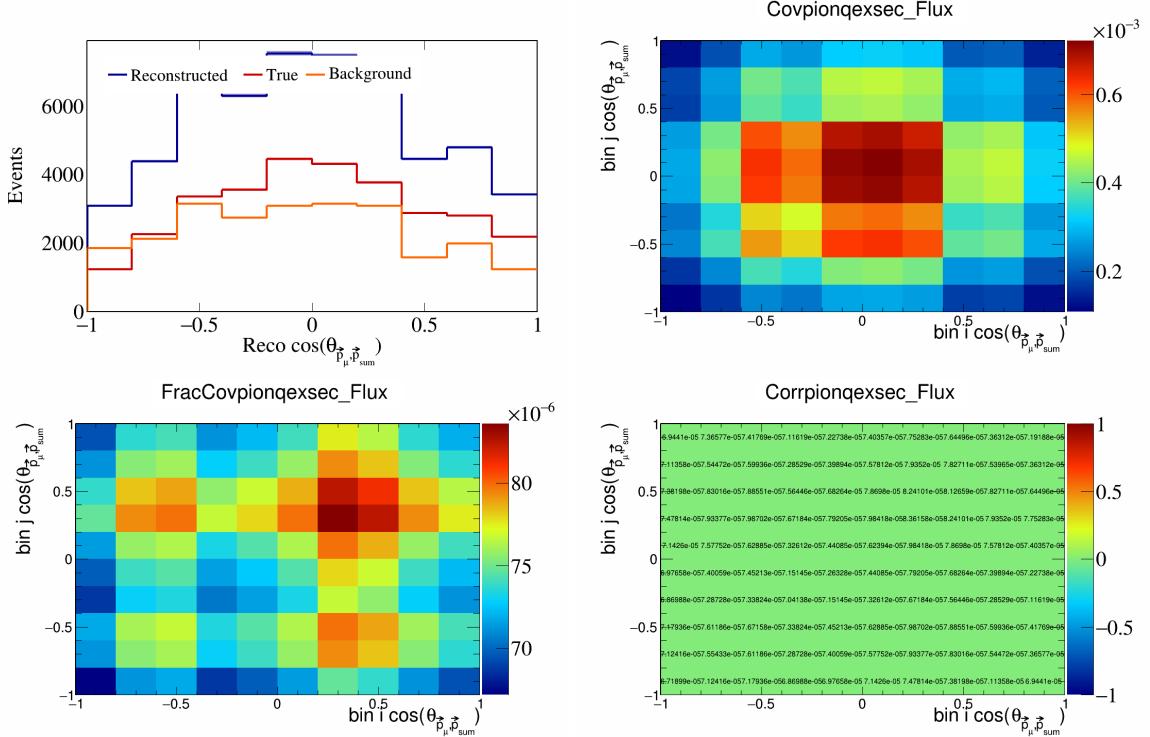


Figure 628: PionQeXSec variations for $\cos(\theta_{\vec{p}_\mu, \vec{p}_{\text{sum}}})$.

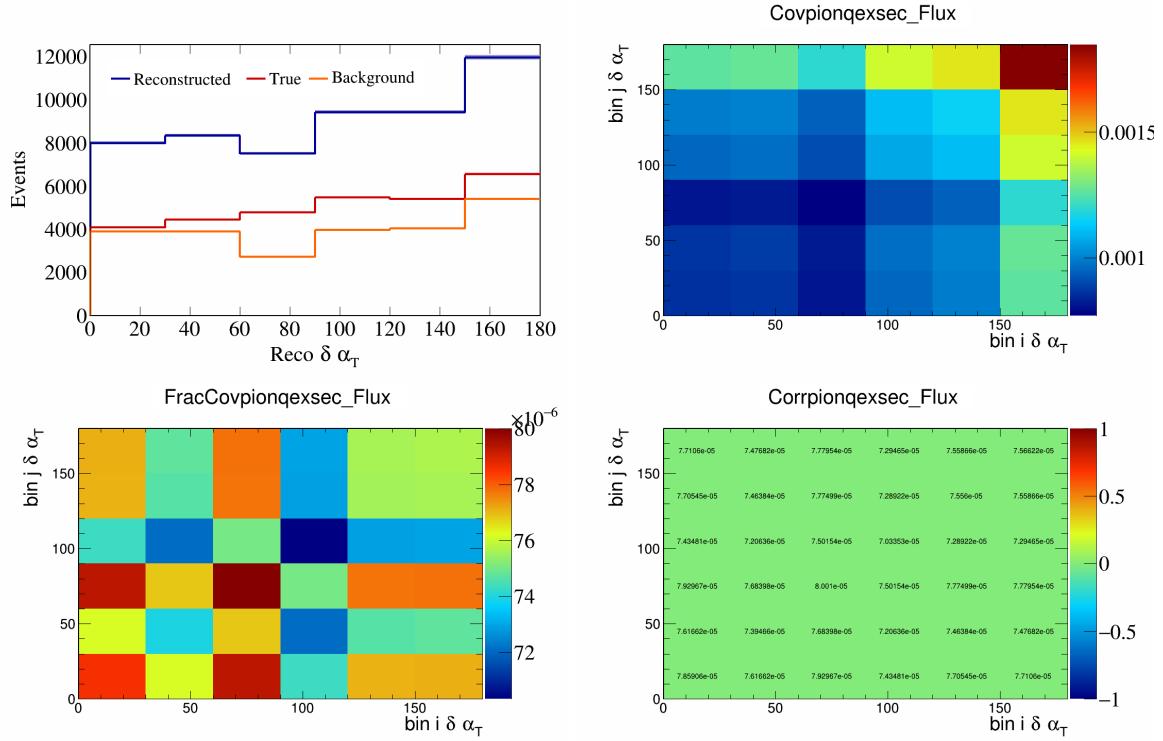


Figure 629: PionQeXSec variations for $\delta\alpha_T$.

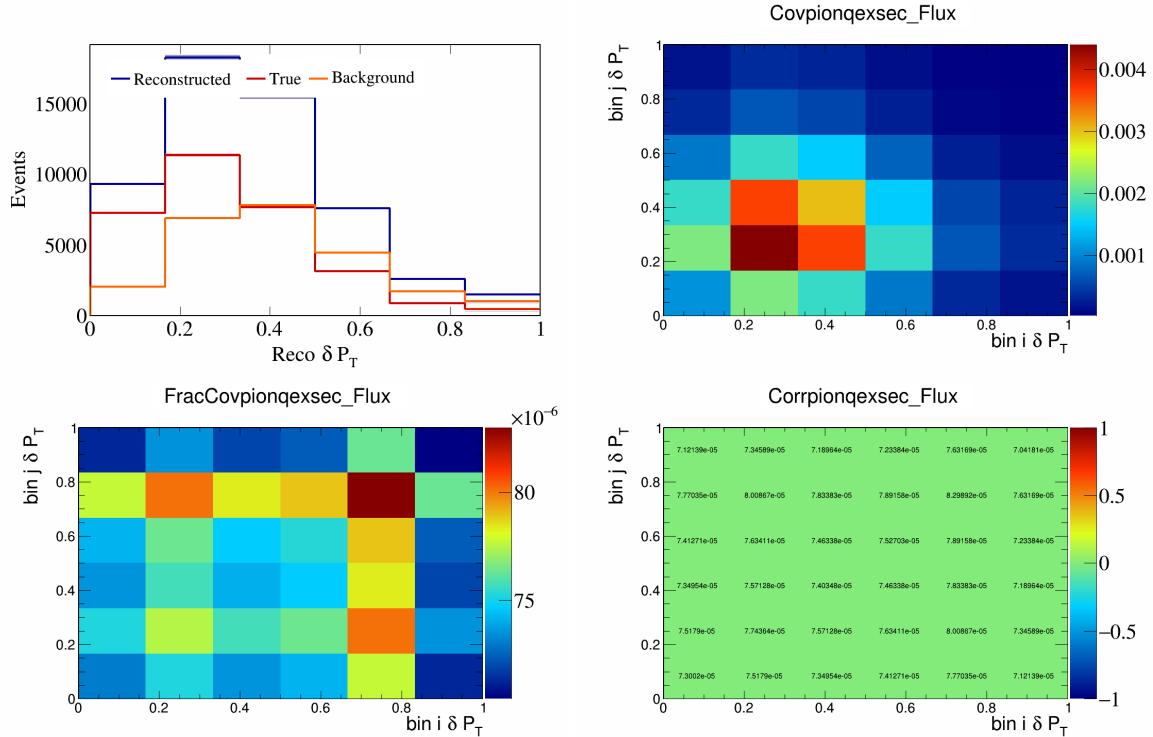


Figure 630: PionQeXSec variations for δP_T .

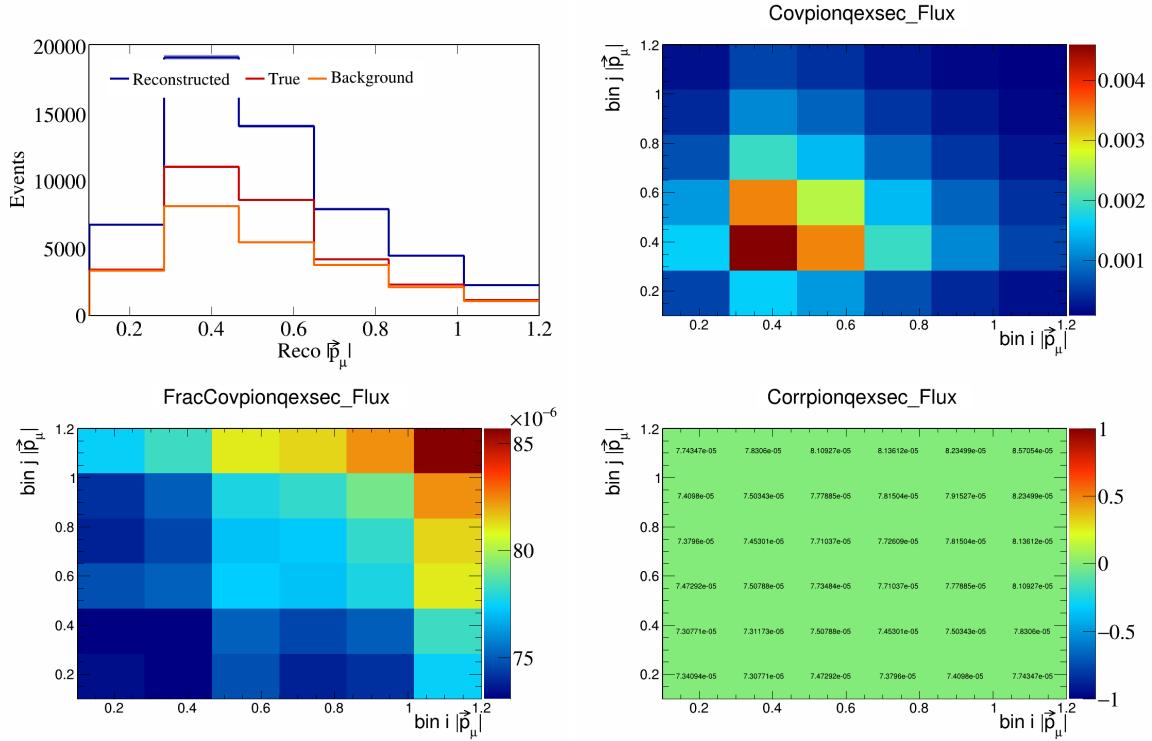


Figure 631: PionQeXSec variations for $|\vec{p}_\mu|$.

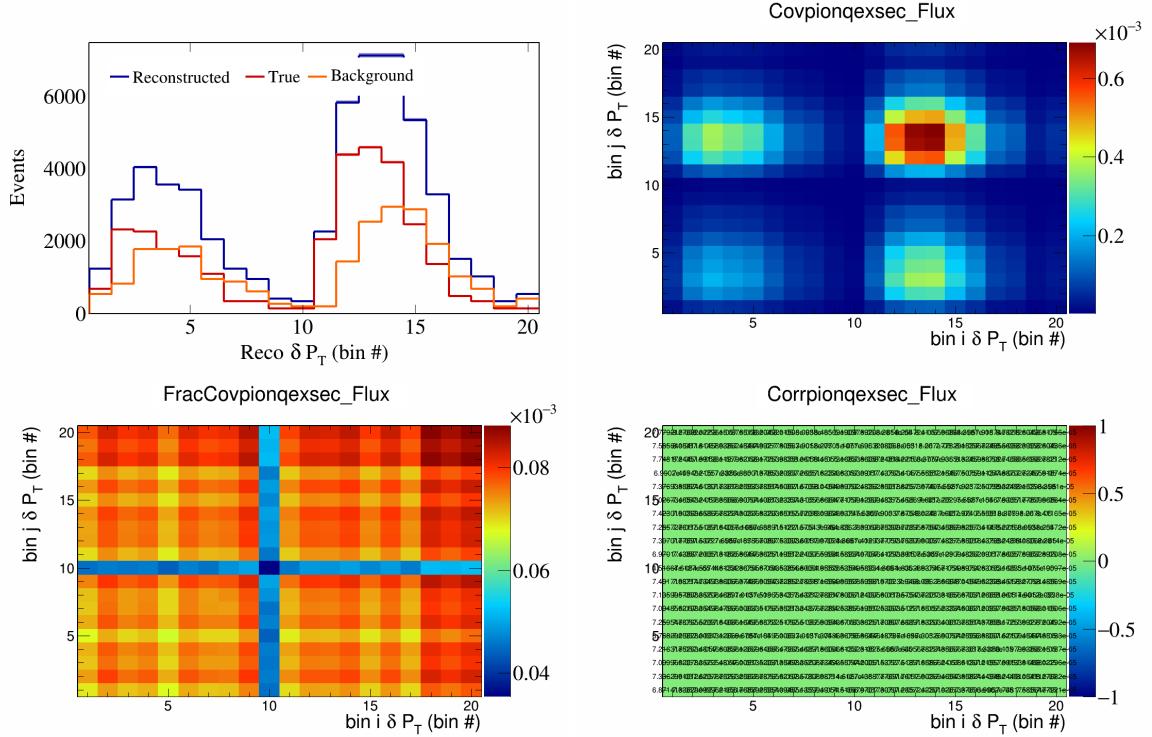


Figure 632: PionQeXSec variations for δP_T in $\cos(\theta_{\vec{p}_\mu})$.

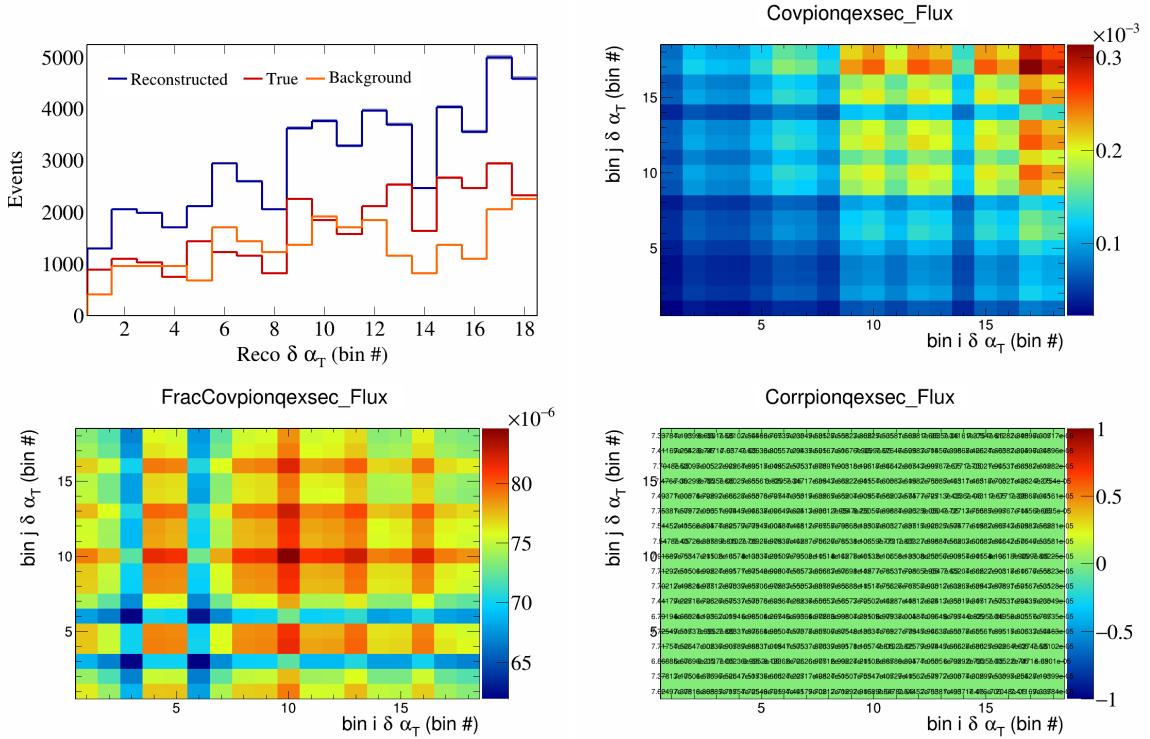


Figure 633: PionQeXSec variations for $\delta\alpha_T$ in $\cos(\theta_{\vec{p}_\mu})$.

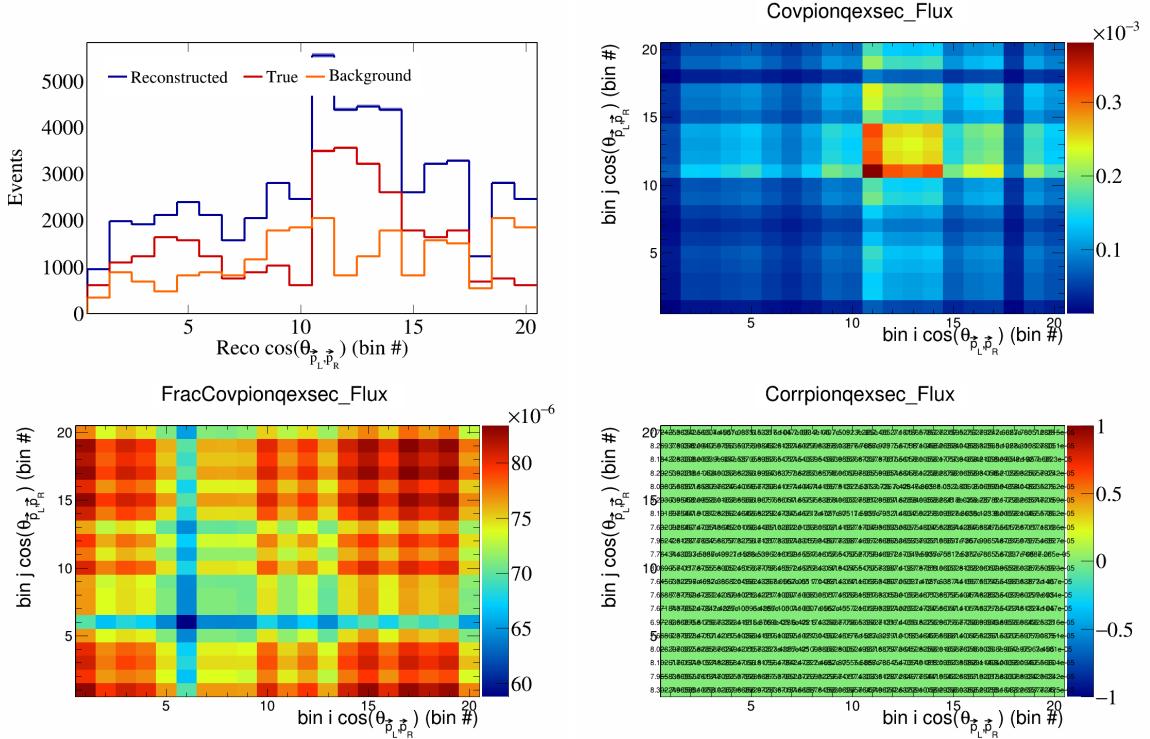


Figure 634: PionQeXSec variations for $\cos(\theta_{\vec{p}_L, \vec{p}_R})$ in $\cos(\theta_{\vec{p}_\mu})$.

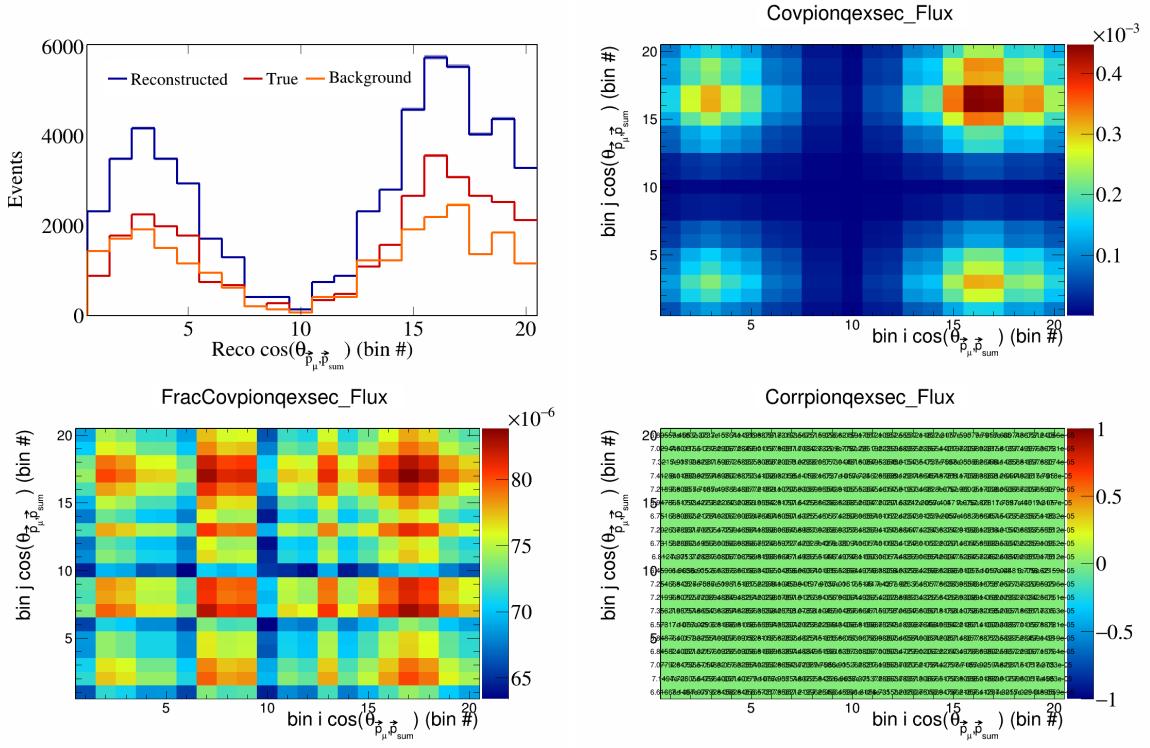


Figure 635: PionQeXSec variations for $\cos(\theta_{\vec{p}_\mu}^*)$ in $\cos(\theta_{\vec{p}_\mu}^*)$.

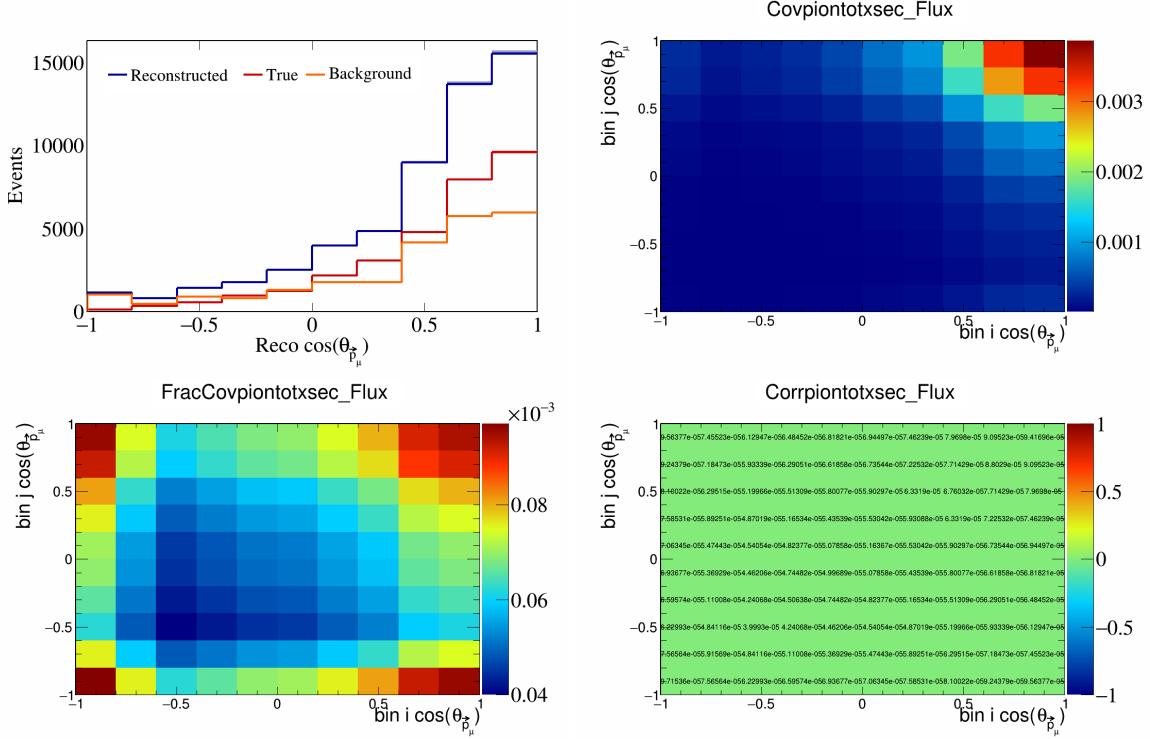


Figure 636: PionTotXSec variations for $\cos(\theta_{\vec{p}_\mu}^*)$.

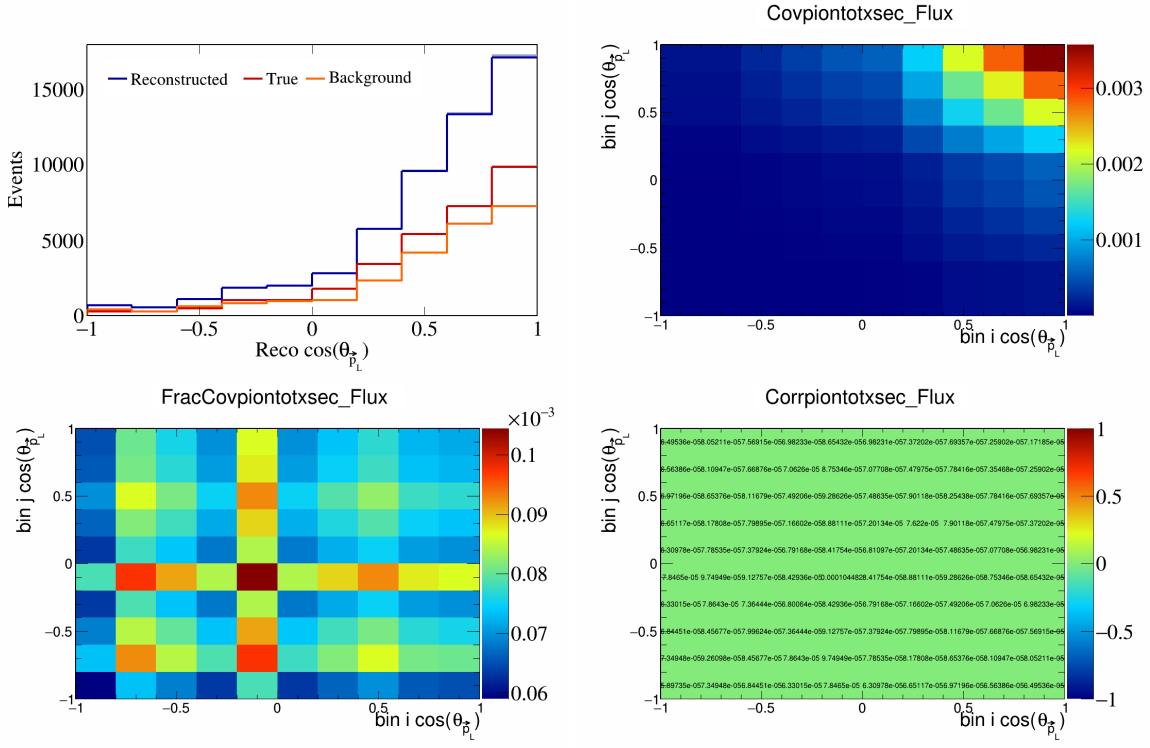


Figure 637: PionTotXSec variations for $\cos(\theta_{\vec{p}_L})$.

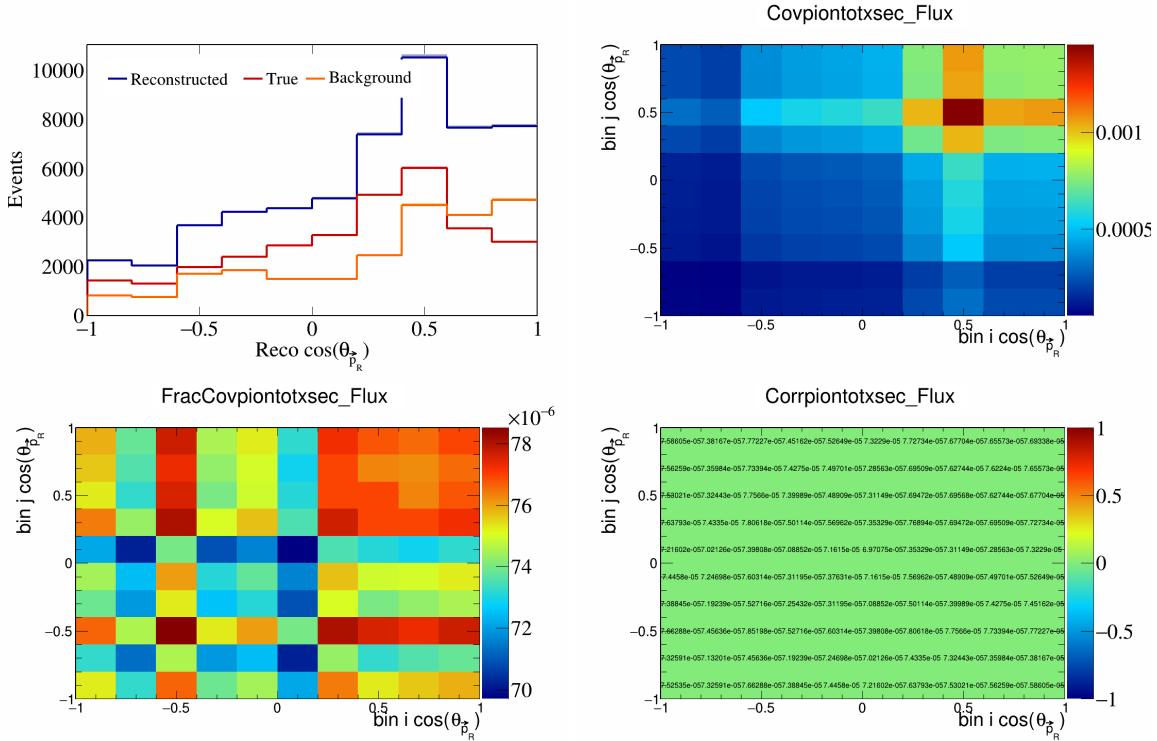


Figure 638: PionTotXSec variations for $\cos(\theta_{\vec{p}_R})$.

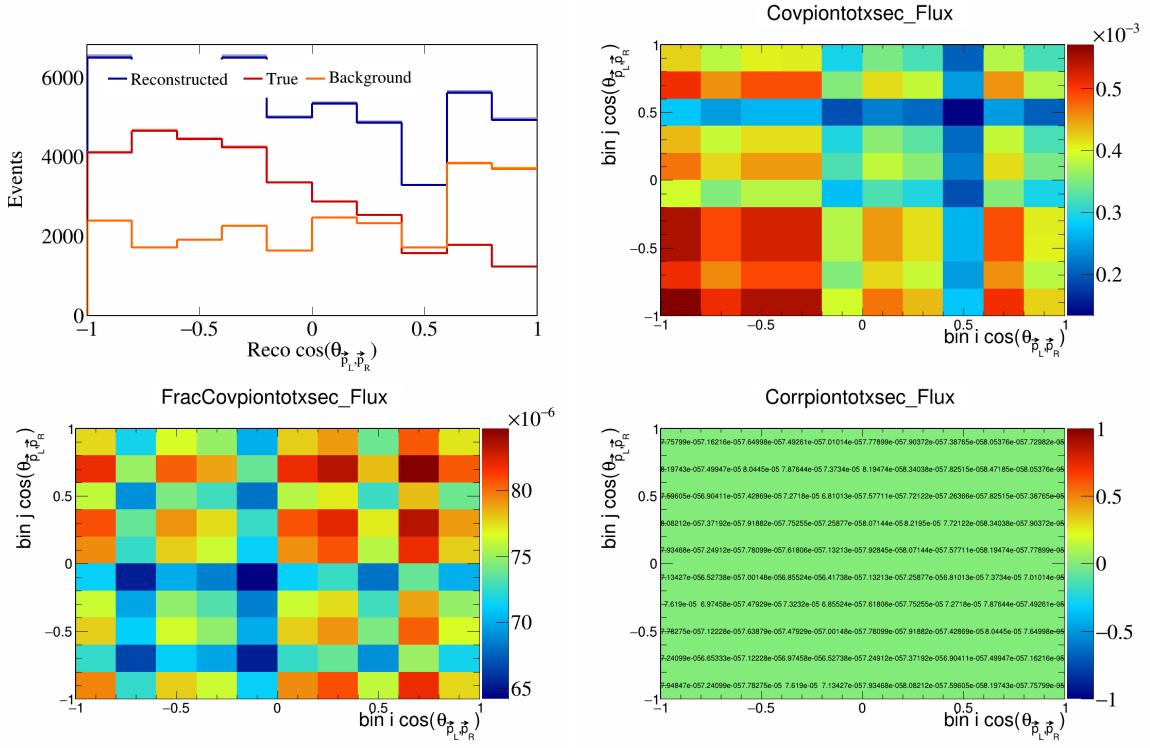


Figure 639: PionTotXSec variations for $\cos(\theta_{\vec{p}_L, \vec{p}_R})$.

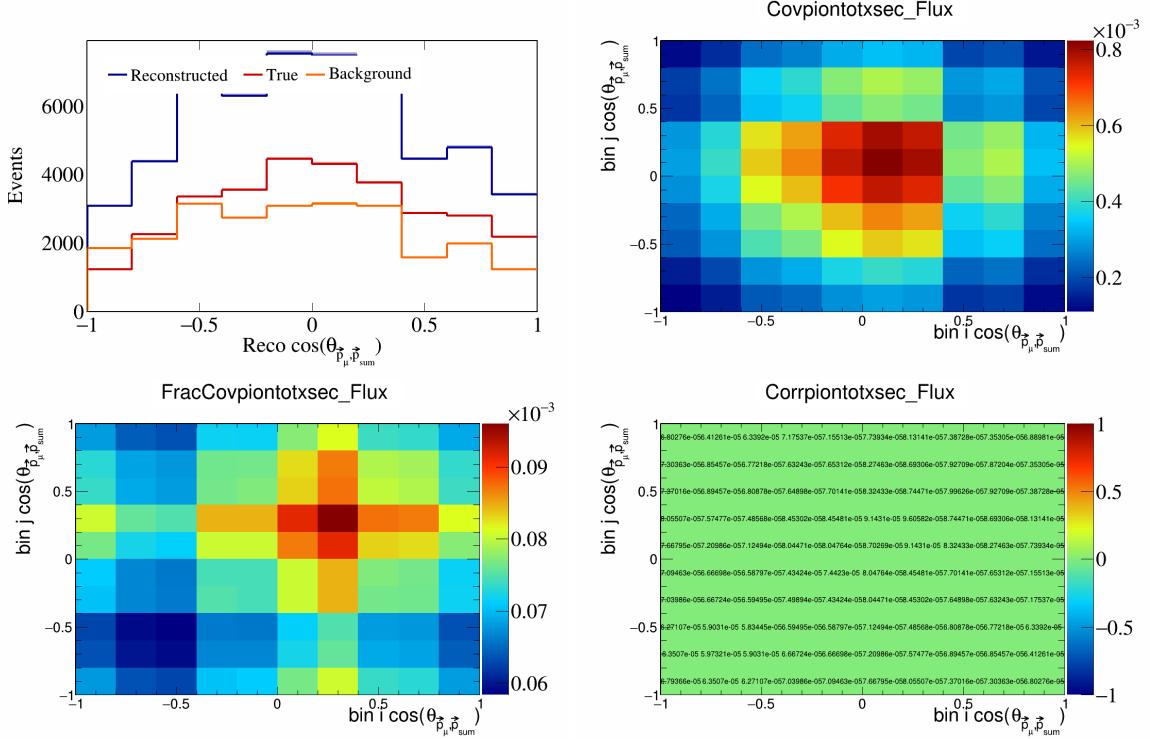


Figure 640: PionTotXSec variations for $\cos(\theta_{\vec{p}_\mu, \vec{p}_{\text{sum}}})$.

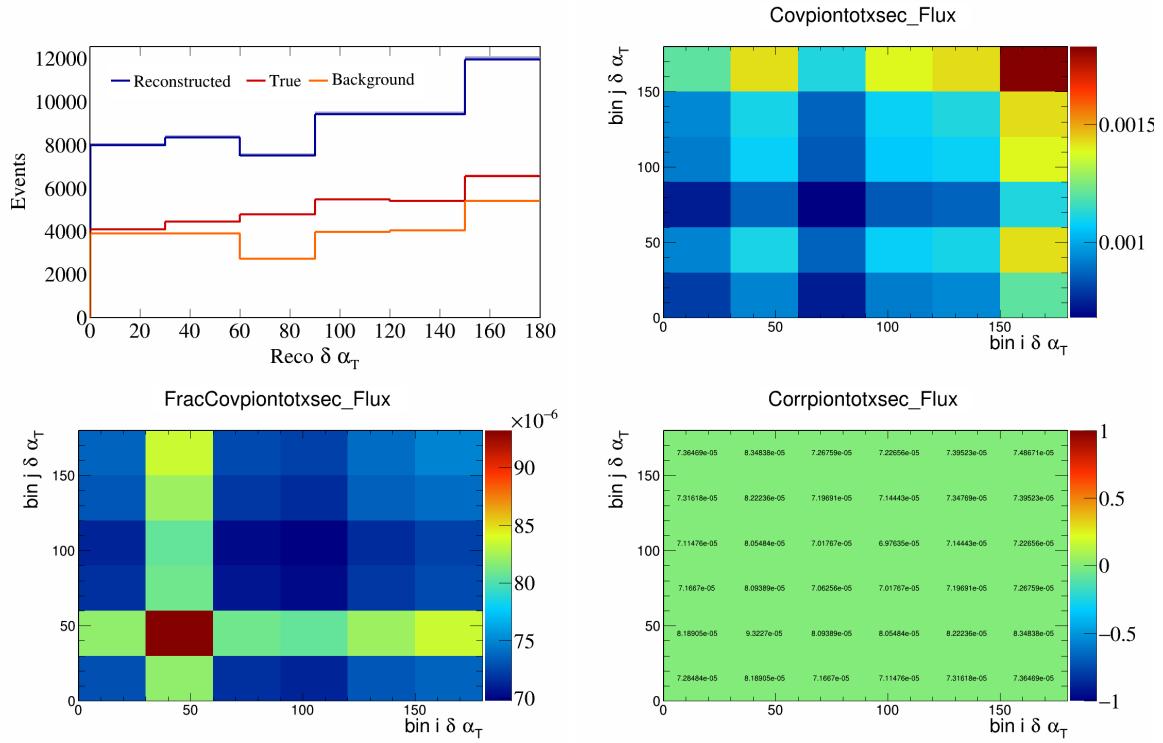


Figure 641: PionTotXSec variations for $\delta\alpha_T$.

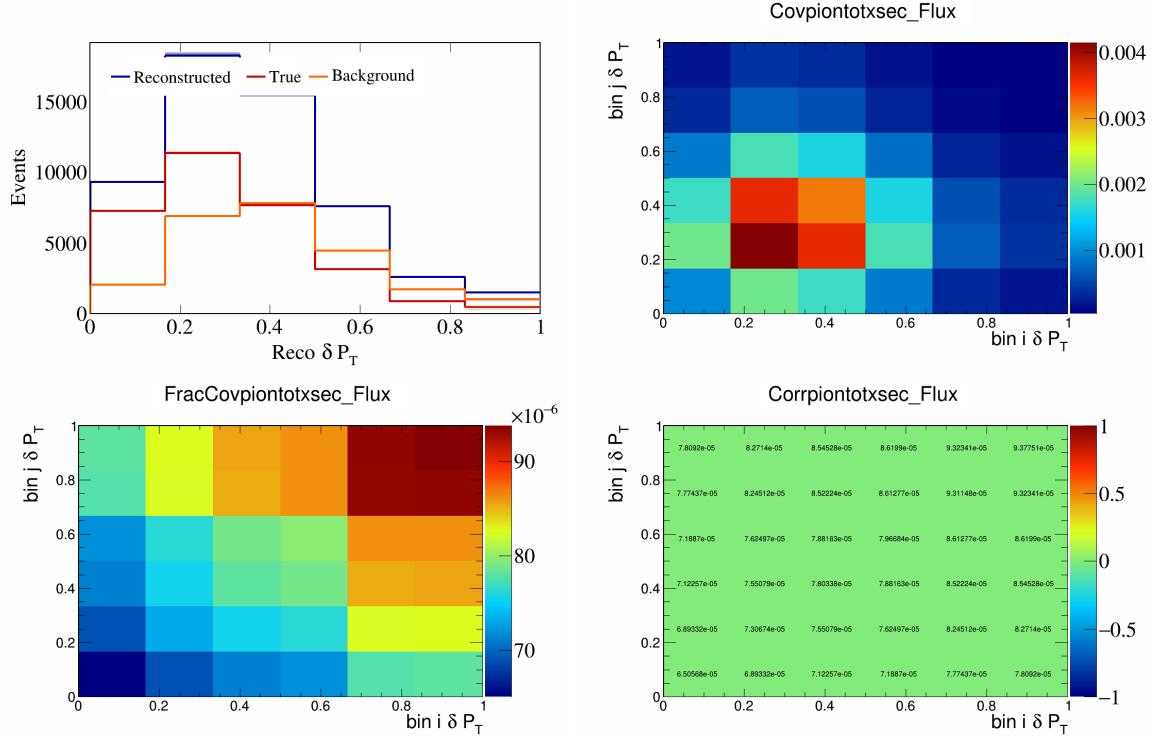


Figure 642: PionTotXSec variations for δP_T .

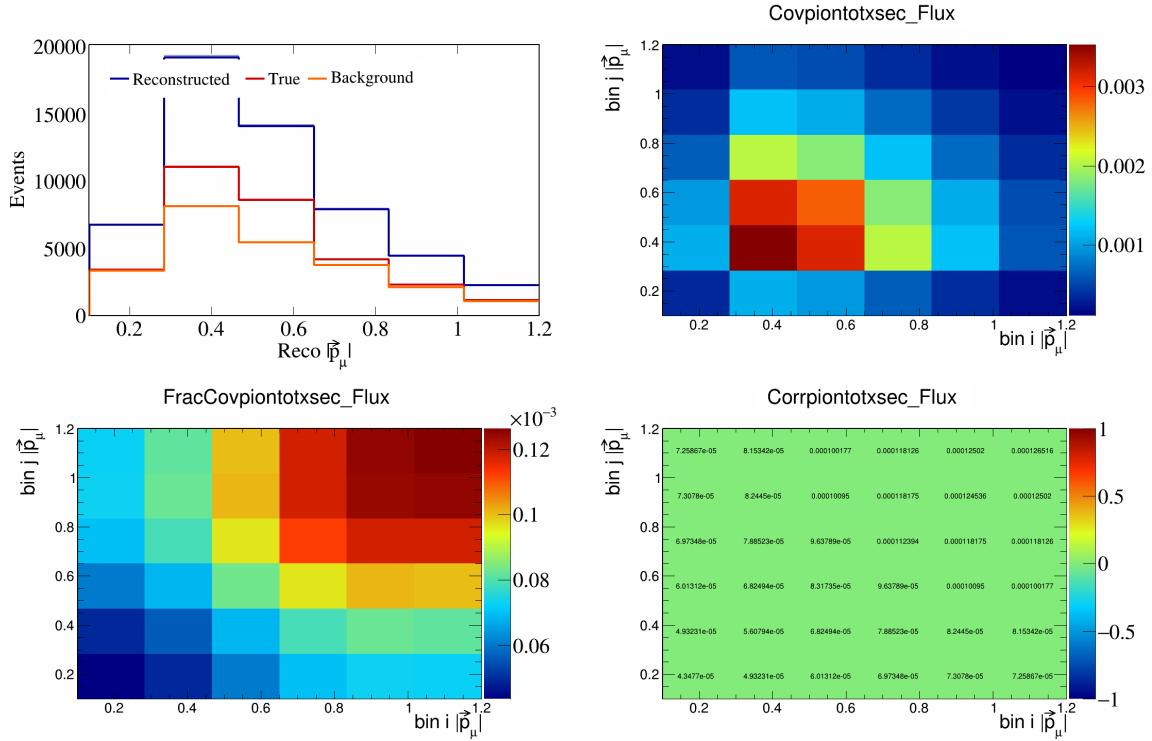


Figure 643: PionTotXSec variations for $|\vec{p}_\mu|$.

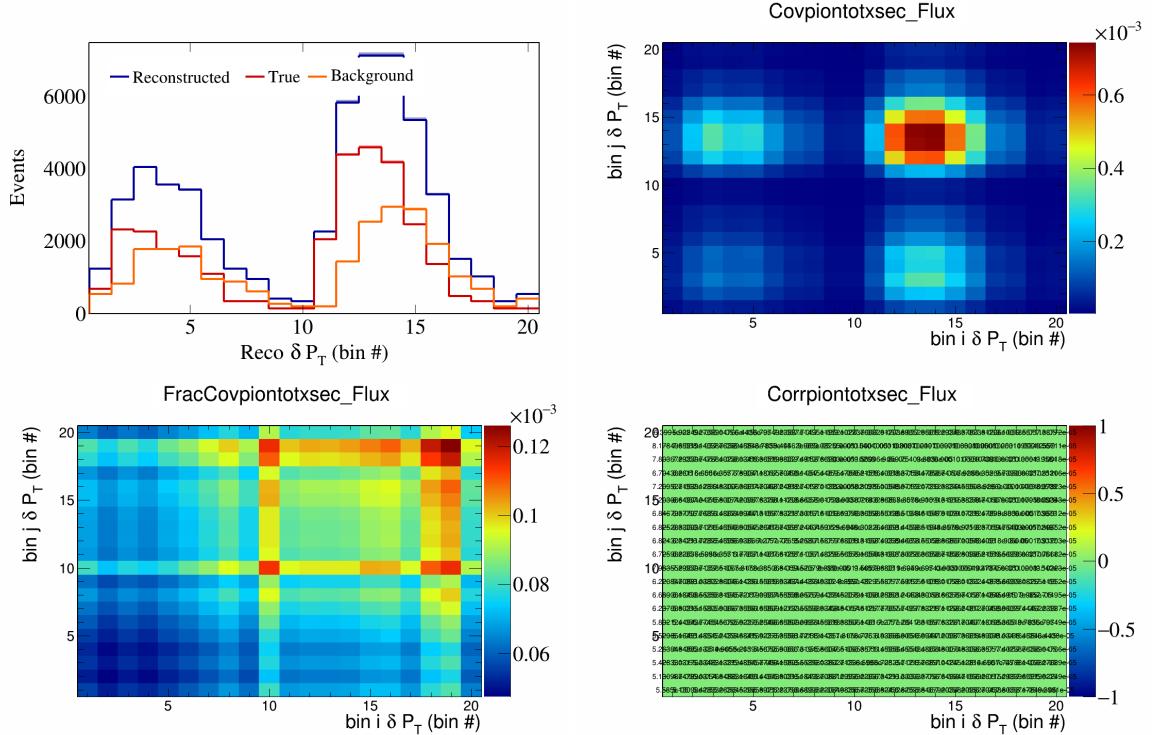


Figure 644: PionTotXSec variations for δP_T in $\cos(\theta_{\vec{p}_\mu})$.

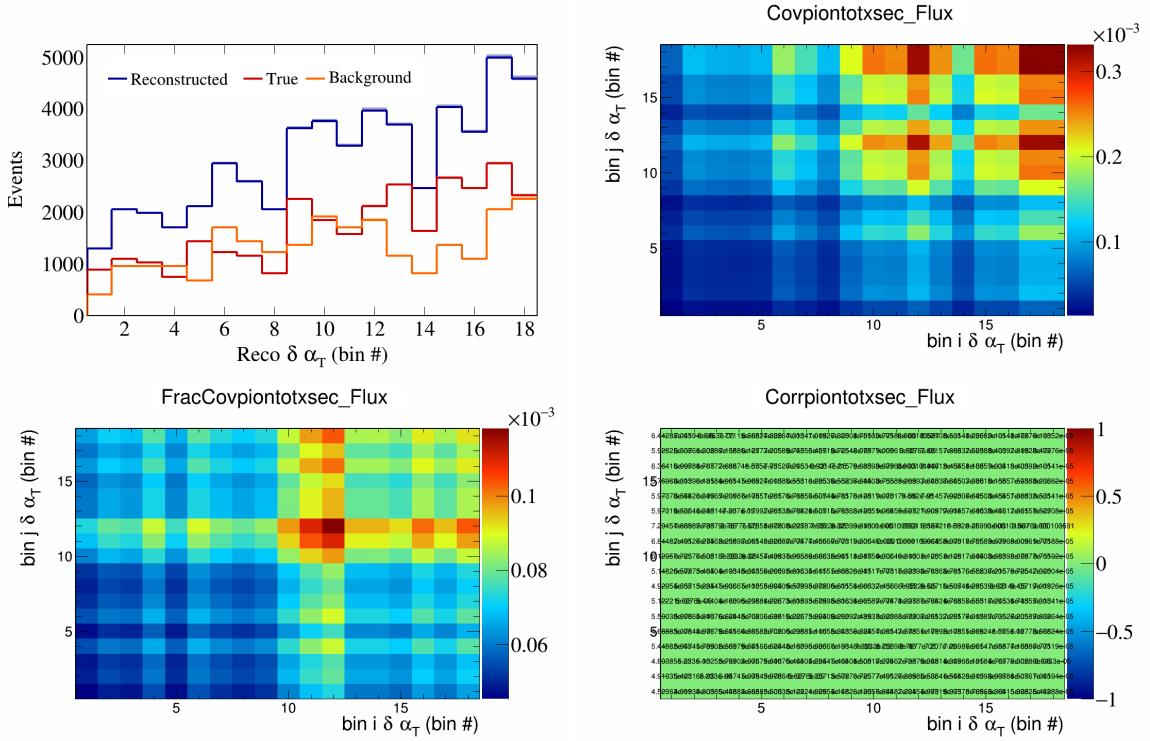


Figure 645: PionTotXSec variations for $\delta \alpha_T$ in $\cos(\theta_{\vec{p}_\mu})$.

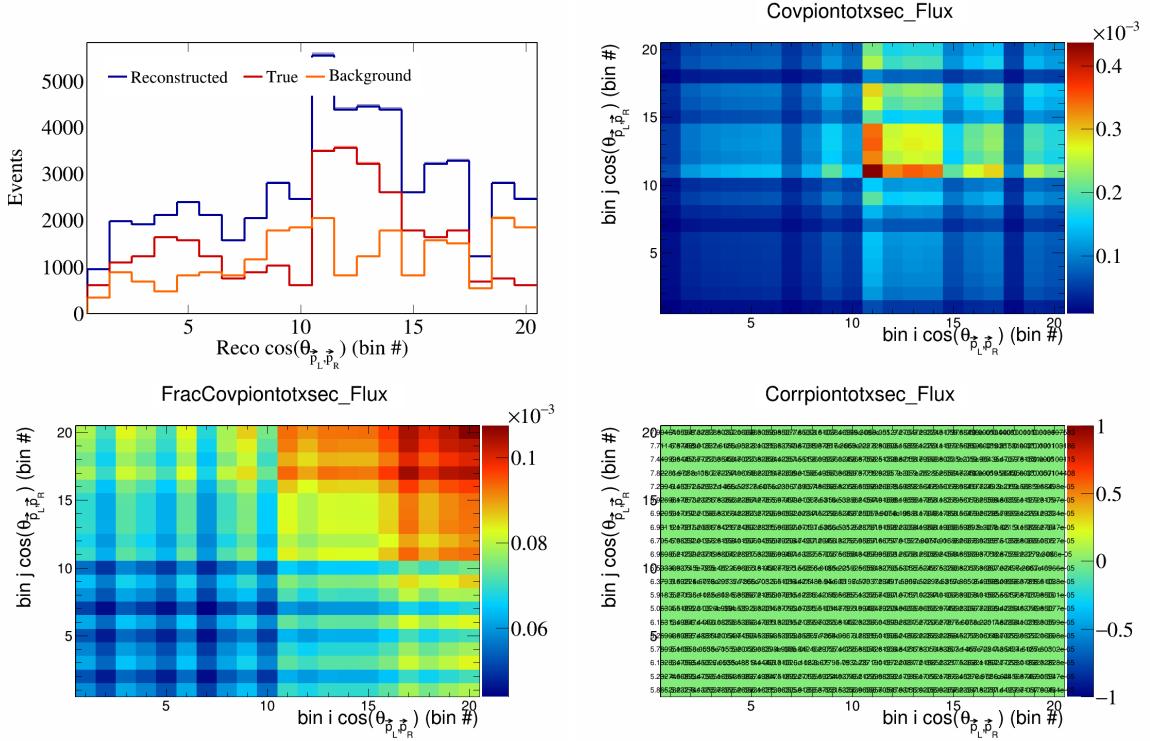


Figure 646: PionTotXSec variations for $\cos(\theta_{\vec{p}_L, \vec{p}_R})$ in $\cos(\theta_{\vec{p}_\mu})$.

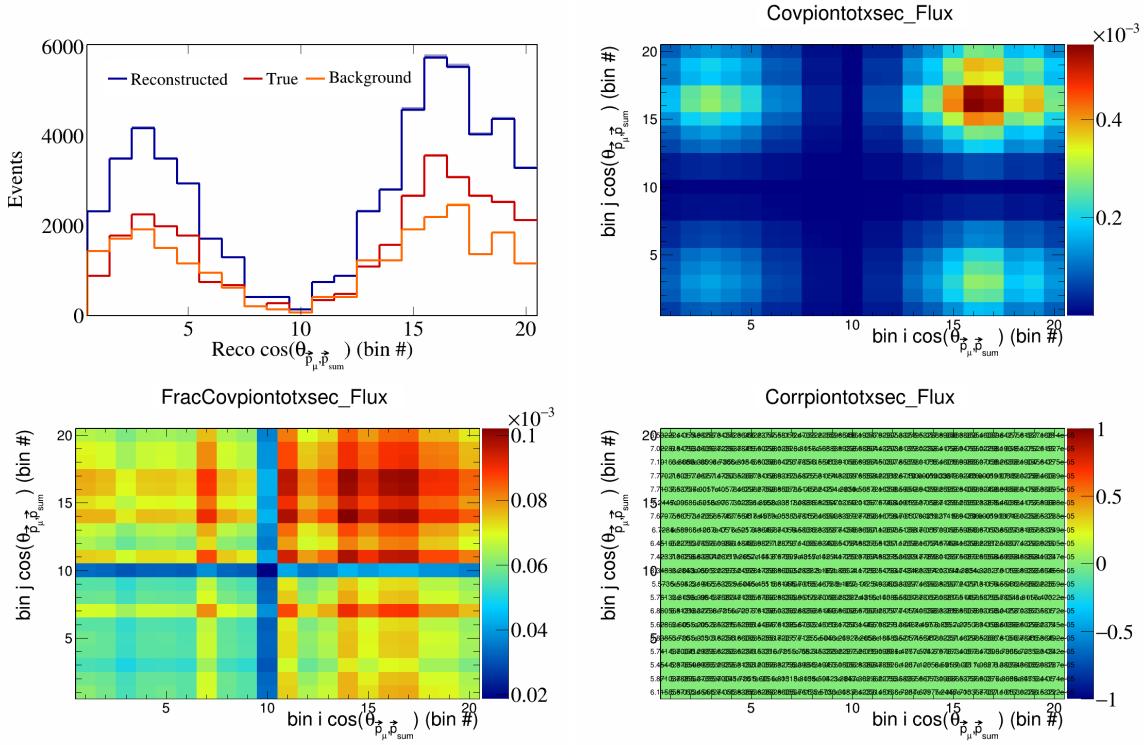


Figure 647: PionTotXSec variations for $\cos(\theta_{\vec{p}_\mu, \vec{p}_{\text{sum}}})$ in $\cos(\theta_{\vec{p}_\mu})$.

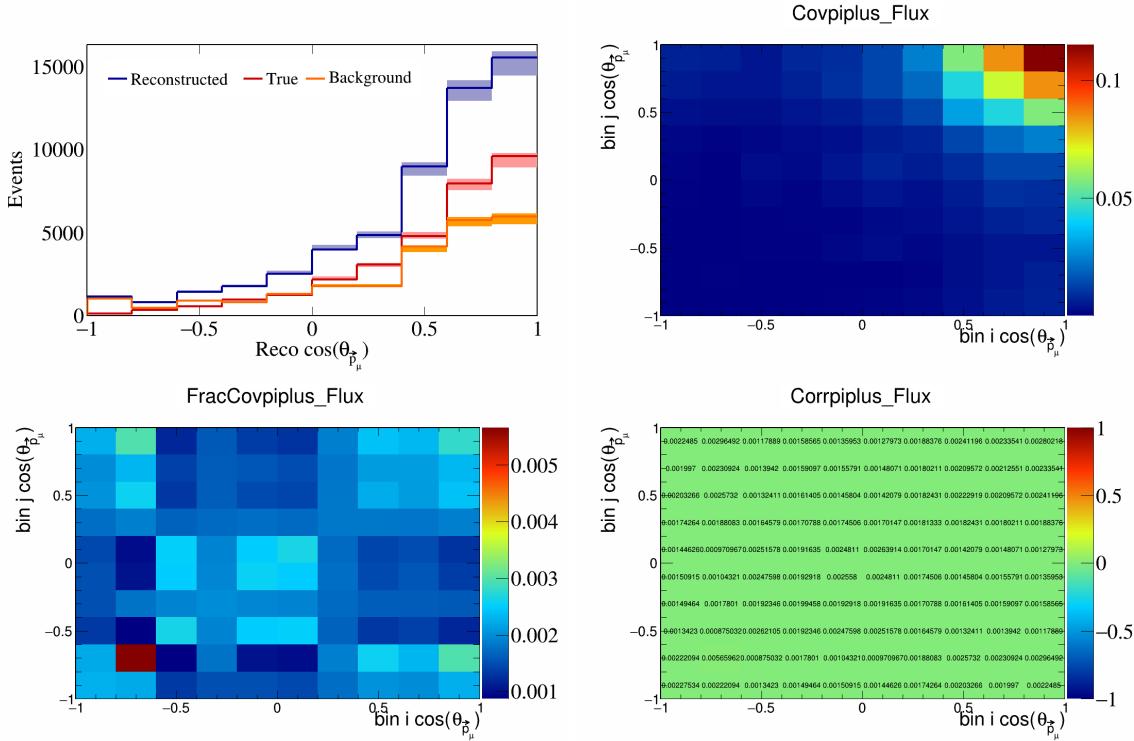


Figure 648: PiPlus variations for $\cos(\theta_{\vec{p}_\mu})$.

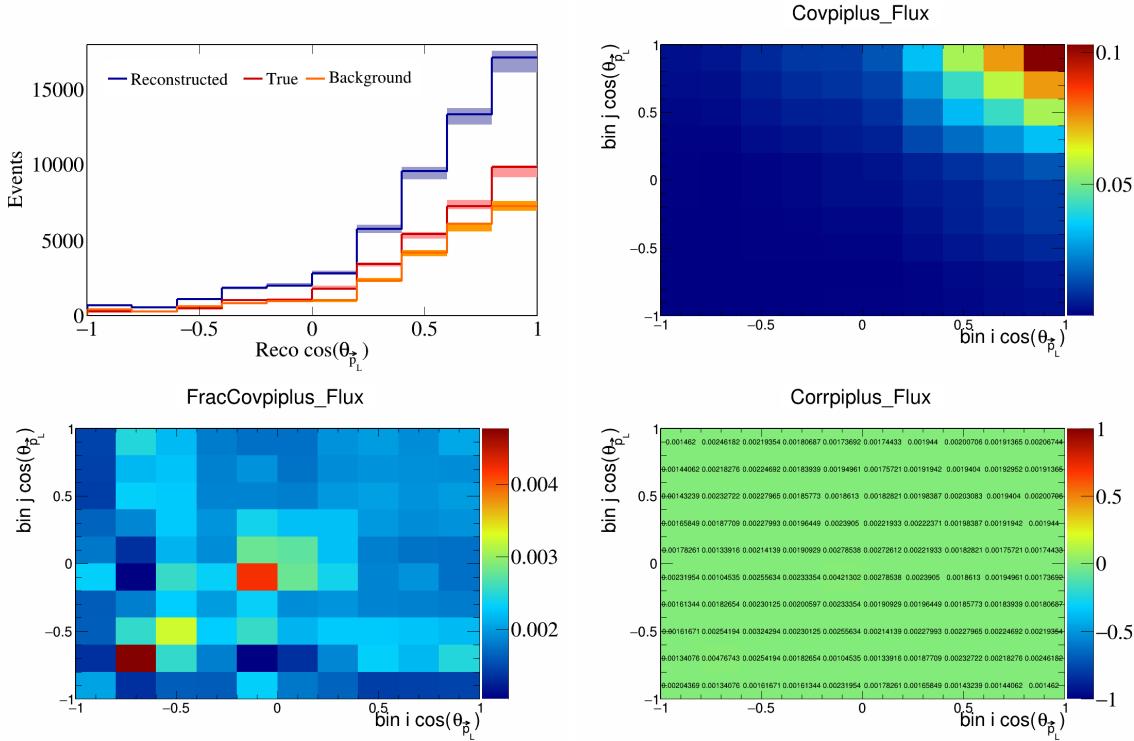


Figure 649: PiPlus variations for $\cos(\theta_{\vec{p}_L})$.

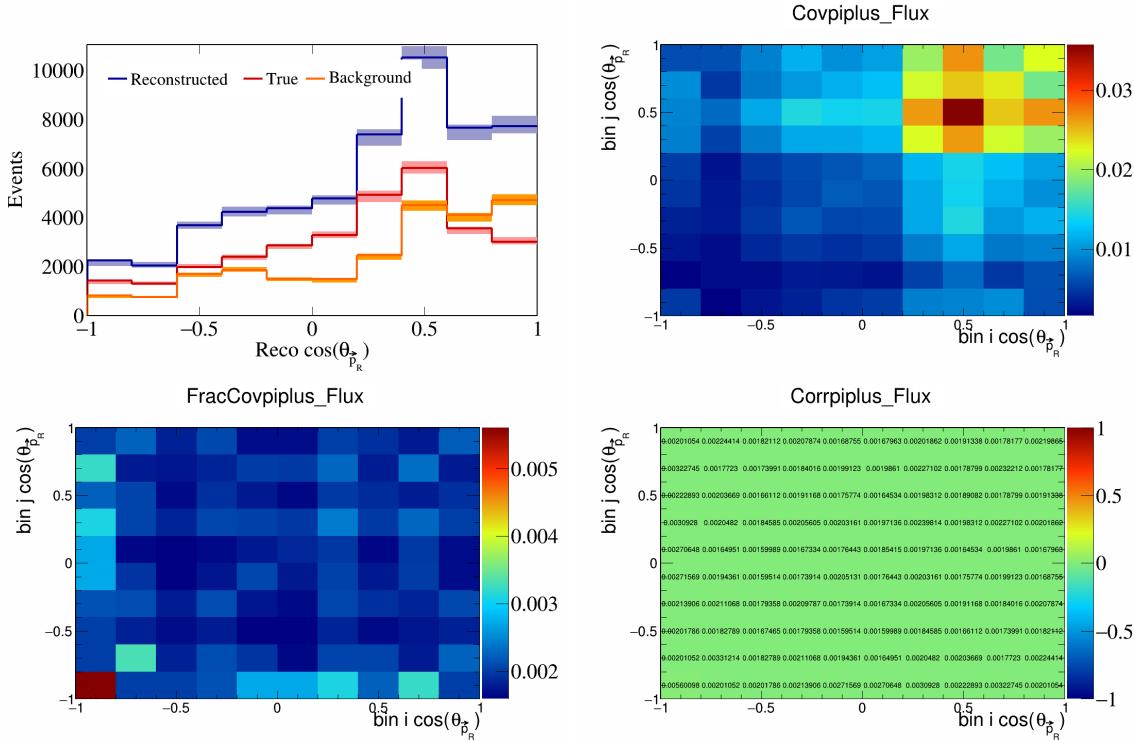


Figure 650: PiPlus variations for $\cos(\theta_{\vec{p}_R})$.

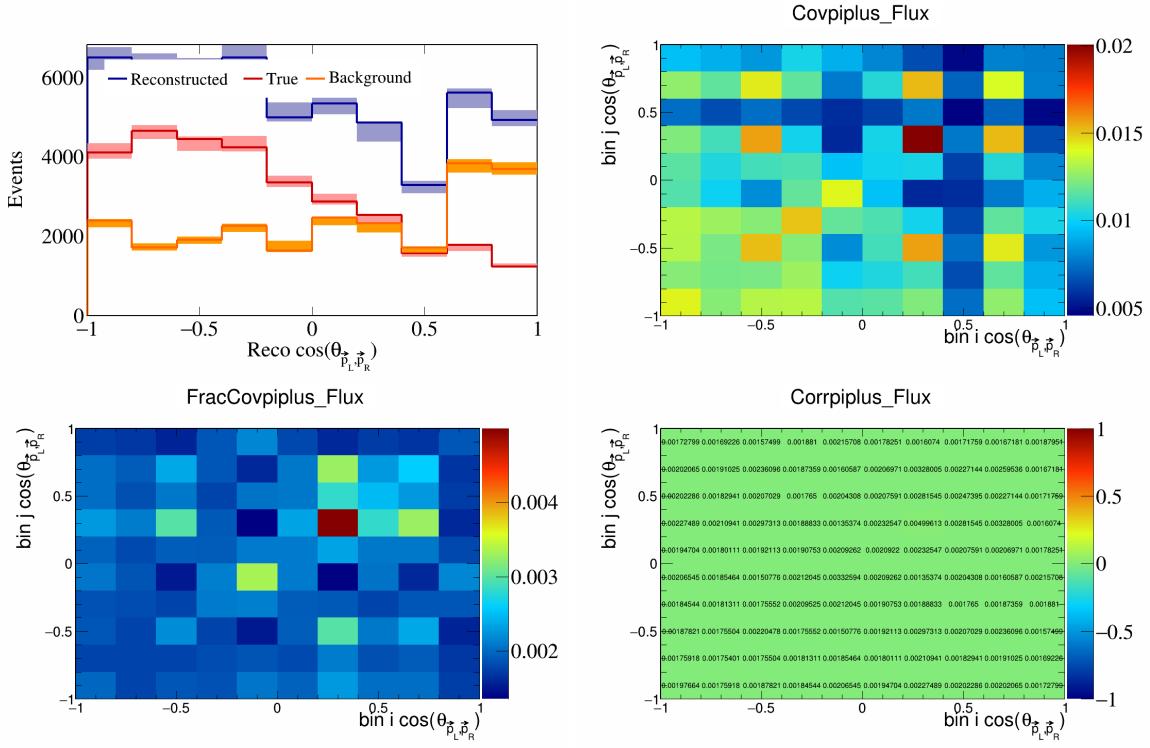


Figure 651: PiPlus variations for $\cos(\theta_{\vec{p}_L, \vec{p}_R})$.

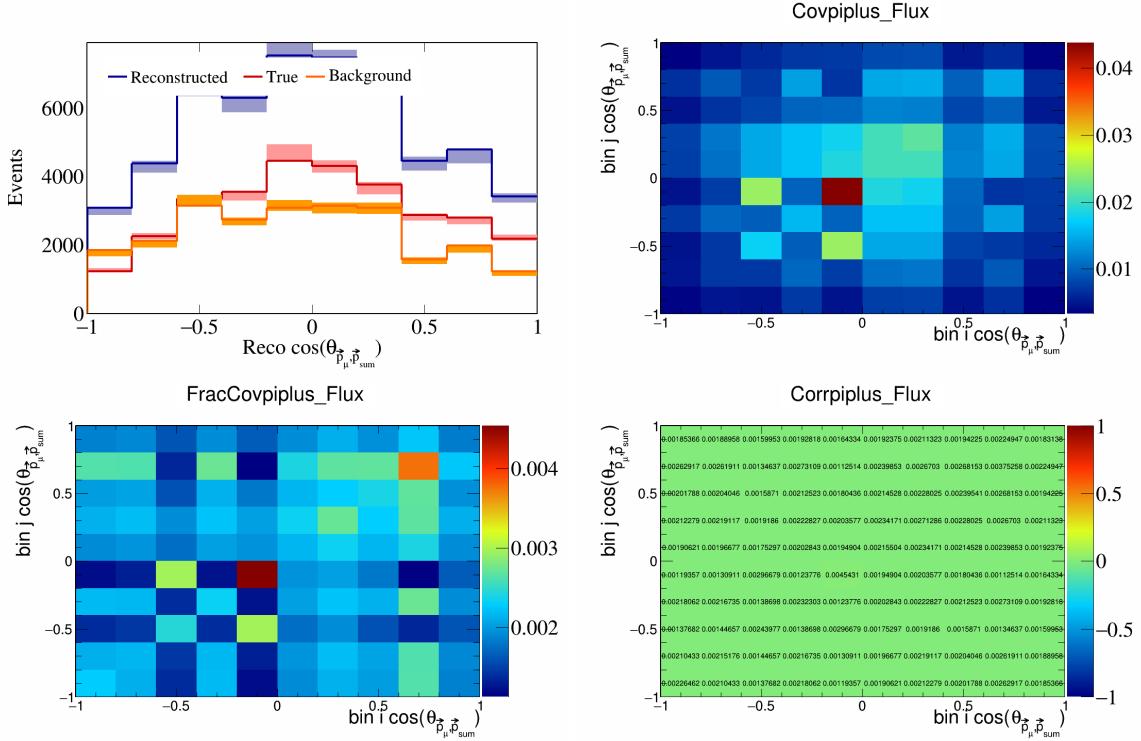


Figure 652: PiPlus variations for $\cos(\theta_{\vec{p}_\mu, \vec{p}_{\text{sum}}})$.

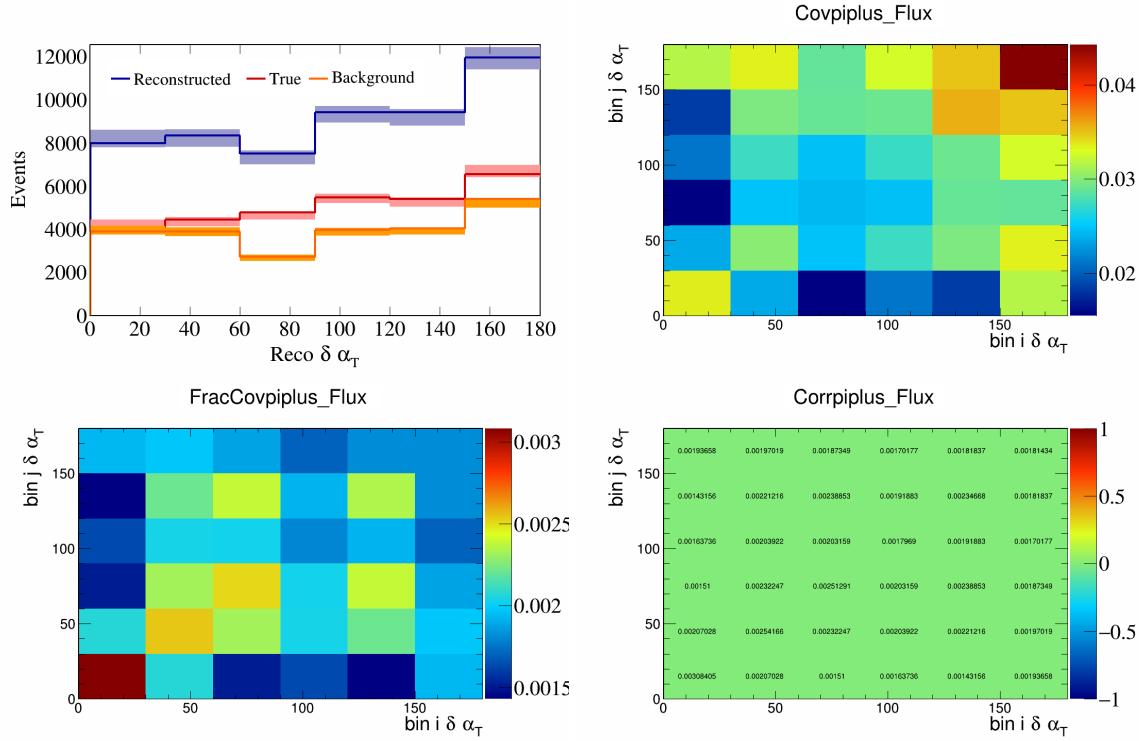


Figure 653: PiPlus variations for $\delta\alpha_T$.

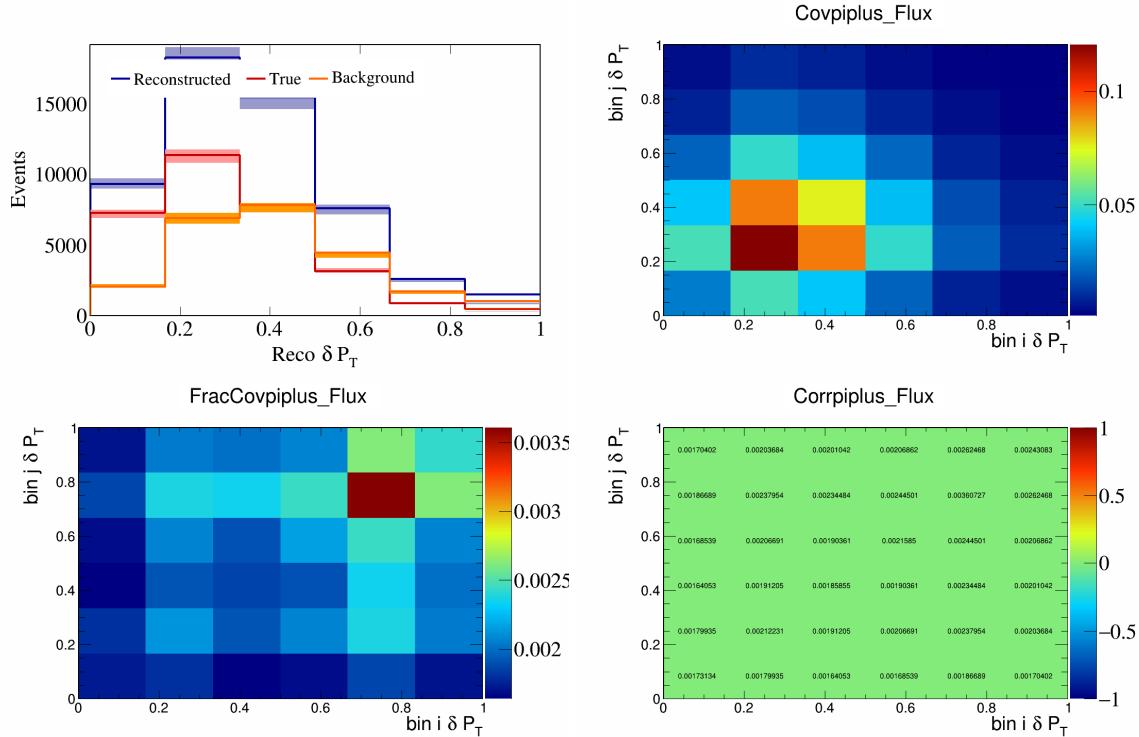


Figure 654: PiPlus variations for δP_T .

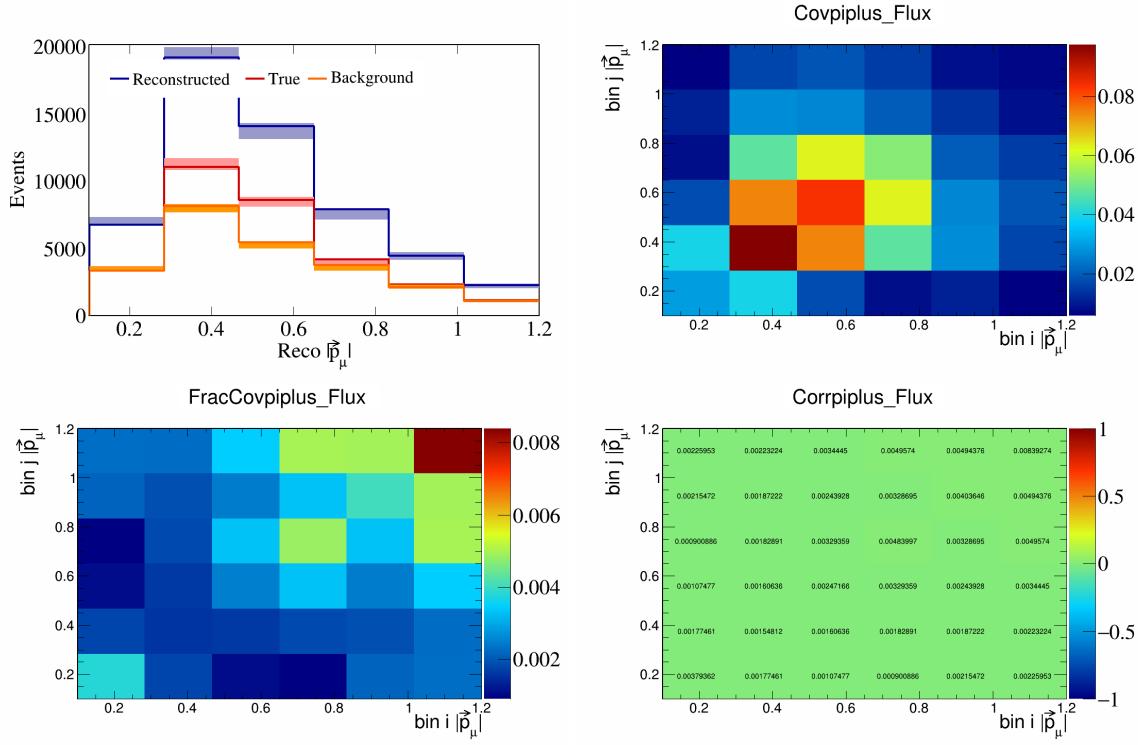


Figure 655: PiPlus variations for $|\vec{p}_\mu|$.

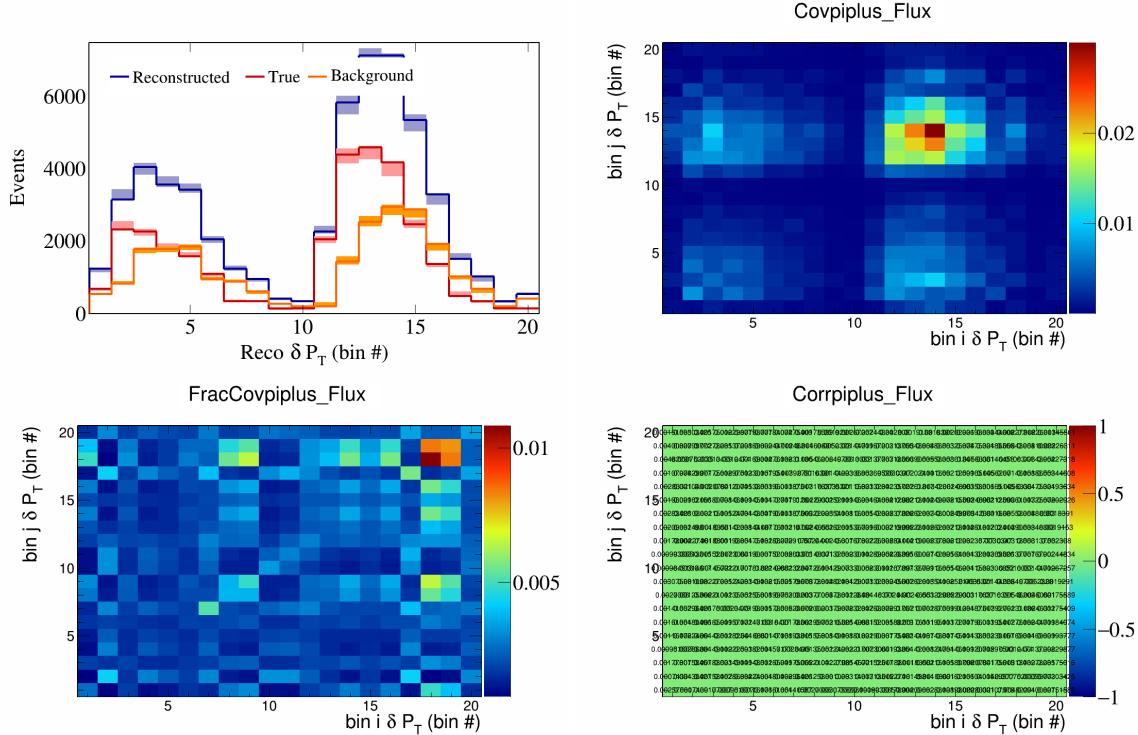


Figure 656: PiPlus variations for $\delta P_T \cos(\theta_{\vec{p}_\mu})$.

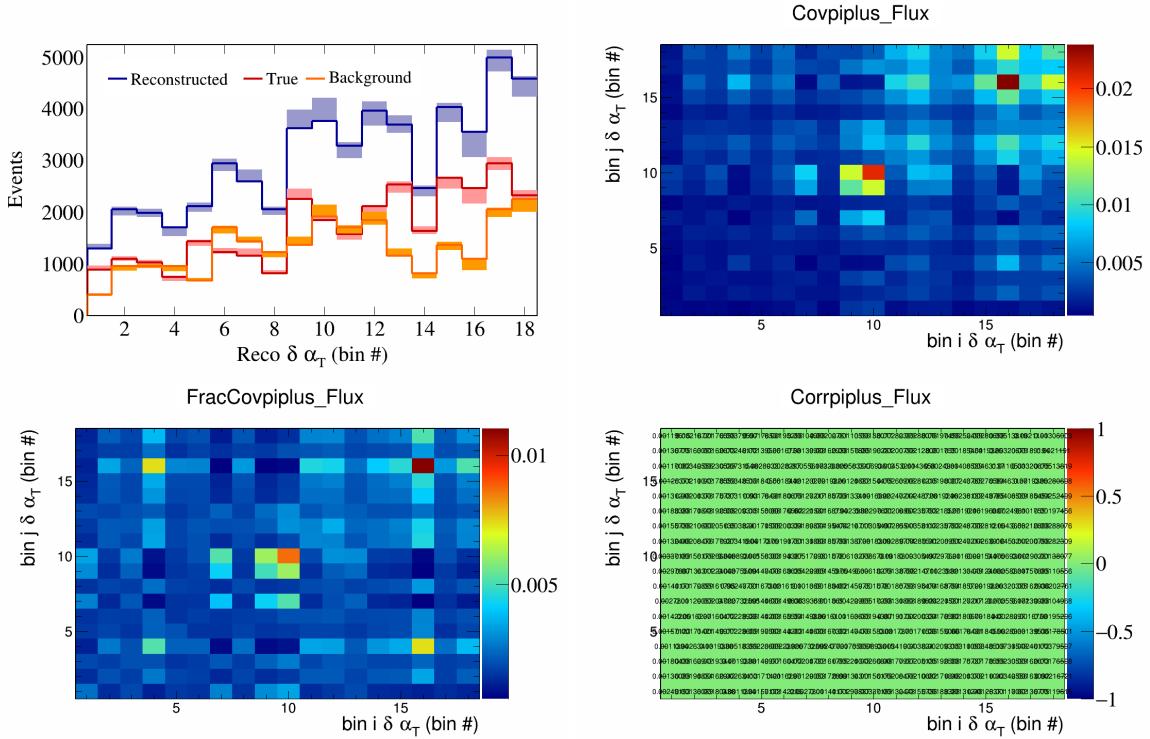


Figure 657: PiPlus variations for $\delta \alpha_T$ in $\cos(\theta_{\vec{p}_\mu})$.

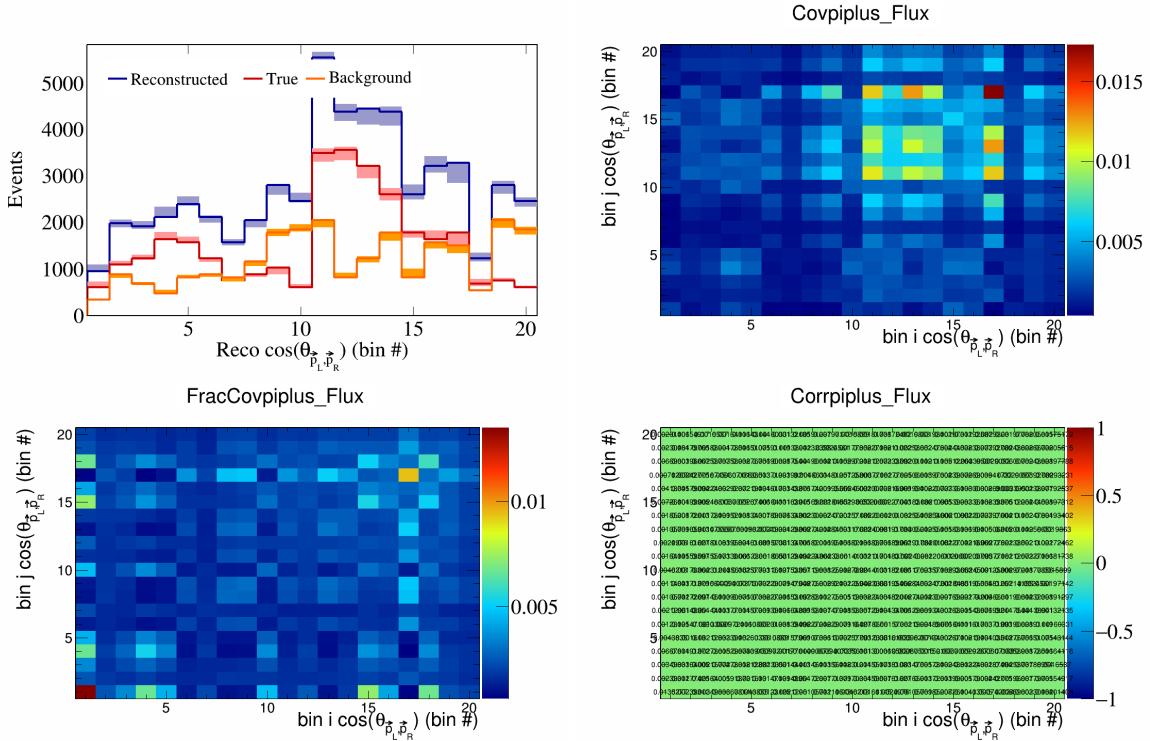


Figure 658: PiPlus variations for $\cos(\theta_{\vec{p}_L, \vec{p}_R})$ in $\cos(\theta_{\vec{p}_\mu})$.

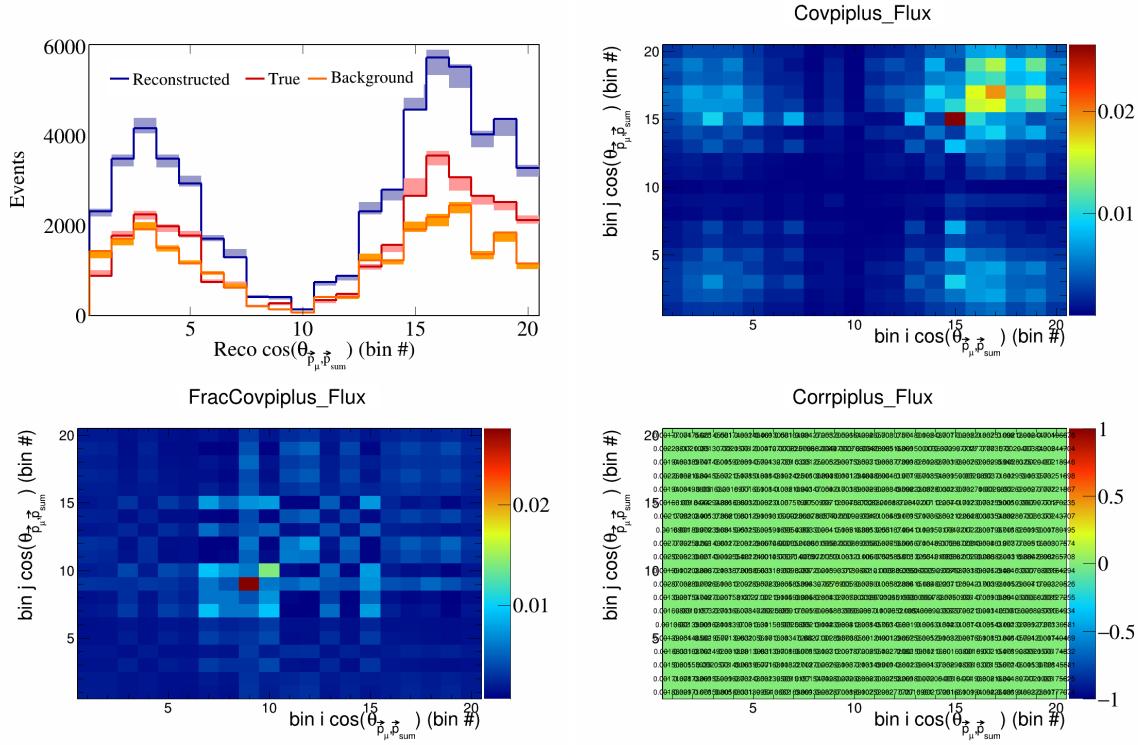


Figure 659: PiPlus variations for $\cos(\theta_{\vec{p}_\mu} \vec{p}_{\text{sum}})$ in $\cos(\theta_{\vec{p}_\mu})$.

215 **6 References**

- 216 [1] R. Acciarri, C. Adams, J. Asaadi, B. Baller, T. Bolton, C. Bromberg, F. Cavanna, E. Church, D. Edmunds, A. Ereditato, S. Farooq, B. Fleming, H. Greenlee, G. Horton-Smith, C. James, E. Klein, K. Lang, P. Laurens, R. Mehdiyev, B. Page, O. Palamara, K. Partyka, G. Rameika, B. Rebel, M. Soderberg, J. Spitz, A. M. Szelc, M. Weber, T. Yang, and G. P. Zeller. Detection of back-to-back proton pairs in charged-current neutrino interactions with the argoneut detector in the numi low energy beam line. *Phys. Rev. D*, 90:012008, Jul 2014.
- 217 [2] C. Andreopoulos, A. Bell, D. Bhattacharya, F. Cavanna, J. Dobson, S. Dytman, H. Gallagher, P. Guzowski, R. Hatcher, P. Kehayias, A. Meregaglia, D. Naples, G. Pearce, A. Rubbia, M. Whalley, and T. Yang. The genie neutrino monte carlo generator. *Nuclear Instruments and Methods in Physics Research Section A: Accelerators, Spectrometers, Detectors and Associated Equipment*, 614(1):87–104, 2010.
- 222 [3] Costas Andreopoulos, Christopher Barry, Steve Dytman, Hugh Gallagher, Tomasz Golan, Robert Hatcher, Gabriel Perdue, and Julia Yarba. The genie neutrino monte carlo generator: Physics and user manual, 2015.
- 227 [4] D. Ashery, I. Navon, G. Azuelos, H. K. Walter, H. J. Pfeiffer, and F. W. Schlepütz. True absorption and scattering of pions on nuclei. *Phys. Rev. C*, 23:2173–2185, May 1981.
- 232 [5] P. S. Auchincloss, R. Blair, C. Haber, E. Oltman, W. C. Leung, M. Ruiz, S. R. Mishra, P. Z. Quintas, F. J. Sciulli, M. H. Shaevitz, W. H. Smith, F. S. Merritt, M. Oreglia, P. Reutens, R. Coleman, H. E. Fisk, D. Levinthal, D. D. Yovanovitch, W. Marsh, P. A. Rapidis, H. B. White, A. Bodek, F. Borcherding, N. Giokaris, K. Lang, and I. E. Stockdale. Measurement of the inclusive charged-current cross section for neutrino and antineutrino scattering on isoscalar nucleons. *Zeitschrift für Physik C Particles and Fields*, 48(3):411–431, Sep 1990.
- 238 [6] Ch. Berger and L. M. Sehgal. Lepton mass effects in single pion production by neutrinos. *Phys. Rev. D*, 76:113004, Dec 2007.
- 240 [7] Ch. Berger and L. M. Sehgal. Partially conserved axial vector current and coherent pion production by low energy neutrinos. *Phys. Rev. D*, 79:053003, Mar 2009.
- 242 [8] B. Bourguille, J. Nieves, and F. Sánchez. Inclusive and exclusive neutrino-nucleus cross sections and the reconstruction of the interaction kinematics. *Journal of High Energy Physics*, 2021(4):4, Apr 2021.
- 244 [9] R.C. Carrasco and E. Oset. Interaction of real photons with nuclei from 100 to 500 mev. *Nuclear Physics A*, 536(3):445–508, 1992.
- 246 [10] R. Cruz-Torres, D. Lonardoni, R. Weiss, N. Barnea, D. W. Higinbotham, E. Piasetzky, A. Schmidt, L. B. Weinstein, R. B. Wiringa, and O. Hen. Many-body factorization and position-momentum equivalence of nuclear short-range correlations. *Nature Phys.*, 17(3):306–310, 2021.
- 249 [11] Jonathan Engel. Approximate treatment of lepton distortion in charged-current neutrino scattering from nuclei. *Phys. Rev. C*, 57:2004–2009, Apr 1998.
- 251 [12] T. Golan, J.T. Sobczyk, and J. Źmuda. Nuwro: the wrocław monte carlo generator of neutrino interactions. *Nuclear Physics B - Proceedings Supplements*, 229-232:499, 2012. Neutrino 2010.
- 253 [13] Krzysztof M. Graczyk and Jan T. Sobczyk. Form factors in the quark resonance model. *Phys. Rev. D*, 77:053001, Mar 2008.
- 255 [14] Yoshinari Hayato and Luke Pickering. The neut neutrino interaction simulation program library. *The European Physical Journal Special Topics*, 230(24):4469–4481, Dec 2021.
- 257 [15] Teppei Katori. Meson exchange current (MEC) models in neutrino interaction generators. *AIP Conference Proceedings*, 1663(1):030001, 05 2015.

- 259 [16] Konstantin S. Kuzmin, Vladimir V. Lyubushkin, and Vadim A. Naumov. Lepton polarization in neutrino–nucleon interactions. *Modern Physics Letters A*, 19(38):2815–2829, 2004.
- 260
- 261 [17] T. Leitner, L. Alvarez-Ruso, and U. Mosel. Charged current neutrino-nucleus interactions at intermediate energies. *Phys. Rev. C*, 73:065502, Jun 2006.
- 262
- 263 [18] C.H. Llewellyn Smith. Neutrino reactions at accelerator energies. *Physics Reports*, 3(5):261–379, 1972.
- 264 [19] Selection of numu charged current induced interactions with $N > 0$ protons and performance of events with $N = 2$ protons in the final state in the MicroBooNE detector from the BNB, Oct 2018.
- 265
- 266 [20] First Extraction of Single Differential Cross-Sections on Argon for CC1 μ 2p0 π Event Topologies in the MicroBooNE Detector. May 2022.
- 267
- 268 [21] Ulrich Mosel. Neutrino event generators: foundation, status and future. *Journal of Physics G: Nuclear and Particle Physics*, 46(11):113001, Sep 2019.
- 269
- 270 [22] J. Nieves, J. E. Amaro, and M. Valverde. Inclusive quasielastic charged-current neutrino-nucleus reactions. *Phys. Rev. C*, 70:055503, Nov 2004.
- 271
- 272 [23] J. Nieves, F. Sánchez, I. Ruiz Simo, and M. J. Vicente Vacas. Neutrino energy reconstruction and the shape of the charged current quasielastic-like total cross section. *Phys. Rev. D*, 85:113008, Jun 2012.
- 273
- 274 [24] J. Nieves, I. Ruiz Simo, and M. J. Vicente Vacas. Inclusive charged-current neutrino-nucleus reactions. *Phys. Rev. C*, 83:045501, Apr 2011.
- 275
- 276 [25] J. Schwehr, D. Cherdack, and R. Gran. Genie implementation of ific valencia model for qe-like 2p2h neutrino-nucleus cross section, 2017.
- 277
- 278 [26] Torbjörn Sjöstrand, Stephen Mrenna, and Peter Skands. Pythia 6.4 physics and manual. *Journal of High Energy Physics*, 2006(05):026, may 2006.
- 279
- 280 [27] W. Tang, X. Li, X. Qian, H. Wei, and C. Zhang. Data unfolding with wiener-svd method. *Journal of Instrumentation*, 12(10):P10002–P10002, October 2017.
- 281
- 282 [28] Júlia Tena-Vidal, Costas Andreopoulos, Adi Ashkenazi, Christopher Barry, Steve Dennis, Steve Dytman, Hugh Gallagher, Steven Gardiner, Walter Giele, Robert Hatcher, Or Hen, Libo Jiang, Igor D. Kakorin, Konstantin S. Kuzmin, Anselmo Meregaglia, Vadim A. Naumov, Afroditi Papadopoulou, Gabriel Perdue, Marco Roda, Vladyslav Syrotenko, and Jeremy Wolcott. Neutrino-nucleon cross-section model tuning in genie v3. *Phys. Rev. D*, 104:072009, Oct 2021.
- 283
- 284 [29] U. K. Yang and A. Bodek. Parton distributions, d/u , and higher twist effects at high x . *Phys. Rev. Lett.*, 82:2467–2470, Mar 1999.
- 285
- 286